

Volume 70
Number 4/5, 1998

International Journal of
QUANTUM
CHEMISTRY

Editor-in-Chief
PER-OLOV LÖWDIN

Editors

ERKKI BRÄNDÅS
YNGVE ÖHRN

Associate Editors

OSVALDO GOSCIŃSKI
STEN LUNELL
JOHN R. SABIN
MICHAEL C. ZERNER

Proceedings of the
International Symposium on
**Atomic, Molecular, and
Condensed Matter Theory**

Held at the Ponce de Leon Resort,
St. Augustine, Florida,
February 21–27, 1998

Editor-in-Chief: Per-Olov Löwdin
Special Editors: Yngve Öhrn
John R. Sabin
Michael C. Zerner



A Wiley-Interscience Publication
John Wiley & Sons, Inc.
Visit Wiley Journals Online
www.interscience.wiley.com

ISSN 0020-4598

Quantum Chemistry

Editor-in-Chief

Per-Olov Löwdin
University of Florida at Gainesville, USA
Uppsala University, Sweden

Editors

Erkki Brändas
Uppsala University, Sweden

Yngve Öhrn
University of Florida at Gainesville, USA

Associate Editors

Osvaldo Goscinski
Uppsala University, Sweden

Sten Lunell
Uppsala University, Sweden

John R. Sabin
University of Florida at Gainesville, USA

Michael C. Zerner
University of Florida at Gainesville, USA

Assistant Editor

Leif Eriksson
Uppsala University, Sweden

Honorary Editors

Gerhard Herzberg
National Research Council,
Ottawa, Ontario, Canada

Jerome Karle
Naval Research Laboratory at
Washington, DC, USA

Rudy Marcus
California Institute of Technology at
Pasadena, USA

Editorial Board

Jiri Čížek
University of Waterloo, Ontario, Canada

Enrico Clementi
Université Louis Pasteur, Strasbourg, France

Raymond Daudej
Académie Européene de Arts, des Sciences
et des Lettres, Paris, France

Ernest Davidson
Indiana University at Bloomington, USA

George G. Hall
University of Nottingham, UK

Laurens Jansen
Kusnacht, Switzerland

Norman H. March
University of Oxford, UK

Roy McWeeny
Università di Pisa, Italy

Saburo Nagakura
Graduate University for Advanced Studies,
Yokohama, Japan

Kimio Ohno
Hokkaido Information University, Japan

Josef Paldus
University of Waterloo, Ontario, Canada

Robert G. Parr
University of North Carolina at Chapel Hill, USA

Ruben Pauncz
Technion, Haifa, Israel

John A. Pople
Northwestern University at Evanston, Illinois, USA

Alberte Pullman
Institut de Biologie Physico-Chimique,
Paris, France

Paul von Ragué Schleyer
Universität Erlangen-Nürnberg,
Erlangen, Germany

Harrison Shull
Naval Postgraduate School,
Monterey, California, USA

Tang Au-Chin
Jilin University, Changchun, China

Rudolf Zahradník
Czech Academy of Sciences,
Prague, Czech Republic

Advisory Editorial Board

Teijo Åberg
Helsinki University of Technology, Espoo,
Finland

Axel D. Becke
Queen's University, Kingston, Ontario, Canada

Gian Luigi Bendazzi
Università di Bologna, Italy

Jerzy Cioslowski
The Florida State University at Tallahassee, USA

Timothy Clark
Universität Erlangen-Nürnberg, Germany

Mireille Defranccheschi
DPEL/SERGD/LMVT,
Fontenay Aux Roses, France

Karl F. Freed
The University of Chicago, Illinois, USA

Odd Groen
University of Tromsø, Norway

Trygve Helgaker
University of Oslo, Norway

Ming-Bao Huang
Academia Sinica,
Beijing, People's Republic of China

Hiroshi Kashiwagi
Kyushu Institute of Technology, Fukuoka, Japan

Eugene S. Kryachko
Academy of Sciences of Ukraine, Kiev, Ukraine

Sven Larsson
Chalmers University of Technology,
Gothenburg, Sweden

Lucas Lathouwers
Universitair Centrum (RUCA), Antwerp, Belgium

Shyi-Long Lee
National Chung Chang University,
Taiwan, Republic of China

Josef Michl
University of Colorado at Boulder, USA

Nimrod Moiseyev
Israel Institute of Technology, Israel

John D. Morgan III
University of Delaware at Newark, USA

Cleanthes A. Nicolaides
National Hellenic Research Foundation, Greece

J. Vincent Ortiz
Kansas State University at Manhattan, USA

Lars Pettersson
University of Stockholm, Sweden

Leon Phillips
University of Canterbury,
Christchurch, New Zealand

Martin Quack
ETH Zürich, Switzerland

Leo Radom
Australian National University, Australia

William Reinhardt
University of Washington at Seattle, USA

Sten Rettrup
H. C. Ørsted Institut, Copenhagen, Denmark

C. Magnus L. Rittby
Texas Christian University at Fort Worth, USA

Michael Robb
King's College, London, UK

Mary Beth Ruskai
University of Massachusetts at Lowell, USA

Harold Scheraga
Cornell University at Ithaca, New York, USA

Vipin Srivastava
University of Hyderabad, India

Nicolai F. Stepanov
Moscow State University, Russia

Jiazong Sun
Jilin University, Changchun,
People's Republic of China

Donald G. Truhlar
University of Minnesota at Minneapolis, USA

Peter Wolynes
University of Illinois at Urbana, USA

Robert E. Wyatt
The University of Texas at Austin, USA

REPORT DOCUMENTATION PAGE

*Form Approved
OMB No. 0704-0188*

Public reporting burden for this collection of information is estimated to average 1 hour per response, including the time for reviewing instructions, searching existing data sources, gathering and maintaining the data needed, and completing and reviewing the collection of information. Send comments regarding this burden estimate or any other aspect of this collection of information, including suggestions for reducing this burden, to Washington Headquarters Services, Directorate for Information Operations and Reports, 1215 Jefferson Davis Highway, Suite 1204, Arlington, VA 22202-4302, and to the Office of Management and Budget, Paperwork Reduction Project (0704-0188), Washington, DC 20503.

1. AGENCY USE ONLY (<i>Leave blank</i>)	2. REPORT DATE	3. REPORT TYPE AND DATES COVERED	
	3/23/99	FINAL 10/1/97 - 9/30/98	
4. TITLE AND SUBTITLE PARTIAL SUPPORT OF 1998 SANIBEL SYMPOSIUM			5. FUNDING NUMBERS G N00014-98-1-0215
6. AUTHOR(S) YNGVE ÖHRN			
7. PERFORMING ORGANIZATION NAMES(S) AND ADDRESS(ES) UNIVERSITY OF FLORIDA QUANTUM THEORY PROJECT PO BOX 118435 GAINESVILLE, FL 32611-8435			8. PERFORMING ORGANIZATION REPORT NUMBER 1
9. SPONSORING / MONITORING AGENCY NAMES(S) AND ADDRESS(ES) OFFICE OF NAVAL RESEARCH CHEMISTRY DIVISION CODE 313 800 NORTH QUINCY STREET ARLINGTON, VA22217-5000			10. SPONSORING / MONITORING AGENCY REPORT NUMBER TECHNICAL REPORT 1
11. SUPPLEMENTARY NOTES			
a. DISTRIBUTION / AVAILABILITY STATEMENT APPROVED FOR PUBLIC RELEASE AND SALE		12. DISTRIBUTION CODE UNLIMITED	
13. ABSTRACT (<i>Maximum 200 words</i>) PROCEEDINGS OF THE 1998 SANIBEL SYMPOSIUM			
14. SUBJECT TERMS			15. NUMBER OF PAGES
			16. PRICE CODE
17. SECURITY CLASSIFICATION OF REPORT UNCLASSIFIED	18. SECURITY CLASSIFICATION OF THIS PAGE UNCLASSIFIED	19. SECURITY CLASSIFICATION OF ABSTRACT UNCLASSIFIED	20. LIMITATION OF ABSTRACT UL

International Journal of QUANTUM CHEMISTRY

Quantum Chemistry Symposium No. 32

*Proceedings of the
International Symposium on
Atomic, Molecular, and Condensed Matter Theory*

Held at Ponce de Leon Resort, St. Augustine, Florida,
February 21–27, 1998

Editor-in-Chief: Per-Olov Löwdin

Special Editors: Yngve Öhrn, John R. Sabin, and
Michael C. Zerner

an Interscience® Publication
published by JOHN WILEY & SONS

DTIC QUALITY INSPECTED 4

19990329039

DISTRIBUTION STATEMENT A

Approved for Public Release
Distribution Unlimited

The *International Journal of Quantum Chemistry* (ISSN 0020-7608) is published semi-monthly with one extra issue in January, March, May, July, August, and November by John Wiley & Sons, Inc., 605 Third Avenue, New York, New York 10158.

Copyright © 1998 John Wiley & Sons, Inc. All rights reserved. No part of this publication may be reproduced in any form or by any means, except as permitted under section 107 or 108 of the 1976 United States Copyright Act, without either the prior written permission of the publisher, or authorization through the Copyright Clearance Center, 222 Rosewood Drive, Danvers, MA 01923, (508) 750-8400, fax (508) 750-4470. Periodicals postage paid at New York, NY, and at additional mailing offices.

The code and the copyright notice appearing at the bottom of the first page of an article in this journal indicate the copyright owner's consent that copies of the article may be made for personal or internal use, or for the personal or internal use of specific clients, on the condition that the copier pay for copying beyond that permitted by Sections 107 or 108 of the US Copyright Law.

This consent does not extend to the other kinds of copying, such as copying for general distribution, for advertising or promotional purposes, for creating new collective work, or for resale. Such permission requests and other permission inquiries should be addressed to the Permissions Dept.

Subscription price (Volumes 66–70, 1998): \$4,439.00 in the US, \$4,739.00 in Canada and Mexico, \$4,964.00 outside North America. All subscriptions outside US will be sent by air. Personal rate (available only if there is an institutional subscription): \$195.00 in North America, \$375.00 outside North America. Subscriptions at the personal rate are available only to individuals. Payment must be made in US dollars drawn on a US bank. Claims for undelivered copies will be accepted only after the following issue has been received. Please enclose a copy of the mailing label. Missing copies will be supplied when losses have been sustained in transit and where reserve stock permits.

Please allow four weeks for processing a change of address. For subscription inquiries, please call (212) 850-6645; e-mail: SUBINFO@Wiley.com.

Postmaster: Send address changes to *International Journal of Quantum Chemistry*, Caroline Rothaug, Director, Subscription Fulfillment and Distribution, Subscription Department, John Wiley & Sons, Inc., 605 Third Avenue, New York, NY 10158.

Advertising Sales: Inquiries concerning advertising should be forwarded to Advertising Sales Manager, Advertising Sales, John Wiley & Sons, Inc., 605 Third Avenue, New York, NY 10158; (212) 850-8832. Advertising Sales, European Contacts: Bob Kern or Nicky Douglas, John Wiley & Sons, Ltd., Baffins Lane, Chichester, West Sussex PO19 1UD, England. Tel.: 44 1243 770 350/367; Fax: 44 1243 770 432; e-mail: adsales@wiley.co.uk.

Reprints: Reprint sales and Inquiries should be directed to the customer service department, John Wiley & Sons, Inc. 605 Third Ave., New York, NY 10158. Tel: 212-850-8776.

Manuscripts should be submitted in triplicate and accompanied by an executed Copyright Transfer Form to the Editorial Office, *International Journal of Quantum Chemistry*, Quantum Chemistry Group, Uppsala University, Box 518, S-75120, Uppsala, Sweden. Authors may also submit manuscripts to the Editorial Office, *International Journal of Quantum Chemistry*, Quantum Theory Project, 2301 NP Building #92, P.O. Box 118435, Museum Road and North South Drive, University of Florida, Gainesville, Florida 32611-8435. **Information for Contributors** appears in the first and last issue of each volume.

All other correspondence should be addressed to the *International Journal of Quantum Chemistry*, Publisher, Interscience Division, Professional, Reference, and Trade Group, John Wiley & Sons, Inc., 605 Third Avenue, New York, New York 10158, U.S.A. The contents of this journal are indexed or abstracted in *Chemical Abstracts*, *Chemical Titles*, *Chemical Database*, *Current Contents/Physical, Chemical, and Earth Sciences*, *Research Alert (ISI)*, *Science Citation Index (ISI)*, and *SCISEARCH Database (ISI)*.

Contents

Introduction

- N. Y. Öhrn, J. R. Sabin, and M. C. Zerner* **529**

- List of Participants **531**

3,5-Contracted Schrödinger Equation: Determining Quantum Energies
and Reduced Density Matrices Without Wave Functions

- D. A. Mazziotti* **557**

Nonconventional Partitioning of the Many-Body Hamiltonian for
Studying Correlation Effects

- P. R. Surján, M. Kállay, and Á. Szabados* **571**

Unambiguous Exchange–Correlation Energy Density for
Hooke's Atom

- K. Burke, F. G. Cruz, and K.-C. Lam* **583**

SCF Calculations with Density-Dependent Local-Exchange Potential

- V. Karasiev, E. V. Ludeña, and R. López-Boada* **591**

Investigation of an Asymmetric Triple-Excitation Correction for
Coupled-Cluster Energies

- T. D. Crawford and J. F. Stanton* **601**

Excitation Energies in Brillouin–Wigner-Based Multireference
Perturbation Theory

- W. Wenzel* **613**

More About the Leaky Aquifer Function

- F. E. Harris* **623**

(continued)

Visit Wiley Journals Online

 **InterScience®**

www.interscience.wiley.com

Use of a Fast Fourier Transform (FFT) 3D Time-Dependent Schrödinger Equation Solver in Molecular Electronic Structure <i>B. Ritchie and C. A. Weatherford</i>	627
Modern Valence Bond Descriptions of Molecular Excited States: An Application of CASVB <i>T. Thorsteinsson and D. L. Cooper</i>	637
Approximate Brueckner Orbitals and Shakeup Operators in Electron Propagator Calculations: Applications to F ⁻ and OH ⁻ <i>J. V. Ortiz</i>	651
Density Functional Theory Without the Born–Oppenheimer Approximation and Its Application <i>Y. Shigeta, H. Takahashi, S. Yamanaka, M. Mitani, H. Nagao, and K. Yamaguchi</i>	659
Analytical Asymptotic Structure of the Pauli, Coulomb, and Correlation–Kinetic Components of the Kohn–Sham Theory Exchange–Correlation Potential in Atoms <i>Z. Qian and V. Sahni</i>	671
Excited States in Density Functional Theory <i>Á. Nagy</i>	681
A Density Functional Study of Small Nickel Clusters <i>M. C. Michelini, R. Pis Diez, and A. H. Jubert</i>	693
Stable and Efficient Numerical Method for Solving the Schrödinger Equation To Determine the Response of Tunneling Electrons to a Laser Pulse <i>M. J. Hagmann</i>	703
Excited Electronic States of Carotenoids: Time-Dependent Density-Matrix-Response Algorithm <i>S. Tretiak, V. Chernyak, and S. Mukamel</i>	711
Balanced Complete Active Space Choices with the Multiconfigurational Spin Tensor Electron Propagator Method: The Vertical Ionization Potentials of NH ₂ <i>A. J. McKellar, D. Heryadi, and D. L. Yeager</i>	729

(continued)

Effect of Heavy Atom on the Second Hyperpolarizability of
Tetrahydrofuran Homologs Investigated by Ab Initio Molecular
Orbital Method

- K. Kamada, M. Ueda, H. Nagao, K. Tawa, T. Sugino,
Y. Shimizu, and K. Ohta* **737**

Structure Dependence of the Low-Lying Excited States and the
First Dipole Hyperpolarizability of Phenol Blue

- A. Serrano and S. Canuto* **745**

Nonresonant Frequency Dispersion of the Electronic Second
Hyperpolarizability of *All-Trans* Polysilane Chains: An Ab Initio
TDHF Oligomeric Approach

- B. Champagne, É. A. Perpète, and J.-M. André* **751**

Computation of the Electromagnetic Harmonics Generation by
Stratified Systems Containing Nonlinear Layers

- A. Calderone and J.-P. Vigneron* **763**

Theory and Calculations of Electric Field Effects on
Hyperfine Interactions

- S. P. Karna* **771**

Differential Equations for Ground-State Electron Density and Slater
Sum in Atoms and Molecules With and Without External Fields

- N. H. March* **779**

Ground States of Atoms and Molecules in Strong Magnetic Fields

- P. Schmelcher* **789**

Some Aspects of Data Processing for an Optical Absorption
Experiment in a Pulsed 1000-Tesla Magnet

- L. G. Butler, A. W. Maverick, C. H. Gallegos, J. D. Goettee,
B. R. Marshall, C. M. Fowler, D. G. Rickel, J. M. Gonzales, and
L. J. Tabaka* **797**

Optimal Decoupling of Positive- and Negative-Energy Orbitals in
Relativistic Electronic Structure Calculations Beyond Hartree–Fock

- C. F. Bunge, R. Jáuregui, and E. Ley-Koo* **805**

Second-Order Multiconfigurational Dirac–Fock Calculations on
Boronlike Ions

- M. J. Vilcas, Y. Ishikawa, and K. Koc* **813**

(continued)

Relativistic Effects on the Structural Phase Stability of Molybdenum <i>J. C. Boettger</i>	825
Water Cluster Approach To Study Hydrogen-Bonded Pattern in Liquid Water: Ab Initio Orientational Defects in Water Hexamers and Octamers <i>E. S. Kryachko</i>	831
Intramolecular Proton Transfer in Monohydrated Tautomers of Cytosine: An Ab Initio Post-Hartree–Fock Study <i>L. Gorb and J. Leszczynski</i>	855
Intramolecular Hydrogen Bonding in Resonance-Stabilized Systems <i>L. A. Schmiedekamp-Schneeweis, and J. O. Payne</i>	863
Quantum Chemical Study of the Interaction of Nitrate Anion with Water <i>C. Ebner, R. Sansone, and M. Probst</i>	877
The Interface of Electronic Structure and Dynamics for Reactions in Solution <i>Y.-Y. Chuang, C. J. Cramer, and D. G. Truhlar</i>	887
The Development of Semiclassical Dynamical Methods and Their Application to Vibrational Relaxation in Condensed-Phase Systems <i>M. F. Herman</i>	897
Single-Electron-Capture Cross Sections by Alpha-Particles from Ground State $K(4s)$ and $Rb(5s)$: A Molecular-State Approach <i>A. Kumar, B. C. Saha, and C. A. Weatherford</i>	909
Bethe–Bloch Stopping-Power Parameters for GaAs and ZnSe <i>L. E. Porter</i>	919
Searches on the Potential Energy Hypersurfaces of $GeCH_2$, $GeSiH_2$, and Ge_2H_2 <i>A. J. Boone, D. H. Magers, and J. Leszczyński</i>	925
Excited-State Potential Energy Curves from Time-Dependent Density-Functional Theory: A Cross Section of Formaldehyde's 1A_1 Manifold <i>M. E. Casida, K. C. Casida, and D. R. Salahub</i>	933

(continued)

Effective Potential for e-Neon and e-Argon Scattering by DCS Minimization at Intermediate Energies <i>J. M. Paikeday and A. Longstreet</i>	943
Ab Initio SCF-MO Study of the Topology of the Charge Distribution of Acid Sites of Zeolites <i>H. Soscún, J. Hernández, O. Castellano, G. Díaz, and A. Hinchliffe</i>	951
Singlet-Triplet Splitting and the Activation of C—H Bond for (η^5 -C ₅ H ₅)M(CO) Isoelectronic Fragments: A Theoretical Study <i>M.-D. Su and S.-Y. Chu</i>	961
Structural and Electronic Properties of Silicon Nitride Materials <i>F. De Brito Mota, J. F. Justo, and A. Fazzio</i>	973
Analysis of Three-Dimensional Molecular Shape Using Surface Area and Molecular Volume Scaling Descriptors <i>G. A. Arteca</i>	981
Approximations of the Mulliken Charges for the Oxygen and Silicon Atoms of Zeolite Frameworks Calculated with a Periodic Hartree-Fock Scheme <i>A. V. Larin and D. P. Vercauteren</i>	993
Structure and Properties of NH ₅ ²⁺ : A Dication with Two 2-Electron 3-Center Bonds <i>J. E. Del Bene, J. D. Watts, and R. J. Bartlett</i>	1003
C ₆₀ Carbyne Knots (from 0 ₁ to 6 ₃): Theoretical NMR Spectra <i>J. Cz. Dobrowolski and A. P. Mazurek</i>	1009
Perturbed Ellipsoidal Wave Functions for Quantum Scattering <i>T. Levitina and E. J. Brändas</i>	1017
Photochemical Reaction Pathways of Ethylene <i>L. Freund and M. Klessinger</i>	1023
Theoretical Studies on Hydrogen Activation by Iridium Dimers <i>S. Castillo, V. Bertin, E. Solano-Reyes, H. Luna-García, A. Cruz, and E. Poulain</i>	1029

(continued)

Electron Propagator Theory of Conformational Effects on Anisole and Thioanisole Photoelectron Spectra <i>O. Dolgounitcheva, V. G. Zakrzewski, J. V. Ortiz, and G. V. Ratovski</i>	1037
Advantages of the Fourier Space RHF Band Structure Approach: Application to Polyoxymethylene Using a Distributed Basis Set of s-Type Gaussian Functions <i>I. Flamant, J. G. Fripiat, and J. Delhalle</i>	1045
Periodic INDO Calculations of Organic Adsorbates on a TiO_2 Surface <i>P. Persson, A. Stashans, R. Bergström, and S. Lunell</i>	1055
Sign of the Interaction Parameter in Disordered Fe–Al Alloys <i>S. Dorfman, D. Fuks, and V. Liubich</i>	1067
Possibility of Charge-Mediated Superconductors in the Intermediate Region of Metal–Insulator Transitions <i>H. Nagao, M. Mitani, M. Nishino, Y. Shigeta, Y. Yoshioka, and K. Yamaguchi</i>	1075
Embedded Cluster and Supercell Study of the Structurre of the Interstitial Cu–C Solid Solutions <i>D. E. Ellis, S. Dorfman, D. Fuks, R. Evenhaim, and K. Mundim</i>	1085
Atomic Motion at Germanium Surfaces: Scanning Tunneling Microscopy and Monte Carlo Simulations <i>J.-P. Vigneron, A. Benaissa, I. Derycke, A. Wiame, and R. Sporken</i>	1093

Introduction

The 38th Annual Sanibel Symposium, organized by the faculty, students, and staff of the Quantum Theory Project of the University of Florida, was held on February 21–27, 1998. Again, the Ponce de Leon Conference Center in St. Augustine, Florida, was the site of the gathering of more than 300 scientists.

The symposium followed the established format with plenary and poster sessions. A compact 7-day integrated program of quantum biology, quantum chemistry, and condensed matter physics provided for intense and lively cross-disciplinary interactions. The topics of the sessions covered by these proceedings included Density Functional Theory (DFT) and Applications, Time-Dependent DFT, Femtosecond Dynamics, Dynamics of Electronically Excited States, Molecular Properties, Proton Transfer Dynamics, Methodological Developments in Quantum Chemistry, Relativistic Quantum Mechanics, Condensed Phase Chemistry, Hydrogen Bonding, and Molecular Properties in High Magnetic Fields.

The articles have been subjected to the ordinary refereeing procedures of the *International Journal of Quantum Chemistry*. The articles presented in the sessions on quantum biology and associated poster sessions are published in a separate volume of the *International Journal of Quantum Chemistry*.

The organizers acknowledge the following sponsors for their support of the 1998 Sanibel Symposium:

- Army Research Office Grant # DAAG55-98-1-0117
"The views, opinions, and/or findings con-

tained in this report are those of the author(s) and should not be construed as an official Department of the Army position, policy, or decision, unless so designated by other documentation."

- The Office of Naval Research through Grant # N00014-98-1-0215
"This work relates to Department of the Navy Grant # N00014-98-1-0215 issued by the Office of Naval Research. The United States Government has the royalty-free license throughout the world in all copyrightable material contained herein."
- IBM Corporation
- HyperCube, Inc.
- Q-Chem, Inc.
- The University of Florida

Very special thanks go to the staff of the Quantum Theory Project of the University of Florida for handling the numerous administrative, clerical, and practical details. The organizers are proud to recognize the contributions of Mrs. Judy Parker, Mrs. Coralu Clements, Ms. Sandra Weakland, Dr. Greg Pearl, and Mr. Cristián Cárdenas. All the graduate students of the Quantum Theory Project who served as "gofers" are gratefully recognized for their contributions to the 1998 Sanibel Symposium.

N. Y. Öhrn
J. R. Sabin
M. C. Zerner

List of Participants

Albert, Katrin
University of Florida
Quantum Theory Project
P.O. Box 118435
Gainesville, FL 32611-8435
USA
Phone: 352-392-1597
Fax: 352-392-8722
albert@qtp.ufl.edu

Arteca, Gustavo A.
Laurentian University
Departments of Chemistry and Biochemistry
Ramsey Lake Road
Sudbury, Ontario P3E 2C6
Canada
Phone: 705-675-1151
Fax: 705-675-4844
gustavo@nickel.laurentian.ca

Baeck, Kyoung-Koo
Kang-Nung University
Department of Chemistry
Ji-Byun-Dong, 123
Kang-Won-Do 210-702
South Korea
Phone: 82-391-640-2307
Fax: 82-391-647-1183
baeck@chem.kangnung.ac.kr

Bartlett, Rodney J.
University of Florida
Quantum Theory Project
P.O. Box 118435
Gainesville, FL 32611-8435
USA
Phone: 352-392-1597
Fax: 352-392-8722
bartlett@qtp.ufl.edu

Bernhardsson, Anders
Lund University
Theoretical Chemistry
Box 124
Lund 221 00
Sweden
Phone: 46-46-2220384
Fax: 46-46-2224543
anders.bernhardsson@teokem.lu.se

Beveridge, David
Wesleyan University
Department of Chemistry
Hall-Atwater Laboratories
Middletown, CT 06457
USA
Phone: 860-685-2575
Fax: 860-685-2211
dbeveridge@wesleyan.edu

Bicca de Alencastro, Ricardo
Universidade Federal de Rio de Janeiro
Inst. de Quimica
Bloco A-CT Sala 622, Cidade Univ.
Rio de Janeiro RJ 21949-900
Brazil
Phone: 55-021-590-3544
Fax: 55-021-2904746
bicca@iq.ufrj.br

Billing, Gert D.
University of Copenhagen
H.C. Ørsted Institute
Department of Chemistry
Copenhagen
Denmark
Phone: 453-532-0252
Fax: 453-532-0259
gdb@moldyn.ki.ku.dk

LIST OF PARTICIPANTS

Bishop, David M.
University of Ottawa
Department of Chemistry
10 Marie Curie
Ottawa, Ontario K1M 0Z3
Canada
Phone: 613-562-5181
Fax: 613-562-5170
dbishop@science.uottawa.ca

Bouferguene, Ahmed
Florida A & M University
Department of Physics
205 Jones Hall
Tallahassee, FL 32307
USA
Phone: 850-599-3470
Fax: 850-599-3577
boufer@cennas.nhmfl.gov

Boettger, Jonathan C.
Los Alamos National Laboratory
Group T-1
MS B221
Los Alamos, NM 87545
USA
Phone: 505-667-7483
Fax: 505-665-5757
jn@lanl.gov

Brändas, Erkki J.
Uppsala University
Department of Quantum Chemistry
P.O. Box 518
Uppsala S-75120
Sweden
Phone: 46-18-4713263
Fax: 46-18-502402
erkki@kvac.uu.se

Bögel, Horst
University of Halle
Inst Phys. Chem. (Merseburg)
Geusaerstr.
Halle D-06099
Germany
Phone: 49-3461-46-2127
Fax: 49-3461-46-2381
boegel@chemie.uni-halle.de

Broo, Anders
Chalmers University of Technology
Physical Chemistry
Kernivagen 3
Göteborg 41296
Sweden
Phone: 46-31-772-3051
Fax: 46-31-772-3858
broo@phc.chalmers.se

Boone, Amy
University of Florida
Department of Chemistry
P.O. Box 117200
Gainesville, FL 32611-7200
USA
Phone: 352-392-0541
Fax: 352-392-0872
boone@chem.ufl.edu

Brown, Richard E.
Michigan Technological University
Chemistry Department
Houghton, MI 49931
USA
Phone: 906-487-2383
Fax: 906-487-2061
rebrown@MTU.edu

Boudreaux, Edward A.
University of New Orleans
Department of Chemistry
Lake Front
New Orleans, LA 70148
USA
Phone: 504-286-6311
Fax: 504-286-6860

Bunge, Carlos F.
Universidade Nacional Autonoma de Mexico
Institute of Physics
AP 20-364
Mexico City DF 01000
Mexico
Phone: 525-622-5014
Fax: 525-622-5015
bunge@fenix.ifisicacu.unam.mx

LIST OF PARTICIPANTS

Burke, Kieron
Rutgers University
Department of Chemistry
1019 West High St.
Kadoon Heights, NJ 08035
USA
Phone: 609-225-6156
Fax: 609-225-6506
kieron@crab.rutgers.edu

Butler, Leslie G.
Louisiana State University
Department of Chemistry
1126 Beakenham Dr.
Baton Rouge, LA 70808
USA
Phone: 504-769-9751
Fax: 504-388-3458
les.butler@chemgate.chem.lsu.edu

Calderone, Anna
Facultes Universitaires Notre Dame de la Paix
Physics Department
rue de Bruxelles
Namur 5000
Belgium
Phone: 32-81-724705
Fax: 32-81-724707
anna.calderone@scf.fundp.ac.be

Canuto, Sylvio
Universidade de São Paulo
Instituto de Fisica
CPX 66318
São Paulo 05389-970
Brazil
Phone: 55-11-818-6983
Fax: 55-11-818-6831
canuto@if.usp.br

Cao, Jianshu
University of California, San Diego
Department of Chemistry
9500 Gilman Dr. 0339
La Jolla, CA 92093
USA
Phone: 619-534-0290
Fax: 619-534-7654
jcao@ucsd.edu

Càrdenas-Lailhacar, Cristiàñ
University of Florida
Quantum Theory Project
P.O. Box 118435
Gainesville, FL 32611-8440
USA
Phone: 352-392-6713
Fax: 352-392-8722
cardenas@qtp.ufl.edu.

Casida, Mark
Universite de Montreal
Department of Chemistry
C.P. 6128, Succ Centre-ville
Montreal, Quebec H3C 3J7
Canada
Phone: 514-343-6111 x-3901
Fax: 514-343-2458
casida@chimie.umontreal.ca

Castillo, Sidonio
Universidad Autonoma Metropolitana-Azcapotzalco
Ciencias Basicas
Av San Pablo #180
Mexico DF 02200
Mexico
Phone: 52-5-724-4218
Fax: 52-5-723-5940
sca@hp9000a1.uam.mx

Castro, Eduardo A.
Universidad Nacional de La Plata
Facultad de Ciencias Exactas
Calles 47 y 115, C.C. 962
La Plata 1900
Argentina
Phone: 54-1-21-214037
Fax: 54-1-21-259485
castro@nahuel.biol.unlp.edu.ar

Challacombe, Matt
Los Alamos National Laboratory
Group T-12
MS B268
Los Alamos, NM 87545
USA
Phone: 505-665-5905
Fax: 505-665-3909
mchalla@lanl.gov

LIST OF PARTICIPANTS

Champagne, Benoît

FUNDP
CTA Lab
Rue de Bruxelles 61
Namur B-5000
Belgium
Phone: 32-81-724557
Fax: 32-81-724530
benoit.champagne@fundp.ac.be

Chatfield, David

Florida International University
Department of Chemistry
Miami, FL 33199
USA
Phone: 305-348-3977
Fax: 305-348-3772
chatfiel@fiu.edu

Cheng, Hai-Ping

University of Florida
Quantum Theory Project
P.O. Box 118435
Gainesville, FL 32611-8435
USA
Phone: 352-392-1597
Fax: 352-392-8722
cheng@qtp.ufl.edu

Chou, Mei-Yin

Georgia Institute of Technology
Department of Physics
Atlanta, GA 30332
USA
Phone: 404-894-4688
Fax: 404-894-9958
meiyin.chou@physics.gatech.edu

Chu, San-Yan

National Tsing Hua University, Taiwan
Department of Chemistry
Hsinchu, Taiwan 30043
Republic of China
Phone: 866-35-721634
Fax: 866-35-711082
sychu@chem.nthu.edu.tw

Chun, Paul

University of Florida
Department of Biochemistry & Molecular Biology
Box 100245
Gainesville, FL 32610-0245
USA
Phone: 352-392-3356
Fax: 352-392-2953
pwchun@pine.circa.ufl.edu

Clark, Tim

University Erlangen-Nurnberg
CCC
Naegelshachstr. 25
Erlangen D-91052
Germany
Phone: 49-9131-852948
Fax: 49-9131-856565
clark@organik.uni-erlangen.de

Coffin, James

IBM, Computational Chemistry
Computational Chemistry
8632 Forest Glenn
Irving, TX 75063
USA
Phone: 972-432-9701
Fax: 800-706-6351 Pager
jmcoffi@us.ibm.com

Colgate, Sam

University of Florida
Department of Chemistry
P.O. Box 117200
Gainesville, FL 32611-7200
USA
Phone: 352-392-5876
Fax: 352-392-0872
colgate@physical4.chem.ufl.edu

Cooper, David L.

University of Liverpool
Department of Chemistry
P.O. Box 147
Liverpool L69 7ZD
UK
Phone: 44-151-794-3532
Fax: 44-151-794-3588
dlc@liv.ac.uk

Cory, Marshall

University of Florida
Quantum Theory Project
P.O. Box 118435
Gainesville, FL 32611-8435
USA
Phone: 352-392-1597
Fax: 352-392-8722
cory@qtp.ufl.edu

LIST OF PARTICIPANTS

Coutinho, Kaline

Universidade de Mogi das Cruzes
Cx.P. 411
Mogi das Cruzes SP 08701-970
Brazil
kaline@onsager.if.usp.br

Coutinho-Neto, Mauricio

University of Florida
Quantum Theory Project
P.O. Box 118435
Gainesville, FL 32611-8435
USA
Phone: 352-392-7184
Fax: 352-392-8722
coutinho@qtp.ufl.edu

Crawford, T. Daniel

University of Georgia
Department of Chemistry
Center for Computational Quantum Chemistry
Athens, GA 30602
USA
Phone: 706-542-7738
Fax: 706-542-0406
crawdad@otanes.ccqc.uga.edu

Cuan, Angeles

Instituto Mexicano del Petroleo
Gerencia de Catalizadores
Eje Central Lazaro Cardenas 152
Gustavo A. Madero DF 07730
Mexico
Phone: 52-5-567-2927
Fax: 52-5-567-2927
angeles@briseida.ind.imp.mx

Da Costa, Herbert

University of Florida
Quantum Theory Project
P.O. Box 118435
Gainesville, FL 32611-8435
USA
Phone: 352-392-3010
Fax: 352-392-8722
dacosta@qtp.ufl.edu

Dalskov, Erik K.

University of Lund
Theoretical Chemistry—Chemical Center
P.O. Box 124
Lund S-221 00
Sweden
Phone: 46-46-222-4915
Fax: 46-46-222-4543
teoekd@garm.teokem.lu.se

Das, Guru P.

Wright Laboratory
MLBP
654, Area B
Wright Patterson AFB, OH 45433
USA
Phone: 937-429-2307
Fax: 937-255-9147
dasgp@picard.ml.wpafb.af.mil

Davidson, Ernest

Indiana University
Department of Chemistry
Bloomington, IN 47405
USA
Phone: 812-855-6013
Fax: 812-855-8300
davidson@indiana.edu

De Kee, Dan

University of Florida
Quantum Theory Project
P.O. Box 118435
Gainesville, FL 32611-8435
USA
Phone: 352-392-9306
Fax: 352-392-8722
dekee@qtp.ufl.edu

Del Bene, Janet E.

Youngstown State University
Department of Chemistry
One University Plaza
Youngstown, OH 44555
USA
Phone: 330-742-3466
Fax: 330-742-1579
fro42008@ysub.ysu.edu

LIST OF PARTICIPANTS

Deleuze, Michael S.D.

Limburgs Universitqire Centrum
SBG
Gebow D
Diepenbeek B-3590
Belgium
Phone: 32-11-26-83-03
Fax: 32-11-26-83-01
deleuze@luc.ac.be

Enevoldsen, Thomas

Odense University
Department of Chemistry
Campusvej 55
Odense M DK-5230
Denmark
Phone: 45-6557-2568
tec@dou.dk

Deumens, Erik

University of Florida
Quantum Theory Project
P.O. Box 118435
Gainesville, FL 32611-8435
USA
Phone: 352-392-1597
Fax: 352-392-8722
deumens@qtp.ufl.edu

Estiu, Guillermina L.

Universidad Nacional de La Plata
Dept. Quimica
Calle 47 Y 115 CC962
La Plata, Buenos Aires 1900
Argentina
Phone: 54-21-210784 EX 41
Fax: 54-21-259485
estiu@nahuel.biol.unlp.edu.ar

Dobrowolski, Jan Cz.

Drug Institute
Lab. Theor. Meth. and Calc.
30/34 Chelmska Street
Warsaw 00-725
Poland
Phone: 48-22-412940
Fax: 48-22-410652
janek@urania.il.waw.pl

Fazzio, Adelberto

University of San Paulo
Materials Science
CP 66318
Sao Paulo SP 05315-570
Brazil
Phone: 55-11-818-6983
Fax: 55-11-818-6831
fazzio@if.usp.br

Dombroski, Jeremy P.

Q-Chem, Inc.
Four Triangle Drive, Suite 160
Export, PA 15632-9255
USA
Phone: 412-325-9969
Fax: 412-325-2062
jack@q-chem.com

Feller, David F.

Battelle PNNL
K1-96
Richland, WA 99352
USA
Phone: 509-375-2617
Fax: 509-375-6631
d3el02@emsl.pnl.gov

Ehara, Masahiro

Kyoto University
Synthetic Chemistry and Biological Chemistry
Sakyo-ku
Kyoto 606-01
Japan
Phone: 81-75-753-5660
Fax: 81-75-753-5910
ehara@sbchem.kyoto-u.ac.jp

Ferris, Kim F.

National Laboratory Pacific Northwest
Environmental & Energy Science
P.O. Box 999, MS-K2-44
Richland, WA 99352
USA
Phone: 509-375-3754
Fax: 509-375-2186
kim@darter.pnl.gov

LIST OF PARTICIPANTS

Fischer, Sighart

Technische Universität München
Theoretische Physik T 38
James-Franck-Str. 12
Garching B München 85747
Germany
Phone: 49-089-289-12393
Fax: 49-089-289-12444
fischer@venus.t30.physik.tu-muenchen.de

Flamant, Isabelle

Universitaires Notre-Dame de la Paix
Lab de Chimie Theorique Appliquee FUNDP
Rue de Bruxelles 61
Namur 5000
Belgium
Phone: 32-81-724530
Fax: 32-81-724530
isabelle.flamant@fundp.ac.be

Flock, Michaela

University of Leuven
Department of Chemistry
Celestynenlaan 200F
Heverlee-Leuven B-3000
Belgium
Phone: 32-16-327-984
Fax: 32-16-32-7992
michaela@hartree.quantchem.kuleuven.ac.be

Folland, Nathan O.

Kansas State University
Physics Department
Cardwell Hall
Manhattan, KS 66506-2601
USA
Phone: 785-532-1615
Fax: 785-841-3038
nof@ksu.edu

Fuks, David

Ben-Gurion University of the Negev
Materials Eng. Department
P.O. Box 653
Beer-Sheva 84105
Israel
Phone: 972-7-6461460
Fax: 972-7-6472946
fuks@bgumail.bgu.ac.il

Gill, Peter

University of Cambridge
Department of Chemistry
Cambridge CB2 1EW
UK
Phone: 44-1223-336-344
Fax: 44-1223-336-362
pmg@euler.ch.cam.ac.uk

Giribet, Claudia G.

University of Buenos Aires
Physics
Ciudad Universitaria-Pab. 1
Buenos Aires 1428
Argentina
Phone: 54-1-788-9101
Fax: 54-1-782-7647
giribet@df.uba.ar

Goldman, Barbara M.

John Wiley & Sons, Inc.
605 Third Avenue
New York, NY 10158-0012
Phone: 212-850-6007
Fax: 212-850-6264
bgoldman@wiley.com

Goodman, Lionel

Rutgers, The State University of New Jersey
Department of Chemistry
P.O. Box 939
Piscataway, NJ 08854
USA
Phone: 908-445-2603
Fax: 908-445-5312
goodman@rutchem.rutgers.edu

Gubanov, Vladimir

San Jose State University
Physics Department
One Washington Square
San Jose, CA 95192-0106
USA
Phone: 408/924-5249
Fax: 408/924-4815
vgubanov@msn.com

Hagmann, Mark J.

Florida International University
Department of Electrical &
Computer Engineering
Miami, FL 33199
USA
Phone: 305-348-3017
Fax: 305-348-3707
hagmann@eng.fiu.edu

LIST OF PARTICIPANTS

Hall, Michael B.

Texas A & M University
Chemistry Department
Mailstop 3255
College Station, TX 77843-3255
USA
Phone: 409-845-1843
Fax: 409-845-4719
hall@chemux.tamu.edu

Handy, Nicholas C.

University of Cambridge
Department of Chemistry
Lensfield Road
Cambridge CB2 1EW
UK
Phone: 44-1223-336373
Fax: 44-1223-336362
nch1@cam.ac.uk

Harris, Frank E.

University of Utah
Department of Chemistry
Salt Lake City, UT 84112
USA
Phone: 801-581-8445
Fax: 801-581-8433
harris@dirac.chem.utah.edu

Havel, Timothy F.

Harvard Medical School
Department of BCMP
240 Longwood Avenue
Boston, MA 02115
USA
Phone: 617-432-3242
Fax: 617-738-0516
havel@menelaus.med.harvard.edu

Hedström, Magnus

University of Florida
Quantum Theory Project
P.O. Box 118435
Gainesville, FL 32611-8435
USA
Phone: 352-392-6973
Fax: 352-392-8722
hedstrom@qtp.ufl.edu

Herman, Michael

Tulane University
Chemistry Department
New Orleans, LA 70118
USA
Phone: 504-862-3582
Fax: 504-865-5596

Hess, Bernd A.

Inst fuer Physikalische and Theoretische Chemie
Theoretical Chemistry
Wegelerstrasse 12
Bonn 53115
Germany
Phone: 49-228-732920
Fax: 49-228-739064
hess@uni-bonn.de

Hill, Susan E.

Pacific Northwest National Lab
EMSL
MS D1-96
Richland, WA 99352
USA
Phone: 509-375-6370
Fax: 509-375-6631
sehill@boys.pnl.gov

Hillebrand, Claudia

University of Florida
Quantum Theory Project
P.O. Box 118435
Gainesville, FL 32611
USA
Phone: 352/392-1597
Fax: 352/392-8722
hildebrand@qtp.ufl.edu

Hirata, So

The Graduate University for Advanced Studies
and School of Mathematical & Physical Science
Myodaiji
Okazaki Aichi 444
Japan
Phone: 81-564-55-7261
Fax: 81-564-53-4660
soh@ims.ac.jp

Hobza, Pavel

J. Heyrovsky Institute of Physical Chemistry
Dolejskova 3
Prague 8 18223
Czech Republic
Phone: 420 2 66052056
Fax: 420 2 8582307
hobza@indy.jh-inst.cas.cz

LIST OF PARTICIPANTS

Hogreve, H. J.

CNRS
Centre de Physique Theorique
Luminy, Case 907
Marseille Cedex 9 F-13288
France
Phone:
Fax: 33-491-269553
hogreve@cpt.univ-mrs.fr

Hu, Zhenming

Kyoto University, Graduate School of Engineering
Dept. of Synth. Chemistry and Biological
Chemistry
Kyoto-606-01
Sakyo-Ku, Kyoto 606-01
Japan
Phone: 81-75-753-5659
Fax: 81-75-753-5910
hu@quantl.synchem.kyoto-u.ac.jp

Ishikawa, Yasuyuki

University of Puerto Rico
Chemistry Department
P.O. Box 23346
San Juan, Puerto Rico 00931-3346
Phone: 787-764-0000 EST 7399
Fax: 787-751-0625
ishikawa@rrpac.upr.clu.edu

Itskowitz, Peter

University of North Carolina
Department of Physics and Astronomy
CB #3255
Chapel Hill, NC 27599
USA
Phone: 919-962-0165
Fax: 919-962-0480
itskowitz@physics.unc.edu

Ivanov, Stanislav

University of Florida
Quantum Theory Project
P.O. Box 118435
Gainesville, FL 32611-8435
USA
Phone: 352-392-6973
Fax: 352-392-8722
ivanov@qtp.ufl.edu

Jamorski, Christine

University of Florida
Quantum Theory Project
P.O. Box 118435
Gainesville, FL 32611-8435
USA
Phone: 352-392-6711
Fax: 352-392-8722
jamorski@qtp.ufl.edu

Jauregui-Renaud, Rocio

Universidad Nacional Autonoma de Mexico
Instituto de Fisica
Apdo Postal 20-364
Mexico DF 01000
Mexico
Phone: 525-622-5014
Fax: 525-622-5015
rocio@fenix.ifisicacu.unam.mx

Johnson, Walter R.

Notre Dame University
Department of Physics
334 Nieuwland Science Bldg.
Notre Dame, IN 46556
USA
Phone: 219-631-6651
Fax: 219-631-5952
WRJ@atomic3.phys.ND.edu

Jubert, Alicia H.

Universidad Nacional de La Plata
Facultad de Ciencias Exactas
CC 962
La Plata, Buenos Aires 1900
Argentina
Phone: 54-1-214037
Fax: 54-1-259485
jubert@nahuel.biol.unlp.edu.ar

Karashev, Valentin

Instituto Venezolano de Investigaciones Cientificas
Centro de Quimica
Apto. 21827
Caracas 1020-A
Venezuela
Phone: 58-2-504-13-57
Fax: 58-2-504-13-50
vkarasev@maria.ivic.ve

LIST OF PARTICIPANTS

Karle, Jerome

Naval Research Laboratory
Laboratory for the Structure of Matter
Code 6030 Naval Research Laboratory
Washington, DC 20375-5341
USA
Phone: 202-767-2665
Fax: 202-767-0953
williams@herker.nrl.navy.mil

Karna, Shashi

U.S. Air Force Phillips Laboratory, VTM
Space Mission Technologies Div
3550 Aberdeen Ave SE
Kirtland AFB, NM 87117-5776
USA
Phone: 505-853-3158
Fax: 505-846-2290
karnas@plk.af.mil

Kaschner, Roland

Forschungszentrum Jülich
IFF
Jülich D-52425
Germany
Phone: 49-2461-612859
Fax: 49-2461-612850
r.kaschnerafz-juelich.de

Kasha, Michael

Florida State University
Institute of Molecular Biophysics
452 Molecular Biophysics
Tallahassee, FL 32306
USA
Phone: 850-644-6452
Fax: 850-561-1406
kasha@sb.fsu.edu

Kedziora, Gary S.

Northwestern University
Chemistry
2145 Sheridan Avenue
Evanston, IL 60208-3113
USA
Phone: 847-467-4857
Fax: 847-491-7713
kedziora@chem.nwu.edu

Keshari, Vijaya

University of Puerto Rico
Department of Chemistry
Avenida R Barcelo
Cayey, Puerto Rico 00736
USA
Phone: 787-738-0702
Fax: 787-738-6962
shlok@mailexcite.com

King, James W.

Foundation for Chemistry
P.O. Box 116
Balsam, NC 28707-0116
USA
Phone: 704-452-7570
Fax: 704-452-5432
jwking@sprynet.com

King, Rollin A.

University of Georgia
Center for Computational Quantum Chemistry
Chemistry Building
Athens, GA 30602
USA
Phone: 706-542-7738
Fax: 706-542-0406
rking@tigranes.ccqc

King-Smith, Dominic

Molecular Simulations, Inc.
9685 Scranton Road
San Diego, CA 92121-3752
USA
Phone: 619-458-9990
dko@msi.com

Kirchner, Eric

Harvard-Smithsonian Center for Astrophysics
60 Garden Street
Cambridge, MA 02138
USA
Phone: 617/495-7237

Kirtman, Bernard

University of California, Santa Barbara
Department of Chemistry
Santa Barbara, CA 93106
USA
Phone: 805-893-2217
Fax: 805-893-4120
kirtman@chem.ucsb.edu

LIST OF PARTICIPANTS

Klessinger, Martin
Universität Münster
Organisch-Chemisches Institut
Corrensstr. 40
Muenster D-48149
Germany
Phone: 49-251-8333-241
Fax: 49-251-8339-772
klessim@uni-muenster.de

Korkin, Anatoli
Motorola, Inc.
SPS
2200 W. Broadway, MD M350
Mesa, AR 85202
USA
Phone: 602-655-3171
Fax: 602-655-2285
korkin@act.sps.mot.com

Krause, Jeffrey L.
University of Florida
Quantum Theory Project
P.O. Box 118435
Gainesville, FL 32611-8435
USA
Phone: 352/392-1597
Fax: 352/392-8722
krause@qtp.edu

Krauss, Morris
National Institute of Science Technology
Center for Advanced Research Biotechnology
9600 Gudelsky Drive
Rockville, MD 20850
USA
Phone: 301-738-6242
Fax: 301-738-6255
krauss@ibm9.carb.nist.gov

Kryachko, Eugene
The John Hopkins University
Department of Chemistry
3400 N. Charles Street
Baltimore, MD 21218
USA
Phone: 410-546-7462
Fax: 410-546-8420
eugene@jhunix.hcf.jhu.edu

Krylov, Anna
University of California, Berkeley
Department of Chemistry
308
Berkeley, CA 94720
USA
Phone: 510-643-2935
Fax: 510-643-1255
anna@elba.cchem.berkeley.edu

Kubli-Garfias, Carlos
National Autonomous University of Mexico
Lab of Hormonal Chemistry
Apartado Postal 70-469
Mexico City 04511
Mexico
Phone: 525-6-223815
Fax: 525-5-500048
kubli@servidor.unam.mx

Kumar, Anil
Florida A & M University
Department of Physics
Tallahassee, FL 32307
USA
Phone: 850-599-3470
Fax: 850-599-3577

Ladik, Janos
Universität Erlangen-Nürnberg
Inst. of Theoretical Chemistry
Egerlandstrasse 3
Erlangen D-97058
Germany
Phone: 49-9131-857766
Fax: 49-9131-857736
ladik@pctc.chemie.uni-erlangen.de

Laidig, William D.
Procter & Gamble Co.
Miami Valley Laboratories
P.O. Box 538707
Cincinnati, OH 45253-8707
USA
Phone: 513-627-2857
Fax: 513-627-1233
laidig@pg.com

Lanig, Harald
Computer-Chemie-Centrum
Naegelsbachstrasse 25
Erlangen D-91052
Germany
Phone: 49-9131-852948
Fax: 49-9131-856565
clark@organik.uni-erlangen.de

LIST OF PARTICIPANTS

Lazzeretti, Paolo
University of Modena
Dipartimento di Chimica
Via Campi 183
Modena 41100
Italy
Phone: 39-59-378450
Fax: 39-59-373543
lazzeret@c220.unimo.it

Levy, Ronald
Rutgers University
Department of Chemistry
P.O. Box 939
Piscataway, NJ 08855-0939
USA
Phone: 732-445-3947
Fax: 732-445-5958
ronlevy@lutece.rutgers.edu

Lee, Michael S.
University of California, Berkeley
Department of Chemistry
Head-Gordon Group, 31 Lewis
Berkeley, CA 94720
USA
Phone: 510-848-5296
Fax:
lee@bastille.cchem.berkeley.edu

Light, John C.
University of Chicago
Department of Chemistry
5735 S. Ellis Avenue
Chicago, IL 60637
USA
Phone: 773-702-7197
Fax: 773-702-8314
light@pclight.uchicago.edu

Leininger, Matt L.
University of Georgia
Center for Computational Chemistry
Chemistry Building
Athens, GA 30602
USA
Phone: 706-542-7738
Fax: 706-542-0406
mleinin@harpagos.ccqc.uga.edu

Loew, Gilda
Molecular Research Institute
845 Page Mill Road
Palo Alto, CA 94304
USA
Phone: 650-424-9924
Fax: 650-424-9501
loew@montara.molres.org

Lengsfield, Byron H.
IBM Almaden Research Center
650 Harry Road
San Jose, CA 95120
USA
Phone: 408-927-2032
Fax:
bbyron@almaden.ibm.com

Lohr, Lawrence
University of Michigan
Department of Chemistry
Ann Arbor, MI 48109-1055
USA
Phone: 313-764-3148
Fax: 313-647-4865
llohr@emich.edu

Leszczynski, Jerzy
Jackson State University
Department of Chemistry
17910
Jackson, MS 39217
USA
Phone: 601-973-3482
Fax: 601-973-3674
jerzy@tiger.jsums.edu

Lopez-Boada, Roberto
Florida State University
Department of Chemistry
Tallahassee, FL 32306-3006
USA
Phone: 850-644-3810
Fax: 850-644-8281
rboada@dirac.fsu.edu

LIST OF PARTICIPANTS

Lotrich, Victor F.
University of Delaware
Department of Physics
Sharp Lab
Newark, DE 19716
USA
Phone: 302-831-3512
Fax: 302-831-1637
lotrich@udel.edu

Löwdin, Per-Olov
University of Florida
Quantum Theory Project
P.O. Box 118435
Gainesville, FL 32611-8435
USA
Phone: 352-392-1597
Fax: 352-392-8722
lowdin@kvac.uu.se

Luna-Garcia, Hector
Universidad Autonoma Metropolitana-
Azcapotzalco
Ciencias Basicas
Av San Pablo 180
Mexico City DF 02200
Mexico
Phone: 915-724-4218
lghm@hp9000al.uam.mx

Magers, David H.
Mississippi College
Department of Chemistry
Box 4065
Clinton, MS 39058
USA
Phone: 617-495-4767
magers@mc.edu

Makri, Nancy
University of Illinois
Department of Chemistry
505 South Mathews Avenue
Urbana, IL 61801
USA
Phone: 217-333-6589
Fax: 217-244-0789
nancy@makri.scs.uiuc.edu

March, Norman
Oxford University
6 Northcroft Road
Egham, Surrey TW20 ODU
UK

Martens, Craig C.
University of California, Irvine
Department of Chemistry
Irvine, CA 92697-2025
USA
Phone: 714-824-8768
Fax: 714-824-8571
cmartens@uci.edu

Martin, Charles H.
University of Florida
Quantum Theory Project
P.O. Box 118435
Gainesville, FL 32611-8435
USA
Phone: 352-392-6711
Fax: 352-392-8722
martin@qtp.ufl.edu

Massa, Lou
City University of New York
Chemistry
695 Park Avenue
New York, NY 10021
USA
Phone: 212-772-5330
Fax: 212-772-5332
massa@mva.gr.hunter.cuny.edu

Mayer, Istvan
Chemical Research Center Hungarian Academy
Institute for Chemistry
P.O. Box 17
Budapest H-1525
Hungary
Phone: 361-325-7900 ext. 295
Fax: 36-1-325-7554/325-7750
mayer@cric.chemres.hu

LIST OF PARTICIPANTS

Mazziotti, David A.
Harvard University
Department of Chemistry
12 Oxford St.
Cambridge, MA 02138
USA
Phone: 617-547-1974
Fax: 617-495-1792
damazz@fas.harvard.edu

Monkhorst, Hendrik J.
University of Florida
Quantum Theory Project
P.O. Box 118435
Gainesville, FL 32611-8435
USA
Phone: 352-392-1597
Fax: 352-392-8722
monkhors@qtp.ufl.edu

McGlynn, Sean P.
Louisiana State University
Department of Chemistry
329 Choppin
Baton Rouge, LA 70803
USA
Phone: 504-769-0021
Fax: 504-388-3458
sean.mcglynn@chemgate.chem.lsu.edu

Mora-Delgado, Marco Antonio
Universidad Autonoma Metropolitana-Iztapalapa
Dpto de Quimica
Av Michoacan y La Purisima, Col Vicentina
Iztapalapa DFCP 09340
Mexico
Phone: 52-5-724-4675
Fax: 52-5-724-4666
mam@xanum.uam.mx

Micha, David A.
University of Florida
Quantum Theory Project
P.O. Box 118435
Gainesville, FL 32611-8435
USA
Phone: 352-392-1597
Fax: 352/392-8722
micha@qtp.ufl.edu

Morales, Jorge A.
University of Florida
Quantum Theory Project
P.O. Box 118435
Gainesville, FL 32611-8435
USA
Phone: 352-392-7184
Fax: 352-392-8722
morales@qtp.ufl.edu

Miller, William H.
University of California, Berkeley
Department of Chemistry
Berkeley, CA 94707
USA
Phone: 510-642-0653
Fax: 510-642-6262
miller@neon.cchem.berkeley.edu

Morgan III, John D.
University of Delaware
Department of Physics
Newark, DE 19716
USA
Phone: 302-831-2661
Fax: 302-831-1637
32399@udel.edu

Mogensen, Benny
University of Florida
Quantum Theory Project
P.O. Box 118435
Gainesville, FL 32611-8435
USA
Phone: 352/392-8113
Fax: 352/392-8722
benny@qtp.ufl.edu

Morita, Akihiro
Kyoto University
Department of Chemistry
Kitashirakawa, Sakyo-Ku
Kyoto 606
Japan
Phone: 81-75-753-4005
Fax: 81-75-753-4000
morita@kuchem.kyoto-u.ac.jp

LIST OF PARTICIPANTS

Mosley, David H.
University of Namur
Lab. de CTA
Rue de Bruxelles 61
Namur B-5000
Belgium
Phone: 32-81-72-4554
Fax: 32-81-72-4567
david.mosley@fundp.ac.be

Motta, Carlos Augusto M.
Facultes Universitaires de Namur
Department of Organic Chemistry
Centro De Tec, Bloco A, Sala 609A, Cidade Uni.
68563
Rio De Janeiro 21947-900
Brazil
Phone: 55-021-590-3544
Fax: 55-021-290-4746
guto@pc140.iq.ufrj.br

Mukamel, Shaul
University of Rochester
Department of Chemistry
Hutchison Hall, 500 Wilson Blvd.
P.O. RC Box 270216
Rochester, NY 14627-0216
USA
Phone: 716/275-3080
Fax: 716-473-6889
mukamel@chem.rochester.edu

Nagao, Hidemi
Institute of Molecular Science
Myodaiji
Okasaki, Aichi 444
Japan
Phone: 81-6-850-5405
Fax: 81-6-850-5550
nagao@chem.sci.osaka-u.ac.jp

Nagel, Bengt
Royal Institute of Technology
Theoretical Physics
Stockholm S-100 44
Sweden
Phone: 46-8-790168
Fax: 46-8-10 48 79
nagel@theophys.kth.se

Nagy, Ágnes
Kossuth Lajos University
Institute of Theoretical Physics
P.O. Box 5
Debrecen H-4010
Hungary
Phone: 36-52-417266
Fax: 36-52-431722-1291
nalev@tigris.klte.hu

Nakano, Haruyuki
University of Tokyo
Department of Applied Chemistry
7-3-1 Hongo, Bunkyo-ku
Tokyo 113
Japan
Phone: 81-3-5802-3757
Fax: 81-3-5802-3757
nakano@qcl.t.u-tokyo.ac.jp

Nakayama, Akira
University of Tokyo
Department of Chem. System Eng.
7-3-1 Hongo
Bunkyo-ku, Tokyo 113
Japan
Phone: 81-3-3812-2111 x7286
Fax: 81-3-3818-5643
nakayama@tcl.t.u-tokyo.ac.jp

Nicholas, John B.
PNNL
EMSL
1502 SE Oxford
Richland, WA 99352
USA
Phone: 509-375-6559
Fax: 509-375-6631
jb-nicholas@pnl.gov

Nicholson, Donald M.
Oak Ridge National Laboratory
Building 4500-S
Oak Ridge, TN 37831-6114
USA
Phone: 423-574-5873
Fax: 423-574-7659
nicholsondm@ornl.gov

LIST OF PARTICIPANTS

Nooijen, Marcel
Princeton University
Department of Chemistry
Frick Lab #123B
Princeton, NJ 08540
USA
Phone: 609-258-3168
Fax: 609-258-6746
nooijen@princeton.edu

Öhrn, Yngve
University of Florida
Quantum Theory Project
P.O. Box 118435
Gainesville, FL 32611-8435
USA
Phone: 352-392-1597
Fax: 352-392-8722
ohrn@qtp.ufl.edu

Ohta, Koji
Osaka National Research Institute, AIST, MITI
Department of Optical Materials
1-8-31 Midorigaoka
Ikeda, Osaka 563-8577
Japan
Phone: 81-627-51-9523
Fax: 81-627-51-9628
ohta@onri.go.jp

Olsen, Jeppe
University of Lund
Theoretical Chemistry Dept.
P.O. Box 124
Lund 22100
Sweden
Phone: 46-46-222-8240
Fax: 46-46-222-4543
teojeo@garm.teokem.lu.se

Ortiz, Vincent
Kansas State University
Department of Chemistry
Manhattan, KS 66506
USA
Phone: 913-532-6665
Fax: 913-532-6666
ortiz@ksu.edu

Ostlund, Neil S.
Hypercube, Inc.
2135 NW 15th Ave
Gainesville, FL 32605
USA
Phone: 352-378-9776
Fax: 352-392-8722
ostlund@hyper.com

Ozment Payne, Judy
Penn State University
Division of Science and Engineering
1600 Woodland Road
Abington, PA 19001
USA
Phone: 215-881-7471
Fax: 215-881-7623
o96@psu.edu

Paikeday, Joseph M.
Southeast Missouri State University
Department of Physics
One University Plaza MS 6600
Cape Girardeau, MO 63701-4799
USA
Phone: 573-651-2393
Fax: 573-651-2223
c314scp@semovm.semo.edu

Pandey, Ravindra
Michigan Technological University
Physics Department
1400 Townsend Drive
Houghton, MI 49931
USA
Phone: 906-487-2831
Fax: 906-487-2933
pandey@mtu.edu

Pearl, Greg Martin
University of Florida
Quantum Theory Project
P.O. Box 118435
Gainesville, FL 32611-8435
USA
Phone: 352-392-6713
Fax: 352-392-8722
pearl@qtp.ufl.edu

LIST OF PARTICIPANTS

Perera, Ajith
University of Florida
Quantum Theory Project
P.O. Box 118435
Gainesville, FL 32611-8435
USA
Phone: 352-392-6973
Fax: 352-392-8722
perera@qtp.ufl.edu

Politzer, Peter
University of New Orleans
Chemistry Department
Lakefront Campus
New Orleans, LA 70148-2820
USA
Phone: 504/286-6850
Fax: 504/286-6860
papcm@uno.edu

Perpete, Eric A.
Facultes Universitaires de Namur
C.T.A.
Rue de Bruxelles, 61
Namur 5000
Belgium
Phone: 32-81-724557
Fax: 32-81-729530
eperpete@messiaen.scf.fundp.ac

Pople, John
Northwestern University
Department of Chemistry
2145 N. Sheridan Road
Evanston, IL 60208-3113
USA
Phone: 847-491-3403
Fax: 847-491-7713
pople@lithium.chem.nwu.edu

Person, Willis
University of Florida
Department of Chemistry
P.O. Box 117200
Gainesville, FL 32611-7200
USA
Phone: 352-392-0528
Fax: 352-392-0872
person@pine.circa.ufl.edu

Porter, Leonard E.
Washington State University
Radiation Safety Office
Nuclear Radiation Center
Pullman, WA 99164-1302
USA
Phone: 509-335-7057
Fax: 509-335-1615
porterl@mail.wsu.edu

Persson, Petter
Uppsala University
Department of Quantum Chemistry
Box 518
S-751 20 Uppsala
Sweden
Phone: 46-18-4713579
Fax: 46-18-502402
petter@kvac.uu.se

Poulain, Enrique
Instituto Technologico de Tlalnepantla
Division de Estudios de Posgrado
Apdo Postal 750
Tlalnepantla de Baz DF 54070
Mexico
Phone: 52-5-390-0310
Fax: 52-5-565-3910
sca@hp9000a1.uam.mx

Piecuch, Piotr
University of Florida
Department of Chemistry
P.O. Box 118435
Gainesville, FL 32611-8435
USA
Phone: 352-392-9227
Fax: 352-392-8722
piecuch@qtp.ufl.edu

Priyadarshy, Satyam
University of Pittsburgh
Department of Chemistry
219 Parkman Avenue
Pittsburgh, PA 15260
USA
Phone: 412-624-8200
Fax: 412-624-8552
satyam@vms.cis.pitt.edu

LIST OF PARTICIPANTS

Probst, Michael
Innsbruck University
Department of Inorganic Chemistry
Innrain 520
Innsbruck A-6020
Austria
Phone: 43-512-5075153
Fax: 43-512-5072934
michael.probst@uibk.ac.at

Purvis, George D.
Oxford Molecular
P.O. Box 4003
Beaverton, OR 97076
USA
Phone: 503-526-5006
Fax: 503-526-5099
gpurvis@oxmol.com

Pyykkö, Pekka
University of Helsinki
Department of Chemistry
P.O. Box 55
Helsinki FIN-00014
Finland
Phone: 358-9-191-40171
Fax: 358-9-191-40169
pekka.pyyKKO@helsinki.fi

Quintao, Andrea D.
Universidade Federal de Minas Gerais
Dept. of Fisica
Av. Antoio Carlos 6627, Pampulha
Belo Horizonte Minas Gerais 30123-970
Brazil
Phone: 55-031-4995633
Fax: 55-031-499-5600
aquintao@fisica.ufmg.br

Ramek, Michael
Technical University of Graz
Physics & Theoretical Chemistry
Brockmanngasse 27
Graz A-8010
Austria
Phone: 43-316-873-8227
Fax: 43-316-873-8720
ramek@ptc.tu-graz.ac.at

Randic, Milan
Drake University
Department of Math & Computer Science
Des Moines, IA 50311
USA
Phone: 515-271-2163
Fax: 515-271-2055

Rassolov, Vitaly A.
Northwestern University
Department of Chemistry
2145 Sheridan Road
Evanston, IL 60208-3113
USA
Phone: 847-491-3423
Fax: 847-491-7713
rassolov@chem.nwu.edu

Ratner, Mark A.
Northwestern University
Chemistry Department
2145 Sheridan Rd
Evanston, IL 60208-3113
USA
Phone: 847-491-5652
Fax: 847-491-7713
ratner@chem.nwu.edu

Récamier, Jose
Universidad Nacional Autonoma de Mexico
Lab Cuernavaca
Apdo Postal 48-3
Cuernavaca Morelos 62251
Mexico
Phone: 52-5-622-7763
Fax: 52-73-173077
pepe@ce.itisicam.unam.mx

Reyes, Andres
University of Florida
Quantum Theory Project
P.O. Box 118435
Gainesville, FL 32611-8435
USA
Phone: 352-392-3010
Fax: 352-392-8722
reyes@qtp.ufl.edu

Ritchie, Adam B.
Lawrence Livermore National Lab.
Livermore, CA 94550
USA
Phone: 510-423-9180
Fax: 510-422-5102
ritchie1@llnl.gov

LIST OF PARTICIPANTS

Roos, Bjorn
University of Lund
Theoretical Chemistry Department
P.O. Box 124
Lund S-221 00
Sweden
Phone: 46-46-2228251
Fax: 46-46-2224543
teobor@garm.teokem.lu.se

Saha, B. C.
Florida A & M University
Department of Physics
112A Jones Hall
Tallahassee, FL 32307
USA
Phone: 850-599-3470
Fax: 850-599-3577
saha@cennas.nhmfl.gov

Ruiz de Azua, Martin C.
Universidad de Buenos Aires
Dpto. de Fisica
Cdad Universitaria, Pab. 1
Buenos Aires 1428
Argentina
Phone: 54-1-782-1007
Fax: 54-1-782-7647
azua@df.uba.ar

Sahni, Virah
Brooklyn College of CUNY
Department of Physics
2900 Bedford Avenue
Brooklyn, NY 11210-2889
USA
Phone: 718-951-5785
Fax: 718-951-4407
vvvbc@cunyvm.cuny.edu

Rychlewski, Jacek
A. Mickiewicz University
Department of Chemistry
Grunwaldzka 6
Poznan 60-780
Poland
Phone: 48-61-8699181 X-275
Fax: 48-61-8658008
rycmlew@man.poznan.pl

Santana, Pedro
University of Florida
Quantum Theory Project
P.O. Box 118435
Gainesville, FL 32611-8435
USA
Phone: 352-392-1597
Fax: 352-392-8722
santana@qtp.ufl.edu

Sabin, John R.
University of Florida
Quantum Theory Project
P.O. Box 118435
Gainesville, FL 32611-8435
USA
Phone: 352-392-1597
Fax: 352-392-8722
sabin@qtp.ufl.edu

Santilli, Ruggero M.
Institute for Basic Research
Box 1577
Palm Harbor, FL 34682
USA
Phone: 813-934-9593
Fax: 813-934-9275
ibr@gte.net

Sadeghi, Raymond
University of Florida
Quantum Theory Project
P.O. Box 118435
Gainesville, FL 32611-8435
USA
Phone: 352-392-6973
Fax: 352-392-8722
rsadeghi@qtp.ufl.edu

Satoh, Katsuhiko
Institute of Molecular Science
Theoretical Studies
Okazaki 444-8585
Japan
Phone: 81-564-55-7308
Fax: 81-564-53-4660
ksatoh@ims.ac.jp

LIST OF PARTICIPANTS

Saue, Trond
Universite Paul Sabatier
IRSAMC-LPQ
118 Route de Narbonne
Toulouse 31400
France
Phone: 33-516556948
Fax: 33-561556065
tsaue@irsamc1.ups-tlse.fr

Schmelcher, Peter
University of Heidelberg
Theoretical Chemistry Department
Im Neuenheimer Feld 253
Heidelberg D-69120
Germany
Phone: 49-6221-545208
Fax: 49-6221-545221
peter@tc pci.uni-heidelberg.de

Schmidt, Peter
Office of Naval Research
Chemistry Division
800 North Quincy Street Code 1113
Arlington, VA 22217-5000
USA
Phone: 703-696-4362
schmidt@onrhq.onr.navy.mil

Schmiedekamp, Lumelle A.
Penn State University
Physics Department
1600 Woodland Road
Abington, PA 19001
USA
Phone: 215-881-7572
Fax: 215-881-7623
ams@psu.edu

Schuch, Dieter
JW Goethe-Universität
Inst. fur Theoretische Physik
Robert-Mayer-Str. 8-10
Frankfurt D-60054
Germany
Phone: 49-69-319523
Fax: 49-69-3088997
schuch@th.physik.uni-frankfurt.de

Schwegler, Eric
Minnesota Supercomputer Institute
1200 Washington Avenue South
Minneapolis, MN 55415
USA
Phone: 612-626-0763
Fax: 612-624-8861
schwiegler@chem.umn.edu

Seel, Max
Michigan Technological University
Physics Department
1400 Townsend Drive
Houghton, MI 49931-1295
USA
Phone: 906-487-2156
Fax: 906-487-3347
seel@mtu.edu

Sekusak, Sanja
Rugjer Boskovic Institute
Department of Chemistry
Bijenicka 54
Zagreb
Croatia
Phone: 385-1-4561-089
Fax: 385-1-4680-084
sanja@indigo.irb.hr

Serrano, Lourdes M.
Lake Forest College
Department of Chemistry
Box 1122 555 N. Sheridan Road
Lake Forest, IL 60045
USA
Phone: 847-735-5867
Fax: 847-735-6194
serralm@student.lfc.edu

Seybold, Paul
Wright State University
Department of Chemistry
Dayton, OH 45355
USA
Phone: 937-775-2407
Fax: 937-775-2717
pseybold@wright.edu

LIST OF PARTICIPANTS

Sherrill, David C.
University of California, Berkeley
Department of Chemistry
Box 308
Berkeley, CA 94720-1460
USA
Phone: 510-643-2935
Fax: 510-643-1255
sherrill@alum.mit.edu

Shields, George
Lake Forest College
Department of Chemistry
555 N. Sheridan Road
Lake Forest, IL 60045
USA
Phone: 708/735-5092
Fax: 708/735-6291
gshields@ifmail.lfc.edu

Shigeta, Yasuteru
Osaka University
Department of Chemistry
Machikane ya ma Machi
Toyonaka 560
Japan
Phone: 81-06-850-5405
Fax: 81-06-850-5550
shigeta@chem.sci.osaka-u.ac.jp

Shillady, Donald D.
Virginia Commonwealth University
Department of Chemistry
1001 W. Main Street, Kapp Hall
Richmond, VA 23284-8599
USA
Phone: 804-367-1298
Fax: 804-828-8599
dhillad@saturn.vcv.edu

Smeijers, Yves G.
Superior Council for Scientific Investigations
Institute of Matter Structure
Calle Serrano No 123
Madrid E-28006
Spain
Phone: 34-1-5855404
Fax: 34-1-5642431
emsmeijers@roca.csic.es

Smith, Vedene H.
Queen's University
Department of Chemistry
Kingston, Ontario K7L 3N6
Canada
Phone: 613-545-2650
Fax: 613-545-6669
vhsmith@chem.queens.ca

Soscun, Humberto
Universidad de Zulia
Fac. of Sciences, Dept. de Quimica
Grano de Oro, Mod. 2
Maracaibo Zulia AP 526,
Venezuela
Phone: 58-61-317902
Fax: 58-61-311348
humberto@sinamaica.ciens.luz.ve

Squire, Richard H.
Marshall University
Department of Chemistry
901 W. DuPont Avenue
Belle, WV 25015
USA
Phone: 304-357-1292
Fax: 304-357-1230
richard.h.squire@USA.dupont.com

Stanton, Christopher
University of Florida
Department of Physics
P.O. Box 118440
Gainesville, FL 32611-8440
USA
Phone: 352-392-8753
Fax:

Stavrev, Krassimir K.
Hypercube, Inc.
1115 NW 4th Street
Gainesville, FL 32601
USA
Phone: 352-371-7744
Fax: 352-371-3662
stavrev@hyper.com

LIST OF PARTICIPANTS

Stevens, Walter J.

National Institute of Standards and Technology
Computational Chemistry
Building 221, Room A111
Gaithersburg, MD 20899
USA
Phone: 301-975-5968
Fax: 301-869-4020
walter.stevens@nist.gov

Tamm, Toomas

University of Helsinki
Department of Chemistry
P.O. Box 55
Helsinki FIN-00014
Finland
Phone: 358-9-191-40174
Fax: 358-9-191-40169
toomas@chem.helsinki.fi

Sun, Jun-Qiang

University of Florida
Quantum Theory Project
P.O. Box 118435
Gainesville, FL 32611-8435
USA
Phone: 352-392-6715
Fax: 352-392-8722
sun@qtp.ufl.edu

Thakkar, Ajit J.

University of New Brunswick
Chemistry Department
Bag Service #45222
Fredericton NB E3B 6E2
Canada
Phone: 506-453-4629
Fax: 506-453-4981
ajit@unb.ca

Surjan, Peter R.

Eötvös University
Theoretical Chemistry
P.O. Box 32
Budapest 1518
Hungary
Phone: 36-1-209-0555-1632
Fax: 36-1-209-0602
surjan@para.chem.elte.hu

Thorndyke, Brian

University of Florida
Quantum Theory Project
P.O. Box 118435
Gainesville, FL 32611-8435
USA
Phone: 352-392-6365
Fax: 352-392-8722
thorndyke@qtp.ufl.edu

Talham, Dan

University of Florida
Department of Chemistry
P.O. Box 117200
Gainesville, FL 32611-7200
USA
Phone: 352-392-9016
Fax: 352-392-3255
talham@chem.ufl.edu

Tobita, Motoi

University of Florida
Quantum Theory Project
P.O. Box 118435
Gainesville, FL 32611-8435
USA
Phone: 352-392-6365
Fax: 352-392-8722
tobita@qtp.ufl.edu

Talman, James

University of Western Ontario
Department of Applied Mathematics
WSC 173
London, Ontario N6A 5B7
Canada
Phone: 519-679-2111 EXT 8800
Fax: 519-661-3523
jdt@apmaths.uwo.ca

Törning, Jens T.

J. W. Goethe-Universitaet
Chemistry
Marie Curie Street, 11
Frankfurt am Main D-60439
Germany
Phone: 49-69-798-29786
Fax: 49-69-798-29404
toerring@chemie.uni-frankfurt.de

LIST OF PARTICIPANTS

Tozer, David J.
University of Cambridge
Department of Chemistry
LCI, Bat. 420
Cambridge CB2 1EW
UK

Trickey, Samuel B.
University of Florida
Quantum Theory Project
P.O. Box 118435
Gainesville, FL 32611-8435
USA
Phone: 352-392-1597
Fax: 352-392-8722
trickey@qtp.ufl.edu

Trindle, Carl
University of Virginia
Chemistry Department
McCormick Road
Charlottesville, VA 22903
USA
Phone: 804-924-3168
Fax: 804-924-3710
cot@virginia.edu

Truhlar, Donald
University of Minnesota
Chemistry Department
207 Pleasant Street, S.E.
Minneapolis, MN 55455-0431
USA
Phone: 612-624-7555
Fax: 612-626-7541
truhlar@umn.edu

Tschumper, Gregory S.
University of Georgia
Center for Computational Quantum Chemistry
Chemistry Annex, Room 515
Athens, GA 30602-2556
USA
Phone: 706-542-7373
Fax: 706-542-0406
tschumpr@xerxes.ccqc.uga.edu

Tsurusawa, Takeshi
Institute for Molecular Science
Theoretical Studies
Myodaiji-Cho, Okazaki
Okazaki Aichi 444-8585
Japan
Phone: 81-564-55-7308
Fax: 81-564-53-4660
ztakeshi@ims.ac.jp

Turner, Rebecca B.
Lake Forest College
Department of Chemistry
LFC Box 1188, 555 N. Sheridan Road
Lake Forest, IL 60045
USA
Phone: 847-735-5374
Fax: 847-735-6194
turnerb@student.lfc.edu

Ugalde, Jesus M.
Euskal Herriko Unibertsitatea
Kimika Fakultatea
P.K. 1072
Donostia 20080
Spain
Phone: 34-43-216-600
Fax: 34-43-212236
ugalde@sq.ehu.es

Vanderbilt, David
Rutgers University
Department of Physics and Astronomy
61 Robert Rd.
Princeton, NJ 08540
USA
Phone: 732-445-2514
Fax: 732-445-4400
dhv@physics.rutgers.edu

Vercauteren, Daniel
University of Namur
Chemistry Department
Rue de Bruxelles, 61
Namur B-5000
Belgium
Phone: 32-81-724534
Fax: 32-81-724530
daniel.vercauteren@sef.fundp.ac.be

LIST OF PARTICIPANTS

Vergenz, Robert

University of North Florida
Department of Natural Sciences
3456 St. Johns Bluff Road S.
Jacksonville, FL 32225-2645
USA
Phone: 904-721-1934

Watts, John

University of Florida
Quantum Theory Project
P.O. Box 118435
Gainesville, FL 32611-8435
USA
Phone: 352-392-1597
Fax: 352-392-8722
watts@qtp.ufl.edu

Vigneron, Jean-Pol

Universitaires Notre-Dame de la Paix
Department of Physics
Rue de Bruxelles 61
Namur 5000
Belgium
Phone: 32-81-724711
Fax: 32-81-724707
jean-pol.vigneron@scf.fundp.ac.be

Weatherford, Charles A.

Florida A & M University
Department of Physics
205 Jones Hall
Tallahassee, FL 32307
USA
Phone: 850-599-3470
Fax: 850-599-3577
weatherf@cennas.nhmfl.gov

Vilkas, Jonas M.

University of Puerto Rico
Department of Chemistry
P.O. Box 23346
San Juan, Puerto Rico 00931-3346
Phone: 787-764-0000 x-5908
Fax: 787-756-7717
vilkas@pauli.uprr.pu

Weiner, Brian

Pennsylvania State University
Department of Physics
College Place
Dubois, PA 15801
USA
Phone: 814-375-4700
Fax: 814-375-4784
bqw@psu.edu

Wagner-Brown, Katrina B.

Conceptual Mindworks
4318 Woodcock Dr. #210
San Antonio, TX 78228
USA
Phone: 210-536-4822
Fax: 210-536-2952
wagner@delta.broks.ad.mil

Wenzel, Wolfgang

Dortmund University
Theoretical Physics
Otto-Hahn-Str 4
Dortmund D-44221
Germany
Phone: 49-251-755-3551
Fax: 49-251-755-3551
wenzel@wap.physik.uni-dortmund.de

Warshel, Arieh

University of Southern California
Chemistry Department
1008 Westholme Ave.
Los Angeles, CA 90024
USA
Phone: 213-740-4114
Fax: 213-740-2701

Wilson, Kenneth

University of Florida
Quantum Theory Project
P.O. Box 118435
Gainesville, FL 32611-8435
USA
Phone: 352-392-6365
Fax: 352-392-8722
wilson@qtp.ufl.edu

LIST OF PARTICIPANTS

Xantheas, Sotiris S.
Pacific Northwest National Lab
Environmental Molecular Sciences Lab
902 Batelle Blvd., MS K1-96
Richland, WA 99352
USA
Phone: 509-375-6878
Fax: 509-375-6631
ss_xantheas@pnl.edu

Yamada, Satoru
Osaka University
Department of Chemistry
Machikaneyama-cho 1-1
Toyonaka 560
Japan
Phone: 81-6-850-5405
Fax: 81-6-850-5550
yamada@chem.sci.osaka-u.ac.jp

Yau, Anthony
University of Florida
Quantum Theory Project
P.O. Box 118435
Gainesville, FL 32611-8435
USA
Phone: 352-392-6365
Fax: 352-392-8722
yau@qtp.ufl.edu

Yeager, Danny L.
Texas A & M University
Chemistry Department
MS-3255
College Station, TX 77843-3255
USA
Phone: 409-845-3436
Fax: 409-845-4719
yeager@chemvx.tamu.edu

Yi, Zhigang
University of Florida
Quantum Theory Project
P.O. Box 118435
Gainesville, FL 32611-8435
USA
Phone: 352/392-3010
Fax: 352/392-8722
yi@qtp.ufl.edu

Yoshioka, Yasunori
Osaka University
Department of Chemistry
Toyonaka, Osaka 560
Japan
Phone: 81-6-850-5406
Fax: 81-6-850-5550
yyoshi@chem.sci.osaka-u.ac.jp

Zakrzewski, Vyacheslav
Kansas State University
Department of Chemistry
111 Willard Hall
Manhattan, KS 66506-3701
USA
Phone: 785-532-6072
Fax: 913-532-6666
vgz@ksu.edu

Zerner, Michael C.
University of Florida
Quantum Theory Project
P.O. Box 118435
Gainesville, FL 32611-8435
USA
Phone: 352-392-1597
Fax: 352-392-8722
zerner@qtp.ufl.edu

Zeroka, Daniel
Lehigh University
Chemistry Department
Bldg. E5554, SCBRD-RTE, ERDEC
Aberdeen Proving Ground, MD 21010-5423
USA
Phone: 410-671-4825
Fax: 410-671-1120
dz00@lehigh.edu

Zhu, Chaoyuan
Institute for Molecular Science
Division of Theoretical Studies
Myodaiji Okazaki 444
Japan
Phone: 81-564-55-7309
Fax: 81-564-53-4660
zhu@ims.ac.jp

3,5-Contracted Schrödinger Equation: Determining Quantum Energies and Reduced Density Matrices Without Wave Functions

DAVID A. MAZZIOTTI

Department of Chemistry, 12 Oxford Street, Harvard University, Cambridge, Massachusetts 02138

Received 18 March 1998; accepted 28 April 1998

ABSTRACT: Through the 3,5-contracted Schrödinger equation (3,5-CSchE) quantum energies and 3-particle reduced density matrices (3-RDMs) are determined directly without wave functions. Since the 3,5-CSchE involves the 5-RDM, its solution is indeterminate without N -representability conditions. However, the indeterminacy of the 3,5-CSchE may be removed through a reconstruction strategy for building the 4- and 5-RDMs from the 3-RDM. We present a systematic procedure for obtaining corrections for Valdemoro's reconstruction functionals from two complementary approaches, the particle-hole duality and the theory of cumulants. With the cumulants we are able to demonstrate that we have obtained all terms in the reconstruction functionals which may be written as antisymmetric products of the lower rdms. The cumulants allow us to understand the reconstruction functionals in terms of a renormalized many-body perturbation theory. The reconstruction functionals also lead to a natural generalization of Wick's theorem for evaluating expectation values of fermionic annihilation and creation operators with respect to correlated reference states. Previous work [Phys. Rev. A 57, 4219 (1998)] has explored the determination of correlation energy and 2-RDMs through the 2,4-CSchE, also known as the density equation. Because the reconstruction functionals employed with the 3,5-CSchE depend only on the antisymmetric products of lower RDMs in contrast to those used with the 2,4-CSchE, the 3,5-CSchE method presented here does not require the solution of systems of linear equations during reconstruction or the storage of the reconstructed RDMs. Application of the 3,5-CSchE technique to a quasi-spin model generates ground-state energies and 2-RDMs similar in accuracy to single-double configuration interaction (SDCI). We employ a simple iterative procedure for the solution of the 3,5-CSchE without traditional diagonalization. The CSchE techniques offer an approximate solution of the N -representability problem and a new approach to electron correlation. © 1998 John Wiley & Sons, Inc. Int J Quant Chem 70: 557–570, 1998

Contract grant sponsor: National Science Foundation.

Key words: electron correlation; reduced density matrices; N -representability; cumulants; particle-hole duality

Introduction

For atoms and molecules with any number N of electrons the repulsions between electrons are treated pairwise within the Hamiltonian. A consequence of this is that the energy and other properties of molecular systems may be calculated with only a knowledge of the 2-particle reduced density matrix (2-RDM). This result suggests a simplification for the many-body problem for pairwise-interacting particles in which calculation of the N -particle wave function is circumvented through a direct determination of the 2-RDM. Many attempts to obtain the 2-RDM variationally have not succeeded because simple yet complete conditions for ensuring that the 2-RDM corresponds to a realistic N -particle system have not been found (N -representability problem) [1, 2]. Recently, however, we have presented an accurate technique for determining directly the 2-RDM through the 2,4-contracted Schrödinger equation (2,4-CSchE) [3].

In 1976 both Cohen and Frishberg [4] and Nakatsuji [5] derived the $(p, p + 2)$ -CSchE as an integro-differential equation where $p \geq 1$. Matrix formulations were later developed by Harriman [6] and Valdemoro [7]. However, the $(p, p + 2)$ -CSchE alone cannot be employed to determine the p -RDM because it also requires a knowledge of the $(p + 2)$ -RDM. In 1993 Valdemoro offered a practical solution for the indeterminacy of the 2,4-CSchE by deriving functionals for reconstructing the 3- and 4-RDMs approximately from a knowledge of the 2-RDM [8–12]. Yasuda and Nakatsuji have employed Valdemoro's formulas for the 3- and 4-RDMs with corrections to solve the 2,4-CSchE for closed-shell molecules with as many as 14 active electrons [13, 14]. We have recently derived corrections for Valdemoro's 3- and 4-RDM reconstruction functionals through the particle-hole duality [3]. Our correction for the 4-RDM functional from the particle-hole perspective agrees with the term proposed by Yasuda and Nakatsuji from the theory of Green's functions, but our approach for correcting the 3-RDM is different. We have also proposed a new reconstruction strategy without functionals, known as the ensemble representabil-

ity method (ERM), in which contraction and positive semidefinite conditions are imposed on the 3- and 4-RDMs. The functional and ERM reconstructions were separately employed with the 2,4-CSchE to solve a quasi-spin model with the number of particles between 4 and 40. For both methods we obtained ground-state energies as accurate as single-double configuration interaction (SDCI) and 2-RDMs which were about an order of magnitude better than SDCI.

In the present work we explore the possibility of obtaining accurate energies and 2-RDMs through the solution of the 3,5-CSchE. By contracting the Schrödinger equation through the use of test functions, we provide a clear derivation of the 3,5-CSchE in second quantization. Two different approaches for deriving a correction to Valdemoro's functional for the 5-RDM in terms of lower RDMs are explored: (i) the particle-hole duality and (ii) the theory of cumulants. We show how these two perspectives interrelate and complement each other. Furthermore, through the cumulant expansion we demonstrate how to obtain *all* of the terms for the p -RDM functional which may be written as antisymmetrized products of the lower RDMs. This leads us to a natural division of the RDM functionals into an *unconnected* part which may be expressed as a product of lower RDMs and a *connected* remainder. The notion of *connected* will allow us to elucidate the relationship between the reconstruction functionals and many-body perturbation theory (MBPT) [15–17] for RDMs. Reconstruction for two different RDMs (the $p + 1$ - and $p + 2$ -RDMs) must be employed to remove the indeterminacy of the $(p, p + 2)$ -CSchE. Ideally, we would like these functionals to be accurate through the same order of MBPT, that is scheme consistent [18, 19]. While the 4-RDM, constructed from the lower RDMs, may be shown to be exact through second order, the 3-RDM functional, we will indicate, cannot be made consistent through second order without a correction to the connected portion. In contrast, both the 4- and 5-RDMs, correct through second order of MBPT, may be built from products of the 3-RDM and lower RDMs. This suggests a possible advantage for solving systems with pairwise interactions through the 3,5-CSchE.

Solution of the 3,5-CSchE with the reconstruction functionals for the 4- and 5-RDMs is explored

through calculations of a quasi-spin system with as many as 50 particles. The spin model, employed in a previous study to illustrate the 2,4-CSchE, was originally used by Lipkin [20] as a benchmark to test various many-body methods for solving fermionic systems. The results are compared with those of the 2,4-CSchE as well as more traditional approaches to electron correlation like MBPT and SDCI. As mentioned above, the second-order correction for the 3-RDM in the 2,4-CSchE requires the solution of a system of equations in Nakatsuji and Yasuda's approach as well as our own, but the equivalent corrections for the 4- and 5-RDMs in the 3,5-CSchE may be written as explicit functionals of the 3-RDM and lower RDMs. For this reason the 3,5-CSchE may be solved iteratively without storing the 4- or 5-RDMs.

Derivation

To generate the 3,5-contracted Schrödinger equation, we begin with the N -particle Schrödinger equation

$$H|\psi\rangle = E|\psi\rangle \quad (1)$$

where the wave function ψ may represent any state of the system and the Hamiltonian is defined in second quantization as

$$H = \frac{1}{2} \sum_{i_4, i_5, j_4, j_5} {}^2K_{j_4, j_5}^{i_4, i_5} a_{i_4}^\dagger a_{i_5}^\dagger a_{j_5} a_{j_4}. \quad (2)$$

Index labeling begins with 4 since we wish to reserve the lower integers for later use. The 2-particle reduced Hamiltonian matrix 2K has elements defined by

$$K_{j_4, j_5}^{i_4, i_5} = V_{j_4, j_5}^{i_4, i_5} + \frac{1}{N-1} (\epsilon_{i_4, j_4} \delta_{i_5, j_5} + \epsilon_{i_5 j_5} \delta_{i_4, j_4}) \quad (3)$$

in which ϵ and V represent the one- and two-particle contributions, respectively. For an atomic system with nuclear charge Z these terms are given explicitly by

$$\epsilon_{i_4, j_4} = \left\langle \phi_{i_4} \left| -\frac{\nabla_1^2}{2} - \frac{Z}{r_1} \right| \phi_{j_4} \right\rangle \quad (4)$$

and

$$V_{j_4, j_5}^{i_4, i_5} = \left\langle \phi_{i_4}(1) \phi_{i_5}(2) \left| \frac{1}{r_{12}} \right| \phi_{j_4}(1) \phi_{j_5}(2) \right\rangle, \quad (5)$$

with ϕ_i denoting the one-electron spin orbitals.

Multiplying the Schrödinger equation on the right by the function $\langle \psi |$, we obtain the expression for exact energy E as a linear function of the 2-particle density matrix 2D (2-RDM):

$$E = \sum_{i_4, i_5, j_4, j_5} {}^2K_{j_4, j_5}^{i_4, i_5} {}^2D_{j_4, j_5}^{i_4, i_5} = \text{Tr}({}^2K {}^2D), \quad (6)$$

where we define the 2-RDM in second quantization as

$${}^2D_{j_4, j_5}^{i_4, i_5} = \frac{1}{2!} \langle \psi | a_{i_4}^\dagger a_{i_5}^\dagger a_{j_5} a_{j_4} | \psi \rangle. \quad (7)$$

The normalization of the 2-RDM is $(N(N-1))/2$ in this notation. As discussed in the introduction, direct determination of the ground-state 2-RDM through variational minimization of the energy is not yet a practical alternative to traditional approaches for the many-body problem because simple conditions for keeping the 2-RDM ensemble N -representable have not been discovered.

Relationships more general than Eq. (6), however, may be obtained by testing the Schrödinger equation with a set of functions $\{\langle \Phi_i | \}$ rather than just the wave function $\langle \psi |$. Let us consider the set of one-, two-, and three-particle excitations by defining the test functions

$$\langle \Phi_{j_1, j_2, j_3}^{i_1, i_2, i_3} | = \langle \psi | a_{i_1}^\dagger a_{i_2}^\dagger a_{i_3}^\dagger a_{j_3} a_{j_2} a_{j_1} |. \quad (8)$$

Multiplying Eq. (1) by these test functions produces the equations

$$\sum_{i_4, i_5, j_4, j_5} {}^2K_{j_4, j_5}^{i_4, i_5} R_{j_1, j_2, j_3, j_4, j_5}^{i_1, i_2, i_3, i_4, i_5} = 12E {}^3D_{j_1, j_2, j_3}^{i_1, i_2, i_3}, \quad (9)$$

where

$$R_{j_1, j_2, j_3, j_4, j_5}^{i_1, i_2, i_3, i_4, i_5} = \langle \psi | a_{i_1}^\dagger a_{i_2}^\dagger a_{i_3}^\dagger a_{j_3} a_{j_2} a_{j_1} a_{i_4}^\dagger a_{i_5}^\dagger a_{j_5} a_{j_4} | \psi \rangle. \quad (10)$$

By rearranging the creation and annihilation operators in the expression for R , we can write the elements of R as linear combinations of 3-, 4-, and 5-RDMs. Use of a graphical rule not only facilitates the rearrangement of the operators but produces a result which is independent of whether the N particles under consideration obey boson or fermion statistics [21]. We obtain the following expres-

sion for the elements of R in terms of RDMs:

$$\begin{aligned}
 R_{j_1, j_2, j_3, j_4, j_5}^{i_1, i_2, i_3, i_4, i_5} = & 5! \left({}^5D_{j_1, j_2, j_3, j_4, j_5}^{i_1, i_2, i_3, i_4, i_5} \right) \\
 & + 4! \left({}^4D_{j_4, j_2, j_3, j_5}^{i_1, i_2, i_3, i_5} \delta_{j_1}^{i_4} + {}^4D_{j_5, j_2, j_3, j_4}^{i_1, i_2, i_3, i_4} \delta_{j_1}^{i_5} \right. \\
 & + {}^4D_{j_1, j_4, j_3, j_5}^{i_1, i_2, i_3, i_5} \delta_{j_2}^{i_4} + {}^4D_{j_1, j_5, j_3, j_4}^{i_1, i_2, i_3, i_4} \delta_{j_2}^{i_5} \\
 & + {}^4D_{j_1, j_2, j_4, j_5}^{i_1, i_2, i_3, i_5} \delta_{j_3}^{i_4} + {}^4D_{j_1, j_2, j_5, j_4}^{i_1, i_2, i_3, i_4} \delta_{j_3}^{i_5} \\
 & + 3! \left({}^3D_{j_3, j_4, j_5}^{i_1, i_2, i_3} \left(\delta_{j_1}^{i_4} \delta_{j_2}^{i_5} + \delta_{j_2}^{i_4} \delta_{j_1}^{i_5} \right) \right. \\
 & \left. + {}^3D_{j_1, j_4, j_5}^{i_1, i_2, i_3} \left(\delta_{j_2}^{i_4} \delta_{j_3}^{i_5} + \delta_{j_3}^{i_4} \delta_{j_2}^{i_5} \right) \right) \\
 & + {}^3D_{j_2, j_4, j_5}^{i_1, i_2, i_3} \left(\delta_{j_3}^{i_4} \delta_{j_1}^{i_5} + \delta_{j_1}^{i_4} \delta_{j_3}^{i_5} \right) \quad (11)
 \end{aligned}$$

in which the p -RDMs are given by the general second-quantized definition

$${}^p D_{j_1, j_2, \dots, j_p}^{i_1, i_2, \dots, i_p} = \frac{1}{p!} \langle \psi | a_{i_1}^\dagger a_{i_2}^\dagger \dots a_{i_p}^\dagger a_{j_1} a_{j_2} \dots a_{j_{p-1}} | \psi \rangle. \quad (12)$$

The p -RDMs are normalized to $N!/(p!(N-p)!)$. Collectively, the equations in (9) with the expression for elements of R in Eq. (11) compose the 3,5-CSchE. Other CSchEs may be generated by using different test functions $\{\Phi_i\}$ in Eq. (8). The 1,3-CSchE requires a set of single excitations while the 2,4-CSchE requires both single and double excitations.

When the RDMs in the 3,5-CSchE are restricted to the set of pure N -representable matrices, they will constitute a solution of the 3,5-CSchE if and only if they may be formed from the contraction of an N -particle pure density matrix ${}^N D(\psi)$ whose associated wave function ψ satisfies the Schrödinger equation (SE). This result, known as Nakatsuji's theorem, was demonstrated by Nakatsuji in 1976 for an integro-differential version of the CSchE [5]. We recently presented the first formal proof of the theorem for the second-quantized 2,4-CSchE [3]. Proof that a ψ satisfying the SE contracts to RDMs, which solve the 3,5-CSchE, follows directly from the above derivation of the 3,5-CSchE from the SE. We may demonstrate the other direction of the proof by showing that within a pure N -representable space the 3,5-CSchE implies the following dispersion condition:

$$\langle \psi | H^2 | \psi \rangle - \langle \psi | H | \psi \rangle^2 = 0, \quad (13)$$

which is true if and only if the SE is satisfied. Hence, solution of the 3,5-CSchE implies solution

of the SE. Details of the derivation mirror those given for the 2,4-CSchE. Since the Hamiltonian in Eq. (13) is defined in second quantization by Eq. (2), the resulting theorem is valid for both complete and incomplete basis sets. This proof does not work for the 1,3-CSchE which may have pure N -representable solutions which do not correspond to the wave function solution of the SE. In any correlated system the Hartree–Fock RDMs as well as the correlated 1-, 2-, and 3-RDMs will satisfy the 1,3-CSchE.

Reconstruction

While Nakatsuji's theorem guarantees that the 3,5-CSchE may be solved directly for the correct 3-, 4-, and 5-RDMs within a pure N -representable space, simple necessary-and-sufficient conditions for keeping these RDMs N -representable are not known. The framework of the 3,5-CSchE, however, allows us to recast N -representability as a reconstruction problem. If we knew how to build from the 3-RDM to the 5-RDM, the 3,5-CSchE in Eq. (9) furnishes us with enough equations to solve iteratively for the 3-RDM. Two approaches for reconstruction have been explored in a previous study [3] on the 2,4-CSchE: (i) the explicit representation of higher RDMs as functionals of lower RDMs and (ii) the construction of a family of higher RDMs from lower RDMs by imposing ensemble representability conditions. In the following two sections we will develop the functional approach for the 3,5-CSchE from two different perspectives, the particle–hole duality and the theory of cumulants.

PARTICLE–HOLE DUALITY

Many-body problems in quantum mechanics are usually described by the number of particles N in the system and the probabilities of finding those particles at different locations in space. If the rank of the one-particle basis is a finite number r , an equally valid description of the system may be given by specifying the number of holes $r-N$ in the system and the probabilities of finding these holes at different locations in space. This possibility for an equivalent representation of the system by particles or holes is known as the particle–hole duality. By using the fermion anticommutation relation to rearrange the creation and annihilation operators in the definition equation (2) of the

Hamiltonian such that all of the annihilators appear to the left of the creators, we generate a hole representation of the Hamiltonian \bar{H} whose expectation value with the $(r - N)$ -hole density matrix ${}^{(r-N)}\bar{D}$ produces the energy E :

$$E = \text{Tr}(\bar{H}^{(r-N)}\bar{D}) \quad (14)$$

$$= \text{Tr}({}^2\bar{K}\bar{D}). \quad (15)$$

As shown in the second line, like the expression for the energy E as a function of the 2-RDM, the energy E may also be expressed as a linear functional of the 2-hole reduced density matrix ${}^2\bar{D}$ (2-HRDM) and the 2-hole reduced Hamiltonian ${}^2\bar{K}$. Direct minimization of the energy to determine the 2-HRDM would require $(r - N)$ -representability conditions. The definition for the p -hole reduced density matrices in second quantization is given by

$${}^p\bar{D}_{i_1, i_2, \dots, i_p}^{j_1, j_2, \dots, j_p} = \frac{1}{p!} \langle \psi | a_{j_1} a_{j_2} \cdots a_{j_p} a_{i_1}^\dagger a_{i_2}^\dagger \cdots a_{i_p}^\dagger | \psi \rangle. \quad (16)$$

Normalization of the p -HRDM in second quantization is $(r - N)! / (p!(r - N - p)!)$.

Because the hole and particle perspectives offer equivalent physical descriptions, the p -RDMs and p -HRDMs are related by a linear mapping [22, 23]. Thus, if one of them is known, the other one is easily determined. The same linear mapping relates the p -particle and p -hole reduced Hamiltonian matrices (2K and ${}^2\bar{K}$). An explicit form for the mapping may be readily determined by using the fermion anticommutation relation to convert the p -HRDM in Eq. (16) to the corresponding p -HRDM. For $p = 1$ the result is simply

$${}^1\bar{D}_i^i = {}^1\delta_j^i - {}^1D_j^i, \quad (17)$$

which is equivalent to taking the expectation of the fermion anticommutation relation. Similarly, for $p = 2$ we obtain the relation

$$\begin{aligned} {}^2\bar{D}_{i_1, i_2}^{j_1, j_2} &= (\delta_{j_1}^{i_1} \delta_{j_2}^{i_2} - \delta_{j_1}^{i_2} \delta_{j_2}^{i_1})/2 \\ &- {}^1D_{j_1}^{i_1} \delta_{j_2}^{i_2} + {}^1D_{j_2}^{i_1} \delta_{j_1}^{i_2} + {}^2D_{j_1, j_2}^{i_1, i_2}, \end{aligned} \quad (18)$$

which contains a sum of three different kinds of terms that have: (i) one 2-RDM, (ii) one 1-RDM multiplying one δ , and (iii) two δ 's. This expression represents the commutation relation for a composite particle consisting of two fermions. By

anticommuting the creation and annihilation operators, we can generate analogous expressions for composite particles consisting of more than two fermions.

Before introducing the general expression, we express Eq. (18) more concisely through the antisymmetric wedge product \wedge from Grassmann algebra [24]. The wedge product between two matrices pD and qD involving p and q particles produces an antisymmetric matrix involving $p + q$ particles defined by

$${}^pD \wedge {}^qD = A_N {}^pD \otimes {}^qDA_N, \quad (19)$$

where the A_N is the N -particle antisymmetrization operator and \otimes is the tensor product. More details about evaluating wedge products may be found in Appendix A of [3]. For the 2-HRDM as a functional of RDMs we obtain

$${}^2\bar{D}_{i_1, i_2}^{j_1, j_2} = {}^2I_{j_1, j_2}^{i_1, i_2} - {}^2D_{j_1}^{i_1} \wedge {}^1I_{j_2}^{i_2} + {}^2D_{j_1, j_2}^{i_1, i_2} \quad (20)$$

where 1I is the identity matrix

$${}^1I_{j_1}^{i_1} = \delta_{j_1}^{i_1} \quad (21)$$

and

$${}^2I_{j_1, j_2}^{i_1, i_2} = {}^1I_{j_1}^{i_1} \wedge {}^1I_{j_2}^{i_2}. \quad (22)$$

In general, the linear relation between the p -HRDM and p -RDM may be expressed as

$${}^p\bar{D} = {}^pI + \sum_{n=1}^{p-1} (-1)^n \binom{p}{n} {}^nD \wedge {}^{(p-n)}I + (-1)^p {}^pD. \quad (23)$$

Indices for the RDMs are not shown for notational clarity. The p -RDM as a functional of the p -HRDM may be easily obtained by switching ${}^p\bar{D}$ and pD in the above equation.

Valdemoro [8] realized that these particle-hole relations could be written in the following form:

$${}^p\bar{D} + (-1)^{p+1} {}^pD = f({}^{p-1}\bar{D}) + (-1)^{p+1} f({}^{p-1}D), \quad (24)$$

where $f({}^{p-1}\bar{D})$ is a functional of the $(p - 1)$ -HRDM and lower HRDMs and $f({}^{p-1}D)$ has the same functional form as $f({}^{p-1}\bar{D})$ with the HRDMs replaced with the corresponding RDMs. With the appropriate f functional for each p the relation in Eq. (24) is *exact* and *equivalent* to Eq. (23).

Valdemoro then obtains functionals for the p -RDM and p -HRDM by assuming that

$${}^p D \approx {}^p D_{\text{Vald}} = f({}^{p-1} D) \quad (25)$$

and

$${}^p \bar{D} \approx {}^p \bar{D}_{\text{Vald}} = f({}^{p-1} \bar{D}). \quad (26)$$

These formulas are approximate because some of the terms for the particle and hole RDMs cancel in relation (24). Rearranging Eq. (23) for each p as originally described by Valdemoro will produce the functionals f . We have found an easier method for extracting the functionals f which, however, does not show the equivalence between Eqs. (23) and (24). Since Valdemoro's method appears in the literature [8], we explain our technique which generates f from Eq. (23) through the following two substitutions: (i) replace ${}^1 I$ with ${}^1 D$, which is equivalent to assuming that ${}^1 \bar{D} = 0$ in Eq. (17), and (ii) set ${}^p \bar{D} = 0$. The technique works because it assumes a separation of particles and holes by setting all of the hole matrices in the expression to zero to produce f . For p from 2 to 5 the resulting RDM functionals are represented by the portions of the functionals in Table I that are not underlined. The underlined corrections will be determined below through an extension of the particle-hole arguments and later through cumulant expansions.

Corrections for the 4-RDM and 5-RDM functionals may be obtained by searching for some terms involving the wedge products of lower RDMs which cancel with the corresponding corrections for the HRDM functionals. Consider the matrices ${}^2 \Delta$ and ${}^3 \Delta$ describing the errors in Valdemoro's reconstruction functionals for the 2- and 3-RDMs as well as the matrices ${}^2 \bar{\Delta}$ and ${}^3 \bar{\Delta}$ describing the errors in Valdemoro's reconstruction functionals

for the 2- and 3-HRDMs:

$${}^2 \Delta = {}^2 D - {}^2 D_{\text{Vald}} \quad (27)$$

$$= {}^2 \bar{D} - {}^2 \bar{D}_{\text{Vald}} \quad (28)$$

$$= {}^2 \bar{\Delta} \quad (29)$$

and

$${}^3 \Delta = {}^3 D - {}^3 D_{\text{Vald}} \quad (30)$$

$$= -({}^3 \bar{D} - {}^3 \bar{D}_{\text{Vald}}) \quad (31)$$

$$= -{}^3 \bar{\Delta}. \quad (32)$$

An appropriate correction for the 4-RDM and 4-HRDM functionals is

$${}^4 D_{\text{corr}} = k_4 {}^2 \Delta \wedge {}^2 \Delta \quad (33)$$

$$= k_4 {}^2 \bar{\Delta} \wedge {}^2 \bar{\Delta} \quad (34)$$

$$= {}^4 \bar{D}_{\text{corr}}, \quad (35)$$

because this term has the same functional form for particles and holes and yet, since they are equal, they cancel in the commutation relation (24). The proportionality factor k_4 is equal to the number of distinct ways of distributing the four particles in two groups of two particles. The possibilities are {12}{34}, {13}{24}, and {14}{23}; hence, $k_4 = 3$. The 5-RDM and 5-HRDM functionals have the following corrections:

$${}^5 D_{\text{corr}} = k_5 {}^3 \Delta \wedge {}^2 \Delta \quad (36)$$

$$= -({}^k_5 {}^3 \bar{\Delta} \wedge {}^2 \bar{\Delta}) \quad (37)$$

$$= -{}^5 \bar{D}_{\text{corr}}. \quad (38)$$

Again this term has the same functional form for particles and holes. Note that for odd p the corrections must have opposite signs to cancel in the anticommutation relation (24). As with k_4 , the proportionality factor k_5 is equal to the number of distinct ways of distributing the five particles be-

TABLE I
Approximate reconstruction functionals for the p -RDMs in terms of lower RDMs where corrections to Valdemoro's functionals are underlined.

${}^2 D \approx {}^2 D_{\text{Vald}} = {}^1 D^2$
${}^3 D \approx {}^3 D_{\text{Vald}} = {}^1 D^3 + 3({}^2 D - {}^1 D^2) \wedge {}^1 D$
${}^4 D \approx {}^4 D_{\text{Vald+corr}} = {}^1 D^4 + 4({}^3 D - {}^1 D^3) \wedge {}^1 D - 6({}^2 D - {}^1 D^2) \wedge {}^1 D^2 + 3 \underline{{}^2 \Delta \wedge {}^2 \Delta}$
${}^5 D \approx {}^5 D_{\text{Vald+corr}} = {}^1 D^5 + 10({}^2 D - {}^1 D^2) \wedge {}^1 D^3 - 10({}^3 D - {}^1 D^3) \wedge {}^1 D^2 + 5({}^4 D - {}^1 D^4) \wedge {}^1 D + 10 \underline{{}^3 \Delta \wedge {}^2 \Delta}$

tween a group of three particles and a group of two particles; thus, $k_5 = 10$.

Cumulants

The reconstruction functionals, derived in the previous section through the particle-hole duality, may also be produced through the theory of cumulants [25–28]. We begin by constructing a functional whose derivatives with respect to probe variables generate the reduced density matrices in second quantization. Because we require that additional derivatives increase the number of second-quantization operators, we are led to the following exponential form:

$$G(J) = \langle \psi | O \left(\exp \left(\sum_k J_k a_k^\dagger + J_k^* a_k \right) \right) | \psi \rangle, \quad (39)$$

where the J_k and its conjugate J_k^* are Schwinger probe variables. For fermions these Schwinger probes have the property that they anticommute, $\{J_k, J_l\} = 0$. Differentiation of $G(J)$ with respect to the probes leads to the accumulation of creation and annihilation operators before the exponential. Because the annihilation and creation operators do not commute, we need to impose a specific ordering for these operators which appear before the exponential after differentiation. Since we wish to form functionals for RDMs, we define that the creation operators should always appear to the left of the annihilation operators independent of the order in which we differentiate with respect to the probes. If we wished to produce the corresponding HRDM functionals, we would order the annihilators to the left of the creators. We represent this ordering convention through the ordering operator O in the definition of $G(J)$. This ordering process is analogous to the time ordering of the creation and annihilation operators which appears in the theory of Green's functions [29].

The general relation between the differentiation of $G(J)$ with respect to the Schwinger probes and the RDMs may be characterized as

$$\begin{aligned} {}^p D_{j_1, j_2, \dots, j_p}^{i_1, i_2, \dots, i_p} \\ = \lim_{J \rightarrow 0} \frac{1}{p!} \frac{\partial^p G}{\partial J_{i_p} \partial J_{i_{p-1}} \dots \partial J_{i_2} \partial J_{i_1} \partial J_{j_1}^* \partial J_{j_{p-1}}^* \partial J_{j_p}^*} \end{aligned} \quad (40)$$

$$= \frac{1}{p!} \langle \psi | a_{i_1}^\dagger a_{i_2}^\dagger \dots a_{i_p}^\dagger a_{j_p} a_{j_{p-1}} \dots a_{j_1} | \psi \rangle. \quad (41)$$

The coefficients of the multivariable Taylor series expansion of $G(J)$ about the point where the Schwinger probes vanish are elements of the RDMs. Thus, $G(J)$ is known as the *generating functional* for RDMs. Mathematically, the RDMs of the functional $G(J)$ are known as the *moments*. The moment-generating functional $G(J)$ may be used to define another functional $W(J)$, known as the cumulant-generating functional, by the relation

$$G(J) = \exp(W(J)). \quad (42)$$

Just as the moments are formed from $G(J)$ as in Eq. (41), the *cumulants* ${}^p \Delta$ are produced from $W(J)$ by

$$\begin{aligned} {}^p \Delta_{j_1, j_2, \dots, j_p}^{i_1, i_2, \dots, i_p} \\ = \lim_{J \rightarrow 0} \frac{1}{p!} \frac{\partial^p W}{\partial J_{i_p} \partial J_{i_{p-1}} \dots \partial J_{i_2} \partial J_{i_1} \partial J_{j_1}^* \partial J_{j_{p-1}}^* \partial J_{j_p}^*}, \end{aligned} \quad (43)$$

and the cumulants are defined as the coefficients of the multivariable Taylor series expansion of $W(J)$ about the point where the Schwinger probes vanish. The introduction of another generating functional $W(J)$ in Eq. (42) may seem unnecessary. The set of cumulants ${}^p \Delta$ for p ranging from 1 to q contains the same information as the set of moments ${}^p D$ for the same range of p , but the information is distributed differently. This different distribution of information will allow us to determine the reconstruction functionals for building higher RDMs from lower RDMs.

As explained by Kubo [25], cumulants have the special property that they vanish if and only if one of their particles is statistically independent of the rest. Thus, for a mean field approximation (Hartree-Fock) where each of the N particles is treated independently all cumulants except ${}^1 \Delta$ vanish. Another way of interpreting this property of cumulants is to say that the p -particle cumulant ${}^p \Delta$ represents the part of the p -RDM which cannot be written as a simple wedge product of lower RDMs. The formula for ${}^3 D_{\text{vald}}$ from Table I accounts for situations where two of the particles are close enough to interact while the remaining particle is sufficiently separated in space for us to assume that it is statistically independent of the others. Therefore, approximating the 3-RDM as a func-

tional of the lower RDMs is equivalent to assuming that ${}^3\Delta$ vanishes. Similarly, the remaining functionals in Table I which express the given p -RDM as a functional of lower RDMs do not accurately represent configurations in which all p particles are close enough to be simultaneously influenced by pairwise interactions. They assume that ${}^p\Delta$ vanishes. By analogy with the convention for Green's functions in quantum field theory [29], we define the p -particle *unconnected* RDM (p -URDM) as the part of the p -RDM which can be written as wedge products of lower RDMs while the p -particle *connected* RDM (p -CRDM) is the remaining portion of the RDM which cannot be expressed as antisymmetrized products of lower RDMs. Hence, the connected RDMs are just the cumulants.

We may express the p -RDM in terms of the q -CRDMS for q between 1 and p by differentiating Eq. (42) with respect to the Schwinger probes as in Eq. (40) and taking the limit as the probes approach zero. The derivatives of the generating functional $G(J)$ produce the p -RDM while differentiation of $\exp(W)$ on the right side produces products of elements from the CRDMs according to Eq. (43). Because the formula for an element of the p -RDM must treat the permutation of the upper and lower indices antisymmetrically, the products between elements of CRDMs may be replaced with wedge products. As before, this allows us to write the formulas concisely through the wedge products of Grassmann algebra. The results for the p -RDMs through $p = 6$ are summarized in Table II. These functionals for the p -RDMs are exact, but they include the p -CRDM. An approximation for the p -RDM in terms of lower RDMs may be achieved by setting the connected portion ${}^p\Delta$ to zero. In this way we recover the functionals for the p -RDMs in Table I with corrections. Thus, through the particle-hole duality we

were able to generate the unconnected portion of the p -RDM exactly. Again the terms missing in Valdemoro's approximation are denoted by an underline. In general any terms involving only ${}^q\Delta$ where $q > 1$ will cancel with the corresponding p -HRDM correction and not appear in Valdemoro's approximation.

The reconstruction functionals may be understood as substantially renormalized many-body perturbation expansions. When exact lower RDMs are employed in the functionals, contributions from *all* orders of perturbation theory are contained in the reconstructed RDMs. As mentioned previously, the reconstruction exactly accounts for configurations in which at least one particle is statistically isolated from the others. Since we know the unconnected p -RDM exactly, all of the error arises from our imprecise knowledge of the p -CRDM. The connected nature of the p -CRDM will allow us to estimate the size of its error. For a Hamiltonian with no more than 2-particle interactions the p -CRDM will have its first nonvanishing term in the $(p - 1)$ order of the MBPT with a Hartree-Fock reference. This assertion may be understood by noticing that the minimum number of pairwise potentials V required to connect p particles completely is $(p - 1)$. It follows from this that as the number of particles p in the reconstructed RDM increases, the accuracy of the functional approximation improves. The reconstruction formula in Table I for the 2-RDM is equivalent to the Hartree-Fock approximation since it assumes that the two particles are statistically independent. Correlation corrections first appear in the 3-RDM functional which is correct through first order of MBPT, and the 4-RDM functional is correct through second order of MBPT.

The iterative solution of the 2,4-CSchE requires the reconstruction of both the 3- and 4-RDMs from

TABLE II
Reconstruction functionals for the p -RDMs in terms of the p -CRDM and lower CRDMs where corrections beyond Valdemoro's approximation are underlined.

$$\begin{aligned}
 {}^1D &= {}^1\Delta \\
 {}^2D &= {}^1\Delta \wedge \underline{{}^1\Delta} + {}^2\Delta \\
 {}^3D &= {}^1\Delta^3 + 3 \underline{{}^2\Delta} \wedge {}^1\Delta + {}^3\Delta \\
 {}^4D &= {}^1\Delta^4 + 6 \underline{{}^2\Delta} \wedge {}^1\Delta^2 + 4 \underline{{}^3\Delta} \wedge {}^1\Delta + 3 \underline{{}^2\Delta^2} + {}^4\Delta \\
 {}^5D &= {}^1\Delta^5 + 10 \underline{{}^2\Delta} \wedge {}^1\Delta^3 + 10 \underline{{}^3\Delta} \wedge {}^1\Delta^2 + 15 \underline{{}^2\Delta^2} \wedge {}^1\Delta + 5 \underline{{}^4\Delta} \wedge {}^1\Delta + 10 \underline{{}^3\Delta} \wedge {}^2\Delta + {}^5\Delta \\
 {}^6D &= {}^1\Delta^6 + 15 \underline{{}^2\Delta} \wedge {}^1\Delta^4 + 20 \underline{{}^3\Delta} \wedge {}^1\Delta^3 + 45 \underline{{}^2\Delta^2} \wedge {}^1\Delta^2 + 15 \underline{{}^4\Delta} \wedge {}^1\Delta^2 + 60 \underline{{}^3\Delta} \wedge {}^2\Delta \wedge {}^1\Delta \\
 &\quad + 6 \underline{{}^5\Delta} \wedge {}^1\Delta + 15 \underline{{}^2\Delta^3} + 15 \underline{{}^4\Delta} \wedge {}^2\Delta + 10 \underline{{}^3\Delta^2} + {}^6\Delta
 \end{aligned}$$

the 2-RDM. Since the 3-RDM formula is missing some second-order corrections while the 4-RDM functional is exact through second order, the resulting 4-RDM will only be accurate to first order when we build from the 2-RDM with a functional of unconnected RDMs. We would like to achieve scheme consistency for the 3- and 4-RDM reconstructions such that they both are correct through second order [19]. In a previous study [3] we introduced a technique for building a 3-RDM which includes the second-order correction of the 4-RDM. This is achieved by contracting the 4-RDM functional in Table I to the 3-RDM:

$$\begin{aligned} {}^3D_{\text{impr}} = & \frac{4}{N-3} L_4^3 ({}^1D^4 + 4 {}^3\Delta ({}^3D_{\text{impr}}) \wedge {}^1D \\ & + 6 {}^2\Delta \wedge {}^1D^2 + 3 {}^2\Delta \wedge {}^2\Delta), \quad (44) \end{aligned}$$

where L_4^3 is the contraction operator which represents the necessary summation to obtain the 3-RDM from a 4-RDM. Because the 3-RDM appears in the 4-RDM formula, this process generates a system of equations whose solution yields an improved 3-RDM ${}^3D_{\text{impr}}$. The contraction mapping from the 4-RDM to the 3-RDM maps each order of the perturbative expansion of the 4-RDM to the same order in the 3-RDM. Therefore, when we only neglect ${}^4\Delta$ in our approximation for the 4-RDM, we have a 4-RDM which is correct through second order; after contraction this translates into a system of equations for the 3-RDM which is correct through second order. Using the connection between RDMs and Green's functions, Yasuda and Nakatsuji have employed Feynman–Dyson perturbation theory to estimate the second-order correction for the 3-CRDM [14]. In the present study we explore a third approach for achieving a 3-RDM which is correct to second order with the 3,5-CSchE. To remove the indeterminacy of the 3,5-CSchE, we need to build both the 4- and 5-RDMs from the 3-RDM. Reconstruction of the 5-RDM from the 4-RDM is correct through third order while building the 4-RDM from the 3-RDM is correct through second order. While not scheme consistent, this method is already accurate through second order. However, we can also achieve scheme consistency by using Valdemoro's formula for the 5-RDM without the term $10 {}^3\Delta \wedge {}^2\Delta$ since this term is the third-order correction. Unlike the available approaches for solving the 2,4-CSchE through second order, the solution of the 3,5-CSchE allows us to

perform all reconstructions through the wedge products of lower RDMs *without* solving large systems of linear equations.

Application

To explore the accuracy of solving many-body systems with the 3,5-CSchE and the derived reconstruction functionals, we solve for the ground-state energies and 2-particle density matrices of a quasi-spin model which we previously employed to compare solutions of the 2,4-CSchE with traditional wave function techniques for electronic structure. The model was originally used by Lipkin as a benchmark to investigate fermionic correlation phenomena [20, 30]. The Lipkin model consists of N degenerate states with an energy of $-\epsilon/2$ and another N degenerate states with an energy of $+\epsilon/2$. For each state there is a unique pair of quantum numbers m and p . The quantum number m indicates whether the state is a member of the upper ($m = +1$) or lower ($m = -1$) energy level, and the quantum number p , ranging from 1 to N , specifies the position of the state in a given level. These energy levels are filled with N fermions where at most only one fermion can occupy a given state. For noninteracting fermions, the configuration of lowest energy $-Ne/2$ is achieved when each of the N fermions occupies one of the N states in the lower energy level $-\epsilon/2$. We add an interaction to the noninteracting system according to the Hamiltonian

$$\begin{aligned} H = & \frac{\epsilon}{2} \sum_{m, p} m a_{m, p}^\dagger a_{m, p} \\ & + V \sum_{p_1, p_2, m} a_{m, p_1}^\dagger a_{m, p_2}^\dagger a_{-m, p_2} a_{-m, p_1}, \quad (45) \end{aligned}$$

where V is the interaction strength. By the nature of the V interaction term, the noninteracting ground-state configuration only mixes with configurations in which each fermion has a different p quantum number. Hence, for a nonzero value of the V parameter a total of 2^N configurations may contribute to the correlated ground state of the system. Because of the model's symmetry, however, we can group the configurations into $N+1$ classes. This reduction in basis size and additional computational details may be found elsewhere [3].

The 3,5-CSchE in Eq. (9) is solved iteratively. The following scheme resembles the one employed by Valdemoro:

- Choose a trial 3-RDM and reconstruct the 4- and 5-RDMs.
- Use these 3-, 4- and 5-RDMs to build the corresponding R matrix through Eq. (11).
- Evaluate the left-hand side of the 3,5-CSchE in Eq. (9) with R .
- Divide the resulting matrix from the previous step by the energy of the original trial 3-RDM to generate a new trial 3-RDM.
- Antisymmetrize and normalize the new trial 3-RDM.
- Repeat all steps with the new trial 3-RDM until suitable convergence is achieved.

This procedure is equivalent to the power method for an uncontracted eigenvalue equation [3]. A similar scheme is employed for the 2,4-CSchE except for the obvious difference that we iterate and reconstruct with the 2-RDM. To accelerate convergence, we use polynomial extrapolation [31] of the trial 3-RDMs after every three iterations to achieve a better estimate for the next trial 3-RDM. The three consecutive 3-RDMs are assigned to the first three values in the integer series for $1/n$ ($1, \frac{1}{2}$, and

$\frac{1}{3}$), and then we extrapolate to zero which gives us a guess for the result after an infinite number of iterations.

The energies from solving the Lipkin model with the 3,5-CSchE are summarized in Table III for the number of fermions N ranging from 5 to 50. The error in the correlation energy is also reported as a percentage where the sign indicates the direction of the energy error. The energies in Table III are dimensionless because we perform calculations with the scaled Hamiltonian obtained by dividing the H in Eq. (45) by ϵ . The dimensionless interaction strength $\tilde{V} (= V/\epsilon)$ is chosen for each N to make the ratio of correlation energy to total energy in the Lipkin model consistent with the values reported in the literature for atoms with the corresponding number N of electrons [32, 33]. In Table IV we report the errors in the calculated 2-RDMs which were measured by the square norm of the difference between the exact and approximate RDMs. Two different 3,5-CSchE calculations are given Table III and IV: (V) where the 5-RDM is constructed using Valdemoro's formula and (U) where the 5-RDM is built with Valdemoro's formula plus the additional underlined correction in Table I. Both methods employ Valdemoro's functional for the 4-RDM with the unconnected correction. Since the reconstruction from the 3-RDM to the 4-RDM neglects the 4-CRDM which contains

TABLE III
Ground-state energies from the CSchE methods are compared to the values from traditional wave function approaches for a range of N within the Lipkin model.

N	CSchE methods			Wave function methods				
	3,5 (V)	3,5 (U)	2,4	HF	RS2	RS3	SDCI	FCI
\tilde{V}	Energy							
	Error in correlation energy as a percentage							
5	-2.512467	-2.512478	-2.512396	-2.5	-2.512554	-2.512522	-2.512476	-2.512546
0.050108	0.62	0.53	1.19	100	-0.06	0.18	0.55	0
10	-5.015357	-5.014338	-5.015778	-5	-5.015761	-5.016192	-5.015639	-5.015869
0.026467	3.22	9.65	0.57	100	0.68	-2.03	1.45	0
20	-10.011923	-10.011820	-10.012600	-10	-10.012483	-10.012924	-10.012406	-10.012595
0.015438	5.33	6.15	-0.03	100	0.88	-2.61	1.49	0
30	-15.013404	-15.013613	-15.014257	-15	-15.014062	-15.014698	-15.013965	-15.014225
0.011463	5.76	4.29	-0.22	100	1.13	-3.32	1.82	0
40	-20.012436	-20.012598	-20.012983	-20	-20.012804	-20.013363	-20.012723	-20.012947
0.009170	3.94	2.69	-0.27	100	1.10	-3.21	1.72	0
50	-25.012525	-25.012721	-25.013016	-25	-25.012828	-25.013408	-25.012746	-25.012976
0.008040	3.47	1.96	-0.30	100	1.14	-3.32	1.76	0

TABLE IV

Errors in the 2-RDMs from the CSchE methods are compared to the errors from traditional wave function approaches for a range of N within the Lipkin model.^a

N	CSchE methods			Wave function methods				
	3,5 (V)	3,5 (U)	2,4	HF	RS2	RS3	SDCI	FCI
5	6.10×10^{-5}	6.50×10^{-5}	1.92×10^{-4}	2.70×10^{-2}	4.35×10^{-5}	2.13×10^{-5}	3.03×10^{-4}	0
10	1.43×10^{-4}	3.17×10^{-4}	8.50×10^{-5}	1.49×10^{-2}	2.09×10^{-4}	5.62×10^{-5}	4.48×10^{-4}	0
20	1.02×10^{-4}	1.26×10^{-4}	2.35×10^{-5}	6.48×10^{-2}	1.20×10^{-4}	3.21×10^{-5}	2.02×10^{-4}	0
30	9.46×10^{-5}	1.22×10^{-4}	2.19×10^{-5}	4.61×10^{-2}	1.10×10^{-4}	3.19×10^{-5}	1.76×10^{-4}	0
40	9.61×10^{-5}	1.17×10^{-4}	2.17×10^{-5}	3.27×10^{-2}	7.56×10^{-5}	2.13×10^{-5}	1.18×10^{-4}	0
50	1.03×10^{-4}	1.15×10^{-4}	2.33×10^{-5}	2.62×10^{-2}	6.28×10^{-5}	1.78×10^{-5}	9.68×10^{-5}	0

^a The errors are measured by computing the square norm of the difference between an approximate 2-RDM and the exact 2-RDM.

third-order terms, the addition of the third-order correction to the 5-RDM in method (U) should not improve the reconstruction. Indeed the resulting energies and 2-RDMs are similar in accuracy throughout the range of N .

For comparison the solutions of the 2,4-CSchE are also given as well as the results from more traditional wave function approaches such as Hartree–Fock (HF), second- and third-order Rayleigh–Schrödinger perturbation theory (RS2 and RS3) for the 2-RDM, single–double configura-

tion interaction (SDCI), and full configuration interaction (FCI). The 2,4-CSchE is solved with the correction for the 3-RDM in Eq. (44) and Valdemoro's functional for the 4-RDM with corrections. Attempts to solve the 2,4-CSchE with only the unconnected reconstruction functionals in Table I led to the divergence of the 2-RDMs after a few iterations. Similar divergence was reported by Nakatsuji and Yasuda [13, 14]. Comparisons of the energies and 2-RDMs are easily visualized in Figures 1 and 2 which plot the 3,5-CSchE (V), the

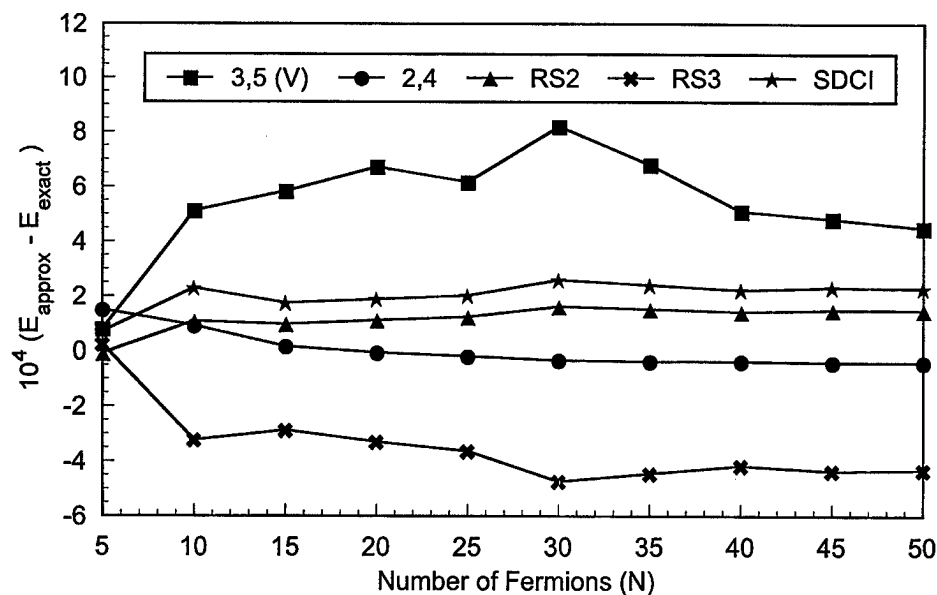


FIGURE 1. Difference between the approximate energy and the FCI energy is presented as a function of N for the 2,4 and 3,5-CSchE methods as well as three wave function methods, second- and third-order RS perturbation theory for the 2-RDMs and SDCl.

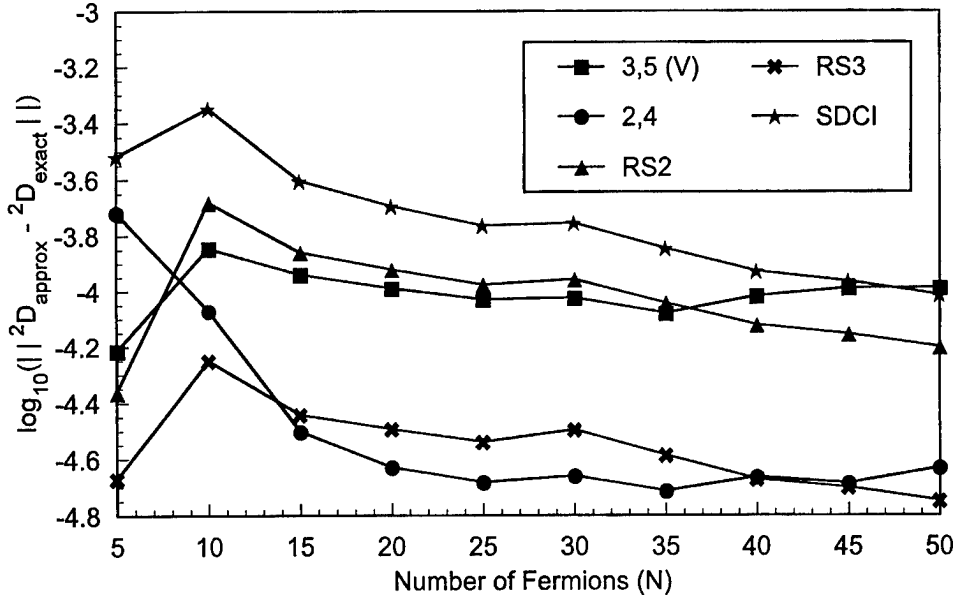


FIGURE 2. Logarithmic errors in the approximate 2-RDMs, generated by the 2,4 and 3,5-CSchE methods as well as SDCI and second- and third-order RS perturbation theory for 2-RDMs, are shown for a range of N . We measure the error in an approximate 2-RDM by taking the square norm of its deviation from the exact 2-RDM.

2,4-CSchE, and the wave function methods. The 3,5-CSchE produces energies that are similar in accuracy to those from RS3 and 2-RDMs similar to those from RS2 but slightly better than those from SDCI. While the reconstruction formulas employed to solve both the 2,4-CSchE and the 3,5-CSchE are exact through second order of MBPT for the RDMs, the 2,4-CSchE gives energies and 2-RDMs which are an order of magnitude better than those from the 3,5-CSchE. Unlike the 2,4 solution, however, the 3,5-CSchE employs only reconstruction with unconnected terms.

Discussion

Solution of the 2,4 or 3,5-CSchE depends on the reconstruction of higher RDMs from lower RDMs. The importance of the reconstruction represents a similarity between the CSchE formalism and density functional theory (DFT). The universal energy functional within DFT may be considered as a reconstruction strategy from the 1-density to the 2-RDM since the energy may be written explicitly as the expectation value of the 2-RDM with the 2-particle reduced Hamiltonian 2K . Within the CSchE techniques the higher RDMs are built from either the 2- or 3-RDMs. Yet the reconstruction methods for DFT and the CSchE have an impor-

tant difference. While the theorem of Hohenberg–Kohn (HK) states that the 1-density and the particle number N uniquely determine the ground-state energy and wave function for an electronic system, it requires that information about the Hamiltonian's kinetic and electron–electron repulsion terms be conveyed through the unknown functional. The reconstruction functionals which we have presented, however, do not explicitly contain any information about the Hamiltonian. They may correspond to electronic, quasi-spin, and many other systems. Either the 1-density or the 1-RDM alone is insufficient for reconstructing the N -particle wave function (preimage) of a correlated system without more specific information concerning the Hamiltonian. From a recent result by Coleman [34] it follows that every 1-RDM, deriving from a Hamiltonian which is invariant under time-reversal [35], may be obtained from the contraction of some pure N -particle density matrix corresponding to an antisymmetrized geminal power (AGP) wave function even if the preimage of interest is not an AGP function. In contrast to the 1-RDM, without any specific information about the Hamiltonian other than that it contain no more than pairwise interactions, a ground-state 2-RDM contains enough information to determine its preimage exactly (Rosina's theorem) [3, 36]. Therefore, Rosina's theorem, rather than the HK theorem,

provides the foundation for reconstruction from the 2- and 3-RDMs within the CSchE methods.

The reconstruction functionals were derived by two different paths, the particle–hole duality and the theory of cumulants. From the particle–hole perspective the functional for the p -RDM reflects the complexity of the commutation (if p even) or anticommutation (if p odd) relation for a composite particle containing p fermions. The resulting functionals, which we call Valdemoro's functionals, are approximate because some terms which are equal in the particle and hole functionals cancel with each other in the particle–hole relations. We are able to infer some of these missing terms from the lower relations. The statistical theory of cumulants [25, 28] provides us with a systematic procedure for obtaining *all* of the terms for the p -RDM functional which may be expressed as simple wedge products of lower RDMs, the unconnected terms. The functionals from the cumulant approach agree with those obtained through the particle–hole duality with inferred corrections. Assuming that the *connected* portion of the p -RDM vanishes is equivalent to accounting correctly for configurations where at least one particle may be assumed to be statistically independent of the remaining $p - 1$ particles. However, correlated systems will always have configurations in which all p fermions are close enough to interact pairwise even though these configurations may be less important than the others. Thus, while the p -CRDM may be small, we would not expect the p -CRDM to vanish completely in a real system of correlated particles. Related to this idea is a theorem which proves that the vanishing of the p -CRDMs for all $p \geq q$ where $q \geq 3$ would violate the necessary positivity of the moment generating functional $G(J)$ [37–39]. Note that this is only for $p \geq 3$. In systems of independent particles, as in Hartree–Fock models, all of the higher RDMs may be expressed exactly as unconnected wedge products of the 1-RDM with itself because the p -CRDMs for $p \geq 2$ vanish.

The notion of connected allows us to forge relationships between the reconstruction functionals and renormalization of MBPT. Since the reconstruction functionals depend on the exact lower RDMs, they contain contributions from all orders of perturbation theory. Furthermore, we were able to demonstrate that the neglected p -CRDM has its first nonvanishing contribution from the $p - 1$ term of the MBPT expansion of the RDM. The p -RDM functional is thus exact through the first

$p - 2$ perturbative corrections beyond Hartree–Fock. For a noninteracting system the p -RDM reconstruction formulas in Table I become equal to the 1-RDM wedged with itself p times. These simplified formulas ${}^1D^p$ may be interpreted as a statement of Wick's theorem [29]. Recall that the time-independent Wick's theorem states that the expectation value of creation and annihilation operators with a noninteracting wave function may be evaluated by the sum of all complete contractions. Applying this rule to the p -RDM generates the wedge products of the 1-RDM with itself. Since any expression of creation and annihilation operators may be rearranged by the anticommutation relation so that all creation operators appear to the left of the annihilation operators as in the definition for the p -RDM, we can use this formula for the p -RDM, which is equivalent to Wick's theorem, to evaluate the expectation value of fermion operators in any order with respect to a noninteracting reference. Furthermore, the complete reconstruction functionals in Table II represent a generalization of Wick's theorem for interacting particles. We can utilize these functionals to express the expectation values of annihilation and creation operators with correlated references in terms of CRDMs. Expectation values, accurate to the $(p - 1)$ order of MBPT, may be formed by neglecting the p -CRDM and higher CRDMs. This may be useful for multireference coupled cluster and MBPT schemes. A related extension of Wick's theorem has recently been reported [40].

Two techniques currently exist for making the 3- and 4-RDM reconstruction functionals scheme consistent in the 2,4-CSchE. The relation between renormalized MBPT and the functionals indicates that building the 3-RDM from unconnected lower RDMs is accurate through first order while reconstruction of the 4-RDM from lower RDMs is correct through second order. To make these two schemes consistent through second order, we must add a connected correction to the 3-RDM. Yasuda and Nakatsuji have estimated the second-order correction through arguments involving Green's functions [14]. We have obtained a different correction by contracting the functional for the 4-RDM to the 3-RDM and then solving the resulting system of equations for an improved 3-RDM as indicated in Eq. (44) [3]. In this study we have presented a new approach based on the 3,5-CSchE for achieving a renormalized scheme for the 3-RDM that is correct through second order. We may think of the reconstruction of the 3-RDM as being per-

formed by the 3,5-CSchE with which we solve for the 3-RDM at each step of the algorithm. Although the size of the 5-RDM may seem prohibitive, the unconnected and hence explicit dependence of the 4- and 5-RDM functionals on the 3-RDM allows us for large systems and basis sets to solve the 3,5-CSchE iteratively without storing either the 4- or 5-RDMs. The ability to reach second-order accuracy without any connected corrections may represent an important advantage for the 3,5-CSchE approach. Comparison of the 3,5-CSchE with the 2,4-CSchE as well with traditional methods like MBPT for RDMs and SDCI gives promising results. By determining the 2-RDM directly, the 3,5 as well as the 2,4-CSchEs offer an approximate solution to the N -representability problem and a fresh approach for electron correlation.

ACKNOWLEDGMENTS

The author wishes to express his gratitude to Professor Dudley R. Herschbach, Professor A. J. Coleman, and Dr. Alexander R. Mazziotti for their advice and encouragement. The National Science Foundation is also acknowledged for supporting the work through a research fellowship.

References

1. A. J. Coleman, Rev. Mod. Phys. **35**, 668 (1963).
2. R. Erdahl and V. Smith, Eds., *Density Matrices and Density Functionals*, Proceedings of the A. J. Coleman Symposium, Kingston, Ontario, 1985 (Reidel, Dordrecht, 1987).
3. D. A. Mazziotti, Phys. Rev. A **57**, 4219 (1998).
4. L. Cohen and C. Frishberg, Phys. Rev. A **13**, 927 (1976).
5. H. Nakatsuji, Phys. Rev. A **14**, 41 (1976).
6. J. E. Harriman, Phys. Rev. A **19**, 1893 (1979).
7. C. Valdemoro, in *Density Matrices and Density Functionals*, Proceedings of the A. J. Coleman Symposium, Kingston, Ontario, 1985, R. Erdahl and V. Smith, Eds. (Reidel, Dordrecht, 1987).
8. F. Colmenero, C. Perez del Valle, and C. Valdemoro, Phys. Rev. A **47**, 971 (1993).
9. F. Colmenero and C. Valdemoro, Phys. Rev. A **47**, 979 (1993).
10. F. Colmenero and C. Valdemoro, Int. J. Quant. Chem. **51**, 369 (1994).
11. C. Valdemoro, in *Strategies and Applications in Quantum Chemistry*, Y. Ellinger and M. Defrancheschi, Eds. (Kluwer, Netherlands, 1996), p. 55.
12. C. Valdemoro, L. M. Tel, and E. Perez-Romero, Adv. Quant. Chem. **28**, 33 (1997).
13. H. Nakatsuji and K. Yasuda, Phys. Rev. Lett. **76**, 1039 (1996).
14. K. Yasuda and H. Nakatsuji, Phys. Rev. A **56**, 2648 (1997).
15. A. L. Fetter and J. D. Walecka, *Quantum Theory of Many-Particle Systems* (McGraw-Hill, New York, 1971).
16. D. A. Mazziotti, M. K. Mishra, and H. A. Rabitz, J. Phys. Chem. **99**, 112 (1995).
17. D. A. Mazziotti and H. A. Rabitz, Mol. Phys. **89**, 171 (1996).
18. A. Tarantelli and L. S. Cederbaum, Phys. Rev. A **46**, 81 (1992).
19. A. Tarantelli and L. S. Cederbaum, Phys. Rev. A **49**, 3407 (1994).
20. H. J. Lipkin, N. Meshkov, and A. J. Glick, Nucl. Phys. **62**, 188, 199, 211 (1965).
21. J. Planelles, C. Valdemoro, and J. Karwowski, Phys. Rev. A **41**, 2391 (1990).
22. R. M. Erdahl, J. Math. Phys. **13**, 1608 (1972).
23. M. B. Ruskai, J. Math. Phys. **11**, 3218 (1970).
24. W. Słobodziński, *Esterior Forms and their Applications* (Polish Scientific Publishers, Warsaw, 1970).
25. R. Kubo, J. Phys. Soc. (Japan) **17**, 1100 (1962).
26. C. W. Gardiner, *Handbook of Stochastic Methods for Physics, Chemistry and the Natural Sciences* (Springer, New York, 1983).
27. K. Kladko and P. Fulde, Int. J. Quant. Chem. **66**, 377 (1998).
28. D. A. Mazziotti, Chem. Phys. Lett., submitted.
29. J. W. Negele and H. Orland, *Quantum Many-particle Systems* (Addison-Wesley, New York, 1988).
30. M. V. Mihailović and M. Rosina, Nucl. Phys. **A130**, 386 (1969).
31. W. H. Press, S. A. Teukolsky, W. T. Vetterling, and B. P. Flannery, *Numerical Recipes in FORTRAN: The Art of Scientific Computing*, 2nd ed. (Cambridge University Press, New York, 1992).
32. S. J. Chakravorty, S. R. Gwaltney, E. R. Davidson, F. A. Parpia, and C. F. Fischer, Phys. Rev. A **47**, 3659 (1993).
33. E. Clementi and G. Corongiu, Int. J. Quan. Chem. **62**, 571 (1997).
34. A. J. Coleman, Int. J. Quant. Chem. **63**, 23 (1997).
35. D. W. Smith, Phys. Rev. A **147**, 896 (1966).
36. M. Rosina, in *Reduced Density Operators with Application to Physical and Chemical Systems*, Queens Papers in Pure and Applied Mathematics No. 11, A. J. Coleman and R. M. Erdahl, Eds. (Queen's University, Kingston, Ontario, 1968).
37. J. Marcinkiewicz, Math. Z. **44**, 612 (1939).
38. D. W. Robinson, Commun. Math. Phys. **1**, 89 (1965).
39. A. K. Rajagopal and E. C. G. Sudarshan, Phys. Rev. A **10**, 1852 (1974).
40. W. Kutzelnigg and D. Mukherjee, J. Chem. Phys. **107**, 432 (1997).

Nonconventional Partitioning of the Many-Body Hamiltonian for Studying Correlation Effects

PÉTER R. SURJÁN, MIHÁLY KÁLLAY, ÁGNES SZABADOS

Department of Theoretical Chemistry, Eötvös University, H-1518 Budapest 112, POB 32, Hungary

Received 21 February 1998; revised 24 June 1998; accepted 10 July 1998

ABSTRACT: For the treatment of electron correlation, one most often uses the Møller-Plesset (MP) partition which defines the zero-order Hamiltonian through the spectral resolution of the Fockian. We investigate how the MP partitioning can be improved while still using the Hartree-Fock (HF) reference state; and how the HF wave function can be substituted by a correlated one preserving the formal simplicity of the HF-based approach. To improve the MP n result, we introduce a fine tuning of energy denominators replacing the HF orbital energies with the ionization potentials obtained from the second-order Dyson equation. As this equation usually tends to close the gaps, a slight decrease of the denominators is expected, inducing an improvement of low-order correlation energies. We keep the simplicity of the MP partitioning and handle Dyson corrections as simple level shifts. Substituting doubly filled HF orbitals by strongly orthogonal geminals, one introduces a correlated reference state which is variational, size-consistent, and properly describes single-bond dissociation. This wave function, the antisymmetrized product of strongly orthogonal geminals (APSG), offers a good starting point for further corrections. We show that the use of an APSG reference state in the equation-of-motion technique leads to Tamm-Dankoff approach (TDA) equations which account for correlation effects in electronic excitation energies. © 1998 John Wiley & Sons, Inc. *Int J Quant Chem* 70: 571–581, 1998

Key words: partitioning; level shift; quasi-degenerate PT; Dyson equation; geminals; excited states

Correspondence to: P. R. Surján.
Contract grant sponsor: OTKA.
Contract grant number: T021179-T023052.

Introduction

Perturbation theory, with a variety of its formalisms [1], has been a powerful tool for taking small interactions into account. In some cases the splitting of the total Hamiltonian comes up naturally, being motivated by the physics of the problem (cf. molecules in external fields), while in other situations the partitioning is ambiguous and can only be governed by mathematical and numerical considerations. An example for this latter case is represented by many-body perturbation theory (MBPT) as applied to the calculation of electronic energies in molecules. Here the partitioning of the total electronic Hamiltonian is motivated by selecting a zeroth order which is easily soluble—a practical rather than unambiguous factor.

In the most widely used partitioning of this type one chooses the Hartree–Fock (HF) level to define the zeroth order. This choice still allows for various possibilities. The most straightforward idea is to consider the diagonal elements of the configuration interaction (CI) matrix as zero-order levels, while the off-diagonals represent the perturbation (Epstein–Nesbet, EN, partitioning [2, 3]). Much better numerical results are obtained from the Møller–Plesset (MP) partitioning [4], where one chooses the Fockian as zeroth-order operator. Though the n th order (MP_n) corrections do not offer an upper bound to the energy, general experience tells us that they usually underestimate the correlation energy for small n .

Standard MP_n corrections with a simple closed-shell reference state are applicable only if the restricted HF determinant is an acceptable approximation. Dissociation curves or other quasi-degenerate situations require a multireference approach [5–14], special damping techniques [15–17], or a repartitioning of the Hamiltonian by a suitable level shift [10, 18–20] to remove quasidegeneracies from the zeroth-order spectrum. A different sort of repartitioning has been applied by Kapuy et al. [21–23] in their MBPT with localized molecular orbitals (LMOs): They select the diagonal elements of the Fockian in LMO basis as zero-order energies and treat the off-diagonals as one-electron perturbations.

In approximating the exact energy, it is not necessary to start at the HF level. One may quote

the old idea of the PCILO method [24] where approximate, strictly localized MOs are used at the zeroth order. Correlation and delocalization effects are treated by PT on an equal footing, thus the zeroth-order approximation in PCILO is weaker than HF. Oppositely, one may use a zeroth order which is better than HF (cf. the multireference PT approaches [5–10] or attempts to improve geminal approximations perturbatively [25–30]).

In this study we shall investigate two kinds of repartitioning in MBPT. In the following section, level shifts will be introduced within the framework of closed-shell MP theory, while in the third section the use of the antisymmetrized product of strongly orthogonal geminals (APSG) reference state will be discussed. A small number of preliminary test calculations will be reported in both cases.

Repartitioning by Level Shifts

REAL SHIFTS

In MP theory, one considers the partitioning

$$\hat{H} = \sum_i \epsilon_i a_i^+ a_i + \hat{W}, \quad (1)$$

where \hat{H} is the total many-body electronic Hamiltonian, ϵ_i 's are the canonical Hartree–Fock orbital energies, while a_i^+ and a_i are creation and annihilation operators for molecular spin-orbitals.

Applying a shift λ_i to level i corresponds to the repartitioning

$$\hat{H} = \sum_i \epsilon_i a_i^+ a_i + \hat{W}', \quad (2)$$

where

$$\epsilon_i' = \epsilon_i + \lambda_i \quad (3)$$

are the shifted one-particle energies.

Using Eq. (2), the second-order correction becomes

$$\Delta E^{(2)} = -\frac{1}{4} \sum_{pq, rs} \frac{[pq||rs]^2}{\epsilon_r + \epsilon_s - \epsilon_p - \epsilon_q} \quad (4)$$

with usual notations, p, q referring to occupied, r, s to virtual levels. The third-order correction undergoes a similar modification and, due to the diagonal perturbation represented by the level shift

operators, it is augmented by the term

$$-\frac{1}{4} \sum_{pq, rs} \frac{[rs \parallel pq]^2}{(\epsilon_r + \epsilon_s - \epsilon_p - \epsilon_q)^2} (\lambda_r + \lambda_s - \lambda_p - \lambda_q). \quad (5)$$

Such level shifts have been discussed previously by several authors [10, 18–20]. Recently [31], we started to investigate the idea of replacing ϵ_i with correlation-corrected ionization potentials or electron affinities ϵ_i obtained from the second-order inverse Dyson equation:

$$\begin{aligned} \epsilon_i = \epsilon_i + \frac{1}{2} \sum_{pqr} \frac{[ir \parallel pq]^2}{\epsilon_i + \epsilon_r - \epsilon_p - \epsilon_q} \\ + \frac{1}{2} \sum_{prs} \frac{[ip \parallel rs]^2}{\epsilon_i + \epsilon_p - \epsilon_r - \epsilon_s}. \end{aligned} \quad (6)$$

This formula originates from the theory of one-particle Green's functions [32–35] by truncating the self-energy at second order. Although it is not a good approximation to obtain accurate ionization potentials and electron affinities, it shifts the Koopmans values in a way to reduce energy gaps [e.g., highest occupied molecular orbital and lowest unoccupied molecular orbital (HOMO–LUMO) differences] in most cases. This feature of Eq. (6) is utilized in solid-state theory to compute correlation-corrected band structures [36, 37]. The slightly smaller energy denominators, received by substituting the Koopmans values ϵ_i by the Dyson-corrected ones ϵ_i , yield slightly larger MP2 corrections, thus a larger fraction of the correlation energy.

The nonlinear equations (6) for ϵ_i have to be solved iteratively. This is straightforward* if the root of the equation is far from all singularities (poles). In the general case, however, one has to introduce a complex damping of strength η

$$\begin{aligned} \epsilon_i = \epsilon_i + \frac{1}{2} \sum_{pqr} \frac{[ir \parallel pq]^2}{\epsilon_i + \epsilon_r - \epsilon_p - \epsilon_q - i\eta} \\ + \frac{1}{2} \sum_{prs} \frac{[ip \parallel rs]^2}{\epsilon_i + \epsilon_p - \epsilon_r - \epsilon_s + i\eta}, \end{aligned} \quad (7)$$

where η tends to zero. Separating the real and imaginary parts of this equation one may arrive at

* 50% damping is usually sufficient to ensure convergence of the standard iterative series.

the following damped expression:

$$\begin{aligned} \epsilon_i = \epsilon_i + \frac{1}{2} \sum_{pqr} \frac{[ir \parallel pq]^2 (\epsilon_i + \epsilon_r - \epsilon_p - \epsilon_q)}{(\epsilon_i + \epsilon_r - \epsilon_p - \epsilon_q)^2 + \eta^2} \\ + \frac{1}{2} \sum_{prs} \frac{[ip \parallel rs]^2 (\epsilon_i + \epsilon_p - \epsilon_r - \epsilon_s)}{(\epsilon_i + \epsilon_p - \epsilon_r - \epsilon_s)^2 + \eta^2}, \end{aligned} \quad (8)$$

which can be successfully used to avoid false roots and to ensure convergence. An example for the use of Eq. (8) is shown in Figure 1.

An even simpler, iteration-free, correction to the Koopmans values is obtained by standard MP2

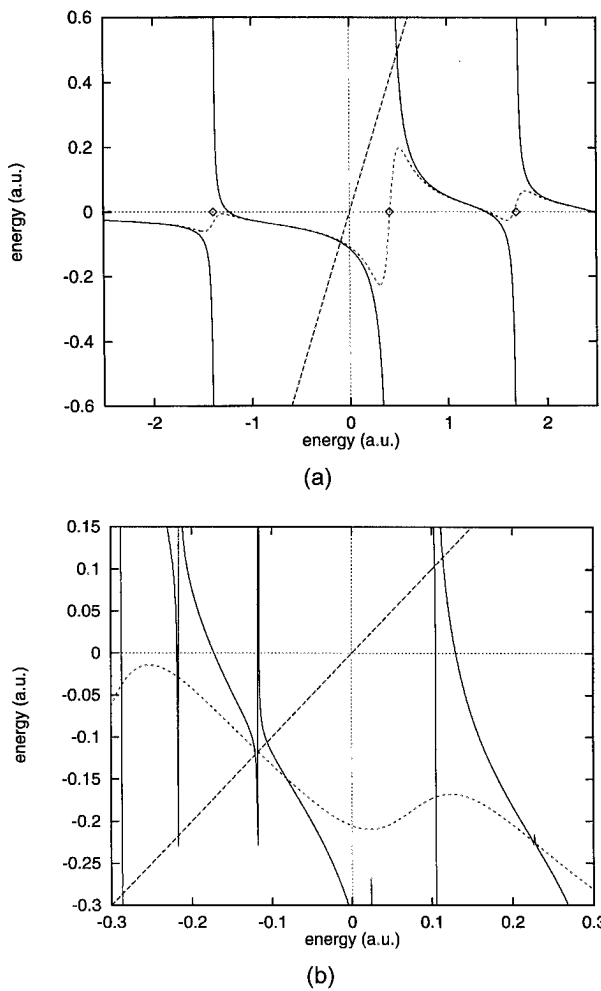


FIGURE 1. Solution of the second-order Dyson equation $\epsilon = f(\epsilon)$ with (dashed line) and without (solid line) damping. The straight dashed line is the left-hand side while the curves are plots of $f(\epsilon)$ at the right-hand side. (a) H_2 molecule 3-21G** basis, HOMO; (b) N_2 molecule 6-311G** basis, MO No.21.

theory to ionization energies

$$\epsilon_i^{\text{MP2}} = \epsilon_i + \frac{1}{2} \sum_{pqr} \frac{[ir||pq]^2}{\epsilon_i + \epsilon_r - \epsilon_p - \epsilon_q} + \frac{1}{2} \sum_{prs} \frac{[ip||rs]^2}{\epsilon_i + \epsilon_p - \epsilon_r - \epsilon_s}. \quad (9)$$

Clearly, this corresponds to the first iteration of Eq. (6). This formula has also been used to correct band structures in periodic systems [38–40].

IMAGINARY LEVEL SHIFTS

Similarly to the damping of Dyson equation, cf. Eq. (7), one can introduce an imaginary level shift in the energy denominator of the MP2 formula

$$\Delta E_{\text{complex}}^{[2]} = - \sum_k \frac{|W_{0k}|^2}{E_k - E_0 + i\Gamma_k}. \quad (10)$$

While in the case of Dyson equation the actual value of η is immaterial as, after achieving convergence to the correct root, the $\eta \rightarrow 0$ limit has to be considered, in the case of Eq. (10) a suitable choice for Γ has to be made, in order to make Eq. (10) valid in quasi-degenerate (QD) situations. Another question is how to extract a real number from $\Delta E_{\text{complex}}^{[2]}$ of Eq. (10). In Ref. [16], we took the term-by-term absolute value of this expression and determined Γ by requiring the resulting formula to be exact for a fully degenerate two-level system [16] ($\Gamma_k = W_{0k}$), or by fitting Γ to the relevant term of the fourth-order expression [41, 42] ($\Gamma_k = 2W_{0k}$). In a recent study, Forsberg and Malmqvist [43] took the real component of Eq. (10), just like Eq. (8). This has the advantage that it can also be

applied for excited states (negative excitation energies), but has the disadvantage that it kills a fully degenerate term completely, thus it is inadequate, e.g., for a degenerate two-level system. Forsberg and Malmqvist do not aim to prescribe the value of Γ but check the results for several values.

Taking the absolute value of each term in Eq. (10), preserving the overall negative sign and using $\Gamma_k = 2W_{0k}$, we get the formula

$$\Delta E^{\text{QD2}} = - \sum_k \frac{|W_{0k}|^2}{\sqrt{(E_k - E_0)^2 + 4|W_{0k}|^2}}. \quad (11)$$

This was found to work properly in quasi-degenerate situations which can otherwise be handled by the substantially more complicated quasi-degenerate PT formalism [11]. We note that another type of straightforward modification of the MP2 formula was proposed by Assfeld et al. [44], who applied the unexpanded square root which occurs in the exact formula of the corresponding 2-by-2 problem for each state. As this expression does not contain energy denominators, it may also be useful in quasi-degenerate situations.

NUMERICAL EXAMPLES

The efficiency of the above ideas has been tested calculating a few examples which are to be considered as forming a preliminary rather than representative set. Table I presents correlation energies for He and Ne atoms, the LiH molecule, and a cluster of 8 hydrogen atoms arranged in a linear chain with an equidistant (“metallic”) geometry of $R = 1$ Å. Second-and third-order (MP n) energies are evaluated with standard partitioning (denoted by MP n -Koopmans in Table I), with the imaginary

TABLE I Second- and third-order correlation energies (a.u.) in various partitionings as compared to CISD and QCISD(T).

Method	He(TZ2P)	Ne(TZP)	LiH(6-31G**)	H ₈ (6-31G**)
MP2-KOOPMANS	-0.029972	-0.227947	-0.035922	-0.132450
QD2	-0.029937	-0.227865	-0.035897	-0.132324
MP2-MP2	-0.030496	-0.243533	-0.037183	-0.145077
MP2-DYSON2	-0.030476	-0.242371	-0.037054	-0.142052
MP3-KOOPMANS	-0.035344	-0.227353	-0.037054	-0.157396
MP3-MP2	-0.035524	-0.225853	-0.043847	-0.161541
MP3-DYSON2	-0.035518	-0.226016	-0.043813	-0.160911
CISD	-0.036487	-0.224202	-0.045674	-0.158255
QCISD(T)		-0.231893		-0.168463

level shift introduced in Ref. [16] [QD2 of Eq. (11)], with real level shifts obtained both by MP2 [Eq. (9)] and by second-order Dyson correction [Eq. (6)] to the one-particle energies (MP n -MP2 and MP n -Dyson, respectively). Variational configuration interaction with singles and doubles (CISD) values are given for comparison, and for Ne and H₈ the QCISD(T) (T stands for triples) estimates are also indicated. We see that the small imaginary level shifts do not affect correlation energies appreciably, systems in Table I not being (quasi)degenerate. The applied real shifts are much larger. Values presented for He, Ne, and LiH give one a feeling that a pretty good improvement may be achieved by this repartitioning, although at the second-order standard MP-Koopmans values appear to be more balanced. This can be seen from the example of Ne where the MP2-Dyson and especially the MP2-MP2 repartitionings apparently exhibit an overcorrection. At third order, however, the improvement toward the variational values is remarkable in each case. The performance of the correction is especially advantageous for the H chain for which the gap-closing effect of the Dyson equation is well established.

It may be of interest to check not only absolute values but also chemical energy differences. In Table II we report the inversion barrier for ammonia where the effect of repartitioning is very small but mostly steps in the good direction. The improvement of the second- and third-order total energies is substantial. The second-order barrier in the Epstein-Nesbet (EN2) partitioning is also included in the table, and it seems to be the best among second-order results. This is not the case in general, however, upon checking the cis and trans barrier of peroxide, Dyson-corrected values proved to be rather bad and EN2 results were simply

TABLE II
Second- and third-order total energies and inversion barrier (a.u.) of the NH₃ molecule in 6-311G** basis set.

	Pyramidal	Planar	Barrier
SCF	-56.210397	-56.200814	0.009583
MP2	-56.427497	-56.417689	0.009808
QD2	-56.427428	-56.417598	0.009830
EN2	-56.480479	-56.470515	0.009964
DY2	-56.443469	-56.433693	0.009776
MP3	-56.439803	-56.429630	0.010173
DY3	-56.440335	-56.430095	0.010240
QCISD(T)	-56.447435	-56.437057	0.010378

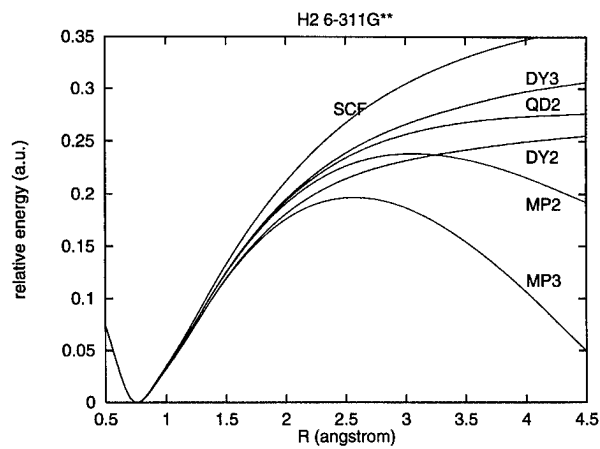


FIGURE 2. Potential curve of H₂ molecule in 6-311G** basis set, obtained with imaginary (QD) and real level shift (DY2, DY3) technique. Closed-shell HF SCF and MP curves are shown for comparison.

pathological. The occasionally catastrophic behavior of the EN2 partitioning was also reported by other authors [45], though in other cases it was used successfully with multiconfigurational reference states [45–47].

Potential curves of H₂, F₂, and N₂ are presented in Figures 2–4 including large interatomic distances for which the single-reference MP n corrections fail. We computed the curves also by second-order imaginary level shift technique [16] (denoted by QD2) which is designed for quasi-degenerate problems using $\Gamma_k = 2W_{0k}$ as the damping constant. As reported in previous studies [16, 17, 42], the dissociation is described in a qualitatively correct manner by the QD2 approach in each case. It was interesting to us to realize that the Dyson-corrected level shifts may also result in

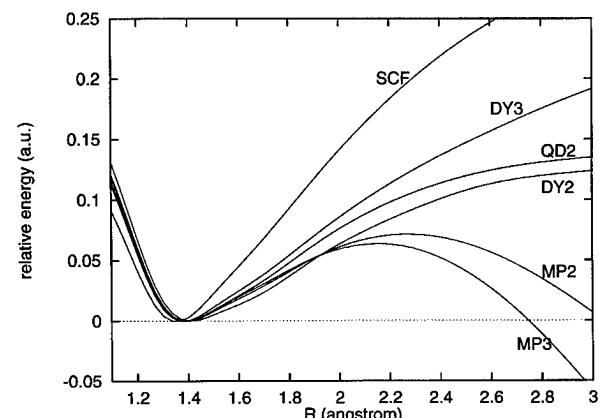


FIGURE 3. The same as Fig. 2, for the F₂ molecule.

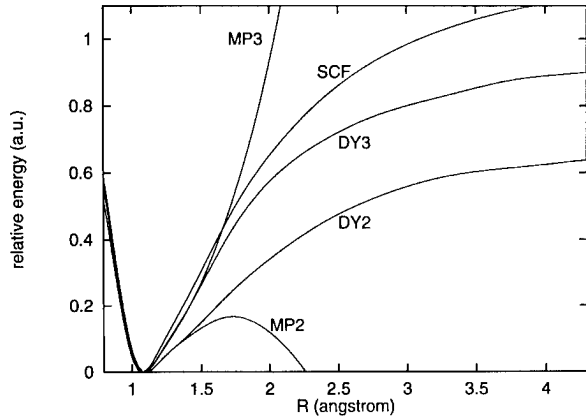


FIGURE 4. Potential curve of N_2 molecule in 6-311G** basis set, using RHF-based perturbation theory with different partitionings; DY2 and DY3 indicates real denominator shift.

potential curves with a roughly acceptable dissociation behavior (DY2 and DY3 in Figs. 2–4) within the investigated range. The reason for this is that for large interatomic distances the second-order Dyson equation [Eq. (6)] does not tend to close the HOMO–LUMO gaps as it usually does at around equilibrium geometries, but conversely, it tends to remove quasi-degeneracies. This is equally seen for each case studied including N_2 with multiple-bond dissociation. We do not claim, however, that this latter level shift technique can be used as a general and automatic tool for dissociation studies.

APSG Reference State

GROUND STATE

The use of Dyson- or MP2-corrected one-electron energies involves that, in some way, correlation effects are included already at the zeroth order. This can be done, however in a more systematic manner. Various attempts to use multireference (MR) PT [5–10] or MR coupled-cluster [12–14] approaches reflect the importance of this issue. Here we discuss the idea of using strongly orthogonal geminals to construct the zeroth order and evaluating perturbation corrections to this reference state. Such an approach has been initiated a long time ago [25, 26] and has been discussed recently for approximate geminals [27–30].

We define the ground-state wave function for a system of N (even) electrons as

$$\Psi_0^{\text{APSG}} = \psi_1^+ \psi_2^+ \dots \psi_{N/2}^+ |\text{vac}\rangle. \quad (12)$$

The strongly orthogonal geminals ψ_i^+ are expanded as

$$\psi_i^+ = \sum_{\mu < \nu}^{(i)} C_{\mu\nu}^i a_\mu^+ a_\nu^+, \quad i = 1, 2, \dots, \frac{N}{2}, \quad (13)$$

where the superscript (i) on the summation indicates that only those indices μ and ν are considered which belong to the subspace assigned to geminal i . In Eq. (13) operators a_μ^+ ($\mu \in i$) create electrons on orbitals spanning the i th subspace. The subspaces i can be built up by mutually exclusive sets of orthogonal one-electron functions which maintain strong orthogonality [48–50]. The expansion coefficients $C_{\mu\nu}^i$ can be optimized variationally by solving a set of coupled local 2-electron Schrödinger equations [27, 30, 51] for each subspace. Optimization of the subspaces themselves leads to the so-called APSG wave function [48–50] which represents the variational minimum within the wave function class specified by Eq. (12). The APSG method is size-consistent and, being trivially exact for a two-electron system, it describes properly the single-bond dissociation. It does not give, however, a sufficiently large fraction of correlation energy which motivated the development of extended geminal schemes [52–56]. Here we discuss the possibility of using the APSG wave function as a reference state in MBPT.

Dealing with geminals in a many-body theory is easier if we study their algebraic properties. The commutators between creation/annihilation operators for the composite quasi-particles can be written as

$$[\psi_i^+, \psi_k^+] = [\psi_i^-, \psi_k^-] = 0, \quad (14)$$

$$[\psi_i^-, \psi_k^+] = \delta_{i,k} \hat{Q}_i, \quad (15)$$

where the quasiparticle commutator has the form [27, 30, 51, 57, 58]

$$\hat{Q}_i = 1 - \sum_{\mu\nu}^{(i)} P_{\nu\mu}^i a_\mu^+ a_\nu^- \quad (16)$$

with P^i being the first-order density matrix for geminal i , for which, using the convention $C_{\mu\lambda}^i = -C_{\lambda\mu}^i$ for $\mu > \lambda$, we get [30, 51, 57, 59]:

$$P_{\nu\mu}^i = \langle \psi_i | a_\mu^+ a_\nu^- | \psi_i \rangle = \sum_{\lambda} C_{\mu\lambda}^i C_{\nu\lambda}^i. \quad (17)$$

Relation (15), which is a consequence of the strong orthogonality of the geminals [57], is extremely important as it tells us that the quasi-particle creation and annihilation operators commute for different geminals. This permits us to use an analogous algebra in the evaluation of matrix elements as if we had a single-reference function.

The above equations are valid only if one considers a single geminal within each subspace. This is normally the ground-state solution of each two-electron problem. For the treatment of excited states and PT corrections one needs locally excited geminals as well:

$$\psi_{ia}^+ = \sum_{\mu < \nu}^{(i)} C_{\mu\nu}^{ia} a_\mu^+ a_\nu^+, \quad (18)$$

where a labels the excited state of the i th geminal. The algebraic properties are defined by the following quasi-particle commutator:

$$[\psi_{ja}^-, \psi_{ib}^+] = \delta_{ij} \hat{Q}_{ab}^i, \quad (19)$$

$$\hat{Q}_{ab}^i = \delta_{ab} - \sum_{\alpha\beta}^{(i)} P_{\alpha\beta}^{iab} a_\alpha^+ a_\beta. \quad (20)$$

(For the transition density matrix P^{iab} , see below.)

While the optimization of the expansion coefficients is a trivial and fast algorithm, finding the proper one-electron functions which span the subspaces is difficult and can be quite demanding computationally. This can be done by successive orbital rotations governed by the appropriate gradients $g_{\mu\nu}$ used also for optimizing multiconfiguration self-consistent field (MCSCF) orbitals [60]:

$$g_{\mu\nu} = 2(F_{\mu\nu} - F_{\nu\mu}) \quad (21)$$

for the rotation of the geminal pair μ, ν , where F is the generalized Fock matrix which, for geminals reads:

$$F_{\mu\nu} = \sum_{\lambda}^{(i)} h_{\mu\lambda} P_{\lambda\nu}^i + \sum_{\sigma\kappa\lambda}^{(i)} [\sigma\lambda | \kappa\mu] \Gamma_{\kappa\nu\sigma\lambda}^i + \sum_{\lambda}^{(k)} \sum_{j(\neq i)}^{(j)} \sum_{\kappa\sigma} [\sigma\lambda | \kappa\mu] \Gamma_{\kappa\nu\sigma\lambda}^{ji} \quad (22)$$

($\mu \in k, \nu \in i, k \neq i$) in terms of spatial orbitals; $\Gamma_{\kappa\nu\sigma\lambda}^i$ is the element of the second-order density matrix where κ, ν, σ , and λ belong to the i th geminal. It takes the particularly simple form

$$\Gamma_{\kappa\nu\sigma\lambda}^i = 2C_{\kappa\nu}^i C_{\sigma\lambda}^i. \quad (23)$$

If κ belongs to the j th subspace and ν to the i th, we get the following expression for the second-order density matrix:

$$\Gamma_{\kappa\nu\sigma\lambda}^{ji} = P_{\sigma\kappa}^j P_{\lambda\nu}^i - \frac{1}{2} P_{\lambda\kappa}^j P_{\sigma\nu}^i. \quad (24)$$

Note that the intrageminal contribution (23) factorizes to the product of geminal coefficients, while the intergeminal contribution (24) has the structure of the second-order density matrix of HF theory, thus using matrix Γ requires neither extra computations nor extra storage. The $k \neq i$ restriction in Eq. (22) reflects that intrageminal orbital pairs need not be rotated during optimization as the two-electron problems are exactly solved within each subspace.

The convergence of such an optimization procedure may nevertheless be slow, so the selection of initial orbitals is of extreme importance. An example is provided by Table III where the total energy of the LiH molecule is shown at different levels. Although the basis is very small (minimal STO-6G), the subspace optimization is not trivial as shown by the second row of Table III. The corresponding energy was thought to be optimized if Ref. [61], but using Boys LMOs as initial guess one gets a better energy without any optimization. Varying the Boys orbitals one still gets an energy lowering of 0.05 mH. (The acronym SLG in Table III and below means strictly localized geminals, expressing that the geminals are not fully optimized but are expanded in arbitrarily selected orthogonal subspaces.)

The fact that Boys LMOs represent an appropriate initial guess can also be inferred from Figure 5. We plot there the variation of the total energy of some molecules as a function of a single selected orbital rotation parameter. The scale is chosen so that the Boys LMOs correspond to 0°. It is apparent that in two of the cases the variational minimum is

TABLE III
Test calculations for LiH in STO-6G basis for comparison to another optimized APSG method (a.u.).

Method	Energy
HF	-7.96663
Optimized in Ref. [61]	-7.97981
SLG-Boys	-7.98085
Opt.-APSG	-7.98090

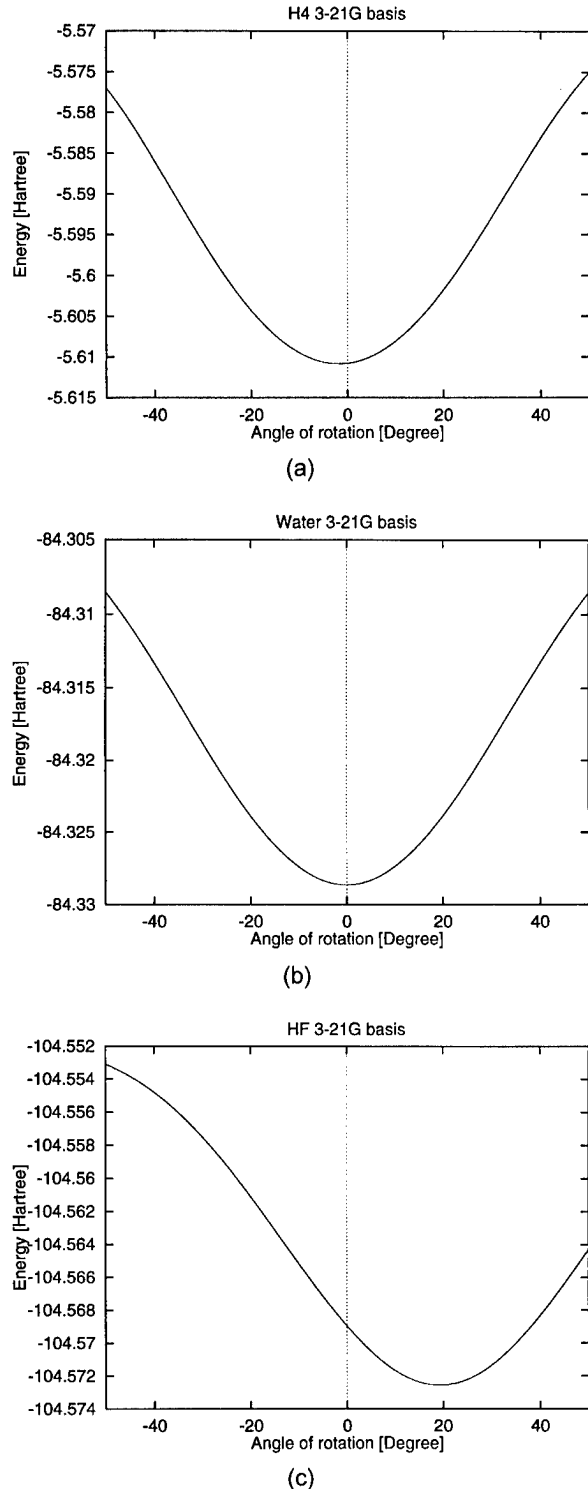


FIGURE 5. Variation of total energies as function of orbital rotation parameters near to SLG-Boys wave function (3-21G basis). (a) H₄, mixing the occupied bonding LMOs of the H₂ molecules; (b) H₂O, mixing the lowest occupied bonding LMO of the O—H bonds; (c) HF, mixing the lowest occupied bonding LMO of the H—F bond and the lowest nonbonding LMO of F.

almost at 0°, while for the hydrogen fluoride it is at around 20°, but it is still closer to the Boys limit than, say, to the canonical MOs.

Having obtained the reference state, it may be useful for a subsequent perturbation treatment. The relevant second-order formulas have already been published in Refs. [27–29]. Among these, delocalization-type corrections due to single-electron transfers vanish if the orbitals are fully optimized, while one still can evaluate the second-order intergeminal dispersion energy:

$$\Delta E(\text{disp})$$

$$= - \sum_{j < l} \sum_{ab}^{(M_S=0)} \frac{|[j_0 l_0 | j_a l_b] - \frac{1}{2} [j_0 l_0 | l_b j_a]|^2}{E_l^b + E_j^a - E_l^0 - E_j^0} - \frac{1}{4} \sum_{j < l} \sum'_{ab} \frac{|[j_0 l_0 | j_a l_b]|^2}{E_l^b + E_j^a - E_l^0 - E_j^0}, \quad (25)$$

where the prime means the restriction $M_S^{a,b} = \pm 1$, $M_S^a + M_S^b = 0$, j_a is the a th excited state of the j th geminal, and the transformed integrals over geminal labels can be expanded as

$$[j_0 l_0 | j_a l_b] = \sum_{\mu\nu}^{(j)} \sum_{\lambda\sigma}^{(l)} [\mu\lambda | \sigma\nu] P_{\mu\nu}^{j_0 a} P_{\lambda\sigma}^{l_0 b}. \quad (26)$$

The first-order transition density matrix element between the ground and a th state of the j th geminal reads as:

$$P_{\mu\nu}^{j_0 a} = \sum_{\lambda} (C_{\mu\lambda}^{j_0} C_{\nu\lambda}^{j_0 a} + C_{\lambda\mu}^{j_0} C_{\lambda\nu}^{j_0 a}). \quad (27)$$

Though the APSG wave function represents a highly correlated multiconfiguration reference state, derivation of this result is straightforward due to the simple algebraic rules of the composite-particle geminal operators [Eqs. (14)–(15)]. To arrive at Eq. (25), one defines the zero-order Hamiltonian in terms of ground- and excited-state geminals as

$$\hat{H}_0 = \sum_i^{(i)} \sum_a E_i^a \psi_{ia}^+ \psi_{ia}^-, \quad (28)$$

which has the property that the ground-state APSG wave function of Eq. (12) as well as similar wave functions in which one or more geminal is excited, are eigenfunctions of \hat{H}_0 . The pairwise interaction of two such local excitations results in Eq. (25) by standard second-order Rayleigh-Schrödinger PT.

TABLE IV
Energies of model systems (a.u.).

Basis	Method	H ₄	H ₂ O	HF
STO-3G	HF	-1.652457	-74.964107	-98.572412
	SLG-Boys	-1.695297	-75.003767	-98.593229
	Opt.-APSG	-1.695760	-75.010899	-98.597985
	Opt.-APSG + disp2	-1.698419	-75.015881	-98.597985
	MP2	-1.686618	-75.004157	-98.590632
	CISD	-1.715532	-75.019737	-98.599827
	HF	-1.827905	-75.582739	-99.460219
	SLG-Boys	-1.873473	-75.613209	-99.488554
	Opt.-APSG	-1.875250	-75.648392	-99.515423
	Opt.-APSG + disp2	-1.879222	-75.688531	-99.572902
3-21G	MP2	-1.869325	-75.707172	-99.581585
	CISD	-1.889984	-75.710692	-99.582181

In Tables IV and V, a few numbers are given illustrating the effect of orbital optimization in very small basis sets. (We do not have yet numbers for larger molecules and/or larger bases.) The bond length of HF was optimized at the HF/3-21G level, while for the water molecule we used $r(\text{OH}) = 1.01 \text{ \AA}$ and $\alpha(\text{HOH}) = 104^\circ$. The H₄ cluster was constructed in a distorted arrangement: $r_{12} = r_{34} = 0.74 \text{ \AA}$, $r_{23} = 1.0 \text{ \AA}$, $\alpha(123) = 80^\circ$, $\alpha(234) = 70^\circ$, and the (1234) dihedral angle was 20° .

One can observe that in minimal basis the Boys localized orbitals represent a rather good initial guess to fully optimized ones, while in split-shell basis the optimization is more essential. It is also important that, with the exception of the H₄ system, the dispersion energies, collected separately in Table V, are quite sensitive to the optimization.

To judge the amount of correlation energy which can be described by the APSG + PT approach, one will need to see calculations in larger basis sets, at least of double ζ polarized (DZP) quality. The small basis results of Table IV already indicate that the dispersive correction alone is not sufficient to reach the MP2 or CISD quality. At the APSG +

disp level, all local excitations have been accounted for, as well as the intrageminal single electron transfers which vanish upon optimization. However, delocalization of the geminals involving two electron transfers are missing from this approximation and may become important in larger systems and/or larger basis sets.

EXCITED STATES

The APSG wave function may be a useful reference state for the calculation of electronically excited states, too [62]. In the Tamm-Dankoff approach (TDA) [63], essentially equivalent to the equation-of-motion (EOM) technique [60], one defines the excitation operator \hat{O}_n^+ for the n th excited state $|n\rangle$

$$\hat{O}_n^+|0\rangle = |n\rangle \quad (29)$$

and expands it as

$$\hat{O}_n^+ = \sum_K X_K^n \hat{A}_K^+. \quad (30)$$

TABLE V
Dispersion contributions to the energy of model systems (a.u.).

Basis	Method	H ₄	H ₂ O	HF
STO-3G	SLG-Boys	-0.002661	-0.005452	-0.000000
	Opt.-APSG	-0.002659	-0.004982	-0.000000
3-21G	SLG-Boys	-0.003917	-0.008690	-0.020686
	Opt.-APSG	-0.003972	-0.040139	-0.057479

For the expansion coefficients X_K^n the general TDA equations are written as

$$\sum_K \mathcal{A}_{LK} X_K^n = \omega_n \sum_K \mathcal{S}_{LK} X_K^n, \quad (31)$$

where $\omega_n = E_n - E_0$ are the excitation energies and the TDA matrices are defined as

$$\begin{aligned} \mathcal{A}_{LK} &= \langle 0 | [\hat{A}_L^-, [\hat{H}, \hat{A}_K^+]] | 0 \rangle \\ &= \langle 0 | \hat{A}_L^- (\hat{H} - E_0) \hat{A}_K^+ | 0 \rangle \end{aligned} \quad (32)$$

and

$$\mathcal{S}_{LK} = \langle 0 | [\hat{A}_L^-, \hat{A}_K^+] | 0 \rangle. \quad (33)$$

We recall that the general TDA equations (31) are exact as far as the state $|0\rangle$ is the true ground state and the operator expansion of Eq. (30) is complete. Substituting $|0\rangle$ with the Hartree-Fock state and limiting the expansion to single excitations, one arrives at the CI with singles (CIS) scheme, a simple, popular but not very accurate approximation to the general TDA equations.

An important consistency requirement of the TDA equations is expressed by

$$\hat{O}_n^- |0\rangle = 0 \quad (34)$$

(the ground state cannot be deexcited). The CIS equations satisfy this requirement, but their improvement within TDA is not trivial as better reference states or larger operator manifolds may easily violate Eq. (34).

It may be interesting to investigate whether an APSG reference state could be useful for this goal. Formally, the answer is positive. Taking Eq. (12) as the approximation for the ground state, and defining the excitation operator manifold as

$$\hat{A}_K^+ = \psi_{pa}^+ \psi_{i0}^-, \quad (35)$$

where ψ_{i0}^- annihilates a ground-state geminal and ψ_{pa}^+ creates one in the a th excited state, Eq. (34) remains valid and the APSG-TDA matrices become

$$\mathcal{A}_{LK} = \langle \Psi_0^{\text{APSG}} | \psi_{j0}^+ \psi_{qa}^- \hat{H} \psi_{pb}^+ \psi_{i0}^- | \Psi_0^{\text{APSG}} \rangle - E_0 \mathcal{S}_{LK} \quad (36)$$

and

$$\mathcal{S}_{LK} = \langle \Psi_0^{\text{APSG}} | \psi_{j0}^+ \psi_{qa}^- \psi_{pb}^+ \psi_{i0}^- | \Psi_0^{\text{APSG}} \rangle. \quad (37)$$

It is to be mentioned that geminal-type wave functions may be useful not only in connection with TDA but also with the random-phase approximation (RPA). In particular, Öhrn and Linderberg have shown that the so-called antisymmetrized geminal power (APG) wave function, where each geminal is identical, serves as an appropriate reference state for RPA calculations [64, 65].

Evaluation of matrix elements in Eqs. (36) and (37) is lengthy but straightforward by the algebraic rules given earlier. For example, matrix \mathcal{S} is obtained as

$$\mathcal{S}_{LK} = \delta_{ij} \delta_{pq} \left(\delta_{iq} \delta_{ab} + (1 - \delta_{iq}) \langle \hat{Q}_{ab}^q \rangle \right), \quad a, b \neq 0, L = \{jq\alpha\}, K = \{ipb\}. \quad (38)$$

The excitation space represented by Eq. (35) describes several types of single and double excitations (in terms of electrons); thus it may be more adequate to describe electronic excitations than the CIS scheme. However, intergeminal charge-transfer-type single-electron excitations are missing from Eq. (35)—they should be accounted for by a suitable perturbation of the TDA equations. We do not have yet any numerical results for excitation energies obtained by this scheme; work in both lines is now in progress.

ACKNOWLEDGMENTS

We are indebted to A. Lázár for useful discussions. This work was supported in part by the grant OTKA T021179-T023052.

References

1. P.-O. Löwdin, Int. J. Quant. Chem. **2**, 867 (1968).
2. P. S. Epstein, Phys. Rev. **28**, 695 (1926).
3. R. K. Nesbet, Proc. Roy. Soc. (London) **A230**, 312 (1955).
4. C. Møller and M. S. Plesset, Phys. Rev. **46**, 618 (1934).
5. S. Kucharski and R. Bartlett, Int. Quant. Chem. S **22**, 383 (1988).
6. K. Wolinski and P. Pulay, J. Chem. Phys. **90**, 3647 (1989).
7. R. Murphy and R. P. Messmer, Chem. Phys. Lett. **183**, 443 (1991).
8. W. Duch and G. H. Diercksen, Phys. Rev. A **46**, 95 (1992).
9. K. Andersson, P.-Å. Malmqvist, and B. O. Roos, J. Chem. Phys. **96**, 1218 (1992).
10. S. Zarabian and J. Paldus, Int. Quant. Chem. **38**, 761 (1990).
11. I. Shavitt and L. T. Redmon, J. Chem. Phys. **73**, 5711 (1980).
12. X. Li and J. Paldus, J. Chem. Phys. **103**, 1024 (1995).
13. S. Berkovic and U. Kaldor, J. Chem. Phys. **98**, 3090 (1993).

14. P. G. Szalay and R. Bartlett, *J. Chem. Phys.* **103**, 3600 (1995).
15. X. Assfeld, J. L. Almlöf, and D. G. Truhlar, *Chem. Phys. Lett.* **241**, 438 (1995).
16. P. R. Surján and Á. Szabados, *J. Chem. Phys.* **104**, 3320 (1996).
17. P. R. Surján and Á. Szabados, *Acta Univ. Debreceniensis PC* **30**, 97 (1995).
18. D. Hegarty and M. A. Robb, *Mol. Phys.* **37**, 1455 (1979).
19. J. Mášik, I. Hubač, and P. Mach, *Int. J. Quant. Chem.* **53**, 207 (1995).
20. U. Kaldor, *Int. Quant. Chem.* **28**, 103 (1985).
21. E. Kapuy, F. Bartha, F. Bogár, and C. Kozmutza, *Theor. Chim. Acta* **72**, 337 (1987).
22. E. Kapuy, F. Bartha, C. Kozmutsa, and F. Bogár, *J. Mol. Struct. (THEOCHEM)* **170**, 59 (1988).
23. E. Kapuy, F. Bartha, F. Bogár, Z. Csépes, and C. Kozmutsa, *Int. Quant. Chem.* **37**, 139 (1990).
24. S. Diner, J.-P. Malrieu, and P. Clavery, *Theor. Chim. Acta* **13**, 1, 18 (1969).
25. E. Kapuy, *Theor. Chim. Acta* **6**, 281 (1966).
26. E. Kapuy, *Theor. Chim. Acta* **12**, 397 (1968).
27. P. R. Surján, I. Mayer, and I. Lukovits, *Phys. Rev. A* **32**, 748 (1985).
28. P. R. Surján, *Int. J. Quant. Chem.* **52**, 563 (1994).
29. P. R. Surján, *Int. J. Quant. Chem.* **55**, 109 (1995).
30. P. R. Surján, in *Theoretical Models of Chemical Bonding*, Vol. 2, *The Concept of the Chemical Bond*, Z. B. Maksić (ed.) (Springer, Berlin–Heidelberg, 1990), p. 205.
31. P. R. Surján and Á. Szabados, to appear.
32. B. T. Pickup and O. Goscinski, *Mol. Phys.* **26**, 1013 (1973).
33. J. Öhrn and G. Born, *Adv. Quant. Chem.* **13**, 1 (1981).
34. J. Oddershede, in *Advances in Chemical Physics* (Wiley, New York, 1987), Vol. 69, p. 201.
35. W. Kutzelnigg and D. Mukherjee, *J. Chem. Phys.* **90**, 5578 (1989).
36. J. Palmer and J. Ladik, *J. Comput. Chem.* **15**, 814 (1994).
37. F. Bogar, W. Förner, E. Kapuy, and J. Ladik, *J. Mol. Struct. (THEOCHEM)* **391**, 193 (1997).
38. S. Suhai, *Phys. Rev. B* **27**, 3506 (1983).
39. S. Suhai, *Phys. Rev. B* **52**, 1674 (1995).
40. J. Sun and R. J. Bartlett, *J. Chem. Phys.* **104**, 8553 (1996).
41. P. R. Surján, Á. Szabados, F. Bogár, and J. Ladik, *Solid State Commun.* **103**, 639 (1997).
42. P. R. Surján and Á. Szabados, *J. Chem. Phys.* **107**, 5677 (1997).
43. N. Forsberg and P.-Å. Malmqvist, *Chem. Phys. Lett.* **274**, 196 (1997).
44. X. Assfeld, J. E. Almlöf, and D. G. Truhlar, *CPL* **241**, 438 (1995).
45. R. B. Murphy and R. P. Messmer, *J. Chem. Phys.* **97**, 4170 (1992).
46. A. O. Mitrushenkov and P. Palmieri, *Chem. Phys. Lett.* **278**, 285 (1997).
47. A. O. Mitrushenkov, *J. Chem. Phys.* **105**, 10487 (1996).
48. T. Arai, *J. Chem. Phys.* **33**, 95 (1960).
49. W. Kutzelnigg, *J. Chem. Phys.* **40**, 3640 (1964).
50. K. J. Miller and K. Ruedenberg, *J. Chem. Phys.* **48**, 3444 (1968).
51. P. R. Surján, *Phys. Rev. A* **30**, 43 (1984).
52. I. Røeggen, *J. Chem. Phys.* **79**, 5520 (1983).
53. I. Røeggen, *J. Chem. Phys.* **89**, 441 (1988).
54. I. Røeggen, *J. Chem. Phys.* **85**, 262 (1986).
55. I. Røeggen, *Mol. Phys.* **70**, 353 (1990).
56. P. Wind and I. Røeggen, *Chem. Phys.* **174**, 345 (1993).
57. P. R. Surján, *Croatica Chemica Acta* **62**, 579 (1989).
58. P. R. Surján *Second Quantized Approach to Quantum Chemistry* (Springer, Heidelberg, 1989).
59. C. Valdemoro, *Phys. Rev. A* **31**, 2114 (1985).
60. R. McWeeny, *Methods of Molecular Quantum Mechanics* (Academic, London, 1989).
61. S. Polezzi and P. Fantucci, *Mol. Phys.* **36**, 1835 (1978).
62. P. R. Surján, to appear.
63. D. J. Rowe, *Rev. Mod. Phys.* **40**, 153 (1968).
64. Y. Öhrn and J. Linderberg, *Int. J. Quant. Chem.* **12**, 161 (1977).
65. Y. Öhrn and J. Linderberg, *Int. Quant. Chem.* **15**, 343 (1979).

Unambiguous Exchange–Correlation Energy Density for Hooke's Atom

KIERON BURKE, FEDERICO G. CRUZ, KIN-CHUNG LAM

Department of Chemistry, Rutgers University, 815 Penn Street, Camden, New Jersey 08102

Received 21 February 1998; revised 24 June 1998; accepted 24 June 1998

ABSTRACT: Recently, we used Helmholtz's theorem to construct an unambiguous exchange–correlation energy density for use in density functional theory. This energy density requires only knowledge of the density dependence of the exchange–correlation energy functional, E_{XC} , for its calculation. We calculate this energy density for Hooke's atom in three different regimes: the high-density (or weakly correlated) limit; a moderate density, comparable to that of the He atom; and a low density, in which the system is strongly correlated. We compare the exact unambiguous energy density with approximate energy densities found from approximate energy functionals. The exchange–correlation energy can be deduced directly from the density in the highly correlated limit and a new formula for the high-density limit of the correlation energy is given. © 1998 John Wiley & Sons, Inc. *Int J Quant Chem* 70: 583–589, 1998

Introduction

A principal aim of quantum chemistry is the calculation of ground-state electronic properties in an accurate and reliable fashion [1]. Traditional approaches based on the wave function have recently been complimented by those of density functional theory [2]. Density functional calculations are typically much less expensive computationally and so become the method of choice for larger systems [3]. This advance has been made

possible by the increase in accuracy of generalized gradient approximations (GGAs) [4–9] (and hybrids of GGAs with exact exchange [10–14]) over the local density approximation (LDA).

The only quantity which must be approximated in a Kohn–Sham spin-density functional calculation [15] is the exchange–correlation energy as a functional of the spin densities, $E_{XC}[\rho_\alpha, \rho_\beta]$, since its functional derivative, $v_{XC,\sigma}(\mathbf{r}) = \delta E_{XC}/\delta \rho_\sigma(\mathbf{r})$, is the only unknown in the Kohn–Sham equations. There are several popular approximations to E_{XC} , including LDA, GGA, and hybrids. These approximations can be tested by calculation of the properties of the system, such as total energies, ionization potentials, binding energies, bond lengths, vibrational frequencies, and transition-state barriers and

Correspondence to: K. Burke.
Contract grant sponsor: Research Corp.

by comparing them either with more accurate calculations or with experiment [16, 17]. However, all these properties are determined entirely by E_{XC} , evaluated on different densities, which is a quantity integrated over the system. To better understand how these approximate functionals work, one would like to examine quantities *other* than just E_{XC} . If your energy in a given calculation comes out poorly, where will you look to find out why?

A simple choice might be to study the spin densities themselves. However, many approximate calculations (Hartree–Fock, LDA, GGA, etc.) yield very similar spin densities [18], so it is not easy to study an approximate density to determine the error in the corresponding energy functional approximation. Furthermore, for stretched H₂, some approximate functionals can have quite incorrect spin densities, while still yielding accurate total energies [19, 20]. Thus, the relation between the self-consistent spin densities and the total energy may be too subtle to easily learn about one from the other.

Another feature which has been studied is the exchange–correlation hole surrounding an electron in the system [4, 6, 21–24]. One can consider the LDA and GGA energy functionals as models for the exact system-averaged exchange correlation hole. Certain aspects of the exact hole are well approximated in LDA [25], because the LDA energy functional replaces the hole by that of another system: the uniform electron gas. Thus, various sum-rules and nonpositivity conditions are shared by the exact hole and its local approximation [26]. This reasoning was extended by Perdew and coworkers to construct a sequence of GGAs (PW86 [4, 5], PW91 [6], and PBE [7]) in which the gradient expansion for the hole was corrected to include these good features. However, only the system and spherical average of these holes is accurately reproduced [24, 26] and, even then, the complications of calculating these approximate holes mean that few systems have been tested. (On the other hand, the potential in LDA arises from an unspherical charge distribution [27].) Similar remarks are true for the LYP correlation functional [9], which is based on the Colle–Salvetti approximations to the pair correlation function [28, 29].

Such comparisons as mentioned in the previous paragraph suffer from the need for detailed knowledge of the construction of a given approximation. But an approximation might not carry with it a derivation which suggests such a comparison. For

a practical calculation, all one really needs is an approximate spin-density functional for E_{XC} . This naturally suggests study of $v_{XC,\alpha}(\mathbf{r})$ itself. For the exact case, one needs only a highly accurate density, as several methods now exist for then solving for the Kohn–Sham potential and orbitals [30–34] and so deducing the exchange–correlation contribution to the potential. Thus, comparison of approximate and exact potentials could be hoped to yield insight into how approximate functionals work.

Unfortunately [18, 35, 36], potentials corresponding to accurate functionals do not look much like the exact potentials. Thus, the study of potentials appears to provide little guidance for the construction of approximate energy functionals. There are several ways to rationalize how these potentials can look so poor:

First, focusing on correlation alone ignores a wealth of experience in functional approximations, in which the exchange and correlation errors cancel. This can be understood simply in terms of the specific effects which occur for pure exchange [12], which are not captured by LDA and GGA, but which wash out when the Coulomb interaction between electrons is included.

Next, as discussed above, system-averaging is important in studying the behavior of density functionals [37]. Many properties of approximate functionals are incorrect in, for example, the asymptotic limit far from a finite system [38], but these have little effect on the total energy or even on energy differences involving only valence electrons.

Furthermore, approximate functionals which incorporate only the density and its gradient cannot have any derivative discontinuities with respect to particle number, which are known to occur in the exact functional [39–42]. These discontinuities lead to constants in the potential which are missed by approximate functionals and so can make the corresponding potentials look poorer.

An alternative to studying the exchange–correlation potential might be provided by the exchange–correlation energy density, that is, a function of \mathbf{r} which, when integrated over all space, yields the exchange–correlation energy. Unfortunately, such a requirement does not uniquely specify which among an infinite number of choices, as the addition of any function whose integral over all space vanishes will produce another energy density. In fact, several choices have been suggested in the past. A popular one, especially for

chemical purposes, is that of Baerends and Gritsenko [43], who defined their energy density in terms of the potential contribution to the exchange–correlation hole, plus the difference of the kinetic energy density from the interacting and noninteracting density matrices. While this energy density can be extracted from an accurate wavefunction calculation, there is no reason why any of the conventional approximate energy densities, used to define the integrated energy, should look much like this one. Indeed, the LYP functional [9] has been integrated by parts in order to remove inconvenient Laplacian terms [44]. Similar arguments apply to the definition in terms of the coupling-constant integrated exchange–correlation hole [26].

Similarly, the work of Harbola and Sahni [45, 46] and others [47] has led to an energy density in terms of potential and kinetic exchange–correlation fields. But the construction of, for example, the potential fields, is based on the exchange–correlation hole (at full coupling strength), which is modeled only in some GGAs. Comparisons of these energy densities with exact ones can only be made with those GGAs which provide a model for this hole [46].

The remainder of this article is devoted to the construction of an unambiguous exchange–correlation energy density, that is, one which is solely determined by the density dependence of E_{XC} . The full details of the construction are given elsewhere [49], but a pedagogical derivation is given here. Results on the Hooke's atom (two electrons in an external oscillator potential) are presented for three cases: moderate correlation, strong correlation, and weak correlation. Atomic units ($e^2 = \hbar = m_e = 1$) are used throughout.

Construction of Unambiguous Energy Density

In this section, we review the construction of the unambiguous energy density. For simplicity, we restrict ourselves to density functionals, but all results are easily generalized to spin-density functionals.

We begin with the virial theorem [50]:

$$2T = \langle \Psi | \sum_{i=1}^N \mathbf{r}_i \cdot \nabla_i V(\mathbf{r}_1, \dots, \mathbf{r}_n) | \Psi \rangle, \quad (1)$$

where T is the kinetic energy; Ψ , the ground-state many-body wave function; N , the number of electrons; and V , the potential energy. This may easily be derived by uniformly scaling the coordinates of the wave function [51]. We apply this theorem to both the physical system and the noninteracting Kohn–Sham system. In the former case, $V = V_{ee} + V_{ext}$, where V_{ee} is the electron–electron Coulomb repulsion and V_{ext} is the external potential. This yields

$$2T = -V_{ee} + \int d^3r \rho(\mathbf{r}) \mathbf{r} \cdot \nabla v_{ext}(\mathbf{r}), \quad (2)$$

since V_{ee} is homogeneous of degree -1 in the coordinates. Similarly, for the noninteracting Kohn–Sham system,

$$\begin{aligned} 2T_S &= \int d^3r \rho(\mathbf{r}) \mathbf{r} \cdot \nabla v_s(\mathbf{r}) \\ &= \int d^3r \rho(\mathbf{r}) \mathbf{r} \cdot \nabla (v_{ext}(\mathbf{r}) + v_{XC}(\mathbf{r})) - U, \end{aligned} \quad (3)$$

where $v_s(\mathbf{r})$ is the Kohn–Sham potential and U is the Hartree energy. Subtraction of Eq. (3) from Eq. (2) yields

$$2(T - T_S) + V_{ee} - U = - \int d^3r \rho(\mathbf{r}) \mathbf{r} \cdot \nabla v_{XC}(\mathbf{r}). \quad (4)$$

The second term on the left can be identified as the potential contribution to E_{XC} , so that the addition of one factor of $T_C = T - T_S$, the kinetic contribution, yields E_{XC} . Thus,

$$E_{XC} + T_C = - \int d^3r \rho(\mathbf{r}) \mathbf{r} \cdot \nabla v_{XC}(\mathbf{r}). \quad (5)$$

This powerful result was proven for the exact functional by Levy and Perdew [51].

The integrand of Eq. (5) is an energy density which is unambiguously determined by the density dependence of the exchange–correlation energy functional, via the potential, its derivative. Unfortunately,

1. It is an energy density not for exchange–correlation, but for exchange–correlation plus kinetic–correlation.
2. Its value depends on the choice of origin. If the origin is shifted, the energy density changes (see Fig. 8 of [52]).

3. This energy density does not reduce to the familiar $e_{XC}^{\text{unif}}(\rho(\mathbf{r}))$, the energy density of a uniform gas, when v_{XC}^{LDA} is inserted on the right.

The first of these shortcomings was easily solved, using the adiabatic connection formula of density functional theory [53]. A coupling-constant λ is introduced to multiply the electron-electron repulsion and is varied while keeping the density fixed. All quantities can then be considered functions of λ . In particular, Bass' relation [54] relates T_C to E_C^λ , via

$$T_C^\lambda = E_C^\lambda - \lambda \frac{dE_C^\lambda}{d\lambda}. \quad (6)$$

Using this on the generalization of Eq. (5) to arbitrary λ , we found [49] a virial for the exchange-correlation energy itself:

$$E_{XC} = - \int d^3r \rho(\mathbf{r}) \mathbf{r} \cdot \nabla \tilde{v}_{XC}(\mathbf{r}), \quad (7)$$

where

$$\tilde{v}_{XC}(\mathbf{r}) = \int_1^\infty \frac{d\lambda}{\lambda^3} v_{XC}^\lambda(\mathbf{r}) \quad (8)$$

is called the exchange-hypercorrelated potential, as it includes contributions from $\lambda > 1$, at which the system is more strongly correlated than at $\lambda = 1$. This potential can also be written as [55]

$$\tilde{v}_{XC}[\rho](\mathbf{r}) = \int_0^1 \frac{d\gamma}{\gamma} v_{XC}[\rho_\gamma](\mathbf{r}/\gamma), \quad (9)$$

where

$$\rho_\gamma(\mathbf{r}) = \gamma^3 \rho(\gamma \mathbf{r}) \quad (10)$$

is a uniformly scaled density. Thus, the integrand on the right of Eq. (7) forms an unambiguous exchange-correlation energy density, as it is completely determined by the density dependence of E_{XC} itself, via its potential, evaluated on scaled densities. In particular, it is very straightforward to modify any approximate functional to calculate $\tilde{v}_{XC}(\mathbf{r})$ instead of $v_{XC}(\mathbf{r})$ simply by scaling the density arguments, according to Eq. (9).

To overcome the second two difficulties, we generalized an argument of Levy and Perdew [51], which they used to show that the virial theorem was satisfied by LDA for a slowly varying electron gas. This generalization amounts to making the

following exact identification:

$$3\rho(\mathbf{r}) \nabla \tilde{v}_{XC}(\mathbf{r}) = \nabla e_{XC}(\mathbf{r}) + \nabla \times \mathbf{a}_{XC}(\mathbf{r}). \quad (11)$$

Insertion of Eq. (11) into Eq. (7), followed by an integration by parts, shows that the \mathbf{a}_{XC} term does not contribute to the energy, while the e_{XC} term is our unambiguous energy density. By use of the Helmholtz theorem of vector calculus, we can write an integral form for e_{XC} :

$$e_{XC}(\mathbf{r}') = \frac{3}{4\pi} \int d^3r \rho(\mathbf{r}) \nabla \tilde{v}_{XC}(\mathbf{r}) \cdot \nabla \frac{1}{|\mathbf{r} - \mathbf{r}'|}. \quad (12)$$

This is an exact energy density that depends solely on the density dependence of the exchange-correlation energy functional. Thus, unambiguous comparisons of exact and approximate results can be made. Furthermore, if E_{XC}^{LDA} is used on the right, $e_{XC}^{\text{unif}}(\rho(\mathbf{r}))$ comes out on the left. Thus, all plots of $e_{XC}^{\text{unif}}(\rho(\mathbf{r}))$ can be interpreted as approximate plots of the exact unambiguous $e_{XC}(\mathbf{r})$.

The right-hand side of Eq. (12) contains the exchange-hypercorrelated potential, that is, the potential integrated over coupling constants greater than 1, as defined in Eq. (8). This is necessary to produce the exchange-correlation energy density on the left. Alternatively, if $v_{XC} = v_{XC}^{\lambda=1}$ is inserted on the right, an energy density $e_{XC}(\mathbf{r}) + t_C(\mathbf{r})$ emerges on the left, as can be seen from Eq. (5). For any approximate functional, it is straightforward to calculate either quantity. However, for the *exact* functional, we only have $v_{XC}(\mathbf{r})$ for a few model systems, where the exact density was evaluated by a highly accurate wave-function calculation and v_{XC} calculated from it. Thus, for purposes of comparison, it is more convenient to study $e_{XC} + t_C$. Ongoing studies of the adiabatic connection should allow construction of \tilde{v}_{XC} in the future. We anticipate little difference in the qualitative features of the comparison, as the hypercorrelated potential is a smooth distortion of the correlated potential (see Fig. 6 of [56]).

Results

To illustrate this energy density, we calculate it for several values of the spring constant in Hooke's atom, which consists of two electrons in an external oscillator potential [57, 58]. This model has been used to study many density functional properties [36, 59, 60].

MODERATE CORRELATION

We begin with a moderately correlated example, $\omega = 1/2$, in which $E_C/E_X \sim 7\%$ and $T_C/|E_C| \sim 75\%$. In Figure 1, we plot the radial unambiguous exchange-correlation plus kinetic-correlation energy density, both exactly and within several functional approximations. We see that, indeed, the LDA curve underestimates the exact one almost everywhere, while the GGA curves reduce the maximum error significantly. The best GGA curve in this case is BLYP (but see real atoms in [49]). Note that the decay of this energy density at large distances is given in [49] and depends on the ionization potential and is not captured by any present-day approximate functionals.

STRONG CORRELATION

Next, we consider the highly correlated (or low-density) limit. We choose $\omega = 10^{-4}$, at which value the density is very close to semiclassical, that is, a Gaussian centered on the classical electrostatic equilibrium position [58]. At the maximum, $\rho \sim 10^{-8}$ or $r_s \sim 270$. Values for the components of the energy are given in Table I, from which we see that $E_C/E_X \sim 40\%$ and $T_C/|E_C| \sim 4\%$. Thus, correlation has become comparable to exchange and is almost entirely static. In this extreme regime, we do not expect too much from our approximate functionals, and Figure 2 shows that the GGA corrections to the LSD energy density do not show

TABLE I
Energy components in milliHartrees for two extreme values of ω , evaluated on the exact densities.

Component	Exact	LSD	PBE	BLYP
$\omega = 10^{-4}$				
E_X	-3.00	-2.90	-3.40	-3.54
E_C	-1.24	-2.29	-1.67	-0.55
T_C	0.05	0.20	0.17	0.003
$E_C + T_C$	-1.19	-2.09	-1.50	-0.55
$\omega = 100$				
E_X	-7,923	-6,773	-7585	-7717
E_C	-49	-221	-77	-29
T_C	48	164	72	33
$E_C + T_C$	-0.9	-57	-4	5

Values for $\omega = 1/2$ and 0.00189 are in [56].

a pointwise improvement. In fact, in this regime, the exact energy density appears more similar to LSD than above.

An important question was raised by Morrison and Parr [48], which can be stated as follows: Given the exact density of some $N > 1$ electronic problem, can you find the exact ground-state energy without solving an $N > 1$ problem? Recently, we pointed out that the answer is yes when $N = 2$ for spin-unpolarized systems [56], since the asymptotic decay of the density determines the ionization potential, so that one is left with a

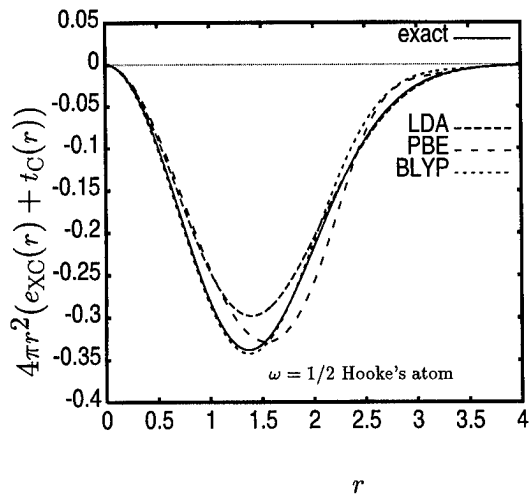


FIGURE 1. Radial unambiguous exchange-correlation plus kinetic-correlation energy density for $\omega = 1/2$ Hooke's atom (atomic units).

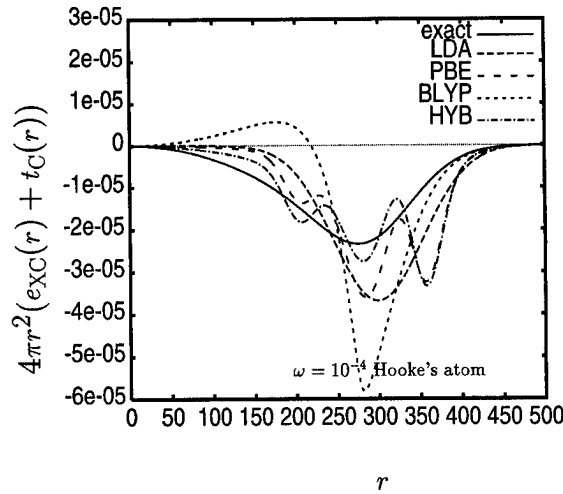


FIGURE 2. Radial unambiguous exchange-correlation plus kinetic-correlation energy density for $\omega = 10^{-4}$ Hooke's atom (atomic units).

one-electron problem to solve. Here, we point out that it is also true in the extreme high-correlation (or low-density) limit, since $T_C \rightarrow 0$, so that the virial of the exchange–correlation potential yields the exchange–correlation energy.

WEAK CORRELATION

Finally, we consider the weakly correlated (or high-density) limit, by studying $\omega = 100$. Now, $E_C/E_X \sim 0.5\%$, while $T_C/|E_C| \sim 98\%$. In this limit, it becomes appropriate to separate correlation from exchange, since Görling–Levy perturbation theory applies [61]. In Figure 3, we plot the radial unambiguous correlation plus kinetic correlation energy densities and their functional approximations. We now see a true limitation of LDA, in that its energy density does not change sign, so that there is no cancellation in the integral. The exact curve integrates to zero in the $\omega \rightarrow \infty$ limit. The GGAs do better, and this is reflected in their energies, although the BLYP curve does not follow the shape of the exact curve. Figure 3 also highlights an undesirable feature of the new energy density. The integrated quantity vanishes, so should not the integrand vanish also? It would be preferable if the energy density never changed sign (as, indeed, the uniform gas energy density does not), since then the allocation of energy densities throughout the system would be cumulative, and one could more

easily define averages over the distribution. Since the prescription described here does not uniquely specify the choice of energy density, the question of whether such a variation can be found remains open.

The high-density limit also raises a slight conundrum: Using Levy scaling [62], one finds $v_C^\lambda \approx \lambda^2 v_C^{(2)}$, in the high-density limit, where $v_C^{(2)}$ is the finite correlation potential when the density is scaled to the high-density limit, that is, $v_C^{(2)}(\mathbf{r}) = \lim_{\gamma \rightarrow \infty} v_C[\rho_\gamma](\gamma \mathbf{r})$. Insertion of this λ -dependence directly into Eq. (12) would cause the hypercorrelated potential to diverge everywhere. In reality, this does not happen, because $E_C \rightarrow -\text{constant}$, even in the low-density limit. This implies that $v_C^\lambda \approx O(\lambda)$ as $\lambda \rightarrow \infty$, and this change in behavior always occurs for some $\lambda \sim O(r_s)$ for any real system, making the integral converge. Thus, the high-density limit cannot be taken *before* the coupling-constant integration.

This raises an interesting point about Eq. (12) in the high-density limit, since it yields the correlation energy in terms of an integral which stretches down to the low-density (highly correlated) limit. For two-electron systems, one may show that the virial theorem becomes

$$E_C^{(2)} = -\frac{1}{2} \int d^3r \rho(\mathbf{r}) \mathbf{r} \cdot \nabla \int_1^\infty \frac{d\lambda}{\lambda^2} \frac{\delta V_{ee}^\lambda}{\delta \rho(\mathbf{r})}, \quad (13)$$

where V_{ee}^λ is the expectation value of the interelectronic Coulomb repulsion evaluated on the wave function at coupling-constant λ , and $E_C^{(2)} = \lim_{\gamma \rightarrow \infty} E_C[\rho_\gamma]$. One may, of course, apply the Helmholtz construction to this expression also to yield an origin-independent energy density as in Eq. (12).

Conclusions

To summarize, we have presented a new tool for the exploration of density functionals. The unambiguous energy density provides several interesting advantages over earlier constructions, and preliminary calculations of this energy density are promising [49].

ACKNOWLEDGMENT

This work was supported by an award from the Research Corp.

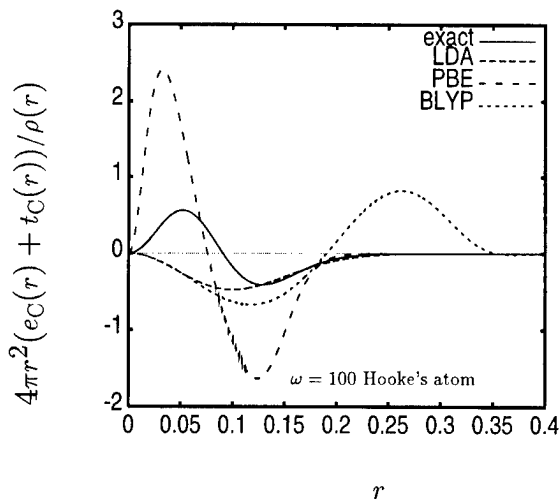


FIGURE 3. Radial unambiguous exchange–correlation plus kinetic–correlation energy density for $\omega = 100$ Hooke’s atom (atomic units).

References

1. P. Fulde, *Electron Correlations in Molecules and Solids* (Springer-Verlag, Berlin, 1991).
2. J. M. Seminario and P. Politzer, Eds., *Modern Density Functional Theory: A Tool for Chemistry*, (Elsevier, Amsterdam, 1995).
3. P. Carloni, W. Andreoni, and M. Parrinello, Phys. Rev. Lett. **79**, 761 (1997).
4. J. P. Perdew, Phys. Rev. B **33**, 8822 (1986); *Ibid* **34**, 7406 (1986).
5. J. P. Perdew and Y. Wang, Phys. Rev. B **33**, 8800 (1986); *Ibid* **40**, 3399 (1989).
6. J. P. Perdew, in *Electronic Structure of Solids '91*, P. Ziesche and H. Eschrig, Eds. (Akademie Verlag, Berlin, 1991), p. 11.
7. J. P. Perdew, K. Burke, and M. Ernzerhof, Phys. Rev. Lett. **77**, 3865 (1996); *Ibid* **78**, 1396 (1997).
8. A. D. Becke, Phys. Rev. A **38**, 3098 (1988).
9. C. Lee, W. Yang, and R. G. Parr, Phys. Rev. B **37**, 785 (1988).
10. A. D. Becke, J. Chem. Phys. **98**, 5648 (1993).
11. A. Becke, J. Chem. Phys. **104**, 1040 (1996).
12. K. Burke, M. Ernzerhof, and J. P. Perdew, Chem. Phys. Lett. **265**, 115 (1997).
13. J. P. Perdew, M. Ernzerhof, and K. Burke, J. Chem. Phys. **105**, 9982 (1996).
14. M. Ernzerhof, Chem. Phys. Lett. **263**, 499 (1996).
15. W. Kohn and L. J. Sham, Phys. Rev. A **140**, 1133 (1965).
16. A. Zupan, K. Burke, M. Ernzerhof, and J. P. Perdew, J. Chem. Phys. **106**, 10184 (1997).
17. J. P. Perdew, M. Ernzerhof, A. Zupan, and K. Burke, J. Chem. Phys. **108**, 1522 (1998).
18. C. Filippi, C. Umrigar, and X. Gonze, Phys. Rev. A **54**, 4810 (1996).
19. J. P. Perdew, A. Savin, and K. Burke, Phys. Rev. A **51**, 4531 (1995).
20. J. P. Perdew, M. Ernzerhof, K. Burke, and A. Savin, Int. J. Quantum Chem. **61**, 197 (1997).
21. J. P. Perdew, K. Burke, and Y. Wang, Phys. Rev. B **54**, 16533 (1996); *Ibid* **57**, 14999 (1998).
22. K. Burke, J. P. Perdew, and Y. Wang, in *Electronic Density Functional Theory: Recent Progress and New Directions*, J. F. Dobson, G. Vignale, and M. P. Das, Eds. (Plenum, New York, 1997), p. 81.
23. K. Burke, in *Electronic Density Functional Theory: Recent Progress and New Directions*, J. F. Dobson, G. Vignale, and M. P. Das, Eds. (Plenum, New York, 1997), p. 19.
24. M. Ernzerhof and J. P. Perdew, J. Chem. Phys., submitted.
25. O. Gunnarsson, M. Jonson, and B. I. Lundqvist, Phys. Rev. B **20**, 3136 (1979).
26. M. Ernzerhof, J. P. Perdew, and K. Burke, in *Density Functional Theory*, R. Nalewajski, Ed. (Springer-Verlag, Berlin, 1996).
27. M. Slamet and V. Sahni, Phys. Rev. A, **51**, 2815 (1995).
28. R. Colle and O. Salvetti, Theor. Chim. Acta **37**, 329 (1975).
29. T. Grabo, T. Kreibich, S. Kurth, and E. K. U. Gross, in *Strong Coulomb Correlations in Electronic Structure: Beyond the Local Density Approximation*, V. I. Anisimov, Ed. (Gordon and Breach, Tokyo, 1998).
30. Q. Zhao and R. G. Parr, Phys. Rev. A **46**, 2337 (1992).
31. A. Görling, Phys. Rev. A **46**, 3753 (1992).
32. Y. Wang and R. G. Parr, Phys. Rev. A **47**, R1591 (1993).
33. C. J. Umrigar and X. Gonze, in *Proceedings of the Mardi Gras 1993 Conference*, D. A. Browne et al., Ed. (World Scientific, Singapore, 1993).
34. R. van Leeuwen and E. J. Baerends, Phys. Rev. A **49**, 2421 (1994).
35. C. J. Umrigar and X. Gonze, Phys. Rev. A **50**, 3827 (1994).
36. C. Filippi, C. J. Umrigar, and M. Taut, J. Chem. Phys. **100**, 1290 (1994).
37. K. Burke, J. P. Perdew, and M. Ernzerhof, J. Chem. Phys., accepted.
38. M. Ernzerhof, K. Burke, and J. P. Perdew, J. Chem. Phys. **105**, 2798 (1996).
39. J. P. Perdew, R. G. Parr, M. Levy, and J. L. Balduz, Jr., Phys. Rev. Lett. **49**, 1691 (1982).
40. J. P. Perdew, in *Density Functional Methods in Physics*, R. M. Dreizler and J. da Providencia, Eds. (Plenum, New York, 1985), p. 265.
41. L. Kleinman, Phys. Rev. B **56**, 12042 (1997); *Ibid* **56**, 16029 (1997).
42. J. P. Perdew and M. Levy, Phys. Rev. B **56**, 16021 (1997).
43. E. J. Baerends and O. V. Gritsenko, J. Phys. Chem. A **101**, 5383 (1997).
44. B. Miehlich, A. Savin, H. Stoll, and H. Preuss, Chem. Phys. Lett. **157**, 200 (1989).
45. M. K. Harbola and V. Sahni, Phys. Rev. Lett. **62**, 489 (1989).
46. V. Sahni, Phys. Rev. A **55**, 1846 (1997).
47. A. Holas and N. H. March, Phys. Rev. A **51**, 2040 (1995).
48. R. C. Morrison and R. G. Parr, Phys. Rev. A **53**, R2918 (1996).
49. K. Burke, F. G. Cruz, and K. C. Lam, J. Chem. Phys., accepted.
50. J. P. Perdew and S. Kurth, in *Proceedings of the Merensee Summer School, S.A.*, Jan. 1997, D. Joubert, Ed. (Springer, Berlin, 1998).
51. M. Levy and J. P. Perdew, Phys. Rev. A **32**, 2010 (1985).
52. F. G. Cruz, K.C. Lam, and K. Burke, J. Phys. Chem. A, accepted.
53. D. C. Langreth and J. P. Perdew, Solid State Commun. **17**, 1425 (1975).
54. R. Bass, Phys. Rev. B **32**, 2670 (1985).
55. R. van Leeuwen and E. J. Baerends, Phys. Rev. A **51**, 170 (1995).
56. K. C. Lam, F. G. Cruz, and K. Burke, Int. J. Quantum Chem., **69**, 533 (1998).
57. N. R. Kesiner and O. Sinanoglu, Phys. Rev. **128**, 2687 (1962).
58. M. Taut, J. Phys. A **27**, 1045 (1994).
59. S. Kais, D. R. Herschbach, N. C. Handy, C. W. Murray, and G. J. Laming, J. Chem. Phys. **99**, 417 (1993).
60. K. Burke, J. P. Perdew, and D. C. Langreth, Phys. Rev. Lett. **73**, 1283 (1994).
61. S. Ivanov, K. Burke, and M. Levy, Phys. Rev. A, in preparation.
62. M. Levy, in *Recent Developments and Applications of Modern Density Functional Theory*, J. Seminario, Ed. (Elsevier, Amsterdam, 1996).

SCF Calculations with Density-Dependent Local-Exchange Potential

V. KARASIEV,¹ E. V. LUDEÑA,¹ R. LÓPEZ-BOADA^{1,2}

¹Centro de Química, Instituto Venezolano de Investigaciones Científicas, IVIC, Apartado 21827, Caracas 1020-A, Venezuela

²Department of Chemistry and Supercomputer Computations Research Institute, Florida State University, Tallahassee, Florida 32306-3006

Received 17 March 1998; revised 18 June 1998; accepted 25 June 1998

ABSTRACT: A new model for the exchange potential in the framework of DFT is proposed. The potential is defined as $2\alpha_x\epsilon_x^{appr}$, where ϵ_x^{appr} is the exchange-energy density and α_x is not a constant but a functional $\alpha_x[\rho]$ to be determined iteratively. The exact Fock expression and the LDA, GEA, and Becke88 approximations were used as ϵ_x^{appr} . We provide results for atoms showing that this model potential yields total and exchange energies and other atomic properties that are in good agreement with Hartree–Fock values. In addition, total energies obtained by adding to the $\alpha_x[\rho]$ approach correlation energy corrections computed via the WL and LYP functionals are in close accord with experimental values. © 1998 John Wiley & Sons, Inc. Int J Quant Chem 70: 591–600, 1998

Introduction

The one-particle equations appearing in the context of the independent particle model of electronic structure are, in general, coupled partial

integrodifferential equations for which it is not possible, due to their complexity, to obtain analytical solutions. For this reason, they are treated approximately by means of a self-consistent-field (SCF) iterative procedure. In the Hartree approximation [1], the “field” or effective potential in which a particle moves is an explicit functional of the one-particle density $\rho(\mathbf{r})$ and comprises the external potential and the Coulomb potential exerted by the charge distribution. In the Hartree–Fock approximation [2], an additional exchange potential arises from the antisymmetry condition

Correspondence to: V. Karasiev.

Contract grant sponsor: 38th Sanibel Symposium.

Contract grant sponsor: Comission of European Communities.

Contract grant number: CI1*-CT93-0333.

on the N -particle wave function. In general, however, this additional term is not a simple functional of the one-particle density.

In 1951, Slater [3] introduced an approximation to the exchange potential corresponding to a weighted mean of the average exchange charges. The advantage of such an approximation was that it led to a single potential field for all electrons. When this averaged exchange charge was replaced by the free electron-gas expression, an exchange potential depending on just the one-particle density $\rho(\mathbf{r})^{1/3}$ was obtained. In this way, a natural connection between the local-density approximation (LDA) [4, 5] and the SCF method was established.

This approach was further extended by Gáspár [6] and Kohn and Sham [7] and was basic to the formulation of the X_α method by Slater and Johnson [8]. However, these methods did not provide a satisfactory description of exchange and, in consequence, density functional calculations based generally on the LDA approximation lead to substantial error. Moreover, exchange potentials derived from these functionals do not show the correct asymptotic behavior at large distances.

To correct these shortcomings of LDA, the use of gradient-corrected density functionals has been advocated. In this direction, for example, Becke proposed a semiempirical exchange density functional [9] that produces more accurate exchange energies and better exchange potentials. Becke's semiempirical functional was reparametrized by Lee and Zhou [10]. But these exchange functionals fail to reproduce the correct asymptotic behavior of v_x .

Recently, Lembarki et al. [11] introduced gradient-corrected exchange potentials with the correct asymptotic behavior. They built two model exchange potentials with one and four parameters. The parameters were determined by fitting them to the values of the highest occupied molecular orbital (HOMO) energies of three atoms. In addition, the virial relation of Levy and Perdew [12] was employed to reproduce the exchange energy. In a different context [13, 14] (namely, that of the local-scaling transformation version of density functional theory), exchange functionals with the correct asymptotic behavior were constructed for closed- and open-shell atoms.

In the present article, based on Slater's [3] initial formulation of a weighted mean of the average exchange charges, we advance a new model where

the approximate exchange potential is of the form

$$v_x^{app}([\rho]; \mathbf{r}) = 2\alpha_x([\rho])\epsilon_x^{app}([\rho]; \mathbf{r}). \quad (1)$$

Here, $\alpha_x([\rho])$ is a functional and $\epsilon_x^{app}([\rho]; \mathbf{r})$ is some given approximation to the exchange energy density.

The reason why $\alpha_x([\rho])$ was selected to be a functional is that in this way one can devise a parameter-free method which retains, nevertheless, the formal simplicity of the $X\alpha$ method. One must bear in mind, however, that in our present model, the determination of $\alpha_x([\rho])$ must proceed through a self-consistent-field approach.

In the next section, we describe the particular form that we have adopted for the functional $\alpha_x([\rho])$. In the third section, we carry out calculations involving the SCF determination of the functional $\alpha_x([\rho])$ for various choices of the exchange energy density $\epsilon_x^{app}([\rho]; \mathbf{r})$ and present results some selected atoms. In particular, we discuss the case where $\epsilon_x^{app}([\rho]; \mathbf{r})$ is the exact weighted mean of the average exchange charges and report, in addition, results that include correlation effects calculated using the Wilson-Levy (WL) [15] and the Lee-Yang-Parr (LYP) [16] functionals. These results are compared with those of Becke-Lee-Yang-Parr (BLYP) as well as with those based on the orbital-dependent potentials of Grabo and Gross [17].

The Model Exchange Potential

The exchange energy component of the exchange-only energy density functional in DFT is defined by

$$E_x[\rho] = \int d^3\mathbf{r}_1 \rho(\mathbf{r}_1)\epsilon_x([\rho]; \mathbf{r}_1). \quad (2)$$

The exchange-only potential of DFT arises from the variation of the functional $E_x[\rho]$ of Eq. (2) with respect to the density $\rho(\mathbf{r})$:

$$v_x([\rho]; \mathbf{r}) = \epsilon_x([\rho]; \mathbf{r}) + \rho(\mathbf{r}) \frac{\delta \epsilon_x([\rho]; \mathbf{r})}{\delta \rho(\mathbf{r})}. \quad (3)$$

Assuming that the Kohn-Sham determinant is formed from the spin-orbital set $\{\psi_i(\mathbf{r}, s) \equiv \phi_i(\mathbf{r})v_{m_{s_i}}(s)\}_{i=1}^N\}$, then we have that the weighted

mean of the averaged exchange charges $\epsilon_x([\rho]; \mathbf{r})$ is given by

$$\begin{aligned}\epsilon_x([\rho]; \mathbf{r}) = & -\frac{1}{\rho(\mathbf{r})} \sum_{i,j=1}^N \delta(m_{s_i}, m_{s_j}) \phi_i^*(\mathbf{r}) \phi_j(\mathbf{r}) \\ & \times \int \frac{\phi_j^*(\mathbf{r}') \phi_i(\mathbf{r}')}{|\mathbf{r}' - \mathbf{r}|} d\mathbf{r}',\end{aligned}\quad (4)$$

where the orbitals $\{\phi_i(\mathbf{r})\}_{i=1}^N$ are the solutions to the exchange-only Kohn–Sham equations:

$$\begin{aligned}\left(-\frac{1}{2}\nabla^2 + v(\mathbf{r}) + v_H([\rho]; \mathbf{r}) + v_x([\rho]; \mathbf{r})\right) \phi_i(\mathbf{r}) \\ = \mathcal{E}_i \phi_i(\mathbf{r}).\end{aligned}\quad (5)$$

For the case of the two-electron system, the first and second terms on the rhs of Eq. (3) are the same and, hence, we can write the exact expression $v_x([\rho]; \mathbf{r}) = 2\epsilon_x([\rho]; \mathbf{r})$. Of course, in general, this is not true, but it may be assumed that for systems having more than two electrons a good approximation for v_x is still given by $v_x([\rho]; \mathbf{r}) \approx 2\epsilon_x([\rho]; \mathbf{r})$. In fact, Slater's [3] initial replacement of the Hartree–Fock (HF) exchange potential v_x by the weighted mean of the average exchange charges, given by Eq. (4), is precisely based on this assumption.

The connection with DFT appears when $\epsilon_x([\rho]; \mathbf{r})$ is approximated by the free-electron expression. Due to the nonuniqueness of this approximation, one obtains the Slater term $\epsilon_x^S([\rho]; \mathbf{r})$ and the Gáspár–Kohn–Sham term $\epsilon_x^{GKS}([\rho]; \mathbf{r})$, which are related by $\epsilon_x^S = 2/3\epsilon_x^{GKS}$. Moreover, the representation of the exchange potential by means of

$$v_x^{\alpha_x}([\rho]; \mathbf{r}) = 2\alpha_x \epsilon_x^S([\rho]; \mathbf{r}), \quad (6)$$

where α_x is a parameter, has been an interesting and widely exploited alternative in quantum-chemical and solid-state calculations.

Owing to the linear dependence of the exchange potential Eq. (6) on α_x , there does not exist a minimum principle associated with the total energy of the system which may be applied for the variational determination of an optimum parameter α_x . For this reason, there has been much debate in the context of the $X\alpha$ method [8] concerning the best manner to determine this parameter. One such possible way [18] is to compute α_x by requiring that the total $X\alpha$ energy be equal to the precise HF energy. This way of fixing α_x , nevertheless, limits the application of the model potential given by Eq. (6) to many-electron systems for which total

HF energies are known. Another way [19, 21] is to minimize the total HF energy for the single-determinantal wave function constructed from the $X\alpha$ orbitals.

DEFINITION OF α_x

In the present work, we assume that $\alpha_x[\rho]$ is the functional

$$\alpha_x[\rho] = \frac{\int d^3\mathbf{r} \rho(\mathbf{r}) \epsilon_x([\rho]; \mathbf{r})}{-2 \int d^3\mathbf{r} \rho(\mathbf{r}) \mathbf{r} \cdot \nabla \epsilon_x^{app}([\rho]; \mathbf{r})}. \quad (7)$$

The rationale for selecting the above functional comes from the requirement that the exchange energy $E_x[\rho]$ computed through Eq. (2) be equal to the Levy–Perdew virial expression:

$$E_x[\rho] = -\int d^3\mathbf{r} \rho(\mathbf{r}) \mathbf{r} \cdot \nabla v_x^{app}([\rho]; \mathbf{r}). \quad (8)$$

Clearly, when we introduce in Eq. (8) the potential $v_x^{app}([\rho]; \mathbf{r})$ given by Eq. (1), one obtains Eq. (7). In addition, the following exchange-only Kohn–Sham equation ensues:

$$\begin{aligned}\left(-\frac{1}{2}\nabla^2 + v(\mathbf{r}) + v_H([\rho]; \mathbf{r}) + 2\alpha_x([\rho]; \mathbf{r})\right. \\ \left.\times \epsilon_x^{app}([\rho]; \mathbf{r})\right) \phi_i(\mathbf{r}) = \mathcal{E}_i \phi_i(\mathbf{r}).\end{aligned}\quad (9)$$

The above procedure can be implemented by computing $\alpha_x([\rho]; \mathbf{r})$ through Eq. (7) at each iteration until the value

$$\alpha_x^{SCF} \equiv \alpha_x[\rho_{opt}] \quad (10)$$

is attained for the optimal density ρ_{opt} computed from the orbital set $\{\phi_i(\mathbf{r})\}$ formed by the converged solutions to the Kohn–Sham equations (9). As can be seen from Eq. (7) and Eq. (1), the choice of some approximate form for the exchange energy density $\epsilon_x^{app}([\rho]; \mathbf{r})$ is needed in order to evaluate $\alpha_x[\rho]$ and the exchange potential v_x^{app} . Notice that $\epsilon_x([\rho]; \mathbf{r})$ appearing in the numerator of Eq. (7) is given by Eq. (4) where the orbitals $\{\phi_i(\mathbf{r})\}$ are the solutions to the Kohn–Sham equations at each iterative step of the SCF procedure.

VARIATIONAL ASPECTS

Consider the following approximate exchange energy functional:

$$E_x^{app}[\rho] = \int d^3\mathbf{r} \rho(\mathbf{r}) \epsilon_x^{app}([\rho]; \mathbf{r}), \quad (11)$$

where, of course, we assume a known (although not necessarily very accurate) $\epsilon_x^{appr}([\rho]; \mathbf{r})$. This definition is to be contrasted with that of the exchange energy given by Eq. (2), where $\epsilon_x([\rho]; \mathbf{r})$ [as given by Eq. (4)] is defined in terms of an orbital set which must be determined through the self-consistent solution of the Kohn-Sham equations. A compromise between these two exchange functionals can be reached by introducing the following functional:

$$\tilde{E}_x[\rho] = \alpha[\rho] E_x^{appr}[\rho], \quad (12)$$

where $\alpha[\rho]$ is given by Eq. (7).

We define the exchange potential v_x^{appr} as the functional derivative of $\tilde{E}_x[\rho]$ with respect to ρ :

$$\begin{aligned} v_x^{appr} &= \frac{\delta \alpha[\rho]}{\delta \rho} E_x^{appr}[\rho] + \alpha[\rho] \frac{\delta E_x^{appr}[\rho]}{\delta \rho} \\ &= \frac{\delta \alpha[\rho]}{\delta \rho} E_x^{appr}[\rho] + \alpha[\rho] \\ &\times \left(\epsilon_x^{appr}([\rho]; \mathbf{r}) + \rho(\mathbf{r}) \frac{\delta \epsilon_x^{appr}([\rho]; \mathbf{r})}{\delta \rho} \right). \end{aligned} \quad (13)$$

It is seen from this equation that the exact variational potential for the present ansatz contains terms which are not easily manageable. For this reason, we advance the conjecture (to be warranted by numerical results) that

$$\begin{aligned} (\delta \alpha_x[\rho]/\delta \rho) E_x^{appr}[\rho] + \alpha[\rho] \rho(\mathbf{r}) \\ \times (\delta \epsilon_x^{appr}([\rho]; \mathbf{r})/\delta \rho) \approx \alpha[\rho] \epsilon_x^{appr}([\rho]; \mathbf{r}). \end{aligned}$$

Thus, we are led to the approximate variational potential given by Eq. (1).

PROPERTIES OF v_x^{appr}

Clearly, the properties of the exchange potential $v_x^{appr}([\rho]; \mathbf{r})$ are going to be dictated by the approximation used for $\epsilon_x^{appr}([\rho]; \mathbf{r})$. For the particular case when $\epsilon_x^{appr}([\rho]; \mathbf{r}) = \epsilon_x([\rho]; \mathbf{r})$ (this alternative can be implemented by the SCF procedure discussed above), we observe that $v_x^{appr}([\rho]; \mathbf{r})$ has the following properties:

- It has the correct scaling behavior. This follows from the fact that

$$v_x^{appr}([\rho_\lambda]; \mathbf{r}) = \lambda v_x^{appr}([\rho]; \lambda \mathbf{r}), \quad (14)$$

where $\rho_\lambda(\mathbf{r}) = \lambda^3 \rho(\lambda \mathbf{r})$.

- It has a reasonable behavior at infinity. Since $v_x^{appr}([\rho_\lambda]; \mathbf{r}) \rightarrow -\alpha[\rho]/r$ for $r \rightarrow \infty$, we see that this behavior is very close to the correct one, $-1/r$, because $\alpha[\rho] \approx 1$.
- It is finite at the nucleus. This follows from the fact that $v_x^{appr}([\rho_\lambda]; \mathbf{r}) = \text{constant}$ for $|\mathbf{r}| = 0$. In this respect, it behaves like the optimized Kohn-Sham x -only potential [22].

Results and Discussion

The numerical results are presented for selected closed- and open-shell atoms. The converged values of α_x^{SCF} are listed in Table I. These values are calculated assuming that $\epsilon_x^{appr}([\rho]; \mathbf{r})$ appearing in Eq. (7) is given by Eq. (4). The values α_x^{Best} also listed in this table are obtained by requiring that the total energy be equal to the corresponding HF (SCF) one. The differences between α_x^{SCF} and α_x^{Best} lie in the range 0.001–0.002 for all atoms discussed here. It should be emphasized that the total energies are quite sensitive to the α_x values.

The ground-state energies are calculated as the expectation values of the HF Hamiltonian with respect to a single Slater determinant constructed from the Kohn-Sham orbitals. This Slater determinant corresponds to one of the degenerate microstates of the ground-state spectroscopic term. The actual evaluation was carried out numerically using a modified version of Froese Fischer's atomic program [23].

TABLE I
Values of the parameter α_x for the ground states of selected neutral atoms (see notation in text).

Atom	α_x^{SCF}	α_x^{Best}	$\alpha_x^{Best}/\alpha_x^{SCF}$
He	1.00000	1.00000	1.00000
Be	0.87587	0.87784	1.00225
B	0.84684	0.84913	1.00270
C	0.82907	0.83120	1.00257
N	0.81978	0.82173	1.00238
O	0.80407	0.80565	1.00197
F	0.79576	0.79716	1.00176
Ne	0.79247	0.79376	1.00163
Mg	0.76947	0.77060	1.00147
Ar	0.75094	0.75169	1.00100
Kr	0.71508	0.71548	1.00056

With respect to the exchange energy, however, it is worthwhile to notice that due to the definition of the model potential given by Eqs. (1) and (7) it follows that $E_x[\rho]$ may be equivalently calculated by the expression

$$E_x[\rho] = -2\alpha_x \int d^3r \rho(\mathbf{r}) \mathbf{r} \cdot \nabla \epsilon_x^{app}([\rho]; \mathbf{r}) \quad (15)$$

or by the HF expression obtained from Eqs. (2) and (4).

Table II shows the ground-state energies for the atoms considered in this work for the case when $\alpha_x = \alpha_x^{SCF}$ (clearly, when $\alpha_x = \alpha_x^{Best}$, the HF energies are reproduced). For convenience, we introduce the notation SC-F for the exchange potential $2\alpha_x \epsilon_x^{app}$, for the case when α_x is obtained self-consistently, that is, $\alpha_x = \alpha_x^{SCF}$, and $\epsilon_x^{app} = \epsilon_x$ is given by the Fock expression [Eq. (4)]. For completeness, we compare these results with the exchange-only results of Lembarki et al. [11] and Harbola and Sahni (HS) [25] and also with the OEP values of Talman [26] and Krieger, Li, and Iafrate (KLI) [27]. In the *x-only* calculations of Lembarki et al. [11], two gradient-corrected exchange potentials having the proper asymptotic behavior are used. The first one is characterized by a single parameter and the second by four parameters

(cases *a* and *b* in Table II, respectively). The mean deviations ($\bar{\Delta}$) and the maximum deviations (Δ_{MAX}) from the HF values are given for all the cases considered in the two last rows of Table II. One may infer from these results that the exchange potential SC-F is more accurate than is the Lembarki et al. [11] one-parameter case (a) and has the same accuracy as the four-parameter case (b).

It should be mentioned that the exchange potential SC-F leads to total energies which are slightly higher than the corresponding HF values. This follows from the variational principle as the total energy is computed as the expectation value of the Hamiltonian with respect to the single Slater determinant formed by the solution to the approximate Kohn-Sham *x-only* equations. The equivalence of the exchange-energy expressions given by Eqs. (2) and (8) guarantees that this variational property is maintained when the exchange energy is calculated by using Eq. (2).

The values of the exchange energy for several *x-only* SCF calculations are listed in Table III. Results for $\alpha_x = \alpha_x^{SCF}$ (SC-F) and $\alpha_x = \alpha_x^{Best}$ are compared with those of cases (a) and (b) of Lembarki et al. [11]. For completeness, we have also included values corresponding to the exchange potential of Becke taken from [28], and values from OEP, KLI, and HS calculations. The two last rows show $\bar{\Delta}$ and Δ_{MAX} deviations from the HF values.

TABLE II
Total energies of selected first- and second-row atoms for several self-consistent *x-only* calculations
(in Hartrees, negative).

Atom	SC-F	L1 ^a	L2 ^b	OEP	KLI	HS	HF ^c
He	2.86168	2.851	2.864	2.86167		2.862	2.86168
Be	14.5670	14.531	14.575	14.5725	14.5723	14.571	14.5730
B	24.5188	24.541	24.532	24.5278	24.5281	24.526	24.5291
C	37.6756	37.675	37.683	37.6865	37.68865	37.685	37.6886
N	54.3853	54.386	54.416	54.3980	54.4030	54.396	54.4009
O	74.7933	74.822	74.805	74.8075	74.8117	74.805	74.8094
F	99.3918	99.387	99.440	99.4075	99.4088	99.405	99.4093
Ne	128.5276	128.573	128.563	128.5455	128.5448	128.542	128.5471
Mg	199.5912	199.694	199.630	199.6115	199.6107	199.606	199.6146
Ar	526.7874	526.838	526.820	526.81	526.8105	526.804	526.8175
Kr	2752.003			2752.04	2752.0398	2752.030	2752.055
$\bar{\Delta}^d$	0.020	0.087	0.021	0.003	0.002	0.007	
Δ_{MAX}^e	0.042	0.37	0.081	0.006	0.005	0.014	

^{a,b} Lembarki et al.'s SCF calculations with exchange-only potential: ^a Eq. (7) and ^b Eq. (8) of [11].

^c HF values from [24].

^d Mean deviation from the HF results for the column (%).

^e Maximum deviation from the HF results for the column (%).

TABLE III
Absolute values of ground-state exchange energies from self-consistent *x-only* calculations for selected neutral atoms (in hartrees).

Atom	α_x^{SCF}	α_x^{Best}	L1 ^a	L2 ^b	Becke ^c	OEP ^d	KLI ^e	HS ^f	HF ^g
He	1.0258	1.0258	1.010	1.110	1.0273	1.026	1.026	1.0258	1.0258
Be	2.6706	2.6714	2.625	2.672	2.6692	2.666	2.667	2.6665	2.6669
B	3.7430	3.7442	3.694	3.732	3.7679			3.7429	3.7587
C	5.0321	5.0334	5.021	5.040	5.0765			5.0428	5.0647
N	6.5671	6.5687	6.567	6.560	6.6080	6.604	6.603	6.5947	6.5968
O	8.1415	8.1430	8.105	8.157	8.2345			8.1806	8.2020
F	9.9581	9.9596	10.010	10.005	10.0811			10.0135	10.0340
Ne	12.0456	12.0472	12.166	12.125	12.1619	12.105	12.099	12.1218	12.1080
Mg	15.9787	15.9803	15.977	16.072	16.0334	15.988	15.983	16.0034	15.9950
Ar	30.1393	30.1407	30.187	30.155	30.1845	30.175	30.174	30.1888	30.1780
Kr	93.7685	93.7702	93.892	93.876	93.8270	93.833		93.8635	93.8100
$\bar{\Delta}^h$	0.36	0.35	0.75	1.1	0.23	0.04	0.05	0.15	
Δ_{MAX}^i	0.76	0.74	1.72	8.21	0.40	0.11	0.09	0.43	

^{a,b} Lembarki et al.'s SCF calculation with exchange-only potential, ^a Eq. (7) and ^b Eq. (8) of [11].

^c Becke's values are taken from Ref. [28].

^d Exact OEP data from [29].

^e KLI data from [17].

^f The HS results are obtained by using a modified version of Froese-Fischer's [23] program.

^g HF values from [28].

^h Mean deviation from the HF results for the column (%).

ⁱ Maximum deviation from the HF results for the column (%).

In Table IV, we present the energies $-\epsilon_{HOMO}$ of the highest occupied orbitals for the atoms considered in this work. Again, we compare them to values obtained by Lembarki et al. [11] and to the HF values. It can be seen from this table that the orbital energies $-\epsilon_{HOMO}[\alpha_x^{SCF}\epsilon_x]$ as well as $\epsilon_{HOMO}[\alpha_x^{Best}\epsilon_x]$ calculated by the present method lie consistently (by almost the same factor) above the HF ones. Let us recall that free parameters of the exchange potentials of Lembarki et al. were determined through a fit on the OEP HOMO energies of three atoms and, hence, these exchange potentials yield quite accurate ϵ_{HOMO} energies.

The exchange potentials $2\alpha_x^{SCF}\epsilon_x$ plotted in Figures 1 and 2 for the carbon and neon atoms, respectively, are in good accord with the "exact" KS *x-only* potentials. The latter were calculated in the present work by the local scaling transformation (LST) method [30] employing even-tempered orbitals (8-term for *s*-states and 6-term for *p*-states). The potentials $2\alpha_x^{SCF}\epsilon_x$ differ from the "exact" ones in the intermediate region by about 10%. For comparison, we reproduce GEA and LDA exchange potentials, which decay more rapidly for large values of *r* and which differ from the "exact" ones

(also in the intermediate region) by about 30%. Note that the GEA exchange potential diverges near the origin.

In the first and second columns of Table V, we list total energies obtained by combining the exchange potential, computed via SC-F, with the correlation potential obtained from the Wilson-Levy (WL) [15] and the Lee-Yang-Parr (LYP) [16] functionals, respectively. For comparison purposes, we also include the total energy values reported by Grabo and Gross [17], the energies obtained by using the BLYP functional, the CI values, and the "exact" results. As it may be inferred from this table, the combinations SC-F & WL and SC-F & LYP yield excellent approximations to the total energy. In fact, in both cases, the mean deviation is smaller than the corresponding one for the BLYP functional. In Table VI, we further analyze the present approach based on the SC-F & WL and SC-F & LYP functionals and compare the ionization potentials (obtained from the ϵ_{HOMO} energies) with the experimental values. For completeness, we also present the values calculated both by Grabo and Gross [17] and those resulting from the BLYP functional. By and large,

TABLE IV
 ϵ_{HOMO} energies for atoms (in Hartrees, negative); notation as in Table III.

Atom	α_x^{SCF}	α_x^{Best}	L1 ^a	L2 ^b	HF ^c
He	0.918	0.918	0.924	0.910	0.918
Be	0.283	0.283	0.334	0.313	0.309
B	0.247	0.248	0.335	0.319	0.310
C	0.339	0.340	0.432	0.426	0.433
N	0.442	0.443	0.550	0.548	0.568
O	0.512	0.513	0.552	0.487	0.632
F	0.600	0.602	0.713	0.655	0.730
Ne	0.704	0.705	0.840	0.830	0.850
Mg	0.213	0.214	0.317	0.278	0.253
Ar	0.472	0.472	0.601	0.592	0.591
Kr	0.400	0.400			0.524

^{a,b} SCF calculations with exchange-only potential, ^a Eq. (7) and ^b Eq. (8) from [11].

^c HF values from [24].

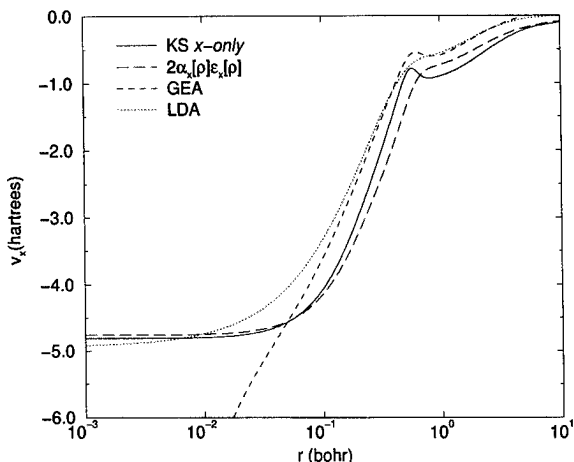


FIGURE 1. “Exact” and approximated exchange potentials for the C atom.

we observe an improvement of the ionization potentials computed via the SC-F & WL and SC-F & LYP functionals as compared with those coming from SC-F alone. We see that the former are in closer agreement with the experimental values than are those obtained from the BLYP functional.

As the possibility of using different types of approximations for $\epsilon_x^{app}(|\rho|; \mathbf{r})$ is open, we performed calculations for the total energy using $\epsilon_x^{app} = \epsilon_x^{LDA}, \epsilon_x^{GEA}, \epsilon_x^{Becke88}$:

$$\epsilon_x^{LDA} = A_x \rho^{1/3}$$

$$\epsilon_x^{GEA} = A_x \rho^{1/3} \left(1 + \frac{C_x}{2^{2/3} A_x} x^2 \right)$$

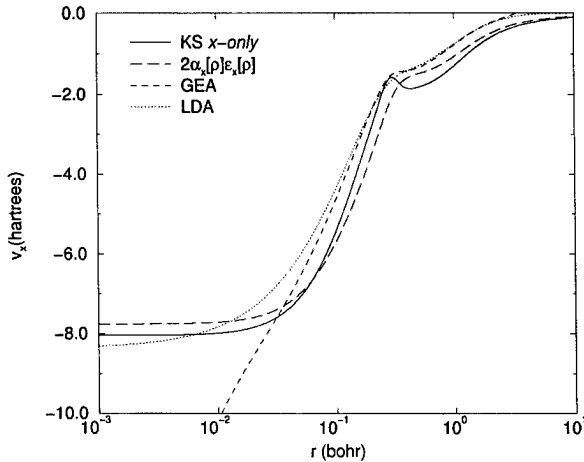


FIGURE 2. “Exact” and approximated exchange potentials for the Ne atom.

$$\epsilon_x^{Becke88} = A_x \rho^{1/3} \left(1 - \frac{\beta}{2^{1/3} A_x} \frac{x^2}{1 + 6\beta x \sinh^{-1}(x)} \right), \quad (16)$$

where

$$A_x = -3/4(3/\pi)^{1/3}, \quad C_x = -7/(432\pi(3\pi^2)^{1/3}),$$

$$\beta = 0.0042, \quad \text{and} \quad x = 2^{1/3}|\nabla\rho|/\rho^{4/3}.$$

Results of these calculations are presented in Table VII (noted as SC-LDA, SC-GEA, and SC-B88), where we have also included the values obtained directly from the LDA, GEA, and Becke88 functionals and energies calculated employing LDA, GEA, and Becke88 orbitals and the exact exchange

TABLE V

Total ground-state energies from various SCF calculations (in Hartrees, negative).

Atom	SC-F & WL	SC-F & LYP	Grabo-Gross ^a	BLYP ^a	CI ^a	Exact ^a
He	2.9039	2.9055	2.9033	2.9071		2.9037
Be	14.6649	14.6618	14.6651	14.6615	14.6657	14.6674
B	24.6546	24.6516	24.6564	24.6458	24.6515	24.6539
C	37.8549	37.8522	37.8490	37.8430	37.8421	37.8450
N	54.6124	54.6100	54.5905	54.5932	54.5854	54.5893
O	75.0693	75.0684	75.0717	75.0786	75.0613	75.067
F	99.7203	99.7201	99.7302	99.7581	99.7268	99.734
Ne	128.9118	128.9113	128.9202	128.9730	128.9277	128.939
Mg	200.0364	200.0514	200.062	200.093		200.059
Ar	527.5791	527.5385	527.553	527.551		527.604
Kr	2753.905	2753.7523				
$\bar{\Delta}^b$	0.016	0.022	0.009	0.030	0.009	
Δ_{MAX}^c	0.042	0.062	0.016	0.12	0.012	

^a Values taken from [17].^b Mean deviation from the "exact" results for the column (%).^c Maximum deviation from the "exact" results for the column (%).**TABLE VI**

Ionization potential from the HOMO energies of few neutral atoms (in Hartrees).

Atom	SC-F & WL	SC-F & LYP	Grabo-Gross ^a	BLYP ^a	Expt. ^a
He	0.949	0.950	0.945	0.585	0.903
Be	0.321	0.303	0.329	0.201	0.343
B	0.281	0.271	0.328	0.143	0.305
C	0.376	0.367	0.448	0.218	0.414
N	0.482	0.473	0.579	0.297	0.534
O	0.553	0.546	0.559	0.266	0.500
F	0.643	0.636	0.714	0.376	0.640
Ne	0.748	0.742	0.884	0.491	0.792
Mg	0.243	0.233	0.273	0.168	0.281
Ar	0.521	0.504	0.619	0.373	0.579
Kr	0.446	0.430			0.514 ^b

^a Values taken from [17].^b Value from [31].

energy expression Eq. (2). It is interesting to note that the present approach leads to a substantial improvement for the LDA and GEA cases. For example, the mean deviation $\bar{\Delta}$ goes from 1.56 to 0.011 for LDA and SC-LDA, respectively. Similarly, we observe an improvement from 0.33 for GEA to 0.044 for SC-GEA. This effect is less pronounced, albeit present, for the Becke functional. The energies $E_{HF}[\Phi^{LDA}]$ and $E_{HF}[\Phi^{GEA}]$ are closer to the HF values than those of LDA and GEA (i.e., calculated with the original LDA and GEA exchange energy expressions). The mean deviation $\bar{\Delta}$

for $E_{HF}[\Phi^{GEA}]$ has the same value as for SC-LDA (0.011) and is smaller than $\bar{\Delta}$ for SC-GEA (0.044).

We should note that a virial relation holds (up to three or more decimals) for all methods employed. However, for the LDA and GEA functionals, the virial relation holds only if we calculate the exchange energy with the original LDA or GEA exchange-energy expressions.

More detailed results of SCF calculations with $\epsilon_x^{app} = \epsilon_x^{LDA}$ (or $\epsilon_x^{app} = \epsilon_x^S \equiv \frac{3}{2}\epsilon_x^{LDA}$) are given in Table VIII. The modified LDA results presented in Table VIII are surprisingly accurate. Let us remark

TABLE VII

Comparison of total energies of spherically symmetric first- and second-row atoms from SCF x-only calculations with different $\epsilon_x^{appr} = \epsilon_x^{LDA}, \epsilon_x^{GEA}, \epsilon_x^{Becke}$, and LDA, GEA, and Becke88 results.^a

Method / Atom	He	Be	Ne	Mg	Ar	Kr	$\bar{\Delta}^b$	Δ_{MAX}^c
SC-LDA	2.8609	14.5707	128.5332	199.6007	526.7981	2752.015	0.011	0.027
LDA	2.7236	14.2233	127.4907	198.2488	524.5174	2746.866	1.56	4.83
$E_{HF}[\Phi^{LDA}]$	2.8578	14.5681	128.5275	199.5973	526.7950	2752.011	0.033	0.14
SC-GEA	2.8563	14.5679	128.5164	199.5959	526.7862	2752.002	0.044	0.19
GEA	2.8423	14.4871	128.2215	199.1364	525.9354	2749.877	0.33	0.68
$E_{HF}[\Phi^{GEA}]$	2.8606	14.5712	128.5371	199.6050	526.8060	2752.026	0.011	0.038
SC-B88	2.8608	14.5706	128.5330	199.6006	526.7978	2752.015	0.012	0.031
B88	2.8634	14.5664	128.5901	199.6320	526.7998	2752.101	0.025	0.060
HF	2.86168	14.5730	128.5471	199.6146	526.8175	2752.055		

^a All values were obtained by means of a modified version of the program described in [23].

^b Mean deviation from the HF results for the column (%).

^c Maximum deviation from the HF results for the column (%).

TABLE VIII

Orbital, exchange, and total energies computed for selected closed- and open-shell atoms using SC-LDA and comparison of total energy with HF results

Atom	ϵ_{HOMO}	E_x	E_{Total}	E_{HF}
He	0.582	1.0175	2.8609	2.86168
Be	0.195	2.6633	14.5707	14.5730
B	0.125	3.7355	24.5252	24.5291
C	0.190	5.0253	37.6824	37.6886
N	0.261	6.5592	54.3911	54.4009
O	0.330	8.1468	74.8000	74.8094
F	0.404	9.9728	99.3983	99.4093
Ne	0.485	12.0654	128.5332	128.5471
Mg	0.155	15.9739	199.6007	199.6146
Ar	0.360	30.1653	526.7981	526.8175
Kr	0.316	93.7936	2752.0147	2752.055

All values are in Hartrees, negative.

for clarity that since in the present approach α_x^{SCF} is calculated self-consistently it is not—as in the case of the original LDA or HF-Slater methods—a parameter that we can adjust to fit some given result. It is for this reason that we regard the present approach as a parameter-free method.

In Table IX, we present results obtained by solving the Kohn-Sham equations where in addition to the exchange potential generated from SC-LDA we have added the WL correlation potential. Again, we observe that the results are quite accurate.

While this article was under review, there appeared an article by Cortona [32] where he pre-

TABLE IX

Calculations for selected atoms using SC-LDA for exchange plus the WL functional for electron correlation.

Atom	ϵ_{HOMO}	E_x	E_{Total}	E_{Total}^{exacta}
He	0.611	1.0226	2.9032	2.9037
Be	0.232	2.6736	14.6697	14.6674
B	0.155	3.7514	24.6615	24.6539
C	0.223	5.0453	37.8623	37.8450
N	0.297	6.5832	54.6189	54.5893
O	0.367	8.1719	75.0764	75.067
F	0.443	9.9998	99.7272	99.734
Ne	0.526	12.0948	128.9178	128.939
Mg	0.186	15.9961	200.0465	200.059
Ar	0.407	30.2106	527.5904	527.604
Kr	0.361	93.8509	2753.9173	

All values are in Hartrees, negative. For comparison, the “exact” values of total energy are listed.

^a Values taken from [17].

sented a method quite similar to the one advanced here. In fact, Cortona’s approach corresponds to the particular instance where $\epsilon_x^{appr} = \epsilon_x^{LDA}$. His results are in complete agreement with ours (up to all decimals reported in [32]) for closed-shell atoms. For open-shell atoms, his results differ from ours due to the fact that he used a spin-unrestricted approach.

ACKNOWLEDGMENTS

One of us (V. K.) acknowledges financial support from the 38th Sanibel Symposium organizers.

R. L. B. is grateful to Conicet of Venezuela for an S3 travel grant and thanks a financial support by the National Science Foundation under Grant No. CHEM-9632706. This work was partially supported by the Comission of European Communities through Contract No. CI1*-CT93-0333.

References

1. D. R. Hartree, *The Calculation of Atomic Structures* (Wiley, New York, 1957).
2. J. C. Slater, *Quantum Theory of Atomic Structure* (McGraw-Hill, New York, 1960), Vol. II.
3. J. C. Slater, Phys. Rev. **81**, 385 (1951); *Ibid.*, **82**, 538 (1951); *Ibid.*, J. Chem. Phys. **43**, S228 (1965).
4. F. Bloch, Z. Phys. **57**, 545 (1929).
5. P. A. M. Dirac, Proc. Camb. Philos. Soc. **26**, 376 (1930).
6. R. Gáspár, Acta Phys. Hung. **3**, 263 (1954).
7. W. Kohn and L. J. Sham, Phys. Rev. A **140**, 1133 (1965); B. Y. Tong and L. J. Sham, Phys. Rev. **144**, 1 (1966).
8. J. C. Slater and K. H. Johnson, Phys. Rev. B **5**, 844 (1972).
9. A. D. Becke, Phys. Rev. A **38**, 3098 (1988).
10. Ch. Lee and Z. Zhou, Phys. Rev. A **44**, 1536 (1991).
11. A. Lembarki, F. Rogemond, and H. Chermette, Phys. Rev. A **52**, 3704 (1995).
12. M. Levy and J. P. Perdew, Phys. Rev. A **32**, 2010 (1985).
13. E. S. Kryachko, E. V. Ludeña, R. López-Boada, and J. Maldonado, in *Condensed Matter Theories*, L. Blum and F. Bary Malik, Eds. (Plenum, New York, 1993), Vol. 8.
14. R. López-Boada, R. Pino, and E. V. Ludeña, Int. J. Quantum Chem. **63**, 1025 (1997).
15. L. C. Wilson and M. Levy, Phys. Rev. B **41**, 12930 (1990).
16. C. Lee, W. Yang, and R. G. Parr, Phys. Rev. B **37**, 785 (1988).
17. T. Grabo and E. K. U. Gross, Chem. Phys. Lett. **240**, 141 (1995).
18. K. Schwarz, Phys. Rev. B **5**, 2466 (1972).
19. I. Lindgren, Phys. Rev. Lett. **19**, 382 (1965).
20. J. H. Wood, Int. J. Quantum Chem. **S3** 747 (1970).
21. E. A. Kmetko, Phys. Rev. A **1**, 37 (1970).
22. O. V. Gritsenko, R. van Leeuwen, and E. J. Baerends, Int. J. Quantum. Chem. **57**, 17 (1996).
23. C. Froese Fischer, Comput. Phys. Commun. **43**, 355 (1987).
24. C. Froese Fischer, *The Hartree-Fock Method for Atoms* (Wiley, New York, 1977).
25. V. Sahni, Y. Li, and M. K. Harbola, Phys. Rev. A **45**, 1434 (1992).
26. J. D. Talman, Comp. Phys. Commun. **54**, 85 (1989); K. Aashmar, T. M. Luke, and J. D. Talman, At. Data. Nucl. Data Tab. **22**, 443 (1978).
27. Y. Li, J. B. Krieger, and G. J. Iafrate, Phys. Rev. A **47**, 165 (1993).
28. N. H. March, *Electron Density Theory of Atoms and Molecules*, (Academic Press, London, 1992).
29. E. Engel and S. H. Vosko, Phys. Rev. **47**, 13164 (1993).
30. E. V. Ludeña, J. Maldonado, and R. López-Boada, J. Chem. Phys. **102**, 318 (1995).
31. N. A. Cordero, K. D. Sen, J. A. Alonso, and L. C. Balbas, J. Phys. II Fr. **5**, 1277 (1995).
32. P. Cortona, Phys. Rev. A **57**, 4306 (1998).

Investigation of an Asymmetric Triple-Excitation Correction for Coupled-Cluster Energies

T. DANIEL CRAWFORD, JOHN F. STANTON

Institute for Theoretical Chemistry, Departments of Chemistry and Biochemistry, The University of Texas, Austin, Texas 78712-1167

Received 22 February 1998; revised 1 May 1988; accepted 13 May 1988

ABSTRACT: A correction for the effects of connected triple excitations to the coupled-cluster singles and doubles energy is studied. The approach relies on the fact that the ground-state coupled-cluster energy may be viewed as an eigenvalue of an effective (similarity transformed) Hamiltonian with associated left and right eigenvectors. Taking these as zeroth-order wave functions and using a conventional partitioning of the bare electronic Hamiltonian, the lowest order triple-excitation correction to the correlation energy is found to have an asymmetric form that involves cluster amplitudes as well as components of the left eigenvector. The popular (T) correction may be viewed as an approximation to the present approach, though the latter is approximately a factor of 2 more expensive to compute. The method is applied to a number of difficult cases, including the harmonic vibrational frequencies of ozone and the equilibrium bond length of N₂. In addition, the theory of analytic gradients for the method is outlined and some aspects regarding its implementation are discussed. © 1998 John Wiley & Sons, Inc. Int J Quant Chem 70: 601–611, 1998

Key words: coupled-cluster theory; triple-excitation corrections; equation-of-motion coupled-cluster theory; perturbation theory; analytic energy gradient theory

Correspondence to: T. D. Crawford.

Contract grant sponsors: National Science Foundation;
Robert A. Welch Foundation; Alfred P. Sloan Foundation.

Introduction

The importance of higher excitations in the description of dynamic electron correlation effects has been well understood for several years. In the absence of a multiconfiguration reference, for example, it has been shown that up to hextuply excited determinants must be included in the correlated wave function in order to obtain even qualitatively correct predictions of bond-breaking processes, particularly in multiply bonded systems [1]. For regions of the potential energy surface near the equilibrium structure, however, the outlook is not quite so bleak. In systems for which a single-determinant reference wave function provides a reasonable zeroth-order approximation, only single, double, and triple excitations may be necessary in order to obtain quantitatively accurate predictions of molecular properties.

In the coupled-cluster (CC) model of electron correlation [2–5], the inclusion of all triply excited determinants (CCSDT) [6–8] is, in general, too computationally intensive to apply to all but the smallest molecular systems, and much effort has been devoted to the construction of reliable approximations. Both iterative [9–11] and noniterative [10, 12, 13] approaches have been examined, and the so-called CCSD(T) method, which includes all singles and doubles [14, 15] as well as a perturbational estimate of connected triple excitations [12, 13, 16–19], provides perhaps the best balance between accuracy and affordability of any single-reference approach [5, 20–23].

Recently, it has been shown [24] that equation-of-motion coupled-cluster theory (EOM-CC) [25–30] provides a unique perspective on the CCSD(T) method. Instead of taking the Hartree–Fock determinant as the zeroth-order wave function and subsequently decomposing the CCSD equations in terms of the many-body perturbation expansion, as is usually done, the CCSD wave function is taken as zeroth-order and the energy viewed as the lowest eigenvalue of an effective Hamiltonian with associated left and right eigenvectors. By substituting converged CCSD cluster amplitudes in place of the left eigenvector in the lowest-order energy correction, the usual (T) energy expression is obtained. In this work, we examine the alternative correction obtained by avoiding this final substitution and preserving the

left eigenvector in the equation. [This approach was used previously [31] to develop a closely related triple-excitation correction for the equation-of-motion coupled-cluster method for ionized states (EOMIP-CC). Footnote 19 of Ref. [31] compares this to the triples correction investigated in this work.] The resulting formula is more expensive to calculate than the (T) correction. In the following section, we outline the theoretical basis for the energy expression and discuss its efficient implementation. In the third section we apply the method to selected systems for which triple excitations are particularly important.

Theory and Implementation

In EOM-CC theory, the normal-ordered electronic Hamiltonian (\hat{H}) undergoes a similarity transformation of the form

$$\bar{H} \equiv e^{-\hat{T}} \hat{H} e^{\hat{T}}, \quad (1)$$

where the cluster operator (\hat{T}) that parametrizes the transformation may be taken from a related, ground-state coupled-cluster wave function. The resulting operator (\bar{H}) is then diagonalized within a selected space of determinants [usually chosen to be the reference ($|0\rangle$) and all excitations generated from it by \hat{T}]. The lowest eigenvalue is the ground-state CC energy, E_{CC} , which, due to the non-Hermiticity of \bar{H} , has distinct biorthogonal right and left eigenvectors,

$$\bar{H}|0\rangle = E_{\text{CC}}|0\rangle \quad (2)$$

and

$$\langle 0|\hat{\mathcal{L}}\bar{H} = \langle 0|\hat{\mathcal{L}}E_{\text{CC}}, \quad (3)$$

respectively. If the diagonalization space is defined to include all possible excitations from $|0\rangle$, the similarity transformed Hamiltonian has an eigenvalue spectrum identical to that of the nontransformed (full configuration interaction) Hamiltonian. However, this space is usually truncated to produce only singly and doubly excited determinants, defining the so-called EOM-CCSD approximation.

We may partition the complete determinant space $|\mathbf{h}\rangle$ into the reference $|0\rangle$, $|\mathbf{g}\rangle$ (all singly and doubly excited determinants generated from $|0\rangle$ by the truncated \hat{T}) and $|\mathbf{q}\rangle$ (all remaining determinants). By defining $|\mathbf{p}\rangle \equiv |0\rangle \cup |\mathbf{g}\rangle$, the effective

Hamiltonian may be written as

$$\bar{H} = \begin{bmatrix} \bar{H}_{pp} & \bar{H}_{pq} \\ \bar{H}_{qp} & \bar{H}_{qq} \end{bmatrix}. \quad (4)$$

We may use Löwdin's partitioning approach [32] to solve for an eigenvalue of the complete Hamiltonian in terms of the projections of the left ($\hat{\mathcal{L}}$) and right ($\hat{\mathcal{R}}$) eigenvectors onto the $|p\rangle$ space to give

$$E_{\text{exact}} = \hat{\mathcal{L}}_p \bar{H}_{pp} \hat{\mathcal{R}}_p + \hat{\mathcal{L}}_p \bar{H}_{pq} (E_{\text{exact}} \mathbf{1}_{qq} - \bar{H}_{qq})^{-1} \bar{H}_{qp} \hat{\mathcal{R}}_p. \quad (5)$$

The second term on the right-hand side of Eq. (5) may be considered as the exact correction to an approximate eigenvalue obtained by diagonalizing \bar{H} within the $|p\rangle$ space. By first choosing a partitioning of \bar{H} and subsequently expanding the inverse in Eq. (5) in a power series [32], one may obtain a variety of iterative approaches for calculating the eigenvalue E_{exact} . (If the operator used in Eq. (5) is the bare electronic Hamiltonian \hat{H} instead of its similarity-transformed counterpart \bar{H} , a power series expansion provides the usual Rayleigh–Schödinger or Brillouin–Wigner perturbation theories, as discussed by Löwdin [32].)

A many-body perturbation theory partitioning of the (nontransformed) electronic Hamiltonian into zeroth- and first-order components, viz.

$$\hat{H} = \hat{H}^{[0]} + \hat{H}^{[1]}, \quad (6)$$

leads to an order-by-order expansion of the similarity-transformed Hamiltonian [33]:

$$\bar{H} = \bar{H}^{[0]} + \bar{H}^{[1]} + \bar{H}^{[2]} + \dots, \quad (7)$$

and an analogous expansion of the energy

$$E_{\text{exact}} = E^{[0]} + E^{[1]} + E^{[2]} + E^{[3]} + \dots. \quad (8)$$

If we further define the $|p\rangle$ space projection of \bar{H} to be zeroth-order (along with its corresponding left and right eigenvectors), order-by-order corrections toward the exact energy may be obtained which depend strictly on the partitioning of the bare electronic Hamiltonian used in Eq. (6). Here we choose the Møller–Plesset partitioning [34] such that the Fock operator (\hat{F}) is used as $\hat{H}^{[0]}$. Since $\hat{\mathcal{R}}_p = \mathbf{1}$ (i.e., the CCSD equations have been solved), it can be shown that the lowest order correction to

the CCSD energy appears in third order as [24]

$$\Delta E^{[3]} = \langle 0 | \hat{\mathcal{L}} | \mathbf{S} \rangle \langle \mathbf{S} | \bar{H}^{[1]} | \mathbf{T} \rangle \mathbf{D}_3 \langle \mathbf{T} | \bar{H}^{[2]} | 0 \rangle + \langle 0 | \hat{\mathcal{L}} | \mathbf{D} \rangle \langle \mathbf{D} | \bar{H}^{[1]} | \mathbf{T} \rangle \mathbf{D}_3 \langle \mathbf{T} | \bar{H}^{[2]} | 0 \rangle, \quad (9)$$

where the notation $\hat{\mathcal{L}}$ is intended to imply only the left eigenvector of \bar{H}_{pp} rather than the p-space projection of the exact left eigenvector, $|\mathbf{S}\rangle$, $|\mathbf{D}\rangle$, and $|\mathbf{T}\rangle$ denote singly, doubly, and triply excited determinants relative to $|0\rangle$, respectively, and \mathbf{D}_3 is a shorthand notation for the usual energy denominator, $[\langle \mathbf{T} | \hat{H}^{[0]} | \mathbf{T} \rangle]^{-1}$.

As pointed out previously [24], the form of Eq. (9) is identical to the conventional (T) correction if the adjoint of the cluster operator \hat{T}^\dagger is used in place of the left eigenvector $\hat{\mathcal{L}}$. The first term on the right-hand side of Eq. (9) is therefore analogous to the fifth-order E_{ST} component of the (T) correction, while the second corresponds to the fourth-order E_{DT} component [18]. The difference in perturbational order between these terms is due to the fact that the earliest contribution of \hat{T}_2 in Møller–Plesset theory is to the first-order wave function, while that of \hat{T}_1 is to the second-order wave function. Both terms contribute to the third-order correction in the present framework, where $\hat{\mathcal{L}}$ is retained in Eq. (9), because both single- and double-excitation components of the left-hand eigenvector are zeroth order.

In the more conventional (T) approach, the energy expression has a more symmetric form due to the presence of cluster operators on both sides of each term in the equation. As a result, only one \mathcal{N}^7 term (namely $\bar{H}^{[1]} \hat{T}_2 \rightarrow \hat{T}_3$) must be evaluated. In the current theory, however, the energy expression contains components of the left eigenvector on one side and cluster operators on the other. Thus, two \mathcal{N}^7 expressions must be evaluated: the same \hat{T}_2 containing term as in the (T) correction, as well as an analogous term involving $\hat{\mathcal{L}}$. In addition, the number of \mathcal{N}^6 steps which must be evaluated is doubled for the present theory since the ground-state left eigenvector must be constructed as well. (The so-called $\hat{\Lambda}$ equations, which were developed within the framework of coupled-cluster gradient theory [35–38] must be solved via an \mathcal{N}^6 procedure in order to obtain the left eigenvector from the relation $\hat{\mathcal{L}} = \mathbf{1} + \hat{\Lambda}$.) Hence, the proposed asymmetric triple-excitation correction, which we will hereafter refer to as a-CCSD(T), is approximately a factor of 2 more expensive to evaluate than that defined by CCSD(T). This triples correc-

tion has also been independently examined recently by Kucharski and Bartlett [39] who compared this approach to a series of similar methods obtained using several different coupled-cluster energy functionals. We have implemented the a-CCSD(T) method in a local version of the ACESII program system [40].

Test Applications

POTENTIAL ENERGY CURVE OF H₂O

Due in part to the availability of full configuration interaction (FCI) data [41–44], a popular test of approximate electron correlation approaches has been computation of single-point energies of H₂O at equilibrium and stretched $r(\text{O}-\text{H})$ bond lengths [6, 9, 13, 44–46]. Using the geometries reported previously by Saxe and co-workers (R_e) [41], Harrison and Handy (1.5 R_e and 2.0 R_e) [42], and Olsen and co-workers (2.5 R_e and 3.0 R_e) [44], as well as additional structures at 1.25 R_e , 1.75 R_e , and 2.25 R_e summarized in Table I, we have computed a-CCSD(T) energies using the cc-pVDZ basis set of Dunning [47]. For comparison to the FCI and CCSDT results reported by Olsen and co-workers [44], no orbitals were frozen in the correlated calculations. It should also be noted that the spin-restricted Hartree–Fock (RHF) reference determinants used at the longer bond lengths (specifically 2.5 R_e and 3.0 R_e) are those which correlate back to the lowest-energy RHF wave function at the equilibrium structure, but are not energetically optimum.

Table II summarizes the total energies at the RHF, CCSD, CCSD(T), a-CCSD(T), CCSDT, and FCI levels of theory, as well as differences from the FCI and CCSDT energies for each method. In addition, Figure 1 provides a plot of the FCI data points reported in Ref. 44 and the potential energy curve for each of the coupled-cluster methods. The FCI data points show the expected asymptotic behavior near -79.911 E_h while a characteristic nonvariational “collapse” of each coupled cluster potential energy curve can be observed as the bonds are stretched. This gradual failure of the approximate methods is a consequence of the increasing inadequacy of the single-determinant RHF reference wave function. The infinite-order CCSD and CCSDT methods show resistance to this collapse even as far out on the potential curve as 3.0 R_e . The CCSD(T) method, on the other hand,

TABLE I Nonzero components of the Cartesian coordinates of the 1.25 R_e , 1.75 R_e , and 2.25 R_e H₂O geometries used in this work.^a

xR_e	O_z	H_y	H_z
1.25	−0.14687455	1.89407696	1.16550258
1.75	−0.20562438	2.65170774	1.63170361
2.25	−0.26437420	3.40933853	2.09790464

^aOther geometries are the same as those used in Ref. 44. C_{2v} symmetry is assumed with the C_2 axis coincident with the z axis and the molecule lying in the yz plane.

fails much sooner and shows a strong decrease in curvature as early as 2.25 R_e , while the a-CCSD(T) introduced here begins to collapse further out (near 2.75 R_e). As the O–H bonds are stretched, the a-CCSD(T) energy remains somewhat closer to FCI than does CCSD(T). Most important, however, the a-CCSD(T) potential energy curve follows the full CCSDT curve very closely from above across the entire range of geometries and finally crosses it only once the longest bond lengths are reached.

HARMONIC VIBRATIONAL FREQUENCIES OF O₃

One of the most challenging problems for state-of-the-art correlated methods is the prediction of the harmonic vibrational spectrum of ozone. Numerous studies have appeared in recent years which make direct comparisons between experimentally derived harmonic frequencies [48, 49] and those obtained using configuration interaction [50–52] or coupled-cluster methods [12, 53–60]. In order to compare the performance of a-CCSD(T), CCSD(T), and CCSDT, we have computed optimized geometries and harmonic vibrational frequencies for ozone using DZP [61] and cc-pVTZ [47] basis sets. The core electrons were not correlated with either basis set, and the three highest-lying virtual orbitals were deleted for all calculations carried out with the smaller DZP basis. These results are summarized in Table III.

With both basis sets, the a-CCSD(T) prediction of the equilibrium geometry lies slightly further away from the CCSDT prediction than CCSD(T), though the differences are small. For the problematic asymmetric stretching frequency (ω_3), however, the a-CCSD(T) method provides considerably better agreement with CCSDT than does CCSD(T). With the DZP basis set, the a-CCSD(T) frequency

TABLE II

Total energies (in $E_h + 75$), energy differences (in mE_h) from the FCI energy (in parentheses) and from the CCSDT energy (in brackets) for restricted Hartree – Fock and a number of approximate coupled-cluster methods for H_2O at equilibrium and stretched geometries using a cc-pVDZ basis set.^a

Method	R_e	$1.25R_e$	$1.5R_e$	$1.75R_e$	$2.0R_e$	$2.25R_e$	$2.5R_e$	$3.0R_e$
RHF	-1.024039 (217.821)	-0.930811 —	-0.802387 (269.961)	-0.685657 —	-0.587711 (363.954)	-0.506904 —	-0.441244 (476.747)	-0.344392 (567.554)
	[217.328]	[238.455]	[268.538]	[310.294]	[365.359]	[433.431]	[501.499]	[607.680]
	-1.238116 (3.744)	-1.164159 —	-1.062305 (10.043)	-0.981683 —	-0.929633 (22.032)	-0.904385 —	-0.897684 (20.307)	-0.901097 (10.849)
CCSD	[3.251]	[5.107]	[8.620]	[14.268]	[23.437]	[35.950]	[45.059]	[50.975]
	-1.241202 (0.658)	-1.169006 —	-1.070717 (1.631)	-0.996436 —	-0.955485 (-3.820)	-0.946101 —	-0.960555 (-42.564)	-1.002458 (-90.512)
	[0.165]	[0.260]	[0.208]	[0.485]	[2.415]	[5.766]	[17.812]	[50.386]
CCSD(T)	-1.241162 (0.698)	-1.168878 —	-1.070217 (2.131)	-0.994754 —	-0.950967 (0.698)	-0.936454 —	-0.939937 (-21.946)	-0.953788 (-41.842)
	[0.205]	[0.388]	[0.708]	[1.197]	[2.103]	[3.881]	[2.806]	[1.716]
	-1.241367 (0.493)	-1.169266 [0.000]	-1.070925 (1.423)	-0.995951 —	-0.953070 (-1.405)	-0.940335 —	-0.942743 (-24.752)	-0.952072 (-40.126)
a-CCSD(T)	[0.000]	[0.000]	[0.000]	[0.000]	[0.000]	[0.000]	[0.000]	[0.000]
	-1.241860 (0.000)	—	-1.072348 (0.000)	—	-0.951665 (0.000)	—	-0.917991 (0.000)	-0.911946 (0.000)
	[-0.493]	—	[-1.423]	—	[1.405]	—	[24.752]	[40.126]

^aFCI and CCSDT results at R_e , $1.5R_e$, $2.0R_e$, $2.5R_e$, and $3.0R_e$ were taken from Ref. 44.

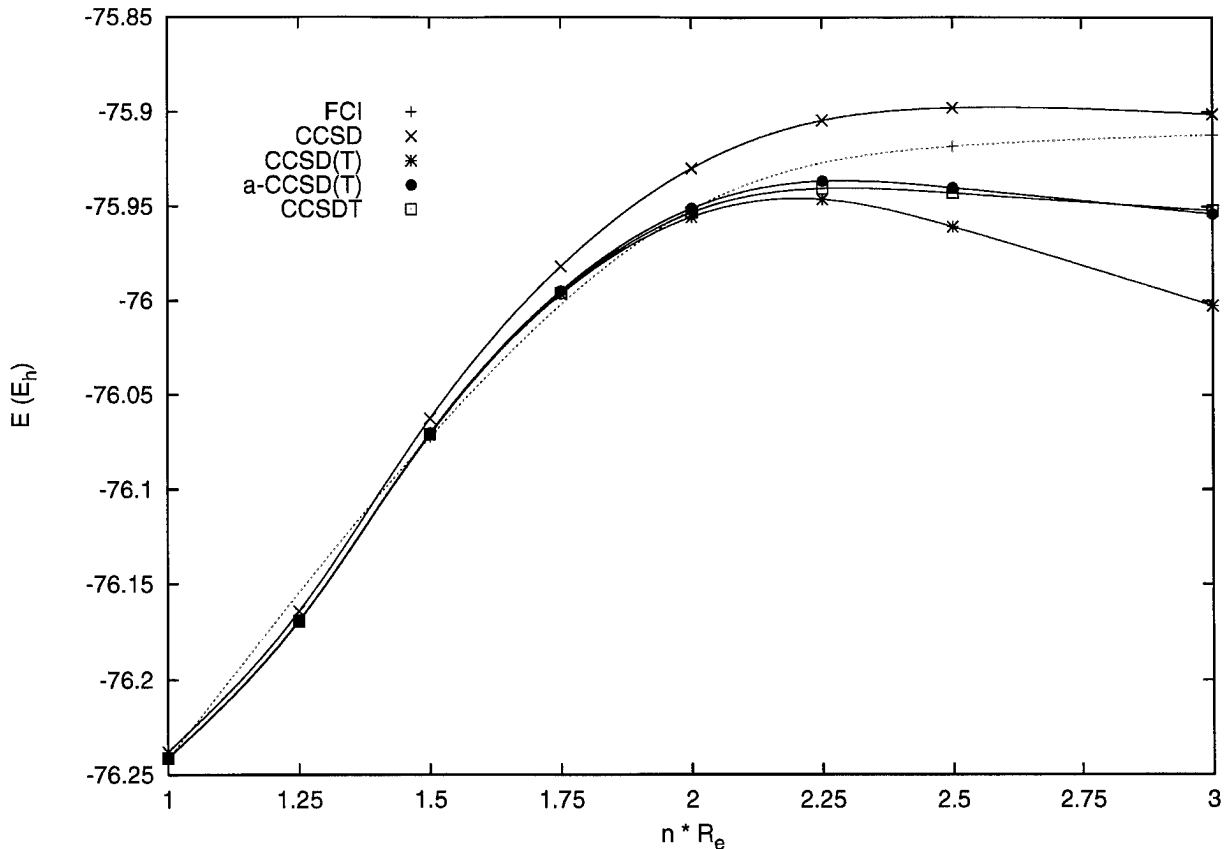


FIGURE 1. FCI and coupled-cluster potential energy curves (in E_h) for H_2O at equilibrium and stretched geometries using a cc-pVDZ basis set.

TABLE III
Coupled-cluster predictions of the equilibrium geometry and harmonic vibrational frequencies of ozone.

	DZP basis				cc-pVTZ basis				
	CCSD	CCSD(T)	a-CCSD(T)	CCSDT ^a	CCSD	CCSD(T)	a-CCSD(T)	CCSDT ^b	Expt. ^c
r_e	1.26291	1.28690	1.28293	1.286	1.24993	1.27550	1.27143	1.274	1.272
θ_e	117.369	116.798	116.939	116.7	117.584	116.948	117.084	116.8	116.8
ω_1	1255.79	1129.84	1156.55	1141	1277.66	1153.10	1179.17	1163	1135
ω_2	747.91	702.82	710.97	705	762.97	715.69	724.05	717	716
ω_3	1237.42	977.12	1059.02	1077	1265.94	1054.32	1130.51	1117	1089

^aRef. 58.^bRef. 60.^cRefs. 48 and 49.

of 1059 cm^{-1} lies only 18 cm^{-1} below the full CCSDT result, while CCSD(T) gives a value that is 100 cm^{-1} too small. As the one-electron basis is improved to cc-pVTZ, the CCSD(T) prediction for ω_3 still lies about 63 cm^{-1} below the CCSDT value of 1117 cm^{-1} recently reported by Watts and Bartlett [60], while the a-CCSD(T) prediction moves even closer to only 13 cm^{-1} above the CCSDT result. Although there has recently been some speculation as to the adequacy of correlated methods which do not include the effects of connected quadruple excitations for the ozone problem [60], the a-CCSD(T) method clearly provides results which closely approximate those of the substantially more expensive CCSDT approach.

EQUILIBRIUM BOND LENGTH OF N_2

In recent work examining the basis-set convergence of the CCSDT method, Halkier and co-workers [62] determined equilibrium geometries for a number of closed-shell molecules using the series of correlation-consistent basis sets developed by Dunning [45]. Of particular interest in their work was the comparison between CCSD(T) and CCSDT predictions using the large cc-pVQZ basis set. For nearly all of the molecules they examined, the differences between the two methods were less than 0.0001 \AA . The only exception was for the equilibrium bond length of N_2 where a difference of 0.0006 \AA was noted. As a third test of the a-CCSD(T) method, we have optimized the geometry of N_2 within the cc-pVQZ basis set for comparison to the results reported by Halkier and co-workers [62]. These data are summarized in Table IV. The CCSD(T) method predicts an equi-

librium bond distance of 1.09780 \AA , a difference of only 0.0003 \AA from the CCSDT result. The a-CCSD(T) method therefore represents a significant improvement over the CCSD(T) (relative to CCSDT) in this example.

Conclusions

A noniterative triple-excitation correction for the CCSD energy has been studied. This approach, denoted a-CCSD(T), is obtained by using the left and (trivial) right eigenvectors of the similarity-transformed Hamiltonian corresponding to the CCSD energy as zeroth-order wave functions in a perturbation expansion of the exact energy. The conventional (T) correction, which is approximately a factor of 2 less expensive to compute than a-CCSD(T), may be considered an approximation to the present approach obtained by substituting cluster amplitudes (\hat{T}) in place of the components of the left eigenvector in the energy expression.

We have shown that the a-CCSD(T) method provides predictions of molecular properties that compare closely to those of the very expensive CCSDT method, including difficult cases such as

TABLE IV
Equilibrium bond length (in \AA) of N_2 determined within the cc-pVQZ basis set of Dunning [47] using a number of coupled-cluster methods.^a

	CCSD	CCSD(T)	a-CCSD(T)	CCSDT
r_e	1.09089	1.09809	1.09780	1.09746

^aFull CCSDT results have been taken from Ref. 62.

the harmonic vibrational spectrum of ozone and the equilibrium bond length of N₂. [We have also computed single-point energies for 10 molecules studied previously [63]. Using the geometries and basis sets given in Ref. [63] for CH₄, H₂O, HF, N₂, F₂, NO⁺, O₃, C₂, BeO, and CN⁺, the a-CCSD(T) method gives an average absolute error (relative to CCSDT) of 711 μE_h compared to 762 mE_h for CCSD(T), 14296 μE_h for CCSD, 2418 μE_h for CCSDT-1a [9], 1914 μE_h for CCSDT-1b [10, 11] 1037 μE_h for CCSDT-2 [10, 11], 1236 μE_h for CCSDT-3 [10, 11], and 1257 μE_h for CCSDT-4 [6].]

Although additional comparisons are clearly needed before any conclusion regarding the relative accuracies of the a-CCSD(T) and CCSD(T) methods can be drawn, the present results are encouraging. Due to its higher computational expense, it is, however, most unlikely that a-CCSD(T) will ever achieve the popularity of the CCSD(T) method.

Appendix A: Analytic Gradient Theory for the a-CCSD(T) Method

This appendix provides the outline for an efficient method to calculate derivatives of the a-CCSD(T) energy analytically and a brief discussion of how the computational requirements differ from those associated with CCSD(T) energy derivative evaluation. In a-CCSD(T), the triples energy correction depends on two sets of wave function parameters: the cluster amplitudes \hat{T} obtained by solving the CCSD equations and the $\hat{\mathcal{L}}$ amplitudes that account for the response of the \hat{T} amplitudes to external perturbations. Although the energy is stationary with respect to neither the \hat{T} nor $\hat{\mathcal{L}}$ amplitudes, the $2n + 1$ rule of perturbation theory guarantees that the energy derivative can be expressed entirely in terms of the unperturbed wave function parameters. Developing such an expression for a-CCSD(T) requires some care, and this aspect of the derivation is stressed in what follows.

The triples energy correction $\Delta E_T \equiv \Delta E^{[3]}$ of a-CCSD(T) can be represented compactly as

$$\Delta E_T = \langle 0 | \hat{\mathcal{L}} \hat{W} D_3 \hat{W} \hat{T}_2 | 0 \rangle, \quad (\text{A1})$$

where \hat{W} is the part of $\bar{H}^{[1]}$ that comprises the two-electron integrals and $\hat{\mathcal{L}}$, \hat{T}_2 , and D_3 are defined earlier. Straightforward differentiation of ΔE_T

with respect to the generic perturbation χ yields

$$\begin{aligned} \frac{\partial \Delta E_T}{\partial \chi} = & \langle 0 | \frac{\partial \hat{\mathcal{L}}}{\partial \chi} \hat{W} | \mathbf{T} \rangle \langle \mathbf{T} | \hat{T}_3 | 0 \rangle \\ & + \langle 0 | \hat{\mathcal{L}} \frac{\partial \hat{W}}{\partial \chi} | \mathbf{T} \rangle \langle \mathbf{T} | \hat{T}_3 | 0 \rangle \\ & + \langle 0 | \hat{\mathcal{L}} \hat{W} | \mathbf{T} \rangle \langle \mathbf{T} | \frac{\partial \hat{T}_3}{\partial \chi} | 0 \rangle, \quad (\text{A2}) \end{aligned}$$

where

$$\langle \mathbf{T} | \hat{T}_3 | 0 \rangle \equiv D_3 \langle \mathbf{T} | \hat{W} \hat{T}_2 | 0 \rangle. \quad (\text{A3})$$

It is easily shown that

$$\langle \mathbf{T} | \frac{\partial \hat{T}_3}{\partial \chi} | 0 \rangle = D_3 \left[\langle \mathbf{T} | \frac{\partial \hat{W}}{\partial \chi} \hat{T}_2 | 0 \rangle + \langle \mathbf{T} | \hat{W} \frac{\partial \hat{T}_2}{\partial \chi} | 0 \rangle \right. \\ \left. - \langle \mathbf{T} | \frac{\partial \hat{F}}{\partial \chi} | \mathbf{T} \rangle \langle \mathbf{T} | \hat{T}_3 | 0 \rangle \right], \quad (\text{A4})$$

where \hat{F} represents the zeroth-order electronic Hamiltonian that comprises the occupied-occupied and virtual-virtual projections of the Fock operator. Substituting this result into Eq. (A2) allows the derivative of the triples energy to be expressed as:

$$\begin{aligned} \frac{\partial \Delta E_T}{\partial \chi} = & \langle 0 | \frac{\partial \hat{\mathcal{L}}}{\partial \chi} \hat{W} | \mathbf{T} \rangle D_3 \langle \mathbf{T} | \hat{W} \hat{T}_2 | 0 \rangle \\ & + \langle 0 | \hat{\mathcal{L}} \frac{\partial \hat{W}}{\partial \chi} | \mathbf{T} \rangle D_3 \langle \mathbf{T} | \hat{W} \hat{T}_2 | 0 \rangle \\ & + \langle 0 | \hat{\mathcal{L}} \hat{W} | \mathbf{T} \rangle D_3 \langle \mathbf{T} | \frac{\partial \hat{W}}{\partial \chi} \hat{T}_2 | 0 \rangle \\ & + \langle 0 | \hat{\mathcal{L}} \hat{W} | \mathbf{T} \rangle D_3 \langle \mathbf{T} | \hat{W} \frac{\partial \hat{T}_2}{\partial \chi} | 0 \rangle \\ & - \langle 0 | \hat{\mathcal{L}} \hat{W} | \mathbf{T} \rangle D_3 \langle \mathbf{T} | \frac{\partial \hat{F}}{\partial \chi} | \mathbf{T} \rangle D_3 \langle \mathbf{T} | \hat{W} \hat{T}_2 | 0 \rangle. \quad (\text{A5}) \end{aligned}$$

In the gradient expression given above, the first and fourth terms contain contributions from the perturbed wave function parameters. It is widely appreciated in quantum chemistry that such terms are undesirable from a computational point of view and that they may always be eliminated by a

procedure known as either the "Z-vector" [64] or "Dalgarno-Stewart interchange" [65] method. Accomplishing this for a-CCSD(T) is relatively straightforward although somewhat more tedious than for CCSD(T). To this end, first consider the equations that govern the unperturbed \hat{T} and $\hat{\mathcal{L}}$ amplitudes:

$$\langle \mathbf{g} | \bar{H} | 0 \rangle = 0, \quad (\text{A6})$$

$$\langle 0 | \hat{\mathcal{L}} \bar{H} | \mathbf{g} \rangle = 0. \quad (\text{A7})$$

Differentiating both sides of Eqs. (A6) and (A7) provides explicit equations for the first-order \hat{T} and $\hat{\mathcal{L}}$ amplitudes, viz.

$$\langle \mathbf{g} | \frac{\partial \hat{T}}{\partial \chi} | 0 \rangle = -[\langle \mathbf{g} | \bar{H} | \mathbf{g} \rangle]^{-1} \langle \mathbf{g} | \bar{H}^\chi | 0 \rangle, \quad (\text{A8})$$

$$\langle 0 | \frac{\partial \hat{\mathcal{L}}}{\partial \chi} | \mathbf{g} \rangle = -\langle 0 | \hat{\mathcal{L}} | \mathbf{g} \rangle \langle \mathbf{g} | \frac{\partial \bar{H}}{\partial \chi} | \mathbf{g} \rangle [\langle \mathbf{g} | \bar{H} | \mathbf{g} \rangle]^{-1}, \quad (\text{A9})$$

where the shorthand notation

$$\bar{H}^\chi \equiv e^{-\hat{T}} \frac{\partial \hat{H}}{\partial \chi} e^{\hat{T}} \quad (\text{A10})$$

has been introduced. By expanding the derivative of \bar{H} that appears in the expression for the derivative $\hat{\mathcal{L}}$ operator, one can show that Eq. (A9) is equivalent to

$$\begin{aligned} \langle 0 | \frac{\partial \hat{\mathcal{L}}}{\partial \chi} | \mathbf{g} \rangle &= - \left\{ \langle 0 | \hat{\mathcal{L}} | \mathbf{g} \rangle \langle \mathbf{g} | \bar{H}^\chi | \mathbf{g} \rangle \right. \\ &\quad \left. + \langle 0 | \hat{\mathcal{L}} | \mathbf{g} \rangle \langle \mathbf{g} | \bar{H} \frac{\partial \hat{T}}{\partial \chi} | \mathbf{g} \rangle \right\} [\langle \mathbf{g} | \bar{H} | \mathbf{g} \rangle]^{-1}, \end{aligned} \quad (\text{A11})$$

where terms involving $\bar{H}(\partial \hat{T} / \partial \chi)$ products in the second term enclosed by braces are restricted to those that have a connected diagrammatic representation.

Armed with the identities provided by Eqs. (A8) and (A11), let us return to the energy derivative contributions that depend on the perturbed wave function parameters. The second of these

involves $\partial \hat{T}_2 / \partial \chi$ and can hence be rewritten as:

$$\begin{aligned} &\langle 0 | \hat{\mathcal{L}} \hat{W} | \mathbf{T} \rangle D_3(\mathbf{T}) \hat{W} \frac{\partial \hat{T}_2}{\partial \chi} | 0 \rangle \\ &\Downarrow \\ &-\langle 0 | \hat{\mathcal{L}} \hat{W} | \mathbf{T} \rangle D_3(\mathbf{T}) \hat{W} | \mathbf{D} \rangle \langle \mathbf{D} | \mathbf{g} \rangle [\langle \mathbf{g} | \bar{H} | \mathbf{g} \rangle]^{-1} \langle \mathbf{g} | \bar{H}^\chi | 0 \rangle, \end{aligned} \quad (\text{A12})$$

in which the explicit dependence on the $\partial \hat{T}_2 / \partial \chi$ amplitudes has been eliminated.

The term involving $\partial \hat{\mathcal{L}} / \partial \chi$,

$$\frac{\partial \Delta E_T}{\partial \chi} \leftarrow \langle 0 | \frac{\partial \hat{\mathcal{L}}}{\partial \chi} W | \mathbf{T} \rangle D_3(\mathbf{T}) \hat{W} \hat{T}_2 | 0 \rangle, \quad (\text{A13})$$

requires a somewhat more involved analysis. Using Eq. (A11), one immediately obtains

$$\begin{aligned} &- \left\{ \langle 0 | \hat{\mathcal{L}} | \mathbf{g} \rangle \langle \mathbf{g} | \bar{H}^\chi | \mathbf{g} \rangle + \langle 0 | \hat{\mathcal{L}} | \mathbf{g} \rangle \langle \mathbf{g} | \bar{H} \frac{\partial \hat{T}}{\partial \chi} | \mathbf{g} \rangle \right\} \\ &\times [\langle \mathbf{g} | \bar{H} | \mathbf{g} \rangle]^{-1} \langle \mathbf{g} | \hat{W} \hat{T}_3 | 0 \rangle, \end{aligned} \quad (\text{A14})$$

which succeeds in removing the perturbed $\hat{\mathcal{L}}$ amplitudes but reintroduces the perturbed \hat{T} amplitudes. To address this difficulty, we define a new excitation operator \hat{T} by

$$\langle \mathbf{g} | \hat{T} | 0 \rangle \equiv [\langle \mathbf{g} | \bar{H} | \mathbf{g} \rangle]^{-1} \langle \mathbf{g} | \hat{W} \hat{T}_3 | 0 \rangle, \quad (\text{A15})$$

thereby allowing Eq. (A14) to be recast as:

$$\begin{aligned} &-\langle 0 | \hat{\mathcal{L}} | \mathbf{g} \rangle \langle \mathbf{g} | \bar{H}^\chi \hat{T} | 0 \rangle - \langle 0 | \hat{\mathcal{L}} | \mathbf{g} \rangle \langle \mathbf{g} | \bar{H} \frac{\partial \hat{T}}{\partial \chi} \hat{T} | 0 \rangle. \end{aligned} \quad (\text{A16})$$

Since both \hat{T} and \hat{T} are excitation operators, they commute and their order can be interchanged in the second term of the expression above. Doing this, and substituting Eq. (A8) for the perturbed \hat{T} amplitudes leads to

$$\begin{aligned} &-\langle 0 | \hat{\mathcal{L}} | \mathbf{g} \rangle \langle \mathbf{g} | \bar{H}^\chi \hat{T} | 0 \rangle \\ &- \langle 0 | \hat{\mathcal{L}} | \mathbf{g} \rangle \langle \mathbf{g} | \bar{H} \hat{T} | \mathbf{g} \rangle [\langle \mathbf{g} | \bar{H} | \mathbf{g} \rangle]^{-1} \langle \mathbf{g} | \bar{H}^\chi | 0 \rangle. \end{aligned} \quad (\text{A17})$$

This is a desirable expression in the sense that only the unperturbed wave function parameters appear. The contraction line appearing in the preceding equation means that at least one quasiparticle an-

nihilation line attached to \bar{H} must not be contracted with \hat{T} , thereby maintaining consistency with Eq. (A16). It is further convenient to define the triple deexcitation operator $\hat{\mathcal{L}}_3$ by

$$\langle 0 | \hat{\mathcal{L}}_3 | \mathbf{T} \rangle \equiv \langle 0 | \hat{\mathcal{L}} \hat{W} | \mathbf{T} \rangle D_3, \quad (\text{A18})$$

so that Eq. (A12) becomes

$$-\langle 0 | \hat{\mathcal{L}}_3 \hat{W} | \mathbf{D} \rangle \langle \mathbf{D} | \mathbf{g} \rangle [\langle \mathbf{g} | \bar{H} | \mathbf{g} \rangle]^{-1} \langle \mathbf{g} | \bar{H}^x | 0 \rangle. \quad (\text{A19})$$

Combining Eq. (A19) and the second term of Eq. (A17) permits the identification of a deexcitation operator $\hat{\Pi}$ defined on the space of \mathbf{g} determinants as the solution to the system of inhomogeneous linear equations:

$$\begin{bmatrix} \langle 0 | \hat{\Pi} | \mathbf{S} \rangle \\ \langle 0 | \hat{\Pi} | \mathbf{D} \rangle \end{bmatrix} = - \begin{bmatrix} \langle 0 | \hat{\mathcal{L}} \bar{H} \hat{T} | \mathbf{S} \rangle \\ \langle 0 | \hat{\mathcal{L}} \bar{H} \hat{T} | \mathbf{D} \rangle + \langle 0 | \hat{\mathcal{L}}_3 \hat{W} | \mathbf{D} \rangle \end{bmatrix} \times \begin{bmatrix} \langle \mathbf{S} | \bar{H} | \mathbf{S} \rangle & \langle \mathbf{S} | \bar{H} | \mathbf{D} \rangle \\ \langle \mathbf{D} | \bar{H} | \mathbf{S} \rangle & \langle \mathbf{D} | \bar{H} | \mathbf{D} \rangle \end{bmatrix}^{-1}. \quad (\text{A20})$$

The total correlation energy in the a-CCSD(T) approximation is given by the usual CCSD energy (E_{CCSD}) plus ΔE_T . Accordingly, the first derivative of the correlation energy is obtained by simply adding the CCSD energy gradient expression [35–38]

$$\frac{\partial E_{\text{CCSD}}}{\partial \chi} = \langle 0 | \hat{\mathcal{L}} \bar{H}^x | 0 \rangle \quad (\text{A21})$$

to $\partial \Delta E_T / \partial \chi$, i.e.,

$$\begin{aligned} \frac{\partial E_{\text{a-CCSD(T)}}}{\partial \chi} = & \langle 0 | \hat{\mathcal{L}} \frac{\partial \hat{W}}{\partial \chi} \hat{T}_3 | 0 \rangle + \langle 0 | \hat{\mathcal{L}}_3 \frac{\partial \hat{W}}{\partial \chi} \hat{T}_2 | 0 \rangle \\ & - \langle 0 | \hat{\mathcal{L}}_3 \frac{\partial \hat{F}}{\partial \chi} \hat{T}_3 | 0 \rangle \\ & + \langle 0 | (\hat{\mathcal{L}} + \hat{\Pi}) \bar{H}^x | 0 \rangle - \langle 0 | \hat{\mathcal{L}} \bar{H}^x \hat{T} | 0 \rangle, \end{aligned} \quad (\text{A22})$$

where the first three terms differ only in notation from the second, third, and fifth terms of Eq. (A5). Contributions involving the \hat{T} and $\hat{\Pi}$ operators are those that account for the nonstationary nature of ΔE_T with respect to variation of $\hat{\mathcal{L}}$ and \hat{T} , respectively.

In CCSD(T) gradient theory, an operator with the same form as $\hat{\Pi}$ appears, but it is handled in a

particularly efficient way. Specifically, the inhomogeneous term associated with this operator is simply combined with that of the CCSD $\hat{\mathcal{L}}$ equation, and the resulting composite operator is obtained by solving a system of linear equations. This, of course, is not possible in a-CCSD(T) since both of the individual operators $\hat{\mathcal{L}}$ and $\hat{\Pi}$ are needed, and not just their sum. Hence, additional computational steps are necessary in a-CCSD(T) gradients to evaluate both $\hat{\Pi}$ and \hat{T} [which has no counterpart in CCSD(T) gradient theory]. Both of these are defined on the space of the \mathbf{g} determinants and their amplitudes are obtained by solving a system of linear equations. The computational scaling associated with both is precisely the same as that for the unperturbed $\hat{\mathcal{L}}$ equations, as all involve iterative steps that scale with the sixth power of the basis set size (\mathcal{N}^6). In terms of iterative steps, a-CCSD(T) gradient calculations require four distinct \mathcal{N}^6 procedures to solve for the amplitudes of \hat{T} , $\hat{\mathcal{L}}$, $\hat{\Pi}$, and \hat{F} , while CCSD(T) gradients require only \hat{T} and the composite operator alluded to above. Once all of these are available, gradient evaluation can proceed in the usual way where terms are recast as contractions between an effective one- and two-particle density and matrix elements of the differentiated electronic Hamiltonian.

In methods involving triple excitation effects, the noniterative \mathcal{N}^7 steps involving formation of three-particle operators or contraction of these with other quantities can often dominate the cost of calculation. The a-CCSD(T) method is again twice as expensive as CCSD(T) since two sets of \mathcal{N}^7 contractions are needed to form contributions to the effective two-particle density matrix ($\hat{\mathcal{L}} \hat{T}_3$ and $\hat{\mathcal{L}}_3 \hat{T}_2$ are required), while only one such set of contractions is needed in CCSD(T). Hence, both the number of iterative \mathcal{N}^6 and noniterative \mathcal{N}^7 steps required in a-CCSD(T) energy (as discussed in the body of the text) and gradient calculations (additional steps discussed above) are twice those associated with CCSD(T), as might well be expected since the former is an inherently asymmetric theory while the latter is based on the approximation $\hat{\mathcal{L}} = \hat{T}^\dagger$.

ACKNOWLEDGMENTS

This research was supported by grants from the National Science Foundation, the Robert A. Welch Foundation, and the Alfred P. Sloan Foundation.

References

1. R. J. Bartlett and J. F. Stanton, in *Reviews in Computational Chemistry*, K. B. Lipkowitz and D. B. Boyd, Eds. (VCH, New York, 1994), Vol. 5, Chap. 2, pp. 65–169.
2. J. Čížek, *J. Chem. Phys.* **45**, 4256 (1966).
3. R. J. Bartlett, *J. Phys. Chem.* **93**, 1697 (1989).
4. R. J. Bartlett, in *Modern Electronic Structure Theory*, No. 2 in *Advanced Series in Physical Chemistry*, D. R. Yarkony, Ed. (World Scientific, Singapore, 1995), Chap. 16, pp. 1047–1131.
5. T. J. Lee and G. E. Scuseria, in *Quantum Mechanical Electronic Structure Calculations with Chemical Accuracy*, S. R. Langhoff, Ed. (Kluwer Academic, Dordrecht, 1995), pp. 47–108.
6. J. Noga and R. J. Bartlett, *J. Chem. Phys.* **86**, 7041 (1987), erratum: **89**, 3401 (1988).
7. G. E. Scuseria and H. F. Schaefer, *Comm. Phys. Lett.* **152**, 382 (1988).
8. J. D. Watts and R. J. Bartlett, *J. Chem. Phys.* **93**, 6104 (1990).
9. Y. S. Lee, S. A. Kucharski, and R. J. Bartlett, *J. Chem. Phys.* **81**, 5906 (1984).
10. M. Urban, J. Noga, S. J. Cole, and R. J. Bartlett, *J. Chem. Phys.* **83**, 4041 (1985).
11. J. Noga, R. J. Bartlett, and M. Urban, *Chem. Phys. Lett.* **134**, 126 (1987).
12. K. Raghavachari, G. W. Trucks, J. A. Pople, and M. Head-Gordon, *Chem. Phys. Lett.* **157**, 479 (1989).
13. R. J. Bartlett, J. D. Watts, S. A. Kucharski, and J. Noga, *Chem. Phys. Lett.* **165**, 513 (1990), erratum: **167**, 609 (1990).
14. G. D. Purvis and R. J. Bartlett, *J. Chem. Phys.* **76**, 1910 (1982).
15. M. Rittby and R. J. Bartlett, *J. Phys. Chem.* **92**, 3033 (1988).
16. G. E. Scuseria, *Chem. Phys. Lett.* **176**, 27 (1991).
17. J. Gauss, W. J. Lauderdale, J. F. Stanton, J. D. Watts, and R. J. Bartlett, *Chem. Phys. Lett.* **182**, 207 (1991).
18. J. D. Watts, J. Gauss, and R. J. Bartlett, *J. Chem. Phys.* **98**, 8718 (1993).
19. T. D. Crawford, T. J. Lee, and H. F. Schaefer, *J. Chem. Phys.* **107**, 7943 (1997).
20. J. R. Thomas, B. J. DeLeeuw, G. Vacek, and H. F. Schaefer, *J. Chem. Phys.* **98**, 1336 (1993).
21. J. R. Thomas, B. J. DeLeeuw, G. Vacek, T. D. Crawford, Y. Yamaguchi, and H. F. Schaefer, *J. Chem. Phys.* **99**, 403 (1993).
22. T. Helgaker, J. Gauss, P. Jørgensen, and J. Olsen, *J. Chem. Phys.* **106**, 6430 (1997).
23. J. M. L. Martin and P. R. Taylor, *J. Chem. Phys.* **106**, 8620 (1997).
24. J. F. Stanton, *Chem. Phys. Lett.* **281**, 130 (1997).
25. H. J. Monkhorst, *Int. J. Quant. Chem. Symp.* **11**, 421 (1977).
26. D. Mukherjee and P. K. Mukherjee, *Chem. Phys.* **39**, 325 (1979).
27. K. Emrich, *Nucl. Phys. A* **351**, 379 (1981).
28. S. Ghosh and D. Mukherjee, *Proc. Indian Acad. Sci. (Chem. Sci.)* **93**, 947 (1984).
29. H. Sekino and R. J. Bartlett, *Int. J. Quant. Chem. Symp.* **18**, 255 (1984).
30. J. F. Stanton and R. J. Bartlett, *J. Chem. Phys.* **98**, 7029 (1993).
31. J. F. Stanton and J. Gauss, *Theor. Chim. Acta* **93**, 303 (1996).
32. P. O. Löwdin, *J. Math. Phys.* **3**, 969 (1962).
33. J. F. Stanton and J. Gauss, *J. Chem. Phys.* **103**, 1064 (1995).
34. C. Møller and M. S. Plesset, *Phys. Rev.* **46**, 618 (1934).
35. L. Adamowicz, W. D. Laidig, and R. J. Bartlett, *Int. J. Quant. Chem. Symp.* **18**, 245 (1984).
36. A. C. Scheiner, G. E. Scuseria, J. E. Rice, T. J. Lee, and H. F. Schaefer, *J. Chem. Phys.* **87**, 5361 (1987).
37. E. A. Salter, G. W. Trucks, and R. J. Bartlett, *J. Chem. Phys.* **90**, 1752 (1989).
38. J. F. Stanton and J. Gauss, in *Recent Advances in Coupled-Cluster Methods*, R. J. Bartlett, Ed. (World Scientific, Singapore, 1997), pp. 49–79.
39. S. A. Kucharski and R. J. Bartlett, *J. Chem. Phys.* **108**, 5243 (1998).
40. J. F. Stanton, J. Gauss, J. D. Watts, W. J. Lauderdale, and R. J. Bartlett, ACES II. The package also contains modified versions of the MOLECULE Gaussian integral program of J. Almlöf and P. R. Taylor, the ABACUS integral derivative program written by T. U. Helgaker, H. J. Aa. Jensen, P. Jørgensen, and P. R. Taylor, and the PROPS property evaluation integral code of P. R. Taylor.
41. P. Saxe, H. F. Schaefer, and N. C. Handy, *Chem. Phys. Lett.* **79**, 202 (1981).
42. R. J. Harrison and N. C. Handy, *Chem. Phys. Lett.* **95**, 386 (1983).
43. C. W. Bauschlicher and P. R. Taylor, *J. Chem. Phys.* **85**, 2779 (1986).
44. J. Olsen, P. Jørgensen, H. Koch, A. Balkova, and R. J. Bartlett, *J. Chem. Phys.* **104**, 8007 (1996).
45. P. J. Knowles, K. Somasundram, N. C. Handy, and K. Hirao, *Chem. Phys. Lett.* **113**, 8 (1985).
46. S. A. Kucharski and R. J. Bartlett, *J. Chem. Phys.* **97**, 4282 (1992).
47. T. H. Dunning, *J. Chem. Phys.* **90**, 1007 (1989).
48. T. Tanaka and Y. Morino, *J. Mol. Spectrosc.* **33**, 538 (1970).
49. A. Barbe, C. Secroun, and P. Jouve, *J. Mol. Spectrosc.* **49**, 171 (1974).
50. T. J. Lee, W. D. Allen, and H. F. Schaefer, *J. Chem. Phys.* **87**, 7062 (1987).
51. P. Borowski, J. Andersson, P.-A. Malmqvist, and B. O. Roos, *J. Chem. Phys.* **97**, 5568 (1992).
52. M. L. Leininger and H. F. Schaefer, *J. Chem. Phys.* **107**, 9059 (1997).
53. J. F. Stanton, W. N. Lipscomb, D. H. Magers, and R. J. Bartlett, *J. Chem. Phys.* **90**, 1077 (1989).
54. G. E. Scuseria, T. J. Lee, A. C. Scheiner, and H. F. Schaefer, *J. Chem. Phys.* **90**, 5635 (1989).
55. K. Raghavachari, G. W. Trucks, J. A. Pople, and E. Replogle, *Chem. Phys. Lett.* **158**, 207 (1989).
56. D. H. Magers, W. N. Lipscomb, R. J. Bartlett, and J. F. Stanton, *J. Chem. Phys.* **91**, 1945 (1989).
57. T. J. Lee and G. E. Scuseria, *J. Chem. Phys.* **93**, 489 (1990).
58. J. D. Watts, J. F. Stanton, and R. J. Bartlett, *Chem. Phys. Lett.* **178**, 471 (1991).

ASYMMETRIC TRIPLE-EXCITATION CORRECTION

59. P. G. Szalay and R. J. Bartlett, *Chem. Phys. Lett.* **214**, 481 (1993).
60. J. D. Watts and R. J. Bartlett, *J. Chem. Phys.* **108**, 2511 (1998).
61. T. H. Dunning, *J. Chem. Phys.* **53**, 2823 (1970). The polarization exponent used with this basis was $\alpha_d(O) = 1.211$, as optimized by L. T. Redmon, G. D. Purvis, and R. J. Bartlett, *J. Am. Chem. Soc.* **101**, 2856 (1979).
62. A. Halkier, P. Jørgensen, J. Gauss, and T. Helgaker, *Chem. Phys. Lett.* **274**, 235 (1997).
63. G. E. Scuseria and T. J. Lee, *J. Chem. Phys.* **93**, 5851 (1990).
64. N. C. Handy and H. F. Schaefer, *J. Chem. Phys.* **81**, 5031 (1984).
65. A. Dalgarno and A. L. Stewart, *Proc. R. Soc. London Ser. A* **247**, 245 (1958).

Excitation Energies in Brillouin–Wigner-Based Multireference Perturbation Theory

W. WENZEL

Theoretical Physics I, Department of Physics, Dortmund University, D-44221 Dortmund, Germany

Received 27 March 1998; accepted 19 May 1998

ABSTRACT: We present the formalism for the treatment of several states of the same symmetry in basis-set reduction (BSR), a form of second-order Brillouin–Wigner multireference perturbation theory, which incorporates the first-order correction of the primary-space wave function with respect to its orthogonal complement. We benchmark this method for some valence and some Rydberg excitations of four small molecules (O_2 , CO, ethene, and ozone). In direct comparison with the underlying MR–SDCI benchmark results, we find an average accuracy of 0.2 eV or better for the excitation energies of the molecules considered and demonstrate the stability of the method with increasing size of the basis set and primary space. We argue that the configuration-based approach in BSR allows an accurate description of dynamical correlation effects with minimal primary space wave functions, containing far fewer configurations than are required for a CASSCF-based perturbative treatment of the molecules. © 1998 John Wiley & Sons, Inc. Int J Quant Chem 70: 613–622, 1998

Key words: excitation energies; dynamic correlation effects; perturbation theory; MBPT; multireference perturbation theory

Introduction

In recent years, second-order multireference perturbation theory has been established as one of the most effective and accurate tools for the computation of vertical excitation energies in a wide variety of systems. The application of various diagrammatic formulations [1–8] of this method,

most notably that of CASPT2 [9–11], has demonstrated an astonishing accuracy for many molecules with a significantly reduced computational effort in comparison to accurate benchmark techniques, such as MRCI and generalized coupled-cluster approaches. The computational efficiency has allowed the treatment of comparatively large molecules and motivated this investigation into an alternate nondiagrammatic approach to second-order perturbation theory, basis-set reduction (BSR), which is based on a Brillouin–Wigner (BW) perturbation expansion [12, 13]. The results of our

Contract grant sponsor: DFG.

Contract grant number: KEI 164/11-1.

initial investigations into this method [14–16] demonstrated that accurate results for some low-lying (adiabatic) excitations of small, but difficult to treat, organic molecules and radicals could be obtained.

Our approach was motivated by a number of useful features that BW perturbation theory offers in comparison to its diagrammatic cousins: (i) By using a fully correlated energy in the denominator of the perturbation expansion, the BW approach generates a rapidly converging perturbation series that avoids the level crossing problem of diagrammatic perturbation theory (PT). (ii) Through use of an implicit summation technique, our formulation treats near degeneracies between active space configurations and secondary space configurations particularly well—since a fully dressed energy appears in the denominator of the perturbation expansion, a BW approach is free of level crossing problems almost by definition. Reexpanded in a diagrammatic context, second-order BW–PT corresponds to the summation of an entire class of diagrams. (iii) While using an orbital-based partitioning scheme to define the primary space, the overall Hilbert space of BSR is defined as the MR–SDCI space for a given, preselected set of reference configurations. Thus, a change in the size of the primary space does not affect the size of the overall Hilbert space, which results in only modest increases in the computational cost with an increasing size of the primary partition. (iv) The relaxation of the primary space wave function with respect to its orthogonal complement in the primary space allows the application of this method in cases where the eigenfunctions of the bare zero-order Hamiltonian are a poor starting point for the perturbation expansion.

The overall aim of this approach was to reduce the size of the primary space, which ultimately determines the cost of calculation, to the absolute minimum required for the description of the target states. The major, as of yet uncorrected, drawbacks of the BW approach are the lack of orbital invariance and the lack of extensivity, which both severely affect the accuracy of energy differences between different points of the potential energy surface (PES). Regarding the calculation of vertical excitation energies, however, both deficiencies are less important. We have demonstrated previously that while the absolute BSR energies can depend strongly on the choice of the secondary-space orbitals, energy differences depend little on the con-

sistent adaptation of some particular choice. The two primary goals of this article were (i) the presentation of the formalism in which excited states of the same symmetry can be computed in the BSR framework (second section) and (ii) the demonstration that vertical excitations energies for some “canonical” benchmark molecules are reproduced to within 0.1–0.3 eV even for very small primary spaces (third section). In comparison to published data of various other approaches to MRPT, we present results for O₂, CO, ethene, and ozone. We explicitly demonstrate the convergence of the results with increasing basis-set size and increasing size of the primary space in direct comparison to the underlying MRCI benchmark calculations, which are approximated by the BSR method.

Methodology

In BSR, the many-body wave function

$$|\Psi\rangle = \sum c_i |\phi_i\rangle, \quad (1)$$

where $|\phi_i\rangle$ labels an individual configuration, is partitioned according to its orbital occupation [12] into

$$|\Psi_p\rangle = P|\Psi\rangle \quad \text{and} \quad (2)$$

$$\begin{aligned} |\Psi_q\rangle &= Q|\Psi\rangle \\ &= \sum_{q \in Q} c_q |\phi_q\rangle, \end{aligned} \quad (3)$$

the primary- and the secondary-space wave functions, respectively. Using an orbital-based partitioning scheme, the primary space wave function is defined to contain only configurations comprising a set of primary-space orbitals. Throughout this article, we denote primary (secondary)-space quantities with subscripts p (q), respectively.

We obtain an initial estimate of the primary wave function for state $k|\Psi_{kp}^{(0)}\rangle$ and the many-body energy $E_k^{(0)}$ by diagonalizing PHP , where P designates the many-body projection operator onto the primary space. We then compute an approximation of the secondary-space wave function $|\Psi_{kq}^{(1)}\rangle$ through the diagonalization of each two-dimensional subspace spanned by the primary many-body wave function and *each individual* secondary-space configuration [14, 16]. For each sec-

secondary-space configuration $|\phi_q\rangle$, we solve the secular equation:

$$\begin{pmatrix} E_k^{(0)} & \langle \Psi_{kp}^{(0)} | H | \phi_q \rangle \\ \langle \phi_q | H | \Psi_{kp}^{(0)} \rangle & \langle \phi_q | H | \phi_q \rangle \end{pmatrix} \begin{pmatrix} 1 \\ c_{kq} \end{pmatrix} = (E^{(0)} + \delta E_q) \begin{pmatrix} 1 \\ c_{kq} \end{pmatrix}, \quad (4)$$

where we have assumed $\langle \Psi_p^{(0)} | \Psi_p^{(0)} \rangle = 1$ without loss of generality.

To facilitate the relaxation of the primary-space wave function in the presence of $Q\Psi_{kq}$, we compute and store the components of $|\chi\rangle = PHQ|\Psi_{kq}\rangle$ during the evaluation of Eq. (4). We then obtain an improved approximation $|\Psi_p^{(1)}\rangle$ for the primary-space wave function, minimizing the functional:

$$\begin{aligned} \mathcal{F}(\Psi_p) &= \frac{\langle \Psi_p | H | \Psi_p \rangle + (\langle \Psi_p | H | \Psi_q^{(1)} \rangle + h.c.) + E_Q^{(1)}}{\langle \Psi_p | \Psi_p \rangle + N_Q^{(1)}} \\ &= \frac{\langle \Psi_p | H | \Psi_p \rangle + (\langle \Psi_p | \chi^{(1)} \rangle + h.c.) + E_Q^{(1)}}{\langle \Psi_p | \Psi_p \rangle + N_Q^{(1)}}, \end{aligned} \quad (5)$$

under the constraint that all pairs of states $|\Psi_k\rangle$ and $|\Psi_l\rangle$ remain mutually orthogonal:

$$\langle \Psi_k | \Psi_l \rangle = \delta_{kl}. \quad (6)$$

The secondary-space contributions to energy and norm in Eq. (5) arise as

$$\begin{aligned} E_{kQ} &= \sum_{q \in Q} \langle \phi_{kq} | H | \phi_{kq} \rangle c_{kq}^2 \quad \text{and} \\ N_{kQ} &= \sum_{q \in Q} c_{kq}^2. \end{aligned} \quad (7)$$

The enforcement of the orthogonality constraint in Eq. (6) complicates the primary-space relaxation both conceptionally and numerically. Since the calculation of the secondary-space coefficients in Eq. (4) is strongly nonlinear, the external components of the various states are not allowed to mix in the primary-space relaxation step. We have thus modified the Davidson procedure to accommodate this constraint. Given a set of converged states $\{\Psi_k | 0 \leq k < N\}$ and a set of primary-space trial states $\{\phi_m | 0 \leq m < M\}$ and a fixed secondary-space wave function Ψ_{Nq} for the N -th state, we determine an

optimal $\Psi = \sum_m \alpha_m \phi_m + \Psi_{Nq}$ by minimizing

$$\frac{\langle \Psi | H | \Psi \rangle}{\langle \Psi | \Psi \rangle}, \quad (8)$$

with respect to the coefficients α_m . To this end, we consider a basis consisting of the N given states (including their secondary-space component), a single artificial state consisting Ψ_{Nq} , and the set of primary-space trial wave functions ϕ_m . We compute the $(N + K + 1) \times (K + 1)$ overlap matrix S between the basis and the $K + 1$ trial states, using secondary–secondary overlaps computed in the previous perturbative step. We embed this matrix in an $(N + K + 1) \times (N + K + 1)$ matrix \tilde{S} , filling the columns with zeros. The nullspace $\{\mathbf{a}_i | 0 \leq i < K\}$ of \tilde{S} , which is determined in a singular value decomposition, defines a basis

$$\phi'_i = \sum a_{ik} \phi_k \quad (9)$$

that automatically satisfies the orthogonality constraints. Note that this basis could be constructed without the evaluation of any secondary-space overlap matrix elements during the relaxation step. In our numerical experience, the subsequent solution of the eigenvalue problem in this basis can be numerically unstable, when all trial states become near-collinear. Such instabilities are avoided by the explicit construction of a further nondegenerate, orthogonal auxiliary basis ϕ''_k by singular value decomposition of the overlap matrix in ϕ'_k , such that all vectors associated with singular values less than $\epsilon \approx 10^{-8}$ are ignored.

Application

For all molecules considered here, we followed the same computational strategy for the determination of the vertical excitation energies. First, we determined the minimal reference space to account for the individual target states in each symmetry, selecting the one to four most important configurations for each state. Given this set of references, we iteratively determined BSR-approximate natural orbitals from the state-average density matrices for all states of a given symmetry [16, 17]. As a check, we performed a separate calculation for the ground state alone and verified that the ground-state energies in the two different approximate natural orbital basis sets did not differ by more than 0.1 eV. All excitation energies that we report here refer to the difference with respect to the ground-state

energy in state-averaged approximate natural orbitals. Since BSR directly approximates an MR-SDCI calculation with the same reference set in the chosen basis, we also performed the underlying MR-SDCI calculations to provide a basis for comparison for the excitation energies here. This comparison eliminates the influence of basis set and reference choice from the comparison.

TWO REPRESENTATIVE FIRST-ROW DIMERS

As a first test, we computed the vertical excitation energies of O₂ and CO as simple representative examples for which data for other diagrammatic approaches are available. Both molecules have been subject to numerous studies [22–25] and Tables I and II summarize our results for two primary spaces in comparison to a small subset of other available data. In the smaller 2s/2p primary space, labeled BSR-1, we selected the relevant reference configurations, which determine the overall size of the Hilbert space. This primary space was chosen to coincide with that of the other methods to facilitate the comparison of the results. The larger primary space, labeled BSR-2, additionally includes the six most important secondary-space orbitals based on their approximate NO occupa-

tion and corresponds to a different partitioning of the same Hilbert space as the previous set of calculations. Since the cost of the BSR calculation is primarily determined by the number of reference configurations, which is the same in both calculations, the choice of these somewhat large primary spaces is easily affordable. To demonstrate basis-set convergence and gauge the inherent errors at the level of the MR-SDCI benchmark, we performed calculations in the cc-pVDZ and cc-pVTZ basis [26, 27] sets, respectively. As can be expected for the states under consideration, the cc-pVDZ basis set performs adequately at the MR-SDCI level and the cc-pVDZ excitation energies differ by no more than 0.1 eV from the corresponding cc-pVTZ energies for all states considered. For both basis sets, we find that the excitations energies for the low-lying states are well reproduced even for the smaller primary space but find a (still tolerable) increase of the absolute errors for the higher excitations. As expected, an increase of the primary space significantly reduces these errors to within 0.1 (0.15) eV of the MR-SDCI values for the cc-pVDZ (cc-pVTZ) basis sets, respectively. These excitation energies are also reproduced very well in the third-order effective valence-shell Hamiltonian method [28, 29]. However, since this method is

TABLE I
BSR vertical excitation energies of O₂ in the cc-pVDZ and cc-pVTZ basis sets at R = 2.28 au for two different primary spaces in comparison to MR-SDCI results for the same reference set and in comparison to the third-order effective valence shell Hamiltonian method (for a double-zeta basis at R = 2.30 au).

State	MR-SDCI	BSR-1	Error	BSR-2	Error	EVSH(3)
cc-pVDZ						
¹ Δ _g	1.08	1.03	(-0.05)	1.04	(-0.04)	1.08
¹ Σ _g ⁺	1.73	1.82	(+0.09)	1.73	(+0.00)	1.77
¹ Σ _u ⁻	6.08	6.39	(+0.21)	6.14	(+0.06)	6.15
³ Δ _u	6.34	6.66	(+0.32)	6.41	(+0.07)	6.37
³ Σ _u ⁺	6.49	6.80	(+0.31)	6.56	(+0.07)	6.51
³ Σ _u ⁻	8.19	8.03	(-0.16)	8.15	(-0.04)	9.47
cc-pVTZ						
¹ Δ _g	0.99	0.96	(-0.03)	0.96	(-0.03)	
¹ Σ _g ⁺	1.68	1.75	(+0.07)	1.75	(+0.07)	
¹ Σ _u ⁻	5.99	6.32	(+0.33)	6.10	(+0.11)	
³ Δ _u	6.23	6.58	(+0.35)	6.38	(+0.15)	
³ Σ _u ⁺	6.37	6.72	(+0.35)	6.52	(+0.15)	
³ Σ _u ⁻	8.20	8.04	(-0.16)	8.18	(-0.02)	

The primary spaces labeled BSR-1 refers to a (2s/2p) CAS primary space; in BSR-2, the primary space of BSR-1 was additionally augmented by the six most important orbitals of the secondary space in the BSR-1 calculation.

based on a quasidegenerate treatment of the primary space, third-order quasidegenerate perturbation theory is required to reach the accuracy a BW approach obtains already in second order.

The results for CO in Table II are similarly encouraging. The MR-SDCI results compare favorably with benchmark calculations, MR-CC [19] and EOM-CCSD [20], as well as with "experimental" results [21]. As for the oxygen molecule, the BSR results in the small primary space are adequate. Increasing the size of the primary space, we find only a very slight improvement of the energies to within about 0.1 eV of the MR-SDCI results, indicating that at this level of theory the residual error of the BSR approximation has been reached and that a substantial (and computationally prohibitive) increase in the primary space is required to significantly improve the results. It is interesting to compare these results with those of the third-order quasidegenerate Hilbert-space MRPT method of Kaldor [5, 6] and its further extension by Kucharski and Bartlett [7], which are summarized under the heading MR-MBPT(3) [8, 18] in the table. The accuracy of this method corresponds roughly to that of BSR-1 and Meissner and Bartlett [30] speculated that fourth-order MR-MBPT may be required to obtain benchmark accuracy, which for this simple molecule is already attained in second-order with either of these two valence spaces in BSR. Again, the quasidegeneracy assumption for the primary space is likely one significant contributing factor to the comparatively slow convergence of the MR-MBPT perturbation expansion. One must stress, however, that the

MR-MBPT formulation is an explicitly extensive formulation, which is not possible in the BW approach pursued here.

ETHYLENE

The understanding of excited states of short polyenes has long been a subject of intense interest in quantum chemistry. As its simplest example, the ethylene molecule has long served as one of the standard benchmarks for vertical excitation energies for a variety of methods [31, 32–35]. Its spectrum is dominated by an intense $\pi-\pi^*$ transition (N-V) at approximately 7.66 eV, which corresponds not to a vertical transition, but to a slightly distorted geometry of the molecule. The accurate reproduction of its vertical excitation energy has been the subject of numerous studies because of the challenge to account both for the dynamical correlation effects and significant valence-Rydberg mixing at the same time. To compare with one of the more recent studies [32], we performed the calculations in the augmented ANO-type basis set used in the CASPT2 calculation [32], consisting of $4s3p2d$ functions for carbon and $3s2p$ for hydrogen, which were augmented by sets of diffuse $2s2p1d$ functions on carbon (for the exponents of the diffuse functions, see [32]). All calculations were performed in D_{2h} symmetry with $R(CC) = 1.339 \text{ \AA}$, $R(HC) = 1.086 \text{ \AA}$, and $\gamma(HCC) = 117.6^\circ$.

Our results are summarized in Table III. The primary space was chosen to coincide with that of the CASPT2 study with (σ : $3a_g 1b_{3u} 1b_{2u} 1b_{1g} \pi$: $2b_{1u} 2b_{2g} 1b_{3g}$) active orbitals and two active elec-

TABLE II
BSR vertical excitation energies for CO (at $R = 2.132 \text{ au}$) in comparison to MR-SDCI, MR-MBPT(3) [18], MRCC [19], and EOM-CCSD [20] and experiment [21] in a cc-pVDZ basis.

	MRCI	BSR-1	Error	BSR-2	Error	MR MBPT(3)	MRCC	EOM CCSD	Exp.
$^3\pi$	6.47	6.42	(-0.05)	6.43	(-0.04)	6.20	6.32	6.34	6.32
$^3\Sigma^+$	8.46	8.52	(-0.06)	8.40	(-0.06)	8.83	8.26	8.36	8.51
$^1\pi$	8.98	8.92	(-0.06)	9.06	(+0.08)	8.51	8.79	8.64	8.51
$^3\Delta$	9.80	10.09	(+0.29)	9.98	(+0.18)	9.75	9.18	9.33	9.36
$^3\Sigma^-$	9.36	9.37	(+0.01)	9.27	(-0.09)	10.35	9.92	9.85	9.88
$^1\Sigma^-$	10.02	9.88	(-0.14)	10.04	(+0.02)	10.52	9.92	10.05	9.88
$^1\Delta$	10.35	10.56	(-0.21)	10.42	(+0.07)	10.71	10.10	10.26	10.23

The primary space in BSR-1 consists of the $(2s/2p)$ orbitals, the $1s$ orbitals are frozen in all calculations. The primary space in BSR-2 includes one additional natural orbital per symmetry channel. The errors of the BSR energies have been computed with respect to the MRCI energies that they approximate.

TABLE III
Excitation energies of ethene in an augmented ANO-type basis for a (3221|2210) primary space with two active electrons.

	BSR	MRCI	CIS	PTD	CASPT2	PTF	Exp.
1^1B_{3u}	7.04	(+0.15)	6.91	(-0.20)	7.10	6.62	7.17
1^1B_{1g}	7.72	(+0.13)	7.59	(-0.21)	7.68	7.27	7.85
1^1B_{2g}	7.62	(-0.09)	7.71	(-0.19)	7.83	7.37	7.95
1^1B_{1u}	8.00	(+0.00)	8.00	(0.00)	7.78	7.97	8.40
2^1A_g	8.22	(+0.08)	8.14	(-0.14)	8.10	8.05	8.40
2^1B_{3u}	8.45	(+0.12)	8.33	(-0.29)	8.71	8.11	8.66
2^1B_{1u}	8.75	(-0.31)	9.06	(-0.27)		8.88	9.31
1^1B_{2u}	8.87	(+0.06)	8.81	(-0.24)	8.88	8.73	9.18
3^1A_g	8.74	(+0.01)	8.73		8.83	8.44	8.94
1^3B_{1u}	4.05	(-0.22)	4.27	(-0.09)	3.54	3.97	4.39
1^3B_{3u}	6.94	(+0.13)	6.81	(-0.17)	6.87	6.49	7.05
1^3B_{1g}	7.65	(+0.09)	7.56	(-0.23)	7.59	7.25	7.80
1^3B_{2g}	7.75	(+0.07)	7.67	(-0.12)	7.71	7.31	7.90
1^3A_g	8.00	(-0.22)	8.22	(+0.07)	7.75	7.84	8.26
1^3A_u	8.94	(+0.21)	8.73				8.15
1^3B_{2u}	8.72	(-0.02)	8.74			8.66	9.09

All energies are in eV; the errors for the MRCI column were computed with respect to the experimental results and those of the BSR column with respect to the MRCI calculations that they approximated. The CIS results are from [31] and CASPT2 and experimental results (mostly adiabatic energies) quoted from [32].

trons. We selected one to three configurations for each desired state according to their primary-space occupation and computed state-averaged approximate natural orbitals for each spin and symmetry segment. We first note that virtually all MR-SDCI energies are somewhat low by the same amount (≈ 0.2 eV) in comparison to their experimental counterparts, pointing to a somewhat inadequate description of the ground-state correlations. Since more elaborate MR-SDCI studies [34] yield better agreement, this indicates that our minimal choice of a single-reference configuration for the ground state proved to be a somewhat drastic approximation compared to the more elaborate treatment of the other states. On the other hand, we recover the excitation energy of the 1^1B_{1u} V-state to 8.00 eV, which is in good agreement with other recent MR-SCDI calculations [35].

To obtain an unbiased measure of these errors of BSR for a given reference set and basis, we compute the errors of the BSR calculations with respect to the underlying MRCI results, even though the agreement between experiment and BSR is often better than that between experiment and MRCI. With the exception of the 2^1B_{1u} state (error -0.31 eV), the errors of BSR are small (RMS

error 0.14 eV) and compare well with CASPT2. The agreement for the V-state is particularly striking, although its only accidental that its numerical accuracy is so much better than the average 0.15 eV. We note that the CASSCF energy is closer to the expected value than that of CASPT2F, a fact attributed by Serrano-Andrés et al. [32] to the difficulty to reproduce the partial Rydberg character of the π^* orbital. By designing a separate orbital optimization scheme, which forces some Rydberg character into this orbital, an improved, if not perfect, value for this excitation energy could be obtained in CASPT2F. In contrast to CASPT2, the orbitals used in the correlation calculation here are computed in the approximate BSR-NO scheme employed throughout this study. These orbitals are constructed from an approximate density matrix computed from the entire (primary and perturbative secondary) wave function, which includes some correlation effects not present in the CAS-SCF calculations. In a number of examples [16], we could show that the MR-SDCI energies in the approximate NOs reproduce those of standard NOs. For this reason, the Rydberg-valence mixing of the π^* orbital of ethylene is likely to be taken into account in the optimization of this orbital

under the BSR-NO scheme, which explains the superior behavior of this method with respect to this state.

OZONE

As a more complicated example, we present data on the vertical excitation energies of ozone [36], which have been obtained with the same computational strategy. Again, we selected the most important configurations for the description

of the various states based on their occupation in a CASSCF wave function. Using these fixed reference sets, we conducted MR-SDCI calculations in the cc-pVDZ, cc-pVTZ, and cc-pVQZ basis sets. The calculations in the largest basis set, which comprise up to 4×10^6 configurations, were carried out on four nodes of an IBM-SP2 using a parallel MR-SDCI program [37]. Comparing the excitation energies in the columns labeled MRCI in Table IV, these calculations demonstrate that the excitation energies under consideration are well

TABLE IV
Vertical excitation energies of ozone in the cc-pVDZ, cc-pVTZ, and cc-pVQZ basis sets for a (2s / 2p) primary partition.

	PRIM		BSR		MRCI	MRD-CI
	ΔE	Error	ΔE	Error	ΔE	ΔE
Basis: cc-pVDZ						
3B_2	0.81	(-0.63)	1.46	(+0.01)	1.45	
3B_1	1.38	(-0.42)	1.85	(+0.05)	1.80	
3A_2	1.35	(-0.56)	1.98	(+0.07)	1.91	
1A_2	1.45	(-0.68)	2.20	(+0.07)	2.13	
1B_1	1.58	(-0.64)	2.25	(+0.03)	2.22	
3B_2	2.68	(-1.25)	3.80	(-0.13)	3.93	
1A_1	3.01	(-1.16)	4.48	(+0.31)	3.95	
1B_2	7.14	(+0.88)	7.06	(+0.80)	6.26	
3A_2	6.46	(-0.02)	6.53	(+0.05)	6.48	
3A_1	8.15	(-0.05)	8.01	(-0.19)	8.20	
Basis: cc-pVTZ						
3B_2	0.79	(-0.59)	1.53	(+0.16)	1.38	1.69
3B_1	1.38	(-0.43)	2.03	(+0.18)	1.81	1.85
3A_2	1.38	(-0.51)	2.03	(+0.03)	1.89	2.00
1A_2	1.45	(-0.65)	2.19	(+0.03)	2.10	2.16
1B_1	1.59	(-0.61)	2.26	(+0.16)	2.20	2.10
3B_2	2.56	(-1.30)	3.70	(-0.17)	3.86	3.87
1A_1	2.96	(-1.20)	4.40	(-0.09)	4.16	4.49
1B_2	7.21	(+0.84)	7.35	(+0.98)	6.37	
3A_2	6.48	(-0.16)	6.91	(+0.27)	6.64	6.01
3A_1	8.10	(-0.04)	8.34	(+0.20)	8.14	
Basis: cc-pVQZ						
3B_2	0.79	(-0.61)	1.34	(-0.06)	1.40	
3B_1	1.47	(-0.34)	1.88	(+0.06)	1.82	
3A_2	1.44	(-0.45)	1.86	(-0.04)	1.90	
1A_2	1.47	(-0.64)	2.15	(+0.03)	2.12	
1B_1	1.61	(-0.52)	2.20	(-0.07)	2.13	
3B_2	2.56	(-1.41)	3.47	(-0.42)	3.90	
1A_1	3.05	(-1.01)	4.27	(+0.21)	4.06	
1B_2	7.16	(+0.76)	7.60	(+1.21)	6.39	
3A_2	6.53	(-0.15)	6.80	(+0.12)	6.68	
3A_1	8.09	(+0.28)	8.01	(+0.20)	7.81	

All calculations were carried out in C_{2v} symmetry at $R = 2.413$ au and $\gamma = 116.8^\circ$. All energies in eV. The errors of the BSR calculations are computed with respect to the corresponding MR-SDCI results.

converged in the cc-pVTZ basis and, furthermore, furnish a rough estimate of the overall accuracy of these numbers, approximately 0.1 eV, which can be compared with the errors of the perturbative approach. Our cc-pVTZ results also agree well with the MRD-CI [36] results for a triple-zeta quality basis with bond-center functions. Under the heading PRIM, Tables IV and V show the excitation energies computed in the primary space, which differ from BSR by more than about 0.6 (0.3) eV for the small (larger) primary space, respec-

tively, and indicate that substantial differential correlation effects must be incorporated in the perturbative treatment to obtain quantitatively acceptable results. For the BSR-1 calculations, this is accomplished with the exception of the 1B_2 state, which shows an altogether unacceptable error. The BSR-2 calculation shows more satisfactory results for all states and basis sets, reducing the RMS error for the cc-pVQZ basis to 0.17 eV, where the majority of the errors arise for states with excitation energies larger than 4 eV, for which such

TABLE V

Vertical excitation energies of ozone in the cc-pVDZ, cc-pVTZ, and cc-pVQZ basis sets for a (2s / 2p) primary partition augmented with the most important NO in each symmetry channel.

	PRIM		BSR		MRCI
	ΔE	Error	ΔE	Error	ΔE
Basis: cc-pVDZ					
3B_2	1.02	(-0.43)	1.42	(-0.03)	1.45
3B_1	1.12	(-0.68)	1.77	(-0.03)	1.80
3A_2	1.27	(-0.63)	1.92	(+0.01)	1.91
1A_2	1.49	(-0.63)	2.13	(+0.00)	2.13
1B_1	1.54	(-0.67)	2.20	(-0.02)	2.22
3B_2	2.99	(-0.93)	3.83	(-0.10)	3.93
1A_1	3.54	(-0.62)	4.53	(+0.36)	3.95
1B_2	5.51	(-0.75)	6.25	(+0.01)	6.26
3A_2	5.71	(-0.76)	6.21	(-0.27)	6.48
3A_1	7.70	(-0.49)	8.07	(-0.13)	8.20
Basis: cc-pVTZ					
3B_2	1.47	(+0.09)	1.33	(-0.05)	1.38
3B_1	1.63	(-0.18)	1.73	(-0.07)	1.81
3A_2	1.77	(-0.11)	1.80	(-0.09)	1.89
1A_2	1.79	(-0.21)	2.05	(-0.10)	2.10
1B_1	1.89	(-0.21)	2.10	(-0.10)	2.20
3B_2	3.39	(-0.47)	3.59	(-0.27)	3.86
1A_1	3.83	(-0.33)	4.18	(+0.02)	4.16
1B_2	5.95	(-0.42)	5.81	(-0.55)	6.37
3A_2	6.18	(-0.46)	6.23	(-0.40)	6.64
3A_1	8.12	(-0.02)	8.12	(-0.02)	8.14
Basis: cc-pVQZ					
3B_2	1.47	(+0.07)	1.37	(-0.03)	1.40
3B_1	1.64	(-0.18)	1.71	(-0.11)	1.82
3A_2	1.78	(-0.12)	1.81	(-0.09)	1.90
1A_2	1.77	(-0.34)	2.06	(-0.06)	2.12
1B_1	1.88	(-0.24)	2.15	(+0.02)	2.13
3B_2	3.38	(-0.52)	3.70	(-0.20)	3.90
1A_1	3.84	(-0.21)	4.24	(+0.18)	4.06
1B_2	6.03	(-0.36)	6.10	(-0.20)	6.39
3A_2	6.15	(-0.53)	16.42	(-0.26)	6.68
3A_1	8.11	(-0.30)	8.05	(+0.24)	7.81

All calculations were carried out in C_{2v} symmetry at $R = 2.413$ au and $\gamma = 116.8^\circ$. The BSR calculations were performed in approximate NO basis sets optimized using the larger primary space, while the MR-SDCI calculations are the same as in Table IV.

deviations can be more easily tolerated, particularly if one takes into account that the BSR-2 (BSR-1) calculations are a factor of 2000 (12,000) more efficient than the underlying MR-SDCI calculations (based on the number of nonzero symmetry-allowed matrix elements).

Discussion

The understanding and accurate description of excitation states is one of the central challenges of quantum chemistry and recent years have seen tremendous progress in this regard. In particular, through the application of diagrammatic or many-body based, multireference perturbation theory, it became possible to investigate many molecules that are still inaccessible to benchmark methods. Many of the prevalent prescriptions for multireference perturbation theory rely on a zero-order CASSCF wave function as a starting point. The number of active electrons which can be treated efficiently within this framework has emerged as one of the crucial bottlenecks in this approach. While the use of a contracted primary-space wave functions allows the treatment of very large CASSCF spaces, it complicates the relaxation of the primary-space wave function with respect to its orthogonal complement. In this investigation, we thus explored an alternate approach, which sought to facilitate such a relaxation of the primary space at least in lowest order. Since we must deal with the individual configurations of the primary space, their number must be kept at an absolute minimum to ensure the computational viability of the resulting method. This, in turn, necessitates the use of a perturbation expansion, which will converge very quickly even for such a minimalistic zero-order description of the problem. The results presented here for both valence and Rydberg excitations in some simple organic molecules demonstrate that a BW-based approach offers a promising avenue toward this goal. The key difference between the BW perturbation expansion and diagrammatic many-body techniques lies in the different origin of the energy gap between the primary and the secondary space. While the numerators of the different expansions are closely related, BWPT features a fully correlated energy in its denominator, which ensures a comparatively large difference between the reference energy and that of the perturbatively treated configurations.

In this study, we were able to reproduce the excitation energies to an accuracy of on average 0.2 eV for some $\pi-\pi^*$ and $\sigma-\pi$ transitions and some Rydberg states of the four molecules studied, which indicates a balanced performance of the method. It is desirable, but more difficult than in CASSCF-based methods, to develop the methodology for the computation of transition moments. Such a development is presently under way, but is complicated by the lack of orthogonality of the primary-space orbitals for different symmetry segments. Motivated by the results reported here, we are presently extending our study to larger polyenes, azabenzenes, and some transition-metal compounds. To make the methodology presented in this work applicable to a wider range of problems, we are presently investigating extensions, which enforce the orbital invariance of energies and render it at least approximately extensive.

ACKNOWLEDGMENTS

I am grateful for the advice from and stimulating discussion with I. Shavitt and M. M. Steiner during the course of this work. The development of the parallel MR-SDCI code, which was used for the benchmark calculations of ozone, was supported by DFG grant (KEI 164/11-1).

References

1. B. H. Brandow, Rev. Mod. Phys. **39**, 771 (1967).
2. B. H. Brandow, Int. J. Quantum Chem. **15**, 207 (1979).
3. S. Iwata and K. F. Freed, Chem. Phys. **11**, 433 (1974).
4. S. Iwata and K. F. Freed, Chem. Phys. Lett. **28**, 176 (1974).
5. G. Hose and U. Kaldor, Phys. Scr. **21**, 357 (1980).
6. G. Hose, J. Chem. Phys. **84**, 4505 (1986).
7. S. A. Kucharski and R. J. Bartlett, Int. J. Quantum Chem. Symp. **22**, 383 (1988).
8. L. Meissner, S. A. Kucharski, and R. J. Bartlett, J. Chem. Phys. **91**, 6187 (1989).
9. K. Andersson, P. A. Malmqvist, B. O. Roos, A. J. Sadlej, and K. Wolinski, J. Phys. Chem. **94**, 5483 (1990).
10. K. Andersson and B. O. Roos, J. Chem. Phys. **96**, 1218 (1992).
11. B. O. Roos, K. Andersson, and M. P. Fülscher, Chem. Phys. Lett. **192**, 5 (1992).
12. P.-O. Löwdin, Phys. Rev. **97**, 1509 (1955).
13. Z. Gershgorn and I. Shavitt, Int. J. Quantum Chem. **2**, 751 (1968).
14. W. Wenzel and K. G. Wilson, Phys. Rev. Lett. **68**, 800 (1992).
15. W. Wenzel, M. M. Steiner, J. W. Wilkins, and K. G. Wilson, Int. J. Quantum Chem. **S30**, 1325 (1996).

16. W. Wenzel and M. M. Steiner, *J. Chem. Phys.* **108**, 4714 (1998).
17. P. J. Hay, *J. Chem. Phys.* **59**, 2468 (1973).
18. L. Meissner, S. A. Kucharski, and R. J. Bartlett, *J. Chem. Phys.* **93**, 1847 (1990).
19. S. Pal, M. Rittby, R. J. Bartlett, D. Sinha, and D. Mukherjee, *J. Chem. Phys.* **88**, 4357 (1988).
20. J. Geersten, M. Rittby, and R. J. Bartlett, *Chem. Phys. Lett.* **164**, 57 (1989).
21. J. Oddershede, in *Ab Initio Methods in Quantum Chemistry II*, K. P. Lawley, Ed. (Wiley, New York, 1987).
22. R. J. Bunker and S. D. Peyerimhoff, *Chem. Phys. Lett.* **36**, 415 (1975).
23. R. P. Saxon and B. Liu, *J. Chem. Phys.* **67**, 5432 (1977).
24. S. K. Shih, W. Butscher, R. J. Bunker, and S. D. Peyerimhoff, *Chem. Phys.* **29**, 241 (1978).
25. E. Nilsen, P. Jorgensen, and J. Oddershede, *J. Chem. Phys.* **73**, 6256 (1980).
26. D. E. Woon and T. H. Dunning, *J. Chem. Phys.* **100**, 2975 (1995).
27. T. H. Dunning, *J. Chem. Phys.* **90**, 1007 (1989).
28. T. Takada and K. F. Freed, *J. Chem. Phys.* **80**, 3696 (1984).
29. A. W. Kanzler and K. F. Freed, *J. Chem. Phys.* **94**, 3779 (1991).
30. L. Meissner and R. J. Bartlett, *J. Chem. Phys.* **94**, 6670 (1991).
31. J. B. Foresma, M. Head-Gordon, J. A. Pople, and M. J. Frisch,
32. L. Serrano-Andrés, M. Merchán, I. Nebot-Gill, R. Lindh, and B. O. Roos, *J. Chem. Phys.* **98**, 3151 (1993).
33. L. E. McMurchie and E. R. Davidson, *J. Chem. Phys.* **67**, 5613 (1977).
34. C. Petrongolo, R. J. Bunker, and S. D. Peyerimhoff, *J. Chem. Phys.* **76**, 3655 (1982).
35. R. Lindh and B. O. Roos, *Int. J. Quantum Chem.* **35**, 813 (1989).
36. A. Banichevich and S. Peyerimhoff, *Chem. Phys.* **174**, 93 (1993).
37. F. Stephan and W. Wenzel, *J. Chem. Phys.* **108**, 1015 (1998).

More About the Leaky Aquifer Function

FRANK E. HARRIS

Department of Chemistry, University of Utah, Salt Lake City, Utah 84112 and Quantum Theory Project, Departments of Physics and Chemistry, University of Florida, Gainesville, Florida 32611

Received 25 February 1998; accepted 25 February 1998

ABSTRACT: The leaky aquifer function $W(x, y)$ is an incomplete Bessel function which has had application in hydrology and more recently in electronic-structure calculations. This article presents an expansion which improves the efficiency of the calculation of W in the only part of its range not treated adequately by previously published methods, namely, the regime where x and y are both larger than unity but one is much larger than the other. © 1998 John Wiley & Sons, Inc. Int J Quant Chem 70: 623–626, 1998

Introduction

In an article published recently in this journal [1], we introduced an expansion which improved the efficiency of the calculation of the incomplete Bessel function known to hydrologists as the *leaky aquifer function*, defined as follows:

$$W(x, y) = \int_1^{\infty} \frac{e^{-xt-y/t}}{t} dt; \quad (1)$$

for some purposes, it is convenient to restate Eq. (1) as

$$W(x, y) = L(u, v) = \int_v^{\infty} \frac{e^{-u(t+1/t)}}{t} dt, \quad (2)$$

where $u = (xy)^{1/2}$ and $v = (x/y)^{1/2}$. Previous work by others [2–7] had established convenient methods for the calculation of W when either x or y was small (less than unity), and our recent article [1] provided an expansion which was optimum when the ratio x/y was near unity, with no requirement that either be small. While proper choices among all these methods enabled at least moderate efficiency for all values of x and y , it remained desirable to find a method that would become optimum when x and y were both large, but at ratios far from unity. Unfortunately, we had no solution to this problem when we wrote our previous article.

We have now found an additional expansion that is efficient in the range previously causing problems and which can be regarded, at least asymptotically, as an expansion in powers of $y/(x+y)$. We present here the new expansion and, to

make this communication reasonably self-contained, the other formulas constituting a complete set of evaluation algorithms. Readers desiring a more detailed survey of the relevant previous work and its use in electronic-structure calculations are referred to our earlier article [1] and the work of Delhalle et al. [8, 9].

This article also includes some data illustrative of the convergence rate of the new expansion. Interested readers may make further calculations by using our computer program, written in Maple V [10], which is available at the author's World Wide Web site [11].

Previously Derived Formulas

An expansion which converges rapidly for small y is [4]

$$W(x, y) = \sum_{n=0}^{\infty} \frac{(-y)^n}{n!} E_{n+1}(x), \quad (3)$$

where E_n is a generalized exponential integral of definition

$$E_n(x) = \int_1^{\infty} \frac{e^{-xt}}{t^n} dt. \quad (4)$$

TABLE I
Expansion coefficients $C_n(u)$ occurring in Eqs. (6) and (7).

n	$C_n(u)$
1	-1
2	1/2
3	$(u - 1)/3$
4	$(-2u + 1)/4$
5	$(-u^2 + 6u - 2)/10$
6	$(3u^2 - 8u + 2)/12$
7	$(u^3 - 18u^2 + 30u - 6)/42$
8	$(-2u^3 + 15u^2 - 18u + 3)/24$
9	$(-u^4 + 40u^3 - 180u^2 + 168u - 24)/216$
10	$(5u^4 - 80u^3 + 252u^2 - 192u + 24)/240$
11	$(u^5 - 75u^4 + 700u^3 - 1680u^2 + 1080u - 120)/1320$
12	$(-6u^5 + 175u^4 - 1120u^3 + 2160u^2 - 1200u + 120)/1440$
13	$(-u^6 + 126u^5 - 2100u^4 + 10080u^3 - 16200u^2 + 7920u - 720)/9360$
14	$(7u^6 - 336u^5 + 3780u^4 - 14400u^3 + 19800u^2 - 8640u + 720)/10080$

If x is small but y is not, their roles can be interchanged by invoking the formula [5]

$$W(x, y) = 2K_0(2\sqrt{xy}) - W(y, x), \quad (5)$$

where K_0 is a modified Bessel function of the second kind (cf. Abramowitz and Stegun [12]).

If neither x nor y is small, but their ratio is near unity, rapid convergence can be achieved from one of the expansions [1]

$$L(u, v) = K_0(2u) + e^{-2u} \sum_{n=1}^{\infty} C_n(u)(v - 1)^n \quad (v < 1), \quad (6)$$

$$L(u, v) = K_0(2u) - e^{-2u} \sum_{n=1}^{\infty} C_n(u)(v^{-1} - 1)^n \quad (v > 1), \quad (7)$$

where the C_n are the polynomials listed in Table I.

New Formula

To obtain a formula that is efficient when both x and y are large and their ratio is far from unity,

we rearrange Eq. (1) to the form

$$\begin{aligned} W(x, y) &= \int_1^\infty \frac{e^{-(x+y)t} e^{y(t-1/t)}}{t} dt \\ &= \sum_{n=0}^{\infty} \frac{D_n(x+y)y^n}{n!}, \end{aligned} \quad (8)$$

where

$$D_n(z) = \int_1^\infty \frac{e^{-zt}}{t} \left(t - \frac{1}{t} \right)^n dt. \quad (9)$$

Equation (8) will be shown to be efficient when $y < x$; if $y > x$, their roles should be interchanged using Eq. (5) before applying Eq. (8).

One way to evaluate the $D_n(z)$ involves the explicit introduction of their derivatives:

$$D'_n(z) = - \int_1^\infty e^{-zt} \left(t - \frac{1}{t} \right)^n dt; \quad (10)$$

using partial integrations, we can establish the recurrence formulas

$$\begin{aligned} D_n(z) &= -D'_{n-1}(z) \\ &+ \frac{1}{n} [zD_{n-1}(z) - 2(n-1)D_{n-2}(z)] \end{aligned} \quad (n > 1), \quad (11)$$

$$D'_n(z) = \frac{n}{z} [2D'_{n-1}(z) + D_n(z)] \quad (n > 0). \quad (12)$$

These formulas can be used for upward recursion in n , starting from

$$D_0(z) = E_1(z), \quad (13)$$

$$D'_0(z) = -\frac{e^{-z}}{z}, \quad (14)$$

$$D_1(z) = -D'_0(z) - E_2(z). \quad (15)$$

To understand the formal convergence properties of Eq. (8), it is useful to note that in the limit of large n (for fixed z)

$$D_n(z) \sim \frac{(n-1)!}{z^n}, \quad (16)$$

so that the n th term of Eq. (8) approaches $n^{-1}y^n/(x+y)^n$. We thus have formal convergence for all relevant values of x and y . However, as a practical matter, we are also interested in the behavior of $D_n(z)$ when n/z is small; in this

instance,

$$D_n(z) \approx \frac{2^n n! e^{-z}}{z^{n+1}}, \quad (17)$$

causing the n th term of Eq. (8) to be approximately $(2y)^n e^{-(x+y)} / (x+y)^{n+1}$. For large $x+y$, we thus see that successive initial terms will decrease rapidly only if y/x is significantly less than unity. The generation of the D_n by upward recurrence, using Eqs. (11) and (12), is numerically unstable, but causes no practical difficulties at the parameter values for which Eq. (8) is recommended.

Numerical

Calculations using the new formula were carried out to supplement those reported previously. As before, we used Maple V [10], with the precision set to 14 decimal digits and with results reported here to 10. The generalized exponential integrals needed for the recurrence formulas were generated as in previous work [1]. All the programs used in these calculations are available to any interested reader [11].

Figure 1 shows the number of terms needed to achieve convergence to an absolute accuracy of 1×10^{-10} in $W(x, y)$ as a function of x and y for the new formula, Eq. (8). We used absolute (rather than relative) accuracy because that is likely to be a more relevant criterion in electronic-structure studies. These expansion lengths may be compared with those found previously where calculations were carried out using Eqs. (3) and (7) of the present article. While the expansion length may be an imperfect measure of the computational effort, it is surely qualitatively informative; we find a significant range of x and y for which the new expansion is better than those previously reported. The x, y values for which the new expansion is best are marked in Figure 1 by asterisks. Values of x, y lying above the asterisked points are best computed using Eq. (7), and those falling below the asterisked points are optimally reached using Eq. (3).

Our overall conclusion is that, when the new expansion is included as an option, satisfactorily convergent methods are available for the computation of $W(x, y)$ for all positive values of x and y to the accuracy needed in electronic structure calculations.

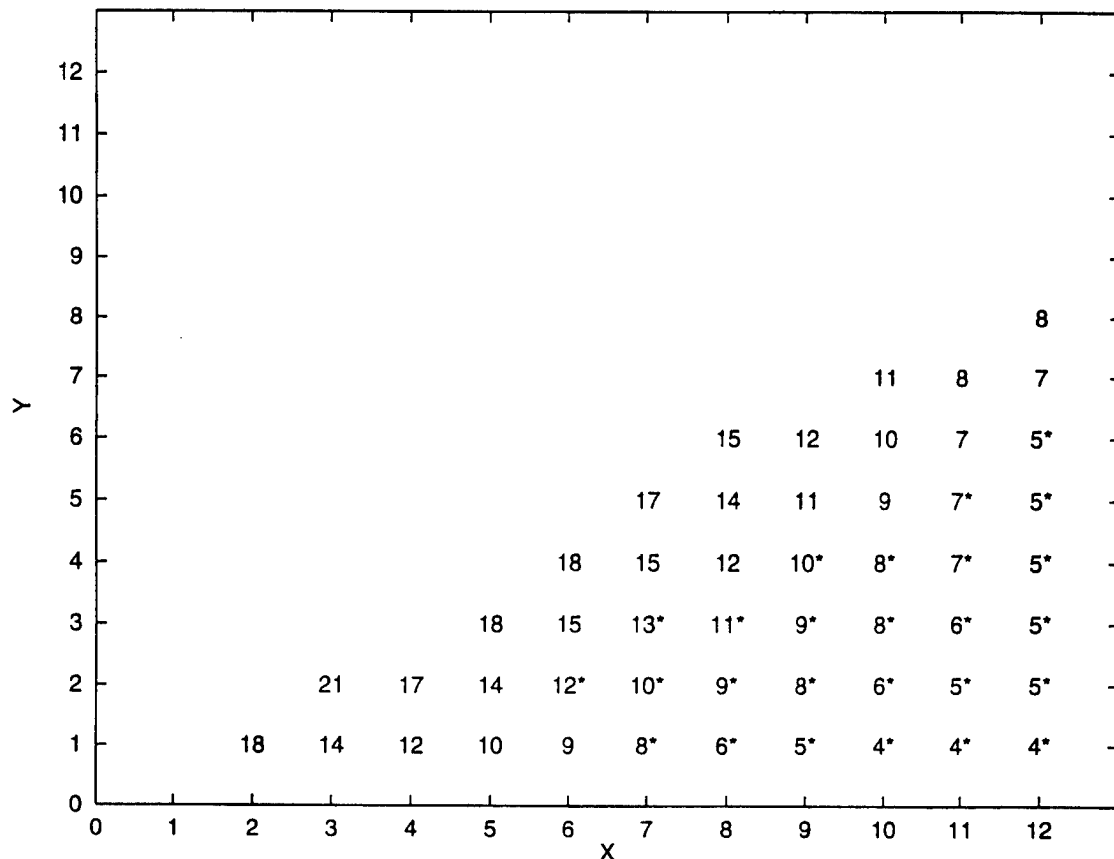


FIGURE 1. Numbers of terms in the expansion of Eq. (8) needed to attain an absolute accuracy of $\pm 1 \times 10^{-10}$ in $W(x, y)$, shown for integer values of x and y . Asterisked entries identify (x, y) pairs for which this expansion converges more rapidly than any of the previously reported expansions.

ACKNOWLEDGMENTS

The author is pleased to acknowledge useful discussions with Professors Joseph Delhalle and J. G. Fripiat and with Dr. Isabelle Flamant at Facultés Universitaires Notre-Dame de la Paix in Namur, Belgium.

References

1. F. E. Harris, Int. J. Quantum Chem. **63**, 913 (1997).
2. M. S. Hantush and C. E. Jacob, Trans. Am. Geophys. Union **36**, 95 (1955).
3. M. S. Hantush, Trans. Am. Geophys. Union **37**, 702 (1956).
4. C. M. Case and J. C. Addiego, J. Hydrol. **32**, 393 (1977).
5. B. Hunt, J. Hydrol. **33**, 179 (1977).
6. G. W. Thomas, R. G. Keys, and A. C. Reynolds, J. Hydrol. **36**, 173 (1978).
7. R. Terras, J. Comput. Phys. **39**, 233 (1981).
8. J. Delhalle and F. E. Harris, Phys. Rev. B **31**, 6755 (1985).
9. I. Flamant, J. G. Fripiat, and J. Delhalle, Int. J. Quantum Chem. S **30**, 275 (1996).
10. *Maple V* Is a product of the Symbolic Computation Group at the University of Waterloo, Ontario, Canada.
11. URL <http://www.chem.utah.edu>; click on "faculty," then "Frank E. Harris," then "available software."
12. M. Abramowitz and I. Stegun, Eds., *Handbook of Mathematical Functions* (Dover, New York, 1970).

Use of a Fast Fourier Transform (FFT) 3D Time-Dependent Schrödinger Equation Solver in Molecular Electronic Structure

BURKE RITCHIE,¹ CHARLES A. WEATHERFORD²

¹*University of California, Lawrence Livermore National Laboratory, Livermore, California 94550*

²*Physics Department, Florida A & M University, Tallahassee, Florida 32307*

Received 23 February 1998; revised 11 May 1998; accepted 21 May 1998

ABSTRACT: An implicit split-operator FFT algorithm for the numerical solution of the time-dependent Schrödinger equation is implemented for the electronic structure of H_2^+ and H_2 . The covalent versus separated-atoms behavior is described by two distinct steady states to which the imaginary-time Schrödinger solution evolves for small or large internuclear distances, respectively. © 1998 John Wiley & Sons, Inc. *Int J Quant Chem* 70: 627–635, 1998

Introduction

The exponentiated split operator (esop) fast Fourier transform (FFT) method of Feit and coworkers [1] has been used extensively in optical

Correspondence to: C. A. Weatherford.

Contract grant sponsor: U.S. Dept. of Energy/Lawrence Livermore National Laboratory.

Contract grant number: W-7405-ENG-48.

Contract grant sponsor: Lawrence Livermore National Laboratory Research Collaboration Program for Historically Black Colleges and Universities and Minority Institutions/NSF.

Contract grant number: HDR-9707076.

Contract grant sponsor: Army High Performance Computing Research Center, Dept. of the Army, Army Research Laboratory.

Contract grant numbers: DAAH04-95-2-0003/DAAH04-95-C-0008.

and chemical physics; however, it has not found use in electronic structure or scattering problems because the explicit form of the temporal advancement algorithm does not conserve energy except for impractically small time steps. The method of choice which overcomes this difficulty is the Peaceman–Rachford alternating direction implicit (ADI) algorithm used extensively by Kulander [2] and others; however, this method is limited to 2D applications and is difficult to implement because the use of three-point spatial differences to represent a component of the Laplacian requires a tridiagonal matrix inversion at each time step and at each spatial grid point of the other component of the Laplacian, with this set of operations carried out twice over a single temporal interval. In this article, we implement an algorithm appropriate for 3D applications which is implicit and thus over-

comes the nonconservation of energy difficulty. Furthermore, it uses the FFT algorithm to advance the Laplacian and thus avoids the labor of spatial differencing methods since the solution of an implicit advancement equation in transform space requires only a single scalar operation.

Implicit Split-Operator Algorithm

The implicit split-operator (isop) FFT method, with applications to the hydrogen atom, was presented earlier by Ritchie and Riley [3], and another version appropriate for radiation transfer through optically thick media was presented by Ritchie and coworkers [4]. We are solving the time-dependent Schrödinger equation. For the case of one particle in a potential V (e.g., H_2^+), the time-dependent Schrödinger equation may be written, in atomic units, as

$$\hat{H}(\mathbf{r})\Psi(\mathbf{r}, t) = i \frac{\partial}{\partial t} \Psi(\mathbf{r}, t) \quad (1)$$

where \hat{H} is the time-independent Hamiltonian operator

$$\hat{H}(\mathbf{r}) = -\frac{1}{2}\nabla^2 + V(\mathbf{r}). \quad (2)$$

For completeness, however, we present the isop algorithm again [applied to Eq. (1)], in slightly different form from that of [3]:

$$\begin{aligned} \left[1 + \frac{dt}{8i}\nabla^2\right]\Psi_{1/3} &= \left[1 - \frac{dt}{8i}\nabla^2\right]\Psi_r, \\ \left[1 - \frac{dt}{4i}V\right]\Psi_{2/3} &= \left[1 + \frac{dt}{4i}V\right]\Psi_{1/3} \quad (3) \\ \left[1 + \frac{dt}{8i}\nabla^2\right]\Psi_a &= \left[1 - \frac{dt}{8i}\nabla^2\right]\Psi_{2/3}, \end{aligned}$$

where the subscripts, r , $1/3$, $2/3$, and a refer to the known solution at a previous time step t , to intermediate solutions within the interval, and to the advanced solution at $t + dt$. The net advancement algorithm is derived by operating successively from the left on the third equation by the left-handed operators of the second and first equations and using the results given by the second and the first equations respectively. The symmetry of the equations is such that we can write for the

net algorithm

$$\begin{aligned} \left[1 + \frac{dt}{4i}\nabla^2 - \frac{dt}{2i}V\right]\Psi_a \\ = \left[1 - \frac{dt}{4i}\nabla^2 + \frac{dt}{2i}V\right]\Psi_r + O(dt^3). \quad (4) \end{aligned}$$

Equation (4) has the form of the Crank–Nicolson algorithm, which, of course, is implicit and second-order accurate. The first and third equations of Eq. (3) are evaluated in transform space and the middle equation is evaluated in real space. As we pointed out earlier, the evaluation of the equations containing the Laplacian in transform space averts the use of spatial differences and the need to invert matrices to find the advanced solution. Please note that we are showing the equations in terms of the real time t . The actual solution is accomplished using imaginary time τ such that $t = -i\tau$.

Hartree Approximation

For the case of two interacting electrons, as is the case for the hydrogen molecule, H_2 , the time-dependent Schrödinger equation is

$$\hat{H}(\mathbf{r}_1, \mathbf{r}_2)\Psi(\mathbf{r}_1, \mathbf{r}_2, t) = i \frac{\partial}{\partial t} \Psi(\mathbf{r}_1, \mathbf{r}_2, t), \quad (5)$$

where the Hamiltonian has the form

$$\hat{H}(\mathbf{r}_1, \mathbf{r}_2) = -\frac{1}{2}\nabla_1^2 - \frac{1}{2}\nabla_2^2 + V(\mathbf{r}_1, \mathbf{r}_2). \quad (6)$$

The solution to Eq. (5) is a function of six spatial dimensions and one time dimension. To set a more computationally tractable problem, we make a Hartree ansatz for the wave function

$$\Psi(\mathbf{r}_1, \mathbf{r}_2, t) \equiv F(\mathbf{r}_1, t) \times G(\mathbf{r}_2, t), \quad (7)$$

where F and G are complex functions. We would like to derive a pair of coupled equations for F and G which involve three spatial dimensions and one time dimension for each function. We could use an action principal, in the manner of Kermin and Koonin [5] with the Hartree ansatz [Eq. (7)] instead of an Hartree–Fock one as they do, and arrive easily at the equations

$$\begin{aligned} i\dot{F}(1) &= \langle G(2)|\hat{H}(1, 2)|G(2)\rangle_2 F(1) \\ i\dot{G}(2) &= \langle F(1)|\hat{H}(1, 2)|F(1)\rangle_1 G(2), \end{aligned} \quad (8)$$

where the dot over F and G means a time derivative and we have suppressed the explicit time dependence in F and G . The subscript on the kets in Eq. (8) indicates the spatial integration variables. In arriving at Eq. (8), normalization of F and G at $t = 0$ is all that is required since the isop preserves the norm. It is not necessary to require orthogonality ($\langle F | G \rangle = 0$). A key point in the use of the action principal is the independent variation of F and G .

Alternatively, we may use a projection procedure. Use the Hartree ansatz [Eq. (7)] in Eq. (5) and first multiply from the left by $G^*(2)$ and integrate over r_2 . Then, multiply Eq. (5) [again using Eq. (7)] by $F^*(1)$ and integrate over r_1 . Using normality conservation for F and G then results in

$$\begin{aligned} i\dot{F}(1) + iF(1)\langle G(2) | \dot{G}(2) \rangle_2 \\ = \langle G(2) | \hat{H}(1, 2) | G(2) \rangle_2 F(1) \\ i\dot{G}(2) + iG(2)\langle F(1) | \dot{F}(1) \rangle_1 \\ = \langle F(1) | \hat{H}(1, 2) | F(1) \rangle_1 G(2). \end{aligned} \quad (9)$$

The difference between Eqs. (8) and (9) is the presence of the overlaps with the time derivatives in the integrand. If we define the following transformation:

$$\begin{aligned} F(1) &= f(1)e^{-\int^t dt' \langle G(2) | \dot{G}(2) \rangle_2} \\ G(2) &= g(2)e^{-\int^t dt' \langle F(1) | \dot{F}(1) \rangle_1}, \end{aligned} \quad (10)$$

then we obtain the same form as in Eqs. (8):

$$\begin{aligned} if'(1) &= \langle g(2) | \hat{H}(1, 2) | g(2) \rangle_2 f(1) \\ ig'(2) &= \langle f(1) | \hat{H}(1, 2) | f(1) \rangle_1 g(2). \end{aligned} \quad (11)$$

Note again that we are suppressing the time dependence of F and G in the notation. The physics is not changed by the phase transformation defined in Eqs. (10).

To facilitate the use of the isop algorithm, we use Eq. (6) in Eq. (11):

$$\begin{aligned} if'(1) &= -\frac{1}{2}\nabla_1^2 f(1) \\ &\quad + \langle g(2) | -\frac{1}{2}\nabla_2^2 + V(1, 2) | g(2) \rangle_2 f(1) \\ ig'(2) &= -\frac{1}{2}\nabla_2^2 g(2) \\ &\quad + \langle f(1) | -\frac{1}{2}\nabla_1^2 + V(1, 2) | f(1) \rangle_1 g(2) \end{aligned} \quad (12)$$

Realizing that the particle labels are "dummy" in Eq. (12) because $V(1, 2) = V(2, 1)$, we may define the matrix equation, using $\psi \equiv [\begin{smallmatrix} f \\ g \end{smallmatrix}]$, as

$$i\dot{\psi} = -\frac{1}{2}\nabla^2 \psi + \underline{V}\psi, \quad (13)$$

where \underline{V} represents a diagonal potential matrix with diagonal elements defined by

$$\begin{aligned} V_{11}(1) &= \langle g(2) | -\frac{1}{2}\nabla_2^2 + V(1, 2) | g(2) \rangle_2 \\ V_{22}(1) &= \langle f(2) | -\frac{1}{2}\nabla_2^2 + V(1, 2) | f(2) \rangle_2. \end{aligned} \quad (14)$$

Thus, the isop algorithm, in matrix form, may be applied to Eq. (13).

In any numerical treatment of the Coulomb potential, it is necessary to sample the potential at small enough radius to represent the ground state accurately. This is achieved for a given numerical grid using the smoothing procedure given earlier [3], for which the radial cut off is $r_0 = [(2dxdydz)/(9\pi)]^{1/3}$. In the two-electron problem, the Hartree potential is evaluated by solving Poisson's equation for a density given by the squared modulus of the wave function. This equation is also solved in transform space, where it is necessary to cut off the Coulomb potential, which goes as $1/k^2$. Using similar smoothing arguments, the cutoff [6] in the radial k variable is $k_0 = 1/\sqrt{3}[(3dk_x dk_y dk_z)/(4\pi)]^{1/3}$. This cutoff has been tested against Coulomb integrals evaluated analytically in real space and found to give results of acceptable accuracy [6].

Results and Discussion

Our results are shown in Figures 1–13. The Schrödinger equation is integrated in imaginary time to evolve an assumed initial Gaussian wave function into the ground-state wave function. First, we solve the H_2^+ problem. In Figure 1 we show snapshots of the initial Gaussian electronic density centered about a proton fixed at 1 au on the positive z axis and then the evolved wave function density after 20 au of elapsed time, centered symmetrically about the molecular midpoint with peaks centered about the proton positions. This picture is a slice along the z axis for $x = y = 0$. The convergence to the molecular covalent state can be followed in time by observing the orbital dipole moment (Fig. 2), which begins at 1 au, as

given by the initial Gaussian, and ends at zero as the orbital evolves into a covalent orbital with a center of inversion. Finally, Figure 3 gives the expectation value of the Hamiltonian, which compares favorably with the exact energy of -1.1026 [7]. This calculation for the energy (Fig. 3) uses a spatial grid of $64 \times 64 \times 64$ points for a box of dimension $16 \times 16 \times 16$ au and a temporal grid of 1601 points for a maximum of 20 au of time. A less accurate but numerically stable result is obtained for 401 temporal points for the same duration (Figs. 1 and 2), in which case the energy is graphically found to be about -1.118 au; thus, the energy does not converge from above in these numerical solutions. The less accurate calculation takes about 19 min of CPU time on a Livermore Cray YMP machine.

Figures 4–13 show the results for the Hartree model of H_2^+ . Figures 4–12 show calculations which are performed on the same spatial grid of Figures 1–3, but with a sufficient number of temporal points such that $dt = 0.05$ au. Figure 13 shows our results with $dt = 0.02$ au for the H_2^+ potential energy curve, compared with three time-indepen-

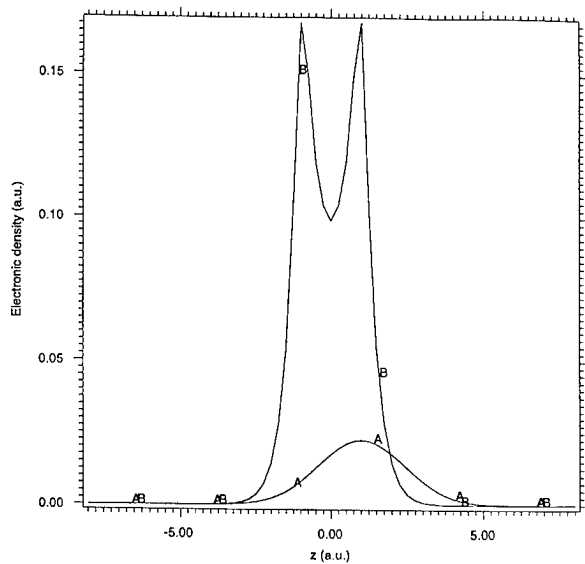


FIGURE 1. Time-dependent Schrödinger calculation of electronic density versus Cartesian coordinate z for H_2^+ , where two protons are fixed at plus or minus $z/2$. (A) Initial Gaussian orbital centered on the proton at $z/2$. (B) The orbital after 20 au of time. In the evolution of the motion, the initial orbital goes awash over the neighboring nucleus such that eventually it reaches a covalent state with a center of inversion about the molecular midpoint (covalent steady state).

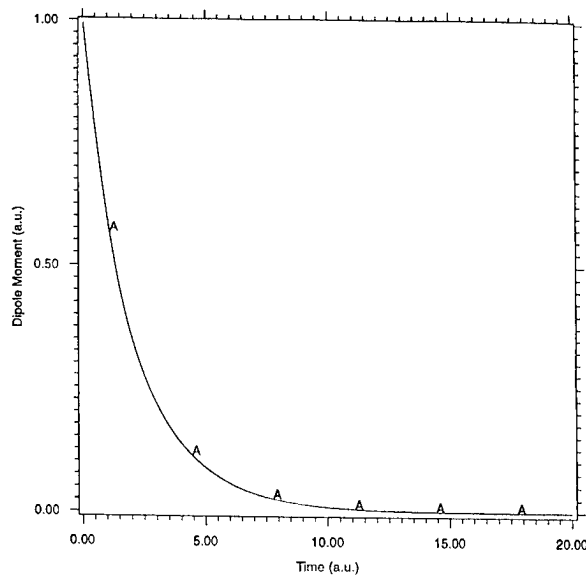


FIGURE 2. (A) Orbital dipole moment versus time for the evolution to the covalent state shown in Figure 1.

dent calculations. Figure 4 shows snapshots of two Gaussian orbital densities, initially centered over the protons, and the evolved densities after the elapse of 40 au of time. Each initial Gaussian has gone awash over its neighboring proton, but has remained primarily centered about its own proton, as Figure 5, which shows orbital dipoles which converge to steady-state equal and opposite values, confirms. On the other hand, at smaller inter-

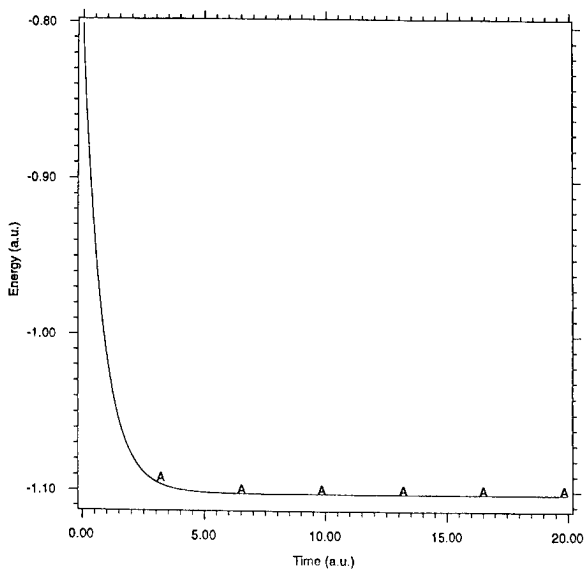


FIGURE 3. (A) Orbital energy versus time for the evolution to the covalent state shown in Figure 1.

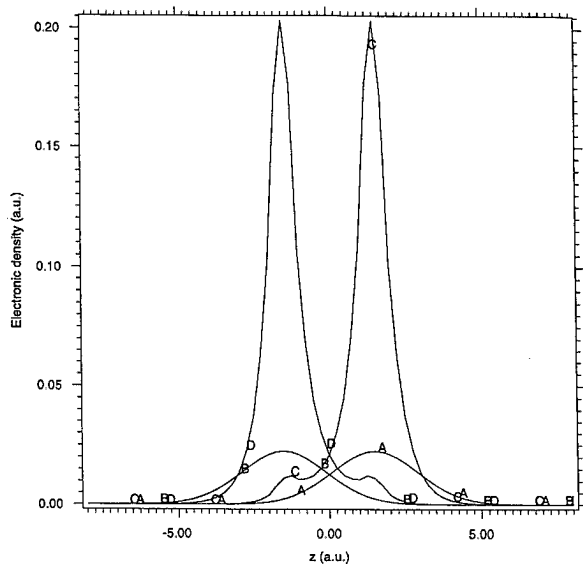


FIGURE 4. Time-dependent Schrödinger calculation of electronic density versus Cartesian coordinate z for H_2 , where two protons are fixed at plus or minus $z/2$. (A, B) Initial Gaussian orbitals centered on the protons. (C, D) Orbitals after 40 au of time. The motion reaches a steady state in which the two orbitals remain centered primarily about their originally assigned nuclei with leakage of density about the neighboring nuclei (separated-atoms steady state).

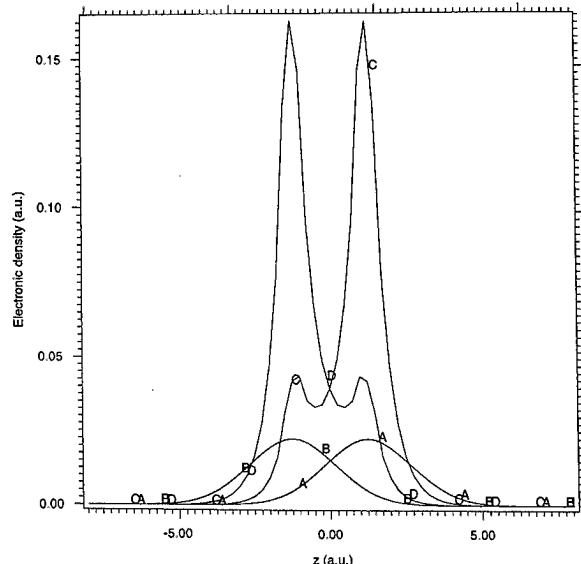


FIGURE 6. Time-dependent Schrödinger calculation of electronic density versus Cartesian coordinate z for H_2 , where two protons are fixed at plus or minus $z/2$. (A, B) Initial Gaussian orbitals centered on the protons. (C, D) The orbitals after 30 au of time. In the evolution of the motion, the initial orbits go awash over the neighboring nuclei such that, eventually, the two orbitals become identical and each has a center of inversion about the molecular midpoint (covalent steady state).

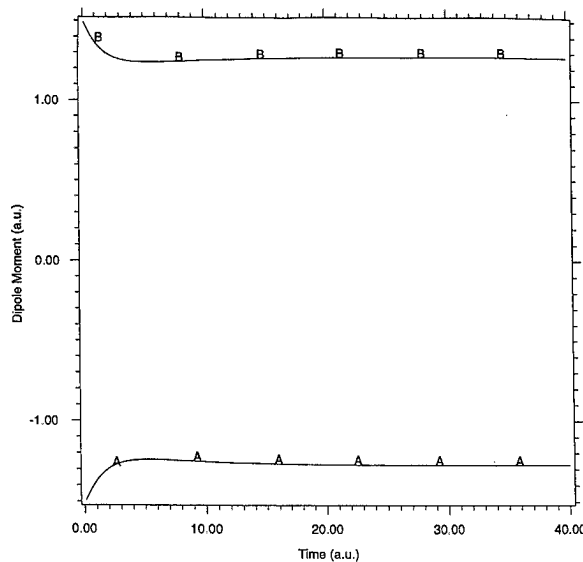


FIGURE 5. Orbital dipole moments versus time. (A, B) The orbitals of Figure 4. The equal and opposite dipole moments are characteristic of the separated-atoms steady state.

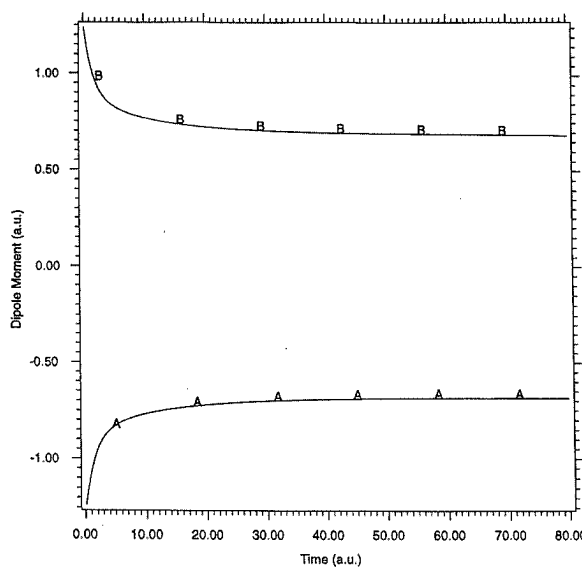


FIGURE 7. Orbital dipole moments versus time. (A, B) The orbital dipole moments for the orbitals of Figure 6. Each orbital dipole moment now individually goes very slowly to zero as the two orbitals awash over the nuclei in Figure 6 become identical.

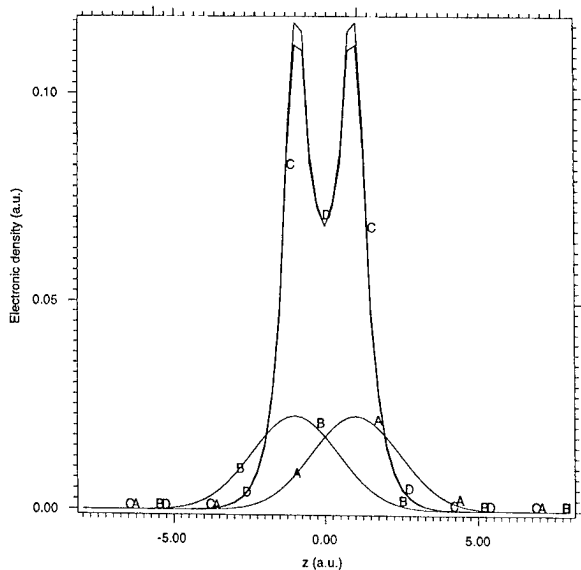


FIGURE 8. Time-dependent Schrödinger calculation of electronic density versus Cartesian coordinate z for H_2 , where two protons are fixed at plus or minus $z/2$. (A, B) Initial Gaussian orbitals centered on the protons. (C, D) The orbitals after 40 au of time. In the evolution of the motion, the initial orbitals go awash over the neighboring nuclei such that, eventually, the two orbitals become identical and each has a center of inversion about the molecular midpoint (covalent steady state).

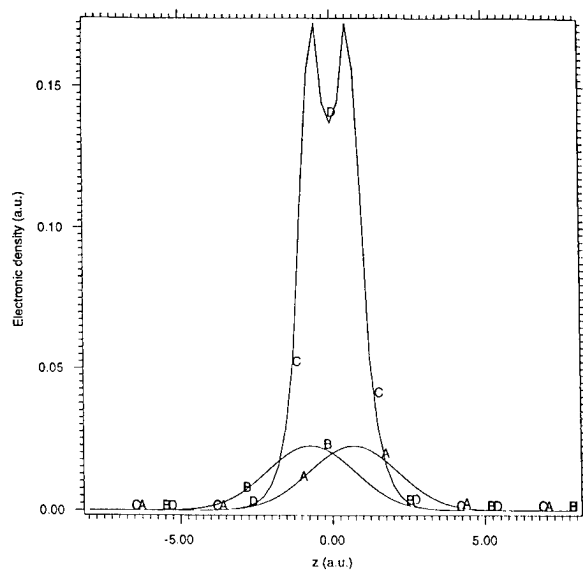


FIGURE 10. Time-dependent Schrödinger calculation of electronic density versus Cartesian coordinate z for H_2 , where two protons are fixed at plus or minus $z/2$. (A, B) Initial Gaussian orbitals centered on the protons. (C, D) The orbitals after 20 au of time. In the evolution of the motion, the initial orbitals go awash over the neighboring nuclei such that the two orbitals have become identical and each has a center of inversion about the molecular midpoint (covalent steady state).

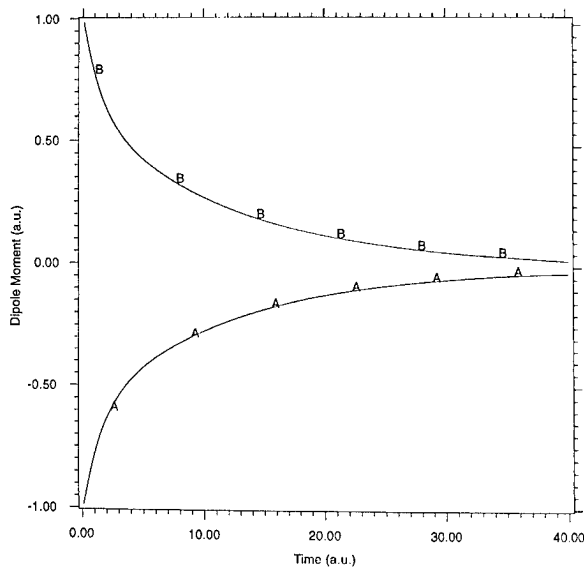


FIGURE 9. Orbital dipole moments versus time. (A, B) The orbital dipole moments for the orbitals of Figure 8. Each orbital dipole moment now individually goes to zero as the two orbitals awash over the nuclei in Figure 6 become identical.

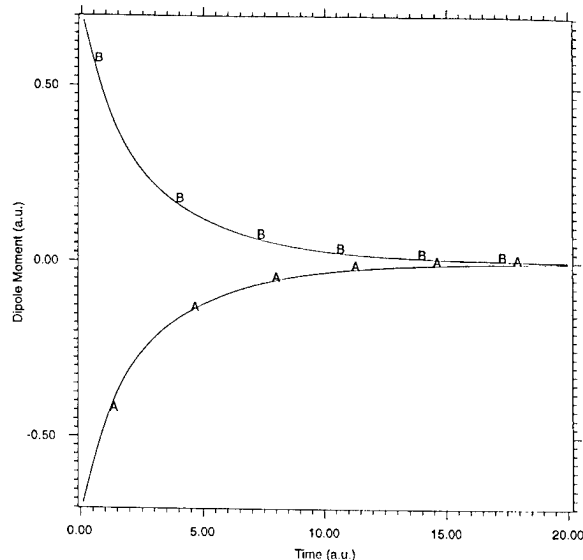


FIGURE 11. Orbital dipole moments versus time. (A, B) The orbital dipole moments for the orbitals of Figure 10. Each orbital dipole moment now individually goes to zero as the two orbitals awash over the nuclei in Figure 10 become identical.

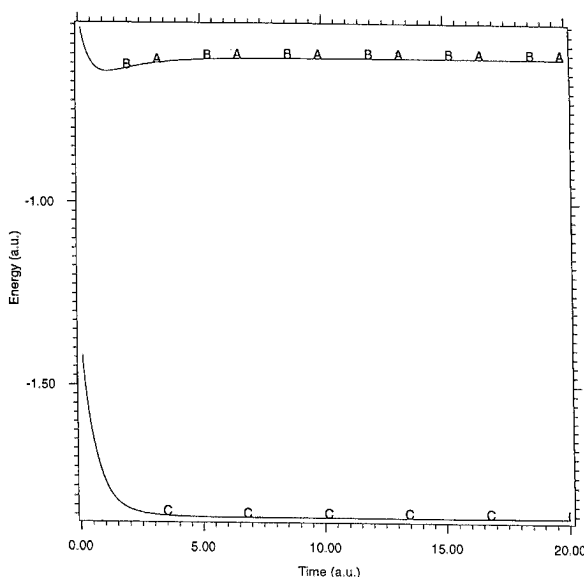


FIGURE 12. (A, B) Orbital energies versus time and (C) total energy versus time. Accounting for the binding energy (total energy – separated atoms energy + internuclear Coulomb energy) gives close to 80% of the accurately known binding energy of the hydrogen molecule, consistent with the interelectronic interaction model used here.

nuclear distances, Figures 6 and 7 show densities and orbital dipoles which appear to be converging to a covalent rather than to a separated-atoms steady-state limit. This is clear from Figure 7, where the equal and opposite orbital dipoles are far from converged after the elapse of 80 au of time, but whose small-magnitude temporal slopes are positive and negative for dipoles which are rising and declining toward the z axis, respectively; thus, with sufficient time, unless the slopes converge to zero for finite equal and opposite dipoles, we would expect an eventual evolution into two identical covalent orbitals with zero dipole moment, as in Figures 1 and 2. Figures 8–11 support this conclusion: In Figures 8 and 9 for the smaller internuclear distance for H_2 , the orbitals have almost converged to identical, zero-dipole orbitals after the elapse of 40 au of time, and in Figures 10 and 11, which are at the equilibrium internuclear distance for H_2 , the orbitals have indeed converged to identical, zero-dipole orbitals after the elapse of 20 au of time.

The convergence to identical covalent orbitals, even though the initial orbitals form an unsymmetrized product centered about each nucleus, can be understood from the work of Riley et al. [8], which shows that the Pauli principle is satisfied starting from an unsymmetrized product, if the symmetry of the Hamiltonian with respect to interchange of the two electrons is represented in a converged perturbation-theoretic calculation. In our calculation, at small enough internuclear distances, the initially nuclei-centered orbitals can migrate to neighboring nuclei such that, with sufficient time, the interchange symmetry of the Hamiltonian is properly represented after the two orbitals have become identical, in analogy to the calculation of Riley et al., after many orders of perturbation theory. Thus, for small enough internuclear distances, the Pauli principle is automatically satisfied finally, even though it is not satisfied initially. We have convinced ourselves of this conclusion by repeating the calculations of Figures 8–11, starting with two identical initial Gaussian orbitals centered on the midpoint between the two nuclei, in which case these orbitals remain identical and converge (with different rates of convergence from those of Figs. 8–11) to the same results as those of Figures 8–11. On the other hand, when identical Gaussians are centered at the midpoint for the larger internuclear distances of Figures 4–7, the calculations converge to identical orbitals having a covalent form, but whose orbital energies are

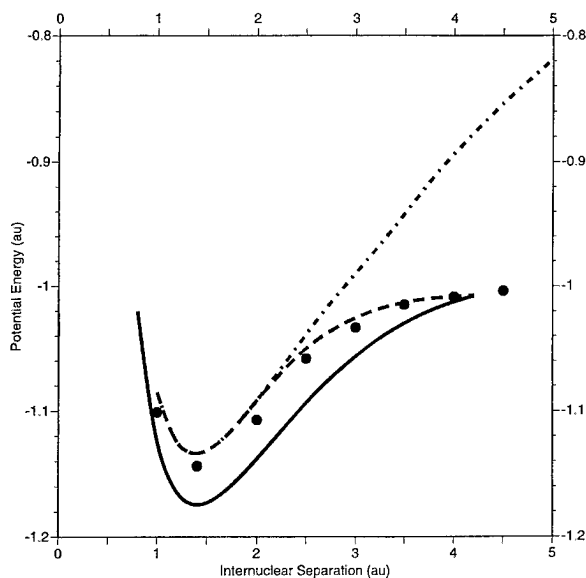


FIGURE 13. H_2 potential energy curves in atomic units: (—) time-independent 40-term variational calculation of [8]; (●●) present time-dependent Hartree calculation; (—) unrestricted time-independent Hartree–Fock [11]; (---) restricted time-independent Hartree–Fock [11].

significantly larger than those of the separated atoms (unlike the orbital energies of Figs. 4–7, which are always below the separated-atoms energies). We reject these results as unphysical since it is clear that at large enough internuclear distances one must obtain the separated-atoms result, and, indeed, the results of Figures 4–7, in which the initial Gaussians are nuclei-centered, exhibit the appropriate separated-atoms behavior. This point emphasizes a characteristic which we have noticed in other calculations, namely, that a poor choice for the initial Gaussian can lead to a numerically converged result which is unphysical; clearly, Gaussians centered initially at the molecular midpoint will not migrate properly to the nuclear positions at large internuclear distances unless they have greater widths than those used here.

Thus, Figures 6 and 7 show results near a critical internuclear distance separating two distinct steady states: a separated-atoms state at larger and a covalent state at smaller internuclear distances. To our knowledge, this is the first description of molecular covalency as a unique steady state of the time-dependent Schrödinger equation whose onset occurs at internuclear distances smaller than a certain critical internuclear distance (Figs. 6 and 7).

Figure 12 shows the orbital energies and total energy versus time corresponding to Figures 10 and 11. The total energy is about -1.857 au, which corresponds to a binding energy of 3.88 eV, which is slightly better than the elliptical-coordinate nine-term variational Hartree–Fock energy of 3.6360 eV obtained by Kolos and Roothaan [9]. This is approximately 81.7% of the binding energy of H_2 (4.75 eV [7]) and is much better than what one would expect for the present Hartree model based on our knowledge of the variational LCAO–MO Hartree model, whose binding energy is only 2.65 eV [10]. The present binding energy compares favorably with that of the Heitler–London model with an optimized exponent [10], namely, 3.76 eV. We repeated the calculation using $dt = 0.02$ au temporal points and found that our results change slightly. At this time step, we got a total energy of -1.858 au, giving a binding energy of 3.91 eV. This is 82.3% of the essentially exact value of 4.75 eV from [7]. Our result was converged to the significant figures shown for the $dt = 0.02$ au time step.

Finally, Figure 13 shows our potential energy curve for H_2 at a time step of $dt = 0.02$ eV, compared with the time-independent 40-term varia-

tional calculation of [8] and restricted Hartree–Fock and unrestricted Hartree–Fock calculations using Gaussian94 [11]. It is clear from Figure 13 that our present time-dependent Hartree results are closer to the exact values for all internuclear calculations than either the restricted or unrestricted time-independent Hartree–Fock results. At large internuclear separations, our results are even slightly better than the best theory from [8]. At $R = 4.5$ Bohr, we obtain a binding energy of 0.11 eV.

Conclusion

The utility of the time-dependent description of molecular electronic structure, in our opinion, lies in the capability of the theory to predict covalent versus separated-atoms states. This is why the simple product of states for H_2 leads to a superior result than that for the LCAO–MO Hartree result, which is based on writing a trial wave function which has equal weighting for components describing the dissociation of the molecule into the ions H^+ and H^- and for components describing the dissociation into the neutral atoms H and H . Clearly, a physically compelling weighting must favor dissociation in the neutral atoms. This example illustrates the difficulty of time-independent variational calculations in which one does not know the steady-state wave function and, hence, must construct it using a trial wave function whose basis-set selection is judgmental. On the other hand, the time-dependent calculation evolves the wave function naturally, depending on the internuclear distance, into states which predict covalent or noncovalent binding. Thus, to use a variational analogy, the time-dependent calculation selects the basis set appropriate for a given internuclear distance.

We would expect the binding energy to show considerable improvement if we based our time-dependent equations on a symmetrized product of orbitals appropriate for singlet-state symmetry. Here, we would expect the two orbitals not to be identical in the covalent steady state. This calculation is at a higher level of difficulty owing to the coupling of the two-orbital equations through exchange and overlap terms and will be forthcoming in future work.

Finally, we comment briefly that time-dependent Hartree–Fock (TDHF) theory [5] appears not to have achieved a high level of regard for useful-

ness in structure and other problems. However, we believe that this is in large part due to its restrictive nature, namely, that the equations be derived from a variational ansatz for a set of orthonormal orbitals. Clearly, this is a too restrictive mathematical environment to describe even the simple H_2 model that we have considered here, in which the two nonorthogonal orbitals are propagated in imaginary time until they evolve either into predominantly atomic orbitals with small leakage of density about another nucleus (Figs. 4 and 5) or into covalent molecular orbitals (Figs. 6–11) which contain a much larger fraction of the binding energy than that based on the well-known LCAO-MO variational *ansatz*. Thus, although we have called our calculation the Hartree model for H_2 , it is not the TDHF model in the usual sense, and we believe that the full model based on the symmetrized product of orbitals holds much promise in the description of electronic structure and scattering problems.

ACKNOWLEDGMENTS

This work was performed under the auspices of the U.S. Department of Energy by the Lawrence Livermore National Laboratory under Contract No. W-7405-ENG-48. C. A. W. was also partially supported by the Lawrence Livermore National Laboratory Research Collaboration Program for Historically Black Colleges and Universities and Minority

Institutions, NSF Cooperative Agreement Number HDR-9707076, and by the Army High Performance Computing Research Center under the auspices of the Department of the Army, Army Research Laboratory Cooperative Agreement Number DAAH04-95-2-0003/contract number DAAH04-95-C-0008. One of the authors (B. R.) is grateful to Merle Riley for helpful discussions. C. A. W. also acknowledges useful conversations with Mario Encinosa and Bidhan Saha.

References

1. M. D. Feit, J. A. Fleck, Jr., and A. Steiger, *J. Comput. Phys.* **47**, 412 (1982).
2. K. Kulander, *Phys. Rev. A* **35**, 445 (1987); *Ibid.*, **36**, 2726 (1987).
3. B. Ritchie and M. E. Riley, *Sandia Report Sand97-1205*, UC-401 (1997).
4. B. Ritchie, P. Dykema, and D. Braddy, *Phys. Rev. E* **56**, 2217 (1997).
5. A. K. Kermin and S. E. Koonin, *Ann. Phys.* **100**, 332 (1976).
6. M. E. Riley, private communication.
7. W. Kolos and L. Wolniewicz, *J. Chem. Phys.* **49**, 404 (1968).
8. M. E. Riley, J. M. Schulman, and J. I. Musher, *Phys. Rev. A* **5**, 2255 (1972).
9. W. Kolos and C. C. Roothaan, *Rev. Mod. Phys.* **32**, 205 (1960).
10. H. Eyring, J. Walter, and G. Kimball, *Quantum Chemistry* (Wiley, New York, 1944), pp. 212–216.
11. Calculations by Ahmed Bouferguene using Gaussian94; private communication.

Modern Valence Bond Descriptions of Molecular Excited States: An Application of CASVB

THORSTEIN THORSTEINSSON,¹ DAVID L. COOPER²

¹*Chemistry Laboratory IV, Copenhagen University, Universitetsparken 5, DK-2100 Copenhagen Ø, Denmark*

²*Department of Chemistry, University of Liverpool, P.O. Box 147, Liverpool L69 7ZD, United Kingdom*

Received 21 February 1998; accepted 17 August 1998

ABSTRACT: The valence bond description of excited states is considered in the context of the CASVB approach, with emphasis on the simultaneous optimization of orbitals and structure coefficients for highly general types of wave function, as well as the close connection to the complete active space self-consistent field (CASSCF) method. In addition to fully variational optimization of modern valence bond (VB) wave functions, one may also generate compact representations of CASSCF wave functions, essentially irrespective of their nature. Consequences of generalizing the CASVB methodology to other than the lowest-lying state of a given symmetry are explored for both the overlap- and energy-based optimization criteria. The methodology is illustrated by means of applications to the 2^1A_g state of *trans*-1,3-butadiene, the \tilde{c}^1A_1 state of methylene, and the first excited singlet state of benzene. © 1998 John Wiley & Sons, Inc. *Int J Quant Chem* 70: 637–650, 1998

Key words: excited states; modern valence bond theory; CASVB; spin-coupled wave function

Correspondence to: D. L. Cooper.

Contract grant sponsor: EEC under the TMR program.

Contract grant number: ERBFMRXCT960088.

Contract grant sponsor: Danish Natural Science Research Council.

Introduction

The description of electronically excited states presents significant problems in quantum chemistry. Unquestionably the presently most accurate approaches for smaller systems involve the initial multiconfiguration self-consistent field (MCSCF) optimization of the reference function(s) prior to a configuration interaction (CI) step, or alternatively a perturbational step, to take proper account of dynamical correlation effects. A useful introduction, in the context of the complete active space self-consistent field (CASSCF) method, is the series of articles by Roos and co-workers [1–3]. At present, modern valence bond theory [4] cannot compete with the most accurate results that may be achieved by such methods, but it may instead play an important role in the visualization of the electronic structure. This is the aim of the current work.

Modern valence bond descriptions of excited states have used two main strategies. Perhaps the most straightforward approach is to follow an orbital optimization procedure by a nonorthogonal CI treatment [5]. This last places particular demands on the quality of the orbital representation, especially if all the orbitals are obtained from a treatment of the lowest state. In the most commonly employed procedure based on a spin-coupled wave function, all of the “virtual” orbitals are generated by diagonalizing generalized Fock operators [6]:

$$\hat{F}^{(\mu)}\phi_{\nu}^{(\mu)} = \varepsilon_{\nu}^{(\mu)}\phi_{\nu}^{(\mu)}. \quad (1)$$

This procedure yields a series of “stacks” of orbitals. Each occupied orbital in the reference function leads to an eigenvalue equation of the form shown in Eq. (1) and may be identified as one of its solutions. Excitation into the low-lying virtuals in each stack may then provide excellent approximations to excited states, and accurate results may be obtained with CI expansions of very moderate size. The overcompleteness of the orbital basis thus defined does not lead to significant problems, provided a critical selection of excitations is carried out. One example of this procedure is an application to the notoriously difficult excited states of benzene [7]. Alternative choices for spin-

coupled virtual orbitals have been investigated recently by Clarke, Sironi, and co-workers [8, 9].

In an alternative to the standard spin-coupled approach, the Fock operators of Eq. (1) may be diagonalized in an iterative procedure until self-consistency is reached. Although such an approach has been applied to the optimization of ground-state wave functions [6], it is not likely to compare favorably with a fully second-order optimization scheme [10, 11] in terms of either computational efficiency or convergence characteristics. The main advantage of this type of approach is instead its straightforward extension to the description of excited states, which may be achieved simply by choosing higher-lying solutions to the Fock eigenvalue problems. Such a procedure has been applied to some smaller systems by Doggett et al. [12–14], using an approach formulated as a super-CI scheme. Their results seem very promising, but an open question is the application to excited states that are not well described as a single excitation from the ground state.

While the optimization of modern valence bond wave functions for ground states has come very far, there is little doubt that there is still some scope for development in the case of excited states. Our newly developed method for optimization of general types of valence bond wave functions, CASVB [15–22], possesses some important advantages in this respect, and we consider its extension to the treatment of excited states in the following sections. Main features include the very flexible forms for the wave function and the natural connection to molecular-orbital-based procedures. Fully variational optimization of the wave function is possible, which may provide benchmarks for other valence bond strategies. Our CASVB program is now available as part of the quantum chemistry package MOLPRO [23], in which it is interfaced to a sophisticated CASSCF program [24]. We foresee a much wider distribution in the near future.

CASVB Approach

Prior to considering the optimization of excited states within the CASVB framework, we review briefly some of the main characteristics of the method [15–22].

The cornerstone of the CASVB approach is the efficient transformation of CASSCF spaces. The structures defining such spaces may be either Slater

determinants or configuration state functions (CSFs), and the subsequent expressions remain equally valid for both, but there are many advantages associated with a determinant approach, not least being that of computational simplicity [17].

The CASSCF wave function may in general incorporate a core term, Φ^{core} , which is common to all structures Φ_I :

$$\Phi_I = \mathcal{A}(\Phi^{\text{core}} \times \Phi_I^{\text{act}}). \quad (2)$$

In practice, Φ^{core} is normally based on $1/2 N_{\text{core}}$ doubly occupied orbitals. The active parts of the structures, Φ_I^{act} , are then constructed as an N in m full CI expansion compatible with a total spin of S . It is well known that a full CI is invariant to nonsingular transformations of the defining orbitals, and this observation forms the basis for the CASVB strategy:

$$\{\phi'\} = \{\phi\}\mathbf{O} \Rightarrow \{\Phi'\} = \{\Phi\}\mathbf{T}(\mathbf{O}). \quad (3)$$

Here $\{\}$ denotes a row-vector of either the active orbitals, ϕ , or many-electron functions, Φ . A very efficient algorithm for obtaining $\mathbf{T}(\mathbf{O})$ is based on rewriting the orbital transformation, \mathbf{O} , as a product of m^2 updates of the form

$$\mathbf{O}_{\mu\nu}(\lambda): \phi_\nu \rightarrow \phi_\nu + \lambda \phi_\mu, \quad (4)$$

for which the corresponding full CI transformations are trivial to evaluate [15,17,25].

The modern valence bond (VB) wave function that we consider in this context takes the form of a single spatial configuration of N singly occupied orbitals (i.e., a spin-coupled wave function [4]):

$$\Psi_{\text{VB}} = \mathcal{A}(\Phi^{\text{core}} \phi_1^{\text{VB}} \phi_2^{\text{VB}} \dots \phi_N^{\text{VB}} \Theta_{SM}^N), \quad (5)$$

or limited multiconfiguration variants thereof. As usual [4], Θ_{SM}^N is an appropriate fully optimized N -electron spin function. Assuming that Ψ_{VB} can be expressed as a linear combination of (nonorthogonal) "N-in- m " CASSCF structures, we can transform to a representation based on orthogonal CSFs, according to:

$$\Psi_{\text{VB}} = \sum_I c_I \mathcal{A}(\Phi^{\text{core}} \times \Phi_I^{\text{VB}}) = \sum_I c_I (\{\Phi\}\mathbf{T}(\mathbf{O}^{\text{VB}}))_I. \quad (6)$$

Here \mathbf{O}^{VB} defines the transformation from CASSCF molecular orbitals (MOs) to valence bond orbitals, as in Eq. (3). Optimization of Ψ_{VB} will normally be carried out both with respect to the linear struc-

ture coefficients; c_I , and to the nonlinear orbital parameters which define the matrix \mathbf{O}^{VB} .

For the case of a ground-state CASSCF wave function, we have in previous work considered two basic criteria for optimizing Ψ_{VB} :

$$\text{maximize } S_{\text{VB}} = \frac{\langle \Psi_{\text{CAS}} | \Psi_{\text{VB}} \rangle}{\langle \Psi_{\text{VB}} | \Psi_{\text{VB}} \rangle^{1/2}} \quad (7)$$

or

$$\text{minimize } E_{\text{VB}} = \frac{\langle \Psi_{\text{VB}} | \hat{H} | \Psi_{\text{VB}} \rangle}{\langle \Psi_{\text{VB}} | \Psi_{\text{VB}} \rangle}. \quad (8)$$

Each quantity is optimized with respect to the valence bond parameters considered above. As a powerful extension, optimization according to Eq. (8) may be combined with the core-active, core-virtual, and active-virtual (orthogonal) orbital rotations inherent in a CASSCF procedure, such that a fully variational modern valence bond solution is obtained.

It is worth emphasizing the special difficulties associated with optimization of a valence bond wave function of this form. First, the optimization problem is nonlinear, necessitating an exact second-order optimization procedure with trust region control for reliable convergence. We have opted for the method by Fletcher [26,27], in which an equation of the form

$$\delta = -(\mathbf{G} - \alpha \mathbf{I})^{-1} \mathbf{g}, \quad \|\delta\| \leq h \quad (9)$$

is solved for the update, δ . Second, as a non-orthogonal orbital optimization, it may not always be possible to avoid linear dependency problems. One may need to invoke some form of constraints on some of the wave function parameters and we have adopted a simple elimination scheme for this purpose [21]. Alternatively, when appropriate, facilities for symmetry adaptation may be used [18], possibly in combination with other constraints.

Excited-State Optimization

The extension of the criteria in Eqs. (7) and (8) to excited states that are lowest within a given symmetry is trivial, since such optimizations can be carried out by simply symmetry adapting the wave function [18]. In the following, we consider

instead the optimization of states that are second or higher within a particular symmetry.

Perhaps most straightforward is the use of the overlap-based criterion since, given a set of CASSCF solutions for each electronic state, $\{\Psi_{\text{CAS}}^{(1)}, \Psi_{\text{CAS}}^{(2)}, \dots\}$, one can simply maximize

$$S_{\text{VB}} = \frac{\langle \Psi_{\text{CAS}}^{(i)} | \Psi_{\text{VB}}^{(i)} \rangle}{\langle \Psi_{\text{VB}}^{(i)} | \Psi_{\text{VB}}^{(i)} \rangle^{1/2}}, \quad (10)$$

to get the i th VB solution, $\Psi_{\text{VB}}^{(i)}$. A fairly standard optimization of an appropriate CASSCF wave function may therefore pave the way for a modern valence bond description of a given excited state.

Generalization of the energy-based criterion is somewhat less straightforward. Two natural requirements for *consistent* representations of different states in a given symmetry are

$$\langle \Psi^{(i)} | \Psi^{(j)} \rangle = \delta_{ij} \quad \text{and} \quad \langle \Psi^{(i)} | \hat{H} | \Psi^{(j)} \rangle = E^{(i)} \delta_{ij}. \quad (11)$$

However, neither of these requirements will in general be satisfied within MCSCF procedures, a fact that must have some bearing on calculated excitation energies and transition properties. While the errors involved may in the majority of cases be relatively small [1], more rigorous procedures that avoid these problems are clearly to be recommended. A natural choice is the CASSCF state interaction approach (CASSI) [28] in which the solutions obtained in preliminary MCSCF optimizations are used to form a secular problem that leads to more accurate representations of the required states.

A significant amount of attention has been paid to the proper definition of excited-state representations in nonlinear optimization procedures. We believe that a very natural approach is to consider the space generated by first-order variations in the variational parameters:

$$\Psi_{\text{SCI}} = \left\{ \Psi(\mathbf{x}_0), \frac{\partial}{\partial x_1} \Psi(\mathbf{x}_0), \frac{\partial}{\partial x_2} \Psi(\mathbf{x}_0), \dots \right\},$$

for a wave function, Ψ , which depends parametrically on the set of variables \mathbf{x} . For $\Psi(\mathbf{x}_0)$ to be a representation of the i th state, it must occur as the i th root in the secular equations formed from this

super-CI space. While it is possible to implement this condition directly in an iterative super-CI optimization procedure, such strategies generally show very poor convergence characteristics.

Perhaps the most widely used approach is therefore to take as a starting point the stationary point for which the second derivative matrix has $i - 1$ negative eigenvalues; this can be shown to be closely related to the super-CI requirement outlined above. In the context of MCSCF optimization, this problem has been considered extensively by Olsen et al. [29, 30].

A particularly useful account of various possible second-order optimization schemes has been presented by Helgaker [31]. Two main families of strategies exist: the stabilized Newton–Raphson scheme (see, e.g., Ref. [27]), and the so-called augmented Hessian method (see, e.g., Refs. [32, 33]). A main advantage of the Newton–Raphson-type schemes is their natural and efficient trust region control. We believe the most natural generalization of such approaches to saddle-point optimization to be the “trust region image minimization” (or TRIM) algorithm proposed by Helgaker [34]. Details of our implementation of this procedure for excited-state optimization are given in an appendix. In the next section, we describe applications of our procedures to the 2^1A_g state of *trans*-1,3-butadiene, the \tilde{c}^1A_1 state of methylene, and the first excited singlet state of benzene.

Problems associated with multiple stationary points for nonlinear optimization procedures are well known [35] and these are likely to be significantly more pronounced for excited-state optimization. Compared with the more straightforward ground-state optimization, special techniques may therefore be required to obtain convergence onto a particular solution. An attractive option is likely to be in the form of a partitioning of the optimization problem. By employing a two-step (or, in general, n -step) optimization procedure, convergence onto stationary points corresponding to particular types of orbital excitations may be obtained. Using such a strategy, we have obtained a similar functionality to the procedure described by Doggett et al. [12–14] and, as such, we have been able to reproduce their results. Olsen et al. [29] have stressed the importance of taking the coupling between optimization problems into account for two-step optimization procedures, and we foresee a need to address this question for treatments of more complicated systems.

Results

SECOND 1A_g STATE OF TRANS-1,3-BUTADIENE

Polyenes possess low-lying valence excited states with the same 1A_g symmetry as the ground state [3], but it is well known that only a relatively small part of the 2^1A_g wave function can be ascribed to single excitations from the ground state. In a recent study, Serrano-Andrés et al. [3] attributed a figure of 58% to such single excitations.

A ground-state geometry determined by electron diffraction spectroscopy [36] was adopted in all of the present calculations and we used Dunning's pVTZ basis sets [37], consisting of (10s5p $2d$ /5s2p) Cartesian Gaussians contracted to [4s3p $2d$ /3s2p] for C/H. Energies from 4-in-4 CASSCF calculations for the ground and 2^1A_g states are given in Table I. In order to assess the suitability of 4-in-4 treatments of these states, we examined also the corresponding 4-in-6 calculations. Energy lowerings of just 4.9 and 5.5 millihartree, respectively, for the ground and excited state suggest that the 4-in-4 spaces are quite reasonable. A further consideration, in our case, is the nature of the subsequent CASVB interpretations;

TABLE I
Energies for various calculations on butadiene.^a

State	Calculation	E , hartree
1^1A_g	SCF	-154.969332
2^1A_g	4-in-4 CAS (MOs from 1^1A_g)	-154.735740
2^1A_g	4-in-4 CASSCF	-154.776292
2^1A_g	4-in-6 CASSCF	-154.781744
1^1A_g	4-in-4 CAS (MOs from 2^1A_g)	-155.007687
1^1A_g	4-in-4 CASSCF	-155.023870
1^1A_g	4-in-6 CASSCF	-155.028809

^a Further details are given in the text.

TABLE II
Values of S_{vb} and E_{vb} for butadiene, calculated with various sets of orbitals.

VB (CAS)	S_{vb}	E_{vb}
1^1A_g (1^1A_g)	0.999889	-155.023628
2^1A_g (2^1A_g)	0.999982	-154.776258
2^1A_g (1^1A_g)	0.999930	-154.735622

multiconfiguration VB wave functions would be required to recover the additional correlation taken into account by the larger CASSCF models.

The results of valence bond representations of the 4-in-4 CASSCF solutions are summarized in Tables II-IV and illustrated in Figures 1 and 2. The overlap-based optimizations are in all cases achieved simply by maximizing the overlap (S_{vb}) between a modern VB wave function of spin-coupled form and the appropriate CASSCF function. The energy-based results were obtained either by minimization onto the ground state or by saddle-point optimization to obtain descriptions of the excited state.

The values of S_{vb} and E_{vb} listed in Table II show that the CASSCF wave functions are represented with great accuracy by the corresponding VB solutions. This is to be expected for active spaces of this size. What is noticeable in this context, however, is the ability of the saddle-point E_{vb} optimization to reproduce the $\max(S_{vb})$ results. The trust region image minimization algorithm therefore seems very viable for use in MCSCF-type optimization problems.

Compared to the ground state, the excited state may to a good approximation thought of as an "excitation" in the spin space (cf. Table IV). As such, the orbitals remain *qualitatively* the same, although a significant increase of the $\langle \phi_2 | \phi_3 \rangle$ overlap, as well as a general "expansion" of the orbitals, may be detected. These simple observa-

TABLE III
Symmetry-unique overlap integrals for butadiene solutions.

Solution	$\langle \phi_1 \phi_2 \rangle$	$\langle \phi_2 \phi_3 \rangle$	$\langle \phi_1 \phi_3 \rangle$	$\langle \phi_1 \phi_4 \rangle$
1^1A_g (S_{vb})	0.65086	0.29400	0.07759	0.03223
1^1A_g (E_{vb})	0.65048	0.29547	0.07984	0.03685
2^1A_g (S_{vb})	0.70369	0.56370	0.21140	0.01383
2^1A_g (E_{vb})	0.70154	0.56416	0.21081	0.01358
2^1A_g (S_{vb} , 1^1A_g)	0.73781	0.49884	0.15976	-0.00943
2^1A_g (E_{vb} , 1^1A_g)	0.73311	0.50420	0.16257	-0.00878

TABLE IV

Weights $w_{pp} = (c_{pp})^2$ of the perfectly paired spin function, expressed as percentages of the total spin function in the Kotani or Serber bases.

VB (CAS)	$w_{pp} (S_{vb})$	$w_{pp} (E_{vb})$
1^1A_g (1^1A_g)	99.22	98.15
2^1A_g (2^1A_g)	2.79	2.83
2^1A_g (1^1A_g)	1.60	1.66

tions may go a long way to explaining the properties of the 2^1A_g state in this and longer polyenes, as well as, of course, why no such state is found for ethene.

The effect of orbital relaxation on the descriptions of the two states may be gauged, for example, by basing the excited-state description on the ground-state CASSCF MOs, giving an energy some 40 millihartree higher than that of the fully optimized excited state (see Table I). Relaxation is thus a very substantial effect, which underlines the aptness of a CASSI [28], or similar, approach for ensuring consistent treatments of the two states. Examination of the VB representations suggests that a major factor in the orbital relaxation is the aforementioned increased diffuseness of the participating orbitals.

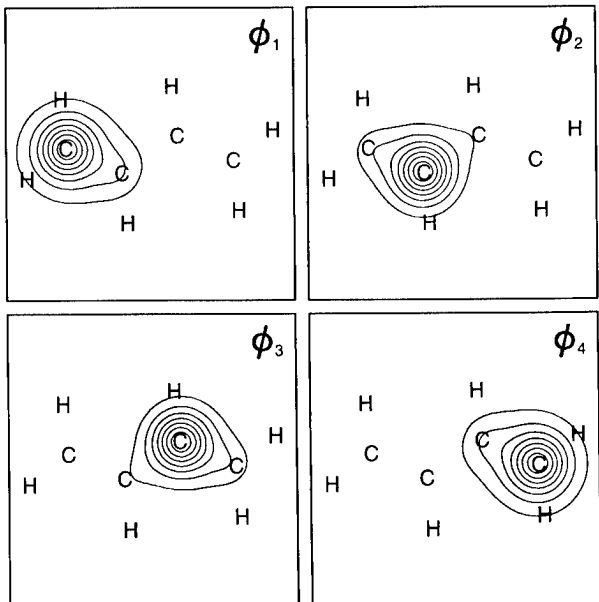


FIGURE 1. CASVB orbitals for butadiene: overlap-based representation of the 1^1A_g ground-state CASSCF wave function. Orbitals are plotted 1 bohr above the molecular plane and (projected) positions of the nuclei are marked by their chemical symbols.

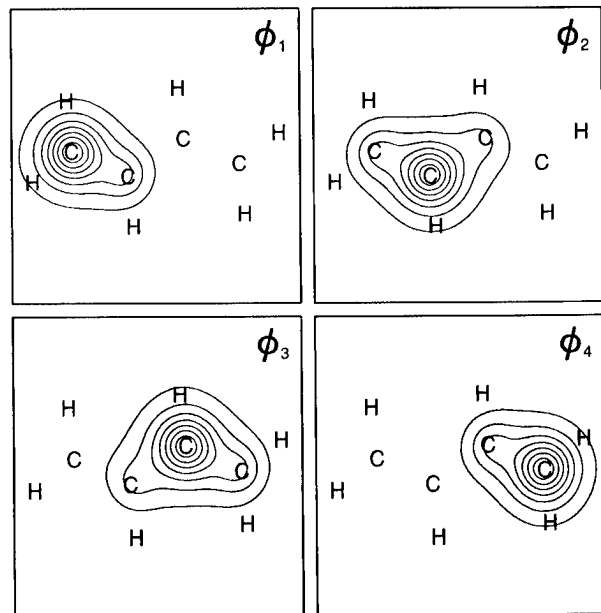


FIGURE 2. CASVB orbitals for butadiene: overlap-based representation of the 2^1A_g excited state CASSCF wave function, plotted as in Figure 1.

THE \tilde{c}^1A_1 STATE OF METHYLENE

Low-lying electronic states of CH_2 have been subject to much attention, especially the problem of describing accurately the splitting between the 3B_1 ground state and the first excited state (\tilde{a}^1A_1). The spin-coupled descriptions of these two states have been reported previously in several publications [38–40]. Furthermore, the CASVB representation of the \tilde{a}^1A_1 state has been found to resemble closely the spin-coupled results [15,16] and the same is true for the CASVB description of the triplet ground state.

For our calculations on the \tilde{c}^1A_1 state, we employed the same pVTZ basis sets as for butadiene and used an ab initio geometry of $r_{\text{CH}} = 1.064 \text{ \AA}$ and $\theta(\text{HCH}) = 171.6^\circ$ [41]. As a starting point for the CASVB representations, an all-valence CASSCF calculation was performed keeping $1s^2$ as an optimized core, so that the active MOs can then be classified as $2a_1$, $1b_2$, $3a_1$, $1b_1$, $2b_2$, and $4a_1$ in C_{2v} symmetry. The CASSCF solution of interest can be identified at convergence as the second CI eigenvector of 1A_1 symmetry. The energies obtained in the SCF and CASSCF calculations are collected in Table V.

Initial investigations of the CASVB solutions were carried out using the simple overlap-based

TABLE V
Energies for various calculations on CH_2 .^a

Calculation	E , hartree
SCF ($\tilde{\alpha}^1\text{A}_1$)	-38.837861
CASSCF $\tilde{\alpha}^1\text{A}_1$	-38.855187
CAS $\tilde{\alpha}^1\text{A}_1$ (MOs from $\tilde{\alpha}^1\text{A}_1$)	-38.891603
CASSCF $\tilde{\alpha}^1\text{A}_1$	-38.893050

^a Further details are given in the text.

criterion, because this is computationally the least expensive. We shall endeavor to describe the series of calculations in sufficient detail to illustrate the way in which a degree of common sense must necessarily be employed to obtain reasonable results for the $\tilde{\alpha}^1\text{A}_1$ state. It seemed natural first to investigate a solution based on an orbital description analogous to that of the lower $\tilde{\alpha}^1\text{A}_1$ state. However, an energy difference of 29 millihartrees from the CASSCF wave function seems to indicate that such a model of the $\tilde{\alpha}^1\text{A}_1$ state, which we label 1a in Table VI, is not very realistic: Corresponding

TABLE VI
Values of S_{vb} and E_{vb} for singlet methylene, calculated with various models, as described in the text.

Model	S_{vb}	E_{vb}	$E_{vb} - E_{\text{CAS}}$
1a	0.991724	-38.826331	0.028856
1b	0.993414	-38.838868	0.016319
1c	0.993412	-38.838872	0.016315
1d	0.994545	-38.865023	-0.009836

values for ground-state calculations are typically 10 millihartrees. Furthermore, as is shown in Figure 3, the forms of the optimized orbitals are rather unphysical. Indeed, the near-linear dependence, due to high orbital overlaps $\langle \phi_1 | \phi_2 \rangle$ and $\langle \phi_4 | \phi_6 \rangle$ (see Table VII), also gave rise to some convergence problems.

The shortened bond lengths for this state relative to the lowest ${}^1\text{A}_1$ state (1.064 versus 1.117 Å [42]) do not suggest any partial breaking of the

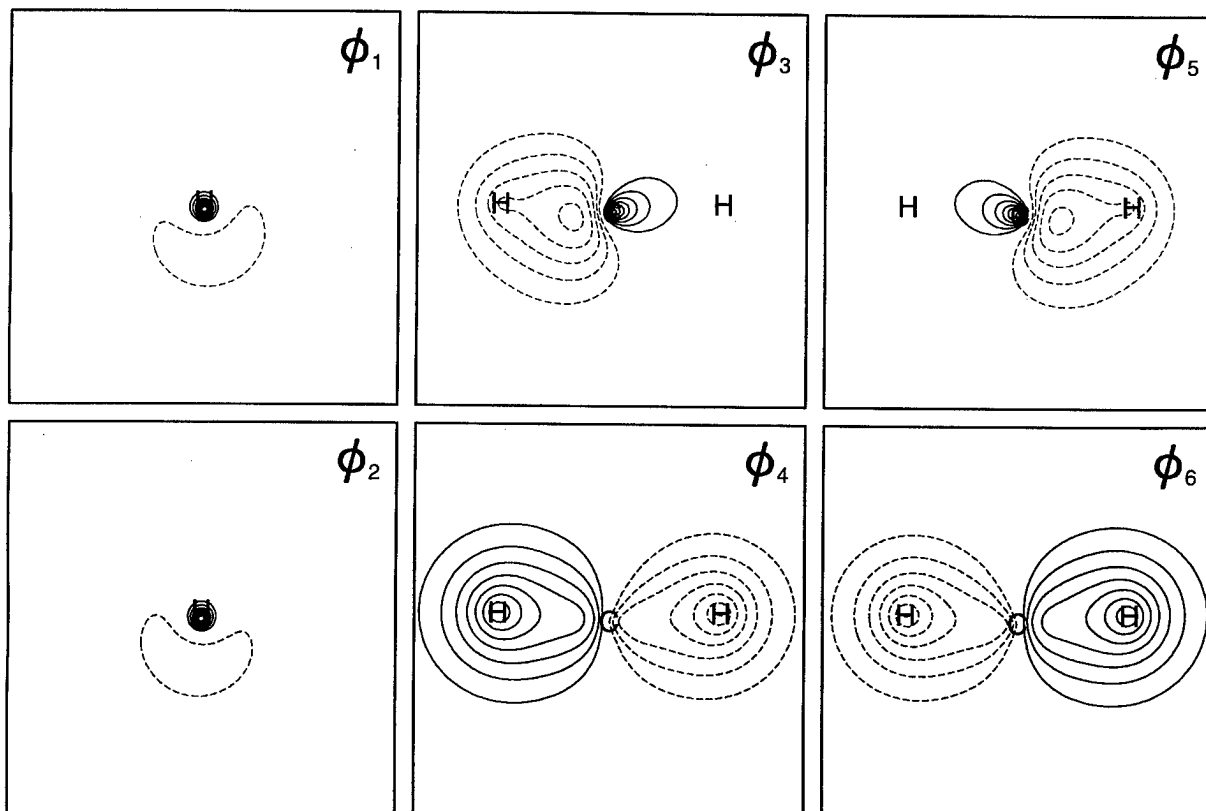


FIGURE 3. CASVB orbitals for singlet methylene: model 1a with $\phi_3 - \phi_6$ shown in the molecular plane and $\phi_1 - \phi_2$ in the perpendicular mirror plane.

TABLE VII
Overlap matrices for models 1a–1d, obtained by maximizing S_{VB} .

Solution 1a

	ϕ_1	ϕ_2	ϕ_3	ϕ_4	ϕ_5	ϕ_6
ϕ_1	1					
ϕ_2	0.997	1				
ϕ_3	0.641	0.641	1			
ϕ_4	0.057	0.057	0.771	1		
ϕ_5	0.641	0.641	-0.177	-0.698	1	
ϕ_6	0.057	0.057	-0.698	-0.990	0.771	1

Solution 1b

	ϕ_1	ϕ_2	ϕ_3	ϕ_4	ϕ_5	ϕ_6
ϕ_1	1					
ϕ_2	-0.646	1				
ϕ_3	0.132	0.132	1			
ϕ_4	0.053	0.053	0.791	1		
ϕ_5	0.132	0.132	0.601	0.248	1	
ϕ_6	0.053	0.053	0.248	-0.074	0.791	1

Solution 1c

	ϕ_1	ϕ_2	ϕ_3	ϕ_4	ϕ_5	ϕ_6
ϕ_1	1					
ϕ_2	0.004	1				
ϕ_3	0.221	0.221	1			
ϕ_4	0.092	0.092	0.792	1		
ϕ_5	0.221	0.221	0.600	0.249	1	
ϕ_6	0.092	0.092	0.249	-0.072	0.792	1

Solution 1d

	ϕ_1	ϕ_2	ϕ_3	ϕ_4	ϕ_5	ϕ_6
ϕ_1	1					
ϕ_2	0.897	1				
ϕ_3	0.243	-0.054	1			
ϕ_4	0.052	-0.036	0.785	1		
ϕ_5	0.243	-0.054	0.625	0.263	1	
ϕ_6	0.052	-0.036	0.263	-0.087	0.785	1

C—H bonds, and a very natural way of improving the solution 1a is therefore to add configurations in which the nonbonding orbitals become doubly occupied:

$$\Psi_{1b} = \mathcal{A}((1s)^2 \times \{c_1\phi_1\phi_2\phi_3\phi_4\phi_5\phi_6\Theta_{00}^6 + c_2(\phi_1\phi_1\phi_3\phi_4\phi_5\phi_6 + \phi_2\phi_2\phi_3\phi_4\phi_5\phi_6)\Theta_{00}^2\Theta_{00}^4\}), \quad (12)$$

This represents a significant improvement, such that the energy difference from the CASSCF is reduced to 16 millihartree, and the bond-forming orbitals (see Fig. 4) now conform to the description found for C—H bonds in a wide variety of sys-

tems. The spin-coupling coefficients also seem much more realistic (see Table VIII). We noticed that the ionic configurations are dominant in the 1b model and so we repeated the calculations leaving out the covalent part:

$$\Psi_{1c} = \mathcal{A}((1s)^2 \times (\phi_1\phi_1\phi_3\phi_4\phi_5\phi_6 + \phi_2\phi_2\phi_3\phi_4\phi_5\phi_6)\Theta_{00}^2\Theta_{00}^4), \quad (13)$$

The associated decrease in quality is not noticeable (see model 1c in Table VI and Fig. 5), so one must prefer this wave function on grounds of simplicity. Based on these various results, we conclude that excitations $\phi_1 \rightarrow \phi_2$ and $\phi_2 \rightarrow \phi_1$, relative to the \tilde{a}^1A_1 state, provide a very acceptable description of the electronic structure of the \tilde{c}^1A_1 state. Examining the full CASSCF CI vector transformed according to the orbitals of Eq. (13), we find that 98.7% of the CASSCF wave function is of the form shown in Eq. (13) (cf. Table VI) and that most of the 1.3% not accounted for (1.1%) is made up of configurations in which ϕ_1 and ϕ_2 are both doubly occupied.

Even within this active space, it is possible to improve slightly the description of the nonbonding electrons by incorporating a degree of radial correlation. Even if ϕ_1 and ϕ_2 are not related by symmetry, correct overall symmetry can be ensured by use of a projection operator [18]. Formally this is equivalent to a wave function of the form

$$\Psi_{1d} = \mathcal{A}((1s)^2 \times (\phi_1\phi_2\phi_3\phi_4\phi_5\phi_6 + (\hat{\sigma}_v\phi_1)(\hat{\sigma}_v\phi_2)\phi_3\phi_4\phi_5\phi_6)\Theta_{00}^2\Theta_{00}^4), \quad (14)$$

and the orbitals resulting from such a calculation (1d) are shown in Figure 6. Obtaining the description of the excited state by maximization of the overlap with the CASSCF wave function is not variational in the energy. The fact that the expectation value of the energy for model 1d is slightly lower than that from a CASSCF calculation for the same state and with the same active space must indicate some overlap of the VB wave function with the corresponding CASSCF solution for the lower state of this symmetry.

The nonbonding orbitals for the \tilde{c}^1A_1 state adopt far greater 2p character (Figs. 3–6) than do those for the lower \tilde{a}^1A_1 state [38–40], for which a dominant 2s component is observed. When the spin-coupled covalent configuration is excluded, as in 1c, the angle between the 2p-type orbitals approaches 90° (Fig. 5) and their overlap becomes

TABLE VIII
Weights $w_{pp} = (c_{pp})^2$ of the perfectly paired spin function, expressed as percentages of the total spin function in the Kotani or Serber bases.

Model	w_{pp}
1a	75.00
1b	100
1c	100
1d	99.67

small (Table VII). As a consequence, the bond-forming orbitals can adopt significantly greater s character, an observation which is consistent both with the increased bond angle (102.4° to 171.6°) as well as the diminished bond lengths relative to the $\tilde{\alpha}^1A_1$ state.

S_1 STATE OF BENZENE

The first excited singlet state (S_1) of benzene is the lowest one of ${}^1B_{2u}$ symmetry but, rather than simply symmetry adapting the wave function and

using the standard “ground-state” approaches, we decided to use this system as a further test of our “excited-state” procedures. Invoking σ/π separation, 6-in-6 CASSCF calculations were performed in D_{2h} symmetry using the same geometry and basis set as in a previous CASVB study [22] of the ${}^1A_{1g}$ ground state (S_0). Explicitly, the basis set is the same as used above for butadiene and methylene, except that the two d functions on carbon and the two p functions on hydrogen were replaced by functions with exponents $d_c = 0.8$ and $p_H = 1.0$. We number the carbon atoms consecutively around the ring. The CASSCF excitation energy of 4.96 eV compares rather well with the experimental value of 4.90 eV quoted in Ref. [7] and taken from Lassetre et al [43].

For our modern VB descriptions, we adopted a spin-coupled (SC) model of the form:

$$\Psi = \mathcal{A}(\Phi^{\text{core}} \times \phi_1 \phi_2 \phi_3 \phi_4 \phi_5 \phi_6 \Theta_{00}^6) \quad (15)$$

and started by maximizing S_{VB} for the S_1 state. This resulted in six p_π -like functions, each associated with a particular carbon atom and resembling

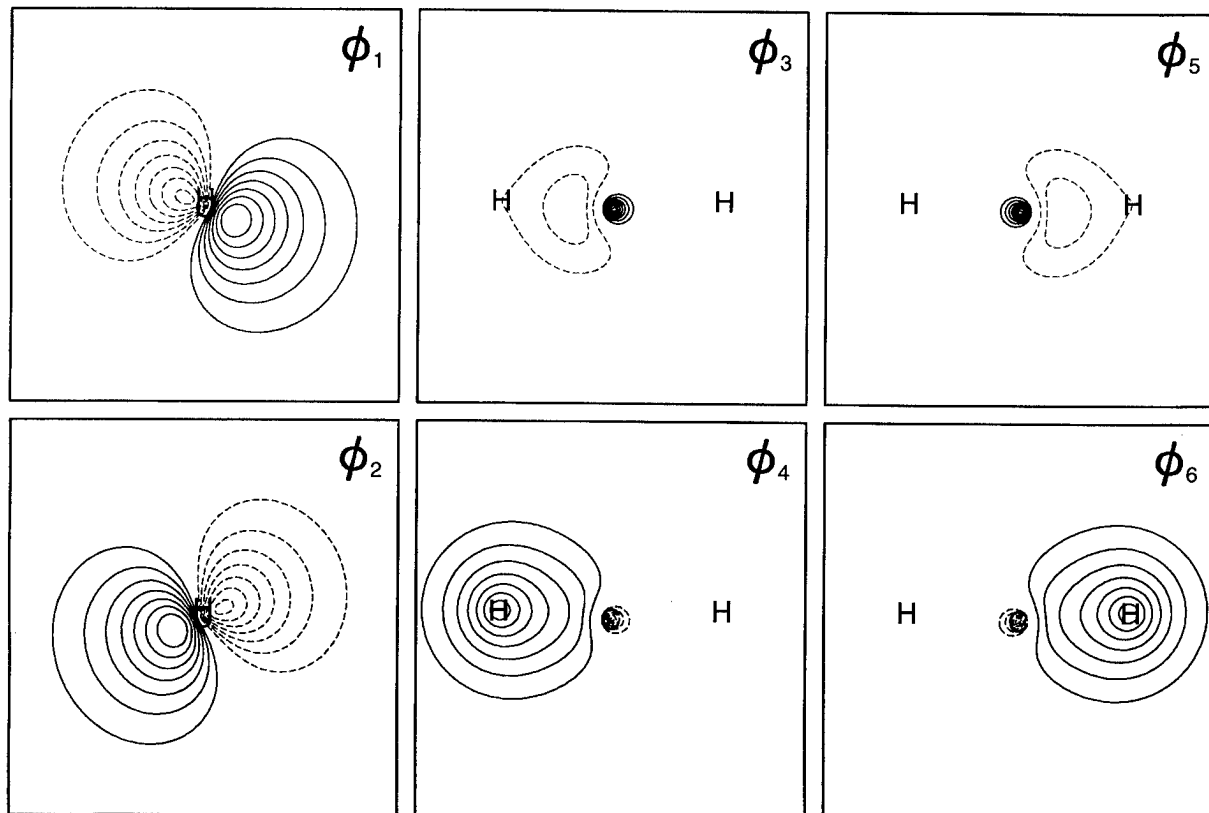


FIGURE 4. CASVB orbitals for singlet methylene: model 1b, plotted as in Figure 3.

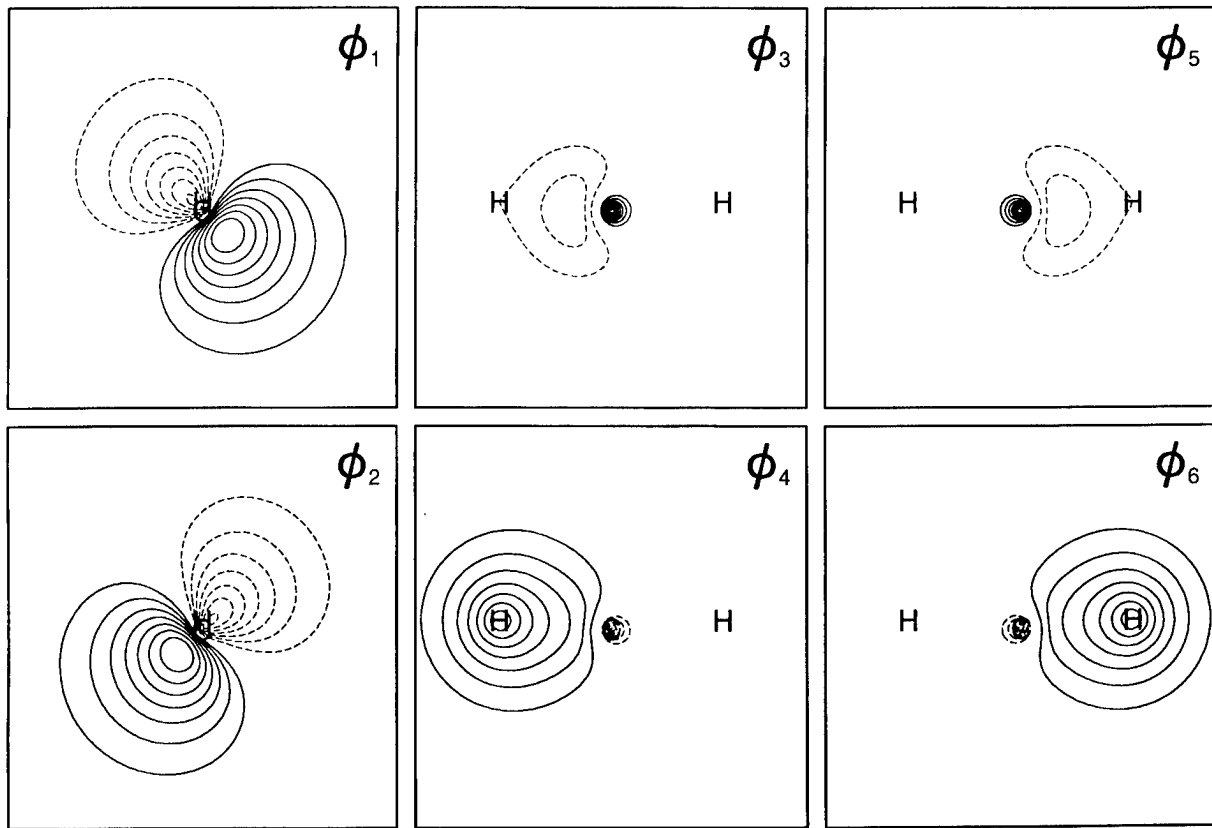


FIGURE 5. CASVB orbitals for singlet methylene: model 1c, plotted as in Figure 3.

fairly closely those from a fully variational treatment of the ground state [22]. However, as was also the case for the corresponding unconstrained $\max(S_{VB})$ representation of the S_0 CASSCF function [18], we observed some symmetry breaking. For all subsequent calculations, we constrained the orbitals ϕ_1 – ϕ_6 to be related to one another by successive \hat{C}_6 rotations, and it is convenient to number them according to the carbon atoms with which they are associated. Use of the overlap criterion to obtain a modern VB representation of the S_1 state then resulted in a very creditable $S_{VB} = 0.99874$ and a corresponding energy that is only ca. 2 millihartree inferior to that from the CASSCF calculation (see Table IX). This energy difference is reduced only very slightly on choosing instead to minimize E_{VB} , and the further change on performing a fully variational SC optimization is almost negligible. Plots of the orbitals from the three different procedures were exceedingly difficult to distinguish by eye, and so we present here only a symmetry-unique orbital from the fully variational SC calculation (see Fig. 7, which illustrates the

similarity to the corresponding picture for the ground state [22]). The various orbital overlaps (see Table IX) are larger than in the case of the ground state (cf. the earlier results for butadiene). Expressing the spin function in the traditional Rumer basis, we find, of course, that all three modern VB descriptions of the S_1 state correspond exactly to the out-of-phase combination of two Kekulé-like structures, as was anticipated in the extensive spin-coupled valence bond studies reported in Ref. [7].

Conclusions

The molecular excited states considered here may all, to a very good approximation, be rationalized in terms of single orbital excitations or a recoupling of the electron spins, relative to the ground-state descriptions. In general, of course, low-lying excited states are likely to be derived from first-order variations in the wave function parameters, but secondary effects may become very

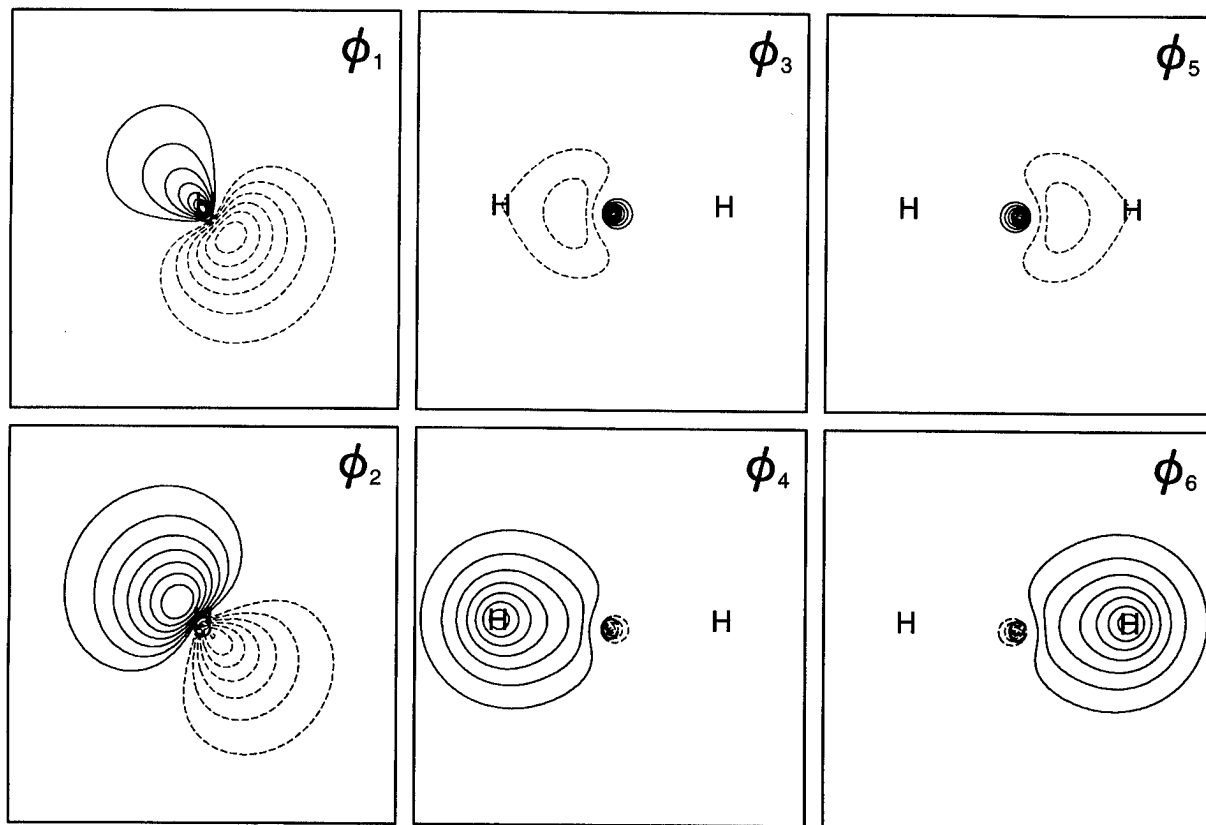


FIGURE 6. CASVB orbitals for singlet methylene: model 1d, plotted as in Figure 3.

important even for these cases. Such secondary effects include the relaxation of active and core orbital spaces, and possibly also induced changes in the geometry. An observation for both cases of spin recoupling considered here, *trans*-1,3-butadiene and benzene, was an associated significant expansion of the spin-coupled orbitals. Particularly for gaining an understanding of such secondary changes in electronic structure, it may be important to allow free optimization of orbitals

and structure coefficients in each excited state. An additional consideration in this context is the requirement of a *balanced* treatment of the various molecular states, for which separate optimization of each state would ultimately seem unavoidable.

It is useful to consider separately orbital excitations within the valence space and those going into the virtual orbital space, because the nature of the consequent valence bond descriptions will be somewhat different. Assuming that the ground-

TABLE IX
Energies and (where appropriate) orbital overlaps from calculations on benzene.

State	Calculation	E , hartree	$\langle \phi_1 \phi_2 \rangle$	$\langle \phi_1 \phi_3 \rangle$	$\langle \phi_1 \phi_4 \rangle$
S_0	6-in-6 CASSCF	-230.836822	—	—	—
S_0	Fully variational SC	-230.829332	0.5238	0.0294	-0.1570
S_1	6-in-6 CASSCF	-230.654383	—	—	—
S_1	Fully variational SC	-230.652205	0.5962	0.2893	0.2787
S_1	$\min(E_{VB})$	-230.652197	0.5961	0.2881	0.2768
S_1	$\max(S_{VB})$	-230.652162	0.5721	0.1705	0.0621

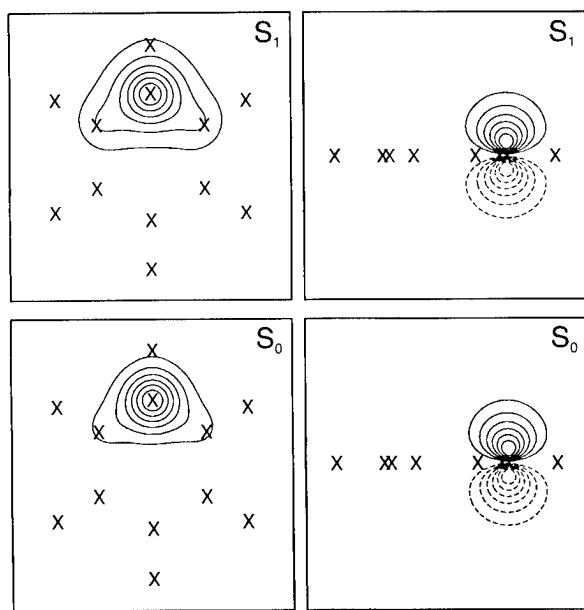


FIGURE 7. Contours of spin-coupled orbital for the S_1 and S_0 states of benzene, with projected positions of the nuclei marked \times . (Left) In the plane 1 bohr above the molecular plane. (Right) In a vertical mirror plane.

state VB picture is based on a spin-coupled wave function consisting of relatively well separated orbitals, a valence excitation will lead to a configuration with "ionic" character. As seen in the case of the \tilde{c}^1A_1 state of CH_2 , a standard spin-coupled covalent structure may then be unsuitable, and could lead to linear dependency problems. However, applying common sense in selecting the form of modern VB wave function is likely to resolve any such difficulties.

The need for a full optimization of states derived by excitations out of the valence space (including those leading to Rydberg states) may be less pronounced than for the valence excited states. In this context, a nonorthogonal CI treatment certainly has the unquestionable advantage of generating representations of a large number of states in one single step. However, the application of our CASVB methodology to such cases presents no formal difficulties and, since there are unlikely to be any problems associated with linear dependence, such optimizations may very well be significantly simpler than the corresponding optimizations for valence excited states. Early tests of our strategy involved reproducing a series of results for Rydberg-type excited states [12–14]. Although no significant difficulties were encountered, the

advantages of invoking a two-step procedure to converge onto particular states soon became clear.

We believe that the CASVB strategy offers a number of advantages for the modern VB description of excited states. In addition to the simultaneous optimization of VB orbitals and structure coefficients, the possibility of simple " $\max(S_{\text{VB}})$ " optimization for *any* given CASSCF solution is a major strength. The requirement for saddle-point optimization in the case of an energy-based optimization is a complication relative to this, but it is likely that our implementation of the TRIM algorithm [34] will deal with this in an efficient manner in most realistic cases. It is reassuring to see that the close harmony between corresponding overlap-based and energy-based results, previously found for ground-state calculations, also holds for applications to excited states.

Appendix: Second-Order Optimization of Excited States

We have had very positive experience with the restricted-step Newton-Raphson approach [26, 27] for the straightforward optimization of simple maxima or minima. Restricted step optimization of excited states is implemented in several MCSCF programs. It seemed reasonable, therefore, to look for a generalization of our ground state scheme to include excited-state optimization. The most natural such generalization, we believe, is the "trust-region image minimization" (TRIM) method developed by Helgaker [34] in the context of transition-state optimization. TRIM represents a further development of the "image function optimization" method proposed by Smith [44]. We review here the main features of the strategy, together with the particular considerations that we found to apply to excited-state optimizations.

It is convenient to transform the optimization problem (i.e., the Hessian matrix, gradient, and update vectors) to the basis of Hessian eigenvectors. The update, δ , can then be expressed as:

$$\delta_i = \frac{-g_i}{G_{ii} - \alpha}, \quad i = 1, \dots, n_{\text{neg}} \quad (16)$$

and

$$\delta_i = \frac{-g_i}{G_{ii} + \alpha}, \quad i = n_{\text{neg}} + 1, \dots, N_{\text{param}}, \quad (17)$$

in which g_i and G_{ii} are the gradient and Hessian elements, respectively, and n_{neg} signifies the number of Hessian negative eigenvalues required at convergence, as determined by the order of saddle point sought. Hessian eigenvalues are assumed to be in ascending order, and the parameter α is chosen larger than $\min(G_{n_{\text{neg}}, n_{\text{neg}}}, -G_{n_{\text{neg}}+1, n_{\text{neg}}+1}, 0)$. Comparing to the standard stabilized Newton-Raphson procedure, Eq. (9), one can see this as a maximization in the space of the first n_{neg} Hessian eigenvectors, equally weighted with minimization within the complementary space. The importance of using a modified Hessian that has the correct number of positive and negative eigenvalues has been pointed out also by other researchers [29]. As in our standard procedure, α is further optimized to achieve an update on, or within, the trust sphere:

$$\|\delta\| \leq h. \quad (18)$$

The trust sphere radius, h , is varied according to the quality of the second-order method, which may be gauged by the ratio r between the actual (Δf) and the predicted changes to the function f :

$$r = \frac{\Delta f}{\delta^T g + 1/2 \delta^T G \delta}. \quad (19)$$

We believe that a number of the important points in the simple stabilized Newton-Raphson procedure are preserved in this approach:

1. The first n_{neg} components of δ seek to maximize f , and the last $N_{\text{parm}} - n_{\text{neg}}$ to minimize f , on, or within, the trust sphere.
2. Close to convergence, the method reduces to the pure Newton-Raphson approach, as the constant α is set to zero.
3. For small updates, the method approaches a steepest ascent procedure in the first n_{neg} variables and steepest descent in the last $N_{\text{parm}} - n_{\text{neg}}$.

The main difference from the simple extremum optimization is that updates for which Δf has the "wrong sign" can no longer necessarily be rejected. The most straightforward way of overcoming this difficulty is to ensure a relatively strict adherence to trust sphere sizes for which the second-order model is valid. In particular, it seems likely that somewhat more "rejections" may be required. The following is an outline of the trust

sphere control scheme as used in our present program:

1. If $r < 0.25$ or $r > 4$, the update is rejected and h is reset to $0.5 \times h$.
2. If $0.75 < r < 1.33$, the update is accepted and h is reset to $2 \times h$.
3. For all other values of r , the update is accepted and h is reset to $1.2 \times h$.

Compared with our standard optimization procedure, this new approach may require more iterations to reach convergence (typically just 1 or 2), but in none of the cases studied so far have the convergence characteristics been severely affected.

ACKNOWLEDGMENTS

This project has received financial support from the EEC under the TMR program (contract ERBFMRXCT960088). One of us (T.T.) gratefully acknowledges the Danish Natural Science Research Council for financial support.

References

1. B. O. Roos, K. Andersson, and M. P. Fülscher, Chem. Phys. Lett. **192**, 5 (1992).
2. M. P. Fülscher, K. Andersson, and B. O. Roos, J. Phys. Chem. **96**, 9204 (1992).
3. L. Serrano-Andrés, M. Merchán, I. Nebot-Gil, R. Lindh, and B. O. Roos, J. Chem. Phys. **98**, 3151 (1993).
4. D. L. Cooper, J. Gerratt, and M. Raimondi, Chem. Rev. **91**, 929 (1991).
5. J. Gerratt and M. Raimondi, Proc. R. Soc. Lond. Ser. A **371**, 525 (1980).
6. J. Gerratt, Adv. Atom. Mol. Phys. **7**, 141 (1971).
7. E. C. da Silva, J. Gerratt, D. L. Cooper, and M. Raimondi, J. Chem. Phys. **101**, 3866 (1994).
8. M. Raimondi, M. Sironi, J. Gerratt, and D. L. Cooper, Int. J. Quant. Chem. **60**, 225 (1996).
9. N. J. Clarke, M. Raimondi, M. Sironi, J. Gerratt, and D. L. Cooper, Theor. Chem. Acc. **99**, 8 (1998).
10. D. L. Cooper, J. Gerratt, M. Raimondi, M. Sironi, and T. Thorsteinsson, Theor. Chim. Acta **85**, 261 (1993).
11. P. B. Karadakov, J. Gerratt, M. Raimondi, and D. L. Cooper, J. Chem. Phys. **97**, 7637 (1992).
12. G. D. Fletcher, G. Doggett, and A. S. Howard, Phys. Rev. A **46**, 5459 (1992).
13. G. Doggett, G. D. Fletcher, and F. R. Manby, J. Mol. Struc. **300**, 191 (1993).
14. F. R. Manby, G. Doggett, and G. D. Fletcher, J. Mol. Struc. **343**, 63 (1995).

15. T. Thorsteinsson, *Development of Methods in Spin-Coupled Theory*, Ph.D. Thesis, University of Liverpool, UK (1995).
16. T. Thorsteinsson, D. L. Cooper, J. Gerratt, P. B. Karadakov, and M. Raimondi, *Theor. Chim. Acta* **93**, 343 (1996).
17. T. Thorsteinsson and D. L. Cooper, *Theor. Chim. Acta* **94**, 233 (1996).
18. T. Thorsteinsson, D. L. Cooper, J. Gerratt, and M. Raimondi, *Theor. Chim. Acta* **95**, 131 (1997).
19. T. Thorsteinsson, D. L. Cooper, J. Gerratt, and M. Raimondi, in *Quantum Systems, in Chemistry and Physics: Trends in Methods and Applications*, R. McWeeny, J. Maruani, Y. G. Smeyers, and S. Wilson, eds. (Kluwer, Dordrecht, 1997).
20. T. Thorsteinsson and D. L. Cooper, *J. Math. Chem.* **23**, 105 (1998).
21. D. L. Cooper, T. Thorsteinsson, and J. Gerratt, *Adv. Quant. Chem.*, to appear.
22. D. L. Cooper, T. Thorsteinsson, and J. Gerratt, *Int. J. Quant. Chem.* **65**, 439 (1997).
23. MOLPRO is a package of ab initio programs written by H.-J. Werner and P. J. Knowles, with contributions from R. D. Amos, A. Berning, D. L. Cooper, M. J. O. Deegan, A. J. Dobbyn, F. Eckert, C. Hampel, T. Leininger, R. Lindh, A. W. Lloyd, W. Meyer, M. E. Mura, A. Nicklaß, P. Palmieri, K. Peterson, R. Pitzer, P. Pulay, G. Rauhut, M. Schütz, H. Stoll, A. J. Stone, and T. Thorsteinsson.
24. H.-J. Werner and P. J. Knowles, *J. Chem. Phys.* **82**, 5053 (1985); P. J. Knowles and H.-J. Werner, *Chem. Phys. Lett.* **115**, 259 (1985).
25. P. Å. Malmqvist, *Int. J. Quant. Chem.* **30**, 479 (1986).
26. S. M. Goldfeld, R. E. Quant, and H. F. Trotter, *Econometrica* **34**, 541 (1966).
27. R. Fletcher, *Practical Methods of Optimization*, 2nd ed. (Wiley, New York, 1987).
28. P. Å. Malmqvist and B. O. Roos, *Chem. Phys. Lett.* **155**, 189 (1989).
29. J. Olsen, D. L. Yeager, and P. Jørgensen, *Adv. Chem. Phys.* **54**, 1 (1983).
30. J. T. Golab, D. L. Yeager and P. Jørgensen, *Chem. Phys.* **78**, 175 (1983).
31. T. Helgaker, in *Lecture Notes in Quantum Chemistry 58: European Summer School in Quantum Chemistry*, B. O. Roos, ed. (Springer, 1992).
32. B. H. Lengsfeld III, *J. Chem. Phys.* **73**, 382 (1980).
33. H. J. Aa. Jensen and P. Jørgensen, *J. Chem. Phys.* **80**, 1204 (1984).
34. T. Helgaker, *Chem. Phys. Lett.* **182**, 503 (1991).
35. J. T. Golab, D. L. Yeager, and P. Jørgensen, *Chem. Phys.* **93**, 83 (1985).
36. W. Haugen and M. Traetteberg, *Acta Chem. Scand.* **20**, 1726 (1966).
37. T. H. Dunning, Jr., *J. Chem. Phys.* **90**, 1007 (1989).
38. M. Sironi, M. Raimondi, D. L. Cooper, and J. Gerratt, *J. Chem. Soc. Faraday Trans. 2* **83**, 1651 (1987).
39. S. C. Wright, D. L. Cooper, M. Sironi, M. Raimondi, and J. Gerratt, *J. Chem. Soc. Perkin Trans. 2*, 369 (1990).
40. M. Sironi, D. L. Cooper, J. Gerratt, and M. Raimondi, *J. Am. Chem. Soc.* **112**, 5054 (1990).
41. Y. Yamaguchi, C. D. Sherrill, and H. F. Schaefer III, *J. Phys. Chem.* **100**, 7911 (1996).
42. C. W. Bauschlicher and P. R. Taylor, *J. Chem. Phys.* **85**, 6510 (1986).
43. E. N. Lassetre, A. Skerbele, M. A. Dillon, and K. J. Ross, *J. Chem. Phys.* **48**, 5066 (1968).
44. C. M. Smith, *Theor. Chim. Acta* **74**, 85 (1988); C. M. Smith, *Int. J. Quant. Chem.* **37**, 773 (1990).

Approximate Brueckner Orbitals and Shakeup Operators in Electron Propagator Calculations: Applications to F⁻ and OH⁻

J. V. ORTIZ

Department of Chemistry, Kansas State University, Manhattan, Kansas 66506-3701

Received 22 March 1998; revised 31 March 1998; accepted 6 April 1998

ABSTRACT: Vertical electron detachment energies of F⁻ and OH⁻ have presented difficulties for perturbative electron propagator methods. A recently derived, nondiagonal, renormalized approximation and two additional improvements are studied here. These improvements are replacement of the Hartree-Fock reference determinant by a determinant of approximate Brueckner orbitals generated by a coupled-cluster doubles calculation and retention of correlation terms in the 2hp-2hp block of the superoperator Hamiltonian matrix. Agreement with experiment is significantly better with these methods. When Hartree-Fock orbitals are used, electron detachment energies are underestimated, but approximate Brueckner orbitals lead to overestimates. © 1998 John Wiley & Sons, Inc. Int J Quant Chem 70: 651–658, 1998

Key words: electron propagator; propagator theory; Brueckner orbitals; anions

Introduction

Electron propagator theory [1–8] is a versatile vehicle for the study of unusual molecular anions. Electron detachment energies of carbon cluster anions [9–13], dianions [14, 15]; and quad-

ranions [16] have been calculated with propagator methods. Multiply charged, anionic complexes of transition metals that are stable in the gas phase have been identified with the aid of electron propagator techniques [17]. Double Rydberg anions [18] and bound, excited states of organic anions [19] have been studied as well.

Several perturbative, electron propagator approximations [20, 21] have been subjected to systematic tests of accuracy in the calculation of vertical electron detachment energies of small, closed-shell anions [22]. Average, absolute errors are ap-

Contract grant sponsor: National Science Foundation.

Contract grant number: CHE-9321434.

Contract grant sponsor: Petroleum Research Fund.

Contract grant number: 29848-AC6.

Contract grant sponsor: Gaussian Inc.

proximately equal to 0.2 eV for the partial third-order (P3) approximation [23], a method that is easily applied to larger anions.

Two anions, however, continue to challenge perturbative approaches. Calculations on F^- and OH^- with a variety of low-order and renormalized methods consistently produce vertical electron detachment energies that are in serious disagreement with accurate experiments [22]. Some of these results are summarized in Tables I and II for Koopmans's theorem, as well as for second-order, third-order [24], outer valence Green's function [8], and P3 [23] diagonal self-energy approximations. These difficulties are not due to basis sets, for additional improvements are likely to favor the anionic reference state over the neutral final state, leading to larger errors. While the P3 method performs better than its predecessors of equal or greater computational difficulty, its errors are still unacceptable large: approximately 0.7 eV for F^- and OH^- with a triple ζ basis augmented with diffuse and polarization functions. Nondiagonal, renormalized self-energy approximations based on perturbative improvements to reference state density matrices, such as 3 + [10, 20], do not fare much better. The inability of currently implemented methods to describe F^- and OH^- impedes study of the many anion-molecule clusters and metal-ligand complexes where these anions occur. More powerful techniques therefore must be considered.

Two improvements on a nondiagonal, renormalized method that has appeared recently [25] are considered here. The first is employment of

TABLE I
 F^- electron detachment energies (eV).

Basis	KT	2	3	OVGF	P3	3 +	Expt.
6-311 + G(2df)	4.83	1.23	5.69	4.39	3.72	4.34	
aug-cc-p VDZ	4.93	1.03	6.61	5.05	3.79	4.84	
aug-cc-p VTZ	4.92	1.21	6.75	5.00	4.15	4.78	3.40

operator manifolds based on approximate Brueckner orbitals [26] instead of Hartree-Fock orbitals. For cases where ground-state correlation is qualitatively important, such as anions, radicals or transition-metal complexes, this option may be generally useful. The second concerns treatment of superoperator matrix elements between shakeup operators. (These operators annihilate two electrons in a reference determinant while creating an electron in a virtual spin-orbital.) This improvement is coupled to the first, for rotations between occupied and virtual orbitals may require equivalent treatment of simple annihilation operators and shakeup operators.

After a review of previously derived methods, the present modifications are defined in a common notation. Test calculations on these two improvements are performed independently and in combination. The best basis set of the previous study on anions [22] is used initially so that comparisons between new and old methods may be made. Basis saturation is demonstrated by additional augmentations. Conclusions on the utility of Brueckner orbitals and higher order treatments of shakeup operators are reached.

Theory

PHYSICAL INTERPRETATION

In its spectral form, the r, s element of the electron propagator matrix is

$$\begin{aligned}
 G_{rs}(E) &= \langle\langle a_r^\dagger; a_s \rangle\rangle \\
 &= \lim_{\eta \rightarrow 0} \left\{ \sum_n \frac{\langle N|a_r^\dagger|N-1, n\rangle\langle N-1, n|a_s|N\rangle}{E + E_n(N-1) - E_0(N) - i\eta} \right. \\
 &\quad \left. + \sum_m \frac{\langle N|a_s|N+1, m\rangle\langle N+1, m|a_r^\dagger|N\rangle}{E - E_m(N+1) + E_0(N) + i\eta} \right\}. \tag{1}
 \end{aligned}$$

TABLE II
 OH^- electron detachment energies (eV).

Basis	KT	2	3	OVGF	P3	3 +	Expt.
6-311 + + G(2df,2pd)	2.88	-0.01	3.59	2.38	2.12	2.45	
aug-cc-p VDZ	2.95	-0.17	4.22	2.86	2.11	2.84	
aug-cc-p VTZ	2.97	-0.02	4.43	2.86	2.48	2.82	1.83

The propagator matrix is energy-dependent; poles occur when E equals a electron detachment energy, $E_0(N) - E_n(N - 1)$, or an electron attachment energy, $-E_0(N) + E_m(N + 1)$. Corresponding residues, such as $\langle N|a_r^\dagger|N - 1, n\rangle\langle N - 1, n|a_s|N\rangle$ or $\langle N|a_s|N + 1, m\rangle\langle N + 1, m|a_r^\dagger|N\rangle$, are related to the Feynman–Dyson amplitudes (FDAs), where

$$U_{r,n} = \langle N - 1, n|a_r|N\rangle \quad (2)$$

or

$$U_{r,n} = \langle N + 1, n|a_r^\dagger|N\rangle. \quad (3)$$

FDAs suffice for constructing Dyson orbitals (DOs) for electron detachments and attachments, where

$$\phi_n^{\text{Dyson}}(x) = \sum_r \phi_r(x) U_{r,n}. \quad (4)$$

In the former case, the DO is related to initial and final-state wave functions via

$$\begin{aligned} \phi_n^{\text{Dyson}}(x_1) &= \int \Psi_N(x_1, x_2, x_3, \dots, x_N) \\ &\quad \times \Psi_{N-1,n}^*(x_2, x_3, x_4, \dots, x_N) dx_2 dx_3 \\ &\quad \times dx_4 \cdots dx_N, \end{aligned} \quad (5)$$

while for the latter case,

$$\begin{aligned} \phi_n^{\text{Dyson}}(x_1) &= \int \Psi_N^*(x_2, x_3, x_4, \dots, x_{N+1}) \\ &\quad \times \Psi_{N+1,n}(x_1, x_2, x_3, \dots, x_{N+1}) \\ &\quad \times dx_2 dx_3 dx_4 \cdots dx_{N+1}. \end{aligned} \quad (6)$$

The pole strength, P_n , for final state n is given by

$$P_n = \int |\phi_n^{\text{Dyson}}(x_1)|^2 dx_1. \quad (7)$$

DIAGONAL APPROXIMATIONS

Approximate electron propagator methods are often classified by their treatment of the self-energy matrix that occurs in the Dyson equation. A computationally convenient form of this equation is

$$\mathbf{G}^{-1}(E) = \mathbf{G}_0^{-1}(E) - \Sigma(E). \quad (8)$$

The inverse of the zeroth-order, propagator matrix that recovers the Koopmans approximation for electron binding energies has a simple form in the canonical orbital basis,

$$[\mathbf{G}_0^{-1}(E)]_{rs} = (E - \epsilon_r)\delta_{rs}, \quad (9)$$

where ϵ_r is the r th orbital energy. Relaxation and correlation corrections reside in the self-energy matrix, $\Sigma(E)$. Poles of the propagator matrix are values of E that satisfy

$$\det\{\mathbf{G}^{-1}(E)\} = 0. \quad (10)$$

This requirement is satisfied by searching for E such that $\mathbf{G}^{-1}(E)$ has a zero eigenvalue. The accompanying eigenvectors provide the Feynman–Dyson amplitudes. For valence electron detachment energies, these eigenvectors are usually close to unit vectors. Correlation corrections to these electron binding energies are found chiefly in diagonal elements of $\Sigma(E)$.

Diagonal approximations in the self-energy matrix therefore have been employed widely. Here, one needs only search for E such that

$$E = \epsilon_p + \Sigma_{pp}(E). \quad (11)$$

Three iterations generally suffice for convergence to 10^{-5} a.u. when a Newton procedure is used. Diagonal approximations also generate a simple picture of electron detachment where electrons assigned to unperturbed canonical orbitals are subject to a relaxation–correlation potential represented by the diagonal elements of $\Sigma(E)$.

Diagonal and nondiagonal expressions for $\Sigma(E)$ in second and third order of the fluctuation potential have been characterized in detail [24]. Second-order results generally overestimate corrections to the canonical orbital energy for valence ionization energies of molecules, and third-order results display the opposite trend. Several recipes for scaling third-order terms depend on ratios of second-order and third-order self-energy diagrams; they have been used widely in the diagonal approximation. These three procedures are known collectively as the outer valence Green's function (OVGF) and numerical criteria for choosing the best result have been prepared [8,27].

The recently derived P3 self-energy [23] possesses several advantages of efficiency and accuracy over its predecessors. It produced an average absolute error of less than 0.2 eV in calculations on the ionization energies of typical, closed-shell molecules. This method eliminated contractions with OV^4 dependence on the number of occupied (O) and virtual (V) orbitals that are the arithmetic bottlenecks in third-order (and therefore OVGF) calculations. P3's most difficult steps scale as O^2V^3 . Calculations on the electron binding ener-

gies of closed-shell molecules with over 300 basis functions are now routine on relatively modest workstations [28–30].

NONDIAGONAL, RENORMALIZED APPROXIMATIONS

There are inherent limitations in diagonal approximations. Dyson orbitals must remain equal to canonical orbitals, and final states with major relaxation effects therefore may be poorly described. Diagonal approximations are inappropriate for states with small pole strengths, such as those occurring in inner-valence photoelectron spectra [31].

Nondiagonal approximations with infinite order corrections, or renormalizations, can be expressed succinctly in terms of the superoperator Hamiltonian matrix. The propagator matrix may be written as

$$\mathbf{G}(E) = [\mathbf{1} \quad \mathbf{0}] \begin{bmatrix} E\mathbf{1} - (\mathbf{a} | \hat{H}\mathbf{a}) & -(\mathbf{a} | \hat{H}\mathbf{f}) \\ -(\mathbf{f} | \hat{H}\mathbf{a}) & E\mathbf{1} - (\mathbf{f} | \hat{H}\mathbf{f}) \end{bmatrix}^{-1} \times \begin{bmatrix} 1 \\ 0 \end{bmatrix}, \quad (12)$$

where the primary operator space of simple field operators, \mathbf{a} , is partitioned from the orthogonal, secondary space of product field operators, \mathbf{f} . In this notation [32],

$$(\mu | \nu) = \langle N | [\mu^\dagger, \nu]_+ | N \rangle, \quad (13)$$

and elements of the superoperator Hamiltonian matrix are given by

$$(\mu | \hat{H}\nu) = \langle N | [\mu^\dagger, [\nu, H]]_+ | N \rangle. \quad (14)$$

Poles and FDAs thus correspond to eigenvalues and to primary space eigenvector components, respectively, of the superoperator Hamiltonian matrix.

Each of the blocks of $\hat{\mathbf{H}}$ may be evaluated in various orders of the fluctuation potential. For example, the primary operator block evaluated through order n has constituents in each order according to

$$(\mathbf{a} | \hat{H}\mathbf{a})^{(n)} = (\mathbf{a} | \hat{H}\mathbf{a})_0 + (\mathbf{a} | \hat{H}\mathbf{a})_1 + (\mathbf{a} | \hat{H}\mathbf{a})_2 + (\mathbf{a} | \hat{H}\mathbf{a})_3 + \dots + (\mathbf{a} | \hat{H}\mathbf{a})_n. \quad (15)$$

For this block, the first- and second-order terms vanish for closed-shell reference states; \mathbf{f}_3 is the vector of two-particle, one-hole and two-hole,

one-particle ($2ph$ and $2hp$, respectively) operators defined with respect to a reference configuration. For the $(\mathbf{a} | \hat{H}\mathbf{f}_3)$ and $(\mathbf{f}_3 | \hat{H}\mathbf{a})$ blocks, only the zeroth-order term vanishes, while the $(\mathbf{f}_3 | \hat{H}\mathbf{f}_3)$ block has nonzero contributions in all orders.

Several approximate propagators can be defined in terms of superoperator Hamiltonian matrix elements. For example, poles corresponding to the nondiagonal, second-order self-energy approximation are recovered by setting

$$\hat{\mathbf{H}} = \begin{bmatrix} (\mathbf{a} | \hat{H}\mathbf{a})^{(0)} & (\mathbf{a} | \hat{H}\mathbf{f}_3)^{(1)} \\ (\mathbf{f}_3 | \hat{H}\mathbf{a})^{(1)} & (\mathbf{f}_3 | \hat{H}\mathbf{f}_3)^{(0)} \end{bmatrix}. \quad (16)$$

The minimal choice needed to recover all third-order terms in the self-energy is

$$\hat{\mathbf{H}} = \begin{bmatrix} (\mathbf{a} | \hat{H}\mathbf{a})^{(3)} & (\mathbf{a} | \hat{H}\mathbf{f}_3)^{(2)} \\ (\mathbf{f}_3 | \hat{H}\mathbf{a})^{(2)} & (\mathbf{f}_3 | \hat{H}\mathbf{f}_3)^{(1)} \end{bmatrix}. \quad (17)$$

The latter approximation also generates other terms in all orders and is henceforth denoted by 3+ [10, 20]. Self-consistent treatments of the $(\mathbf{a} | \hat{H}\mathbf{a})$ block may provide further refinements. Procedures of this kind are employed in the extended $2ph$ Tamm-Dancoff approximation (TDA), or third order algebraic diagrammatic construction (ADC)(3), methods [8, 20].

A recently developed, nondiagonal, renormalized method (NR2) may be explained in similar terms by separating the p and h subsets of \mathbf{a} and the $2hp$ and $2ph$ subsets of \mathbf{f}_3 . Diagonalization of the NR2 superoperator Hamiltonian matrix, defined by

$$\hat{\mathbf{H}} = \begin{bmatrix} \hat{\mathbf{H}}_{h,h}^{(0)} & \hat{\mathbf{H}}_{h,p}^{(0)} & \hat{\mathbf{H}}_{h,2hp}^{(1)} & \hat{\mathbf{H}}_{h,2ph}^{(1)} \\ \hat{\mathbf{H}}_{p,h}^{(0)} & \hat{\mathbf{H}}_{p,p}^{(0)} & \hat{\mathbf{H}}_{p,2hp}^{(1)} & \hat{\mathbf{H}}_{p,2ph}^{(1)} \\ \hat{\mathbf{H}}_{2hp,h}^{(2)} & \hat{\mathbf{H}}_{2hp,p}^{(1)} & \hat{\mathbf{H}}_{2hp,2hp}^{(1)} & \hat{\mathbf{H}}_{2hp,2ph}^{(0)} \\ \hat{\mathbf{H}}_{2ph,h}^{(1)} & \hat{\mathbf{H}}_{2ph,p}^{(1)} & \hat{\mathbf{H}}_{2ph,2hp}^{(0)} & \hat{\mathbf{H}}_{2ph,2ph}^{(0)} \end{bmatrix}, \quad (18)$$

is equivalent to solving the Dyson equation with a nondiagonal, renormalized self-energy that is complete in second order, but not third order, in the fluctuation potential. All terms present in the P3 approximation are recovered in the NR2 method.

To take advantage of programs used for traditional configuration interaction calculations, eigenvalues of the symmetrized matrices, $\frac{1}{2}(\hat{\mathbf{H}} + \hat{\mathbf{H}}^\dagger)$,

are computed. Errors in the self-energy matrix introduced by this procedure occur initially in fourth order.

IMPROVED REFERENCE STATES AND OPERATORS

Two extensions of the NR2 approximation are considered here. This method may not be properly balanced in its treatment of final states with appreciable shakeup ($2hp$) character. It retains terms through second order in the $\hat{H}_{h,2hp}$ and $\hat{H}_{h,h}$ blocks, but only first-order terms in the $\hat{H}_{2hp,2hp}$ block are kept. (In the canonical orbital basis, first- and second-order terms in the $\hat{H}_{h,h}$ block vanish.) Therefore, second-order terms in the $\hat{H}_{2hp,2hp}$ block are added to restore balance to the treatment of h and $2hp$ operators.

A second extension of the NR2 method considers replacement of canonical orbitals by approximate Brueckner orbitals. Exact Brueckner orbitals form a reference determinant such that single excitation coefficients vanish in the full configuration interaction wave function [26]. Approximate Brueckner orbitals may be obtained from limited configuration interaction wave functions by requiring single excitation coefficients to be zero [33]. Coupled-cluster wave functions may employ a reference determinant, $|\text{Brueckner}\rangle$, defined in a similar manner [34]. In the so-called Brueckner doubles (BD) [35] approximation,

$$|\text{BD}\rangle = e^{T_2} |\text{Brueckner}\rangle, \quad (19)$$

where orbitals and double replacement coefficients occurring in T_2 are simultaneously optimized. In this study, the double replacement coefficients, t , of

$$T_2 = \sum_{ij}^{\text{occ}} \sum_{ab}^{\text{vir}} t_{ij}^{ab} a_a^\dagger a_b^\dagger a_i a_j \quad (20)$$

replace their counterparts from the first-order wave function of many-body perturbation theory [36]. Superoperator matrix elements are evaluated with the following metric:

$$\langle \mu | \nu \rangle = \langle \text{Brueckner} | [\mu^\dagger, \nu]_+ e^{T_2} | \text{Brueckner} \rangle. \quad (21)$$

This choice produces nonhermitian superoperator matrices and is motivated by the following considerations. Employment of this metric in combination with a complete operator manifold (\mathbf{u}) for the

propagator final states has implications for ground-state properties. Insertion of a propagator defined thus in the contour integral expression for total energies [37],

$$\langle N | H | N \rangle = \text{Tr} \frac{1}{4\pi i} \int_C \{ \mathbf{h}^{(1)} + E \mathbf{1} \} \mathbf{G}(E) dE, \quad (22)$$

where $\mathbf{h}^{(1)}$ is the matrix of the one-electron part of the Hamiltonian and C encloses only the ionization energy poles, yields the BD ground-state energy. Specification of a well-defined reference state total energy is useful in the evaluation of final state energies and properties [9, 38]. The choice of Eq. (21) forces only one major modification in programs written for canonical orbitals. In the Brueckner orbital basis, elements of the $\hat{H}_{h,p}$ block of the superoperator Hamiltonian matrix no longer vanish. The $\hat{H}_{h,h}$ and $\hat{H}_{p,p}$ blocks may be diagonalized without altering the BD ansatz.

Computational Methods

Calculations were performed with augmented, correlation-consistent basis sets and the 6-311++G(2df,2pd) [39] basis. These sets contain many polarization and diffuse functions [40]. Because of the inability of current propagator-based programs to accept integrals over g functions, these contributions have been omitted from the aug-cc-pVQZ basis. For the sake of balance, f functions on hydrogen have been omitted as well. The resultant (6s,5p,4d,3f/5s,4p,3d) basis is subsequently supplemented by additional diffuse functions whose exponents are obtained by multiplying the previously smallest exponent of each angular momentum type by 0.3. This (7s,6p,5d,4f/6s,5p,4d) basis is the largest used here.

The OH bond length is 0.98 Å; 1s orbitals on F and O are omitted from propagator calculations. Calculations are performed with modified versions of Gaussian 95 [41].

Results and Discussion

Tables I and II demonstrate the difficulties encountered by previously derived methods in describing the vertical electron detachment energies of F^- and OH^- . Errors with respect to experiment [42] obtained with Koopmans's theorem (KT) are between 1 and 2 eV and are not unusual for

closed-shell molecules and anions. In the columns labeled 2, 3, OVGF, and P3, results of diagonal approximations are listed. Corrections to canonical orbital energies are overestimated with the second-order self-energy and have the wrong sign when the third-order self-energy is used. OVGF predictions, as usual, lie between these two extremes, but still exhibit major discrepancies with experiment. The P3 self-energy produces the best results in the diagonal approximation, for the errors with the aug-cc-pVTZ basis are less than 1 eV. The nondiagonal 3+ self-energy contains all third-order terms and many higher order terms; it is therefore considered a generalization of the third-order and OVGF diagonal approximations. Agreement between 3+ and OVGF results is often observed and differences between these two approximations are less than 0.22 eV in Tables I and II. Unfortunately, 3+ results remain in serious disagreement with experiment. Additional improvements in basis sets are unlikely to provide a remedy for the failures of these approximate self-energies, for all results, with the exception of second order, are too large. Second-order errors in the limit of basis set saturation are likely to exceed 1 eV.

Results that employ four alternative approximations are shown in Tables III and IV. The first, a nondiagonal, renormalized generalization of the P3 self-energy, is the previously derived NR2 method [25]. The original form of NR2 used Hartree-Fock orbitals and reference states. Here, this method is labeled NR2-HF. Substitution of approximate Brueckner orbitals in this treatment of the superoperator Hamiltonian matrix defines the NR2-BD method. Retention of second-order terms in the $\hat{H}_{2hp,2hp}$ block of the superoperator Hamiltonian matrix may be called a second-order description of shakeup states and is therefore labeled SH2. This choice can be made with Hartree-Fock or approximate Brueckner orbitals, thus leading to the SH2-HF and SH2-BD columns of Tables III and IV.

TABLE III
F⁻ electron detachment energies (eV).

Basis	NR2-HF	NR2-BD	SH2-HF	SH2-BD	Expt.
aug-cc-p VTZ	2.99	3.55	3.02	3.60	
6s,5p,4d,3f	3.16	3.55	3.16	3.61	
7s,6p,5d,4f	3.12	3.56	3.16	3.62	3.40

TABLE IV
OH⁻ electron detachment energies (eV).

Basis	NR2-HF	NR2-BD	SH2-HF	SH2-BD	Expt.
aug-cc-p VTZ	1.54	1.85	1.58	1.92	
6s,5p,4d,3f/5s,4p,3d	1.60	1.85	1.64	1.94	
7s,6p,5d,4f/6s,5p,4d	1.61	1.89	1.65	1.97	1.83

Comparison of NR2-HF and P3 results with the aug-cc-pVTZ basis reveals major discrepancies. For ionization energies of closed-shell molecules, the two methods are usually in close agreement [25]. NR2-HF, unlike P3, underestimates both vertical electron detachment energies. As additional basis functions are added, the predictions of this column rise by less than 0.15 eV. Pole strengths are approximately 0.9 for all three basis sets and contributions from canonical, virtual orbitals to the Dyson orbitals are negligible. It is therefore likely that the source of NR2-HF's superiority is the renormalization that derives from the nondiagonal, first-order $\hat{H}_{2hp,2hp}$ block of the superoperator Hamiltonian matrix.

When second-order terms in this block are added, the SH2-HF model results. Some modest improvements are realized. Basis set augmentations beyond 7s,6p,5d,4f/6s,5p,4d will lead to slightly better agreement with experiment. The behavior of pole strengths and Dyson orbitals is similar to the NR2-HF results. Because generation of second-order $\hat{H}_{2hp,2hp}$ terms is not computationally difficult, this approximation may be useful for other anions. Remaining errors are near 0.2 eV.

The NR2 method also may be improved by replacement of Hartree-Fock orbitals by approximate Brueckner orbitals. Substantial improvements over the NR2-HF method are displayed in the NR2-BD columns. Pole strengths are 0.89 for F⁻ and 0.88 for OH⁻. One orbital in the Brueckner determinant dominates the normalized Dyson orbital with a coefficient in excess of 0.99 for all basis sets. For F⁻, coefficients near 0.1 for $a_{2p}^\dagger a_{2p}^\dagger a_{4p}$ shakeup operators appear in the eigenvectors of the superoperator Hamiltonian matrix. While the propagator calculation is no more difficult with the new orbital choice, a substantial investment must be made in obtaining the BD reference state.

From a computational perspective, the additional work required by the $\hat{H}_{2hp,2hp}$ terms that depend on the coupled-cluster wave function amplitudes is minor. Somewhat larger increases in the

vertical electron detachment energies accompany the inclusion of these terms when approximate Brueckner orbitals are used. Pole strengths, Dyson orbitals, and shakeup operator participation are approximately the same. With the largest basis, the SH2-BD model overestimates vertical electron detachment energies by 0.22 eV for F^- and by 0.14 eV for OH^- .

The SH2-BD model is perhaps the most satisfactory considered here, for the next set of improvements must include $3h2p$ operators. These contributions probably improve the description of the electron-detached final state, but their influence on the initial state (through triple and quadruple excitations achieved by coupling to the p and $2ph$ operators) is likely to be relatively minor. These effects will decrease electron detachment energies. A slight overestimate may be expected with the present set of operators.

Conclusions

Previously derived diagonal approximations in the self-energy matrix and the nondiagonal, renormalized generalization represented by the 3+ method fail to produce satisfactory predictions for the vertical electron detachment energies of F^- and OH^- . Saturation of basis sets provides no remedy for this conclusion. The best of these methods is the partial third-order, diagonal approximation.

The recently derived, nondiagonal, renormalized generalization of the latter method, known as NR2, produces much smaller errors, approximately 0.2 eV. Small improvements are realized when second-order terms in the $\hat{H}_{2hp,2hp}$ block of the superoperator Hamiltonian matrix are added. Both of these methods underestimate the electron detachment energies.

Replacement of Hartree-Fock orbitals in the reference determinant by approximate Brueckner orbitals generated in a Brueckner doubles, coupled-cluster calculation produces values that overestimate experiment, but the absolute errors are smaller. When $\hat{H}_{2hp,2hp}$ terms that depend on cluster amplitudes are added, agreement with experiment grows slightly worse.

The new approximations tested here are significant improvements over the older techniques and are a promising foundation for additional method-

ological developments and applications to anion chemistry.

ACKNOWLEDGMENTS

This work was supported by the National Science Foundation under grant CHE-9321434, the Petroleum Research Fund under grant 29848-AC6, and by Gaussian, Incorporated.

References

1. J. Linderberg and Y. Öhrn, *Propagators in Quantum Chemistry* Academic, New York, (1973).
2. B. Pickup and O. Goscinski, *Mol. Phys.* **26**, 1013 (1973).
3. L. S. Cederbaum and W. Domcke, *Adv. Chem. Phys.* **26**, 206 (1977).
4. J. Simons, *Theor. Chem. Adv. Persp.* **3**, 1 (1978).
5. J. Simons, *Ann. Rev. Phys. Chem.* **28**, 15 (1977).
6. Y. Öhrn and G. Born, *Adv. Quant. Chem.* **13**, 1 (1981).
7. M. F. Herman, K. F. Freed, and D. L. Yeager, *Adv. Chem. Phys.* **48**, 1 (1981).
8. W. von Niessen, J. Schirmer, and L. S. Cederbaum, *Comput. Phys. Rep.* **1**, 57 (1984).
9. J. V. Ortiz, *J. Chem. Phys.* **97**, 7531 (1992).
10. J. V. Ortiz, *J. Chem. Phys.* **99**, 6716 (1993).
11. J. V. Ortiz, *Chem. Phys. Lett.* **216**, 319 (1993).
12. J. V. Ortiz and V. G. Zakrzewski, *J. Chem. Phys.* **100**, 6614 (1994).
13. M. Ohno, V. G. Zakrzewski, J. V. Ortiz, and W. von Niessen, *J. Chem. Phys.* **106**, 3258 (1997).
14. V. G. Zakrzewski and J. V. Ortiz, *J. Chem. Phys.* **102**, 294 (1995).
15. O. Dolgounitcheva, V. G. Zakrzewski, and J. V. Ortiz, *J. Chem. Phys.*, in press.
16. M. Enlow, J. V. Ortiz, and H. P. Lüthi, *Mol. Phys.* **92**, 441 (1997).
17. M. Gutowski, A. I. Boldyrev, J. V. Ortiz, and J. Simons, *J. Am. Chem. Soc.* **101**, 9262 (1994).
18. J. V. Ortiz, *J. Phys. Chem.* **94**, 4762 (1990); M. Gutowsky and J. Simons, *Chem. Rev.* **91**, 669 (1991).
19. V. G. Zakrzewski, O. Dolgounitcheva, and J. V. Ortiz, *J. Chem. Phys.* **105**, 5872 (1996).
20. J. V. Ortiz, in *Computational Chemistry, Reviews of Current Trends*, Vol. 2, J. Leszczynski, Ed. (World Scientific, Singapore, 1997).
21. J. V. Ortiz, V. G. Zakrzewski, and O. Dolgounitcheva, in *Conceptual Trends in Quantum Chemistry*, Vol. 3, E. S. Kryachko, Ed., (Kluwer, Dordrecht, 1997), p. 465.
22. O. Dolgounitcheva, V. G. Zakrzewski, and J. V. Ortiz, *Int. J. Quant. Chem.* **65**, 463 (1997).
23. J. V. Ortiz, *J. Chem. Phys.* **104**, 7599 (1996).
24. J. Simons and W. D. Smith, *J. Chem. Phys.* **58**, 4899 (1973); L. S. Cederbaum, *Theor. Chim. Acta* **31**, 239 (1973); G. D. Purvis and Y. Öhrn, *Chem. Phys. Lett.* **33**, 396 (1975).

ORTIZ

25. J. V. Ortiz, *J. Chem. Phys.* **108**, 1008 (1998).
26. K. A. Brueckner, *Phys. Rev.* **96**, 508 (1954).
27. V. G. Zakrzewski, J. V. Ortiz, J. A. Nichols, D. Heryadi, D. L. Yeager, and J. T. Golab, *Int. J. Quant. Chem.* **60**, 29 (1996).
28. V. G. Zakrzewski, O. Dolgounitcheva, and J. V. Ortiz, *J. Chem. Phys.* **105**, 8748 (1996).
29. O. Dolgounitcheva, V. G. Zakrzewski, and J. V. Ortiz, *J. Phys. Chem. A* **101**, 8554 (1997).
30. V. G. Zakrzewski, O. Dolgounitcheva, and J. V. Ortiz, *J. Chem. Phys.* **107**, 7906 (1997).
31. L. S. Cederbaum, W. Domcke, J. Schirmer, and W. von Niessen, *Adv. Chem. Phys.* **65**, 115 (1986).
32. O. Goscinski and B. Lukman, *Chem. Phys. Lett.* **7**, 573 (1970).
33. I. Shavitt, B. J. Rosenberg, and S. Palalikit, *Int. J. Quant. Chem. Quant. Chem. Symp.* **10**, 33 (1976); W. Meyer, *J. Chem. Phys.* **64**, 2901 (1976); C. E. Dykstra, *Chem. Phys. Lett.* **45**, 466 (1977).
34. J. Cizek and J. Paldus, *Physica Scripta* **21**, 251 (1980); R. J. Bartlett and G. D. Purvis, *Physica Scripta* **21**, 255 (1980); R. A. Ciles and C. E. Dykstra, *J. Chem. Phys.* **74**, 4544 (1981).
35. N. C. Handy, J. A. Pople, M. Head-Gordon, K. Ragavachari, and G. W. Trucks, *Chem. Phys. Lett.* **164**, 185 (1989).
36. R. J. Bartlett, *Ann. Rev. Phys. Chem.* **32**, 359 (1981).
37. J. V. Ortiz, *J. Chem. Phys.* **103**, 5630 (1995); J. V. Ortiz, *Int. J. Quant. Chem., Quant. Chem. Symp.* **29**, 331 (1995).
38. J. Cioslowski and J. V. Ortiz, *J. Chem. Phys.* **96**, 8379 (1992); J. V. Ortiz *Int. J. Quant. Chem., Quant. Chem. Symp.* **26**, 1 (1992).
39. R. Krishnan, J. S. Binkley, R. Seeger, and J. A. Pople, *J. Chem. Phys.* **72**, 650 (1980) and references therein; M. J. Frisch, J. A. Pople and J. S. Binkley, *J. Chem. Phys.* **80**, 3265 (1984); T. Clark, J. Chandrasekhar, G. W. Spitznagel, and P.V.R. Schleyer, *J. Comp. Chem.* **4**, 294 (1983).
40. T. H. Dunning, *J. Chem. Phys.* **90**, 1007 (1989); R. A. Kendall, T. H. Dunning, and R. J. Harrison, *J. Chem. Phys.* **96**, 6796 (1992).
41. M. J. Frisch, G. W. Trucks, H. B. Schlegel, P.M.W. Gill, B. G. Johnson, M. A. Robb, J. R. Cheeseman, T. A. Keith, G. A. Peterson, J. A. Montgomery, K. Ragavachari, M. A. Al-Laham, V. G. Zakrzewski, J. V. Ortiz, J. B. Foresman, J. Cioslowski, B. B. Stefanov, A. Nanayakkara, M. Challacombe, C. Y. Peng, P. Y. Ayala, W. Chen, M. W. Wong, J. L. Andres, E. S. Replogle, R. Gomperts, R. L. Martin, D. J. Fox, J. S. Binkley, D. J. Defrees, J. Baker, J. J. P. Stewart, M. Head-Gordon, C. Gonzales, and J. A. Pople, *Gaussian 95*, Development Version, Gaussian, Inc., Pittsburgh, PA, 1995.
42. F⁻: H. Hotop and W. C. Lineberger, *J. Phys. Chem. Ref. Data* **4**, 539 (1975). OH⁻: F. A. Schultz, R. D. Mead, P. L. Jones, and W. C. Lineberger, *J. Chem. Phys.* **77**, 1153 (1982).

Density Functional Theory Without the Born–Oppenheimer Approximation and Its Application

Y. SHIGETA,¹ H. TAKAHASHI,² S. YAMANAKA,¹ M. MITANI,¹
H. NAGAO,³ K. YAMAGUCHI¹

¹Department of Chemistry, Graduate School of Science, Osaka University, Toyonaka 560, Japan

²Department of Chemical Engineering, Graduate School of Engineering Science, Osaka University, Toyonaka 560, Japan

³Institute for Molecular Science, Myodaiji, Okazaki 444, Japan

Received 21 February 1998; revised 3 June 1998; accepted 5 June 1998

ABSTRACT: A procedure for the calculation of molecular properties in the full quantum mechanical treatment is presented. We formulate the non-Born–Oppenheimer density functional theory and propose its numerical scheme. We numerically calculate the energy, particle densities, interparticle distance, and (hyper)polarizability of the hydrogen molecule and its isotopes using this method and discuss isotope effects on the physical properties. © 1998 John Wiley & Sons, Inc. *Int J Quant Chem* 70: 659–669, 1998

Introduction

The Born–Oppenheimer approximation (BOA) [1], which allows one to separate electronic and nuclear motions, is often used to calculate physical properties of a molecular system in molecular physics and quantum chemistry. Within the BOA, solutions of the electronic Hamiltonian describe electronic energies depending parametrically upon nuclear coordinates. The solutions give a very effective and practical concept of the potential energy surface (PES). There are many advan-

tages of the PES concept, for example, the equilibrium interatomic distance of the lowest point of the PES, the excitation among electronic and rovibrational states, and the transition states. They give crucial information on chemical reactions and spectroscopic data.

In chemical physics, there is, however, a wealth of problems where quantum effects of nuclei are essential. It is difficult to describe these nuclear quantum phenomena within the BOA. The near (avoid) crossing such as the Jahn–Teller effect manifests that the separation is not accurate. For an old problem, we can find a phase transition of solid molecular hydrogen under a pressure at a low temperature due to the quantum effect of the

Correspondence to: Y. Shigeta.

protons. We also know that proton tunneling plays an important role in phase transitions between various phases of water. In small systems such as a hydrogen molecule and hydrogen molecular ion, solving the Schrödinger equation without the BOA has been tried by employing the specialized trial function [2–5].

There are many ideas and methods grounded on the non-Born–Oppenheimer (NBO) treatments for molecular systems in both static [6–12] and dynamic [13–15] cases. Recently, we developed the NBO Hartree–Fock method based upon the generator coordinate method (GCM) [11, 12] and calculated molecular vibrational spectra and molecular wave functions directly. The NBO density functional theory (NBO–DFT) was formulated by Capitani et al. in 1982 [9]. DFT [16–18] is one of many useful and simple methods for calculating electronic properties and structural informations for molecular systems. One of recent topics in this field is molecular dynamics (MD) based upon the DFT, which was initiated by Car and Parrinello in 1985 [19]. Some algorithms and computational codes based upon the real-space grid (RSG) method have been proposed for years [20–26].

Capitani et al. introduced a chemical potential for both the electron and nucleus by solving the Euler equation for each particle and discussed the meanings of the chemical potentials from the viewpoint of a chemical reaction. They also showed a relationship between the NBO–DFT and the NBO–HF methods and pointed out its equality. Although Capitani et al. formulated the NBO–DFT method, realistic exchange–correlation potentials were *not* expressed and a concrete numerical calculation for molecular systems was *not* also examined.

In this article, we present a general NBO–DFT calculation technique based upon the RSG. Our aim in this work was to show the possibilities of this method and a strategy of improvement in calculations for realistic systems. In the second section, we review details of the NBO–DFT formalism. We also remark on a calculation scheme using the RSG method. We used the Fast Fourier Transform (FFT) method and the local spin density (LSD) approximation through this work for a first approximation. The third section is concerned with numerical calculation examples of some physical properties of the hydrogen molecule and its isotopomers. In the fourth section, we briefly outline the program for future theoretical and numerical

developments to the NBO–DFT. The fifth section contains a summary and concluding remarks.

Theory and Technique

NON-BORN–OPPENHEIMER DENSITY FUNCTIONAL THEORY

The full Hamiltonian \hat{H} for a molecular system consisting of N electrons and M nuclei is given as (atomic units are used throughout in this text)

$$\begin{aligned} \hat{H} = & \frac{1}{2} \sum_i^N \nabla_i^2 + \sum_a^M \frac{1}{2m_a} \nabla_a^2 + \frac{1}{2} \sum_{i \neq j}^N \frac{1}{|\mathbf{r}_i - \mathbf{r}_j|} \\ & + \frac{1}{2} \sum_{a \neq b}^M \frac{Z_a Z_b}{|\mathbf{R}_a - \mathbf{R}_b|} - \sum_i^N \sum_a^M \frac{Z_a}{|\mathbf{r}_i - \mathbf{R}_a|}, \end{aligned} \quad (1)$$

where \mathbf{r}_i and \mathbf{R}_a are the coordinate for i -th electron and for a -th nucleus, respectively. Z_a and m_a denote the atomic number of a -th nucleus and its mass. One defines a particle density for an electron with σ spin:

$$\rho_c^\sigma(\mathbf{r}_1) = \int d\tau |\Psi(r_i, \sigma_i, R_a, I_a)|^2, \quad (2)$$

and an α -type nucleus with I_α spin:

$$\rho_\alpha^{I_\alpha}(\mathbf{R}_{\alpha_1}) = \int d\tau' |\Psi(r_i, \sigma_i, R_a, I_a)|^2, \quad (3)$$

where $d\tau$ ($d\tau'$) denotes the product form of all spin–space volume elements except for $d\sigma_1 d\mathbf{r}_1$ ($dI_{\alpha_1} d\mathbf{R}_{\alpha_1}$). Note that the index of α specifies the kinds of the nuclei, for example, proton, deuteron, and so on, whereas the index of a in Eq. (1) denotes an order corresponding to one nucleus.

We now define a ground-state energy density functional for the NBO as

$$E[\{\rho_c^\sigma\}, \{\rho_\alpha^{I_\alpha}\}] = \min \langle \Psi_{\{\rho_c^\sigma\}, \{\rho_\alpha^{I_\alpha}\}} | \hat{H} | \Psi_{\{\rho_c^\sigma\}, \{\rho_\alpha^{I_\alpha}\}} \rangle. \quad (4)$$

E searches all wave functions in the domain of the full Hamiltonian \hat{H} of Eq. (1) of appropriate symmetries and statistics of particles. We can now construct the well-known Kohn–Sham equation for each particle using sets of one-particle wave functions for both electrons $\{\phi_i^\sigma(\mathbf{r})\}$ and nuclei $\{\chi_i^{I_\alpha}(\mathbf{r})\}$:

$$\begin{aligned} \hat{F}_c^\sigma \phi_i^\sigma(\mathbf{r}) &= \epsilon_i^\sigma \phi_i^\sigma(\mathbf{r}), \\ \hat{F}_\alpha^{I_\alpha} \chi_i^{I_\alpha}(\mathbf{R}) &= \epsilon_i^{I_\alpha} \chi_i^{I_\alpha}(\mathbf{R}), \end{aligned} \quad (5)$$

where \hat{F}_e^σ and $\hat{F}_\alpha^{I_\alpha}$ mean the Kohn–Sham operators defined in the usual manner [16–18]. Explicit forms of these operators for calculations are stated in the next subsection.

Next, let us consider a molecular system interacting with a static external electronic field characterized by the scalar potential ϕ . The total Hamiltonian \hat{H}' for such a system is

$$\hat{H}' = \hat{H} + \sum_{i=1}^N \phi(\mathbf{r}_i) - \sum_{i=\alpha}^M Z_\alpha \phi(\mathbf{R}_\alpha), \quad (6)$$

where \hat{H} is defined in Eq. (1). Similarly, we yield the ground-state energy functional including the scalar potential ϕ which is a unique functional of set of particle densities, $\{\rho_e^\sigma\}$ and $\{\rho_\alpha^{I_\alpha}\}$:

$$\begin{aligned} \tilde{E}[\{\rho_e^\sigma\}, \{\rho_\alpha^{I_\alpha}\}] &= E[\{\rho_e^\sigma\}, \{\rho_\alpha^{I_\alpha}\}] + \sum_\sigma \int d\mathbf{r} \rho_e^\sigma(\mathbf{r}) \phi(\mathbf{r}) \\ &\quad - \sum_{\alpha, I_\alpha}^M Z_\alpha \int d\mathbf{R} \rho_\alpha^{I_\alpha}(\mathbf{R}) \phi(\mathbf{R}). \end{aligned} \quad (7)$$

For the ϕ -representable densities, $E[\{\rho_e^\sigma\}, \{\rho_\alpha^{I_\alpha}\}]$ coincides with the functional of Eq. (4).

NUMERICAL TECHNIQUE

We mention here a detail of a calculation scheme using the RSG. We adopt the higher-order expansions for the kinetic operator in Eq. (1) by using a uniform grid. We approximate $\nabla_r^2 \phi_e(x_i, y_j, z_k)$ as

$$\begin{aligned} \nabla_r^2 \phi_e^\sigma(x_i, y_j, z_k) &= \sum_{n_x=-N_h}^{N_h} C_{n_x} \phi_e^\sigma(x_i + n_x h, y_j, z_k) \\ &\quad + \sum_{n_y=-N_h}^{N_h} C_{n_y} \phi_e^\sigma(x_i, y_j + n_y h, z_k) \\ &\quad + \sum_{n_z=+N_h}^{N_h} C_{n_z} \phi_e^\sigma(x_i, y_j, z_k + n_z h), \end{aligned} \quad (8)$$

where h is a grid spacing; C_i , constants in the differential method; and N_h , a positive integer describing the accuracy of this approximation. The accuracy is ordered as $O(h^{2N_h+2})$. The nuclear kinetic terms are also represented in analogical forms. Other approximations for the kinetic operator are referred to in [22, 26]. With these kinetic operators

in Eq. (8) and the local spin density approximation (LSD), we can construct a one-particle Schrödinger equation over the grid. We then yield the Kohn–Sham equation from Eq. (5) as

$$\begin{aligned} \hat{F}_e^\sigma \phi_i^\sigma(x_i, y_j, z_k) &= [\hat{T}_e + \hat{V}_e^\sigma(x_i, y_j, z_k)] \phi_i^\sigma(x_i, y_j, z_k) \\ &= \epsilon_i^\sigma \phi_i^\sigma(x_i, y_j, z_k), \\ \hat{F}_\alpha^{I_\alpha} \chi_i^{I_\alpha}(X_i, Y_j, Z_k) &= [\hat{T}_\alpha + \hat{V}_\alpha^{I_\alpha}(X_i, Y_j, Z_k)] \chi_i^{I_\alpha}(X_i, Y_j, Z_k) \\ &= \epsilon_i^{I_\alpha} \chi_i^{I_\alpha}(X_i, Y_j, Z_k), \end{aligned} \quad (9)$$

where \hat{T}_e (\hat{T}_α), \hat{V}_e^σ ($\hat{V}_\alpha^{I_\alpha}$), and ϵ_i^σ ($\epsilon_i^{I_\alpha}$) are the one-particle kinetic operator, the external potential, and the orbital energy of the i -th state for an electron (for an α -type nucleus), respectively.

These external potentials are defined as

$$\hat{V}_e^\sigma(x_i, y_j, z_k) = \hat{V}_c(x_i, y_j, z_k) + \hat{U}_e^\sigma(x_i, y_j, z_k) \quad (10)$$

and

$$\begin{aligned} \hat{V}_\alpha^{I_\alpha}(X_i, Y_j, Z_k) &= -Z_\alpha \hat{V}_c(X_i, Y_j, Z_k) \\ &\quad + \hat{U}_\alpha^{I_\alpha}(X_i, Y_j, Z_k), \end{aligned} \quad (11)$$

where \hat{V}_c is a classical Coulomb potential and \hat{U}_e^σ ($\hat{U}_\alpha^{I_\alpha}$) is a exchange–correlation potential for the electron with spin σ (for the α -type nucleus with spin I_α). The classical Coulomb potential, which does not depend upon the spins of two particles, is given as

$$\hat{V}_c(\mathbf{s}) = \int d\mathbf{s}' \frac{\rho^t(\mathbf{s}')}{|\mathbf{s} - \mathbf{s}'|}, \quad (12)$$

where ρ^t means a generalized total density of the molecular system defined as

$$\rho^t(\mathbf{s}) = - \sum_\alpha \sum_{I_\alpha} Z_\alpha \rho_\alpha^{I_\alpha}(\mathbf{s}) + \sum_\sigma \rho_e^\sigma(\mathbf{s}). \quad (13)$$

For isolated systems, we can yield \hat{V}_c by the FFT in forcing the supercell periodicity, which is commonly used in the calculations of the band structures. Other treatments to obtain the \hat{V}_c are the multigrid method solving the Poisson equation [23, 26] and the direct summation method [21].

On the other hand, the exchange–correlation potentials, which depend on the spins of particles, consist of three parts, which are the exchange part, the correlation with identical particles, and correlation with other particles. The exchange–correlation potential in Eqs. (10) and (11) can be represented as

$$\hat{U}_e^\sigma = \hat{v}_{ex}^\sigma + \hat{v}_c^\sigma + \hat{v}_{en}^\sigma, \quad (14)$$

$$\hat{U}_\alpha^{I_\alpha} = \hat{u}_{ex}^{I_\alpha} + \hat{u}_c^{I_\alpha} + \hat{u}_{en}^{I_\alpha}. \quad (15)$$

Because practical forms of the exchange–correlation potentials are *not* known yet, then we consider a *bold* approximation for the potentials. In this work, we chose an exchange–correlation potential for an electron as the X_α potential ($\alpha = 0.7$ for an electron in the hydrogen atom). The nuclear–nuclear correlation and electron–nuclear correlation terms, which are the second term in Eq. (15) and the third terms in Eqs. (14) and (15), are ignored for a first-order approximation as $\hat{v}_{en}^\sigma = \hat{u}_{en}^{I_\alpha} = \hat{u}_{cn}^{I_\alpha} = 0$.

We can obtain the ground state by using the reduction technique [14], which is available from the Taylor expansion of an imaginary time evolution operator,

$$\begin{aligned} \phi_i^\sigma(t + dt) &= N_i(\phi_i^\sigma(t) - dt \hat{F}_e^\sigma(t) \phi_i^\sigma(t)) \\ &\quad + O(dt^2), \\ \chi_i^{I_\alpha}(t + dt) &= N'_i(\chi_i^{I_\alpha}(t) - dt \hat{F}_\alpha^\sigma(t) \chi_i^{I_\alpha}(t)) \\ &\quad + O(dt^2), \end{aligned} \quad (16)$$

where N_i and N'_i are normalization constants, and $\hat{F}_e^\sigma(t)$ and $\hat{F}_\alpha^{I_\alpha}(t)$ are generated by means of the set of the wave functions $\{\phi_e^\sigma(t), \chi_\alpha^{I_\alpha}(t)\}$ at time t .

Numerical Result and Discussion

In this section, we present numerical results of the physical properties of the hydrogen molecule and its isotopomers using the NBO–DFT.

PARAMETERS

Table I summarizes various parameters of the initial conditions adapted in numerical calculations. We assume that the range of molecular spacing is $L_{max} = 44.61$ (au), and we divide L_{max} into 128 grids ($N = 128$). The grid interval h is, therefore, about 0.3512 au. The corresponding cutoff energies for wave functions in the FFT is about 40 au. For an initial single-particle wave function for the H_2 molecule, we set Gaussian functions with an exponent of 21.95 located at $(X_1, Y_1, Z_1) = (62, 64, 64)$ for the up-spin proton and $(X_2, Y_2, Z_2) = (66, 64, 64)$ for the down-spin proton. These exponents for nuclei are determined by the full variational molecular orbital (FVMO) method proposed by Tachikawa et al. [27]. Parameters for the HD and D_2 are also listed in Table I. On the other hand, initial electronic wave functions are set at (X_1, Y_1, Z_1) and (X_2, Y_2, Z_2) , and the exponent 0.271 is used for all isotopomers. Note that the initial wave function for the electrons is put at the same grid point of nuclei and that exponents of the wave function are different from those of nuclei.

TABLE I
Calculation of initial constants (au).

	L_{max}	h	Initial location	Initial exponent	Initial mass	Spin
H_2 electron 1	44.61	0.351	$r_1 = (62, 64, 64)$	0.271	1.0	↑
H_2 electron 2	44.61	0.351	$r_2 = (66, 64, 64)$	0.271	1.0	↓
H_2 nucleus 1	44.61	0.351	$R_1 = (62, 64, 64)$	21.95	1836.0	↑
H_2 nucleus 2	44.61	0.351	$R_2 = (66, 64, 64)$	21.95	1836.0	↓
HD nucleus 1	44.61	0.351	$R_1 = (62, 64, 64)$	21.88	1836.0	↑
HD nucleus 2	44.61	0.351	$R_2 = (66, 64, 64)$	33.13	3672.0	↓
D_2 nucleus 1	44.61	0.351	$R_1 = (62, 64, 64)$	32.43	3672.0	↑
D_2 nucleus 2	44.61	0.351	$R_2 = (66, 64, 64)$	32.43	3672.0	↓

The intermolecular distance for initial location is almost 1.4 au. We set $N_h = 4$ in Eq. (8).

TOTAL ENERGY AND INTERPARTICLE DISTANCE

The total energies of the hydrogen molecule and its isotopomers are listed in Table II. The total energies yielded by the BO X_α method and HF in the Gaussian 94 package [28] and the NBO–HF method [11] are also shown in Table II. Note that the energies obtained from the NBO procedure include the so-called the zero-point vibration energy. Our results are comparable to the NBO–HF method. From Table II, we find that the tendency of the increment for the total energy of the isotopomers agrees with the results obtained from other methods [4, 11], qualitatively. Note that the results obtained from the present NBO–DFT scheme do not include the nuclear–nuclear and electron–nuclear correlation terms.

The average interparticle distance between electron and electron ($e-e$), electron and nucleus ($e-n$), and nucleus and nucleus ($n-n$) is indicated in Table III. All the tendencies of the interparticle distances are $H_2 > HD > D_2$. We should note that the $n-n$ distance does not mean the equilibrium distance R_e which is available from the BOA, but corresponds to the average distance $\langle R \rangle$ over a nuclear and electronic ground state. We can explain a relationship between R_e and $\langle R \rangle$ by using the PES concept shown in Figure 1. R_e is the lowest point of the PES. On the other hand, $\langle R \rangle$ is the expectation value averaged over a vibrational ground state.

DENSITY

We define here the densities for the electron and nucleus as

$$\begin{aligned} P_e(x_i) &= \sum_{\sigma} \sum_{j,k} \rho_e^{\sigma}(x_i, y_j, z_k) h^3, \\ P_n(X_i) &= \sum_{\alpha} \sum_{I_{\alpha}} \sum_{j,k} \rho_n^{I_{\alpha}}(X_i, Y_j, Z_k) h^3. \end{aligned} \quad (17)$$

The densities for the electron and nucleus are shown in Figures 2 and 3, respectively. Comparing Figure 3(a) with (b) and (c), we can find the isotope effect on the densities explicitly. The highest amplitudes of the proton and the deuteron in each molecule indicate that the average range where a

TABLE II
Total energy of hydrogen molecule (au).

	H_2	HD	D_2
NBO–DFT	−1.052804	−1.059503	−1.065855
NBO–HF	−1.048296	−1.060542	−1.072764
BO–DFT(X_α) ^a	−1.066319	—	—
BO–HF ^a	−1.126755	—	—

^a Obtained from Gaussian 94 using the 6-31G basis at 1.4 au.

nucleus moves differ in each case. The protonic density in H_2 is slightly different from that in HD [see Fig. 3(a) and (b)]. The electronic density of HD is not symmetric due to the nuclear density.

In Eqs. (10) and (11), each potential is determined from the densities of the other particles. The density of each particle, therefore, also depends upon the densities of the other particles through the coupled Kohn–Sham equations of Eq. (5). The electronic properties depend not only on the atomic number of nuclei but also on its mass because of the behavior of the nuclear density. We conclude that all electronic properties are diversified by a

TABLE III
Interparticle distance of hydrogen molecule (au).

	$e-e$	$n-e$	$n-n$
H_2	2.115571	1.795880	1.406685
HD	2.086376	1.771450	1.405375
D_2	2.085256	1.770079	1.405226

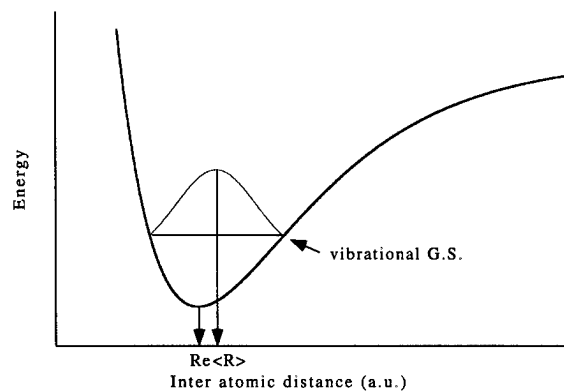


FIGURE 1. A relationship between the equilibrium interatomic distance and average nuclear distance of the vibrational ground state using the PES.

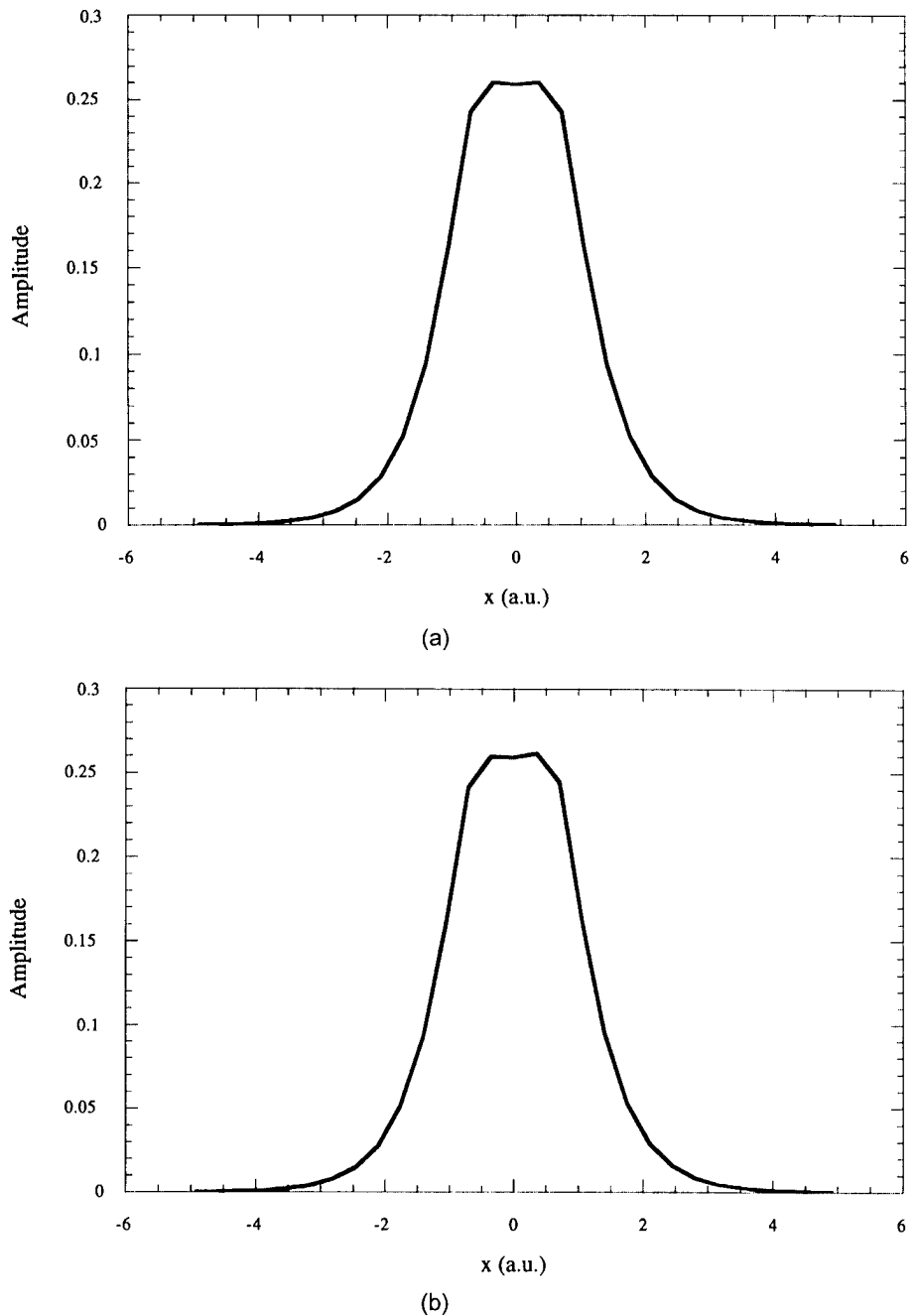
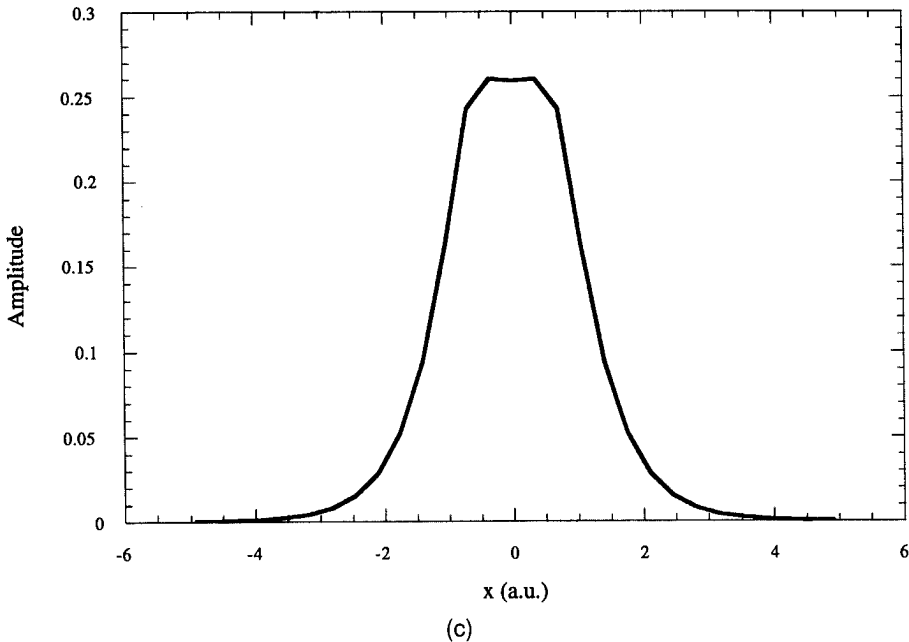


FIGURE 2. Electronic density of (a) H_2 , (b) HD , and (c) D_2 (au) using converged wave functions. The range of the figures are from $i = 48$ to 80 (from $x_{48} = -5.62$ to $x_{80} = 5.62$).

**FIGURE 2.** (Continued)

circumstance by which electrons move around, for example, the nuclear motions and kinds of nuclei of which molecular systems consist.

POLARIZABILITY AND HYPERPOLARIZABILITY

We calculated the linear and nonlinear optical properties of these systems. In Eqs. (6) and (7), we extended the NBO-DFT to molecular systems in a static external field of $\phi(\mathbf{s})$. The static (hyper)polarizabilities are defined as

$$\alpha_{ij}(0) = \left(\frac{\partial^2 \tilde{E}}{\partial F_i \partial F_j} \right)_{\mathbf{F} \rightarrow 0}, \quad (18)$$

$$\beta_{ijk}(0) = \left(\frac{\partial^3 \tilde{E}}{\partial F_i \partial F_j \partial F_k} \right)_{\mathbf{F} \rightarrow 0}, \quad (19)$$

where

$$\begin{aligned} \tilde{E}(\mathbf{F}) &= E(0) - \mu_0 \mathbf{F} \\ &- \frac{1}{2!} \alpha \mathbf{F}^2 - \frac{1}{3!} \beta \mathbf{F}^3 - \frac{1}{4!} \gamma \mathbf{F}^4 - \dots \end{aligned} \quad (20)$$

$\tilde{E}(\mathbf{F})$ is the molecular total energy in the presence of a static electric field $\phi(\mathbf{s})$. $\phi(\mathbf{s})$ is approximated as $\mathbf{F} \cdot \mathbf{s}$ in Eq. (7), where \mathbf{F} is a field amplitude and \mathbf{s} represents a coordinate. We can obtain (hyper)

polarizabilities by solving Eqs. (18) and (19) numerically by using the finite-field method. Table IV indicates the (hyper)polarizability α_{xx} and β_{xxx} of the hydrogen molecules and isotopomers by the BO and by the NBO-DFT. The α_{xx} values obtained from the NBO-DFT increases in the order of the nuclear mass, that is, $\text{H}_2 < \text{HD} < \text{D}_2$. From Table IV, the β_{xxx} value of the HD molecule has a nonzero value, but that of the other symmetric molecules are equal to zero, due to the unsymmetric system shown as Figures 2(b) and 3(b). Within the conventional BO procedure, it is difficult to obtain the β_{xxx} value of the HD because the nuclear mass effect on the electronic properties is omitted.

Future Program

In this section, problems which need to be improved on are mentioned briefly.

EXCITED STATES AND REAL-TIME DYNAMICS

For dynamic cases, we presented the molecular wave packet (MWP) method to investigate the isotope effect on the (hyper)polarizability of the one-dimensional hydrogen molecule and its iso-

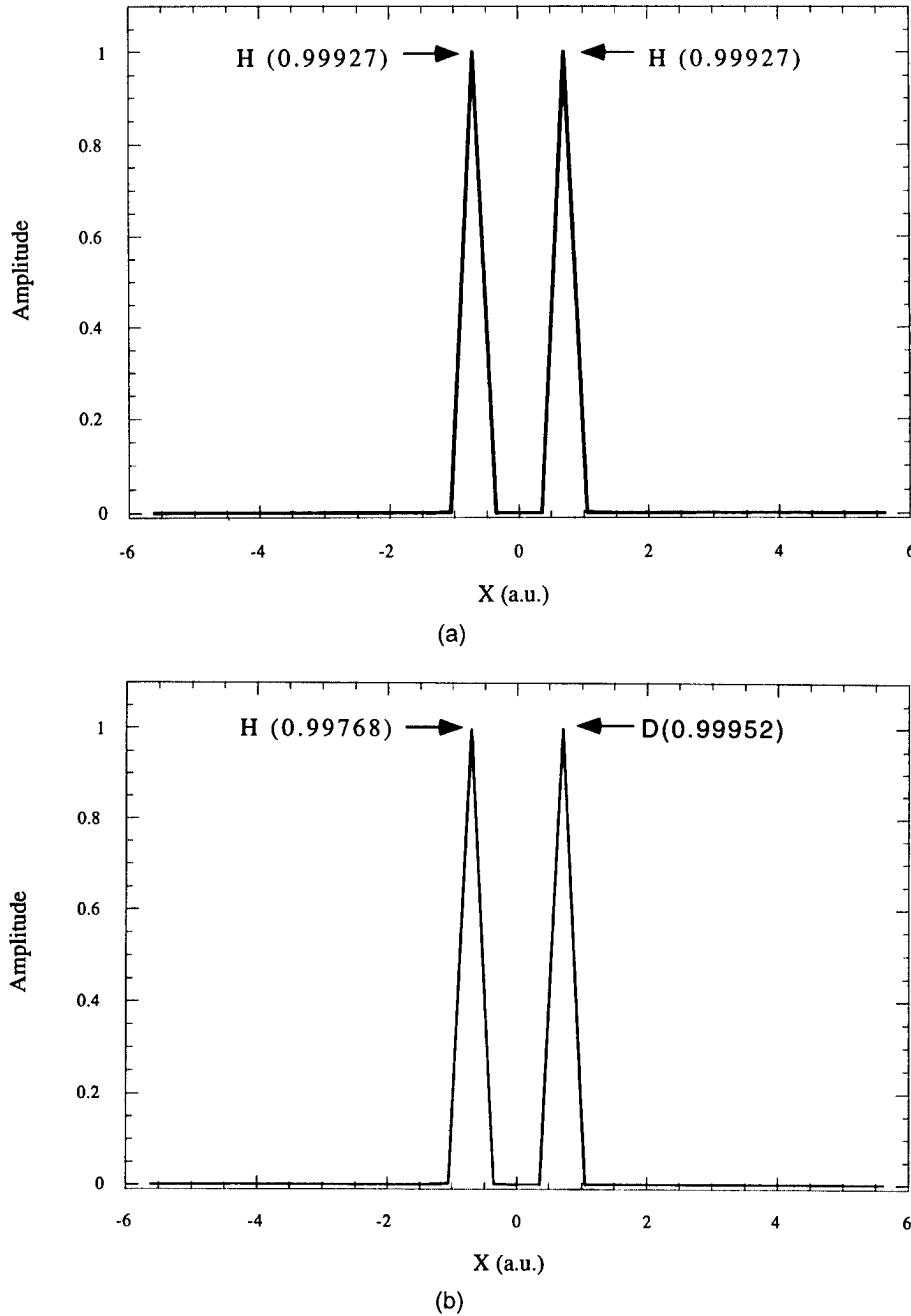


FIGURE 3. Nuclear density of (a) H_2 , (b) HD, and (c) D_2 (au) using converged wave functions. The range of figures are from $i = 48\text{--}80$. H and D represent the proton and deuteron, respectively. The numbers in a parentheses denote the maximum density.

topomers [14]. It is, however, actually difficult to extend this method into three-dimensional many-particle systems, because the method is computationally demanding. To reduce the computational efforts, it is necessary to introduce an approximation as a possible retaining accuracy.

Although the present NBO-DFT method also enables one to extend a real-time evolution scheme straightforwardly once the exact ground state is determined, the method deals only with the ground state. To tackle the realistic cases where the BOA breaks down, this method must be reconstructed

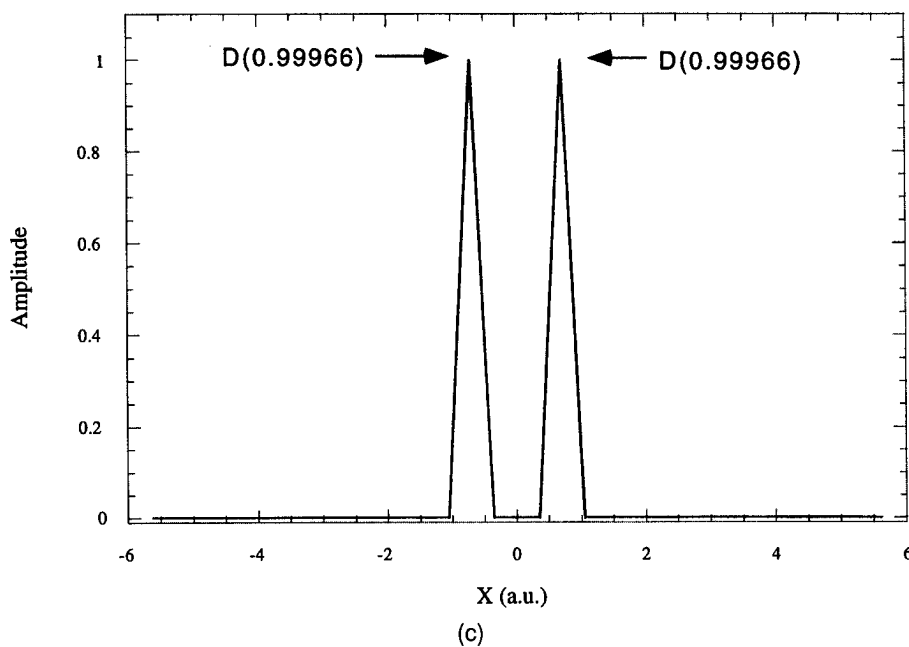


FIGURE 3. (Continued)

in order to treat the excited states. Several extensions of the ground-state DFT have been contrived to cope with excited states. They are based either on the Reyleigh-Ritz principle for the lowest eigenstate of each symmetry class [29, 30] or on the variational principle for ensembles [31, 32]. The crucial problem is how to determine the exchange-correlation energy functionals for excited states. Recently, Görling suggested a computational scheme for the treatment of excited states within the DFT [33] and the time-dependent Kohn-Sham formalism which is generalization of the DFT perturbation [34]. Gross et al. also derived another time-dependent DFT with excited states [35]. At the next stage, making use of these methods may enable us to treat the time-dependent

molecular dynamics including both ground and excited states using the DFT.

EXCHANGE AND CORRELATION ENERGY FUNCTIONAL FOR ELECTRON AND NUCLEI

Quite independent of the problems connected with the exchange-correlation energy functionals for the excited states, there are some questions of how to uniquely choose the functionals for both the fermion and boson nuclei and for electron-nuclear coupling. At this stage, we have neglected such effects in Eqs. (14) and (15). Here, we will make some remarks about it briefly.

For the fermion nucleus, due to the anticommutation relation or Hund's rule, the identical nuclear-nuclear exchange-correlation terms may be represented as the same form for the electronic-electronic ones. On the other hand, the boson nuclei satisfy the commutation relation. For the boson nucleus, the Kohn-Sham equation may be represented as only one differential equation with a density. The identical exchange-correlation terms may be obtained from the imperfect Bose gas model, taking all these considerations into account. Electron-nucleus correlation terms which are the third terms on the right-hand side of Eqs. (14) and (15) and different nuclear-nuclear correlation terms are indispensable for describing the nonadi-

TABLE IV
(Hyper)polarizability of hydrogen molecule (au).

	α_{xx}	β_{xxx}
H ₂	6.3020	0.0
HD	6.3025	$4.10 \times e^{-4}$
D ₂	6.3029	0.0
H ₂ (BO-DFT) ^a	6.6436	0.0

^a Obtained from Gaussian 94 by using 6-31G basis at 1.4 au.

abatic effects. We can *never* neglect these coupling terms. There are many cases for calculating such terms, for example, a correlation between the electron and fermion or boson nucleus and between fermion and boson nuclei. Although the last terms are very small in comparison with the other terms, when one investigates a deuteron in metallic hydrogen and a mixture system of ^3He and ^4He , the last terms seem to be very significant. Much progress is exceedingly expected to search them.

We now prepare for a construction of the exact functional beyond the LSD using the GW approximation [36, 37] and the generalized gradient approximation [38] methods, taking advantage of the scaling law generated by the virial theorem [39].

Concluding Remarks

An NBO-DFT calculation scheme based upon the real-space grid method was presented to apply to molecular systems. A numerical calculation for a simple system such as the hydrogen molecule was attempted. We evaluated total energies, densities, interparticle distances, and (hyper)polarizabilities of the hydrogen molecule. Calculations of the (hyper)polarizability α_{xx} and β_{xxxx} were also performed using the finite-field method. The unsymmetry of the HD molecule is affected by the β_{xxxx} , which is difficult to obtain by the BO procedures. We pointed out that all electronic and nuclear properties depend upon the charges and masses of particles of which a system consists, because the densities of particles are determined from the coupled Kohn-Sham equation of Eq. (5). We showed that it is possible to discuss isotope effects among the hydrogen molecule and its isotopomers at least qualitatively, although only a poor correlation term is used. Many works are needed to implement the NBO-DFT method, but the nuclear kinetic effects on the quantum chemistry and molecular physics seem to be well understood.

ACKNOWLEDGMENTS

The authors would like to thank Prof. Nishikawa, Dr. M. Nakano, and Dr. Y. Yoshioka for their continued encouragement and helpful discussions throughout this work. We also wish to express our grateful acknowledgment to Mr. T. Kawakami, Mr. S. Yamada, Mr. T. Kobayashi, and Mr. D. Yamaki for their instructive discussions.

References

1. M. Born and R. Oppenheimer, Ann. Phys. **84**, 457 (1927).
2. W. Kolos and L. Wolniewicz, Rey. Mod. Phys. **35**, 473 (1963).
3. D. M. Bishop, Mol. Phys. **28**, 1397 (1974).
4. D. M. Bishop and L. M. Cheung, Phys. Rev. A **16**, 640 (1977).
5. P. M. Kozlowski and L. Adamowicz, Chem. Rev. **97**, 2007 (1993).
6. I. L. Thomas, Phys. Rev. **185**, 90 (1969); I. L. Thomas, Phys. Rev. A2, 728, 1675 (1970); I. L. Thomas and H. W. Joy, *Ibid.* A2, 1200 (1970); I. L. Thomas, *Ibid.* A3, 565 (1971); I. L. Thomas, *Ibid.* A4, 457 (1971); I. L. Thomas, *Ibid.* A5, 1104 (1972).
7. B. A. Pettitt, Chem. Phys. Lett. **130**, 399 (1986).
8. H. J. Monkhorst, Phys. Rev. A **36**, 1544 (1987).
9. J. F. Capitani, R. F. Nalewajski, and R. G. Parr, J. Chem. Phys. **76**, 568 (1982).
10. L. Lathouwers, P. Van Leuven, and M. Bouting, Chem. Phys. Lett. **52**, 439 (1977); L. Lathouwers, Phys. Rev. A **18**, 2150 (1978); E. Deumens, Y. Öhrn, L. Lathouwers, and P. Van Leuven, J. Chem. Phys. **84**, 3944 (1986); J. Broeckhove, L. Lathouwers, and P. Van Leuven, J. Math. Chem. **6**, 207 (1991).
11. Y. Shigeta, K. Kodama, H. Kawabe, H. Nagao, and K. Nishikawa, Chem. Phys. Lett., submitted.
12. Y. Shigeta, Y. Ozaki, K. Kodama, H. Kawabe, H. Nagao, and K. Nishikawa, Int. J. Quantum Chem. (in press).
13. S. Chelkowski, C. Foisy, and A. D. Bandrauk, Int. J. Quantum Chem. **65**, 503 (1997).
14. H. Nagao, K. Kodama, Y. Shigeta, K. Nishikawa, H. Kawabe, and K. Yamaguchi, Int. J. Quant. Chem. **60**, 49 (1996); K. Kodama, H. Nagao, Y. Shigeta, K. Nishikawa, H. Kawabe, M. Nakano, and K. Yamaguchi, Chem. Phys. Lett., submitted.
15. E. Deumens, A. Diz, R. Longo, and Y. Öhrn, Rev. Mod. Phys. **66**, 917 (1994).
16. P. Hohenberg and W. Kohn, Phys. Rev. B **136**, 864 (1964).
17. W. Kohn and L. J. Sham, Phys. Rev. A **140**, 1133 (1965).
18. R. G. Parr and W. Yang, *Density Functional Theory of Atoms and Molecules* (Oxford University Press, New York, 1989), and references therein.
19. R. Car and M. Parrinello, Phys. Rev. Lett. **55**, 2471 (1985).
20. A. D. Becke, J. Chem. Phys. **76**, 6037 (1982).
21. J. R. Chelikowsky, N. Troullier, and Y. Saad, Phys. Rev. Lett. **72**, 1240 (1994); J. R. Chelikowsky, N. Troullier, K. Wu, and Y. Saad, Phys. Rev. B **50**, 11355 (1994); X. Jing, N. Troullier, D. Dean, N. Binggeli, J. R. Chelikowsky, K. Wu, and Y. Saad, *Ibid.* **50**, 12234 (1994); J. R. Chelikowsky, X. Jing, K. Wu, and Y. Saad, *Ibid.* **53**, 12071 (1996); X. Jing, J. R. Chelikowsky, and N. Troullier, Solid State Commun. **96**, 231 (1996).
22. T. Hoshi, M. Arai, and T. Fujiwara, Phys. Rev. B **52**, R5459 (1995).

23. M. P. Merrick, K. A. Iyer, and T. L. Beck, *J. Phys. Chem.* **99**, 12478 (1995); K. A. Iyer, M. P. Merrick, and T. L. Beck, *J. Chem. Phys.* **103**, 227 (1995); T. L. Beck, *Int. J. Quantum Chem.* **65**, 477 (1997).
24. F. Gygi and G. Galli, *Phys. Rev. B* **52**, R2229 (1995).
25. G. Zumbach, N. A. Modine, and E. Kaxiras, *Solid State Commun.* **99**, 57 (1996).
26. E. L. Briggs, D. J. Sullivan, and J. Bernholc, *Phys. Rev. B* **52**, R5471 (1995); E. L. Briggs, D. J. Sullivan, and J. Bernholc, *Ibid.* **54**, 14362 (1996), J. Bernholc, J.-Y. Yi, and D. J. Sullivan, *Faraday Discuss.* **92**, 217 (1991); and J. Bernholc, E. L. Briggs, D. J. Sullivan, C. J. Brabec, M. B. Nardelli, K. Rapcewicz, C. Roland, and M. Wense, *Int. J. Quantum Chem.* **65**, 531 (1997).
27. M. Tachikawa, K. Mori, and H. Nakai, private communication.
28. M. J. Frisch, G. W. Trucks, H. B. Schlegel, P. M. W. Gill, B. G. Johnson, M. A. Robb, J. R. Cheeseman, T. A. Keith, G. A. Petersson, J. A. Montgomery, K. Raghavachari, M. A. Al-Laham, V. G. Zakrzewski, J. V. Ortiz, J. B. Foresman, J. Cioslowski, B. B. Stefanov, A. Nanayakkara, M. Challacombe, C. Y. Peng, P. Y. Ayala, W. Chen, M. W. Wong, J. L. Andres, E. S. Replogle, R. Gomperts, R. L. Martin, D. J. Fox, J. S. Binkley, D. J. Defrees, J. Baker, J. P. Stewart, M. Head-Gordon, C. Gonzalez, and J. A. Pople, *Gaussian 94* (Gaussian, Inc., Pittsburgh, PA, 1995).
29. O. Gunnarsson and B. I. Lundqvist, *Phys. Rev. B* **13**, 4274 (1976).
30. U. von Barth, *Phys. Rev. A* **20**, 1693 (1979).
31. A. K. Theophilou, *J. Phys. C* **12**, 5419 (1979); N. Hadjisavvas and A. K. Theophilou, *Phys. Rev. A* **32**, 720 (1985).
32. W. Kohn, *Phys. Rev. A* **34**, 737 (1986); E. K. U. Gross, L. N. Oliveira, and W. Kohn, *Phys. Rev. A* **37**, 2805, 2809 (1988); L. N. Oliveira, E. K. U. Gross, and W. Kohn, *Phys. Rev. A* **37**, 2821 (1988).
33. A. Görling, *Phys. Rev. A* **54**, 3912 (1996).
34. A. Görling, *Phys. Rev. A* **55**, 2630 (1997).
35. C. A. Ullrich, U. J. Gossman, and E. K. U. Gross, *Phys. Rev. Lett.* **73**, 2915 (1995).
36. M. S. Hybertsen and S. G. Louie, *Phys. Rev. B* **34**, 5390 (1986).
37. F. Aryasetiawan and O. Gunnarsson, *Rep. Prog. Phys.* **61**, 237 (1998).
38. J. P. Perdew, K. Burke, and M. Ernzerhof, *Phys. Rev. Lett.* **77**, 3865 (1996).
39. P. O. Löwdin, *J. Mol. Spect.* **3**, 67 (1959).

Analytical Asymptotic Structure of the Pauli, Coulomb, and Correlation–Kinetic Components of the Kohn–Sham Theory Exchange–Correlation Potential in Atoms

ZHIXIN QIAN, VIRAHT SAHNI

Department of Physics, Brooklyn College of the City University of New York, Brooklyn, New York 11210, and The Graduate School and University Center of the City University of New York, 33 West 42nd Street, New York, New York 10036

Received 21 February 1998; revised 3 April 1998; accepted 13 April 1998

ABSTRACT: In this article, we derive the analytical asymptotic structure in the classically forbidden region of atoms of the Kohn–Sham (KS) theory exchange–correlation potential defined as the functional derivative $\nu_{xc}(\mathbf{r}) = \delta E_{xc}^{KS}[\rho]/\delta\rho(\mathbf{r})$, where $E_{xc}^{KS}[\rho]$ is the KS exchange–correlation energy functional of the density $\rho(\mathbf{r})$. The derivation is via the exact description of KS theory in terms of the Schrödinger wave function. As such, we derive the explicit contribution to the asymptotic structure of the separate correlations due to the Pauli exclusion principle and Coulomb repulsion, and of correlation–kinetic effects which are the source of the difference between the kinetic energy of the Schrödinger and KS systems. We first determine the asymptotic expansion of the wave function, single-particle density matrix, density, and pair–correlation density up to terms of order involving the quadrupole moment. For atoms in which the N - and $(N - 1)$ -electron systems are orbitally nondegenerate, the structure of the potential is derived to be $\nu_{xc}(\mathbf{r}) \underset{r \rightarrow \infty}{\sim} -1/r - \alpha/2r^4 + 8\kappa_0\chi/5r^5$, where α is the polarizability; χ , an expectation value of the $(N - 1)$ -electron ion; and $\kappa_0^2/2$, the ionization potential. The derivation shows the leading and second terms to arise directly from the KS Fermi and Coulomb hole charges, respectively, and the last to be a correlation–kinetic contribution. For atoms in which the N -electron system is orbitally degenerate, there are additional contributions

Correspondence to: V. Sahni.

Contract grant sponsor: Research Foundation of the City University of New York.

of $O(1/r^3)$ and $O(1/r^5)$ due to Pauli correlations. We show further that there is no $O(1/r^5)$ contribution due to Coulomb correlations. © 1998 John Wiley & Sons, Inc. Int J Quant Chem 70: 671–680, 1998

Key words: density-functional theory; exchange–correlation potential

Introduction

In this article, we derive for atoms in the classically forbidden region the analytical asymptotic structure of the Kohn-Sham [1] (KS) density functional theory [2] exchange–correlation potential $\nu_{xc}(\mathbf{r})$. This potential is defined as the functional derivative $\delta E_{xc}^{KS}[\rho]/\delta\rho(\mathbf{r})$, where $E_{xc}^{KS}[\rho]$ is the KS exchange–correlation energy functional of the density $\rho(\mathbf{r})$. The energy functional, and thus its derivative, incorporate electron correlations due to the Pauli exclusion principle, Coulomb repulsion, and correlation–kinetic effects which are the source of the difference between the interacting Schrödinger and noninteracting KS system kinetic energies. Our derivation is within the framework of the exact interpretation [3–6] of KS theory in terms of the Schrödinger wave function Ψ . A principal advantage of this interpretation is that it delineates the contribution of each type of correlation to both the energy and potential. In this manner it is then possible to derive the explicit contribution to the asymptotic structure of $\nu_{xc}(\mathbf{r})$ due to Pauli and Coulomb correlations and correlation–kinetic effects. This understanding not only provides insights into the theory, but also allows for the meaningful construction of approximate exchange–correlation energy functionals and potentials, which is one major focus of research in density functional theory. (We note that correlations due to the Pauli exclusion principle are usually referred to as exchange effects. However, in KS theory, the “exchange” potential contains correlations resulting from the Pauli principle as well as those due to part of the correlation–kinetic effects. In the present work, we refer to correlations arising from the Pauli principle as Pauli correlations, and those due to Coulomb repulsion, as Coulomb correlations.)

The systems that we consider are those for which the N -electron atom may be orbitally degenerate, but the $(N - 1)$ -electron ion is always orbitally nondegenerate except for the twofold spin degen-

eracy for example, B and Mg atoms and their ions. For the case when both the N - and $(N - 1)$ -electron systems are nondegenerate, we obtain the asymptotic structure of $\nu_{xc}(\mathbf{r})$ to be

$$\nu_{xc}(\mathbf{r}) \underset{r \rightarrow \infty}{\sim} -\frac{1}{r} - \frac{\alpha}{2r^4} + \frac{8\kappa_0\chi}{5r^5} + \dots, \quad (1)$$

where α is the polarizability; χ , an expectation value of the $(N - 1)$ -electron ion; and $\kappa_0^2/2$, the ionization potential. The $(-1/r)$ term is shown to arise directly from the KS Fermi hole charge, and the $(-\alpha/2r^4)$, from the KS Coulomb hole. Neither Pauli nor Coulomb correlations contribute to $O(1/r^5)$. The last term is further shown [7] to be a correlation–kinetic contribution. For these assignments to $O(1/r^5)$, the wave function is expanded in the classically forbidden region to include terms involving the quadrupole moment tensor. For the case when the N -electron atom is orbitally degenerate, we obtain

$$\nu_{xc}(\mathbf{r}) \underset{r \rightarrow \infty}{\sim} -\frac{1}{r} - \frac{Q}{r^3} - \frac{\alpha}{2r^4} + \frac{8\kappa_0\chi}{5r^5} - \frac{R}{r^5} + \dots, \quad (2)$$

where the additional $O(1/r^3)$ and $O(1/r^5)$ terms are Pauli-correlation contributions, and Q and R , multipole moments of the density. The physics of the other terms remains unchanged.

Prior to proceeding with our derivation, we briefly discuss the previous work of others. The first two terms of the structure of Eq. (1) have also been obtained quantum mechanically by Almbladh and von Barth [8]. These authors first derived the differential equation for the quasiparticle amplitudes which are the interacting system counterparts of the single-particle orbitals of the noninteracting system. Then, on comparison with the KS equation, they determine $\nu_{xc}(\mathbf{r})$ to $O(1/r^4)$ to be

$$\nu_{xc}(\mathbf{r}) = \nu_H^{(N-1)}(\mathbf{r}) - \nu_H(\mathbf{r}) - \frac{1}{2r^4} \sum_{\alpha\beta} \hat{f}_\alpha \hat{f}_\beta \alpha_{\alpha\beta}, \quad (3)$$

where $\nu_H(\mathbf{r}) = \int d\mathbf{r}' \rho(\mathbf{r}')/|\mathbf{r} - \mathbf{r}'|$ and $\nu_H^{(N-1)}(\mathbf{r})$ are the Hartree potentials for the N - and $(N - 1)$ -

electron systems, $\alpha_{\alpha\beta}$ is the polarizability tensor of the $(N - 1)$ -electron ion, subscripts α and β represent Cartesian coordinates, and \hat{r}_α is a component of the unit vector \hat{r} . For the case when both the N - and $(N - 1)$ -electron systems are nondegenerate, asymptotically, the potentials $v_H^{(N-1)}(\mathbf{r}) \sim_{r \rightarrow \infty} (N - 1)/r$ and $v_H(\mathbf{r}) \sim N/r$ to exponential accuracy and $\alpha_{\alpha\beta} = \alpha \delta_{\alpha\beta}$. The leading $-1/r$ term of Eq. (1) arises as the difference between two Hartree potentials. The authors, however, ascribe this term to the Fermi hole which has a total charge of (negative) unity and, thus, to Pauli correlations. But the KS Fermi hole charge does not appear in the derivation so that the basis for the assignation is unclear. The $(-\alpha/2r^4)$ term is attributed to Coulomb correlations. However, this assignation is based on a comparison with a classical calculation of an ion and an asymptotic test charge. Once again, there is no direct relationship between this term and the KS Coulomb hole charge or other equivalent representation of Coulomb correlations within KS theory. Of course, in the classical calculation, even the $-1/r$ term is due to Coulomb correlations. It is interesting to note that, classically, higher-order contributions [9] are of $O(1/r^6, 1/r^8)$, etc., and thus of even order. There are no terms of $O(1/r^5)$ in the classical calculation. Such terms are strictly a consequence of quantum effects and KS theory.

The leading $(-1/r)$ term of $v_{xc}(\mathbf{r})$ was also derived by Sham [10]. In the asymptotic limit, the integral equation relating $v_{xc}(\mathbf{r})$ to the nonlocal exchange-correlation component $\Sigma_{xc}(\mathbf{r}, \mathbf{r}'; \omega)$ of the self-energy $\Sigma(\mathbf{r}, \mathbf{r}'; \omega)$ reduces to

$$v_{xc}(\mathbf{r}) = \frac{1}{2\phi_i(\mathbf{r})} \int d\mathbf{r}' \Sigma_{xc}(\mathbf{r}, \mathbf{r}'; \mu) \phi_i(\mathbf{r}') + \frac{1}{2\phi_i^*(\mathbf{r})} \int d\mathbf{r}' \Sigma_{xc}(\mathbf{r}, \mathbf{r}'; \mu) \phi_i^*(\mathbf{r}'), \quad (4)$$

where $\phi_i(\mathbf{r})$ are the KS orbitals, μ is the chemical potential, and the electron is in the highest occupied orbital. By considering the leading exchange term in a diagrammatical analysis, the $(-1/r)$ term is obtained, and, thus, this structure can be attributed to Pauli correlations.

Finally, according to Harbola and Sahni [5], the asymptotic structure of $v_{xc}(\mathbf{r})$ is given by $W_x^{KS}(\mathbf{r})$, which is the work done to move an electron in the field of the KS Fermi hole. The $(-1/r)$ structure is

then obtained because the total charge of the Fermi hole is unity and the fact that it becomes an essentially static charge in the limit of asymptotic positions of the electron. The KS Coulomb hole does not contribute asymptotically to this order since its total charge is zero, and the field due to it vanishes in this region faster than $O(1/r^2)$.

We begin in the next section by defining the KS exchange-correlation potential in terms of its components as described by the quantum mechanical interpretation. We first determine the asymptotic structure of the wave function, single-particle density matrix, and pair-correlation density up to terms including the quadrupole contribution in the third section. In the fourth section, we then derive the asymptotic structure of the quantum mechanical Pauli-Coulomb component of the KS exchange-correlation potential and separately that of the Pauli and Coulomb correlation parts. In the fifth section, we derive the structure of the correlation-kinetic component. In the concluding section, we summarize what has been understood and discuss future work. We also discuss how the present derivation helps explain the accuracy of previous results on the ionization potential of atoms.

Definitions

The KS theory exchange-correlation energy and potential can be described exactly in terms of the Schrödinger wave function Ψ . For proofs of this description, we refer the reader to the original literature [3, 6]. Here, we provide those definitions relevant to the present work.

The KS electron-interaction energy functional $E_{ee}^{KS}[\rho] = E_H[\rho] + E_{xc}^{KS}[\rho]$, where $E_H[\rho]$ is the Coulomb self-energy. The corresponding local potential representative of all the electron correlations is then $v_{ee}(\mathbf{r}) = \delta E_{ee}^{KS}[\rho]/\delta\rho(\mathbf{r}) = v_H(\mathbf{r}) + v_{xc}(\mathbf{r})$. This functional derivative is the work done to move an electron in a conservative field $\mathcal{F}(\mathbf{r})$:

$$v_{ee}(\mathbf{r}) = - \int_{\infty}^{\mathbf{r}} \mathcal{F}(\mathbf{r}') \cdot d\mathbf{l}'. \quad (5)$$

The work done is path-independent since $\nabla \times \mathcal{F}(\mathbf{r}) = 0$. The field $\mathcal{F}(\mathbf{r})$ is the sum of an electron-interaction $\mathcal{E}_{ee}(\mathbf{r})$ and correlation-kinetic $\mathbf{Z}_{t_c}(\mathbf{r})$ component.

The field $\mathcal{E}_{ee}(\mathbf{r})$ is determined by Coulomb's law from the pair-correlation density $g(\mathbf{r}, \mathbf{r}')$, so that

$$\mathcal{E}_{ee}(\mathbf{r}) = \int \frac{g(\mathbf{r}, \mathbf{r}')(\mathbf{r} - \mathbf{r}')}{|\mathbf{r} - \mathbf{r}'|^3} d\mathbf{r}', \quad (6)$$

where $g(\mathbf{r}, \mathbf{r}') = P(\mathbf{r}, \mathbf{r}')/\rho(\mathbf{r})$, and $P(\mathbf{r}, \mathbf{r}')$ is the probability of simultaneously finding electrons at \mathbf{r} and \mathbf{r}' :

$$P(\mathbf{r}, \mathbf{r}') = N(N-1) \sum_{\sigma\sigma'} \int \Psi^*(\mathbf{r}\sigma, \mathbf{r}'\sigma', \mathbf{x}_3, \dots, \mathbf{x}_N) \times \Psi(\mathbf{r}\sigma, \mathbf{r}'\sigma', \mathbf{x}_3, \dots, \mathbf{x}_N) d^{N-2}\mathbf{x}. \quad (7)$$

(Here, $\mathbf{x} = \mathbf{r}\sigma$, $\int d\mathbf{x} = \sum_{\sigma} \int d\mathbf{r}$, $\int d^{n-2}\mathbf{x} = \int d\mathbf{x}_3 \dots d\mathbf{x}_N$, and σ is the spin index.)

The field $\mathbf{Z}_{t_c}(\mathbf{r})$ is the difference of two fields $\mathbf{z}(\mathbf{r})$ and $\mathbf{z}_s(\mathbf{r})$, which are derived from the kinetic energy-density tensors $t_{\alpha\beta}(\mathbf{r})$ and $t_{s,\alpha\beta}(\mathbf{r})$ for the interacting Schrödinger and noninteracting KS systems, respectively. Thus,

$$\mathbf{Z}_{t_c}(\mathbf{r}) = \frac{1}{\rho(\mathbf{r})} [\mathbf{z}_s(\mathbf{r}; [\gamma_s] - \mathbf{z}(\mathbf{r}; [\gamma])], \quad (8)$$

where the component of the field $\mathbf{z}(\mathbf{r})$ is $z_{\alpha}(\mathbf{r}) = 2\sum_{\beta} (\partial/\partial r_{\beta}) t_{\alpha\beta}(\mathbf{r}; [\gamma])$, $t_{\alpha\beta}(\mathbf{r}; [\gamma]) = (1/4)(\partial^2/\partial r'_{\alpha} \partial r''_{\beta} + \partial^2/\partial r'_{\beta} \partial r''_{\alpha})\gamma(\mathbf{r}', \mathbf{r}'')|_{\mathbf{r}'=\mathbf{r}''=\mathbf{r}}$, and $\gamma(\mathbf{r}, \mathbf{r}')$ is the spinless single-particle density matrix

$$\gamma(\mathbf{r}, \mathbf{r}') = N \sum_{\sigma} \int \Psi^*(\mathbf{r}\sigma, \mathbf{x}_2, \dots, \mathbf{x}_N) \times \Psi(\mathbf{r}'\sigma, \mathbf{x}_2, \dots, \mathbf{x}_N) d^{N-1}\mathbf{x}. \quad (9)$$

The field $\mathbf{z}_s(\mathbf{r})$ is similarly obtained from the idempotent Dirac density matrix $\gamma_s(\mathbf{r}, \mathbf{r}') = \sum_{\sigma} \sum_i \phi_i^*(\mathbf{r}\sigma) \phi_i(\mathbf{r}'\sigma)$ constructed from the KS orbitals $\phi_i(\mathbf{x})$. The density $\rho(\mathbf{r})$ is the diagonal matrix element $\gamma(\mathbf{r}, \mathbf{r})$.

For spherically symmetric atoms, or nonspherically symmetric atoms in the central field approximation, etc., the curl of the fields $\mathcal{E}_{ee}(\mathbf{r})$ and $\mathbf{Z}_{t_c}(\mathbf{r})$ separately vanish. For such systems then, $\nu_{ee}(\mathbf{r}) = W_{ee}(\mathbf{r}) + W_{t_c}(\mathbf{r})$, where

$$W_{ee}(\mathbf{r}) = - \int_{\infty}^{\mathbf{r}} \mathcal{E}_{ee}(\mathbf{r}') \cdot d\mathbf{l}', \quad (10)$$

and

$$W_{t_c}(\mathbf{r}) = - \int_{\infty}^{\mathbf{r}} \mathbf{Z}_{t_c}(\mathbf{r}') \cdot d\mathbf{l}', \quad (11)$$

and each work done is path-independent.

Asymptotic Structure of Wave Function, Single-Particle Density Matrix, and Pair-Correlation Density

In this section, we derive the asymptotic structure of the wave function Ψ , of the single-particle density matrix $\gamma(\mathbf{r}, \mathbf{r}')$ and, hence, of the density $\rho(\mathbf{r})$ and the pair-correlation density $g(\mathbf{r}, \mathbf{r}')$.

WAVE FUNCTION

The ground-state Schrödinger equation for a system of N -electrons in a local external potential described by the operator $\hat{V} = \sum_i \nu(\mathbf{r}_i)$ is $\hat{H}\Psi = E_0\Psi$, where $\hat{H} = -(1/2)\sum_i \nabla_i^2 + \sum_i \nu(\mathbf{r}_i) + (1/2)\sum_{ij} 1/|\mathbf{r}_i - \mathbf{r}_j|$, and Ψ and E_0 are the wave function and the energy, respectively. The complete set of eigenfunctions and eigenenergies of the $(N-1)$ -electron system are defined by the equation $\hat{H}^{(N-1)}\Psi_s^{(N-1)} = E_s^{(N-1)}\Psi_s^{(N-1)}$. We first expand the wave function Ψ in terms of the eigenfunctions $\Psi_s^{(N-1)}$:

$$\Psi(\mathbf{r}\sigma, \mathbf{x}_2, \dots, \mathbf{x}_N) = \sum_s C_{s\sigma}(\mathbf{r}) \Psi_s^{(N-1)}(\mathbf{x}_2, \dots, \mathbf{x}_N), \quad (12)$$

and rewrite the N -electron Schrödinger equation as

$$\begin{aligned} & \left\{ -\frac{1}{2} \nabla^2 + \nu(\mathbf{r}) + \sum_{i=2}^N \frac{1}{|\mathbf{r} - \mathbf{r}_i|} - \frac{1}{2} \sum_{i=2}^N \nabla_i^2 \right. \\ & \left. + \sum_{i=2}^N \nu(\mathbf{r}_i) + \frac{1}{2} \sum_{i \neq j \neq 1} \frac{1}{|\mathbf{r}_i - \mathbf{r}_j|} \right\} \sum_s C_{s\sigma}(\mathbf{r}) \Psi_s^{(N-1)} \\ & = E_0 \sum_s C_{s\sigma}(\mathbf{r}) \Psi_s^{(N-1)}. \end{aligned} \quad (13)$$

For asymptotic positions of the electron, we have by Taylor expansion

$$\frac{1}{|\mathbf{r} - \mathbf{r}_i|} = \frac{1}{r} + \frac{\mathbf{r}_i \cdot \mathbf{r}}{r^3} + \frac{1}{2} \sum_{\alpha, \beta} \mathbf{r}_{i\alpha} \mathbf{r}_{i\beta} \frac{\partial^2}{\partial r_{\alpha} \partial r_{\beta}} \frac{1}{r}, \quad (14)$$

so that Eq. (13) may be rewritten as

$$\begin{aligned} & \left\{ -\frac{1}{2}\nabla^2 + \nu(\mathbf{r}) + \frac{N-1}{r} \right. \\ & \quad \left. + \sum_{i=2}^N \left[\frac{\mathbf{r}_i \cdot \mathbf{r}}{r^3} + \frac{1}{2} \sum_{\alpha, \beta} r_{i\alpha} r_{i\beta} \frac{\partial^2}{\partial r_\alpha \partial r_\beta} \frac{1}{r} \right] \right\} \\ & \times \sum_s C_{s\sigma}(\mathbf{r}) \Psi_s^{(N-1)} + \hat{H}^{(N-1)} \sum_s C_{s\sigma}(\mathbf{r}) \Psi_s^{(N-1)} \\ & = E_0 \sum_s C_{s\sigma} \Psi_s^{(N-1)}, \end{aligned} \quad (15)$$

which reduces further to

$$\begin{aligned} & \left[-\frac{1}{2}\nabla^2 + \nu(\mathbf{r}) + \frac{N-1}{r} \right] \sum_s C_{s\sigma}(\mathbf{r}) \Psi_s^{(N-1)} \\ & + \sum_{i=2}^N \left[\frac{\mathbf{r}_i \cdot \mathbf{r}}{r^3} + \frac{1}{2} \sum_{\alpha, \beta} r_{i\alpha} r_{i\beta} \frac{\partial^2}{\partial r_\alpha \partial r_\beta} \frac{1}{r} \right] \\ & \times \sum_s C_{s\sigma}(\mathbf{r}) \Psi_s^{(N-1)} \\ & = \sum_s [E_0 - E_s^{(N-1)}] C_{s\sigma}(\mathbf{r}) \Psi_s^{(N-1)}. \end{aligned} \quad (16)$$

Multiplying Eq. (16) from the left by $\Psi_s^{(N-1)*}$ and using the orthonormality condition $\langle \Psi_s^{(N-1)} | \Psi_s^{(N-1)} \rangle = \delta_{ss'}$, we have

$$\begin{aligned} & \left[-\frac{1}{2}\nabla^2 + \nu(\mathbf{r}) + \frac{N-1}{r} \right] C_{s\sigma}(\mathbf{r}) + \frac{\mathbf{r}}{r^3} \cdot \sum_{s'} C_{s'\sigma}(\mathbf{r}) \mathbf{P}_{ss'} \\ & + \frac{1}{2} \sum_{\alpha, \beta} \frac{\partial^2}{\partial r_\alpha \partial r_\beta} \frac{1}{r} \sum_{s'} C_{s'\sigma}(\mathbf{r}) (Q_{ss'})_{\alpha\beta} \\ & = [E_0 - E_s^{(N-1)}] C_{s\sigma}(\mathbf{r}), \end{aligned} \quad (17)$$

where

$$\begin{aligned} \mathbf{P}_{ss'} &= \sum_{i=2}^N \int \Psi_s^{(N-1)*}(\mathbf{x}_2, \dots, \mathbf{x}_N) \mathbf{r}_i \\ &\quad \times \Psi_{s'}^{(N-1)}(\mathbf{x}_2, \dots, \mathbf{x}_N) d^{N-1}\mathbf{x} \end{aligned} \quad (18)$$

and

$$\begin{aligned} (Q_{ss'})_{\alpha\beta} &= \sum_{i=2}^N \int \Psi_s^{(N-1)*}(\mathbf{x}_2, \dots, \mathbf{x}_N) r_{i\alpha} r_{i\beta} \\ &\quad \times \Psi_{s'}^{(N-1)}(\mathbf{x}_2, \dots, \mathbf{x}_N) d^{N-1}\mathbf{x}. \end{aligned} \quad (19)$$

Here, $\mathbf{P}_{ss'}$ is the dipole moment, and $(Q_{ss'})_{\alpha\beta}$, the quadrupole moment tensor of the $(N-1)$ electron system. With the definitions

$$D_{ss'}(\hat{r}) = \hat{r} \cdot \mathbf{P}_{ss'} \quad (20)$$

and

$$Q_{ss'}(\hat{r}) = \frac{1}{2} \sum_{\alpha, \beta} (3\hat{r}_\alpha \hat{r}_\beta - \delta_{\alpha\beta}) (Q_{ss'})_{\alpha\beta}, \quad (21)$$

Eq. (17) becomes

$$\begin{aligned} & \left[-\frac{1}{2}\nabla^2 + \nu(\mathbf{r}) + \frac{N-1}{r} \right] C_{s\sigma}(\mathbf{r}) \\ & + \left[\frac{1}{r^2} \sum_{s'} D_{ss'}(\hat{r}) + \frac{1}{r^3} \sum_{s'} Q_{ss'}(\hat{r}) \right] \\ & \times C_{s'\sigma}(\mathbf{r}) = \epsilon_s C_{s\sigma}(\mathbf{r}), \end{aligned} \quad (22)$$

where $\epsilon_s = E_0 - E_s^{(N-1)}$. This is the same equation as derived by Almbladh and von Barth for the quasiparticle amplitudes, but it is derived here via the wavefunction and carried to $O(1/r^3)$. The asymptotic structure of the coefficients $C_{s\sigma}(\mathbf{r})$ for $s \neq 0$ is then obtained from Eq. (22) as

$$C_{s\sigma}(\mathbf{r}) = - \left[\frac{1}{r^2} D_{s0}(\hat{r}) + \frac{1}{r^3} Q_{s0} \right] \frac{C_{0\sigma}(\mathbf{r})}{\omega_s}, \quad (23)$$

where $\omega_s = \epsilon_0 - \epsilon_s = E_s^{(N-1)} - E_0^{(N-1)}$ is an excitation of the $(N-1)$ -electron system. Thus, the asymptotic structure of the wave function to $O(1/r^3)$ is derived.

SINGLE-PARTICLE DENSITY MATRIX

On substituting Eq. (12) for Ψ into Eq. (9) and using the orthonormality condition of the $\Psi_s^{(N-1)}$, we obtain the asymptotic structure of $\gamma(\mathbf{r}, \mathbf{r}')$ as

$$\begin{aligned} \gamma(\mathbf{r}, \mathbf{r}') &= N \sum_{\sigma} \sum_s C_{s\sigma}^*(\mathbf{r}) C_{s\sigma}(\mathbf{r}') \\ &= N \sum_{\sigma} C_{0\sigma}^*(\mathbf{r}) C_{0\sigma}(\mathbf{r}') \\ &\quad \times \left\{ 1 + \sum_s' \frac{1}{\omega_s^2} \left[\frac{D_{s0}^*(\hat{r})}{r^2} \frac{D_{s0}(\hat{r}')}{r'^2} \right. \right. \\ &\quad + \frac{D_{s0}^*(\hat{r})}{r^2} \frac{Q_{s0}(\hat{r}')}{r'^3} + \frac{Q_{s0}^*(\hat{r})}{r^3} \frac{D_{s0}(\hat{r}')}{r'^2} \\ &\quad \left. \left. + \frac{Q_{s0}^*(\hat{r})}{r^3} \frac{Q_{s0}(\hat{r}')}{r'^3} \right] \right\}. \end{aligned} \quad (24)$$

(Here, $\Sigma'_s = \Sigma_{s \neq 0}$.) The dipole-quadrupole cross terms in Eq. (24) can be shown to vanish by rewriting each term as

$$\begin{aligned} \sum_s \frac{1}{\omega_s^2} \frac{D_{s0}(\hat{r})}{r^2} \frac{Q_{s0}^*(\hat{r}')}{r'^3} \\ = \frac{1}{r^2} \cdot \frac{1}{r'^3} \sum_{\alpha\beta\lambda} \hat{r}'_\alpha \hat{r}'_\beta r_\lambda \\ \times \left\langle \Psi_0^{(N-1)} \left| \hat{q}_{\alpha\beta} \frac{1 - \hat{P}}{[\hat{H} - E_0^{(N-1)}]^2} \hat{d}_\lambda \right| \Psi_0^{(N-1)} \right\rangle, \end{aligned} \quad (25)$$

where $\mathbf{d} = \int \mathbf{r} \delta\hat{\rho}(\mathbf{r}) d\mathbf{r}$, $\hat{q}_{\alpha\beta} = \int r_\alpha r_\beta \delta\hat{\rho}(\mathbf{r}) d\mathbf{r}$, $\delta\hat{\rho}(\mathbf{r}) = \hat{\rho}(\mathbf{r}) - \langle \Psi_0^{(N-1)} | \hat{\rho}(\mathbf{r}) | \Psi_0^{(N-1)} \rangle$, $\hat{\rho} = \sum_i \delta(\mathbf{r} - \mathbf{r}_i)$, and $\hat{P} = |\Psi_0^{(N-1)}\rangle \langle \Psi_0^{(N-1)}|$ is the projector onto the $(N-1)$ -electron ground state. [Note that the dipole \mathbf{d} and quadrupole $\hat{q}_{\alpha\beta}$ moment operators are the same as in Eqs. (18) and (19) since the second term of the operator $\delta\hat{\rho}(\mathbf{r})$ does not contribute on account of the fact that the $(N-1)$ -electron system is spherically symmetric.] Now, the operators \hat{P} , \hat{H} , and $\hat{q}_{\alpha\beta}$ are invariant under the inversion operator \hat{I} , while \hat{d}_λ changes sign. Thus, the dipole-quadrupole term vanishes. The density matrix is then

$$\begin{aligned} \gamma(\mathbf{r}, \mathbf{r}') \underset{r, r' \rightarrow \infty}{\sim} N \sum_\sigma C_{0\sigma}^*(\mathbf{r}) C_{0\sigma}(\mathbf{r}') \\ \times \left\{ 1 + \sum'_s \frac{1}{\omega_s^2} \left[\frac{D_{s0}^*(\hat{r})}{r^2} \frac{D_{s0}(\hat{r}')}{r'^2} \right. \right. \\ \left. \left. + \frac{Q_{s0}^*(\hat{r})}{r^3} \frac{Q_{s0}(\hat{r}')}{r'^3} \right] \right\}. \end{aligned} \quad (26)$$

The asymptotic structure of the density $\rho(\mathbf{r})$ is given by the diagonal matrix element $\gamma(\mathbf{r}, \mathbf{r})$ so that to $O(1/r^6)$

$$\begin{aligned} \rho(\mathbf{r}) \underset{r \rightarrow \infty}{\sim} N \sum_\sigma |C_{0\sigma}(\mathbf{r})|^2 \\ \times \left\{ 1 + \sum'_s \frac{1}{\omega_s^2} \left[\frac{|D_{s0}(\hat{r})|^2}{r^4} + \frac{|Q_{s0}(\hat{r})|^2}{r^6} \right] \right\}. \end{aligned} \quad (27)$$

For the systems considered, the leading term of $\gamma(\mathbf{r}, \mathbf{r}')$ as $r, r' \rightarrow \infty$ is from Eqs. (26) and (27):

$$\gamma(\mathbf{r}, \mathbf{r}') \underset{r, r' \rightarrow \infty}{\sim} \sqrt{\rho(\mathbf{r})} \sqrt{\rho(\mathbf{r}')}, \quad (28)$$

which is a well-known result [2, 11, 12].

PAIR-CORRELATION DENSITY

On substituting Eq. (12) for Ψ into the definition of $P(\mathbf{r}, \mathbf{r}')$ in Eq. (7), we have

$$\begin{aligned} P(\mathbf{r}, \mathbf{r}') &= N(N-1) \\ &\times \sum_{\sigma\sigma'} \int \left[C_{0\sigma}^*(\mathbf{r}) \Psi_0^{(N-1)*}(\mathbf{r}'\sigma', \mathbf{x}_3, \dots, \mathbf{x}_N) \right. \\ &+ \sum'_s C_{s\sigma}^*(\mathbf{r}) \Psi_s^{(N-1)*}(\mathbf{r}'\sigma', \mathbf{x}_3, \dots, \mathbf{x}_N) \Big] \\ &\times \left[C_{0\sigma}(\mathbf{r}) \Psi_0^{(N-1)}(\mathbf{r}'\sigma', \mathbf{x}_3, \dots, \mathbf{x}_N) \right. \\ &+ \sum'_{s'} C_{s'\sigma}(\mathbf{r}) \Psi_{s'}^{(N-1)}(\mathbf{r}'\sigma', \mathbf{x}_3, \dots, \mathbf{x}_N) \Big] d^{N-2} \mathbf{x} \\ &= N \sum_\sigma \left[|C_{0\sigma}(\mathbf{r})|^2 \rho^{(N-1)}(\mathbf{r}') \right. \\ &+ \sum'_s C_{0\sigma}^*(\mathbf{r}) C_{s\sigma}(\mathbf{r}) \rho_{0s}^{(N-1)}(\mathbf{r}') \Big] \\ &+ \sum'_s C_{s\sigma}^*(\mathbf{r}) C_{0\sigma}(\mathbf{r}) \rho_{s0}^{(N-1)}(\mathbf{r}') \\ &+ \sum'_{ss'} C_{s\sigma}^*(\mathbf{r}) C_{s'\sigma}(\mathbf{r}) \rho_{ss'}^{(N-1)}(\mathbf{r}'), \end{aligned} \quad (29)$$

where

$$\begin{aligned} \rho_{ss'}^{(N-1)}(\mathbf{r}') &= (N-1) \sum_{\sigma'} \int \Psi_s^{(N-1)*}(\mathbf{r}'\sigma', \mathbf{x}_3, \dots, \mathbf{x}_N) \\ &\times \Psi_{s'}^{(N-1)}(\mathbf{r}'\sigma', \mathbf{x}_3, \dots, \mathbf{x}_N) d^{N-2} \mathbf{x}. \end{aligned} \quad (30)$$

Thus, the asymptotic structure of the pair-correlation density $g(\mathbf{r}, \mathbf{r}')$, on substituting for $C_{s\sigma}(\mathbf{r})$ from Eq. (23), is to $O(1/r^6)$

$$\begin{aligned} g(\mathbf{r}, \mathbf{r}') \underset{r \rightarrow \infty}{\sim} \frac{1}{\rho(\mathbf{r})} \sum_\sigma |C_{0\sigma}(\mathbf{r})|^2 \left\{ \rho^{(N-1)}(\mathbf{r}') \right. \\ - 2 \operatorname{Re} \sum'_s \frac{1}{\omega_s} \left[\frac{D_{s0}(\hat{r})}{r^2} + \frac{Q_{s0}(\hat{r})}{r^3} \right] \rho_{s0}^{(N-1)}(\mathbf{r}') \\ + \sum'_{ss'} \frac{1}{\omega_s \omega_{s'}} \left[\frac{D_{s0}^*(\hat{r}) D_{s'0}(\hat{r})}{r^4} \right. \\ \left. + \frac{Q_{s0}^*(\hat{r}) Q_{s'0}(\hat{r})}{r^6} \right] \rho_{ss'}^{(N-1)}(\mathbf{r}'). \end{aligned} \quad (31)$$

For the systems considered, the leading term of $g(\mathbf{r}, \mathbf{r}')$ in the asymptotic limit is $\rho^{(N-1)}(\mathbf{r}')$, which is also a well-known result [11–13]. Here, we have provided the higher-order contributions.

Asymptotic Structure of the Electron-interaction Potential and Its Pauli and Coulomb Correlation Components

We begin this section by determining the asymptotic structure of the quantum mechanical electron-interaction component $W_{ee}(\mathbf{r})$ of the KS electron-interaction potential $\nu_{ee}(\mathbf{r})$. Substituting Eq. (31) for the pair-correlation density $g(\mathbf{r}, \mathbf{r}')$ into Eq. (6) for the electron-interaction field $\mathcal{E}_{ee}(\mathbf{r})$, we obtain

$$\mathcal{E}_{ee}(\mathbf{r}) \underset{r \rightarrow \infty}{\sim} -\nabla \left[\frac{N-1}{r} - \sum_s' \frac{D_{s0}^*(\hat{r}) D_{s0}(\hat{r})}{\omega_s} \frac{1}{r^4} \right], \quad (32)$$

to the accuracy of $O(1/r^6)$. Thus, asymptotically, the work done in this field is

$$W_{ee}(\mathbf{r}) \underset{r \rightarrow \infty}{\sim} \frac{N-1}{r} - \frac{\alpha}{2r^4}, \quad (33)$$

where

$$\alpha = 2 \sum_s' \frac{D_{s0}^*(\hat{r}) D_{s0}(\hat{r})}{\omega_s} \quad (34)$$

is the ground-state polarizability of the $(N-1)$ -electron system. Note that the result for $W_{ee}(\mathbf{r})$ is to the accuracy of $O(1/r^5)$. In other words, there are no $O(1/r^5)$ contributions to $\nu_{ee}(\mathbf{r})$ due to Pauli and Coulomb correlations. The results of Eqs. (32) and (33) are valid for when the N -electron system is either orbitally degenerate or nondegenerate.

We next determine the separate KS Pauli and Coulomb correlation contributions to the asymptotic structure of $W_{ee}(\mathbf{r})$. The pair-correlation density may also be expressed [3] as $g(\mathbf{r}, \mathbf{r}') = \rho(\mathbf{r}') + \rho_{xc}(\mathbf{r}, \mathbf{r}')$, where $\rho_{xc}(\mathbf{r}, \mathbf{r}')$ is the quantum mechanical Fermi–Coulomb hole charge. In turn, $\rho_{xc}(\mathbf{r}, \mathbf{r}')$ can be written [3] as $\rho_{xc}(\mathbf{r}, \mathbf{r}') = \rho_x^{KS}(\mathbf{r}, \mathbf{r}') + \rho_c^{KS}(\mathbf{r}, \mathbf{r}')$, where $\rho_x^{KS}(\mathbf{r}, \mathbf{r}')$ and $\rho_c^{KS}(\mathbf{r}, \mathbf{r}')$ are KS Fermi and Coulomb holes, respectively. The Fermi hole is expressed in terms of the KS orbitals $\phi_i(\mathbf{x})$ as $\rho_x^{KS}(\mathbf{r}, \mathbf{r}') = -|\gamma_s(\mathbf{r}, \mathbf{r}')|^2 / 2\rho(\mathbf{r})$. Thus [3], the

electron-interaction potential $W_{ee}(\mathbf{r}) = \nu_H(\mathbf{r}) + W_x^{KS}(\mathbf{r}) + W_c^{KS}(\mathbf{r})$, where

$$W_x^{KS}(\mathbf{r}) = - \int_{\infty}^{\mathbf{r}} \mathcal{E}_x^{KS}(\mathbf{r}') \cdot d\mathbf{l}' \text{ and} \\ \times W_c^{KS}(\mathbf{r}) = - \int_{\infty}^{\mathbf{r}} \mathcal{E}_c^{KS}(\mathbf{r}') \cdot d\mathbf{l}', \quad (35)$$

with

$$\mathcal{E}_x^{KS}(\mathbf{r}) = \int \frac{\rho_x^{KS}(\mathbf{r}, \mathbf{r}')(\mathbf{r} - \mathbf{r}')}{|\mathbf{r} - \mathbf{r}'|^3} d\mathbf{r}' \text{ and} \\ \mathcal{E}_c^{KS}(\mathbf{r}) = \int \frac{\rho_c^{KS}(\mathbf{r}, \mathbf{r}')(\mathbf{r} - \mathbf{r}')}{|\mathbf{r} - \mathbf{r}'|^3} d\mathbf{r}' \quad (36)$$

being the Pauli and Coulomb correlation fields, respectively. It is evident that the N/r term of $W_{ee}(\mathbf{r})$ of Eq. (33) of the KS potential $\nu_{ee}(\mathbf{r})$ is due to the Hartree potential $\nu_H(\mathbf{r})$.

Since in KS theory only the highest occupied orbital $\phi_N(\mathbf{x})$ contributes to the asymptotic structure, we have to exponential accuracy $\gamma_s(\mathbf{r}, \mathbf{r}') \sim \sum_{\sigma} \phi_N^*(\mathbf{r}\sigma) \phi_N(\mathbf{r}'\sigma)$. Thus, asymptotically,

$$\mathcal{E}_x^{KS}(\mathbf{r}) \underset{r \rightarrow \infty}{\sim} \frac{4}{2\rho(\mathbf{r})} |\phi_N(\mathbf{r})|^2 \left(\nabla \frac{1}{r} \right) \int |\phi_N(\mathbf{r}')|^2 d\mathbf{r}' \\ \underset{r \rightarrow \infty}{\sim} -\frac{\mathbf{r}}{r^3}, \quad (37)$$

so that

$$W_x^{KS}(\mathbf{r}) \underset{r \rightarrow \infty}{\sim} -\frac{1}{r} \quad (38)$$

to exponential accuracy. Thus, the $(-1/r)$ asymptotic structure of the KS electron-interaction potential $\nu_{ee}(\mathbf{r})$ is due entirely to Pauli correlations. As a consequence [and from Eqs. (33) and (38)], we have

$$W_c^{KS}(\mathbf{r}) \underset{r \rightarrow \infty}{\sim} -\frac{\alpha}{2r^4}, \quad (39)$$

so that the term of $O(1/r^4)$ in $\nu_{ee}(\mathbf{r})$ is strictly due to Coulomb correlations, arising from the KS Coulomb hole charge.

The Hartree $\nu_H(\mathbf{r})$ and Pauli $W_x^{KS}(\mathbf{r})$ potentials will have higher-order contributions for the case when the N -electron system is orbitally degenerate since the density $\rho(\mathbf{r})$ is no longer spherically sym-

metric. Expanding $1/|\mathbf{r} - \mathbf{r}'|$ in Legendre polynomials $P_n(x)$, we have

$$\nu_H(\mathbf{r}) \underset{r \rightarrow \infty}{\sim} \frac{N}{r} + \frac{Q}{r^3} + \frac{R}{r^5} + \dots \quad (40)$$

and

$$\mathcal{E}_x^{KS}(\mathbf{r}) \underset{r \rightarrow \infty}{\sim} -\frac{\mathbf{r}}{r^3} - \frac{3\mathbf{r}}{r^5} Q - \frac{5\mathbf{r}}{r^7} R + \dots, \quad (41)$$

so that

$$W_x^{KS}(\mathbf{r}) \underset{r \rightarrow \infty}{\sim} -\frac{1}{r} - \frac{Q}{r^3} - \frac{R}{r^5} + \dots, \quad (42)$$

where

$$Q = \int \rho(\mathbf{r}') r'^2 P_2(\cos \theta') d\mathbf{r}', \quad (43)$$

$$R = \int \rho(\mathbf{r}') r'^4 P_4(\cos \theta') d\mathbf{r}'. \quad (44)$$

Note that the terms of $O(1/r^3)$ and $O(1/r^5)$ in $\nu_H(\mathbf{r})$ and $W_x^{KS}(\mathbf{r})$ cancel out. Thus, for both the orbitally degenerate and nondegenerate N -electron systems, the asymptotic structure of $W_c^{KS}(\mathbf{r})$ is the same to $O(1/r^5)$ and is given by Eq. (39).

Asymptotic Structure of the Correlation-Kinetic Potential $W_{t_c}(\mathbf{r})$

In this section, we determine the asymptotic structure of the correlation-kinetic field $\mathbf{Z}_{t_c}(\mathbf{r})$ and potential $W_{t_c}(\mathbf{r})$. These results have been previously derived by us [7], employing quasiparticle amplitudes, and the physics and details of the calculations are the same. Primarily, the asymptotic structure of the density $\rho(\mathbf{r})$ and idempotent density matrix $\gamma_s(\mathbf{r}, \mathbf{r}')$ are governed by the highest occupied KS orbital $\phi_N(\mathbf{x})$. Since the densities of the interacting and noninteracting systems are the same, the asymptotic structure of $\phi_N(\mathbf{r})$ is obtained from Eq. (27) as [8, 11, 13]

$$\begin{aligned} \phi_N(\mathbf{r}) &= \sqrt{N} \sum_{\sigma} |C_{0\sigma}(\mathbf{r})| \\ &\times \left\{ 1 + \sum_s' \frac{1}{\omega_s^2} \left[\frac{|D_{s0}(\hat{r})|^2}{r^4} + \frac{|Q_{s0}(\hat{r})|^2}{r^6} \right] \right\}^{1/2}. \end{aligned} \quad (45)$$

The asymptotic structure of $\gamma_s(\mathbf{r}, \mathbf{r}')$ is thus known. With that of $\gamma(\mathbf{r}, \mathbf{r}')$ given by Eq. (26), the asymp-

totic structure of the field $\mathbf{Z}_{t_c}(\mathbf{r})$ of Eq. (8) is derived to be

$$\mathbf{Z}_{t_c}(\mathbf{r}) \underset{r \rightarrow \infty}{\sim} \frac{8\kappa_0 \chi \mathbf{r}}{r^7}, \quad (46)$$

where $\kappa_0^2/2 = E_0^{(N-1)} - E_0$ is the ionization potential and χ is an expectation of the spherically symmetric $(N-1)$ -electron system defined by $\chi_{\alpha\beta} = \chi \delta_{\alpha\beta}$, where

$$\chi_{\alpha\beta} = \left\langle \Psi_0^{(N-1)} \left| \mathbf{d}_{\beta} \frac{1 - \hat{P}}{[\hat{H} - E_0^{(N-1)}]^2} \mathbf{d}_{\alpha} \right| \Psi_0^{(N-1)} \right\rangle \quad (47)$$

and where the operator \mathbf{d} and \hat{P} are defined in the Single-particle Density Matrix section. Thus, the correlation-kinetic component of the KS potential $\nu_{ee}(\mathbf{r})$ decays asymptotically as

$$W_{t_c}(\mathbf{r}) \underset{r \rightarrow \infty}{\sim} \frac{8\kappa_0 \chi}{5r^5}. \quad (48)$$

Conclusions

There are two facets to this article: First, we have derived the asymptotic structure of the wave function, single-particle density matrix, the density, and pair-correlation density in the classically forbidden region of atoms. The results are specific to those atoms for which the N -electron system maybe orbitally degenerate, but the $(N-1)$ -electron system is orbitally nondegenerate. The derivation differs from as well as goes beyond that of previous work in that higher-order quadrupole moment terms are included. In the second part of the article, we employed these expressions within the exact description of KS theory in terms of the wave function Ψ to derive the analytical asymptotic structure of the KS exchange-correlation potential to terms of $O(1/r^5)$. Although terms of $O(1/r^4)$ have been obtained previously, the present derivation provides an independent confirmation of these results. However, the derivation via this interpretation provides the understanding that the $O(1/r)$ term is due to Pauli correlations; that of $O(1/r^4)$, to Coulomb correlations; and that of $O(1/r^5)$, to correlation-kinetic effects. For systems for which the N -electron atom is orbitally degenerate, Pauli correlations also contribute terms of $O(1/r^3)$ and $O(1/r^5)$. There are no quantum me-

chanical Coulomb correlation contributions to $O(1/r^5)$. For these rigorous assignations to be made, it was necessary to expand the wave function, density matrix, etc., to include terms up to the quadrupole moment. We note that the asymptotic structure derived is valid for the Coulomb external potential. For external potentials that are not Coulombic, such as in the Hooke's atom model [4], the asymptotic structure is different. The present procedure can be extended to systems where the $(N - 1)$ -electron system is degenerate, in which case the asymptotic structure will have an angular dependence [12]. We expect to extend our calculations to such systems in the future.

The KS exchange-correlation potential $\nu_{xc}(\mathbf{r})$ is also conventionally written as a sum of its exchange $\nu_x(\mathbf{r})$ and correlation $\nu_c(\mathbf{r})$ potentials, where $\nu_x(\mathbf{r}) = \delta E_x^{KS}[\rho]/\delta\rho(\mathbf{r})$ and $\nu_c = \delta E_c^{KS}[\rho]/\delta\rho(\mathbf{r})$, and $E_x^{KS}[\rho]$ and $E_c^{KS}[\rho]$ are the KS exchange and correlation energy functionals, respectively. Recently, it has been shown [14] that

$$\nu_x(\mathbf{r}) = W_x^{KS}(\mathbf{r}) - W_{t_c}^{(1)}(\mathbf{r}), \quad (49)$$

where $W_{t_c}^{(1)}(\mathbf{r})$ is the work done in the field $\mathbf{Z}_{t_c}^{(1)}(\mathbf{r}) = \mathbf{z}(\mathbf{r}; [\gamma_1^c])/\rho(\mathbf{r})$, with $\gamma_1^c(\mathbf{r}, \mathbf{r}')$ being the first-order correction to the KS density matrix $\gamma_s(\mathbf{r}, \mathbf{r}')$ as obtained via adiabatic connection perturbation theory by an expansion of the system wave function in terms of the electron-interaction coupling constant at fixed electron density. The sum of the work $[W_x^{KS}(\mathbf{r}) - W_{t_c}^{(1)}(\mathbf{r})]$ is path-independent. Thus, $\nu_c(\mathbf{r}) = W_c^{KS}(\mathbf{r}) + W_{t_c}^{(1)}(\mathbf{r}) + W_{t_c}^{(1)}(\mathbf{r})$. Solomatin and Sahni [15] studied the field $\mathbf{Z}_{t_c}^{(1)}(\mathbf{r})$ and potential $W_{t_c}^{(1)}(\mathbf{r})$ in atoms numerically and showed them to be of much shorter range than $\mathcal{E}_x^{KS}(\mathbf{r})$ and $W_x^{KS}(\mathbf{r})$, vanishing within the last occupied shell. However, for the nonuniform electron gas at a metal surface, these authors determined [15–18] the potentials $\nu_x(\mathbf{r})$, $W_x^{KS}(\mathbf{r})$, and $W_{t_c}^{(1)}(\mathbf{r})$ analytically and showed that $W_{t_c}^{(1)}(\mathbf{r})$ is long-ranged both in the classically forbidden vacuum region as well as in the metal bulk. We are presently working on determining the analytical asymptotic structure of $W_{t_c}^{(1)}(\mathbf{r})$ and that of the higher-order contributions to $\nu_c(\mathbf{r})$ in atoms.

Finally, the results derived help explain the accuracy of the results [3, 19] for the ionization potential of atoms as obtained by the highest occupied eigenvalue of the Work-Hartree-Fock approximation [19, 20]. In the Work-Hartree-Fock

approximation, the KS exchange-correlation potential $\nu_{xc}(\mathbf{r})$ is replaced by the work $W_x(\mathbf{r})$ done in the field $\mathcal{E}_x(\mathbf{r})$ of the Fermi hole generated by the corresponding differential equation. The highest occupied eigenvalue of the KS equation is [8, 13, 21] (minus) the ionization potential. Further, this eigenvalue is governed principally by the asymptotic structure of $\nu_{xc}(\mathbf{r})$. Now, since Coulomb correlation and correlation-kinetic effects are of $O(1/r^4)$ and $O(1/r^5)$, respectively, the asymptotic structure of $\nu_{xc}(\mathbf{r}) \sim W_x^{KS}(\mathbf{r})$. Thus, the asymptotic structure of $\nu_{xc}(\mathbf{r}) \xrightarrow{r \rightarrow \infty}$ is determined exactly by solving the Work-Hartree-Fock differential equation. This then explains why the highest occupied eigenvalue of this differential equation closely approximates the experimental [19] ionization potential. For a comparison of the highest occupied Work-Hartree-Fock eigenvalues to those of exact KS theory, see [3].

ACKNOWLEDGMENT

This work was supported in part by a grant from the Research Foundation of the City University of New York.

References

1. P. Hohenberg and W. Kohn, Phys. Rev. B **136**, 864 (1964); W. Kohn and L. J. Sham, Phys. Rev. A **140**, 1133 (1965).
2. R. G. Parr and W. Yang, *Density Functional Theory of Atoms and Molecules* (Oxford University Press, Oxford, 1989); R. M. Dreizler and E. K. U. Gross, *Density Functional Theory* (Springer-Verlag, Berlin, 1990); N. H. March, *Electron Density Theory of Atoms and Molecules* (Academic Press, London, 1992).
3. V. Sahni, Phys. Rev. A **55**, 1846 (1997); V. Sahni, in *Density Functional Theory III, Topics in Current Chemistry* Vol. 182, R. Nalewajski, Ed. (Springer-Verlag, Heidelberg, 1996).
4. Z. Qian and V. Sahni, Phys. Rev. A **57**, 2527 (1998).
5. M. K. Harbola and V. Sahni, Phys. Rev. Lett. **62**, 489 (1989); V. Sahni and M. K. Harbola, Int. J. Quantum Chem. Symp. **24**, 569 (1990).
6. A. Holas and N. H. March, Phys. Rev. A **51**, 2040 (1995).
7. Z. Qian and V. Sahni, Phys. Rev. A **57**, 4041 (1998).
8. C.-O. Almbladh and U. von Barth, Phys. Rev. B **31**, 3231 (1985); A. R. Williams and U. von Barth, in *Theory of the Inhomogeneous Electron Gas*, S. Lundqvist and N. H. March, Eds. (Plenum, New York, 1983).
9. C. J. Umrigar and X. Gonze, Phys. Rev. A **50**, 3827 (1994).
10. L. J. Sham, Phys. Rev. B **32**, 3876 (1985).

11. J. Katriel and E. R. Davidson, Proc. Natl. Acad. Sci. U.S.A. **77**, 4403 (1980); Y. Tal and R. F. Bader, Int. J. Quantum Chem. Symp. **12**, 153 (1978); N. H. March, Phys. Lett. **84**, 319 (1981); N. H. March and R. Pucci, J. Chem. Phys. **75**, 496 (1981).
12. M. Ernzerhof, K. Burke, and J. P. Perdew, J. Chem. Phys. **105**, 2798 (1996).
13. M. Levy, J. P. Perdew, and V. Sahni, Phys. Rev. A **30**, 2745 (1984).
14. M. Levy and N. H. March, Phys. Rev. A **55**, 1885 (1997).
15. A. Solomatin and V. Sahni, Int. J. Quantum Chem. **65**, 893 (1997).
16. V. Sahni, Prog. Surf. Sci. **54**, 115 (1997).
17. A. Solomatin and V. Sahni, Phys. Rev. B **56**, 3655 (1997); *Ibid.*, Ann. Phys. **259**, 97 (1997); *Ibid.*, Phys. Lett. A **212**, 263 (1996).
18. A. Solomatin and V. Sahni, Ann. Phys. (1998).
19. V. Sahni, Y. Li, and M. K. Harbola, Phys. Rev. A **45**, 1434 (1992).
20. V. Sahni, Int. J. Quantum Chem., **56**, 265 (1995); J. L. Calais and E. Kryachko, Eds., *Structure and Dynamics of Atoms and Molecules: Conceptual Trends*, (Kluwer, Dordrecht, 1995).
21. J. P. Perdew, R. G. Parr, M. Levy, and J. L. Balduz, Phys. Rev. Lett. **49**, 1691 (1982).

Excited States in Density Functional Theory

Á. NAGY

Institute of Theoretical Physics, Kossuth Lajos University, H-4010 Debrecen, Hungary

Received 21 February 1998; revised 20 April 1998; accepted 20 April 1998

ABSTRACT: Density functional theory for a single excited state is presented using Kato's theorem and the concept of adiabatic connection. The degenerate case is also detailed. The optimized potential method is generalized. The generalized Krieger, Li, and Iafrate (KLI) approximation is derived. © 1998 John Wiley & Sons, Inc. *Int J Quant Chem* 70: 681–691, 1998

Key words: excited states; Kato's theorem; adiabatic connection; optimized potential method; KLI approximation

1 Introduction

Density functional theory was originally developed for the ground state [1]. It has been generalized for the lowest energy state in each symmetry class [2, 3]. To calculate excitation energies Slater [4] introduced the so-called transition-state method. The density functional theory was first rigorously generalized for excited states by Theophilou [5]. Formalisms for excited states have also been provided by Fritsche [6] and English et al. [7]. A more general treatment was given by Gross et al. [8]. Several calculations have been done with this method [9–15]. The relativistic generalization of this formalism has also been done [16]. The optimized potential method has recently

been generalized for ensembles of excited states [17]. The ensemble theory has the disadvantage that one has to calculate all the ensemble energies lying under the given ensemble energy to obtain the desired excitation energy. It is especially inconvenient to use it if one is interested in highly excited states.

An alternative theory, worth mentioning, is time-dependent density functional theory (TD DFT) [18, 19] in which transition energies are obtained from the poles of dynamic linear response properties. While TD DFT cannot obtain the energies and properties of excited states directly, it is complementary to the ensemble method and the approach to excited states presented here.

The work formalism proposed by Sahni and co-workers [20] has also been applied in excited-state density functional calculations [21].

Recently, Görling [22] presented a new density functional formalism for excited states generalizing a recent perturbation theory [23].

Contract grant sponsor: Hungarian Ministry of Culture and Education.

Contract grant numbers: OTKA No. T 16623; FKFP 0314/1997.

It is also possible, however, to treat a single excited state in the density functional theory. This approach is based on Kato's theorem [24] and is valid for Coulomb external potential (i.e., atoms, molecules, and solids).

The outline of this study is as follows: In Section 2 the ensemble theory of excited states is summarized. In Section 3 Görling's theory for excited states via adiabatic connection and perturbation theory is outlined. Section 4 introduces a new method treating a single excited state. Section 4.1 presents this new approach of density functional theory of excited states utilizing Kato's theorem and the concept of the adiabatic connection. In Section 4.2 important expressions for the coupling-constant-dependent energies and potentials are derived. Section 4.3 addresses the problem of degenerate states. The optimized potential method is presented in Section 4.4. A generalized Krieger, Li, and Iafrate (KLI) potential is derived in Section 4.5. Section 4.6 presents several illustrative examples. Some important points of the different approaches described in this work are discussed in Section 5.

2 Review of Ensemble Density Functional Theory for Excited States

First, the ensemble theory of Gross, Oliveira, and Kohn [8] is summarized. The eigenvalue problem of the Hamiltonian \hat{H} is given by

$$\hat{H}\Psi_k = E_k\Psi_k, \quad (k = 1, \dots, M), \quad (1)$$

where

$$E_1 \leq E_2 \leq \dots \quad (2)$$

are the energy eigenvalues. The generalized Rayleigh–Ritz variational principle [8] can be applied to the ensemble energy

$$\mathcal{E} = \sum_{k=1}^M w_k E_k, \quad (3)$$

where $w_1 \geq w_2 \geq \dots \geq w_M \geq 0$. The weighting factors w_i are chosen as

$$w_1 = w_2 = \dots = w_{M-g} = \frac{1-wg}{M-g}, \quad (4)$$

$$w_{M-g+1} = w_{M-g+2} = \dots = w_M = w, \quad (5)$$

$$0 \leq w \leq \frac{1}{M}, \quad (6)$$

and

$$1 \leq g \leq M-1. \quad (7)$$

The limit $w = 0$ corresponds to the eigenensemble of $M-g$ states ($w_1 = \dots = w_{M-g} = 1/(M-g)$ and $w_{M-g+1} = \dots = w_M = 0$). The case $w = 1/M$ leads to the eigenensemble of M states ($w_1 = w_2 = \dots = w_M = 1/M$). The generalized Hohenberg–Kohn theorems read as follows:

1. The external potential $v(\mathbf{r})$ is determined within a trivial additive constant, by the ensemble density n defined as

$$n = \sum_{k=1}^M w_k n_k. \quad (8)$$

2. For a trial ensemble density $n'(\mathbf{r})$ such that

$$n'(\mathbf{r}) \geq 0 \quad (9)$$

and

$$\int n'(\mathbf{r}) d\mathbf{r} = N, \quad (10)$$

$$\mathcal{E}[n] \leq \mathcal{E}[n']. \quad (11)$$

The ensemble functional \mathcal{E} takes its minimum at the correct ensemble density n . Using the variation principle, the Euler equation can be obtained:

$$\frac{\delta \mathcal{E}}{\delta n} = \mu. \quad (12)$$

Kohn–Sham equations for the ensemble can also be derived:

$$\left[-\frac{1}{2}\nabla^2 + v_{\text{KS}} \right] u_i(\mathbf{r}) = \epsilon_i u_i(\mathbf{r}). \quad (13)$$

The ensemble Kohn–Sham potential

$$v_{\text{KS}}(\mathbf{r}; n_w) = v(\mathbf{r}) + \int \frac{n_w(\mathbf{r}')}{|\mathbf{r} - \mathbf{r}'|} d\mathbf{r}' + v_{\text{xc}}(\mathbf{r}; w, n_w) \quad (14)$$

is a functional of the ensemble density

$$\begin{aligned} n_w^I(\mathbf{r}) &= \frac{1-wg_I}{M_{I-1}} \sum_{m=1}^{M_{I-g_I}} \sum_j \lambda_{mj} |u_j(\mathbf{r})|^2 \\ &\quad + w \sum_{m=M_{I-g_I}+1}^{M_I} \sum_j \lambda_{mj} |u_j(\mathbf{r})|^2, \end{aligned} \quad (15)$$

where g_I is the degeneracy of the I th multiplet.

$$M_I = \sum_{i=1}^I g_i \quad (16)$$

is the multiplicity of the ensemble and

$$0 \leq w \leq 1/M_I. \quad (17)$$

λ_{mj} are the occupation numbers. The ensemble exchange–correlation potential v_{xc} is the functional derivative of the ensemble exchange–correlation energy functional E_{xc}

$$v_{xc}(\mathbf{r}; w, n) = \frac{\delta E_{xc}[n, w]}{\delta n(r)}. \quad (18)$$

Using the Hellmann–Feynmann theorem for the ensemble [12], the adiabatic connection formula for the ensemble exchange–correlation energy can be derived [12].

3 Review of Adiabatic Connection and Perturbation Density Functional Theory for Excited States

Recently, Görling [22] has shown that the density functional theory can be extended to excited states via the adiabatic connection and making use of perturbation theory [23]. The adiabatic connection characterized by the Schrödinger equation

$$\hat{H}^\alpha |\Psi_k^\alpha\rangle = E_k^\alpha |\Psi_k^\alpha\rangle, \quad (19)$$

$$\hat{H}^\alpha = \hat{T} + \alpha \hat{V}_{ee} + \hat{V}_\alpha \quad (20)$$

represents a continuous connection between a non-interacting system and the real system. Here not only the ground-state but also the k th eigenstate Ψ_k^α of the coupling constant Hamiltonian is considered. The additional assumption here is that the energetic order of eigenstates Ψ_k^α of \hat{H}^α of the same symmetry is preserved along the adiabatic connection. So the coupling constant path establishes a continuous connection between the k th eigenstates of the noninteracting and interacting Hamiltonians. The energy of the k th eigenstate

$$E_k^\alpha = \langle \Phi_k[n_0] | \hat{T} | \Phi_k[n_0] \rangle + J_k[n_0] + E_{x,k}[n_0] + E_{c,k}^\alpha[n_0] + \int v^\alpha(\mathbf{r}) n_k^0(\mathbf{r}) d\mathbf{r} \quad (21)$$

is a functional of the ground-state density n_0 which is kept fixed in the coupling-constant path.

In order to treat excited states in the Kohn–Sham formalism, first, the ground-state Kohn–Sham equations have to be solved, i.e., the ground-state one-electron energies and orbitals have to be determined. To obtain the excited-state exchange and correlation energy functionals, $E_{x,k}[n_0]$ and $E_{c,k}^\alpha[n_0]$, the density functional perturbation theory can be applied. It has already been shown by several authors (see, e.g., [19]) that the ground-state one-electron energies are not just auxiliary quantities without physical meaning. Görling [22] pointed out that their difference provides zeroth-order approximation to excitation energies.

Table I presents excitation energies in this zeroth-order approximation for a couple of atoms. Calculations were performed using a method of the author for determining the potential if the density is available [25]. Hartree–Fock densities [26] were applied. For comparison Hartree–Fock values are also presented. Recently, excitation energies for certain atoms and ions have been calculated in first-order coupling-constant perturbation theory [27].

4 Density Functional Theory for a Single Excited State

The ground-state density functional theory states that a knowledge of the ground-state electron density is sufficient in principle to determine all molecular properties. This can be simply understood following Bright Wilson's [28] argument: A well-known theorem of quantum mechanics, Kato's theorem [24] states that

$$Z_\beta = -\frac{1}{2n(r)} \left. \frac{\partial n(r)}{\partial r} \right|_{r=R_\beta}, \quad (22)$$

where the partial derivatives are taken at the nuclei β . So the cusps of the density tell us where the nuclei are (R_β) and what the atomic numbers Z_β are. On the other hand, the integral of the density

TABLE I
Hartree–Fock and exchange-only density functional excitation energies (in Ry).

	HF	DF
Li($2s^1 \rightarrow 2p^1$)	0.1353	0.1342
Na($3s^1 \rightarrow 3p^1$)	0.1450	0.1462
K($4s^1 \rightarrow 4p^1$)	0.1033	0.1024
K($4s^1 \rightarrow 3d^1$)	0.1782	0.1785

gives us the number of electrons:

$$N = \int n(\mathbf{r}) d\mathbf{r}. \quad (23)$$

Thus from the density the Hamiltonian can be readily obtained from which every property can be determined. Of course, the Bright Wilson's argument does not apply to, e.g., a molecule in a uniform electric field, since the field itself is not identified by a cusp in the density.

Kato's theorem is valid not only for the ground state but also for the excited states. In the following we use it to obtain a density functional theory for a single excited state.

4.1 DENSITY FUNCTIONAL THEORY FOR A SINGLE EXCITED STATE USING KATO'S THEOREM AND THE CONCEPT OF ADIABATIC CONNECTION

As Kato's theorem holds also for excited states, if the density n_i of the i th electron states is known, the Hamiltonian \hat{H} is also in principle known and its eigenvalue problem

$$\hat{H}\Psi_k = E_k\Psi_k, \quad (k = 1, \dots, i, \dots) \quad (24)$$

can be solved.

The adiabatic connection [2, 29] is a key concept in the density functional theory. This will be now applied for a single excited state. It is not only supposed that the electron density is the same for both the interacting and noninteracting systems, but there exists a continuous path between them. A coupling-constant path is defined by the Schrödinger equation

$$\hat{H}_i^\alpha\Psi_k^\alpha = E_k^\alpha\Psi_k^\alpha, \quad (25)$$

where

$$\hat{H}_i^\alpha = \hat{T} + \alpha\hat{V}_{ee} + \hat{V}_i^\alpha. \quad (26)$$

The subscript i denotes that the density of the given excited state is supposed to be the same for any value of the coupling constant α ; $\alpha = 1$ corresponds to the fully interacting case, while $\alpha = 0$ gives the Kohn–Sham system:

$$\hat{H}_i^0\Psi_k^0 = E_k^0\Psi_k^0. \quad (27)$$

For $\alpha = 1$ the Hamiltonian \hat{H}_i^α is independent of i . For any other values of α the "adiabatic" Hamiltonian depends on i , we have different Hamiltonians

for different excited states. Thus even the Kohn–Sham Hamiltonian, the one corresponding to the noninteracting ($\alpha = 0$) case is different for different excited states.

In the ground-state density functional theory the first Hohenberg–Kohn theorem [1] states that the external potential $v(\mathbf{r})$ is determined within a trivial additive constant by the knowledge of the electron density $n(\mathbf{r})$. As we have seen, the present theory also provides the external potential $v(\mathbf{r})$ if the density $n_i(\mathbf{r})$ of the i th excited state is known. Through the adiabatic connection the Kohn–Sham equations and the Kohn–Sham potential are also constructed.

4.2 EXPRESSIONS FOR THE COUPLING-CONSTANT-DEPENDENT ENERGIES AND POTENTIALS

Following the ground-state definitions [23, 30], the correlation energy is defined:

$$E_c^\alpha[n_i] = [\langle\Psi_i^\alpha|\hat{T}|\Psi_i^\alpha\rangle - \langle\Psi_i^0|\hat{T}|\Psi_i^0\rangle] + \alpha[\langle\Psi_i^\alpha|\hat{V}_{ee}|\Psi_i^\alpha\rangle - \langle\Psi_i^0|\hat{V}_{ee}|\Psi_i^0\rangle]. \quad (28)$$

It can also be written as

$$E_c^\alpha[n_i] = F^\alpha[n_i] - F^0[n_i] - \alpha(U[n_i] + E_x[n_i]), \quad (29)$$

where the functional $F^\alpha[n_i]$ is defined:

$$F^\alpha[n_i] = T\langle\Psi_i^\alpha|\hat{T} + \alpha\hat{V}_{ee}|\Psi_i^\alpha\rangle. \quad (30)$$

The classical Coulomb and the exchange energies are given by

$$U[n_i] = \frac{1}{2} \int \frac{n_i(\mathbf{r}_1)n_i(\mathbf{r}_2)}{r_{12}} d\mathbf{r}_1 d\mathbf{r}_2 \quad (31)$$

and

$$E_x[n_i] = (\langle\Psi_i^0|\hat{V}_{ee}|\Psi_i^0\rangle - U[n_i]), \quad (32)$$

respectively. The energy $E^\alpha[n_i]$ can be expressed in the following way:

$$E^\alpha[n_i] = \langle\Psi_i^\alpha|\hat{H}^\alpha|\Psi_i^\alpha\rangle = \langle\Psi_i^\alpha|\hat{T} + \alpha\hat{V}_{ee}|\Psi_i^\alpha\rangle + \int v_i^\alpha(\mathbf{r})n_i(\mathbf{r}) d\mathbf{r}. \quad (33)$$

Equations (30) and (33) lead to the Hamiltonian:

$$\begin{aligned}\hat{H}_i^\alpha &= \hat{T} + \alpha \hat{V}_{ee} \\ &\quad + \sum_{k=1}^N \left[v(\mathbf{r}_k) + \frac{\delta(F^1[n_i] - F^\alpha[n_i])}{\delta n(\mathbf{r}_k)} \right] \\ &= \hat{T} + \alpha \hat{V}_{ee} \\ &\quad + \sum_{k=1}^N \left[v(\mathbf{r}_k) + (1 - \alpha)(v_F^i(\mathbf{r}_k) + v_x^i(\mathbf{r}_k)) \right. \\ &\quad \left. + \frac{\delta E_c^{\alpha=1}[n_i]}{\delta n(\mathbf{r}_k)} - \frac{\delta E_c^\alpha[n_i]}{\delta n(\mathbf{r}_k)} \right] \\ &= \hat{T} + \alpha \hat{V}_{ee} + \sum_{k=1}^N v_i^\alpha(\mathbf{r}_k),\end{aligned}\quad (34)$$

where

$$\begin{aligned}v_i^\alpha(\mathbf{r}) &= v_{i0}(\mathbf{r}) - \alpha(v_F^i(\mathbf{r}) + v_x^i(\mathbf{r})) \\ &\quad + \frac{\delta E_c^{\alpha=1}[n_i]}{\delta n(\mathbf{r})} - \frac{\delta E_c^\alpha[n_i]}{\delta n(\mathbf{r})}.\end{aligned}\quad (35)$$

v_F^i and v_x^i are the classical Coulomb and the exchange potentials

$$v_F^i(\mathbf{r}) = \int \frac{n_i(\mathbf{r}')}{|\mathbf{r} - \mathbf{r}'|} d\mathbf{r}' \quad (36)$$

and

$$v_x^i(\mathbf{r}) = \frac{\delta E_x[n_i]}{\delta n(\mathbf{r})}, \quad (37)$$

respectively. v_i^0 is the Kohn–Sham potential of the noninteracting system corresponding to the excited state considered.

4.3 DEGENERATE EXCITED STATE

All stated above in this section is valid for both degenerate and nondegenerate excited state. For a degenerate excited state starting out from a density n_i , we can determine the Hamiltonian \hat{H} , and we find out that there are several eigenfunctions with energy E_i . But, the densities corresponding to these eigenfunctions are different. The concept of adiabatic connection can be applied as for the nondegenerate state.

However, concerning the approximations one inevitably should apply in actual calculations, a slightly different approach may be more useful. This approach that has been already proposed for

the ground state [31] is based on using density matrices instead of the density.

Consider the solutions of the symmetry Γ of the Schrödinger equation:

$$\hat{H}|\Psi_\gamma^i\rangle = E^i|\Psi_\gamma^i\rangle, \quad (\gamma = 1, 2, \dots, g_i), \quad (38)$$

where g_i is the degeneracy. Instead of treating one wave function Ψ_γ^i , the density matrix defined in subspace S^i

$$\hat{D}^i = \sum_{\gamma=1}^{g_i} w_\gamma |\Psi_\gamma^i\rangle\langle\Psi_\gamma^i|, \quad (39)$$

is introduced, where the weighting factors w_γ^i should satisfy the conditions

$$1 = \sum_{\gamma=1}^{g_i} w_\gamma^i \quad (40)$$

and

$$w_\gamma^i \geq 0. \quad (41)$$

In principle, any set of weighting factors w_γ^i satisfying conditions (40) and (41) can be used. The subspace density is defined as

$$n^i = \sum_{\gamma=1}^{g_i} w_\gamma^i \int |\Psi_\gamma^i|^2 ds_1 d\mathbf{x}_2, \dots, d\mathbf{x}_N, \quad (42)$$

where \mathbf{x} stands for both the coordinates and the spin. The superscript i in n^i and the subspace density matrix denotes that they are constructed from wave functions that belong to the subspace S^i . One is free to select the values of the weighting factors w_γ^i ; they only should satisfy the conditions (40) and (41). If the weighting factors w_γ^i are all equal, the density has the property of transforming according to the totally symmetric irreducible representation. So, for instance, for atoms the density will be spherically symmetric. But it is possible to select other values for the weighting factors w_γ^i .

This approach has the advantage that with equal weighting factors the density has the symmetry of the external potential.

The concept of adiabatic connection can also be applied for the subspace density n^i . It is supposed that the subspace density is the same in the coupling-constant path. Now, the Schrödinger equa-

tion has the form

$$\hat{H}_i^\alpha |\Psi_\gamma^{i,\alpha}\rangle = E^{i,\alpha} |\Psi_\gamma^{i,\alpha}\rangle, \quad (\gamma = 1, 2, \dots, g_i), \quad (43)$$

where

$$\hat{H}_i^\alpha = \hat{T} + \alpha \hat{V}_{ee} + \hat{V}_i^\alpha. \quad (44)$$

The subscript i denotes that the subspace density n^i is supposed to be the same for any value of the coupling constant α ; $\alpha = 1$ corresponds to the fully interacting case, while $\alpha = 0$ gives the Kohn–Sham system:

$$\hat{H}_i^0 |\Psi_\gamma^{i,0}\rangle = E^{i,0} |\Psi_\gamma^{i,0}\rangle, \quad (\gamma = 1, 2, \dots, g_i). \quad (45)$$

For $\alpha = 1$ the Hamiltonian \hat{H}_i^α is independent of i . For any other values of α the adiabatic Hamiltonian depends on i . Thus the Kohn–Sham Hamiltonian is different for different degenerate excited states.

4.4 OPTIMIZED POTENTIAL METHOD

In order to perform calculations, one needs explicit expressions for the functionals. In the ground-state theory, exchange can be treated exactly via the optimized potential method [32]. Now, this method is generalized for a single excited state.

In the optimized potential method the following problem is solved: Find the potential such that when it is given a small variation, the energy of the system remains stationary. It can also be written as

$$\frac{\delta E}{\delta V} = 0. \quad (46)$$

Now, we show that from the fact that the energy is stationary at the true wave function it follows that the energy is stationary at the true potential. It is well-known that considering the energy as a functional of the wave function $E[\Psi]$, the eigenvalues of the Hamiltonian are stationary points of E :

$$\frac{\delta E}{\delta \Psi_k} = 0, \quad (k = 1, \dots, i, \dots), \quad (47)$$

and only the eigenvalues are stationary points.

From our arguments above from the density of a given excited state n_i , one can obtain the Hamil-

tonian, the eigenvalues, and eigenfunctions and through adiabatic connection the Kohn–Sham potential $V_i^{\alpha=0}$, and certainly the solution of the Kohn–Sham equations leads to the density n_i :

$$n_i \rightarrow \hat{H} \rightarrow E_k, \Psi_k (k = 1, \dots, i, \dots) \rightarrow V_i^0 \rightarrow n_i. \quad (48)$$

Thus, we can consider the total energy as a functional of the Kohn–Sham potential:

$$E[\Psi_i] = E[\Psi_i[V_i^0]]. \quad (49)$$

Making use of Eq. (47) we obtain

$$\frac{\delta E}{\delta V_i^0} = \int \frac{\delta E}{\delta \Psi_i} \frac{\delta \Psi_i}{\delta V_i^0} + \text{c.c.} = 0. \quad (50)$$

Thus, from the fact the energy is stationary at the true wave function follows that the energy is stationary at the true potential.

The fact, however, that the energy is only stationary and not minimum at the true density makes it more difficult to find adequate approximations. The Kohn–Sham wave function should be orthogonal to the exact Kohn–Sham wave function(s) of the lower state(s). Since the exact Kohn–Sham wave functions are not known, one is satisfied if approximate orthogonality with respect to the approximate lower Kohn–Sham wave function(s) is assured.

In the ground-state theory exchange can be treated exactly via the optimized potential method [32]. Now, this method is generalized for excited states. Following the usual method [32] deriving the optimal potential, the well-known integral equation for the effective exchange potential V_x can be obtained.

The total energy E_i is considered as a functional of the one-electron orbitals u_j^i , which are eigenfunctions of the local effective potential V_i^0 :

$$\hat{h}_i u_j^i = \left(-\frac{1}{2} \nabla^2 + V_i^0 \right) u_j^i = \epsilon_j^i u_j^i. \quad (51)$$

From Eq. (50) we obtain

$$\frac{\delta E_i}{\delta V_i^0} = \sum_j \int \frac{\delta E_i}{\delta u_j^{i*}(\mathbf{r}')} \frac{\delta u_j^{i*}(\mathbf{r}')}{\delta V_i^0(\mathbf{r})} d\mathbf{r}' + \text{c.c.} = 0. \quad (52)$$

The functional derivative of the one-electron orbitals u_j with respect to the local effective potential V_i^0 can be calculated with the help of Green's

function:

$$\frac{\delta u_j^{i*}(\mathbf{r}')}{\delta V_i^0(\mathbf{r})} = -G_j^i(\mathbf{r}', \mathbf{r}) u_j^i(\mathbf{r}), \quad (53)$$

$$(\hat{h}_i - \epsilon_j^i) G_j^i(\mathbf{r}', \mathbf{r}) = \delta(\mathbf{r} - \mathbf{r}') - u_j^i(\mathbf{r}) u_j^{i*}(\mathbf{r}'). \quad (54)$$

Using Eqs. (51)–(54) an integral equation for the effective exchange–correlation potential v_{xc}^i follows:

$$\int L_j^i(\mathbf{r}, \mathbf{r}') v_{xc}^i(\mathbf{r}') d\mathbf{r}' = Q^i(\mathbf{r}), \quad (55)$$

$$L^i(\mathbf{r}, \mathbf{r}') = \sum_j u_j^{i*}(\mathbf{r}) G_j^i(\mathbf{r}, \mathbf{r}') u_j^i(\mathbf{r}'), \quad (56)$$

$$Q^i(\mathbf{r}) = \sum_j \int d\mathbf{r}' u_j^{i*}(\mathbf{r}) G_j^i(\mathbf{r}, \mathbf{r}') v_{xc,j}^i(\mathbf{r}') u_j^i(\mathbf{r}'). \quad (57)$$

The orbital dependent potential $v_{xc,j}^i$ is given by

$$v_{xc,j}^i(\mathbf{r}) = \frac{\delta E_{xc,i}[u_j^i]}{u_j^i(\mathbf{r}) \delta u_j^{i*}(\mathbf{r})}. \quad (58)$$

Turning to the degenerate case the total subspace energy can be written as [33]:

$$E^i = E_{av}^i + \sum_j C_j^i B_j^i, \quad (59)$$

where E_{av}^i is the average energy of the configuration considered; C_j^i and B_j^i are quantities characteristic to the multiplet i . For instance, if we consider spherically symmetric systems (atoms or atomic ions) in the case $nsmp^2$, the energies of the multiplets have the form [34]:

$$E^i(^4P) = E_{av}^i - \frac{3}{25} F^2(pp) - \frac{1}{5} G^1(sp), \quad (60)$$

$$E^i(^2P) = E_{av}^i - \frac{3}{25} F^2(pp) + \frac{2}{3} G^1(sp), \quad (61)$$

$$E^i(^2D) = E_{av}^i + \frac{3}{25} F^2(pp), \quad (62)$$

$$E^i(^2S) = E_{av}^i + \frac{12}{25} F^2(pp). \quad (63)$$

$F^2(pp)$ and $G^1(sp)$ are the Slater integrals:

$$F^2(pp) = \int \int R_{mp}^2(r_1) R_{mp}^2(r_2) \frac{r_<^2}{r_>^3} dr_1 dr_2 \quad (64)$$

and

$$G^1(sp) = \int \int R_{ns}(r_1) R_{mp}(r_2) R_{mp}(r_1) R_{ns}(r_2) \times \frac{r_<}{r_>} dr_1 dr_2, \quad (65)$$

where R_{ns} and R_{mp} are the radial wave function of the ns and mp electrons. $r_<$ means r_1 if it is smaller than r_2 and r_2 if it is smaller than r_1 .

In the degenerate case beyond the orbital-dependent exchange potential $v_{xc,j}^i$ there is an extra orbital-dependent exchange potential:

$$w_j^i = \sum_k C_k^i \frac{1}{P_j^i} \frac{dB_k^i}{dP_j^i}, \quad (66)$$

$$\text{where } P_j^i = r R_j^i.$$

To find the optimized potential is very tedious even in the ground-state. However, Krieger, Li, and Iafrate [35] introduced a very accurate approximation that can be used here, too. Recently, an alternative derivation of the KLI approximation to the optimized potential method has been presented [36]. This method can be readily generalized to excited states.

4.5 APPROXIMATE POTENTIAL

Let us first treat the nondegenerate case. We start from the Hartree–Fock equations for the excited state under consideration:

$$-\frac{1}{2} \nabla^2 \psi_j^i(\mathbf{r}) + (v(\mathbf{r}) + v_j^i(\mathbf{r})) \psi_j^i(\mathbf{r}) - \int d\mathbf{r}' w^i(\mathbf{r}, \mathbf{r}') \psi_j^i(\mathbf{r}') = \epsilon_j^i \psi_j^i(\mathbf{r}), \quad (67)$$

where v is the external potential and v_j^i is the classical Coulomb potential:

$$v_j^i(\mathbf{r}) = \int \frac{dr' n_i(r')}{|\mathbf{r} - \mathbf{r}'|}. \quad (68)$$

The total electron density n_i can be expressed with the Hartree–Fock spin-orbitals ψ_j^i :

$$n_i(\mathbf{r}) = \sum_j |\psi_j^i(\mathbf{r})|^2, \quad (69)$$

while the exchange kernel $w^i(\mathbf{r}, \mathbf{r}')$ takes the form

$$w^i(\mathbf{r}, \mathbf{r}') = \sum_j \frac{\psi_j^{i*}(\mathbf{r}') \psi_j^i(\mathbf{r})}{|\mathbf{r} - \mathbf{r}'|}. \quad (70)$$

Now, we introduce the functions K_j^i with the following definition:

$$\psi_j^i = n_i^{1/2} K_j^i. \quad (71)$$

Substituting Eq. (71) into (67), multiplying with K_j^i , summing for all orbitals and making use of the relation

$$1 = \sum_j |K_j^i|^2, \quad (72)$$

then adding the complex conjugate we arrive at the following equation:

$$\begin{aligned} \frac{\delta T_w}{\delta n} \Big|_{n=n_i} + \frac{1}{2} \sum_j |\nabla K_j^i|^2 + v + v_j^i + v_s^i \\ = \sum_j \epsilon_j^i |K_j^i|^2; \end{aligned} \quad (73)$$

where v_s^i is the Slater potential.

$$v_s^i(\mathbf{r}) = -\frac{1}{2} \int d\mathbf{r}' n_i(\mathbf{r}') \frac{\left| \sum_j K_j^{i*}(\mathbf{r}') K_j^i(\mathbf{r}) \right|^2}{|\mathbf{r} - \mathbf{r}'|} \quad (74)$$

and $\delta T_w / \delta n$ is the functional derivative of the full Weizsäcker kinetic energy functional:

$$T_w = \frac{1}{8} \int d\mathbf{r} \frac{(\nabla n)^2}{n} \quad (75)$$

with respect to the density n .

Let us consider now the Kohn-Sham equations

$$-\frac{1}{2} \nabla^2 u_j^i + v_{KS}^i u_j^i = \epsilon_j^i u_j^i \quad (76)$$

leading to the same electron density n_i . The Kohn-Sham potential has the form

$$v_{KS}^i = v + v_j^i + v_x^i, \quad (77)$$

where v_x^i is the exchange potential. Introducing new functions k_j^i with the definition

$$u_j^i = n^{1/2} k_j^i, \quad (78)$$

substituting into Eq. (76), multiplying with k_j^i , summing for all orbitals, and using the relation between k_j^i

$$1 = \sum_j |k_j^i|^2, \quad (79)$$

and adding the complex conjugate of the equation obtained we arrive at the following equation:

$$\frac{\delta T_w}{\delta n} \Big|_{n=n_i} + \frac{1}{2} \sum_j |\nabla k_j^i|^2 + v_{KS}^i = \sum_j \epsilon_j^i |k_j^i|^2. \quad (80)$$

Now, we compare the Hartree-Fock and Kohn-Sham type equations (73) and (80). We treat the case when both equations provide the same (Hartree-Fock) density n_i , i.e., the Hartree-Fock method is posed as a density functional theory. From Eqs. (73) and (80) then follows:

$$\begin{aligned} v_x^i = v_s^i + \sum_j (\epsilon_j^i - \epsilon_j^i) |k_j^i|^2 - \sum_j \epsilon_j^i (|K_j^i|^2 - |k_j^i|^2) \\ - \frac{1}{2} \sum_j [|\nabla k_j^i|^2 - |\nabla K_j^i|^2]. \end{aligned} \quad (81)$$

In earlier studies [22, 25, 37] it was found that in the ground state the Hartree-Fock wave functions are very close to the orbitals satisfying the Kohn-Sham equations (80) with the Hartree-Fock density. Supposing the same for the i th excited state, we obtain the following approximate exchange potential:

$$v_x^i = v_s^i + \sum_j (\epsilon_j^i - \epsilon_j^i) |k_j^i|^2. \quad (82)$$

As shown, this expression is equivalent to the KLI potential for the ground state. It can also be written as

$$V_x^i = v_s^i + \sum_j \frac{|u_j^i|^2}{n_i} (\bar{v}_{xj}^i - \bar{v}_{xj}^{\text{HF}}), \quad (83)$$

where \bar{v}_{xj}^i and \bar{v}_{xj}^{HF} are the expectation values of the exchange potential V_x^i (83) and the Hartree-Fock exchange potentials v_{xj}^{HF} defined in the usual way with respect to orbital u_j^i .

Turning to the degenerate case, only spherically symmetric systems are considered. The weighting factors in Eq. (39) are selected to be equal. Then the Hartree-Fock-like radial equations can be obtained from Eq. (59):

$$\begin{aligned} \left(-\frac{1}{2} \frac{d^2}{dr^2} + \frac{l_j^i(l_j^i + 1)}{r^2} + v + v_j^i + v_{x,j}^i + w_j^i \right) \\ \times P_j^i = \epsilon_j^i P_j^i. \end{aligned} \quad (84)$$

Now starting out from Eq. (84) instead of Eq. (67) and repeating the whole derivation above, we arrive at the Kohn-Sham potential having the form

$$v_{KS}^i = v + v_j^i + v_x^i + w^i, \quad (85)$$

where v_x^i is the exchange potential

$$v_x^i = v_S^i + \sum_j (\epsilon_j^i - \epsilon_j^i) |k_j^i|^2 \quad (86)$$

and

$$w^i = \sum_j (k_j^i)^2 w_j^i = \sum_k (k_j^i)^2 \sum_l C_l^i \frac{1}{P_k^i} \frac{dB_l^i}{dP_k^i} \quad (87)$$

is the potential which is responsible for the multiplet separation.

4.6 ILLUSTRATIVE APPLICATIONS

To illustrate the present method, total energies are calculated for a couple of ground and excited

states for first-row atoms using the generalized KLI approximation. In a recent work [38], nondegenerate systems have been considered. Here, degenerate states are studied.

Table II presents total energies for atoms from Be to Ne. In a couple of cases exact orthogonality is assured by the fact that these excited states have different symmetries than the ground states. Total energies are also presented for states that are not the lowest of a symmetry species. Here, only an approximate orthogonality is ensured through the orbital representation of the functionals. For comparison Hartree–Fock values [39] are also shown. Result of the generalized KLI calculations are very close to the Hartree–Fock values. The accuracy of the generalized KLI results is about the same as

TABLE II
Total energies of ground and excited states of several atoms (in Ry).

Atom	Configuration	State	Total energy HF	Total energy DF
Be	[He]2s ²	¹ S	29.1460464	29.1445640
	[He]2s ¹ 2p ¹	³ P	29.0230038	29.0180909
		¹ P	28.7894708	28.7518996
B	[He]2s ² 2p ¹	² P	49.0581214	49.0551763
	[He]2s ¹ 2p ²	⁴ P	48.9013152	48.8884686
		² D	48.6237378	48.6215037
		² S	48.4961812	48.4893193
		² P	48.3580864	48.3519425
C	[He]2s ² 2p ²	³ P	75.3772380	75.3707497
		¹ D	75.2626626	75.2603155
		¹ S	75.0992218	75.0946642
	[He]2s ¹ 2p ³	⁵ S	75.1984292	75.1722258
		³ D	74.7887394	74.7828623
		³ P	74.6754332	74.6717829
		¹ D	74.3392354	74.3373082
		³ S	74.2842284	74.2811503
		¹ P	74.2315796	74.2262289
	[He]2s ² 2p ³	⁴ S	108.801868	108.788938
N		² D	108.592339	108.588113
		² P	108.456204	108.454229
	[He]2s ¹ 2p ⁴	⁴ P	107.976570	107.963937
		² D	107.567282	107.564494
		² S	107.366819	107.363890
O	[He]2s ² 2p ⁴	² P	107.167882	107.166816
		² P	149.618797	149.612502
		¹ D	149.458529	149.455621
		¹ S	149.222041	149.220299
Ne	[He]2s ¹ 2p ⁵	³ P	148.367817	148.360439
		¹ P	147.744071	147.744346
	[He]2s ² 2p ⁶	¹ S	257.094196	257.089024
[He]2s ² sp ⁵ 3s ¹		³ P	255.984628	255.975597
		¹ P	255.972424	255.968182

that of the original KLI for the ground state [35]. There is only one exception (the 5S state of the C atom) probably because of the high spin. It has been shown that the HF total energy is lower than the KLI one [22, 35, 37]. It is true for the present results, too.

5 Discussion

In this section the present approach is compared with the theories of excited states proposed by Theophilou [5] and Gross, Oliveira, and Kohn [8] and by Görling [22].

In the ensemble theory one has to calculate all the ensemble energies lying under the given ensemble energy in order to obtain the desired excitation energy. A disadvantage is that one has to do several self-consistent calculations in order to obtain the excitation energy of a single state. It is especially inconvenient to use it if one is interested in highly excited states. The present approach, on the other hand, can be applied to a single excited state.

In the theory proposed by Görling, the adiabatic connection is applied in the usual way, i.e., the ground-state density is kept fixed. (In the present approach the density of the excited state considered remains unchanged in the adiabatic connection.) The coupling-constant path establishes a continuous connection between the k th eigenstate of noninteracting and the interacting Hamiltonian. This statement is true in both approaches. However, the noninteracting Hamiltonian is different in the two methods, as the Kohn–Sham potentials are different. The reason for it is the following: In Görling's method, the Kohn–Sham potential ensures that the noninteracting ground-state density be equal to the interacting ground-state density. In the present approach, on the other hand, the Kohn–Sham potential ensures that the noninteracting excited-state density under consideration be equal to the corresponding interacting excited-state density.

ACKNOWLEDGMENTS

The grant "Széchenyi" from the Hungarian Ministry of Culture and Education is gratefully acknowledged. This work was supported by the grants OTKA No. T 16623 and FKFP 0314/1997.

References

1. P. Hohenberg and W. Kohn, Phys. Rev. B **136**, 864 (1964).
2. O. Gunnarsson and B. I. Lundqvist, Phys. Rev. B **13**, 4274 (1976); O. Gunnarsson, M. Jonson, and B. I. Lundqvist, Phys. Rev. B **20**, 3136 (1979).
3. U. von Barth, Phys. Rev. A **20**, 1693 (1979).
4. J. C. Slater, *Quantum Theory of Molecules and Solids*, Vol. 4 (McGraw-Hill, New York, 1974).
5. A. K. Theophilou, J. Phys. C **12**, 5419 (1978).
6. L. Fritzsche, Phys. Rev. B **33**, 3976 (1986); Int. J. Quant. Chem. **21**, 15 (1987).
7. H. English, H. Fieseler, and A. Haufe, Phys. Rev. A **37**, 4570 (1988).
8. E. K. U. Gross, L. N. Oliveira, and W. Kohn, Phys. Rev. A **37**, 2805, 2809, 2821 (1988).
9. Á. Nagy, Phys. Rev. A **42**, 4388 (1990).
10. Á. Nagy, J. Phys. B **24**, 4691 (1991).
11. Á. Nagy and I. Andrejkovics, J. Phys. B **27**, 233 (1994).
12. Á. Nagy, Int. J. Quant. Chem. **56**, 225 (1995).
13. Á. Nagy, J. Phys. B **29**, 389 (1996).
14. Á. Nagy, Int. J. Quant. Chem. S. **29**, 297 (1995).
15. Á. Nagy, Adv. Quant. Chem. **29**, 159 (1997).
16. Á. Nagy, Phys. Rev. A **49**, 3074 (1994).
17. Á. Nagy, Int. J. Quant. Chem., to appear.
18. E. U. K. Gross, J. F. Dobson, and M. Petersilka, in *Density Functional Theory*, R. Nalewajski, Ed., Topics in Current Chemistry (Springer, Heidelberg, 1996), vol. 181, p. 81.
19. M. F. Casida, in *Recent Advances in the Density Functional Methods* (Recent Advances in Computational Chemistry, Vol. 1), D. P. Chong, Ed. (World Scientific, Singapore, 1996), p. 155.
20. M. K. Harbola and V. Sahni, Phys. Rev. Lett. **62**, 489 (1989); see also V. Sahni, in Nato ASI Series Vol. B **337**, E. K. U. Gross and R. M. Dreizler, Eds. (Plenum, New York, 1995) and in *Density Functional Theory, Topics in Current Chemistry*, R. Nalewajski, Ed. (Springer, Berlin, 1996), Vol. 182, p. 1.
21. K. D. Sen, Chem. Phys. Lett. **168**, 510 (1992); R. Singh and B. M. Deb, Proc. Indian Acad. Sci. **106**, 1321 (1994); J. Mol. Struc. Theochem **361**, 33 (1996); J. Chem. Phys. **104**, 5892 (1996); A. K. Roy, R. Singh, and B. M. Deb, J. Phys. B **30**, 4763 (1997); Int. J. Quant. Chem. **65**, 317 (1997); A. K. Roy and B. M. Deb, Phys. Lett. A **234**, 465 (1997).
22. A. Görling, Phys. Rev. A **54**, 3912 (1996).
23. A. Görling and M. Levy, Phys. Rev. B **47**, 13105 (1993); Phys. Rev. A **50**, 196 (1994); Int. J. Quant. Chem. S. **29**, 93 (1995).
24. T. Kato, Commun. Pure Appl. Math. **10**, 151 (1957); E. Steiner, J. Chem. Phys. **39**, 2365 (1963); N. H. March, *Self-Consistent Fields in Atoms* (Pergamon, Oxford, 1975).
25. Á. Nagy, J. Phys. B **26**, 43 (1993); Phil. Mag. B **69**, 779 (1994).

EXCITED STATES IN DENSITY FUNCTIONAL THEORY

26. E. Clementi and A. Roetti, At. Data Nucl. Data Tables **14**, 177 (1974).
27. C. Filippi, C. J. Umrigar, and X. Gonze, J. Chem. Phys. **107**, 9994 (1997).
28. see in N. C. Handy, in *Quantum Mechanical Simulation Methods for Studying Biological Systems*, D. Bicout and M. Field, Eds. (Springer, Heidelberg, 1996), p. 1.
29. J. Harris and R. O. Jones, J. Phys. F **4**, 1170 (1974); J. Harris, Phys. Rev. A **29**, 1648 (1984).
30. M. Levy and J. P. Perdew, Phys. Rev. A **33**, 2010 (1985).
31. Á. Nagy, Phys. Rev. A, to appear.
32. R. T. Sharp and G. K. Horton, Phys. Rev. A **30**, 317 (1953); K. Aashamar, T. M. Luke, and J. D. Talman, At. Data Nucl. Data Tables, **22**, 443 (1978).
33. Á. Nagy, Phys. Rev. A, submitted.
34. J. C. Slater, *Quantum Theory of Atomic Structure* (McGraw-Hill, New York, 1960), Vol. 1.
35. J. B. Krieger, Y. Li, and G. J. Iafrate, Phys. Lett. A **146**, 256 (1990); Int. J. Quant. Chem. **41**, 489 (1992); Phys. Rev. A **45**, 101 (1992); Phys. Rev. A **46**, 5453 (1992); in *Density Functional Theory*, E. K. U. Gross and R. M. Dreizler, Eds. (Plenum, New York, 1995).
36. Á. Nagy, Phys. Rev. A **55**, 3465 (1997).
37. A. Holas and N. H. March, in *Density Functional Theory*, R. Nalewajski, Ed., Topics in Current Chemistry, Vol. 180 (Springer, Heidelberg, 1996).
38. To be submitted to *Electron Correlations and Materials Properties*, A. Gonis and N. Kioussis, Eds. (Plenum, New York).
39. H. Tatewaki, T. Koga, Y. Sakai, and A. J. Thakkar, J. Chem. Phys. **101**, 4945 (1994).

A Density Functional Study of Small Nickel Clusters

M. C. MICHELINI, R. PIS DIEZ, A. H. JUBERT

CEQUINOR, Centro de Química Inorgánica (CONICET, UNLP) Departamento de Química, Facultad de Ciencias Exactas, UNLP, C. C. 962, 1900 La Plata, Argentina

Received 22 February 1998; revised 6 May 1998; accepted 25 June 1998

ABSTRACT: Small nickel clusters up to the tetramer are investigated within the framework of the local spin density functional theory. Several competitive states are studied for the dimer. Both the geometry and the spin state are optimized for several starting symmetries in the case of the trimer and the tetramer. Moreover, all those calculations are followed by a vibrational analysis in order to discriminate between real minima and saddle points on the potential energy surface. It is found that Jahn-Teller deformations play an important role in determining transition-metal cluster geometries. Equilibrium geometries, electronic configurations, binding energies, magnetic moments, and harmonic frequencies are reported in this work. © 1998 John Wiley & Sons, Inc. Int J Quant Chem 70: 693–701, 1998

Introduction

Clusters are useful as models for surfaces, and as such, they have been used in the analysis of surface processes from a theoretical point of view [1]. The cluster approach focuses on the properties of a variety of surface sites, taking into account their local geometries and enabling the use of accurate quantum mechanical methods.

The rapid development of experimental techniques in recent years has made it possible both to obtain size-controlled transition-metal clusters and to study their reactivity against chemisorption processes [2, 3]. Although, in principle, metal clusters

and metal surfaces seem to behave in a very similar way against chemisorbed species, small transition-metal clusters show highly size-dependent properties such as their geometries and magnetic moments [4]. This intriguing behavior can be attributed to the fact that transition metals have unfilled valence *d* orbitals characterized by their localization and high density of states. As a consequence of this, a variety of geometries and electronic states are available for a given cluster composition. Let us say, for example, that the nickel dimer presents almost 30 electronic states located in an energy range of only 0.75 eV [5].

Because of their important catalytic and magnetic properties and the just-mentioned complexity of the electronic structure of low-lying excited states, nickel clusters seem to be a challenge for

Correspondence to: A. H. Jubert.

any ab initio calculation. A description of the ground-state electronic and magnetic properties of small nickel clusters was offered by Bash et al. [6] by means of effective core potential Hartree–Fock and configuration interaction calculations. Tomonari and coworkers [7] also investigated small nickel clusters using an all-electron basis set at both Hartree–Fock and configuration interaction levels of theory assuming bulk nickel interatomic distances for bond lengths. Mlynarski and Salahub [8] studied Ni₄ and Ni₅ using an all-electron basis within the local and nonlocal density functional formalisms. Reuse and Khanna [9] performed a systematic study of the geometry, electronic structure, and magnetic properties of small nickel clusters. Their calculations were carried out using norm-conserving, nonlocal pseudopotentials within the local density functional framework. Surprisingly, none of these authors reported any vibrational analysis to confirm that their findings correspond to true minima and not to saddle points in the potential energy surface of a given conformer. On the other hand, Castro et al. [10] performed all-electron local and nonlocal density functional calculations on nickel clusters up to the pentamer. These authors report not only structural and magnetic properties but they also properly characterize the clusters using the calculation of vibrational frequencies. Finally, Bérces [11] reported the vibrational frequencies of several optimized geometries for Ni₃ calculated using the nonlocal density functional formalism. It is important to remark that other recent works based on empirical molecular dynamics calculations on nickel clusters exist [12] but we prefer to restrict our comparison and discussion to first-principles results only.

As mentioned above, only Reuse and Khanna [9] and Castro et al. [10] made a systematic study on small nickel clusters. However, their results are rather different, especially for Ni₄. In [10, p. 140], Castro et al. also states that “*the precise source(s) of these discrepancies is not currently understood. Further work, with the use of different DFT codes and in different laboratories, on these small nickel clusters will be required to understand the shortcomings or limitations that the available DFT techniques possess in the description of transition metal cluster.*”

It was the aim of the present work to contribute to that very interesting, challenging, and actual topic. To this end, a systematic study of the geometry, electronic structure, and magnetic and vibrational properties of small nickel clusters up to the tetramer is presented.

Computational Details

Density functional calculations within the local spin density approximation (LSDA) [13] were performed on small nickel clusters up to the tetramer using the ADF package [14]. This code is based on Slater-type orbitals (STO) instead of the usual Gaussian-type functions. Furthermore, a set of auxiliary STOs are available to fit the electronic density in order to get a faster evaluation of the Coulomb potential.

The local correlation functional due to Vosko, Wilk, and Nussair [15] was used. The triple-zeta basis set of STOs available as set IV in the package was also used. That basis set does not include polarization functions. The frozen-core approximation up to the 3p orbital (included) was utilized.

The geometries and spin multiplicities of the Ni₂, Ni₃, and Ni₄ clusters were optimized with the default convergence thresholds, that is, 10⁻³ au for the energy, 10⁻² au for the gradients, and 10⁻⁶ for the self-consistent cycle. The integration accuracy parameter was also set to its default value of 4.0 (see [14b] for details about the numerical integration technique). Several symmetries were considered for the trimer and the tetramer (see the next section for details). The optimizations were symmetry-constrained in all cases. Several different starting geometries were considered for each symmetry.

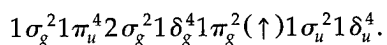
The frequency calculations were carried out using the default convergence and accuracy thresholds, that is, 10⁻³ au for the energy, 10⁻² au for the gradients, 10⁻⁶ for the self-consistent cycle, and 6.0 for the integration accuracy parameter. It is a well known fact that transition-metal cluster calculations are very difficult to converge [9, 16]. The *electron smearing* technique is a very useful trick that can help to solve that problem. It creates an energy window around the Fermi level and all the molecular orbitals inside that window are allowed to have fractional occupation numbers. Thus, when some of our calculations revealed convergence problems, the program’s *smearq* keyword was activated. When this was the case, several subsequent calculations were carried out by letting the *smearq* parameter to tend gradually to zero. This must be performed because the true self-consistency is only achieved when the energy window width is set to zero, that is, when all the occupation numbers become integers.

Results and Discussion

Atomic calculations using the basis set mentioned in the last section indicate that the 3D (d^9s^1) state is the ground state at the present LSDA level of theory. The binding energies reported in this work are then calculated using that value as the reference atomic energy. The 3F (d^8s^2) and 1S (d^{10}) states were also calculated. Our results are in qualitative agreement with J -averaged experimental results [17] and show the same trends that other LSDA calculations (see [8]). Table I shows our atomic calculations results and the experimental values [17].

Ni₂

The ground state of the nickel dimer is found to be $^3\Sigma_g^-$ according to our LSDA calculations. The binding energies of the ground state and the low-lying excited states of Ni₂ are reported in Table II. The two unpaired electrons in the ground state are located on a π_g molecular orbital (MO) as can be seen from the electronic configuration



Due to the near degeneracy found among the $1\pi_g$, $1\sigma_u$, and $1\delta_u$ MOs, all of them around the Fermi level, other configurations were studied to obtain a deeper understanding on the variety of electronic states of Ni₂ near the ground state. The detail of the configurations studied as well as their bond lengths and binding energies are presented in Table III for comparison. It can be seen that minor modifications take place when one goes from state I to state II. On the other hand, when the δ_u MO becomes depopulated, states III and IV, the bond length increases its value and, accordingly, the binding energy lowers its magnitude.

TABLE I
Energy of different atomic states of nickel.

Atomic state	This work	Experimental [17]
$^3D(d^9s^1)$	0.00	0.00
$^3F(d^8s^2)$	1.42	0.03
$^1S(d^{10})$	1.85	1.83

The values are given in eV and the ground state is taken as the reference value. The experimental values [17] are weighted averages over the J components.

TABLE II
Binding energies (BE) of ground and low-lying excited states of Ni₂. The energies are given in eV, with S the total electronic spin.

S	BE
0	1.33
1	1.67
2	0.86

Since the three MOs considered have antibonding character, a closer look at the antibonding overlap population between the nickel atoms could help to understand that behavior. The σ_u , π_g , δ_u , and total antibonding overlap populations are presented in Table IV. It can be seen from that table that the total antibonding overlap population increases when passing from state I to state IV. Moreover, it is clear that the σ_u and π_g MOs are mainly responsible for the antibonding overlap between the nickel atoms. The δ_u MO, on the other hand, shows only a weak antibonding character. Thus, an increase in the total antibonding character must be expected when the δ_u MO becomes depopulated in favor of the π_g MO. These facts are consistent with the variations observed in the binding energies and the bond lengths (see Table III).

TABLE III
Comparison of different triplet states of Ni₂.

Electronic configuration	Electronic state	r	BE
$(1\sigma_u)^2 (1\delta_u)^4 (1\pi_g)^2$ (I)	$^3\Sigma_g^-$	2.07	1.67
$(1\sigma_u)^1 (1\delta_u)^4 (1\pi_g)^3$ (II)	$^3\Pi_u$	2.06	1.60
$(1\sigma_u)^2 (1\delta_u)^3 (1\pi_g)^3$ (III)	$^3\Pi_u$ or $^3\Phi_u$	2.11	1.56
$(1\sigma_u)^2 (1\delta_u)^2 (1\pi_g)^4$ (IV)	$^3\Sigma_g^-$	2.16	1.26

Only the relevant molecular orbitals of each configuration are given. Bond lengths (r, in Å) and binding energies (BE, in eV/at) are shown.

TABLE IV
 σ_u , π_g , δ_u , and total antibonding overlap populations for the states I–IV of Ni₂.

	I	II	III	IV
σ_u	0.0442	0.0223	0.0551	0.0713
π_g	0.0561	0.0877	0.0815	0.1029
δ_u	0.0048	0.0031	0.0071	0.0080
Total	0.1051	0.1131	0.1437	0.1822

TABLE V
Comparison of different triplet states of Ni₂.

Electronic configuration	Electronic state	r	BE
(1σ _u) ² (1δ _u) ⁴ (1π _g) ²	¹ Σ _g ⁺	2.08	1.33
(1σ _u) ¹ (1δ _u) ³ (1π _g) ⁴	¹ Δ _g	2.10	1.33
(1σ _u) ² (1δ _u) ³ (1π _g) ³	¹ Π _u or ¹ Φ _u	2.12	1.31
(1σ _u) ¹ (1δ _u) ⁴ (1π _g) ³	¹ Π _u	2.06	1.31
(1σ _u) ⁰ (1δ _u) ⁴ (1π _g) ⁴	¹ Σ _g ⁺	2.05	1.13
(1σ _u) ² (1δ _u) ² (1π _g) ⁴	¹ Σ _g ⁺ or ¹ Γ _g	2.16	0.92

Only the relevant molecular orbitals of each configuration are given. Bond lengths (r, in Å) and binding energies (BE, in eV/at) are shown.

According to Table II, the singlet state is close in energy to the triplet state. Moreover, some experimental results indicate that the Ni₂ ground state would be a singlet state [5]. Due to this fact, several singlet states were also investigated. The results are collected in Table V. It can be seen from that table that four singlet states are within only 0.02 eV/at. Although those singlet states are close in energy to the triplet states discussed above, our calculations clearly favor the triplet state as the ground state for Ni₂.

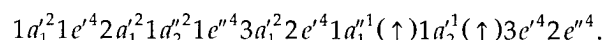
The bond length, binding energy, and vibrational frequency of the ground state of Ni₂ are reported in Table VI together with other theoretical results and the corresponding experimental values. It can be seen from the table that, although

different codes were used, the present calculations are in good agreement with the other LSDA results. Moreover, they show the usual tendencies attributed to LSDA, that is, shorter bond distances and larger binding energies than experimental values. The vibrational frequency is reproduced with great accuracy.

Ni₃

The starting symmetries studied in the case of the trimer were the $D_{\infty h}$ linear structure, the C_{3v} equilateral triangle, and the acute and obtuse C_{2v} isosceles triangles. A $^5\Sigma_u^-$ state was found to be the ground state of the $D_{\infty h}$ Ni₃ cluster. The binding energies of the ground state and the low-lying excited states of the linear trimer are collected in Table VII. No Renner-Teller effect should be expected due to the absence of degeneracies in the electronic state of the cluster. Nevertheless, the vibrational analysis reveals one degenerate imaginary frequency that can be attributed to near-degeneracy effects between frontier orbitals. It is concluded that the linear trimer is not a real minimum on the potential energy surface of Ni₃.

In the case of the equilateral triangle, an $^3A_2'$ state was found to be the ground state. The binding energies of the ground and the low-lying excited states of the D_{3h} trimer are listed in Table VII. The valence electronic configuration of the ground state is



No first-order Jahn-Teller (FOJT) effect [18] should be expected for this cluster. The vibrational analysis confirms that this is a real minimum in the Ni₃ potential energy surface.

In the case of the C_{2v} acute and obtuse triangles, all the geometry optimizations converge to the equilateral triangle irrespective of the starting

TABLE VI
Comparison of bond length (r, in Å), binding energy (BE, in eV/at), magnetic moment (μ , in bohr magneton/at), and vibrational frequency (ω_e , in cm⁻¹) of Ni₂ calculated in this work with other theoretical calculations and experimental results.

Method	State	r	BE	μ	ω_e
[6] ^a	³ Σ _u ⁺	2.33	0.71	1.00	211
[7] ^b	³ Σ _u ⁺	2.30 ^c	0.24	1.00	—
[8] ^d	³ Σ _g ⁻	2.03	1.82	1.00	379
[9]	Triplet	2.00	1.61	1.00	—
[10] ^d	Triplet	2.05	1.82	1.00	354
This work	³ Σ _g ⁻	2.07	1.67	1.00	353
Exp. [5]	— ^e	2.20	1.03	—	381

^a Only CI results are shown.

^b Only SCF results are shown.

^c The bond length was kept fixed at this value.

^d Only LSDA results are shown.

^e A wide variety of states lie around the true ground state, making difficult its assignment. Nevertheless, the possibilities seem to be ³Σ_u⁺, ³Σ_g⁻, ¹Σ_u⁻, ¹Σ_g⁺, ¹Γ_g, or ³Π_u.

S	$D_{\infty h}$	D_{3h}
0	—	1.98
1	1.79	2.20
2	1.86	2.00
3	1.11	—

The energies are given in eV. S is the total electronic spin.

geometries used. The variation of the total energy with respect to the apex angle opening was also studied. Only the minimum corresponding to the equilateral triangle was identified in that curve. This is in agreement with the results reported in the previous paragraph.

A summary of our results as well as their comparison with other theoretical calculations and some experimental results is shown in Table VIII.

It can be seen from that table that the characterization of the nickel trimer is a difficult task. Bash et al. [6] reported a quintet linear trimer as the most stable one. It must be noted, however, that the geometry of the equilateral triangle was kept fixed and all the calculations were performed at a Hartree–Fock level of theory only. Tomonari and coworkers [7] only performed calculations on the equilateral triangle with fixed bond lengths and also at a Hartree–Fock level of theory. They found the quintet to be the most stable state. Reuse and Khanna [9], on the other hand, performed pseudopotential LSDA calculations, finding a triplet C_{2v} ground state with an apex angle of 61°, very close to the equilateral triangle conformation found in this work. Castro et al. [10] reported all-electron local and nonlocal density functional calculations on Ni_3 . These authors found an equilateral triangular structure in a triplet electronic state for the trimer and it is characterized using a vibrational

analysis. Bérces [11] found using nonlocal density functional calculations that the lowest-energy conformation was a triplet D_{3h} structure closely followed by two C_{2v} structures also in triplet electronic states with apex angles of 62.1° and 58.3°, respectively.

The amount of experimental information is scarce. The ground state is characterized only by the C_{2v} symmetry and an apex angle in the range 90–100° [19] and two vibrational frequencies [20]. It is important to note that irrespective of some differences in the calculation methodology within the LSDA both the results in [9, 10] and the results in this work agree to predict the Ni–Ni bond lengths and the binding energy to be about 2.15–2.18 Å and 1.96–2.40 eV/at, respectively. Since no frequency calculations were performed in [6], [7], or [9] the minimum characterization presented there is uncompleted from our point of view. On the other hand, the frequencies calculated in the present work are in excellent agreement with those reported in [10] and in good agreement with those shown in [11], especially the higher ones. The disagreement found in the lower frequencies can be attributed to the fact that local frequencies tend to be higher than nonlocal ones (see [10, 16] for some examples). Unfortunately, the scarcity of experimental results makes the comparison very difficult.

TABLE VIII

Comparison of the binding energy (BE, in eV / at), geometrical parameters (r , in Å; θ , the apex angle, in degrees), magnetic moment (μ , in bohr magneton / at), and vibrational frequencies (ω_e , in cm⁻¹) of different Ni_3 conformers calculated in this work with other theoretical calculations and some experimental results.

Method	Symmetry-State	r , θ	BE	μ	ω_e
[6] ^a	$D_{\infty h}$ –quintet	2.38, 180	0.51	1.34	—
[6] ^a	D_{3h} – ⁵ E'	2.49, ^b 60	0.45	1.34	—
[7] ^a	D_{3h} – ⁵ E'	2.49, ^b 60	0.19	1.34	—
[9]	C_{2v} –triplet	2.15, 61	1.96	0.67	—
[10] ^c	D_{3h} –triplet	2.16, 60	2.40	0.67	228, 230, 352
[11]	D_{3h} – ³ A' ₁	2.21, 60	—	0.67	142, 356
[11]	C_{2v} – ³ B ₂	2.21, 62.1	—	0.67	—
[11]	C_{2v} – ³ A ₁	2.25, 58.3	—	0.67	213, 228, 349
[19]	C_{2v}	—, 90–100	—	—	—
[20]	—	—	—	—	100 ± 5, 230 ± 5
This work	D_{3h} – ³ A'' ₂	2.18, 60	2.20	0.67	229 (e'), 359 (a' ₁)

Symmetry assignment of frequencies is given in parentheses.

^aOnly SCF are shown.

^bThe bond length was kept fixed to this value.

^cOnly LSDA results are shown.

Ni₄

The study of the nickel tetramer is more complex than in the previous cases since more structures are involved. To simplify the analysis, we investigated two-dimensional (2D) and three-dimensional (3D) structures separately. Our results are then presented in two different subsections.

2D Structures

We started our study with the most symmetrical 2D structure, that is, D_{4h} . An 5E_g electronic state was found to be the ground state for the square conformer. The binding energies of the ground and the low-lying excited states of the D_{4h} tetramer are listed in Table IX. The presence of FOJT deformations due to the nature of the electronic state can be expected. A vibrational analysis confirmed the existence of two imaginary frequencies along the B_{1g} and B_{2g} modes. These modes would lead to a rectangular structure and a rhombic structure, respectively, both of symmetry D_{2h} , after distortion.

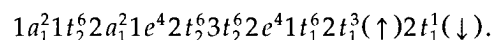
We were not able to get any rectangular, D_{2h} , structure. Despite the starting geometry used, the final geometry always became a perfect square.

On the other hand, two different rhombic structures were obtained characterized by the 5A_g and $^5B_{3u}$ electronic states. The binding energies of the ground and the low-lying excited states of the D_{2h} tetramers are shown in Table IX. A vibrational analysis shows one imaginary frequency along the B_{1u} mode for the first conformer, and two imaginary frequencies along the B_{1u} and A_g modes for the second one. When the deformation along the B_{1u} mode was investigated, the two rhombi led to the same 3D, C_{2v} , structure that will be considered in the next subsection. The deformation along the A_g mode in the second conformer, on the other

hand, led to the first conformer characterized by the 5A_g electronic state.

3D Structures

We start our study with the most symmetrical 3D structure, that is, T_d . Two different states, 3T_1 and 5T_2 , were found to have the same minimum energy within 0.01 eV/at and almost the same geometrical parameters within 0.01 Å. The binding energies of the ground and the low-lying excited states of the T_d tetramers are collected in Table IX. FOJT deformations due to the nature of the electronic states can be expected. The quintet state shows an imaginary frequency along the E mode, in agreement with the Jahn-Teller theorem. This mode leads to a D_{2d} structure that will be considered later. Surprisingly, the 3T_1 electronic state does not present any imaginary frequency, contrary to what is expected from the Jahn-Teller theorem. Additional frequency calculations with more stringent conditions than those used as defaults were performed but the same results were obtained. Although this could be an error coming from the LSDA model, we decided to report this nickel conformer as a real minimum on the potential surface of the tetramer. The valence electronic configuration of the 3T_1 state (a from now on) is



C_{3v} structures were also studied. An 5E state was found to be the ground state. The binding energies of the ground and the low-lying excited states of the C_{3v} tetramers are listed in Table IX. However, the nature of the electronic state anticipates that this conformer is not a true minimum on the potential surface of the tetramer. The vibrational analysis shows an imaginary frequency along the E mode. Unfortunately, we were not able to

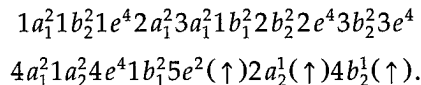
TABLE IX
Binding energies of the ground and low-lying excited states of Ni₄ in different symmetries.

S	D_{4h}	$D_{2h}-^5A_g$	$D_{2h}-^5B_{3u}$	T_d	C_{3v}	D_{2d}	$C_{2v}(\mathbf{c})$	$C_{2v}(\mathbf{d})$	C_{2v}
0	—	—	—	2.43	—	—	—	—	—
1	2.37	2.42	2.38	2.52	2.45	2.52	2.37	2.43	2.46
2	2.39	2.51	2.44	2.52	2.46	2.53	2.51	2.51	2.51
3	2.38	2.34	2.30	2.32	2.30	2.34	2.35	2.30	2.30

The energies are given in eV. S is the total electronic spin. For C_{2v} , the letters **c** and **d** indicate the stable conformers, whereas the C_{2v} column without any letter indicates the conformer that lead to imaginary frequencies.

complete our study on the deformation along this mode due to convergence problems.

The analysis of the D_{2d} structures (including that structure coming from the FOJT distortion of the tetrahedron mentioned above) leads to an 5A_2 state (**b** from now on) characterized by the valence electronic configuration



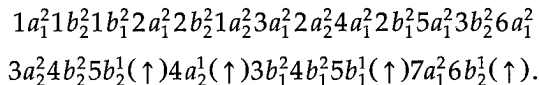
The binding energies of the ground state and the low-lying excited states of the D_{2d} tetramers are shown in Table IX. This conformer does not show imaginary frequencies and then can be reported as a real minimum on the potential energy surface of the nickel tetramer.

Finally C_{2v} structures were studied including that structure coming from the distortion of the D_{2h} rhombi along the B_{1u} mode mentioned above. Three different ground states were found characterized by the same electronic states 5B_1 . The binding energies of the ground state and the low-lying excited states of the C_{2v} tetramers are shown in Table IX.

The vibrational analysis reveals that one of the conformers has one imaginary frequency along the A_2 mode. When the geometry and spin state are optimized according the distortion suggested by

the imaginary mode, the **b** structure mentioned in the last paragraph is obtained.

The other two conformers, on the other hand, have only real frequencies, indicating that these are true minima on the potential energy surface of the nickel tetramer. Their valence electronic configurations are also the same:



To facilitate the report of the geometric parameters and the vibrational frequencies, these conformers are labeled **c** and **d** respectively.

A summary of our results as well as their comparison with other theoretical calculations is reported in Table X. The geometrical parameters of conformers **a-d** are shown in Figure 1.

The results reported in [6, 7] were obtained at a Hartree–Fock level of theory, without including correlation effects. Only the most symmetrical structures were studied. Moreover, the interatomic distances were kept fixed. Mlynarski and Salahub [8] studied only the tetrahedron finding a quintet state and a binding energy of 3.35 eV/at when the geometry is optimized. Reuse and Khanna [9] performed LSDA calculations on the D_{4h} and D_{2d} structures only. They found a septet state and the same binding energy (2.34 eV/at) for both. No

TABLE X
Comparison of the binding energy (BE, in eV / at), magnetic moment (μ , in bohr magneton / at), and vibrational frequencies (ω_e , in cm^{-1}) of different Ni_4 conformers calculated in this work with other theoretical calculations.

Method	Symmetry-State	BE	μ	ω_e
[6] ^a	$D_{\infty h}$ -quintet	0.58 ^b	1.00	—
[6] ^a	D_{4h} - $^7B_{1g}$	0.58 ^b	1.50	—
[6] ^a	T_d - 7T_2	0.32 ^b	1.50	—
[7] ^a	D_{4h} - $^7B_{1g}$	0.50 ^b	1.50	—
[8] ^a	T_d -quintet	2.99 ^c	1.00	—
[8] ^d	T_d -quintet	3.35 ^c	1.00	—
[9]	D_{2d} -septet	2.34	1.50	—
[9]	D_{4h} -septet	2.34	1.50	—
[10] ^c	D_{2d} -quintet	2.78	1.50	147, 172 (e), 199, 300, 363
This work	T_d - 3T_1 (a)	2.52	0.50	124 (e), 216 (t_2), 356(a_1)
This work	D_{2d} - 5A_2 (b)	2.53	1.00	144 (b_1), 163 (e), 197 (a_1), 297 (b_2), 362 (a_1)
This work	C_{2v} - 5B_1 (c)	2.51	1.00	51 (a_1), 183 (b_1), 213 (a_2), 225 (a_1), 307 (b_2), 344 (a_1)
This work	C_{2v} - 5B_1 (d)	2.51	1.00	23 (a_1), 176 (b_2), 209 (a_2), 228 (a_1), 305 (b_1), 349 (a_1)

Symmetry assignment of frequencies is given in parentheses.

^aThe bond length was kept fixed to 2.49 Å.

^bOnly SCF results are shown.

^cOnly LSDA results are shown.

^dThe bond length was optimized to 2.23 Å.

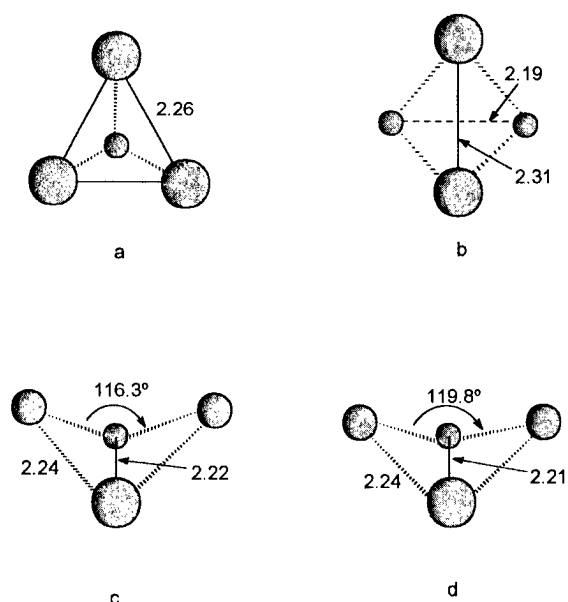


FIGURE 1. Geometric parameters of the four conformers of Ni_4 : (a) $T_d - ^3T_1$; (b) $D_{2d} - ^5A_2$; (c) $C_{2v} - ^5B_1$; (d) $C_{2v} - ^5B_1$. Distances are in Å and angles in degrees.

vibrational analysis was made in [6–9]. Castro and coworkers [10], on the other hand, investigated the T_d , D_{2d} , and D_{2h} structures. They found that only the D_{2d} conformer in a quintet electronic state is a real minimum, whereas the other two are saddle points on the potential energy surface of Ni_4 . The binding energy of the D_{2d} structure was 2.78 eV/at. Those authors also reported the vibrational frequencies. The binding energy of the D_{2d} conformer found in this work is rather lower than that from [10] and rather higher than those reported in [9]. Our vibrational frequencies, on the other hand, are in excellent agreement with those given in [10]. Moreover, we found three new conformers for Ni_4 , all of them being within an energy range of 0.02 eV/at.

Conclusions

A systematic LSDA study of the geometry, electronic structure, and magnetic and vibrational properties of small nickel clusters up to the tetramer is presented in this work. The main conclusions can be summarized as follows:

- (a) A $^3\Sigma_g^-$ state characterized by a bond length of 2.07 Å was found for the nickel dimer. The binding energy is found to be 1.67 eV/at and the vibrational frequency is 353 cm^{-1} .

(b) An equilateral triangle characterized by an $^3A''_2$ state and a bond length of 2.18 Å is found to be the ground state of the nickel trimer. Its binding energy is 2.20 eV/at, and the corresponding magnetic moment and vibrational frequencies that confirm that this is a real minimum on the potential energy surface of the trimer are also reported in this work. It should be noted that a stable linear trimer was also found but it was impossible to complete the vibrational analysis due to convergence problems.

(c) Four different stable conformers were found for the nickel tetramer: a distorted tetrahedron (D_{2d}), a perfect tetrahedron, and two butterfly structures (C_{2v}). The spin states are triplets and quintets. The binding energies ranges from 2.51 to 2.53 eV/at. The corresponding vibrational frequencies that confirm that these are real minima on the potential energy surface of the tetramer as well as their geometric parameters and magnetic moments are also shown in this work.

The results presented in this work show an excellent agreement with the results reported by Castro et al. [10]. Thus, the present work represents a contribution to clarify the dilemma posed by those authors concerning the reliability of the present DFT codes. Moreover, a more complete description of the potential energy surface of Ni_4 is given.

ACKNOWLEDGMENTS

M. C. M. is a fellow from CONICET, Argentina. R. P. D. is member of the Scientific and Technological Researcher Career, CONICET. A. H. J. is a member of the Scientific Researcher Career, CI-CPBA, Argentina. The authors acknowledge the Albuquerque Resource Center at the University of New Mexico for providing computing time.

References

1. G. Pacchioni, P. S. Bagus, and F. Parmigiani, Eds., *Clusters Models for Surface and Bulk Phenomena* (Plenum, New York, 1992).
2. A. Kaldor, D. M. Cox, and M. R. Zakin, *Adv. Chem. Phys.* **70**, 211 (1988).
3. (a) D. J. Trevor, R. L. Whetten, D. M. Cox, and A. Kaldor, *J. Am. Chem. Soc.* **107**, 518 (1985); (b) M. R. Zakin, D. M. Cox,

SMALL NICKEL CLUSTERS

- and A. Kaldor, *J. Phys. Chem.* **91**, 5224 (1987); (c) M. R. Zakin, D. M. Cox, R. O. Brickman, and A. Kaldor, *J. Phys. Chem.* **93**, 6823 (1989).
4. I. Panas, P. Siegbahn, and U. Wahlgren, in *The Challenge of d and f Electrons. Theory and Computation*, D. R. Salahub and M. C. Zerner, Eds. ACS Symposium Series No. 394 (American Chemical Society, Washington, DC, 1989), Chap. 9.
 5. M. D. Morse, *Chem. Rev.* **86**, 1049 (1986).
 6. H. Bash, M. D. Newton, and J. W. Moskowitz, *J. Chem. Phys.* **73**, 4492 (1980).
 7. M. Tomonari, H. Tatewaki, and T. Nakamura, *J. Chem. Phys.* **85**, 2875 (1986).
 8. P. Mlynarski and D. R. Salahub, *J. Chem. Phys.* **95**, 6050 (1991).
 9. F. A. Reuse and S. N. Khanna, *Chem. Phys. Lett.* **234**, 77 (1995).
 10. M. Castro, C. Jamorski, and D. R. Salahub, *Chem. Phys. Lett.* **271**, 133 (1997).
 11. A. Bérces, *Spectrochim. Acta A* **53**, 1257 (1997).
 12. (a) N. N. Lathiotakis, A. N. Andriotis, M. Menon, and J. Connolly, *J. Chem. Phys.* **104**, 992 (1996); (b) S. K. Nayak, S. N. Khanna, B. K. Rao, and P. Jena, *J. Phys. Chem. A* **101**, 1072 (1997).
 13. (a) P. Hohenberg and W. Kohn, *Phys. Rev.* **136**, B864 (1964); (b) W. Kohn and L. J. Sham, *Phys. Rev.* **140**, B1133 (1965); (c) R. G. Parr and W. Yang, *Density Functional Theory of Atoms and Molecules* (Oxford University Press, New York, 1989).
 14. ADF 2.3.0, Theoretical Chemistry, Vrije Universiteit, Amsterdam: (a) E. J. Baerends, D. E. Ellis, and P. Ros, *Chem. Phys.* **2**, 41 (1973); (b) G. te Velde and E. J. Baerends, *J. Comp. Phys.* **99**, 84 (1992); (c) C. Fonseca Guerra et al., METECC-95 305 (1995).
 15. S. H. Vosko, L. Wilk, and M. Nusair, *Can. J. Phys.* **58**, 1200 (1980).
 16. C. Jamorski, A. Martinez, M. Castro, and D. R. Salahub, *Phys. Rev. B* **55**, 10905 (1997).
 17. C. E. Moore, *Atomic Energy Levels* (National Bureau of Standards Circ. 467, 1952).
 18. I. B. Bersuker, *The Jahn-Teller Effect and Vibronic Interactions in Modern Chemistry* (Plenum, New York, 1984).
 19. (a) M. Moskowits and J. E. Hulse, *J. Chem. Phys.* **66**, 3988 (1977); (b) M. Moskowits and D. P. DiLella, *J. Chem. Phys.* **72**, 2267 (1980).
 20. J. R. Woodward, S. H. Cobb, and J. L. Gole, *J. Phys. Chem.* **92**, 1404 (1984).

Stable and Efficient Numerical Method for Solving the Schrödinger Equation To Determine the Response of Tunneling Electrons to a Laser Pulse

MARK J. HAGMANN

*Department of Electrical and Computer Engineering, Florida International University, Miami,
Florida 33199*

ABSTRACT: The form $\Psi(x, t) = [F_0(x) + F_1(x, t)e^{-i\omega t} + F_{-1}(x, t)e^{i\omega t}]e^{-iEt/\hbar}$ is used for the wave function in the transient solutions. This expression is similar to the three dominant terms in the steady-state solution from the Floquet theory, except that now F_1 and F_{-1} depend on t as well as x . The function F_0 is the static solution, and separate partial differential equations are given for F_1 and F_{-1} . Polynomial extrapolation is used to satisfy boundary conditions at the ends of the grid. The numerical solutions are shown to converge and to be numerically stable even for simulated times exceeding 2000 cycles of the radiation field. The examples show delays corresponding to the semiclassical tunneling transit time, the classical time for traversing the inverted barrier. A resonance is seen when electrons promoted above the barrier by absorbing quanta from the radiation field have the closed line integral of momentum between the turning points equal to an integral multiple of Planck's constant. A second resonance occurs when the period of oscillation for the radiation equals the semiclassical tunneling transit time for electrons that absorb one photon from the radiation but are still below the barrier. This resonance decays at a rate corresponding to the tunneling dwell time, and, thus, it is not present in the steady state. These observations suggest a semiclassical picture of the tunneling process. © 1998 John Wiley & Sons, Inc. Int J Quant Chem 70: 703–710, 1998

Introduction

Laser-assisted scanning tunneling microscopy, in which laser radiation is coupled to the tip-sample junction of a scanning tunneling microscope (STM), has been used to generate microwave

Contract grant sponsor: NSF.

Contract grant number: 9500007.

mixing signals which have been used for feedback control [1] as well as for imaging the local conductivity of the sample [2]. These procedures show promise for obtaining atomic resolution with samples having high electrical resistivity, increasing the speed of imaging, and extending the list of the types of data that can be imaged. Our simulations [3] show that a single amplitude-modulated laser focused on the tip-sample junction of an STM will generate a tunneling current at the modulation

frequency, and this was verified in preliminary experiments. Other simulations and experiments suggest that optical mixing in laser-assisted field emission could be used to generate and detect signals over bandwidths as large as 100 THz [4].

All these simulations used either single-electron solutions [3] or density functional theory with the approximation that the time-averaged response for electrons in the metal is the same as in the static problem, and screening of the radiation fields was described classically [4–5]. It was the objective of this study to find a numerically stable and computationally efficient method for obtaining transient solutions of the Schrödinger equation so that this method may subsequently be combined with iterative dynamic corrections to the potential from density functional theory to obtain self-consistency. A number of methods have already been used to obtain transient solutions of the Schrödinger equation. The method of finite differences was used with alternating-direction implicit propagation [6], a split-operator propagator [7], and a fourth-order predictor–corrector [8]. Other methods include finite elements [9], a modification of finite elements using complex-coordinate contours [10], split-operator spectral techniques with fast-Fourier transforms [11], quadratures with expansions in Vokolov states [12], and a formulation in which the wave function is divided by the steady-state solution [13].

Analysis

We begin with the dipole approximation [14] of the one-dimensional time-dependent Schrödinger equation for an electron in a static potential plus a radiation field with axial polarization,

$$\frac{-\hbar^2}{2m} \frac{\partial^2 \Psi}{\partial x^2} + [V_0 + exE_0 U(t)\sin(\omega t)]\Psi = i\hbar \frac{\partial \Psi}{\partial t}, \quad (1)$$

where $U(t)$ is the unit step function (1 for $t > 0$, else 0), and both the static potential V_0 and the magnitude of the electric vector of the radiation field E_0 may be functions of the axial coordinate x . In the steady state, Floquet's theorem [15] may be used to write the solution of Eq. (1) as

$$\Psi = \sum_{-\infty}^{\infty} \psi_N \exp[-i(E + N\hbar\omega)t/\hbar], \quad (2)$$

where the ψ_N are functions of x only. Now, for a transient solution, we take the three dominant terms of the Floquet series [16] and generalize their time dependence as follows:

$$\Psi = [F_0(x) + F_1(x, t)e^{-i\omega t} + F_{-1}(x, t)e^{i\omega t}]e^{-iEt/\hbar}. \quad (3)$$

Substituting Eq. (3) into Eq. (1) and separating the resulting expression results in the following set of three equations:

$$\begin{aligned} \frac{\hbar^2}{2m} \frac{\partial^2 F_1}{\partial x^2} + i\hbar \frac{\partial F_1}{\partial t} \\ + [E + \hbar\omega - V_0 - U(t)V_1 \sin(\omega t)]F_1 \\ = \frac{i}{2} U(t)V_1 F_0 \end{aligned} \quad (4a)$$

$$\begin{aligned} \frac{\hbar^2}{2m} \frac{\partial^2 F_{-1}}{\partial x^2} + i\hbar \frac{\partial F_{-1}}{\partial t} \\ + [E - \hbar\omega - V_0 - U(t)V_1 \sin(\omega t)]F_{-1} \\ = \frac{-i}{2} U(t)V_1 F_0 \end{aligned} \quad (4b)$$

$$\frac{\hbar^2}{m} \frac{d^2 F_0}{dx^2} + [E - V_0]F_0 = 0. \quad (4c)$$

To solve this system of equations, first, the static solution F_0 is determined by using shooting methods [17] to solve Eq. (4c). Then, F_1 and F_{-1} are determined by solving Eqs. (4a) and (4b) by time stepping using finite differences with the initial condition that both F_1 and F_{-1} are identically zero for $t \leq 0$ at all values of x . In the finite-difference approximations, the time derivatives are approximated by the midpoint method [18]. For example, the approximation of Eq. (4a) is

$$\begin{aligned} F_{1, I, J+1} = F_{1, I, J-1} \\ + \frac{i\hbar\Delta t}{m(\Delta x)^2} [F_{1, I+1, J} - 2F_{1, I, J} + F_{1, I-1, J}] \\ + \frac{2i\Delta t}{\hbar} [E + \hbar\omega - V_0(I \cdot \Delta x) \\ - U(J \cdot \Delta t) \cdot V_1(I \cdot \Delta x) \sin(\omega \cdot J \cdot \Delta t)] \\ \times F_{1, I, J} \\ + \frac{\Delta t \cdot U(J \cdot \Delta t) \cdot V_1(I \cdot \Delta x)}{\hbar} F_0(I \cdot \Delta x), \end{aligned} \quad (5)$$

where we use the notation $F_{1,I,J} \equiv F_1(I \cdot \Delta x, J \cdot \Delta t)$ and $V_1 \equiv exE_0$. We find that the criterion $\Delta t < m(\Delta x)^2/2\hbar$ must be satisfied for numerical stability, and all solutions obtained using different values of the time step which satisfy this criterion are numerically equivalent.

Our numerical solutions show that, in general, $|F_0| \gg |F_1| \gg |F_{-1}|$, so we have also tested a second formulation in which F_{-1} is deleted and Eq. (3) is replaced with the following equation:

$$\Psi = [F_0(x) + F_1(x, t)e^{-i\omega t}]e^{-iEt/\hbar}. \quad (6)$$

Substituting Eq. (6) into Eq. (1) and separating the resulting expression leads to the following set of two equations:

$$\begin{aligned} \frac{\hbar^2}{2m} \frac{\partial^2 F_1}{\partial x^2} + i\hbar \frac{\partial F_1}{\partial t} \\ + [E + \hbar\omega - V_0 - U(t)V_1 \sin(\omega t)]F_1 \\ = \frac{i}{2}U(t)V_1 F_0(1 - e^{2i\omega t}) \end{aligned} \quad (7a)$$

$$\frac{\hbar^2}{2m} \frac{d^2 F_0}{dx^2} + [E - V_0]F_0 = 0. \quad (7b)$$

Our numerical solutions show that the two formulations [Eqs. (3), (4a), (4b), and (4c) and Eqs. (6), (7a), and (7b)] give equivalent values for the probability density and that these two formulations have similar numerical stability. However, in the second formulation, the term $F_1 e^{-i\omega t}$ must include all time-dependent effects, and so we find that even for large values of t the function $F_1(x, t)$ has appreciable time dependence. By contrast, with the first formulation, we find that in the asymptotic limit as t becomes large $F_1(x, t)$ and $F_{-1}(x, t)$ approach functions of x only. The first formulation was used for all of the examples that are presented in this article.

Conditions Imposed at the Ends of the Grid

At each time step, Eq. (5) and the corresponding equation for F_{-1} are used to update all values of F_1 and F_{-1} with the exception of those at the points at the ends of the grid. These two equations may not be used at the ends of the grid because the finite difference approximation used for the Laplacian operator requires values on both sides of

the point where the function is to be updated. Others have used various types of absorbing boundary conditions [19], or, equivalently, complex-coordinate contours [10], to avoid interference by reflections at the ends of the grid. However, there are two alternatives to this procedure and both of them have the advantage that they do not require an increased number of points as is necessary with absorbing boundary conditions. One approach is to use forward-only and backward-only differences to approximate the Laplacian operator at the two ends of the grid, and the second is to use extrapolants approximating the functions near the ends of the grid to update the values at the end points. We examined both of these methods and chose to use extrapolation because it offers greater flexibility and appears to have greater numerical stability.

It may be shown that for a uniformly spaced lattice, polynomial extrapolants have the form $C_1 Y_1 = -[C_2 Y_2 + C_3 Y_3 + \dots + C_{N+2} Y_{N+2}]$ where $N-1$ is the degree of the polynomial and the C_i are the binomial coefficients for the expansion of $(x-y)^N$. For example, with a linear extrapolant, $Y_1 = 2Y_2 - Y_3$, and with a quadratic extrapolant, $Y_1 = 3Y_2 - 3Y_3 + Y_4$. It is convenient to define extrapolants with fractional degrees as interpolations between the two adjacent extrapolants having an integer degree. For example, we define the 1.5-degree extrapolant as $Y_1 = 2.5Y_2 - 2Y_3 + 0.5Y_4$. We also define the -1-degree extrapolant as not updating the end point.

Figure 1 shows the results of stability tests in which F_1 and F_{-1} at both ends of the grid were updated by using polynomials for extrapolation. These tests are simulations of laser-assisted field emission using the Fowler-Nordheim model [20] for the potential at the surface of tungsten metal ($\phi = 4.5$ eV, $\epsilon_f = 19.1$ eV) with an applied static field of 5.5 V/nm and making the approximation that all tunneling electrons are at the Fermi level. The potential barrier is approximately triangular in shape, with rounding due to image corrections. The radiation field has a wavelength of 2 μm and a power flux density of 10^8 W/m² and is turned on at time $t = 0$. The 450-point grid has a spacing of $\Delta x = 0.01725$ nm. The criterion $\Delta t < m(\Delta x)^2/2\hbar$ requires that the time step $\Delta t < 0.001285$ fs, and the value used was $\Delta t = 0.001$ fs. The figure shows the logarithm of the simulated duration of the radiation field for the divergence of the calculations versus the degree of the polyno-

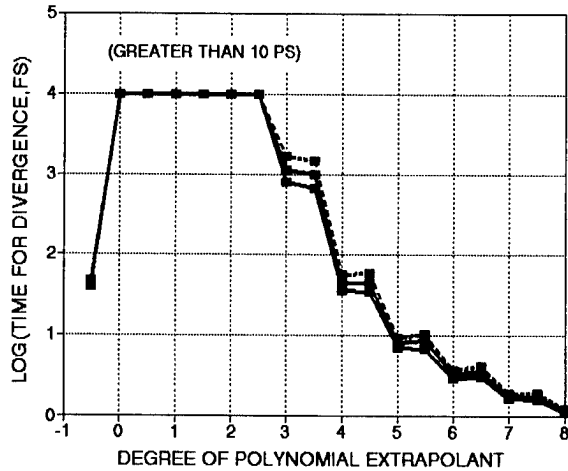


FIGURE 1. Simulated duration of the radiation field for divergence (mean and mean \pm SEM) versus degree of polynomial extrapolant for > 10 ps using polynomials of degrees 0, 0.5, 1, 1.5, 2, and 2.5.

omial extrapolant, where divergence is defined to occur when $|F_1| > 1$ and/or $|F_{-1}| > 1$ at any point in the grid. Tests were made using each extrapolant with five different distances of the metal–vacuum interface from the incident (left) end of the grid (3, 2.5, 2, 1.5, and 1 nm), and the values of the mean and the mean (\pm SEM) are shown. Figure 1 shows that extrapolation causes instability with polynomials having degree less than 0 or greater than 2.5, but there was no evidence of divergence for simulated durations exceeding 10 ps when using extrapolants having degrees 0, 0.5, 1, 1.5, 2, and 2.5.

Figure 2 shows the results of stability tests made using the same model and parameters as in the previous figure. We observed that the errors caused by numerical instability are most severe at the end points of the grid, which would be anticipated because the values at the two end points are evaluated directly by the extrapolation. Figure 2 shows the values of $|F_1|^2$ for both end points at a simulated time of 100 fs. Under the conditions used in these simulations, the radiation field would cause the current to increase by less than 0.1% in the steady state [4]. Thus, Figure 2 shows that there are significant errors at the end points when using extrapolation with polynomials having degree less than 0 or greater than 2.5, which is consistent with Figure 1. The results in Figure 2 suggest that a polynomial of degree 1.5 may be the optimum.

Figure 3 shows the results of stability tests that are similar to those shown in Figure 2 except that

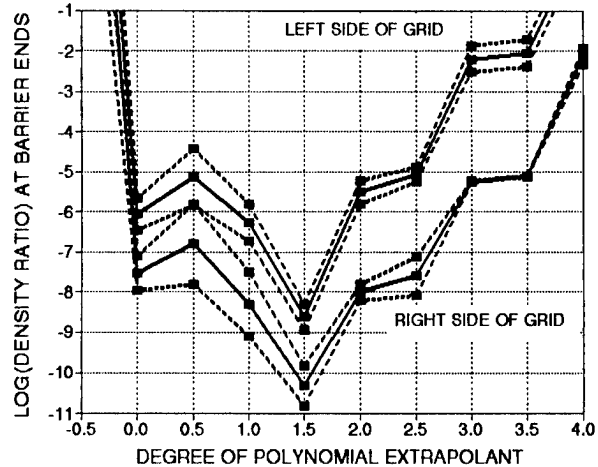


FIGURE 2. Value of $|F_1|^2$ (mean and mean \pm SEM) at the ends of the grid versus degree of polynomial extrapolant for simulations of laser-assisted field emission 100 fs after turning on a radiation field with a power flux density of 10^8 W/m² at $\lambda = 2 \mu\text{m}$.

they were made for 10 eV electrons with a square barrier having a height of 11 eV and a length of 1 nm. The radiation field has a wavelength of 2 μm and a power flux density of 10^8 W/m² and is turned on at time $t = 0$. The 450-point grid has a spacing $\Delta x = 0.00667$ nm. The time step used was $\Delta t = 0.00015$ fs, where the criterion $\Delta t < m(\Delta x)^2/2\hbar$ requires $\Delta t < 0.0001920$ fs. In Figure 3, the values of $|F_1|^2$ are shown for both end points

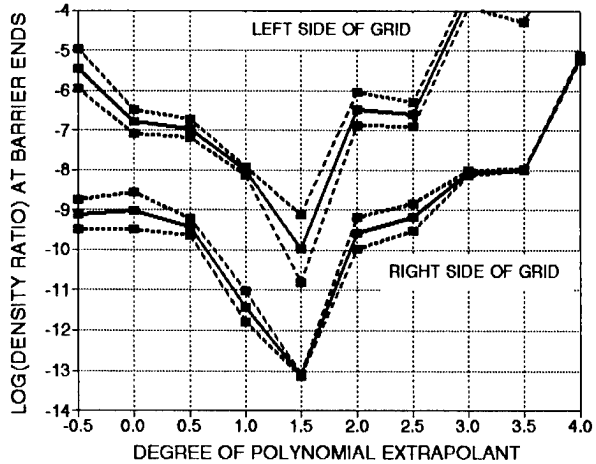


FIGURE 3. Value of $|F_1|^2$ (mean and mean \pm SEM) at the ends of the grid versus degree of polynomial extrapolant for simulations of 10 eV electrons with an 11 eV, 1 nm-square barrier 50 fs after turning on a radiation field with a power flux density of 10^8 W/m² at $\lambda = 2 \mu\text{m}$.

at a simulated time of 50 fs. Tests were made using each extrapolant with five different distances of the barrier from the incident (left) end of the grid (0.5, 0.6, 0.7, 0.8, and 0.9 nm), and values of the mean and the mean \pm SEM are shown. The results shown in Figure 3 are consistent with those in Figure 2 in that they also suggest that degree 1.5 may be the optimum. We observed that the deviation in values of the probability density caused by changing the spacing between the ends of the potential barrier and the ends of the grid is much less pronounced within the grid than at the end points. This aberrant effect appears to be minimum for extrapolants having degrees 1, 1.5, and 2. When using polynomials having each of these three degrees, the solutions show waves that approach the right side of the grid and are transmitted without reflection, whereas the wave structure near the ends of the grid is destroyed by using extrapolation with polynomials of higher degree. We believe that polynomials with degree less than 1 fail to approximate the variation of the wave function within the grid, and polynomials with degree greater than 2 cause oscillations that create numerical instability at the end points.

Numerical Examples

Figure 4 shows the normalized probability density for 10 eV electrons exiting at the far side of a square potential barrier as a function of the time

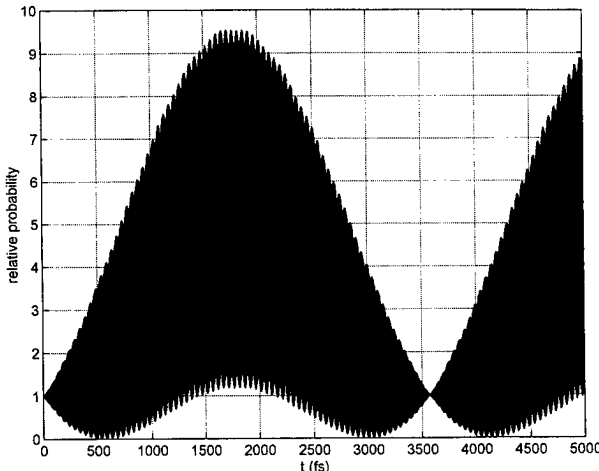


FIGURE 4. Normalized probability density for 10 eV electrons exiting from an 11 eV, 1 nm-square barrier versus time the radiation field is on. The radiation has a power flux density of 10^8 W/m^2 at $\lambda = 900 \text{ nm}$.

since the radiation field was turned on. The square barrier has a height of 11 eV and a length of 1 nm, and the radiation has a wavelength of 900 nm and a power flux density of 10^8 W/m^2 . The total simulated time is 5 ps, corresponding to 3.333×10^7 time steps or 1666 cycles of the radiation field. The figure is dark because of the many cycles, and the fine-scale scalloping does not represent extrema of the individual optical cycles, but is caused by using 10,000 points in the figure, which is only six samples per cycle.

Steady-state solutions obtained with Floquet methods [16] and other procedures [21] show resonances at which the tunneling current is markedly increased by a radiation field. The mechanism for these resonances is that an electron is promoted above the barrier by absorbing one quantum from the radiation field, and the line integral of the (now real) momentum around the closed contour between the classical turning points is an integral multiple of Planck's constant. Thus, the wave function is reinforced. For square barriers, this requires that the length of the barrier is an integer multiple of one-half the de Broglie wavelength, and so the optical wavelength at resonance is given by

$$\lambda = \frac{hc}{(V_0 - E) + \frac{n^2 h^2}{8md^2}}, \quad (8)$$

where m and E are the mass and energy of the particles, V_0 is the barrier height, and n is an integer greater than zero. For 10 eV electrons with an 11 eV, 1 nm-square barrier, the first three resonances are at wavelengths of 905, 506, and 296 nm, for which the barrier length equals $1/2$, $2/2$, and $3/2$ of the de Broglie wavelength for particles absorbing one quantum [13]. We find that in transient solutions, when the frequency of the radiation field is near a resonance, the initial response consists of beating between the two frequencies, with a gradual transition to the steady-state response, which contains only the frequency of the radiation field. The duration of each beat and the time required to reach the steady-state values each vary inversely with the difference between the two frequencies. Thus, at the wavelength used in Figure 4 (900 nm), which is near the first resonance (905 nm), each beat has a duration of 3.56 ps or approximately 1190 cycles of the radiation field.

Measurements with heterostructures and Josephson junctions [22] suggest that a specific

time is required for quantum tunneling, and the question of how to calculate or measure this time has generated much interest and controversy [23]. Our examples are consistent with the semiclassical transit time (T_{sc}), which corresponds to the classical time for traversing the inverted barrier, and they suggest a semiclassical picture of the tunneling process. In each transient solution, we find a delay equal to T_{sc} (1.69 fs for the example in Fig. 4) before the probability density at the far side of the barrier responds to the radiation field. The optical electric field is superimposed on the barrier and so the height of the barrier is modulated at the optical frequency. Each decrease in the barrier height causes increased transmission of electrons through the barrier, and each increase in the barrier height causes decreased transmission. However, in each transient solution, we find a delay equal to $T_{sc}/2$ between each extremum in the instantaneous barrier height and the corresponding extremum in the transmission.

Figure 5 shows values of the probability density as a function of the optical wavelength for 10 eV electrons at the far side of an 11 eV, 1 nm-square barrier for a radiation field with a power flux density of 10^8 W/m^2 . The quantities plotted are the maximum peak-to-peak value for the relative probability density, the maximum values of $|F_1|^2$ and $|F_{-1}|^2$, and the duration of the first beat (first null-to-null, shown dashed). The resonance seen in Figure 5 at $\lambda = 905 \text{ nm}$ corresponds to a barrier

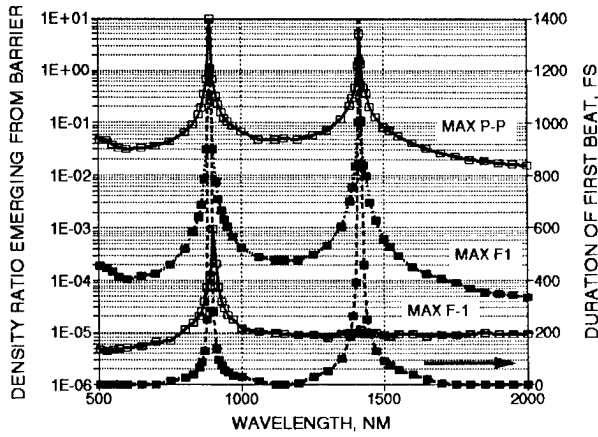


FIGURE 5. Normalized probability density versus optical wavelength for 10 eV electrons exiting from an 11 eV, 1 nm-square barrier for a power flux density of 10^8 W/m^2 . Quantities plotted are maximum peak-to-peak normalized probability density, maximum of $|F_1|^2$ and $|F_{-1}|^2$, and duration of the first beat (dashed).

length equal to $1/2$ of the de Broglie wavelength for particles absorbing one quantum.

There is a second resonance, at $\lambda = 1420 \text{ nm}$, which is not present in the steady state [16, 21]. Our transient solutions show that this resonance decays at a rate that is consistent with the "dwell time" for quantum tunneling [23]. Since the second resonance occurs at a wavelength $\lambda > hc/(V_0 - E) = 1240 \text{ nm}$, the energy of a single photon from the radiation field cannot take an electron above the barrier. This new resonance is a single-photon effect because we find that the current is proportional to the power flux density, and thus the resonance must occur for particles while they are tunneling. From numerical values in the transient solutions, we find that the criterion for the new resonance is that the semiclassical transit time for tunneling electrons that have absorbed one photon from the radiation field is equal to the period of the optical radiation. Thus, an electron entering the barrier at a time when the modulated barrier height is minimum will also exit the barrier when this height is minimum, and, therefore, the transmission is increased because the reflection is reduced in both transitions. For square barriers, the optical wavelength at the new resonance is given by

$$\lambda = \frac{hc}{2(V_0 - E)} \left[1 + \sqrt{1 + \frac{2(V_0 - E)md^2}{h^2}} \right], \quad (9)$$

where m and E are the mass and energy of the particles and V_0 is the barrier height.

Figure 6 shows the normalized probability density for electrons as they exit from the barrier in laser-assisted field emission, as a function of the time since the radiation field was turned on. We used the Fowler-Nordheim model [20] for the potential at the surface of tungsten with an applied static field of 5.5 V/nm and the approximation that all tunneling electrons are at the Fermi level. The radiation field has a wavelength of 660 nm and a power flux density of 10^8 W/m^2 . The 450-point grid has a spacing $\Delta x = 0.01725 \text{ nm}$, and the time step was $\Delta t = 0.001 \text{ fs}$. The degree 1.5 polynomial extrapolant was used in these calculations. For this potential, we found a single resonance at a wavelength of 520 nm , in which an electron absorbing one photon from the radiation field has a momentum line integral equal to Planck's constant. The response shown in Figure

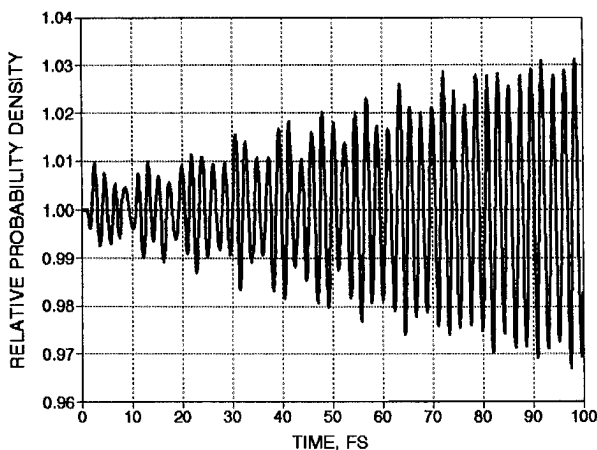


FIGURE 6. Normalized probability density for electrons exiting from the barrier in laser-assisted field emission versus time the radiation field is on. The radiation has a power flux density of 10^8 W/m^2 at $\lambda = 660 \text{ nm}$.

6 illustrates beating with the resonance followed by a transition to approach the steady state. The new resonance seen in Figure 5, which is not present in the steady state, was not found when using the Fowler–Nordheim model for the potential or in any of the other simulations which we have made using models other than a square potential barrier with a single energy.

Figure 7 shows the logarithm of the probability density for electrons in laser-assisted field emission as a function of the location and the time since the radiation field was turned on. As in

Figure 6, we used the Fowler–Nordheim model for tungsten with an applied static field of 5.5 V/nm . The maximum barrier height is 1.684 eV above the Fermi level, which corresponds to one quantum for a radiation field with a wavelength of 736 nm . The radiation field used in the simulation is at the resonant wavelength of 520 nm , with a power flux density of 10^{12} W/m^2 . This figure shows the initial buildup in a small fraction of the first beat period in the response. There is a delay equal to T_{sc} (1.28 fs for the example in Fig. 7) before the density of the exiting electrons responds to the radiation field. The radiation field modulates the barrier height at the optical frequency, and we find a delay equal to $T_{sc}/2$ between each extremum in the barrier height and the corresponding extremum in the density for electrons emerging from the barrier.

Discussion

The two systems of equations which we used [Eqs. (3) and (4a)–(4c) and Eqs. (6), (7a), and (7b)] are each equivalent to Eq. (1). However, an approximation of the steady-state solution is built into Eqs. (3) and (6), and we find that this causes numerical solutions of these two systems to be more stable than solving Eq. (1) directly. Furthermore, in the numerical solutions, we find that in the asymptotic limit as t become large $F_1(x, t)$ and $F_{-1}(x, t)$ approach functions of x only. Prior to this study, we used a product formulation [13] in which the wave function $\Psi(x, t) = F(x, t)\Phi(x)e^{-iEt/\hbar}$, where $\Phi(x)e^{-iEt/\hbar}$ is the static solution and one solves for the function $F(x, t)$ which is defined to be unity for $t \leq 0$ at all values of x . With the product formulation, convergence was demonstrated when simulating short optical pulses, but the solutions were found to be unstable when simulating pulses with durations exceeding four to five periods of the optical field. We attribute this instability to the choice of the static solution, rather than to the steady-state solution, as the basis.

Others have used absorbing boundary conditions [19], or, equivalently, complex-coordinate contours [10] to avoid interference by reflections at the ends of the grid and empirically adjusted “windowing” and “gobbling” [24] and split-operator formulations requiring matrix methods [6–9],

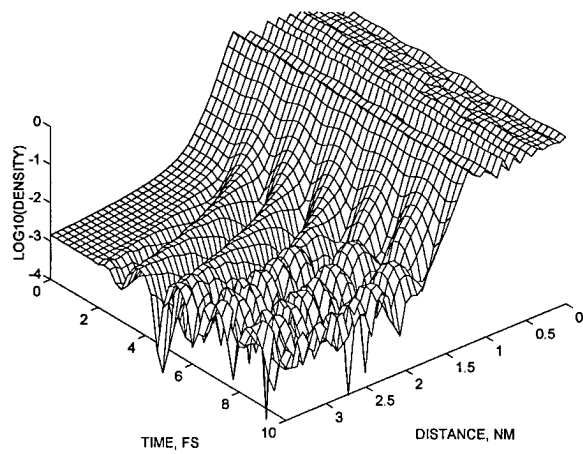


FIGURE 7. Logarithm of the probability density for electrons in laser-assisted field emission as a function of the location and the time that the radiation field is on. The radiation has a power flux density of 10^{12} W/m^2 at $\lambda = 520 \text{ nm}$.

to obtain numerical stability. The present formulation does not use any of these techniques, and it has been shown to be stable for simulated pulse durations exceeding 2000 cycles of the radiation field. We find that the present formulation is much simpler to implement because (1) the end conditions do not require increasing the length of the grid, (2) the solution is explicit so that no matrix is required, and (3) only 5 dimensioned variables are declared which correspond to F_0 and two values of F_1 and F_{-1} . The present calculations were made for single energies instead of wave packets because our objective was to develop stable and efficient techniques to be used with density functional theory in simulating laser-assisted field emission [5] where one is not free to specify a Gaussian or other distribution.

The numerical examples shown in Figures 4–7 offer promise as a new approach to the unsolved problem [23] of evaluating the duration of quantum tunneling. Many different theoretical approaches have been used to examine tunneling times [23], but the only transient solutions considered for this purpose were based on wave packets [25]. Wave-packet solutions show a delay between the incident and transmitted packets, but the interpretation of these solutions has been questioned [26] because there is no valid basis for comparing any part (e.g., peak or centroid) of these two different packets. Furthermore, it appears that the tunneling time is a function of the particle energy, and, therefore, the distribution of energies in a wave packet would smear the effects of tunneling times. Our calculations do not require a distribution of energies, and the examples clearly show the effects of tunneling times. While the result is by no means unanimous [23], 12 different analytical methods used to study tunneling times resulted in the semiclassical transit time [27], which is the classical time for traversing the inverted barrier. Our examples are consistent with the semiclassical transit time, and they also show the effects of the tunneling dwell time, so that they suggest a semiclassical picture for the tunneling process.

ACKNOWLEDGMENTS

The Pentium PC used for the calculations was made possible by NSF Research Equipment Grant No. 9500007.

References

- M. Völcker, W. Krieger, and H. Walther, *J. Appl. Phys.* **74**, 5426 (1993).
- M. Völcker, W. Krieger, and H. Walther, *Phys. Rev. Lett.* **66**, 1717 (1991).
- M. J. Hagmann, *J. Vac. Sci. Technol. B* **14**, 838 (1996).
- M. J. Hagmann and M. Brugat, *J. Vac. Sci. Technol. B* **15**, 405 (1997).
- M. J. Hagmann, *Int. J. Quantum Chem.* **65**, 857 (1997).
- K. C. Kulander, *Phys. Rev. A* **35**, 445 (1987).
- P. L. DeVries, *J. Opt. Soc. Am. B* **7**, 517 (1990).
- K. J. LaGattuta, *J. Opt. Soc. Am. B* **7**, 639 (1990).
- M. S. Pindzola, G. J. Bottrell, and C. Bottcher, *J. Opt. Soc. Am. B* **7**, 659 (1990).
- C. W. McCurdy, C. K. Stroud, and M. K. Wisinski, *Phys. Rev. A* **43**, 5980 (1991).
- M. R. Hermann and J. A. Fleck, Jr., *Phys. Rev. A* **38**, 6000 (1988).
- L. A. Collins and A. L. Merts, *J. Opt. Soc. Am. B* **7**, 647 (1990).
- M. J. Hagmann, *Int. J. Quantum Chem.* **60**, 1231 (1996).
- F. H. M. Faisal, *Theory of Multiphoton Processes* (Plenum, New York, 1987), pp. 8–10.
- A. Pimpale, S. Holloway, and R. J. Smith, *J. Phys. A* **24**, 3533 (1991).
- M. J. Hagmann, *J. Appl. Phys.* **78**, 25 (1995).
- H. B. Keller, *Numerical Methods for Two-Point Boundary-Value Problems* (Dover, New York, 1992), pp. 39–71.
- D. M. Young and R. T. Gregory, *A Survey of Numerical Mathematics* (Addison-Wesley, Reading, MA, 1972), Vol. I, pp. 453–456.
- D. Macias, S. Brouard, and J. G. Muga, *Chem. Phys. Lett.* **228**, 672 (1994).
- R. H. Fowler and L. Nordheim, *Proc. R. Soc. Lond. A* **119**, 173 (1928); L. Nordheim, *Proc. R. Soc. Lond. A* **121**, 626 (1928).
- M. J. Hagmann, *Int. J. Quantum Chem.* **56** (Quantum Symp. Issue No. 29), 289 (1995).
- P. Gueret, E. Marcley, and H. Meier, *Appl. Phys. Lett.* **53**, 1617 (1988); D. Esteve, J. M. Martinis, C. Urbina, E. Turlot, M. H. Devoret, H. Grabert, and S. Linkwitz, *Phys. Scr. T* **29**, 121 (1989).
- R. Landauer and Th. Martin, *Rev. Mod. Phys.* **66**, 217 (1994).
- J. T. Muckerman, R. V. Weaver, T. A. B. Kennedy, and T. Uzer, in *Numerical Grid Methods and Their Applications to Schrödinger's Equation*, C. Cerjan, Ed. (Academic, Dordrecht, 1992).
- C. R. Leavens and G. C. Aers, *Phys. Rev. B* **39**, 1202 (1989); S. Brouard, R. Sala, and J. G. Muga, *Europhys. Lett.* **22**, 159 (1993).
- R. Landauer and Th. Martin, *Solid State Commun.* **84**, 115 (1992).
- M. J. Hagmann, *Int. J. Quantum Chem.* **52** (Quantum Symp. Issue No. 28), 271 (1994).

Excited Electronic States of Carotenoids: Time-Dependent Density-Matrix-Response Algorithm

SERGEI TRETIAK, VLADIMIR CHERNYAK, SHAUL MUKAMEL

Department of Chemistry and Rochester Theory Center for Optical Science and Engineering, University of Rochester, Rochester, New York 14627

Received 30 March 1998; revised 12 August 1998; accepted 13 August 1998

ABSTRACT: The response of the single-electron density matrix of a many-electron system to an external field is calculated using the time-dependent Hartree–Fock (TDHF) technique. A procedure for inverting the resulting nonlinear response functions to obtain an effective quantum multilevel system that has the same response is developed. The number of effective states is gradually increased as higher-order nonlinearities are computed. The complete set of intrastate and interstate density matrices and excited-state energies can be calculated. A favorable N -scaling of computational effort with size can be obtained making use of the localization of the optical transitions in real space. © 1998 John Wiley & Sons, Inc. Int J Quant Chem 70: 711–727, 1998

Key words: density matrix response functions; N -scaling, time-dependent Hartree–Fock, nonlinear response, bosonization, carotenoids

1. Introduction

The complete information on the optical response of a quantum system is contained in its set of many-electron eigenstates $|\nu\rangle, |\eta\rangle, \dots$ and energies $\epsilon_\nu, \epsilon_\eta, \dots$ [1]. Since the number of states

increases exponentially with the number of electrons, exact calculations become impractical even for fairly small molecules with a few atoms. An approximation at some level of configuration interaction (CI) allows to compute the states, and optical susceptibilities may be calculated using a summation over states (SOS) [2–5]. The CI/SOS is computationally expensive. In addition, size consistency is not guaranteed *a priori* and special care needs to be taken when choosing the right configurations.

Using the many-electron wave functions it is possible to calculate all n -body quantities and correlations. Most of this information is, however,

Correspondence to: S. Mukamel.

Contract grant sponsor: Air Force Office of Scientific Research.

Contract grant number: AFOSR-F49620-96-1-0030.

Contract grant sponsor: National Science Foundation.

Contract grant numbers: CHE-9526125, PH494-15583.

rarely used in the calculation of common observables (energies, dipole moments, spectra, etc.), which only depend on the expectation values of one- and two-electron quantities. A reduced description that only keeps a small amount of relevant information is called for. An important example of such a method is density-functional theory (DFT) [6–11], which only retains the ground-state charge density profile:

$$\rho_{nn}^{gg} = \langle g | c_n^+ c_n | g \rangle, \quad (1.1)$$

where $|g\rangle$ denotes the ground-state many-electron wave function and $c_n^+(c_n)$ is the Fermi annihilation (creation) operators for the n th basis set orbital. Hohenberg and Kohn's theorem proves that the ground-state energy is a unique and a universal functional of ρ_{nn} [12, 13], making it possible to compute self-consistently the charge distribution and the ground-state energy. This approach has been remarkably successful, and extensions to excited states have been made as well [10, 11].

In this study we develop a semiclassical approach for calculating the excited-state energies ϵ_ν and density matrices

$$\rho_{nm}^{\nu\eta} \equiv \langle \nu | c_n^+ c_m | \eta \rangle. \quad (1.2)$$

This approach is formally unrelated to DFT. Nevertheless, it shares its basic philosophy of aiming at “the truth but not the whole truth.” We recall that $|\nu\rangle$ and $|\eta\rangle$ represent the global electronic states of the system, whereas n and m denote the atomic basis functions. These quantities carry more information than ρ_{nn}^{gg} , yet considerably less than the complete set of eigenstates. $\rho^{\nu\nu}$ is the reduced single-electron density matrix of state ν . For $\nu \neq \eta$ $\rho^{\nu\eta}$ is the density matrix associated with the transition between ν and η . When the system is driven by an optical field, its wave function becomes a coherent superposition state:

$$\Psi(t) = \sum_\nu a_\nu(t) |\nu\rangle, \quad (1.3)$$

and its density matrix is given by

$$\rho_{nm}(t) \equiv \langle \Psi(t) | c_n^+ c_m | \Psi(t) \rangle = \sum_{\nu\eta} a_\nu^*(t) a_\eta(t) \rho_{nm}^{\nu\eta}. \quad (1.4)$$

Thus $\rho_{nm}^{\nu\eta}$ are the building blocks for the time-dependent single-electron density matrix [14–17]. In addition, the density matrix provides the complete information necessary for computing the matrix

elements of all single-electron operators. Given the operator

$$\mu = \sum_{nm} \mu_{nm} c_n^+ c_n, \quad (1.5)$$

we have

$$\langle \nu | \mu | \eta \rangle = \sum_{nm} \mu_{nm} \rho_{nm}^{\nu\eta}. \quad (1.6)$$

In particular, dipole matrix elements that determine the optical properties have the form of Eq. (1.6).

Our approach starts by coupling the molecule to an external field $\mathcal{E}(t)$ through

$$H_{\text{int}} = -\mu \mathcal{E}(t) \equiv \sum_{nm} \mathcal{E}_{nm}(t) c_n^+ c_m, \quad (1.7)$$

where $\mathcal{E}_{nm}(t) \equiv \mu_{nm} \mathcal{E}(t)$. We can then expand the induced density matrix in powers of the incoming field:

$$\begin{aligned} \rho_{nm}(t) &= \rho_{nm}^{gg} + \int d\tau \sum_{n'm'} S_{nm, n'm'}^{(1)}(t; \tau) \mathcal{E}_{n'm'}(\tau) \\ &\quad + \int \int d\tau_1 d\tau_2 \sum_{\substack{n'm' \\ n''m''}} S_{nm, n'm', n''m''}^{(2)}(t; \tau_1, \tau_2) \mathcal{E}_{n'm'}(\tau_1) \mathcal{E}_{n''m''}(\tau_2) + \dots. \end{aligned} \quad (1.8)$$

The j th-order density matrix response functions (DMRF) $S^{(j)}$ can be conveniently calculated using the time-dependent Hartree–Fock (TDHF) approximation [18–20], which provides a closed system of equations for the reduced single-electron density matrix ρ_{mn} . Since the DMRF can be alternatively expanded in terms of the system energies and matrix elements of the single-electron operators $c_m^+ c_n$, it constitutes a source of information on these quantities. However, it is not easy to interpret the TDHF response in terms of the global eigenstates since the structure of the TDHF expressions is very different from their standard SOS counterparts.

The present article provides an algorithm for inverting the DMRF to obtain an effective multi-level system which has the same response functions, resulting in the eigenvalues and all density matrix elements [Eq. (1.2)]. Note that the DMRFs are more general than the optical response functions since the interaction [Eq. (1.7)] is not limited to the dipole operator. The latter has often selec-

tion rules which limit the information to a few dominant states. The freedom to use any field $\mathcal{E}_{nm}(t)$ in Eq. (1.7) allows us to calculate all possible states.

The effective multilevel system will be constructed in four steps (Fig. 1).

(i) Starting with the original quantum fermion model (QFM), we build its classical limit by considering the space of single Slater determinants \mathbf{M} (the space of coherent states as its phase space). The Poisson bracket on \mathbf{M} and the classical Hamiltonian have been introduced in [21]. We make use of the observation [22] that the TDHF approximation can be considered as a classical limit of the original many-electron system. Hereafter we refer to the classical limit of the QFM as the classical oscillator model (COM). As shown in [22] any classical system can be mapped onto a set of classical coupled oscillators.

(ii) In the vicinity of the stationary solution $\rho^{ss} \in \mathbf{M}$ of the TDHF equation we transform the local variables on \mathbf{M} so that the Poisson bracket assumes a canonical form. This establishes the oscillator representation of the COM. Stated differently, this shows the equivalence of the COM and a classical canonical oscillator model (CCOM) de-

fined as the COM represented in terms of the canonical variables.

(iii) We build the quantum oscillator model (QOM) by quantizing the CCOM, so that the classical limit of the QOM reproduces the CCOM. The classical system of oscillators can therefore be viewed as the classical limit of a system of quantum coupled oscillators. We thus have two quantum models: QFM, which corresponds to the original electronic system, and the system of quantum anharmonic oscillators (QOM). The classical limits for COM and CCOM, respectively, are equivalent, and the COM describes the QFM within the TDHF approximation.

(iv) Finally, using a perturbative approach, we build an effective multilevel system (EMS) whose exact optical response reproduces the classical approximation of the QOM, which is the CCOM and in turn coincides with the TDHF approximation of the original model QFM. In summary, the EMS constitutes a quantum model whose optical response reproduces the TDHF approximation of the original model.

In Section 2 we carry out steps (i) and (ii) and map the original quantum fermion model onto a classical canonical oscillator model. Steps (iii) and (iv) are made in Section 3. Computational details are given in the Appendices. In Section 4 we apply this algorithm to a family of unsubstituted and acceptor-substituted carotenoids [23, 24]. The induced density matrices $\rho_{nm}^{\nu\eta}$ for the states which dominate the linear and the quadratic response are investigated. Finally we discuss and summarize our results in Section 5.

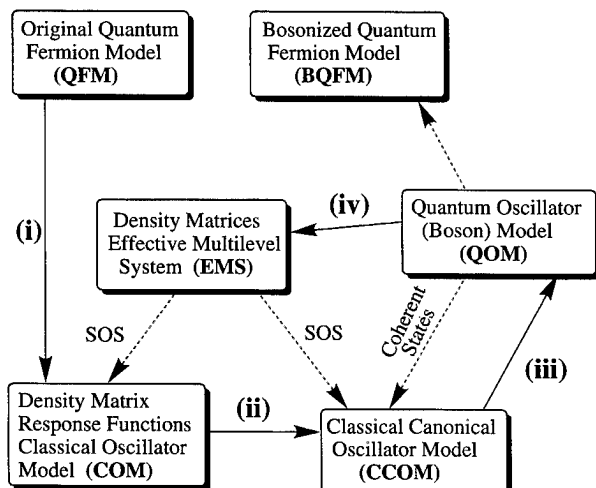


FIGURE 1. Four steps involved in constructing the effective multilevel system (EMS) out of the original quantum Fermion model (QFM). Obtaining a bosonized quantum fermion model (BQFM) out of the quantum oscillator model should allow to reproduce the exact density matrix response functions and not rely on the TDHF. This extension goes beyond the scope of the present work.

2. TDHF APPROACH: CLASSICAL ELECTRONIC OSCILLATORS

We consider a system described by the molecular electronic Hamiltonian [14, 23].

$$\hat{H} = \sum_{mn\sigma} t_{mn} c_{m\sigma}^+ c_{n\sigma} + \sum_{\substack{mnkl \\ \sigma\sigma'}} \langle nm | kl \rangle c_{m\sigma}^+ c_{n\sigma'}^+ c_{k\sigma'} c_{l\sigma} - \mathcal{E}(t) \sum_{mn\sigma} \mu_{mn} c_{m\sigma}^+ c_{n\sigma}, \quad (2.1)$$

where $c_{m,\sigma}^+$ ($c_{m,\sigma}$) are the annihilation (creation) operators of an electron on atomic orbital m with

spin σ which satisfy the Fermi anticommutation relations (assuming an orthogonal basis set):

$$c_{m\sigma} c_{n\sigma'}^+ + c_{n\sigma'}^+ c_{m\sigma} = \delta_{mn} \delta_{\sigma\sigma'}, \quad (2.2)$$

and all other anticommutators of c^+ and c vanish. $\hat{\rho}_{nm}^\sigma = c_{m,\sigma}^+ c_{n,\sigma}$ is the reduced single-electron density operator [14–17]. The first term in Eq. (2.1) is the single-electron (core) Hamiltonian describing the kinetic energy and nuclear attraction of an electron, the second term represents electron–electron (Coulomb) interactions where $\langle mk | nl \rangle$ are the two-electron integrals, and the last term gives the interaction between the electrons and the external electric field $\mathcal{E}(t)$, μ being any single-electron operator [21, 23].

The classical oscillator model is constructed using the procedure for approaching the classical limit outlined in [22]. We start by defining the phase space of the single Slater determinants \mathbf{M} (defined up to a phase) known as the Grassmann manifold $G(M, N; C)$, N being the basis set size and M is the number of electrons. The Grassmann manifold $\mathbf{M} = G(M, N; C)$ can be alternatively represented as the space of hermitian $N \times N$ single-electron reduced density matrices with $\rho^2 = \rho$ and $\text{rank}(\rho) = M$. The classical Hamiltonian is given as

$$H(\rho) = \langle \Omega(\rho) | \hat{H} | \Omega(\rho) \rangle, \quad (2.3)$$

where $\Omega(\rho)$ is the Slater determinant corresponding to ρ . Expressions for $H(\rho)$ in terms of the original parameters of the molecular electronic Hamiltonian [Eq. (2.1)] and for the Poisson bracket were given in [21]. The TDHF equation adopts the form of the equation of motion of Hamilton's classical dynamics on \mathbf{M} . The stationary point of the TDHF equations which corresponds to the minimum of the energy function $H(\rho)$ on \mathbf{M} constitutes the Hartree–Fock (HF) reduced ground-state single-electron density matrix ρ^{ss} which can be found by solving the HF equation [14]:

$$[F(\rho^{ss}), \rho^{ss}] = 0, \quad (2.4)$$

where $F(\rho^{ss})$ is the Fock matrix

$$F(\rho^{ss}) = t + V(\rho^{ss}), \quad (2.5)$$

and the matrix elements of the Coulomb electronic operator V are

$$V(\rho^{ss})_{mn} = \sum_{k,l} \rho_{kl}^{ss} \left[\langle mk | nl \rangle - \frac{1}{2} \langle mn | kl \rangle \right]. \quad (2.6)$$

To construct the classical oscillators [step (ii)] we need to define local coordinates on \mathbf{M} representing deviations from ρ^{ss} . The restricted TDHF scheme [21] allows us to reduce the number of variables from N^2 to particle-hole variables $M(N - M)$ only. To that end we decompose the single-electron density matrix in the form

$$\rho = \rho^{ss} + \xi + T(\xi). \quad (2.7)$$

Here ξ represents the particle–hole whereas $T(\xi)$ is the particle–particle and the hole–hole parts of the deviation of the reduced single-electron density matrix from the ground-state ρ^{ss} . Also ρ^{ss} , ξ , and $T(\xi)$ in Eq. (2.7) are $N \times N$ matrices.* The particle–particle and hole–hole components of the density matrix are not independent variables, since they can be expressed in terms of the particle–hole part [21, 23]. Therefore only the particle–hole components of the density matrix, ξ , need to be calculated explicitly; T can be expanded in a Taylor series which contains only even powers of ξ . For computing DMRF not higher than third order, it is sufficient to retain only the lowest (second-order) term [21, 23].

$$T(\xi) = \frac{1}{2} [[\xi, \rho^{ss}], \xi] = (I - 2\rho^{ss})\xi^2, \quad (2.8)$$

where I is the $N \times N$ unit matrix.

A convenient coordinate system can be introduced by parameterizing the electron–hole component (ξ) of the density matrix. To introduce variables close to canonical (as will be explained latter) it is convenient to use the TDHF equations for $\xi(t)$:

$$\begin{aligned} i \frac{\partial}{\partial t} \xi(t) &= L(\xi) - \mathcal{E}[\mu, \rho] + [V(\xi), \xi + T(\xi)] \\ &\quad + [V(T(\xi)), \xi + \rho^{ss}], \end{aligned} \quad (2.9)$$

where ρ is given by Eq. (2.7) and the Liouville space operator (superoperator) L represents the linear part of the equation [21, 23]:

$$L(\xi) = [t + V(\rho^{ss}), \xi] + [V(\xi), \rho^{ss}]. \quad (2.10)$$

The oscillator variables are computed as the eigenmodes of the linear part of Eq. (2.9) satisfying:

$$L(\xi_\alpha) = \Omega_\alpha \xi_\alpha, \quad L(\xi_{-\alpha}) = -\Omega_\alpha \xi_{-\alpha}. \quad (2.11)$$

* ρ^{ss} and $\xi(t)$ are matrices of rank M , $M < N$.

These oscillators are orthonormal:

$$\text{Tr}(\rho^{gg}[\xi_{-\alpha}, \xi_\beta]) = \delta_{\alpha, -\beta}, \quad (2.12)$$

and the particle-hole part of the density matrix can be expanded in ξ_α [21, 23]

$$\xi(t) = \sum_{\alpha > 0} z_\alpha(t) \xi_\alpha + z_\alpha^*(t) \xi_\alpha^+. \quad (2.13)$$

Each oscillator α is described by two complex operators ξ_α and ξ_α^+ . Following the notation of Ref. [21] we define $\xi_{-\alpha} = \xi_\alpha^+$; z_α and its complex conjugate $z_{-\alpha} = z_\alpha^*$ constitute the complex oscillator amplitudes. A classical picture is obtained by introducing the oscillator coordinates $Q_\alpha \equiv 1/\sqrt{2}(\xi_\alpha + \xi_\alpha^+)$ and the momenta $P_\alpha \equiv i/\sqrt{2}(\xi_\alpha - \xi_\alpha^+)$ [21]. However, it is more convenient to keep the complex ξ_α variables.

Equations (2.13) and (2.7) define a local coordinate system z_α on \mathbf{M} where ρ^{gg} is the origin. Substitution of Eqs. (2.13) and (2.7) into Eq. (2.3) yields the classical Hamiltonian for the variables z_α ; $H(z_\alpha)$ can be calculated in a form of an expansion in powers of z_α . The expression to fourth-order is presented in [21]. For the applications made in this study we only need the Hamiltonian up to third-order:

$$H(z) = \sum_{\alpha > 0} \Omega_\alpha z_{-\alpha} z_\alpha + \frac{1}{3} \sum_{\alpha \beta \gamma} V_{\alpha, \beta \gamma} z_\alpha z_\beta z_\gamma - \mathcal{E}(t) \mathcal{P}(z), \quad (2.14)$$

with the polarization

$$\mathcal{P}(z) = \sum_\alpha \mu_\alpha z_\alpha + \frac{1}{2} \sum_{\alpha \beta} \mu_{\alpha \beta} z_\alpha z_\beta, \quad (2.15)$$

where

$$\mu_\alpha = \text{Tr}([\rho^{gg}, \xi_\alpha][\mu, \rho^{gg}]), \quad (2.16a)$$

$$\mu_{\alpha, \beta} = \text{Tr}([\rho^{gg}, \xi_\alpha][\mu, \xi_\beta]), \quad (2.16b)$$

$$V_{\alpha, \beta \gamma} = \text{Tr}([\rho^{gg}, \xi_\alpha][V(\xi_\beta), \xi_\gamma]) + \text{Tr}([\rho^{gg}, \xi_\alpha] \times [V(\frac{1}{2}[[\xi_\beta, \rho^{gg}], \xi_\gamma]), \rho^{gg}]). \quad (2.16c)$$

All quantities here are $N \times N$ matrices in the single-electron space, and the trace is defined in this space.

The Poisson bracket for the z_α variables is calculated in [21] and to first-order in z_α it has the

canonical form

$$\{z_\alpha, z_\beta\} = i \delta_{\alpha, -\beta}. \quad (2.17)$$

It has the following useful properties:

$$\{z_\alpha, z_\beta\} = -\{z_\beta, z_\alpha\}, \quad (2.18)$$

$$\{z_\alpha, z_\beta z_\gamma\} = \{z_\alpha, z_\beta\} z_\gamma + z_\beta \{z_\alpha, z_\gamma\}. \quad (2.19)$$

The classical Hamilton equation of motion $\dot{z} = \{H, z\}$ obtained using Eqs. (2.14)–(2.16) can be written as

$$i \frac{\partial}{\partial t} z_\alpha = \Omega_\alpha z_\alpha - \mathcal{E} \mu_{-\alpha} - \mathcal{E} \sum_\beta \mu_{-\alpha, \beta} z_\beta + \sum_{\beta \gamma} V_{-\alpha, \beta \gamma} z_\beta z_\gamma. \quad (2.20)$$

These equations are equivalent to Eq. (2.9). The linear and the second-order response functions calculated by solving these equations are given in Appendix A.

Equations (2.14)–(2.20) define the classical oscillator model. The variable z_α describes the α th oscillator, as is clearly seen from the form of the Poisson bracket [Eq. (2.16)]. Higher-order terms of the Hamiltonian can be calculated order by order. Similarly, the Poisson bracket is not strictly canonical and the right-hand side (rhs) of Eq. (2.17) can be expanded in powers of z_α . Second-order corrections have been calculated in [22]. These deviations can, however, be eliminated since the Poisson bracket can be always transformed to a canonical form [25] using a nonlinear transformation of variables

$$z'_\alpha = z_\alpha + \sum_{\alpha \beta \gamma \delta} S_{\alpha, \beta \gamma \delta} z_\beta z_\gamma z_\delta + \dots. \quad (2.21)$$

In practice, the canonical variables can be calculated order by order in z_α . Expressing the Hamiltonian in terms of the canonical variable z'_α allows us to define a CCOM to any given order in z_α . This accomplishes step (ii) of the procedure.

3. Intrastate and Transition Electronic Density Matrices for the Effective Multilevel System

Step (iii) involves the construction of a quantum oscillator model QOM whose classical limit reproduces the CCOM. To that end we associate with each classical variable z_α an annihilation operator

a_α ($z_\alpha = \langle a_\alpha \rangle, \alpha > 0$); $z_{-\alpha} = z_\alpha^*$ is associated with a creation operator a_α^+ ($z_\alpha^* = \langle a_\alpha \rangle^+$). These satisfy the boson commutation relations:

$$[a_\alpha, a_\beta^+] = \delta_{\alpha\beta}. \quad (3.1)$$

We define the QOM Hamiltonian H_1 by

$$H_1 = :H(a_\alpha, a_\alpha^+):, \quad (3.2)$$

where $H(a_\alpha, a_\alpha^+)$ is the classical Hamiltonian of the CCOM, which is given by Eqs. (2.14) and (2.15) up to third order, and $: \dots :$ stands for normal ordering. We then have

$$\begin{aligned} H_1 = & \sum_\alpha \Omega_\alpha a_\alpha^+ a_\alpha + \frac{1}{3!} \left(\sum_{\alpha\beta\gamma} V_{\alpha, \beta\gamma} a_\alpha a_\beta a_\gamma \right. \\ & + 3 \sum_{\alpha\beta\gamma} V_{-\alpha, \beta\gamma} a_\alpha^+ a_\beta a_\gamma + h.c. \Big) \\ & - \mathcal{P}(a_\alpha^+, a_\alpha), \end{aligned} \quad (3.3)$$

with

$$\begin{aligned} \mathcal{P}(a_\alpha^+, a_\alpha) = & \sum_\alpha \mu_\alpha a_\alpha \\ & + \frac{1}{2!} \left(\sum_{\alpha\beta} \mu_{\alpha\beta} a_\alpha a_\beta + \sum_{\alpha\beta} \mu_{-\alpha\beta} a_\alpha^+ a_\beta + h.c. \right), \end{aligned} \quad (3.4)$$

and the summation in Eqs. (3.3) and (3.4) runs over $\alpha, \beta, \gamma > 0$.

The classical limit of the QOM can be obtained by requiring that each oscillator α remain in a coherent state parameterized by z_α at all times. This amounts to the following factorizations $\langle a_\alpha a_\beta \rangle = z_\alpha z_\beta$ and $\langle a_\alpha^+ a_\beta \rangle = z_\alpha^* z_\beta$. Using these factorizations, the Heisenberg equation of motion $\dot{a}_\alpha = i/\hbar [H_1, a_\alpha]$ with H_1 given by Eq. (3.3) coincides with the classical equation of motion [Eq. (2.20)]. The CCOM is thus the classical limit of the QOM and step (iii) is accomplished.

We turn now to step (iv), namely constructing the effective multilevel system EMS whose response reproduces the classical limit of QOM (which, in turn, coincides with the TDHF approximation of the QFM). This will be based on the picture established in [22] that the semiclassical expansion is a reexpansion of the optical response in the anharmonicities of the Hamiltonian and nonlinearities of the polarization operator in a and a^+ . This is carried out for the response up to second order in Appendix B. In particular, the linear response in the classical approximation is

obtained by setting $V_{\alpha, \beta\gamma} = 0$ and $\mu_{\alpha\beta} = 0$ (i.e., using the model of a set of linearly driven uncoupled harmonic oscillators) whereas the second-order response also depends on the terms proportional to $V_{\alpha, \beta\gamma}$ and $\mu_{\alpha\beta}$.

The QOM is improved successively by incorporating higher-order responses. We will concentrate on the lower-energy excited states, which can be constructed using the linear and the second-order responses. For the linear response we set $V_{\alpha, \beta\gamma} = 0$ and $\mu_{\alpha\beta} = 0$ and obtain a system of harmonic oscillators with the polarization linear in a and a^+ . Since the polarization is represented by the most general operator given by linear and bilinear combinations $c_m^+ c_n$ of fermion operators, we can obtain the matrix elements of $c_m^+ c_n$ between the ground state and single-excited oscillator states involved in the linear response. The second-order response depends on the anharmonicities to the first order. This leads to first-order corrections to the oscillator wave functions, whereas the eigenvalues remain the same (since they only contain higher-order corrections). This implies that in this order of perturbation theory, which corresponds to the classical limit, the system remains harmonic and simply attains new matrix elements of $c_m^+ c_n$.

It follows from Eqs. (2.1) and (3.3) together with Eqs. (2.16) that the operator $c_m^+ c_n$ can be represented in terms of the oscillator operators in the following form:

$$\begin{aligned} c_m^+ c_n = & \rho_{mn}^{gg} + \sum_\alpha \{ (\xi_\alpha^+)_m a_\alpha^+ + (\xi_\alpha)_m a_\alpha \} \\ & + \frac{1}{2} \sum_{\alpha\beta} \{ ([\xi_\alpha^+, \rho^{gg}] \xi_\beta^+) \}_{mn} a_\alpha^+ a_\beta^+ \\ & + ([\xi_\alpha^+, \rho^{gg}] \xi_\beta^+) \}_{mn} a_\alpha^+ a_\beta \\ & + ([\xi_\alpha, \rho^{gg}] \xi_\beta^+) \}_{mn} a_\alpha a_\beta^+ \\ & + ([\xi_\alpha, \rho^{gg}] \xi_\beta) \}_{mn} a_\alpha a_\beta \}. \end{aligned} \quad (3.5)$$

The EMS is constructed as a system of harmonic oscillators with the eigenstates $|k\alpha, l\beta, \dots\rangle$ and eigenenergies $E = k\Omega_\alpha + l\Omega_\beta + \dots$, where the integers $k, l = 0, 1, 2, \dots$ label the excited states of the various oscillators. The EMS are calculated to first-order in V in terms of the oscillator states of QOM in Appendix B. The contributions to the response functions $S^{(j)}$ can, therefore, be classified according to the matrix elements of the effective oscillator system $\langle k\alpha, \dots | c_m^+ c_n | l\beta, \dots \rangle$.

The effective level scheme that reproduces the linear response $S^{(1)}$ [Eq. (A3)] consists of the

ground-state $|g\rangle$ and all single excitations $|1\alpha\rangle$. The relevant density matrix elements are

$$\langle g|c_m^+ c_n|g\rangle = \rho_{mn}^{gg}, \quad (3.6a)$$

$$\langle g|c_m^+ c_n|1\alpha\rangle = (\xi_\alpha)_{mn}. \quad (3.6b)$$

Equations (3.6a) and (3.6b) simply recover our input, i.e., the ground-state density matrix and the TDHF electronic modes contributing to the linear response.

The second-order response $S^{(2)}$ [Eq. (A4)] is represented by an effective system consisting of the ground-state $|g\rangle$, single $|1\alpha\rangle$, and double $|1\alpha 1\beta\rangle$ excited states. These are given by Eqs. (B3) to first order in V . (The state $|2\alpha\rangle$ is the special case of $|1\alpha 1\beta\rangle$ when $\alpha = \beta$.) The necessary additional matrix elements are obtained by combining Eqs. (B3) and (3.5):

$$\begin{aligned} \langle g|c_m^+ c_n|1\alpha 1\beta\rangle &= \frac{([\xi_\alpha, \rho^{gg}] \xi_\beta])_{mn}}{2} \\ &+ 2 \sum_\gamma \left\{ \frac{V_{\alpha\beta-\gamma}(\xi_\gamma)_{mn}}{\Omega_\alpha + \Omega_\beta - \Omega_\gamma} - \frac{V_{\alpha\beta\gamma}(\xi_\gamma^+)_{mn}}{\Omega_\alpha + \Omega_\beta + \Omega_\gamma} \right\}, \end{aligned} \quad (3.7a)$$

$$\begin{aligned} \langle 1\alpha|c_m^+ c_n|1\beta\rangle &= \rho_{mn}^{gg} \delta_{\alpha\beta} + ([\xi_\alpha^+, \rho^{gg}] \xi_\beta)_{mn} \\ &+ \sum_\gamma \left\{ \frac{V_{-\alpha-\beta\gamma}(\xi_\gamma)_{mn}}{-\Omega_\alpha + \Omega_\beta - \Omega_\gamma} + \frac{V_{\alpha\beta-\gamma}(\xi_\gamma^+)_{mn}}{\Omega_\alpha - \Omega_\beta - \Omega_\gamma} \right\}, \end{aligned} \quad (3.7b)$$

$$\langle 1\alpha|c_m^+ c_n|1\beta 1\gamma\rangle = (\xi_\gamma)_{mn} \delta_{\alpha\beta} + (\xi_\beta)_{mn} \delta_{\alpha\gamma}, \quad (3.7c)$$

where $V_{\alpha\beta\gamma}$ is given by Eq. (2.16c).

Equation (3.7a) gives transition density matrices involving the ground state. Equation (3.7b) expresses the transition density matrices between singly excited states obtained from $S^{(1)}$, and Eq. (3.7c) gives the transitions between singly and doubly excited states. The first term in Eqs. (3.7a) and (3.7b) represents the interband (particle-particle and hole-hole) part of the density matrix and involves only two electronic modes. The second (intraband, particle-hole, and hole-particle) term, involves a summation over all electronic modes. These matrices provide an approximation for the density matrices between states contributing to the first- and to the second-order optical responses. The corresponding energies are

$$\Omega_{1\alpha} = \Omega_\alpha; \quad \Omega_{1\alpha 1\beta} = \Omega_\alpha + \Omega_\beta. \quad (3.8)$$

Taking higher-order anharmonicities into account will allow us to compute density matrix elements involving new states. For example, the third-order response $S^{(3)}$ includes higher lying excitations: $\langle g|c_m^+ c_n|1\alpha 1\beta 1\gamma\rangle$, $\langle 1\alpha|c_m^+ c_n|1\beta 1\gamma 1\delta\rangle$, $\langle 1\alpha 1\beta|c_m^+ c_n|1\gamma 1\delta 1\zeta\rangle$, and $\langle 1\alpha 1\beta|c_m^+ c_n|1\gamma 1\delta\rangle$. In general, $S^{(j)}$ involves all transitions contributing to the lower order responses, j transitions from the ground, single, double, ..., $(j-1)$ th excited states to the j th excited state, and transitions between $(j-1)$ th excited states.

By using an arbitrary single-particle operator μ_{mn} in Eqs. (3.7) we can compute the full density matrix response function, which depends on all electronic modes. When μ_{mn} is taken to be the dipole operator, we only obtain those modes that dominate the optical response. The ability to focus on the dominant modes alone has proved to be very useful for calculating the optical response [23, 26–29]. However, in order to compute the excited-state density matrices we need to capture all the modes (optically bright and dark).

When only few modes are known, Eqs. (3.7a) and (3.7b) are dominated by the interband term ($[\xi_\alpha, \rho^{gg}] \xi_\beta$). The summation over available modes gives a negligible contribution because, in general, $V_{\alpha\beta\gamma} \ll 1$. The resulting transition matrices ($\langle 1\alpha|c_m^+ c_n|1\beta\rangle$, $\langle g|c_m^+ c_n|1\alpha 1\beta\rangle$) will, therefore, preserve all localization properties of the ground-state ρ^{gg} and electronic modes ξ_α and ξ_β . On the other hand, the summation over all TDHF modes significantly increases the contribution of the second term in Eqs. (3.7a) and (3.7b) yielding the transition matrices which do not depend on the way the molecule interacts with the optical field (molecular dipole) but represent intrinsic molecular properties.

4. Density Matrices of Acceptor-Substituted Carotenoids

We have applied the present algorithm to a family of symmetric nonpolar (N) and polar (P) conjugated polyenes whereby one end is substituted with a strong acceptor group (see Fig. 2). The linear absorption and the electronic modes responsible for the optical response of these molecules were studied in [23, 24]. The Hartree-Fock ground-state density matrices were calculated first. Optimal ground-state geometries were obtained at the AM1 level using Gaussian-94. The ZINDO

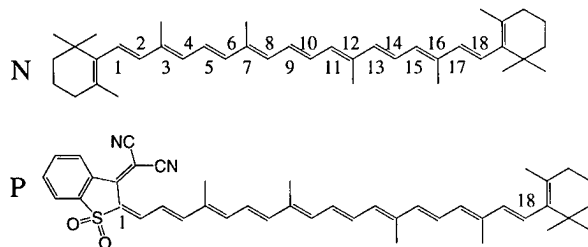


FIGURE 2. Structures and atom labeling of the neutral *N* and polar *P* (substituted by the strong acceptor) molecules.

code was utilized to generate INDO/S [30–32] Hamiltonian, and the collective electronic oscillator (CEO) procedure [23, 26, 28] was then applied to compute the dominant electronic modes and the corresponding dipole moments $\mu_{\nu}^{(j)}$ which contribute to the first- and second-order off-resonant optical response:^{*}

$$\xi^{(j)} = \sum_{\nu} \mu_{\nu}^{(j)} \xi_{\nu} + (\mu_{\nu}^{(j)})^* \xi_{\nu}^+, \quad j = 1, 2. \quad (4.1)$$

Satisfactory convergence of the response to within $\sim 10^{-3}$ was achieved using 10–15 effective electronic modes.

In Figure 3 we display the dipole moments [Eq. (4.1)] of the dominant modes vs. mode frequencies Ω_{ν} , calculated using the first- and the second-order response. Since the *N* molecule has an inversion symmetry, the first-order response depends only on antisymmetric (B_u) oscillators (panel *A*) whereas the second-order response depends on symmetric (A_g) oscillators (panel *B*). The figure shows that the response of the neutral (*N*) molecule is dominated by a single electronic mode. In contrast, the polar (*P*) molecule shows four major peaks in each order of the response, and its electronic oscillators do not possess any symmetry.

* INDO/S Hamiltonian was initially parameterized to reproduce electronic spectra at Configuration Interaction Singles (CIS) level. However, we found that it works also extremely well without further reparameterization with the CEO for a broad range of molecules: Computed linear absorptions of acceptor-substituted carotenoids [23], stilbenoid aggregates [33], phenylacetylene dendrimers [28], porphins [34, 35], and static second-order polarizabilities of donor/acceptor-substituted polyenes [29] compared well with experiment. The input to these calculations, the ground-state structures, could be obtained using other semiempirical (e.g., AM1), ab initio optimized molecular geometries, experimental X-ray diffraction, or nuclear magnetic resonance (NMR) data. The issue of optimizing INDO/S Hamiltonian parameters for the CEO approach or using other Hamiltonians is an open problem that lies beyond the scope of the present work.

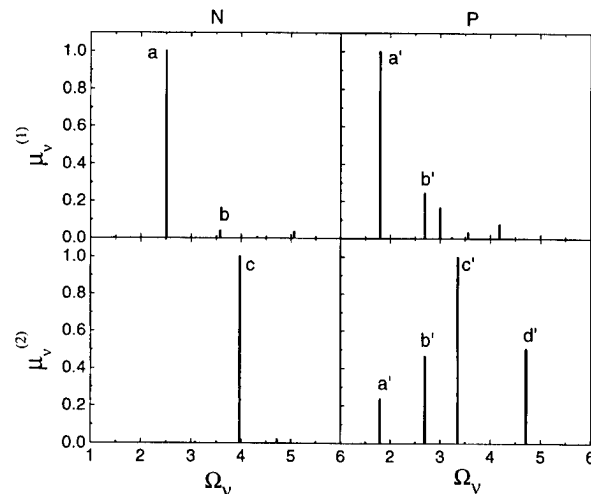


FIGURE 3. The dipole moments μ_{ν} are displayed vs. electronic mode frequencies Ω_{ν} for the molecules shown in Figure 2. Shown are the dominant modes in the first two orders of nonlinearity. The dipoles are given in arbitrary units.

The same modes (*a* and *b*) with different dipoles show up in both responses.

We next examine the single-electron density matrices ρ_{nm}^{rr} for the states corresponding to peaks *a*, *b*, and *c* in *N* and *a'b'*, *c'*, and *d'* in *P*. These density matrices computed using Eqs. (3.6) and (3.7) represent the projection of the full matrix which contributes to the first- and second-order response, because only the electronic modes which dominate the linear and the quadratic optical responses were used in the calculations. Other components of the matrix do not have a dipole moment and, therefore, do not contribute to the optical response. The acceptor's effect on the molecular properties can be illustrated using contour plots of the density matrices. The absolute value of the reduced ground-state density matrix ρ^{gg} of *N* is shown in the upper left panel of Figure 4. The axes represent carbon atoms. The ground-state density matrix is dominated by diagonal and near-diagonal elements, reflecting the bonds between nearest neighbors. The ($\times 1$) scaling factor indicates that the largest values of the matrix shown by the blue color are equal to 1. The diagonal elements represent the electronic charges on each carbon atom. The absolute values of the matrix $\Delta \rho^{aa} \equiv \rho^{aa} - \rho^{gg}$ [panel *N*(ρ^{aa})] is the difference between the density matrix of state *a* and the ground-state density matrix. The matrix is delocalized over the entire molecule. The $\times 10$ factor

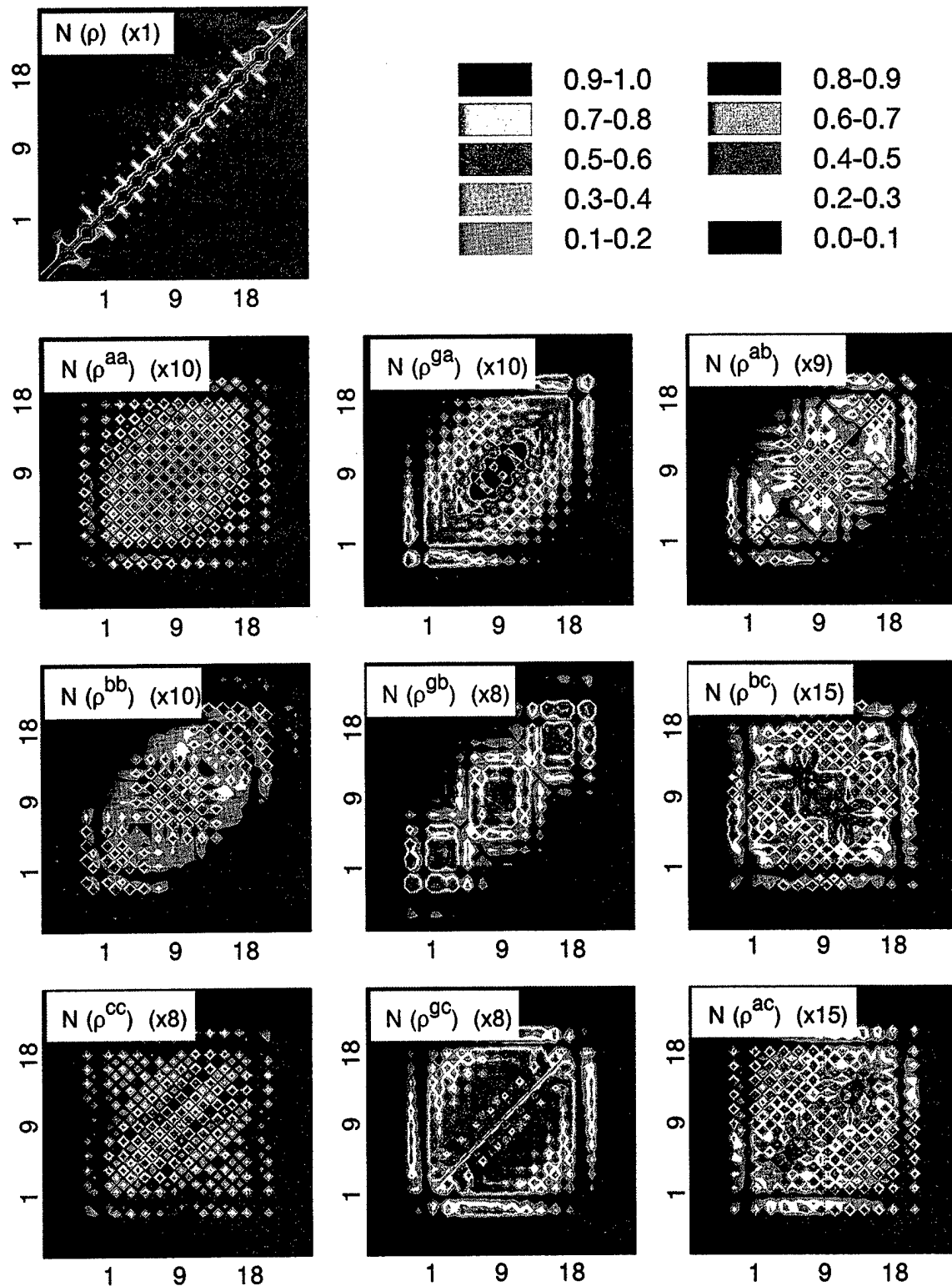
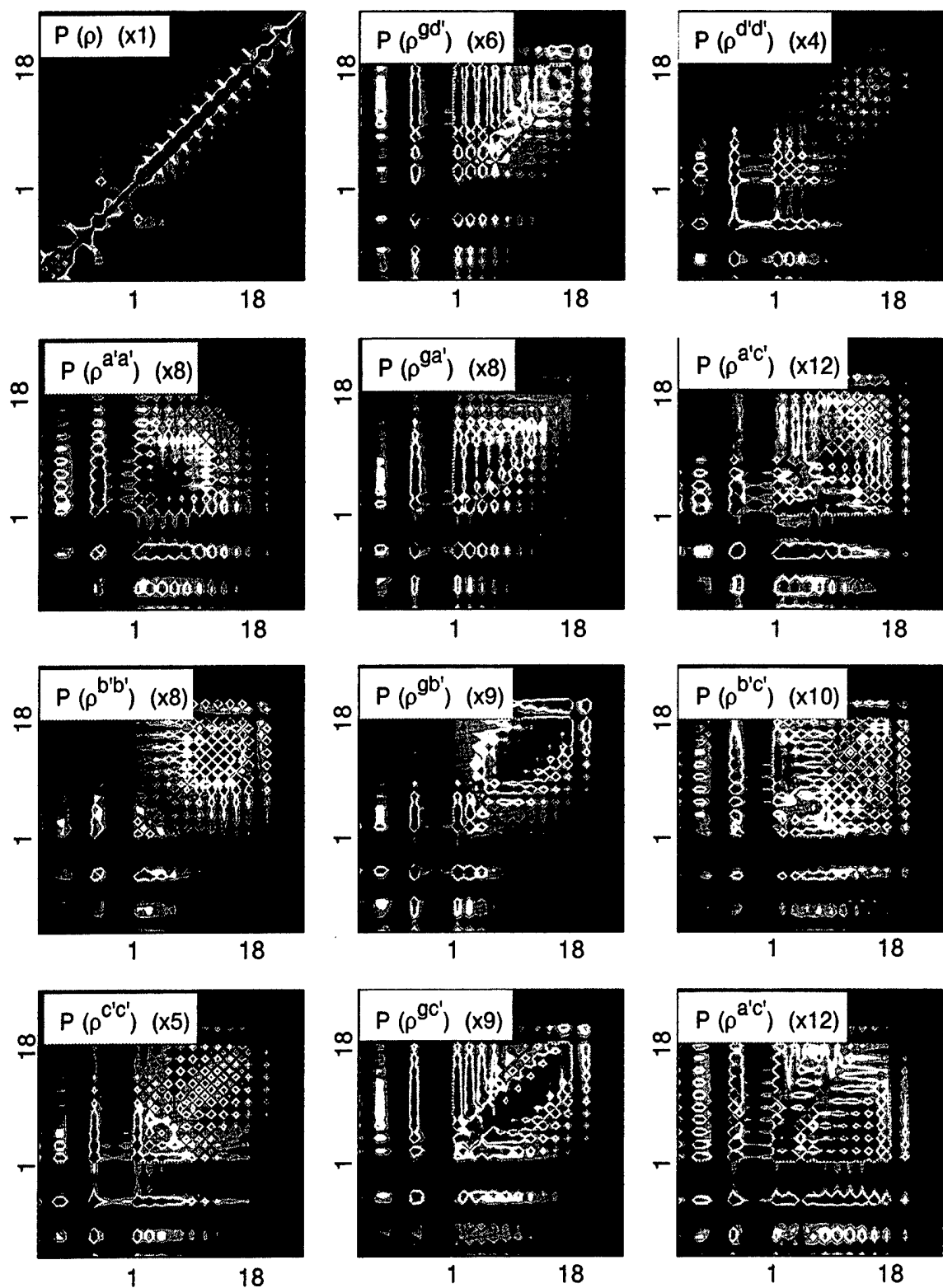


FIGURE 4. Contour plots of ground- and excited-state density matrices which dominate the linear absorption of molecules N . The axis labels represent the individual carbon atoms as labeled in Figure 2. Panel labels indicate the molecule (Fig. 2) and the state corresponding to the peak in Figure 3: ρ^{gg} ground-state density matrix; $\Delta\rho^{\nu\nu} \equiv \rho^{\nu\nu} - \rho^{gg}$ the difference between the density matrices of state ν and the ground state; $\rho^{\nu\eta}$ the transition density matrices.

FIGURE 5. Same as in Figure 4 but for the polar molecule P .

implies that the part of the excited-state density matrix which contributes to the second-order optical response only changes slightly compared to the ground state. The difference for the density matrix of state $b\Delta\rho^{bb}$ [panel $N(\rho^{bb})$] is less delocalized compared with $\Delta\rho^{aa}$. In addition it is nonuniform along the diagonal, which leads to diagonal localization sizes. $\Delta\rho^{cc}$ corresponding to the electronic mode contributing to the second-order optical response possesses a delocalization and magnitude similar to $\Delta\rho^{aa}$. For all excited-state matrices, the off-diagonal elements are much larger than the diagonal. This means that upon optical excitation of the unsubstituted molecule the changes in the bonding pattern are much more significant compared with the charge redistribution.

The transition density matrices are displayed in the middle and the right columns of Figure 4. Transitions involving the ground state are described by the electronic modes (ρ^{ga} , ρ^{gb} , and ρ^{gc}). Their role in the optical response has been analyzed in [23]. They have delocalization properties very similar to the corresponding states density matrices, because in the calculations of the latter these modes make the dominant contribution. Similarly, the transition density matrices between excited states shown in the right column of Figure 4 are symmetric and delocalized over the entire molecule. The largest coherences appear to be at the center of the matrices because the density matrices of states a , b , and c have the strongest bonding pattern at the center.

Figure 5 displays the absolute values of the calculated density matrices of P . The strong acceptor perturbs the ground state, as shown by the reduction of the electronic density toward the acceptor in panel $P(\rho^{gg})$. The difference $\Delta\rho^{a'a'}$ for state a' is localized in the acceptor end [panel $P(\rho^{a'a'})$], whereas $\Delta\rho^{b'b'}$ for state b is localized on the neutral end of the molecule [panel $P(\rho^{b'b'})$]. Note that $\Delta\rho^{a'a'}$ has very large diagonal and off-diagonal elements implying that excitation to state a changes the charge distribution as well as the bonding pattern compared to the ground state. In contrast, $\Delta\rho^{b'b'}$ is dominated by off-diagonal elements, which makes it similar to the excited-state density matrices of the unsubstituted molecule. This reflects the fundamental difference between states a' and b' . $\Delta\rho^{c'c'}$ and $\Delta\rho^{d'd'}$ corresponding to the electronic mode contributing to the second-order optical response are both localized at the

acceptor end and are dominated by a few large diagonal and off-diagonal elements. The former has a stronger bulk contribution.

The transition density matrices between the ground and the excited states (electronic modes $\rho^{ga'}$ and $\rho^{gb'}$) are highly asymmetric and delocalized, reflecting the motions of charges along the molecule upon optical excitation. The x and the y axis label the electron and the hole, respectively. The diagonal elements ρ_{nn} show induced charges on various atoms whereas the off-diagonal elements ρ_{nm} represent the probability amplitude of finding an excess electron at the m th atomic orbital and a hole on the n th atomic orbital. Electronic modes $\rho^{gc'}$ and $\rho^{gd'}$ corresponding to the high-frequency excited states and contributing to the second-order response are less asymmetric than the former and delocalized over the entire molecule (compared with $\rho^{c'c'}$ and $\rho^{d'd'}$). The transition density matrices shown in the right column of Figure 5 are delocalized over the entire molecule. The largest coherences appear where the density matrices of corresponding states have the strongest bonding patterns. Note that these density matrix elements are smaller ($\times 10-12$) compared to the other displayed matrices ($\times 4-9$), because states a' , b' , and c' are localized in different regions.

5. Discussion

The TDHF uses the single-electron density matrix $\langle g|c_m^+c_n|g \rangle$ to calculate the single-electron transition density matrices (electronic modes) between the ground state and the excited electronic states $\langle g|c_m^+c_n|1\alpha \rangle$ which contribute to the linear response. In this article we made one step further: using the ground-state density matrix and the electronic modes we calculated additional density matrices: between the ground state and the excited states $\langle g|c_m^+c_n|1\alpha\beta \rangle$, which contribute to the second-order response, and transition density matrices between states $\langle 1\alpha|c_m^+c_n|1\beta \rangle$ as well as the single-electron density matrices of the excited states $\langle 1\alpha|c_m^+c_n|1\alpha \rangle$ which contribute to the linear response.

The TDHF procedure maps the quantum many-electron system onto a system of classical oscillators. The present approach is based on inverting the optical response function and mapping

the original system onto an effective set of quantum states. An algorithm is developed for calculating DMRF for excited electronic states using the TDHF approximation. The DMRF carries additional excited-state information about charge distributions and bonding patterns as well as the dynamical changes induced in these quantities by the external field.

The present analysis has several advantages. First, it connects the TDHF representation with the quantum mechanical treatments of the optical response in terms of global many-electron eigenstates. The latter may be useful for representing the properties of optically excited molecules. The procedure is further numerically inexpensive. The absence of long-range electronic coherence may be used to reduce the number of density matrix elements from $\sim N^2$ to $\sim NN_c$ where N_c denotes the number of orbital points of closely lying atoms [36] which communicate coherently upon optical excitation. Typically $N_c \ll N$ results in favorable linear N -scaling of computational effort with size. For example, $N_c \sim 20$ heavy atoms (~ 100 atomic orbitals in semiempirical Hamiltonian) in polyenes. This is analogous to similar developments in ground-state calculations [37]. We anticipate to achieve $\sim N$ and $\sim N^2$ scaling of memory and total computational time with molecular size, respectively.*

The present approach can be extended to compute vibronic structure of electronic transitions [38, 39] by including the dependence of the electronic modes on nuclear coordinates.

Finally, the present analysis was based on the TDHF approximation for the DMRF. The resulting EMS is not equivalent to the original QFM. It simply reproduces its TDHF response. It is possible, however, to extend this approach and obtain an exact EMS. To that end the QOM should be deformed to yield a bosonized quantum fermion model (BQFM) which will be equivalent to QFM [40–43] (see Fig. 1). The TDHF is then used only to define a convenient set of collective coordinates. These coordinates may then be used to compute the exact DMRF, and we no longer rely on the

* To calculate the electronic modes of carotenoids (see Section 4) we used the Density Matrix Spectral Moments Algorithm (DSMA) [23] which implements a Lanczos-type algorithm and gives $\sim N^2$ and $\sim N^3$ size scaling of memory and computational time, respectively. We considered molecules of moderate size (~ 40 heavy atoms). These computations are inexpensive and therefore the N -scaling procedure was not implemented.

TDHF. This should result in extending the TDHF equation to include higher-order oscillator variables [22]. The TDHF is then a classical approximation which follows the evolution of a point in phase space. These extensions are semiclassical since they follow the evolution of wavepackets, which amounts to including higher moments of the classical variables.

In this study we have used the single Slater determinants, which constitute a set of generalized coherent states [44] for the many-electron problem, to construct the classical limit of the original model. This allowed us to introduce the boson language, which has been demonstrated to be useful for developing various approximation schemes. The coherent states form an overcomplete basic set which leads to certain difficulties in using them to describe quantum dynamics. However, they possess the property of the unit operator decomposition [44] which eliminates the difficulties. There are several ways how the coherent states can be used to generate new approximate descriptions of the original many-bodied problem [18, 19]. One way is to start with the BQFM which is equivalent to the original QFM, as described here, and derive closed equations of motion for one- and two-boson variables in full analogy with the Frenkel exciton systems [45]. Another way is to use variational dynamical approach by applying Ansätze for the many-body wave function and representing it as a wavepacket in the space of coherent states [18, 19]. Finally the coherent states can be used to formulate nontraditional configuration interaction (CI) approaches. Usually the CI schemes take into account certain important configurations which are classified and truncated according to the number of electron–hole pairs, i.e., single CI, double CI, etc. The coherent states allow to introduce new types of configurational spaces. This can be accomplished by defining the configurational space as spanned onto a certain subspace of coherent states. The space of coherent states \mathbf{M} as stated here form a Grassmannian manifold which has a complex analytical structure. We can immerse the complex projective line \mathbb{CP}^1 (which is a one-dimensional compact complex manifold) into \mathbf{M} and form a vector subspace in the many-body space of states as generated by the coherent states which belong to \mathbb{CP}^1 . This should result in a configurational space with the same dimensionality of single CI, which nevertheless contains an arbitrary number of electron–hole pairs.

Appendix A: Classical TDHF Response

To compute the DMRF we recast Eq. (2.20) in the form

$$\begin{aligned} i \frac{\partial z_\alpha(t)}{\partial t} = & \Omega z_\alpha(t) + \sum_{\beta\gamma} (V_{-\alpha-\beta-\gamma} z_\beta^*(t) z_\gamma^*(t) \\ & + 2V_{-\alpha-\beta\gamma} z_\beta^*(t) z_\gamma(t) \\ & + V_{-\alpha\beta\gamma} z_\beta(t) z_\gamma(t)) \\ & - \mathcal{E}(t) \left[\mu_{-\alpha} + \sum_\beta (\mu_{-\alpha-\beta} z_\beta^*(t) \right. \\ & \left. + \mu_{-\alpha\beta} z_\beta(t)) \right], \end{aligned} \quad (\text{A1})$$

where the summation goes over $\alpha, \beta, \gamma > 0$. This nonlinear equation may be solved by expanding $z(t)$ ($z^*(t)$) in powers of the external field $\mathcal{E}(t)$: $z(t) = z^{(1)}(t) + z^{(2)}(t) + \dots$. Using the time-domain Green function

$$G_\alpha(t) = \exp(-i\Omega_\alpha t), \quad (\text{A2})$$

the first-order solution of Eq. (A1) is

$$z_\alpha^{(1)}(t) = i \int_{-\infty}^t d\tau \mathcal{E}(\tau) \mu_{-\alpha} G_\alpha(t - \tau). \quad (\text{A3})$$

To second order we obtain

$$\begin{aligned} z_\alpha^{(2)}(t) = & \int_{-\infty}^t \int_{-\infty}^{\tau_2} d\tau_2 d\tau_1 \mathcal{E}(\tau_2) \mathcal{E}(\tau_1) \\ & \times \sum_\beta (\mu_{-\alpha-\beta} \mu_\beta G_\beta^*(\tau_2 - \tau_1) \\ & - \mu_{-\alpha\beta} G_\beta(\tau_2 - \tau_1)) \\ & \times G_\alpha(t - \tau_2) + i \int_{-\infty}^t \int_{-\infty}^t d\tau_2 d\tau_1 \\ & \times \mathcal{E}(\tau_2) \mathcal{E}(\tau_1) \int_{\tau_2}^t d\tau \\ & \times \sum_{\beta\gamma} (V_{-\alpha-\beta-\gamma} \mu_\beta \mu_\gamma G_\beta^*(\tau - \tau_2) \\ & \times G_\gamma^*(\tau - \tau_1) \\ & - 2V_{-\alpha\beta-\gamma} \mu_{-\alpha} \mu_\beta \mu_\gamma G_\alpha(\tau - \tau_2) \\ & \times G_\beta^*(\tau - \tau_1) G_\gamma(t - \tau) \\ & + V_{-\alpha\beta\gamma} \mu_{-\alpha} \mu_{-\beta} \mu_\gamma G_\alpha(\tau - \tau_2) G_\beta(\tau - \tau_1) \\ & \times G_\gamma(t - \tau)) G_\alpha(t - \tau). \end{aligned} \quad (\text{A4})$$

The time-dependent linear and second-order polar-

izabilities are given by

$$\mathcal{P}^{(1)} = \sum_\alpha \mu_{-\alpha} z_\alpha^{*(1)}(t) + \mu_\alpha z_\alpha^{(1)}(t), \quad (\text{A5})$$

$$\begin{aligned} \mathcal{P}^{(2)} = & \sum_\alpha \mu_{-\alpha} z_\alpha^{*(2)}(t) + \mu_\alpha z_\alpha^{(2)}(t) \\ & + \frac{1}{2!} \sum_{\alpha\beta} (\mu_{-\alpha-\beta} z_\alpha^{*(1)}(t) z_\beta^{*(1)}(t) \\ & + 2\mu_{-\alpha\beta} z_\alpha^{*(1)}(t) z_\beta^{(1)}(t) \\ & + \mu_{\alpha\beta} z_\alpha^{(1)}(t) z_\beta^{(1)}(t)), \end{aligned} \quad (\text{A6})$$

where $z^{(1)}(t)$ ($z^{*(1)}(t)$) and $z^{(2)}(t)$ ($z^{*(2)}(t)$) are given by Eqs. (A3) and (A4) and their hermitian conjugates. Linear and second-order time-domain response functions are defined by

$$\mathcal{R}^{(1)} = \int d\tau \mathcal{E}(\tau) R^{(1)}(t; \tau), \quad (\text{A7})$$

$$\mathcal{R}^{(2)} = \int d\tau_2 d\tau_1 \mathcal{E}(\tau_2) \mathcal{E}(\tau_1) R^{(2)}(t; \tau_1, \tau_2). \quad (\text{A8})$$

Comparing Eqs. (A7) and (A5) [Eqs. (A8) and (A6)] and using Eqs. (A3) and (A4) we obtain for linear and second-order time-domain response function

$$R^{(1)}(t; \tau) = - \sum_\alpha \mu_{-\alpha} \mu_\alpha (G_\alpha(t - \tau) G_\alpha^*(t - \tau)), \quad (\text{A9})$$

$$\begin{aligned} R^{(2)}(t; \tau_1, \tau_2) = & i \sum_{\alpha\beta\gamma} \int_{\tau_2}^t d\tau (V_{-\alpha-\beta-\gamma} \mu_\alpha \mu_\beta \mu_\gamma G_\alpha^*(\tau - \tau_2) \\ & \times G_\beta^*(\tau - \tau_1) G_\gamma(t - \tau) \\ & - 2V_{-\alpha\beta-\gamma} \mu_{-\alpha} \mu_\beta \mu_\gamma G_\alpha(\tau - \tau_2) \\ & \times G_\beta^*(\tau - \tau_1) G_\gamma(t - \tau) \\ & + V_{-\alpha\beta\gamma} \mu_{-\alpha} \mu_{-\beta} \mu_\gamma G_\alpha(\tau - \tau_2) G_\beta(\tau - \tau_1) \\ & \times G_\gamma(t - \tau)) + h.c. \\ & + \frac{1}{2!} \sum_{\alpha\beta} (2\mu_{-\alpha-\beta} \mu_\alpha \mu_\beta G_\alpha^*(\tau_2 - \tau_1) \\ & - \mu_{-\alpha\beta} \mu_{-\alpha} \mu_\beta G_\alpha(\tau_2 - \tau_1)) G_\beta(t - \tau_2) + h.c. \\ & - (\mu_{-\alpha-\beta} \mu_\alpha \mu_\beta G_\alpha^*(t - \tau_1) G_\beta^*(t - \tau_2) \\ & + \mu_{\alpha\beta} \mu_{-\alpha} \mu_{-\beta} G_\alpha(t - \tau_1) G_\beta(t - \tau_2) \\ & - 2\mu_{\alpha\beta} \mu_{-\alpha} \mu_\beta G_\alpha(t - \tau_1) G_\beta^*(t - \tau_2)). \end{aligned} \quad (\text{A10})$$

Applying the Fourier transform

$$\begin{aligned} f(\omega) &= \int dt f(t) \exp(-i\omega t); \\ f(t) &= \frac{1}{2\pi} \int d\omega f(\omega) \exp(i\omega t) \end{aligned} \quad (\text{A11})$$

to Eqs. (A10) and (A9), we obtain the frequency-dependent linear and second-order polarizabilities:

$$\begin{aligned} P^{(1)}(-\omega_s; \omega) &= \int \frac{d\omega}{2\pi} 2\pi \delta(-\omega_s + \omega) \\ &\times \alpha(-\omega_s; \omega) \mathcal{E}(\omega), \end{aligned} \quad (\text{A12})$$

$$\begin{aligned} P^{(2)}(-\omega_s; \omega_1, \omega_2) &= \int \frac{d\omega_1}{2\pi} \frac{d\omega_2}{2\pi} \\ &\times 2\pi \delta(-\omega_s + \omega_1 + \omega_2) \beta(-\omega_s; \omega_1, \omega_2) \\ &\times \mathcal{E}(\omega_1) \mathcal{E}(\omega_2). \end{aligned} \quad (\text{A13})$$

The final expressions for the linear and the second-order polarizabilities are:

$$\alpha(\omega) = \sum_{\alpha} \frac{2\mu_{-\alpha} \mu_{\alpha} \Omega_{\alpha}}{\Omega_{\alpha}^2 - \omega^2}, \quad (\text{A14})$$

$$\begin{aligned} \beta(-\omega_s = \omega_1 + \omega_2; \omega_1, \omega_2) &= -\frac{1}{4} \sum_{\alpha\beta\gamma} (V_{\alpha\beta\gamma} \mu_{-\alpha} \mu_{-\beta} \mu_{-\gamma} + h.c.) \\ &\times \left(\frac{1}{(\Omega_{\alpha} - \omega_1)(\Omega_{\beta} - \omega_2)(\Omega_{\gamma} + \omega_1 + \omega_2)} \right. \\ &+ \frac{1}{(\Omega_{\alpha} + \omega_1)(\Omega_{\beta} + \omega_2)(\Omega_{\gamma} - \omega_1 - \omega_2)} \Big) \\ &+ (2V_{\alpha-\beta-\gamma} \mu_{-\alpha} \mu_{\beta} \mu_{\gamma} + h.c.) \\ &\times \left(\frac{1}{(\Omega_{\alpha} + \omega_1)(\Omega_{\beta} - \omega_2)(\Omega_{\gamma} + \omega_1 + \omega_2)} \right. \\ &+ \frac{1}{(\Omega_{\alpha} - \omega_1)(\Omega_{\beta} + \omega_2)(\Omega_{\gamma} + \omega_1 + \omega_2)} \\ &+ \frac{1}{(\Omega_{\alpha} - \omega_1)(\Omega_{\beta} + \omega_2)(\Omega_{\gamma} - \omega_1 - \omega_2)} \Big) \\ &+ \frac{1}{(\Omega_{\alpha} + \omega_1)(\Omega_{\beta} - \omega_2)(\Omega_{\gamma} - \omega_1 - \omega_2)} \Big) \\ &+ (V_{-\alpha\beta\gamma} \mu_{\alpha} \mu_{-\beta} \mu_{-\gamma} + h.c.). \end{aligned}$$

$$\begin{aligned} &\times \left(\frac{1}{(\Omega_{\alpha} + \omega_1)(\Omega_{\beta} + \omega_2)(\Omega_{\gamma} + \omega_1 + \omega_2)} \right. \\ &+ \frac{1}{(\Omega_{\alpha} - \omega_1)(\Omega_{\beta} - \omega_2)(\Omega_{\gamma} - \omega_1 - \omega_2)} \Big) \\ &+ \frac{1}{4} \frac{1}{2!} \sum_{\alpha\beta} (\mu_{\alpha\beta} \mu_{-\alpha} \mu_{-\beta} + h.c.) \\ &\times \left(\frac{1}{(\Omega_{\alpha} - \omega_1)(\Omega_{\beta} + \omega_1 + \omega_2)} \right. \\ &+ \frac{1}{(\Omega_{\alpha} - \omega_2)(\Omega_{\beta} + \omega_1 + \omega_2)} \\ &+ \frac{1}{(\Omega_{\alpha} - \omega_1)(\Omega_{\beta} - \omega_2)} \\ &+ \frac{1}{(\Omega_{\alpha} + \omega_1)(\Omega_{\beta} - \omega_1 - \omega_2)} \\ &+ \frac{1}{(\Omega_{\alpha} + \omega_2)(\Omega_{\beta} - \omega_1 - \omega_2)} \\ &+ \frac{1}{(\Omega_{\alpha} + \omega_1)(\Omega_{\beta} + \omega_2)} \Big) \\ &+ 2\mu_{-\alpha\beta} \mu_{\alpha} \mu_{-\beta} \left(\frac{1}{(\Omega_{\alpha} + \omega_1)(\Omega_{\beta} + \omega_1 + \omega_2)} \right. \\ &+ \frac{1}{(\Omega_{\alpha} + \omega_2)(\Omega_{\beta} + \omega_1 + \omega_2)} \\ &+ \frac{1}{(\Omega_{\alpha} + \omega_1)(\Omega_{\beta} - \omega_2)} \\ &+ \frac{1}{(\Omega_{\alpha} - \omega_1)(\Omega_{\beta} - \omega_1 - \omega_2)} \\ &+ \frac{1}{(\Omega_{\alpha} - \omega_2)(\Omega_{\beta} - \omega_1 - \omega_2)} \\ &+ \frac{1}{(\Omega_{\alpha} + \omega_1)(\Omega_{\beta} - \omega_2)} \Big). \end{aligned} \quad (\text{A15})$$

Appendix B: Sum-Over-States Polarizabilities of the Effective Multilevel System

In this appendix we calculate optical polarizabilities for the quantum model QOM using the standard sum-over-states expressions [1]. The lin-

ear and the quadratic polarizabilities are given by

$$\alpha(\omega) = \sum_n \frac{2\omega_{ng} r_{gn} r_{ng}}{\omega_{ng}^2 - \omega^2} \quad (\text{B1})$$

$$\begin{aligned} \beta(-\omega_s = \omega_1 + \omega_2; \omega_1, \omega_2) &= -\frac{1}{4} \sum_{n, n'} r_{gn} r_{nn'} r_{n'g} \\ &\times \left(\frac{1}{(\omega_{n'g} + \omega_1 + \omega_2)(\omega_{ng} + \omega_1)} \right. \\ &+ \frac{1}{(\omega_{n'g} - \omega_1 - \omega_2)(\omega_{ng} - \omega_1)} \\ &+ \frac{1}{(\omega_{n'g} + \omega_1 + \omega_2)(\omega_{ng} + \omega_2)} \\ &+ \frac{1}{(\omega_{n'g} - \omega_1 - \omega_2)(\omega_{ng} - \omega_2)} \\ &+ \frac{1}{(\omega_{n'g} + \omega_1)(\omega_{ng} + \omega_1 + \omega_2)} \\ &+ \frac{1}{(\omega_{n'g} - \omega_1)(\omega_{ng} - \omega_1 - \omega_2)} \\ &+ \frac{1}{(\omega_{n'g} + \omega_2)(\omega_{ng} + \omega_1 + \omega_2)} \\ &+ \frac{1}{(\omega_{n'g} - \omega_2)(\omega_{ng} - \omega_1 - \omega_2)} \\ &+ \frac{1}{(\omega_{n'g} - \omega_2)(\omega_{ng} + \omega_1)} \\ &+ \frac{1}{(\omega_{n'g} + \omega_2)(\omega_{ng} - \omega_1)} \\ &+ \frac{1}{(\omega_{n'g} - \omega_1)(\omega_{ng} + \omega_2)} \\ &+ \left. \frac{1}{(\omega_{n'g} + \omega_1)(\omega_{ng} - \omega_2)} \right), \quad (\text{B2}) \end{aligned}$$

where the sum runs over all excited states n and n' , and g stands for the ground state; $r_{kl} = \langle k | \mathcal{P} | l \rangle$ ($r_{lk} = r_{kl}^*$) is the transition dipole between k th and l th states.

We start with the Hamiltonian [Eq. (3.3)] representing N quantum oscillators with the electronic polarizability operator $\mathcal{P}(a^+, a)$ [Eq. (3.4)]. To calculate the transition dipoles we first compute the

wave functions of our oscillator system to first order in V :

$$\phi^{(0)} = |g\rangle_0 - \frac{1}{3!} \sum_{\alpha\beta\gamma} \frac{V_{-\alpha-\beta-\gamma}}{\Omega_\alpha + \Omega_\beta + \Omega_\gamma} a_\alpha^+ a_\beta^+ a_\gamma^+ |g\rangle_0, \quad (\text{B3a})$$

$$\phi_\alpha^{(1)} = a_\alpha^+ |g\rangle_0 + \frac{1}{3!} \sum_{\beta\gamma} \frac{V_{\alpha-\beta-\gamma}}{\Omega_\alpha - \Omega_\beta - \Omega_\gamma} a_\beta^+ a_\gamma^+ |g\rangle_0, \quad (\text{B3b})$$

$$\begin{aligned} \phi_{\beta\gamma}^{(2)} &= a_\beta^+ a_\gamma^+ |g\rangle_0 - \frac{1}{3!} \sum_\alpha \frac{2V_{-\alpha\beta\gamma}}{\Omega_\alpha - \Omega_\beta - \Omega_\gamma} a_\alpha^+ |g\rangle_0 \\ &+ \frac{1}{3!} \sum_{\delta\zeta} \left(\frac{V_{-\gamma-\delta\zeta} a_\beta^+}{\Omega_\gamma - \Omega_\delta - \Omega_\zeta} + \frac{V_{-\delta-\zeta\beta} a_\gamma^+}{\Omega_\beta - \Omega_\delta - \Omega_\zeta} \right) \\ &\times a_\delta^+ a_m^+ |g\rangle_0, \end{aligned} \quad (\text{B3c})$$

where $V_{\alpha\beta\gamma}$ is given by Eq. (2.16c) and $|g\rangle_0$, $a_\alpha^+ |g\rangle_0$, $a_\alpha^+ a_\beta^+ |g\rangle_0$, and $a_\alpha^+ a_\beta^+ a_\gamma^+ |g\rangle_0$ denote the ground, single, double, and triple excited states of the uncoupled system, respectively.

The transition dipoles among the ground and the first two excited states are given by:

$$\langle \phi^{(0)} | \mathcal{P} | \phi^{(0)} \rangle = 0, \quad (\text{B4a})$$

$$\langle \phi^{(0)} | \mathcal{P} | \phi_\alpha^{(1)} \rangle = \mu_\alpha, \quad (\text{B4b})$$

$$\begin{aligned} \langle \phi^{(0)} | \mathcal{P} | \phi_{\alpha\beta}^{(2)} \rangle &= \frac{1}{2!} \mu_{\alpha\beta} + 2 \sum_\gamma \left\{ \frac{V_{\alpha\beta-\gamma} \mu_\gamma}{\Omega_\alpha + \Omega_\beta - \Omega_\gamma} \right. \\ &\left. - \frac{V_{\alpha\beta\gamma} \mu_{-\gamma}}{\Omega_\alpha + \Omega_\beta + \Omega_\gamma} \right\}, \end{aligned} \quad (\text{B4c})$$

$$\begin{aligned} \langle \phi_\alpha^{(1)} | \mathcal{P} | \phi_\beta^{(1)} \rangle &= \mu_{-\alpha\beta} + \sum_\gamma \left\{ \frac{V_{\alpha\beta-\gamma} \mu_{-\gamma}}{\Omega_\alpha - \Omega_\beta - \Omega_\gamma} \right. \\ &\left. + \frac{V_{-\alpha-\beta\gamma} \mu_\gamma}{-\Omega_\alpha + \Omega_\beta - \Omega_\gamma} \right\}, \end{aligned} \quad (\text{B4d})$$

$$\langle \phi_\alpha^{(1)} | \mathcal{P} | \phi_{\alpha\beta}^{(2)} \rangle = \mu_\beta. \quad (\text{B4e})$$

Substituting these transitions dipoles in Eqs. (B1) and (B2) we obtain expressions for the linear and the second-order polarizabilities which coincide with Eqs. (A14) and (A15). This proves the equivalence of the linear and the second-order polarizabilities of the QOM calculated in the classical limit and using the sum-over-states expression.

Appendix C: Nonlinear Response of Systems with Coordinate-Dependent Anharmonicities

When the anharmonicities in Eqs. (3.3) and (3.4) only depend on coordinates $q_\alpha = (a_\alpha^+ + a_\alpha^-)q_{0\alpha}/\sqrt{2}$ (and not on the momenta $p_\alpha = (a_\alpha^+ - a_\alpha^-)p_{0\alpha}/\sqrt{2}$) the DMRF are simplified considerably. In this case we have

$$\begin{aligned} V_{\alpha\beta\gamma} &= V_{-\alpha-\beta-\gamma} = V_{-\alpha\beta\gamma} \\ &= V_{-\alpha-\beta\gamma} \equiv V_{\alpha\beta\gamma}^q \frac{q_{0\alpha} q_{0\beta} q_{0\gamma}}{(\sqrt{2})^3}, \end{aligned} \quad (\text{C1})$$

$$\mu_{-\alpha-\beta} = \mu_{\alpha\beta} = \mu_{-\alpha\beta} \equiv \mu_{\alpha\beta}^q \frac{q_{0\alpha} q_{0\beta}}{(\sqrt{2})^2}, \quad (\text{C2})$$

$$\mu_\alpha = \mu_\alpha \equiv \mu_\alpha^q \frac{q_{0\alpha}}{\sqrt{2}}. \quad (\text{C3})$$

The time-domain response [Eq. (A10)] then becomes

$$\begin{aligned} R(t; \tau_1, \tau_2) &= - \int_{\tau_2}^t d\tau \sum_{\alpha\beta\gamma} V_{\alpha\beta\gamma}^q \mu_\alpha^q \mu_\beta^q \mu_\gamma^q \\ &\times \frac{(q_{0\alpha} q_{0\beta} q_{0\gamma})^2}{8} C_\alpha(\tau - \tau_2) \\ &\times C_\beta(\tau - \tau_1) C_\gamma(t - \tau) \\ &+ \sum_{\alpha\beta} \mu_{\alpha\beta}^q \mu_\alpha^q \mu_\beta^q \frac{(q_{0\alpha} q_{0\beta})^2}{4} \\ &\times (2C_\alpha(\tau_2 - \tau_1) C_\beta(\tau - \tau_2) \\ &+ C_\alpha(\tau - \tau_1) C_\beta(\tau - \tau_2)), \end{aligned} \quad (\text{C4})$$

where

$$C_\alpha(t) = i(G_\alpha(t) - G_\alpha^*(t)) = 2 \sin(\Omega_\alpha t) \quad (\text{C5})$$

is the classical linear response of a harmonic oscillator.

Similarly Eq. (A15) reduces to

$$\begin{aligned} \beta(-\omega_s = \omega_1 + \omega_2; \omega_1, \omega_2) &= - \sum_{\alpha\beta\gamma} \frac{V_{\alpha\beta\gamma}^q \mu_\alpha^q \mu_\beta^q \mu_\gamma^q}{M_\alpha M_\beta M_\gamma} \\ &\times \frac{1}{(\Omega_\alpha^2 - \omega_1^2)(\Omega_\beta^2 - \omega_2^2)(\Omega_\gamma^2 - (\omega_1 + \omega_2)^2)} \end{aligned}$$

$$\begin{aligned} &+ \sum_{\alpha\beta} \frac{\mu_{\alpha\beta}^q \mu_\alpha^q \mu_\beta^q}{M_\alpha M_\beta} \\ &\times \left(\frac{1}{(\Omega_\alpha^2 - \omega_1^2)(\Omega_\beta^2 - (\omega_1 + \omega_2)^2)} \right. \\ &+ \frac{1}{(\Omega_\alpha^2 - \omega_2^2)(\Omega_\beta^2 - (\omega_1 + \omega_2)^2)} \\ &\left. + \frac{1}{(\Omega_\alpha^2 - \omega_1^2)(\Omega_\beta^2 - \omega_2^2)} \right). \end{aligned} \quad (\text{C6})$$

ACKNOWLEDGMENTS

One of us (S.M.) wishes to thank the Alexander Van Humboldt award, the Guggenheim Fellowship, and the kind hospitality of Prof. E. Schlag at the Technical University of Munich. The support of the Air Force Office of Scientific Research Grant No. AFSOR-F49620-96-1-0030, and the National Science Foundation through Grants No. CHE-9526125 and No. PHY94-15583 is gratefully acknowledged. The calculations were conducted using the resources of the Cornell Theory Center, which receives major funding from the NSF and New York State.

References

1. J. F. Ward, Rev. Mod. Phys. **37**, 1 (1965); B. J. Orr and J. F. Ward, Mol. Phys. **20**, 513 (1971).
2. J. Zyss and D. S. Chemla, eds., *Nonlinear Optical Properties of Organic Molecules and Crystals*, Vols. **1** and **2** (Academic, Orlando, FL, 1987).
3. D. R. Kanis, M. A. Ratner, and T. J. Marks, Chem. Rev. **94**, 195 (1994).
4. J. L. Brédas, C. Adant, P. Tackx, A. Persoons, and B. M. Pierce, Chem. Rev. **94**, 243 (1994).
5. S. A. Kicharski and R. J. Bartlett, J. Chem. Phys. **97**, 4282 (1992); J. Chem. Phys. **95**, 8227 (1991); H. Sekino and R. J. Bartlett, J. Chem. Phys. **94**, 3665, (1991).
6. J. A. Pople, P. M. W. Gill, and B. J. Johnson, Chem. Phys. Lett. **199**, 557 (1992).
7. A. D. Becke, Phys. Rev. A **38**, 3098 (1988).
8. E. K. U. Gross, J. F. Dobson, and M. Petersilka, in *Density Functional Theory*, Vol. 181, R. F. Nalewajski, ed. (Springer, Berlin, 1996), pp. 1–81.
9. R. G. Parr and W. Yang, *Density-Functional Theory of Atoms and Molecules* (Oxford University Press, Oxford, 1994).
10. M. E. Casida, in *Recent Advances in Density-Functional Methods, Part I*, Vol. 3, D. A. Chong, ed. (World Scientific, Singapore, 1995), pp. 151–192.
11. C. Jamorski, M. E. Casida, and D. R. Salahub, J. Chem. Phys. **104**, 5134 (1996).

EXCITED ELECTRONIC STATES OF CAROTENOIDS

12. P. Hohenberg and W. Kohn, Phys. Rev. B **136**, 864 (1964).
13. W. Kohn and L. J. Sham Phys. Rev. A **140**, 1133 (1965).
14. A. Szabo and N. S. Ostlund, *Modern Quantum Chemistry: Introduction to Advanced Electronic Structure Theory* (McGraw-Hill, New York, 1989).
15. R. McWeeny and B. T. Sutcliffe, *Methods of Molecular Quantum Mechanics* (Academic, New York, 1976); E. R. Davidson, *Reduced Density Matrices in Quantum Chemistry* (Academic, New York, 1976).
16. P. O. Lowdin, Phys. Rev. **97**, 1474, (1955); Adv. Phys. **5**, 1, (1956).
17. R. S. Milliken, J. Chem. Phys., **23**, 1833, 1841, 2338, 2343, (1955).
18. P. Ring and P. Schuck, *The Nuclear Many-Body Problem* (Springer, New York, 1980).
19. J.-P. Blaizot and G. Ripka, *Quantum Theory of Finite Systems* MIT Press, Cambridge, MA, 1986.
20. H. Sekino and R. J. Bartlett, J. Chem. Phys. **98**, 3022 (1993).
21. V. Chernyak and S. Mukamel, J. Chem. Phys. **104**, 444 (1996).
22. V. Chernyak and S. Mukamel, J. Chem. Phys. **108**, 5812 (1998).
23. S. Tretiak, V. Chernyak, and S. Mukamel, JACS **119**, 11408 (1996).
24. V. Ricci, Large Enhancement of Third Order Susceptibility, MS Thesis, Dept. of Electrical Engineering, University of Central Florida (1995).
25. L. D. Landau and E. M. Lifshitz, *Mechanics*, 3rd ed. (Pergamon, Oxford, 1976).
26. S. Mukamel, S. Tretiak, T. Wagersreiter, and V. Chernyak, Science **277**, 781 (1997).
27. S. Tretiak, V. Chernyak, and S. Mukamel, Chem. Phys. Lett. **259**, 55 (1996); S. Tretiak, V. Chernyak, and S. Mukamel, J. Chem. Phys. **105**, 8914 (1996).
28. S. Tretiak, V. Chernyak, and S. Mukamel, J. Phys. Chem. B **102**, 3310 (1998).
29. S. Tretiak, V. Chernyak, and S. Mukamel, Chem. Phys. Lett. **287**, 75 (1998), S. Tretiak, V. Chernyak, and S. Mukamel (unpublished).
30. J. Ridley and M. C. Zerner, Theor. Chim. Acta **32**, 111 (1973).
31. M. C. Zerner, G. H. Loew, R. F. Kirchner, and U. T. Mueller-Westerhoff, J. Am. Chem. Soc. **102**, 589 (1980).
32. J. A. Pople and G. A. Segal, J. Chem. Phys. **43**, S136 (1965); J. A. Pople, D. L. Beveridge, and P. Dobosh, J. Chem. Phys. **47**, 2026 (1967).
33. G. C. Bazan, W. J. Oldham, Jr., R. J. Lachicotte, S. Tretiak, V. Chernyak, and S. Mukamel, J. Am. Chem. Soc., to appear.
34. J. Baker and M. Zerner, Chem. Phys. Lett. **175**, 192, (1990).
35. S. Tretiak, V. Chernyak, and S. Mukamel (unpublished).
36. O. Dubovsky and S. Mukamel, J. Chem. Phys. **95**, 7828 (1991).
37. E. Schwegler, M. Challacombe, and M. Head-Gordon, J. Chem. Phys. **106**, 9708 (1997).
38. Y. Yamaguchi, M. Frisch, J. Gaw, H. F. Schaefer, and J. S. Binkley, J. Chem. Phys. **84**, 2262 (1986); B. G. Johnson and M. J. Fisch, J. Chem. Phys. **100**, 7429 (1994).
39. H. B. Schlegel, J. S. Binkley, and J. A. Pople, J. Chem. Phys. **80**, 1976 (1984).
40. F. J. Dyson, Phys. Rev. **102**, 1217 (1956).
41. V. M. Agranovich and B. S. Toshich, Zh. Éksp. Teor. Fiz. **53**, 281 (1967) [Sov. Phys. JETP **26**, 188 (1968)].
42. T. Holstein and H. Primakoff, Phys. Rev. B **58**, 1098 (1940).
43. V. Chernyak, Phys. Lett. A **163**, 117 (1992).
44. A. Perelomov, *Generalized Coherent States and Their Applications* (Springer, Berlin, 1986).
45. S. Mukamel, *Principles of Nonlinear Optical Spectroscopy* (Oxford, New York, 1995).

Balanced Complete Active Space Choices with the Multiconfigurational Spin Tensor Electron Propagator Method: The Vertical Ionization Potentials of NH₂

ALEXANDER J. MCKELLAR, DODI HERYADI, DANNY L. YEAGER

Texas A & M University, Chemistry Department, MS-3255, P.O. Box 300012, College Station, Texas 77842-3012

Received 30 March 1998; revised 21 May 1998; accepted 29 May 1998

ABSTRACT: With electron propagator methods, vertical ionization potentials (IPs) and electron affinities can be calculated directly. Our implementation, known as the multiconfigurational spin tensor electron propagator method (MCSTEP), is specifically designed for open-shell and highly correlated initial states. The initial state that is usually used in MCSTEP is a complete active space (CAS) MCSCF state. We have previously demonstrated that a small balanced CAS is the optimal choice for the MCSTEP initial state. In this article, we examine two ways of determining this balanced CAS for the MCSTEP initial state. With these choices, we calculate the low-lying vertical MCSTEP IPs of NH₂ and compare them with experiment for the three lowest IPs. With (aug-)cc-pVTZ, (aug-)cc-pVQZ, and extrapolated complete basis set limits, the MCSTEP IPs for both CAS choices are in very good agreement with experiment. We also calculate the next two vertical IPs where no accurate experimental estimates are as yet available. The "SCF-balanced" CAS choice is advantageous to use with MCSTEP because of simplicity, while the "SDCI-balanced" CAS is appropriate for use with MCSTEP when the initial MCSCF has undesired properties. © 1998 John Wiley & Sons, Inc. Int J Quant Chem 70: 729–736, 1998

Key words: ionization potentials; electron propagator; MCSTEP; NH₂; Green's function

Correspondence to: D. L. Yeager.

Contract grant sponsor: The Robert A. Welch Foundation.

Contract grant number: A-770.

Introduction

With electron propagator methods, vertical ionization potentials (IPs) and electron affinities (EAs) are determined directly [1, 2]. Traditionally, these methods have been based on a single-configurational initial state (also called the “reference” state) corrected by perturbation theory [3–12]. Although these perturbational Green’s function techniques have occasionally been successfully applied to more general cases, they are usually restricted in applicability to closed-shell atoms and molecules with only dynamical correlation in their initial states.

The multiconfigurational spin-tensor electron propagator method (MCSTEP) was specifically designed to consistently and reliably determine low-lying, vertical principal IPs and EAs for open-shell and highly correlated (nondynamical correlation) initial-state atoms and molecules [13, 14]. Of course, closed-shell atoms and molecules with only dynamical initial-state correlation effects can be handled as well. Several recent calculations have demonstrated the accuracy and reliability of MCSTEP for determining the low-lying principal vertical IPs for general atoms and molecules [13–24].

With MCSTEP, a small multiconfigurational self-consistent-field (MCSCF) calculation is first required to obtain the initial state. For calculational simplicity, we usually choose a complete active space (CAS) reference state. In previous work, we showed that a “balanced” CAS composed of three strongly occupied and three weakly occupied orbitals for the MCSCF reference state in MCSTEP calculations gives superior IPs over other CAS choices [21, 24].

We recently determined an optimal way to choose the active orbitals for this CAS [21–24]. This involves a balanced CAS where three CAS orbitals are the symmetries of the highest occupied in the (single configuration) SCF and three CAS orbitals are the symmetries lowest unoccupied. The initial MCSCF orbital guess has also been these SCF orbitals. We will refer to this CAS as an “SCF-balanced” CAS.

This scheme for choosing a CAS for the MCSCF calculation is very straightforward and works very well, in general, for the initial state for the determination of low-lying, principal vertical IPs and

EAs with MCSTEP [21–24]. However, occasionally, a fully optimized MCSCF reference state is obtained which has undesired characteristics. When this MCSCF reference state is used in subsequent MCSTEP calculations, lower-quality IPs are obtained. An approximate MCSCF reference state with the same CAS choice has then been obtained for use in MCSTEP calculations which when used in subsequent MCSTEP calculations gives, in general, excellent vertical IPs [21–24].

In this article, a different balanced CAS choice is presented for the MCSCF state to use with MCSTEP calculations. Instead of choosing the CAS orbitals using the SCF orbital energies as a criterium, as was utilized previously, the occupation numbers of the natural orbitals obtained from a single (SCF)-reference singles and doubles configuration interaction (SDCI) calculation are used to choose the six active orbitals. We refer to this CAS as “SDCI-balanced.”

As we report below, the use of either CAS with MCSTEP for NH_2 gives very good IPs compared with experiment. The fully optimized SCF-balanced CAS MCSCF gives an undesired reference state so an approximate MCSCF state must be used for the MCSTEP calculations. The SDCI-balanced CAS MCSCF state does not have undesired characteristics, and, hence, the true, fully optimized MCSCF state is used for the MCSTEP calculations. The use of the SDCI-balanced CAS in MCSTEP calculations gives low-lying vertical IPs for NH_2 in even better agreement with experiment compared with the SCF-balanced choice.

Theory

MULTICONFIGURATIONAL SPIN TENSOR ELECTRON PROPAGATOR METHOD (MCSTEP)

In this section, some of the theory relevant to MCSTEP is very briefly discussed. The intent is not to be complete, but, instead, to be indicative of the methodology. For a more complete discussion, interested readers are directed to the original articles on MCEP [13] and MCSTEP [14]. For a summary on MCEP and MCSTEP longer than given here, interested readers should examine [15].

The poles of the single-particle Green’s function are the IPs and EAs of a system [1, 2]. In general, these poles cannot be obtained exactly. Therefore,

approximations have to be made. There are two principal approximations: For the initial or reference state and for the complete operator manifold that describes the ionization or attachment processes [2–24].

The single-particle Green's function equations for closed-shell atoms and molecules were traditionally solved by approximating the reference state by a single-determinant Hartree–Fock state corrected by Møller–Plesset perturbation theory [2–12]. In these techniques, operators were included in the operator manifold to assure the solution of the resulting equations correctly through a certain order in the electron–electron interaction. To obtain reliable IPs for outer-valence principal IPs for closed-shell systems that had initial states well described by Møller–Plesset perturbation theory, it was found that for IPs the equations needed to be solved at least through third order in the electron–electron interaction. Some higher-order terms are sometimes required in the perturbational Green's function solution in order to obtain accurate IPs.

Although these third- and third + -order perturbative Green's function methods have been very successful [25–27], they are somewhat limited in applicability. Perturbative approaches often cannot handle reliably or handle at all systems with initial states that are open-shell and/or highly correlated (nondynamical correlation) for either IPs or EAs.

With MCSTEP, these problems are solved by using a multiconfigurational reference state and explicitly coupling tensor ionization and attachment operators to a tensor initial state. For calculational simplicity, an MCSCF reference state is used in MCSTEP, although, in principle, a CI state or other nonperturbatively correlated state could also be used. The operator manifold chosen for MCSTEP includes simple electron addition and destruction operators, $N - 1$ transfer operators which remove an electron from the occupied/partially occupied orbitals and allow all possible rearrangements of the remaining electrons in the partially occupied space, and $N + 1$ transfer operators which add an electron to the unoccupied/partially unoccupied orbitals and allow all possible rearrangements of the remaining electrons in the partially occupied space [13–15].

MCSTEP IPs and EAs are obtained from the generalized eigenvalue equation

$$\mathbf{M} X_f = \omega_f \mathbf{N} X_f, \quad (1)$$

where

$$M_{r,p} = \sum_{\Gamma} (-1)^{S_0 - \Gamma - S_f - \gamma_r} W(\gamma_r \gamma_p S_0 S_0; \Gamma S_f) \times (2\Gamma + 1)^{1/2} \times \langle \langle NS_0 | \{ h_r^+(\bar{\gamma}_r), H, h_p(\gamma_p) \}^{\Gamma} | NS_0 \rangle \rangle \quad (2)$$

and

$$N_{r,p} = \sum_{\Gamma} (-1)^{S_0 - \Gamma - S_f - \gamma_r} W(\gamma_r \gamma_p S_0 S_0; \Gamma S_f) \times (2\Gamma + 1)^{1/2} \times \langle \langle NS_0 | \{ h_r^+(\bar{\gamma}_r), h_p(\gamma_p) \}^{\Gamma} | NS_0 \rangle \rangle \quad (3)$$

ω_f is an IP or EA to the final ion tensor state $|N \pm 1S_f\rangle\rangle$, which has spin S_f . W is the usual Racah coefficient; $h_p(\gamma_p)$ and $h_r^+(\bar{\gamma}_r)$ are tensor operator versions of members of the operator manifold with ranks γ_p and γ_r , respectively; $\{ , \}$ is the anticommutator

$$\{A, B\} = AB + BA; \quad (4)$$

and $\{ , , \}$ is the symmetric double anticommutator

$$\{A, B, C\} = \frac{1}{2}\{A, [B, C]\} + \frac{1}{2}\{[A, B], C\}. \quad (5)$$

We have demonstrated that MCSTEP is very accurate and reliable for lower-lying (in energy) IPs [13–24]. These are the IPs corresponding to processes that are primarily simple electron removal (i.e., the principal IPs) of the outer-valence electrons. Higher-lying inner valence and core principal IPs and shake-up IPs (where the primary processes correspond to simple electron removal with excitation of the remaining electrons) can, in principle, also be determined with MCSTEP; however, they are usually at best only of qualitative accuracy.

MCSTEP IPs are incorrect when important contributions from processes that are simple electron removal + excitation of the remaining electrons to diffuse orbitals are necessary for an accurate description. (This is true regardless of the number of diffuse functions in the basis set.) These IPs are usually higher in energy and include most inner-valence and core IPs as well as most of the shake-up IPs. We have previously shown that these higher-lying IPs can be accurately determined by an extension of MCSTEP known as the repartitioned multiconfigurational spin-tensor electron

propagator method (RMCSTEP) [14]. RMCSTEP is considerably more complicated than is MCSTEP.

REFERENCE MCSCF STATE AND EIGENVALUES OF THE LAGRANGIAN

In MCSTEP, we first perform an MCSCF calculation in order to obtain an MCSCF reference state and the needed MCSCF orthogonal compliment states. The CAS choices for the MCSCF for MCSTEP involve a few strongly occupied orbitals and a few weakly occupied orbitals as discussed above for the SCF-balanced and SDCI-balanced CAS choices. Since MCSTEP is designed to calculate outer-valence IPs and EAs, for a "desired" MCSCF state, the eigenvalues of the Lagrangian corresponding to the partially occupied orbitals should be above the eigenvalues of the doubly occupied orbitals. The Lagrangian is defined:

$$\epsilon_{ir} = \sum_j \gamma(rj) h(ij) + 2 \sum_{jkl} \Gamma(rjkl)(ij|kl), \quad (6)$$

where γ is the one-body density matrix and Γ is the two-body density matrix. Note that in the limit of a closed-shell single determinant the eigenvalues of the Lagrangian correspond to the canonical orbital energies.

In some cases, the Lagragian eigenvalues for some of the MCSCF active orbitals are below the eigenvalues of the doubly occupied orbitals. We refer here to such an obtained MCSCF state as "undesired" (at least for use in subsequent MCSTEP calculations).

When an undesired MCSCF state is obtained, a desired but approximate MCSCF state with the same CAS can usually be obtained by reoptimizing the MCSCF while neglecting one or more orbital rotations in the MCSCF iterations [21]. When this approximate MCSCF state is used as the reference state, the obtained CAS orbitals, while obviously not fully variational, are still used in forming the ket-bra states used in the transfer operators.

COMPLETE BASIS SET (CBS) LIMIT

The basis sets that we used in the calculations for NH_2 are the Dunning correlation consistent basis sets, cc-pVDZ, cc-pVTZ, and cc-pVQZ, and the Dunning augmented correlation consistent basis sets, aug-cc-pVDZ, aug-cc-pVTZ, and aug-cc-pVQZ [28, 29]. The aug-cc-pVXZ sets have addi-

tional diffuse functions added to the corresponding cc-pVXZ sets.

We then apply a three-parameter exponential fitting function of [30] to estimate values at the CBS limit:

$$A(x) = A_{\text{CBS}} + Be^{-Cx} \quad (7)$$

where $x = 2, 3$, and 4 for the DZ, TZ, and QZ basis sets.

Calculational Results

The ground state of NH_2 is of ${}^2\text{B}_1$ symmetry. The principal configuration of the ground state is $1a_1^2 2a_1^2 1b_2^2 3a_1^2 1b_1^1$. Since it is open shell, the usual perturbative Green's function methods cannot, in general, be used to determine ionizations from this state.

In Tables I–III, low-lying principal vertical IPs are listed using MCSTEP with balanced CAS choices and several different basis sets at the experimental ground-state ${}^2\text{B}_1$ geometry [31–34] (i.e., the HNH angle is 103.3° and the NH bond length is 1.93508 au). The low-lying, principal vertical IPs of NH_2 determined with MCSTEP using the SCF-balanced CAS are given in Table I. The CAS used in these calculations consists of five electrons in the $(1b_2 3a_1 1b_1 2b_2 4a_1 3b_2)$ orbitals. For neutral B_1 states, this involves only 52 determinants. This CAS was chosen by the SCF-balanced scheme described above, that is, the three occupied (single-configuration) SCF orbitals with the highest orbital energies and three unoccupied SCF orbitals with the lowest orbital energies were used as an initial orbital guess for the active orbitals for the subsequent MCSCF.

Upon examination of the fully optimized MCSCF states used as the MCSTEP reference states, it was found that the MCSCF states had an undesired ordering of the Lagrangian eigenvalues. The $3a_1$ orbital which was included in the active space had a lower eigenvalue than the $2a_1$ orbital which was doubly occupied. The resulting MCSTEP IPs using this state are not of the same quality as are the MCSTEP IPs obtained from a more "desired" initial state.

To correct this, rotations between the $2a_1$ and $3a_1$ were neglected in the MCSCF optimizations, and approximate MCSCF states with the correct ordering of the Lagrangian eigenvalues were obtained. Use of these approximate MCSCF states

TABLE I
Low-lying principal vertical ionization potentials for NH₂^{a,b}, with the MCSTEP calculations using the SCF-balanced (1b₂3a₁1b₁2b₂4a₁3b₂) CAS.^c

Ion state	MCSTEP cc-pVDZ basis ^d	MCSTEP cc-pVTZ basis ^d	MCSTEP cc-pVQZ basis ^d	MCSTEP CBS limit ^e	Experiment ^f
X̃ ³ B ₁ (3a ₁) ⁻¹	11.40	11.67	11.74	11.77	12.00
Ā ¹ A ₁ (1b ₁) ⁻¹	12.09	12.30	12.34	12.36	12.45
¹ B ₁ (3a ₁) ⁻¹	13.82	14.03	14.07	14.09	14.27
³ A ₂ (1b ₂) ⁻¹	16.48	16.68	16.73	16.75	
¹ A ₂ (1b ₂) ⁻¹	17.87	18.08	18.13	18.15	

^a All results are in electron volts.^b The ground-state neutral experimental geometry is from [31–34].^c The CAS used for the MCSTEP calculations is all possible configurations with five electrons in the (1b₂3a₁1b₁2b₂4a₁2b₂) orbitals.^d pVDZ, pVTZ, and pVQZ basis sets are from [28]. The cc-pVDZ calculations include all six Cartesian d components; the cc-pVTZ calculations include all six Cartesian d components and all 10 Cartesian f components; and the cc-pVQZ calculations include the five spherical d components, seven spherical f components, and nine spherical g components.^e Equation (7).^f [35, 36]. The authors report their experimental vertical IPs to hundredths of an electron volt.

yields MCSTEP IPs which were considerably better. This problem has manifested itself previously in MCSCF calculations of O₃ [23], HCN [21], HNC [21], and several others. The energies of these approximate MCSCF ²B₁ ground states are, respectively, -55.614410, -55.6339520, and -55.638503 au for the cc-pVDZ, cc-pVTZ, and cc-pVQZ basis sets.

The MCSTEP IPs reported in Table I were obtained with the SCF-balanced CAS approximate MCSCF initial states using cc-pVDZ, cc-pVTZ, and cc-pVQZ basis sets. The results show that the cc-

pVDZ basis set is not adequate for obtaining low-lying principal vertical MCSTEP IPs, while the cc-pVTZ and cc-pVQZ results are very similar and in very good agreement with experiment. With the best basis set results reported in Table I (i.e., with the pVQZ basis set), the MCSTEP results differ by -0.26, -0.11, and -0.20 eV from experiment [35, 36] for IPs to the X̃³B₁(3a₁)⁻¹, Ā¹A₁(1b₁)⁻¹, and ¹B₁(3a₁)⁻¹ states, respectively. [Note that the experimental vertical IPs are reported to hundredths of electron volts in [35, 36]. Although we do not think that such experimental accuracy is possible

TABLE II
Low-lying principal vertical ionization potentials for NH₂^{a,b}, with the MCSTEP calculations using the SDCI-balanced (1b₂3a₁1b₁2b₂4a₁5a₁) CAS.

Ion state	MCSTEP cc-pVDZ basis ^d	MCSTEP cc-pVTZ basis ^d	MCSTEP cc-pVQZ basis ^d	MCSTEP CBS limit ^e	Experiment ^f
X̃ ³ B ₁ (3a ₁) ⁻¹	11.34	11.63	11.71	11.74	12.00
Ā ¹ A ₁ (1b ₁) ⁻¹	12.11	12.32	12.38	12.40	12.45
¹ B ₁ (3a ₁) ⁻¹	13.84	14.05	14.12	14.15	14.27
³ A ₂ (1b ₂) ⁻¹	16.55	16.72	16.78	16.81	
¹ A ₂ (1b ₂) ⁻¹	17.80	17.97	18.04	18.09	

^{a,b} See footnotes a and b to Table I.^c The CAS used for the MCSTEP calculations is all possible configurations with five electrons in the (1b₂3a₁1b₁2b₂4a₁5a₁) orbitals.^d cc-pVDZ, cc-pVTZ, and cc-pVQZ basis sets are from [28]. The cc-pVDZ calculations include all six Cartesian d components; the cc-pVTZ calculations include all six Cartesian d components and all 10 Cartesian f components; and the cc-pVQZ calculations include the five spherical d components, seven spherical f components, and nine spherical g components.^{e,f} See footnotes e and f to Table I.

TABLE III

Low-lying principal vertical ionization potentials for NH_2 ^{a,b}, with the MCSTEP calculations using the SDCI-balanced ($1b_2 3a_1 1b_1 2b_2 4a_1 5a_1$) CAS and with the basis sets including diffuse functions.^{c,d}

Ion state	MCSTEP avg-cc-pVDZ basis ^d	MCSTEP avg-cc-pVTZ basis ^d	MCSTEP avg-cc-pVQZ basis ^d	MCSTEP CBS limit ^e	Experiment ^f
$\tilde{X}^3\text{B}_1(3a_1)^{-1}$	11.71	11.75	11.76	11.77	12.00
$\tilde{A}^1\text{A}_1(1b_1)^{-1}$	12.40	12.41	12.42	12.42	12.45
$^1\text{B}_1(3a_1)^{-1}$	14.11	14.15	14.16	14.17	14.27
$^3\text{A}_2(1b_2)^{-1}$	16.82	16.83	16.84	16.84	
$^1\text{A}_2(1b_2)^{-1}$	18.05	18.08	18.09	18.10	

^{a,b} See footnotes a and b to Table I.

^c The CAS used for the MCSTEP calculations is all possible configurations with five electrons in the ($1b_2 3a_1 1b_1 2b_2 4a_1 5a_1$) orbitals.

^d aug-cc-pVDZ, aug-cc-pVTZ, and aug-cc-pVQZ basis sets are from [28, 29]. The aug-cc-pVDZ calculations include all six Cartesian *d* components; the aug-cc-pVTZ calculations include all six Cartesian *d* components and all 10 Cartesian *f* components; and the aug-cc-pVQZ calculations include the five spherical *d* components, seven spherical *f* components, and nine spherical *g* components.

^{e,f} See footnotes e and f to Table I.

(see the next section), for comparison purposes, we report the MCSTEP IPs to the same accuracy.] The CBS extrapolated limit values differ from experiment by -0.23 , -0.09 , and -0.18 eV.

Vertical NH_2 MCSTEP IPs using the SDCI-balanced CAS are reported in Tables II and III.

Performing an SDCI calculation including all single and double excitations from the $1a_1^2 2a_1^2 1b_1^2 3a_1^2 1b_1^1$ single-configuration SCF state, obtaining the natural orbitals, and choosing the three lowest occupancy strongly occupied orbitals and the three highest occupancy weakly occupied orbitals gives a ($1b_2 3a_1 1b_1 2b_2 4a_1 5a_1$) CAS. This MCSCF CAS includes all possible configurations of five electrons in the ($1b_2 3a_1 1b_1 2b_2 4a_1 5a_1$) orbitals. For neutral B_1 states, this involves only 76 determinants.

The fully optimized $^2\text{B}_1$ ground-state SDCI-balanced CAS MCSCF energies are, respectively, -55.620342 , -55.634819 , and -55.639730 au for the cc-pVDZ, cc-pVTZ, and cc-pVQZ basis sets. Furthermore, the orbitals with these basis sets had the desired order of the Lagragian eigenvalues, that is, the MCSCF active orbitals had Lagragian eigenvalues higher than those of the MCSCF doubly occupied orbitals.

The MCSTEP IPs reported in Table II were obtained with this SDCI-balanced CAS using cc-pVDZ, cc-pVTZ, and cc-pVQZ basis sets. The results also show that the cc-pVDZ basis set is not adequate for obtaining low-lying principal vertical MCSTEP IPs, while the cc-pVTZ and cc-pVQZ results are very similar and are in very good

agreement with experiment. With the best basis set reported in Table II (i.e., with the cc-pVQZ basis set), the MCSTEP results differ by -0.29 , -0.07 , and -0.15 eV from experiment for IPs to the $\tilde{X}^3\text{B}_1(3a_1)^{-1}$, $\tilde{A}^1\text{A}_1(1b_1)^{-1}$, and $^1\text{B}_1(3a_1)^{-1}$ states, respectively. The CBS-extrapolated limit values differ from experiment by -0.26 , -0.05 , and -0.12 eV.

The MCSTEP vertical IPs with the augmented basis sets and the SDCI-balanced CAS are even better compared to the reported experimental values. The $^2\text{B}_1$ ground-state MCSCF energies are, respectively, -55.623540 , -55.636853 , and -55.640393 au for the aug-cc-pVDZ, aug-cc-pVTZ, and aug-cc-pVQZ basis sets. Furthermore, the fully optimized MCSCF orbitals had the desired order of the Lagragian eigenvalues, that is, the active orbitals in the CAS had Lagragian eigenvalues higher than those of the MCSCF doubly occupied orbitals.

The MCSTEP IPs reported in Table III were obtained with this SDCI-balanced CAS using aug-cc-pVDZ, aug-cc-pVTZ, and aug-cc-pVQZ basis sets. The results show that the aug-cc-pVDZ, the aug-cc-pVTZ, and aug-cc-pVQZ results are very similar to each other and are in even better agreement with experiment compared to the corresponding non-aug basis sets with the same SDCI-balanced CAS. This is undoubtedly due to the extra functions added to the cc-pVXZ basis sets. With the best basis-set results reported in Table III (i.e., with the aug-cc-pVQZ basis set), the MCSTEP results differ by -0.24 , -0.03 , and -0.11

eV from experiment for IPs to the $\tilde{X}^3B_1(3a_1)^{-1}$, $\tilde{A}^1A_1(1b_1)^{-1}$, and ${}^1B_1(3a_1)^{-1}$ states, respectively. The CBS-extrapolated limit values differ from experiment by -0.23, -0.03, and -0.10 eV.

Summary, Discussion, and Conclusions

The lowest three MCSTEP vertical, principal IPs for NH₂ are in very good agreement with experiment with either the SCF-balanced CAS or the SDCI-balanced CAS for cc-pVTZ, cc-pVQZ, and cc-CBS limit estimates. For the aug-cc basis sets, the MCSTEP IPs are also in excellent agreement at the pVDZ level as well. For the three lowest vertical IPs, the MCSTEP values are slightly low compared with the experimentally obtained values.

For all these experimentally determined vertical IPs, however, it should be kept in mind that since NH₂ is a free radical it is very reactive. Hence, the experimental photoelectron spectrum is very cluttered and is difficult to interpret [35, 36]. There has been some controversy where it was argued that the $\tilde{X}^3B_1(3a_1)^{-1}$ IP of [35, 36] was too high by approximately 0.30–0.35 eV [37, 38]. Of course, it is also often difficult or impossible to interpret exactly (i.e., within hundredths of an electron volt) where the vertical is experimentally from a PES that may have, for example, some vibrational structure, even when the spectrum is uncluttered. Other good theoretical results have likewise been reported lower than experiment by similar amounts or even more (see [35–38]).

Because of the accuracy of the MCSTEP calculations reported here and other previously reported MCSTEP IP calculations as well, the MCSTEP vertical IPs to the ${}^3A_2(1b_2)^{-1}$ and ${}^1A_2(1b_2)^{-1}$ states at around 16.8 and 18.2 eV, respectively, can also be assumed to be very accurate. This region of the NH₂ photoelectron spectrum is even more difficult to interpret due to contaminant clutter and low peak intensity [35, 36].

While both the SCF-balanced CAS and the SDCI-balanced CAS give very good vertical IPs in NH₂ compared to experiment, use of the SDCI-balanced CAS is advantageous when the two CASs differ or when the SCF-balanced CAS gives an “undesired” MCSCF state (i.e., meaning here one with partially occupied orbitals having Lagrangian eigenvalues lower than the eigenvalues for some of the doubly occupied orbitals). While we have devised a computational scheme to obtain an ap-

proximate MCSCF state when the true MCSCF state is undesired—by neglecting a rotation or two in MCSCF optimization [21]—it is sometimes unclear which rotation(s) need to be ignored to obtain this approximate MCSCF state. Also, if too many rotations are neglected in the MCSCF optimization, the obtained approximate MCSCF state may be so far from the true quantum mechanical state as to be useless for use as the MCSTEP reference state.

Hence, in general, the best CAS choice for the MCSCF initial state used in MCSTEP is the SCF-balanced CAS. This is because this CAS is straightforwardly obtained from a simple SCF calculation. If, however, the MCSCF state using the SCF-balanced CAS is “undesired,” then the SDCI-balanced CAS MCSCF state should be used instead. A similar analysis applies for the MCSTEP initial state for H₂O and other molecules as well.

ACKNOWLEDGMENTS

We would like to acknowledge support for this research, in part, from The Robert A. Welch Foundation, Grant No. A-770. We also especially thank Jack Simons from the University of Utah for providing the MESSKIT suite of codes which we used to obtain MCSCF wave functions and Dr. Jeff Nichols of Pacific Northwest Laboratory for advice and helpful discussions.

References

1. J. Linderberg and Y. Öhrn, *Propagators in Quantum Chemistry* (Academic Press, London, 1973).
2. P. Jørgensen and J. Simons, *Second Quantization-Based Methods in Quantum Chemistry* (Academic Press, New York, 1981).
3. J. Simons, *Annu. Rev. Phys. Chem.* **28**, 15 (1977).
4. C. W. McCurdy, T. Rescigno, D. L. Yeager, and V. McKoy, in *Methods of Electronic Structure*, H. F. Schaefer III, Ed. (Plenum, New York, 1977).
5. L. S. Cederbaum, G. Hohneicher, and W. von Niessen, *Chem. Phys. Lett.* **18**, 503 (1973).
6. L. S. Cederbaum, W. Domcke, J. Schirmer, and W. von Niessen, *Adv. Chem. Phys.* **65**, 115 (1986).
7. J. Oddershede, *Adv. Quantum Chem.* **11**, 257 (1978).
8. J. Oddershede, P. Jørgensen, and D. L. Yeager, *Comp. Phys. Rep.* **2**, 33 (1984).
9. J. Oddershede, *Adv. Chem. Phys.* **69**, 201 (1987).
10. Y. Öhrn and G. Born, *Adv. Quantum Chem.* **13**, 1 (1981).
11. M. F. Herman, K. F. Freed, and D. L. Yeager, *Adv. Chem. Phys.* **48**, 1 (1981).

12. J. V. Ortiz, R. Basu, and Y. Öhrn, *Chem. Phys. Lett.* **103**, 29 (1983).
13. J. T. Golab and D. L. Yeager, *J. Chem. Phys.* **87**, 2925 (1987).
14. J. A. Nichols, D. L. Yeager, and P. Jørgensen, *J. Chem. Phys.* **293** (1984).
15. D. L. Yeager, in *Applied Many-Body Methods in Spectroscopy and Electronic Structure*, D. Mukherjee, Ed. (Plenum, New York, 1992).
16. D. L. Yeager, J. A. Nichols, and J. T. Golab, *J. Chem. Phys.* **97**, 8841 (1992).
17. D. L. Yeager, J. A. Nichols, and J. T. Golab, *J. Chem. Phys.* **98**, 8790 (1993).
18. J. A. Nichols, D. Heryadi, D. L. Yeager, and J. T. Golab, *J. Chem. Phys.* **100**, 2947 (1994).
19. D. L. Yeager, J. A. Nichols, and J. T. Golab, *J. Chem. Phys.* **100**, 6514 (1994).
20. D. Heryadi, D. L. Yeager, J. T. Golab, and J. A. Nichols, *J. Chem. Phys.* **102**, 9444 (1995).
21. D. Heryadi, D. L. Yeager, J. T. Golab, and J. A. Nichols, *Theor. Chim. Acta* **90**, 273 (1995).
22. D. L. Yeager, *J. Chem. Phys.* **105**, 8170 (1996).
23. A. J. McKellar, D. L. Yeager, J. A. Nichols, and J. T. Golab, *J. Chem. Phys.* **105**, 9927 (1996).
24. D. Heryadi, C. Jones, and D. L. Yeager, *J. Chem. Phys.* **107**, 5088 (1997).
25. J. V. Ortiz, in *Computational Chemistry: Reviews of Current Trends*, Vol. 2, J. Leszczynski, Ed. (World Scientific, Singapore, 1997), p. 1.
26. J. V. Ortiz, V. G. Zakrzewski, and O. Dolgounitcheva, in *Conceptual Trends in Quantum Chemistry*, E. S. Kryachko, Ed. (Kluwer, Dordrecht, 1997), Vol. 3, p. 465.
27. J. V. Ortiz, *J. Chem. Phys.* **99**, 6716 (1993).
28. T. H. Dunning, *J. Chem. Phys.* **90**, 1007 (1989).
29. R. A. Kendall, T. H. Dunning, and R. J. Harrison, *J. Chem. Phys.* **96**, 6796 (1992).
30. K. A. Peterson and T. H. Dunning, *J. Chem. Phys.* **102**, 2032 (1995).
31. G. Herzberg and D. A. Ramsey, *J. Chem. Phys.* **20**, 347 (1952).
32. G. Herzberg and D. A. Ramsey, *Discuss. Faraday Soc.* **14**, 11 (1953).
33. K. Dressler and D. A. Ramsay, *J. Chem. Phys.* **27**, 971 (1957).
34. G. Herzberg, *Electronic Spectra of Polyatomic Molecules* (Van Nostrand, Princeton, 1967).
35. S. J. Dunlavey, J. M. Dyke, N. Jonathan, and A. Morris, *Mol. Phys.* **39**, 1121 (1980).
36. J. M. Dyke, N. Jonathan, and A. Morris, *Int. Rev. Phys. Chem.* **2**, 3 (1982).
37. R. L. Graham, J. T. Golab, and D. L. Yeager, *J. Chem. Phys.* **88**, 2572 (1988).
38. S. Te Gibson, J. P. Greene, and J. Berkowitz, *J. Chem. Phys.* **83**, 4319 (1985).

Effect of Heavy Atom on the Second Hyperpolarizability of Tetrahydrofuran Homologs Investigated by Ab Initio Molecular Orbital Method

KENJI KAMADA,¹ MINORU UEDA,¹ HIDEKI NAGAO,^{1,*}
KEIKO TAWA,¹ TAKUSHI SUGINO,² YO SHIMIZU,² KOJI OHTA¹

¹ Department of Optical Materials, Osaka National Research Institute, AIST, MITI, 1-8-31
Midorigaoka, Ikeda, Osaka 563-8577, Japan

² Department of Organic Materials, Osaka National Research Institute, AIST, MITI, 1-8-31
Midorigaoka, Ikeda, Osaka 563-8577, Japan

Received 30 March 1998; accepted 19 May 1998

ABSTRACT: Static second hyperpolarizabilities were calculated for molecules including tetrahydrofuran homologs by ab initio molecular orbital methods at the Hartree-Fock and various correlation levels. Substitution of the heteroatom with a heavier atom is found to be effective for increase of the second hyperpolarizability of these homologs. Comparison between the present results and previous results for furan homologs shows that π -conjugation is not effective for the increase of second hyperpolarizability of the molecules when the heteroatom is heavier. © 1998 John Wiley & Sons, Inc. Int J Quant Chem 70: 737–743, 1998

Introduction

Nonlinear optical properties of molecular materials are important because of possible future photonics applications. In this field, the struc-

ture–property correlation has been extensively studied. For the third-order nonlinear optical properties, however, this correlation is not well established.

Molecular orbital calculations are a useful tool for investigating structure–property correlation at the molecular level [1–9] because they give individual molecular properties directly. This information is complementary to statistically averaged properties obtained by most experimental techniques from the condensed phase.

Correspondence to: K. Ohta.

*Present address: Department of Chemistry, Graduate School of Science, Osaka University, 1-1 Machikaneyamacho, Toyonaka, 560-0043, Japan.

We have extensively studied the third-order nonlinear optical properties of molecules containing second- or higher-row atoms by molecular orbital calculation [6–8]. Some of these molecules containing heteroatoms are important because of their large third-order nonlinearities. We have revealed, by experiment and molecular orbital calculation [9, 10], the effect of variation of the heteroatom on the nonlinearity of the homologs of thiophene. These materials are not only the simplest unsaturated heterocyclics but are also the constitutive unit of the potential nonlinear optical materials such as polythiophene.

In this article, we report the static hyperpolarizability, γ , of tetrahydrofuran homologs (saturated derivatives of furan homologs) studied by ab initio molecular orbital methods. By comparing the γ values of furan and tetrahydrofuran homologs, we investigated the influence of π -conjugation on the molecular second hyperpolarizabilities of furan homologs and the effect of heavier heteroatom substitution. Finally, we compared the present calculations with the observations obtained by the optical Kerr effect (OKE) experiments which have been done in our laboratory [9, 10].

Calculation Method

Here, we describe the calculation method used in this study. The Gaussian 94 program [11] was used for the ab initio molecular orbital calculations throughout this study. Finite-field methods were used for the calculation of static second hyperpolarizability. At the Hartree–Fock level, we used the following equation for the first-order numerical derivative of the first hyperpolarizability values β :

$$\gamma_{iijj} = [8\{\beta_{iij}(F_j) - \beta_{iij}(-F_j)\} - \{\beta_{iij}(2F_j) - \beta_{iij}(-2F_j)\}]/12F_j, \quad (1)$$

with $i, j = x, y, z$. Individual $\beta_{iij}(F_j)$ values can be obtained under the application of a uniform electric field by the optional routine in the Gaussian program [6]. In this case, the minimum finite electric-field value F_j was set at 0.0025 au [6].

Various kinds of correlation methods including MP2, MP3, MP4, CCSD, and CCSD(T) models were used for examining the effect of electron correlation on the hyperpolarizability. For this purpose, we used the following equations for the fourth-

order numerical derivative of the total energy E :

$$\begin{aligned} \gamma_{iiii} = & -[56E(0) - 39\{E(F_i) + E(-F_i)\} \\ & + 12\{E(2F_i) + E(-2F_i)\} \\ & - \{E(3F_i) + E(-3F_i)\}]/6F_i^4 \end{aligned} \quad (2)$$

$$\begin{aligned} \gamma_{iiji} = & -[72E(0) - 38\{E(F_i) + E(-F_i) \\ & + E(F_j) + E(-F_j)\} \\ & + 2\{E(2F_i) + E(-2F_i) + E(2F_j) + E(-2F_j)\} \\ & + 20\{E(F_i, F_j) + E(F_i, -F_j) \\ & + E(-F_i, F_j) + E(-F_i, -F_j)\} \\ & - \{E(2F_i, F_j) + E(2F_i, -F_j) \\ & + E(-2F_i, F_j) + E(-2F_i, -F_j) \\ & + E(F_i, 2F_j) + E(F_i, -2F_j) \\ & + E(-F_i, 2F_j) + E(-F_i, -2F_j)\}]/12F_i^2F_j^2, \end{aligned} \quad (3)$$

with $i, j = x, y, z$. In this case, the minimum finite electric-field values F_i and F_j were set at 0.005 au [8]. It should be noted that γ in eqs. (1)–(3) is defined as the coefficient of the next Taylor expansion of total electric dipole moment, μ , with respect to the applied electric field \mathbf{F} :

$$\mu = \mu_0 + \alpha\mathbf{F} + \beta\mathbf{FF}/2 + \gamma\mathbf{FFF}/6 + , \quad (4)$$

where μ_0 is the permanent electric dipole moment and α is the linear polarizability. The orientationally averaged value of the second hyperpolarizability γ_s is evaluated as

$$\begin{aligned} \gamma_s = & (\gamma_{xxxx} + \gamma_{yyyy} + \gamma_{zzzz} + 2\gamma_{xxyy} \\ & + 2\gamma_{xxzz} + 2\gamma_{yyzz})/5. \end{aligned} \quad (5)$$

This can be directly compared to the electronic component of the experimental Kerr coefficients observed for the isotropic gas or liquid phase.

Basically, the 6-31G basis set was used for light atoms in the present calculation. For carbon, oxygen, and sulfur atoms, two different basis sets augmented with diffuse orbitals were used. First, the 6-31G + pd basis set is the 6-31G basis set augmented with diffuse p and d orbitals on the atoms. Second, the 6-31G + pdd basis set is made by adding another semidiffuse d orbital to the 6-31G + pd basis set.

For the calculations of (hyper)polarizability, the contribution from the electrons in the outer region

of molecules is considered to be more essential than are the electrons of the inner shell. This gives a reasonable basis for using the effective core potential (ECP) for the calculation of (hyper)polarizability [3, 4]. In our previous work [7], we used the ECP method for the calculation of linear polarizability of the molecules containing selenium and tellurium in order to clarify the mechanism of third-order nonlinear optical properties of those molecules observed by picosecond degenerate four-wave mixing method. In this study, the contribution of core electrons in selenium and tellurium atoms was estimated using Wadt-Hay's effective core potential (LANL1DZ) [12] augmented with the *pd* (LANL1DZ + *pd*) and *pdd* (LANL1DZ + *pdd*) diffuse orbitals. The procedure for determining the orbital exponents of the diffuse functions is the same as previously reported [7, 8]. The exponents of the orbitals augmented to the 6-31G and LANL1DZ basis sets are summarized in Table I.

In principle, it would be better to calculate the electronic response properties for the optimized geometry. However, tetrahydrofuran and its homologs are known to have flat potential energy surfaces with respect to the distortion of the molecular plane and we have confirmed that there is little difference between the calculated γ values of the distorted and the plane geometries. Therefore, for simplicity, molecular geometries optimized at the plane configuration (for each basis set at the Hartree-Fock level) were used for the calculation of γ . The molecular axis for designating the tensor component of γ is shown in Figure 1.

Results and Discussion

Static hyperpolarizability values calculated for tetrahydrofuran (C_4H_8O), tetrahydrothiophene (C_4H_8S), tetrahydroselenophene (C_4H_8Se), and tetrahydrotellurophene (C_4H_8Te) are summarized in Tables II–V, respectively. Various approximation

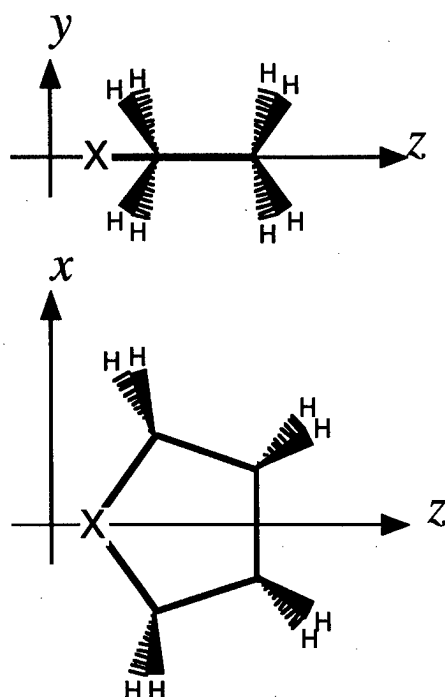


FIGURE 1. Molecular fixed Cartesian coordinates used in the present calculation for tetrahydrofuran homologs C_4H_8X ($X = O, S, Se, Te$).

levels including the Hartree-Fock method are shown. For the correlated results, the last digit in every γ component under 10 au was neglected due to the lack of stability which may have occurred in the numerical differentiation.

First, we discuss the basis-set dependence of the calculated second hyperpolarizability for the molecules at both Hartree-Fock level and correlation methods. As described before, it is necessary to augment the basis set with the diffuse orbital having large orbital exponents for the calculation of hyperpolarizability [1–6]. Once the diffuse *p* and *d* orbitals are added to the basis set, the obtained γ values become quite stable to further augmentation. However, there still seems some

TABLE I
Orbital exponents for functions augmented to the 6-31G and LANL1DZ basis sets

Basis set	C		O		S		Se		Te	
	<i>p</i>	<i>d</i>								
+ <i>pd</i>	0.0438	0.0438	0.0845	0.0845	0.0405	0.0405	0.0367	0.0367	0.0301	0.0301
+ <i>pdd</i>	0.0438	0.18719	0.0845	0.26	0.0405	0.16225	0.0367	0.11558	0.0301	0.08709
		0.0438		0.0845		0.0405		0.0367		0.0301

TABLE II
**Individual components of the second hyperpolarizability of tetrahydrofuran (C_4H_8O) calculated with
 6-31G + *pd* and 6-31G + *pdd* basis sets (atomic units).^a**

Method	γ_{xxxx}	γ_{yyyy}	γ_{zzzz}	γ_{xxyy}	γ_{xxzz}	γ_{yyzz}	γ_s
6-31G + <i>pd</i>							
HF	7591 (1.00)	3465 (1.00)	6989 (1.00)	2377 (1.00)	2131 (1.00)	1567 (1.00)	6039 (1.00)
MP2	13,310 (1.75)	5320 (1.54)	12,700 (1.82)	4110 (1.73)	3480 (1.63)	2530 (1.61)	10,310 (1.71)
MP3	11,180 (1.47)	4840 (1.40)	10,390 (1.49)	3480 (1.46)	2950 (1.38)	2180 (1.39)	8730 (1.45)
MP4D	11,300 (1.49)	4830 (1.39)	10,670 (1.53)	3550 (1.49)	2980 (1.40)	2210 (1.41)	8860 (1.47)
MP4DQ	11,440 (1.51)	4890 (1.41)	10,780 (1.54)	3590 (1.51)	3010 (1.41)	2230 (1.42)	8960 (1.48)
MP4SDQ	13,430 (1.77)	5410 (1.56)	12,930 (1.85)	4260 (1.79)	3440 (1.61)	2570 (1.64)	10,470 (1.73)
MP4SDTQ	14,820 (1.95)	5800 (1.67)	14,370 (2.06)	4570 (1.96)	3780 (1.77)	2800 (1.79)	11,500 (1.90)
CCSD	13,520 (1.78)	5370 (1.55)	12,630 (1.81)	4360 (1.83)	3410 (1.60)	2540 (1.62)	10,420 (1.73)
CCSD(T)	14,620 (1.93)	5750 (1.66)	13,690 (1.96)	4640 (1.95)	3670 (1.72)	2710 (1.73)	11,220 (1.86)
6-31G + <i>pdd</i>							
HF	7457 (1.00)	3922 (1.00)	6281 (1.00)	2507 (1.00)	2013 (1.00)	1671 (1.00)	6008 (1.00)
MP2	13,090 (1.76)	5530 (1.41)	11,150 (1.78)	4140 (1.65)	3290 (1.63)	2500 (1.50)	9930 (1.65)
MP3	10,710 (1.44)	5000 (1.27)	9030 (1.44)	3470 (1.38)	2750 (1.37)	2160 (1.29)	8300 (1.38)
MP4D	10,830 (1.45)	4940 (1.26)	9210 (1.47)	3510 (1.40)	2770 (1.38)	2170 (1.30)	8380 (1.39)
MP4DQ	11,010 (1.48)	5020 (1.28)	9340 (1.49)	3560 (1.42)	2810 (1.40)	2200 (1.32)	8500 (1.41)
MP4SDQ	13,120 (1.76)	5480 (1.40)	11,190 (1.78)	4250 (1.70)	3230 (1.60)	2480 (1.48)	9940 (1.65)
MP4SDTQ	14,620 (1.96)	5890 (1.50)	12,520 (1.99)	4670 (1.86)	3570 (1.77)	2700 (1.62)	10,980 (1.83)
CCSD	12,800 (1.72)	5330 (1.36)	10,740 (1.71)	4180 (1.67)	3120 (1.55)	2400 (1.44)	9650 (1.61)
CCSD(T)	14,020 (1.88)	5870 (1.50)	11,650 (1.85)	4330 (1.73)	3360 (1.67)	2580 (1.54)	10,410 (1.73)

^aNos. in parentheses are ratios to the Hartree-Fock values.

TABLE III
**Individual components of the second hyperpolarizability of tetrahydrothiophene (C_4H_8S) calculated with
 6-31G + *pd* and 6-31G + *pdd* basis sets (atomic units).^a**

Method	γ_{xxxx}	γ_{yyyy}	γ_{zzzz}	γ_{xxyy}	γ_{xxzz}	γ_{yyzz}	γ_s
6-31G + <i>pd</i>							
HF	10,617 (1.00)	10,481 (1.00)	19,020 (1.00)	3112 (1.00)	4106 (1.00)	5059 (1.00)	12,934 (1.00)
MP2	17,420 (1.64)	16,920 (1.61)	29,570 (1.55)	4750 (1.53)	7060 (1.72)	7880 (1.56)	20,660 (1.60)
MP3	15,610 (1.47)	16,260 (1.55)	26,630 (1.40)	4390 (1.41)	6370 (1.55)	7310 (1.44)	18,930 (1.46)
MP4D	15,430 (1.45)	15,910 (1.52)	26,160 (1.38)	4320 (1.39)	6300 (1.53)	7180 (1.42)	18,620 (1.44)
MP4DQ	15,640 (1.47)	16,170 (1.54)	26,520 (1.39)	4380 (1.41)	6400 (1.56)	7270 (1.44)	18,880 (1.46)
MP4SDQ	17,100 (1.61)	17,730 (1.69)	28,980 (1.52)	4750 (1.53)	7010 (1.71)	7960 (1.57)	20,650 (1.60)
MP4SDTQ	18,460 (1.74)	18,790 (1.79)	31,230 (1.64)	5070 (1.63)	7550 (1.84)	8490 (1.68)	22,140 (1.71)
CCSD	17,070 (1.61)	19,130 (1.83)	28,810 (1.51)	4780 (1.54)	7080 (1.72)	8140 (1.61)	21,000 (1.62)
CCSD(T)	18,300 (1.72)	20,030 (1.91)	30,700 (1.61)	5010 (1.61)	7520 (1.83)	8550 (1.69)	22,240 (1.72)
6-31G + <i>pdd</i>							
HF	9609 (1.00)	10,857 (1.00)	16,982 (1.00)	3060 (1.00)	3849 (1.00)	5290 (1.00)	12,369 (1.00)
MP2	15,550 (1.62)	16,420 (1.51)	26,020 (1.53)	4450 (1.45)	6300 (1.64)	7770 (1.47)	19,000 (1.54)
MP3	13,460 (1.40)	15,510 (1.43)	22,750 (1.34)	3990 (1.30)	5510 (1.43)	7100 (1.34)	16,980 (1.37)
MP4D	13,280 (1.38)	14,930 (1.38)	22,250 (1.31)	3930 (1.28)	5410 (1.41)	6890 (1.30)	16,580 (1.34)
MP4DQ	13,520 (1.41)	15,300 (1.41)	22,680 (1.34)	3990 (1.30)	5520 (1.43)	7040 (1.33)	16,920 (1.37)
MP4SDQ	14,980 (1.56)	16,580 (1.53)	24,940 (1.47)	4320 (1.41)	6110 (1.59)	7620 (1.44)	18,520 (1.50)
MP4SDTQ	16,400 (1.71)	17,700 (1.63)	27,210 (1.60)	4640 (1.52)	6670 (1.73)	8180 (1.55)	20,060 (1.62)
CCSD	14,710 (1.53)	17,050 (1.57)	24,380 (1.44)	4260 (1.39)	6050 (1.57)	7610 (1.44)	18,390 (1.49)
CCSD(T)	16,090 (1.67)	18,070 (1.66)	26,020 (1.53)	4330 (1.42)	6460 (1.68)	7980 (1.51)	19,540 (1.58)

^aNos. in parentheses are ratios to the Hartree-Fock values.

HEAVY ATOM EFFECT ON SECOND HYPERPOLARIZABILITY

TABLE IV

Individual components of the second hyperpolarizability of tetrahydroselenophene (C_4H_8Se) calculated with 6-31G + *pd* and 6-31G + *pdd* basis sets and ECP methods (atomic units).^a

Method	γ_{xxxx}	γ_{yyyy}	γ_{zzzz}	γ_{xxyy}	γ_{xxzz}	γ_{yyzz}	γ_s
6-31G + <i>pd</i> for C, ECP (LANL1DZ + <i>pd</i>) for Se							
HF	12,669 (1.00)	20,698 (1.00)	27,382 (1.00)	4253 (1.00)	5553 (1.00)	8516 (1.00)	19,479 (1.00)
MP2	20,310 (1.60)	31,990 (1.55)	40,460 (1.48)	6300 (1.48)	9270 (1.67)	12,540 (1.47)	29,790 (1.53)
MP3	18,460 (1.46)	31,990 (1.55)	37,360 (1.36)	6030 (1.42)	8600 (1.55)	12,060 (1.42)	28,240 (1.45)
MP4D	18,270 (1.44)	31,170 (1.51)	36,590 (1.34)	5930 (1.39)	8480 (1.53)	11,800 (1.39)	27,690 (1.42)
MP4DQ	18,510 (1.46)	31,750 (1.53)	37,120 (1.36)	6010 (1.41)	8620 (1.55)	11,970 (1.41)	28,120 (1.44)
MP4SDQ	19,930 (1.57)	34,300 (1.66)	39,890 (1.46)	6410 (1.51)	9280 (1.67)	12,860 (1.51)	30,250 (1.55)
MP4SDTQ	21,420 (1.69)	36,000 (1.74)	42,680 (1.56)	6780 (1.59)	9920 (1.79)	13,590 (1.60)	32,140 (1.65)
CCSD	19,780 (1.56)	37,380 (1.81)	39,810 (1.45)	6630 (1.56)	9390 (1.69)	13,280 (1.56)	31,110 (1.60)
CCSD(T)	21,140 (1.67)	38,980 (1.88)	42,310 (1.55)	6940 (1.63)	9950 (1.79)	13,900 (1.63)	32,800 (1.68)
6-31G + <i>pdd</i> for C, ECP (LANL1DZ + <i>pdd</i>) for Se							
HF	10,796 (1.00)	21,263 (1.00)	22,939 (1.00)	4050 (1.00)	5142 (1.00)	8217 (1.00)	17,963 (1.00)
MP2	17,230 (1.60)	30,850 (1.45)	34,020 (1.48)	5770 (1.42)	8200 (1.59)	11,600 (1.41)	26,650 (1.48)
MP3	15,070 (1.40)	30,260 (1.42)	30,430 (1.33)	5380 (1.33)	7360 (1.43)	10,980 (1.34)	34,640 (1.37)
MP4D	14,900 (1.38)	28,930 (1.36)	29,660 (1.29)	5260 (1.30)	7210 (1.40)	10,630 (1.29)	23,930 (1.33)
MP4DQ	15,150 (1.40)	29,740 (1.40)	30,250 (1.32)	5350 (1.32)	7360 (1.43)	10,860 (1.32)	24,460 (1.36)
MP4SDQ	16,610 (1.54)	31,770 (1.49)	32,830 (1.43)	5720 (1.41)	8020 (1.56)	11,590 (1.41)	26,370 (1.47)
MP4SDTQ	18,120 (1.68)	33,560 (1.58)	35,570 (1.55)	6100 (1.51)	8690 (1.69)	12,290 (1.50)	28,280 (1.57)
CCSD	16,200 (1.50)	32,790 (1.54)	32,190 (1.40)	5680 (1.40)	7930 (1.54)	11,660 (1.42)	26,340 (1.47)
CCSD(T)	17,530 (1.62)	34,330 (1.61)	34,310 (1.50)	5860 (1.45)	8430 (1.64)	12,160 (1.48)	27,820 (1.55)

^aNos. in parentheses are ratios to the Hartree–Fock values.

TABLE V

Individual components of the second hyperpolarizability of tetrahydrotellurophene (C_4H_8Te) calculated with 6-31G + *pd* and 6-31G + *pdd* basis sets and ECP methods (atomic units).^a

Method	γ_{xxxx}	γ_{yyyy}	γ_{zzzz}	γ_{xxyy}	γ_{xxzz}	γ_{yyzz}	γ_s
6-31G + <i>pd</i> for C, ECP (LANL1DZ + <i>pd</i>) for Te							
HF	17,938 (1.00)	52,229 (1.00)	45,390 (1.00)	8600 (1.00)	9414 (1.00)	17,810 (1.00)	37,441 (1.00)
MP2	27,660 (1.54)	75,700 (1.45)	63,640 (1.40)	12,370 (1.44)	14,650 (1.56)	24,590 (1.38)	54,050 (1.44)
MP3	25,510 (1.42)	77,570 (1.49)	59,850 (1.32)	12,350 (1.44)	13,870 (1.47)	24,330 (1.37)	52,800 (1.41)
MP4D	25,230 (1.41)	75,590 (1.45)	58,540 (1.29)	12,100 (1.41)	13,610 (1.45)	23,790 (1.34)	51,670 (1.38)
MP4DQ	25,580 (1.43)	77,090 (1.48)	59,400 (1.31)	12,300 (1.43)	13,860 (1.47)	24,160 (1.36)	52,540 (1.40)
MP4SDQ	27,230 (1.52)	81,720 (1.56)	63,180 (1.39)	13,000 (1.51)	14,730 (1.56)	25,500 (1.43)	55,720 (1.49)
MP4SDTQ	29,140 (1.62)	84,910 (1.63)	67,150 (1.48)	13,610 (1.58)	15,650 (1.66)	26,660 (1.50)	58,610 (1.57)
CCSD	26,970 (1.50)	88,230 (1.69)	63,040 (1.39)	13,700 (1.59)	14,840 (1.58)	26,260 (1.47)	57,570 (1.54)
CCSD(T)	28,740 (1.60)	91,710 (1.76)	66,770 (1.47)	14,300 (1.66)	15,690 (1.67)	27,350 (1.54)	60,380 (1.61)
6-31G + <i>pdd</i> for C, ECP (LANL1DZ + <i>pdd</i>) for Te							
HF	14,883 (1.00)	49,836 (1.00)	36,069 (1.00)	7971 (1.00)	8317 (1.00)	15,364 (1.00)	32,818 (1.00)
MP2	22,750 (1.53)	67,580 (1.36)	50,860 (1.41)	10,800 (1.35)	12,490 (1.50)	20,430 (1.33)	45,730 (1.39)
MP3	20,190 (1.36)	68,100 (1.37)	46,370 (1.29)	10,620 (1.33)	11,450 (1.38)	19,980 (1.30)	43,750 (1.33)
MP4D	19,920 (1.34)	64,840 (1.30)	45,050 (1.25)	10,240 (1.28)	11,160 (1.34)	19,270 (1.25)	42,240 (1.29)
MP4DQ	20,280 (1.36)	66,830 (1.34)	46,030 (1.28)	10,490 (1.32)	11,430 (1.37)	19,730 (1.28)	43,290 (1.32)
MP4SDQ	21,880 (1.47)	69,830 (1.40)	49,230 (1.36)	10,980 (1.38)	12,200 (1.47)	20,630 (1.34)	45,710 (1.39)
MP4SDTQ	23,750 (1.60)	73,010 (1.47)	52,970 (1.47)	11,560 (1.45)	13,090 (1.57)	21,640 (1.410)	48,460 (1.48)
CCSD	21,320 (1.43)	72,000 (1.44)	48,420 (1.34)	11,130 (1.40)	12,050 (1.45)	20,840 (1.36)	45,960 (1.40)
CCSD(T)	22,980 (1.54)	75,260 (1.51)	51,510 (1.43)	11,530 (1.45)	12,780 (1.54)	21,700 (1.41)	48,350 (1.47)

^aNos. in parentheses are ratios to the Hartree–Fock values.

basis-set dependence, depending on tensor components and molecular species. For example, the $+pdd$ basis set gives 10–20% smaller molecular planar components γ_{xxxx} and γ_{zzzz} compared with the $+pd$ basis set at the Hartree–Fock level. On the other hand, the $+pdd$ basis set gives a larger component γ_{yyyy} concerning the axis perpendicular to the molecular plane than the $+pd$ basis set (except for C_4H_8Te).

Electron correlation increases all tensor components of γ . This increase depends on the contributions from different excitation types to the total MP4 or CCSD(T) results and is similar to the case of carbon disulfide [8]. As pointed out previously for carbon disulfide [8], the smaller $+pd$ basis set can tend to exaggerate the effect of electron correlation on the hyperpolarizability. A similar tendency can also be observed for the present case by comparing the results between the Hartree–Fock and correlation methods. For example, the γ_{yyyy} component becomes larger with the $+pd$ basis set than with the $+pdd$ basis set at any correlation level while it is larger with the $+pdd$ basis set than with the $+pd$ basis set at the Hartree–Fock level (except for C_4H_8Te). Also, the $+pd$ basis set gives a larger γ for almost all components compared to the $+pdd$ basis set at MP4SDTQ or CCSD(T) levels, irrespective of molecular structure.

Now let us examine the effect that substitution of the heteroatom with a heavier atom has on the second hyperpolarizability based on the CCSD(T) models with the $+pdd$ basis set. As can be seen from the comparison among Tables II–V, all the

components of γ monotonically increase as the heteroatom becomes heavier. The γ_s values show the increase due to the heavier heteroatom, illustrating clearly the effect of heavy atom on the resultant third-order optical nonlinearity of these homologs. However, this increase is not uniform depending on the components. The γ_{xxxx} component, which is the planar component, of C_4H_8Te is within twice that of C_4H_8O . On the other hand, the γ_{yyyy} component, which is the component perpendicular to the molecular plane, of C_4H_8Te is more than 10 times that of C_4H_8O , implying that the out-of-plane orbitals of the heavy atom play an essential role in the increase of the γ value.

It should be noted that the electron correlation effect on the hyperpolarizability is smaller for the homologs with heavier heteroatoms. This variation seems systematic, although it is difficult to explain the origin of this phenomenon at the present time.

Comparison of the present results with those for the furan homologs is important for the examination of the effect of π -conjugation on the nonlinear optical properties of furan homologs. Here, we consider the static γ_s value from the 6-31G + pdd basis set and CCSD(T) method as the best calculation value. Table VI summarizes the orientationally averaged values obtained by the present ab initio calculations and the OKE experiments, with the results for furan (C_4H_8O), thiophene (C_4H_8S), selenophene (C_4H_8Se), and tellurophene (C_4H_8Te). The experimental procedure was described in previous articles [9, 10]. The C_4H_8O and C_4H_8S molecules give, respectively, smaller γ_s values

TABLE VI
Comparison between the orientationally averaged second hyperpolarizabilities obtained by the present ab initio calculations and OKE experiment.^a

Molecule	au	Calculation ^b		Experiment ^c 10^{-36} esu (ratio)
		10^{-36} esu (ratio)		
Tetrahydrofuran	10,410	5.2 (0.71)		5.3 (0.71)
Tetrahydrothiophene	19,540	9.8 (1.3)		11.3 (1.5)
Tetrahydroselphenone	27,820	14.0 (1.9)		N.A. ^d (N.A.)
Tetrahydrotellurophene	48,350	24.4 (3.3)		N.A. (N.A.)
Furan	14,750	7.4 (1.0)		7.5 (1.0)
Thiophene	19,990	10.1 (1.4)		13.2 (1.7)
Selenophene	25,460	12.8 (1.7)		17.2 (2.3)
Tellurophene	38,800	19.5 (2.6)		N.A. (N.A.)

^aNos. in parentheses are ratios to the values for furan molecule.

^bPresent CCSD(T) results, 6-31G + pdd , ECP for Se and Te.

^cMeasured at 790 nm. See [10].

^dN.A., not available.

than do C_4H_4O and C_4H_4S both experimentally and theoretically. This clearly indicates that the presence of π -conjugation enhances optical nonlinearity at the molecular level. Conversely, C_4H_8Se and C_4H_8Te with the heavier heteroatom give larger γ_s values than the corresponding C_4H_4Se and C_4H_4Te . This means that the effect of π -conjugation contributes little to the larger second hyperpolarizability of the heterocyclic compounds with the heavier heteroatoms. In other words, we can state that the increasing effect of γ due to the heavier atom originates from the electrons localized on the heteroatoms in these homologs.

Finally, we would like to point out that agreement of the present calculations with experimental results is excellent, especially for the molecules with atoms of smaller atomic numbers when considering the higher correlation effects. In the case of selenophene, there is some discrepancy between the experimental observations and the theoretical calculations. Possible cause of this discrepancy will be discussed in detail in a separate article with the extensive calculational results for the furan homologs [13]. At present, no experimental data are available for the C_4H_8Se and C_4H_8Te molecules. However, we may expect larger γ values for molecules without π -conjugation compared to those with π -conjugation.

Concluding Remarks

In this study, static second hyperpolarizabilities were calculated for tetrahydrofuran homologs by ab initio molecular orbital methods. We found that substitution of the heteroatom with a heavier atom increases the second hyperpolarizability of the tetrahydrofuran homologs. Comparison of the present results with those for furan homologs shows that π -conjugation does not increase the second hyperpolarizability as the heteroatom becomes heavier. Use of effective core potential (ECP) together with diffuse functions is found to be efficient for calculation of second hyperpolarizability of molecules containing heavy atoms. Good corre-

lation between the experimental results and the present calculations is observed with the inclusion of the effect of electron correlation.

ACKNOWLEDGMENTS

Some of the computations were performed on the Cray C916 at the Research Information Processing System (RIPS) at Tsukuba Research Center of Agency of Industrial Science and Technology (AIST). Other parts of the computations were performed on the Cray J912 at this Institute.

References

1. G. J. B. Hurst, M. Dupuis, and E. Clementi, *J. Chem. Phys.* **89**, 385 (1988).
2. P. Chopra, L. Carlacci, H. F. King, and P. N. Prasad, *J. Phys. Chem.* **93**, 7120 (1989).
3. S. P. Karna, M. Dupuis, E. Perrin, and P. N. Prasad, *J. Chem. Phys.* **92**, 7418 (1990).
4. S. P. Karna and M. Dupuis, *Chem. Phys. Lett.* **171**, 201 (1990).
5. M. Dory, L. Beudels, J. G. Fripiat, J. Delhalle, J. M. Andre, and M. Dupuis, *Int. J. Quantum Chem.* **42**, 1577 (1992).
6. K. Ohta, T. Fukumi, and T. Sakaguchi, *Nonlin. Opt.* **6**, 215 (1994).
7. T. Sugino, N. Kambe, N. Sonoda, T. Sakaguchi, and K. Ohta, *Chem. Phys. Lett.* **251**, 125 (1996).
8. K. Ohta, T. Sakaguchi, K. Kamada, and T. Fukumi, *Chem. Phys. Lett.* **274**, 306 (1997).
9. K. Kamada, M. Ueda, T. Sakaguchi, K. Ohta, and T. Fukumi, *J. Opt. Soc. Am. B* **15**, 838 (1998).
10. K. Kamada, M. Ueda, T. Sakaguchi, K. Ohta, and T. Fukumi, *Chem. Phys. Lett.* **263**, 215 (1996); *Ibid., Erratum* **267**, 402 (1997).
11. M. J. Frisch, G. W. Trucks, H. B. Schlegel, P. M. W. Gill, B. G. Johnson, M. A. Robb, J. R. Cheeseman, T. Keith, G. A. Petersson, J. A. Montgomery, K. Reghavachari, M. A. Al-Laham, V. G. Zakrzewski, J. V. Ortiz, J. B. Foresman, C. Y. Peng, P. Y. Ayala, W. Chen, M. W. Wong, J. L. Andres, E. S. Replogle, R. Gomperts, R. L. Martin, D. J. Fox, J. S. Binkley, D. J. Defrees, J. Baker, J. P. Stewart, M. Head-Gordon, C. Gonzalez, and J. A. Pople, *Gaussian 94, Revision B.3* (Gaussian, Inc., Pittsburgh PA, 1995).
12. W. R. Wadt and P. J. Hay, *J. Chem. Phys.* **82**, 284 (1985).
13. K. Kamada, M. Ueda, H. Nagao, K. Tawa, T. Sugino, Y. Shimizu, and K. Ohta, to be submitted.

Structure Dependence of the Low-Lying Excited States and the First Dipole Hyperpolarizability of Phenol Blue

AGOSTINHO SERRANO, SYLVIO CANUTO

Instituto de Física, Universidade de São Paulo, CP 66318, 05315-970 São Paulo, SP, Brazil

Received 17 March 1998; accepted 23 June 1998

ABSTRACT: $(\text{CH}_3)_2\text{NC}_6\text{H}_4\text{NC}_6\text{H}_4\text{O}$ is a merocyanine dye that exists in resonance between the two extreme conformations of a keto and an eno form. The keto form is more stable in the gas phase and the eno form is believed to be more stable in solution. We show that the keto form can prevail in nonpolar solvents, but in polar solvents like chloroform, the eno form should be dominant. Analysis is made of the solvent effects in the low-lying absorption transition and its consequence in the first dipole hyperpolarizability. We show by explicit calculations that the hyperpolarizability of the eno form is one order of magnitude greater than in the keto form. We then contend that this structure dependence may also lead to very large changes of the hyperpolarizability of similar molecules and polymers in solvents. © 1998 John Wiley & Sons, Inc. *Int J Quant Chem* 70: 745–750, 1998

Introduction

4-[(4-Dimethylamino)phenyl]imino]-2,5-cyclohexadien-1-one (DIA), also known as phenol blue, is a merocyanine dye with promising nonlinear optical properties, especially enhanced in the chloroform environment [1]. However, the precise location of its low-lying excited states is not known and this is of great importance to the understanding of the large nonlinear response. Moreover, the influence of the solvent on the low-lying transi-

tions of DIA is of primary importance. This is the subject of this article.

DIA may exist in two possible configurations, as shown in Figure 1. Configuration (I) is expected to be more stable in isolated form, but due to its larger dipole moment, configuration (II) is believed to be more stable in solution. Brooker and Sprague [2] measured the low-lying excitations in different solvents and noticed a red shift of the first absorption transition that is increased as the polarity of the solvent increases. Lushkov and Warshel [3] made interesting theoretical studies of the two low-lying excited states and noticed that the experimental data could be best reproduced using configuration (I). Karelson and Zerner [4]

Correspondence to: S. Canuto.

Contract grant sponsors: CNPq; FAPESP (Brazil).

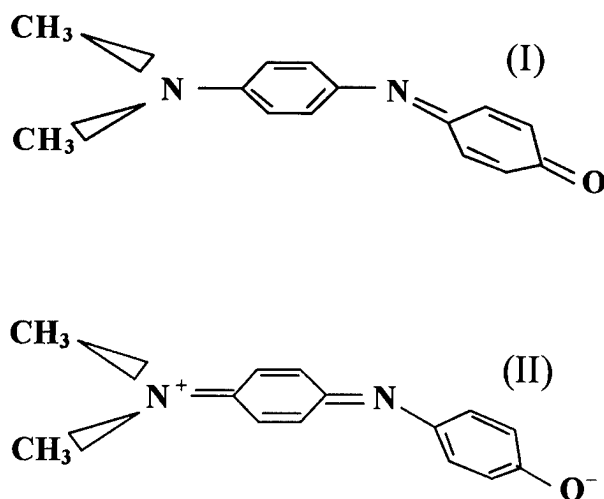


FIGURE 1. The two extreme configurations of the resonance form of DIA.

also used configuration (I) to analyze spectral shifts in different solvents. Thus, it is natural that most of the effort should be concentrated in configuration (I), but, as we shall see, some interesting results will emerge for configuration (II).

Methods and Results

We first performed a gas-phase full geometry optimization of configuration (I) using ab initio methods and the Gaussian 94 program [5]. Some of our results are shown in Figure 2 (which defines the geometrical parameters) and Table I. Only the most relevant structural parameters are shown. With all theoretical methods used, the C₁—O and the N₁—C₃ distances are compatible with a double bond as is the case of configuration (I). Similarly, the N₁—C₄ distance is compatible with a single bond. The bending angle C₃—N₁—C₄ varies from one model to the other but keeps around a value of 120°. The molecule shows a rather pro-

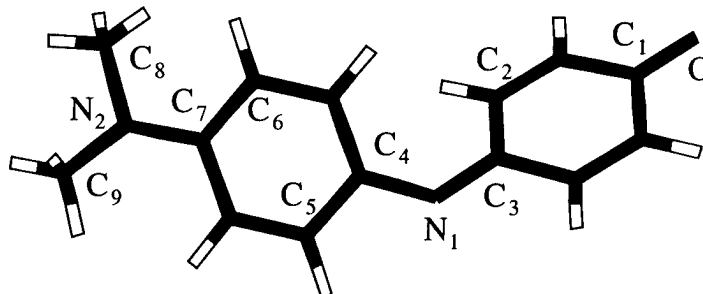


FIGURE 2. The optimized geometry of isolated DIA. The atomic indices are used to define the geometric parameters and the atomic sites for Figures 3 and 4 and Tables I–III.

TABLE I
Comparison of the calculated geometries for configuration (I) using different ab initio theoretical methods.

Geometry (A and degree)	HF / STO-3G	HF / 3-21G	HF / 6-31G*	MP2 / 6-31G*
R(C ₁ —O)	1.228	1.218	1.197	1.241
R(N ₁ —C ₃)	1.290	1.269	1.263	1.313
R(N ₁ —C ₄)	1.460	1.408	1.407	1.400
θ(C ₃ —N ₁ —C ₄)	119.6	127.7	123.9	120.6
φ(C ₃ —N ₁ —C ₄ —C ₅)	122.9	143.9	128.8	139.1
φ(C ₂ —C ₃ —N ₁ —C ₄)	350.0	353.1	354.7	350.0
φ(C ₆ —C ₇ —N ₂ —C ₈)	10.4	0.4	18.7	3.4
φ(C ₆ —C ₇ —N ₂ —C ₉)	241.2	181.6	243.3	229.1
Energy (au)	−713.04979	−717.98145	−722.01735	−724.38968

Geometric parameters are defined in Figure 2.

nounced interring modification at the central N₁ atom, as given by the angles $\theta(C_3-N_1-C_4)$, $\varphi(C_3-N_1-C_4-C_5)$, and $\varphi(C_2-C_3-N_1-C_4)$. This comes from the steric interaction between the *ortho* hydrogens of the ring. Comparison between the results obtained at the HF/6-31G* and MP2/6-31G* levels shows that the C₁—O distance and the out-of-plane angle $\varphi(C_3-N_1-C_4-C_5)$ are the geometric parameters most affected by the inclusion of correlation effects. However, it is the angle $\theta(C_3-N_1-C_4)$ that is found to have the largest influence in the calculated spectrum for this case of configuration (I). Overall, we notice the usual trend that improving the basis set decreases the distances and including correlation effects increases these distances, giving the reason for the generally good performance of the HF/STO-3G model for obtaining geometries for this type of system.

Using the HF/STO-3G geometry, we calculated next the low-lying transition energies. This was made at the semiempirical INDO/CIS level using ZINDO [6]. The lowest state is an $n-\pi^*$ state with an intraring character, whereas the second state is an allowed $\pi-\pi^*$ state that results from an interring charge transfer. The calculated value (see Table II) of 26,000 cm⁻¹ seems too high. There is no experimental result to make a direct comparison. However, the first-allowed absorption transition was measured in several solvents [2]. This transition lies at 18,100 cm⁻¹ for cyclohexane, 17,200 cm⁻¹ for acetone, 16,400 cm⁻¹ for methyl alcohol, and 15,000 cm⁻¹ for water. By interpolating these results for the dielectric constant of chloroform, we could expect a transition energy close

to 17,000 cm⁻¹. This indicates that our gas-phase result is indeed too large, as an unexpectedly large red shift is necessary to have a good agreement. At this level, the calculated value for the static hyperpolarizability of DIA using the sum-over-states method [7] (including over 200 excited states) is $\beta_{vec} = 6.7 \times 10^{-30}$ cm⁵/esu, which is certainly too low compared to the experimentally measured value of about 106.0×10^{-30} cm⁵/esu [1]. This large underestimate is corroborated by ab initio calculations: Using the HF method with the 6-311 + + G** basis, which includes as many as 472 contracted Gaussian-type functions, we obtained the value of 7.2×10^{-30} cm⁵/esu.

To include some of the solvent effects, supermolecular calculations of DIA in chloroform were made. These supermolecular structures were obtained from a separate Monte Carlo simulation [8]. The simulation used a Lennard-Jones plus Coulomb 12–6–1 interatomic potential. The Lennard-Jones parameters were obtained from the OPLS suggestion of Jorgensen et al. [9]. The Coulomb charges were obtained from CHELPG calculations [5, 10] at the HF/6-31G** level. Our first interest in this stage is the possible role of the hydrogen bonding between the DIA molecule and the CHCl₃ solvent. Figure 3 thus shows the pairwise radial distribution function of the two N and O atoms of DIA and the H atom of CHCl₃. All three functions exhibit a peak around 2.5 Å, characteristic of hydrogen bonds. Integration of these three peaks in a volume space shows that, on average, there are two hydrogen bonds formed on the O site and one hydrogen bond on each of the N atoms. This is illustrated in Figure 4, which shows the four hy-

TABLE II
Calculated values for the first $n-\pi^*$ and $\pi-\pi^*$ transitions (in 1000 cm⁻¹) and the first static hyperpolarizability β_{vec} (in 10^{-30} cm⁵/esu) of DIA both isolated and including the hydrogen-bonded chloroforms (see Fig. 4).

	$n-\pi^*$ Transition	$\pi-\pi^*$ Transition	β_{vec}
DIA (isolated)	23.48 (0.002)	26.14 (0.104)	6.7
DIA(N ₁) ... HCCl ₃	23.29 (0.003)	25.79 (0.095)	5.5
DIA(N ₂) ... HCCl ₃	23.55 (0.002)	26.85 (0.101)	4.6
DIA(O) ... 2HCCl ₃	23.46 (0.005)	24.99 (0.117)	10.5
DIA ... 4HCCl ₃	23.13 (0.001)	25.96 (0.149)	9.1
Experiment (in HCCl ₃)		16.95 ^a	106 ^b

^a All values are obtained with the INDO/CI method as implemented in the ZINDO program [6]. Nos. in parentheses are the calculated oscillator strengths. See text.

^b Interpolated from the experimental results of [2].

^b Experimental result [1] within the uncertainty of 10%.

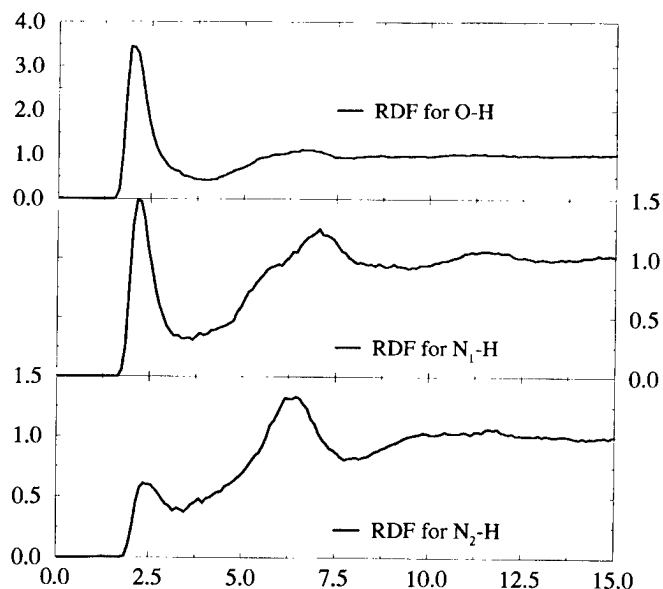


FIGURE 3. The pairwise radial distribution function between the corresponding atomic sites of DIA and the H atom of HCCl_3 , as obtained from the Monte Carlo simulation.

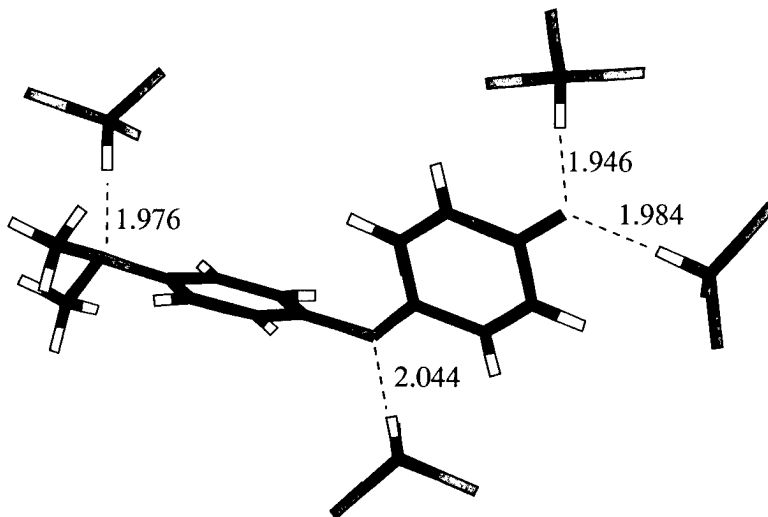


FIGURE 4. Illustration of the four hydrogen bonds formed between the O and N atomic sites of DIA and HCCl_3 . Also shown are the optimized hydrogen bond distances.

hydrogen bonds. The influence of these hydrogen bonds are shown in Table II. As can be seen, these four hydrogen bonds do have some influence on the low-lying transitions. The separate contribution of the hydrogen bonds in each site is given. The (two) hydrogen bonds on the O site have the largest influence on the $\pi-\pi^*$ shift. Although relatively large, this shift is not enough to bring the calculated transition even close to the experimen-

tal result. A similar conclusion can be reached from the still very low calculated value of $\beta_{vec} = 9.1 \times 10^{-30} \text{ cm}^5/\text{esu}$. We should mention that the results we obtained for a dipolar self-consistent field using a spherical cavity are similar to the gas-phase result. This is, of course, expected, as the reaction field depends on the inverse cubic power of the cavity radius. Other attempts to include the solvent effects via supermolecular calcu-

lations including the first solvation shell after the four hydrogen bonds have, similarly, given poor results compared to experiment.

The results obtained for configuration (II) are more promising. It is important to mention that full geometry optimization of configuration (II) is not very simple. Several attempts made at the HF level converged back to the lowest energetic configuration (I). However, by including some correlation contribution and some restraints, we were able to obtain at the MP2/STO-3G level the geometry shown in Table III. Now, the C₁—O and the N₁—C₃ distances are compatible with a single bond as in the case of configuration (II). The bending angle (C₃—N₁—C₄) is lower than 120°. Using this ab initio MP2/STO-3G geometry, we again calculated the lowest excited states of isolated DIA using INDO/CIS. The second excited state is an n—π* state at 18,600 cm⁻¹ with an intraring nature and a low transition moment. The lowest calculated excited state is the π—π* interring charge transfer calculated at 17,000 cm⁻¹, in excellent agreement with the experimental result. The calculated static β_{vec} is now 91.2 × 10⁻³⁰ cm⁵/esu, which is one order of magnitude larger than that for configuration (I) and now in good agreement with the experimental value [1]. The explicit use of configuration (II) leads to an improved description of the low-lying states of DIA in solution. To make

a direct comparison between the two configurations, the results obtained using the same theoretical procedure for obtaining the geometries (MP2/STO-3G) are given in Table III. The relative location of the π—π* is reversed with the n—π in the two configurations. The reversal of the n—π* and the π—π* states in going from nonpolar to polar solvents has also been noted elsewhere [11]. It is interesting to note the large difference in the calculated dipole moment. It can be seen that configuration (II) gives a π—π* transition that is red-shifted by nearly 8000 cm⁻¹ as compared with configuration (I) and has also a much larger oscillator strength (given in parentheses). These have clear consequences in the calculated β_{vec}, which is now in considerable improvement and makes the two-level approximation [1, 7] work better for configuration (II) than for configuration (I).

There is an interesting and complementary argument relative to the competition between configurations (I) and (II): In the case of nonpolar solvents, it is expected that configuration (I) could still be more stable. For instance, for the case of DIA in cyclohexane, the experimental value [1] is around 15.0 × 10⁻³⁰ cm⁵/esu, which is, indeed, in accord with our results for configuration (I). There is, of course, no reason to believe that these arguments should not prevail in other similar systems.

TABLE III
Comparison of the calculated geometries, dipole moment, first dipole hyperpolarizability, and transition energies for configurations (I) and (II).

Geometry (Å and degree)	Configuration (I)	Configuration (II)
R(C ₁ —O)	1.28	1.31
R(N ₁ —C ₃)	1.36	1.49
R(N ₁ —C ₄)	1.49	1.36
R(N ₂ —C ₇)	1.48	1.45
θ(C ₃ —N ₁ —C ₄)	115.2	117.0
φ(C ₃ —N ₁ —C ₄ —C ₅)	123.1	152.6
φ(C ₃ —C ₃ —N ₁ —C ₄)	355.6	341.4
Properties		
μ(D)	2.7	7.4
β _{vec} (total) in 10 ⁻³⁰ cm ⁵ /esu	10.3	91.2
β _{vec} (two-level) in 10 ⁻³⁰ cm ⁵ /esu	24.1	130.9
Transition energies (1000 cm ⁻¹)	23.2 (0.009) n—π*	17.0 (1.153) π—π*
	24.9 (0.174) π—π*	18.6 (0.029) n—π*

Geometric parameters are defined in Figure 2. See text.

In particular, it is known that some polymers increase the value of the first hyperpolarizability by an order of magnitude when in a solvent media.

Conclusions

Summarizing, this paper gives the ab initio-optimized geometry of DIA in the most stable configuration (**I**). As in solution configuration (**II**) is expected to be more stable than configuration (**I**), we have given some attention to its determination. It is seen from the calculated results that the molecular properties change with the configuration considered. It is thus expected that a large contribution of the solvent effects comes from the structure variation induced by the solvent. Of course, the usual solvent effects in the low-lying excitation spectrum, as given by the difference in stabilization energies in the ground and excited states due to the different contributions of the intermolecular forces, still play an important role. However, this article emphasizes the strong structure dependence of the low-lying excited states that are of great importance for the understanding of the solvent effects, with dramatic consequences for the first dipole hyperpolarizability.

ACKNOWLEDGMENTS

We are grateful to Dr. R. Bicca de Alencastro (Univ. Fed. Rio de Janeiro) for discussions and for reading the manuscript. We also acknowledge continuous discussions with Dr. K. Coutinho (Univ. Mogi das Cruzes) and Dr. M. C. Zerner (Univ. of Florida). Part of these calculations were performed using the LCCA-USP and CENAPAD-SP computa-

tional facilities. This work was partially supported by CNPq and FAPESP (Brazil).

References

- S. R. Marder, D. N. Beratan, and L. T. Chang, *Science* **252**, 103 (1991).
- L. G. S. Brooker and R. H. Sprague, *J. Am. Chem. Soc.* **63**, 3214 (1941); L. G. S. Brooker, A. C. Craig, D. W. Haseltine, P. W. Jenkins, and, L. L. J. Lincoln, *J. Am. Chem. Soc.* **87**, 2443 (1965).
- V. Lukshov and A. Warshel, *J. Am. Chem. Soc.* **113**, 4491 (1991).
- M. M. Karelson and M. C. Zerner, *J. Phys. Chem.* **96**, 6949 (1992).
- M. J. Frisch, G. W. Trucks, H. B. Schlegel, P. M. W. Gill, B. G. Johnson, M. A. Robb, J. R. Cheeseman, T. Keith, G. A. Petersson, J. A. Montgomery, K. Raghavachari, M. A. Al-Laham, V. G. Zakrzewski, J. V. Ortiz, J. B. Foresman, J. Cioslowski, B. B. Stefanov, A. Nanayakkara, M. Challacombe, C. Y. Peng, P. Y. Ayala, W. Chen, M. W. Wong, J. L. Andres, E. S. Replogle, R. Gomperts, R. L. Martin, D. J. Fox, J. S. Binkley, D. J. Defrees, J. Baker, J. P. Stewart, M. Head-Gordon, C. Gonzalez, and J. A. Pople, *Gaussian 94, Revision E.1* (Gaussian, Inc., Pittsburgh, PA, 1995).
- M. C. Zerner, ZINDO: A semiempirical program package (University of Florida, Gainesville, FL 32611).
- D. R. Karmis, M. A. Ratner, and T. J. Marks, *Chem. Rev.* **94**, 195 (1994); N. P. Prasad and D. J. Williams, *Introduction to Nonlinear Optical Effects in Molecules and Polymers* (Wiley, New York, 1991).
- K. Coutinho and S. Canuto, DICE: A Monte Carlo program for molecular liquid simulation (University of São Paulo, São Paulo, Brazil).
- W. L. Jorgensen, E. R. Laird, T. B. Nguyen, and J. Tirado-Rives, *J. Comp. Chem.* **14**, 206 (1993); W. L. Jorgensen, J. M. Briggs, and M. L. Contreras, *J. Phys. Chem.* **94**, 1683 (1990).
- C. N. Breneman and K. B. Wiberg, *J. Comp. Chem.* **11**, 361 (1990).
- L. A. Diverdi and M. R. Topp, *J. Phys. Chem.* **88**, 3447 (1984).

Nonresonant Frequency Dispersion of the Electronic Second Hyperpolarizability of *All-Trans* Polysilane Chains: An Ab Initio TDHF Oligomeric Approach

BENOÎT CHAMPAGNE,* ÉRIC A. PERPÈTE,[†] JEAN-MARIE ANDRÉ

Laboratoire de Chimie Théorique Appliquée, Facultés Universitaires Notre-Dame de la Paix, rue de Bruxelles, 61, B-5000 Namur, Belgium

Received 21 February 1998; revised 8 April 1998; accepted 20 April 1998

ABSTRACT: The frequency-dependent electronic second hyperpolarizability of increasingly large polysilane chains is computed for the most common nonlinear optical (NLO) processes at the time-dependent Hartree-Fock level with the 6-31G atomic basis set. Due to σ -conjugation, the longitudinal component (γ_L^e) turns out to be dominant. Its nonresonant dispersion relations are described by the coefficients of the power expansion formula, $\gamma_L^e(-\omega_\sigma; \omega_1, \omega_2, \omega_3) = \gamma_L^e(0; 0, 0, 0)[1 + A\omega_L^2 + B\omega_L^4 + C\omega_L^6 + \dots]$, where $\omega_L^2 = \omega_\sigma^2 + \omega_1^2 + \omega_2^2 + \omega_3^2$ and $\gamma_L^e(0, 0, 0)$ is the static limit value. In the infinite chain length limit, the CHF/6-31G static longitudinal electronic second hyperpolarizability per Si₂H₄ unit cell is estimated to attain $463 \pm 10 \times 10^3$ a.u. whereas the A coefficient reaches 27.8 ± 0.9 a.u. The accuracy that could be reached from using this power expansion expression for estimating the second hyperpolarizability for other optical frequencies is discussed. © 1998 John Wiley & Sons, Inc. Int J Quant Chem 70: 751–761, 1998

Key words: electronic second hyperpolarizability; polysilane; frequency dispersion

* Research Associate of the National Fund for Scientific Research (Belgium).

[†] Scientific Collaborator of the National Fund for Scientific Research (Belgium).

Correspondence to: B. Champagne.

Contract grant sponsor: FNRS-FRFC.

Contract grant number: 2.4519.97.

Contract grant sponsor: Belgian National Interuniversity Research Program.

Contract grant number: PAI/IUAP No. P4/10.

Introduction

The design of new compounds for nonlinear optical (NLO) applications is a domain of intense activity where quantum chemistry provides efficient tools to highlight the physical underlying phenomena and to determine structure–property relationships [1]. In particular, two recent theoretical reviews have considered the potential of large conjugated oligomers and polymers for NLO and have addressed the importance of the vibrational contributions with respect to (w.r.t.) the electronic counterpart, the effects of the surroundings, as well as the influence of including electron correlation and taking into account the frequency dispersion [2–3].

Due to a high degree of electron delocalization, π -conjugated organic oligomers and polymers are the preferred materials for exhibiting large NLO responses. Nevertheless, π -conjugation could also be the cause of a lack of stability with respect to air exposure, laser irradiation, and processing conditions. In addition, the corresponding bandgap being small, absorption of the second- and third-harmonic-generated light consists in another limitation for their applications. Polysilylenes, most of the time named polysilanes (PSi) exhibit also favorable NLO properties [4] which are combined with good electrical, mechanical, and thermal properties [5]. In addition, PSi presents a larger bandgap and is, therefore, more often transparent w.r.t. the generated higher harmonics than π -conjugated systems. These exceptional properties of PSi are due to their σ -conjugation and are at the origin of the increasing attention paid to their photoluminescence, piezochroïsm, thermochroïsm, conductivity, nonlinear optical properties, etc.

Many theoretical studies have already concerned the PSi chains. The discovery of the thermochromic conformational transitions in PSi have directed the initial theoretical studies toward the relative energy of the various backbone conformations and their associated spectra [6]. The effects of the conformational modifications on the ionization energies of small oligosilanes have been addressed by Ortiz and co-workers [7] and have been rationalized in terms of phase relationships between bond and antibond orbitals localized in the Si–Si bond regions. Band structure calculations have de-

termined the nature of electronic states and their evolution upon substitution by alkyl and aryl groups [8] as well as the shape of the energy dispersion curves [9]. Other theoretical calculations have revealed that the lowest energy excitation in small oligosilanes is characterized by a weakly dipole-allowed σ – π^* transition whereas larger chains present a strong σ – σ^* transition [10]. The σ -conjugation in PSi leads to a decrease of the lowest excitation energy with the size of the oligosilane just as the π – π^* excitation energy decreases with the polyacetylene (PA) chain length. These effects of electron delocalization were expected to lead to substantial linear and nonlinear polarizabilities.

Linear and nonlinear electronic responses of PSi and related oligomers have already been considered several times. The first of these studies, carried out at the MNDO semiempirical level, claimed that PSi chains are more polarizable than the π -conjugated PA chains of the same length [11]. Following studies have confirmed the highly (hyper)polarizable character of PSi chains but have pointed out that PSi exhibits a similar linear polarizability per unit cell to PA whereas its second hyperpolarizability per unit cell is one order of magnitude smaller. In particular, at the coupled Hartree–Fock (CHF/6-31G) level, Kirtman and Hasan [12] have calculated the electronic static polarizability, $\alpha^e(0; 0)$, and second hyperpolarizability $\gamma^e(0; 0, 0, 0)$ of PSi chains up to $\text{Si}_{15}\text{H}_{32}$. In the infinite chain length limit, the longitudinal static electronic polarizability, $\alpha_L^e(0; 0)$, per Si_2H_4 unit amounts to 131.4 ± 0.2 a.u.* whereas the longitudinal static electronic second hyperpolarizability, $\gamma_L^e(0; 0, 0, 0)$, attains $5.16 \pm 0.14 \times 10^5$ a.u.[†] per unit cell which is one order of magnitude smaller than in π -conjugated PA [13] and polydiacetylene [14]. Coupled and uncoupled Hartree–Fock polarizability calculations performed on the infinite periodic PSi have revealed that this large $\alpha_L^e(0; 0)$ is due to the highest occupied crystalline orbitals, which are built from Si_{3p} functions oriented parallel to the polymer axis [15]. More recently, Ortiz and Rohlffing have shown that the linear polariz-

* 1.0 a.u. of polarizability = $1.6488 \times 10^{-41} \text{ C}^2 \text{ m}^2 \text{ J}^{-1} = 0.14818 \text{ \AA}^3$.

[†] 1.0 atomic unit of second hyperpolarizability = $6.235377 \times 10^{-65} \text{ C}^4 \text{ m}^4 \text{ J}^{-3} = 7.0423 \times 10^{-54} \text{ m}^5 \text{ V}^{-2} = 5.0367 \times 10^{-40}$ esu.

ability of poly(phenylsilane) oligomers slightly increases when the PSi backbone leaves its *all-trans* conformation to become helical [16].

Several aspects of the structure–property relationships for PSi chains remain to be tackled in order to point out the main structural properties which should be tuned for optimizing their NLO responses. One important aspect is the evaluation of the vibrational contribution to the second hyperpolarizability which, for trisilane and pentasilane, has been shown by Kirtman and Hasan to modulate strongly γ as a function of the NLO process [12]. A forthcoming study is in fact devoted to the determination of the γ^v contributions in increasingly large PSi chains with inclusion of the lowest-order anharmonicity contributions [17]. The present study determines at the time-dependent Hartree–Fock (TDHF) level the nonresonant frequency dependence of γ_L^e for the most common NLO processes: the electro-optic Kerr effect (dc-Kerr), the electric-field-induced second harmonic generation (ESHG), the third harmonic generation (THG), and the intensity-dependent refractive index or degenerate four-wave mixing (DFWM) phenomena. Future works will consider the effects of the surrounding and of the substituents upon the second hyperpolarizability of PSi's.

Methodological and Computational Aspects

The second hyperpolarizability (γ) is the third-order response of the dipole moment with respect to the external electric fields:

$$\begin{aligned} \mu_\zeta(\omega_\sigma) = & \mu_\zeta^0 + \sum_{\eta} \alpha_{\zeta\eta}(-\omega_\sigma; \omega_1) E_\eta(\omega_1) \\ & + \frac{1}{2} K^{(2)} \sum_{\eta\xi} \beta_{\zeta\eta\xi}(-\omega_\sigma; \omega_1, \omega_2) \\ & \times E_\eta(\omega_1) E_\xi(\omega_2) \\ & + \frac{1}{6} K^{(3)} \sum_{\eta\xi\chi} \gamma_{\zeta\eta\xi\chi}(-\omega_\sigma; \omega_1, \omega_2, \omega_3) \\ & \times E_\eta(\omega_1) E_\xi(\omega_2) E_\chi(\omega_3) + \dots, \quad (1) \end{aligned}$$

where $\omega_\sigma = \sum_i \omega_i$ and the summations are running over the field indices η , ξ , and χ , associated to the Cartesian coordinates; μ_ζ^0 is one element of the

permanent dipole moment; $K^{(2)}$ and $K^{(3)}$ are such that the β and γ of different NLO processes converge toward the same static value. The static, dc-Kerr, ESHG, THG, and DFWM responses are therefore given by $\gamma(0; 0, 0, 0)$, $\gamma(-\omega; \omega, 0, 0)$, $\gamma(-2\omega; \omega, \omega, 0)$, $\gamma(-3\omega; \omega, \omega, \omega)$, and $\gamma(-\omega; \omega, -\omega, \omega)$, respectively. The two main approaches to evaluate the hyperpolarizabilities are based either upon perturbation theory methods which provide summation-over-states (SOS) expressions, or upon response function schemes. In the latter case, the response can be determined numerically (leading to the finite field schemes) or analytically.

Perturbation theory provides general SOS expressions for molecular second hyperpolarizabilities [18]. Ordinarily, the electronic second hyperpolarizability (γ^e) is evaluated within the canonical or clamped nucleus (CN) approximation [19] which means that the field effects upon the electrons and nuclei are considered sequentially. Various approaches can approximate the exact CN frequency-dependent SOS *electronic* second hyperpolarizability. The TDHF [20] procedure is probably the most common procedure in ab initio calculations. In this approach, a term representing the interaction between an external electric field (which contains both static and dynamic components) and the molecular dipole is added to the Fock matrix. Its effects upon the density matrix are obtained by expanding the TDHF equation as a power series in the external electric fields and by solving it self-consistently order by order. The successive density matrix responses are then used to evaluate the hyperpolarizabilities. The static limit of the TDHF procedure is referred to as the coupled-perturbed Hartree–Fock (CPHF) scheme [21] and has been presented under a convenient computational formulation by Dykstra and Jasien [22]. The CPHF procedure is in fact equivalent to the Hartree–Fock finite field (HF-FF) technique where the electronic hyperpolarizabilities are obtained as successive numerical derivatives of the field-dependent electronic dipole moment with respect to the static external electric field. In this approach, the field dependence of the electronic dipole moment is built in the self-consistent field (SCF) procedure, via the $-\sum_{\eta} \hat{\mu}_{\eta}^e E_{\eta}$ coupling term where $\hat{\mu}_{\eta}^e$ is one component of the dipole moment operator. Similar HF-FF approaches can be based upon the energy (E), the electronic polarizability (α^e), or the electronic first hyperpolarizability (β^e). Indeed, at the

HF level, one has:

$$\begin{aligned}\gamma_{\xi\xi\xi\xi}^e(0; 0, 0, 0) &= - \left(\frac{\partial^4 E}{\partial E_\xi^4} \right)_{E=0} = \left(\frac{\partial^3 \mu_\xi^e}{\partial E_\xi^3} \right)_{E=0} \\ &= \left(\frac{\partial^2 \alpha_{\xi\xi}^e}{\partial E_\xi^2} \right)_{E=0} = \left(\frac{\partial \beta_{\xi\xi\xi}^e}{\partial E_\xi} \right)_{E=0}. \quad (2)\end{aligned}$$

Both the CPHF and TDHF schemes are atomic-orbital-based methods which are particularly well suited to deal with large organic compounds. Their sister method, the random phase approximation (RPA) technique [23] gives equivalent hyperpolarizability values which are obtained from a computationally more demanding molecular orbital-based procedure. However, in the RPA scheme, once the superoperator resolvent has been worked out, the hyperpolarizabilities for a large range of optical frequencies and processes can be calculated at a low computational cost whereas the TDHF equations must be solved for each frequency of interest.

For computing γ^e , we use the conventional CPHF and TDHF schemes as implemented in the HONDO95-3 [24] computer program. As a matter of fact, our approach is a fully relaxed Hartree-Fock procedure which neglects the effects of the instantaneous interactions between electrons having opposite spin. Future works will investigate the importance of including these corrections which, on one hand, turn out to be significant for α_L , and especially, for γ_L , of π -conjugated carbon-based oligomers [25] whereas, on the other hand, their effects estimated at the MP2 level is rather small for $\alpha_L^e(0; 0)$ of PSi chains [26]. The 6-31G basis set [27] has been employed for computing the static and frequency-dependent electronic second hyperpolarizabilities because it has already proven many times its adequacy for computing at a lower computational cost accurate electronic (hyper)polarizabilities of extended σ - and π -conjugated oligomers [12, 28]. Indeed, when the chain is lengthened, the gap between the 6-31G and extended basis sets bearing diffuse functions becomes negligible as a result of the cooperation of the neighboring atomic functions.

Dispersion formulas for $\gamma^e(-\omega_\sigma; \omega_1, \omega_2, \omega_3)$ are expressible in power expansions in squares of the optical frequencies. Indeed, since γ is real [$\gamma^e(-\omega_\sigma; \omega_1, \omega_2, \omega_3) = \gamma^e(-\omega_\sigma; \omega_1, \omega_2, \omega_3)^*$] and since changing the sign of all the optical frequency is equivalent to taking the conjugate complex [$\gamma^e(\omega_\sigma; -\omega_1, -\omega_2, -\omega_3) = \gamma^e(-\omega_\sigma; \omega_1, \omega_2, \omega_3)^*$], it follows that $\gamma^e(-\omega_\sigma;$

$\omega_1, \omega_2, \omega_3) = \gamma^e(\omega_\sigma; -\omega_1, -\omega_2, -\omega_3)$. A useful form for comparing responses obtained with different processes consists in expressing $\gamma^e(-\omega_\sigma; \omega_1, \omega_2, \omega_3)$ in a power expansion in $\omega_L^2 = \omega_\sigma^2 + \omega_1^2 + \omega_2^2 + \omega_3^2$. Indeed, for the diagonal, $\gamma_{\xi\xi\xi\xi}^e$, second hyperpolarizability tensor components, we have the relation:

$$\begin{aligned}\gamma_{\xi\xi\xi\xi}^e(-\omega_\sigma; \omega_1, \omega_2, \omega_3) &= \gamma_{\xi\xi\xi\xi}^e(0; 0, 0, 0) \\ &\times [1 + A\omega_L^2 + B\omega_L^4 + C\omega_L^6 + \dots], \quad (3)\end{aligned}$$

where A is the same for all optical processes (the process dependence being accounted for in ω_L^2) but depends on the molecule. Originally this fact was pointed out experimentally [29]. Then, it was demonstrated for atoms and centrosymmetric molecules [30] as well as for noncentrosymmetric molecules [31]. With the exception that it is identical for dc-Kerr and ESHG, B depends upon the molecule and the NLO process. Depending upon the relative importance of the two terms involved in B [31], there could also exist molecules for which B is *quasi* process independent. The hyperpolarizability expressions due to Hättig [32] expanded in terms of symmetrized-frequency products also highlight these relations while, in addition, in this formalism, dispersion coefficients are dropped out systematically when the NLO process involves static fields. To our knowledge, this is also the first study dealing with C and D coefficients [32]. In conjugated systems, the longitudinal tensor component is often dominant and therefore, these equivalence relations hold also for the isotropically average quantity, $\bar{\gamma} = \frac{1}{15} \sum_\xi \sum_\eta (\gamma_{\xi\xi\eta\eta} + \gamma_{\xi\eta\xi\eta} + \gamma_{\xi\eta\eta\xi})$ which reduces to $\bar{\gamma} = \frac{1}{5} \gamma_L$. Consequently, for the most common NLO processes, the $\{[\gamma_L^e(-\omega_\sigma; \omega_1, \omega_2, \omega_3)/\gamma_L^e(0; 0, 0)] - 1\}$ quantity will obey the simple ratio rule 6:3:2:1 for THG:ESHG:DFWM:dc-Kerr, respectively, provided the optical frequency is small enough. Divergence with respect to this ratio rule is expected when ω increases and particularly when ω approaches resonances which are defined by simple ratios of the excitation energies.

Most of the time in conjugated systems, $\gamma^e(-\omega_\sigma; \omega_1, \omega_2, \omega_3)$ is dominated by a strong low-lying dipole-allowed transition which also determines the three-photon resonance. This is the case in PSi for which Hasegawa et al. [4f, 4g] have highlighted the crucial role of this low-lying state in determining the third-order NLO response. From

analyzing the frequency dependence of the linear polarizability $\{[\alpha^e(-\omega; \omega)/\alpha^e(0; 0)] - 1\} = A'\omega_L^2 + B'\omega_L^4 + C'\omega_L^6 + \dots$, an upper bound to this first excitation energy (ΔE) is given by $1/\sqrt{A'}$, its [1,0] Padé approximant [33].

Results

The fully optimized RHF/6-31G *all-trans* $\text{Si}_{2N}\text{H}_{4N+2}$ chains belonging to the C_{2h} point group have been employed for the second hyperpolarizability calculations. As described in Refs. [13 and 17], the evolution with chain length of the geometrical parameters saturates rapidly and the parameters of the central unit cell are already converged for $N = 5$. Figure 1 summarizes the polymeric RHF/6-31G unit cell geometry.

The CHF/6-31G $\gamma_L^e(0; 0, 0, 0)$ values as a function of the PSi chain length are listed in Table I. In order to address the polymeric limit, it has become usual to define the second hyperpolarizability per unit cell as the difference between the γ of oligomers containing N and $N - 1$ units: $\Delta\gamma[N] = \gamma[N] - \gamma[N - 1]$. In our study, the unit cell is

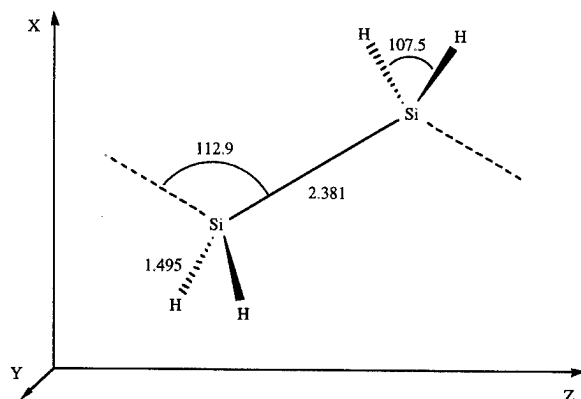


FIGURE 1. RHF/6-31G PSi converged geometrical parameters (in Å and degrees). The PSi chains are oriented in such a way that the middle point of the central and end Si–Si bonds belong to the Z axis which is therefore referred as the longitudinal axis. The Si–Si bond of Si_2H_6 forms a 33.55° angle with the Z axis in order to foresee the orientation of the Si–Si bonds in growing PSi chains. The unit cell length is 3.970 Å.

TABLE I
CHF/6-31G $\gamma_L^e(0; 0, 0, 0)[N]$ and $\Delta\gamma_L^e(0; 0, 0, 0)[N] = \gamma_L^e(0; 0, 0, 0)[N] - \gamma_L^e(0; 0, 0, 0)[N - 1]$ as a function of the number of Si_2H_4 unit cells (N).^a

N cells	$\gamma_L^e(0; 0, 0, 0)$	$\Delta\gamma_L^e(0; 0, 0, 0)$	$\frac{\gamma_L^e(0; 0, 0, 0)}{\bar{\gamma}_L^e(0; 0, 0, 0)}$
1	5526		2.111
2	35075	29549	3.407
3	137392	102317	4.197
4	335709	198317	4.501
5	620245	284536	4.635
6	967513	347268	4.705
7	1356506	388993	4.745
8	1772593	416087	4.770
9	2206288	433695	4.787
10	2651690	445402	4.800

^a The γ values are given in a.u. (1.0 a.u. of second hyperpolarizability = $6.235377 \times 10^{-65} \text{ C}^4 \text{ m}^4 \text{ J}^{-3} = 7.0423 \times 10^{-54} \text{ m}^5 \text{ V}^{-2} = 5.0367 \times 10^{-40} \text{ esu}$). The last column lists the ratio between the longitudinal and average γ .

the Si_2H_4 fragment. The chain length dependence of $\Delta\gamma_L^e(0; 0, 0, 0)$, given in Table I and represented in Figure 2, is typical of conjugated systems where, due to electron delocalization, it first increases, then it saturates toward an asymptotic polymeric value.

Another evidence of this one-dimensional electron delocalization is demonstrated by the $[\gamma_L^e/\bar{\gamma}^e]$ ratio, which is close to the value of 5.0, that would have been obtained if all the tensor components except γ_L^e were equal to zero. By adopting the procedure described [13, 34] and employed in previous investigations [14] for extrapolating to the infinite chain length the NLO properties of conjugated materials, we obtain a value of $463 \pm 10 \times 10^3$ a.u. for the asymptotic limit of $\Delta\gamma_L^e(0; 0, 0, 0)$. This value can be compared to the previous result of Kirtman and Hasan [12] who obtained from fitting their data to a $1/N$ power series expansion a value of $516 \pm 14 \times 10^3$ a.u. The difference between the two polymeric values originates from (i) slightly different geometrical parameters and (ii) the use in Ref. [12] of only the $1/N$ power series expansion for extrapolating $\Delta\gamma_L^e(0; 0, 0, 0)$, which generally yields larger polymeric values. In order to compare PSi to other conjugated compounds, it is suitable to consider the γ_L^e per unit length given by $\Delta\gamma_L^e/a$ where a is the unit cell length. The static

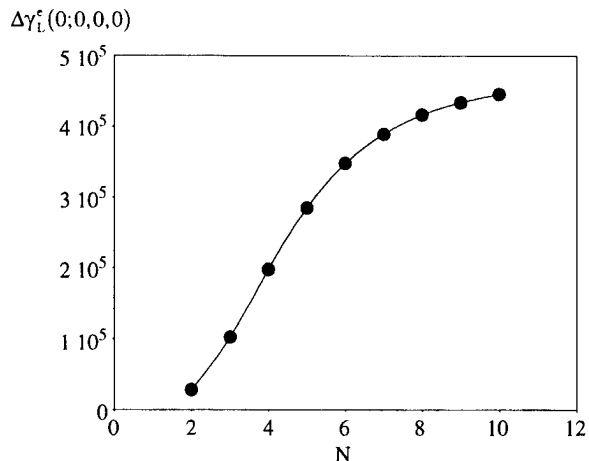


FIGURE 2. CHF/6-31G $\Delta\gamma_L^e(0; 0, 0, 0)$ (in a.u.) as a function of the number of Si_2H_4 unit cells.

$\Delta\gamma_L^e/a$ value of PSi, PA, polyyne (PY), polydiacetylene (PDA), and polybutatriene (PBT) are in the ratio 1.0:24.8.4:7.7:365, showing the more hyperpolarizable character of the π - versus σ -conjugated compounds.

For the $N = 1-7$ oligomers, we have evaluated the dynamic second hyperpolarizabilities by adopting the TDHF scheme. The results for the dc-Kerr, ESHG, THG, and DFWM processes are listed in Tables II-V for frequencies ranging be-

TABLE II
TDHF/6-31G $\gamma_L^e(-\omega; \omega, 0, 0)$ (in a.u.) as a function of the number of Si_2H_4 unit cells (N) and the frequency of the optical light.^a

$\hbar\omega$ (eV) \ N	1	2	3	4	5	6	7
0.2	5531	35128	137669	336498	621846	970163	1360326
0.4	5549	35290	138504	338881	626682	978173	1372020
0.6	5578	35562	139911	342906	634861	991732	1391823
0.8	5620	35945	141916	348656	646564	1011156	1420222
1.0	5673	36453	144555	356250	662061	1036922	1457934
A	9.69	14.15	18.62	21.72	23.84	25.30	26.33
B ($\times 10$)	8	15	25	33	40	45	48
C ($\times 100$)	-10	10	34	49	67	77	80
$\gamma_L^e(-\omega; \omega, 0, 0) _{\lambda=6328 \text{ \AA}}$							
TDHF	6125	40831	168056	425207	804674	1276276	1810650
Estimated	6119	40817	168074	425119	804514	1275764	1809238
	(-0.09%)	(-0.03%)	(+0.01%)	(-0.02%)	(-0.01%)	(-0.04%)	(-0.08%)

^a The corresponding A , B , and C parameters (in a.u.) obtained by fitting Eq. (3) are listed in the middle section. An estimate of the dc-Kerr effect at $\lambda = 6328 \text{ \AA}$ ($\hbar\omega = 1.959 \text{ eV} = 0.0720 \text{ a.u.}$) by using Eq. (3) is compared to the TDHF result at the bottom of the table; in parentheses are given the differences in percent.

TABLE III
TDHF/6-31G $\gamma_L^e(-2\omega; \omega, \omega, 0)$ (in a.u.) as a function of the number of Si_2H_4 unit cells (N) and the frequency of the optical light.^a

$\hbar\omega$ (eV) \ N	1	2	3	4	5	6	7
0.2	5543	35236	138225	338084	625064	975493	1368106
0.4	5596	35727	140765	345354	639840	999992	1403896
0.6	5687	36567	145151	357971	665578	1042776	1466511
0.8	5814	37793	151627	376755	704116	1107093	1560915
1.0	5986	39461	160581	403027	758448	1198275	1695269
<i>A</i>	9.78	14.15	18.61	21.73	23.85	25.31	26.31
<i>B</i> ($\times 10$)	5	15	25	33	39	44	48
<i>C</i> ($\times 100$)	2	16	35	55	73	87	90
$\gamma_L^e(-2\omega; \omega, \omega, 0) _{\lambda=6943 \text{ \AA}}$							
TDHF	7207	52418	235894	637097	1262927	2070506	3009001
Estimated	7268	52293	234312	629667	1292651	2029088	2929065
(+0.8%)	(−0.2%)	(−0.7%)	(−1.2%)	(−1.6%)	(−2.0%)	(−2.7%)	

^a The *A*, *B*, and *C* parameters (in a.u.) obtained by fitting Eq. (3) are listed in the middle section. An estimate of the ESHG at $\lambda = 6943 \text{ \AA}$ ($\hbar\omega = 1.786 \text{ eV} = 0.0563 \text{ a.u.}$) by using Eq. (3) is compared to the TDHF result at the bottom of the table; in parentheses are given the differences in percent.

tween $\hbar\omega = 0.2 \text{ eV}$ to $\hbar\omega = 1.0 \text{ eV}$. The corresponding dispersion curves plotted in Figure 3 for Si_4H_{10} and $\text{Si}_{12}\text{H}_{26}$ show the order $\gamma_L^e(-\omega, 0, 0) < \gamma_L^e(-\omega; \omega, -\omega, \omega) < \gamma_L^e(-2\omega; \omega, \omega, 0) < \gamma_L^e(-3\omega; \omega, \omega, \omega)$. The differences between the values associated with the different NLO processes increase with the energy of the optical frequency as well as with the size of the PSi chain. This could be explained by a dominant dipole-allowed transition of which the corresponding excitation energy decreases with chain length. Similar effects have already been noted for PA chains [35–37].

These data have been used for fitting [Eq. (3)] and obtaining the *A*, *B*, and *C* coefficients that are also given in Tables II–V. We have found a good agreement between the *A* parameters obtained from the different NLO processes; the differences being due to the numerical accuracy on the $\gamma_L^e(-\omega_\sigma; \omega_1, \omega_2, \omega_3)$ values and, subsequently, due to the effects of truncating the fitting function.

An asymptotic value, $A(\infty)$, of $27.8 \pm 0.9 \text{ a.u.}$ has been determined by considering the extrapolations of the four frequency-dependence sets and by using various analytical functions to fit the $A(N)$

TABLE IV
TDHF/6-31G $\gamma_L^e(-3\omega; \omega, \omega, \omega)$ (in a.u.) as a function of the number of Si_2H_4 unit cells (N) and the frequency of the optical light.^a

$\hbar\omega$ (eV) \ N	1	2	3	4	5	6	7
0.2	5561	35398	139064	340484	629939	983571	1379901
0.4	5668	36397	144264	355418	660367	1034109	1453824
0.6	5852	38159	153591	382514	716017	1127055	1590314
0.8	6125	40849	168222	425817	806108	1278899	1814783
1.0	6505	44754	190303	492981	948569	1522342	2178249
<i>A</i>	9.70	14.15	18.65	21.79	23.94	25.43	26.46
<i>B</i> ($\times 10$)	7	15	24	32	37	41	44
<i>C</i> ($\times 100$)	5	20	47	77	104	127	144

^a The *A*, *B*, and *C* parameters (in a.u.) obtained by fitting Eq. (3) are listed in the bottom section.

TABLE V
TDHF/6-31G $\gamma_L^e(-\omega; \omega, \omega, -\omega)$ (in a.u.) as a function of the number of Si_2H_4 unit cells (N) and the frequency of the optical light.^a

$\hbar\omega$ (eV) \ N	1	2	3	4	5	6	7
0.2	5537	35182	137946	337289	623451	972821	1364205
0.4	5573	35507	139626	342089	633197	988970	1387787
0.6	5632	36058	142486	350287	649881	1016656	1428254
0.8	5716	36850	146621	362197	674197	1057098	1487469
1.0	5826	37903	152175	378295	707209	1112158	1568275
A	9.68	14.15	18.62	21.72	23.84	25.30	26.33
B ($\times 10$)	8	14	23	30	36	40	46
C ($\times 100$)	-9	15	30	40	52	58	67

^a The A , B , and C parameters (in a.u.) obtained by fitting Eq. (3) are listed in the bottom section.

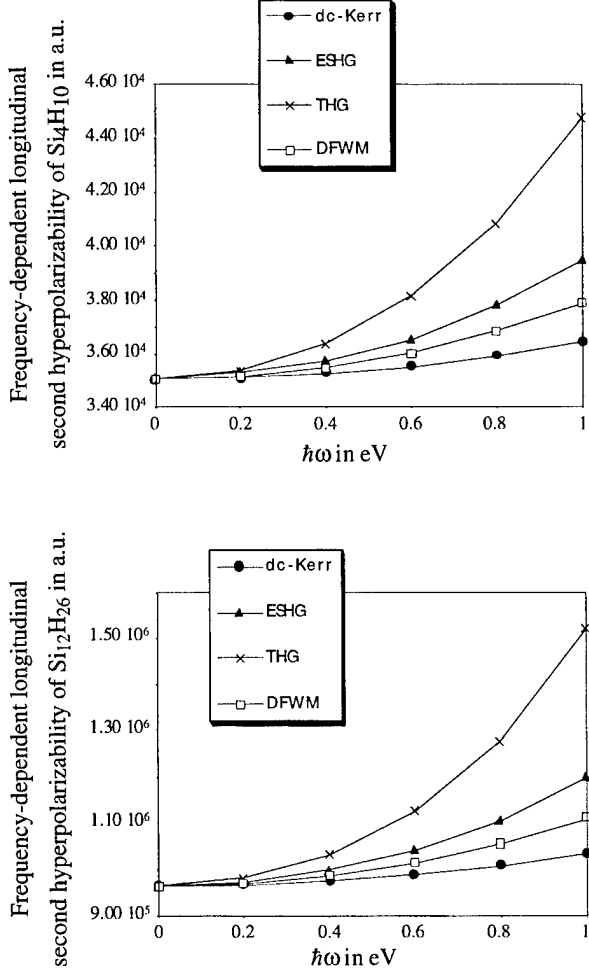


FIGURE 3. TDHF/6-31G dispersion of $\gamma_L^e(-\omega_\sigma; \omega_1, \omega_2, \omega_3)$ (in a.u.) for the most common NLO processes.

data [13, 34]. This value should therefore help in determining $\gamma_L^e(-\omega_\sigma; \omega_1, \omega_2, \omega_3)$ for any NLO process and for any light frequency. Determination of an asymptotic value for the B and C coefficients, that are going to play a more and more important role when ω increases, is, however, difficult because of their slow convergence with chain length as well as of their decreased numerical accuracy. The numerical accuracy on the B coefficients can be addressed simply by comparing the B values obtained from the dc-Kerr and ESHG data which, in principle, should be identical.

It is also interesting to define a frequency range in which the $A\omega_L^2$ term accounts for most of the frequency dispersion of γ_L^e . To do so, we have calculated the $\hbar\omega_1$ below which $B\omega_L^4 < A\omega_L^2/10$, i.e., the $A\omega_L^2$ contribution is about 10 times larger than the next term. For Si_8H_{18} , $\hbar\omega_1$ is equal to 1.55, 0.90, 0.65, and 1.15 eV for the dc-Kerr, ESHG, THG, and DFWM processes, respectively, whereas for $\text{Si}_{14}\text{H}_{30}$, the corresponding energy limits are 1.42, 0.82, 0.61, and 1.03 eV. We have also determined the $\hbar\omega_{II}$ values for which $A\omega_L^2 = B\omega_L^4$. In the same order, they are equal for Si_8H_{18} to 3.46, 2.02, 1.46, and 2.57 eV, whereas for $\text{Si}_{14}\text{H}_{30}$, they are 3.18, 1.83, 1.36, and 2.30 eV. We see that $\hbar\omega_1$ and $\hbar\omega_{II}$ decrease with chain length as expected from the chain length dependence of ΔE . A similar treatment has been applied for the $C\omega_L^6$ w.r.t. the $B\omega_L^4$ terms. Keeping the same order for the NLO processes, the corresponding $\hbar\omega_1$ are equal to 1.82, 0.86, 0.50, and 1.19 eV for Si_8H_{18} , whereas for $\text{Si}_{14}\text{H}_{30}$ the energy limits are 1.49, 0.82, 0.43, and 1.10 eV. We have also determined the corresponding $\hbar\omega_{II}$ values which are equal for Si_8H_{18}

to 4.07, 1.92, 1.13, and 2.65 eV, whereas for $\text{Si}_{14}\text{H}_{30}$ they are 3.33, 1.82, 0.97, and 2.46 eV. For the purpose of the following discussion, we could assume in first approximation that $\hbar\omega_1$ and $\hbar\omega_{II}$ for the $C\omega_L^6$ versus $B\omega_L^4$ terms are roughly the same as for the $B\omega_L^4$ versus $A\omega_L^2$ terms. Consequently, for a light beam of energy smaller or equal to $\hbar\omega_1$, the $A\omega_L^2$ term makes the major contribution, $B\omega_L^4$ and $C\omega_L^6$ contributing for *circa* 10 and 1%, respectively. The situation for $\hbar\omega_{II}$ is totally different because the three contributions are roughly of the same importance. This also suggests that higher-order terms should not be excluded for determining γ_L^e and that the validity of using the truncated Eq. (3) is questionable.

Another approach to delimit the region of validity of Eq. (3) consists in locating the first resonance for each process. Indeed, Eq. (3) is no more valid in the vicinity of resonance. As is discussed in the last paragraph of this section, an upper bound to the excitation energy of the lowest-energy one-photon absorption, ΔE , is 7.41 and 6.74 eV for Si_8H_{18} and $\text{Si}_{14}\text{H}_{30}$, respectively. ΔE corresponds to the position of the first one-photon resonance for the dc-Kerr and DFWM processes whereas for ESHG and THG the first dipole-allowed resonance occurs at $\Delta E/2$ and $\Delta E/3$, respectively. In the case of Si_8H_{18} and $\text{Si}_{14}\text{H}_{30}$, these resonances are located at 3.70 and 3.37 eV for ESHG and at 2.47 and 2.25 eV for THG, respectively. Approximately, these resonances are located at energies twice as large as $\hbar\omega_{II}$. Moreover there also exist two-photon resonances which can play an important role in the dispersion [4d, 4f, 4g] but cannot be assessed from the dispersion of the linear polarizability.

Further assessment of the pertinence of using Eq. (3) to guess $\gamma_L^e(-\omega_\sigma; \omega_1, \omega_2, \omega_3)$ has been carried out by comparing the TDHF/6-31G $\gamma_L^e(-\omega; \omega, 0, 0)|_{\lambda=6328 \text{ \AA}}$ and $\gamma_L^e(-2\omega; \omega, \omega, 0)|_{\lambda=6943 \text{ \AA}}$ to their respective estimated values. The source wavelengths are typical of dc-Kerr and ESHG experiments. For the dc-Kerr results, the $\hbar\omega$ value of 1.959 eV falls well below the $\hbar\omega_{II}$ (close to $\hbar\omega_1$) limit, and the $\gamma_L^e(-\omega; \omega, 0, 0)$ estimates are in good agreement with the true TDHF value, with an error smaller than 0.1%. The estimations of $\gamma_L^e(-2\omega; \omega, \omega, 0)$ are also of good quality even if the relative difference attains nearly -3% for the largest PSi chain considered. These larger deviations should be related to the fact that $\hbar\omega = 1.786$ eV is twice as large as $\hbar\gamma_1$ and is very close to the $\hbar\omega_{II}$ limit.

The $\gamma_L^e(-\omega_\sigma; \omega_1, \omega_2, \omega_3)$ frequency dispersion curves of conjugated systems are often dominated by a strong low-lying dipole-allowed transition. We have estimated its excitation energy by fitting the $[\alpha_L^e(-\omega; \omega)/\alpha_L^e(0; 0)]$ ratio to a power series expression in ω^2 . From Si_2H_6 to $\text{Si}_{14}\text{H}_{30}$, ΔE is successively equal to 10.48, 8.86, 7.93, 7.41, 7.09, 6.88, and 6.74 eV. Extrapolation to the infinite chain limit yields $\Delta E = 6.50 \pm 0.07$ eV. This upper bound to the ΔE of the infinite stereoregular PSi chain can also be compared to the Hartree-Fock 3-21G band gap of 9.63 eV that has been evaluated from a crystal orbital calculation [38] which does not include the electron-hole interactions and which therefore overestimates ΔE . In addition it can be compared to the numerous theoretical investigations of the PSi band gap, including explicitly (local density functional methods) or implicitly (valence effective Hamiltonian) electron correlation effects, which provide ΔE values ranging between 3.75 and 4.53 eV and assign it to a $\sigma - \sigma^*$ transition [8].

Further Discussions

It is tempting to relate our theoretical estimates to the available experimental quantities. First of all, one should only consider experiments carried out under nonresonant conditions. Second, it is necessary to make the connections between the macroscopic measured $\chi^{(3)}$ values and the microscopic calculated γ values by using appropriate local field factors as well as density of Si-Si units. The relation between $\chi^{(3)}$ and $\Delta\gamma$ can be expressed as

$$\begin{aligned} \chi^{(3)}(-\omega_\sigma; \omega_1, \omega_2, \omega_3) &= \frac{1}{30} f_{\omega_\sigma} f_{\omega_1} f_{\omega_2} f_{\omega_3} N_v \times \Delta\gamma_L(-\omega_\sigma; \omega_1, \omega_2, \omega_3), \end{aligned} \quad (4)$$

where the factor $\frac{1}{30}$ comes from the difference of convention to define the experimental and theoretical quantities and from a $\frac{1}{5}$ factor which relates $\bar{\gamma}$ to the dominant longitudinal γ_L value. N_v represents the number of Si_2H_4 unit cells per unit volume and is given by $N_A \times (d/M)$ where N_A is the Avogadro's number, d the weight density, and M the molecular weight of the unit cell.

Kajzar et al. [4a] have determined a $\chi^{(3)}(-3\omega; \omega, \omega, \omega)$ value of 1.5×10^{-12} esu for films of

poly(methyl-phenylsilane) at $\lambda = 1064$ nm. For THG, the pure vibrational contribution can be assumed to be negligible and therefore the NLO response is dominated by the electronic response and its zero point vibrational averaging (ZPVA) correction. The local field factors have been estimated from the simple Onsager/Lorentz expressions, $f_\omega = (\epsilon_\omega + 2)/3$. An ϵ_ω value of 2.5 has been chosen ($f_\omega = 1.5$). It corresponds to the dielectric constant of poly(di-*n*-hexylsilane) [4e] which depends weakly upon the energy of the light in range of use for NLO measurements. By using $d = 1.06 \text{ g/cm}^3$ from Ref. [4d], one obtains $\Delta\gamma_L(-3\omega; \omega, \omega, \omega)_{\lambda=1064 \text{ nm}} = 6.6 \times 10^6 \text{ a.u.}$ whereas theoretically we have calculated $7.5 \times 10^5 \text{ a.u.}$ It is important to remember that the experimentally derived value is the third-order NLO response per $(\text{SiMePh})_2$ unit, i.e., in first approximation, the response of both the Si_2 unit and the four substituents. For instance $\Delta\bar{\gamma}(-3\omega; \omega, \omega, \omega)_{\lambda=1064 \text{ nm}} = 2.1 \times 10^4 \text{ a.u.}$ for benzene as computed by Karna et al. [39]. Another THG experiment [4b] of thin films of poly(methyl-phenylsilane) and poly(di-*n*-hexylsilane) has provided $\chi^{(3)}(-3\omega; \omega, \omega, \omega)_{\lambda=1907 \text{ nm}}$ values equal to $4.2 \times 10^{-12} \text{ esu}$ and $1.3 \times 10^{-12} \text{ esu}$, respectively which, using the same procedure as above, corresponds to $\Delta\gamma_L(-3\omega; \omega, \omega, \omega)_{\lambda=1907 \text{ nm}} = 1.9 \times 10^7 \text{ a.u.}$ and $9.7 \times 10^6 \text{ a.u.}$ whereas the theoretical estimates is $5.5 \times 10^5 \text{ a.u.}$ Baumert et al. [4b] have also highlighted the conformational dependence of $\chi^{(3)}$ via its temperature dependence.

McGrath et al. [4c] have determined for poly(di-*n*-octylsilane) what they called the electronic and orientational contributions to $\chi^{(3)}(-\omega; \omega, -\omega, \omega)$ at $\lambda = 532$ nm. Their electronic contribution, which in fact contains both electronic and vibrational terms, amounts to $1.8 \pm 0.5 \times 10^{-12} \text{ esu}$. By using $d = 1.06 \text{ g/cm}^3$ and $f_\omega = 1.5$, the estimated $\Delta\gamma_L(-\omega; \omega, -\omega, \omega)_{\lambda=532 \text{ nm}}$ attains $1.7 \times 10^7 \text{ a.u.}$, whereas our theoretical electronic estimate attains only $8.4 \times 10^5 \text{ a.u.}$ Yang et al. [4d] have measured the $\chi^{(3)}(-\omega; \omega, -\omega, \omega)$ of poly(phenyl-methylsilane) in THF solution at $\lambda = 1064$ nm. Their $\chi^{(3)}(-\omega; \omega, -\omega, \omega)$ value extrapolated to the solid film ($d = 1.06 \text{ g/cm}^3$) is $5.0 \times 10^{-13} \text{ esu}$. The local field factors have been estimated from the simple Onsager/Lorentz expression, which for THF amounts to $f_\omega = 1.32$. The corresponding experimentally derived $\Delta\gamma_L(-\omega; \omega, -\omega, \omega)_{\lambda=1064 \text{ nm}}$ is equal to $3.7 \times 10^6 \text{ a.u.}$, whereas our theoretical estimate amounts to $5.6 \times 10^5 \text{ a.u.}$

Systematically, the theoretical estimates are one order of magnitude smaller than the experimentally derived quantities. This discrepancy could originate from different factors: (i) the crystal packing effects which are not properly accounted for by using simple local field factors, (ii) the vibrational contribution of which the pure vibrational part—as opposed to the ZPVA correction—depends strongly upon the NLO process but is negligible for THG, (iii) the lack of electron correlation, and (iv) the effects of the substituents. The importance of the vibrational contribution is assessed in another work [17]. On the other hand, the substituents have a double effect upon $\chi^{(3)}$. Indeed they possess their own $\chi^{(3)}$ contribution, but they also modify the electronic structure and the conformation of the PSi backbone. In particular, they decrease the band gap and therefore they enhance the NLO response; the extent of which remains to be assessed.

ACKNOWLEDGMENTS

Two of us (B.C. and E.A.P) thank the Belgian National Fund for Scientific Research for their Research Associate and Scientific Collaborator positions, respectively. They would also like to thank Prof. B. Kirtman for constructive remarks. The calculations have been performed on the IBM SP2 of the Namur Scientific Computing Facility (Namur-SCF) for which the authors gratefully acknowledge the financial support of the FNRS-FRFC, the Loterie Nationale for the convention No. 2.4519.97 and the Belgian National Interuniversity Research Program on Sciences of Interfacial and Mesoscopic Structures (PAI/IUAP No. P4/10).

References

1. (a) S. P. Karna and A. T. Yeates, Eds., *Theoretical and Computational Modeling of NLO and Electronic Materials* (ACS Symposium Series, New York, 1995). (b) *Chemical Reviews*, thematic issue on Optical Nonlinearities in Chemistry **94**(1) (1994), J. Michl, Ed. (c) *Int. J. Quant. Chem.*, special issue on Molecular Nonlinear Optics **43**(1) (1992), P. O. Löwdin, Ed.
2. B. Kirtman, in *Theoretical and Computational Modeling of NLO and Electronic Materials*, S. P. Karna and A.T. Yeates, Eds. (ACS Symposium Series, New York, 1996), Vol. 628, p. 58.
3. B. Kirtman and B. Champagne, *Int. Rev. Phys. Chem.* **16**, 389 (1997).
4. (a) F. Kajzar, J. Messier, and C. Rosilio, *J. Appl. Phys.* **60**, 3040 (1986). (b) J. C. Baumert, G. C. Bjorklund, D. H. Jundt,

- M. C. Jurich, H. Looser, R. D. Miller, J. Rabolt, R. Sooriyakumaran, J. D. Swaelen, and R. J. Twieg, *Appl. Phys. Lett.* **53**, 1147 (1988). (c) D. J. McGraw, A. E. Siegman, G. M. Wallraff, and R. D. Miller, *Appl. Phys. Lett.* **54**, 1713 (1989). (d) L. Yang, R. Dorsinville, R. R. Alfano, W. K. Zou, and N. L. Yang, *Opt. Lett.* **16**, 758 (1991). (e) F. M. Schellenberg, R. L. Byer, R. D. Miller, R. H. French, S. S. Kano, Y. Takahashi, Y. Shiraki, and R. Ito, in *Inorganic and Organometallic Oligomers and Polymers*, J. F. Harrod and R. M. Laine, Eds. (Kluwer, The Netherlands, 1991), p. 73. (f) T. Hasewaga, Y. Iwasa, H. Kishida, T. Koda, Y. Tokura, H. Tachibana, and Y. Kawabata, *Phys. Rev.* **45**, 6317 (1992). (g) H. Kishida, T. Hasegawa, Y. Iwasa, T. Koda, Y. Tokura, H. Tachibana, M. Matsumoto, S. Wada, T. T. Lay, and H. Tashiro, *Phys. Rev. B* **50**, 7786 (1994).
5. (a) R. West, *J. Organomet. Chem.* **300**, 433 (1989). (b) R. D. Miller and J. Michl, *Chem. Rev.* **89**, 1359 (1989). (c) J. Michl, *Synth. Metals* **49/50**, 367 (1992).
 6. (a) H. Teramae and K. Takeda, *J. Am. Chem. Soc.* **109**, 4140 (1987). (b) J. V. Ortiz and J. W. Mintmire, *J. Am. Chem. Soc.* **110**, 4522 (1988). (c) J. W. Mintmire, *Phys. Rev. B* **39**, 13350 (1989). (d) M. Sprinborg, *Phys. Rev. B* **40**, 7839 (1989). (e) H. Teramae and K. Takeda, *J. Am. Chem. Soc.* **111**, 1281 (1989). (f) N. Matsumoto and H. Teramae, *J. Am. Chem. Soc.* **113**, 4481 (1991). (g) S. Suhai, *Int. J. Quant. Chem.* **S27**, 130 (1993).
 7. (a) J. V. Ortiz and J. W. Mintmire, *J. Phys. Chem.* **95**, 8609 (1991). (b) J. V. Ortiz, *J. Chem. Phys.* **94**, 6064 (1991). (c) J. V. Ortiz, *Polyhedron* **10**, 1285 (1991). (d) J. V. Ortiz and C. McMichael Rohlfsing, *Macromolecules* **26**, 7282 (1993).
 8. (a) K. Takeda, H. Teramae, and N. Matsumoto, *J. Am. Chem. Soc.* **108**, 8186 (1986). (b) R. Crespo, M. C. Piqueras, E. Ortí, and F. Tomàs, *Synth. Met.* **54**, 173 (1993). (c) K. Takeda, *J. Phys. Soc. Jap.* **63**, 1 (1994).
 9. J.-M. André, *Int. J. Quant. Chem.* **S24**, 65 (1990).
 10. V. Balaji and J. Michl, *Polyhedron* **10**, 1265 (1991). Z. Liu, K. Terakura, S. Abe, and J. F. Harris, *J. Chem. Phys.* **105**, 8237 (1996).
 11. R. W. Bigelow and K. M. McGraene, *J. Polym. Phys.* **24**, 1233 (1986).
 12. B. Kirtman and M. Hasan, *J. Chem. Phys.* **96**, 470 (1992).
 13. B. Kirtman, J. L. Toto, K. A. Robins, and M. Hasan, *J. Chem. Phys.* **102**, 5350 (1995).
 14. E. A. Perpète, B. Champagne, and B. Kirtman, *J. Chem. Phys.* **107**, 2463 (1997).
 15. B. Champagne and J.-M. André, *Int. J. Quant. Chem.* **45**, 1009 (1992). B. Champagne and J.-M. André, *Nonlinear Optics* **9**, 25 (1995).
 16. J. V. Ortiz and C. McMichael Rohlfsing, *Chem. Phys. Lett.* **280**, 239 (1997).
 17. E. A. Perpète, J. M. André, and B. Champagne, *J. Chem. Phys.*, **109** (1998).
 18. B. J. Orr and J. F. Ward, *Mol. Phys.* **20**, 513 (1971). D. M. Bishop, *J. Chem. Phys.* **100**, 6535 (1994).
 19. D. M. Bishop, B. Kirtman, and B. Champagne, *J. Chem. Phys.* **107**, 5780 (1997).
 20. H. Sekino and R. J. Bartlett, *J. Chem. Phys.* **85**, 976 (1986). S. P. Karna and M. Dupuis, *J. Comp. Chem.* **12**, 487 (1991).
 21. For example, see P. W. Langhoff, M. Karplus, and R. P. Hurst, *J. Chem. Phys.* **44**, 505 (1966); T. C. Caves and M. Karplus, *J. Chem. Phys.* **50**, 3649 (1969).
 22. C. E. Dykstra and P. G. Jasien, *Chem. Phys. Lett.* **109**, 388 (1984).
 23. J. Linderberg and Y. Öhrn, *Propagators in Quantum Chemistry* (Academic, New York, 1973). J. Oddershede, P. Jørgensen, and D. L. Yeager, *Comput. Phys. Rev.* **2**, 33 (1984). P. Norman, D. Jonsson, O. Vahtas, and H. Ågren, *Chem. Phys. Lett.* **242**, 7 (1995).
 24. M. Dupuis, A. Marquez, and E. R. Davidson, HONDO95-3 from CHEM-Station, 1995, IBM Corporation, Neighborhood Road, Kingston, New York 12401. For the purpose of comparison, it should be noted that the default 6-31G basis set in HONDO95-3 is slightly different from Ref. 26.
 25. J. L. Toto, T. T. Toto, C. P. de Melo, M. Hasan, and B. Kirtman, *Chem. Phys. Lett.* **244**, 59 (1995). J. L. Toto, T. T. Toto, and C. P. de Melo, *Chem. Phys. Lett.* **245**, 660 (1995).
 26. B. Champagne, E. A. Perpète, J.-M. André, and B. Kirtman, *J. Chem. Soc. Faraday Trans.* **91**, 1641 (1995).
 27. W. J. Hehre, R. Ditchfield, and J. A. Pople, *J. Chem. Phys.* **56**, 2257 (1972).
 28. G. J. B. Hurst, M. Dupuis, and E. Clementi, *J. Chem. Phys.* **89**, 385 (1988).
 29. D. P. Shelton, *J. Chem. Phys.* **84**, 404 (1985).
 30. D. M. Bishop and D. W. De Kee, *J. Chem. Phys.* **104**, 9876 (1996).
 31. D. M. Bishop and D. W. De Kee, *J. Chem. Phys.* **105**, 8247 (1996).
 32. C. Hättig, *Mol. Phys.*, **94**, 455 (1998).
 33. P. W. Langhoff and M. Karplus, *J. Chem. Phys.* **52**, 1435 (1970).
 34. B. Champagne, D. Jacquemin, J. M. André, and B. Kirtman, *J. Phys. Chem. A* **101**, 3158 (1997).
 35. S. P. Karna, G. B. Talapatra, W. M. K. M. Wijekoon, and P. N. Prasad, *Phys. Rev. A* **45**, 2763 (1992).
 36. Y. Luo, H. Ågren, H. Koch, P. Jørgensen, and T. Helgaker, *Phys. Rev. B* **51**, 14949 (1995).
 37. M. Hasan, S. J. Kim, J. L. Toto, and B. Kirtman, *J. Chem. Phys.* **105**, 186 (1996).
 38. B. Champagne, unpublished results.
 39. S. P. Karna, G. B. Talapatra, and P. N. Prasad, *J. Chem. Phys.* **95**, 5873 (1991).

Computation of the Electromagnetic Harmonics Generation by Stratified Systems Containing Nonlinear Layers

ANNA CALDERONE, JEAN-POL VIGNERON

Institute for Studies in Interface Sciences, Facultés Universitaires Notre-Dame de la Paix, rue de Bruxelles 61, 5000 Namur, Belgium

Received 21 February 1998; revised 17 March 1998; accepted 18 March 1998

ABSTRACT: We propose a computational technique to evaluate the reflectivity and the transmission of the harmonics generated by a planar-stratified material containing nonlinear layers. Maxwell's equations are solved and the scattering boundary conditions are implemented using a transfer matrix technique. As our goal beyond this study is to model sum-frequency generation spectra, our approach is limited to second-order processes. The great advantage of this algorithm is that owing to a self-consistent procedure the nonlinear scattering problem is reduced to the repeated solving of linear equations. © 1998 John Wiley & Sons, Inc. *Int J Quant Chem* 70: 763–770, 1998

Key words: electromagnetism; nonlinear optics; stratified system; Maxwell's equations; transfer matrix

Introduction

Since the advent of lasers that produce highly coherent beams of light that can be extremely intense, a continued interest has been devoted to nonlinear optics [1–3]. Nonlinear processes are being increasingly exploited in a variety of optoelec-

tronic and photonic applications, for instance, in the area of telecommunications. Furthermore, nonlinear optical techniques, such as second harmonic generation (SHG) and sum-frequency generation (SFG) [4], which rely on specific second-order optical processes, have emerged as useful tools to study various types of surfaces and interfaces [5, 6].

Due to the complexity of nonlinear optical processes, their theoretical modeling can be very helpful for a better understanding and a proper exploitation of the experimental techniques. In this

Correspondence to: A. Calderone.

Contract grant sponsors: Belgian Programs on Interuniversity Attraction Poles; FNRS/FRFC.

way, the study of the interaction of an electromagnetic wave with a nonlinear medium depends on many parameters such as anisotropy, polarization of the light, and the structure of the sample. While most of the physics of the linear electromagnetic wave propagation in a stratified system is known from previous work in optics [7–9], much less has been undertaken to develop the required algorithmic tools for nonlinear materials.

In this study, we propose a computational technique that allows for the evaluation of the contributions of harmonics in the waves reflected and transmitted by a planar-stratified material. The algorithm, described in the following section, is based on the resolution of Maxwell's equations and uses a transfer matrix technique [10] to compute the needed electromagnetic transmission coefficients. Since our goal, beyond this study, is to attempt to model SFG spectra, we have limited our approach to second-order processes. The great advantage of our algorithm is that because of a self-consistent procedure, the nonlinear scattering problem is reduced to sequentially solving a system of linear equations. Another specificity lies in the mode of propagating the fields through the nonlinear medium. Indeed, this one is cut in sufficiently thin slices to consider that the fields in each of them are constant, so that an exact solution to Maxwell's equations can be obtained, in contrast to most standard integrators which are based on truncation techniques. An application related to the scattering of electromagnetic waves through a nonlinear organic film deposited on a glass substrate will be presented in the third section.

Algorithm for the Computation of Electromagnetic Energy Transfer Through Nonlinear Anisotropic Films

GEOMETRY

The stratified system considered here consists of a stack of nonlinear anisotropic films deposited on a dielectric substrate (Fig. 1). We will refer to the nonlinear films as "the active nonlinear medium." Moreover, the system contains a third medium, the wave emitter, in which the incident and the reflected waves propagate. The incident plane defines the yz plane: the y axis is oriented in the direction of incidence and the z axis is perpendicular to the surface.

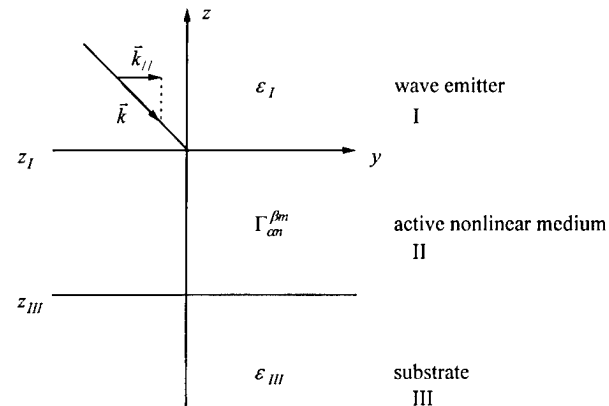


FIGURE 1. Geometry of interest for the nonlinear stratified system. The $\Gamma_{\alpha n}^{\beta m}$ contain the dielectric functions and the second-order susceptibility tensors characterizing the nonlinear medium.

The incident wave may present a transverse-electric (TE) or a transverse-magnetic (TM) polarization depending on whether the electric field is perpendicular or parallel to the incident plane, respectively. However, due to the presence of the nonlinear medium, the polarization of the resulting transmitted waves can be mixed.

The macroscopic polarization P induced in a nonlinear material due to the application of an intense electromagnetic field can be written as a Taylor series:

$$P(\mathbf{r}, t)$$

$$\begin{aligned} &= P_0 + \chi^{(1)}(\mathbf{r})E(\mathbf{r}, t) + \frac{1}{2!}\chi^{(2)}(\mathbf{r})E(\mathbf{r}, t)E(\mathbf{r}, t) \\ &\quad + \frac{1}{3!}\chi^{(3)}(\mathbf{r})E(\mathbf{r}, t)E(\mathbf{r}, t)E(\mathbf{r}, t) + \dots, \end{aligned} \quad (1)$$

where P_0 is the permanent polarization which exists in the material prior to when the field is applied, $\chi^{(1)}$ is the linear susceptibility tensor, and $\chi^{(2)}$ and $\chi^{(3)}$ are the second-order and third-order susceptibility tensors, respectively. In our algorithm, we have limited the polarization to the second order; this is sufficient for simulated SHG or SFG. Due to the stratified structure considered in this work, the space-varying dielectric and susceptibility anisotropic tensors depend only on the normal coordinate z .

TIME-DEPENDENT FIELD EQUATIONS AND THE HARMONIC REPRESENTATION

The active nonlinear media induces a local distortion of the incident signal, which we write as a Fourier series:

$$\mathbf{E}(\mathbf{r}, t) = \sum_{\beta} \sum_{n=-\infty}^{+\infty} E_{\beta n}(z) e^{in(k_y y - \omega t)} \quad (2)$$

$$\mathbf{H}(\mathbf{r}, t) = \sum_{\beta} \sum_{n=-\infty}^{+\infty} H_{\beta n}(z) e^{in(k_y y - \omega t)}, \quad (3)$$

where β represents the spatial coordinates x , y , and z . This representation represents the fact that the interaction of an incident wave at frequency ω with the nonlinear medium can lead to the formation of new waves (which are the reflected or transmitted waves) at frequencies $\omega, 2\omega, 3\omega, \dots$ and that the lateral momentum is conserved (therefore, if we transform a frequency ω into a frequency 2ω , we must collapse two photons with an energy $\hbar\omega$ into one photon with an energy $2\hbar\omega$).

With this representation, we shall write Maxwell's equations. The Gauss electric equation is:

$$\nabla \cdot \mathbf{D} = 0. \quad (4)$$

For a nonlinear interaction up to the second order, the α component of the displacement vector \mathbf{D} can be written in the international mks system units as:

$$D_{\alpha} = \epsilon_0 \sum_{n=-\infty}^{+\infty} \sum_{\beta} \sum_{m=-\infty}^{+\infty} \left[\epsilon_{\alpha\beta} \delta_n^m + \frac{1}{2!} \sum_j \chi_{\alpha j \beta}^{(2)} \cdot E_{jn-m}(z) \right] E_{\beta m}(z) e^{in(k_y y - \omega t)}, \quad (5)$$

where both j , α , and β represent the spatial coordinates x , y , and z . To simplify, we will introduce the notation:

$$\Gamma_{\alpha n}^{\beta m} = \epsilon_{\alpha\beta} \delta_n^m + \frac{1}{2!} \sum_j \chi_{\alpha j \beta}^{(2)} E_{jn-m}(z). \quad (6)$$

As explained in the next section, in order to render the problem linear, we introduce a self-consistent approach and consolidate the values of the electric fields appearing in $\Gamma_{\alpha n}^{\beta m}$ to their values calculated in the previous iteration step. Finally, the Gauss

electric equation (4) becomes:

$$\frac{d}{dz} \left[\sum_{\beta, m} \Gamma_{zn}^{\beta m} E_{\beta m} \right] = -ink_y \sum_{\beta, m} \Gamma_{yn}^{\beta m} E_{\beta m}, \quad \forall n = -\infty \text{ to } +\infty. \quad (7)$$

The Gauss magnetic equation

$$\nabla \cdot \mathbf{H} = 0 \quad (8)$$

becomes:

$$\frac{dH_{zn}}{dz} = -ink_y H_{yn}, \quad \forall n = -\infty \text{ to } +\infty. \quad (9)$$

And Faraday's law

$$\nabla \times \mathbf{E}(\mathbf{r}, t) = -\mu_0 \frac{\partial \mathbf{H}(\mathbf{r}, t)}{\partial t} \quad (10)$$

can be written, for each n going from $-\infty$ to $+\infty$, as:

$$\frac{dE_{yn}}{dz} = ink_y E_{zn} - in\mu_0 \omega H_{xn}, \quad (11)$$

$$\frac{dE_{xn}}{dz} = in\mu_0 \omega H_{yn}, \quad (12)$$

$$H_{zn} = -\frac{k_y}{\mu_0 \omega} E_{xn}. \quad (13)$$

Finally, Ampère's law

$$\nabla \times \mathbf{H}(\mathbf{r}, t) = \frac{\partial \mathbf{D}(\mathbf{r}, t)}{\partial t} \quad (14)$$

becomes for each n going from $-\infty$ to $+\infty$:

$$\frac{dH_{yn}}{dz} = ink_y H_{zn} + in\omega\epsilon_0 \sum_{\beta, m} \Gamma_{xn}^{\beta m} E_{\beta m}, \quad (15)$$

$$\frac{dH_{xn}}{dz} = -in\omega\epsilon_0 \sum_{\beta, m} \Gamma_{yn}^{\beta m} E_{\beta m}, \quad (16)$$

$$H_{xn} = \epsilon_0 \frac{\omega}{k_y} \sum_{\beta, m} \Gamma_{zn}^{\beta m} E_{\beta m}, \quad (17)$$

where the sum over β runs over the three coordinates x , y , and z while the sum on m goes from $-\infty$ to $+\infty$.

It should be noted that the time dependence in Maxwell's equations has now disappeared. It should also be noticed that since Eqs. (16) and (12)

can be obtained by combining Eqs. (7) and (17) and Eqs. (9) and (13), respectively, Eqs. (7) and (9) can be ignored, as redundant.

SELF-CONSISTENT APPROACH TO NONLINEAR SCATTERING PROBLEMS

At this stage, the system of equations [(11)–(13) and (15)–(17)] can be rewritten in such a way as to eliminate the normal component of the fields. The H_{zn} component is automatically eliminated by Eq. (13):

$$H_{zn} = -\frac{k_y}{\mu_0 \omega} E_{xn}. \quad (18)$$

Concerning the E_{zn} component, if we develop the sum over β appearing in Eq. (17), we obtain:

$$\sum_m \Gamma_{zn}^{zm} E_{zm} = \frac{k_y}{\epsilon_0 \omega} H_{xn} - \sum_m (\Gamma_{zn}^{xm} E_{xm} + \Gamma_{zn}^{ym} E_{ym}). \quad (19)$$

If we denote θ_p^n the inverse matrix of Γ_{zn}^{zm} :

$$\sum_n \theta_p^n \Gamma_{zn}^{zm} = \delta_p^m. \quad (20)$$

By introducing Eq. (20) into Eq. (19), the E_{zn} component is found to be:

$$E_{zn} = \frac{k_y}{\epsilon_0 \omega} \sum_p \theta_p^n H_{xp} - \sum_m \left(\sum_p \theta_p^n \Gamma_{zp}^{xm} \right) E_{xm} - \sum_m \left(\sum_p \theta_p^n \Gamma_{zp}^{ym} \right) E_{ym}. \quad (21)$$

Using Eqs. (18) and (21), the normal components of fields can be eliminated in the tangential-fields differential equations [(11), (12), (15), and (16)]:

$$\frac{dE_{xn}}{dz} = i(\mu_0 c) \left(\frac{n \omega}{c} \right) H_{yn}, \quad (22)$$

$$\begin{aligned} \frac{dE_{yn}}{dz} &= \sum_q \left[(-ink_y) \sum_p \theta_p^n \Gamma_{zp}^{xq} \right] E_{xq} \\ &\quad + \sum_q \left[(-ink_y) \sum_p \theta_p^n \Gamma_{zp}^{yq} \right] E_{yq} \\ &\quad + \sum_q \left[i \frac{(nk_y)^2}{(n \omega / c)} \mu_0 c \theta_q^n \right] H_{xq} \\ &\quad - i(\mu_0 c) \left(\frac{n \omega}{c} \right) H_{xn}, \end{aligned} \quad (23)$$

$$\begin{aligned} \frac{dH_{xn}}{dz} &= \sum_q \left[-i \left(\frac{n \omega}{c} \right) \frac{1}{\mu_0 c} \right. \\ &\quad \cdot \left. \left(\Gamma_{yn}^{xq} - \sum_m \sum_p \Gamma_{yn}^{zm} \theta_m^p \Gamma_{zp}^{xq} \right) \right] E_{xq} \\ &\quad + \sum_q \left[-i \left(\frac{n \omega}{c} \right) \frac{1}{\mu_0 c} \right. \\ &\quad \cdot \left. \left(\Gamma_{yn}^{yq} - \sum_m \sum_p \Gamma_{yn}^{zm} \theta_m^p \Gamma_{zp}^{yq} \right) \right] E_{yq} \\ &\quad + \sum_q \left[(-ink_y) \sum_m \Gamma_{yn}^{zm} \theta_m^q \right] H_{xq}, \end{aligned} \quad (24)$$

$$\begin{aligned} \frac{dH_{yn}}{dz} &= -i \frac{(nk_y)^2}{\mu_0 c (n \omega / c)} E_{xn} \\ &\quad + \sum_q \left[-i \left(\frac{n \omega}{c} \right) \frac{1}{\mu_0 c} \right. \\ &\quad \cdot \left. \left(\Gamma_{xn}^{xq} - \sum_m \sum_p \Gamma_{xn}^{zm} \theta_m^p \Gamma_{zp}^{xq} \right) \right] E_{xq} \\ &\quad + \sum_q \left[-i \left(\frac{n \omega}{c} \right) \frac{1}{\mu_0 c} \right. \\ &\quad \cdot \left. \left(\Gamma_{xn}^{yq} - \sum_m \sum_p \Gamma_{xn}^{zm} \theta_m^p \Gamma_{zp}^{yq} \right) \right] E_{yq} \\ &\quad + \sum_q \left[(ink_y) \sum_m \Gamma_{xn}^{zm} \theta_m^q \right] H_{xq}, \end{aligned} \quad (25)$$

Finally, we have to resolve for each value of n (which in practice has a finite value) a system of four differential equations [(22)–(25)] which depend on the tangential components of the fields E_x , E_y , H_x , and H_y . The normal components are afterwards explicitly given by Eqs. (18) and (21). However, $\Gamma_{\alpha n}^{\beta m}$ (and thus the θ_p^n), appearing in this system of equations, also depend on the electric fields. As pointed out above, we propose to introduce a self-consistent approach to make the scattering problem linear. In practice, our algorithm first solves the system of equations [(22)–(25), (18), and (21)] in the linear case, by considering that $\Gamma_{\alpha n}^{\beta m} = \epsilon_{\alpha \beta} \delta_n^m$. Then, the nonlinearity is introduced in a self-consistent manner. In the first iteration step, the values of the electric fields appearing in the $\Gamma_{\alpha n}^{\beta m}$ [see (6)] are those calculated in the linear

case. Then, in each following iteration, a new $\Gamma_{\alpha n}^{\beta m}$ is constructed where the values of the electric fields are fixed to those calculated at the previous step. After each step, a convergence test is performed on the convergence of the multifrequency reflection value. The nonlinear scattering problem is therefore reduced to repeated solution of linear equations.

SCATTERING BOUNDARY CONDITIONS AND TRANSFER MATRIX

On a plane with a constant value of the coordinate z , the tangential component of the electric field ($E_{||}$) is a continuous function of z , even if the dielectric function $\epsilon(z)$ contains a discontinuity. Moreover, for nonmagnetic materials ($\mu = 1$), the tangential component of the magnetic field ($H_{||}$) is also continuous across the interface.

In emitter region I and in collector region III, the dielectric function ϵ_1 and ϵ_{III} are constant over space. In such homogeneous regions, the electric field can be represented as a superposition of plane waves, with polarization vectors normal to the propagation direction. For an incident wave with lateral wave vector $\mathbf{k}_{||}$ (that is to say k_y in the chosen geometry), the polarization vector $\boldsymbol{\eta}$, defined as being the direction of the electric field in a local transverse electric configuration, corresponds simply to \mathbf{e}_x :

$$\boldsymbol{\eta} = \frac{\mathbf{k}_{||} \times \mathbf{e}_z}{|\mathbf{k}_{||} \times \mathbf{e}_z|} = \mathbf{e}_x, \quad (26)$$

while the direction of the corresponding magnetic field $\boldsymbol{\mu}$ is defined as

$$\boldsymbol{\mu}_I^+ = \boldsymbol{\chi}_I - \frac{k_y}{\sqrt{\epsilon_1 \omega/c}} \mathbf{e}_z \quad (27)$$

for a wave which propagates in the direction of \mathbf{e}_z , and

$$\boldsymbol{\mu}_I^- = -\boldsymbol{\chi}_I - \frac{k_y}{\sqrt{\epsilon_1 \omega/c}} \mathbf{e}_z \quad (28)$$

in the case of a backward propagation along \mathbf{e}_z . The tangential part of these complementary polar-

ization vectors ($\boldsymbol{\chi}_I$) is given by:

$$\boldsymbol{\chi}_I = \frac{\sqrt{\epsilon_1 \frac{(n\omega)^2}{c^2} - (nk_y)^2}}{\sqrt{\epsilon_1} \frac{n\omega}{c}} \mathbf{e}_y,$$

with $\Re e \left[\sqrt{\epsilon_1 \frac{\omega^2}{c^2} - k_y^2} \right] > 0. \quad (29)$

Similar expressions exist for region III, with ϵ_{III} as dielectric function. We now write the general form of the fields in the emitter region as a superposition of plane waves with both directions of propagation along the normal \mathbf{e}_z and both polarizations:

$$\mathbf{E}_{||n}(z) = N_{In}^+ \boldsymbol{\eta} e^{ink_I(z-z_I)} + N_{In}^- \boldsymbol{\eta} e^{-ink_I(z-z_I)} \\ + X_{In}^+ \boldsymbol{\chi}_I e^{ink_I(z-z_I)} - X_{In}^- \boldsymbol{\chi}_I e^{-ink_I(z-z_I)}, \quad (30)$$

while the magnetic field is expressed as:

$$\mathbf{H}_{||n}(z) = \frac{\sqrt{\epsilon_1}}{\mu_0 c} (N_{In}^+ \boldsymbol{\chi}_I e^{ink_I(z-z_I)} - N_{In}^- \boldsymbol{\chi}_I e^{-ink_I(z-z_I)} \\ - X_{In}^+ \boldsymbol{\eta} e^{ink_I(z-z_I)} - X_{In}^- \boldsymbol{\eta} e^{-ink_I(z-z_I)}). \quad (31)$$

Similar expressions can be written for the collector region (III), with in this case the set of coefficients $N_{III,n}^+$, $X_{III,n}^+$, $N_{III,n}^-$, $X_{III,n}^-$, and ϵ_{III} as dielectric function.

Applying scattering boundary conditions amounts to finding the amplitude of the reflected wave so that, combined with a single incident wave, the field in region I provides initial conditions to propagate across the nonlinear medium and leaves in region III only outgoing waves (that is to say that $N_{III,n}^+$ and $X_{III,n}^+$ are both zero). Obtaining the correct coefficients is merely a matter of choosing the appropriate superposition of plane waves in both regions, with the constraint that they connect according to the propagation equations [(22)–(25), (18), and (21)].

The set of coefficients \bar{N}_I^+ , \bar{X}_I^+ , \bar{N}_I^- , \bar{X}_I^- and \bar{N}_{III}^+ , \bar{X}_{III}^+ , \bar{N}_{III}^- , \bar{X}_{III}^- (the overbar denotes an entire column of components corresponding to the different frequencies and labeled by the n indices) are representations of the wave in the incidence and emergence regions, respectively. If these coefficients are known, the wave can be reconstructed

using the explicit field expressions given above. In particular, if the coefficients \bar{N}_{III}^+ , \bar{X}_{III}^+ , \bar{N}_{III}^- , \bar{X}_{III}^- are known, the fields at $z = z_{III}$ are given by:

$$\mathbf{E}_{||n}(z_{III}) = N_{III,n}^+ \mathbf{\eta} + N_{III,n}^- \mathbf{\eta} + X_{III,n}^+ \mathbf{X}_{III} - X_{III,n}^- \mathbf{X}_{III} \quad (32)$$

$$\mathbf{H}_{||n}(z_{III}) = \frac{\sqrt{\varepsilon_{III}}}{\mu_0 c} (N_{III,n}^+ \mathbf{X}_{III} - N_{III,n}^- \mathbf{X}_{III} - X_{III,n}^+ \mathbf{\eta} - X_{III,n}^- \mathbf{\eta}). \quad (33)$$

Conversely, if we know the field values on the interface $z = z_I$, we can reconstruct the corre-

sponding wave coefficients by inverting the above formulas, relocalized at the edge of region I. The computation of the wave coefficients is then reduced to a simple four-order matrix multiplication:

$$\begin{bmatrix} N_{In}^+ \\ X_{In}^+ \\ N_{In}^- \\ X_{In}^- \end{bmatrix} = T^{-1} \begin{bmatrix} E_{xn}(z_I) \\ E_{yn}(z_I) \\ (\mu_0 c / \sqrt{\varepsilon_1}) H_{xn}(z_I) \\ (\mu_0 c / \sqrt{\varepsilon_1}) H_{yn}(z_I) \end{bmatrix}, \quad (34)$$

where

$$T^{-1} = \begin{bmatrix} \frac{1}{2} & 0 & 0 & \frac{\sqrt{\varepsilon_1} \omega}{2c \sqrt{\varepsilon_1 \frac{\omega^2}{c^2} - k_y^2}} \\ 0 & \frac{\sqrt{\varepsilon_1} \omega}{2c \sqrt{\varepsilon_1 \frac{\omega^2}{c^2} - k_y^2}} & -\frac{1}{2} & 0 \\ \frac{1}{2} & 0 & 0 & -\frac{\sqrt{\varepsilon_1} \omega}{2c \sqrt{\varepsilon_1 \frac{\omega^2}{c^2} - k_y^2}} \\ 0 & -\frac{\sqrt{\varepsilon_1} \omega}{2c \sqrt{\varepsilon_1 \frac{\omega^2}{c^2} - k_y^2}} & -\frac{1}{2} & 0 \end{bmatrix}. \quad (35)$$

On the other hand, due to the linearity of Maxwell's equations, Eqs. (22)–(25), (18), and (21), there exists a transfer matrix that connects the coefficients in region I with those in region III. This relation is written as:

$$\begin{bmatrix} \bar{N}_I^+ \\ \bar{X}_I^+ \\ \bar{N}_I^- \\ \bar{X}_I^- \end{bmatrix} = \begin{bmatrix} M_{NN}^{++} & M_{NX}^{++} & M_{NN}^{+-} & M_{NX}^{+-} \\ M_{XN}^{++} & M_{XX}^{++} & M_{XN}^{+-} & M_{XX}^{+-} \\ M_{NN}^{-+} & M_{NX}^{-+} & M_{NN}^{--} & M_{NX}^{--} \\ M_{XN}^{-+} & M_{XX}^{-+} & M_{XN}^{--} & M_{XX}^{--} \end{bmatrix} \begin{bmatrix} \bar{N}_{III}^+ \\ \bar{X}_{III}^+ \\ \bar{N}_{III}^- \\ \bar{X}_{III}^- \end{bmatrix}. \quad (36)$$

If the matrix is applied to a basis vector (in which all components are zero, except the one

appearing in position q), the result of the multiplication in Eq. (36) is column q of the matrix. Therefore, the transfer matrix will be computed by putting all wave coefficients \bar{N}_{III}^+ , \bar{X}_{III}^+ , \bar{N}_{III}^- , and \bar{X}_{III}^- to zero, except one of them which will be set to 1. Then, using Eqs. (32) and (33), the corresponding fields are computed at $z = z_{III}$ and these values are taken as initial conditions to solve the system of equations [(22)–(25), (18), and (21)] and to propagate the electromagnetic waves through the nonlinear medium. In fact, to do this, the nonlinear medium is cut in different slices sufficiently thin to consider that the fields are homogeneous in each of these layers. As the tangential fields are continuous at each interface, the system

of differential equations [(22)–(25)] is solved exactly for each layer, by using the values of the fields calculated in the previous slice as an initial condition. In this way, the waves are propagated from the interface at $z = z_{\text{III}}$ to the interface at $z = z_1$ where the coefficients \bar{N}_1^+ , \bar{X}_1^+ , \bar{N}_1^- , \bar{X}_1^- are built using (34). These correspond to a whole column of the transfer matrix. All columns are obtained in this way. We have tested this method of integration of the fields on known linear scattering problems, and we have obtained very good results. The exact algorithm is expected to perform much better than standard integrators (like Runge-Kutta) which have to deal with truncation techniques.

Once the transfer matrix is available, the scattering boundary conditions can be implemented by specifying that, on one hand, the incident wave and thus its \bar{N}_1^- , \bar{X}_1^- coefficients are known and, on the other hand, there is no back-traveling wave in the emergence region, e.g., $\bar{N}_{\text{III}}^+ = 0$ and $\bar{X}_{\text{III}}^+ = 0$. Once introduced into Eq. (36), this provides a direct relationship between the coefficients of the transmitted waves and those of the incident wave. The transmission coefficients can be obtained from a system of linear equations:

$$\begin{bmatrix} \bar{N}_{\text{III}}^- \\ \bar{X}_{\text{III}}^- \end{bmatrix} = \begin{bmatrix} M_{NN}^{--} & M_{NX}^{--} \\ M_{XN}^{--} & M_{XX}^{--} \end{bmatrix}^{-1} \begin{bmatrix} \bar{N}_1^- \\ \bar{X}_1^- \end{bmatrix}. \quad (37)$$

It is apparent that only a fraction of the transfer matrix is needed.

Finally, the energy transfer which corresponds to the surface integral (J) of the Poynting vector over the unit surface σ :

$$J = \frac{\sigma}{2} \Re e [\mathbf{E}_{||n}(z) \times \mathbf{H}_{||n}^*(z) \cdot \mathbf{e}_z] \quad (38)$$

can be obtained directly from the computed coefficients, using

$$J = \frac{\sigma}{2\mu_0\omega} (|N_{\text{III},n}^-|^2 + |X_{\text{III},n}^-|^2) \sqrt{\varepsilon_{\text{III}} \frac{(n\omega)^2}{c^2} - nk_y^2} \cdot \Theta \left(\varepsilon_{\text{III}} \frac{(n\omega)^2}{c^2} - nk_y^2 \right). \quad (39)$$

The Heaviside Θ -function (1 for positive arguments, 0 otherwise) ensures that only radiative emerging waves transfer energy.

Application

As an application, we have modeled the scattering of electromagnetic waves through a very thin nonlinear organic film of 5×10^{-9} m deposited on a glass substrate. The nonlinear film is composed of *trans*-1-dicyano, 14-aminotetradecaheptaene molecules which are planar and lie perpendicular to the incident plane, their long axis oriented along the y axis. The dielectric function and second-order susceptibility tensors are both anisotropic and are calculated from the corresponding polarizabilities and first hyperpolarizabilities provided by AM1/FF (Austin Model 1/Finite Field) quantum chemistry calculations performed by Geskin [11]. In this way, we have taken as real parts of the dielectric function tensor: $\varepsilon_{xx} = 1.0300$, $\varepsilon_{yy} = 1.1452$, $\varepsilon_{zz} = 1.0000$, $\varepsilon_{xy} = \varepsilon_{yx} = 1.0014$.

The other components and the imaginary part of all components are taken as zero and for the real parts of the second-order susceptibility tensor: $\chi_{xyx}^{(2)} = \chi_{yxx}^{(2)} = 4.8 \times 10^{-5}$ m/V, $\chi_{xyy}^{(2)} = \chi_{yyx}^{(2)} = 1.59 \times 10^{-4}$ m/V, $\chi_{yyy}^{(2)} = -7.510 \times 10^{-3}$ m/V; the other components and the imaginary part of all components are zero. The power of the incident beam is 20×10^{-3} W and its wavelength is about 0.632×10^{-6} m; these parameters correspond to those of a weak infrared laser. The polarization of the incident wave is TE.

In Figure 2, we present the total reflectivity and the contributions of the first to fourth harmonics obtained at angles of incidence ranging from 0° to 90° . As expected, the reflectivities calculated for the third and fourth harmonics are very weak. The reflectivity of the first harmonic is close to the total one, it starts from 0.04 at 0° (which corresponds to the value obtained at normal incidence at the vacuum/glass interface) and increases to one at 90° . The high reflectivity at grazing incidence limits the penetration into the nonlinear medium and explains the fact that the contributions of the other harmonics fall to zero. On the other hand, we have noted that they increase with the thickness of the nonlinear film.

Conclusions

We have built an algorithm which evaluates the electromagnetic harmonic generation by stratified

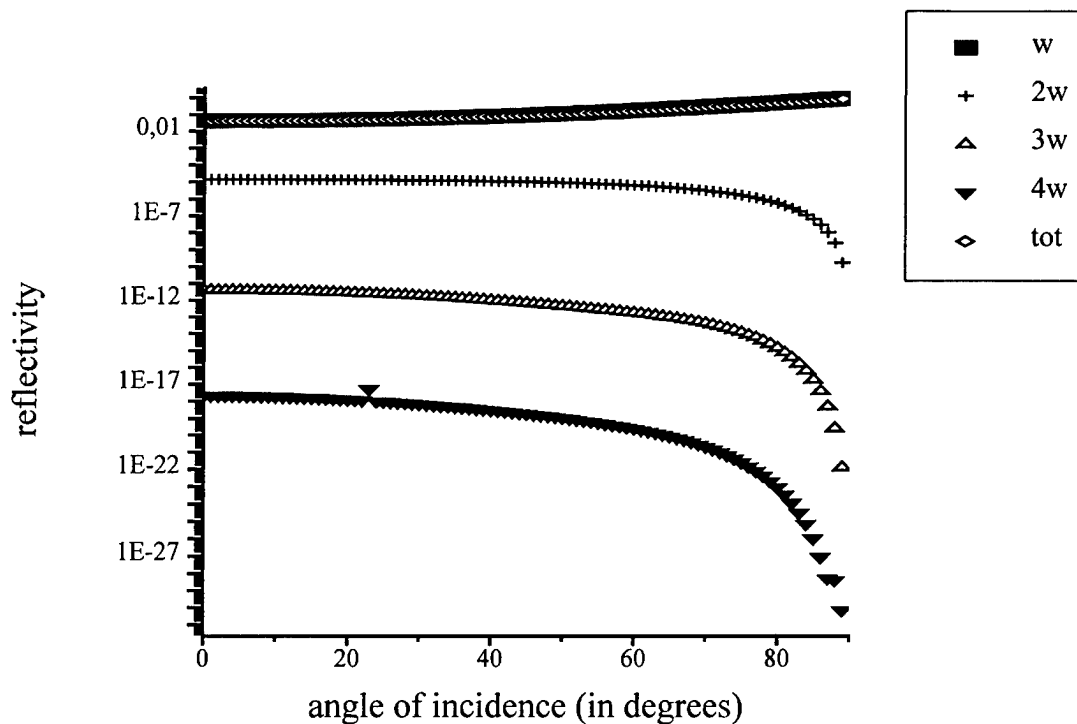


FIGURE 2. Total reflectivity (tot) and the contributions of the first to fourth harmonics calculated, at different angles of incidence, for a nonlinear film of *trans*-1-dicyano, 14-aminotetradecaheptaene deposited on glass.

systems containing nonlinear layers. It is based on the direct solution of Maxwell's equations and it is limited to second-order processes. The scattering boundary conditions are implemented using a transfer matrix technique, and the integration of the fields through the active nonlinear medium is carried out by an exact approach. The great advantage of this algorithm is that because of a self-consistent procedure, we have reduced the nonlinear scattering problem to the repeated solution of a system of linear equations. The first results obtained in the case of an organic nonlinear film deposited on a glass substrate show promise. Our future goal is the modeling of sum-frequency generation in order to help the interpretation of experimental spectra.

ACKNOWLEDGMENTS

This work is partly supported by the Belgian Programs on Interuniversity Attraction Poles and FNRS/FRFC.

References

1. P. N. Butcher and D. Cotter, *The Elements of Nonlinear Optics* (Cambridge University Press, Cambridge, 1990).
2. P. N. Prasad and D. J. Williams, *Introduction to Nonlinear Optical Effects in Molecules and Polymers* (Wiley Interscience, New York, 1991).
3. R. W. Boyd, *Nonlinear Optics* (Academic, New York, 1992).
4. P. F. Brevet, *Surface Second Harmonic Generation* (Presses polytechniques et universitaires romandes, Lausanne, 1997).
5. J. M. Chen, J. R. Bower, C. S. Wang, and C. H. Lee, *Optics Commun.* **9**, 132 (1993).
6. A. Tadjeeddine and A. Peremans, *J. Electroanal. Chem.* **409**, 115 (1996).
7. M. Born and E. Wolf, *Principles of Optics* (Pergamon, London, 1958), p. 50.
8. A. Dereux, J. P. Vigneron, Ph. Lambin, and A. A. Lucas, *Phys. Rev. B* **38**, 5438 (1988).
9. J. P. Vigneron, F. Forati, D. André, A. Castiaux, I. Derycke, and A. Dereux, *Ultramicroscopy* **61**, 21 (1995).
10. J. B. Pendry, *J. Mod. Optics* **41**, 209 (1994).
11. V. Geskin, unpublished results.

Theory and Calculations of Electric Field Effects on Hyperfine Interactions

SHASHI P. KARNA

Air Force Research Laboratory, Space Electronics and Protection Branch, 3550 Aberdeen Ave, SE, Kirtland AFB, New Mexico 87117-5776

Received 30 March 1998; accepted 14 August 1998

ABSTRACT: A recently published theory of electric field effects on electron spin resonance hyperfine couplings [Phys. Ref. Lett. 79, 379, (1997)] is extended to nuclear quadrupole coupling. With the use of the ab initio coupled Hartree-Fock approach and augmented Sadlej basis set, results are obtained for the first-order corrections to the isotropic and anisotropic parts of hyperfine coupling tensor and the electronic part of the electric field gradient tensor for ^{17}O and ^2H nuclei in OH radical. The first-order coefficients exhibit a number of interesting features. The calculated results, in general, appear to be insensitive to the bond-centered polarization functions used in the calculation. © 1998 John Wiley & Sons, Inc. Int J Quant Chem 70: 771–778, 1998

Key words: electric field effects; hyperfine interactions

Introduction

Effects of electric field on the hyperfine interaction in a paramagnetic system was first predicted by Bloembergen [1]. According to Bloembergen, if a nucleus or paramagnetic ion with $I > \frac{1}{2}$ occupies a site in a crystal lattice without inversion symmetry, an externally applied field will cause, in general, a change in the quadrupole coupling constant linearly proportional to the strength of the applied field. Later, Bloembergen [2] also predicted that the effective g -tensor and

nuclear spin-electron spin hyperfine coupling (HFC) tensor \mathbf{A} of a magnetic nucleus located at a noncentrosymmetric site in the lattice will experience changes which are linear in electric field strength.

The linear electric field effect, or the *Bloembergen effect* as it is called now [3], has been observed in numerous nuclear quadrupole resonance (NQR) and electron spin resonance (ESR) experiments on crystalline [4–15] materials. Due to its ability to provide information on the spatial symmetry of a paramagnetic site as well as the strength of the local electric field near it, there is currently interest in measuring Bloembergen effect on ESR HFC of

point defects in amorphous materials, such as $a\text{-SiO}_2$, in metal–oxide–semiconductor (MOS) devices [16].

In contrast to the experimental measurements, theoretical treatments of the electric field effects on hyperfine interaction have been rather few and generally concerned with phenomenological description [2, 17, 18] or semiempirical calculations [19]. In a recent letter [3], a general theory of the electric field effects on the nuclear spin (\mathbf{I})–electron spin (\mathbf{S}) hyperfine interaction within the perturbation approach was presented. Results for the first-order corrections corresponding to the Bloembergen effect on the ESR HFC constants of ^2H and ^{17}O nuclei in OH radical were also presented.

In this study, the theory presented in Ref. [3] is extended to nuclear quadrupole coupling constant. Expressions are derived for the coefficients representing electric-field corrections to HFC parameters and electric field gradient (EFG) tensors in terms of the matrix elements of HFC operators and perturbed spin/total density matrices. Using the theory presented here, results are obtained for the first-order corrections to HFC and EFG tensor for OH radical. Effects of bond-centered functions in the basis set on the calculated results are also investigated and discussed.

Theory

The nuclear–electron hyperfine coupling tensor \mathbf{A} appearing in the interaction Hamiltonian

$$H' = \mathbf{I} \cdot \mathbf{A} \cdot \mathbf{S} \quad (1)$$

is a combination of two terms:

$$\mathbf{A} = a + \mathbf{T}, \quad (2)$$

where, a , known as the *isotropic hyperfine coupling constant*, is a scalar quantity which results from the interaction of the electron spin magnetic moment in contact with the nuclear magnetic moment. The second term in Eq. (2), known as the *anisotropic hyperfine coupling tensor*, results from the classical dipolar interaction between electron spin magnetic moment and nuclear spin magnetic moment. The anisotropic term, \mathbf{T} , is a second-rank, traceless tensor whose principal components give the dipolar part of the HFC constant (HFCC).

For a magnetic nucleus N , with $I_N \geq 1$, there is also quadrupole moment Q_N associated with the nucleus. This quadrupole moment interacts with EFG around the nucleus leading to the splitting of

NQR spectrum. The hyperfine splitting resulting from nuclear quadrupole interaction is described by a tensor, χ , defined as

$$\chi = e\mathbf{q}Q, \quad (3)$$

where e is the electronic charge and $e\mathbf{q}$ represents the EFG tensor. For the sake of simplicity in notation, we shall denote the EFG tensor $e\mathbf{q}$ by \mathbf{R} , so that Eq. (3) can be written as

$$\chi = \mathbf{R}Q. \quad (4)$$

Similar to the anisotropic HFC tensor \mathbf{T} , χ is a second-rank, traceless tensor. In the principal axis system, the component of χ parallel to the direction of the applied field, say z , gives nuclear quadrupole coupling (NQC) constant. If we treat Q as a constant and use its scalar value, as is often done, it is clear from Eq. (4) that χ is essentially described by EFG, \mathbf{R} , which is a second-rank, traceless tensor. The EFG tensor is a sum of a nuclear term and an electronic term written as

$$\mathbf{R} = \mathbf{R}_{\text{nuc}} + \mathbf{R}_{\text{el}}. \quad (5)$$

The nuclear term \mathbf{R}_{nuc} results from the EFG due to all nuclei in the system other than the nucleus under consideration and depends on the nuclear charge and positions. The electronic part, \mathbf{R}_{el} , on the other hand, depends on EFG due to electronic charge and depends on electronic charge density. In the presence of an external electric field, both \mathbf{R}_{nuc} and \mathbf{R}_{el} would be affected: the former due to ionic movement and the latter due to polarization of electronic charge distribution. Thus, for a complete treatment of the electric field effects on χ , changes in \mathbf{R}_{nuc} as well as \mathbf{R}_{el} need to be considered. However, treating both terms at the same time quickly complicates the mathematical derivation. Therefore, in the present study, we focus our attention on the electronic part only. The effects of electric field on the nuclear part will be treated in a separate work.

Taking the scalar value of Q for a given nucleus, we can write the *electronic part* of χ tensor as

$$\chi_{\text{el}} = Q\mathbf{R}_{\text{el}}. \quad (6)$$

At this point it is useful to introduce some constant terms and matrix elements of various operators to be used. Let us define,

$$G_c = (8\pi/3)G_d, \quad (7)$$

$$G_d = (\frac{1}{2})g_e\beta_e g_N \beta_N. \quad (8)$$

The spin density, ρ^z , at a point P in space is defined as

$$\rho^z(P) = \langle \Psi | \sum_k 2S_{zk} \delta(\mathbf{r}_k) | \Psi \rangle. \quad (9)$$

The total charge density, $\rho(P)$, at point P is defined as

$$\rho(P) = \langle \Psi | \sum_k \delta(\mathbf{r}_k) | \Psi \rangle. \quad (10)$$

The matrix element, $V_{\mu\nu}^c$, of the Dirac delta operator is defined as

$$V_{\mu\nu}^c = \langle \phi_\mu | \delta(\mathbf{r}_N) | \phi_\nu \rangle. \quad (11)$$

The matrix elements, $V_{\mu\nu}^{ij}$, of the electron-nucleus dipolar interaction operator is given by

$$V_{\mu\nu}^{ij} = \langle \phi_\mu | r_N^{-5} (3r_{N_i} r_{N_j} - r_N^2 \delta_{ij}) | \phi_\nu \rangle. \quad (12)$$

In the above equations, g_e is the electronic g factor, β_e is the Bohr magneton, g_N is the nuclear g factor, β_N is the nuclear magneton, S_z is the eigenvalue of the z -component of the spin angular momentum operator, $\delta(\mathbf{r}_N)$ is the Dirac delta operator, r_N is the radius vector of an electron from nucleus N , δ_{ij} is the Kronecker delta, Ψ is the total wave function of the system, ϕ_μ , ϕ_ν represent the μ th and ν th atomic orbitals in the system, i , j represent Cartesian axes (x , y , z), and k represents the k th electron in the system. The summation index k in the definition of the spin and total charge density runs over all the electrons in the system.

Using these definitions and notations, the hyperfine and EFG terms can be written in the matrix form as

$$a = G_c \text{tr}[V^c \rho^z], \quad (13)$$

$$T_{ij} = G_d \text{tr}[V^{ij} \rho^z], \quad (14)$$

$$R_{ij} = \text{tr}[V^{ij} \rho]. \quad (15)$$

Here, tr stands for *trace*. So far it has been assumed that the system is free from any external field.

Let us now assume that an external electric field represented by $\mathbf{E}(\mathbf{r}, t) = E(r)\cos \omega t$ is applied to the system. For the sake of generality, an electric field with arbitrary frequency has been used. If this field is only sufficiently large to polarize the spin and charge distributions, we can describe the

HFCC and EFG tensor by Taylor series expansions in the applied electric field, so that

$$a(E) = a^{(0)} + \sum_k a_k^{(1)} E_k + \frac{1}{2!} \sum_k \sum_l a_{kl}^{(2)} E_k E_l + \dots, \quad (16)$$

$$T_{ij}(E) = T_{ij}^{(0)} + \sum_k T_{ijk}^{(1)} E_k + \frac{1}{2!} \sum_k \sum_l T_{ijkl}^{(2)} E_k E_l + \dots, \quad (17)$$

$$R_{ij}(E) = R_{ij}^{(0)} + \sum_k R_{ijk}^{(1)} E_k + \frac{1}{2!} \sum_k \sum_l R_{ijkl}^{(2)} E_k E_l + \dots. \quad (18)$$

In writing the above expansions, the frequency-dependent part of the electric field has been dropped for the sake of brevity. Here, $a^{(0)}$ is the field-free isotropic hyperfine coupling constant and $a_i^{(1)}$ and $a_{ij}^{(2)}$ represent the first- and the second-order corrections, respectively, to the contact term. Similarly, $T_{ij}^{(0)}$ and $R_{ij}^{(0)}$ represent the field-free terms, while $T_{ijk}^{(1)}$, $R_{ijk}^{(1)}$ and $T_{ijkl}^{(2)}$, $R_{ijkl}^{(2)}$ are the first- and second-order corrections to the anisotropic HFC tensor and EFG tensor, respectively.

The zero-order dipolar terms $\mathbf{T}^{(0)}$ and $\mathbf{R}^{(0)}$ are tensor quantities of rank 2 and their n th-order correction terms are tensor quantities of rank $m = n + 2$. The zero-order contact term, $a^{(0)}$, is a scalar and the first-order correction term, $a^{(1)}$, is a vector. The second- and higher-order corrections to the contact term are tensor quantities of ranks 2 and higher. The first-order terms $\mathbf{a}^{(1)}$ and $\mathbf{T}^{(1)}$ together describe the Bloembergen effect [1, 2] and vanish for a paramagnetic center at a site with center of inversion. Similarly, first-order EFG term, $R_{ijk}^{(1)}$, vanishes for a nucleus located at a centrosymmetric site. It is trivial to show that the first-order correction to the nuclear quadrupole coupling tensor, $\chi_{ijk}^{(1)}$, at a center with center of inversion vanishes. In fact, this is true for all odd-rank \mathbf{T} and \mathbf{R} tensors, i.e., for a nucleus located at a site with center of inversion [20],

$$\mathbf{T}^{(1)} = \mathbf{T}^{(3)} = \dots = 0. \quad (19)$$

Similarly,

$$\mathbf{R}^{(1)} = \mathbf{R}^{(3)} = \dots = 0. \quad (20)$$

The even-rank tensors $\mathbf{T}^{(0)}$, $\mathbf{T}^{(2)}$, and $\mathbf{R}^{(0)}$, $\mathbf{R}^{(2)}$ etc., on the other hand, do not have this inversion symmetry restrictions. However, the following

trace relations [20]

$$\sum_i T_{ii}^{(0)} = \sum_i T_{ij}^{(1)} = \sum_i T_{ijk}^{(2)} = 0; \quad i, j, k = x, y, z \quad (21)$$

and

$$\sum_i R_{ii}^{(0)} = \sum_i R_{ij}^{(1)} = \sum_i R_{ijk}^{(2)} = 0; \quad i, j, k = x, y, z \quad (22)$$

hold for \mathbf{T} and \mathbf{R} in all orders.

Similar to the HFC parameters, the spin density matrix, ρ^z , and the total density matrix, ρ , can be expanded in the Taylor series of the applied electric field as

$$\rho^z(E) = \rho^{z(0)} + \sum_k \rho_k^{z(1)} E_k + \frac{1}{2!} \sum_k \sum_l \rho_{kl}^{z(2)} E_k E_l + \dots, \quad (23)$$

$$\rho(E) = \rho^{(0)} + \sum_k \rho_k^{(1)} E_k + \frac{1}{2!} \sum_k \sum_l \rho_{kl}^{(2)} E_k E_l + \dots, \quad (24)$$

Substituting Eqs. (16) and (17) on the left-hand side of Eqs. (13) and (14), respectively, substituting Eq. (23) for the spin density matrix on the right-hand side, and separating terms with the equal coefficients in the resulting two equations, we obtain

$$a^{(0)} = G_c \text{tr}[\mathbf{V}^c \rho^{z(0)}], \quad (25)$$

$$a_i^{(1)} = G_c \text{tr}[\mathbf{V}^c \rho_i^{z(1)}], \quad (26)$$

$$a_{ij}^{(2)} = G_c \text{tr}[\mathbf{V}^c \rho_{ij}^{z(2)}] \quad (27)$$

⋮

and

$$T_{ij}^{(0)} = G_d \text{tr}[\mathbf{V}^{ij} \rho^{z(0)}], \quad (28)$$

$$T_{ijk}^{(1)} = G_d \text{tr}[\mathbf{V}^{ij} \rho_k^{z(1)}], \quad (29)$$

$$T_{ijkl}^{(2)} = G_d \text{tr}[\mathbf{V}^{ij} \rho_{kl}^{z(2)}] \quad (30)$$

⋮

Similarly, substituting Eq. (18) on the left-hand side and Eq. (24) for the charge density matrix, ρ , on the right-hand side of Eq. (15) and separating terms with equal coefficients, we get

$$R_{ij}^{(0)} = \text{tr}[\mathbf{V}^{ij} \rho^{(0)}], \quad (31)$$

$$R_{ijk}^{(1)} = \text{tr}[\mathbf{V}^{ij} \rho_k^{(1)}], \quad (32)$$

$$R_{ijkl}^{(2)} = \text{tr}[\mathbf{V}^{ij} \rho_{kl}^{(2)}] \quad (33)$$

⋮

In deriving the above expressions, it has been assumed that the matrix elements of the contact operator, $V_{\mu\nu}^c$, and the dipolar interaction operator, $V_{\mu\nu}^{ij}$, over atomic functions are not affected by the external electric field. Although it is rigorously true only in the limit of the complete basis set, the effects of the electric field on the basis functions, in general, are too small to invalidate the assumptions made here.

Equations (25)–(33) provide a means to calculate electric field effects to HFC interaction from a knowledge of the matrix elements of the Dirac delta operator, dipolar interaction operator, and perturbed spin and total density matrices. The calculation of the matrix elements $V_{\mu\nu}^c$ and $V_{\mu\nu}^{ij}$ is rather trivial. However, the same is not true for the calculation of the perturbed spin density and the charge density matrices. The simplest and a straightforward approach to calculate the static as well as the dynamic density matrices is the time-dependent coupled Hartree–Fock (TDCHF) theory [21]. In this work we use the TDCHF approach to calculate the first-order coefficients.

Calculations

We calculated the elements of the first-order coefficients $a^{(1)}$, $\mathbf{T}^{(1)}$, and $\mathbf{R}^{(1)}$ along with their zero-order counterparts for the ^{17}O and ^2H nuclei in OH radical. The first-order density matrices, $\rho^{z(1)}(\omega)$ and $\rho^{(1)}(\omega)$, were calculated via spin-unrestricted time-dependent Hartree–Fock (TDHF) method [22]. The calculations were performed at an internuclear distance $R(\text{OH}) = 1.95$ bohr using Sadlej basis set [23]. The Sadlej basis was further augmented by successively adding an $s(3.80)$, a $p(1.85)$, and a $d(0.925)$ function centered in the middle of the O–H bond. Numbers inside parentheses are the exponents of the auxiliary functions. Frequency-dependent calculations were performed at an optical wavelength, $\lambda = 694.3$ nm.

Results and Discussion

The calculated results are listed in Tables I through VII. For the sake of completeness, the

calculated values of the dipole moment, μ , and electric polarizability, α , are also listed in Table I along with the total energy. The bond functions systematically lower the total energy (Table I). However, the calculated properties (Tables I–VII), in general, seem to be insensitive to the additions of the bond functions. The Sadlej basis set [23] is fairly large and includes appropriate functions to accurately describe the core and valence regions of the molecule. Therefore, it is possible that additional s , p , and d functions in the middle of the bond do not modify the charge and spin distributions. On the other hand, the exponents of the bond functions, chosen somewhat arbitrarily, may

be too large. An optimized set of functions would perhaps exhibit noticeable effect.

The zero-order HFC parameters for the ^2H nucleus in OH are available from gas-phase ESR experiments [24, 25]. Results of the present calculations are compared with experiment in Table V. The calculated values of ${}^2\text{H}(a^{(0)})$ are about twice as large as their experimental counterpart. On the other hand, the calculated values of the principal components of ${}^2\text{H}(\mathbf{T}^{(0)})$ are in good agreement with experiment. These results are consistent with other studies [26], whereby it is known that the unrestricted Hartree–Fock theory, as used in the present calculations, generally overestimates the

TABLE I
Calculated values of total energy, E (a.u.), dipole moment, μ (D), and polarizability, α (10^{-24} cm^3)^a of OH.

Basis set ^b	A	A + s	A + p	A + sp	A + spd
$E(-75.0 - x)^c$	0.411732	0.412041	0.412290	0.412482	0.413052
μ	1.806	1.805	1.806	1.805	1.805
$\alpha_{xx}(0)$	0.8441	0.8442	0.8445	0.8447	0.8471
$\alpha_{yy}(0)$	0.9916	0.9916	0.9923	0.9923	0.9937
$\alpha_{zz}(0)$	1.3007	1.3011	1.3010	1.3012	1.3003
$\langle \alpha(0) \rangle$	1.0455	1.0457	1.0459	1.0461	1.0470
$\alpha_{xx}(\omega)$	0.8547	0.8549	0.8552	0.8554	0.8578
$\alpha_{yy}(\omega)$	1.0050	1.0050	1.0056	1.0057	1.0071
$\alpha_{zz}(\omega)$	1.3167	1.3173	1.3172	1.3174	1.3165
$\langle \alpha(\omega) \rangle$	1.0588	1.0591	1.0594	1.0595	1.0604

^a $\alpha(\omega)$ calculated at $\lambda = 694.3$ nm.

^b A = Sadlej basis.

^c x is the number listed in this row.

TABLE II
Calculated values of zero-order isotropic HFC constant, $a^{(0)}$, anisotropic HFC tensor, $\mathbf{T}^{(0)}$, NQC tensor, $\chi^{(0)}$, and asymmetry parameter, η , for ${}^{17}\text{O}$ in OH radical.^a

Basis set	A	A + s	A + p	A + sp	A + spd
$a^{(0)}$	-84.92	-84.77	-85.33	-85.42	-85.21
$T_{xx}^{(0)}$	-269.60	-269.60	-269.02	-269.98	-270.58
$T_{yy}^{(0)}$	138.09	138.14	137.55	137.62	138.52
$T_{zz}^{(0)}$	131.51	131.46	131.47	131.36	132.06
$\chi_{xx}^{(0)}$	-3.80	-3.90	-3.52	-3.63	-3.90
$\chi_{yy}^{(0)}$	-12.82	-12.78	-12.86	-12.81	-12.86
$\chi_{zz}^{(0)}$	16.62	16.68	16.38	16.44	16.76
η^b	0.5426	0.5325	0.5407	0.5583	0.5348

^a All results, except for the values of η , are in MHz.

^b $\eta = |\chi_{xx}^{(0)} - \chi_{yy}^{(0)}| / \chi_{zz}^{(0)}$.

TABLE III
Nonzero components of $\mathbf{a}^{(1)}$ and $\mathbf{T}^{(1)}$ for ^{17}O in OH radical.^{a,b}

Basis set	A	A + s	A + p	A + sp	A + spd
$a_z^{(1)}(0)$	-79.68	-79.21	-79.99	-79.54	-79.01
$a_z^{(1)}(\omega)$	-82.23	-81.70	-82.51	-82.04	-81.50
$T_{xxz}^{(1)}(0)$	5.62	5.80	5.54	5.72	5.47
$T_{yyz}^{(1)}(0)$	-12.60	-12.47	-12.63	-12.48	-12.29
$T_{zxx}^{(1)}(0)$	30.78	30.88	30.69	30.65	31.69
$T_{zyy}^{(1)}(0)$	2.16	1.98	2.19	2.03	2.24
$T_{zzz}^{(1)}(0)$	6.97	6.67	7.08	6.76	6.83
$T_{xxz}^{(1)}(\omega)$	5.58	5.63	5.36	5.54	5.29
$T_{yyz}^{(1)}(\omega)$	-13.12	-13.09	-13.26	-13.11	-12.92
$T_{zxx}^{(1)}(\omega)$	38.24	38.36	38.25	38.23	39.43
$T_{zyy}^{(1)}(\omega)$	2.79	2.65	2.87	2.70	2.92
$T_{zzz}^{(1)}(\omega)$	7.54	7.45	7.90	7.56	7.63

^aAll results are in the units of (10^{-11} MHz m/V).

^bFrequency-dependent coefficients calculated at $\lambda = 694.3$ nm.

isotropic HFC of first-row elements by about a factor of 2 but yields fairly accurate values for the dipolar terms. We, therefore, believe that the dipolar terms calculated in this work are fairly accurate, whereas the coefficients involving Dirac delta operator should be in error by a factor of about 2. We also believe, however, that the ratio ($a^{(1)}/a^{(0)}$) describing the Bloembergen shift in the ESR hyper-

fine spectrum due to s-type electrons should be reasonably accurate.

An inspection of the results for the first-order coefficients, $\mathbf{a}^{(1)}$, $\mathbf{T}^{(1)}$, and $\mathbf{R}^{(1)}$, reveals a number of interesting features. First, we note that the magnitude of the nonzero element of $\mathbf{a}^{(1)}$ is considerably larger than any component of $\mathbf{T}^{(1)}$. We also note that whereas for ^{17}O , $a_z^{(1)}$ has the same sign as its

TABLE IV
Components of $\mathbf{R}_{\text{el}}^{(0)}$ (a.u.) and $\mathbf{R}_{\text{el}}^{(1)}$ (10^{-11} a.u. m/V) for ^{17}O in OH radical.^a

Basis set	A	A + s	A + p	A + sp	A + spd
$R_{xx}^{(0)}$	-2.2519	-2.2444	-2.2586	-2.2495	-2.2577
$R_{yy}^{(0)}$	2.6098	2.6180	2.5693	2.5791	2.6314
$R_{zz}^{(0)}$	-0.3579	-0.3736	-0.3107	-0.3296	-0.3737
$R_{xxz}^{(1)}(0)$	-0.7025	-0.7024	-0.7060	-0.7066	-0.7061
$R_{yyz}^{(1)}(0)$	-0.9314	-0.9318	-0.9252	-0.9262	-0.9324
$R_{zxx}^{(1)}(0)$	0.5800	0.5785	0.5854	0.5845	0.5958
$R_{zyy}^{(1)}(0)$	0.2887	0.2817	0.2957	0.2899	0.2914
$R_{zzz}^{(1)}(0)$	1.6339	1.6342	1.6311	1.6328	1.6385
$R_{xxz}^{(1)}(\omega)$	-0.7140	-0.7142	-0.7179	-0.7185	-0.7180
$R_{yyz}^{(1)}(\omega)$	-0.9499	-0.9504	-0.9436	-0.9447	-0.9511
$R_{zxx}^{(1)}(\omega)$	0.6757	0.6739	0.6829	0.6815	0.6945
$R_{zyy}^{(1)}(\omega)$	0.3114	0.3046	0.3191	0.3130	0.3146
$R_{zzz}^{(1)}(\omega)$	1.6639	1.6646	1.6615	1.6632	1.6691

^aFrequency-dependent coefficients calculated at $\lambda = 694.3$ nm.

TABLE V

Results for the zero-order isotropic HFC constant $a^{(0)}$, anisotropic HFC tensor, $T^{(0)}$, NQC tensor, $\chi^{(0)}$, and asymmetry parameter, η , for ^2H in OH radical.^a

Basis set	A	A + s	A + p	A + sp	A + spd	Expt. ^b
$a^{(0)}$	-125.52	-124.08	-121.21	-121.47	-121.66	-64.74
$T_{xx}^{(0)}$	-25.43	-24.51	-24.64	-24.08	-21.20	-17.514
$T_{yy}^{(0)}$	-66.55	-65.61	-66.03	-65.43	-68.18	-60.326
$T_{zz}^{(0)}$	91.98	90.12	90.67	89.52	89.38	77.56
$\chi_{xx}^{(0)}$	-0.0780	-0.0732	-0.0705	-0.0680	-0.0682	
$\chi_{yy}^{(0)}$	-0.1311	-0.1262	-0.1242	-0.1217	-0.1181	
$\chi_{zz}^{(0)}$	0.2091	0.1994	0.1947	0.1897	0.1863	
η^c	0.2536	0.2658	0.2761	0.2833	0.2678	

^a Units for a and the components of T and χ are MHz.

^b Ref. [24].

^c See footnote of Table II for the definition.

zero-order counterpart, in the case of the ^2H nucleus the sign of $a_z^{(1)}$ is opposite to that of $a_z^{(0)}$. This suggests that an external electric field may cause either an increase or a decrease in the ESR HFC splitting.

Second, we note that the elements of static as well as dynamic $T^{(1)}$ and $R^{(1)}$ obey the trace relations given in Eqs. (21) and (22), respectively. It is also interesting to note that the elements of the dipolar terms $T^{(1)}$ and $R^{(1)}$ do not exhibit a permutational symmetry known as the Kleinman symmetry [27] that is exhibited by the electric hyperpolarizability tensor, β , in the static field limit.

Finally, we note that the elements of $a^{(1)}$, $T^{(1)}$, and $R^{(1)}$ exhibit considerable frequency dependence. Thus, the extent of Bloembergen shift in ESR or NQR hyperfine splitting will depend on the frequency of the external field.

Summary

We have presented here a general theory of electric field effects on hyperfine parameters. With the help of the ab initio TDCHF approach and extended set of basis functions, results were ob-

TABLE VI

Nonzero components of $a^{(1)}$ and $T^{(1)}$ for ^2H in OH radical.^a

Basis set	A	A + s	A + p	A + sp	A + spd
$a_z^{(1)}(0)$	51.70	50.97	51.33	50.82	49.50
$a_z^{(1)}(\omega)$	54.39	54.91	55.32	54.78	53.40
$T_{xxz}^{(1)}(0)$	3.76	3.86	3.85	3.91	3.38
$T_{yyz}^{(1)}(0)$	11.95	12.02	12.02	12.07	12.98
$T_{zxx}^{(1)}(0)$	-13.65	-13.62	-13.67	-13.65	-12.83
$T_{zyy}^{(1)}(0)$	7.08	7.06	7.20	7.20	7.30
$T_{zzz}^{(1)}(0)$	-15.71	-15.88	-15.87	-15.98	-16.36
$T_{xxz}^{(1)}(\omega)$	4.07	4.27	4.26	4.32	3.80
$T_{yyz}^{(1)}(\omega)$	12.26	12.44	12.44	12.49	13.42
$T_{zxx}^{(1)}(\omega)$	-12.18	-12.15	-11.87	-11.84	-10.87
$T_{zyy}^{(1)}(\omega)$	7.30	7.30	7.44	7.44	7.53
$T_{zzz}^{(1)}(\omega)$	-16.33	-16.71	-16.70	-16.81	-17.21

^a Frequency-dependent coefficients calculated at $\lambda = 694.3$ nm. The unit is 10^{-11} MHz m/V.

TABLE VII
Components of $R_{el}^{(0)}$ (a.u.) and $R_{el}^{(1)}$ (10^{-11} a.u. m/V) for ^2H in OH radical.^a

Basis set	A	A + s	A + p	A + sp	A + spd
$R_{xx}^{(0)}$	-0.9628	-0.9700	-0.9740	-0.9777	-0.9774
$\dots 06 R_{yy}^{(0)}$	-0.8838	-0.8911	-0.8940	-0.8978	-0.9031
$R_{zz}^{(0)}$	1.8466	1.8611	1.8680	1.8755	1.8805
$R_{xxz}^{(1)}(0)$	-0.0673	-0.0659	-0.0664	-0.0655	-0.0651
$R_{yyz}^{(1)}(0)$	-0.0890	-0.0876	-0.0884	-0.0875	-0.0863
$R_{zxx}^{(1)}(0)$	0.0523	0.0522	0.0525	0.0523	0.0512
$R_{zyy}^{(1)}(0)$	0.0273	0.0272	0.0276	0.0275	0.0258
$R_{zzz}^{(1)}(0)$	0.1563	0.1535	0.1548	0.1530	0.1513
$R_{xxz}^{(1)}(\omega)$	-0.0684	-0.0670	-0.0676	-0.0667	-0.0662
$R_{yyz}^{(1)}(\omega)$	-0.0902	-0.0888	-0.0896	-0.0887	-0.0872
$R_{zxx}^{(1)}(\omega)$	0.0491	0.0490	0.0493	0.0491	0.0497
$R_{zyy}^{(1)}(\omega)$	0.0265	0.0265	0.0270	0.0269	0.0251
$R_{zzz}^{(1)}(\omega)$	0.1586	0.1558	0.1572	0.1554	0.1534

^a Frequency-dependent coefficients calculated at $\lambda = 694.3$ nm.

tained for the first-order corrections to ESR HFC parameters and EFG tensor for OH radical. These coefficients exhibit some very interesting features which may be useful in probing microscopic structure and properties of paramagnetic sites in solids. For a reliable prediction of these coefficients, particularly the contact terms, a more accurate theoretical technique than TDUHF is required. We hope that the present work will serve as a stimulus for further theoretical development and calculations and experimental exploration of the electric field effects on hyperfine interaction.

ACKNOWLEDGMENT

Helpful discussions with Dr. Gerry Lushington and Professor Henry Kurtz are gratefully acknowledged.

References

- N. Bloembergen, Science **133**, 1363 (1961).
- N. Bloembergen, Phys. Rev. Lett. **7**, 90 (1961).
- S. P. Karna, Phys. Rev. Lett. **79**, 379, 4516 (1997).
- G. W. Ludwig and H. H. Woodbury, Phys. Rev. Lett. **7**, 240 (1961).
- P. S. Pershan and N. Bloembergen, Phys. Rev. Lett. **7**, 165 (1961).
- J. O. Artman and J. C. Murphy, Bull. Am. Phys. Soc. **7**, 14 (1962).
- J. J. Kerbs, Bull. Am. Phys. Soc. **8**, 259 (1963).
- E. B. Royce and N. Bloembergen, Phys. Rev. **131**, 1912 (1963).
- W. B. Mims, Phys. Rev. **133**, A835 (1964).
- L. G. Rowan, E. L. Hahn, and W. B. Mims, Phys. Rev. **137**, A61 (1965).
- W. B. Mims, Phys. Rev. **140**, A531 (1965).
- A. Kiel and W. B. Mims, Phys. Rev. **153**, 378 (1967).
- W. B. Mims and J. Peisach, J. Chem. Phys. **64**, 1074 (1976).
- W. B. Mims, J. Peisach, and J. L. Davis, J. Chem. Phys. **64**, 5536 (1977).
- W. B. Mims, *The Linear Electric Field Effect in Paramagnetic Resonance* (Clarendon, Oxford, 1976).
- M. Lilis, P. M. Lenahan, H. A. Kurtz, and S. P. Karna, *Proceedings of the 28th IEEE Semiconductor Specialists Conference*, Charleston, SC, December 4–7, 1997.
- F. S. Ham, Phys. Rev. Lett. **7**, 242 (1961).
- A. Kiel, Phys. Rev. **148**, 247 (1966).
- B. S. Gerstman and A. S. Brill, Phys. Rev. A **39**, 5903 (1989).
- J. Armstrong, N. Bloembergen, and D. Gill, Phys. Rev. Lett. **7**, 11 (1961).
- H. Sekino and R. J. Bartlett, J. Chem. Phys. **85**, 976 (1986).
- S. P. Karna, J. Chem. Phys. **104**, 6590, (1990); *Ibid.*, **105**, 6091 (1996).
- A. D. Sadlej, Theor. Chem. Acta **79**, 123 (1991).
- K. Toriyama and M. Iwasaki, J. Chem. Phys. **55**, 1890 (1971).
- H. E. Radford, Phys. Rev. **122**, 114 (1961).
- S. P. Karna and F. Grein, Int. J. Quant. Chem. **36**, 265 (1989).
- D. A. Kleinman, Phys. Rev. **126**, 1977 (1962).

Differential Equations for Ground-State Electron Density and Slater Sum in Atoms and Molecules With and Without External Fields

N. H. MARCH

University of Oxford, Oxford, England

Received 21 February 1998; accepted 8 June 1998

ABSTRACT: The ground-state density amplitude $\{\rho(\mathbf{r})\}^{1/2}$ for atoms and molecules satisfies a Schrödinger equation in which the customary one-body potential energy $V(\mathbf{r})$ of density functional theory is supplemented by the addition of the Pauli potential $V_p(\mathbf{r})$. Since neither the exchange-correlation potential V_{xc} or V_p are presently known as functionals of the electron density $\rho(\mathbf{r})$, approximations are currently unavoidable. Here, widespread use is made of semiclassical approximations, within a self-consistent field framework both with and without magnetic fields. The importance of low-order gradient quantities $\nabla^2\rho/\rho$ and $(\nabla\rho/\rho)^2$ is one focal point, while a generalized low-density approximation is another. New relativistic differential equations are given. Then, the arguments are generalized to embrace the so-called Slater sum $P(\mathbf{r}, \beta)$: $\beta = (k_B T)^{-1}$, of statistical mechanics, generated by the one-body potential $V(\mathbf{r})$. This is a generalized partition function, and differential equations are set up for this quantity $P(\mathbf{r}, \beta)$ with and without external fields. Finally, some potentially fruitful directions for treating cylindrically symmetric inhomogeneous electron liquids are outlined, following the very recent work of Amovilli and March. These include modeling the Slater sum along the electric field direction for the Stark effect in a hydrogenlike atom. © 1998 John Wiley & Sons, Inc. *Int J Quant Chem* 70: 779–788, 1998

Correspondence to: N. H. March, 6 Northcroft Road, Egham, Surrey TW20 0DU, England.

Contract grant sponsor: Office of Naval Research.

1. Introduction

Even for atoms described by the nonrelativistic Schrödinger equation, for the number of electrons N exceeding a certain rather small integer, the many-electron wave function $\Psi(\mathbf{r}_1 \dots \mathbf{r}_N; \sigma_1 \dots \sigma_N)$ with \mathbf{r}_n and σ_n representing space and spin coordinates of the n th electron contains a great deal of redundant information. Therefore, Löwdin [1], Coleman [2], McWeeny [3], and others proposed to work with reduced density matrices, defined from Ψ in a way described for example by Löwdin [1]. For a customary nonrelativistic Hamiltonian H , the ground-state energy E is well known to be determined by the first-order spinless density matrix (1 DM) $\gamma(\mathbf{r}_1, \mathbf{r}'_1)$ and the (diagonal element of the) second-order matrix (2 DM) $\gamma_2(\mathbf{r}_1 \mathbf{r}_2; \mathbf{r}'_1 \mathbf{r}'_2)$.

In density functional theory, theorems exist [4] which show formally that $E = E[\rho]$ and the important exchange-correlation potential energy $V_{xc}[\rho]$, related to the energy component $E_{xc}[\rho]$ of $E[\rho]$ containing exchange plus correlation contributions by the functional derivative relation

$$V_{xc}[\rho] = \frac{\delta E_{xc}[\rho]}{\delta \rho(\mathbf{r})}, \quad (1.1)$$

are, as indicated notationally above, functionals of the electron density $\rho(\mathbf{r})$, related to 1 DM $\gamma(\mathbf{r}_1, \mathbf{r}'_1)$ by

$$\rho(\mathbf{r}) = \gamma(\mathbf{r}, \mathbf{r}). \quad (1.2)$$

Very recently, Holas and March [5, 6] obtained $V_{xc}[\rho]$ exactly in terms of γ and γ_2 , plus the single-electron reference system defined formally by the Slater-Kohn-Sham (SKS) Schrödinger equations [7] characterized by the one-body potential $V(\mathbf{r})$. Holas and March [5] described this reference system, not, of course, exactly available because of the as yet unknown V_{xc} , by noninteracting density matrices γ_s and γ_{2s} defined from a single Slater determinant formed from the occupied SKS one-electron orbitals, that is,

$$V_{xc} \equiv V_{xc}[\gamma, \gamma_2; \gamma_s, \gamma_{2s}]. \quad (1.3)$$

The N -representability problem arises with γ and γ_2 : namely, how one knows that approximate forms of, say, γ_2 came from an antisymmetric

N -electron ground-state wave function Ψ . One must expect especially from the work of Coleman [2] (see also Young and March [8] on the jellium model) that ad hoc approximations to V_{xc} in atoms and molecules can lead to ground-state energies below the exact ground-state energy E , in spite of the variational basis of density functional theory. Therefore, Holas and March [6] subsequently proposed a method which, in principle, can bypass the N -representability problem associated with Eq. (1.3) by employing diffraction experiments. It remains to be seen, however, what accuracy can be achieved for $V_{xc}(\mathbf{r})$ for a specific system (e.g., Be metal: Brown [9], Coppens [10], and Massa et al. [11]) by the Holas-March proposal. Of course, one must hope that, if this approach has useful accuracy for $V_{xc}(\mathbf{r})$, building up a body of results of $V_{xc}(\mathbf{r})$ will lead one toward the construction of "variationally acceptable" approximations to $V_{xc}[\rho]$.

However, all this is for the future, and in the present article, we focus directly on the differential equation satisfied by the ground-state density amplitude $\{\rho(r)\}^{\frac{1}{2}}$. This equation takes the form

$$\nabla^2 \rho^{\frac{1}{2}} + \frac{2m}{\hbar^2} [-|I| - V_p(\mathbf{r}) - V(\mathbf{r})] \rho^{\frac{1}{2}} = 0, \quad (1.4)$$

with $|I|$ the ionization potential. The historical background of this equation was discussed by Levy and Görling [12]: the potential energy $V_p(\mathbf{r})$ being termed the Pauli potential ([13], see also Herring and Chopra [14] and Holas and March [15]).

In Eq. (1.4), $V(\mathbf{r})$, of course, as defined above characterizes the SKS Schrödinger equations, while $V_p(\mathbf{r})$ is a one-electron quantity defined by

$$V_p(\mathbf{r}) = \frac{\delta T_s[\rho]}{\delta \rho(\mathbf{r})} - \frac{\delta T_w[\rho]}{\delta \rho(\mathbf{r})}. \quad (1.5)$$

While $T_w[\rho]$, the von Weizäcker inhomogeneity kinetic energy, has the form [7]

$$T_w[\rho] = \frac{\hbar^2}{8m} \int \frac{(\nabla \rho)^2}{\rho} d\mathbf{r}, \quad (1.6)$$

the single-particle kinetic energy functional $T_s[\rho]$ remains unknown (and current practice, of course, is to bypass it by calculating single-particle kinetic energies from the one-electron orbitals generated by the SKS equations). It will be useful below to write the effective potential $V_{eff}(\mathbf{r})$ entering the

density amplitude Eq. (1.4) as

$$\begin{aligned} V_{eff}(\mathbf{r}) &= V_p(\mathbf{r}) + V(\mathbf{r}) \\ &= V_p(\mathbf{r}) + V_H(\mathbf{r}) + V_{xc}(\mathbf{r}), \end{aligned} \quad (1.7)$$

where $V_H(\mathbf{r})$ is the Hartree potential generated by $\rho(\mathbf{r})$ and the potential energy of the nuclear framework of the molecule under investigation. Evidently, except at point nuclei, Poisson's equation relates $V_H(\mathbf{r})$ to the ground-state density $\rho(\mathbf{r})$ by

$$\nabla^2 V_H(\mathbf{r}) = -4\pi\rho(\mathbf{r})e^2, \quad (1.8)$$

which expresses the requirement of self-consistency. Equation (1.8) plays a crucial role in the setting up of explicit, although, of course, approximate, equations for the electron density $\rho(\mathbf{r})$ below. Let us begin by using the simplest semiclassical approach, the Thomas–Fermi statistical method, the forerunner of modern density functional theory [7, 16].

2. Semiclassical Differential Equation for Ground-State Electron Density $\rho(\mathbf{r})$

Using the variational principle

$$\delta [E - N\mu] = 0, \quad (2.1)$$

where μ is the Lagrange multiplier taking care of the density normalization

$$\int \rho d\mathbf{r} = N, \quad (2.2)$$

having the physical significance that it is the constant chemical potential of the electronic charge cloud throughout the inhomogeneous density distribution $\rho(\mathbf{r})$, one has in Thomas–Fermi (TF) theory, with $T_s(\rho) = c_k \int \rho(\mathbf{r})^{5/3} d\mathbf{r}$:

$$\mu = \frac{5}{3}c_k \rho^{2/3} + V_n(\mathbf{r}) + V_e(\mathbf{r}), \quad (2.3)$$

where $V_n(\mathbf{r}) + V_e(\mathbf{r})$ is the Hartree potential $V_H(\mathbf{r})$ already introduced in Eq. (1.7) above, n denoting the nuclei, and e , the electrostatic potential of the electronic charge cloud $\rho(\mathbf{r})$, and $c_k = (3\hbar^2/10m) \times (3/8\pi)^{2/3}$.

Operating with the Laplacian ∇^2 on Eq. (2.3) and utilizing Poisson's Eq. (1.8) then yields after a short calculation the result [17]

$$\frac{\nabla^2 \rho}{\rho} - \frac{1}{3} \left(\frac{\nabla \rho}{\rho} \right)^2 = \frac{\rho^{1/3}}{l_1}, \quad (2.4)$$

where the length l_1 is a pure number given by

$$l_1 = \frac{1}{4} \left(\frac{\pi}{3} \right)^{1/3} a_0 : a_0 = \hbar^2/me^2. \quad (2.5)$$

Equation (2.4) is the simplest of the self-consistent-field equations for the electron density to be displayed in the present study.

2.1. MODIFICATION OF ZERO-FIELD EQ. (2.4) FOR ATOMS IN INTENSE MAGNETIC FIELDS OF STRENGTH B

Solving Eq. (2.3) yields $\rho(\mathbf{r}) \propto [\mu - V_H(\mathbf{r})]^{3/2}$, which is the three-dimensional TF density-potential relation. However, for atoms in intense fields, the cyclotron radius l_B defined by

$$l_B = \frac{1}{B^{1/2}} \left(\frac{\hbar}{e} \right)^{1/2} \quad (2.6)$$

must enter the equation for $\rho(\mathbf{r}, B)$. Motion along the magnetic field is still determined by V_H through a one-dimensional TF factor $[\mu_B - V_H(\mathbf{r})]^{1/2}$, where the chemical potential now depends on the field strength B . But this is proportional to a number of electrons/unit length, and, hence, the number $\rho(\mathbf{r}, B)$ per unit volume has the form

$$\rho(\mathbf{r}, B) = \frac{\text{constant} [\mu_B - V_H(\mathbf{r})]^{1/2}}{l_B^2}. \quad (2.7)$$

Kadomtsev [18] was the first to derive Eq. (2.7) (see also Banerjee et al. [19]) and the explicit form is

$$\rho(\mathbf{r}, B) = \text{constant } B [\mu - V_H(\mathbf{r})]^{1/2}, \quad (2.8)$$

where the constant is as in [18] and [19]. Thus, squaring Eq. (2.8), one has

$$\mu_{TF}^{(B)} = \frac{\text{constant } \rho^2(\mathbf{r}, B)}{B^2} + V_H(\mathbf{r}). \quad (2.9)$$

Of course, Eq. (2.9) cannot be employed for other than large B . A form unifying Eqs. (2.3) and (2.9) was given by Pfalzner and March [20] but we shall not go into this generalization here.

Combining Eq. (2.9) with Poisson's Eq. (1.8) yields then

$$0 = -4\pi e^2 \rho(r) + \frac{\text{constant}}{B^2} \nabla^2 [\rho^2(\mathbf{r}, B)]$$

or

$$\frac{1}{\pi^3 \rho a_0^4} = \frac{\nabla^2 \rho}{\rho} + \left(\frac{\nabla \rho}{\rho} \right)^2. \quad (2.10)$$

For atoms, solutions of this equation can be constructed from the earlier work of Hill et al. [21] who solved for the Hartree potential $V_H(r)$ for atomic ions. In the above TF theory, the atoms remain spherical, and so in some sense, the semiclassical limit corresponds to “small” B . Lieb et al. [22] showed, in fact, that one must distinguish for atoms regimes of both B and atomic number Z large, but still one can have $B/Z^3 \ll 1$, $B/Z^3 \sim 1$ and $B/Z^3 \gg 1$ regimes. The first is the TF regime, while the last is the hyperstrong (HS) field regime in which atoms become “needles.”

3. Density Amplitude Differential Equation for Atomic Needles

Following Lieb et al. [22], one can construct a density matrix theory which eventually yields a differential equation for the density amplitude $\rho^{1/3}(z) \equiv \psi(z)$, with z along the field. This equation takes the form

$$-\psi''(z) - \delta(z)\psi(o) + \psi^3(z) = \text{const } \psi(z), \quad (3.1)$$

with physical solution, for $\lambda = N/Z < 2$,

$$\psi(z) = \frac{2^{1/2}(2 - \lambda)}{4 \sinh[\frac{1}{4}(2 - \lambda)|z| + c]}, \quad (3.2)$$

with $\tanh c = (2 - \lambda)/2$. For $\lambda \leq 2$, the energy is given by

$$E^{HS}(\lambda) = -\frac{1}{4}\lambda + \frac{1}{8}\lambda^2 - \frac{1}{48}\lambda^3 \quad (3.3)$$

and the corresponding chemical potential equation is

$$Z\mu_{HS} = -\frac{1}{4} + \frac{1}{4}\lambda - \frac{\lambda^2}{16}. \quad (3.4)$$

Lehmann and March [23] discussed the Pauli potential V_p from Eq. (3.1). This method shows that atomic needles can bind $2Z$ electrons to an atomic nucleus carrying charge Ze . One must expect ter-

restrial chemistry to be totally changed in the atmosphere of a neutron star [24].

We do not, presently, have a theory to enable us to pass smoothly from the semiclassical high-field TF theory characterized by the differential Eq. (2.10) to the Lieb et al. [22] eq. (3.1), that is, from spherical atoms to needles.

4. Inclusion of Exchange

So far, we have neglected the potential $V_x(r)$ in the original density amplitude equation. Let us next incorporate the Dirac-Slater (DS) exchange potential

$$V_x^{DS}(\mathbf{r}) = -\frac{4}{3}c_x \rho^{1/3} : c_x = \frac{3e^2}{4} \left(\frac{3}{\pi} \right)^{1/3}. \quad (4.1)$$

Then, the chemical potential equation of the Thomas-Fermi-Dirac [16, 7] theory reads

$$\mu_{TFD} = \frac{5}{3}c_k \rho(r)^{2/3} + V_H(r) - \frac{4}{3}c_x \rho^{1/3}. \quad (4.2)$$

Again, let us take the Laplacian of Eq. (4.2) to find

$$0 = \frac{5}{3}c_k \nabla \left\{ \frac{2}{3}\rho^{-\frac{1}{3}}\nabla\rho \right\} - 4\pi\rho e^2 - \frac{4}{3}c_x \nabla \left\{ \frac{1}{3}\rho^{-\frac{2}{3}}\nabla\rho \right\} \quad (4.3)$$

or

$$4\pi\rho e^2 = \frac{10}{9}c_k \left[\rho^{-\frac{1}{3}}\nabla^2\rho - \frac{1}{3}\rho^{-\frac{4}{3}}(\nabla\rho)^2 \right] - \frac{4}{9}c_x \left[\rho^{-\frac{2}{3}}\nabla^2\rho - \frac{2}{3}\rho^{-\frac{5}{3}}(\nabla\rho)^2 \right]. \quad (4.4)$$

Defining

$$L^{(i)} = \frac{\nabla^2 \rho}{\rho} - \frac{i}{3} \left(\frac{\nabla \rho}{\rho} \right)^2, \quad (4.5)$$

we find from Eq. (4.4)

$$4\pi\rho^{1/3}e^2 = \frac{10}{9}c_k L^{(1)} - \frac{4}{9}c_x \rho^{-\frac{4}{3}}[L^{(2)}]. \quad (4.6)$$

Equation (4.6) generalizes Eq. (2.4) to include the effect of Dirac-Slater exchange. The relativistic generalization of Eqs. (2.4) and (4.6) is effected in Appendix 1 below. The high-field Eq. (2.10) also has a relativistic analog, which is derived in Appendix 2.

5. Inclusion of Gellmann–Brueckner High-Density Correlation Energy

We next treat the effect on the differential Eq. (4.6) for the ground-state density of including the Gellmann–Brueckner [25] correlation energy, as obtained from the high-density limit of the jellium model. This has been achieved in the work of March et al. [26].

The chemical potential equation becomes then

$$\mu_{TFDC} = \frac{5}{3} c_k \rho^{2/3}(\mathbf{r}) - \frac{4}{3} c_x \rho^{1/3}(\mathbf{r}) - c_c \ln \rho(\mathbf{r}) + V_H(\mathbf{r}). \quad (5.1)$$

When we apply the Laplacian operator to Eq. (5.1), we find the new term beyond the TFD theory to have the form

$$\nabla^2 \ln \rho = \nabla \cdot \left(\frac{\nabla \rho}{\rho} \right) = \frac{\nabla^2 \rho}{\rho} - \left(\frac{\nabla \rho}{\rho} \right)^2 \equiv L^{(3)}. \quad (5.2)$$

Hence, as March et al. [26] emphasized, the dependence of the self-consistent-field problem on the reduced density gradient variables $\nabla^2 \rho / \rho$ and $(\nabla \rho / \rho)^2$ remains intact.

6. Proposal of Generalized Local Density Approximation and Use of Experimentally Determined Ground-State Density

The three zero-field Eqs. (5.2), (4.6), and (2.4) all are embraced by the equation

$$\frac{\nabla^2 \rho}{\rho} S(\rho) + \frac{\nabla \rho}{\rho} \cdot \nabla_r S(\rho) = 1. \quad (6.1)$$

It can immediately be verified that if one substitutes the self-consistent atomic TF density $\rho_{TF}(\mathbf{r})$ obtained by solving Eq. (2.4) with the appropriate atomic boundary conditions then $S(\rho)$ follows from Eq. (6.1) as

$$S_{TF}(\rho) = l_1 \rho_{TF}^{-\frac{1}{3}} \quad (6.2)$$

and nothing new is obtained. Similarly, substituting $\rho_{TFD}^{(n)}$ from (4.6), one finds

$$S_{TFD}(\rho) = l_1 \rho_{TFD}^{-\frac{1}{3}} + l_2 \rho_{TFD}^{-\frac{2}{3}}, \quad (6.3)$$

and adding Gell–Mann and Brueckner correlation, the generalization

$$S_{TFDC}(\rho) = l_1 \rho_{TFDC}^{-\frac{1}{3}} + l_2 \rho_{TFDC}^{-\frac{2}{3}} + l_3 \rho_{TFDC}^{-\frac{3}{3}} \quad (6.4)$$

follows.

If one now asserts that a “generalized” local density approximation consistent with the sequence (6.2)–(6.4) is described by

$$S(\rho) = \sum_{i=1}^{\infty} l_i \rho^{-\frac{i}{3}}, \quad (6.5)$$

then Eq. (6.1) follows.

Of course, one must input $\rho(r)$ to extract $S(r)$ by solution of the first-order differential equation (6.1). The proposal here is to take $\rho(r)$ from measured X-ray or electron scattering experiments on Xe. This will then yield, to within “experimental” error, $S(r)$ for Xe from Eq. (6.1). But atomic densities $\rho(r)$ decrease monotonically from the nucleus and, hence, $S(\rho)$ can be found for Xe. We expect $S(\rho)$ to converge to a unique limit as the atomic number is increased in a nonrelativistic theory. If we then go to radon, to test the convergence of $S(\rho)$, the “experimental” $\rho(r)$ may need correction in the K shell due to relativistic effects.

It seems intriguing to contemplate that information on the “jellium” model in the form of $S(\rho)$ defined through Eqs. (6.5) and (6.1) might be extracted from “atomic” densities, but that is, in fact, part of the underlying philosophy of DFT and, indeed, the entire basis for the TFDc theory given above and characterized completely by Eq. (6.4), with l_i , $i = 1–3$, taken from jellium calculations.

7. Slater Sum: or Generalized Partition Function

We turn from the ground-state electron density to the generalized partition function, or Slater sum $P(\mathbf{r}, \beta)$, with $\beta = (k_B T)^{-1}$. Again, we focus on normalized eigenfunctions $\psi_i(\mathbf{r})$ and corresponding eigenvalues ϵ_i generated by the one-body potential $V(\mathbf{r})$. Then, the definition of $P(\mathbf{r}, \beta)$ is

$$P(\mathbf{r}, \beta) = \sum_{all \ i} \psi_i(\mathbf{r}) \psi_i^*(\mathbf{r}) \exp(-\beta \epsilon_i). \quad (7.1)$$

It will be convenient this time to begin with the external-field problem. In particular, let us treat initially free electrons described by plane-wave

functions $\exp(i\mathbf{k} \cdot \mathbf{r})$ in a constant electric field F along the z axis.

7.1. SLATER SUM $P(z, \beta, F)$ FOR FREE ELECTRONS IN CONSTANT ELECTRIC FIELD OF STRENGTH F

Thomas-Fermi theory would simply move each energy level by a "constant" amount— Fz , leaving the wave functions as the original plane waves. The approximation to the Slater sum is then

$$P_{TF}(z, \beta, F) = P_0(\beta) \exp(\beta F z). \quad (7.2)$$

This, in fact, needs to be corrected by a factor given by Jannussis [27] and by Harris and Cina [28] to yield the exact form

$$\begin{aligned} P(z, \beta, F) &= P_0(\beta) \exp\left(\beta F z + \frac{\beta^3 F^2}{24}\right) : P_0(\beta) \\ &= (2\pi\beta)^{-3/2}. \end{aligned} \quad (7.3)$$

Lehmann and March [29] constructed the differential equation satisfied by $P(z, \beta, F)$ in Eq. (7.3) as

$$\frac{1}{8} \frac{\partial^3 P}{\partial z^3} - \left(-Fz + \frac{\partial}{\partial \beta}\right) \left(\frac{\partial P}{\partial z}\right) - \frac{1}{2} P = 0, \quad (7.4)$$

for this free-field problem with arbitrary field strength F .

7.2. SLATER SUM OF BARE COULOMB POTENTIAL — Ze^2/r

March and Murray [30, see also 31] in early work on central-field problems analyzed $P(r, \beta)$ into l waves and, hence, constructed a differential equation for the partial wave term $P_l(r, \beta)$. This has the form

$$\begin{aligned} \frac{1}{8} \frac{\partial^3}{\partial r^3} (r^2 P_l) - \frac{l(l+1)}{2r} \frac{\partial}{\partial r} (r P_l) - \frac{1}{2} \frac{\partial V}{\partial r} r^2 P_l \\ - V \frac{\partial}{\partial r} (r^2 P_l) - \frac{\partial^2}{\partial \beta \partial r} (r^2 P_l) = 0, \end{aligned} \quad (7.5)$$

but for a general central field $V(r)$, it has not, to date, proved possible to sum over l to obtain the desired differential equation for $P(r, \beta)$.

However, for a bare Coulomb field $V(r) = -Ze^2/r$, such a differential equation has been constructed independently by Cooper [31] and by Pfalzner et al. [32, 33] as

$$\begin{aligned} \frac{1}{8} \frac{\partial^3 P}{\partial r^3} + \frac{1}{2r} \frac{\partial^2 P}{\partial r^2} + \frac{1}{4r^2} \left(\frac{\partial V}{\partial r} - V - \frac{\partial}{\partial \beta} \right) \frac{\partial P}{\partial r} \\ + \frac{1}{2} V' P = 0, \end{aligned} \quad (7.6)$$

where V is the bare Coulomb potential energy $-Z/r$.

To date, no completely general result has proved possible for central fields described by $V(r)$, for reasons analyzed by Amovilli and March [33, 34]. These workers pointed out that, with presently available techniques, progress can be made only when there is a simple relation between the kinetic energy density tensor and the kinetic energy density itself. Such a relation always exists in one dimension, and, therefore, in this case, a differential equation for the Slater sum $P(x, \beta)$ can always be written down [30].

However, it remains of considerable interest to be able to find a synthesis of Eqs. (7.4) and (7.6) appropriate to treat the Stark effect in the hydrogenlike atom. Therefore, in Section 7.3, we outline the recent progress of Amovilli and March [35] toward a differential equation for the Slater sum, but now restricted to the axis of the electric field.

7.3. SLATER SUM ALONG AXIS FOR CYLINDRICALLY SYMMETRIC FIELDS

Attention is focused here [35] on a variety of cylindrically symmetric inhomogeneous electron liquids. These include separable potentials in which a general variation along the (z) axis of cylindrical symmetry is combined with isotropic harmonic confinement in the (x, y) plane. In this case, an explicit differential equation is derived for the Slater sum along the z axis by projecting out of the (off-diagonal) canonical density matrix the states with zero angular momentum about the axis of symmetry. Some attention is then given to the calculation of the Slater sum for a hydrogenlike atom in a uniform electric field of arbitrary strength. The model of a separable potential with harmonic confinement, although no longer exact, is shown to lead directly to a (now approximate) equation for the Slater sum along the z axis for the Stark effect in hydrogen.

7.3.a. Harmonic Confinement of Electrons in a General Potential Varying Along the z Axis

It is of some interest to discuss an example in which perpendicularly to the axis of cylindrical symmetry is switched on a harmonic force, and along the z axis, a more general field. The potential has the separable form $(1/2)\omega^2\rho^2 + V(z)$. Inserting this potential into the Bloch equation for the (off-diagonal) Slater sum, expanding to work then with the diagonal form $P(\mathbf{r}, \beta)$ only, Amovilli and March [35] showed that one has finally for $P(z, \beta)$

$$\frac{1}{8}P''' - \left[\omega \coth(\beta\omega) + V + \frac{\partial}{\partial\beta} \right] P' - \frac{1}{2}V'P = 0, \quad (7.7)$$

which is valid for any given potential V varying along z .

These workers then linked the exact differential equation (7.7), valid for a wide class of cylindrically symmetric problems, with the Stark effect; we summarize their approach very briefly below. One has now to deal with the specific cylindrically symmetric potential about the field (z) axis:

$$V = -\frac{Z}{\rho^2 + z^2} - Fz : \rho = (x^2 + y^2)^{1/2}. \quad (7.8)$$

Although this potential is not contained in the class of potentials satisfying Eq. (7.7), we follow Amovilli and March [35] in linking that equation approximately with the Stark problem.

7.3.b. Modeling the Stark Effect by Harmonic Confinement

The potential (7.8), referring to the Stark effect, can be expanded, near the z axis and for large z , up to second order in ρ , namely,

$$V(\rho, z) = -Fz - \frac{Z}{|z|} \left(1 - \frac{\rho^2}{2z^2} \right) + \dots \quad (7.9)$$

In this regime perpendicularly to the axis, the electron is subjected to elastic forces of "constant"

$$\omega^2 = \frac{Z}{|z|^3}. \quad (7.10)$$

This consideration has led us [35] to formulate an approximate differential equation for the Slater

sum substituting ω from Eq. (7.10), as a function of z now, into Eq. (7.7) in order to build a model for the Stark effect along the axis of symmetry. The equation

$$\frac{1}{8}P''' - \left[\omega(z) \coth(\beta\omega(z)) + V(z) + \frac{\partial}{\partial\beta} \right] P' - \frac{1}{2}V'(z)P = 0, \quad (7.11)$$

where $\omega(z)$ is to be obtained from Eq. (7.10), is the equation derived by Amovilli and March [35] as an approximate equation for the Slater sum for the Stark effect in hydrogen, with $V(z) = -Z/|z| - Fz$. This equation should eventually be amenable to numerical solution techniques.

8. Summary and Proposed Future Directions

A sequence of zero external-field differential equations in which Hartree self-consistency has been imposed leads rather naturally to the "generalized" local density approximation $S(\rho)$ defined formally in Eq. (6.5). It has been stressed that it will be of interest for the future to input experimental data on $\rho(r)$ for Xe and, hence, to integrate the first-order differential equation (6.1) for $S(r)$. But since $\rho(r)$ is monotonically decreasing from the nucleus, knowledge of r determines ρ and, hence, S can be plotted against ρ . We expect $S(\rho)$ to converge to a unique limit for nonrelativistic closed-shell atoms. Unfortunately, even for radon, relativistic corrections would have to be applied, should $\rho(r)$ prove measurable. Nevertheless, the route to this "generalized" local density approximation is conceptually attractive and, in some sense, is the inverse procedure to the sequence TF, TFD, and TFDc as set out in some detail above.

Considerable attention has then been focused on differential equations for both the ground-state electron density and the Slater sum for atoms in intense external fields. For magnetic fields of arbitrary strength, equations are set up for the ground-state density both in nonrelativistic and in relativistic semiclassical theory. For the case of electric fields, progress has proved possible via the Slater sum, Eqs. (7.4), (7.6), (7.7), and (7.11) affording specific examples of differential equations for this sum $P(\mathbf{r}, \beta)$. Further progress on the Stark

effect in atoms is to be expected along such directions in future studies.

ACKNOWLEDGMENTS

Many valuable discussions with Drs. C. Amovilli, A. Holas, and A. Nagy are gratefully acknowledged. The work on atoms and molecules in intense external fields was supported in part by the Office of Naval Research. It is a particular pleasure to thank Dr. P. Schmidt of that office for much stimulation and continuous encouragement.

Appendix 1: Inclusion of Exchange in Relativistic Thomas-Fermi Theory

Following MacDonald and Vosko [36], the exchange energy density $\epsilon_{x\alpha}$ in relativistic electron gas theory can be written (see also March and Santamaria [37]) as

$$\epsilon_{x\alpha} = \epsilon_{x0} F(\beta), \quad (\text{A1.1})$$

where α is the fine structure constant. ϵ_{x0} is the usual Dirac nonrelativistic result [16]:

$$\epsilon_{x0} = -c_x \rho^{4/3} : c_x = \frac{3}{4} e^2 \left(\frac{3}{\pi} \right)^{\frac{1}{3}}. \quad (\text{A1.2})$$

In Eq. (A1.1),

$$\begin{aligned} F(\beta) &= 1 - \frac{3}{2} \left\{ (1 + \beta^2)^{\frac{1}{2}} \right. \\ &\quad \left. - \ln \left[\beta + (1 + \beta^2)^{\frac{1}{2}} \right] \right\}^2 / \beta^4; \\ \beta &= b \rho^{\frac{1}{3}}, \end{aligned} \quad (\text{A1.3})$$

where

$$b = (3\pi^2)^{1/3} (\hbar/mc). \quad (\text{A1.4})$$

In this local density theory, with kinetic energy density $t_\alpha(\rho)$, the chemical potential μ_α , constant throughout the entire charge cloud of the atom or molecule under consideration, is given by

$$\mu_\alpha = \frac{\partial t_\alpha}{\partial \rho} + V_{\text{Hartree}}(\mathbf{r}) + \frac{\partial \epsilon_{x\alpha}}{\partial \rho}. \quad (\text{A1.5})$$

Acting on Eq. (A1.5) with the Laplacian operator ∇^2 and utilizing again Poisson's equation for ∇^2

V_{Hartree} yields

$$0 = \nabla^2 \left\{ \frac{\partial t_\alpha}{\partial \rho} \right\} - 4\pi\rho(\mathbf{r})e^2 + \nabla^2 \left\{ \frac{\partial \epsilon_{x\alpha}}{\partial \rho} \right\}. \quad (\text{A1.6})$$

Putting the exchange contribution equal to zero, Eq. (A1.6) reduces to the differential equation already derived [38] for the relativistic TF ground-state electron density.

It remains to write the exchange term in Eq. (A1.6) explicitly using Eqs. (A1.1)–(A1.4). Taking for simplicity of presentation the atomic case with spherical symmetry, and writing $\partial\rho(\mathbf{r})/\partial r = \rho'$, etc., one readily obtains

$$\nabla^2 \left\{ \frac{\partial \epsilon_{x\alpha}}{\partial \rho} \right\} = \rho'^2 \frac{\partial^3 \epsilon_{x\alpha}}{\partial \rho^3} + \left(\rho'' + \frac{2}{r} \rho' \right) \frac{\partial^2 \epsilon_{x\alpha}}{\partial \rho^2}, \quad (\text{A1.7})$$

and, hence, from Eqs. (A1.6) and (A1.7),

$$\begin{aligned} 0 &= \nabla^2 \left\{ \frac{\partial t_\alpha}{\partial \rho} \right\} - 4\pi\rho(r)e^2 + \rho'^2 \frac{\partial^3 \epsilon_{x\alpha}}{\partial \rho^3} \\ &\quad + \left(\rho'' + \frac{2}{r} \rho' \right) \frac{\partial^2 \epsilon_{x\alpha}}{\partial \rho^2}. \end{aligned} \quad (\text{A1.8})$$

Using the analogous result to Eq. (A1.7) for $\nabla^2 \{(\partial t_\alpha)/(\partial \rho)\}$, one reaches the desired differential equation for $\rho(r)$ in this relativistic TF atomic theory including exchange:

$$\begin{aligned} 4\pi\rho(r)e^2 &= \rho'^2 \left[\frac{\partial^3(t_\alpha + \epsilon_{x\alpha})}{\partial \rho^3} \right] \\ &\quad + \left(\rho'' + \frac{2}{r} \rho' \right) \left[\frac{\partial^2(t_\alpha + \epsilon_{x\alpha})}{\partial \rho^2} \right]. \end{aligned} \quad (\text{A1.9})$$

Writing finally

$$\frac{1}{4\pi e^2} \frac{\partial^2}{\partial \rho^2} (t_\alpha + \epsilon_{x\alpha}) \equiv g_\alpha(\rho), \quad (\text{A1.10})$$

an evidently local density function, the shape of the final differential equation in relativistic TF theory plus exchange is given by

$$\rho(r) = (\nabla \rho)^2 \frac{\partial g_\alpha}{\partial \rho} + (\nabla^2 \rho) g_\alpha(\rho). \quad (\text{A1.11})$$

Evidently, $g_\alpha(\rho)$ is determined quite explicitly by the known forms of $t_\alpha(\rho)$ and $\epsilon_{x\alpha}(\rho)$, the latter being given in Eqs. (A1.1)–(A1.4). The final form

$$\left(\frac{\nabla^2\rho}{\rho}\right)g_\alpha(\rho) + \left(\frac{\nabla\rho}{\rho}\right)^2 \left(\rho \frac{\partial g_\alpha}{\partial\rho}\right) = 1 \quad (\text{A1.12})$$

shows again the central role played by the reduced Laplacian $(\nabla^2\rho/\rho)$ and the "local wave number" $\nabla\rho/\rho$, the latter quantity being discussed for closed-shell atoms, but now in nonrelativistic quantum mechanics, by Nagy and March [39]. Equation (A1.11) naturally reduces to the earlier relativistic TF equation [38] when $\epsilon_{x\alpha}$ is set equal to zero. To the writer's knowledge, Eq. (A1.12), with $g_\alpha(\rho)$ given by Eq. (A1.10) has not been derived hitherto.

Appendix 2: Relativistic Generalization of Eq. (2.10) for Atoms in Intense Magnetic Fields

The kinetic energy density $t_\alpha(\rho)$ in relativistic theory for electrons in intense magnetic fields was discussed by the writer in the context of the virial [40]. As the fine structure constant $\alpha = e^2/hc$ is allowed to tend to zero, the result $t_0(\rho) \propto \rho^3$ is recovered, which affords an alternative route to Eq. (2.9) above, utilizing the variational principle (2.1).

The relativistic generalization of Eq. (2.9) then can be written as

$$\mu_{\text{TF}}^{(B, \alpha)} = \frac{\partial t_\alpha}{\partial\rho(\mathbf{r})} + V_H(\mathbf{r}). \quad (\text{A2.1})$$

Utilizing once more the constancy of the chemical potential throughout the entire electronic distribution, one can operate with ∇^2 on Eq. (A2.1) to find, using, again, Eq. (1.8),

$$4\pi\rho e^2 = \frac{\nabla^2\partial t_\alpha}{\partial\rho(\mathbf{r})}. \quad (\text{A2.2})$$

Utilizing spherical symmetry as in Appendix 1 (such a state is variationally the best, not withstanding the magnetic field), Eq. (A2.2) is readily cast into the form

$$\frac{\nabla^2\rho}{\rho}G_\alpha(\rho) + \left(\frac{\nabla\rho}{\rho}\right)^2 \left(\rho \frac{\partial G_\alpha}{\partial\rho}\right) = 1 \quad (\text{A2.3})$$

where $G_\alpha(\rho)$ is given in terms of t_α by

$$G_\alpha(\rho) = \frac{1}{4\pi e^2} \frac{\partial^2}{\partial\rho^2} t_\alpha, \quad (\text{A2.4})$$

where $(\partial t_\alpha/\partial\rho)$ is given explicitly in [40].

In early work, Hill et al. [21] solved numerically the complementary problem for the Hartree potential for an assumed B field of strength 10^{14} Gauss (motivated by neutron stars) and atomic number $Z = 100$. Their results can be utilized to derive the density $\rho(r)$ satisfying Eq. (A2.3). However, it is to be noted that there is a region, having the size of the nuclear radius, in which they transcend Eq. (A2.3) in order to effect the normalization of $\rho(r)$. We remind the reader that this should occasion no surprise in a relativistic theory, for the Dirac one-electron wave function for the H atom ground state has a weak (although still normalizable) singularity at a point nucleus.

References

1. P. O. Löwdin, Phys. Rev. **97**, 1490 (1955).
2. A. J. Coleman, Rev. Mod. Phys. **35**, 668 (1963).
3. R. McWeeny, *Methods of Molecular Quantum Mechanics* (Academic Press, New York, 1989).
4. See P. Hohenberg and W. Kohn, Phys. Rev. **136**, 864 (1964).
5. A. Holas and N. H. March, Phys. Rev. **51**, 2040 (1995).
6. A. Holas and N. H. March, Phys. Rev. B (in press).
7. See, e.g., R. G. Parr and W. Yang, *Density Functional Theory of Atoms and Molecules* (Oxford University Press, New York, 1989).
8. W. H. Young and N. H. March, Proc. R. Soc. **A256**, 62 (1960).
9. P. J. Brown, Philos. Mag. **26**, 1377 (1972).
10. P. Coppens, *X-Ray Charge Densities and Chemical Bonding* (Oxford, New York, 1997).
11. L. Massa, L. Huang and J. Karle, Int. J. Quantum Chem. Symp. **29**, 371 (1995).
12. M. Levy and A. Görling, Philos. Mag. B **69**, 763 (1994).
13. N. H. March, Phys. Lett. A **113**, 66 (1985); *Ibid.* **113**, 476 (1985).
14. C. Herring and M. Chopra, Phys. Rev. A **37**, 31 (1988).
15. A. Holas and N. H. March, Phys. Rev. A **44**, 5521 (1991).
16. See N. H. March, *Electron Density Theory of Atoms and Molecules* (Academic Press, New York, 1992).
17. N. H. March, Phys. Rev. A **56**, 1025 (1997).
18. B. B. Kadomtsev, Sov. Phys. JETP **31**, 945 (1970).
19. B. Banerjee, D. H. Constantinescu, and P. Rehak, Phys. Rev. D **10**, 2384, (1974).
20. S. Pfalzner and N. H. March, J. Math. Phys. **34**, 549 (1993).

MARCH

21. S. H. Hill, P. J. Grout, and N. H. March, *J. Phys. B* **16**, 2301 (1983); *J. Phys. B* **18**, 4665 (1985).
22. E. H. Lieb, J. P. Solovej, and J. Yngvason, *Phys. Rev. Lett.* **69**, 749 (1992).
23. H. Lehmann and N. H. March, *Pure Appl. Chem.* **67**, 457 (1995).
24. G. R. Freeman and N. H. March, *J. Phys. Chem.* **100**, 4331 (1996).
25. M. Gell-Mann and K. A. Brueckner, *Phys. Rev.* **106**, 364 (1957).
26. N. H. March, A. Holas, and A. Nagy, *Int. J. Quantum Chem.*, in press.
27. A. D. Jannussis, *Phys. Stat. Sol.* **36**, K17 (1969).
28. R. Harris and J. Cina, *J. Chem. Phys.* **79**, 1381 (1983).
29. H. Lehmann and N. H. March, *Phys. Chem. Liq.* **27**, 65 (1994).
30. N. H. March and A. M. Murray, *Phys. Rev.* **120**, 830 (1960).
31. I. L. Cooper, *Phys. Rev. A* **50**, 1040 (1994).
32. S. Pfalzner, H. Lehmann, and N. H. March, *J. Math. Chem.* **16**, 9 (1994).
33. C. Amovilli and N. H. March, *Phys. Chem. Liq.* **30**, 135 (1995).
34. See also N. H. March, *J. Math. Phys.* **38**, 2037 (1997).
35. C. Amovilli and N. H. March, *Phys. Chem. Liq.* (in press).
36. A. H. MacDonald and S. H. Vosko, *J. Phys. C* **12**, 2977 (1979).
37. N. H. March and R. Santamaria, *Phys. Chem. Liq.* **19**, 187 (1989).
38. N. H. March, *Phys. Chem. Liq.* (in press).
39. A. Nagy and N. H. March, *Mol. Phys.* **90**, 271 (1997).
40. N. H. March, *Phys. Rev. A* **48**, 4778 (1993).

Ground States of Atoms and Molecules in Strong Magnetic Fields

P. SCHMELCHER

Theoretische Chemie, Physikalisch-Chemisches Institut, Im Neuenheimer Feld 253, 69120 Heidelberg,
Federal Republic of Germany

Received 23 March 1998; revised 24 June 1998; accepted 2 July 1998

ABSTRACT: The ground states of small atoms and molecules, namely those of the hydrogen, helium, and lithium atoms and the hydrogen molecular ion and hydrogen molecule, are studied in the presence of an external magnetic field. For the one-electron systems the ground state is of the same symmetry for arbitrary field strengths, and the corresponding binding energy shows a monotonic increase with increasing field strength. More interesting, the two- and three-electron systems show ground-state transitions which involve both transitions in the spin multiplicity and spatial quantum numbers. An outlook on the expected cascade of transitions in many electron atoms and molecules is provided. © 1998 John Wiley & Sons, Inc. Int J Quant Chem 70: 789–795, 1998

Key words: strong magnetic fields; ground states; binding properties; symmetry transitions

Introduction

Atoms and molecules subjected to strong magnetic fields experience severe changes of both their electronic properties as well as dynamical behavior. The term *strong* hereby refers to the ratio of the magnetic and Coulomb binding forces of the considered system: If the magnetic and corresponding Coulomb interaction become comparable, we encounter a variety of nonperturbative and complex phenomena. For a single electron in a magnetic and Coulomb field (fixed nucleus hydrogen atom), the electronic wave function continuously changes its shape with increasing field

strength. For the extreme cases, i.e., for the zero-field case and high-field regime, we have the field-free hydrogenic and the combined Landau and one-dimensional Coulomb behavior, respectively. More interesting is the intermediate regime which bears the transformation between these two configurations. From a dynamical point of view the intermediate regime is characterized by the prevalence of chaotic classical motion in phase space and its corresponding quantum signatures. Due to an enormous effort, i.e., a large number of studies during the past 20 years (see Ref. [1] and references therein), we have a very clear and detailed understanding of the behavior and properties of the hydrogen atom for any regime of field strengths and degree of excitation. This picture

changes, however, dramatically if we turn to more electron atoms and molecules. Already for the helium atom the number of investigations is very limited (see Refs. [2–4] and references therein) and for more than two electrons only a few works are available [3, 5–11]. For molecules the literature is even more scarce. For the parallel configuration of the H_2^+ ion, arbitrary configurations of the H_2^+ ion and for the parallel configuration of the hydrogen molecule we refer the reader to the Refs. [12–15] and references therein, respectively. More electron molecules have been treated, for example, in Refs. [16, 17]. The small amount of available literature is in contrast to the fact that many interesting phenomena have to be expected which possess no counterpart in field-free space and do in particular not occur for the hydrogen atom in a magnetic field. One of the reasons for this lack of investigations is certainly the computational difficulties encountered in a theoretical study of interacting electronic systems in strong magnetic fields: new approaches and techniques have to be developed in order to properly describe the effects of competitive Coulomb and magnetic forces.

The purpose of the present work is to draw a picture of the state of the art concerning the ground states of atoms and molecules in strong magnetic fields and to provide a perspective of possible phenomena with respect to the ground-state transitions of many electron atomic and molecular systems. Since our knowledge on finite particle systems in magnetic fields is very limited, this can at best be a theorist's outline, which hopefully will soon be enriched by many more manifestations of complex magnetic field phenomena discovered in concrete investigations.

Our discussion is as follows. In the following section we focus on atomic systems. After a few comments on the hydrogen atom we discuss the helium and lithium atom. The third section deals with the hydrogen molecular ion and the hydrogen molecule, and the final section contains our conclusions as well as the outlook on many electron atoms and molecules.

Ground States of Small Atomic Systems

Let us first consider the hydrogen atom. The remaining symmetries in the presence of the external magnetic field are the rotations around the magnetic field axis (magnetic quantum number),

which is in the following assumed to be aligned with the z axis, the parity, and, as a combined quantity of the latter operations, the z parity. It is well-known that each of the lowest electronic states of gerade z parity and a given magnetic quantum number show a monotonic increase in binding energy with increasing field strength B [18]. These states uniquely correspond to the field-free hydrogen $1s_0, 2p_{-1}, 3d_{-2}$, etc states. Indeed, their binding energy diverges $E_B \rightarrow \infty$ in the mathematical limit $B \rightarrow \infty$. This means that in particular the ground state is a so-called strongly bound state. The corresponding wave function hereby undergoes a transition from a spherical (field-free space) to a needlelike shape (high field regime) [19, 20].

Next let us turn to the helium atom. The field-free ground state is of 1S_g symmetry and is therefore a spin singlet state. If we turn on a magnetic field, it shows a monotonic increase of binding energy with increasing field strength. However, since the external magnetic field couples to the spin through the spin Zeeman term, we expect that there occurs for some critical field strength B_c a crossing of the lowest state of $^1\Sigma_g$ symmetry with a spin triplet state which has all spins antiparallel to the magnetic field. Indeed, for sufficiently large field strengths, it can be conjectured that any triplet state which is fully spin polarized antiparallel to the field will be lower in energy than the lowest state of $^1\Sigma_g$ symmetry. The question then is: Which is the lowest of those triplet states? In concrete investigations it turns out that this state is of $^3\Pi_u$ symmetry. It shows also a monotonic behavior of its binding energy with increasing field strength. Figure 1 illustrates the total energies of the corresponding states of $^1\Sigma_g$ and $^3\Pi_u$ symmetry as a function of the magnetic field on a logarithmic scale thereby demonstrating the crossover in the global ground state of the helium atom around $B_c \approx 0.7$ (1 a.u. corresponds to 2.35×10^5 Tesla). Having a closer look at the wave function of the $^3\Pi_u$ state in the high-field limit, one finds that the dominant configuration is of $1s \downarrow 2p_{-1} \downarrow$ character. This means that the two electrons are in those magnetized hydrogenic orbitals which correspond to the two energetically lowest above-mentioned strongly bound states of hydrogen. Occupying these states provides therefore the energetically most favorable configuration for the helium atom in the high-field regime. The transition with respect to the ground state at $B \approx 0.7$ involves, therefore, in an effective one-particle

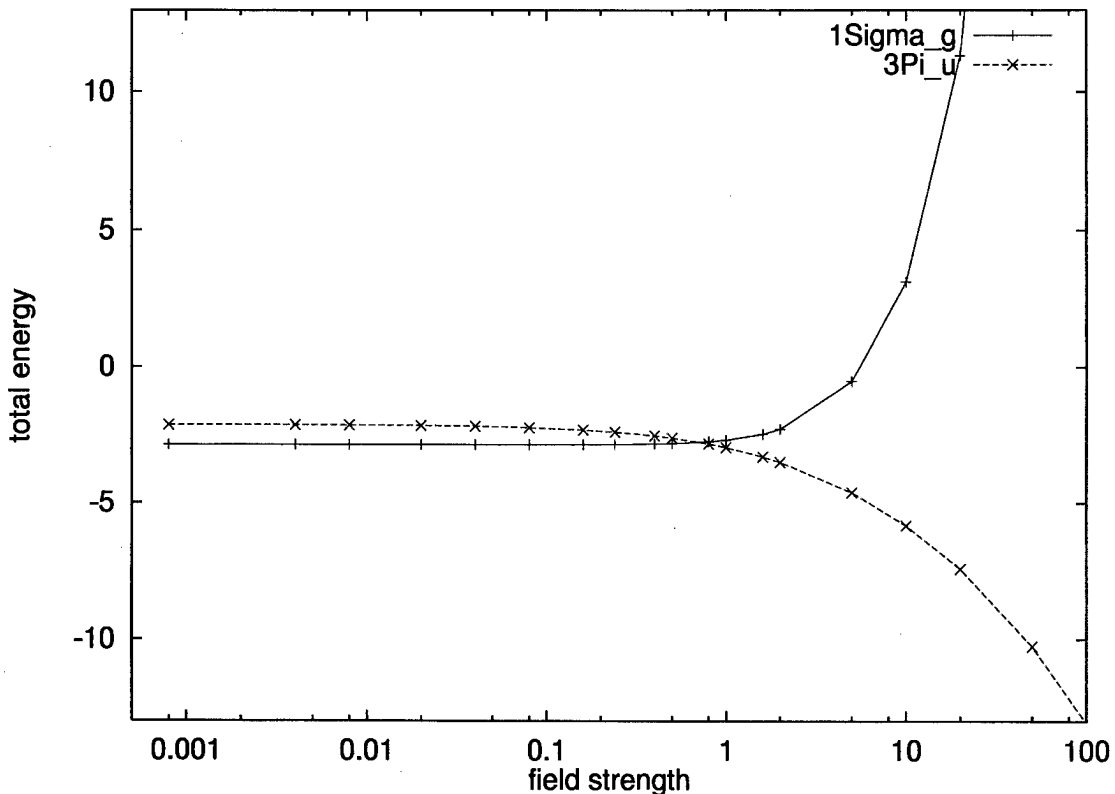


FIGURE 1. Total energy of the $^1\Sigma_g$ (solid line) and $^3\Pi_u$ (broken line) electronic states of helium atom as a function of the field strength on a logarithmic scale. Energy and field strength are given in atomic units ($B = 1$ a.u. corresponds to 2.35×10^5 Tesla).

picture, not only a transition with respect to the total spin and its projection but also a change in the spatial quantum numbers. Obviously other spin triplet states, associated with, for example, the $1s \downarrow 2s \downarrow$ configuration are for any field strength much higher than the above-described ground state.

Considering the Li atom, the literature is already very scarce: There exist only two very recent investigations [3, 10] on the Hartree-Fock level. The field-free ground state is given by the spin doublet $1s^2 2s \downarrow$ configuration. The binding energy of this state increases monotonic with increasing field strength. Since it is not a fully spin-polarized state, we again expect that there occurs a transition with respect to the ground state of the Li atom with increasing field strength to a spin quartet state. The numerical investigation [10], however, shows that the situation is more complex than originally assumed. Of course, starting with the field-free situation and increasing the field strength, we observe that the $1s^2 2s \downarrow$ configuration represents the ground state of the Li atom for

a certain regime of field strengths. This is the case up to $B_{c_1} \approx 0.176$ a.u. where the first transition takes place. The new ground state above B_{c_1} is constituted by the $1s^2 2p_{-1} \downarrow$ configuration, and therefore we do not encounter a transition with respect to the spin and its projection but a transition purely with respect to the spatial quantum numbers: The weakly bound $2s$ magnetized hydrogenic orbital is replaced by the strongly bound $2p_{-1}$ orbital. Obviously, this transition is prior to a spin flip transition.

The $1s^2 2p_{-1} \downarrow$ spin doublet configuration is the global ground state of the Li atom in the regime $0.176 < B < 2.153$ a.u. At $B_{c_2} = 2.153$ a.u. a second transition takes place, and for $B > 2.153$ a.u. the new ground state is represented by the fully spin polarized $1s \downarrow 2p_{-1} \downarrow 3d_{-2} \downarrow$ configuration [10]. Figure 2 shows the corresponding total energies as a function of the magnetic field on a logarithmic scale. Above B_{c_2} the three electrons are therefore in the three lowest strongly bound magnetized hydrogenic orbitals $1s$, $2p_{-1}$, and $3d_{-2}$ which, together with the fact of antiparallel spins

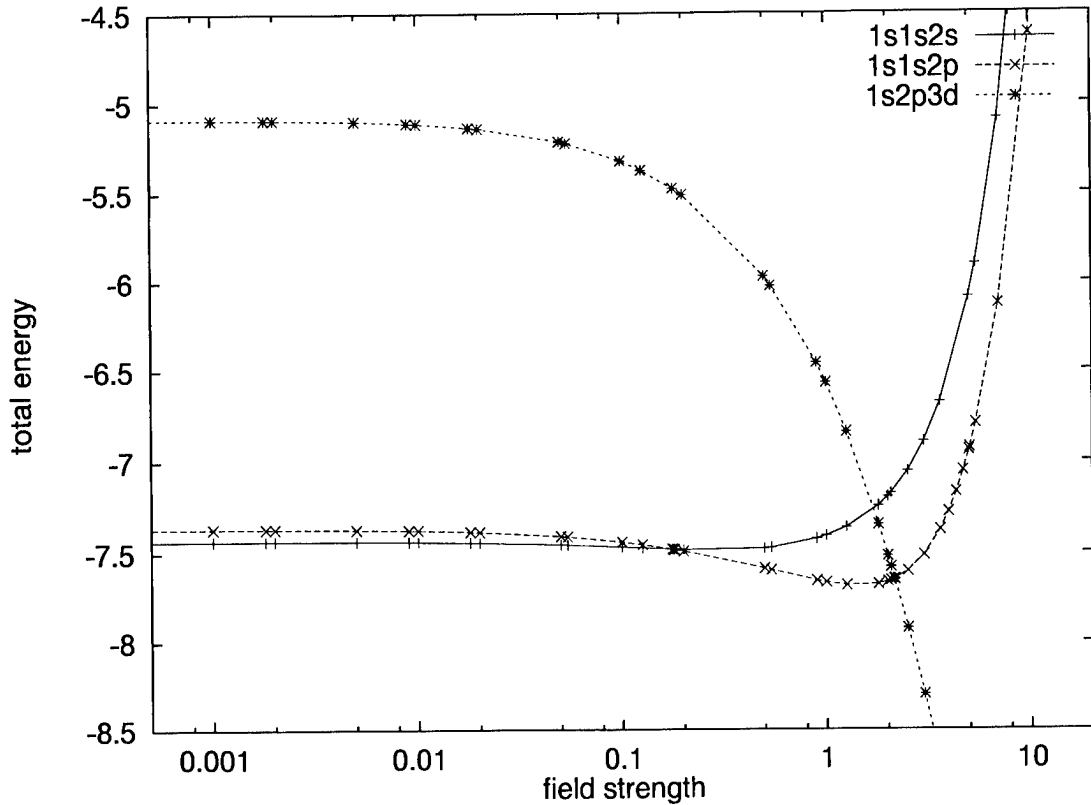


FIGURE 2. Total energy of the electronic configurations $1s^22s$ (solid line), $1s^22p_{-1}$ (broken line with crosses), and $1s2p_{-1}3d_{-2}$ (broken line with stars) of the lithium atom as a function of the field strength on a logarithmic scale in atomic units.

with respect to the magnetic field, represent the energetically lowest configuration in the high field regime. This means the electronic configuration does not change for $B > B_{c_2}$.

For heavier atoms there exist a few investigations (see, e.g., Refs. [5–8]) which, however, deal only with the ground state in the high field limit. Therefore no information is now available on the ground-state transitions of atoms with more than three electrons.

Ground States of the Hydrogen Molecular Ion and the Hydrogen Molecule

Before entering the discussion of the global ground state of a specific molecule, let us provide some general features of diatomic molecules in strong magnetic fields. The electronic potential energy, defined through an adiabatic approximation in a magnetic field [21], depends on the internu-

clear distance R and the angle Θ between the magnetic field and the internuclear axis and represents therefore a two-dimensional surface, i.e., $\epsilon = \epsilon(R, \Theta)$. In Ref. [22] it has been shown that the parallel and perpendicular configurations are distinguished by their higher symmetry and that the diabatic energy curves exhibit extrema at these positions. The positions $\Theta = 0^\circ$ and $\Theta = 90^\circ$ are therefore good candidates for becoming the global equilibrium configuration of the ground state. However, there is to our knowledge no fundamental reason why the positions $\Theta \neq 0^\circ, 90^\circ$ should be excluded from representing the global equilibrium configuration in particular if one takes into account vibronic interaction effects.

Most of the investigations on the hydrogen molecular ion have been performed for the parallel configuration (see Ref. [12] and references therein). Studies of the full potential energy surfaces (see Ref. [13] and references therein) have shown that the parallel configuration represents the global equilibrium configuration for the ground state for

arbitrary field strengths. The latter is of $1\sigma_g$ symmetry, and its binding as well as dissociation energy increases monotonically with increasing field strength. Simultaneously the bond length decreases. In particular there occur, of course, no transitions for the ground state, i.e., the dominant contribution comes from the molecular orbital of gerade parity which is built up from the lowest $1s$ magnetized hydrogenic orbital.

Considering the hydrogen molecule, the situation is much more complicated and was unresolved until recently. For the literature on the hydrogen molecule in the parallel configuration, we refer the reader to Refs. [14, 15] and references therein. References [14, 15] clarified the question for the global ground state of the molecule for this configuration in arbitrary field strengths. In field-free space the ground state is well-bound and of $^1\Sigma_g^+$ symmetry, i.e., in particular a spin singlet state. In the presence of a magnetic field the diamagnetic term causes an increase in the total energy with increasing field strength. At the same

time the spin-Zeeman shift tends to lower the total energy for triplet states with $M_s = -1$. As a result a ground state crossing between the potential energy curves of the singlet $^1\Sigma_g$ and triplet $^3\Sigma_u$ state occurs at $B \approx 0.18$ a.u. (see Fig. 3). For $B_{c_1} > 0.18$ a.u. the potential energy curve of the $^3\Sigma_u$ state is lower in energy than that of the $^1\Sigma_g$ state and represents therefore the global ground state of the hydrogen molecule. Since the potential energy curve of the $^3\Sigma_u$ state is, apart from a very shallow van der Waals minimum, a purely repulsive curve the hydrogen molecule is unstable in the corresponding regime of field strengths, i.e., for $B_{c_1} < B < B_{c_2}$. And $B_{c_2} = 12.3$ a.u. is another crossing field strength above which the unbound $^3\Sigma_u$ state is no more the ground state but an excited state. The new ground state above B_{c_2} is of $^3\Pi_u$ symmetry and a strongly bound state. This state includes the two strongly bound hydrogenic orbitals $1s$ and $2p_{-1}$ and represents the ground state in the high-field regime. To summarize we have two ground-state transitions for the hydrogen molecule in a

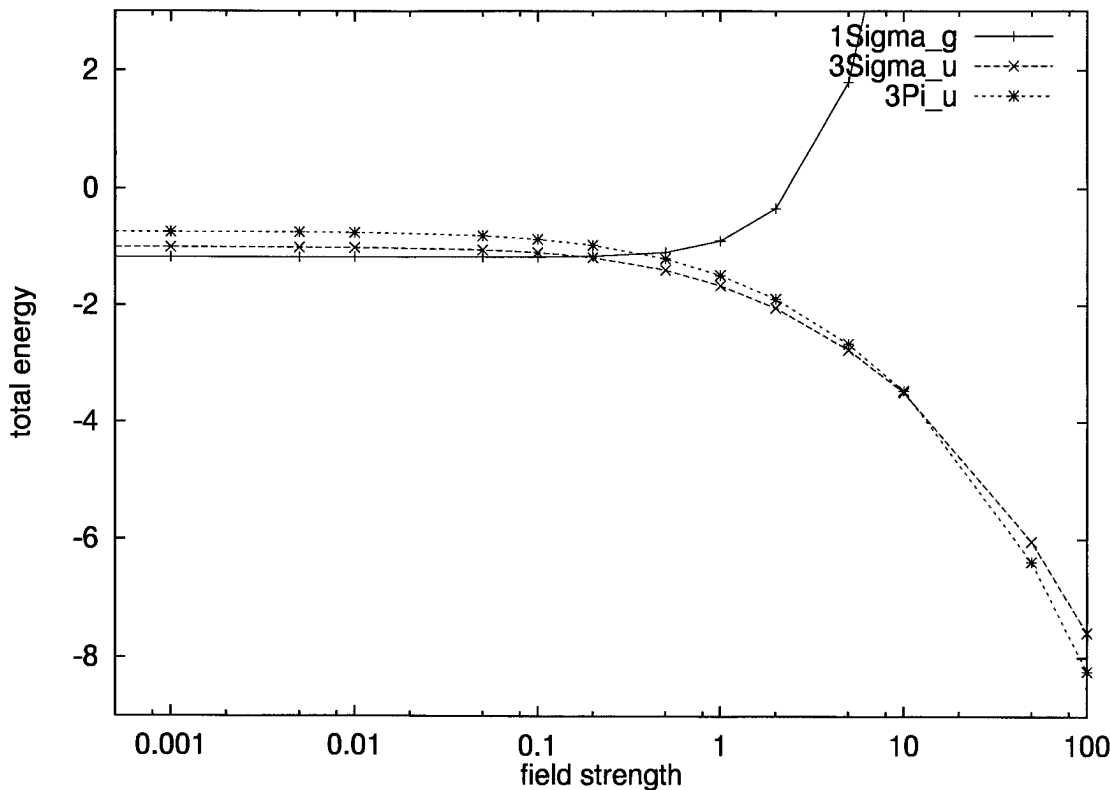


FIGURE 3. Total energy of the electronic equilibrium configurations $^1\Sigma_g$ (solid line), $^3\Sigma_u$ (broken line with crosses), and $^3\Pi_u$ (broken line with stars) of the hydrogen molecule as a function of the field strength on a logarithmic scale in atomic units.

magnetic field: In the weak field regime $B < B_{c_1}$ the ground state is of ${}^1\Sigma_g$ symmetry, and strongly bound. In the intermediate regime defined by $B_{c_1} < B < B_{c_2}$ the ground state is the triplet ${}^3\Sigma_u$ state which is almost purely repulsive and provides no bound H_2 molecule. Beyond B_{c_2} , i.e., in the high-field regime, the ${}^3\Pi_u$ state represents the ground-state configuration and is in particular a strongly bound state of the molecule. Let us conclude this section with the remark that the above-described results on the hydrogen molecule are strictly valid for $\Theta = 0^\circ$ only. However, we do expect from the way the mixing of different magnetic quantum numbers takes place for $\Theta \neq 0^\circ$ that the above-drawn picture holds also for $\Theta \neq 0^\circ$.

The available literature on more electron molecules is very scarce and restricted to the high-field regime (see, e.g., Refs. [16, 17])

Conclusions for General Atoms and Molecules

In view of the existing results of investigations on small atoms and molecules in strong magnetic fields, which have been sketched in the previous sections, let us try to draw a picture of the ground-state transitions in general atoms and molecules. As already mentioned this can at best be considered as an intuitive outline of partially speculative character.

The discussed features of the ground states of few electron systems demonstrate that the global ground state of any atom or linear molecule in the high-field limit should not only be fully spin polarized but should at least within a Hartree–Fock effective one-particle picture be constituted by the $1s, 2p_{-1}, 3d_{-2}, \dots, Nz_{-N+1}$ magnetized hydrogenic orbitals (N is the number of electrons of the system, z indicates the highest possible angular momentum in the N th shell) [10]. For example, for the carbon atom with six electrons the high-field ground state is given by $1s \downarrow 2p_{-1} \downarrow 3d_{-2} \downarrow 4f_{-3} \downarrow 5g_{-4} \downarrow 6h_{-5} \downarrow$ configuration. The high-field ground state of multielectron systems possesses therefore a total angular momentum component $-\frac{1}{2}N(N - 1)$. For polyatomic molecules the situation might be more intricate. Either the global ground-state geometry is linear (chains) in which case the above arguments hold or the geometry is nonlinear in which case one could at least in principle imagine that the molecular bonding modifies the above picture of the selection of strongly bound

hydrogenic orbitals for the ground state of the molecular system.

What does happen with increasing field strength on the way to the high-field limit? Obviously, a number of spin polarization transitions finally yielding the fully spin polarized state have to occur. However, it can certainly not be said *a priori* over what regime of field strength these transitions take place. In particular we have also the transitions of the orbitals to the series of hydrogenic magnetized orbitals ($1s, 2p_{-1}, 3d_{-2}, \dots$) which represent the strongly bound orbitals in the high-field limit. It can be conjectured that the sequence of the transitions which belong to changes in spatial quantum numbers is given by the hierarchy ($1s, 2p_{-1}, 3d_{-2}, \dots$). However, there is a great variety in the possible sequences of spin polarization and spatial quantum numbers, which are to a large extent independent from each other and indeed one might expect that also other orbitals could be involved in the cascade of transitions depending on the individual system under consideration. A great complexity of ground-state transitions will therefore be encountered for multielectron atoms. Including correlation effects might in addition change the transitions and in particular their appearance as a function of the field strength.

For heavy systems it might well be that, with increasing field strength, not all inner shell orbitals are “converted” to hydrogenic magnetized and strongly bound orbitals before relativistic corrections due to the external magnetic field become relevant (relativistic corrections to the Coulomb interaction are assumed not to change the picture drawn above for the high-field limit). In addition mass corrections are known to be relevant in the very high field regime and might additionally have some impact on the scenario sketched above.

ACKNOWLEDGMENTS

The author acknowledges fruitful discussions during the CECAM workshop “Atoms in Strong Magnetic Fields” in Lyons.

References

1. H. Friedrich and D. Wintgen, Phys. Rep. **183**, 37 (1989).
2. M. V. Ivanov, J. Phys. B **27**, 4513 (1994).
3. M. D. Jones, G. Ortiz, and D. M. Ceperley, Phys. Rev. A **54**, 219 (1996).
4. M. D. Jones, G. Ortiz, and D. M. Ceperley, Phys. Rev. E **55**, 6202 (1997).

GROUND STATES IN STRONG MAGNETIC FIELDS

5. E. Müller, Astron. Astrophys. **130**, 415 (1984).
6. D. Neuhauser, S. E. Koonin, and K. Langanke, Phys. Rev. A **33**, 2084 (1986).
7. D. Neuhauser, K. Langanke, and S. E. Koonin, Phys. Rev. A **36**, 4163 (1987).
8. B. M. Relovsky and H. Ruder, Phys. Rev. A **53**, 4068 (1996).
9. M. V. Ivanov, Phys. Lett. A **239**, 72 (1998).
10. M. V. Ivanov and P. Schmelcher, Phys. Rev. A **57**, 3793 (1998).
11. N. H. March in *Atoms and Molecules in Strong External Fields* (Plenum, New York and London 1998), p. 255.
12. U. Kappes and P. Schmelcher, Phys. Rev. A **51**, 4542 (1995).
13. U. Kappes and P. Schmelcher, Phys. Rev. A **54**, 1313 (1996).
14. T. Detmer, P. Schmelcher, F. K. Diakonos, and L. S. Cederbaum, Phys. Rev. A **56**, 1825 (1997).
15. Yu. P. Kravchenko and M. A. Liberman, Phys. Rev. A **56**, R2510 (1997).
16. A. M. Abrahams and S. L. Shapiro, Astrophys. J. **382**, 233 (1991).
17. M. Demeur, P. H. Heenen, and M. Godefroid, Phys. Rev. A **49**, 176 (1994).
18. J. E. Avron, I. W. Herbst, and B. Simon, Phys. Rev. A **20**, 2287 (1979).
19. H. Friedrich, Phys. Rev. A **26**, 1827 (1982).
20. W. Rösner, G. Wunner, H. Herold, and H. Ruder, J Phys. B **17**, 29 (1984).
21. P. Schmelcher, L. S. Cederbaum, and H. D. Meyer, Phys. Rev. A **38**, 6066 (1988).
22. P. Schmelcher and L. S. Cederbaum, Phys. Rev. A **41**, 4936 (1990).

Some Aspects of Data Processing for an Optical Absorption Experiment in a Pulsed 1000-Tesla Magnet

LESLIE G. BUTLER,¹ ANDREW W. MAVERICK,¹
CENOPIO H. GALLEGOS,³ JEFFREY D. GOETTEE,²
BRUCE R. MARSHALL,⁴ C. MAXWELL FOWLER,²
DWIGHT G. RICKEL,² JOSEPH M. GONZALES,²
LEONARD J. TABAKA²

¹*Department of Chemistry, Louisiana State University, Baton Rouge, Louisiana 70803-1804*

²*National High Magnetic Field Laboratory, Los Alamos National Laboratory, Los Alamos, New Mexico 87545*

³*Bechtel-Nevada, Los Alamos, New Mexico 87544*

⁴*Special Technologies Laboratory, Bechtel-Nevada, Santa Barbara, California 93111*

Received 30 March 1998; accepted 21 May 1998

ABSTRACT: A procedure is given for the analysis of optical absorption data acquired in the hostile environment of a pulsed 1000-Tesla magnet. © 1998 John Wiley & Sons, Inc.
Int J Quant Chem 70: 797–804, 1998

Key words: pulsed magnetic field; Zeeman effect; quadruple metal bonds; octachlorodirhenate

Introduction

We wish there were many opportunities for performing experiments in magnetic fields approaching 1000 Tesla. The current, highly limited access puts additional pressure on the exper-

imentalist to make maximum use of each event. Ideally, a complete experiment can be accomplished in a single event. An optical absorption experiment requires attention to sample preparation, the optical apparatus, time and wavelength calibrations, and light leaks. The 1000-Tesla magnetic field is achieved with an explosive charge which generates a shock wave that travels toward the sample [1–4]. As the shock wave reaches the

Correspondence to: L. G. Butler.

optical path, the beginnings of a light leak, caused by the shock wave, distort the absorption spectrum of the sample. Light leaks are, for the 1000-Tesla magnet, an inherent feature and occur at or near peak magnetic field. Herein, the experiment is discussed, with an emphasis on measurement and analysis of optical properties of samples in high field.

Sample Holder

Space constraints in the magnet force a small sample. We chose to use a light path that is folded back upon itself, as shown in Figure 1. In this probe design, the incident light beam is carried by a 600- μm diameter optical fiber, and the transmitted light is collected and returned to the spectrograph via a 100- μm fiber. The smaller fiber is sharply bent in a 180° curve with an outside diameter of 5.7 mm. This bend is smaller than the manufacturer's recommendation but was found to be stable for about one day.

The sample, bis(tetrabutylammonium) octachlorodirhenate(III) $[(\text{C}_4\text{H}_9)_4\text{N}]_2[\text{Re}_2\text{Cl}_8]$ was dissolved in dichloromethane, poly(methyl methacrylate) (PMMA) added, and the mixture poured onto a glass slide and allowed to evaporate to produce an approximately 1-mm-thick PMMA film. A disk cut from the film was fixed between

the two ends of the fiber. The surface roughness of the film causes some light scattering. A sample consisting only of PMMA was prepared and its spectrum was measured before the shot; this spectrum serves as the intensity reference (I_0) for the absorption calculation.

Spectrograph and CCD Camera

The light transmitted through the sample is returned to the spectrograph via a 10-m 100- μm optical fiber. The propagation delay of the fiber is 4.93 ns/m (the refractive index is 1.48). Wavelength dispersion in the spectrograph is accomplished with a roof prism; gratings are available for higher resolution work. Time dispersion is done with a streak camera; the spectrum is directed to a photocathode, the ejected electrons retain wavelength dispersion while time dispersion is performed with a rapidly ramped electric field. A scintillator plate converts the electron beam back to visible light which is then detected with a CCD camera.

The fiber optic/prism/streak camera–CCD camera system entails several experimental details. As noted above, the propagation delay from the sample to the spectrograph is significant. The prism requires a wavelength calibration and the streak camera a time calibration. The time calibration

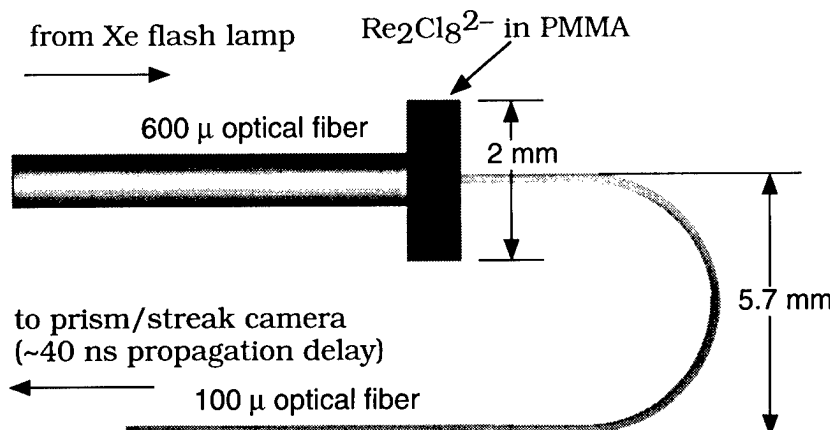


FIGURE 1. Schematic drawing of the sample holder.

data also provide a means to determine and correct for CCD mounting errors, i.e., the CCD pixel array may be misaligned with respect to the wavelength and time axes as displayed on the scintillator. Absorption spectra are calculated from three images—the shot image, an image of a PMMA film, and a CCD background image—and then a search is made for light leaks in the optical system by an analysis of the shot image.

For this run, the CCD camera consisted of a $1k \times 1k$ pixel array with a 16-bit readout. The camera control software was IPLab (Scanalytics, Inc.; www.iplab.com) running on a Macintosh IIfx. The binary data files have a 2120-byte header, with the data consisting of $1k \times 1k$ array of unsigned 2-byte integers, followed by a footer of varying length. Figure 2 shows a gray scale image of a raw data file from the shot. Key features in this image are the Re_2Cl_8^- absorption between columns 750 and 800, the timing comb pulses between columns 952 and 964, the fiducial mark at column 98, row

618 (visible in an expanded plot), and the glow of the crushed optical fiber at row 627 and higher. All of the data processing software was written in Matlab 4.2 and 5.

Wavelength Calibration

Wavelength calibration is done with a set of images acquired with known light sources: a tunable HeNe laser, a semiconductor laser, and the Hg emission lines from the lab's fluorescent lights. The calibration data are listed in the insert to Figure 3; the plot shows a best fit to the transfer function [5], where λ is given in nanometers. The inverse of this function was obtained by linear interpolation between calculated points. The semiconductor laser at 819 nm is labeled "comb" in Figure 3, and, when the laser is remounted on the streak camera, is used to generate the timing comb pulses discussed below. The point labeled "limit"

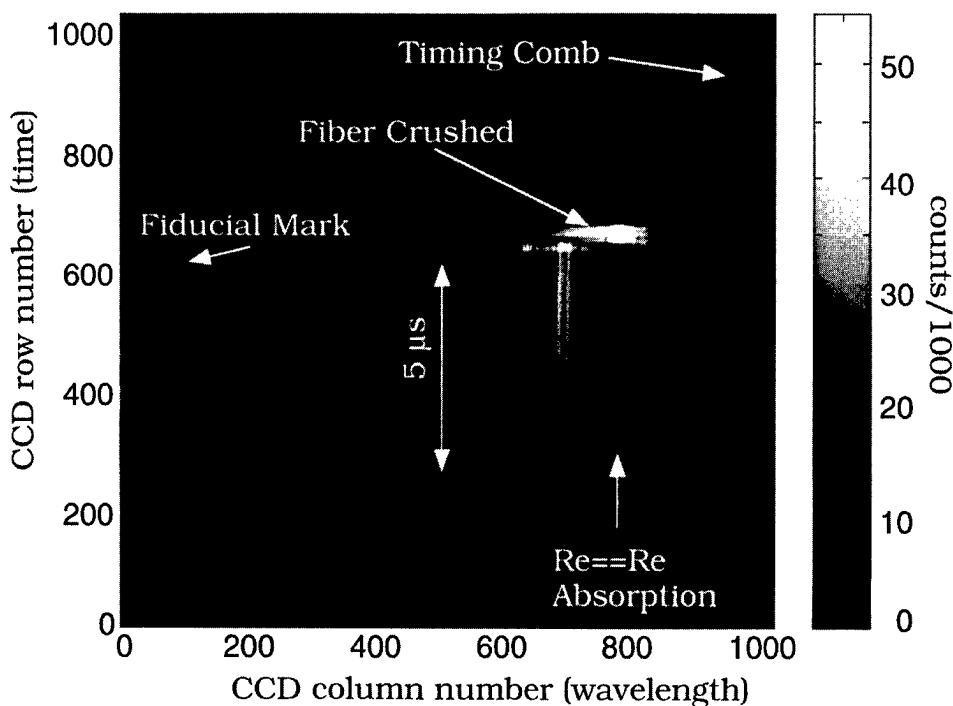


FIGURE 2. Raw data from the shot showing the Re_2Cl_8^- absorption, glow from the fiber crush, the time comb pulses, and the fiducial timing mark. The horizontal axis has the wavelength dispersion, with red to the right. The vertical axis is the time domain.

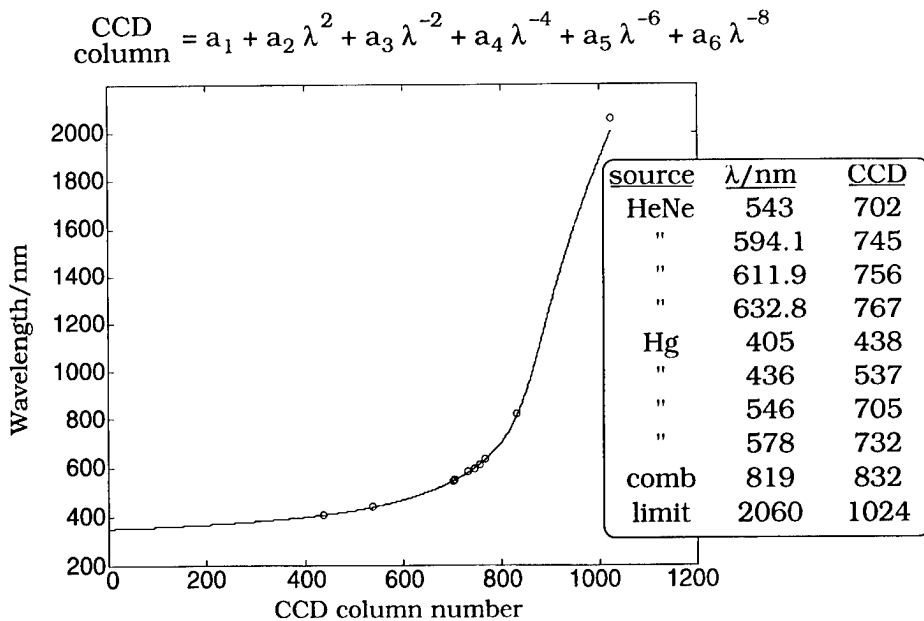


FIGURE 3. Data used to generate a wavelength calibration for the CCD images.

was created to yield a useful functional form to the red of 819 nm.

Time Calibration

The fiducial time mark is displayed in detail in Figure 4. This short duration light pulse is linked to the common time base used for logging the

magnetic field data. Hence, this pulse is the connection between the spectroscopic observation and the magnetic field data. The fiducial timing mark for the spectrograph was measured several days prior to the experiment. To be included separately in our data analysis is the propagation delay from the sample to the spectrograph. Based on the light pulse maximum, CCD row 618 is assigned to 72.853

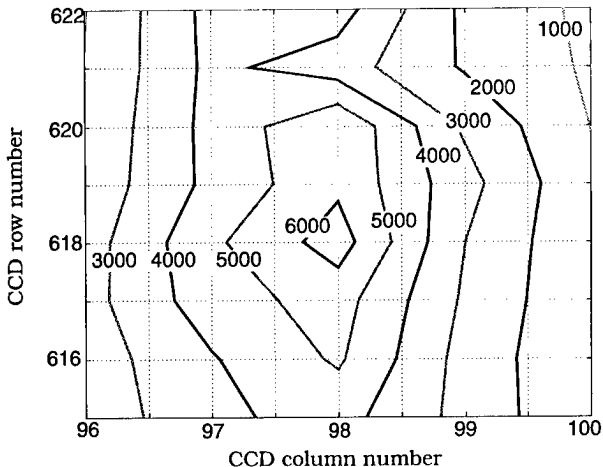


FIGURE 4. Fiducial timing mark at $72.853 \mu\text{s}$ on the common time base.

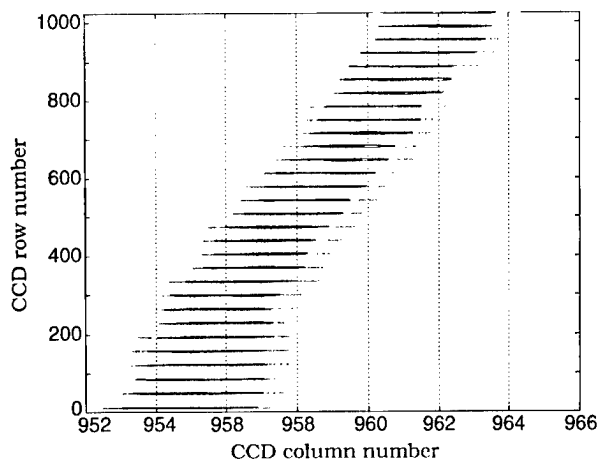


FIGURE 5. Timing comb pulses used to determine the time step per row ($14.32 \text{ ns} / \text{row}$) and the CCD mounting error (a -6 row error at the columns corresponding to the $\text{Re}_2\text{Cl}_8^{2-}$ absorption).

μs , subject to a later correction for CCD mounting error.

The timing comb pulses, shown in Figure 5, are generated by an 819-nm semiconductor laser mounted adjacent to the roof prism. The pulse interval is 500 ns. A fast Fourier transform (FFT) of the comb pulses along the row axis yielded a relative time calibration of 14.32 ns/row. The "tilt" of the timing comb is used to assess the alignment between the CCD pixel array and the electrostatic sweep voltage in the camera, i.e., the time axis. In this run, a slight rotation of the CCD mount is revealed. We assume that the CCD chip itself has orthogonal rows and columns. The application of simple geometry (similar right triangles) shows that the -8 row error in column 960 is a -6 row error in columns defining the $\text{Re}_2\text{Cl}_8^{2-}$ absorption. Thus, row 612 of the $\text{Re}_2\text{Cl}_8^{2-}$ absorption is assigned the absolute time value of $72.853 \mu\text{s}$.

Absorption Spectra

The absorption spectra are calculated in units of absorbance (optical density) for two situations,

preshot and shot, corresponding to zero and high magnetic field, respectively. For each experiment, four data sets were acquired: background (no flash), PMMA, sample preshot, and sample shot. The absorption for the shot is calculated as

$$\text{Abs(shot)} = \log\{(\text{PMMA} - \text{background}) / (\text{Shot} - \text{background})\},$$

where the CCD background image is acquired with the Xe flash lamp disabled; typical photon count was about 50. The PMMA image was acquired a few hours before the shot with an alternate sample holder containing only PMMA film; the fiber length was set to be identical to the sample. The preshot data were acquired a few minutes before the shot. These three data sets are shown in Figure 6. We note that some timing jitter is evident as judged by the leading edge of the light pulse in, for example, column 700. For this reason, the PMMA data set was shifted back in time by 35 rows to obtain a preshot $\text{Re}_2\text{Cl}_8^{2-}$ absorption trace that was constant as a function of time. In the absence of a correction, the $\text{Re}_2\text{Cl}_8^{2-}$

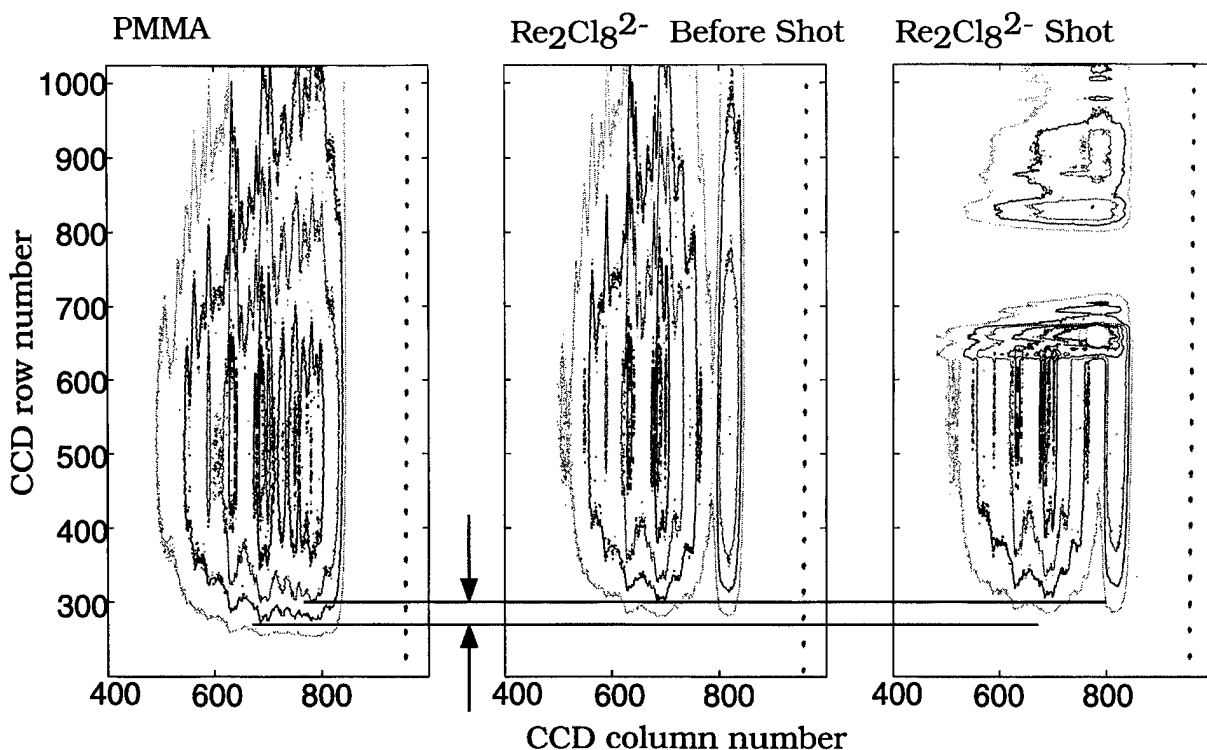


Figure 6. Xe flash lamp jitter as determined from the leading edges for the PMMA, preshot, and shot images.

absorptions in both preshot and shot would have a linear slope with time. We emphasize that Xe flash lamp timing jitter does not affect the absolute time base of the experiment.

Light Leaks and the End of the Experiment

Figure 7 shows the absorption spectrum of octachlorodirhenate during the shot. The next step in data analysis is assessing the end of reliable absorption data. The duration of the magnetic field at its high values can be as short as 50 ns, or roughly 3 CCD rows of data. To better ascertain the "end" of the optical experiment, spectral regions for preshot and shot were integrated, as shown in Figure 8. There is a very close match for preshot and shot $\text{Re}_2\text{Cl}_8^{2-}$ absorption at row 550, corresponding to about 300 Tesla at 1 μs before maximum field. The fiber crush is evident as a sudden change in the baseline at spectral regions away from the $\text{Re}_2\text{Cl}_8^{2-}$ absorption. By this standard, the last good data are in CCD row 626, corresponding

to an absolute time of 73.013 μs [= fiducial mark time + time per row \times row offset – propagation delay = 72.853 μs + 0.01432 $\mu\text{s}/\text{row} \times (626 - 612) - 0.040 \mu\text{s}$]. Interestingly, some of the magnetic field sensors were destroyed by 72.839 μs , CCD row 611 for the $\text{Re}_2\text{Cl}_8^{2-}$ absorption, so we are suspicious of data after this time.

A low-level light leak, probably caused by the shock wave, is difficult to detect in the absorption plot (Figs. 7 and 8) but more easily seen in a reexamination of the raw data. In Figure 9, a portion of the raw data from CCD rows 550 to 626 is shown, along with integrated traces of selected spectral regions. In this plot, we note that the region of maximum $\text{Re}_2\text{Cl}_8^{2-}$ absorption (rows 775–795; 645–690 nm) shows a very low average photon count of 2700 counts/pixel. The baseline regions all have more transmitted light, depending upon the Xe flash lamp. Therefore, a small light leak on the order of 500 counts/pixel will cause a dramatic change in the measured $\text{Re}_2\text{Cl}_8^{2-}$ absorption, while scarcely affecting the absorbance in the "baseline" regions. The region in rows 550–570 has a low average count of 5600, and corresponds

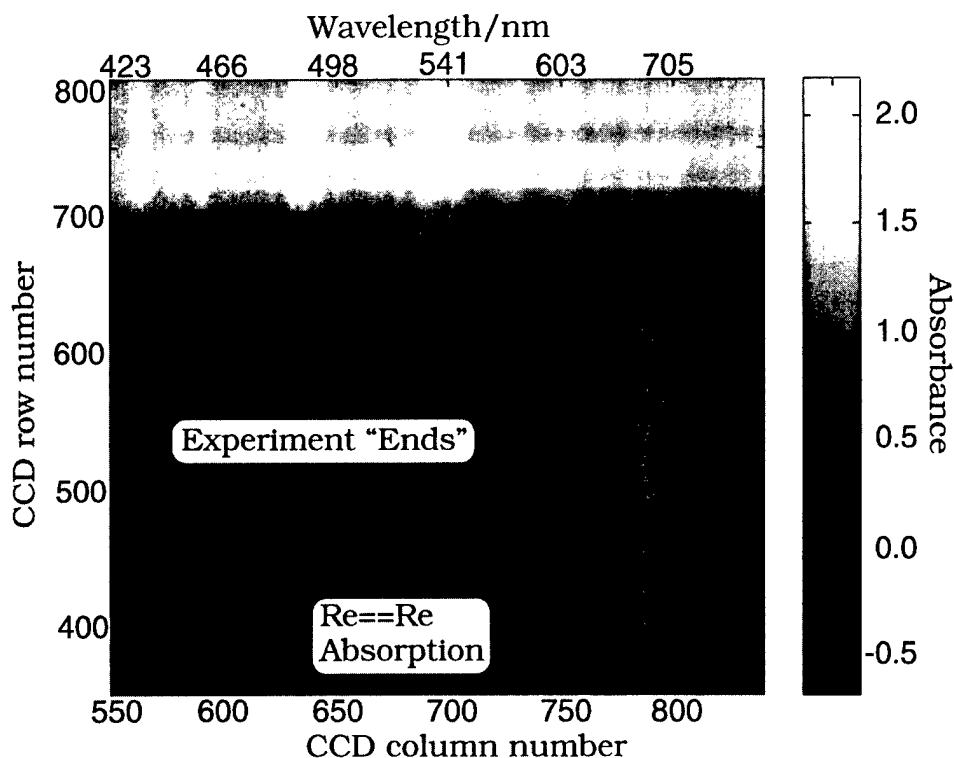


FIGURE 7. Absorption spectrum of octachlorodirhenate during the shot. The $\text{Re}_2\text{Cl}_8^{2-}$ absorption dominates the spectrum prior to the fiber crush near row 627.

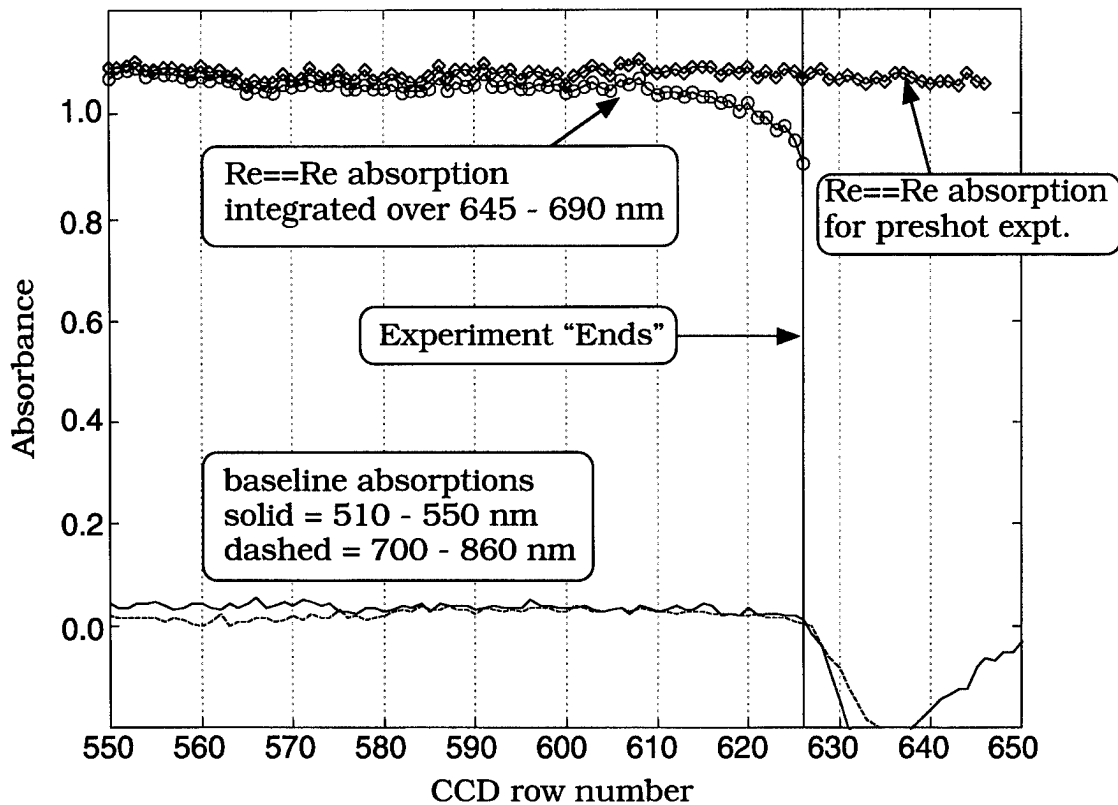


FIGURE 8. Integrated absorptions for preshot and shot $\text{Re}_2\text{Cl}_8^{2-}$ absorptions, and the baseline regions in the shot data. Average absorbances in regions of intense $\text{Re}_2\text{Cl}_8^{2-}$ ground-state absorption, and in “baseline” regions of little or no $\text{Re}_2\text{Cl}_8^{2-}$ ground-state absorption. After row 626, significant changes in baseline regions suggest that data are no longer reliable.

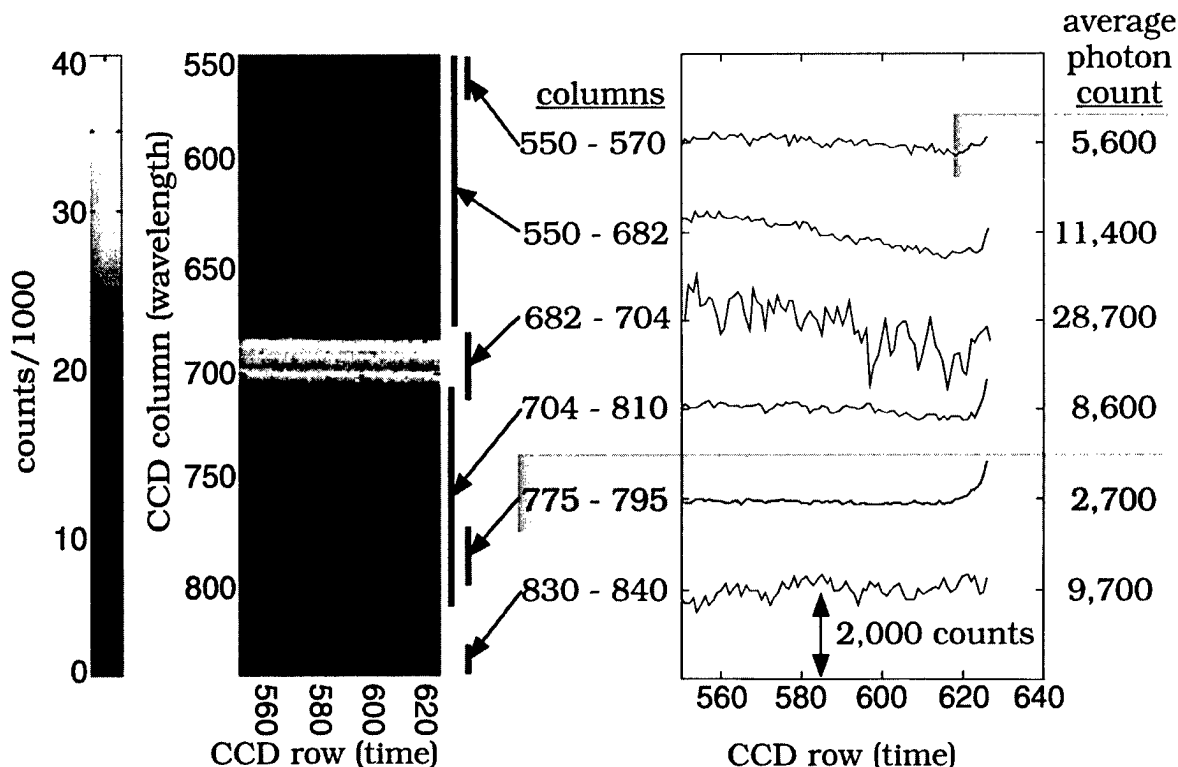


FIGURE 9. A second search for low-level light leaks, caused by the shock wave, based on raw CCD data. The integrated photon count for the $\text{Re}_2\text{Cl}_8^{2-}$ absorption (CCD columns 775–795) shows an increase, indicating a possible reduction of the ground-state absorption as the experiment progresses in time. However, a baseline region with low count rate (CCD columns 775–795) shows an unexplained increase in photon counts starting at CCD row 617. The extra counts are attributed to the onset of a low-level light leak.

to 423–450 nm, a region that does not have a significant $\text{Re}_2\text{Cl}_8^{2-}$ ground-state absorption. However, there is an upturn in the counts beginning at CCD row 617. The most likely explanation of the increased count is a white-light leak from the explosion shock wave as it contacts one of the optical fibers. Hence, we believe that the last reliable optical data to be in row 616, corresponding to an absolute time of 72.870 μs .

The next step in data analysis is the correlation of the absorption change with the magnetic field. This work is ongoing as there is substantial effort involved with determining the magnetic field from the pickup coils and Faraday rotation probes, an interpretation that is done by the magnet team at Los Alamos.

References

1. C. M. Fowler, W. B. Garn, and R. S. Caird, *J. Appl. Phys.* **31**, 588 (1960).
2. A. I. Pavlovskii, N. P. Kolokolchikov, O. M. Tatsenko, A. I. Bykov, M. I. Dolotenko, and A. A. Karpikov, in *Megagauss Physics and Technology*, P. J. Turchi, Ed. (Plenum, New York, 1980).
3. A. I. Pavlovskii, in *Megagauss Fields and Pulsed Power Systems*, V. M. Titov and G. A. Shvetsov, Eds. (Nova Science Publications, New York, 1990).
4. C. M. Fowler and B. L. Freeman, The Los Alamos Arzamas-16 High Magnetic Field Shot Series, Ancho Canyon Site, December 1993, Report #LA-UR-94-2892, Los Alamos National Laboratory, 1994.
5. “Optical Materials,” in *Optics Guide 5*, Melles-Griot, Irvine, CA, 1990, Ch. 3, p. 8.

Optimal Decoupling of Positive- and Negative-Energy Orbitals in Relativistic Electronic Structure Calculations Beyond Hartree–Fock

CARLOS F. BUNGE, ROCIO JÁUREGUI, EUGENIO LEY-KOO

Instituto de Física, Universidad Nacional Autónoma de México Apdo. Postal 20-364, México, 01000, México

Received 25 February 1998; accepted 2 April 1998

ABSTRACT: When the one-body part of the relativistic Hamiltonian H is a sum of one-electron Dirac Hamiltonians, relativistic configuration interaction (CI) calculations are carried out with an *ad hoc* basis of positive-energy orbitals, $\{u_j^+, j = 1, 2, \dots, m\}$ and, more recently, with the full bases of positive-energy and negative-energy orbitals, $\{u_j^+, u_j^-, j = 1, 2, \dots, m\}$. The respective eigenproblems $\mathbf{H}^+ \mathbf{C}_k^+ = E_k^+ \mathbf{C}_k^+$, $k = 1, 2, \dots, \mathcal{N}(m)$, and $\mathbf{H}\mathbf{C}_k = E_k \mathbf{C}_k$; $k = 1, 2, \dots, \mathcal{N}(2m)$ are related through $E_k^+ \leq E_{k+\mathcal{N}(2m)-\mathcal{N}(m)}^-$ [R. Jáuregui et al., Phys. Rev. A **55**, 1781 (1997)]. This inequality becomes an equality for the independent-particle Hartree–Fock model and some other simple multiconfiguration models, leading to an exact decoupling of positive-energy and negative-energy orbitals. Beyond Hartree–Fock, however, it is generally impossible to achieve an equality. By definition, optimal decoupling is obtained when the difference $E_{k+\mathcal{N}(2m)-\mathcal{N}(m)}^- - E_k^+$ is a minimum, which amounts to maximize the energy E_k^+ with respect to any set of m functions in the $2m$ -dimensional space $\{u_j^+, u_j^-, j = 1, 2, \dots, m\}$. Straight maximization is a slowly convergent process. Fortunately, numerical calculations on high-Z atomic states show that optimally decoupled, or best positive-energy orbitals are given, to within 6 decimals in atomic units by the positive-energy natural orbitals of the full eigenfunction $\mathbf{C}_{k+\mathcal{N}(2m)-\mathcal{N}(m)}$. Best orbitals can accurately be obtained through CI-by-parts treatments for later use in large-scale relativistic CI, as illustrated with Ne ground-state calculations. © 1998 John Wiley & Sons, Inc. Int J Quant Chem 70: 805–812, 1998

Key words: negative-energy orbitals; Dirac equation; relativistic configuration interaction; Breit–Dirac–Hartree–Fock; minimax theorem; best orbitals; natural orbitals

Correspondence to: C. F. Bunge.

Introduction

In a previous study [1] we discussed how to incorporate negative-energy orbitals exactly in relativistic variational calculations of electronic bound states. However, except for very small systems, calculations with negative-energy orbitals require formidable computational resources and techniques. The purpose of this study is to show how to determine positive-energy orbitals which minimize, in a strict sense, the energy contribution of negative-energy orbitals. After this, the energy contribution of negative-energy orbitals, always of positive sign [1], can be added from an ab initio estimate obtained with small orbital bases.

We consider a relativistic N -particle Hamiltonian H ,

$$H = H_D + V_{e-e}, \quad (1)$$

where H_D is a sum of one-particle Dirac Hamiltonians h_D ,

$$H_D = \sum_{i=1}^N h_D(i), \quad (2)$$

$$h_D = c\boldsymbol{\alpha} \cdot \mathbf{p} + \beta mc^2 - \frac{Z}{r}, \quad (3)$$

and V_{e-e} is a two-body electron-electron interaction. The V_{e-e} interaction can be the Coulomb repulsion among the electrons, C_{e-e} plus the Breit interaction, B_{e-e} , or any other V_{e-e} which is bounded from below with respect to nonrelativistic trial wave functions. When trying to apply a variational principle in the relativistic realm, the problem with H is that for any normalized N -electron χ , properly built up from Dirac bispinors, the expectation value $\langle \chi | H | \chi \rangle$ is not bounded from below due to the occurrence of small components in the Dirac bispinors.

The study of \mathcal{N} -dimensional representations \mathbf{H} of H in Hilbert space [2] shows that the eigenvalue equation,

$$\mathbf{H}\mathbf{C}_k = E_k \mathbf{C}_k, \quad k = 1, 2, \dots, \mathcal{N} = \mathcal{N}^- + \mathcal{N}^+, \quad (4)$$

$E_k \leq E_{k+1}$, contains two sets of equations with different behavior [2]:

$$\mathbf{H}\mathbf{C}_j = E_j \mathbf{C}_j, \quad j = 1, 2, \dots, \mathcal{N}^-, \quad (5)$$

$$\mathbf{H}\mathbf{C}_{\mathcal{N}^-+i} = E_{\mathcal{N}^-+i} \mathbf{C}_{\mathcal{N}^-+i}, \quad i = 1, 2, \dots, \mathcal{N}^+. \quad (6)$$

In quantum chemistry, Eq. (4) corresponds to a full configuration interaction (CI) expansion.

In Eq. (5), although \mathbf{C}_j represents \mathcal{N} linear variational coefficients, neither these nor E_j can be made stable upon variations in the nonlinear parameters specifying the one-particle basis. Thus, although Eq. (5) is mathematically correct and useful for a given basis set, variational collapse toward minus infinity ensues after legitimate variations in the basis set within Hilbert space.

On the other hand, Eq. (6) yields solutions which are stable upon *any* variations in the basis set. Thus, despite the unboundedness of \mathbf{H} , if one jumps over the lower \mathcal{N}^- eigensolutions of Eq. (4), a genuine variational principle valid for the remaining \mathcal{N}^+ higher-lying eigenvalues is found [1], encompassing the ground and all excited eigenstates. This corresponds to the expected behavior of finite-dimensional representations of operators having a discrete spectrum coexisting with a continuum from minus to plus infinity.

In order to overcome the unboundedness of H , most relativistic electronic structure treatments based on the Dirac-Hamiltonian use the "no-pair" Hamiltonian H^+ [3–5],

$$H^+ = \Lambda^{2+} H \Lambda^{2+}, \quad (7)$$

$$H^+ \Psi_i^+ = E_i^+ \Psi_i^+, \quad (8)$$

where Λ^{2+} is a product of one-particle projection operators,

$$\Lambda^{2+} = \prod_{i=1}^N \lambda^+(i), \quad (9)$$

$$\lambda^+(1) = \sum_{n(\epsilon_j > 0)} |u_j^+(1)\rangle\langle u_j^+(1)|, \quad (10)$$

and the u_j^+ 's are the positive-energy eigenfunctions of a one-particle operator $h_0(1)$ yet to be specified:

$$h_0(1)u_j^+(1) = \epsilon_j u_j^+(1), \quad \epsilon_j > 0. \quad (11)$$

The negative-energy eigenfunctions,

$$h_0(1)u_j^-(1) = \epsilon_j u_j^-(1), \quad \epsilon_j < 0, \quad (12)$$

are defined likewise. The eigenstates of the corresponding finite-basis representation \mathbf{H}^+ satisfy

$$\mathbf{H}^+ \mathbf{C}_i^+ = E_i^+ \mathbf{C}_i^+, \quad i = 1, 2, \dots, \mathcal{N}^+. \quad (13)$$

In some circles, Eq. (13) is considered the fundamental and only valid equation of modern relativistic CI.

The no-pair eigenvalues E_i^+ of Eq. (13) are related to the unique eigenvalues E_{N^-+i} of Eq. (6) by [1],

$$E_i^+ \leq E_{N^-+i}, \quad i = 1, 2, \dots, N^+, \quad (14)$$

indicating that the eigenvalues E_i^+ of relativistic calculations with positive-energy one-particle bases will always lie *below* the eigenvalues E_{N^-+i} of the matrix \mathbf{H} , Eq. (6), whatever choice of positive-energy bases is made. Also, the bound eigenstates of \mathbf{H} (clearly independent of h_0) are devoid of the indefiniteness in the no-pair eigenvalues, caused by the *ad hoc* nature of h_0 .

In Eq. (14), although the eigenvalues E_{N^-+i} are invariant upon linear transformations of the orbital basis, the corresponding E_i^+ are not. The difference between these eigenvalues is equal to the energy contributions of negative-energy orbitals, always a positive quantity on account of (14). In this study we will discuss positive-energy orbitals yielding E_i^+ as close as possible to the E_{N^-+i} . For short, positive-energy and negative-energy orbitals will be denoted by (+) and (-) orbitals, respectively.

Minimax Theorem

The $N(2m)$ eigenvalues of \mathbf{H} are entirely determined by the $\{u_j^+, u_j^-, j = 1, 2, \dots, m\}$ set, independently of any basis of (+) orbitals, $\{u_j^+, j = 1, 2, \dots, m\}$. What happens if we *maximize* the no-pair energies E_i^+ with respect to a nonsingular linear transformation within the entire $\{u_j^+, u_j^-, j = 1, 2, \dots, m\}$? Since the E_i^+ can never be above the E_{N^-+i} , it follows that Eq. (14) contains a variational theorem concerning maximization of E_i^+ . One can then define *best* (+) orbitals for a given bound state i as those for which $E_{N^-+i} - E_i^+$ is a minimum. Since E_{N^-+i} is an invariant, minimization of the above difference amounts to maximization of E_i^+ .

Before setting to maximize E_i^+ , let us discuss the possibility that $E_{N^-+i} - E_i^+ = 0$. It is readily seen that this happens for the case of the lowest state $i = 1$ of a CI singles (a CI with a reference configuration and all singly excited ones) when the CI coefficient of each singly excited configuration is zero, that is, when the Brillouin condition [6] is

satisfied. In that circumstance the reference configuration is the Hartree-Fock solution, and any matrix element of H with the Hartree-Fock function on one side and a single excited configuration on the other is equal to zero, a result known as Brillouin's theorem [7]. The matrix \mathbf{H}^+ consists of just one entry which is equal to the Hartree-Fock energy. The CI singles matrix \mathbf{H} contains \mathbf{H}^+ as its first element, and has zero elements in the remaining of the first column (row), indicating that one of its eigenvalues, E_{N^-+1} , is equal to E_1^+ .

The same result is obtained for some excited states within the same symmetry and also for some simple multireference Hartree-Fock eigenolutions, but it cannot be extended for general wave functions beyond Hartree-Fock. Furthermore, the annihilation of singly excited coefficients provides a completely general method to obtain multireference Hartree-Fock solutions even when $E_{N^-+i} - E_i^+ > 0$ [8].

Best (+) Orbitals for Two-Electron Systems

Let us define an m -dimensional one-particle basis of normalizable Dirac bispinors embracing n_{irr} irreducible representations:

$$\Psi_{n_k l_j m_j}^{(i)} a = \frac{1}{r} \begin{pmatrix} P_{n_k l_j}(r) \mathcal{Y}_{\kappa m_j} \\ i Q_{n_k l_j}(r) \mathcal{Y}_{-\kappa m_j} \end{pmatrix}, \quad k = 1, 2, \dots, k_x(l_j), \quad (15)$$

$$m = \sum_{(l_j)=1}^{n_{\text{irr}}} k_x(l_j). \quad (16)$$

This one-particle basis is called a *single primitive* (SP) basis. An SP basis is not necessarily associated with (+) states, although it can become one after certain transformations that we shall discuss shortly. To date, all many-electron relativistic calculations beyond Hartree-Fock (HF) have been carried out by means of SP bases of one kind or another. However, if one wishes to evaluate accurate relativistic self-consistent field (SCF) wave functions not through SCF equations but rather via Brillouin's theorem [6], negative-energy orbitals need to be included [8] to start the iterative process, although, in the end, the converged relativistic Hartree-Fock orbitals are bona fide (+) orbitals.

The radial functions P belong to a wide family of continuously differentiable radial functions with suitable boundary conditions at the origin and at infinity. In the applications of this study the P 's are Slater-type orbitals (STOs):

$$P_{n_k l_j}(r) = r^{\gamma + n_k - 1} e^{-\lambda_k r}, \quad (17)$$

where $\gamma = \sqrt{\kappa^2 - (\alpha Z)^2} \geq \frac{1}{2}$, viz., $Z \leq 118$. Moreover, each lower component Q_k is coupled to the upper component P_k [9, 10] through the kinetic-balance condition [12]:

$$Q_k(r) = \frac{\alpha}{2} \left(\frac{d}{dr} + \frac{\kappa}{r} \right) P_k(r). \quad (18)$$

Since the final orbitals will contain linear combinations of the upper components differing from the corresponding linear combinations for the lower components, kinetic balance is alien to Hartree-Fock or similar orbitals. The only exceptions to Eqs. (17) and (18) are when $\kappa > 0$ and $n = l + 1$, viz., for $2p_{1/2}$, $3d_{3/2}$, $4f_{5/2}$, etc., and for $1s_{1/2}$ orbitals, where the P_k 's and Q_k 's are chosen to be hydrogenic eigensolutions, that is, eigenfunctions of Dirac's equation with arbitrary charge $Z = n\lambda$.

Following our method to overcome a so-called continuum dissolution [1], we explicitly incorporate, on an equal footing, both (+) and (-) one-particle states into the theory. We do this by supplementing the original m -dimensional SP basis with another complementary m Dirac bispinors,

$$\Psi_{n_k l_j m_j}^{(k+m)} = \frac{1}{r} \begin{pmatrix} P_{n_k l_j}(r) \mathcal{Y}_{\kappa m_j} \\ -i Q_{n_k l_j}(r) \mathcal{Y}_{-\kappa m_j} \end{pmatrix}, \quad (19)$$

differing from the first m in the minus sign preceding the lower components Q_k . In analogy with the SP set, the full $2m$ -dimensional one-particle basis will be called a *double primitive* (DP) set. With one exception [12, 13], all relativistic HF calculations [10, 14] use DP sets, a fact that is important to make explicit.

It is advisable to choose the DP set so as to avoid variational collapse at the one-particle level; if one is going to optimize the nonlinear parameters of the orbital basis at the relativistic level, this requisite becomes mandatory. As is well known [15–19], a matrix representation of a one-particle Dirac Hamiltonian h_D is not a trivial matter. A satisfactory basis must yield positive-energy eigenvalues of the one-particle Dirac equation avoiding

variational collapse and providing *upper bounds* to the exact one-particle eigenvalues. Such bases [20–22] will be said to span the physical domain of h_D .

Distinctively from the SP set, the crucial property of the DP set is that it is invariant under *separate* nonsingular linear transformations of its upper and lower components. A special partitioning of a DP space is a representation of the type $\{u_j^+, u_j^-, j = 1, 2, \dots, m\}$ used above, with the u_j^+, u_j^- given by Eqs. (11) and (12), but this is generally not necessary. We shall now look for a $2m$ -by- $2m$ orthogonal transformation \mathcal{O}^{2m}

$$\mathcal{O}^{2m} \begin{pmatrix} u_1 \\ \dots \\ u_m \\ u_{m+1} \\ \dots \\ u_{2m} \end{pmatrix} = \begin{pmatrix} v_1 \\ \dots \\ v_m \\ v_{m+1} \\ \dots \\ v_{2m} \end{pmatrix} \quad (20)$$

such that E_i^+ is a maximum when H^+ is defined in $\{v_j, j = 1, 2, \dots, p \leq m\}$. The orthonormal set $\{u_j, j = 1, 2, \dots, 2m\}$ is initially given by

$$u_k = \begin{pmatrix} p_k \\ \eta_k q_k \end{pmatrix} \quad (21)$$

with $\eta_k = 1$. After developing the primitive basis, Eqs. (15) and (19), we choose any arbitrary set $\{u_j, j = 1, 2, \dots, m\}$ and maximize E_i^+ with respect to variations in the η_k .

The maximization of E_i^+ will be illustrated with full CI for $U^{90+} 1s^2$ with a DP basis of eighteen $1s_{1/2}$ orbitals. Thus $m = 9$, the CI size is $\mathcal{N}(2m) = 171$, and $\mathcal{N}^-(2m) = 126$. We use Eqs. (15) and (19) with radical functions

$$P_{n_k l_j}(r) = Q_{n_k l_j}(r) = r^\gamma e^{-\lambda_k r}. \quad (22)$$

The orbital exponents λ_k were optimized at the relativistic level by minimizing the CI eigenvalue of order $\mathcal{N}^- + 1 = 127$. After several hundreds of iterations we get:

$$\begin{aligned} \lambda_k = & 12.7255, 17.8156, 28.8820, 40.4350, 56.5954, \\ & 79.5754, 90.7381, 153.449, 213.177, \\ & k = 1, \dots, 9. \end{aligned} \quad (23)$$

The energy E_{127} is given in the first entry of Table I. This is an invariant for the given DP set. The behavior of neighboring eigenvalues and eigenfunctions in a similar situation has been discussed in detail [1].

POSITIVE- AND NEGATIVE-ENERGY ORBITAL

TABLE I
Full CI calculations with the Dirac-Coulomb Hamiltonian for U⁹⁰⁺ 1s² ground state using a DP basis, best (+) orbitals, natural orbitals, and relativistic HF orbitals.^a

Basis	Energy
DP	-9651.3855 029
Best (+) orbitals	-9651.3863 464
(+) natural orbitals	-9651.3863 465
HF orbitals	-9651.3888 435

^aThe four calculations use the same nine s-type STO basis. Energies in a.u., $c = 137.0373$ to conform with literature data.

Next we maximize E_1^+ with respect to the parameters η_k carrying out a CI of order $9 \times 10/2 = 45$. The result appears to be unique, at least in the present case. When HF orbitals (one occupied and eight virtuals) are given as input, iterations take several minutes of CPU time, but when more general orbitals are considered, the CPU time rises to many hours. At this point it is important to control orbital orthogonalization with respect to fixed input orbitals since otherwise, after millions of orthogonalizations, the ensuing loss of precision becomes severe and the optimization process stalls. The maximized E_1^+ is the second entry of Table I, this is the closest one can get to E_{127} with an SP basis.

A conventional no-pair calculation using the nine (+) HF orbitals yields an E_1^+ sinking 3340 μ hartree below the DP basis, as shown in Table I. This is precisely the energy contribution of (-) HF orbitals. In general, HF bases split in an equal number of (+) and (-) orbitals.

We shall now look at results obtained with natural orbitals (NOs) [23]. These are the eigenfunctions of the reduced first-order density matrix $\gamma(1, 1')$,

$$\begin{aligned} \gamma(1, 1') &= N \int \Psi^*(1, 2, \dots, N) \\ &\quad \times \Psi(1', 2, \dots, N) d(2, 3, \dots, N), \quad (24) \end{aligned}$$

$$\gamma(1, 1') = \sum n_i \chi_i^*(1) \chi_i(1'), \quad (25)$$

and they provide a fast-convergent orbital basis for the N -electron CI expansion [23], so it is not surprising that they play a major role in optimal decoupling of (+) and (-) orbitals in the relativistic regime. The eigenvalues n_i of $\gamma(1, 1')$, called occupation numbers, are a measure of the impor-

tance of χ_i in a CI expansion expressed in terms of NOs.

If we solve for the NOs of C_{127} we find only eight (+) NOs. These resemble very closely the first eight best (+) orbitals, and the corresponding energies differ only by 0.1 μ hartree, as shown in Table I. This is a blessing since the latter are very hard to evaluate, while NOs are trivially obtained.

The definition of (+) NOs requires more detail than that of (+) HF orbitals. A (+) NO has positive kinetic energy expectation values and positive expectation value of the mass operator βc^2 . (A positive expectation value of βc^2 is equivalent to a relative weight N_p of the upper component larger than 0.5.)

In Table II we provide pertinent natural orbital data for the ground state 1s² of U⁹⁰⁺. There is an almost perfect splitting between (+) and (-) NOs; however, the fifth NO has a positive kinetic energy expectation value but $N_p < N_Q$ (negative expectation value of the mass operator). Upon using this NO in an SP basis, we find that it behaves as a (-)

TABLE II
Properties of the natural orbitals arising from a relativistically optimized s_{1/2}-type basis set for U⁹⁰⁺ ground state.^a

i	n_k	$\langle c\alpha \cdot p \rangle$	N_p	N_Q
1	2.00	11329.30	0.87	0.13
2	3.85×10^{-6}	26070.61	0.73	0.27
3	1.46×10^{-7}	41440.12	0.57	0.43
4	2.96×10^{-8}	22619.00	0.63	0.37
5	1.68×10^{-8}	10560.19	0.37	0.63
6	3.41×10^{-9}	-8832.77	0.29	0.71
7	7.46×10^{-10}	6350.86	0.86	0.14
8	1.46×10^{-10}	-21428.18	0.26	0.74
9	7.48×10^{-12}	-52371.51	0.23	0.77
10	2.57×10^{-12}	1449.22	0.97	0.03
11	4.14×10^{-13}	-31940.34	0.20	0.80
12	2.49×10^{-14}	-4835.44	0.04	0.96
13	8.69×10^{-15}	846.41	0.96	0.04
14	2.74×10^{-17}	-554.74	0.03	0.97
15	4.89×10^{-19}	89.28	0.92	0.08
16	1.07×10^{-20}	466.88	0.61	0.39
17	3.37×10^{-21}	-982.68	0.28	0.72
18	5.82×10^{-22}	-276.20	0.18	0.82

^aThe dimension of the double-primitive basis is 18. The second column gives the occupation number n_k of orbital k added over the angular momentum quantum number m_j . The expectation value of the kinetic energy operator $c\alpha \cdot p$ is given in the third column. The relative weights N_p and N_Q of the upper P_k and lower Q_k components for each natural orbital are given in the fourth and fifth columns.

NO, that is, in a CI calculation it must be counted as a $(-)$ orbital. Therefore, $(-)$ NOs will be defined as those NOs that are not $(+)$ NOs.

Those NOs with $n_i < 10^{-16}$ may be numerically unreliable and do not yield significant contributions to the wave function, thus $(+)$ NOs with such small n_i may be discarded.

The natural orbitals are closely related to ergonals, the eigenfunctions of the reduced $1-p$ energy-density operator $h_p(1,1')$ [24]:

$$\begin{aligned} h_p(1,1') = & \int \Psi^*(1,2,\dots,N) \\ & \times \frac{1}{2}[H(1,2,\dots,N) + H(1',2,\dots,N)] \\ & \times \Psi(1',2,\dots,N)d(2,3,\dots,N). \end{aligned} \quad (26)$$

If Ψ is a full CI, it holds:

$$h_p(1,1') = \frac{E}{N} \gamma(1,1'), \quad (27)$$

thus ergonals become natural orbitals and their eigenvalues are proportional to the occupation numbers. We have observed that for $2m$ -dimensional DP bases, the eigenvalues of both, h_D and of the Fock-Dirac operator, split into m $(+)$ and m $(-)$ orbitals. Alternatively, there are usually fewer than m $(+)$ NOs, as it may be suspected from the results of Table II. Since the latter are identical with $(+)$ ergonals for full CI, we see that this difference cannot be ascribed to the use of "energy" operators in the first case.

One of the original motivations for introducing NOs [23] was to reduce the number of primitive orbitals. We notice that this expectation is clearly fulfilled in relativistic calculations when condensing a $2m$ -dimensional DP basis into an SP basis of dimension even smaller than m , as illustrated in Tables I and II.

In conclusion, for two-electron systems, $(+)$ NOs are as close to best $(+)$ orbitals as one may hope to get. For the ground state $1s^2$ of U^{90+} , $(+)$ NOs yield an energy only $0.1\ \mu$ hartree below that of best $(+)$ orbitals. Also, the energy contribution of s -type $(-)$ NOs is $844\ \mu$ hartree, four times smaller than that of $(-)$ HF orbitals.

(+) Natural Orbitals for Many-Electron Systems

Maximizations of E_i^+ are very time-consuming. In view of the remarkable coincidence between

best $(+)$ orbitals and $(+)$ NOs for two-electron systems, we will examine the viability of computing $(+)$ NOs of C_{N^-+i} even when N^-+i exceeds practical limits.

Let us consider Ne ground state and settle for a singles and doubles CI approximation. An STO basis of $8s7p6d5f4g3h2i$ orbitals [25] yields a nonrelativistic energy $E = -128.914571$ a.u., recovering about 94% of the correlation energy. The full jj basis is $16S14p14P12d12D10f10F8g8G6h6H4i4I$, where lowercase and uppercase are used for $j = l - \frac{1}{2}$ and $j = l + \frac{1}{2}$, respectively. Here $N = 23586$ and $N^- = 17984$, thus simplifications are warranted. In short, we will calculate approximate NOs through CI by parts. These approximate NOs are quite distinct from the rigorous NOs. However, one hopes that the corresponding $(+)$ NOs will span essentially the same space as the rigorous $(+)$ NOs.

The reliability of our procedure will be tested with small $14S10p10P$ bases which allow both rigorous and approximate treatments to be carried out. Rigorous $(+)$ NOs are a subset of the NOs of the 2283th excited state of a doubles CI of order 2827, with all singles being excluded to allow the HF orbitals to be part of the NO set. Approximate S -type NOs are a subset of the S -type NOs of a CI, including all double substitutions of $1S^2$, $2S^2$, $2p^2$, and $2P^2$, and similarly for the p -type and P -type NOs. In both instances, a full DP base is used. In the first column of Table III we present model CI energies obtained with the full basis, thus a very highly excited state is considered. Columns 2 and 3 report energies obtained with rigorous and approximate $(+)$ NOs, respectively. The fact that both columns are equal means that our approximate $(+)$ NOs essentially span the same space as the rigorous ones.

In Tables IV and V we present model calculations in terms of approximate $(+)$ NOs, using the Dirac-Coulomb and the Breit-Dirac-Coulomb (BDC) Hamiltonians, respectively. Relativistic energy contributions in the last column reflect basis set incompleteness rather than actual convergence. In both cases, however, convergence to within 0.0001 a.u. appears to be achieved, which is a better accuracy than one recently obtained for the nonrelativistic correlation energy [26]. However, this optimism must be tempered by further studies on reliable calculations of energy contributions of $(-)$ orbitals, which are appreciable in Breit-Dirac-Coulomb calculations, even in such small systems as Ne.

TABLE III

Ne ground-state energies for model calculations using the full (+, -) orbital bases, rigorous (+) NOs and approximate (+) NOs, using the Dirac–Coulomb (DC) and the Breit–Dirac–Coulomb (BDC) Hamiltonians.^a

Model	(+, -)	Rigorous (+)	Approximate (+)	(-)
DC, Hartree–Fock	–128.691969	–128.691969		0
BDC, Hartree–Fock	–128.675328	–128.675328		0
DC, CI doubles 7s5p	–128.872829	–128.872829	–128.872829	0
DC, CI singles and doubles 7s5p	–128.874803	–128.874803	–128.874803	0
BDC, CI doubles 7s5p	–128.853822	–128.857090	–128.857090	0.003268
BDC, CI singles and doubles 7s5p	–128.855803	–128.859062	–128.859062	0.003259

^aEnergy contributions of negative-energy orbitals are given in the last column. Energies in a.u., $c = 137.0359895$.

TABLE IV

Ne ground-state energies for model calculations in terms of approximate (+) NOs, using the Dirac–Coulomb (DC) Hamiltonian.^a

Model	Nonrelativistic	DC energy	Difference
Hartree–Fock	–128.547098	–128.691969	0.144871
CI singles and doubles 8s7p	–128.733861	–128.879017	0.145156
CI singles and doubles 8s7p6d	–128.860136	–129.005254	0.145118
CI singles and doubles 8s7p6d5f	–128.896413	–129.041502	0.145089
CI singles and doubles 8s7p6d5f4g	–128.909090	–129.054168	0.145078
CI singles and doubles 8s7p6d5f4g3h	–128.913068	–129.058142	0.145074
CI singles and doubles 8s7p6d5f4g3h2i	–128.914571	–129.059643	0.145072

^aEnergies in a.u., $c = 137.0359895$.

TABLE V

Ne ground-state energies for model calculations in terms of approximate (+) NOs, using the Breit–Dirac–Coulomb (BDC) Hamiltonian.^a

Model	Nonrelativistic	BDC energy	Difference
Hartree–Fock	–128.547098	–128.675321	0.128223
CI singles and doubles 8s7p	–128.733861	–128.863404	0.129543
CI singles and doubles 8s7p6d	–128.860136	–128.989878	0.129742
CI singles and doubles 8s7p6d5f	–128.896413	–129.026174	0.129761
CI singles and doubles 8s7p6d5f4g	–128.909090	–129.038844	0.129754
CI singles and doubles 8s7p6d5f4g3h	–128.913068	–129.042819	0.129751
CI singles and doubles 8s7p6d5f4g3h2i	–128.914571	–129.044321	0.129750

^aEnergies in a.u., $c = 137.0359895$.

The obvious strategy is to calculate those quantities accessible to more exact results, from which one can deduce the less accurate ones. The next challenge is to evaluate accurate quantum electrodynamics corrections. Purely variational nonrelativistic results [26] may be improved by a combination of variational-perturbation and perturbation techniques. Estimates of the energy contributions of (–) orbitals can be made approximately, but more experience is needed to know how reliable these approximate estimates are. Of course, for

two-electron systems, exact incorporation of (–) orbitals is always possible [1].

References

1. R. Jáuregui, C. F. Bunge, and E. Ley-Koo, Phys. Rev. A **55**, 1781 (1997).
2. J. von Neumann, *Mathematical Foundations of Quantum Mechanics* (Princeton University Press, Princeton, 1955).
3. G. E. Brown and D. G. Ravenhall, Proc. Roy. Soc. London, A **208**, 552 (1951).

4. M. H. Mittleman, Phys. Rev. A **4**, 893 (1971); *Ibid.*, **15**, 2395 (1972).
5. J. Sucher, Phys. Rev. A **22**, 348 (1980).
6. C. F. Fisher, *The Numerical Hartree-Fock Method* (Wiley, New York, 1977).
7. L. Brillouin, J. Phys. **3**, 373 (1932).
8. C. F. Bunge, R. Jáuregui, and E. Ley-Koo, Can. J. Phys., to appear.
9. Y. S. Lee and A. D. McLean, J. Chem. Phys. **76**, 735 (1982).
10. Y. Ishikawa, R. C. Binning, and K. M. Sando, Chem. Phys. Lett. **101**, 111 (1983).
11. R. E. Stanton and S. Havriliak, J. Chem. Phys. **81**, 1910 (1984).
12. S. P. Goldman and A. Dalgarno, Phys. Rev. Lett. **57**, 408 (1986).
13. S. P. Goldman, Phys. Rev. A **37**, 16 (1988).
14. A. K. Mohanty and E. Clementi, Chem. Phys. Lett. **157**, 348 (1989).
15. W. Kutzelnigg, Int. J. Quant. Chem. **25**, 107 (1984).
16. S. P. Goldman, Phys. Rev. A **31**, 3541 (1985).
17. G. W. F. Drake and S. P. Goldman, Phys. Rev. A **23**, 2093 (1981).
18. K. G. Dyall, I. P. Grant, and S. Wilson, J. Phys. B **17**, 493 (1984).
19. Y. Ishikawa, R. Baretti, and K. M. Sando, Chem. Phys. Lett. **117**, 444 (1985).
20. I. P. Grant and H. M. Quiney, Adv. At. Mol. Phys. **23**, 37 (1988).
21. G. W. F. Drake and S. P. Goldman, Adv. At. Mol. Phys. **23**, 393 (1988).
22. R. Jáuregui, C. F. Bunge, and E. Ley-Koo, preprint IFUNAM FT96-01.
23. P.-O. Löwdin, Phys. Rev. **97**, 1509 (1955); Adv. Phys. **5**, 1 (1956).
24. C. F. Bunge, Phys. Rev. A **7**, 15 (1973); C. F. Bunge, in *Energy Structure and Reactivity* (D. W. Smith and B. McRae, Eds.) (Wiley, New York, 1973), pp. 68–74.
25. The STOs are available from directory pub/bases/neon via anonymous ftp 132.248.7.246.
26. O. Jitrik and C. F. Bunge, Phys. Rev. A **55**, 2614 (1997).

Second-Order Multiconfigurational Dirac–Fock Calculations on Boronlike Ions

MARIUS JONAS VILKAS,¹ YASUYUKI ISHIKAWA,¹ KONRAD KOC²

¹Department of Chemistry and the Chemical Physics Program, University of Puerto Rico, P.O. Box 23346, San Juan, Puerto Rico 00931-3346

²Department of Physics, Pedagogical University, ul. Podchorazych 2, 30-084, Krakow, Poland

Received 23 February 1998; revised 11 May 1998; accepted 21 May 1998

ABSTRACT: Second-order multiconfigurational Dirac–Fock self-consistent-field calculations are reported for the ground and low-lying excited states of boronlike ions, Ne^{+5} , P^{+10} , Ca^{+15} , Mn^{+20} , Zn^{+25} , and Mo^{+37} . Relativity alters an important class of strong configuration interaction, asymptotic CI, along the isoelectronic sequence, and multiconfigurational Dirac–Fock self-consistent-field calculations including $n = 2$ and $n = 3$ complexes are sufficient to accurately predict fine-structure splittings for larger Z , while for small Z , it is necessary to accurately account for the remaining dynamical correlation. © 1998 John Wiley & Sons, Inc. Int J Quant Chem 70: 813–823, 1998

Introduction

It is widely recognized that accurate predictions of properties of atoms and molecules must take electron correlation into account. In heavy-atom systems and highly ionized high- Z ions, the effects of relativity become important in addition to electron correlation. Further, the effects of relativity and electron correlation in these systems are strongly intertwined. There are two distinct methods for studying the relativistic and correlation effects in atoms and molecules: The first is the use

of nonrelativistic wave functions, the relativistic effects being introduced by perturbation theory. Pyper [1] and Molzberger and Schwarz [2] showed that relativity significantly modifies even the dynamics of valence electrons in heavy atoms. These studies indicate that perturbation theory is less adequate for investigating relativistic effects in heavy atoms or in molecules which contain heavy atoms. The second of the two methods is the direct use of the Dirac Hamiltonian or its two-component variant which incorporates major one-electronlike relativistic effects in variational calculations.

An intense effort in the last decade has been directed toward developing relativistic many-body theories that accurately account for both relativis-

Correspondence to: Y. Ishikawa.

tic and electron correlation effects in heavy-atom systems and highly ionized high-Z ions. Among the relativistic many-body techniques developed recently are numerical finite-difference multiconfiguration (MC) Dirac–Fock self-consistent-field (DF SCF) theory [3–5], relativistic many-body perturbation theory (MBPT) [6–11], relativistic coupled cluster (CC) theory [12–15], and the relativistic configuration interaction (CI) method [16–19]. Discrete basis sets of both “local” [6, 7, 12, 14, 17] and “global” [5, 8–10, 13, 16, 18] functions as well as numerical finite-difference algorithms [3, 4, 11, 15, 19] have been used. Implementations based on expansion in analytic basis functions [5–10, 12–14, 16–18] have the advantage over those based on numerical finite-difference algorithms [3, 4, 11, 19] of providing a compact representation of the complete Dirac spectrum and of providing analytic energy gradients and Hessian matrices of second-energy derivatives.

We recently [20] employed the generalized coupling operator method [21] to construct a single Fock operator for open-shell matrix DF SCF and showed that with such an operator all closed- and open-shell four-component Dirac spinors can be determined. We reported state-specific relativistic MBPT [10] and relativistic CI [18] calculations for open-shell systems. The spinors used in these calculations were obtained in single-configuration matrix DF SCF calculations. Correlated methods based on the single-configuration reference state are very effective in describing dynamical correlation, but do not work well when significant nondynamic correlation (i.e., near-degeneracy) is present. Systems in which only the dynamical correlation is important may be described by single-configuration DF wave functions, whereas systems with significant nondynamical correlation cannot be correctly described within single-configuration DF wave functions. Near-degeneracy of the valence spinors gives rise to a manifold of strongly interacting configurations, that is, strong configuration mixing within a relativistic complex due to asymptotic degeneracy [22], and makes a relativistic multiconfigurational treatment mandatory. The classic examples are the near-degeneracy effects in the beryllium and carbon isoelectronic sequences, open-shell atoms with two or more valence electrons, molecular reactive and excited-state energy surfaces, and multiply bonded molecules.

In the present study, we outlined a recently developed second-order matrix MC DF SCF [23,

24] which is applicable to systems with significant nondynamical correlation effects. Numerical finite-difference and matrix MC DF SCF algorithms based on first-order energy variation often exhibit slow convergence for the ground states of atoms and molecules and are often nonconvergent for their excited states. Second-order optimization of Dirac four-spinors and configuration mixing coefficients in the MC DF SCF is thus necessary to guarantee well-controlled convergence in relatively few iterations. The essential feature of the MC DF SCF is that the multireference technique is employed as a means of treating nondynamical correlation. Once the near-degeneracy effects in the relativistic complex are accounted for by MC DF SCF, the remaining dynamical correlation may be accounted for by multireference (MR) configuration interaction with single and double excitations (CI–SD) out of MC DF reference wave functions or MR perturbation theory. In the second-order MC DF SCF, we develop the MC variational energy up to second order in the unitary rotation parameters and seek the stationary point by employing a quadratic approximation to the energy surface. The approach parallels the second-order algorithm developed in nonrelativistic multiconfigurational SCF calculations [25] and provides excellent convergence once a quadratic basin on the energy surface is entered. In the next section, we briefly outline the quadratically convergent relativistic MC DF SCF [23, 24] and MR CI–SD algorithms implemented with analytic basis sets of Gaussian spinors. In the third section, the results of matrix MC DF SCF calculations on the ground and low-lying excited states of boronlike ions, Ne^{+5} , P^{+10} , Ca^{+15} , Mn^{+20} , Zn^{+25} , and Mo^{+37} , are presented. For low-Z ions, Ne^{+5} and P^{+10} , MR CI–SD calculations that account for the remaining dynamic correlation are also reported.

Theory

The effective N -electron Hamiltonian (in atomic units) for the development of our matrix MC DF SCF algorithm is taken to be the relativistic “no-pair” Dirac–Coulomb (DC) Hamiltonian [26, 27],

$$H_{DC}^+ = \sum_i h_D(i) + \mathcal{L}_+ \left(\sum_{i>j} \frac{1}{r_{ij}} \right) \mathcal{L}_+, \quad (1)$$

where $h_D(i)$ is the Dirac one-electron Hamiltonian:

$$h_D(i) = c\alpha_i \mathbf{p}_i + (\beta_i - 1)c^2 + V_{nuc}(r_i). \quad (2)$$

Here, α and β are the 4×4 Dirac vector and scalar matrices, respectively. $V_{nuc}(r)$ is the nuclear attraction term. The nucleus is modeled as a sphere of uniform proton-charge distribution (Z is the nuclear charge, and R , the radius of the sphere) [28]:

$$V_{nuc}(r) = \begin{cases} -\frac{Z}{r}; & \text{for } r > R \\ -\frac{Z}{2R} \left(3 - \frac{r^2}{R^2}\right); & \text{for } r \leq R. \end{cases} \quad (3)$$

The positive-energy projection operator \mathcal{L}_+ formally takes into account the field-theoretic condition that the negative-energy states are filled [26, 27]. It is defined in terms of the positive-energy spinors obtained from MC DF SCF calculations [27].

Adding the frequency-independent Breit interaction,

$$B_{12} = -\frac{1}{2} [\alpha_1 \cdot \alpha_2 + (\alpha_1 \cdot \mathbf{r}_{12})(\alpha_2 \cdot \mathbf{r}_{12})/r_{12}^2] / r_{12}, \quad (4)$$

to the instantaneous electron-electron Coulomb interaction, in Coulomb gauge, results in the Coulomb-Breit potential, which is correct to order α^2 (α being the fine-structure constant) [26]. Addition of the Breit term yields the no-pair Dirac-Coulomb-Breit (DCB) Hamiltonian [26, 27]:

$$H_{DCB}^+ = \sum_i h_D(i) + \mathcal{L}_+ \left(\sum_{i>j} \left(\frac{1}{r_{ij}} + B_{ij} \right) \right) \mathcal{L}_+, \quad (5)$$

which is covariant to first order and increases the accuracy of calculated fine-structure splittings and inner-shell binding energies. Higher-order QED effects appear first in order α^3 . Studies have appeared that go beyond the no-pair approximation where negative-energy states are needed to evaluate the higher order QED effects [29, 30].

Eigenfunctions of the no-pair DC Hamiltonian are approximated by a linear combination of N -electron configuration state functions (CSFs):

$$\Psi_{MCDFC}(\gamma\mathcal{T}\pi) = \sum_I^{N_{CSF}} C_I^{\gamma\mathcal{T}\pi} \Phi_I(\gamma_I\mathcal{T}\pi). \quad (6)$$

Here, the MC Dirac-Fock-Coulomb self-consistent-field (DFC SCF) wave function $\Psi_{MCDFC}(\gamma\mathcal{T}\pi)$ is an eigenfunction of the angular momentum and parity operators with total angular momentum \mathcal{T} and parity π , and $\Phi_I(\gamma_I\mathcal{T}\pi)$ are the CSFs. γ denotes a set of quantum numbers other than \mathcal{T} and π necessary to specify the state uniquely. In the following, $C_I^{\gamma\mathcal{T}\pi}$ is abbreviated as C_I^γ .

In the atomic case, the total DC energy of the general electronic state $\Psi_{MCDFC}(\gamma\mathcal{T}\pi)$ can be expressed as

$$\begin{aligned} E^{\gamma\mathcal{T}\pi} &= \langle \Psi_{MCDFC}(\gamma\mathcal{T}\pi) | H_{DC}^+ | \Psi_{MCDFC}(\gamma\mathcal{T}\pi) \rangle \\ &= \sum_{I \geq J}^{N_{CSF}} C_I^\gamma C_J^\gamma \langle \Phi_I(\gamma_I\mathcal{T}\pi) | H_{DC}^+ | \Phi_J(\gamma_J\mathcal{T}\pi) \rangle \\ &\quad \times (2 - \delta_{IJ}). \end{aligned} \quad (7)$$

Here, it is assumed that $\Psi_{MCDFC}(\gamma\mathcal{T}\pi)$ and $\Phi_I(\gamma_I\mathcal{T}\pi)$ are normalized. The configuration mixing coefficients $\{C_I^\gamma\}$ and the integrals involved in Eq. (7) may be chosen real in atomic many-electron calculations. The number of terms in the summation has been reduced by using the hermiticity of the Hamiltonian and by having chosen coefficients $\{C_I^\gamma\}$ and integrals real. The total energy can be conveniently expressed in terms of the unique elements of the one- and two-particle radial integrals:

$$E^{\gamma\mathcal{T}\pi} = \sum_{\alpha=1}^{N_t} t_\alpha I(a_\alpha b_\alpha) + \sum_{\beta=1}^{N_V} V_\beta R^{\nu_\beta}(a_\beta b_\beta, c_\beta d_\beta), \quad (8)$$

where N_t and N_V are the numbers of nonzero t_α and V_β coefficients. The short notation for the radial integrals was used:

$$I(ab) = I(n_a \kappa_a n_b \kappa_b) = \langle \phi_{n_a \kappa_a}(r) | h_D(r) | \phi_{n_b \kappa_b}(r) \rangle \quad (9)$$

$$\begin{aligned} R^\nu(ab, cd) &= R^\nu(n_a \kappa_a n_b \kappa_b, n_c \kappa_c n_d \kappa_d) \\ &= \left\langle \phi_{n_a \kappa_a}(r_1) \phi_{n_b \kappa_b}(r_2) \left| \frac{r'_<}{r'_>} \right| \phi_{n_c \kappa_c}(r_1) \phi_{n_d \kappa_d}(r_2) \right\rangle, \end{aligned} \quad (10)$$

where $\{\phi_{n_a \kappa_a}(r)\}$ is an orthonormal set of Dirac one-electron radial spinors of symmetry κ . The symmetry κ is related to spinor angular momentum j by $\kappa = \mp(j + \frac{1}{2})$ for $l = j \mp \frac{1}{2}$, where l is

orbital angular momentum quantum number of the large component spinor. The generalized coefficients t_α and V_β are expressed in terms of nonzero angular coefficients t_α^{IJ} and V_β^{IJ} :

$$t_\alpha = \sum_{\alpha'=1}^{N'_I} t_\alpha^{IJ} \delta(\alpha, \alpha') \{2 - \delta_{IJ}\} C_I^\gamma C_J^\gamma \quad (11)$$

$$V_\beta = \sum_{\beta'=1}^{N'_V} V_\beta^{IJ} \delta(\beta, \beta') \{2 - \delta_{IJ}\} C_I^\gamma C_J^\gamma. \quad (12)$$

The angular coefficients t_α^{IJ} and V_β^{IJ} account for the symmetries of the radial integrals $I(a_\alpha b_\alpha)$ and $R^\nu(a_\beta b_\beta, c_\beta d_\beta)$, and the notations $\alpha = \{a_\alpha b_\alpha\}$ and $\beta = \{\nu_\beta, a_\beta b_\beta, c_\beta d_\beta\}$ were used.

Throughout the section, the following notations are used: The indices e and f denote occupied spinors, the indices p, q, r , and s denote any of the occupied or virtual spinors (both positive and negative energy spinors), the indices I, J , and K denote CI coefficients, and the indices a, b, c, d , and ν are reserved for the sets α and β describing unique radial integrals.

SECOND-ORDER DIRAC-FOCK SELF-CONSISTENT-FIELD ALGORITHM

Given a trial orthonormal set of $2N_\kappa$ one-electron radial spinors $\{\phi_{n_e \kappa_p}(r)\}$, the optimum occupied radial spinors $\{\phi_{n_e \kappa_e}^{opt}\}$ can be found by a unitary transformation $\mathbf{U} = \mathbf{1} + \mathbf{T}$ via

$$\begin{aligned} \phi_{n_e \kappa_e}^{opt}(r) &= \frac{1}{r} \begin{pmatrix} P_{n_e \kappa_e}^{opt}(r) \\ Q_{n_e \kappa_e}^{opt}(r) \end{pmatrix} = \sum_p^{2N_\kappa} \phi_{n_p \kappa_p}(r) U_{pe} \\ &= \sum_p^{2N_\kappa} \phi_{n_p \kappa_p}(r) (T_{pe} + \delta_{pe}). \end{aligned} \quad (13)$$

Here, the summation extends over both negative and positive energy spinors. $P_{n_e \kappa_e}(r)$ and $Q_{n_e \kappa_e}(r)$ are the large and small radial components and are expanded in N_κ Gaussian-type functions (GTF) that satisfy the boundary conditions associated with the finite nucleus [9, 20, 28]. Variation of the energy with respect to the parameters $\{T_{pe}\}$ leads to the Newton-Raphson (NR) equations:

$$g_{pe}^o + \sum_{qf} h_{pe, qf}^{oo} T_{qf} = 0, \quad (14)$$

where the first derivative with respect to T_{pe} is

$$\begin{aligned} g_{pe}^o &= \left. \frac{\partial E^{\gamma\bar{\gamma}\pi}(\mathbf{T})}{\partial T_{pe}} \right|_{T=0} \\ &= \sum_{\alpha=1}^{N_I} t_\alpha [I(p b_\alpha) \delta(e, a_\alpha) + I(a_\alpha p) \delta(e, b_\alpha)] \\ &\quad + \sum_{\beta=1}^{N_V} V_\beta \cdot \{ R^{\nu_\beta}(p b_\beta, c_\beta d_\beta) \delta(e, a_\beta) \\ &\quad + R^{\nu_\beta}(a_\beta p, c_\beta d_\beta) \delta(e, b_\beta) \\ &\quad + R^{\nu_\beta}(a_\beta b_\beta, p d_\beta) \delta(e, c_\beta) \\ &\quad + R^{\nu_\beta}(a_\beta b_\beta, c_\beta p) \delta(e, d_\beta) \} \end{aligned} \quad (15)$$

and the Hessian matrix with respect to T_{pe} and T_{qf} is

$$\begin{aligned} h_{pe, qf}^{oo} &= \left. \frac{\partial^2 E^{\gamma\bar{\gamma}\pi}(\mathbf{T})}{\partial T_{pe} \partial T_{qf}} \right|_{T=0} \\ &= \sum_{\alpha=1}^{N_I} t_\alpha [I(p q) \delta(e, a_\alpha) \delta(f, b_\alpha) \\ &\quad + I(q p) \delta(e, b_\alpha) \delta(f, a_\alpha)] + \sum_{\beta=1}^{N_V} V_\beta \\ &\quad \times \{ R^{\nu_\beta}(p q, c_\beta d_\beta) \delta(e, a_\beta) \delta(f, b_\beta) \\ &\quad + R^{\nu_\beta}(p b_\beta, q d_\beta) \delta(e, a_\beta) \delta(f, c_\beta) \\ &\quad + R^{\nu_\beta}(p b_\beta, c_\beta q) \delta(e, a_\beta) \delta(f, d_\beta) \\ &\quad + R^{\nu_\beta}(a_\beta p, q d_\beta) \delta(e, b_\beta) \delta(f, c_\beta) \\ &\quad + R^{\nu_\beta}(a_\beta p, c_\beta q) \delta(e, b_\beta) \delta(f, d_\beta) \\ &\quad + R^{\nu_\beta}(a_\beta b_\beta, p q) \delta(e, c_\beta) \delta(f, d_\beta) \\ &\quad + R^{\nu_\beta}(q p, c_\beta d_\beta) \delta(f, a_\beta) \delta(e, b_\beta) \\ &\quad + R^{\nu_\beta}(q b_\beta, p d_\beta) \delta(f, a_\beta) \delta(e, c_\beta) \\ &\quad + R^{\nu_\beta}(q b_\beta, c_\beta p) \delta(f, a_\beta) \delta(e, d_\beta) \\ &\quad + R^{\nu_\beta}(a_\beta q, p d_\beta) \delta(f, b_\beta) \delta(e, c_\beta) \\ &\quad + R^{\nu_\beta}(a_\beta q, c_\beta p) \delta(f, b_\beta) \delta(e, d_\beta) \\ &\quad + R^{\nu_\beta}(a_\beta b_\beta, q p) \delta(f, c_\beta) \delta(e, d_\beta) \}. \end{aligned} \quad (16)$$

To account for the orthogonality constraints, terms involving Lagrange multipliers must be added to the energy functional.

The CI coefficients C_I^γ [Eq. (7)] are not constant, and variations over them must also be incorporated in the second-order energy. Consider two

sets of CI coefficients $\mathbf{C}^\gamma = \{C_l^\gamma\}$ (optimum) and $\mathbf{C}^{(0)\gamma} = \{C_l^{(0)\gamma}\}$ (approximate). A Taylor expansion of the energy yields

$$\begin{aligned} E^{\gamma\pi}(\mathbf{T}, \mathbf{C}^\gamma = \mathbf{C}^{(0)\gamma} + \Delta\mathbf{C}^\gamma) \\ = E^{\gamma\pi}(\mathbf{T}, \mathbf{C}^{(0)\gamma}) + \sum_I \frac{\partial E^{\gamma\pi}(\mathbf{T}, \mathbf{C}^\gamma)}{\partial C_l^\gamma} \Big|_{C^{(0)\gamma}} \cdot \Delta C_l^\gamma \\ + \frac{1}{2} \sum_{IJ} \frac{\partial^2 E^{\gamma\pi}(\mathbf{T}, \mathbf{C}^\gamma)}{\partial C_l^\gamma \partial C_j^\gamma} \Big|_{C^{(0)\gamma}} \cdot \Delta C_l^\gamma \Delta C_j^\gamma + \dots \end{aligned} \quad (17)$$

ΔC_l^γ may be expanded in terms of the CI vectors $\{C_l^{(0)\gamma'}\}$:

$$\begin{aligned} \Delta C_l^\gamma = C_l^\gamma - C_l^{(0)\gamma} &= \sum_{\gamma'=1}^{N_{CSF}} A_{\gamma'} C_l^{(0)\gamma'} - C_l^{(0)\gamma} \\ &= \sum_{\gamma'=1}^{N_{CSF}} (A_{\gamma'} - \delta_{\gamma'\gamma}) C_l^{(0)\gamma'} = \sum_{\gamma'=1}^{N_{CSF}} B_{\gamma'} C_l^{(0)\gamma'}. \end{aligned} \quad (18)$$

Now, the second-order energy can be expressed in terms of ΔC_l^γ or $B_{\gamma'}$. By collecting terms with up to second-order in ΔC^γ and \mathbf{T} , we obtain the NR nonlinear equations.

$$\begin{pmatrix} g_{pe}^o \\ g_{\gamma'}^c \end{pmatrix} + \sum_{qf\gamma''} \begin{pmatrix} h_{pe,qf}^{oo} & h_{pe,\gamma''}^{oc} \\ h_{\gamma',qf}^{co} & h_{\gamma',\gamma''}^{cc} \end{pmatrix} \begin{pmatrix} T_{qf} \\ B_{\gamma''} \end{pmatrix} = \begin{pmatrix} 0 \\ 0 \end{pmatrix}, \quad (19)$$

where the additional Hessian matrix elements are defined by

$$\begin{aligned} h_{\gamma',pe}^{co} &= h_{pe,\gamma'}^{oc} \\ &= \sum_I^{N_{CSF}} \left[\sum_\alpha^{N_t} t_\alpha^I \{I(pb_\alpha)\} \delta(e, a_\alpha) \right. \\ &\quad + I(a_\alpha p) \delta(e, b_\alpha) \} \\ &\quad + \sum_{\beta=1}^{N_V} V_\beta^I \cdot \{R^{\nu_\beta}(pb_\beta, c_\beta d_\beta)\} \delta(e, a_\beta) \\ &\quad + R^{\nu_\beta}(a_\beta p, c_\beta d_\beta) \delta(e, b_\beta) \\ &\quad + R^{\nu_\beta}(a_\beta b_\beta, pd_\beta) \delta(e, c_\beta) \\ &\quad \left. + R^{\nu_\beta}(a_\beta b_\beta, c_\beta p) \delta(e, d_\beta) \right] C_l^{(0)\gamma'} \quad (20) \end{aligned}$$

$$h_{\gamma',\gamma''}^{cc} = 2E^\gamma \delta_{\gamma'\gamma''}, \quad (21)$$

with

$$\begin{aligned} t_\alpha^K = \frac{\partial t_\alpha}{\partial C_K^\gamma} \Big|_{C^{(0)\gamma}} &= \sum_{\alpha'=1}^{N_t} t_\alpha^{II} \delta(\alpha, \alpha') \\ &\times \{C_j^{(0)} \delta(I, K) + C_l^{(0)\gamma} \delta(J, K)\} \end{aligned} \quad (22)$$

$$\begin{aligned} V_\beta^K = \frac{\partial V_\beta}{\partial C_K^\gamma} \Big|_{C^{(0)\gamma}} &= \sum_{\beta'=1}^{N_V} V_\beta^{II} \delta(\beta, \beta') \\ &\times \{C_j^{(0)} \delta(I, K) + C_l^{(0)\gamma} \delta(J, K)\} \end{aligned} \quad (23)$$

and the first derivative with respect $B_{\gamma'}$ is

$$g_{\gamma'}^c = 2E^{(0)\gamma} \delta_{\gamma'\gamma'}. \quad (24)$$

As with the spinor orthogonality constraints, the normalization condition $\sum_{\gamma'} A_{\gamma'} A_{\gamma'} = 1$ of the CI vectors must be incorporated. The intermediate coupling is built in through the MC DF SCF process.

The second-order MC DF SCF procedure starts with the construction of CFSs by vector selection. From a set of nonscreened hydrogenic spinors generated by diagonalizing the matrix Dirac one-electron Hamiltonian, positive-energy (electronic) spinors are selected to construct relevant CSFs while negative-energy (positronic) spinors are left unoccupied. Second-order MC DF SCF is thus a *c*-number theory which does not reinterpret the negative-energy solutions as *q*-number theory does. It treats a desired electronic state as an excited state to which the iterative NR equation converges by vector selection. A straightforward application of the iterative NR equations [Eq. (19)] starting from nonscreened hydrogenic spinors, although they are poor initial guesses, exhibits rapid convergence to a targeted electronic state. Further, the solutions of the second-order MC DF SCF equations reveal an extension of Talman's minimax-principle [31] for one-electron systems to many-electron systems. For the lowest electronic state of a given symmetry, the spinor Hessian possesses N_κ positive and N_κ negative eigenvalues corresponding to a minimum and a maximum, respectively, in the space of large and small component parameters. Our second-order optimization procedure is thus equivalent to employing a minimax principle.

RELATIVISTIC MULTIREFERENCE CONFIGURATION INTERACTION

In the previous section, we derived a Newton-Raphson equation to determine optimum MC DFC

SCF wave functions based on the DC Hamiltonian. The effects of the frequency-independent Breit interaction may be excluded or included in the MR CI-SD step. These correspond to MR CI-SD calculations based, respectively, on the no-pair DC and DCB Hamiltonians. In the following, they will be referred to as the DC MR CI-SD and DCB MR CI-SD schemes. In our DC and DCB MR CI-SD schemes, the eigenfunctions of the DC and DCB Hamiltonians are constructed as linear combinations of CSFs generated by single and double excitations out of the reference CSFs $\Phi_l(\gamma_l \mathcal{T}\pi)$ involved in Eq. (6):

$$\begin{aligned} \Psi_{CI}(\gamma \mathcal{T}\pi) &= \sum_I^{N_{CSF}} \left(C_{l0}^{\gamma} \Phi_l(\gamma_l \mathcal{T}\pi) + \sum_i^{n_l^S} C_{li}^{\gamma S} \Phi_{l;e}^r(\gamma_i \mathcal{T}\pi) \right. \\ &\quad \left. + \sum_i^{n_l^D} C_{li}^{\gamma D} \Phi_{l;ef}^{rs}(\gamma_i \mathcal{T}\pi) \right), \end{aligned} \quad (25)$$

where n_l^S (n_l^D) is the total number of singly excited CSFs $\Phi_{l;e}^r$ (doubly excited $\Phi_{l;ef}^{rs}$) constructed by single (double) excitations from the reference CSFs Φ_l . $C_{li}^{\gamma S}$ and $C_{li}^{\gamma D}$ are CI-SD coefficients, which are determined variationally. Since MC SCF calculations provide only occupied and virtual spinors of the same symmetries, virtual spinors of other symmetries are generated via a Fock operator [32] with fractionally occupied MC SCF spinors.

In expansion (25), some of the CSFs coming from different reference states Φ_A may be identical. For example,

$$\Phi_{A;ef}^{rs} = \Phi_{B;e}^r \quad \text{for } A \neq B.$$

In such a case, the expansion coefficients may be factorized, $(C_{Ai} \Phi_{A;ef}^{rs} + C_{Bj} \Phi_{B;e}^r)$, and replaced by

$(C_{Ai} + C_{Bj}) \Phi_{B;e}^r$, leading to summation in (25) only over nonredundant CSFs. If the reference MC DFC SCF wave function includes the most important double excitations from the dominant CSFs, the multireference CI-SD wave function will contain important triple and quadruple excitations.

BASIS-SET EXPANSION METHOD

The large radial components $P_{n\kappa}(r)$ of the Dirac spinors of symmetry κ are expanded in sets of even-tempered GTFs (G-spinors):

$$\chi_{\kappa i}^L = N_{\kappa i}^L r^{n_\kappa} \exp(-\zeta_{\kappa i} r^2), \quad (26)$$

with $n_\kappa = -\kappa$ for $\kappa < 0$, and $n_\kappa = \kappa + 1$ for $\kappa > 0$. $N_{\kappa i}^L$ is the normalization constant. The small component basis set $\{\chi_{\kappa i}^S\}$ is constructed to satisfy the boundary conditions associated with the finite nucleus [28]. The basis-set exponents $\{\zeta_{\kappa i}\}$ in even-tempered GTFs are given in terms of the parameters α and β by the geometric series $\xi_{\kappa i} = \alpha \beta^{i-1}; i = 1, 2, \dots, N_\kappa$. The speed of light is taken to be 137.0359895 au throughout this study. The GTFs that satisfy the boundary conditions associated with the finite nucleus automatically satisfy the so-called kinetic balance condition [33].

Results and Discussion

Table I contains the results of single-configuration DF SCF and MC DF SCF calculations on the odd-parity $J = 1/2$ ground state of boronlike ions Ne^{+5} ($Z = 10$), P^{+10} ($Z = 15$), Ca^{+15} ($Z = 20$), Mn^{+20} ($Z = 25$), Zn^{+25} ($Z = 30$), and Mo^{+37} ($Z = 42$), in increasing number of configurations (N_{CSF})

TABLE I

Computed MC DFC energies, E_{MCDFC} (au), and MC DFB energies, E_{MCDFB} (au), for the ground $J = \frac{1}{2}$ state along the boron isoelectronic sequence in increasing CSF expansion lengths.

	N_{CSF}	$Z = 10$	$Z = 15$	$Z = 20$	$Z = 25$	$Z = 30$	$Z = 42$
E_{MCDFC}	1	-116.061472	-276.927731	-507.799766	-809.698759	-1183.992448	-2388.951640
	2	-116.133428	-277.032602	-507.932284	-809.851457	-1184.156449	-2389.110745
	6	-116.136557	-277.035835	-507.935593	-809.854847	-1184.159931	-2389.114474
	24	-116.141849	-277.041098	-507.940936	-809.860288	-1184.165519	-2389.120492
E_{MCDFB}	1	-116.046411	-276.872623	-507.663422	-809.424886	-1183.509078	-2387.571464
	2	-116.118431	-276.977756	-507.796602	-809.578874	-1183.675199	-2387.735014
	6	-116.121563	-276.980997	-507.799932	-809.582308	-1183.678764	-2387.739052
	24	-116.126857	-276.986270	-507.805304	-809.587817	-1183.684487	-2387.745559

up to $N_{CSF} = 24$. Even-tempered G-spinor basis sets of $23s19p$, $23s19p$, $28s26p$, $29s27p$ and $30s27p$ were used, respectively, for Ne^{+5} , P^{+10} , Ca^{+15} , Mn^{+20} , Zn^{+25} , and Mo^{+37} . The MC DF calculations were performed using both the no-pair DC and DCB Hamiltonians, and in the table they are designated, respectively, as multiconfigurational Dirac-Fock-Coulomb (MC DFC) and multiconfigurational Dirac-Fock-Breit (MC DFB) SCF. Single-configuration DFC and DFB SCF wave functions were derived from the electronic configuration, $(1s_{1/2})^2(2s_{1/2})^2(2p_{1/2})^1$. A set of all configurations of the same parity which are asymptotically degenerate in the hydrogenic limit is called a complex [22]. Within the $n = 2$ complex, there are only two $J = 1/2$ odd-parity CSFs, the $(1s_{1/2})^2(2s_{1/2})^2(2p_{1/2})^1$ and $(1s_{1/2})^2(2p_{1/2})^1(2p_{3/2})^2$. The two-configuration DFC and DFB wave functions are constructed from these CSFs. The 24-configuration DFC and DFB wave functions are a complete active space (CAS) wave function which contains all the CSFs constructed by keeping $(1s_{1/2})^2$ frozen and distributing the three valence electrons over the spinor set $2s_{1/2}$, $2p_{1/2}$, $2p_{3/2}$, $3s_{1/2}$, $3p_{1/2}$, $3p_{3/2}$. All the MC DFC and DFB SCF energies were computed with basis sets of even-tempered $25s23p$ G-spinors for Ne^{+5} and $30s27p$ G-spinors for Mo^{+37} . Calculations were done with a finite nucleus of uniform proton charge distribution. The atomic masses used for Ne^{+5} , P^{+10} , Ca^{+15} , Mn^{+20} , Zn^{+25} , and Mo^{+37} are, respectively, 20.18, 30.97, 40.08, 54.94, 65.37, and 95.94 amu. One- and two-configuration numerical finite-difference MC DFC SCF calculations on Ne^{+5} made with GRASP [4] yielded, respectively, the total energies, -116.061509 and -116.133483 au. The GRASP results were obtained with a finite nucleus of Fermi proton charge distribution. The total energies obtained in our second-order MC DF calculations are in very good agreement with those obtained by the GRASP finite difference program. The discrepancies between the two calculations are on the order of 10 microHartrees.

Two-configuration DFC SCF energies of the ground $J = 1/2$ odd-parity states for the boronlike ions are reproduced in Table II along with the configuration mixing coefficients. The magnitude of the configuration mixing coefficients is a measure of configuration mixing. For $Z = 10$, there is a nonnegligible mixing of the two configurations that arises from the $n = 2$ complex. As Z increases, however, this mixing tends to diminish, and for $Z = 42$, a single-configuration DF wave

TABLE II
Ground state $J = \frac{1}{2}$ two-configurational DFC energies, E_{MCDFC} (au) and configuration mixing coefficients along the boron isoelectronic sequence.

	E_{MCDFC}	$C_{2s^2 2p_{1/2}}$	$C_{2p_{1/2} 2p_{3/2}^2}$
$Z = 10$	-116.133428	0.98148	0.19155
$Z = 15$	-277.032602	0.98425	0.17677
$Z = 20$	-507.932284	0.98649	0.16383
$Z = 25$	-809.851457	0.98884	0.14900
$Z = 30$	-1184.156449	0.99125	0.13201
$Z = 42$	-2389.120492	0.99599	0.08943

function is sufficient to describe the ground $J = 1/2$ odd-parity state. For neutral boron ($Z = 5$), nonrelativistic charge expansion theory [34] applies well because relativistic effects are very small. The strong configuration mixing within a complex due to asymptotic degeneracy is asymptotic CI. The nonrelativistic complex for the isoelectronic sequence consists of $2s^2 2p^1 {}^2P$ and $2p^3 {}^2P$. This asymptotic CI within the nonrelativistic complex produces, for lighter ions, a linear Z -dependence in the energy shift. As Z increases, relativity starts to weaken the configuration mixing predicted nonrelativistically, and a linear Z -dependence of correlation energy typical of the nonrelativistic complex is diminished by the relativistic complex. In the high- Z relativistic hydrogenic limit, relativity causes separation of the $2p_{1/2}$ and $2p_{3/2}$ spinor energies, making $1s_{1/2}^2 2s_{1/2}^2 2p_{1/2}^1$ the dominant configuration for the $J = 1/2$ ground state. Table II displays just such a trend as the nuclear charge increases.

Table III contains the results of single-configuration SCF and MC DF SCF calculations on the lowest odd-parity $J = 3/2$ state of boronlike ions Ne^{+5} ($Z = 10$), P^{+10} ($Z = 15$), Ca^{+15} ($Z = 20$), Mn^{+20} ($Z = 25$), Zn^{+25} ($Z = 30$), and Mo^{+37} ($Z = 42$), in an increasing number of configurations (N_{CSF}) up to $N_{CSF} = 32$. The MC DF calculations again were performed with the no-pair DC and DCB Hamiltonians, and in the table they are designated, respectively, as multiconfigurational Dirac-Fock-Coulomb (MC DFC) and multiconfigurational Dirac-Fock-Breit (MC DFB) SCF. Single-configuration DFC and DFB SCF wave functions were derived from the electronic configuration, $(1s_{1/2})^2(2s_{1/2})^2(2p_{3/2})^1$. Within the $n = 2$ complex, there are four $J = 3/2$ odd-parity CSFs,

TABLE III

Computed MCDFC energies, E_{MCDFC} (au), and MC DFB energies, E_{MCDFB} (au), for lowest $J = \frac{3}{2}$ state along the boron isoelectronic sequence in increasing CSF expansion lengths.

	N_{CSF}	Z = 10	Z = 15	Z = 20	Z = 25	Z = 30	Z = 42
E_{MCDFC}	1	-116.054727	-276.879559	-507.621251	-809.219531	-1182.931208	-2384.410435
	4	-116.126129	-276.984905	-507.757618	-809.383030	-1183.117313	-2384.634446
	8	-116.129243	-276.988118	-507.760889	-809.386351	-1183.120688	-2384.637959
	32	-116.134682	-276.993870	-507.766852	-809.392433	-1183.126835	-2384.644177
E_{MCDFB}	1	-116.040314	-276.827325	-507.492660	-808.962075	-1182.477923	-2383.122386
	4	-116.111751	-276.932807	-507.629353	-809.126181	-1182.665008	-2383.348348
	8	-116.114868	-276.936030	-507.632648	-809.129552	-1182.668475	-2383.352181
	32	-116.120309	-276.941785	-507.638620	-809.135654	-1182.674662	-2383.358555

the $1s_{1/2}^2 2s_{1/2}^2 2p_{3/2}^1$, $1s_{1/2}^2 2p_{1/2}^2 2p_{3/2}^1$, $1s_{1/2}^2 2p_{1/2}^1 2p_{3/2}^2$, and $1s_{1/2}^2 2p_{3/2}^3$. The four-configuration DFC and DFB wave functions are constructed from these CSFs. The 32-configuration DFC and DFB wave functions are a CAS wave function which contains all the CSFs constructed by keeping $(1s_{1/2})^2$ frozen and distributing the three valence electrons over the spinor set $2s_{1/2}$, $2p_{1/2}$, $2p_{3/2}$, $3s_{1/2}$, $3p_{1/2}$, $3p_{3/2}$. The convergence patterns of our second-order MC DFC SCF for Ne^{+5} are demonstrated in Table IV. For the $J = 1/2$ and $J = 3/2$ states, the convergence pattern is shown, respectively, for the 24- and 32-configuration DFC SCF. In the table, $|T + B|$ represents the norm of spinor and CI rotation parameters, and

ΔE , the energy difference between successive Newton-Raphson iterations. Nonscreened hydrogenic spinors were used as initial guesses. The crux of quadratically convergent MC DF SCF is its simplicity and straightforwardness in applying the NR equation [Eq. (19)] to obtain rapid convergence to the solution.

Four-configuration DFC SCF energies of the $J = 3/2$ odd-parity states for the boronlike ions are reproduced in Table V along with the configuration mixing coefficients. For $Z = 10$, there is a nonnegligible mixing of three configurations, $1s_{1/2}^2 2s_{1/2}^2 2p_{3/2}^1$, $1s_{1/2}^2 2p_{1/2}^2 2p_{3/2}^1$, and $1s_{1/2}^2 2p_{3/2}^3$, that arise from the $n = 2$ complex. As Z increases, however, this mixing tends to alter, and for $Z = 42$,

TABLE IV

Convergence of the second-order MC SCF for the Ne^{+5} ion lowest states using 24-configuration space functions for $J = 1/2$ and 32-configuration space functions for $J = 3/2$ ^a, the energies, E_{MCSCF} , $\Delta E^{(2)}$, and ΔE are in atomic units.

NR iteration	$ T + B $	$\Delta E^{(2)}$	ΔE	E_{MCSCF}
<i>J = 1/2</i>				
1	1.19[+0]	-1.16[-2]	-8.33[-3]	-116.130104
2	6.12[-1]	-3.21[-3]	-3.10[-3]	-116.138429
3	4.26[-1]	-3.08[-3]	-3.21[-4]	-116.141525
4	2.66[-2]	-2.32[-6]	-2.62[-6]	-116.141847
5	3.65[-3]	-5.28[-8]	-5.22[-8]	-116.141849
<i>J = 3/2</i>				
1	1.16[+0]	-2.17[-2]	-9.39[-3]	-116.117681
2	6.00[-1]	-7.88[-3]	-6.65[-3]	-116.127072
3	7.00[-1]	-8.92[-4]	-9.42[-4]	-116.133719
4	6.08[-2]	-1.86[-5]	-2.03[-5]	-116.134661
5	6.82[-3]	-2.07[-7]	-2.01[-7]	-116.134682
6	9.97[-4]	-6.80[-9]	-6.81[-9]	-116.134682

^aNonscreened hydrogenic spinors were used as initial guesses.

TABLE V

Lowest $J = \frac{3}{2}$ state 4-configurational DFC energies, E_{MCDFC} (au), and configuration mixing coefficients along the boron isoelectronic sequence.

	E_{MCDFC}	$C_{2s^2 2p_{3/2}}$	$C_{2p_{1/2}^2 2p_{3/2}}$	$C_{2p_{1/2} 2p_{3/2}^2}$	$C_{2p_{3/2}^3}$
Z = 10	-116.126129	0.98135	0.13657	0.00007	0.13529
Z = 15	-276.984905	0.98381	0.12894	0.00023	0.12443
Z = 20	-507.757618	0.98543	0.12542	0.00052	0.11484
Z = 25	-809.383030	0.98691	0.12342	0.00092	0.10381
Z = 30	-1183.117313	0.98831	0.12208	0.00133	0.09127
Z = 42	-2384.634446	0.99101	0.11918	0.00190	0.06074

the $1s_{1/2}^2 2p_{3/2}^3$ CSF mixes much less than for Z = 10 with the other three CSFs because, in the high-Z relativistic hydrogenic limit, relativity separates the $2p_{1/2}$ and $2p_{3/2}$ spinor energies. On the other hand, relativity causes a smaller separation of the $2s_{1/2}$ and $2p_{1/2}$ spinor energies as Z increases (i.e., the $2s_{1/2}$ and $2p_{1/2}$ spinor energies become asymptotically degenerate in the hydrogenic limit

[22]), making $1s_{1/2}^2 2s_{1/2}^2 2p_{3/2}^1$ and $1s_{1/2}^2 2p_{1/2}^2 2p_{3/2}^1$ the two dominant configurations for the $J = 3/2$ state. Table V displays the trend in energies as nuclear charge increases.

The fine-structure separations between the lowest $J = 1/2$ and $J = 3/2$ states for the boronlike ions are displayed in Table VI in increasing CSF expansion lengths. The table also contains the

TABLE VI

Fine-structure separation (cm^{-1}) between the lowest $J = \frac{1}{2}$ and $J = \frac{3}{2}$ states along the boron isoelectronic sequence in increasing CSF expansion lengths.

N_{CSF}	Z = 10	Z = 15	Z = 20	Z = 25	Z = 30	Z = 42
This work						
MC DFC						
1–1	1480	10,573	39,180	105,178	232,915	996,679
2–4	1602	10,468	38,336	102,808	228,064	982,434
MR DC RCI						
2–4	1443.4	10,290				
MC DFB						
1–1	1338	9942	37,478	101,576	226,312	976,460
2–4	1466	9865	36,707	99,355	221,711	962,762
6–8	1469	9869	36,715	99,368	221,733	962,807
24–32	1437	9763	36,583	99,238	221,631	962,836
24–32 + LS ^a	1440	9784	36,659	99,434	222,037	964,390
MR DCB RCI						
2–4	1308.6	9691				
2–4 + LS ^a	1312	9712				
Previous work						
MCDF ($n = 2$) ^b	1465	9871	36,717	99,322	221,481	959,831
Relativistic MBPT ^c	1311	9713	36,631	99,423	222,002	963,920
Nonrelativistic MBPT ^d	1275	9546	35,971			
Experiment ^e	1309(4)	9695(15)	36,615(30)	99,287(110)	222,021	964,255

^aLamb shift (LS) estimated by GRASP [4] ($n = 2$ complex) is added to MC DFB value.

^bCheng et al. [36], $n = 2$ complex MCDF calculations. Lamb shift included.

^cSafranova et al. [35], relativistic second-order MBPT calculations using single-particle orbitals generated in the HF potential of the $(1s^2)$ heliumlike core. Lamb shift included.

^dMerkelis et al. [37], nonrelativistic second-order MBPT calculations using single-particle orbitals generated in the HF-type potential. Breit-Pauli relativistic correction is included.

^eEdlén [38], experimental and recommended values.

fine-structure separations obtained previously by correlated methods and by experiment for comparison. The number of CSFs included in the MC DFC and DFB SCF calculations for the $J = 1/2$ and $J = 3/2$ states to evaluate the fine-structure separations are denoted as 1–1, 2–4, etc., in the first column. For $Z = 10$, the fine-structure splitting, 1480 cm^{-1} , obtained as the difference between the single-configuration DFC SCF energies of the $J = 1/2$ and $J = 3/2$ states (denoted by 1–1 in the table) is much poorer than is the value, 1338 cm^{-1} , obtained in DFB SCF calculations. The latter agrees well with the experimental fine-structure separation: 1309 cm^{-1} . The results indicate that treatment of the Breit interaction is important to accurate determination of fine-structure separations.

For $Z = 10$, the agreement between the computed fine-structure separation and experiment deteriorates as the number of CSFs in the MC DF SCF calculations is increased. Partially accounting for dynamical correlation by including the $n = 3$ complex in MC DF SCF calculations simply causes an imbalance in the recovery of dynamical correlation for each J state. Accurate determination of dynamical correlation is necessary to predict the fine-structure separation. For $Z = 10$ and 15, DC

and DCB MR CI–SD calculations were performed using the $23s19p17d17f16g16h$ basis set to take into account the remaining dynamic correlation. Table VII displays the DC and DCB MR CI energies of Ne^{+5} and P^{+10} in increasing order of partial-wave expansion. The extrapolated energies are given in the last column of the table. The fine-structure separations computed by taking the difference between $J = 1/2$ and $3/2$ extrapolated energies are displayed under MR DCB RCI in Table VI (1308.6 cm^{-1} for Ne^{+5} and 9691 cm^{-1} for P^{+10}) and are in good agreement with experiment. Safronova et al. [35] performed MR relativistic MBPT calculations on boron isoelectronic sequence. The fine-structure separation for $Z = 10$ computed by their relativistic many-body perturbation method is 1311 cm^{-1} , in excellent agreement with experiment.

For ions with large Z , however, the trend observed in $Z = 10$ is reversed and a steady increase in accuracy in the fine-structure splitting is obtained as the number of CSFs in the MC DF SCF calculations is increased. When the Lamb shift for each fine structure level is accounted for, the computed fine-structure separations agree well with experiment.

TABLE VII

Computed MR DC RCI energies, $E_{DC}(I)$ (au) and MR DCB RCI energies, $E_{DCB}(I)$ (au), for the ground $J = \frac{1}{2}$ state and lowest $J = \frac{3}{2}$ state for Ne^{+5} and P^{+10} in increasing partial-wave expansion.^a

	<i>f</i> Limit	<i>g</i> Limit	<i>h</i> Limit	Extrapolated ^b
Ne^{+5}				
$J = \frac{1}{2}$				
$E_{DC}(I)$	–116.231698	–116.232735	–116.233047	–116.233274
$E_{DCB}(I)$	–116.217784	–116.218825	–116.219138	–116.219366
$J = \frac{3}{2}$				
$E_{DC}(I)$	–116.225125	–116.226160	–116.226470	–116.226698
$E_{DCB}(I)$	–116.211826	–116.212864	–116.213176	–116.213404
P^{+10}				
$J = \frac{1}{2}$				
$E_{DC}(I)$	–277.133624	–277.134803	–277.135108	–277.135321
$E_{DCB}(I)$	–277.081201	–277.082390	–277.082698	–277.082912
$J = \frac{3}{2}$				
$E_{DC}(I)$	–277.086743	–277.087919	–277.088224	–277.088436
$E_{DCB}(I)$	–277.037053	–277.038237	–277.038544	–277.038759

^a Two-configuration and four-configuration MC DFC wave functions were used as reference spaces, respectively, for $J = 1/2$ and $J = 3/2$ states.

^b Extrapolation was performed using the formula $\Delta E(I) = a(I + 1/2)^b$.

ACKNOWLEDGMENTS

This work was supported in part by the National Science Foundation. The authors thank Dr. H. M. Quiney for valuable discussions.

References

1. N. Pyper, Chem. Phys. Lett. **74**, 554 (1980).
2. K. Molzberger and W. H. E. Schwarz, Theor. Chim. Acta **94**, 213 (1996).
3. J. P. Desclaux, in *Methods and Techniques in Computational Chemistry: MOTECC-94*, E. Clementi, Ed. (STEF, Cagliari, 1993), Vol. A, *Small Systems*, p. 253.
4. F. A. Parpia, C. Froese Fischer, and I. P. Grant, Comput. Phys. Commun. **94**, 249 (1996).
5. T. Kagawa, Phys. Rev. A **22**, 2340 (1980).
6. W. R. Johnson and J. Sapirstein, Phys. Rev. Lett. **57**, 1126 (1986); W. R. Johnson, S. A. Blundell, and J. Sapirstein, Phys. Rev. A **37**, 307 (1988); W. R. Johnson, S. A. Blundell, and J. Sapirstein, Phys. Rev. A **41**, 1689 (1990).
7. E. Avgoustoglou, W. R. Johnson, D. R. Plante, J. Sapirstein, S. Sheinerman, and S. A. Blundell, Phys. Rev. A **46**, 5478 (1992); E. Avgoustoglou, W. R. Johnson, Z. W. Liu, and J. Sapirstein, Phys. Rev. A **51**, 1196 (1995).
8. H. M. Quiney, I. P. Grant, and S. Wilson, Phys. Scr. **36**, 460 (1987); H. M. Quiney, I. P. Grant, and S. Wilson, in *Many-Body Methods in Quantum Chemistry*, Lecture Notes in Chemistry 52, U. Kaldor, Ed., Springer, Berlin, 1989; H. M. Quiney, I. P. Grant, and S. Wilson, J. Phys. B **23**, L271 (1990).
9. Y. Ishikawa, Phys. Rev. A **42**, 1142 (1990); Y. Ishikawa and H. M. Quiney, Phys. Rev. A **47**, 1732 (1993); Y. Ishikawa and K. Koc, Phys. Rev. A **50**, 4733 (1994).
10. Y. Ishikawa and K. Koc, Phys. Rev. A **53**, 3966 (1996); *Ibid.* **56**, 1295 (1997).
11. K. Koc and J. Migdalek, J. Phys. B **23**, L5 (1990); *Ibid.* **25**, 907 (1992).
12. S. A. Blundell, W. R. Johnson, and J. Sapirstein, Phys. Rev. A **43**, 3407 (1991).
13. E. Eliav, U. Kaldor, and Y. Ishikawa, Phys. Rev. A **49**, 1724 (1994); *Ibid.* **51**, 225 (1995); *Ibid.* **52**, 291 (1995).
14. Z. W. Liu and H. P. Kelly, Phys. Rev. A **43**, 3305 (1991).
15. S. Salomonson and P. Oster, Phys. Rev. A **40**, 5548 (1989); E. Lindroth and S. Salomonson, Phys. Rev. A **41**, 4659 (1990); A. C. Hartly, E. Lindroth, and A.-M. Martensson-Pendrill, J. Phys. B **23**, 1990 (1990).
16. T. Kagawa, Y. Honda, and S. Kiyokawa, Phys. Rev. A **44**, 7092 (1991).
17. M. H. Chen, K. T. Cheng, and W. Johnson, Phys. Rev. A **47**, 3692 (1993).
18. K. Koc, Y. Ishikawa, and T. Kagawa, Chem. Phys. Lett. **231**, 407 (1994).
19. D. R. Beck and Z. Cai, Phys. Rev. A **37**, 4481 (1988); D. R. Beck, *Ibid.* **37**, 1847 (1988); *Ibid.* **45**, 1399 (1992).
20. K. Koc and Y. Ishikawa, Phys. Rev. A **49**, 794 (1994).
21. K. Hirao and H. Nakatsuji, J. Chem. Phys. **59**, 1457 (1973); K. Hirao, J. Chem. Phys. **60**, 3215 (1974).
22. A. W. Weiss and Y.-K. Kim, Phys. Rev. A **51**, 4487 (1995).
23. M. J. Vilkas, K. Koc, and Y. Ishikawa, Chem. Phys. Lett. **280**, 167 (1997).
24. M. J. Vilkas, Y. Ishikawa, and K. Koc, Phys. Rev. E, in press.
25. H.-J. Werner, Adv. Chem. Phys. **69**, 1 (1987).
26. J. Sucher, Phys. Rev. A **22**, 348 (1980).
27. M. Mittleman, Phys. Rev. A **24**, 1167 (1981).
28. Y. Ishikawa, R. Baretti, and R. C. Binning, Jr., Chem. Phys. Lett. **121**, 130 (1985); Y. Ishikawa, H. M. Quiney, and G. L. Malli, Phys. Rev. A **43**, 3270 (1991).
29. S. A. Blundell, P. J. Mohr, W. R. Johnson, and J. Sapirstein, Phys. Rev. A **48**, 2615 (1993).
30. I. Lindgren, H. Persson, S. Salomonson, and L. Labzovsky, Phys. Rev. A **51**, 1167 (1995).
31. J. Talman, Phys. Rev. Lett. **57**, 1091 (1986).
32. K. Hirao, Chem. Phys. Lett. **190**, 374 (1992); *Ibid.* **196**, 397 (1992); *Ibid.* **201**, 59 (1993).
33. W. H. E. Schwarz and H. Wallmeier, Mol. Phys. **46**, 1045 (1982); Y. Ishikawa, R. C. Binning, Jr., and K. M. Sando, Chem. Phys. Lett. **101**, 111 (1983); K. Dyall, I. P. Grant, and S. Wilson, J. Phys. B **17**, 1201 (1984).
34. D. Layzer, Ann. Phys. NY **8**, 271 (1959).
35. M. S. Safranova, W. R. Johnson, and U. I. Safranova, Phys. Rev. A **54**, 2850 (1996).
36. K. T. Cheng, J. K. Kim, and J. P. Desclaux, Atom. Data Nucl. Data Tab. **24**, 111 (1979).
37. G. Merkelis, M. J. Vilkas, G. Gaigalas, and R. Kisielius, Phys. Scr. **51**, 233 (1995).
38. B. Edlén, Phys. Scr. **28**, 483 (1983).

Relativistic Effects on the Structural Phase Stability of Molybdenum

J. C. BOETTGER

Theoretical Division, Los Alamos National Laboratory, Los Alamos, New Mexico 87545

Received 21 February 1998; accepted 18 March 1998

ABSTRACT: The body-centered cubic-face-centered cubic (bcc-fcc) structural phase stability of molybdenum (Mo) is studied as a function of volume with both nonrelativistic and scalar-relativistic linear combinations of Gaussian-type orbitals-fitting functions (LCGTO-FF) calculations. It is demonstrated that relativity has a significant, albeit small effect, on the bcc-fcc structural energy difference, which increases with pressure. The scalar-relativistic structural energy difference curve is shown to be in excellent agreement with an earlier scalar-relativistic calculation using the full-potential linear muffin-tin orbital (FP-LMTO) method, clearly demonstrating the ability of the scalar-relativistic LCGTO-FF method to resolve an extremely subtle relativistic effect. It is argued that relativity will tend to delay pressure-induced structural phase transitions that are triggered by electron band reordering. © 1998 John Wiley & Sons, Inc. Int J Quant Chem 70: 825–830, 1998

Key words: molybdenum; phase stability; relativity; Douglas-Kroll

Introduction

The linear combinations of Gaussian-type orbitals-fitting function (LCGTO-FF) technique is one of the few all-electron, full-potential, density functional theory (DFT) electronic structure techniques able to treat isolated clusters of atoms [1], one-dimensional periodic polymer chains [2], two-dimensional periodic films [3], and crystalline solids [4] on an equal footing. To this extent, the LCGTO-FF method may be viewed as

a “universal” methodology able to bridge the often wide gap between solid-state physics and quantum chemistry. For this reason, the LCGTO-FF method is well-suited for studying systems that do not lie entirely within the scope of either discipline; for example, nanostructures on a surface, impurities in a crystal, catalysis, etc.

One disadvantage of the LCGTO-FF method relative to numerical solid-state electronic structure techniques has been the absence of a stable method for incorporating relativistic effects during calculations on systems that include heavy atoms, an affliction shared by most pure variational methods. This limitation effectively restricts LCGTO-FF

Contract grant sponsor: U.S. Department of Energy.

calculations to systems formed from atoms in the first three rows of the periodic table. Although a number of strategies have been suggested over the years for incorporating relativistic effects into variational calculations [5], most practical calculations still rely on either perturbation theory or some form of relativistic pseudopotential.

A major breakthrough on this venerable problem occurred several years ago when Häberlen and Rösch [6] (HR) demonstrated the feasibility of carrying out scalar-relativistic LCGTO-FF calculations on heavy-atom clusters using an “incomplete” Douglas-Kroll-Hess [7–9] transformation, hereafter, the HR approximation. Since that time, the scalar-relativistic LCGTO-FF cluster technique has been applied to a number of systems containing heavy atoms with apparent success [10]. The HR approximation has also been implemented quite recently [11] in an existing computer program designed to carry out LCGTO-FF calculations on crystalline solids and thin films (GTOFF) [4]. GTOFF was then used to carry out the first all-electron, scalar-relativistic LCGTO calculation on a crystalline solid, gold (Au; Z = 79) [11]. The HR approximation was shown to produce bulk and electronic properties for face-centered cubic (fcc) Au that are nearly indistinguishable from those obtained with numerical scalar-relativistic electronic structure techniques.

In this investigation, GTOFF is used to study the effect of relativity on the equation of state and face-centered cubic–body-centered cubic (fcc–bcc) structural phase stability of Mo. Since Mo is a standard test case for new bulk electronic structure programs, a number of prior calculations of the zero-pressure properties [12–18], both relativistic and nonrelativistic, are available for comparison. In addition, the structural phase stability of Mo has been studied with at least one high-precision, all-electron, scalar-relativistic local density approximation (LDA) technique; the full-potential linear muffin-tin orbital (FP-LMTO) method [19]. Thus the current investigation represents an important test of the scalar-relativistic LCGTO-FF method on a rather subtle relativistic effect.

The scalar-relativistic LCGTO-FF method has been described in detail elsewhere [11], and that discussion will not be repeated here. Instead, this study will begin with a brief discussion of the basis sets used and other computational details. The results obtained here for the bcc and fcc phases of Mo will be presented and compared with prior

calculations in the third section. A few concluding remarks will be given in the final section.

Computational Details

The orbital basis set used here for volumes near ambient was derived from Huzinaga’s $17s11p8d$ atomic basis [20] by replacing the five most diffuse s -type GTOs with more local basis functions and augmenting the p -type basis with one diffuse GTO. The resulting $17s12p8d$ crystalline basis set was then reduced to a $13s8p5d$ basis set by contracting the most local GTOs of each l -type using atomic orbital coefficients from nonrelativistic or scalar-relativistic atomic calculations using the same LDA model as was used in the crystalline calculations, Hedin–Lundqvist (HL) [21]. The charge density and the exchange–correlation (XC) integral kernels were fitted with a single $15s$ GTO basis set, selected on the basis of prior experience with LCGTO-FF calculations. The orbital and fitting function exponents used near the ambient volume of Mo are listed in Table I. For the more highly compressed volumes considered here, the exponents of the most diffuse GTOs were increased as needed to avoid numerical instabilities due to near-linear dependencies. In all cases, the same basis sets were used for a given volume regardless of the crystal structure under consideration.

All Brillouin zone (BZ) integrations were carried out on a uniform mesh with 145 irreducible k -points using a Gaussian-broadened (10 mRy) histogram integration technique. Additional calculations using a sparser mesh with 72 irreducible k -points indicate that the calculations are well converged with respect to the mesh density. The self-consistent field (SCF) cycle was iterated until the total energy varied by less than 0.004 mRy.

Results

Nonrelativistic and scalar-relativistic total energies were calculated for bcc and fcc Mo at 10 volumes ranging from 41.8414 to 113.4905 a.u. Cohesive energies were then obtained by removing atomic energies calculated in a manner consistent with the crystalline calculations. (For the atomic calculations, the basis sets were augmented with diffuse functions to mimic the effect of off-site

TABLE I
GTO exponents for the s-, p-, and d-type primitive orbital basis functions and s-type GTO fitting functions used here for crystalline Mo at low compressions.^a

s	p	d	FF
564811.58	4706.3308	172.75830	40000.00
84340.172	1104.2933	51.005487	11000.00
19223.887	361.17122	19.267661	4000.00
5640.4270	139.14298	7.9229414	1500.00
1935.0108	58.356511	3.3785846	610.00
736.03701	25.821389	1.3293987	270.00
304.54661	10.718475	0.49531799	100.00
134.49152	4.7732916	0.15895673	45.00
50.361750	2.0262457		15.40
22.461279	0.83764641		7.85
7.7112170	0.34208279		3.66
3.9263438	0.12000000		1.78
1.9200000			0.79
0.9600000			0.27
0.4800000			0.12
0.2400000			
0.1200000			

^aThe smaller exponents were increased as needed for the larger compressions; see text.

functions in the crystalline calculations.) The resulting cohesive energies are listed in Table II.

The low-pressure properties of fcc and bcc Mo were obtained by fitting the cohesive energies for the seven largest volumes in Table II with a modified version of the universal equation of state [22]. Table III compares the zero-pressure lattice constant a_0 , bulk modulus B , and pressure derivative of the bulk modulus B' found here for the fcc and bcc structures, both nonrelativistically and scalar-relativistically, with results from a number of other

calculations. Experimental values [23] for a_0 and B are also given in Table III.

Comparison of the theoretical results in Table III reveals several interesting features. First, the LCGTO-FF results are consistent with the previous calculations. For example, the average scalar-relativistic values for the lattice constant and bulk modulus of bcc Mo are 5.9035 a.u. and 287 GPa versus 5.905 a.u. and 292 GPa from the scalar-relativistic LCGTO-FF calculations. In general, the various results in Table III are also consistent with

TABLE II
Nonrelativistic (NR) and scalar-relativistic (SR) cohesive energies (in Ry) for bcc and fcc Mo at 10 atomic volumes (a.u.).

V	NR-bcc	NR-fcc	SR-bcc	SR-fcc
113.4905	-0.524290	-0.496500	-0.566522	-0.537012
108.0000	-0.529628	-0.500762	-0.573288	-0.542308
102.6895	-0.530574	-0.500852	-0.575564	-0.543268
97.5560	-0.526364	-0.496056	-0.572468	-0.539044
92.5965	-0.516046	-0.485698	-0.563186	-0.529066
83.5965	-0.475826	-0.447196	-0.524512	-0.490334
73.1399	-0.376416	-0.353718	-0.425568	-0.369060
62.6877	-0.178588	-0.170688	-0.227942	-0.209874
52.2768	0.196072	0.174362	0.154008	0.144004
41.8414	0.925012	0.866048	0.895774	0.846594

TABLE III
Lattice constant (a_0 ; bohr), bulk modulus (B ; GPa), and pressure derivative of the bulk modulus (B') for bcc and fcc Mo obtained here from nonrelativistic (NR) and scalar-relativistic (SR) LCGTO-FF calculations are compared with other calculations and experiment.

Method	Rel.	Struc.	Ref.	a_0	B	B'
LCGTO-FF	NR	fcc	Present	7.493	246	4.10
LAPW	SR	fcc	13	7.504	247	
APW	SR	fcc	16	7.475	256	
LCGTO-FF	SR	fcc	Present	7.472	269	3.85
KKR	NR	bcc	12	5.91	251	
FP-LMTO	NR	bcc	14	5.97	255	
LMTO-ASA	NR	bcc	15	5.948	265	4.38
LCGTO-FF	NR	bcc	Present	5.930	273	4.12
LAPW	SR	bcc	13	5.917	291	
LMTO-ASA	SR	bcc	15	5.910	248	4.99
APW	SR	bcc	16	5.904	288	
FP-LMTO	SR	bcc	17	5.879	297	
FCD-LMTO	SR	bcc	18	5.906	306	
LCGTO-FF	SR	bcc	Present	5.905	292	4.11
Expt.		bcc	23	5.949	261	

the widely held belief that relativistic effects are quite small for d -bonded materials, making it difficult to judge the reliability of the scalar-relativistic LCGTO-FF method based on the zero-pressure properties of Mo. Still, the -0.025 a.u. shift in the lattice constant found here is in reasonable agreement with the -0.038 a.u. shift found by Moriarty [15] using the more approximate linear muffin-tin orbital-atomic sphere approximation (LMTO-ASA) method. The scalar-relativistic LCGTO-FF results for bcc Mo exhibit the expected small lattice contraction and bulk modulus enhancement, relative to experiment, expected for an LDA calculation.

Figure 1 compares the nonrelativistic and scalar-relativistic bcc-fcc structural energy difference versus volume curves found here with structural energy differences determined from scalar-relativistic FP-LMTO calculations [19]. Figure 1 illustrates two important results: (1) Relativity has a significant, albeit small, effect on the structural energy difference of Mo that initially increases with pressure. (2) The scalar-relativistic LCGTO-FF results are in good agreement with the FP-LMTO results, demonstrating the ability of the LCGTO-FF method to resolve a rather subtle relativistic effect.

Although the relativistic correction to the structural energy difference is fairly small, it significantly delays the onset of the structural phase transition from a relative volume of about 0.57 to roughly 0.53. This delay in the transition has a

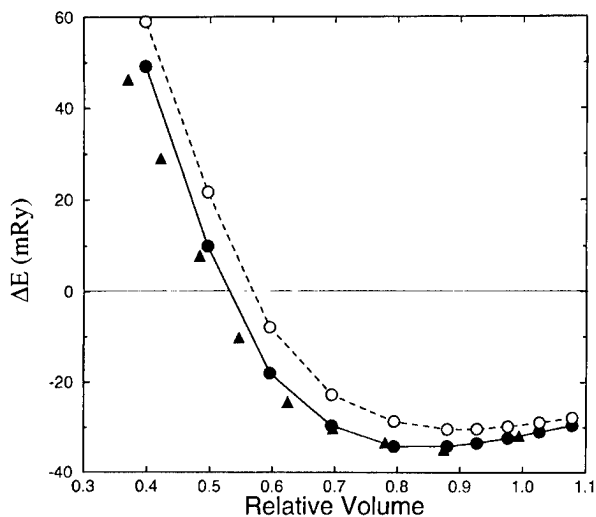


FIGURE 1. Energy difference (ΔE) between the bcc and fcc structures of Mo is shown as a function of relative volume for the current scalar-relativistic (solid circle) and nonrelativistic (open circle) LCGTO-FF calculations. Results from the scalar-relativistic FP-LMTO calculations of [19] are also shown, solid triangles. Negative values imply stability of the bcc structure.

rather simple interpretation. It is well-known that pressure-induced structural phase transitions are frequently associated with a transfer of electrons from low-angular-momentum states to high-angular-momentum states. For example, elemental solids formed from third-row atoms exhibit struc-

tural phase transitions that can be related to a pressure-induced transfer of electrons from the $3s$ state to the $3d$ state [24]. Since relativity tends to reduce the energy of low-angular-momentum states relative to high-angular-momentum states, relativity will tend to delay any structural phase transitions that are triggered by reordering of the electron bands.

Another obvious question is "Why does relativity have such a large effect on the high-pressure properties of Mo but not on the low-pressure properties?" It is well-known that under pressure the (initially fully occupied) $5s$ band of Mo is driven through the partially occupied $4d$ band [15]. Thus, under pressure, Mo first transforms from a d -bonded material (relatively insensitive to relativistic effects) to a mixed s - and d -bonded material (with large relativistic effects) and then returns to a d -bonded material (with small relativistic effects). This process is evident in the relativistic correction to the structural energy difference, shown in Fig. 2 as a function of relative volume. The relativistic correction reaches its maximum at a relative volume of about 0.5 and then begins to decrease as the pressure is increased further. Thus, the present analysis is entirely consistent with what is already known about the $s \rightarrow d$ transition in Mo.

Conclusions

It has been demonstrated here that the scalar-relativistic LCGTO-FF method as embodied in the

program GTOFF produces zero-pressure properties of Mo that are indistinguishable from the results of other scalar-relativistic calculations. More importantly, it has been shown that the LCGTO-FF technique is able to resolve a very subtle relativistic effect; namely, the volume-dependent correction to the bcc-fcc structural energy difference. It is argued that relativity will tend to delay structural phase transitions that are triggered by pressure-induced reordering of electronic states. Finally, the current results suggest that relativity must be taken into consideration when studying the high-pressure properties of materials even if they are unaffected by relativity at low pressures, since pressure can significantly alter the basic nature of the bonding.

ACKNOWLEDGMENTS

This work was supported by the U.S. Department of Energy.

References

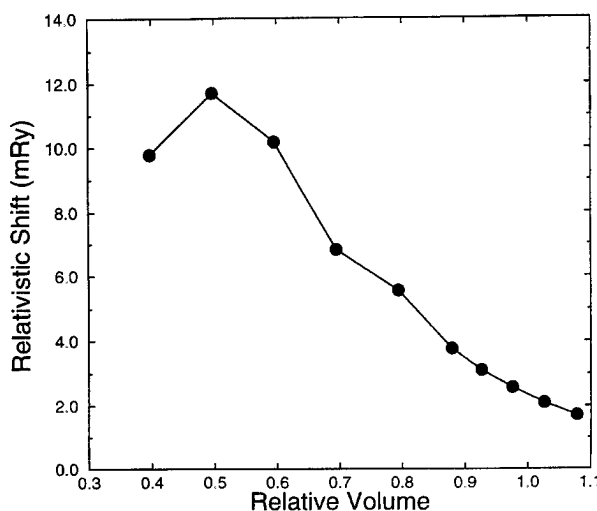


FIGURE 2. Relativistic correction to the bcc-fcc structural energy difference of Mo is shown as a function of relative volume.

1. B. I. Dunlap and N. Rösch, *Adv. Quant. Chem.* **21**, 317 (1990), and references therein.
2. J. W. Mintmire, *Phys. Rev. B* **39**, 13350 (1989), and references therein.
3. J. C. Boettger, *Phys. Rev. B* **53**, 13133 (1996), and references therein.
4. J. C. Boettger, *Int. J. Quant. Chem. Symp.* **29**, 197 (1995).
5. W. Kutzelnigg, *Int. J. Quant. Chem.* **25**, 107 (1984).
6. N. Rösch and O. D. Häberlen, *J. Chem. Phys.* **96**, 6322 (1992); O. D. Häberlen and N. Rösch, *Chem. Phys. Lett.* **199**, 491 (1992); O. D. Häberlen, Ph.D. Thesis, Technische Universität, München, 1993.
7. M. Douglas and N. M. Kroll, *Ann. Phys.* **82**, 89 (1974).
8. B. A. Hess, *Phys. Rev. A* **33**, 3742 (1986).
9. G. Jansen and B. A. Hess, *Phys. Rev. A* **39**, 6016 (1989).
10. N. Rösch, S. Krüger, M. Mayer, and V. A. Nasluzov, in *Recent Developments and Applications of Modern Density Functional Theory*, J. M. Seminario, Ed. (Elsevier, Amsterdam, 1996), p. 497, and references therein.
11. J. C. Boettger, *Phys. Rev. B*, submitted; also see, J. C. Boettger, *Int. J. Quant. Chem.* **65**, 565 (1997).
12. V. L. Moruzzi, J. F. Janak, and A. R. Williams, *Calculated Electronic Properties of Metals* (Pergamon, New York, 1978).
13. L. F. Mattheiss and D. R. Hamann, *Phys. Rev. B* **33**, 823 (1986).
14. M. Alouani, R. C. Albers, and M. Methfessel, *Phys. Rev. B* **43**, 6500 (1991).
15. J. A. Moriarty, *Phys. Rev. B* **45**, 2004 (1992).

16. M. Sigalas, D. A. Papaconstantopoulos, and N. C. Bacalis, Phys. Rev. B **45**, 5777 (1992).
17. V. Ozoliņš and M. Körling, Phys. Rev. B **48**, 18304 (1993).
18. L. Vitos, J. Kollár, and H. L. Skriver, Phys. Rev. B **55**, 13521 (1997).
19. P. Söderind, O. Eriksson, B. Johansson, and J. M. Wills, Phys. Rev. B **49**, 2004 (1994).
20. S. Huzinaga, J. Chem. Phys. **66**, 4245 (1977).
21. L. Hedin and B. I. Lundqvist, J. Phys. C **4**, 2064 (1971).
22. A. Banerjee and J. R. Smith, Phys. Rev. B **37**, 6632 (1988); for the exact form used here see, J. C. Boettger and S. B. Trickey, Phys. Rev. B **53**, 3007 (1996).
23. K. W. Katahara, M. H. Manghnani, and E. S. Fisher, J. Phys. F **9**, 773 (1979).
24. A. K. McMahan and J. A. Moriarty, Phys. Rev. B **27**, 3235 (1983).

Water Cluster Approach To Study Hydrogen-Bonded Pattern in Liquid Water: Ab Initio Orientational Defects in Water Hexamers and Octamers

EUGENE S. KRYACHKO*

Bogoliubov Institute for Theoretical Physics, Kiev-143, Ukraine 252143; Cherry L. Emerson Center for Scientific Computation and Department of Chemistry Emory University, Atlanta, Georgia 30322

Received 30 March 1998; revised 8 June 1998; accepted 23 June 1998

ABSTRACT: Fifteen different structures of the water hexamer found ab initio within the 6-311G(*d, p*) basis set in the interval of 1.75 kcal/mol above the global minimum represent an unprecedented wide range of conformational plasticity of liquid water. The present work also provides the first ab initio demonstration of the existence of pentacoordinated water clusters of an orientational defect type and elaborates their properties. © 1998 John Wiley & Sons, Inc. *Int J Quant Chem* 70: 831–853, 1998

Key words: Liquid water; H-bond pattern; orientational defect; water cluster; “dangling” bond; ab initio HF/6-311(*d, p*) calculation

Introduction

Liquid water is the most abnormal substance ever known. It is formed by hydrogen or H bonds and, in fact, its H-bonded pattern with interconnectivity and tortuosity is believed to play the key role in that liquid water is as it actually is

[1]. It has been known for a long time that H-bonded patterns of liquid water and hexagonal ice Ih are tetrahedral [1], which is why an ice-Ih-like open tetrahedral pattern is often chosen as a reasonable reference, the so-called icelike model, in the study of the H bond one of liquid water. The aforementioned tetrahedrality originates, in fact, from the tetrahedral charge distribution around the oxygen atom in the water monomer possessing two positive partial charges at the positions of the hydrogen atoms and two negative partial charges that refer to a rabbit’s ear-like lone electron pair

Correspondence to: E. S. Kryachko, Department of Chemistry, The Johns Hopkins University, Baltimore, MD 21218.

* Cherry L. Emerson Fellow.

[2]. This is simply expressed by the Bernal–Fowler–Pauling or so-called ice rules [3]:

- (i) There are exactly two hydrogen atoms that belong to each oxygen atom with the O—H bond length of $\sim 1 \text{ \AA}$.
- (ii) There is exactly one hydrogen atom that occupies each O—O bond between any pair of neighboring oxygen atoms.

The “icelikeness” of liquid water is manifested in that each of its oxygen atoms is involved in two covalent and two hydrogen bonds, that is, each water molecule is four-bonded and is surrounded by four nearest-neighbor water molecules composing its first coordination shell. In the Bernal–Fowler–Pauling H-bonded pattern, the oxygen atoms are arranged in such a way that all the O—O—O bond angles between the nearest-neighbor water molecules are tetrahedral, that is, equal to ca. 109.47° . The hydrogen atoms decorate therein the O—O bonds, establishing the so-called hydrogen bigamy. It is clear that this ice like model is good, although to what extent it is appropriate or, in other words, whether this “icelikeness” adequately describes the whole H-bonded pattern of liquid water is *still* a question? Let us put this question in another way: Does liquid water contain some “patches” in its pattern that, in fact, violate the Bernal–Fowler–Pauling ice rules? It is now apparently hard to believe that resolving a liquid water paradigm becomes possible with denying the very existence of such non-icelikeness “patches.” So, to say simply, water can be crudely describable by a “two-state” model with one “state” that obeys the Bernal–Fowler–Pauling rules and the other one violating them.

A “two-state” model satisfies either the energetical or geometrical criterion imposed on a H-bonded pattern [4–6]. The former suggests that two water molecules are H-bonded if their interaction energy $V < V_{HB}$. A negative threshold H-binding energy V_{HB} plays the role of model cutoff parameter. It is allowed to take on a sequence of values, $V_{HB} = -2n\epsilon$, with integer n from interval (10, 41) and $\epsilon = 0.07575 \text{ kcal/mol}$. V_{HB} varies then from -6.2115 to -1.5150 kcal/mol . According to the geometrical criterion (for current references, see [7]), two water molecules are H-bonded if the following three constraints are accomplished altogether: The first one is the constraint on interoxygen separations that must be less than $R_{thr} =$

$3.4\text{--}3.7 \text{ \AA}$ [8]. The R_{thr} determines the position of the first minimum of the g_{OO} radial distribution function and defines, in fact, the boundary of the first coordination shell. It certainly depends on the temperature and pressure. The second constraint is imposed on the distance between the oxygen atom of the acceptor water molecule and the hydrogen atom of the donor one. This is the so-called H-bond length. It should be smaller than $r_{thr} = 2.45 \text{ \AA}$, that is, the distance at which the first minimum of the radial distribution function g_{OH} takes place [8]. The third constraint limits the angle δ_H between the participating oxygen and the hydrogen of the donor molecule and the oxygen atom of the acceptor molecule: $\delta_H > 160^\circ$. This constraint seems to be quite fragile and is often omitted because a reasonable deviation of δ_H from 160° to smaller angles indicates a stronger nonlinearity of a H bond. These constraints are sometimes supplemented by another one imposed on values of the lone pair–oxygen–oxygen angle.

The second “state” is further subdivided into two types: ionic and orientational, depending on which Bernal–Fowler–Pauling ice rule is violated. It is highly worth noticing here two subtle features of liquid water that show how much it is actually distinguished from the Bernal–Fowler–Pauling model. It is obvious that both these features should be incorporated into this non-Bernal–Fowler–Pauling “state” under the assumption that two “states” suffice to describe water correctly. The first feature is related to the O—O radial distribution function g_{OO} of liquid water at 25°C . It is experimentally revealed [8] that its first maximum is sharply peaked at 2.86 \AA and its integral from zero to R_{thr} , which is interpreted as the mean number of water molecules within the first coordination shell, is about 4.5. This clearly implies that liquid water must possess fivefold coordinated “patches,” which obviously violate ice rules. Another feature concerns the O—O—O bond-angle distribution function. According to recent experiments [9] (see also [10]), it possesses two maxima, one of which is very broad and corresponds to the tetrahedral bond angle. The other maximum is peaked at $\angle O—O—O = 60^\circ$, which demonstrates that the corresponding water molecules are settled in nontetrahedral directions.

The present work focuses on orientational defects as such H-bond “patches” that violate the second Bernal–Fowler–Pauling rule. The simplest model of an orientational defect in ice was long ago suggested by Bjerrum [11(a)] (see also [1]).

Bjerrum orientational defects are of two types: The first one is that which corresponds to an "empty" or "dangling" O···O bond. It is called the L-defect.[†] The other one, the D-defect,[‡] is actually a doubly occupied bond O—H···H—O. This definition of orientational defects seems rather schematic and it does not take into account the cooperative nature of H-bonding in liquid water. Progress toward understanding the nature of orientational defects has been made due to the first and, in some sense, semiempirical calculations by Dunitz [12(a)], Cohan and coworkers [12(b)], and Eisenberg and Coulson [12(c)] (see also [12(d–h)]). These calculations show that an orientational defect is some "patch" in the H-bonded pattern around an "empty" or doubly occupied H bond surrounded by some distorted H bonds. Distortion is primarily thought of in terms of a δ_H angle, whose value in the range of 160°–130° describes a leaned or non-linear H bond. The latter converts into a so-called bifurcated H bond when this angle approaches 120°–100°. A physical model of a solitonic-type orientational defect where the central part is some sort of bifurcated H bond was elaborated in [13] (for a recent review, see [14]). A bifurcated H-bond is a specific type of H bond where the hydrogen atom simultaneously participates in or donates two hydrogen bonds. In other words, the hydrogen atom is shared by a couple of oxygen atoms simultaneously [12(e–h), 15]. It is believed that these bonds contribute significantly to the Raman [16] and infrared [1] (see also [13(b)]) spectra of liquid water. It is also believed that they play a major role in the mobility of water. This view was supported experimentally [17] and in computer simulations [10, 18]. However, it should be stressed that all these Bjerrum-type defects rely on the tacit assumption of preserving fourfold coordination. It was recently suggested [10] that a fivefold "patch" is a new type of orientational defect with a bifurcated H bond which appears as a result of the approaching of a fifth water molecule. It was also suggested in [10] that this "patch" facilitates a transition from one Bernal–Fowler–Pauling pattern to another one through a lowered energy barrier. A similar model of a fivefold "patch" cluster was recently discussed by Head-Gordon and Stillinger [19].

[†]Originally from the German word "leer" that means "empty."

[‡]Originally from the German word "doppelt" that means "double."

Following the idea of the early quantum-chemical studies of orientational defects by Dunitz, Eisenberg, and Coulson, Cohan and coworkers, and Newton, it is natural, before invoking a pentacoordinated orientational defect as the second "state" in the H-bonded pattern of liquid water, to quest it in water clusters. This was the principal aim of the present article. Its realization requires a performance of a quite exhaustive ab initio search of the total potential energy surface (PES) of water clusters that is feasible at the Hartree–Fock computational level with the 6-311G(*d, p*) basis set. The layout of the present article is the following: The next section furnishes the computational GAUSSIAN-type methodology. The second section starts with a succinct exposition of the present state of the ab initio hexamer and octamer water clusters. This is the main section that presents the results of a PES search of the water hexamer and octamer clusters, gives the structures of lower-lying pentacoordinated water clusters, and discusses thoroughly their properties. The third section summarizes the present work.

Computational Methodology

All calculations were performed with the Gaussian-94 suite of programs [20] at the Cherry L. Emerson Center for Scientific Computation of Emory University in Atlanta. A search of the total potential energy surface of water clusters was performed at the Hartree–Fock (HF) level of computation with the triply split valence 6-311G(*d, p*) basis set that includes polarization functions on the oxygen and hydrogen atoms in particular [21]. In all computations, no constraints were imposed on the geometry of water clusters. Full geometrical optimization was performed for each water cluster structure, and the attainment of the energy minimum was verified by calculating the vibrational frequencies that result in the absence of negative eigenvalues. Default options were used for the SCF convergence and for the threshold limits determining the final changes in the maximum forces and displacements in the geometry optimization. Vibrational modes and the corresponding frequencies are based on a harmonic force field. Empirical scaling factors were not used. For conciseness, the tables report only the most intensive infrared (IR) and Raman active bands of pentacoordinated

orientational defects for which the IR intensity and Raman activity exceed ca. 200 km/mol and ca. 50 Å⁴/amu, respectively, and also include the scissor and H-stretching vibrational bands.

Pentacoordinated Water Clusters

PRELUDE: HEXAMER AND OCTAMER

The study of water clusters is one of the promising ways to shed light on the liquid water paradigm. It is obvious, on the one hand, that a larger cluster mimics better a bulky water. On the other hand, it is also quite evident that a larger cluster possesses a richer landscape of its PES. Regarding this, deserving to be mentioned is a rather well-spread and reasonable belief that to grasp the nature of water it might be sufficient to study those water cluster structures that occupy lower-lying energy minima on the PES. Water hexamer and octamer clusters are at the primary place in this cluster approach. They were the subject of numerous ab initio studies (see [22, 23] and references therein). In particular, it was shown in [22(d)] that at the HF/6-311G(*d, p*) level of computational theory the global minimum of the hexamer PES is attained by the prism structure. Two lower-lying local minima close to the global one were also found in this work: One corresponds to the monocyclic chair-type structure, whereas the other one is occupied by the boat form. Xantheas and Dunning [22(a)] and Xantheas [22(b)] studied the cyclic water hexamer at the HF and the second-order Møller-Plessett perturbation theory (MP2) levels with an augmented correlation-consistent polarized valence double-zeta basis (aug-cc-pVDZ) basis set. The global minimum of a cage type with eight H bonds was detected by Jordan and coworkers [22(c), 23(d)] at the MP2/aug-cc-pVDZ level. They also found that the prism is a more stable structure by approximately 0.2 kcal/mol compared with the cyclic one. A similar conclusion about the cage as the most stable water hexamer was recently reached by Saykally and coworkers [23(e)], Gregory and Clary [23(f)], and Saykally and coworkers [23(g)].

In the present work, we performed a rather exhaustive search of the landscape of the total PES of the water hexamer around its global minimum. The results of these searches are reported in Table I for the energy, zero-point vibration energy (ZPVE), enthalpy, and entropy and in Table II for

rotational constants and the total dipole moment. They are also displayed in Figure 1. It shows that two prism structures, prism I and prism II, of (H₂O)₆ are at the bottom of the total PES. Prism I is in its global minimum at the present computational level, although prism II lies much closer to it. Their energy difference is only 5.8 cm⁻¹ taking ZPVE into account (see Fig. 2). Four cage-type structures follow them. In the notations of [23(g)], cage I corresponds to {dd}, cage II to {ud}, cage III to {du}*, and, finally, cage IV to {uu} hexamers. They are shown altogether in Figure 3. Table II demonstrates a good agreement of the rotational constants for cages calculated in the present work and reported in [23(g)]. Four lower-lying cages I–IV possess very particular geometries. The interoxygen distances between O₃ and O₄ are 3.466, 3.465, and 3.471 Å, respectively, in the cages I, II, and III. Moreover, in cage II, the distance R(O₉—O₁₅) = 3.699 Å, and in cage IV, R(O₁—O₄) = 3.465 and R(O₉—O₁₄) = 3.692 Å. This implies that, according to the first geometrical constraint, all these pairs of the oxygen atoms form “dangling” bonds, namely, cages I and III possess one “dangling” bond, whereas cages II and IV, two bonds of this sort. Furthermore, some O—O—O interbond angles move away from the tetrahedral value to lower angles thanks to pentacoordination. For example, in cage I, ∠O₃—O₁₄—O₄ = 74.63°; in cage II, ∠O₃—O₁₄—O₄ = 74.61°; in cage III, ∠O₃—O₁₄—O₄ = 74.51°; and in cage IV, ∠O₁—O₁₄—O₄ = 70.94°. Interestingly, the cage structures of the water hexamer mimics the basic unit of one of the high-density polymorphs of ice, ice VI (compare with [1(a)], Fig. 3.8). They are interconnected with each other via flipping of the free O—H bonds of two donor-acceptor monomers.

Proceeding to the next structures, it is worth mentioning that prism V is exactly the one found in [22(d)] at the global minimum. Its isoenergetic isomer, prism IV, is also revealed in the present PES search. They are interconnected through flipping of the two-sided O—H bonds. Even more interestingly, this list includes the pre-opened prism structure shown in Figure 2 with a very high dipole moment of 4.38 D. Another cage structure, cage V, displayed in Figure 4, also possesses a rather high dipole moment equal to 3.45 D. The distance between its oxygen atoms O₂ and O₅ is 3.62 Å, so they form a sort of “dangling” bond. One structure of the water hexamer that was unknown is the so-called propeller-type structure. It is also portrayed in Figure 4. With ZPVE correc-

TABLE I
Energy, enthalpy H , entropy S , and ZPVE of lower-lying water hexamers.

Structure	- Energy +456 Hartrees	ΔE (kcal / mol)	ZPVE (kcal / mol)	- Enthalpy +456 Hartrees	ΔH (kcal / mol)	S (cal / mol K)
Boat	0.354985963	3.4392354 1.5462454 ^a	99.55746	0.179342	2.670025 0.777035 ^a	135.271
Book	0.356340902	2.5890071 1.7422371 ^a	100.60368	0.180000	2.257128 1.410358 ^a	126.412
Chair	0.356702756	2.3619426 0.7666526 ^a	99.85516	0.180874	1.708691 0.113401 ^a	132.506
Cage V	0.357035657	2.1530463 1.6980763 ^a	100.99548	0.180491	1.949024 1.494054 ^a	121.942
Propeller	0.357274355	2.0032625 1.1068525 ^a	100.55404	0.1810310	1.610173 0.713763 ^a	125.363
Preopened prism	0.357431391	1.9047220 1.2040020 ^a	100.74973	0.181046	1.600760 0.900040 ^a	123.652
Prism III	0.358047985	1.5178074 1.3752474 ^a	101.30789	0.181304	1.438864 1.296304 ^a	119.300
Prism V	0.358048203	1.5177980 1.3761080 ^a	101.30876	0.181303	1.439492 1.297757 ^a	119.297
Prism IV	0.358048107	1.5177308 1.3759908 ^a	101.30871	0.181303	1.4394922 1.297752 ^a	119.301
Cage IV	0.358758406	1.0720161 0.6344461 ^a	101.01288	0.182218	0.865327 0.427757 ^a	121.718
Cage III	0.358944226	0.9554135 0.6047335 ^a	101.09977	0.182346	0.785006 0.434326 ^a	121.111
Cage II	0.359012959	0.9122833 0.5649433 ^a	101.10311	0.182409	0.745474 0.398134 ^a	120.983
Cage I	0.359013050	0.9122262 0.5606662 ^a	101.09889	0.182410	0.744846 0.393286 ^a	121.022
Prism II	0.360449222	0.0110239 0.0166139 ^a	101.45604	0.183583	0.008785 0.014375 ^a	118.301
Prism I	0.360466790	0.0 0.0	101.45045	0.183597	0.0 0.0	118.347

^a ZPVE correction is taken into account.

tion, the difference in energies of prism I and the propeller structure is 1.107 kcal/mol. This water hexamer has a rather large dipole moment of 3.74 D and one “dangling” bond between the oxygen atoms O₇ and O₈ with a very short distance of R(O₇—O₃) = 3.104 Å. Because the distance between the oxygen atom O₈ and the hydrogen H₁₀ is 2.564 Å and the angle $\delta_H = \angle O_7—H_{10}—O_8 = 116.67^\circ < 160^\circ$, it is unlikely that they form a hydrogen bond. This “dangling” bond is seen from the oxygen atoms O₄ and O₁₃ under the angles 63.85° and 63.56°. This is the first structure among lower-lying water hexamers that contributes to the second nontetrahedral maximum of the O—O—O bond distribution function.

Table I reports the calculated thermodynamic

properties of all the studied hexamer structures. It is seen there that the boat and chair are characterized by rather high entropies of 135.27 and 132.51 cal/mol T, respectively. Entropies of the book, propeller, and pre-opened prism structures are also quite large compared with that of the prism I structure. This means that despite that the latter is at the global minimum at T = 0 K the energy ordering changes substantially with increasing temperature. For example, prism I remains at the global minimum at T < 130 K. At T ≥ 130 K, the chair structure becomes the lowest one by the free energy. At room temperature, cages I–IV compete with prism I. Interestingly, at T > 300 K, the pre-opened prism becomes more energetically favorable than prism I. Even more interesting to notice

TABLE II
Rotational constants and total dipole moment of lower-lying water hexamer structures.^a

Structure	Rotational constants (GHz)			Dipole moment (D)
Boat	1.23136	1.12844	0.62217	0.8101
Book	1.82085	1.00761	0.76171	2.8858
Chair	1.16607	1.16607	0.59509	0.0
Cage V	2.06059	1.08402	1.07861	3.4507
Propeller	1.65997	1.18276	0.91629	3.7428
Preopened prism	1.57297	1.29319	1.07046	4.3841
Prism III	1.63253	1.28955	1.26493	2.8531
Prism V	1.63298	1.28948	1.26525	2.8512
Prism IV	1.63251	1.28955	1.26522	2.8523
Cage IV	2.11851 (2.1334)	1.08603 (1.1055)	1.02710 (1.0790)	2.0095
Cage III	2.10894 (2.2808)	1.09042 (1.1596)	1.03060 (1.1096)	2.0980
Cage II	2.14024 (2.1336)	1.07891 (1.1021)	1.01597 (1.0755)	1.8667
Cage I	2.13849 (2.1332)	1.07943 (1.1027)	1.01628 (1.0747)	1.8524
Prism II	1.61272	1.32655	1.28996	2.9921
Prism I	1.61452	1.32630	1.29033	2.9038

^a Calculated rotational constants from [23(g)] are in parentheses. For the cage III ({du}, in notations of [23(g)]), these values are approximate (see Table 2, [23(g)]).

is that at room temperature the propeller structure distances from the chair by approximately 2 kcal/mol.

With regard to the water octamer, it is well known that the cubic structure Ca [23(a)] of D_{2d} is the most stable one on the water octamer PES energy surface computed at the HF/6-311G(*d, p*) level. The cubic structure of S_4 symmetry occupies the local minimum that lies 3.49 kcal/mol above the Ca structure. In addition, there have been found another 25 lower-lying octamer structures, among which the ring structure R8a is energetically higher than the Ca one by 12.91 kcal/mol. At room temperature, their free-energy difference diminishes to 0.19 kcal/mol [23(a)].

"DANGLING" BOND IN WATER HEXAMER

Two novel low-energy local-minimum structures of the $(\text{H}_2\text{O})_6$ water cluster are revealed on the water hexamer PES at the HF/6-311G(*d, p*) computational level. They are shown in Figure 5. The first one with a total dipole of 2.47 D

is hereafter named Defect I. It lies above prism V and the chair water hexamers by 2.88 and 2.04 kcal/mol, respectively, and distances from the prism I structure by 4.40 kcal/mol, which reduces to 3.19 kcal/mol when taking ZPVE into account. The ZPVE, enthalpy, and free energy of Defect I and their differences with respect to the corresponding quantities for the prism and chair structures are listed in Table III. One readily figures out that at room temperature the energy of the formation of Defect I is 1.15 kcal/mol with respect to the prism I structure. It is worth mentioning that the Defect I structure and prism VI become almost isoenergetical at room temperature.

The internal coordinates of Defect I are presented in Table IV. One sees there that in Defect I the water molecule $\text{H}_2\text{H}_3\text{O}_1$'s distances from the nearest-neighbor water molecules with which it forms either a covalent or H bond are rather far apart than the typical O—O separation of 2.86 Å inherent for the tetrahedral pattern. To specify, $r(\text{O}_1—\text{O}_4) = 2.93$ Å, $r(\text{O}_1—\text{O}_5) = 3.08$ Å, and $r(\text{O}_1—\text{O}_{15}) = 2.97$ Å. It is, in fact, due to that this water molecule has a fifth nearest-neighbor one that is settled on the oxygen atom O_{10} and characterized by the distance $r(\text{O}_1—\text{O}_{10}) = 3.16$ Å. The latter one is less than R_{thr} and, thus, one might think of these molecules as bonded to each other by a so-called dangling bond. One therefore concludes that this water cluster with a "dangling" bond represents itself as a fivefolded "patch" that may appear among fourfolded ones in the H-bonded pattern of liquid water. The formation of a "dangling" bond promotes the appearance of nonlinear H bonds between O_1 , on the one side, and O_5 and O_{15} , on the other one, with $r(\text{O}_1—\text{H}_9) = 2.34$ Å, $\angle \text{O}_1—\text{H}_9—\text{O}_5 = 134.63^\circ$, $r(\text{O}_1—\text{H}_{18}) = 2.17$ Å, and $\angle \text{O}_1—\text{H}_{18}—\text{O}_{15} = 141.29^\circ$. This is clearly seen in Figure 5. It follows from Table IV that the "dangling" bond causes distortion of the rest of the H-bonded pattern of the Defect I water hexamer that remains fourfolded. For instance, $r(\text{O}_5—\text{O}_{10}) = 2.95$ Å, $r(\text{O}_{10}—\text{H}_8) = 2.07$ Å, $\angle \text{O}_5—\text{H}_8—\text{O}_{10} = 154.30^\circ$, and $r(\text{O}_4—\text{O}_{15}) = 2.90$ Å, with $r(\text{O}_4—\text{H}_{18}) = 2.07$ Å and $\angle \text{O}_4—\text{H}_{18}—\text{O}_{15} = 144.44^\circ$. It is also worth noticing that, compared with the propeller structure, Defect I solidly contributes to the second nontetrahedral maximum of the O—O—O bond distribution function thanks to five O—O—O bond angles which are clustered around 60°. These are, in particular, the following: $\angle \text{O}_4—\text{O}_1—\text{O}_{15} = 62.75^\circ$, $\angle \text{O}_1—\text{O}_4—\text{O}_{15} = 59.57^\circ$,

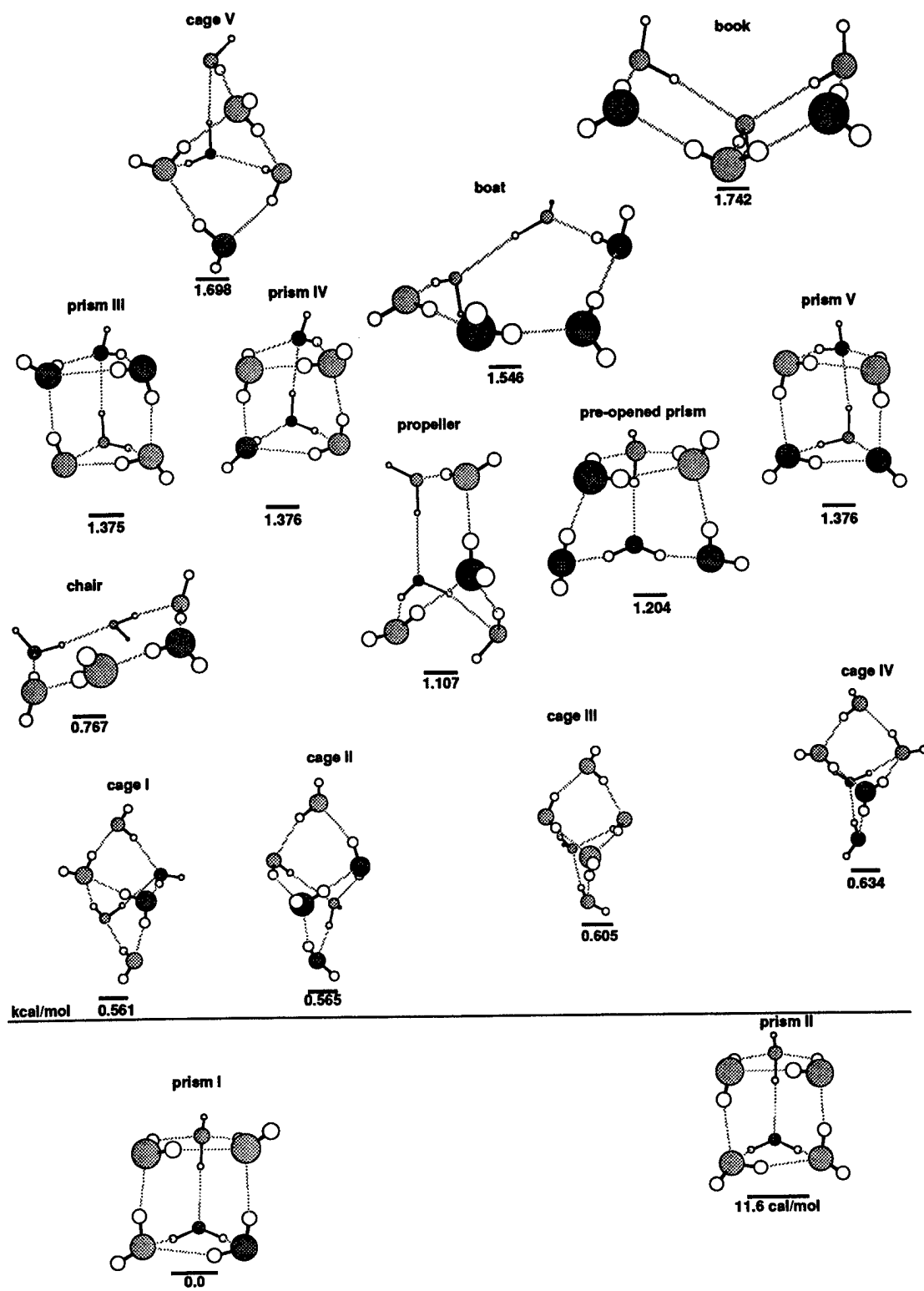


FIGURE 1. Lower-lying structures of water hexamer. (Solid line) O—H, (dashed line) H and (dot-dashed line) “dangling” bonds.

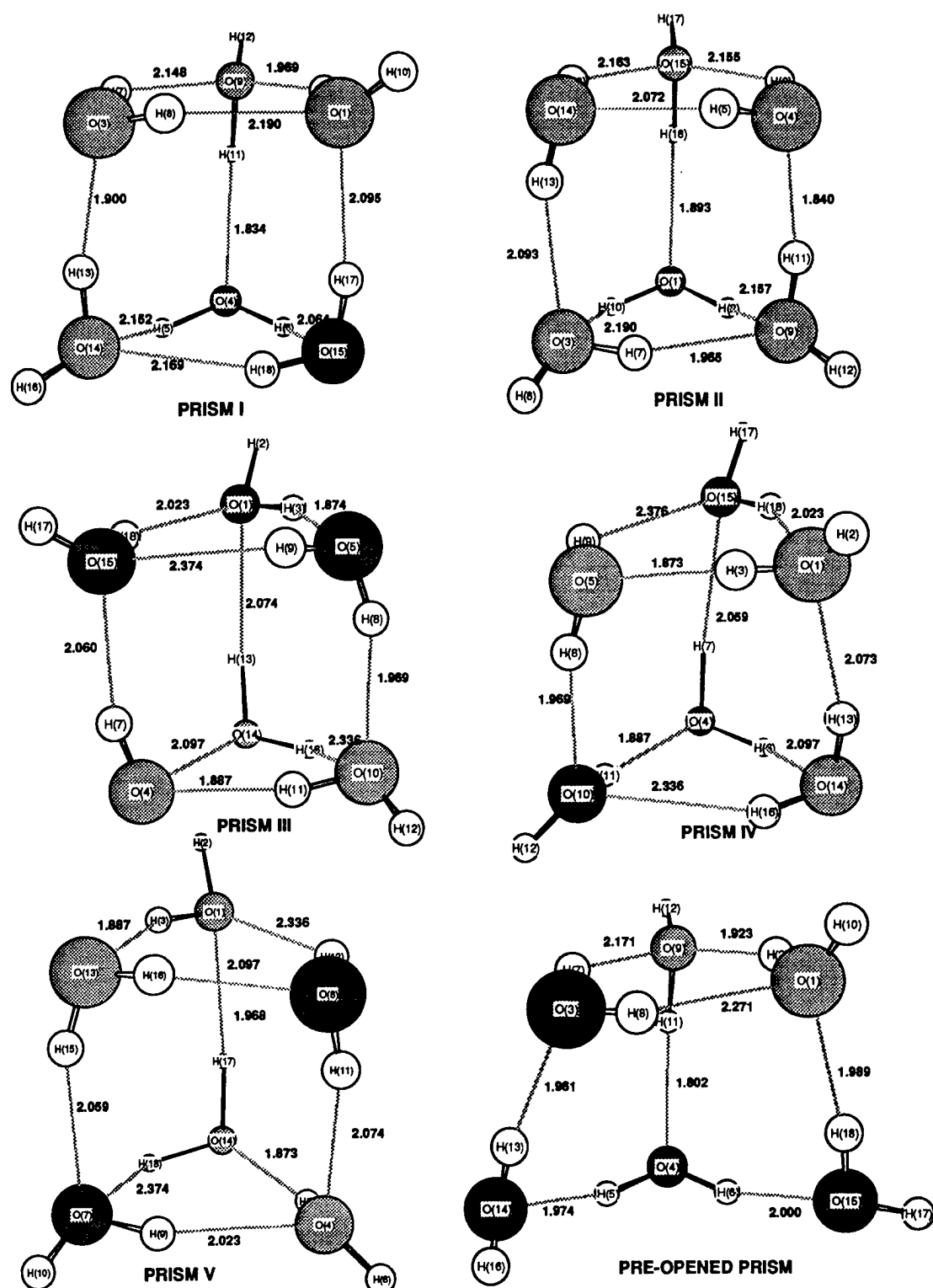


FIGURE 2. Six lower-lying prismlike structures of water hexamer. Symbols same as in Figure 1.

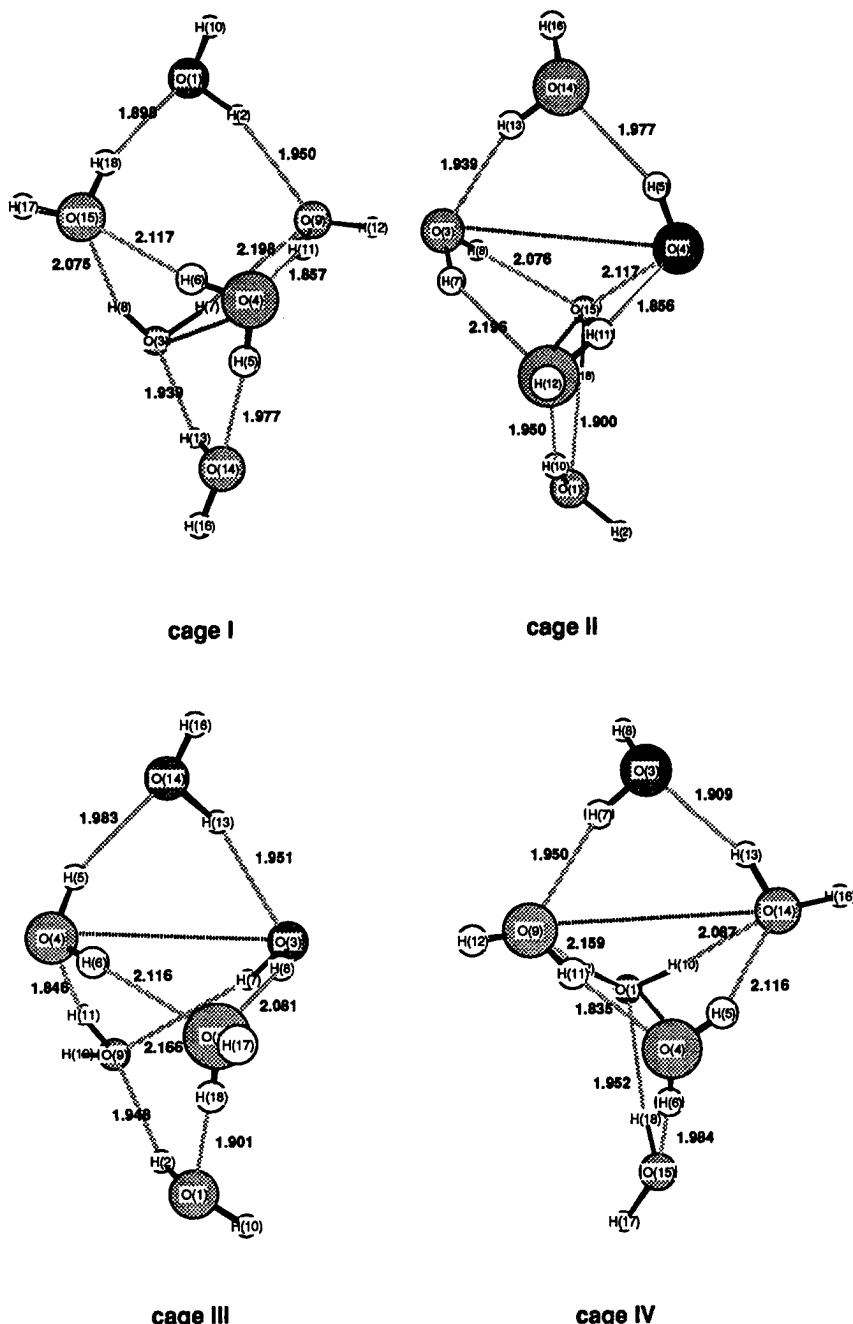


FIGURE 3. Four lowest cage structures of six molecules of water. Symbols same as in Figure 1.

and $\angle O_4—O_{14}—O_5 = 63.41^\circ$. One also sees from Table IV that the lone-pair distribution of O_1 loses its tetrahedrality characterized $\angle O_5—O_1—O_{15} = 87.60^\circ$ due to fivefold coordination. Before ending this paragraph, it is interesting to notice that due to the “dangling” bond the separation between the

oxygen atoms O_1 and O_{14} considered as the second-neighbors is 4.22 \AA .

The assignment of the most active harmonic vibrations of the Defect I “patch” is carried out in Table V. Harmonic frequencies computed for inter- and intramolecular modes of the Defect I structure

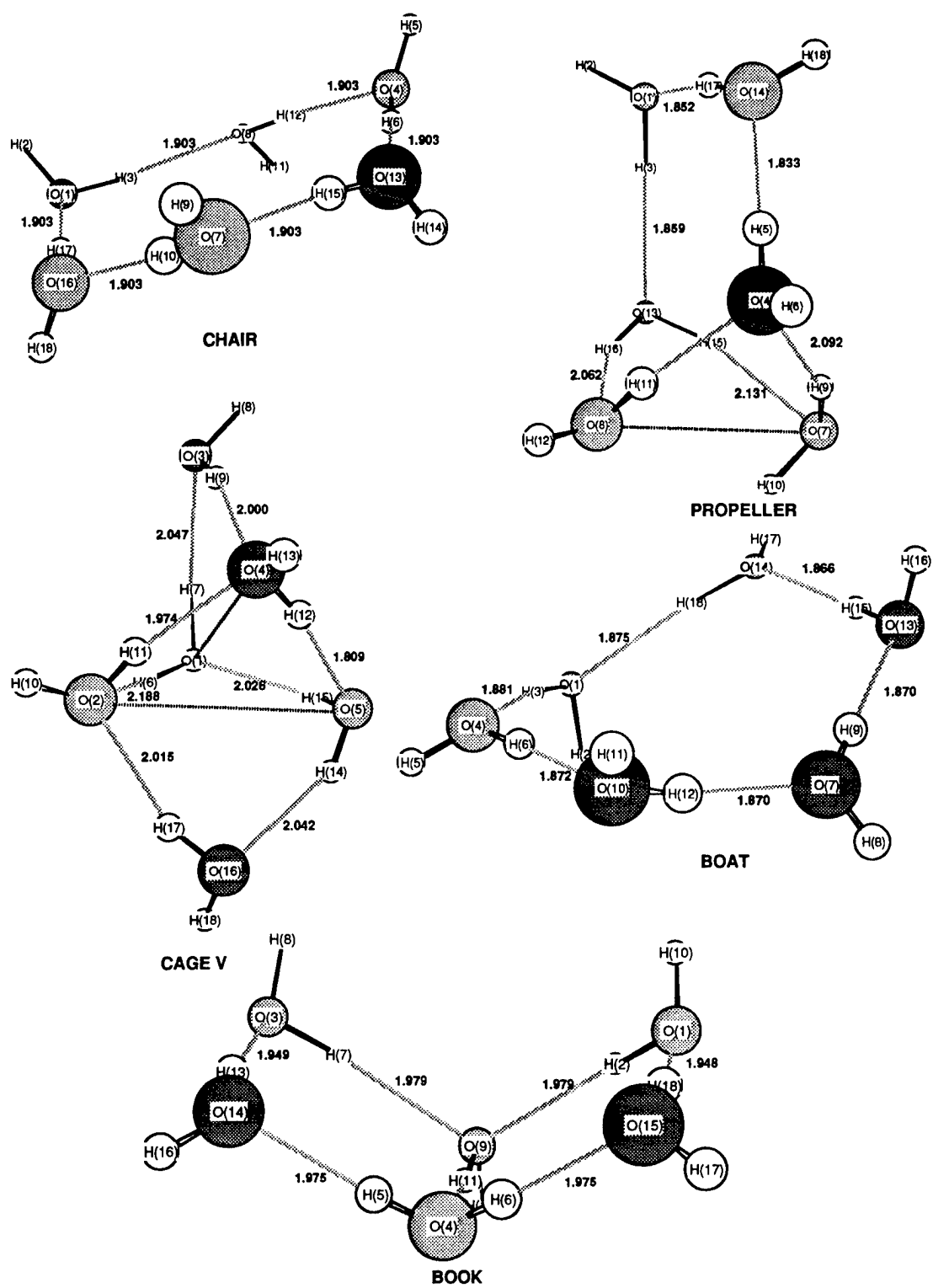


FIGURE 4. Chair, propeller, cage V, boats and book structures. Symbols same as in Figure 1.

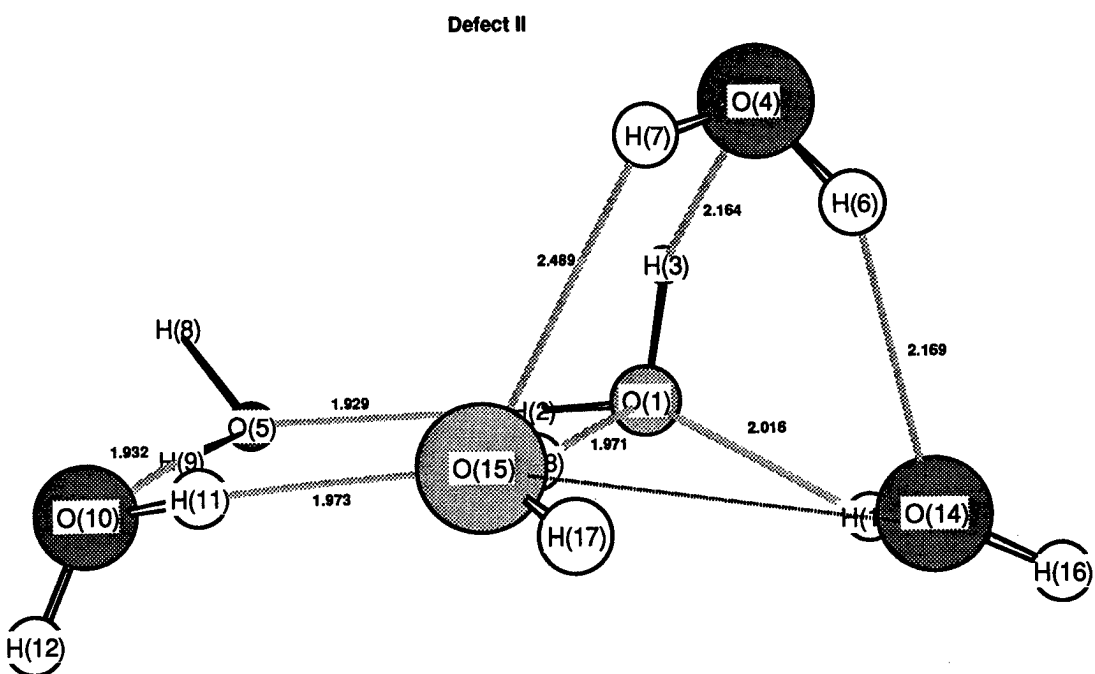
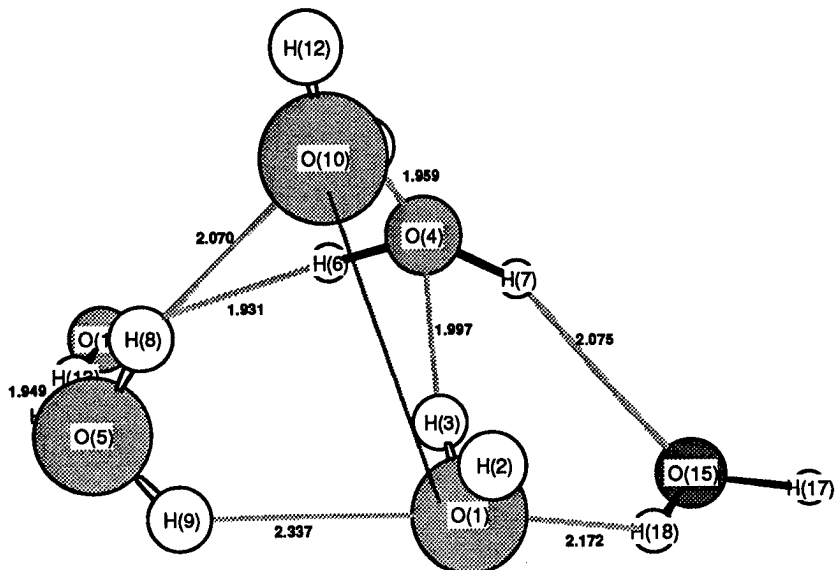


FIGURE 5. Pentacoordinated water hexamer Defects I and II. Symbols same as in Figure 1.

are listed in the second column of this table. Its third and fourth columns report the corresponding theoretical IR intensity and Raman activity. First of all, before inspecting Table V, it deserves to be mentioned that the theoretical spectra of the chair and boat water hexamers do not possess vibrations in the region of $4000\text{--}4200\text{ cm}^{-1}$, implying that the

hydrogen atoms in these structures are solely of two sorts: the hydrogens involved in forming the H bond and the "free" hydrogens participating in unbonded OH groups. On the contrary, the prism hexamers and Defect I do have H-stretching vibrations in this region. The most intensive IR band of Defect I is the librational one centered at 663.5 (IR

TABLE III
Energy (*E*), enthalpy (*H*), entropy (*S*), ZPVE, and free energy of defect water hexamers.

<i>E</i> (Hartree)	<i>H</i> (Hartree)	<i>S</i> (cal / mol K)	ZPVE (kcal / mol)
$\Delta_o E$	$\Delta_o H$	$\Delta_o S$	$\Delta_o G$
$\Delta_p E$	$\Delta_p H$	$\Delta_p S$	$\Delta_p G$
$\Delta_c E$	$\Delta_c H$	$\Delta_c S$	$\Delta_c G$
<i>Defect I</i>			
- 456.3534556	- 456.1773545	127.64111	100.24399
4.40	3.92	9.29	1.15
2.88	2.48	8.34	- 0.01
2.04	2.21	- 4.86	3.66
<i>Defect II</i>			
- 456.3532593	- 456.1771700	126.23200	100.32397
- 4.52	4.03	7.89	1.68
3.01	2.59	6.94	0.52
2.16	2.32	- 6.27	4.19

Prisms I and VI and chair hexamers are chosen as the reference ones. $\Delta_{\text{prism}I} \equiv \Delta_o$, $\Delta_{\text{prism}VI} \equiv \Delta_p$, $\Delta_{\text{chair}} \equiv \Delta_c$. $\Delta_x X$ in kcal / mol, $X = E$, H , and G (at room $T = 298.15$ K); $\Delta_x S$ in cal / mol K, $x = o, p, c$.

intensity 564 km/mol, Raman activity $0.5 \text{ \AA}^4/\text{amu}$) compared with the most IR intensive ones for the prisms, chair, and boat hexamers that fall into the region of H-stretching vibrations. The band at 663.5 cm^{-1} is assigned to the composed libration of the O_4-H_6 , O_5-H_8 , and O_5-H_9 bonds. Other IR intensive bands of Defect I are the following: first of all, the band 467.2 cm^{-1} (343.3, 2.2) associated with the composed librational vibration of O_1-H_3 , O_5-H_8 , O_5-H_9 , and $\text{O}_{15}-\text{H}_{18}$ bonds. The other ones belong to the H-stretching region. These are the bands centered at 4001.96 cm^{-1} (511.8, 22.0) with the O_4-H_6 , $\text{O}_{14}-\text{H}_{13}$ stretching vibration character and the band at 4111.4 cm^{-1} (369.8, 21.3) assigned merely to O_4-H_7 stretching. Regarding the O—H stretching vibrational modes with the frequencies $\nu_1^{\text{theor}} = 4141.9 \text{ cm}^{-1}$ (17.7, 65.5; symmetric) and $\nu_3^{\text{theor}} = 4237.6 \text{ cm}^{-1}$ (57.4, 32.4; asymmetric) computed for the HF/6-311G(*d, p*) water monomer (for comments, see footnote [§]), one may divide the whole stretching region of Defect I into three groupings. The first one spans the range from 3967 to 4069 cm^{-1} and possesses the dominant character of stretching of H-

bonded hydrogen atoms. The band 3967.5 cm^{-1} (79.7, 162.6) describes the composed symmetric stretching vibration of O_4-H_6 and $\text{O}_{14}-\text{H}_{13}$ bonds and is, in fact, the strongest Raman active band. The aforementioned 4002.0 cm^{-1} band corresponds to their asymmetric stretching vibrations. Compared with the stretching bands of a single water molecule, the latter bands of Defect I are both redshifted, considerably enhanced, and become closer to each other by 60 cm^{-1} . The second grouping of bands lies in the interval from 4085 to 4180 cm^{-1} and is primarily contributed to by nonlinear or bent H-bonded hydrogens. The last one consists of bands spanning the interval from 4183 to 4221 cm^{-1} . They are assigned to the stretching vibrations of "orphaned" H-bond donors. These bands are slightly blue-shifted and mainly enhanced in twofold compared with the stretching mode ν_3 of the water monomer.

The second water hexamer displayed in Figure 5 and named Defect II looks more noticeable because its H-bonded imperfection seems to be more spectacular and manifests itself in the following: (1) Table IV shows that the oxygen–oxygen separation between O_{15} and O_{14} reaches 3.12 \AA . On the one hand, this implies that, according to the first geometrical constraint, the corresponding water molecules are bonded. On the other hand, they are also not H-bonded because the hydrogen atoms of one water molecule are settled so far away from the oxygen atom of a possible acceptor water molecule [$r(\text{O}_{14}-\text{H}_{17}) = 2.68 \text{ \AA}$] that the second

[§] See [24(a) and (b)]. Experimental harmonic frequencies of the water molecule are the following: $\nu_1^{\text{expt}} = 3832 \text{ cm}^{-1}$, $\nu_2^{\text{expt}} = 1649 \text{ cm}^{-1}$, and $\nu_3^{\text{expt}} = 3942 \text{ cm}^{-1}$. $\nu_2^{\text{theor}} = 1750.30 \text{ cm}^{-1}$ at the HF/6-311G(*d, p*) level. Scaling factors $f_i = \nu_i^{\text{theor}} / \nu_i^{\text{expt}}$, $i = 1, 2, 3$ are equal to 1.0809, 1.0614, and 1.0750, respectively. The average scaling factor $\langle f \rangle = (f_1 + f_2 + f_3) / 3 = 1.0724$. The scaled frequencies $\nu_i^{\text{sc}} = \nu_i^{\text{theor}} / \langle f \rangle$ [with the relative error, $\delta = (\nu_i^{\text{sc}} - \nu_i^{\text{expt}}) / \nu_i^{\text{expt}}$, %] are 3862.17 cm^{-1} (+0.79%), 1632.09 cm^{-1} (-1.03%), and 3951.43 cm^{-1} (+0.21%).

TABLE IV
Internal coordinates of defect water hexamers.

Defect I			
Interoxygen Distance, (Å)			
$R(O_1-O_4)$	$R(O_1-O_5)$ $R(O_4-O_{10})$ $R(O_5-O_{10})$	$R(O_1-O_{10})$ $R(O_4-O_{14})$ $R(O_5-O_{14})$	$R(O_1-O_{16})$ $R(O_4-O_{15})$ $R(O_{10}-O_{14})$
2.932	3.075 2.842 2.953	3.162 2.824 2.869	2.969 2.897 4.120
H-bond Angle δ_H (deg)			
$O_1-H_3-O_4$ $O_4-H_7-O_{15}$	$O_1-H_9-O_5$ $O_5-H_8-O_{10}$	$O_1-H_{18}-O_{15}$ $O_{10}-H_{11}-O_4$	$O_4-H_6-O_{14}$ $O_{14}-H_{13}-O_5$
167.99 144.44	134.63 154.30	141.29 153.55	155.45 161.84
O—O—O Bond Angle (deg)			
$O_4-O_1-O_{15}$	$O_{10}-O_1-O_{15}$ $O_1-O_4-O_{15}$ $O_{10}-O_5-O_{14}$	$O_5-O_1-O_{15}$ $O_{10}-O_5-O_{14}$ $O_4-O_{14}-O_5$	$O_{14}-O_4-O_{15}$ $O_1-O_5-O_{10}$ $O_1-O_{15}-O_4$
62.75	43.89 59.57 86.70	87.60 86.70 63.41	73.37 93.11 57.67
Defect II			
Interoxygen Distance (Å)			
$R(O_1-O_4)$	$R(O_1-O_5)$ $R(O_4-O_{14})$	$R(O_1-O_{14})$ $R(O_4-O_{15})$ $R(O_{10}-O_{15})$	$R(O_1-O_{15})$ $R(O_5-O_{10})$ $R(O_{14}-O_{15})$
2.916	2.840 3.002	2.836 3.135 2.876	2.910 2.869 3.121
H-bond Angle δ_H (deg)			
$O_1-H_3-O_4$	$O_1-H_2-O_5$ $O_5-H_3-O_{10}$ $O_{15}-H_{18}-O_1$	$O_4-H_6-O_{14}$ $O_{10}-H_{11}-O_{15}$ $O_{14}-H_{17}-O_{15}$	$O_4-H_7-O_{15}$ $O_{14}-H_{13}-O_1$ $O_{14}-H_{18}-O_{15}$
135.44	159.51 168.09 169.35	146.19 158.08 109.09	126.16 143.68 90.02
O—O—O Bond Angle (deg)			
$O_4-O_1-O_{14}$	$O_5-O_1-O_{14}$ $O_5-O_1-O_{15}$	$O_4-O_1-O_{15}$ $O_1-O_{15}-O_{10}$ $O_1-O_5-O_{10}$	$O_4-O_1-O_5$ $O_5-O_{10}-O_{15}$ $O_4-O_1-O_{15}$
62.90	149.64 88.41	65.21 90.65 92.24	121.88 88.50 65.79

TABLE V

Most intensive bands of Defect I water hexamer: vibrational frequencies ν (cm⁻¹) IR intensity (km / mol), Raman activity (Å⁴ / amu), force constant (mdyne / Å), and reduced mass (amu).

No.	ν (cm ⁻¹)	IR intensity	Raman activity	Force constant	Reduced mass Assignment
1	7426.87	191.66	1.32	0.1163	1.0830 $O_1—H_2, O_{15}—H_{17}—H_{18}$ libration
2	467.16	343.34	2.20	0.1357	1.0554 $O_1—H_3, O_5—H_8—H_9, O_{15}—N_{18}$ libration
3	591.19	203.24	4.31	0.2162	1.0497 $O_1—H_3, O_4—H_7$ libration
4	663.51	564.12	0.47	0.2763	1.0651 $O_4—H_6, O_5—H_8—H_9$ libration
5	792.43	292.40	0.88	0.3940	1.0650 $O_4—H_6—H_7, O_5—H_9, O_{14}—H_{13}$ libration
6	1756.83	203.58	3.66	1.9633	1.0797 $H_2—O_1—H_3, H_{11}—O_{10}—H_{12},$ $H_{17}—O_{15}—H_{18}$ scissor
7	1822.21	107.83	3.87	2.1091	1.0781 $H_2—O_1—H_3, H_8—O_5—H_9$ scissor
8	3967.47	79.66	162.57	9.7897	1.0566 $O_4—H_6, O_{14}—H_{13}$ stretch
9	4001.96	511.76	22.01	9.9429	1.0537 $O_4—H_6, O_4—H_7, O_{14}—H_{13}$ stretch
10	4016.36	167.01	25.95	10.0461	1.0570 $O_{10}—H_{11}$ stretch
11	4047.50	227.75	89.05	10.1860	1.0553 $O_1—H_3, O_4—H_6, O_{10}—H_{11}$ stretch
12	4068.80	143.11	36.64	10.2569	1.0516 $O_5—H_8, O_5—H_9$ stretch
13	4085.39	211.26	48.75	10.3511	1.0526 $O_{15}—H_{17}, O_{15}—H_{18}$ stretch
14	4111.36	369.79	21.25	10.7142	1.0758 $O_4—H_7$ stretch
15	4159.71	177.57	29.98	10.9754	1.0766 $O_5—H_9$ stretch
16	4183.20	111.31	32.23	11.0601	1.0727 $O_1—H_2$ stretch
17	4210.83	124.08	51.80	11.2187	1.0739 $O_{10}—H_{12}$ stretch
18	4212.04	81.71	59.75	11.2060	1.0721 $O_{14}—H_{16}$ stretch
19	4220.61	113.57	47.29	11.3126	1.0779 $O_{15}—H_{17}$ stretch

geometrical constraint is not satisfied. Moreover, the angle δ_H in this case is $\angle O_{14}—H_{17}—O_{14} = 109.09^\circ$. Altogether, it results in that this couple of water molecules form a “dangling” bond. (2) The separation between O_4 and O_{15} is quite normal for the nearest neighbors. However, the bond length

of 2.49 Å between O_{15} and H_7 slightly exceeds r_{thr} and the corresponding bond angle $\angle O_4—H_7—O_{15} = 126.16^\circ$ is far beyond the interval of the δ_H inherent for a regular tetrahedral “patch.” Nevertheless, one may suggest that this is, in fact, a H bond, albeit rather weak and strongly nonlinear,

TABLE VI
Most intensive bands of Defect II water hexamer.

No.	ν (cm ⁻¹)	IR intensity	Raman activity	Force constant	Reduced mass Assignment
1	558.00	548.86	2.93	0.1978	1.0782 O_4-H_6 , $O_{10}-H_{11}$, $O_{14}-H_{13}$, $O_{15}-H_{17}-H_{18}$ libration
2	663.55	395.30	1.58	0.2780	1.0716 O_1-H_3 , O_4-H_7 , O_5-H_9 , $O_{10}-H_{11}$ libration
3	695.54	188.50	0.49	0.2959	1.0383 O_1-H_2 , $O_{10}-H_{11}$, $O_{14}-H_{13}$ libration
4	736.56	234.87	0.83	0.3332	1.0425 $O_1-H_2-H_3$, $O_4-H_6-O_{10}-H_{11}$, $O_{14}-H_{13}$, $O_{15}-H_{18}$ libration
5	1761.25	145.79	5.11	1.9704	1.0781 $H_{13}-O_{14}-H_{16}$ scissor
6	1781.83	102.85	3.17	2.0210	1.0804 $H_8-O_5-H_9$, $H_{11}-O_{10}-H_{12}$ scissor
7	1788.81	118.23	4.28	2.0275	1.0754 $H_6-O_4-H_7$, $H_{17}-O_{15}-H_{18}$ scissor
8	1819.17	103.45	2.47	2.1016	1.0779 $H_6-O_4-H_7$, $H_{17}-O_{15}-H_{18}$ scissor
9	3966.58	87.30	191.47	9.7875	1.0558 O_1-H_2 , O_5-H_9 , $O_{10}-H_{11}$, $O_{15}-H_{18}$ stretch
10	4004.87	541.04	23.68	9.9611	1.0541 O_1-H_2 , O_5-H_9 , $O_{15}-H_{18}$ stretch
11	4019.74	482.95	13.43	10.0578	1.0565 O_1-H_2 , $O_{10}-H_{11}$, $O_{14}-H_{13}$, $O_{15}-H_{18}$ stretch
12	4041.97	93.95	71.60	10.1556	1.0550 O_5-H_9 , $O_{10}-H_{11}$, $O_{10}-H_{12}$, $O_{14}-H_{13}$, $O_{15}-H_{18}$ stretch
13	4059.63	105.91	59.50	10.2369	1.0543 O_1-H_2 , $O_{14}-H_{13}$, $O_{15}-H_{18}$ stretch
14	4091.93	185.26	31.57	10.3782	1.0520 O_4-H_6 , O_4-H_7 stretch
15	4113.52	302.18	26.87	10.7087	1.0741 O_1-H_2 , O_1-H_3 , O_4-H_6 stretch
16	4180.60	130.02	21.57	11.1098	1.0789 O_4-H_6 , O_4-H_7 stretch
17	4188.06	127.12	39.50	11.0769	1.0719 $O_{15}-H_{18}$ stretch
18	4205.30	110.69	41.85	11.1851	1.0735 O_5-H_8 , $O_{10}-H_{11}$, $O_{10}-H_{12}$ stretch
19	4207.32	87.44	55.50	11.1803	1.0720 O_5-H_8 stretch
20	4213.11	115.71	56.96	11.2516	1.0759 $O_{14}-H_{13}$, $O_{14}-H_{16}$ stretch

For notations, see caption of Table V.

that is caused by the closer presence of a "dangling" bond. The conclusion to be drawn is that the water molecule $H_{17}H_{18}O_{15}$ in the Defect II structure is fivefold coordinated with one "dangling" bond. Moreover, it is rather interesting to see from Figure 5 that Defect II includes a squarelike substructure formed by four water molecules. Its diagonal takes two values, 4.11 and 4.01 Å, respectively for the $O_1—O_{10}$ and $O_5—O_{15}$ separations. One can easily recognize that, by the structure, Defect II partly resembles a norbornane water heptamer found in [25].

Energetically, Defect II is slightly less stable than is Defect I by 0.13 kcal/mol (see Table III). Their ZPVE difference of 0.08 kcal/mol is almost negligible. The difference in their free energies is 0.53 kcal/mol at room temperature, so that Defect II is slightly less stable than is Defect I. Furthermore, it is less polar than is Defect I by 0.09 D. The assignment of harmonic vibrational modes of Defect II is presented in Table VI. Similarly to Defect I, it also possesses the two most IR-intensive bands. The first one with an IR intensity of 548.86 km/mol belongs to the libration range and is centered at 558.0 cm⁻¹. It is associated with the composed libration of H-bonded $O_4—H_6$, $O_{10}—H_{11}$, and $O_{14}—H_{13}$ bonds. The second one is characterized by an IR intensity of 541.04 km/mol and is peaked at

4004.87 cm⁻¹. It describes the asymmetric stretching vibration of H-bonded hydrogen atoms involved in the squarelike substructure. Their symmetric stretching vibration at 3966.58 cm⁻¹ is the most Raman-active one with a Raman activity of 191.47 Å⁴/amu. Compared with the stretching vibrations of the water molecule, both these vibrations are red shifted by approximately 200 cm⁻¹ and more pronounced. By analogy with the partition of stretching bands of Defect I into three groupings, a similar one exists for Defect II. Regarding the intramolecular or scissor modes of these defect structures, it has to be mentioned first that the harmonic mode $\nu_2^{(monomer)}$ of the water monomer calculated at the HF/6-311G(d, p) level is 1750.30 cm⁻¹. Its IR absorption and Raman activity constitute 79.15 km/mol and 6.38 Å⁴/amu, respectively. Two intramolecular modes of Defect I and four of Defect II listed in Tables V and VI are red-shifted compared with $\nu_2^{(monomer)}$ and more pronounced. Their normal vibration assignment is also shown there. For instance, the first intramolecular mode of Defect I with a frequency 1756.83 cm⁻¹ describes the composed scissor vibrations of the water molecules $H_2H_3O_1$ and $H_{11}H_{12}O_{10}$ bonded to each other via a "dangling" bond. The two last bands of Defect II correspond to the composed symmetric and asymmetric scissor vibra-

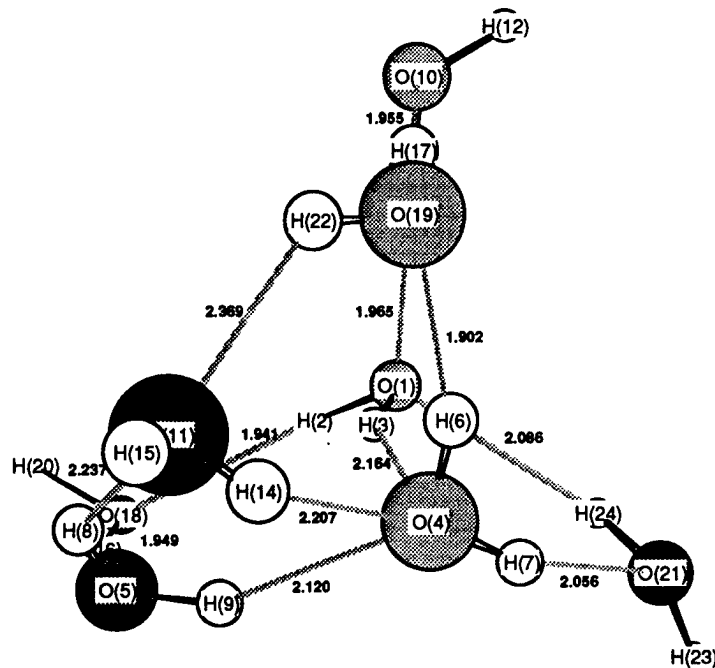


FIGURE 6. Pentacoordinated water octamer Defect III. Symbols same as in Figure 1.

tions of the $\text{H}_6\text{H}_7\text{O}_4$ and $\text{H}_{17}\text{H}_{18}\text{O}_{15}$ molecules of water.

FIVEFOLD COORDINATED WATER OCTAMERS

Figure 6 displays a pentacoordinated water octamer. The distinctive features of this structure are that one of its water molecules forms three H bonds and looks identical to the structure R6c

found in [23(a)], although a slight deviation in their properties is revealed.[#] Its energy, enthalpy, ZPVE, and entropy calculated at the HF/6-311G(*d, p*) computational level are reported in Table VII. Before going further, a word about the studied water clusters should be said. With regard to the cage, propeller, and defect structures of the

[#] The relative properties of Defect III with respect to the R6c structure are $\Delta E = 2 \cdot 10^{-4}$ kcal/mol, $\Delta H = -4 \cdot 10^{-4}$ kcal/mol, and $\Delta S = -21.74$ cal/mol K.

TABLE VII
Energy (*E*), enthalpy (*H*), entropy (*S*), ZPVE, and free energy of defect water octamer.

Defect	<i>E</i> (Hartree) $\Delta_{ca}E$	<i>H</i> (Hartree) $\Delta_{ca}H$	<i>S</i> (cal / mol K) $\Delta_{ca}S$	ZPVE (kcal / mol) $\Delta_{ca}G$
Defect III	-608.4765824 12.291	-608.2403860 10.802	156.181 17.905	134.42923 5.47

The Cubic octamer Ca is chosen as the reference one. For other notations, see caption of Table III.

TABLE VIII
Internal coordinates of defect water octamer.

Interoxygen Distance (Å)			
R(O ₁ —O ₄)	R(O ₁ —O ₁₀)	R(O ₁ —O ₁₈)	R(O ₁ —O ₂₁)
R(O ₄ —O ₅)	R(O ₄ —O ₁₁)	R(O ₄ —O ₁₉)	R(O ₄ —O ₂₁)
R(O ₅ —O ₁₁)	R(O ₅ —O ₁₈)	R(O ₁₀ —O ₁₉)	R(O ₁₁ —O ₁₉)
3.051	2.883	2.842	2.930
2.989	2.972	2.802	2.890
2.990	2.862	2.875	3.061
H-bond Angle δ_H (deg)			
O ₁ —H ₃ —O ₄	O ₄ —H ₉ —O ₅	O ₅ —H ₈ —O ₁₁	O ₁ —H ₁₃ —O ₁₀
O ₄ —H ₁₄ —O ₁₀	O ₁ —H ₂ —O ₁₈	O ₅ —H ₁₆ —O ₁₈	O ₄ —H ₆ —O ₁₉
O ₁₀ —H ₁₇ —O ₁₉	O ₄ —H ₇ —O ₂₁	O ₁₁ —H ₂₂ —O ₁₉	O ₁ —H ₂₄ —O ₂₁
155.49	152.07	136.03	161.78
137.24	157.20	160.34	158.87
162.59	146.57	129.83	147.54
O—O—O Bond Angle (deg)			
O ₁ —O ₁₈ —O ₅	O ₄ —O ₅ —O ₁₈	O ₁₀ —O ₁ —O ₁₈	O ₁₁ —O ₅ —O ₁₈
O ₅ —O ₄ —O ₁₉	O ₁ —O ₁₀ —O ₁₉	O ₄ —O ₁₉ —O ₁₀	O ₁₁ —O ₄ —O ₁₉
	O ₅ —O ₄ —O ₂₁	O ₁₀ —O ₁ —O ₂₁	O ₁₁ —O ₄ —O ₂₁
		O ₁₈ —O ₁ —O ₂₁	O ₁₉ —O ₄ —O ₂₁
77.73	104.14	122.58	138.43
103.22	84.15	99.21	63.95
	113.46	112.69	169.30
		122.74	111.81

water hexamer, it is worth noticing that they serve as an example of that in lower-lying clusters a water molecule may form a first-coordination shell with five water molecules in such a way that an approaching fifth water molecule is bonded to the central water molecule by a "dangling" bond. The Defect III portrayed in Figure 6 refers to an absolutely different type of pentacoordinated water clusters. It is seen there that the oxygen atom O₄ has three elongated and rather weak H bonds with the oxygen atoms O₁, O₅, and O₁₁ separated from it by ca. 3 Å (Table VIII). Despite that, the angle $\angle H_6-O_5-H_7 = 107.13^\circ$ remains, in fact, unchanged compared with the water monomer. However, the lone-pair angular distribution suffers drastic changes that are revealed in the calculated values of the corresponding angles: $\angle H_3-O_4-H_9 = 69.19^\circ$, $\angle H_9-O_4-H_{14} = 70.54^\circ$, and $\angle H_3-O_4-O_{14} = 115.65^\circ$. Its arrangement relative to the H₆—O₄—H₇ plane is determined by the angles $\angle H_3-O_4-H_7 = 88.91^\circ$, $\angle H_6-O_4-H_{14} = 79.56^\circ$, and $\angle H_6-O_4-H_9 = 125.61^\circ$.

As the Ca structure, Defect III possesses 12 H bonds, albeit seven of which may be considered as relatively weak because their lengths exceed 2 Å. What is mostly impressive in the H-bonded pattern of Defect III is that the water molecule H₁₄H₁₅O₁₁ is weakly bonded to its nearest neighbors. This is clearly seen, first, in that the inwarding H bonds such as O₁₁—H₈ and O₁₁—H₂₂ have lengths of 2.24 and 2.37 Å, respectively. The outwarding H-bond O₄—H₁₄ is also strongly elongated to 2.21 Å. Second, the angles $\angle O_5-H_8-O_{11} = 136.03^\circ$, $\angle O_4-H_{14}-O_{11} = 137.24^\circ$, and $\angle O_{11}-H_{22}-O_{19} = 129.83^\circ$ keep, therefore, a very low profile. The angle $\angle O_{11}-O_4-O_{19} = 63.95^\circ$ shows, in particular, a loss of tetrahedrality in this area of the pentacoordinated "patch." It seems worthwhile to discuss right now the distribution of oxygen–oxygen separations beyond the first-coordination shell. It is rather well clustered around 4.65 Å and takes such values as R(O₄—O₁₀) = 4.32 Å, R(O₅—O₁₉) = 4.54 Å, R(O₄—O₁₈) = 4.62 Å, R(O₁₉—O₂₁) = 4.71 Å, R(O₁₀—O₂₁) = 4.84 Å, R(O₅—O₂₁) = 4.92 Å, and R(O₁—O₁₁) = 4.94 Å. However, the oxygen atom is placed in a particularly privileged position because it stays much closer to O₅ and O₁₉, namely, by 3.58 and 3.86 Å, respectively.

The dipole moment of the Defect III "patch" is very low and equal to 0.87 D. Energetically, it is situated 12.30 kcal/mol above the Ca structure. At

room temperature, their difference in free energy is just 5.47 kcal/mol. Regarding the spectrum of this "patch" presented in Table IX, it is worth noticing that the spectrum of Defect III possesses rather strong IR-intensive bands, namely, its most IR-intensive and Raman-active bands fall only in the region of stretching vibrations. This is, first, the band $\nu_{28}^{H_2O} = 4113.9 \text{ cm}^{-1}$ with an IR intensity of 453.6 km/mol attributed chiefly to the stretching of the O₁—H₃ bond. The second one $\nu_{20}^{H_2O} = 3978 \text{ cm}^{-1}$ with a Raman activity of 142.27 Å⁴/amu and an IR intensity of 429.7 km/mol is assigned to the composed symmetric stretching vibration of the O₁—H₂ and O₁₈—H₁₆ bonds. As seen from Table IX, the grouping of the bands in the region 4091–4168 cm⁻¹ correspond to the stretching vibrations of three O—H bonds that establish the fivefold coordination of the H₆H₁₅O₄ water molecule and of another two directed to H₁₄H₁₅O₁₁. Compared with the stretching modes of the water monomer, these bands are slightly red shifted, which indicates their substantial weakness. This grouping of bands borders another one falling to 4205–4215 cm⁻¹ and describing the stretching vibrations of "free" O—H groups. Table IX also lists the most intensive vibrations of the fully deuterated Defect III calculated at the HF/6-31G(d, p) level of computation. Its ZPVE is 87.961 kcal/mol and its entropy is 178.571 cal/mol K. Hence, the ratio ZPVE_{H₂O}/ZPVE_{D₂O} = 1.53E.¹¹ For the deuterium Defect III, the band $\nu_{20}^{D_2O} = 2880.0 \text{ cm}^{-1}$ becomes the most IR and the most Raman active simultaneously contrary to the protium Defect III. It is more interesting to analyze the dependence of ν_{27} assigned to the coupled asymmetric stretching vibrations of O₁₁—H₁₄ and O₅—H₉ bonds under isotopic substitution. In the case of the protium Defect III, this band possesses an IR intensity equal to 48.8 km/mol, whereas it becomes pronounced in about five times for its deuterated isotopomer. In analyzing the second and sixth columns of Table IX, one finds that the calculated harmonic frequen-

¹¹ Compare with for instance, the frequencies ν and reduced masses μ of water isotopomers H₂O and D₂O calculated via the STO-3G basis set, which are the following: $\nu_1^{H_2O(D_2O)} = 4142.29$ (2992.49) cm⁻¹, $\mu_1^{H_2O(D_2O)} = 1.0491$ (2.1747) amu; $\nu_2^{H_2O(D_2O)} = 2169.80$ (1584.65) cm⁻¹, $\mu_2^{H_2O(D_2O)} = 1.0785$ (2.2429) amu; and $\nu_3^{H_2O(D_2O)}(2) = 4393.38$ (3212.88) cm⁻¹, $\mu_3^{H_2O(D_2O)} = 1.0774$ (2.2696) amu. Further, ZPVE_{H₂O} = 15.30 kcal/mol, ZPVE_{D₂O} = 9.94 kcal/mol, and their ratio ZPVE_{H₂O}/ZPVE_{D₂O} = 1.54. Also, $\nu_1^{H_2O}/\nu_1^{D_2O} = 1.38$, $\nu_2^{H_2O}/\nu_2^{D_2O} = \nu_3^{H_2O}/\nu_3^{D_2O} = 1.37$ and $\sqrt{\mu_1^{H_2O}/\mu_1^{D_2O}} = \sqrt{\mu_2^{H_2O}/\mu_2^{D_2O}} = 1.44$, $\sqrt{\mu_3^{H_2O}/\mu_3^{D_2O}} = 1.45$.

TABLE IX
Most intensive bands of defect water octamer.

No.	ν (cm ⁻¹)	IR intensity	Raman activity	Force constant	Reduced mass Assignment
1	167.50 (139.68)	134.88 (66.82) $O_{21}-H_{23}$	2.49 (0.13)	0.0217	1.3153 (2.4140) Translation
2	186.88 (145.25)	188.76 (47.14) $O_{18}-H_{20}$	0.82 (0.50)	0.0286	1.3893 (2.8709) Translation
3	454.54 (329.81)	247.97 (119.39) $O_{19}-H_{22}$	1.45 (0.69)	0.1290	1.0594 (2.2083) Libration
4	479.03 (347.03)	156.33 (94.76) O_1-H_3 , $O_{19}-H_{22}$	3.36 (1.69)	0.1426	1.0549 (2.1971) Libration
5	492.42 (357.49)	217.73 (108.48) $O_{21}-H_{24}$,	0.69 (0.39)	0.1513	1.0592 (2.2157) Libration
6	533.88 (387.10)	161.88 (114.83) O_5-H_8 ,	0.31 (0.43)	0.1781	1.0605 (2.1872) Libration
7	546.94 (395.37)	170.08 (50.61) O_4-H_7 ,	3.40 (1.52)	0.1849	1.0492 (2.1872) Libration
8	601.84 (436.54)	202.77 (116.59) O_5-H_9 ,	1.35 (0.65)	0.2256	1.0571 (2.2097) Libration
9	654.55 (474.21)	134.04 (68.85) O_5-H_9 ,	0.87 (0.46)	0.2673	1.0591 (2.1829) Libration
10	668.36 (486.34)	332.08 (191.89) $O_{18}-H_{16}$,	1.49 (0.75)	0.2802	1.0646 (2.2347) Libration
11	693.47 (501.19)	250.72 (127.85) $O_{19}-H_{17}$,	0.93 (0.42)	0.2975	1.0501 (2.1782) Libration
12	757.18 (548.76)	149.08 (73.69) O_4-H_6 ,	1.94 (0.96)	0.3574	1.0582 (2.1919) Libration
13	798.45 (570.25)	381.95 (234.52) O_1-H_2 ,	0.13 (0.10)	0.3851	1.0488 (2.1742) Libration
14	844.58 (615.41)	177.47 (112.25) O_4-H_7 ,	0.40 (0.13)	0.4484	1.0670 (2.2478) Libration
15	908.64 (654.81)	128.66 (77.92) O_4-H_6 ,	0.64 (0.30)	0.5079	1.0441 (2.1547) Libration
16	1754.08 (1282.64)	132.62 (67.93) $O_{11}-H_{14}-H_{15}$	6.41 (3.41)	1.9589	1.0806 (2.2559) Scissor
17	1774.04 (1295.89)	116.20 (54.80) $O_{21}-H_{23}-H_{24}$	5.05 (2.71)	1.9991	1.0781 (2.2477) Scissor
18	1843.89 (1344.61)	188.18 (100.98) $O_1-H_2-H_3$,	1.93 (1.11)	2.1503	1.0735 (2.2360) scissor
19	3927.49 (2842.71)	257.45 (111.19) O_4-H_6	122.55 (74.23)	9.6031	1.0566 (2.1797) Stretch
20	3978.39 (2880.00)	429.69 (252.81) O_1-H_2 ,	142.27 (77.02)	9.8550	1.0568 (2.1812) Stretch
21	4003.26 (2897.42)	438.73 (199.00) $O_{10}-H_{13}$,	20.23 (11.63)	9.9717	1.0561 (2.1801) Stretch
22	4015.09 (2903.59)	114.94 (48.68) O_1-H_2 ,	36.68 (19.66)	10.0101	1.0539 (2.1756) Stretch
23	4034.36 (2917.34)	345.32 (143.67) $O_{10}-H_{13}$,	38.65 (19.40)	10.1096	1.0542 (2.1738) Stretch
24	4058.52 (2937.93)	61.32 (36.05) $O_{21}-H_{24}$,	96.31 (40.38)	10.2950	1.0608 (2.1743) Stretch
25	4085.48 (2954.27)	426.88 (35.75) O_4-H_7 ,	35.90 (8.48)	10.5052	1.0682 (2.1656) Stretch

(Continued)

TABLE IX
(Continued)

No.	ν (cm ⁻¹)	IR intensity	Raman activity	Force constant	Reduced mass Assignment
26	4091.03 (2955.79)	41.88 (53.56) $O_{11}-H_{14}$,	21.64 (45.36) O_5-H_9	10.3624	1.0509 (2.1632) Stretch
27	4094.86 (2985.00)	48.83 (233.61) $O_{11}-H_{14}$,	67.66 (21.11) O_5-H_9	10.3814	1.0508 (2.2772) Stretch
28	4113.90 (3005.70)	453.56 (233.57) O_1-H_3	37.92 (19.01)	10.6611	1.0692 (2.2742) Stretch
29	4161.77 (3046.49)	96.49 (53.20) O_5-H_8 ,	26.93 (15.75) O_5-H_9 ,	11.0057	1.0785 (2.2812) Stretch
30	4168.43 (3049.50)	256.07 (169.94) $O_{19}-H_{22}$	23.34 (10.82)	11.0101	1.0755 (2.2797) Stretch
31	4205.02 (3072.61)	104.06 (88.09) $O_{10}-H_{12}$	49.36 (23.54)	11.1776	1.0729 (2.2705) Stretch
32	4208.77 (3074.79)	100.10 (85.73) $O_{18}-H_{20}$	52.66 (24.84)	11.1935	1.0725 (2.2691) Stretch
33	4213.47 (3082.78)	116.91 (76.78) $O_{21}-H_{23}$,	43.67 (20.41) $O_{21}-H_{24}$	11.2567	1.0762 (2.2801) Stretch
34	4214.21 (3087.05)	110.76 (88.40) $O_{11}-H_{15}$,	47.58 (19.72) $O_{11}-H_{14}$	11.2964	1.0796 (2.2878) Stretch

For notations, see caption of Table V. Values for fully deuterated Defect III are given in parentheses.

cies and reduced masses of the protium and deuterium Defect III do not show the known isotopic relationships connecting the ratio of frequencies of translational and bending modes ν^{H_2O}/ν^{D_2O} with the square root of the ratio of the corresponding moments of inertia or masses, respectively. Although this is perhaps the common situation with computing harmonic vibrational frequencies,** although in the present case with larger water clusters, this deviation appears more significant than with the water dimer. From Table IX, it follows that, first, for $\nu^{H_2O} = 167.5$ cm⁻¹ the ratio $\nu_1^{H_2O}/\nu_1^{D_2O} = 1.20$, whereas, according to this relationship, it should be $\sqrt{20/18} = 1.05$. Second, one directly obtains further that $\nu_2^{H_2O}/\nu_2^{D_2O} = 1.29$ and $\sqrt{\mu_2^{H_2O}/\mu_2^{D_2O}} = 1.44$. Third, for the rest of vibrations listed in Table VIII, the isotopic frequency ratio behaves rather regularly around 1.37–1.38 with the exception for the 13th and 15th modes when this ratio ratio is 1.40 and 1.39, respectively. The isotopic reduced mass ratio does not reveal such simple regularity, although it is largely clustered near 1.44–1.45. Altogether, this isotopic anal-

** We analyzed the ratio ν^{H_2O}/ν^{D_2O} for the harmonic vibrational frequencies of the water dimer calculated in [26] at the HF/6-31G* and MP2 levels. Following Tables 1 and 2 of [26], one easily derives that this ratio spans the range 1.16–1.18 for all the listed modes.

ysis emphasizes a very anharmonic landscape of the total potential energy surface of water clusters.

Summary

Fifteen different structures of the water hexamer found in the interval of 1.75 kcal/mol around its global minimum at the HF/6-311G(*d, p*) computational level represent an unprecedented wide range of conformational excursions for the water hexamer cluster and obviously, for the PES of liquid water. The richness of the PES landscape of water clusters is not actually a new fact. Tsai and Jordan [22(c), 27(a)], combining the TIP4P water–water potential with ab initio calculations, revealed 135 distinct minima of the water hexamer. Some lower-lying minima were also found in [22(g), 27(b, c)], although they do not show such striking plasticity of the PES landscape of the water hexamer in a rather close, of 1.75 kcal/mol by energy, neighborhood of its global minimum. The results of the present search is actually a challenge to the ability of the model water–water interaction potential to reproduce such high conformational plasticity.

The present work provides the first ab initio demonstration of the pentacoordinated water hex-

amer structure. This structure is not, in fact, the defect one in the common sense of defects in the H-bonded pattern that violate the Bernal–Fowler–Pauling rules or those structures that involve the bifurcated H bond. It actually represents a novel structure of H bonds where an approaching fifth water molecule forms a “dangling” bond with the central water molecule generating in such a way a pentacoordinated “patch” of higher density. This “patch,” being incorporated into the H-bonded pattern of liquid water, on the one hand, contributes partly to nontetrahedral configurations and to the known maximum of the O—O—O bond angle distribution function around 60° in particular. On the other hand, it contributes to tetrahedral configurations as well. Notwithstanding that such hexamer and octamer fivefold coordinated “patches” occupy lower-lying local energetic minima on the total potential energy surfaces, they become energetically accessible at room temperature. One would say that the structure of the propeller and Defects I–III reconcile the concept of an orientational defect as the violation of the second ice rule, on the one hand, and with non-icelikeness specific features of liquid water, on the other hand. In this context, pentacoordinated “patches” within the H-bonded pattern of liquid water is an appealing concept since they constitute an intriguingly simple and, to some extent, rather universal organization principle of the underlying liquid water dynamics.

There is still one question worthy to be pointed out in ending the present work. How significantly are the conclusions that we have drawn sensitive to the computational level? First of all, let us notice that the order of the water hexamer structures displayed in Figure 1 at 0 K would undergo some changes with the varying of computational levels, albeit this is not the main conclusion of the present article. Rather, it aimed to show how the water hexamer and bulky water as well might have so rich and intricate landscape where there are certainly some energetically accessible minima for those clusters that are pentacoordinated, on the one side, and that contribute to the subtle O—O—O angular distribution function peak at ca. 60°, on the other side. Although, speaking precisely, to pose a question of which one of two, say, minima is the lowest, one might not be too essential and perhaps even unresolvable at any computational level for many reasons: One simply is that there is always another superior level. Another reason is that this requires to taking the

ZPVE and basis-set superposition error into account together with including correlation effects that make the post-HF methods with high-level basis sets almost unfeasible for studies of medium-size water clusters, like, for example, the water hexamer. On the contrary, the HF/6-31G* and HF/6-31G** levels show quite accurate energies of “both conformational change and hydrogen bonding” [27] for hydrogen-bonded complexes and they are, in fact, rather feasible in distinction, for instance, to known highly accurate empirical water–water potentials that are unable to reproduce the aforementioned features of liquid water [27]. However, thanks to the thorough analysis by Xantheas and Dunning [22a] and Xantheas [22b] of small water clusters according to which, in particular, the HF level produces larger O—O distances between neighboring water molecules, one may interpolate their conclusion on the O—O distances in cages and may suggest that it is apparently that all present cages will have “dangling” bonds at higher computational levels. There is certainly a powerful alternative to these methods, namely, to employ density functional methods, although following [22e], “ideally, the question of the lowest hexamer structure could thus be answered experimentally by IR spectroscopy.” However, physically speaking, there is probably strong evidence that the prism structure of the water hexamer is the most stable one at 0 K and at normal pressure compared to the cage structure. Otherwise, instead of ices I, ice VI will exist at such conditions that contradict the phase diagram of H₂O given, for instance, in Figure 3.4 by Eisenberg and Kauzmann [1a]. Their mutual order certainly changes at higher temperatures and it is likely to suggest that it will be even interfered with by the ring or cyclic structures in such a manner that these structures will be dominant in some temperature range at least.

ACKNOWLEDGMENTS

The author gratefully acknowledges the kind invitation of M. Kasha and his financial support to participate in the 38th Sanibel Symposium. He also appreciates the partial support by the Organizers of the Sanibel Symposium, and J. R. Sabin, M. Zerner, J. Parker, and S. Weakland, in particular. The author thanks very much J. M. Bowman, K. Morokuma, and J. Musaev for many helpful discussions and warm hospitality during his visit at

Emory University. GAUSSIAN computing resources were provided by the Cherry L. Emerson Center for Scientific Computation at Emory University in Atlanta. He also expresses his thanks to E. Clementi, G. Corongiu, J. P. Dahl, J. P. Devlin, L. Hofacker, Y. Marechal, Yu. Naberukhin, F. Scortino, S. Xantheas, G. Yukhnevich, and G. Zundel for stimulating and helpful discussions. The referee is acknowledged for useful suggestions.

References

1. (a) D. Eisenberg and W. Kauzmann, *The Structure and Properties of Water* (Clarendon, Oxford, 1969); (b) F. Franks, Ed., *Water: A Comprehensive Treatise* (Plenum, New York, 1973), Vols. 1–7 and references therein.
2. (a) A. D. Buckingham, in *Water and Aqueous Solution*, G. W. Neilson and J. E. Enderby, eds. (Adam Hilger, Bristol, 1986), pp. 1–10, and Discussion (1) on pp. 11–13; (b) R. F. W. Bader, *Atoms in Molecules—A Quantum Theory* (Oxford University Press, Oxford, 1990); (c) R. C. Cohen and R. J. Saykally, *J. Chem. Phys.* **98**, 6007 (1993); (d) G. Chalasinski and M. M. Szczesiak, *Chem. Rev.* **94**, 1723 (1994).
3. J. D. Bernal and R. H. Fowler, *J. Chem. Phys.* **1**, 515 (1933); L. Pauling, *J. Am. Chem. Soc.* **57**, 2680 (1933).
4. (a) A. Rahman and F. H. Stillinger, *J. Chem. Phys.* **55**, 3336 (1971); (b) F. H. Stillinger and A. Rahman, *Ibid.* **60**, 1545 (1974).
5. (a) A. Geiger, F. H. Stillinger, and A. Rahman, *J. Chem. Phys.* **70**, 4185 (1979); (b) M. Mezei and D. L. Beveridge, *Ibid.* **74**, 622 (1981).
6. (a) H. E. Stanley and J. Teixeira, *J. Chem. Phys.* **73**, 3404 (1980); (b) H. E. Stanley, J. Teixeira, A. Geiger, and R. L. Blumberg, *Physica A* **106**, 260 (1981); (c) A. Geiger and H. E. Stanley, *Phys. Rev. Lett.* **49**, 1749 (1982); (d) A. Geiger and H. E. Stanley, *Ibid.* **49**, 1895 (1982); (e) R. L. Blumberg, H. E. Stanley, A. Geiger, and P. Mausbach, *J. Chem. Phys.* **80**, 5230 (1984); (f) A. Geiger and P. Mausbach, in *Hydrogen-Bonded Liquids*, J. C. Dore and J. Teixeira, Eds. (Kluwer, Dordrecht, 1991), pp. 171–183.
7. (a) A. Luzar and D. Chandler, *J. Chem. Phys.* **98**, 8160 (1993); *Ibid.*, *Phys. Rev. Lett.* **76**, 928 (1996); (b) J. A. Padró, J. Martí, and E. Guàrdia, *J. Phys.: Condens. Mat.* **6**, 2283 (1994); (c) J. Martí, J. A. Padró, and E. Guàrdia, *J. Chem. Phys.* **105**, 639 (1996).
8. (a) A. H. Narten, M. D. Danford, and H. A. Levy, *Disc. Faraday Soc.* **43**, 97 (1967); (b) A. H. Narten and H. A. Levy, *Science* **165**, 447 (1969); (c) A. K. Soper and M. G. Phillips, *Chem. Phys.* **107**, 47 (1986); (d) F. H. Narten and H. A. Levy, *Science* **217**, 1033 (1982); (e) J. Morgan and B. E. Warren, *J. Chem. Phys.* **6**, 666 (1938).
9. (a) R. Jedlovszky, I. Bakó, G. Pálinskás, T. Radnai, and A. K. Soper, *J. Chem. Phys.* **105**, 245 (1996); (b) F. Bruni, M. A. Ricci, and A. K. Soper, *Phys. Rev. B* **54**, 11876 (1996).
10. (a) F. Sciortino, A. Geiger, and H. E. Stanley, *J. Chem. Phys.* **96**, 3857 (1992); (b) F. Sciortino, A. Geiger, and H. E. Stanley, *Phys. Rev. Lett.* **65**, 3452 (1990).
11. (a) N. Bjerrum, *Danske Vid. Selsk. Mat.-Fys. Medd.* **27**, 3 (1951); *Ibid.*, *Science* **115**, 385 (1952).
12. (a) J. D. Dunitz, *Nature* **197**, 860 (1963); (b) N. V. Cohan, M. Cotti, J. V. Iribarne, and M. Weissmann, *Trans. Faraday Soc.* **58**, 490 (1962); (c) D. Eisenberg and C. A. Coulson, *Nature* **199**, 368 (1963); (d) J. L. Kavanau, *Structure and Function in Biological Membranes* (Holden-Day, San Francisco, 1965), Vol. I, p. 175ff; (e) M. D. Newton, *J. Phys. Chem.* **87**, 4288 (1983); (f) M. D. Newton, G. A. Jeffrey, and S. Takagi, *J. Am. Chem. Soc.* **101**, 1997 (1979); (g) G. A. Jeffrey and W. Saenger, *Hydrogen Bonding in Biological Structures* (Springer, Berlin, 1991), p. 20ff; (h) M. Head-Gordon and T. Head-Gordon, *Chem. Phys. Lett.* **220**, 122 (1994).
13. (a) E. S. Kryachko, *Chem. Phys. Lett.* **141**, 346 (1987); *Ibid.*, *Solid State Phys. (USSR)* **29**, 345 (1987); (b) O. E. Yanovitskii and E. S. Kryachko, *Phys. Stat. Sol. (b)* **147**, 69 (1988); (c) E. S. Kryachko, in *Electron and Proton Transfer in Chemistry and Biology*, A. Müller, H. Ratajczak, W. Junge, and E. Diemann, Eds. (Elsevier, Amsterdam, 1992), pp. 363–385.
14. (a) J. P. Devlin, *Int. Rev. Phys. Chem.* **9**, 29 (1990); (b) M. Fisher and J. P. Devlin, *J. Phys. Chem.* **99**, 11584 (1995); (c) J. P. Devlin and V. Buch, *J. Phys. Chem. B* **101**, 6095 (1997).
15. P. A. Giguere, *J. Raman Spectrosc.* **15**, 354 (1984); *Ibid. J. Chem.* **87**, 4835 (1987).
16. (a) G. E. Walrafen, M. S. Hokmabadi, W.-H. Yang, Y. Chu, and W. B. Monosmith, *J. Phys. Chem.* **93**, 2909 (1989); (b) G. E. Walrafen, M. S. Hokmabadi, and W.-H. Yang, *Ibid.* **92**, 2433 (1988); (c) G. E. Walrafen, *Ibid.* **94**, 2237 (1990).
17. F. X. Prielmeier, E. W. Lang, H. D. Lüdemann, and R. J. Speedy, *Phys. Rev. Lett.* **59**, 1128 (1987).
18. A. Geiger, P. Mausbach, and J. Schnitker, in *Water and Aqueous Solutions*, G. W. Neilson and J. E. Enderby, Eds. (Adam Hilger, Bristol, 1986).
19. T. Head-Gordon and F. H. Stillinger, *J. Chem. Phys.* **98**, 3313 (1993), see Figs. 5 and 20 therein.
20. M. J. Frisch, G. W. Trucks, H. B. Schlegel, P. M. W. Gill, B. G. Johnson, M. A. Robb, J. R. Cheeseman, T. Keith, G. A. Petersson, J. A. Montgomery, K. Raghavachari, M. A. Al-Laham, V. G. Zakrzewski, J. V. Ortiz, J. B. Foresman, C. Y. Peng, P. Y. Ayala, W. Chen, M. W. Wong, J. L. Andres, E. S. Replogle, R. Gomperts, R. L. Martin, D. J. Fox, J. S. Binkley, D. J. Defrees, J. Baker, J. P. Stewart, M. Head-Gordon, C. Gonzalez, and J. A. Pople, *GAUSSIAN 94, Revision B.3* (Gaussian, Inc., Pittsburgh, PA, 1995).
21. (a) R. Krishnan, J. S. Binkley, R. Seeger, and J. A. Pople, *J. Chem. Phys.* **72**, 650 (1980); (b) M. J. Frisch, J. A. Pople, and J. S. Binkley, *Ibid.* **80**, 3265 (1984).
22. (a) S. S. Xantheas and T. H. Dunning, Jr., *J. Chem. Phys.* **99**, 8774 (1993); (b) S. S. Xantheas, *Ibid.* **100**, 7523 (1994); (c) C. J. Tsai and K. D. Jordan, *Chem. Phys. Lett.* **213**, 181 (1993); (d) P. N. Krishnan, J. O. Jensen, and L. A. Burke, *Ibid.* **217**, 311 (1994); (e) D. A. Estrin, L. Paglieri, G. Corongiu, and E. Clementi, *J. Phys. Chem.* **100**, 8701 (1996); (f) B. J. Mhin, J. Kim, S. Lee, J. Y. Lee, and K. S. Kim, *J. Chem. Phys.* **100**, 4484 (1994); (g) K. Laasonen, M. Parrinello, R. Car, C. Lee, and D. Vanderbilt, *Chem. Phys. Lett.* **207**, 208 (1993).
23. (a) J. O. Jensen, P. N. Krishnan, and L. A. Burke, *Chem. Phys. Lett.* **246**, 13 (1995); (b) J. Kim, B. J. Mhin, S. J. Lee, and K. S. Kim, *Ibid.* **219**, 243 (1994); (c) R. Knochenmuss and S. Leutwyler, *J. Chem. Phys.* **96**, 5233 (1992); (d) K. Kim,

ORIENTATIONAL DEFECTS IN WATER CLUSTERS

- K. D. Jordan, and T. S. Zwier, *J. Am. Chem. Soc.* **116**, 11568 (1994); (e) K. Liti, M. G. Brown, C. Carter, R. J. Saykally, J. K. Gregory, and D. C. Clary, *Nature* **381**, 501 (1996); (f) J. K. Gregory and D. C. Clary, *J. Phys. Chem.* **100**, 18014 (1996); (g) K. Liu, M. G. Brown, and R. J. Saykally, *J. Phys. Chem. A* **101**, 8995 (1997).
24. (a) I. M. Mills, in *Theoretical Chemistry*, R. N. Dixon, Ed. (Chemical Society, London, 1974), Vol. I; (b) E. Honegger and S. Leutwyler, *J. Chem. Phys.* **88**, 2582 (1988), Table II and references therein.
25. E. S. Kryachko, *Chem. Phys. Lett.* **272**, 132 (1997).
26. S. Scheiner and M. Čuma, *J. Am. Chem. Soc.* **118**, 1511 (1996).
27. (a) C. J. Tsai and K. D. Jordan, *J. Phys. Chem.* **97**, 5208 (1993); (b) B. J. Mhin, H. S. Kim, H. S. Kim, C. W. Yoon, and K. S. Kim, *Chem. Phys. Lett.* **176**, 41 (1991); (c) M. Masella and J. P. Flamant, *J. Chem. Phys.* **107**, 9105 (1997); (d) P. L. M. Plummer, *J. Phys. Chem.* **101**, 6247 (1997); *J. Mol. Struct. (Theochem)* **417**, 35 (1997); (e) P. R. Rablen, J. W. Lockman, and W. L. Jorgensen, *J. Phys. Chem. A* **102**, 3782 (1998); (f) C. H. Cho, S. Singh, and G. W. Robinson, *Phys. Rev. Lett.* **76**, 1651 (1996).

Intramolecular Proton Transfer in Monohydrated Tautomers of Cytosine: An Ab Initio Post-Hartree-Fock Study

LEONID GORB, JERZY LESZCZYNSKI

Department of Chemistry, Jackson State University P.O. Box 17910, 1325 J.R.L. Lynch Street, Jackson, Mississippi 39217

Received 31 March 1998; revised 28 May 1998; accepted 3 June 1998

ABSTRACT: The results of an ab initio post-Hartree-Fock study of the molecular structures, relative stabilities, and mechanisms of intermolecular proton transfer in isolated and monohydrated cytosine complexes are reported. The geometries of the local minima and transition states were optimized without symmetry restrictions by the gradient procedure at the HF and the MP2 levels of theory and were verified by energy second-derivative calculations. The standard 6-31G(d) basis set was used. The single-point calculations were performed at the MP4(SDQ)/6-31 + G(*d, p*)//MP2/6-31G(*d*) and MP2/6-311++G(*d, p*)//MP2/6-31G(*d*) approximations. All values of the total energies were corrected for scaled zero-point energy contributions. The post-Hartree-Fock ab initio theory predicts the height of the proton-transfer barrier for monohydrated cytosine complexes to be approximately three times lower for the tautomeric oxo-hydroxo reaction compared with non-water-assisted processes. The influence of polar media (Onsager's self-consistent reaction-field model) slightly changes these values according to the order of the stability of the tautomers in a polar solution. The interaction with one water molecule changes the order of the relative stability of cytosine tautomers from the gas

Correspondence to: J. Leszczynski.

Contract grant sponsor: NSF.

Contract grant number: OSR-9452857.

Contract grant sponsor: Office of Naval Research.

Contract grant number: N00014-95-1-0049.

Contract grant sponsor: Army High Performance Computing Research Center/Department of the Army, Army Research Laboratory.

Contract grant number: DAAH04-95-2-0003/DAAH04-95-C-0008.

phase to the one which corresponds to the experimentally measured relative stabilities in polar solutions. In contrast to guanine, we did not find significant water influence on the NH₂-nonplanarity phenomena. © 1998 John Wiley & Sons, Inc. Int J Quant Chem 70: 855–862, 1998

Introduction

The relative stability of the tautomers of DNA bases is of fundamental importance to the structure and functioning of nucleic acids [1]. The occurrence of rare tautomers has been put forward as a possible mechanism for spontaneous mutations [1, 2]. Although the most stable tautomer of each species has been determined experimentally in matrix isolation infrared studies [3] and in solutions [4], the stability and properties of the rare tautomers are difficult to measure. The question concerning the properties of tautomers hydrated by a limited number of water molecules has risen in response to the possibility of local hydration of the DNA bases in the first solvation shell [5]. This is especially important for such DNA bases as cytosine and guanine due to the coexistence of a number of their tautomers in the gas phase as had been established by studies for isolated molecules.

Recently [6], we initiated a comprehensive theoretical investigation of the role of hydration on the properties of DNA bases and base pairs. In particular, the mono- and dihydrated species of the guanine molecules were investigated [6a, b]. Because the main goal of our investigation was the phenomenon of intramolecular proton transfer, only the cyclic forms of the water-hydrated guanine were taken into account. The following new features were established: First of all, we found the unique role of water molecules in controlling the nonplanarity of the NH₂ group of guanine. The influence of water molecules is twofold: They are the source of nonplanarity of the hydroxo forms of guanine, and they also decrease the nonplanarity of the oxo-tautomers. Another interesting peculiarity is the stepwise interaction of guanine with water molecules. We showed [6a, b] that the interaction of guanine tautomers with one and two water molecules monotonically change the order of the gas-phase stability into the order which corresponds to the stability of the guanine tautomers in a polar solvent. Finally, we analyzed the barrier heights for forward and reverse reactions of

intramolecular proton transfer to form rare (hydroxo-) forms of guanine. We concluded that the value of the rate constant in isolated guanine tautomers will be characterized by a nonappreciable rate in both directions. The situation should be completely different in mono- and dihydrated guanine complexes where we expect quite sizable rate constants in the direction yielding the oxo type of guanine tautomers.

In principle, cytosine has an amidic fragment (—NH—CO—) similar to guanine and is able to form the same type of hydrogen bonding as observed for guanine (see Fig. 1). There is, however, one important difference in the chemical structure of cytosine compared with guanine. The NH₂ group of cytosine is placed relatively far from the —NH—CO— amidic moiety. In addition, it is important to remember that cytosine is the complementary base for guanine in DNA.

In the present article, we investigated the influence of the interaction of a water molecule on the nonplanarity phenomena of the oxo- (CYT) and hydroxo- (CYT*) cytosine tautomers, the relative stability of the isolated and monohydrated (CYT · H₂O and CYT* · H₂O) cytosine tautomers, and, finally, the rate of intramolecular proton transfer for these species. All these data are compared with similar data predicted for guanine.

Computational Methods

The ab initio LCAO-MO method was used for the study of the interaction of cytosine tautomers with one water molecule. The calculations were carried out with the Gaussian-94 program [7]. The standard 6-31G(d) basis set was used. All the geometries of the local minima and the transition-state structure were optimized without symmetry restrictions (C_1 symmetry was assumed) by the gradient procedure initially at the HF level and subsequently at the second order of closed-shell restricted Möller-Plesset perturbation theory [8]. The characterization of the local minima and transition states were verified by establishing that the matrices of the energy second derivatives (Hessians) [at the HF/6-31G(d) level] have zero and

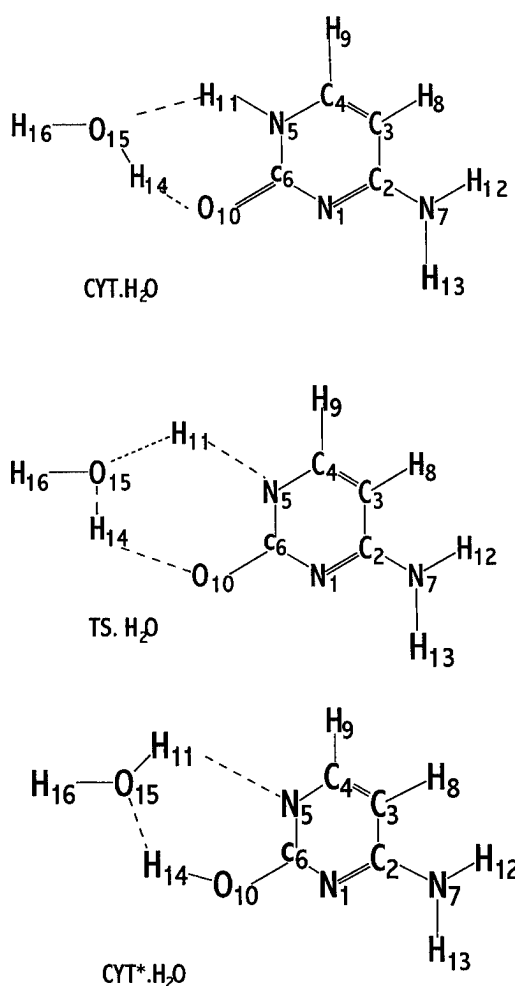


FIGURE 1. Molecular structure of cytosine–water complexes.

one negative eigenvalue, respectively. The single-point calculations were performed at the MP4(SDQ)/6-31 + G(*d, p*)//MP2/6-31G(*d*) level of theory and at the MP2/6-311++G(*d, p*)//MP2/6-31G(*d*) level for all the studied systems. The total energies were corrected for the HF/6-31G(*d*) zero-point energies scaled by a factor of 0.9.

To estimate the effect of the polar medium on the relative stability of cytosine tautomers and their monohydrated complexes, we applied the Onsager reaction-field model [9] as implemented in the Gaussian-94 program. In this model, the solvent is viewed as a continuous dielectric medium of uniform dielectric permittivity ϵ . The solute occupies a spherical cavity within the solvent. We used the relative permittivity $\epsilon = 80.0$ and the cavity radius obtained from the calcula-

tion of the volume (Option Volume of Gaussian-94 program) of a given molecule. The MP2 single-point energy calculated in this way (MP2_{solv}) was also corrected for the scaled zero-point energy.

Results and Discussion

GEOMETRY OF LOCAL MINIMA AND TRANSITION STATE

Before discussing the obtained results, we would like to mention that the MP2-level calculated geometries of cytosine and its monohydrated complexes were already published in a number of articles [10]. Therefore, in the present article, we discuss only the problems that were not revealed in [10].

According to earlier investigations of a large number of hydrogen-bonded systems, the geometry of the A–H \cdots B fragment plays a crucial role in forming the proton-transfer barrier. Especially, it was established in [11] that a low proton-transfer barrier takes place when the A–B distance is $< 2.5 \text{ \AA}$ (A and B atoms are oxygens and/or nitrogens). It was also found that the case of a low proton-transfer barrier corresponds to the so-called strong hydrogen bonds, the energy of formation which exceeds 120 kJ mol^{-1} .

An analysis of the obtained data collected in Table I and drawn in Figure 1 allows us to make the following conclusions:

- (i) Previously [6a, b], based on an analysis of the geometrical parameters of monohydrated guanine, we predicted that hydrogen bonds in this molecule should be classified as rather weak. The geometrical parameters of the monohydrated amidic part of cytosine and guanine are very similar. Current data justified that the same assumption could be made regarding the hydrogen bonds in the monohydrated cytosine species.
- (ii) The most prominent difference in the geometries of the transition states compared to the geometry of the local minima is demonstrated in the decrease in the interatomic distances between heavy atoms involved in the hydrogen bond which are remarkably shorter. They certainly reached the threshold of 2.5 \AA , which divides the strong and weak hydrogen bonds. Thus,

TABLE I
Selected geometrical parameters of cytosine monohydrated species.^a

	CYT · H ₂ O	TS · H ₂ O	CYT* · H ₂ O
R _{H11O15}	1.908 (1.890)	1.285 (1.319)	0.985 (0.985)
R _{O15H14}	0.986 (0.984)	1.230 (1.200)	1.799 (1.777)
R _{H14O10}	1.888 (1.930)	1.210 (1.196)	0.985 (0.986)
R _{O15N5}	2.827 (2.810)	2.425 (2.431)	2.807 (2.810)
R _{O15O10}	2.785 (2.811)	2.410 (2.410)	2.740 (2.740)
< _{N5H11O15}	147.0 (148.0)	149.3 (149.3)	140.8 (141.3)
< _{H11O15H14}	78.9 (80.4)	83.2 (84.5)	81.1 (80.4)
< _{O15H14O10}	149.8 (147.6)	157.8 (156.7)	163.0 (160.3)

^a The values of corresponding geometrical parameters for monohydrated 9-guanine species are given in parentheses [6a].

the rather weak hydrogen bonds in minimum-energy forms become considerably strong for the related transition states.

- (iii) The very similar values of the geometrical parameters characterizing bonds involved in proton transfer in the local minima and transition states of the monohydrated cytosine and guanine species allow us to predict the very close values for the water-assisted proton-transfer barrier in cytosine and guanine.

The nonplanar geometry of the isolated DNA bases has been the subject of a number of articles (see [12] for a review references therein). The importance of the specific interaction with water molecules on the nonplanarity phenomena of guanine tautomers was demonstrated recently [6a, b]. Two structural sources of nonplanarity were revealed: The nonplanarity of the first type is connected with the partial sp^3 hybridization of the amino group which could be characterized by the sum of the CNH and HNH angles of the amino group (ΣAH in Table II). In this case, the degree of

nonplanarity could be estimated as the deviation of ΣAH from 360° (δ in the Table II).

The second source of the nonplanarity is the interaction of amino group hydrogen atoms with the closest atoms belonging to the rest of the DNA base. To analyze the nonplanarity of this type, it is also convenient, instead of $\angle H_{12}N_7C_2N_1$ (see Fig. 1), to introduce the angle $\varphi = 180^\circ - \angle H_{12}N_7C_2N_1$. In this case, it should be clear that the difference between φ and $\angle H_{11}N_7C_2N_1$ (Δ in Table II) is the simplest estimation of the interaction of the H_{12} amino group hydrogen atom with the closest H_8 atom of the cytosine tautomers.

Let us start the analysis of nonplanarity of the calculated cytosine tautomers from the nonplanarity of the first type. There are two important observations: First of all, we should confirm our previous statement [6a] that the nonplanarity of the first type (sp^3 hybridization of the amino group) is the internal property of a particular DNA base and does not depend significantly either on the change of chemical structure of cytosine tautomers or on its interaction with a water molecule. The amino group in cytosine is simply less nonpla-

TABLE II
Selected values of torsion angles of cytosine tautomers^a calculated at the MP2 / 6-31G(d) level.

	CYT	CYT*	CYT · H ₂ O	CYT* · H ₂ O
ΣAH ^b	348.2 (337.9)	346.2 (343.2)	349.3 (340.2)	347.2 (341.5)
δ ^c	11.8 (22.1)	13.8 (16.3)	10.7 19.8	12.8 (18.5)
<H ₁₂ N ₇ C ₂ N ₁	155.8 (140.2)	155.5 (158.1)	157.1 (146.3)	156.3 (153.3)
<H ₁₁ N ₇ C ₂ N ₁	14.3 (11.8)	17.1 (21.9)	14.1 (33.7)	16.4 (26.7)
ω ^d	24.2 (39.8)	24.5 21.9	22.9 33.7	23.7 26.7
Δ ^e	9.9 (28.0)	7.4 (-0.5)	8.8 (18.5)	7.3 (6.2)

^a The calculated distortion of the atoms of heterocycles from planarity is nonsignificant. The values of corresponding torsional angles for 9-guanine species are given in parentheses [6a].

^b ΣAH = <H₁₂N₇C₂ + <H₁₃N₇C₂ + <H₁₃N₇H₁₂.

^c δ = 360.0 - ΣAH.

^d φ = 180.0 - <H₁₂N₇C₂N₁.

^e Δ = ω - <H₁₁N₇C₂N₁.

nar than in guanine as has been shown previously in a number of articles [12].

The characteristics of the second type of nonplanarity are certainly different from those predicted for guanine. They do not depend on the nature of the cytosine tautomers and on its interaction with a water molecule. The origin of such behavior is also clear. As the most important reason for the changes depending on the nature of the guanine tautomers, we have distinguished the interaction of the hydrogen atom of the amino group with the hydrogen atom attached to N1 atom of the guanine ring in the oxo-tautomers. This hydrogen migrates during a tautomeric reaction. So, it is absent in the hydroxyl-tautomers of guanine. In the case of cytosine, a similar atom (H₈) is attached to C3 of the cytosine ring and is not moving during the tautomeric transformation. It is also well known that the polarity of the CH bond is lower than those of the NH bond, so the repulsion of the H₁₂ hydrogen of the amino group by the H₈ atom of the ring should be less pronounced in the cytosine case. The nonplanarity of the second type also does not depend significantly on the interaction with a water molecule because the amino group in cytosine is placed relatively far from the attaching

water molecule, in contrast to guanine where this interaction is significant.

RELATIVE STABILITY

According to the experimental results of matrix isolation IR studies of cytosine tautomers, the CYT* tautomer is the most stable one. The experimental estimated energy difference between CYT and CYT* is 2–5 kJ mol⁻¹ in favor of CYT* [3, 10a]. The experimental stability in a water solution is also known—only the CYT tautomer has been found [4, 10a]. The conclusions of matrix isolation IR studies are supported by the results of high-performance ab initio calculations at the CCSD(T) and MP4(SDTQ) levels. According to these calculations, the energy difference is 4.2 [10b] and 2.3 [10c, d] kJ mol⁻¹ in favor of CYT* at the CCSD(T) and MP4(SDTQ) levels, respectively. The polar solvent which has been taken into account in the framework of a continuum approximation [13] reverses the stability order, and the CYT tautomer predominates over CYT*. Our data at the MP4(SDQ)/6-31 + G(d, p)//MP2/6-31G(d), MP2/6-311 + + G(d, p)//MP2/6-31G(d), and MP2/6-31G(d)//MP2/6-31G(d) levels of theory

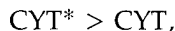
TABLE III
Relative stability (kJ mol^{-1}) of cytosine tautomers and their monohydrated forms.^a

	MP4(SDQ) 6-31 + G(<i>d, p</i>) // MP2 / 6-31G(<i>d</i>)	MP2 / 6-311++G(<i>d, p</i>) // MP2 / 6-31G(<i>d</i>)	MP2 / 6-31G(<i>d</i>) // MP2 / 6-31G(<i>d</i>)	MP2 solv
CYT	0.0	0.0	0.0	0.0
CYT*	0.5	-9.3 (1.2)	-1.3 (-0.2)	13.3 (22.1)
CYT · H ₂ O	0.0	0.0	0.0	0.0
CYT* · H ₂ O	8.1	-1.8 (9.5)	5.3 (15.1)	9.7 (17.2)

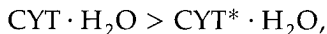
^a The relative stability of corresponding 9-guanine tautomers are given in parentheses [6a].

(Table III) on the isolated bases are in good accord with that mentioned above.

An interesting peculiarity could be seen from the predicted relative stability of the monohydrated species. The data on the isolated tautomers indicate that



where the relative stability of the monohydrated species is reversed,



and approaches the stability of fully hydrated complexes. So, one can conclude that even the interaction with one water molecule is sufficient to reverse the gas-phase relative stability of cytosine tautomers into the order which corresponds to the stability found in a water solution.

PROTON TRANSFER

Discussion of the relative stability of the DNA base tautomers from both theoretical and experimental points of view usually stands on the assumption of the thermodynamic control of these transformations. There are only a few theoretical articles where the questions concerning the rate of these transformations are discussed for the prototypic molecules as formamide and formamidine [14]. Except for the recent work where simple estimations were done for guanine and its mono- and dihydrated species [6a], data on the rate of the proton transfer are not available either from experimental or theoretical studies.

Although the most stable tautomer in the gas phase is CYT*, it is more convenient for compari-

son with the similar data [6a, b] obtained for 9-guanine to define the forward proton transfer reaction from the oxo to the hydroxo form, and the reverse is the reaction in the opposite direction. The calculated values of the proton-transfer barriers in cytosine and their monohydrated complexes are collected in Table IV. Due to the high sensitivity of the barrier height at the correlated level of computation [e.g., for water-assisted proton transfer in formamide, the calculated barrier height is as follows [14b]: 108.3 (QCISD), 941 (MP2), 81.6 (DFT/B3LYP), and 69.0 (DFT/BLYP)], the observed difference between the MP4 and MP2 results is not surprising.

Following a comparative analysis of the geometrical parameters for local minima and transition states of the cytosine and guanine species, we expect very similar behavior for the rate of proton transfer in both bases. An analysis of the data collected in Table IV, completely supports our assumption. The data of the barrier height for cytosine and guanine are different by a few kJ mol^{-1} for the corresponding complexes. In particular, we should distinguish a dramatic decrease in barrier heights (to compare with gas-phase data) when one water molecule participates directly in the proton-transfer reaction. The values of the proton-transfer barriers are decreasing approximately threefold for both forward and reverse reactions. Nevertheless, due to the difference in stability, a preference for the reverse reaction should be remarkable.

The influence of the polar surrounding, included in the framework of the Onsager model on the height of the proton-transfer barrier, is also noticeable. It also corresponds to the change of the relative stability of the tautomers which takes place

TABLE IV
Zero-point-corrected barrier heights for proton transfer of cytosine species (kJ mol^{-1}).^a

	MP4(SDQ) / 6-31 + G(<i>d, p</i>) // MP2 / 6-31G(<i>d</i>)	MP2 / 6-311++G(<i>d, p</i>) // MP2 / 6-31G(<i>d</i>)	MP2 / 6-31G(<i>d</i>) / MP2 / 6-31G(<i>d</i>)	MP2 solv
Forward				
CYT \rightarrow TS	157.0	137.8	142.4 (148.5)	146.7 (150.6)
CYT · H ₂ O \rightarrow TS · H ₂ O	66.4	47.0	56.1 (58.1)	59.4 (56.5)
Reverse				
CYT* \rightarrow TS	156.5	147.2	143.7 (141.0)	133.4 (128.4)
CYT* · H ₂ O \rightarrow TS · H ₂ O	58.2	48.9	50.7 (48.5)	49.7 (47.7)

^a The values of corresponding zero-point-corrected barriers heights for 9-guanine species are given in parentheses [6a].

after dissolving the corresponding species in solution.

As we have already mentioned [6a], a noticeable influence of tunneling in contributing to the barrier height of the proton-transfer reaction in the prototypic molecules does not allow us to use the values from Table IV to directly estimate the rate constant. Nevertheless, a simple comparison is possible, using the following assumptions: The available value of the calculated thermal rate constant for the proton-transfer barrier in formamide (gas phase, nonwater-assisted reaction) amounts to $8.37 \cdot 10^{-14} \text{ s}^{-1}$ (300 K) with a corresponding zero-point energy-corrected barrier height of $189.1 \text{ kJ mol}^{-1}$. The calculated value of the rate constant for a forward water molecule-assisted reaction in formamide–water complexes is $4.6 \times 10^{-4} \text{ s}^{-1}$ (300 K), and the corresponding value of the proton-transfer barriers is 90.8 kJ mol^{-1} . The calculated value of the rate constant for the reverse reaction is 1.0×10^5 (300 K) with a barrier height of 46.0 kJ mol^{-1} . Because these values have been obtained for the same reaction of the prototypic molecules, we can apply these data for estimation of the trends for the proton-transfer reaction of cytosine tautomers placed in the gas phase and in a water surrounding. We expect that the calculated nonwater-assisted gas-phase rate constant for both forward and reverse reactions will never reach the values which characterize any

appreciable rate at room temperature. In other words, the value of the proton-transfer barrier is too large in both directions to be reached with any really observable rate at room temperature. In contrast, the value of water-assisted barriers could produce much higher interconversion rates that should be observable at least in the reverse direction. We expect that a profound preference for the reverse reaction will occur at any temperature of biological importance. These preferences should be increased after surrounding the tautomers in a water solution.

Conclusion

In this article, we reported the results of a comprehensive post-Hartree–Fock investigation of the structural parameters, stabilities, and intermolecular proton-transfer phenomena in monohydrated tautomers of cytosine. The principal conclusions from this study are the following:

1. The similarity of the calculated structural parameters of the monohydrated amidic fragment of cytosine tautomers with the similar fragment of the 9-guanine molecule was shown.
2. Two possible structural sources of nonplanarity of the NH₂ group (sp^3 hybridization

and the interaction of the amino hydrogens with the rest of the molecule) of cytosine tautomers were investigated. The difference in the origin of nonplanarity parameters of the monohydrated cytosine tautomers compared with the similar monohydrated guanine complexes is explained on the basis of the differences in the chemical structures of cytosine compared to guanine.

3. We found that the interaction of the cytosine tautomers with a water molecule changes the gas-phase stability CYT* > CYT into the order which corresponds to the stability of the cytosine tautomers in a polar solvent CYT ≫ CYT*.
4. An analysis of the barrier height of forward and reverse reactions of intermolecular proton transfer of isolated and monohydrated cytosine species was performed. Data similar to guanine were obtained, which is in accord with the similarity of the structural parameters of these complexes. We expect that the value of the rate constant of the isolated cytosine tautomers will be characterized by a nonappreciable rate in both directions at room temperature. The situation should be completely different in monohydrated cytosine complexes where we expect a quite sizable rate constant in the direction yielding to the oxo type of the cytosine tautomers. The influence of the polar solvent should further increase this tendency.

ACKNOWLEDGMENTS

The authors thank the Mississippi Center for Supercomputing Research for the computational facilities. This work was facilitated in part by the NSF Grant OSR-9452857 and by the Office of Naval Research Grant No. N00014-98-7-0592 and the Army High Performance Computing Research Center under the auspices of the Department of the Army, Army Research Laboratory Cooperative Agreement No. DAAH04-95-2-0003/Contract No. DAAH04-95-C-0008, the content of which does not necessarily reflect the position or the policy of the government, and no official endorsement should be inferred.

References

1. P. O. Lowdin, *Adv. Quantum Chem.* **2**, 213 (1965).
2. B. Pullman and A. Pullman, *Adv. Heterocycl. Chem.* **13**, 77 (1971).
3. (a) J. S. Kwiatkowski and B. Pullman, *Adv. Heterocycl. Chem.* **18**, 199 (1975); (b) M. J. Nowak, L. Lapinski, and J. Fulara, *Spectrochim. Acta A* **45**, 229, (1989); (c) I. R. Gould, M. A. Vincent, I. H. Hillier, L. Lapinski, and M. J. Nowak, *Spectrochim. Acta A* **48**, 811 (1992); (d) A. Jaworski, M. Szczepaniak, K. KiBulat, and W. B. Person, *J. Mol. Struct.* **63**, 223, (1990); (e) E. D. Radchenko, G. G. Sheina, N. Smorygo, and Yu. P. Blagoi, *J. Mol. Struct.* **116**, 387 (1984).
4. (a) W. Saenger, *Principles of Nucleic Acid Structure* (Springer-Verlag, New York, 1984); (b) P. Beak, *Acc. Chem. Res.* **10**, 186 (1997).
5. (a) V. I. Poltev, A. V. Teplukhin, and G. G. Malenkov, *Int. J. Quantum Chem.* **42**, 1499 (1992); (b) B. Schneider and H. M. Berman, *Biophys. J.* **69**, 2661 (1995).
6. (a) L. G. Gorb and J. Leszczynski, *J. Am. Chem. Soc.* **112**, 5024 (1990); (b) L. Gorb and J. Leszczynski, *Int. J. Quantum Chem.* **65**, 759, (1997); N. U. Zhanpeisov and J. Leszczynski, *Int. J. Quantum Chem.* **69**, 37 (1998); N. U. Zhanpeisov and J. Leszczynski, *J. Phys. Chem. A* **102**, 6167 (1998).
7. M. J. Frisch, G. W. Trucks, H. B. Schlegel, P. M. W. Gill, B. G. Johnson, M. A. Robb, J. R. Cheeseman, T. Keith, G. A. Petersson, J. A. Montgomery, K. Raghavachari, M. A. Al-Laham, V. G. Zakrzewski, J. V. Ortiz, J. B. Foresman, J. Cioslowski, B. B. Stefanov, A. Nanayakkara, M. Challacombe, C. Y. Peng, P. Y. Ayala, W. Chen, M. W. Wong, J. L. Andres, E. S. Replogle, R. Gomperts, R. L. Martin, D. J. Fox, J. S. Binkley, D. J. Defrees, J. Baker, J. P. Stewart, M. Head-Gordon, C. Gonzalez, and J. A. Pople, *Gaussian 94, Revision E.2* (Gaussian, Inc., Pittsburgh PA, 1995).
8. C. Möller and M. S. Plesset, *Phys. Rev.* **46**, 618 (1934).
9. L. Onsager, *J. Am. Chem. Soc.* **58**, 1486 (1936).
10. (a) J. S. Kwiatkowski and J. Leszczynski, *J. Phys. Chem.* **100**, 941 (1996); (b) A. Les, L. Adamowich, and R. Bartlett *J. Phys. Chem.* **93**, 4001 (1989); (c) I. R. Gould and I. H. Hillier *Chem. Phys. Lett.* **161**, 185, 1989; (d) I. R. Gould, N. A. Burton, R. J. Hall, and I. H. Hillier, *J. Mol. Struct. (Theorchem)* **331**, 147 (1995).
11. (a) G. J. Kearley, F. Filliaux, M. H. Baron, S. Bennington, and J. Tomkinson, *Science* **64**, 1285 (1994); (b) W. W. Cleland and M. M. Kreevoy, *Science* **264**, 1887 (1994); (c) P. Gilli, V. Bertolassi, V. Ferretti and G. J. Gilli, *Am. Chem. Soc.* **116**, 909 (1994).
12. J. Sponer, J. Leszczynski, and P. Hobza, *J. Biomol. Struct. Dynam.* **14**, 117 (1996).
13. (a) M. J. Scanlan and I. H. Hillier, *J. Chem. Soc., Chem. Commun.* **102** (1984); (b) C. Comominas, F. J. Luque, and M. Orozco, *J. Am. Chem. Soc.* **118**, 6811 (1996).
14. (a) R. L. Bell and T. N. Truong, *J. Phys. Chem.* **101**, 10442 (1994); (b) R. L. Bell, D. L. Taveras, T. N. Truong, and J. Simons, *Int. J. Quantum Chem.* **63**, 861 (1997).

Intramolecular Hydrogen Bonding in Resonance-Stabilized Systems

LUMELLE A. SCHMIEDEKAMP-SCHNEEWEIS,
JUDY OZMENT PAYNE

Pennsylvania State University, Abington College, Abington, Pennsylvania 19001

Received 30 March 1998; accepted 1 June 1998

ABSTRACT: The 3-substituted-2-methoxybenzoic acid system exhibits resonance-stabilized intramolecular hydrogen bonding between the 2-methoxy oxygen and the adjacent carboxylic acid. This intramolecular hydrogen bond can be disrupted by adding another substituent with variable size on the neighboring 3-position of the ring. To relieve steric strain, the system must sacrifice hydrogen bonding and/or resonance stabilization. Full-energy optimizations have been done at HF/D95V (valence double-zeta Dunning-Huzinaga), HF/6-31G* (Pople), HF/D95 (full double-zeta Dunning-Huzinaga), HF/D95V(*d, p*), and HF/6-31 + G(*d, p*). Further single-point calculations were done at MP2/D95V, MP2/6-31G*, MP2/D95, MP2/D95V(*d, p*), and MP2/6-31 + G(*d, p*). The thermal populations of various conformational states including the hydrogen-bonding conformation are presented. The computational results were compared with the experimental thermal population of hydrogen bonding determined by nuclear magnetic resonance (NMR) and infrared (IR) spectroscopies. Results indicate that polarization of the second-row elements in intramolecular hydrogen bonding and perturbation-theory calculations that correct for electron correlations are very important for intramolecular hydrogen bonding. Adding polarization and diffuse functions to the hydrogens, while useful, are quite costly for these systems and do not seem to be as important. © 1998 John Wiley & Sons, Inc. *Int J Quant Chem* 70: 863–875, 1998

Introduction

Hydrogen bonding is one of the most important interactions within and between covalent chemical systems. From protein tertiary structures [1, 2] to DNA double-helical structure [3] to the behavior of lipid membranes [4], hydrogen

Correspondence to: J. O. Payne.

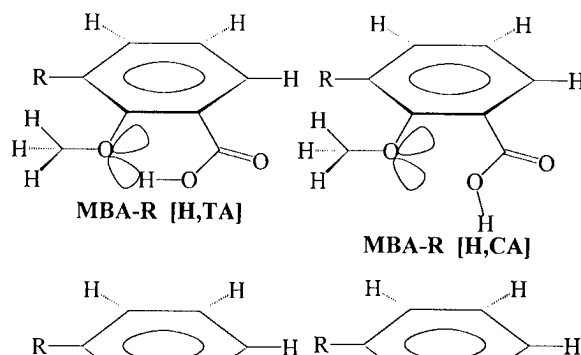
bonding is used to explain key chemical and biological structures and processes. Although the widespread occurrence of hydrogen bonding demonstrates the importance of this interaction, the hydrogen bond is sometimes falsely portrayed as a long-range driving force for molecular conformation preferences. Forces such as ionic attraction, electronic resonance, and steric hindrance are dynamic forces; they act to change the conformation of molecular systems which are “unfavorably ori-

ented" and provide the impetus which moves the atoms to a more favorable position. If "unfavorably oriented" local minima exist at all, their energies are far too high to contribute to a thermal population of conformations. Hydrogen bonding is not such a dynamic force. It has very specific geometry constraints. A molecular system in a nonhydrogen-bonded conformation will not necessarily reorient to take advantage of a possible hydrogen-bonded conformation, and non-hydrogen-bonded conformations often have low enough energy to compete favorably in a thermal population. As a result, hydrogen bonding has more recently been characterized as a stabilizing force rather than as a driving force [5].

Our aim in this work was to investigate the changes in hydrogen bonding in a resonance-stabilized system as it is sterically strained by the addition of a neighboring substituent. The molecule 2-methoxybenzoic acid, called MBA-H in this work (see Fig. 1), is stabilized by an intramolecular hydrogen bond between the carboxylic acid group

and the methoxy oxygen. Both nuclear magnetic resonance (NMR) and infrared (IR) spectroscopies show the contribution of the hydrogen-bonded conformation to a thermal population to be over 90% [6, 7]. However, when another substituent is added to the ring at the position adjacent to the methoxy group (MBA-R, see Fig. 1), steric crowding may interfere with and change the hydrogen bond. The experiments show that the hydrogen-bonded conformation contribution to the thermal population can be far less than 90% in some cases [6, 7]. Therefore, as a tool to compare these systems, we will show a way of characterizing the steric environment for a range of substituents.

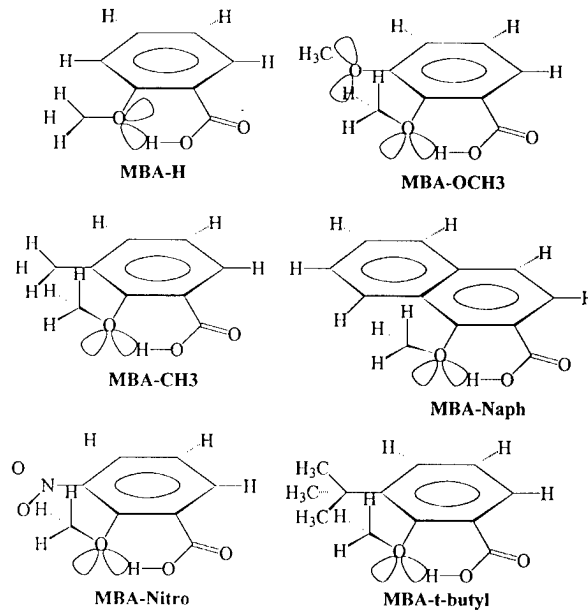
Energetically, there is a measurable stabilizing effect when a hydrogen bond is formed. As an example, each one of the intermolecular hydrogen bonds formed in water dimers provides about 20 kcal/mol [8]. Geometrically, the ideal hydrogen bond is found to have a linear arrangement of the three atoms involved (e.g., the bond angle of N—H · · · N would be 180°). However, a stable hy-



MBA-R Substituents

MBA-H	2-methoxybenzoic acid
MBA-OCH₃	2,3-dimethoxybenzoic acid
MBA-CH₃	3-methyl-2-methoxybenzoic acid
MBA-Naph	1-methoxy-2-naphthoic acid
MBA-Nitro	3-nitro-2-methoxybenzoic acid
MBA-t-butyl	3- <i>t</i> -butyl-2-methoxybenzoic acid

(a)



(b)

FIGURE 1. Nomenclature: (a) specific nomenclature of the various conformations and substitutions for 2-methoxybenzoic acid; (b) six 3-substituted-2-methoxybenzoic acids (MBA-R).

drogen bond can be formed with angles ranging from 130° to 180° when the LUMO of the hydrogen donor is symmetrical (e.g., a commonly reported bond angle for O—H \cdots O is 165° [9]). Sufficient overlap of the LUMO of the donor with the HOMO of the acceptor is possible even when the three atoms are not linearly arranged, as long as their respective sigma planes are still aligned. Hydrogen bonds which deviate significantly from linearity and/or co-planarity will have a reduced orbital overlap and will result in less favorable interactions. For example, the H₂CO \cdots H₂O hydrogen bond is almost 15 kcal/mol less stable when its geometry is changed from linear to approximately 110° [10]. Unless the molecule is very large, intramolecular hydrogen bonds are rarely formed with angles near 180° , due to the ring strain that would be created. This leads us to a conformational investigation of a few key dihedral angles to check coplanarity, as well as the hydrogen-bonded (O \cdots H) distance and angle (O—H \cdots O). We expect that intramolecular hydrogen bonds will be weaker and that they will provide less stabilization compared to their intermolecular counterparts.

Previous theoretical work has been done on related systems. Energy-optimized local minima at the HF/STO-3G level were found for 2-methoxybenzoic acid (MBA-H) [11]. The four primary conformations, called [H, TA], [H, CA], [O, CA], and [O, TA] in this work, are shown in Figure 1. A semiempirical study [12] of various resonance-assisted hydrogen-bonding systems found that no common semiempirical method accurately models intramolecular hydrogen bonding. In 2-hydroxy-nitrobenzene, studied at the HF/6-31G* and MP2/6-31G* levels, [13] aromatic resonance was found to align the hydrogen-bonded atoms. In a study of amide–water and amide–amide hydrogen bonds, [14] it is reported that the polarized Dunning–Huzinaga double-zeta valence (DZP) basis set properly describes relative energetics better and, as a result, represents hydrogen bonding more accurately than does 6-31G*, because the DZP basis set has polarization functions on hydrogen and a larger number of polarization and diffuse functions.

We performed full-energy-optimization calculations in C1 symmetry at the Hartree–Fock level on a series of MBA-R molecules in the hydrogen-bonded conformation, [H, TA] (see Fig. 1), and the three other energetically competitive conformations: [H, CA], [O, CA], and [O, TA]. We compared

the results of the 6-31G* basis set and the Dunning/Huzinaga valence double-zeta basis set (D95V). We compared the effects of adding other polarization and diffuse functions. Using optimized conformational energies from Hartree–Fock as well as conformational energies adjusted for correlation effects using second-order Møller–Plesset perturbation theory, we address the various ab initio methods' ability to recreate the experimental thermal populations. We also report some of the key geometrical features of the energy-optimized hydrogen-bonded conformation. From molecule to molecule, the geometrical results will vary related to their respective steric environment. Also, finally, we examine the flexibility of those basis sets to responding to the changing steric environment.

Calculations

Full-energy-optimization calculations were done at the Hartree–Fock level in C1 symmetry using the Gaussian program [15, 16]. Several basis sets were used: 6-31G* [17], D95V [18], and D95 [18]. The effectiveness of adding basis enhancements for full double-zeta (D95), polarization functions (*d*, *p*), and diffuse functions (+) were investigated. The size of these molecular systems precluded a full study at the higher basis levels. The harmonic frequencies of all optimized structures were calculated to assure that each one represents a local minimum. Single-point energy calculations were done for correlation corrections at the optimal Hartree–Fock-optimized geometries using second-order Møller–Plesset theory (MP2). Spartan 4.1 was used for visualization and generating some geometrical parameters and molecular orbitals.

Thermal populations of various conformational states were calculated using Boltzman's distribution law [19]. The four (or three) significant conformational states were used to approximate the entire ensemble of states. The percent of the *k*th state *N_k* is calculated as follows:

$$\frac{N_k}{N_{tot}} 100\% = \frac{e^{(-E_k/RT)}}{\sum_j e^{(-E_j/RT)}} 100\%,$$

where *E_k* is the optimized energy of the *k*th conformational state, relative to the lowest-energy conformational state, *T* is the temperature in Kelvin (298 K), and *R* is the gas constant (*R* = 1.99×10^{-3} kcal/mol).

Results and Discussion

STERIC ENVIRONMENT

To describe the steric environment, we determined the ability of the 3-substituent (*R*) to cause steric restrictions on the hydrogen-bond acceptor's position. The 2-methoxy group was rotated at 15° intervals from its optimized location and a series of single-point energy calculations was done. With the optimized energy as a reference, the relative energies are plotted in figure (Fig. 2). This provided a qualitative picture of how the hydrogen-bond acceptor is sterically crowded by the acid on one side and the *R* group on the other. In MBA-H, the shape of the rotational potential well is very flat in the region from 0 to 100°. Hence, the 2-methoxy experiences little resistance to moving over that range. However, when the substituent at the 3-position is large, such as *t*-butyl, a steric "wall" impedes the rotation of the 2-methoxy group to a planar orientation and instead forces it

to take a position roughly perpendicular to the plane of the ring (approximately 70–100°). The presence of *t*-butyl creates a more restrictive steric environment. The steric environment was judged by each of the 3-substituents' ability to restrict the motion of the 2-methoxy. The order of the steric environment is the following: MBA-H < MBA-OCH₃ < MBA-CH₃-MBA-Naph < MBA-nitro < MBA-*t*-butyl. The geometric and energetic comparisons shown in this study make use of this order of increasing steric environment as a standard measure.

ENERGIES AND THERMAL POPULATIONS

The optimized energies of the various conformations are presented in Table I. The D95V energies are systematically higher than those of 6-31G*. On the occasions where a comparison is possible, the optimized energies determined by the larger basis sets that include polarization functions on hydrogen as well as diffuse functions are improved. The size of these systems makes the full

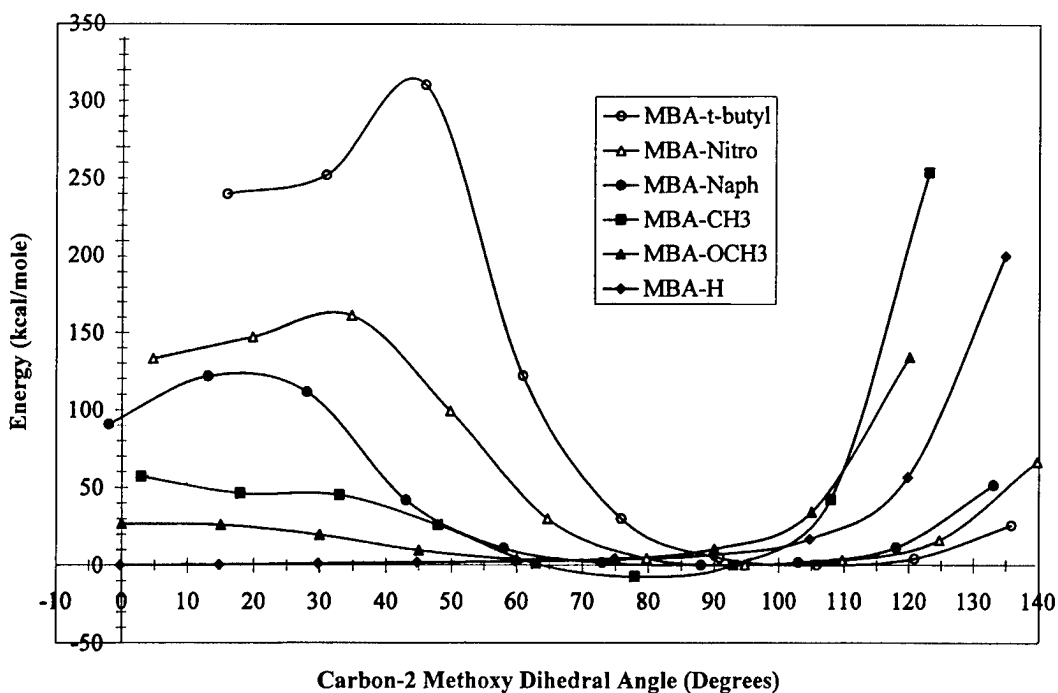


FIGURE 2. Steric environment of hydrogen-bonding conformation [H, TA]. The HF/6-31G* single-point energies (relative to the HF/6-31G*-optimized structure) is calculated at 15° interval rotations of the carbon-2 methoxy dihedral angle. Relative optimized energies are in kcal/mol.

TABLE I
Electronic energies.

Molecule	(a) Electronic energies ^a						
	HF / 6-31G*		HF / D95V		MP2 / 6-31G*		
	Hartrees	kcal / mol	Hartrees	kcal / mol	Hartrees	kcal / mol	
MBA-H	HTA	-532.1979468	0.00	-532.0514002	0.00	-533.7321083	0.00
MBA-H	HCA	-532.1971912	0.47	-532.0444813	4.34	-533.7295838	1.58
MBA-H	OCA	-532.1962527	1.06	-532.0455643	3.66	-533.7291181	1.88
MBA-H	OTA	-532.1853875	7.88	-532.033024	11.53	-533.7205343	7.26
MBA-OCH ₃	HTA	-646.0721633	0.00	-645.8933161	0.00	-647.9162044	0.00
MBA-OCH ₃	HCA	-646.0713499	0.51	-645.8896099	2.33	-647.9130849	1.96
MBA-OCH ₃	OCA	-646.0715925	0.36	-645.8903498	1.86	-647.9135544	1.66
MBA-OCH ₃	OTA	-646.0577271	9.06	-645.8736373	12.35	-647.9007847	9.68
MBA-CH ₃	HTA	-571.2319724	0.61	-571.0712897	0.78	-572.9027139	0.00
MBA-CH ₃	HCA	-571.2321329	0.51	-571.0702316	1.44	-572.8999475	1.74
MBA-CH ₃	OCA	-571.2329496	0.00	-571.0725338	0.00	-572.9010957	1.02
MBA-CH ₃	OTA	-571.219552	8.41	—	—	-572.8894876	8.30
MBA-naph	HTA	-684.8470951	0.87	-684.6552022	1.34	-686.8876913	0.00
MBA-naph	HCA	-684.8479116	0.36	-684.6550519	1.43	-686.8852698	1.52
MBA-naph	OCA	-684.8484785	0.00	-684.6573301	0.00	-686.8861518	0.97
MBA-naph	OTA	-684.8378989	6.64	-684.6449459	7.77	-686.8775765	6.35
MBA-nitro	HTA	-735.6543387	1.26	-735.4322674	2.60	-737.7235245	0.00
MBA-nitro	HCA	-735.6561239	0.14	-735.4342125	1.38	-737.7221738	0.85
MBA-nitro	OCA	-735.656345	0.00	-735.4364086	0.00	-737.7224061	0.70
MBA-nitro	OTA	-735.6444229	7.48	—	—	-737.7133836	6.36
MBA- <i>t</i> -butyl	HTA	-688.3213065	0.66	-688.1241525	1.64	-690.3993874	0.00
MBA- <i>t</i> -butyl	HCA	-688.322361	0.00	-688.1236918	1.93	-690.397936	0.91
MBA- <i>t</i> -butyl	OCA	-688.3223266	0.02	-688.1267639	0.00	-690.3981472	0.78
MBA- <i>t</i> -butyl	OTA	-688.3115509	6.78	—	—	-690.3894247	6.25

TABLE I
(Continued)

Molecule	(b) Electronic energies ^b						
	HF / D95	HF / 6-31+G(<i>d</i> , <i>p</i>)	HF / D95V(<i>d</i> , <i>p</i>)	MP2 / D95	MP2 / 6-31 + G(<i>d</i> , <i>p</i>)	MP2 / D95V(<i>d</i> , <i>p</i>)	Hartrees
	Hartrees	kcal / mol	Hartrees	kcal / mol	Hartrees	kcal / mol	Hartrees
MBA-H	HTA - 532.05983	0.00	-532.3124945	0.00	-532.2306639	0.00	-533.86666944
MBA-H	HCA - 532.04587	4.37	-532.3117946	0.44	-532.229692	0.61	-533.8636513
MBA-H	OCA - 532.00483	30.12	-532.311079	0.89	-532.2288009	1.17	-533.8633316
MBA-CH3HTA - 571.073	0.73	-571.354335	0.79	-571.2669022	0.69	-572.176	0.00
MBA-CH3HCA - 571.07187	1.44	-571.3545542	0.66	-571.2670342	0.61	-572.173	2.28
MBA-CH3OCA - 571.07416	0.00	-571.3555994	0.00	-571.2680049	0.00	-572.175	1.17

^a Full-energy optimizations of various conformational states of all six MBA-R systems were done at the HF level using 6-31G* and D95V basis sets. MP2 / 6-31G* single-point energies were calculated. Absolute electronic energies are given in Hartrees and relative energies are given in kcal / mol.

^b Full-energy optimizations of various conformational states of two of the MBA-R system (MBA-H and MBA-CH3), were done at the HF level using D95, 6-31+G(*d*, *p*), and D95V(*d*, *p*) basis sets. MP2 single-point calculations were done for each of those basis sets. Absolute electronic energies are given in Hartrees and relative energies are given in kcal / mol.

analysis of all six MBA-H systems too costly, so two test cases were chosen: one where the steric strain is minimal, and one where the first significant onset of steric strain is seen, namely, MBA-H and MBA-CH3. The aim of this work was to ascertain which of the lower-level methods preserves most of the results obtained by the larger calculations. One can see that even the relative energy ordering of the three lowest-energy conformers changes at various calculation levels.

It seems that polarizing the second-row elements (*) provides some improvement. Secondary improvement is seen when the hydrogens are also enhanced. The most important energy improvement came with the MP2 single-point calculations to include electron-correlation effects. The 6-31G*-optimal geometries were deemed more closely comparable (energetically and geometrically, described later) to those obtained at the higher levels, so we performed MP2/6-31G* single-point energies on all six MBA-R systems. The relative conformational relationships between the MP2/6-31G* energies in kcal/mol are diagrammed in Figure 3. This figure shows that the [O, TA] conformation has a much higher energy than that of the other three conformations. This may be due to destabilization of the molecule with the acid hydrogen in the "trans" orientation. Under these circumstances, the [O, TA] conformation appears to suffer more notably from oxygen–oxygen repulsion.

In all six MBA-R systems, at the MP2/6-31G* level (Fig. 3), the hydrogen-bonded conformation [H, TA] is the lowest in energy. However, there is a very small difference between the conformational energies (only 0.97–1.7 kcal/mol between [H, TA] and the next lowest conformational state). Therefore, while we do see some stabilization energy, it is smaller than those seen in intermolecular bonds.

The thermal populations of various conformational states were calculated using the relative energies of Boltzman's distribution. Several variations were attempted, including accounting for entropic changes and thermal vibrational and rotational motion, and the best comparisons to experiment are those presented (Table II). As the steric environment increases, there is a general decrease in the percent of hydrogen bonding in the MP2/6-31G* thermal population (Fig. 3). MBA-OCH3 is an exception. The steric environment in this molecule is minimal, since the methyl of the 3-methoxy is able to rotate away from the 2-methoxy.

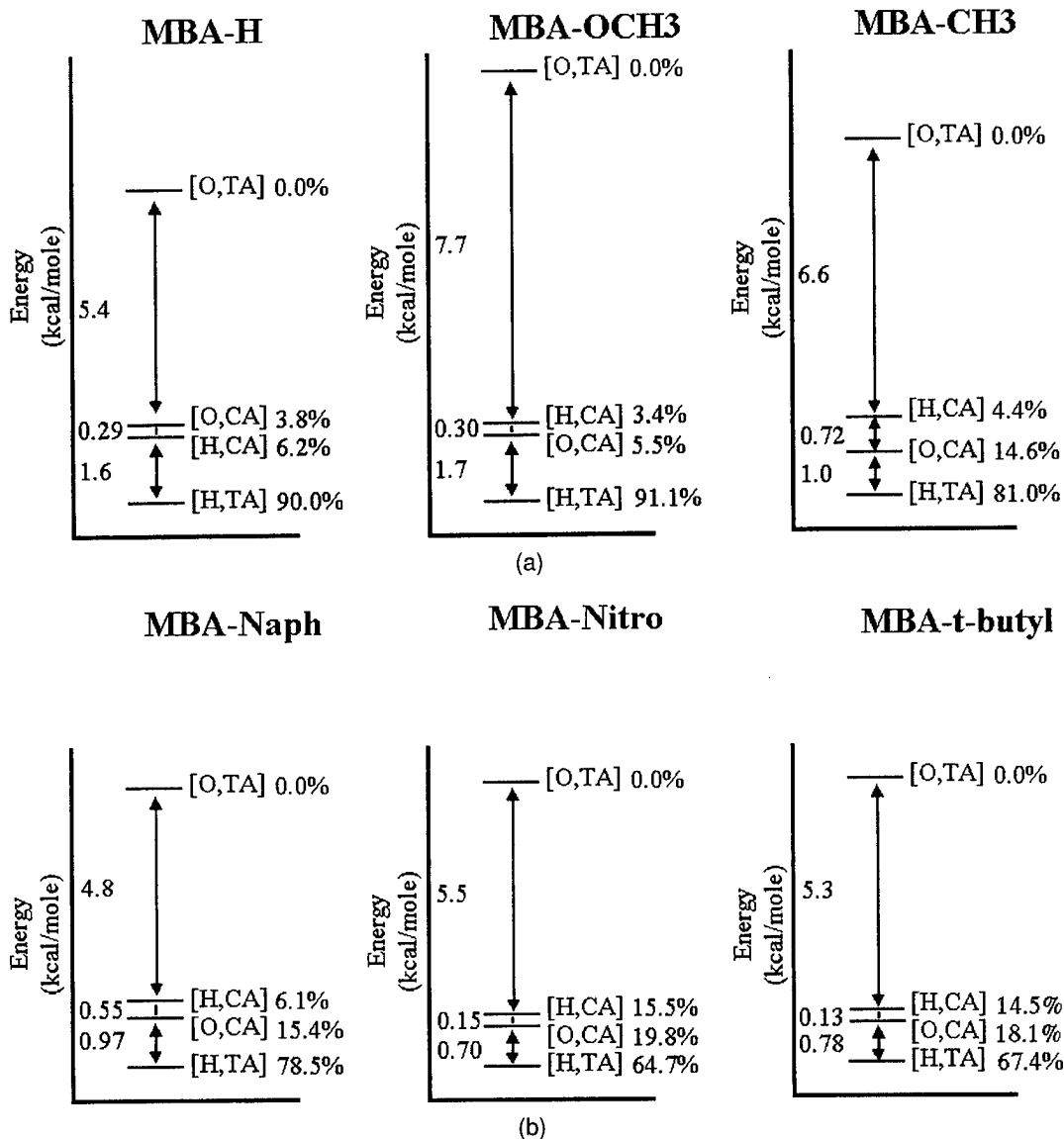


FIGURE 3. MP2 / 6-31G* relative energies and thermal population of states. Relative MP2 / 6-31G* conformational energies are shown for all six of the MBA-R systems, including the percent thermal population of each conformation.

TABLE II
Thermal population of states.

Molecule	(a) Thermal population of states ^a					
	NMR [6]	IR [7]	HF / 6-31G*	HF / D95V	MP2 / 6-31G*	
MBA-H						
MBA-H	HTA	93.8%	93.75%	61.88%	99.73%	89.98%
HCA				27.82%	0.07%	6.22%
OCA				10.30%	0.21%	3.80%
OTA				0.00%	0.00%	0.00%
MBA-OCH₃						
MBA-OCH ₃	HTA	92.3%	92.31%	50.77%	94.06%	91.12%
HCA				21.47%	1.86%	3.36%
OCA				27.75%	4.08%	5.52%
OTA				0.00%	0.00%	0.00%
MBA-CH₃						
MBA-CH ₃	HTA	71.4%	71.43%	20.01%	19.78%	81.04%
HCA				23.71%	6.45%	4.34%
OCA				56.28%	73.77%	14.62%
OTA				0.00%	0.00%	0.00%
MBA-naph						
MBA-naph	HTA	58.3%	12.99%	8.81%	78.54%	
HCA				30.83%	7.51%	6.06%
OCA				56.17%	83.68%	15.40%
OTA				0.00%	0.00%	0.00%
MBA-nitro						
MBA-nitro	HTA	20%	6.26%	1.13%	64.69%	
HCA				41.41%	8.82%	15.49%
OCA				52.33%	90.06%	19.81%
OTA				0.00%	0.00%	0.00%
MBA-t-butyl						
MBA-t-butyl	HTA	23.5%	14.30%	5.70%	67.36%	
HCA				43.63%	3.50%	14.50%
OCA				42.07%	90.80%	18.13%
OTA				0.00%	0.00%	0.00%

^a Thermal populations of various conformational states of all six MBA-R systems were calculated using Boltzman's distribution law and the electronic energies in Table I(a). Experimental populations are provided [6, 7] for comparison.

TABLE II
(Continued)

Molecule	(b) Thermal population of states ^b											
	HF 6-31G*	HF D95V	MP2 6-31G*	HF D95	MP2 D95	HF D95V(d, p)	6-31+G(d, p)	MP2 D95V(d, p)	HF D95V(d, p)	6-31+G(d, p)	MP2 D95V(d, p)	Experiment
MBA-H	HTA	61.88%	99.72%	89.975%	99.94%	99.98%	58.81%	66.81%	93.59%	89.11%	93.8%	
MBA-H	HCA	27.8%	0.0659%	6.22%	0.06%	0.02%	28.04%	23.89%	3.74%	7.05%		
MBA-H	OCA	10.3%	0.207%	3.80%	0.0%	0.0%	13.2%	9.3%	2.7%	3.8%		
MBA-H	OTA	0.000%	0.000%	0.000%								
MBA-CH₃	HTA	20.0%	19.78%	81.04%	21.18%	86.14%	16.47%	18.65%	85.67%	82.37%	71.4%	
MBA-CH ₃	HCA	23.7%	6.45%	4.34%	6.42%	1.84%	20.77%	21.45%	2.79%	2.70%		
MBA-CH ₃	OCA	56.3%	73.8%	14.6%	72.4%	12.0%	62.8%	59.9%	11.5%	14.9%		
MBA-CH ₃	OTA	0.000%		0.000%								

^b Thermal populations of various conformational states of two MBA-R systems were calculated using Boltzman's distribution law and the electronic energies in Table I(b). Experimental populations are provided [6, 7] for comparison.

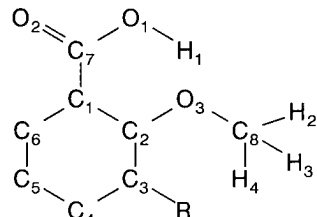
GEOMETRIC CONSIDERATIONS: RELATING RESONANCE STABILIZATION, STERIC EFFECTS, AND HYDROGEN BONDING

Three key parameters related to resonance stabilization and steric effects are given in Table III(a). The two dihedral angles represent the relative orientation of the acid group and the methoxy group, respectively. The degree of planarity of the acid group, designated by O=CCC, indicates the extent of electronic resonance with the acid group with the ring. We found that while there is some minor "puckering" of the hydrogen in the acid group the major change is represented as a simple rotation about the CC bond that connects the acid to the ring; hence, we provide one dihedral angle to indicate that rotation. The dihedral angle of the methoxy group, COCC, indicates the degree of steric crowding as described earlier. The bond angle of the methoxy group, COC, indicates the type and degree of hybridization experienced by the methoxy oxygen for positioning its nonbonding electron pairs. Additionally, all these angles provide some information to address the linearity and planarity of the hydrogen donor and the hydrogen acceptor and the possible positions of the lone pair of electrons on the methoxy oxygen.

At all calculation levels, we see that MBA-H enjoys a completely planar arrangement. It has maximum electronic resonance with the ring, minimal steric strain, and a high percentage of hydrogen bonding. However, the planarity of the acid group is quickly sacrificed once a substituent is placed in the 3-position. All optimizations give similar values for the coplanar dihedral, and all optimizations show a significant rotation of the acid out-of-the-ring plane to compensate for the steric-induced rotation of the 2-methoxy out-of-the-ring plane. These results show that the molecule sacrifices the coplanarity of the acid group with the ring (and thereby sacrifices resonance between the acid group and the ring) in the face of severe steric strain.

Three key parameters related to hydrogen bonding are given in Table III(b). The hydrogen-bonding distance shows the proximity of the hydrogen to the methoxy oxygen. The angle formed between the two oxygens and the shared hydrogen indicate the planarity of the hydrogen bond. The dihedral angle (CO \cdots HO) represents the relative planarity of the atoms involved in the hydrogen bond.

TABLE III
**Selected geometric parameters directly associated with (a) electronic resonance and steric environments and
(b) hydrogen bonding:**



Dihedral angles:	Name
O2-C7-C1-C6	O=CCC
C8-O3-C2-C1	COCC
C2-O3-H1-O1	CO ... HO
Angle:	Name
O1-C7-O2	OCO
Distance:	Name
O3-H1	O ... H

(a) Geometrical parameters related to electronic and steric effects

Molecule	6-31G* O=CCC	6-31G* COCC	6-31G* COC
MBA-H			
HTA	-0.0120	-179.9765	121.0217
HCA	-0.4064	179.9553	120.7769
OCA	166.2833	179.7663	120.8218
MBA-CH ₃			
HTA	15.5994	92.9405	115.7510
HCA	1.9586	86.9137	116.5386
OCA	157.7890	90.8539	116.9619
MBA- <i>t</i> -butyl			
HTA	22.5644	75.6819	115.8312
HCA	25.9563	67.9729	117.2145
OCA	-157.4296	57.4054	121.0111
	D95V O=CCC	D95V COCC	D95V COC
MBA-H			
HTA	0.0059	-179.9962	122.3787
HCA	-28.0228	173.6036	122.2936
OCA	179.9633	-179.9974	122.7225
MBA-CH ₃			
HTA	15.5901	101.2156	118.3933
HCA	-24.3610	96.2190	119.6954
OCA	159.4363	88.0364	120.4005
MBA- <i>t</i> -butyl			
HTA	22.7952	77.4336	117.8380
HCA	20.4457	64.5484	120.4173
OCA	-171.2245	59.5876	123.4954
	6-31 + G(<i>d, p</i>) O=CCC	6-31 + G(<i>d, p</i>) COCC	6-31 + G(<i>d, p</i>) COC
MBA-H			
HTA	-0.0337	-179.9837	121.2265
HCA	-14.3933	179.5488	120.9451
OCA	166.3337	179.5823	121.0716
MBA-CH ₃			
HTA	17.1097	95.2809	116.0413
HCA	-8.5974	91.7560	117.0077
OCA	155.8869	91.4651	117.4040

(Continued)

TABLE III
(Continued)

(a) Geometrical parameters related to electronic and steric effects			
Molecule	6-31 + G(<i>d, p</i>) O=CCC	6-31 + G(<i>d, p</i>) COCC	6-31 + G(<i>d, p</i>) COC
MBA- <i>t</i> -butyl			
HTA	24.9617	75.5732	116.0292
HCA	28.8020	67.3157	117.5005
OCA	-156.5036	56.4168	121.3581
	D95V(<i>d, p</i>) O=CCC	D95V(<i>d, p</i>) COCC	D95V(<i>d, p</i>) COC
MBA-H			
HTA	0.0000	-179.9974	120.7590
HCA	-4.8078	179.8691	120.5065
OCA	173.2467	179.7449	120.5575
MBA-CH ₃			
HTA	16.4571	94.4732	115.4523
HCA	2.6065	86.8947	116.2557
OCA	157.6700	91.0405	116.7127
MBA- <i>t</i> -butyl			
HTA	24.2722	75.9209	115.4643
HCA	27.3619	68.1236	116.9076
OCA	-159.0988	57.9022	120.6949
(b) Geometric parameters related to hydrogen bonding			
Molecule	6-31G* O ··· H	6-31G* O ··· H—O	6-31G* CO ··· HO
MBA-H	HTA	1.8056	144.3140
MBA-CH ₃	HTA	1.8721	139.5956
MBA- <i>t</i> -butyl	HTA	1.9471	139.5956
	D95V O ··· H	D95V O ··· H—O	D95V CO ··· HO
MBA-H	HTA	1.7689	140.7154
MBA-CH ₃	HTA	1.8612	135.2406
MBA- <i>t</i> -butyl	HTA	1.9679	127.9940
	6-31 + G(<i>d, p</i>) O ··· H	6-31 + G(<i>d, p</i>) O ··· H—O	6-31 + G(<i>d, p</i>) CO ··· HO
MBA-H	HTA	1.8075	144.0548
MBA-CH ₃	HTA	1.8816	139.0622
MBA- <i>t</i> -butyl	HTA	1.9767	131.8841
	D95V(<i>d, p</i>) O ··· H	D95V(<i>d, p</i>) O ··· H—O	D95V(<i>d, p</i>) CO ··· HO
MBA-H	HTA	1.8029	144.6997
MBA-CH ₃	HTA	1.8766	139.6923
MBA- <i>t</i> -butyl	HTA	1.9708	132.4931

At all calculation levels, we see that MBA-H has a relatively short hydrogen bond, set essentially planar, with the widest angle of 144°. However, the angle described by the O···O—C is never in the preferred linear arrangement or even at the 165° typical OH-O angle. Therefore, the angular arrangement imposed by the intramolecular nature of these hydrogen bonds is consistent with their small stabilization energy.

As the steric environment becomes more crowded, the hydrogen bond lengthens, the angle narrows, and the planarity decreases. This helps explain why the population of the hydrogen-bonded conformer decreases. These geometrical changes are making the hydrogen bond weaker. The steric crowding reduced the effectiveness of the hydrogen bond and increased the chances that the thermal population will start to favor a less crowded conformation. The changes in the COC angle suggests that that electron density of the nonbonding electron pair on oxygen moves out of the ring plane. The signs (+, -) of the dihedrals for the [H, TA] conformer's acid and the methoxy are always opposite, suggesting that acid hydrogen appears to "follow" that nonbonding electron pair.

Comparing the optimized geometrical parameters of the smaller basis sets (6-31G* and D95V) with those of the larger ones [6-31 + G(*d, p*) and D95V(*d, p*)], we see that in most instances the 6-31G* geometries are better than those of D95V. The H···O, O···H—O, COCC, and COC parameters compare much more favorably with the geometries of the better calculations. In fact, there is only one parameter in D95V that compares better than in 6-31G* and that is the MBA-*t*-butyl hydrogen-bond length. The most striking results are seen in the O=CCC angles of the [H, CA] conformers. Each of the different basis sets optimized at significantly different acid dihedral angles for this particular conformer. According to energetics, we expect the 6-31 + G(*d, p*) to be closest to right, although there are not many significant differences between this and D95V(*d, p*).

When hydrogen bonding is energetically favorable and sterically unhindered, the D95V distances are consistently shorter than for 6-31G*, and when hydrogen bonding becomes less favorable (less than about 75% of the thermal population) and the 3-substituent's steric influence is greater, the D95V distances become smaller than for 6-31G*. The two basis sets optimized the O···H—O angle at signif-

icantly different values. The D95V O···H—O angles are consistently smaller than those in 6-31G*.

Conclusion

We do see some stabilization energy in the conformations of 3-substituted-2-methoxybenzoic acid that are able to form hydrogen bonds, although it is smaller (1–2 kcal/mol) than those seen in some intermolecular bonds. An increase in the 2-methoxy-substituent's steric environment systematically reduces the thermal population of intramolecular hydrogen-bonded structures. The extremely nonlinear and eventually even nonplanar arrangement imposed on these hydrogen bonds by the ring arrangement and the steric environment is consistent with their small stabilization energy. Thermal populations compare within a few percent of experimental when the hydrogen-bonding conformation is the most favored. The best comparison to experiment is achieved with MP2/6-31 + G(*d, p*). However, none of the isolated molecule models studied so far predicts appropriate decreases in the thermal population, in cases where the steric environment becomes significant. Even in the case of MBA-CH₃, the best comparison is 10% off. This lack of consistency suggests that it may be insufficient to compare the results of calculations for isolated molecules to these experimental values. The coplanarity of the acid group and the 2-methoxy group appears to be the key to what small amount of stability there is left in these hydrogen bonds. Comparing the calculation results, we find that the polarization of the second-row elements in intramolecular hydrogen bonding and perturbation theory calculations that correct for electron correlations are very important for intramolecular hydrogen bonding. Adding polarization and diffuse functions to the hydrogens will help, but do not seem to be as important.

ACKNOWLEDGMENTS

We are grateful for Grant CHE960014P from the Pittsburgh Supercomputer Center.

References

- E. N. Baker and R. E. Hubbard, *Prog. Biophys. Mol. Biol.* **44**, 98 (1984).

RESONANCE-STABILIZED HYDROGEN BONDING

2. N. S. Golubev, G. S. Denisov, V. A. Gindin, S. S. Ligay, H.-H. Limbach, and S. N. Smirnov, *J. Mol. Struct.* **322**, 83 (1994). G. Zubay, *Biochemistry*, 3rd ed. (Wm. C. Brown, Dubuque, IA, 1993), pp. 219–251.
3. R. H. Garrett and C. M. Grisham, *Biochemistry* (Saunders, Philadelphia, 1995), pp. 216–218.
4. J. M. Boggs, *Biochim. Biophys. Acta* **906**, 353–404 (1987).
5. K. A. Dill, *Biochemistry* **29**, 7133–7155 (1990).
6. I. I. Schuster, private communication (Penn State University, Abington College, 1997).
7. H. A. Lloyd, K. S. Warren, and H. M. Fales, *J. Am. Chem. Soc.* **88**, 5544 (1966).
8. A. Rauk, *Orbital Interaction Theory of Organic Chemistry* (Wiley-Interscience, New York, 1994), pp. 160–162.
9. J. P. M. Lommerse, S. L. Price, and R. Taylor, *J. Comput. Chem.* **18**, 757 (1997).
10. S. Scheiner, *Acc. Chem. Res.* **27**, 402 (1995).
11. G. Jaccard, P. A. Carrupt, and J. Lauterwein, *Magn. Reson. Chem.* **26**, 239 (1988).
12. M. A. Rios and J. Rodriques, *J. Comput. Chem.* **13**, 860 (1992).
13. C. W. Bock and I. Hargittai, *Struct. Chem.* **5**, 307 (1994).
14. D. A. Dixon, K. D. Dobbs, and J. J. Valentini, *J. Phys. Chem.* **98**, 13435 (1994).
15. M. J. Frisch, G. W. Trucks, H. B. Schlegel, P. M. W. Gill, B. G. Johnson, M. W. Wong, J. B. Foresman, M. A. Robb, M. Head-Gordon, E. S. Replogle, R. Gomperts, J. L. Andres, K. Raghavachari, J. S. Binkley, C. Gonzalez, R. L. Martin, D. J. Fox, D. J. Defrees, J. Baker, J. J. P. Stewart, and J. A. Pople, *Gaussian 92/DFT, Revision G.4* (Gaussian, Inc., Pittsburgh PA, 1993).
16. M. J. Frisch, G. W. Trucks, H. B. Schlegel, P. M. W. Gill, B. G. Johnson, M. A. Robb, J. R. Cheeseman, T. Keith, G. A. Petersson, J. A. Montgomery, K. Raghavachari, M. A. Al-Laham, V. G. Zakrzewski, J. V. Ortiz, J. B. Foresman, J. Cioslowski, B. B. Stefanov, A. Nanayakkara, M. Challacombe, C. Y. Peng, P. Y. Ayala, W. Chen, M. W. Wong, J. L. Andres, E. S. Replogle, R. Gomperts, R. L. Martin, D. J. Fox, J. S. Binkley, D. J. Defrees, J. Baker, J. P. Stewart, M. Head-Gordon, C. Gonzalez, and J. A. Pople, *Gaussian 94, Revision E.2* (Gaussian, Inc., Pittsburgh PA, 1995).
17. R. Ditchfield, W. J. Hehre, and J. A. Pople, *J. Chem. Phys.* **54**, 724 (1971); W. J. Hehre, R. Ditchfield, and J. A. Pople, *J. Chem. Phys.* **56**, 2257 (1972); M. S. Gordon, *Chem. Phys. Lett.* **76**, 163 (1980); P. C. Hariharan and J. A. Pople, *Mol. Phys.* **27**, 209 (1974).
18. Dunning and Hays, in *Modern Theoretical Chemistry*, H. F. Schaefer III, Ed. (Plenum, New York, 1976), pp. 1–28.
19. W. J. Moore, *Physical Chemistry*, 4th ed. (Prentice-Hall, Englewood Cliffs, NJ, 1972), pp. 180–185.

Quantum Chemical Study of the Interaction of Nitrate Anion with Water

CHRISTOPH EBNER, ROLAND SANSONE, MICHAEL PROBST

*Institute of General and Inorganic Chemistry, Innsbruck University, Innrain 52a,
A-6020 Innsbruck, Austria*

Received 29 March 1998; revised 29 June 1998; accepted 10 July 1998

ABSTRACT: The interaction between nitrate anion and water has been investigated by Hartree–Fock calculations with the 6-311 + G(d, p) basis set and by B3LYP density functional calculations with the aug-cc-pVTZ basis set. It is found that the global energy minimum is a planar configuration where both hydrogen atoms of water are coordinated to two oxygen atoms of NO_3^- by distorted hydrogen bonds. In contrast to former studies on $\text{NO}_3^-/\text{H}_2\text{O}$ this configuration is found to be asymmetric at the highest theoretical level employed. The corresponding structure with C_{2v} symmetry is a saddle point at slightly higher energy. A singly hydrogen-bonded configuration is still about 2.4 kcal/mol higher in energy. The shifts in the vibrational frequencies of water and nitrate upon complexation were calculated. A compact analytical potential function of $\text{NO}_3^-/\text{H}_2\text{O}$ for use in statistical thermodynamic simulations was obtained from 390 points of the energy surface and an intramolecular force field for the nitrate anion is presented. © 1998 John Wiley & Sons, Inc. *Int J Quant Chem* 70: 877–886, 1998

Key words: potential functions; nitrate anion; nitrate-water interaction; nitrate-water cluster geometries; vibrational frequencies

Introduction

This work is organized as follows: First, we discuss relevant previous works. In the second section we present the energetic and conformational properties of the system $\text{NO}_3^-/\text{H}_2\text{O}$ and

in the third section its vibrational behavior. An analytical function representing the energy surface of $\text{NO}_3^-/\text{H}_2\text{O}$ as well as an intramolecular potential function for NO_3^- are derived in the fourth section.

Because of their great chemical, biological, and technical importance, many experimental studies have focused on elucidating the properties of aqueous nitrate solutions. Specifically, articles investigating the structure of nitrate solutions by various spectroscopic techniques under a variety

Correspondence to: M. Probst.

Contract grant sponsor: Austrian FWF.

Contract grant number: P10106-MOB.

of conditions have been published (*vide infra*). In contrast, rather few quantum chemical studies dealing with the properties of NO_3^- were reported.

It has been found that NO_3^- can serve as a sensitive probe of the molecular environment, especially via vibrational spectroscopy. The experimental evidences are, for example, reviewed in great detail in [1]. Other important reviews include [2] and [3]. The rotational behavior of NO_3^- was also investigated by nuclear magnetic resonance (NMR) spectroscopy [4, 5]. The easy distortion of the D_{3h} symmetry of the anion causes shifts and splitting of the vibrational bands as well as changes in their intensity. This topic is discussed together with the results of our frequency calculations in the following section.

One of the first theoretical studies on the system $\text{NO}_3^-/\text{H}_2\text{O}$ was performed by Howell et al. [6]. With Hartree–Fock calculations and the 6-31G basis set, a cyclic structure with two distorted hydrogen bonds was found to be most stable with a binding energy of -18.49 kcal/mol versus -17.23 kcal/mol for a singly hydrogen-bonded one.

In Ref. [7] the system $\text{NO}_3^-/\text{H}_2\text{O}$ was studied by Hartree–Fock calculations and compared with the isomeric form $\text{ONOO}^-/\text{H}_2\text{O}$ (as well as with H_2NO_4^- in a subsequent study [8]). The largest basis set used by them was a double zeta basis set with polarization functions [9]. The authors find, similar to [6], the global minimum in a planar conformation with C_{2v} symmetry and two strongly bent hydrogen bonds with a binding energy of -14.9 kcal/mol .

Velders and Feil [10] studied changes in electronic density and geometry of nitrate anion in the presence of a proton and could correlate them with experimental crystal geometries. In a related study, Probst [11] calculated properties of various $\text{NO}_3^-/\text{M}^{n+}$ ion pairs and the intramolecular vibrational frequency shifts caused by the counterions. The binding sites and the frequency shifts were found to depend on the size of the cation.

A computer simulation involving an aqueous silver nitrate solution was performed by Laaksonen and Kovacs [12]. They used a rigid model with a Lennard-Jones force field for the nitrate and the rigid SPC water model. Another molecular dynamics simulation was performed by Kataoka [13] with the Carravetta–Clementi water model and an empirical potential for the nitrate interactions. A series of molecular dynamics simulations investigating the dynamics of NO_3^- in molten salts has been published by Kato et al. [14].

The $\text{NO}_3^-/\text{H}_2\text{O}$ Complex

Geometry optimizations of the nitrate–water complex with all degrees of freedom included have been performed at the HF/6-311G + (d, p) [15, 16] and B3LYP/aug-cc-pVTZ [17] levels. Different starting geometries always resulted in one of two minima on the potential hypersurface. While this is no proof of the nonexistence of other minima, the symmetric structure of NO_3^- makes it plausible that no other minima exist. Our investigations included, for example, a nonplanar configuration with C_{2v} symmetry which is a saddle point, bifurcated structures with two hydrogen atoms adjacent to one oxygen of NO_3^- , and structures with water on top or below the plane of the anion. All of them do not constitute local minima as well. However, as discussed below, generally only small energy differences between various configurations are found and point to the fact that parts of the potential surface are very shallow.

The global minimum is a cyclic structure with two hydrogen bonds. The exact structure of this configuration, however, differs between HF/6-311G + (d, p) and B3LYP/aug-cc-pVTZ calculations. The former method leads to a structure with C_{2v} symmetry similar as in [7] and [6] with a binding energy of -14.0 kcal/mol , while at the B3LYP/aug-cc-pVTZ level the corresponding planar configuration with C_{2v} symmetry exhibits one imaginary frequency. If optimized without symmetry constraints, the B3LYP/aug-cc-pVTZ dimer is asymmetric and -0.1 kcal/mol lower in energy (-14.5 and -14.4 kcal/mol , respectively). Figure 1(a) shows that despite the small energy difference the deviation from C_{2v} symmetry is not negligible and the structure can even be viewed as an intermediate between a cyclic structure and a singly hydrogen-bonded one. The singly hydrogen-bonded structure shown in Figure 1(b) is $+1.9 \text{ kcal/mol}$ higher in energy (-12.6 kcal/mol) and is found to be a local minimum on the potential energy surface. The distance between the oxygen atom of water and the nitrogen is more than 0.3 \AA larger for the singly bonded configuration (3.355 and 3.703 \AA).

A comparison between optimized monomers ($r_{\text{N}-\text{O}}: 1.258 \text{ \AA}$, $r_{\text{O}-\text{H}}: 0.962 \text{ \AA}$, and $\angle_{\text{H}-\text{O}-\text{H}}: 105.1^\circ$) and the dimers (values given in Fig. 1) exhibits only small geometric changes with the exception of $\angle_{\text{H}-\text{O}-\text{H}}$ for the global minimum

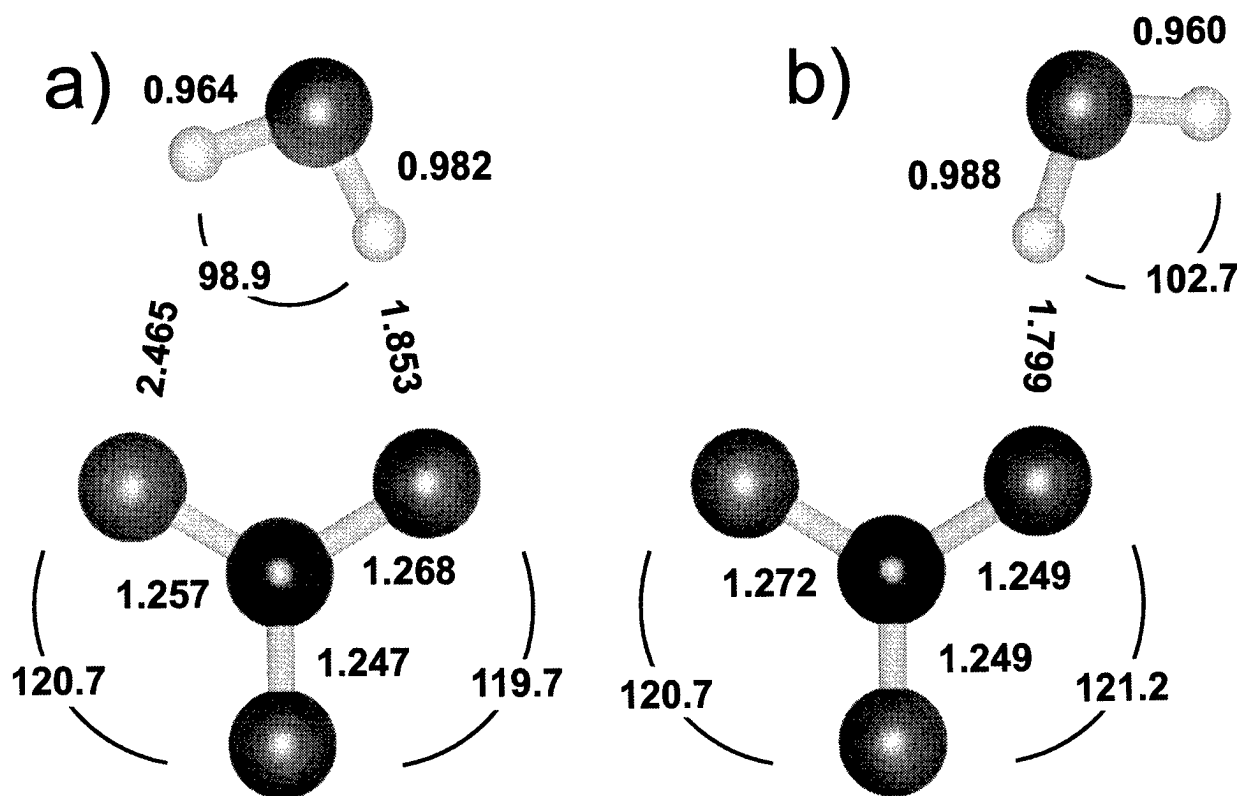


FIGURE 1. Geometries optimized at the B3LYP/aug-cc-pVTZ level. (a) Global minimum and (b) second energy minimum.

configuration which decreases by 6.2° . The largest change in one of the $\angle_{\text{O}-\text{N}-\text{O}}$ angles is less than 1° and the largest changes in $r_{\text{N}-\text{O}}$ and $r_{\text{O}-\text{H}}$ bond lengths are $+0.013$ and $+0.025$ Å, respectively. It can be seen that the values of $r_{\text{O}-\text{H}}$ correspond to the ability of the corresponding atoms to participate in hydrogen bonding.

Vibrations of Nitrate Anion and $\text{NO}_3^-/\text{H}_2\text{O}$

As already mentioned above, nitrate anion is an extremely useful molecule for probing the molecular environment, especially via its vibrational behavior. This stems partially from the fact that NO_3^- , due to its high symmetry, is a “vibrationally deficient” molecule. Symmetry lowering from D_{3h} to C_{2v} can occur easily, leading to infrared (IR) and Raman band splitting and intensity changes. Also IR, Raman, and the ultraviolet (UV) intensities of its electronic transitions depend much on the environment, but this shall not be studied further here. As a tetraatomic molecule, nitrate anion exhibits six vibrational modes: A total symmetric stretch-

ing mode ($\nu_s = \nu_1$), two degenerate asymmetric stretching modes ($\nu_{as} = \nu_3$), two degenerate bending modes ($\delta_{as} = \nu_4$), and one out-of-plane mode ($\nu_{oop} = \nu_2$). While the occurrence of the splitting of the δ_{as} and ν_{as} vibrations in an asymmetric environment is therefore easy to understand in principle, there is yet no concise explanation why this symmetry lowering can even readily be observed in dilute aqueous solutions [1, 2]. Ion pair formation can be ruled out experimentally because the splitting is largely independent of concentration and cation. An explanation by assuming specific hydrogen bonding between the anion and its hydration shell has the drawback that the splitting is neither found in deuterated H_2O nor in other solvents with strong hydrogen bonding to NO_3^- .

Table I gives a comparison of various theoretical methods with experiments. The experimental values were derived from measurements in solution. It can be seen that a high theoretical level and large basis set is needed and that the B3LYP values are closer to the experiment than the more expensive MP4 results. Keeping in mind that experimentally the typical half-height linewidth of

TABLE I
Vibrational frequencies of nitrate anion (cm^{-1}).

Method	E' (δ_{as})	$A2''$ (ν_{oop})	$A1'$ (ν_s)	E' (ν_{as})
NO_3^-				
MP4/aug-cc-pVTZ	689	816	996	1379
B3LYP/aug-cc-pVTZ	707	844	1062	1364
BLYP/aug-cc-pVTZ	663	783	978	1240
MP4(SDQ)/MIDI + **	705	842	1056	1369
HF/MIDI + **	781	959	1200	1516
NO_3^-/K^+				
HF/MIDI + **	785, 796	945	1183	1453, 1688
MP4(SDQ)/MIDI + **	713, 720	832	1029	1263, 1518
$\text{NO}_3^-/\text{H}_2\text{O}$				
B3LYP/aug-cc-pVTZ	712, 718	841	1062	1341, 1402
Solution				
IR, Raman [19]	719	825	1049	1348, 1404
IR, Raman [18]	720	825	1050	1345, 1400

the peaks is 50 cm^{-1} , the B3LYP/aug-cc-pVTZ values seem very reasonable. The largest deviation from the experimental values is 19 cm^{-1} for ν_{oop} (the experimental value for the unperturbed ν_{as} is about 1380 cm^{-1} [18]).

In the optimized $\text{NO}_3^-/\text{H}_2\text{O}$ complex (global minimum), the coordination of water leads to a splitting of the degenerate asymmetric stretching modes at 1364 cm^{-1} into 1341 and 1402 cm^{-1} and of the two degenerate asymmetric bending modes at 707 cm^{-1} into 712 and 718 cm^{-1} (B3LYP/aug-cc-pVTZ values). The out-of-plane and the symmetric stretching modes remain (nearly) unchanged at 844 and 1062 cm^{-1} . These splittings are very similar to the experimental values from Table I.

In order to be able to compare these frequency splittings from hydrogen bonding with the splittings caused by symmetry lowering from ion pair formation, corresponding calculations were performed on an NO_3^-/K^+ contact ion pair. The frequencies obtained with the MP4(SDQ) method and the MIDI basis set augmented with diffuse and polarization functions each [20] (no aug-cc-pVTZ basis set for K has yet been published) are included in Table I. With 255 cm^{-1} , a considerably larger splitting than for H_2O was found for the ν_{as} mode. It is not unlikely that for a hydrated potassium cation ion pair the splitting comes down to a similar range than for H_2O .

It can be concluded that the magnitude of the band splitting found in $\text{NO}_3^-/\text{H}_2\text{O}$ is comparable to the experimental value in solution and that even

a rather weak cation like K^+ causes a larger splitting in the ν_{as} band. In accordance with experiment, the splitting of the other degenerate band, δ_{as} , is much smaller.

Potential Energy Functions

A calculation of the energy surface of $\text{NO}_3^-/\text{H}_2\text{O}$ was performed at the Hartree-Fock level with the 6-311 + G(d, p) basis set. This method was chosen in view of the large computational effort involved in the more accurate B3LYP/aug-cc-pVTZ calculations. Despite the fact that, as discussed above, a symmetric global minimum structure results at the 6-311 + G(d, p) level, the actual binding energies of both methods are very close and, for example, comparable to the approximations introduced by assuming rigid monomers. [The HF/6-311G + (d, p) binding energy at the global minimum obtained with rigid monomers is -13.67 kcal/mol versus -13.97 kcal/mol for a full optimization.] The intramolecular geometries of water and nitrate anion were kept rigid at the experimental values [21] with $r_{\text{N}-\text{O}} = 1.220 \text{ \AA}$, $\angle_{\text{O}-\text{N}-\text{O}} = 120^\circ$, $r_{\text{O}-\text{H}} = 0.957$ and $\angle_{\text{H}-\text{O}-\text{H}} = 104.5^\circ$. No counterpoise correction has been applied since test calculations showed that for this basis set the superposition error at the global minimum is less than 4% of the binding energy.

Fifteen sets of configurations were chosen and for each set 26 energy points were calculated by moving the water molecule along a line. Due to

the high symmetry of nitrate anion the resulting 390 energy points should sufficiently cover the representative regions of interaction.

Figures 2(a) and 2(b) visualize some of the 15 configurations. The configurations which result by water being rotated out of the nitrate plane by 90° are not shown in order to avoid overcrowding the picture: In Figure 2(a), configuration 2 is derived from configuration 1 (nitrate anion and water are in one plane and the atoms N—O⋯H—O are collinear) with water rotated around the N—O⋯H—O axis by 90°. Configurations 4, 7, and 9 (not shown) are derived in the same way from configurations 3, 6, and 8, respectively. Configuration 5 is derived from configuration 9 but has the hydrogen atoms pointing away from the nitrate anion. Configurations in which the oxygen atom of water is located out of the nitrate plane are shown in Figure 2(b). In configurations 10 and 11, the O⋯N axis is inclined by 45° out of the nitrate plane whereas in configurations 12 and 13 it is perpendicular to it. In 10 and 12, one hydrogen atom points toward the nitrogen atom while in 11 and

13 both hydrogen atoms point away from it. Configurations 14 (like 13 but the hydrogen atoms point toward N) and 15 (like 13 but with water below one oxygen atom of NO_3^-) are not shown.

The binding energies corresponding to the various sets of configurations are shown in Figure 3 (circles) as a function of the N—O distance. As can be expected from electrostatic considerations, configurations 5, 6, 7, 11, and 15 are always repulsive. In 12, a hydrogen atom approaches NO_3^- from the top. The attraction from the oxygen atoms predominates in this case and a shallow minimum is found.

The 390 energy points were used to fit a polynomial with 4 adjustable parameters for each site–site interaction:

$$V_{\text{fit}}^{\text{n-w}} = \sum_{k,i} \left[\frac{q_k q_i}{r_{ki}} + \frac{A_{ki}}{r_{ki}^4} + \frac{B_{ki}}{r_{ki}^6} + \frac{C_{ki}}{r_{ki}^8} + \frac{D_{ki}}{r_{ki}^9} \right], \quad (1)$$

where A to D are the parameters to be fitted, q_k and q_i are the partial charges at the centers of

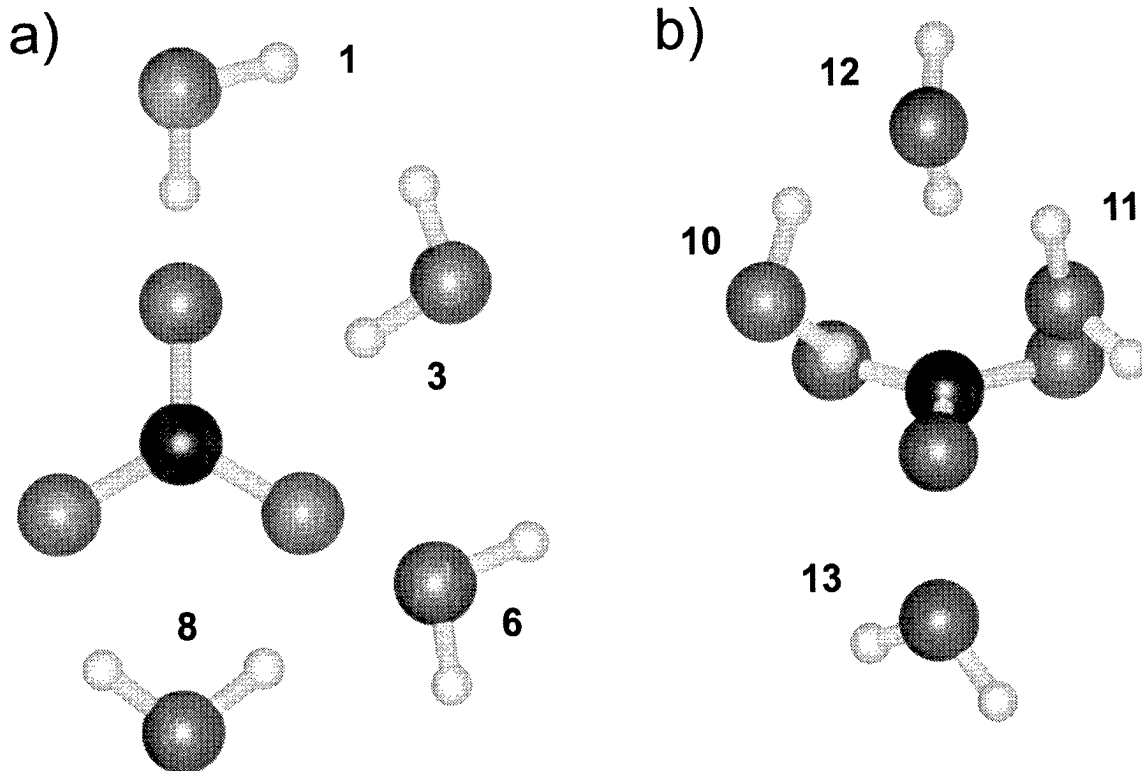


FIGURE 2. Configurations considered in the scan of the potential energy surface. (a) Shows the configurations where water oxygen atom is in the nitrate plane and (b) shows the out-of-plane configurations. See text for further explanations.

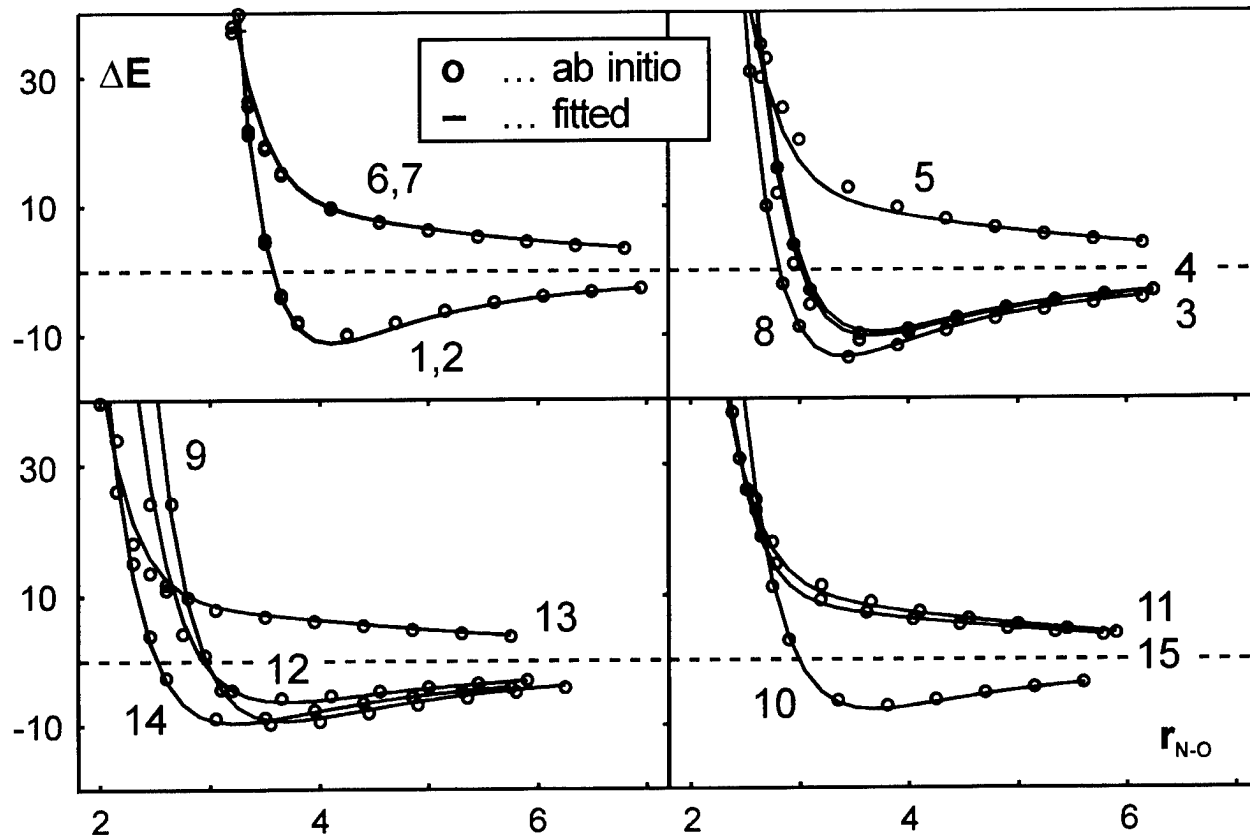


FIGURE 3. Calculated energy points (symbols) and fitted energies (solid lines) for the 15 configurations plotted against the $N \cdots O$ interatomic distance. The energies are given in kcal/mol and the distances in Ångström.

interaction k and i in the two molecules, and $r_{k,i}$ is their distance. A calculation of the q 's by CHELPG [22] population analysis gave charges of +1.298 and -0.766 electrons for nitrogen and oxygen, respectively. Since the potential function is intended to be used in computer simulations of aqueous nitrate solutions, for reasons of electrostatic consistency the partial charges of the well-known MCYL water potential [23] were taken. For O and H atoms of water the charges are -1.434

and +0.717, respectively. The charges were kept constant in the fitting process. Their values, somewhat arbitrary as any charge partition scheme, are larger than the corresponding ones from CHELPG (-0.808 and +0.404, respectively) and are intended to be effective charges for liquid water. The values of the optimized parameters A to D are given in Table II.

The overall standard deviation of the fit (including the electrostatic terms) was 1.17 kcal/mol.

TABLE II
Values of the parameters (kcal / mol, Å) of the analytical pair potential for the nitrate – water interaction in formula (1).

	$O_n - O_w$	$O_n - H_w$	$N_n - O_w$	$N_n - H_w$
A	456.230953	-9.267009	-141.352593	-286.238598
B	-14346.495583	509.57219	8378.086698	1710.782613
C	135881.693843	-1063.771480	-52972.399360	-4740.608610
D	-163716.597217	654.054407	60790.249131	3454.023536

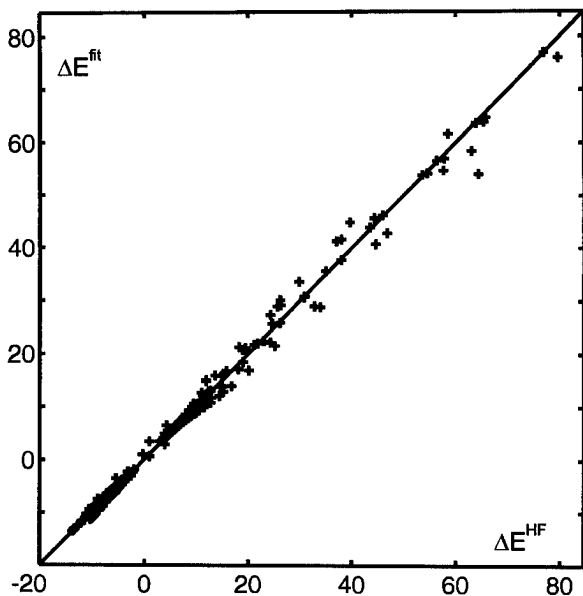


FIGURE 4. Correlation of all fitted energy points versus Hartree-Fock energies (kcal/mol).

Figure 4 shows a reasonably good correlation between ab initio and fitted energies. The solid curves in Figure 3 show the analytical potential. It can be seen that the important characteristics of the ab initio potential curves can be found in the calculated potential. Configuration 8 includes the global minimum and shows that within the method used and under the restriction of rigid monomers, a cyclic structure is somewhat more stable than a single hydrogen bonded one. Structures with linear O—H \cdots O—N hydrogen bonds (configurations 1 and 2) are about as stable as the corresponding configurations where the nitrate molecule is turned by 60° and O—H points to the bisector of O—N—O (configurations 3 and 4). If the nitrogen atom is directly involved, the bonding is much weaker (configuration 12).

Figure 5 shows two-dimensional cuts of the potential energy surface in the plane of NO_3^- for three typical cases. In the left part the orientations of the water molecules are shown and in the right part the corresponding energy surface as contour plot. From the picture on top which includes the configurations with two hydrogen bonds (-13 kcal/mol contour), it can be seen that (if water is thought to move around the anion) bifurcated hydrogen bonds are about 4–5 kcal/mol less stable. For the singly hydrogen-bonded structures (Fig. 5 middle), there is even less difference between lin-

ear hydrogen bonds and bifurcated ones. Finally, the contour diagram at the bottom shows a set of typical repulsive configurations.

The agreement between the calculated points and the fitted potential as discussed above indicates that our potential function is no worse than comparable ion–water potentials published so far. It can be assumed to be more reliable than potentials constructed from standard molecular mechanics parameters or combination rules. Since for our system it describes a shallow energy surface with subtle hydrogen bonding features, it should be mentioned that its parameters are certainly not transferable and that only subsequent computer simulations can demonstrate its accuracy.

No intramolecular potential for NO_3^- seems to have been described in the literature yet. In order to be able to perform future simulation studies with flexible nitrate anion, we prepared a simple intramolecular potential function compatible with the $\text{NO}_3^-/\text{H}_2\text{O}$ potential described above. A comparison of the quantum chemically calculated harmonic spectrum with a force-field-based one was performed. The matrix of the second derivative of the energy with respect to the Cartesian coordinates was obtained by quantum chemical calculations and was converted into a function of the six internal coordinates $\Delta r_{\text{N}-\text{O}}$, $\Delta\angle_{\text{O}-\text{N}-\text{O}}$ and \angle_{OOP} where the Δr and $\Delta\angle$ values are the deviations of the bond length and bond angles from the equilibrium values and \angle_{OOP} is the out-of-plane angle describing the pyramidal distortion of NO_3^- . It can be defined as 90° minus the angle between the vector perpendicular to the $\text{O}_1-\text{N}-\text{O}_2$ plane and the vector from N to O_3 :

$$V_{\text{intra}} = \frac{1}{2} \sum_{i=1}^6 f_{ii} D_i D_i + \sum_{i \neq j=1}^6 f_{ij} D_i D_j. \quad (2)$$

Here the three distances Δr , the two independent angular internal coordinates $\Delta\angle$, and the out-of-plane angle (\angle_{OOP}) are abbreviated D_1-D_6 . This function was used in molecular dynamics calculations, and the vibrational spectrum was subsequently extracted from the trajectories of the atoms by the usual Fourier-transform methods. The results showed that for NO_3^- even modest accuracy in reproducing intramolecular vibrational frequencies requires the inclusion of the terms in the second sum in formula (2), the harmonic cross terms. On the other hand, the inclusion of anhar-

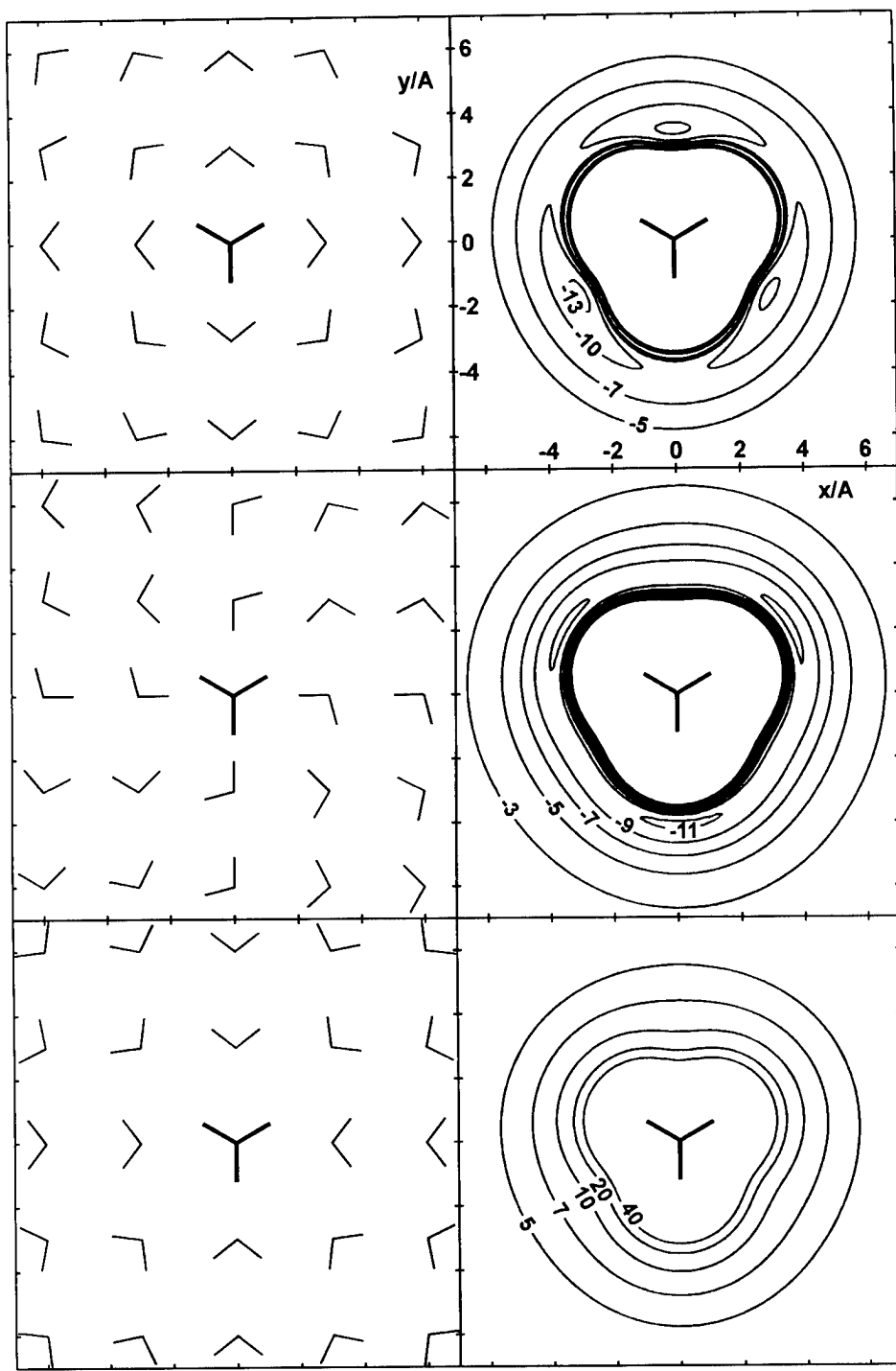


FIGURE 5. Contour plots of the nitrate–water energy surface (right side) together with pictures of the respective water orientations (left side) for three typical orientations. The water molecule is located in the plane of the nitrate anion. The contour map on top contains the global energy minimum at the HF/6-311G + (d, p) level of theory.

monicity has a much smaller effect as was found by augmenting formula (2) by correction terms incorporating the first anharmonicities along the normal modes. The largest anharmonic contribution to the energy is contributed by the cubic force constant f_{444} of the total symmetric mode. Its inclusion gives our final expression for the intramolecular force field:

$$V_{\text{intra}} = \frac{1}{2} \sum_{i=1}^6 f_{ii} D_i D_i + \sum_{i \neq j=1}^6 f_i D_j D_{ij} + \frac{1}{6} f_{444} S_4 S_4 S_4, \quad (3)$$

where S_4 is the coordinate $(\Delta r_{N-O1} + \Delta r_{N-O2} + \Delta r_{N-O3})/\sqrt{3}$.

The values of the force constants are given in Table III. The numerical values of the harmonic force constants were determined by calculations on the MP4/aug-cc-pVTZ level of theory. The cubic force constant f_{444} was obtained from five energy points at displacements of 0, ± 0.05 and ± 0.1 Å along the total symmetric normal mode S_4 by minimizing the least-square difference between their ab initio energies and the energies obtained from formula (3).

Summary

The system $\text{NO}_3^-/\text{H}_2\text{O}$ at the B3LYP/aug-cc-pVTZ level forms a planar complex with C_s symmetry and two distorted hydrogen bonds. The binding energy is -14.5 kcal/mol. The symmetric complex which is found to be stable at a lower theoretical level [HF/6-311G+(d,p)] is a saddle point about $+0.1$ kcal/mol higher in energy. A singly hydrogen-bonded complex is still $+2.4$ kcal/mol higher in energy. The vibrational frequencies of nitrate anion and of the complex

TABLE III
Force constants of the intramolecular potential of NO_3^- (atomic units).

f_{r1-r1}	0.4840
$f_{\alpha 1-\alpha 1}$	0.7130
f_{oop}	0.1748
f_{r1-r2}	0.0583
$f_{\alpha 1-\alpha 2}$	0.3565
$f_{\alpha 1-r1}$	0.0886
f_{444}	-1.3759

$\text{NO}_3^-/\text{H}_2\text{O}$ were calculated and are in good agreement with experimental results. The magnitude of the splitting of the asymmetric stretching mode due to symmetry lowering is similar to the experimental values found for aqueous nitrate solutions. It is therefore—at least in principle—possible that asymmetric anionic hydration causes the observed behavior. However, in view of the rather low binding energies of about 14 kcal/mol the absence of dynamic averaging remains to be understood.

Interaction potentials for $\text{NO}_3^-/\text{H}_2\text{O}$ were obtained from high-level ab initio calculations. Diagrams of the potential energy surface show that little energetic differences between linear, cyclic, or bifurcated hydrogen bonding exist. Configurations with hydrogen bonding from above or below the nitrogen atom are somewhat less favorable but still result in attractive interactions. An intramolecular force field for nitrate anion that includes the most important anharmonic terms was developed.

Work on molecular dynamics simulations of aqueous nitrate solutions incorporating the interaction potentials is in progress.

ACKNOWLEDGMENTS

Financial support from the Austrian FWF (project P10106-MOB) is gratefully acknowledged. The ab initio calculations were performed with the computer programs Gaussian 92 and 94 [24].

References

1. D. E. Irish, M. H. Brooker, in *Advances in Infrared and Raman Spektroskopie*, R. J. Clark and R. E. Hester, Eds. (Heyden, London-New York, 1976), Vol. 2, Chapter 6.
2. B. E. Conway, *Studies in Physical and Theoretical Chemistry* 12, (Elsevier, Amsterdam-Oxford-New York, 1981), Chapter 8.
3. R. E. Verall, in *Water: A Comprehensive Treatise*, F. Franks, Ed. (Plenum, New York, 1973), Vol. 31, Chapter 5.
4. A. M. de P. Nicholas and R. Wasylyshen, Can. J. Chem. 65, 951 (1987) and J. Phys. Chem. 89, 5446 (1985).
5. M. Nakahara, A. Adachi, H. Kiyoyama, A. Shimizu, Y. Taniguchi, and Y. Masuda, J. Phys. Chem. 94, 6179 (1990).
6. J. M. Howell, A. M. Sapse, E. Singman, and G. Snyder, J. Phys. Chem. 86, 2345 (1982).
7. M. Shen, Y. Xie, H. F. Schaefer, and C. A. Deakyne, J. Chem. Phys. 93, 3379 (1990).
8. M. Shen, Y. Xie, H. F. Schaefer, and C. A. Deakyne, Chem. Phys. 151, 187 (1991).

9. T. H. Dunning, Jr., and P. J. Hay, in *Modern Theoretical Chemistry: Methods of Electronic Structure Theory*, H. F. Schaefer III, Ed. (Plenum, New York, 1997), Vol. 3, p. 1.
10. G. Velders and D. Feil, *Theor. Chim. Acta* **84**, 195 (1992).
11. M. Probst, *Int. J. Quant. Chem.* **29**, 559 (1995).
12. A. Laaksonen and H. Kovacs, *Can. J. Chem.* **72**, 2278 (1994).
13. Y. Kataoka, *Bull. Chem. Soc. Jpn.* **66**, 2478 (1993).
14. T. Kato, S. Hayashi, M. Oobatake, and K. Katsunosuke, *J. Chem. Phys.* **99**, 3966 (1993); T. Kato, K. Machidae, M. Oobatake, and S. Hayashi, *J. Chem. Phys.* **93**, 3970 (1990); *J. Chem. Phys.* **92**, 5506 (1990); *J. Chem. Phys.* **89**, 7471 (1988); *J. Chem. Phys.* **89**, 3211 (1988).
15. R. Krishnan, J. S. Binkley, R. Seeger, and J. A. Pople, *J. Chem. Phys.* **72**, 650 (1980).
16. A. D. McLean and G. S. Chandler, *J. Chem. Phys.* **72**, 5639 (1980).
17. T. H. Dunning, Jr., *J. Chem. Phys.* **90**, 1007 (1989); R. A. Kendall, T. H. Dunning, Jr., and R. J. Harrison, *J. Chem. Phys.* **96**, 6796 (1992); D. E. Woon and T. H. Dunning, Jr., *J. Chem. Phys.* **98**, 1358 (1993).
18. T. J. Findlay and M. C. Symons, *J. Chem. Soc. Faraday Trans. II* **72**, 820 (1976).
19. D. E. Irish and A. R. Davis, *Can. J. Chem.* **46**, 943 (1968).
20. S. Huzinaga, J. Andzelm, M. Klobukowski, E. Radzio-Andzelm, Y. Sakai, and H. Tatewaki, in *Gaussian Basis Sets for Molecular Calculations* (Elsevier, Amsterdam, 1984).
21. N. Greenwood, *Chemie der Elemente* (VCh Verlag, Weinheim, 1990), p. 604.
22. C. M. Breneman and K. B. Wiberg, *J. Comp. Chem.* **11**, 361 (1990).
23. G. Lie and E. Clementi, *Phys. Rev. A* **33**, 2679 (1986).
24. M. J. Frisch, G. W. Trucks, H. B. Schlegel, P. M. W. Gill, B. G. Johnson, M. A. Robb, J. R. Cheeseman, T. A. Keith, G. A. Petersson, J. A. Montgomery, K. Raghavachari, M. A. Al-Laham, V. G. Zakrzewski, J. V. Ortiz, J. B. Foresman, C. Y. Peng, P. Y. Ayala, M. W. Wong, J. L. Andres, E. S. Replogle, R. Gomperts, R. L. Martin, D. J. Fox, J. S. Binkley, D. J. Defrees, J. Baker, J. P. Stewart, M. Head-Gordon, C. Gonzalez, and J. A. Pople, *Gaussian 94*, Gaussian, Inc., Pittsburgh, PA, 1995.

The Interface of Electronic Structure and Dynamics for Reactions in Solution

YAO-YUAN CHUANG, CHRISTOPHER J. CRAMER,
DONALD G. TRUHLAR

Department of Chemistry and Supercomputer Institute, University of Minnesota, Minneapolis,
Minnesota 55455

Received 24 March 1998; accepted 25 June 1998

ABSTRACT: We compare two systematic approaches to the calculation of reaction rates in liquid solutions: the separable equilibrium solvation (SES) approximation and the equilibrium solvation path (ESP) approximation. These approaches are tested for two reactions, $\text{ClCH}_3 + \text{NH}_3 \rightarrow \text{Cl}^- + \text{H}_3\text{CNH}_3^+$ (R1) and $\text{NH}_4^+ \cdots \text{N}'\text{H}_3 \rightarrow \text{NH}_3 \cdots \text{N}'\text{H}_4^+$ (R2), both in aqueous solution. The first reaction illustrates the importance of variational optimization of the transition state, and the second illustrates the importance of tunneling. Free energies of solvation are calculated by the Solvation Model 5. All calculations are carried out by the new AMSOLRATE program, which is an interface of the AMSOL and POLYRATE programs. © 1998 John Wiley & Sons, Inc. Int J Quant Chem 70: 887–896, 1998

Introduction

The interface of electronic structure theory with dynamics has received considerable attention in recent years, especially in conjunction with transition-state theory [1]. Most of this work has been concerned with gas-phase reactions, and systematically improved methods [2, 3] have been developed that require the representation of the potential energy only in a valley [4] centered on the minimum-energy path (MEP) or in a somewhat

wider region [5] called the reaction swath. The present article summarizes two systematic ways to extend this kind of theory to reactions in solution and illustrates them for two reactions. Both approaches involve equilibrium solvation; however, in the first approach, the calculation is based on the gas-phase MEP, whereas in the second approach, the calculation is based on the equilibrium solvation path [6] (ESP). For completeness, we should mention a third possible approach, in which solvation is not assumed to be at equilibrium with the solvent at all points along the reaction path [7]. (Nonequilibrium solvation is sometimes called nonadiabatic or dynamic solvation, in which case equilibrium solvation is called adiabatic or static.)

Correspondence to: D. G. Truhlar.

Contract grant sponsor: National Science Foundation.

We will use the following shorthand notation for these three approaches:

SES: Separable equilibrium solvation—The free energy of solvation at a fixed solute geometry is added to the gas-phase free energy using gas-phase geometries for reactants, products, intermediates, and transition states and using gas-phase reaction paths. While the reaction path remains constant in coordinate space, the position of the potential energy (and free energy) maximum *along* the path can be shifted.

ESP: Equilibrium solvation path—One defines a solution-phase potential of mean force by

$$W(\mathbf{R} | T) = V(\mathbf{R}) + \Delta G_s^0(\mathbf{R} | T), \quad (1)$$

where $W(\mathbf{R} | T)$ is the free energy of a solute molecule in a solution as a function of the solute coordinates \mathbf{R} and the temperature T , $V(\mathbf{R})$ is the Born–Oppenheimer potential energy in the gas phase, and $\Delta G_s^0(\mathbf{R} | T)$ is the standard-state free energy of solvation of a solute with geometry \mathbf{R} and temperature T . This represents additional flexibility over SES in the sense that the location of the transition state may now move not only along the gas-phase reaction path but also perpendicular to it in the remaining $3N - 7$ degrees of freedom.

NES: Nonequilibrium solvation—This approach requires including solvent coordinates in the definition of geometries and reaction paths.

A complete microscopic description of a reaction in solution must consider nonequilibrium solvation [7–10],* but we can learn a lot with the SES and ESP approaches. Thus, our first goal was to systematize these approaches. Our motivation for this follows from the observation that systematically defined procedures can be tested, validated, and incorporated in user-friendly computer packages much more readily than can nonsystematized methods.

Solvation effects on transition-state structures have also been considered by previous researchers, notably by Bertrán and Rivail and coworkers [11–13]. Bertrán et al. [12] distinguished three options: Option 1 is identical to the SES approach

with conventional transition-state theory (i.e., assuming the dynamical bottleneck is at the gas-phase saddle point); option 2 is identical to the SES approach with variational transition-state theory; and option 3 is equivalent to the ESP approach. Bertrán et al. [12] did not consider tunneling. In the present article, tunneling in solution is calculated by treating solute modes in the ground-state transmission-coefficient approximation [14–16] and solvent modes by the zero-order canonical mean shape (CMS-0) approximation, which is presented in a previous article [7]. The CMS-0 approximation is discussed further in the second section of this article.

The second section presents the dynamical theory for generalized transition-state theory calculations based on the SES and ESP approaches. The third section discusses the interface of electronic structure theory and dynamics for solution-phase reactions. The fourth section presents applications to two prototype reactions. The applications were carried out with a new computer program called AMSOLRATE. The fifth section contains concluding remarks.

Dynamical Theory

The theory for variational transition-state theory in solution was given previously [9, 10]. The theory for including semiclassical transmission coefficients to account for tunneling was given previously [7]. Here, we summarize the essential formulas.

In canonical variational theory (CVT), the rate constant at temperature T for a bimolecular reaction in solution, assuming it is not diffusion-controlled, is given by [9, 10]

$$k^{\text{CVT}}(T) = \frac{\tilde{k}T}{hC^0} \exp\left\{-[G^0(\text{CVT} | T) - G^0(\mathbf{R} | T)]/\tilde{k}T\right\}, \quad (2)$$

where \tilde{k} is Boltzmann's constant, h is Planck's constant, C^0 is the concentration corresponding to the standard state, $G^0(\mathbf{R} | T)$ is the solution-phase standard-state free energy of reactants at temperature T , and $G^0(\text{CVT} | T)$ is the solution-phase standard-state free energy of the canonical variational transition state at temperature T . The latter is given by

$$G^0(\text{CVT} | T) = \max_s G^0(\text{GT}, s | T), \quad (3)$$

* An extensive review of nonequilibrium solvation theories is given in [1].

where $G^0(\text{GT}, s | T)$ is the solution-phase standard-state free energy at temperature T of a generalized transition state (GT) located at a signed value s of the reaction coordinate. (A generalized transition state is a trial choice of a variational transition state with $s \neq 0$.) The value of s that maximizes $G^0(\text{GT}, s | T)$ is called the canonical variational transition-state location. The free energies are, in turn, given by [17]

$$G^0(X, T) = W(\mathbf{R}_X | T) + G_{\text{RVE}}(X | T), \quad (4)$$

where $W(\mathbf{R}_X | T)$ is given by Eq. (1) for species X (X is R or GT) at its classical equilibrium geometry, which is denoted \mathbf{R}_X , and $G_{\text{RVE}}(X | T)$ is the rovibronic internal free energy of species X at temperature T relative to a nondegenerate, structureless, motionless particle at equilibrium (where X is R) or at position s on the reaction path (when X is GT). Note that $\Delta G_s^0(\mathbf{R} | T)$ in Eq. (1) is evaluated using the same concentration for the standard state in both the gas phase and solution. In the SES approximation, $G_{\text{RVE}}(X | T)$ in Eq. (4) is evaluated from the gas-phase potential $V(\mathbf{R})$, whereas in the ESP approximation, $G_{\text{RVE}}(X | T)$ is evaluated from the potential of mean force $W(X | T)$. At transition states, one omits the imaginary frequency mode (which is the reaction coordinate) in calculating $G_{\text{RVE}}(\text{GT}, s = 0 | T)$ so that $G^0(\text{GT}, s = 0 | T)$ is actually a free energy of activation rather than a true free energy; one also omits the reaction coordinate from $G_{\text{RVE}}(\text{GT}, s | T)$ at generalized transition states, and, therefore, $G^0(\text{GT}, s | T)$ is a generalized free energy of activation. A plot of $G^0(\text{GT}, s | T)$ versus s is sometimes called a free-energy profile.

Tunneling is more complicated. In general, tunneling is included by multiplying $k^{\text{CVT}}(T)$ by a transmission coefficient $\kappa(T)$. For gas-phase reactions, $\kappa(T)$ is evaluated using the ground-state transmission coefficient approximation, as described previously [14–16]. For solution-phase reactions, $\kappa(T)$ is evaluated by treating solute modes by the ground-state transmission-coefficient approximation [14–16] and treating solvent modes by the canonical-mean-shape (CMS) approximation, also described previously [7]. We can express these two approximations in a unified approximation as follows:

$$\kappa(T) = \frac{\int_0^\infty dE P(V_1, V_2 | E) \exp(-E/\tilde{k}T)}{\int_{V_2[s_*^{\text{CVT}}(T)]}^\infty dE \exp(-E/\tilde{k}T)}, \quad (5)$$

where E is total energy, $P(V_1, V_2 | E)$ is the transmission probability at energy E using $V_1(\mathbf{R})$ as the effective multidimensional potential and $V_2(s)$ as the effective adiabatic potential, and $s_*^{\text{CVT}}(T)$ is the location of the canonical variational transition state at temperature T . For gas-phase reactions (ground-state approximation), we have

$$V_1(\mathbf{R}) = V(\mathbf{R}) \quad (6)$$

and

$$V_2(s) = V_a^G(s), \quad (7)$$

where $V_a^G(s)$ is the vibrationally adiabatic ground-state potential given by [14–16]

$$V_a^G(s) = V_{\text{RP}}(s) + G_{\text{RVE}}(\text{GT}, s | T = 0), \quad (8)$$

where $V_{\text{RP}}(s)$ is $V(\mathbf{R})$ evaluated along the reaction path. For solution-phase reactions (ground-state approximation for solute modes and CMS approximation for solvent modes), we have

$$V_1(\mathbf{R} | T) = U(\mathbf{R} | T) \quad (9)$$

and

$$V_2(s) = U_{\text{RP}}(s | T) + V_a^G(s) - V_{\text{RP}}(s), \quad (10)$$

where $U(\mathbf{R} | T)$ is the CMS potential given by

$$U(\mathbf{R} | T) = W(\mathbf{R} | T) + \beta \frac{\partial W(\mathbf{R} | T)}{\partial \beta}. \quad (11)$$

β is $(\tilde{k}T)^{-1}$, and $U_{\text{RP}}(s | T)$ is $U(\mathbf{R} | T)$ evaluated along the reaction path.

We will employ a further approximation, denoted the zero-order canonical mean shape (CMS-0) approximation in our previous work [7], namely, we neglect the temperature derivative in Eq. (11). As pointed out previously [7], the CMS-0 approximation is justified when thermally excited bath-mode frequencies are approximately independent of s over the range of s important for tunneling. This should be a reasonable approximation in many cases.

The meaning of “conventional transition state theory” (TST) is ambiguous for solution-phase reactions. What we shall mean by this is placing the generalized transition state at $s = 0$, which denotes the location of the gas-phase saddle point in SES calculations and denotes the location of the liquid-phase saddle point in ESP calculations. An alternative definition that one might consider for the ESP case is the location of the maximum of U_{MEP} ; we call this choice VTST (max U_{MEP}).

The above formulation is general enough to encompass all of the standard tunneling approximations in the POLYRATE computer program [15, 16, 18], namely zero-curvature tunneling (ZCT) [14], small-curvature tunneling (SCT) [15, 19], large-curvature tunneling (LCT) [15, 20, 21], and microcanonical-optimized multidimensional tunneling (μ OMT) [21].

The formulas given above also apply to unimolecular reactions provided one makes a single change: C^0 is replaced by unity in Eq. (2).

Interface of Dynamics with Electronic Structure

In the SES approximation, stationary points (reactants and products) are optimized using $V(\mathbf{R})$, the reaction path is calculated using $V(\mathbf{R})$, and $G_{\text{RVE}}(X | T)$ is computed using $V(\mathbf{R})$ for gas-phase species. In the ESP approximation, stationary points are optimized using $W(\mathbf{R} | T)$, the reaction path is calculated using $W(\mathbf{R} | T)$, and $G_{\text{RVE}}(X | T)$ is computed using $W(\mathbf{R} | T)$ for solution-phase species.

To carry out the calculations, we interfaced the POLYRATE computer program with the AMSOL computer program using of an interface program called AMSOLRATE [22].

We calculated $V(\mathbf{R})$ by the Parametrized Model 3 (PM3) [23] version of the neglect-of-diatom-differential-overlap [24] molecular orbital theory. Although the PM3 model is not quantitatively accurate for $V(\mathbf{R})$, it is adequate for the present work where the goal is to demonstrate dynamical approximations. We calculated $\Delta G_s^0(\mathbf{R} | T)$ by the SM5.4/PM3 [25] and SM5.2R/PM3 [26] solvation models.

At this point, it might be useful to interject a note about consistency. In particular, we note that the SM5.4 solvation model was parameterized, allowing the solute geometry to relax in solution, while the SM5.2R solvation model was parameterized using gas-phase geometries in solution. Thus, a purist might insist that the SM5.4 model not be used in SES calculations and the SM5.2R model not be used in ESP calculations. But that would be inconsistent with general usage of semiempirical models in other contexts. For example, the gas-phase PM3 model was parameterized for heats of formation, yet is routinely used for predicting electronic energies. Similarly, semiempirical methods are often parametrized by matching fixed- \mathbf{R} dipole

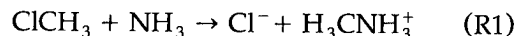
moments to experimental ones, which are vibrationally averaged. In this spirit, one may use either solvation model with either dynamical approximation. In the present article, we used both models with the SES approximation, and the SM5.4 model with the ESP approximation, for a total of three combinations.

The SES calculations will be denoted SM5.4/PM3//PM3 and SM5.2R/PM3//PM3 since they are based on gas-phase PM3 geometries, reaction paths, and vibrational potentials. The ESP calculations will simply be denoted SM5.4/PM3 since solvation is fully included in optimizing geometries and calculating reaction paths and vibration potentials.

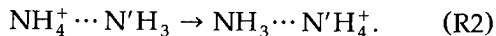
Results

All calculations in this article are for $T = 298 \text{ K}$, and the solvent for all liquid-phase reactions is water. All values of U are evaluated in the CMS-0 approximation. All information (i.e., geometries, energies, gradients, and Hessians) required for the dynamics calculations was obtained from the computer program AMSOL, and the reaction rates were calculated using the AMSOLRATE package [22]. Although solution-phase calculations were carried out with the AMSOLRATE program, as a check we compared gas-phase calculations with AMSOLRATE to gas-phase calculations carried out with the MORATE [20, 27] package, and we obtained the same result within the accuracy afforded by the numerical derivatives.

Two reactions are used to illustrate the differences between the SES and ESP approximations:



and



R1 is the widely studied [12, 28, 29] Menshutkin reaction, and R2 is a symmetrical unimolecular proton-transfer reaction.

Even though there is a van der Waals complex and an ion-pair complex along the reaction path of R1, we treat it as a bimolecular reaction. Although R2 is a unimolecular reaction, we nevertheless considered a Boltzmann-weighted continuum of tunneling energies in Eq. (5).

For both-reactions, we scaled [30] the coordinate system to a reduced mass μ of 1 amu, and the frequencies along the reaction path were evaluated

in the harmonic approximation by a transformation to redundant internal coordinates [31]. Zero-, small-, and large-curvature tunneling calculations were carried out with 30 quadrature points for each action integral, and they were Boltzmann-averaged using 30 energies. For reaction R1, we followed the reaction path with the Page-McIver [32] algorithm with a step size $0.01 a_0$ over the range of $-4.0 a_0 \leq s \leq 2.0 a_0$ for the gas phase and over the range $-2.0 a_0 \leq s \leq 1.56 a_0$ for solution. Hessians were obtained using central differences with a step size of $0.013 a_0$ for the gas phase and $0.009 a_0$ for solution at each step. For reaction R2, we followed the reaction path with the Page-McIver method [32] with a gradient step size equal to $0.015 a_0$ over the range $-1.3 a_0 \leq s \leq 1.3 a_0$ for both the gas and solution phases. Hessians were calculated using the central difference algorithm with a numerical step size of $0.011 a_0$ for both the gas phase and solution at each gradient step.

Table I gives the optimized values of the making and breaking bond distances of the stationary points for reactions R1 and R2 in both the gas phase (PM3) and aqueous solution phase (SM5.4/PM3). Table II gives free energies of solvation, Table III gives values of U at the saddle point and product (both relative to reactants), and Figures 1–4 show $U_{RP}(s | T)$ plotted both as a function of s and as a function of the difference in the making and breaking bond lengths.

We see for reaction R1 that the C—N bond distance at the saddle point is 0.3 Å shorter in the gas phase than in the aqueous solution, and the C—Cl bond is 0.3 Å longer. This results in a large

TABLE I
Bond lengths in Å.

R1-PM3	r_{NC}	r_{CCl}
Reactant	∞	1.764
van der Waals complex	3.785	1.767
Saddle point	1.762	2.269
Ion pair	1.473	2.718
Ionic products	1.495	∞
R1-SM5.4 / PM3	r_{NC}	r_{CCl}
Reactant	∞	1.777
Saddle point	2.063	2.094
Product	1.481	∞
R2-PM3	r_{NH}	r_{NH}
Reactant	1.048	1.721
Saddle point	1.302	1.302
Product	1.721	1.048
R2-SM5.4 / PM3	r_{NH}	r_{NH}
Reactant	1.022	1.789
Saddle point	1.290	1.290
Product	1.789	1.022

shift in the position of the maximum of U in the SES approximation compared to its position in the ESP approximation in Figure 1, and it results in large differences in the SES and ESP free energies of solvation of the stationary points of R1 in Table II. As a consequence, applying conventional transition-state theory with the free energies of solvation added to the gas-phase-optimized stationary points gives a very inaccurate reaction rate for R1, as shown in Table IV. However, this does not mean that the gas-phase reaction path is not useful. In particular, it can still be useful for reasonably accurate calculations on reaction R1 if one employs variational transition-state theory.

TABLE II
Standard-state free energy of solvation in kcal/mol.

		SM5.2R / PM3 // PM3	SM5.4 / PM3 // PM3	SM5.4 / PM3
R1	NH ₃	4.3	−3.5	−3.6
	CH ₃ Cl	−0.8	−0.5	−0.5
	ClCH ₃ ... NH ₃	−4.1	−4.0	
	Cl ... CH ₃ ... NH ₃	−41.5	−40.7	−14.7
	Cl [−] ... CH ₃ NH ₃ ⁺	−32.7	−32.6	
	Cl [−]	−77.0	−77.2	−77.2
	CH ₃ NH ₃ ⁺	−79.1	−78.2	−78.5
R2	NH ₄ ⁺ ... NH ₃	−81.0	−72.7	−73.8
	NH ₃ ... H ⁺ ... NH ₃	−74.6	−69.0	−71.2
	NH ₃ ... NH ₄ ⁺	−81.0	−72.7	−73.8

TABLE III
Energetics of R1 and R2 in kcal/mol.^a

Reaction	Method	$U(s=0) - U^R$	$U^P - U^R$
R1	PM3	41.2	119.9
	SM5.2R / PM3 // PM3	4.0	-32.2
	SM5.4 / PM3 // PM3	4.4	-31.7
	SM5.4 / PM3	21.6	-31.7
R2	PM3	9.5	0.0
	SM5.2R / PM3 // PM3	15.9	0.0
	SM5.4 / PM3 // PM3	13.3	0.0
	SM5.4 / PM3	13.7	0.0

^aR and P denote values at reactant and product, respectively.

In Figure 1, we observe that in the SES approximation the maximum of $U_{RP}(s|T)$ for R1 is shifted $1.47a_0$ (in mass-scaled coordinates) toward the reactant side. However, by plotting $U_{RP}(s|T)$ versus the difference in the C—N and C—Cl bond lengths in Figure 2, we see that both the SES and ESP approximations give similar classical barriers for this reaction. In the ESP approximation, the barrier in $U_{RP}(s|T)$ is 21.6 kcal/mol, whereas in the SES approximation, the variational maxima $U(s|T)$ calculated by the SM5.2R/PM3//PM3 and SM5.4/PM3//PM3 approximations are 22.3 and

21.9 kcal/mol, respectively. Of course, the reaction rates also depend on the geometries and frequencies, and different partition functions are used to compute the reaction rates in the SES and ESP approximations. Thus, Table IV shows that the SM5.4/PM3//PM3 and SM5.4/PM3 estimations of the CVT rate constant differ by factor of 2. We found that the dominant tunneling mechanism is the small-curvature one, and it increases the rate by a factor of 2.5–2.7, which is similar to the magnitude of the tunneling effect in the gas phase [29].

Now we turn to reaction R2. The lowest real frequency mode, which corresponds to the internal rotation of the two NH_3 subgroups around the N—H—N' axis, is hard to calculate precisely without analytical Hessians. In addition, the semiempirical method is not reliable for such a mode. Preliminary calculations with both MORATE and AMSOLRATE and showed that the frequency of this mode does not vary strongly with s . We therefore set the frequency of this mode equal to a constant along the whole reaction path. For the gas-phase calculation, this constant was set equal to 34.6 cm^{-1} , which we obtained using the GAUSSIAN94 program [33] at the MP2/6-31G** level [34, 35] for the reactant com-

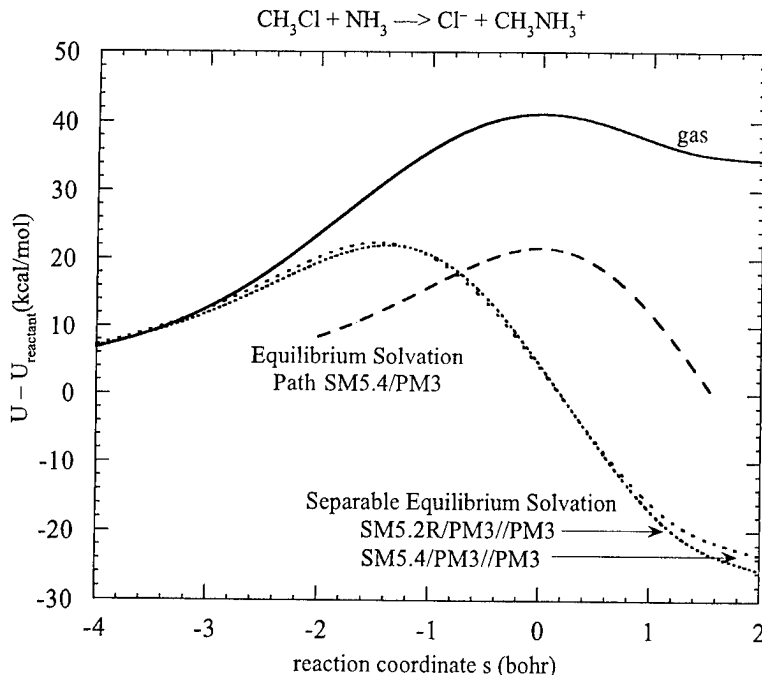


FIGURE 1. Adiabatic potential curves U for reaction R1 in the gas phase as calculated by PM3 and in aqueous solution as calculated by SM5.2R / PM3 // PM3, SM5.4 / PM3 // PM3, and SM5.4 / PM3 as functions of the reaction coordinate s .

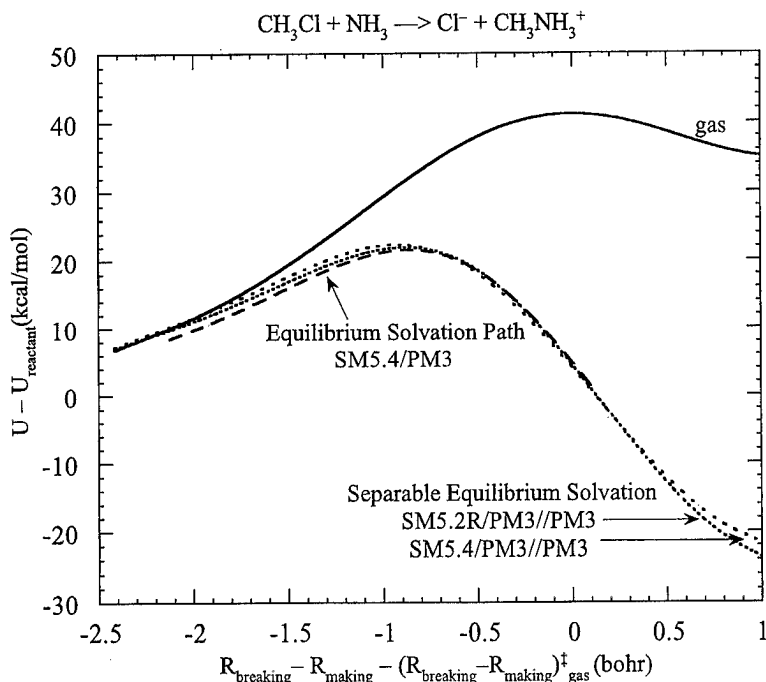


FIGURE 2. Adiabatic potential curves U for reaction R1 in the gas phase as calculated by PM3 and in aqueous solution as calculated by SM5.2R / PM3 // PM3, SM5.4 / PM3 // PM3, and SM5.4 / PM3 as functions of the making and breaking bond distances from the gas-phase saddle-point geometry.

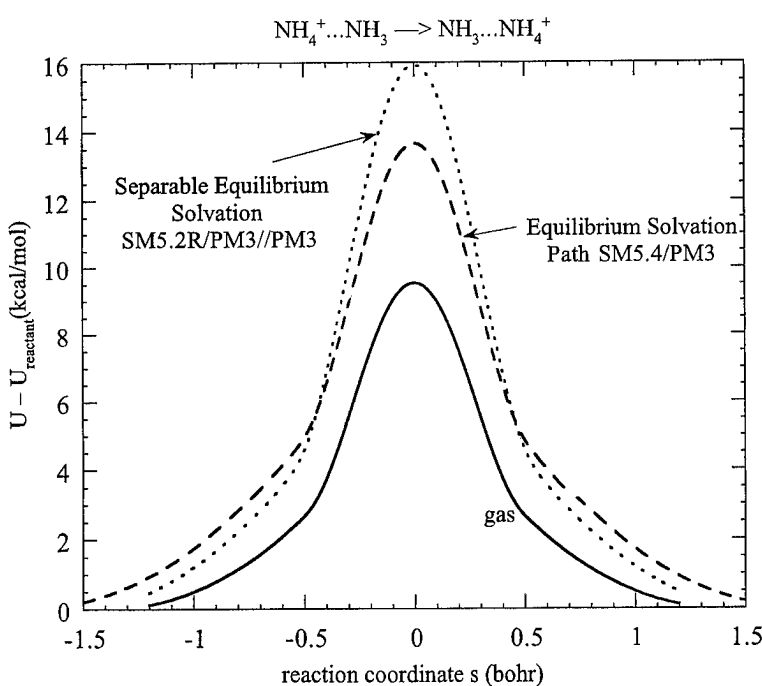


FIGURE 3. Adiabatic potential curves U for reaction R2 in the gas phase as calculated by PM3 and in aqueous solution as calculated by SM5.2R / PM3 // PM3 and SM5.4 / PM3 as functions of the reaction coordinate s .

plex. For the aqueous-phase calculation, this constant was set equal to 50 cm^{-1} , which is an average value from SM5.4//PM3 calculations at different values of s . The partition function of this mode was evaluated by a hindered-rotor approximation [36]. We found that in the gas-phase calculation the hindered-rotor partition function differed by about 5% from the free-rotor limit, and for the solution case, it differed by about 10% from the free-rotor limit. Thus, the results are not sensitive to the frequency of this mode after all.

The SM5.2R//PM3 method overestimates the effective barrier height by 2.3 kcal/mol (Fig. 3), and the SM5.4//PM3 method underestimates it by 0.5 kcal/mol (Fig. 4). Therefore, Table V shows a larger TST reaction rate in the SM5.4//PM3 case than in the SM5.4/PM3 case.

Table V shows the tunneling effect for reaction R2. The tunneling is dominated by the large-curvature mechanism. The increase in the unimolecular rate constant due to tunneling is very sensitive to the level of theory. For quantitatively meaningful results, it is clear that very careful choices of gas- and liquid-phase methods must be made.

Concluding Remarks

In this article, we illustrated two different methods for calculating reaction rates in solution. The SES approximation utilizes the reaction path obtained from a gas-phase calculation and then solvates each configuration along the reaction path. This is compared with the ESP approximation where the free energy of solvation is included while following the reaction path. For the Menshutkin reaction, we observed that even though the saddle-point geometries differ in the gas phase and in solution, the SES approximation is still applicable within a factor of 2 when the same solvation model (SM5.4/PM3) is employed. For proton transfer between ammonium and ammonia, the ESP approximation gives a rate constant about $3\frac{1}{2}$ times smaller than the SES approximation when tunneling is neglected, but tunneling reduces the difference to about a factor of 2. In general, the ESP approximation provides a more complete approach to studying the dynamics in solution; however, the SES method is an affordable

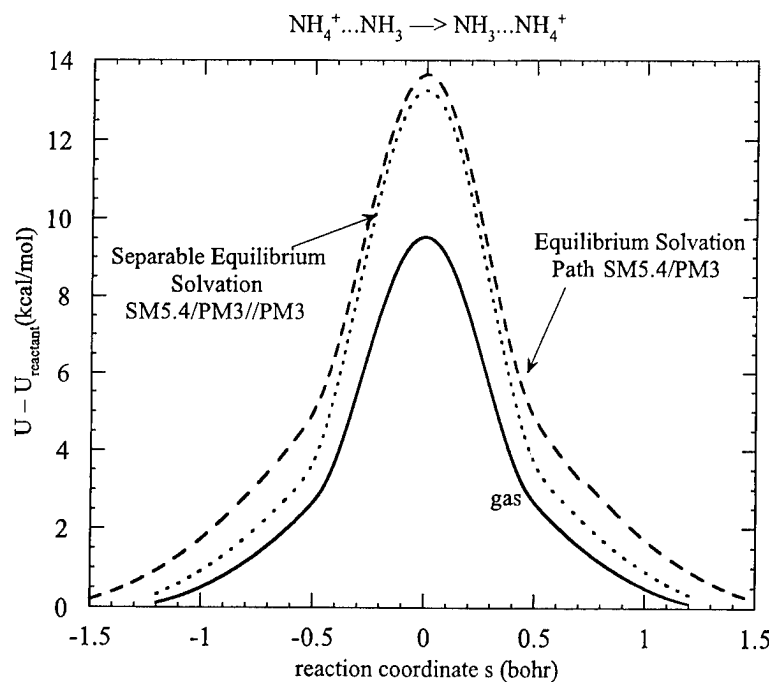


FIGURE 4. Adiabatic potential curves U for reaction R2 in the gas phase as calculated by PM3 and in aqueous solution as calculated by SM5.4 / PM3 // PM3 and SM5.4 / PM3 as functions of the reaction coordinate s .

TABLE IV
Rate constants of reaction R1 at 298 K.

	k (in 10^{-31} cm 3 / molecule $^{-1}$ s $^{-1}$)		
	SES		ESP SM5.4 / PM3
	SM5.2R / PM3 // PM3	SM5.4 / PM3 // PM3	
TST	1.5E13	2.8E12	5.3
VTST(max U_{MEP})	2.6 ^a	2.1 ^b	^c
CVT	2.5 ^d	2.0 ^e	4.6 ^f
CVT / ZCT	5.7	4.6	11.2
CVT / SCT	6.2	4.9	11.8
CVT / LCT	5.8	4.6	11.3
CVT / μ OMT	6.2	4.9	11.8

^a Max of U_{MEP} occurs at $s_*^{MEP} = -1.46$ bohr. Results denoted VTST (max U_{MEP}) are obtained by finding the maximum of $W(GT, s | T)$ rather than $G^0(GT, s | T)$.

^b Max of U_{MEP} occurs at $s_*^{MEP} = -1.40$ bohr.

^c Same as above because the maximum of U_{MEP} occurs at the conventional transition state in the ESP method.

^d Variational transition state occurs at $s_*^{MEP} = -1.41$ bohr.

^e Variational transition state occurs $s_*^{MEP} = -1.35$ bohr.

^f Variational transition state occurs at $s_*^{MEP} = -0.07$ bohr.

TABLE V
Rate constants of reaction R2 at 298 K.

	k (in s $^{-1}$)		
	SES		ESP SM5.4 / PM3
	SM5.2R / PM3 // PM3	SM5.4 / PM3 // PM3	
TST	1.8E4	1.8E6	4.9E5
VTST(max U_{MEP})	1.8E4	1.8E6	^a
CVT	1.8E4	1.8E6	4.9E5
CVT / ZCT	1.4E7	2.7E8	4.7E7
CVT / SCT	5.8E7	6.4E8	1.2E8
VT / LCT	2.5E8	1.6E9	8.1E8
CVT / μ OMT	2.5E8	1.6E9	8.1E8

^a Same as above because the maximum of U_{MEP} occurs at the conventional transition state in the ESP method.

approximation which will often be in reasonable agreement with the ESP method and can be employed economically with a variety of different electronic structure methods (e.g., a variety of ab initio methods) to obtain the gas-phase reaction path.

ACKNOWLEDGMENTS

This work was supported in part by the National Science Foundation.

References

- D. G. Truhlar, B. C. Garrett, and S. J. Klippenstein, *J. Phys. Chem.* **100**, 12771 (1996).

- J. C. Corchado, E. L. Coitiño, Y.-Y. Chuang, P. L. Fast, and D. G. Truhlar, *J. Phys. Chem. A* **102**, 2424 (1998).
- (a) W.-P. Hu, Y.-P. Liu, and D. G. Truhlar, *J. Chem. Soc., Faraday Trans.* **90**, 1715 (1994); (b) D. G. Truhlar, in *The Reaction Path in Chemistry: Current Approaches and Perspectives*, D. Heidrich, Ed. (Kluwer, Dordrecht, 1995), pp. 229–255; (c) Y.-Y. Chuang and D. G. Truhlar, *J. Phys. Chem. A* **101**, 3808 (1997).
- (a) L. Hofacker and Z. Naturforsch., A **18**, 607 (1963); (b) R. A. Marcus, *J. Chem. Phys.* **49**, 2610 (1968); (c) K. Fukui, *Acct. Chem. Res.* **14**, 363 (1981); (d) K. Morokuma and S. Kato, in *Potential Energy Surfaces and Dynamics Calculations*, D. G. Truhlar, Ed. (Plenum, New York, 1981), pp. 243–264; (e) W. H. Miller, *Ibid.*, pp. 265–286; (f) B. C. Garrett, D. G. Truhlar, and R. S. Grev, *Ibid.*, pp. 587–637.
- (a) V. K. Babamov and R. A. Marcus, *J. Chem. Phys.* **74**, 1790 (1978); (b) B. C. Garrett, D. G. Truhlar, A. F. Wagner, and T. H. Dunning, Jr., *J. Chem. Phys.* **78**, 4400 (1983); (c) B. C. Garrett and D. G. Truhlar, *J. Chem. Phys.* **79**, 4931

- (1983); (d) D. G. Truhlar, F. B. Brown, R. Steckler, and A. D. Isaacson, in *The Theory of Chemical Reaction Dynamics*, D. C. Clary, Ed. (D. Reidel, Dordrecht, 1986), pp. 285–329; (e) D. G. Truhlar and M. S. Gordon, *Science* **249**, 491 (1990).
6. S. C. Tucker and D. G. Truhlar, *J. Am. Chem. Soc.* **112**, 3347 (1990).
 7. D. G. Truhlar, Y.-P. Liu, G. K. Schenter, and B. C. Garrett, *J. Phys. Chem.* **98**, 8396 (1994).
 8. (a) J. T. Hynes, in *Theory of Chemical Reaction Dynamics*, M. Baer, Ed. (CRC Press, Boca Raton, FL, 1985), Vol. 4, pp. 172–234; (b) B. J. Gertner, K. R. Wilson, and J. T. Hynes, *J. Chem. Phys.* **90**, 3537 (1989); (c) D. G. Truhlar, G. K. Schenter, and B. C. Garrett, *J. Chem. Phys.* **98**, 5756 (1993); (d) M. V. Basilevsky, G. E. Chudinov, and D. V. Napolov, *J. Phys. Chem.* **97**, 3270 (1993); (e) B. C. Garrett and G. K. Schenter, ACS Symposium Series 568 (American Chemical Society, Washington, DC, 1994), p. 122; (f) C. J. Cramer and D. G. Truhlar, in *Solvent Effects and Chemical Reactivity*, O. Tapia and J. Bertrán, Eds. (Kluwer, Dordrecht 1996), pp. 1–80. (g) J. T. Hynes, *Ibid.*, pp. 231–258.
 9. M. M. Kreevoy and D. G. Truhlar, *Tech. Chem. (N.Y.)* **6**, 13 (1986).
 10. B. C. Garrett and G. K. Schenter, *Int. Rev. Phys. Chem.* **13**, 263 (1994).
 11. I. Tuñon, E. Silla, and J. Bertrán, *J. Chem. Soc., Faraday Trans.* **90**, 1757 (1994).
 12. J. Bertrán, J. M. Lluch, A. Gonzalez-Lafont, V. Dillett, and V. Pérez, ACS Symposium Series 568 (American Chemical Society, Washington, DC, 1994), p. 168.
 13. References are given in a review: J.-L. Rivail and D. Rinaldi, *Comp. Chem. Rev. Curr. Trends* **1**, 139 (1996).
 14. (a) B. C. Garrett and D. G. Truhlar, *J. Chem. Phys.* **72**, 3460 (1980); (b) B. C. Garrett, D. G. Truhlar, R. S. Grev, and A. W. Magnuson, *J. Phys. Chem.* **84**, 1730 (1980); (c) D. G. Truhlar and B. C. Garrett, *Acc. Chem. Res.* **13**, 440 (1980).
 15. D.-h. Lu, T. N. Troung, V. S. Melissas, G. C. Lynch, Y.-P. Liu, B. C. Garrett, R. Steckler, A. D. Isaacson, S. N. Rai, G. C. Hancock, J. G. Lauderdale, T. Joseph, and D. G. Truhlar, *Comp. Phys. Commun.* **71**, 235 (1992).
 16. R. Steckler, W.-P. Hu, Y.-P. Liu, G. C. Lynch, B. C. Garrett, A. D. Isaacson, V. S. Melissas, D.-h. Lu, T. N. Troung, S. N. Rai, G. C. Hancock, J. G. Lauderdale, T. Joseph, and D. G. Truhlar, *Comp. Phys. Commun.* **88**, 34 (1995).
 17. (a) A. Ben-Naim, *Solution Thermodynamics* (Plenum, New York, 1987). (b) A. Ben-Naim, *Statistical Thermodynamics for Chemists and Biochemists* (Plenum, New York, 1992). (c) D. J. Giesen, C. J. Cramer, and D. G. Truhlar, *J. Phys. Chem.* **98**, 4141 (1994).
 18. J. Corchado, Y.-Y. Chuang, P. L. Fast, J. Villa, E. L. Coitino, W.-P. Hu, Y.-P. Liu, G. C. Lynch, K. Nguyen, C. F. Jackels, M. Z. Gu, I. Rossi, S. Clayton, V. Melissas, R. S. Steckler, B. C. Garrett, D.-h. Lu, T. N. Troung, A. D. Isaacson, and D. G. Truhlar, POLYRATE 7.9 (University of Minnesota, 1998 [<http://comp.chem.umn.edu/polyrate>]).
 19. Y.-P. Liu, G. C. Lynch, T. N. Troung, D.-h. Lu, D. G. Truhlar, and B. C. Garrett, *J. Am. Chem. Soc.* **115**, 2408 (1993).
 20. T. N. Troung, D.-h. Lu, G. C. Lynch, Y.-P. Liu, V. S. Melissas, J. J. P. Stewart, R. Steckler, B. C. Garrett, A. D. Isaacson, A. González-Lafont, S. N. Rai, G. C. Hancock, T. Joseph, and D. G. Truhlar, *Comp. Phys. Commun.* **75**, 143 (1993).
 21. Y.-P. Liu, D.-h. Lu, A. González-Lafont, D. G. Truhlar, and B. C. Garrett, *J. Am. Chem. Soc.* **115**, 7806 (1993).
 22. Y.-Y. Chuang, Y.-P. Liu, and D. G. Truhlar, AMSOLRATE version 7.9 (University of Minnesota, 1998), based on POLYRATE version 7.9 [18] and on G. D. Hawkins, D. J. Giesen, G. C. Lynch, C. C. Chamber, I. Rossi, J. W. Storer, J. Li, D. Rinaldi, D. A. Liotard, C. J. Cramer and D. G. Truhlar, AMSOL version 6.5.1, University of Minnesota and Oxford Molecular Group, 1998.
 23. J. J. P. Stewart, *J. Comp. Chem.* **10**, 221 (1989).
 24. J. A. Pople and G. A. Segal, *J. Chem. Phys.* **43**, S129 (1965).
 25. C. C. Chambers, G. D. Hawkins, C. J. Cramer, and D. G. Truhlar, *J. Phys. Chem.* **100**, 16385 (1996).
 26. G. D. Hawkins, C. J. Cramer, and D. G. Truhlar, *J. Phys. Chem. B* **102**, 3257 (1998).
 27. Y.-Y. Chuang, P. L. Fast, W.-P. Hu, G. C. Lynch, Y.-P. Liu, and D. G. Truhlar, MORATE 7.9 (University of Minnesota, 1998) based on POLYRATE version 7.9 [18] and on J. J. P. Stewart, I. Rossi, W.-P. Hu, G. C. Lynch, Y.-P. Liu, and D. G. Truhlar, MOPAC version 507mn, University of Minnesota, 1997 [<http://comp.chem.umn.edu/morate>].
 28. (a) J. Gao, X. Xia, *J. Am. Chem. Soc.* **115**, 9667 (1993). (b) S. Shaik, A. Ioffe, A. C. Reddy, and A. Pross, *J. Am. Chem. Soc.* **116**, 262 (1994). (c) U. Maran, T. A. Pakkanen, and M. Karelson, *J. Chem. Soc., Perkins Trans. 2*, 2445 (1994). (d) U. Berg, M. Chanon, R. Gallo, and M. Rajzmann, *J. Org. Chem.* **60**, 1975 (1995). (e) E. Gawlitza, A. Szylhabbel-Godala, and P. Paneth, *J. Phys. Org. Chem.* **9**, 41 (1996). (f) V. Dillett, D. Rinaldi, J. Bertrán, J.-L. Rivail, *J. Chem. Phys.* **104**, 9437 (1996). (g) X. Fradera, L. Amat, M. Torrent, J. Mestres, P. Constans, E. Besalu, J. Martí, S. Simom, M. Lovato, J. M. Oliva, J. M. Luis, J. L. Andres, M. Sola, R. Carbo, and M. Duran, *Theochem* **271**, 171 (1996). (h) U. Maran, M. Karelson, and T. A. Pakkanen, *Theochem* **397**, 263 (1997). (i) T. N. Truong, T.-T. Y. Truong, and E. V. Stefanovich, *J. Chem. Phys.* **107**, 1881 (1997).
 29. A. González-Lafont, J. Villà, J. M. Lluch, J. Bertrán, R. Steckler, and D. G. Truhlar, *J. Phys. Chem.* **102**, 3420 (1998).
 30. D. G. Truhlar, A. D. Isaacson, and B. G. Garrett, in *Theory of Chemical Reaction Dynamics*, M. Baer, Ed. (CRC Press, Boca Raton, FL, 1985), Vol. 4, pp. 65–137.
 31. Y.-Y. Chuang and D. G. Truhlar, *J. Phys. Chem. A* **102**, 242 (1998).
 32. M. Page and J. W. McIver, Jr., *J. Chem. Phys.* **88**, 922 (1988).
 33. M. J. Frisch, G. W. Trucks, H. B. Schlegel, P. M. W. Gill, B. G. Johnson, M. A. Robb, J. R. Cheeseman, T. Keith, G. A. Petersson, J. A. Montgomery, K. Raghavachari, M. A. Al-Laham, V. G. Zakrzewski, J. V. Ortiz, J. B. Foresman, J. Cioslowski, B. B. Stefanov, A. Nanayakkara, M. Challacombe, C. Y. Peng, P. Y. Ayala, W. Chen, M. W. Wong, J. L. Andres, E. S. Replogle, R. Gomperts, R. L. Martin, D. J. Fox, J. S. Binkley, D. J. Defrees, J. Baker, J. P. Stewart, M. Head-Gordon, C. Gonzalez, and J. A. Pople, GAUSSIAN94 (Gaussian Inc., Pittsburgh, PA, 1995).
 34. M. J. Frisch, M. Head-Gordon, and J. A. Pople, *Chem. Phys. Lett.* **166**, 281 (1990).
 35. W. J. Hehre, R. Ditchfield, and J. A. Pople, *J. Chem. Phys.* **56**, 2257 (1972).
 36. D. G. Truhlar, *J. Comput. Chem.* **12**, 266 (1991).

The Development of Semiclassical Dynamical Methods and Their Application to Vibrational Relaxation in Condensed-Phase Systems

MICHAEL F. HERMAN

Department of Chemistry, Tulane University, New Orleans, Louisiana 70118

Received 23 March 1998; revised 3 June 1998; accepted 8 June 1998

ABSTRACT: A semiclassical surface-hopping propagator for problems involving nonadiabatic transitions is discussed. The propagator is employed in expressions for the probability of transitions between quantum states of molecules in condensed phases. This approach is implemented for the evaluation of the rate of vibrational transitions in liquids, dense gases, and clusters. Results for the rates of relaxation of excited vibrational states of a molecule in a simple solvent are discussed. The use of computationally simplifying short-time approximations for the solvent dynamics are considered. These approximations are tested using calculations on simple model systems. It is found that these simplifying approximations work well as long as the energy difference between the initial and final quantum states is not small. Calculations are also performed for the probability of resonant transfer of vibrational excitation energy between molecules in clusters using a mixed quantum-classical calculational procedure. It is found that quantum coherence effects are observed for several picoseconds in the probability for resonant transfer in these systems. © 1998 John Wiley & Sons, Inc. *Int J Quant Chem* 70: 897–907, 1998

Contract grant sponsor: NSF.

Contract grant number: CHE-9422786.

Contract grant sponsor: Center for Photoinduced Processes
at Tulane University.

Introduction

The rate at which molecules undergo transitions between quantum states in condensed phases plays an important role in energy relaxation and dissipation in these systems. The computational evaluation of these rates present difficult challenges. If the energy difference between the initial and final states is large compared with $K_B T$, then the quantum nature of the transition is often very important and must be accounted for in a calculation of the rate. On the other hand, the fact that these processes take place in condensed-phase systems requires that the evaluation of the rate involves an average over the multitude of configurations that are accessible to the system. Semiclassical approximations [1–3] can often provide useful procedures for studying these types of dynamical processes in condensed-phase systems. Semiclassical methods include important quantum aspects of the problem, including phase interference between different semiclassical amplitudes, while relying only on information obtained along classical trajectories.

In the work described here, semiclassical methods are employed for the calculation of the rate of vibrational energy relaxation in condensed-phase systems. Although this work is specialized on vibrational relaxation [4–21], the semiclassical methods are, in principle, applicable to other quantum transition processes as well. In this semiclassical description of the relaxation process, the rotational and translational degrees of freedom evolve along classical trajectories on the potential energy surface for the system in a given vibrational state. The transitions between vibrational states are accounted for by means of hops from the energy surface corresponding to the system in one vibrational state to the surface corresponding to another vibrational state. The momenta of the rotational and translational degrees of freedom are adjusted so as to conserve energy when the system undergoes the hop. This semiclassical surface hopping procedure is described in the subsection Semiclassical Surface-hopping Expression.... It is then applied to the propagation of the density in the subsection Surface-hopping Treatment.... An alternative quantum/classical propagation procedure that is appropriate for degenerate or very nearly degenerate transitions is described in the

subsection Quantum-Classical Approach.... The results for the time-dependent probability for transitions between vibrational states are presented in the third section. These transition probabilities exhibit quantum interference effects at short times, and this feature is examined in detail through model calculations. In the case of resonant transfer between the same vibrational state of identical molecules, the quantum coherence effects are found to persist for several picoseconds in model calculations.

Theory

SEMICLASSICAL SURFACE-HOPPING EXPRESSION FOR NONADIABATIC TRANSITIONS

It is useful in many problems to divide the system into "fast" coordinates, \mathbf{r} , and "slow" coordinates, \mathbf{R} . The division of molecular systems into "fast" electronic and "slow" nuclear coordinates is a familiar example. A quantum description is generally employed for the electronic coordinates within the Born–Oppenheimer approximation [22]. In many problems, semiclassical approximations [1–3] provide a very useful approach for treating the nuclear degrees of freedom, since semiclassical methods retain the important quantum interference aspects of the problem, while utilizing information from classical trajectories to evaluate approximate wave functions, state energies, transition amplitudes, etc.

The quantum time evolution of a wave function can be expressed as [23]

$$\psi(\mathbf{R}, t) = \int d\mathbf{R}_1 K(\mathbf{R}, \mathbf{R}_1, t) \psi(\mathbf{R}_1, 0), \quad (1)$$

where $K(\mathbf{R}, \mathbf{R}_1, t)$ is the propagator. The semiclassical expression for the propagator is given by [1]

$$K(\mathbf{R}, \mathbf{R}_1, t) = \sum \left[(-2\pi i\hbar)^{-d} \left| \frac{\partial^2 S}{\partial \mathbf{R} \partial \mathbf{R}_1} \right| \right]^{1/2} \times \exp(iS/\hbar), \quad (2)$$

where d is the dimensionality of \mathbf{R} , and $S(\mathbf{R}, \mathbf{R}_1, t)$ is the action for the classical trajectory that travels from \mathbf{R}_1 to \mathbf{R} in time t . The summation in (2) is over all classical trajectories which travel between \mathbf{R}_1 and \mathbf{R} in time t .

The Born–Oppenheimer approximation ignores the action of the kinetic energy operator for the

slow variables on the wave function for the fast degrees of freedom [22]. These neglected terms, which are called the nonadiabatic coupling, are responsible for transitions between the adiabatic (Born–Oppenheimer) states of the fast coordinates. For problems in which two or more adiabatic states are important, there is an energy surface, $E_j(\mathbf{R})$, corresponding to each of these states. These $E_j(\mathbf{R})$ are the fast variable adiabatic-state energies, and they depend on the slow coordinates \mathbf{R} . The semiclassical treatment of the slow degrees of freedom is considerably more difficult when there are several interacting adiabatic states, since there is no longer a *single*-energy surface on which to run the classical trajectories.

Various semiclassical methods have been developed for treating problems with nonadiabatic transitions [3, 24–42]. These include the effective path methods [24–27] which run trajectories on a single-energy surface obtained by averaging the fast variable Hamiltonian over the time-dependent fast variable wave function. The complex trajectory method of Miller and George [28] is another semiclassical technique for problems involving nonadiabatic transitions. This method integrates complex trajectories around the points where the surfaces cross in the space of complex values of the slow coordinates. Surface-hopping techniques represent a third class of semiclassical nonadiabatic methods [29–42]. In these methods, classical trajectories undergo discrete jumps between the different adiabatic energy surfaces. The work described in this article is based upon semiclassical surface-hopping procedures.

It can be shown that the propagator for a multi-surface nonadiabatic problem can be written as [41]

$$\begin{aligned} K_i(\mathbf{R}_f, \mathbf{R}_0, t) &= \varphi_i(\mathbf{R}_0) A_i \exp(iS_i/\hbar) \\ &+ \sum_j \varphi_j(\mathbf{R}_0) \int du_1 A_{ij} \sigma_{ij}(\mathbf{R}_1) \exp(iS_{ij}/\hbar) \\ &+ \sum_j \sum_k \varphi_k(\mathbf{R}_0) \int du_1 \int du_2 A_{ijk} \sigma_{ij}(\mathbf{R}_1) \\ &\quad \times \sigma_{jk}(\mathbf{R}_2) \exp(iS_{ijk}/\hbar) + \dots. \end{aligned} \quad (3)$$

The $\varphi_j(\mathbf{R})$'s are the adiabatic fast coordinate states. $K_i(\mathbf{R}_f, \mathbf{R}_0, t)$ is the semiclassical surface-hopping propagator for the system to be at \mathbf{R}_f in some $\varphi_j(\mathbf{R}_f)$ at time t , given that it was at \mathbf{R}_0 in state

$\varphi_i(\mathbf{R}_0)$ at time zero. The first term on the r.h.s. of (3), $\varphi_i(\mathbf{R}_0) A_i \exp(iS_i/\hbar)$, is the single-surface semiclassical propagator on energy surface $E_i(\mathbf{R})$, corresponding to adiabatic state φ_i . S_i and A_i are defined as in the usual single surface case given by (1) and (2). This term implicitly contains a sum over all classical trajectories on surface i that travel from \mathbf{R}_0 to \mathbf{R}_f in time t . This sum is not explicitly shown to simplify the notation.

The second term on the r.h.s. of (3) includes all contributions to the semiclassical nonadiabatic propagator that are first order in the nonadiabatic coupling. This term contains a summation overall all possible final states φ_j . The nonadiabatic coupling between the initial state φ_i and the final state φ_j is given by

$$\eta_{ij}(\mathbf{R}) = \langle \varphi_j(\mathbf{R}) | \nabla \varphi_i(\mathbf{R}) \rangle, \quad (4)$$

where ∇ is the gradient with respect to the “slow” coordinates, \mathbf{R} , and $\langle \dots \rangle$ denotes integration over the fast coordinates, \mathbf{r} . Since $\nabla \varphi_i(\mathbf{R})$ is a vector function, η_{ij} is also a vector. For a given j , the first-order term in the propagator includes contributions from paths that follow a classical trajectory in the slow coordinates on adiabatic energy surface $E_i(\mathbf{R})$ from \mathbf{R}_0 to a hopping point \mathbf{R}_1 . The trajectory then hops to surface $E_j(\mathbf{R})$ at this point and continues on this surface to the final point \mathbf{R}_f . The term includes all such hopping paths with a total propagation time of t . The energy is conserved in the hop by adjusting P_η , the component of the momentum which is parallel to $\eta_{ij}(\mathbf{R}_1)$. The hopping points, \mathbf{R}_1 , for this set of single-hop trajectories form a one-dimensional curve [41]. The u_1 integration in (3) is an integration over this curve. The condition that energy is conserved during the hop determines the magnitude of P_η , but not its sign. In general, hopping trajectories with both signs of P_η can contribute to the surface-hopping propagator [32]. The action for this hopping trajectory, S_{ij} , is just the sum of the classical actions for the two portions of the trajectory, before the hop and after the hop. The prefactor for the first-order term in the nonadiabatic propagator is given by [41]

$$A_{ij} = \left[(-2\pi i\hbar)^{-d} \left| \frac{P_{\eta j}}{P_{\eta i}} \right| \left| \frac{\partial^2 S_{ij}}{\partial \mathbf{R}_0 \partial \mathbf{R}_f} \right| \right]^{1/2}. \quad (5)$$

This prefactor has the same form as the prefactor for single-surface propagator, except for the addi-

tion of the factor $|P_{\eta_j}/P_{\eta_i}|$, which is the absolute value of ratio of the η component of the momentum after the hop and before the hop at \mathbf{R}_1 . The only remaining factor in the first-order contribution to the surface-hopping propagator is the transition amplitude [41]

$$\sigma_{ij} = - \left[\frac{P_{\eta_i} \pm P_{\eta_j}}{2P_{\eta_j}} \right] \eta_{ij}, \quad (6)$$

where the plus sign is used if P_{η_i} and P_{η_j} have the same sign and the minus sign is used if P_{η_i} and P_{η_j} have opposite signs. P_{η_i} and P_{η_j} are treated as positive quantities in (6), and η_{ij} is the magnitude of η_{ij} multiplied by the sign of $\mathbf{P}_i \cdot \eta_{ij}$.

The n th-order term in (3) contains contributions from trajectories with n intersurface hops. This requires an integration over the variables u_1, u_2, \dots, u_n , which parameterize the n hopping points. (Alternatively, these integrations could be converted into integrations over n hopping times $t_1 < t_2 < \dots < t_n$, with $t_1 > 0$ and $t_n < t$. This change of integration variables would introduce an additional Jacobian factor in the integrand.) The contribution for each n th-order hopping trajectory contains the usual phase factor of the form $\exp(iS/\hbar)$, where S is the classical action for the n hop trajectory; n transition amplitudes; σ_{jk} , given by (6), and a prefactor A , which has the form of (5), except that it contains $n|P_{\eta_k}/P_{\eta_j}|$ factors, one for each transition. The n th-order term is also summed over all sequences of adiabatic states resulting from the n transitions. In addition, recall that the zeroth-order term implicitly includes a summation over different classical trajectories that travel from the \mathbf{R}_0 to \mathbf{R}_f in time t . Each classical trajectory in the zeroth-order term gives rise to a set of surface-hopping trajectories, parameterized by the u_j integrations. Just as is the case for the zeroth-order term, this sum over different sets of trajectories is not explicitly shown in (3).

It has been shown [41] that this form for the semiclassical surface-hopping propagator satisfies the full time-dependent Schrödinger equation, including nonadiabatic coupling terms, to order \hbar . This is the same order that the single-surface semiclassical propagator, (2), satisfies the single-surface time-dependent Schrödinger equation. Other surface-hopping semiclassical procedures [29–31, 33–40] have been developed for nonadiabatic problems. In particular, the fewest-switches method of Tully is a procedure that affords rela-

tive computational simplicity, while providing accurate results [36, 37]. The surface-hopping propagator given by (3) is very useful for the work described in the rest of this article, and it is employed throughout.

SURFACE-HOPPING TREATMENT OF VIBRATIONAL TRANSITION PROBABILITIES

The quantity that we are interested in is the probability that the system, which was in vibrational state i at time $t = 0$, is in vibrational state f at time t . This quantity is formally given by [43]

$$P_{if}(t) = Q_i^{-1} \text{Tr}_s \langle f | \exp(-iHt/\hbar) | i \rangle \times \langle i | \exp(-\beta H) | i \rangle \langle i | \exp(iHt/\hbar) | f \rangle, \quad (7)$$

where Tr_s indicates a trace over the slow degrees of freedom and $Q_i = \text{Tr}_s \langle i | \exp(-\beta H) | i \rangle$. This expression projects the canonical density operator, $\rho = \exp(-\beta H)$, onto the initial vibrational state, $|i\rangle$, using the density projection operator, $|i\rangle\langle i| \dots |i\rangle\langle i|$, and propagates this projected density for time t , $\exp(-iHt/\hbar)\rho_i \exp(iHt/\hbar)$, where $\rho_i = |i\rangle\langle i| \rho |i\rangle\langle i|$. The propagated density is then projected onto the final vibrational state, $|f\rangle$, and a trace over slow coordinates is performed to give the transition probability. In this work, an adiabatic approximation is employed to accomplish the separation of the degrees of freedom into “fast” vibrational coordinates, \mathbf{r} , and “slow” solvent or bath coordinates, \mathbf{R} . In the adiabatic approximation, the vibrational wave functions and energies are \mathbf{R} -dependent, and the bath coordinates evolve on the vibrational energy surfaces. If the coordinate representation is employed for the slow variables, this transition probability takes the form [44]

$$P_{if}(t) = Q_i^{-1} \int d\mathbf{R}_f \int d\mathbf{R}_{ia} \int d\mathbf{R}_{ib} K_{fi}(\mathbf{R}_f, \mathbf{R}_{ia}, t) \times \rho_{ii}(\mathbf{R}_{ia}, \mathbf{R}_{ib}, \beta) K_{fi}(\mathbf{R}_f, \mathbf{R}_{ib}, t)^*, \quad (8)$$

where $\rho_{ii}(\mathbf{R}_{ia}, \mathbf{R}_{ib}, \beta) = \langle i, \mathbf{R}_{ia} | e^{-\beta H} | i, \mathbf{R}_{ib} \rangle$ is the canonical density function for the system in this representation, and $K_{fi}(\mathbf{R}_f, \mathbf{R}_i, t) = \langle f, \mathbf{R}_f | \exp(-iHt/\hbar) | i, \mathbf{R}_i \rangle$ is the nonadiabatic transition propagator corresponding to final state $\varphi_f(\mathbf{R}_f)$. This propagator is given, within the semiclassical approximation, by all terms in the surface-hopping expression, (3), with $\varphi_f(\mathbf{R}_f)$ as the final state.

The lowest-order approximation (in the nonadiabatic coupling) for $P_{if}(t)$ is obtained by using an adiabatic approximation for the canonical density,

$\rho_{ii}(\mathbf{R}_{ia}, \mathbf{R}_{ib}, \beta)$, and the first-order approximation, (3), for the transition propagators. The high-temperature approximation is utilized for the canonical density [44]

$$\begin{aligned} & \rho_{ii}(\mathbf{R}_{ia}, \mathbf{R}_{ib}, \beta) \\ &= (m/2\pi\hbar^2\beta)^{d/2} \exp\left\{-\left(m/2\hbar^2\beta\right)\right. \\ & \quad \times (\mathbf{R}_{ia} - \mathbf{R}_{ib})^2 - \beta[V_i(\mathbf{R}_{ia}) + V_i(\mathbf{R}_{ib})]/2\left.\right\}, \end{aligned} \quad (9)$$

where d is the dimensionality of \mathbf{R} , and $V_i \equiv E_i(\mathbf{R})$ is the adiabatic potential energy for the bath coordinate when the molecule is in vibrational state i . Notice that the semiclassical propagation of the density and the calculation of the transition probability require an integration over pairs of hopping trajectories, since there are two propagators in (8). One of these trajectories travels from \mathbf{R}_{ia} to \mathbf{R}_f with a single hop between the initial and final vibrational states, while the other travels from \mathbf{R}_{ib} to \mathbf{R}_f , also with a single hop. If the \mathbf{R}_f integration is performed by the method of the stationary phase, the stationary-phase condition is that the momentum at \mathbf{R}_f is the same for both paths [44–45]. Since both paths have the same phase space point at \mathbf{R}_f in this case, the two trajectories are identical after they have both hopped. This stationary-phase integration connects the two paths at the point of the second hop and combines the two semiclassical propagators into a single propagator associated with the combined trajectory.

It can be shown [46] that the second-order transition probability, $P_{if}^{(2)}(t)$, depends only on the portion of the trajectories when one trajectory is still on the initial adiabatic surface and the other trajectory has already hopped to the final adiabatic surface. In this case, the transition probability can be reexpressed in the form [46]

$$\begin{aligned} P_{if}^{(2)}(t) = & 2 \operatorname{Re} Q_i^{-1} \int d\mathbf{R}_{1a} d\mathbf{P}_{1af} d\tau(t - \tau) (P_{\eta fa}/m) \\ & \times (P_{\eta fb}/m) J A_{if} \exp(iS_{if}/\hbar) \\ & \times \sigma_{if}(\mathbf{R}_{1a}) \sigma_{if}(\mathbf{R}_{1b}) \rho_{ii}(\mathbf{R}_{ia}, \mathbf{R}_{ib}, \beta), \end{aligned} \quad (10)$$

where \mathbf{R}_{1a} is the point at which the trajectory from \mathbf{R}_{ia} to \mathbf{R}_f hops; \mathbf{R}_{1b} , the hopping point for the trajectory from \mathbf{R}_{ib} to \mathbf{R}_f ; τ , the time between the first and second hops; $P_{\eta fa}$ and $P_{\eta fb}$, the values of $P_{\eta f}$ for the trajectories labeled a and b , respectively; and \mathbf{P}_{1af} , the momentum at \mathbf{R}_{1a} on the final

adiabatic surface. J is the Jacobian for the change of integration variables from \mathbf{R}_{1b} to \mathbf{P}_{1af} that is made in deriving (10). The semiclassical amplitude, $A_{if} \exp(iS_{if}/\hbar)$, corresponds to a trajectory that travels on the final adiabatic surface from \mathbf{R}_{1a} to \mathbf{R}_{1b} in time τ and then hops to surface i and travels backward in time for time τ . This amplitude accounts for the combined amplitudes of the two trajectories on different surfaces in (8).

The derivation [44, 46] of (10) transforms the integration over \mathbf{R}_{ia} , \mathbf{R}_{ib} , u_a , and u_b into an integration over the two hopping points, \mathbf{R}_{1a} and \mathbf{R}_{1b} , the time between the hops, τ , and the time of the first hop. The integrand in this expression does not depend on the time of the first hop, t_1 , and the integration over t_1 simply gives the factor $(t - \tau)$. The \mathbf{R}_{1b} integration is then changed to the \mathbf{P}_{1af} integration in (10). It is assumed in (10) that the hop at \mathbf{R}_{1a} occurs before the hop at \mathbf{R}_{1b} . The opposite possibility is accounted for by taking twice the real part of the contribution when the \mathbf{R}_{1a} hop comes first. According to (10), the calculation of $P_{if}^{(2)}(t)$ requires the integration over all times τ and all single-hop trajectories of the type associated with the semiclassical amplitude in (10).

Since the two branches of the trajectories are on different adiabatic surfaces, the contribution to the integrand is generally small due to phase cancellation unless τ is small [44–48]. We refer to the decay time for the τ integration as the quantum coherence time, τ_c . For times $t \gg \tau_c$, the τ integration can be extended to infinity with introducing serious error. In this case, the only t dependence in the transition probability comes from the t in the $t - \tau$ factor. Therefore, $P_{if}(t)$ takes the form

$$P_{if}(t) = k_{if} t + C, \quad t \gg \tau_c, \quad (11)$$

where the constants k_{if} and C are given by the integrals over τ , \mathbf{R}_{1a} , and \mathbf{P}_{1af} for the terms containing t (after the t has been taken out of the integrand) and τ in (10), respectively. The constant k_{if} is the rate constant for the transition.

If only very short time trajectories contribute significantly to the transition probability due to phase cancellation, then it should be possible to obtain accurate results using short-time approximations for the dynamics of the slow degrees of freedom. Specifically, we considered approximation calculations which treat the forces on the bath coordinates, the difference between the initial and final energy surfaces, and the nonadiabatic coupling as constant [44–48]. The d -dimensional bath

coordinate dynamics become separable into d one-dimensional problems when these approximations are made, and only the direction parallel to the nonadiabatic coupling vector plays a role in the vibrational relaxation. The contributions from remaining perpendicular bath coordinates cancel between the integrals in (10) and the corresponding factors in the partition function, Q_i . Within these approximations, the rate constant can be expressed as a Boltzmann average [44]:

$$k_{if} = Q_i^{-1} \int d\mathbf{R} \exp[-\beta V_i(\mathbf{R})] K_{if}(\mathbf{R}), \quad (12)$$

where $K_{if}(\mathbf{R})$ is the integral over τ and the η component of P_{1af} of $\exp(\beta V_i)$ times the factors multiplying t in (10) for the one-dimensional problem in the η direction.

QUANTUM-CLASSICAL APPROACH FOR RESONANT VIBRATIONAL ENERGY TRANSFER

The semiclassical methods described in the previous section are well suited for the calculation of vibrational energy relaxation rates, when the energy difference between the initial and final vibrational state is large compared with $K_B T$. Resonant transfer of vibrational energy between different molecules represents the opposite extreme. In the adiabatic representation, the intermolecular interactions break the exact degeneracy of the vibrational states of different molecules. However, the energy differences are generally quite small compared to $K_B T$. In this case, it is reasonable to ignore the changes in the bath momentum that accompany changes in the vibrational state of the system. If these momentum changes are ignored, then the bath propagation can be treated as occurring along a single classical trajectory. The vibrational coordinates are set to their equilibrium values, \mathbf{r}_e , during the propagation of the classical trajectory for the bath coordinates.

The evolution of the vibrational degrees of freedom can be treated quantum mechanically in this case [49]. We define a set of N vibrational basis functions for the N molecule system. The j th vibrational basis function, ψ_j^v , is the product of a vibrational wave function for each molecule, with the j th molecule in the excited vibrational state of interest and the remaining molecules in their vibrational ground state. The vibrational Hamiltonian is defined as $H^v = T^v + V^v(r, \mathbf{R})$, where T^v is the vibrational kinetic energy operator and

$V^v(r, \mathbf{R}) = V(r, \mathbf{R}) - V(r_e, \mathbf{R})$. The vibrational Hamiltonian depends on the bath coordinates through $V^v(r, \mathbf{R})$. Within the vibrational subspace of interest, which is defined by the N basis functions, H^v can be expressed as an $N \times N$ matrix, \mathbf{H}^v , and the vibrational wave function is a linear combination of the basis functions

$$\Psi^v(t) = \sum_{j=1}^N c_j(t) \psi_j^v. \quad (13)$$

The \mathbf{R} dependence of \mathbf{H}^v , together with the t dependence of \mathbf{R} along the classical trajectories for the bath variables results in \mathbf{H}^v being time-dependent. Within the $N \times N$ matrix representation of the vibrational transfer problem, the propagation of the vibrational wave function is given by

$$\mathbf{C}(t + \delta t) = \exp(-i\mathbf{H}^v \delta t / \hbar) \mathbf{C}(t), \quad (14)$$

where $\mathbf{C}(t)$ is the column composed of the $c_j(t)$. In the work described here [49, 50] the matrix propagator, $\exp(-i\mathbf{H}^v \delta t / \hbar)$, is evaluated by treating \mathbf{H}^v as independent of time over the short δt interval. \mathbf{H}^v is diagonalized for each interval, $\mathbf{U}^T \mathbf{H}^v \mathbf{U} = \mathbf{D}$ (where \mathbf{D} is diagonal and \mathbf{U} is unitary), and the matrix propagator is expressed as $\exp(-i\mathbf{H}^v \delta t / \hbar) = \mathbf{U} \exp(-i\mathbf{D} \delta t / \hbar) \mathbf{U}^T$.

The appropriate initial condition for the resonant transfer problem is that the vibrational excitation is localized on a single molecule, which is taken to be molecule one without loss of generality. This corresponds to the condition that $c_1(0) = \delta_{1j}$. The probability that the excitation has been transferred to molecule j at time t is given by $|c_j(t)|^2$. This probability is averaged over a canonical ensemble of initial coordinates and momenta for the classical bath coordinate trajectories [49, 50], giving $P_{ij}(t) = \langle |c_j(t)|^2 \rangle_T$, where $\langle \dots \rangle_T$ indicates this ensemble average, which is performed using a Monte Carlo algorithm [51].

Results

Results from Monte Carlo calculations [44, 45] for the relaxation rate for the first excited vibrational state of a diatomic in a simple monoatomic solvent are presented in Table I. The basic system mimics Br₂ in Ar. A Morse potential is employed for the diatomic bond potential and Lennard-Jones potentials are used for the interactions between the different solvent atoms and between the atomic

centers in the diatomic and the atoms in the solvent. The purpose of the calculations is to explore the sensitivity of the relaxation to changes in different physical parameters that define the system, rather than to evaluate the relaxation rate for a specific physical system. Therefore, no attempt was made to optimize the potential for vibrational relaxation calculations. The calculations were performed within the short-time approximations for the surface-hopping dynamics of the solvent that are described in the subsection Surface-hopping Treatment.... The relaxation rate is obtained as a Monte Carlo average over solvent configurations, as described by Eq. (12). The simulation system consists of a single diatomic with 107 solvent atoms in a box with an excluded volume fraction of 0.3 at $T = 300$ K. Periodic boundary conditions are employed. The potential parameters and details of the simulation procedure can be found elsewhere [44, 45].

The results [44, 45] presented in Table I indicate that the relaxation rate of this system is more sensitive to the mass of the solvent atoms than to the mass of the diatomic. We also found that neglecting the components of the nonadiabatic coupling vector corresponding to rotations of the diatomic had a negligible effect on the relaxation rate. These results are reasonable, since the solvent atoms in this system are lighter than the diatomic molecule. Therefore, the diatomic center-of-mass

motion and rotations correspond to relatively low-frequency motions, and the comparatively "high-frequency" solvent motions provide better accepting modes. The relaxation rate is also sensitive to the frequency of the vibrational potential, while it is less sensitive to the Lennard-Jones energy parameter, ϵ , for the diatomic-solvent interactions. Softening the 6–12 Lennard-Jones potential to a 6–9 potential results in a large decrease in the relaxation rate, indicating that the hardness of the repulsive interactions is a significant factor in the vibrational relaxation in this system. On the other hand, replacing the 6–12 potential with a 6–15 potential had little impact on the rate, suggesting that there is a saturation of this repulsive hardness effect.

These calculations are based on short-time approximations for the solvent dynamics. These approximations rely on the argument that the phase difference between two trajectories, one on the initial vibrational energy surface and the other on the final vibration surface, should be a rapidly growing function of time. If this is the case, the averaging of the rate expression over the initial coordinates and momenta for the classical trajectories produces significant phase cancellation, except at early times. To test these approximations, we considered a simple one-dimensional model in which the center of mass of a single molecule moves between two fixed solvent atoms [46–48]. The center-of-mass motion is the lone solvent coordinate in this model. Since there is only a single bath coordinate, it is feasible to numerically perform the integrations over R_{1a} , P_{1af} , and τ in (10) without the use of any simplifying approximations. The results of these calculations can then be compared with those of calculations using the short-time approximations. Results [48] are shown in Figure 1 for the transition probabilities of a system with a triatomic molecule moving between fixed solvent atoms. The potential parameters model CO_2 in Ar. The three curves correspond to the transition from the first excited state of the symmetric stretch to the vibrational ground state, from the first excited state of the asymmetric stretch to the vibrational ground state, and from the asymmetric stretch state to the symmetric stretch state. Details of the calculations and the potentials are provided elsewhere [48]. The short-time approximations provide very good results for this system. The transition probabilities are nonlinear at short times, up to about 0.2 ps, and then the quantum oscillations die out and $P_{if}(t)$ essentially

TABLE I
Rate for $1 \rightarrow 0$ vibrational relaxation for diatomic in simple solvent [44, 45].

System (change from basic system)	Rate (ps^{-1})
Br_2 in Ar (basis system)	0.37×10^{-2}
Solvent mass changed to 20.18 amu	0.99×10^{-2}
Diatomic mass halved (reduced mass held fixed)	0.49×10^{-2}
Diatomic frequency doubled ϵ doubled for $\text{Br} - \text{Ar}$	0.024×10^{-2}
Lennard-Jones potential	0.61×10^{-2}
6–12 $\text{Br} - \text{Ar}$ potential replaced with 6–9 potential	0.072×10^{-2}
6–12 $\text{Br} - \text{Ar}$ potential replaced with 6–15 potential	0.37×10^{-2}
Br_2 in Ar, ignoring rotational components of η_{if}	0.34×10^{-2}
Br_2 in Ar, including only rotational components of η_{if}	0.014×10^{-2}

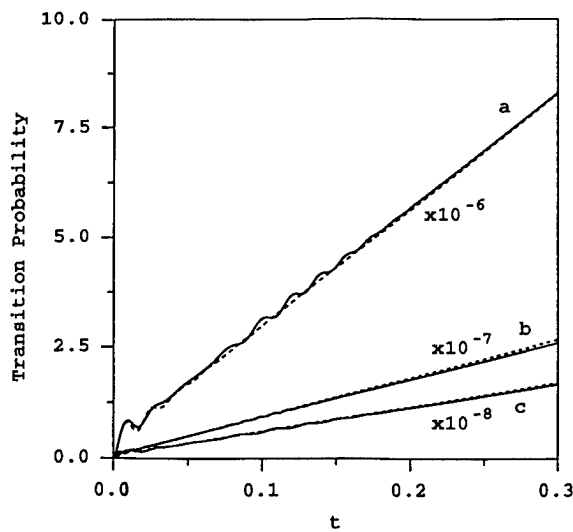


FIGURE 1. Calculated vibrational transition probabilities are plotted versus time for one-dimensional Ar—CO₂—Ar model system [48]. The solid curves are results from the full second-order calculations and the dotted curves are results obtained using short-time approximations for the solvent dynamics. The curves labeled a present $P_{if}(t) \times 10^6$ for the transition from the first excited symmetric stretch vibrational state to the ground state. The curves labeled b give $P_{if}(t) \times 10^7$ for the transition from the first excited asymmetric stretch vibrational state to the ground state. The curves labeled c present $P_{if}(t) \times 10^8$ for the transition from the first excited asymmetric stretch vibrational state to the first excited symmetric stretch state.

becomes a linear function of time. The slope of the $P_{if}(t)$ in the linear region gives the rate constant for the vibrational transition, as discussed in the subsection Surface Hopping Treatment....

Similar model calculations were performed for the Br₂ in the Ar system [46, 47]. In this system, the short-time approximations are again found to provide good results, although the errors are somewhat larger than for the CO₂ in Ar system. The quantum oscillators are also more pronounced and persist for about twice as long as in the Br₂ case as compared with the CO₂ system. This is quite reasonable, since the CO₂ has much stronger bonds and the energy difference between initial and final vibrational states is much larger for the CO₂ transitions than for the Br₂ transition. We also performed similar model calculations which mimic KrF₂ between Ar atoms [48]. This molecule has weak bonds, and the coupling between the bonds is weak, since the central atom is heavy compared with the light end atoms. Due to the weak cou-

pling between the bonds in KrF₂, the energy difference between the first excited states of the asymmetric and symmetric stretches is quite small: 93 cm⁻¹. In this KrF₂ case, the quantum oscillations in the transition probabilities are more pronounced and persist for about 0.5 ps. The short-time approximations are much less accurate, completely breaking down for the asymmetric stretch-to-symmetric stretch transition.

In large condensed-phase simulations, where there are many solvent coordinates, there will be a great deal more averaging than in these one-dimensional model calculations. This increased averaging may result in a decrease in the quantum nonlinearities in the transition probabilities. As a result, the errors introduced by the short-time approximations in the model calculations are expected to be provide an upper limit on the size of the errors introduced by these approximations in the larger simulations. Although the short-time approximations might fare better in a large condensed-phase simulation due to more complete averaging and phase cancellation, these calculations suggest that care must be taken when applying these short-time approximations to systems with very low energy vibrational transitions.

Figure 2 presents results from simulations on two-dimensional clusters of N identical diatomic

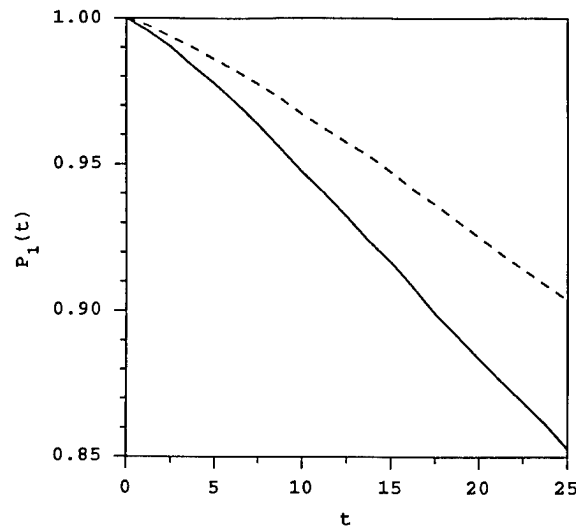


FIGURE 2. Plot of the calculated probability that a vibrational excitation on molecule one at time zero remains on molecule one at time t for two-dimensional Br₂ clusters [50]. The dashed curve is for a cluster of 10 molecules and the solid curve is for a cluster of 20 molecules.

molecules for the resonant transfer of a single quantum of vibrational energy [50]. Results are shown for $N = 10$ and $N = 20$. The quantum-classical simulation method described in the subsection Quantum-Classical Approach... was employed. The use of two-dimensional systems reduces the number of coordinates without changing the essential physics, and it increases the size of the cluster, as measured by the diameter, for a given value of N . The potential parameters are chosen to model a cluster of Br_2 molecules. The individual molecules have harmonic bond potentials with $\omega = 60.06 \text{ ps}^{-1}$. The intermolecular interactions consist of Lennard-Jones interactions between the atoms in different molecules with $\epsilon = 170 \text{ K}$ and $\sigma = 3.6 \text{ \AA}$. An additional harmonic potential is added between the center of mass of each molecule and the origin of the coordinate system. This keeps the cluster from fragmenting. A force constant of $10 \text{ K}/\text{\AA}^2$ is employed for this additional potential in both calculations presented in the figure. The quantity shown, $P_1(t)$, is the probability that the single vibrational quantum, which was localized on molecule one at time zero, is still on molecule one at time t .

The initial-phase space points for the classical trajectories are selected using a Monte Carlo sampling procedure at $T = 300 \text{ K}$. The results shown are the average of the transition probabilities over 400 trajectories [50]. The initial-phase space points for these trajectories are well-separated points in the Monte Carlo sampling to assure a lack of correlation among the trajectories. The quantum-classical simulation procedure for resonant transfer has been tested against a modified version of the semiclassical surface-hopping procedure at short times for a simple model with two Br_2 molecules moving in one dimension between fixed Ar atoms [49]. The results of the two methods agreed to within statistical error, indicating that ignoring the small changes in the bath momentum when the system undergoes a vibrational transition is a good approximation in these resonant transfer calculations.

The interesting feature of the results is that the transition probability is nonlinear for several picoseconds. The total transition probability, $1 - P_1(t)$, appears quadratic at short times and then it crosses over to a linear behavior at about 5 ps. This indicates that the quantum coherence time for these nearly resonant transitions is around 5 ps, which is a somewhat surprising length of time for quantum effects to persist in a cluster at a high temperature.

These results indicate that the possibility of long quantum coherence times must be accounted for in order to accurately evaluate transition rates between degenerate or nearly degenerate states [49, 50].

Discussion

In this article, we have outlined computational methods for studying vibrational relaxation in condensed systems. We have found that semiclassical surface-hopping procedures provide a very useful methodology for vibrational energy relaxation. Model calculations indicate that short-time approximations for the solvent dynamics, which significantly simplify the calculations in condensed-phase systems, yield very accurate results as long as the energy difference between the vibrational states of interest is not small compared with $K_B T$. The results from these model calculations show quantum coherence effects for a few tenths of a picosecond. Calculations of the *resonant transfer* of a vibrational quantum of energy in clusters of identical molecules indicate that the quantum coherence can persist for several picoseconds in this case. It is reasonable to assume that the transfer probabilities for transitions between vibrational levels, which are energetically very close, will also display long quantum coherence times. These quantum coherence times can be expected to vary from a quite long (a few picoseconds) to quite short (a few tenths or hundredths of a picosecond) as the energy difference between the levels varies from very small to quite large compared with $K_B T$.

Bittner and Rossky [52] recently presented a discussion of the decoherence of quantum transition probabilities in a condensed-phase system. Their analysis was based upon the idea that the interaction of the degrees of freedom undergoing the transition (which we simply refer to as the system) with the bath coordinates has the same effect as a measurement of the system, producing a reduction of the mixed state system to a pure state system. The classical trajectories describing the evolution of the bath degrees of freedom depend on the quantum state of the system. The divergence of trajectories, which correspond to different quantum states after the system undergoes a reduction to a pure state density, produces the quantum decoherence. Bittner and Rossky [52] also

demonstrated through model calculations that the transition probability can depend strongly on the quantum coherence time. Bittner and Rossky considered coherence times on the order of 10 fs or less in their model calculations. This is reasonable, since they are modeling electronic transition and the energy differences between quantum states is much higher than is the case for the vibrational transitions considered here. The larger energy differences result in a more rapid divergence of the trajectories and shorter coherence times.

The formalism discussed in the current work contains the decoherence produced by the diverging of the trajectories, which is included in the analysis of Bittner and Rossky [52]. There are two propagators in Eq. (8) for the time-dependent transition probability, one of them complex-conjugated. The calculation of the transition probability requires an integration of all pairs of hopping, and the phase of the integrand is given by the difference in the phases for the two trajectories. Only those times when the two trajectories correspond to the system in different quantum states contribute to the integration [44–50]. The diverging of these trajectories is one of the features that contributes to quantum decoherence in our work. In the quasidegenerate case of resonant vibrational energy transfer, we find that the trajectories diverge very slowly and the phase cancellation increases very slowly as well. In this case, the loss of correlation in the coupling between quantum states as a function of time also plays an important role in the decay of quantum effects [50]. The pair of trajectories describing the evolution of the transition density have different hopping times. The lowest (second)-order transition density contains a factor of the interaction coupling the initial and final states from each of the hops. The values of the coupling at the two hopping times become uncorrelated as the time between the hops increases. This loss of correlation has an impact on the integration over all pairs of trajectories, which is similar to the effect of increasing phase cancellation in those cases where the trajectories are rapidly diverging [50].

In conclusion, the semiclassical surface-hopping method and the quantum-classical simulation procedure appear to provide computationally useful and accurate methods for the large energy gap and nearly degenerate cases, respectively. On the other hand, the development of methods that can systematically and accurately account for the quantum nature of the transition and provide accurate

results for the full range of possibilities, including the intermediate range of energy differences, remains a challenge.

ACKNOWLEDGMENTS

This work was supported by NSF grant CHE-9422786 and by the Center for Photoinduced Processes at Tulane University, which is funded by the Louisiana Board of Regents and NSF.

References

1. W. H. Miller, *Adv. Chem. Phys.* **25**, 69 (1974); *Ibid.* **30**, 77 (1975).
2. E. J. Heller, *Acc. Chem. Res.* **14**, 368 (1981).
3. M. F. Herman, *Annu. Rev. Phys. Chem.* **45**, 83 (1994).
4. D. W. Oxtoby, *Adv. Chem. Phys.* **40**, 1 (1979).
5. D. W. Oxtoby, *Ann. Rev. Phys. Chem.* **32**, 77 (1981).
6. J. C. Owrusky, D. Raftery, and R. M. Hochstrasser, *Annu. Rev. Phys. Chem.* **45**, 519 (1994).
7. R. N. Schwartz, Z. I. Slawsky, and K. F. Herzfeld, *J. Chem. Phys.* **20**, 1591 (1952).
8. S. A. Adelman and R. H. Stote, *J. Chem. Phys.* **88**, 4397 (1988).
9. R. H. Stote and S. A. Adelman, *J. Chem. Phys.* **88**, 4415 (1988).
10. D. Levesque, J.-J. Weis, and D. W. Oxtoby, *J. Chem. Phys.* **79**, 917 (1983).
11. R. M. Whitnell, K. R. Wilson, and J. T. Hynes, *J. Chem. Phys.* **96**, 5354 (1992).
12. P. S. Dardi and R. I. Cukier, *J. Chem. Phys.* **86**, 2264, 6893 (1987); **89**, 4145 (1988).
13. J. K. Brown, C. B. Harris, and J. C. Tully, *J. Chem. Phys.* **89**, 6687 (1988).
14. F. E. Figueirido and R. M. Levy, *J. Chem. Phys.* **97**, 703 (1992).
15. H. Gai and G. A. Voth, *J. Chem. Phys.* **99**, 740 (1993).
16. R. M. Whitnell and I. Benjamin, *Chem. Phys. Lett.* **204**, 45 (1993).
17. S. A. Egorov and J. L. Skinner, *J. Chem. Phys.* **105**, 7047 (1996).
18. M. Cho, *J. Chem. Phys.* **105**, 10755 (1996).
19. R. Rey and J. T. Hynes, *J. Chem. Phys.* **104**, 2356 (1996).
20. V. M. Kendre, A. Tokmakoff, and M. D. Fayer, *J. Chem. Phys.* **101**, 10618 (1994).
21. P. Moore, A. Tokmakoff, T. Keyes, and M. D. Fayer, *J. Chem. Phys.* **103**, 3325 (1995).
22. I. N. Levine, *Quantum Chemistry* (Allyn and Bacon, Boston, 1983).
23. R. P. Feynman and A. R. Hibbs, *Quantum Mechanics and Path Integrals* (McGraw-Hill, New York, 1965).
24. J. B. Delos, W. R. Thorson, and S. K. Knudson, *Phys. Rev. A* **6**, 709 (1972).

DEVELOPMENT OF SEMICLASSICAL DYNAMICAL METHODS

25. N. E. Henriksen, G. D. Billing, and F. Y. Hansen, Chem. Phys. Lett. **199**, 176 (1992).
26. C. W. McCurdy, H. D. Meyer, and W. H. Miller, J. Chem. Phys. **70**, 3177 (1979).
27. H. D. Meyer and W. H. Miller, J. Chem. Phys. **70**, 3214 (1979); *Ibid.* **71**, 2156 (1979); *Ibid.* **72**, 2272 (1980).
28. W. H. Miller and T. F. George, J. Chem. Phys. **56**, 5637, 5668 (1972).
29. P. Pechukas, Phys. Rev. **181**, 166, 174 (1969).
30. R. K. Preston and J. C. Tully, J. Chem. Phys. **54**, 4297 (1971).
31. J. C. Tully and R. K. Preston, J. Chem. Phys. **55**, 562 (1971).
32. M. F. Herman, J. Chem. Phys. **76**, 2949 (1982).
33. M. F. Herman and K. F. Freed, J. Chem. Phys. **78**, 6010 (1983).
34. N. C. Blais and D. G. Truhlar, J. Chem. Phys. **79**, 1334 (1983).
35. N. C. Blais, D. G. Truhlar, and C. A. Mead, J. Chem. Phys. **89**, 6204 (1988).
36. J. C. Tully, J. Chem. Phys. **93**, 1061 (1990).
37. S. Hammes-Schiffer and J. C. Tully, J. Chem. Phys. **101**, 46567 (1994).
38. F. Webster, J. Schnitker, M. S. Friedrichs, R. A. Friesner, and P. J. Rossky, Phys. Rev. Lett. **66**, 3172 (1991).
39. D. F. Coker and L. Xiao, J. Chem. Phys. **102**, 496 (1995).
40. V. S. Batista and D. F. Coker, J. Chem. Phys. **106**, 6923 (1997).
41. M. F. Herman, J. Chem. Phys. **103**, 8081 (1995).
42. M. S. Topaler, M. D. Hack, T. C. Allison, Y.-P. Liu, S. Mielke, D. W. Schwenke, and D. G. Truhlar, J. Chem. Phys. **106**, 8699 (1997).
43. M. F. Herman and E. Kluk, in *Dynamical Processes in Condensed Matter*, M. Evans, Ed. (Wiley, New York, 1985).
44. M. F. Herman, J. Chem. Phys. **87**, 4779, 4794 (1987).
45. R. K. Rudra and M. F. Herman, in *Mathematics Applied to Science*, J. Goldstein, S. Rosencrans, and G. Sod, Eds. (Academic Press, Boston, 1988).
46. M. F. Herman and J. C. Arce, Chem. Phys. **183**, 335 (1994).
47. J. C. Arce and M. F. Herman, J. Chem. Phys. **101**, 7520 (1994).
48. P. Velev and M. F. Herman, Chem. Phys., submitted.
49. F. A. Dodaro and M. F. Herman, J. Chem. Phys. **108**, 2903 (1998).
50. M. F. Herman, J. Chem. Phys., in press.
51. K. Binder, in *Monte Carlo Methods in Statistical Physics*, 2nd ed., K. Binder, Ed. (Springer-Verlag, Berlin, 1986).
52. E. R. Bittner and P. J. Rossky, J. Chem. Phys. **103**, 8130 (1995).

Single-Electron-Capture Cross Sections by Alpha-Particles from Ground State $K(4s)$ and $Rb(5s)$: A Molecular-State Approach

ANIL KUMAR,* BIDHAN C. SAHA, CHARLES A. WEATHERFORD

Department of Physics, Florida A & M University, Tallahassee, Florida 32307

Received 23 February 1998; revised 28 May 1998; accepted 3 June 1998

ABSTRACT: Cross sections for single-electron capture by α -particles from ground state K and Rb were calculated in the low-to-intermediate energy region by employing the molecular expansion method in the framework of impact parameter formulation. The colliding partners are treated as a pseudo-one-electron system and the technique of the pseudopotential is used to account for their mutual interactions. The molecular wave function of the quasimolecule formed during the collision is expanded in terms of basis sets of atomic orbitals on two centers. The resulting coupled equations are solved semiclassically where a straight-line trajectory describes the relative motion of the two nuclei. The effect of electron translation is also suitably incorporated. The calculated cross sections, both total and partial, are presented and compared with the available experimental measurements. © 1998 John Wiley & Sons, Inc. *Int J Quant Chem* 70: 909–917, 1998

Key words: charge transfer; α -particles; alkali atoms; MO expansion; close coupling

Correspondence to: A. Kumar.

*On leave from Department of Physics, J. P. University,
Chapra-841 301, India.

Contract grant sponsor: NASA.

Contract grant number: NAGS-6831.

Contract grant sponsor: NSF-CREST.

Contract grant number: HDR-9707076.

Contract grant sponsor: Army High Performance Computing Research Center/Department of the Army, Army Research Laboratory.

Contract grant number: DAAH04-95-2-0003/DAAH04-95-C-0008.

Contract grant sponsor: Research Corp.

Introduction

Charge-transfer processes involving multiply charged ions and alkali atoms have, lately, been a subject of detailed theoretical and experimental studies (see [1] and [2] for reviews on the subject). Single-electron capture in such reactions often leads to selective population of certain excited states, especially at low and intermediate energies. These special products obviously radiate and, hence, have the potentiality of turning into ultraviolet and X-ray lasers [3]. So, it is not surprising to find in the literature a flurry of activity—theoretical and experimental—on electron capture by α -particles from alkali targets, especially the low-lying alkalies such as Li and Na [4, 5]. Another important reason behind these studies may be the simplicity with which the aforesaid interacting systems can be looked at; they provide a pseudo-one-electron picture. The outermost weakly bound electron of the alkali target hardly allows any one else to participate in the collisional processes leading to single-electron capture by the incident α -particle.

Although Li and Na have enjoyed much attention, recently an attempt was made by Schweinzer and Winter [6] to go beyond this, when they measured the cross sections for single-electron transfer from ground state K to the incoming bare nuclei of He at low impact energies. Previously, Shah and Gilbody [7] also carried out such measurements in the intermediate energy region. These measurements on K and alpha have been a motivating factor for us to examine the process of charge exchange in this reaction from a theoretical point of view. This may also be viewed as a step in the direction of a systematic study of various alkali targets at low and intermediate energies so as to observe the target dependency of these cross sections (see also Nagata [8]), if any. Although similar in electronic structure of their cores, alkali atoms provide a systematic variation in the binding of their outermost electron. This can have a profound effect on the positions of the group of electronic states responsible for charge transfer. With this motivation, we proceed not only to investigate the K- α system for which some measurements are available in the literature, but also go one step ahead and attempt to look into the interesting case of Rb- α . With these calculations, we also intend to

present a comparative overview of single-electron capture by α -particles from different alkali atoms.

Theoretical Methods

We used the standard semiclassical MO expansion method for our present study. In this method (see, e.g., Kumar et al. [9] and references therein), the pseudo-one-electron system is described by a quasi-molecule model, where the active electron is supposed to move in the combined electric field of the two cores (the alkali core and the bare nucleus of He). The dynamics of the relative motion of the two nuclei is described in terms of a straight-line trajectory, and the effective potential, V_{eff} , of the participating electron is accounted for by invoking the technique of the pseudo-potential [10]:

$$V_{eff}(r) = V^{SR}(\mathbf{r}) + V^{LR}(r) + V^{CI}, \quad (1)$$

where the short-range part $V^{SR}(\mathbf{r})$ is given by

$$V^{SR}(\mathbf{r}) = \sum_{l,m} V_l^{SR}(r) |Y_{lm}(\hat{\mathbf{r}})\rangle \langle Y_{lm}(\hat{\mathbf{r}})|. \quad (2)$$

In this expression, $|Y_{lm}(\hat{\mathbf{r}})\rangle$ are the spherical harmonics and $V_l^{SR}(r)$ is the Gaussian-type radial function:

$$V_l^{SR}(r) = A_l \exp(-B_l r^2). \quad (3)$$

The l -dependent pseudopotential parameters A_l and B_l used above were chosen to fit the spectroscopic data and were tabulated by Bardsley [10] for K and Rb. The long-range part, V^{LR} , of the effective potential consists of the polarization terms:

$$V^{LR}(r) = -\left[\frac{\alpha_d}{2(r^2 + d^2)^2} + \frac{\alpha_q}{2(r^2 + d^2)^3} \right] \quad (4)$$

and

$$V^{CI}(r) = 1/r, \quad (5)$$

where α_d and α_q are the dipole and quadrupole polarizabilities, respectively, and d is the cutoff distance. The motion of the bound electron is described quantum mechanically and we performed the structure calculation by expanding the electron wave function in terms of molecular orbitals (MO). They, in turn, are constructed by a linear combination of Slater-type-orbitals (STOs) centered on the core of the alkali atom as well as on the incident α -particle ion. In the present study, we used the STOs provided by Kimura et al. [11] for alkali

targets. The basis set centered on the α -particle is of hydrogenic character and was given by Sato and Kimura [4]. The motion of the electron with respect to the center of mass of the colliding system is also introduced in the calculation via a plane-wave electron translation factor (ETF). Substituting the ETF-modified (see also [12]) electron wave function in the time-dependent Schrödinger equation, we get a standard set of coupled equations:

$$ia_j = \sum_{j \neq i} \mathbf{V} \cdot (\mathbf{P} + \mathbf{A})_{ij} a_i + \varepsilon_j a_j, \quad (6)$$

where \mathbf{P} and \mathbf{A} are the nonadiabatic coupling matrices and the ETF correction, respectively, and ε_j represents the adiabatic electronic energy of the j th state of the quasimolecule. The above coupling matrices are expressed as a sum of radial and angular terms which can be evaluated numerically [11]. We then solve a finite number of coupled equations [see Eq. (6)] for each contributing impact parameter to evaluate the probability of transition to the j th state:

$$P_j(E, b) = |a_j(+\alpha, b)|^2 \quad (7)$$

subject to the initial condition

$$a_i(t = -\alpha) = \delta_{ij}. \quad (8)$$

The transition probability multiplied by the impact parameter is then integrated over all possible b values to yield the integrated cross sections:

$$\sigma_j = 2\pi \int db \cdot P_j(E, b) \cdot b. \quad (9)$$

In the present case, the total number of configurations used by us for obtaining molecular Σ and Π states are 23 and 12, respectively. It may here be pointed out that the previous calculation performed on Na- α by the same method [5] also uses exactly the same number of configurations to obtain molecular states for that reaction. We have, thereafter, carried out a 13-state calculation (8Σ and 5Π) to evaluate cross sections for single-electron capture by α -particles from the two alkali targets K and Rb.

Results and Discussion

ADIABATIC POTENTIAL CURVES

The adiabatic molecular potential energy curves for the K(4s) + He²⁺ system are presented in Fig-

ures 1 and 2. The potential surfaces for the other system, that is, Rb(5s) + He²⁺, also exhibit more or less similar character, but they do vary in details when it comes to various avoided crossings. For convenience, we present the atomic states correlating to various Σ and Π states used in our calculations for the two interacting systems in Table I. We would like to mention at this stage that unlike Na(3s) + He²⁺ capture into He⁺ ($n = 2$) was not found to make any significant contribution toward the total electron capture cross sections for the two systems that we investigated here. We arrived at this conclusion by actually performing a couple of 18-state calculations for the two systems where all the molecular states correlating to He⁺($n = 2$) were taken into account. In addition, the Δ molecular states correlating to He⁺(3d and 4d) were also included in these test calculations. But no significant contributions were made by these states, and, hence, to save on computational efforts, these states were dropped from our final calculation. In this context, it is worth pointing out that Shah and Gilbody [7], while measuring the total single-electron capture cross section on α -K, tried to record the contribution of formation of He^{+(2s)} toward this reaction and also arrived to the same conclusion regarding their relative importance.

Before we talk about the adiabatic potential surfaces of these systems, we would like to point out that Coulomb repulsion plays a dominant role in shaping the nature of these curves related to various outgoing channels of the reaction [He^{+(nl)} + A⁺]. This, in both cases, causes strong avoided crossings with the incoming channel around which appreciable flux transfer is mainly responsible for the single-electron capture. The incoming channel (K4s Σ) has a very strong avoided crossing with the outgoing channel 3d Σ [correlated to He^{+(3d)}] around $R \approx 20a_0$ in K- α . The 3d Σ itself interacts very strongly with 3p Σ in the region of $13a_0 < R < 17a_0$. These two interactions are marked as 1 and 2 in Figure 1 and then are magnified in Figure 2 to show the involved energy defects for these avoided crossings. Another near crossing between the incoming channel and 3d Σ is observed around $R \approx 8a_0$. Exit channels correlating to the excited target, that is, K(4p) and He⁺ ($n = 4$ manifold), have only weak interaction with the incoming channel at still lower R values, which is, therefore expected to be important at only high impact energies. These avoided crossings also manifest them-

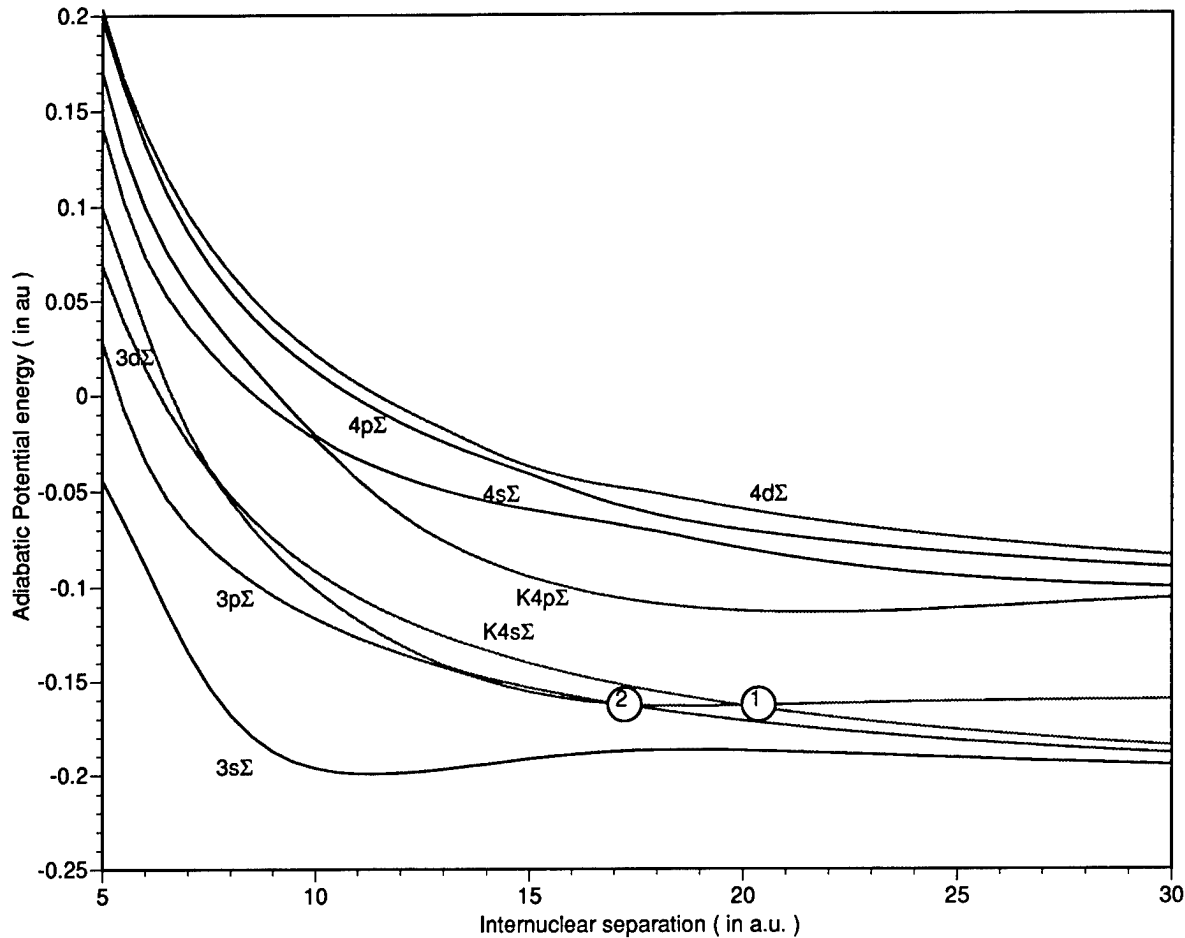


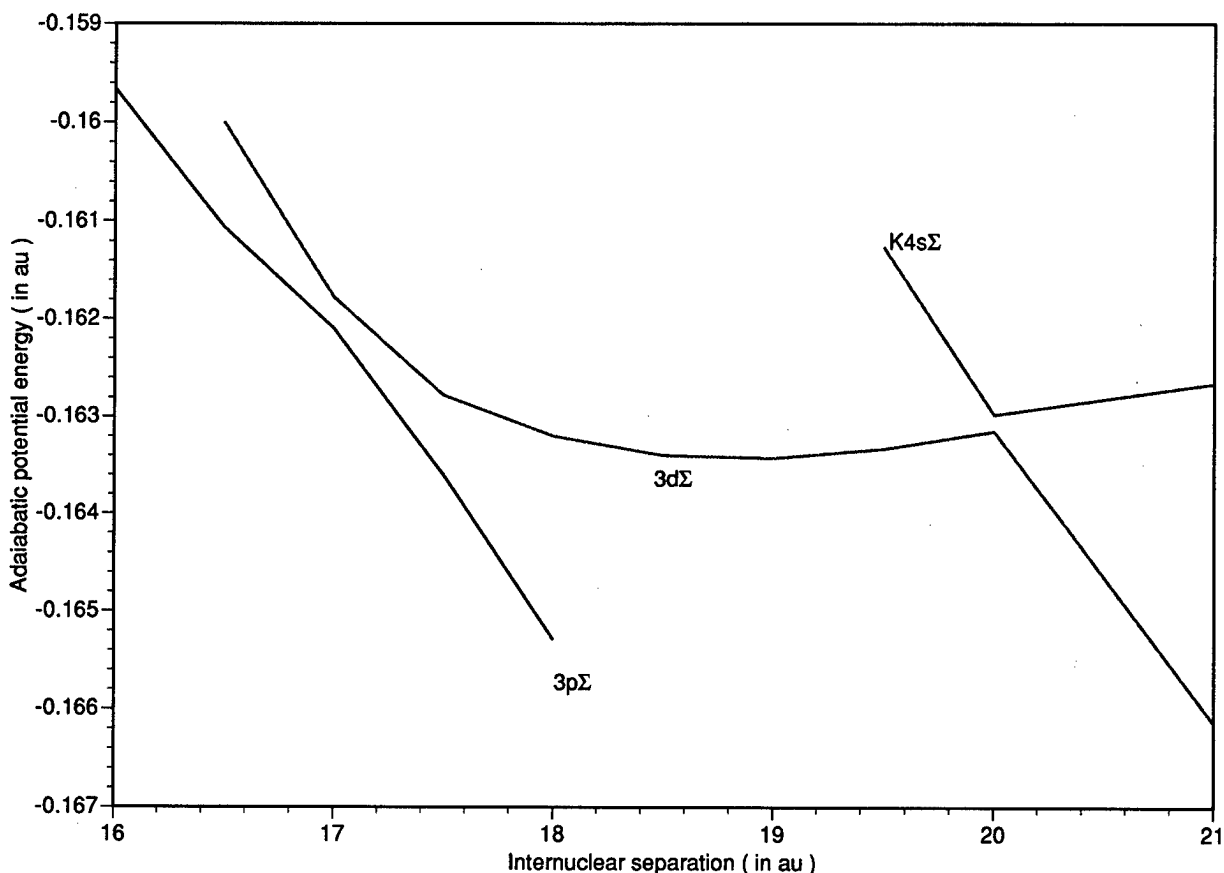
FIGURE 1. Adiabatic potential energies for the quasimolecule $(\text{KHe})^{2+}$. Various channels are marked by their designated symbols as adopted in Table I.

selves through strong radial couplings in the same range of internuclear separation. For example, the $\text{K}4s\Sigma \leftrightarrow 3d\Sigma$ radial coupling has two sharp peaks around $7a_0$ and $20a_0$. These are the strongest of all radial couplings that exist for this system. The incoming channel has only a mild coupling with $3p\Sigma$ at lower R values ($\approx 7a_0$). However, the $3p\Sigma \leftrightarrow 3d\Sigma$ radial coupling exhibits two strong peaks around $R \approx 13.5a_0$ and $17.5a_0$. Perhaps these radial couplings are responsible for the flux finally ending up in $3p\Sigma$, which makes capture into $\text{He}^+(3p)$ the most dominant contributor to the process of single-electron transfer up to 30 keV of the projectile energy. $3p\Sigma$ also couples significantly with $3s\Sigma$ up to $R \approx 7a_0$ and this helps in populating the outgoing channel correlating to $\text{He}^+(3s) + \text{K}^+$.

So far, as the rotational couplings are concerned, they are, more or less, subordinate to the radial

couplings in populating various manifolds of outgoing channels. At this juncture, one may refer to the observations made by Gargaud et al. [13] regarding the relative importance of radial and rotational couplings in the process of charge transfer. They hold the view that the primary mechanism of charge transfer is through the radial couplings; the rotational couplings do have some important secondary effects under favorable circumstances. Here, also, the molecular states of different symmetries correlating to the $n = 3$ manifold of He^+ , for example, $3p\Sigma \leftrightarrow 3p\Pi$ and $3d\Sigma \leftrightarrow 3d\Pi$, are found to have significant rotational couplings in a certain region of internuclear separation. But their effect on the total capture cross section turns out to be moderate and secondary, at least in the energy range of our interest.

A more or less similar situation exists in case of Rb colliding with α -particles. The molecular Σ

FIGURE 2. Avoided crossings among $K4s\Sigma$, $3d\Sigma$, and $3p\Sigma$.

states representing the outgoing channels of $Rb^+ + He^+$ ($n = 3$ manifold) have strong radial couplings with the incoming channel $Rb5s\Sigma$. But the range of these strong avoided crossings shifts slightly toward the lower R values, and their strength, in comparison to $K-\alpha$ case, also diminishes. On the other hand, the initial channel exhibits a bit stronger radial coupling with the $Rb5p\Sigma$

state, which, in turn, has moderate couplings with the states correlating to He^+ ($n = 4$ manifold). This is perhaps responsible for the $n = 4$ states of He^+ being populated with a somewhat larger probability in the case of $Rb-\alpha$.

SINGLE-ELECTRON CAPTURE CROSS SECTION

Both in the case of $K-\alpha$ and $Rb-\alpha$, we performed 13-state calculations to evaluate single-electron capture cross sections at low and intermediate energies. These cross sections, along with the experimental measurements of Schweinzer and Winter [6] and Shah and Gilbody [7], for $K-\alpha$, are graphically presented in Figure 3. Although we do not include the theoretical calculations carried out for $K-\alpha$ by Schweinzer and Winter in this figure, we do compare our results with their estimates. To look into the selectivity of the charge-transfer process in this reaction, we also present partial cross

TABLE I
Different atomic states correlating to Σ and Π states used in the present calculations.

$He^+(3s) + A^+$	$3s\Sigma$	
$He^+(3p) + A^+$	$3p\Sigma$	$3p\Pi$
$He^+(3d) + A^+$	$3d\Sigma$	$3d\Pi$
$He^{2+} + A(4/5s)^a$	$A4/5s\Sigma$	(Initial channel)
$He^{2+} + A(4/5p)$	$A4/5p\Sigma$	$A4/5p\Pi$
$He^+(4s) + A^+$	$4s\Sigma$	
$He^+(4p) + A^+$	$4p\Sigma$	$4p\Pi$
$He^+(4d) + A^+$	$4d\Sigma$	$4d\Pi$

^aA stands for the alkali atom target K/Rb.

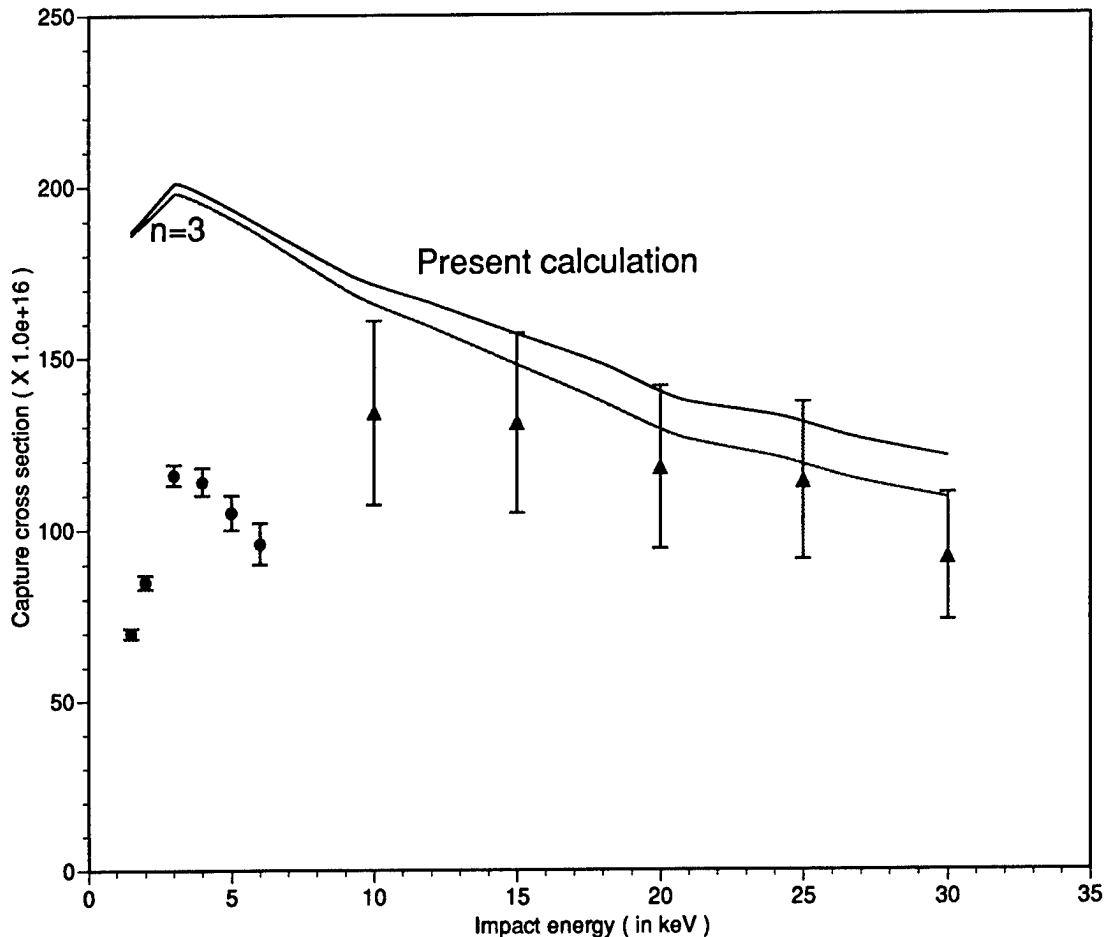


FIGURE 3. Cross sections (in 10^{-16} cm^2) for single-electron capture by α -particles from ground state K: (present cal) calculated cross sections for total capture; ($n = 3$) cross sections for capture into $n = 3$ manifold of He^+ ; (●) experiment by Schweinzer and Winter [6]; (▲) experiment by Shah and Gilbody [7].

sections for single-electron capture into the $n = 3$ manifold of He^+ in this figure.

Our cross section for single-electron capture in the reaction $\text{K}-\alpha$ exhibits a peak around the impact energy 3 keV. This is the region where Schweinzer and Winter also measured the maximum cross section. However, our calculated cross sections are twofold as large as their experimental measurements. In comparison to that, the close-coupling calculations by Schweinzer and Winter, which use the usual AO expansion method, are found to be in better agreement with their own measured values, although these results also lie in the higher side of the experimental results. But this apparent better agreement needs to be judged in the light of the fact that a number of simplifying assumptions have been incorporated into these calculations. As mentioned by Schweinzer and

Winter, instead of including the ETF explicitly in their calculations, they used an approximate scheme put forward by Larsen and Taulbjerg [14] to evaluate their matrix elements. The importance of the proper choice of ETF in such calculations can hardly be emphasized; this may not significantly affect the total capture cross section, but its effect on various individual channels is bound to be appreciable [11]. In fact, one may get unphysical distribution of the total cross section into various individual channels if the ETF is not properly accounted for. Another aspect that has not been taken care of in these calculations is the excitation of the target atom. As shown in Figure 1, the excited target, that is, $\text{K}(4p)$, energetically lies just below the He^+ ($n = 4$) manifold, and, hence, its inclusion in the close-coupling calculation seems to be unavoidable if one wants to get a realistic

picture of flux distribution. We do include these states (for both K and Rb) in our MO calculations and the ETF has also been taken care of in the proper way. Even Schweinzer and Winter [6], while commenting on their AO13 calculations, accept that a larger basis set along with proper treatment of ETF may be needed while investigating such colliding systems.

Agreement of our cross sections with another set of experimental measurements by Shah and Gilbody [7], carried out in intermediate-energy region, is much more satisfactory. Our cross sections, although still at the higher side in absolute magnitude, are much closer to these experimental results which have an accuracy within +20% (shown here in the form of error bars). Also, our observations that capture into He^+ ($n = 2$) is negligibly small in this energy range concur with these measurements. In fact, we found that capture into the $n = 3$ manifold of He^+ is still the most dominant process contributing toward single-electron capture in this energy region. Capture into He^+ ($n = 4$ manifold) increases with increase in the impact energy but its absolute magnitude is slightly more than 10% at the highest impact energy that we have looked into. Here, also, our observations are somewhat different from those of Schweinzer and Winter, who found that the maximum contribution of capture into He^+ ($n = 3$) is limited up to 75%. It may here be pointed out that their AO13 calculations also did not agree with their experimental measurements on the partial capture cross section. We feel that the excited states of these atoms must be included in any close-coupling calculation to obtain a realistic picture of different individual processes contributing toward the single-electron capture by α -particles from alkali atoms. As pointed out earlier, the initial channel $\text{K}4s\Sigma$ couples with those states correlating to He^+ ($n = 4$ manifold) only through $\text{K}4p\Sigma$. This substantially restricts the population of $\text{K}^+ + \text{He}^+$ ($n = 4$) channels in low- and intermediate-energy regions. It is expected that couplings which exist between $\text{K}4p\Sigma$ and different states correlating to He^+ ($n = 4$), at small internuclear separations, will significantly enhance the possibility of capture into the $n = 4$ manifold in high-impact energies. For theoretical interest, it may be pointed out here that capture into Σ molecular states correlating to He^+ ($n = 3$) are found to dominate over capture into Π states, except at very low impact energies where Π states also make significant contributions toward populating the He^+ ($n = 3$) out-

going channel. This is perhaps a manifestation of the relative strengths of various radial and angular couplings that are important and also of the dominant role played by the radial couplings in such colliding systems.

The cross sections for single-charge transfer from Rb to the incident α -particles, along with those for $\alpha\text{-Na}$ and $\alpha\text{-K}$, are graphically presented in Figure 4. The most striking feature of $\alpha\text{-Rb}$ is, more or less, a constant cross section for single-electron capture in the investigated low- and intermediate-energy region. After attaining a peak around 3 keV of the projectile energy, where $\alpha\text{-K}$ also has its peak, the estimated cross section for $\alpha\text{-Rb}$ goes on to acquire a nearly constant value. Also, the relative contribution of capture into He^+ ($n = 4$ manifold) keeps increasing with increase in the impact energy. As discussed earlier, comparatively stronger couplings between $\text{Rb}5p\Sigma$ and other molecular states correlating to $\text{Rb}^+ + \text{He}^+$ ($n = 4$), at smaller R values, are mainly responsible for these individual processes becoming dominant at higher impact energies. Actually, the incoming channel, in both the systems ($\alpha\text{-K}$ and $\alpha\text{-Rb}$), interacts with the above-mentioned outgoing channels only through the molecular state correlating to the excited target atom, that is, $\text{K}4p\Sigma/\Pi$ and $\text{Rb}5p\Sigma/\Pi$. But in the case of the $\alpha\text{-Rb}$ majority of the flux passed onto the $\text{Rb}5p\Sigma$ state finally ends up with the individual channels representing capture into He^+ ($n = 4$ manifold). The difference in the magnitude of the target excitation cross sections in the two cases also agrees with this observation. At the highest impact energy (= 30 keV), the cross sections for excitation to $\text{K}(4p)$ and $\text{Rb}(5p)$ in these reactions are approximately 55 and 40 \AA^2 , respectively. This prompts us to conclude that even though the target excitation may not be an important reaction channel in these collisions its significant role in the selectivity of the electron capture cross section cannot be denied. Another interesting feature of the electron capture in $\alpha\text{-Rb}$, from a theoretical point of view, is the dominance of Π states in populating He^+ ($n = 3$) manifold of the outgoing channel. Obviously, the rotational couplings, in this system, are much stronger than they are in case of $\alpha\text{-K}$.

In Figure 4, we also include the capture cross sections calculated by Kumar et al. [5] for $\alpha\text{-Na}$ in the same energy region. They used exactly the same method as has been employed by us in the present study. The $\alpha\text{-Na}$ cross-section curve has a slightly different characteristic in the low-energy

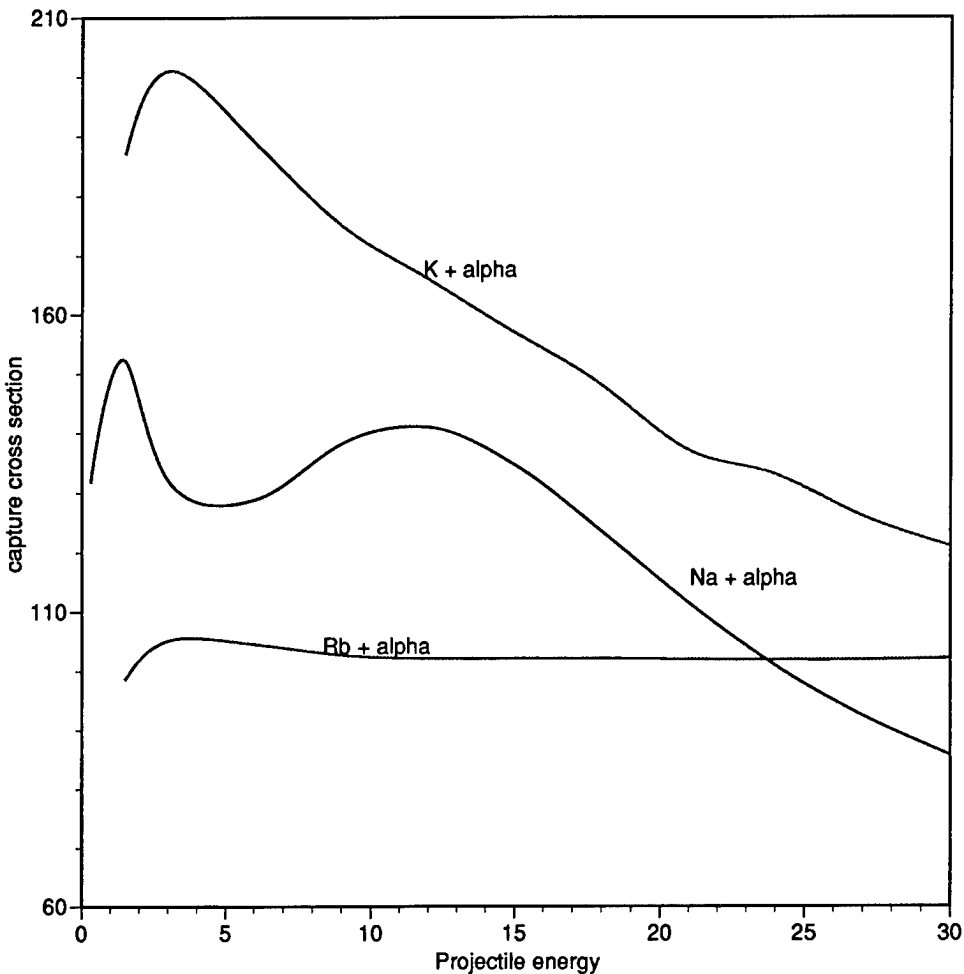


FIGURE 4. Comparison of capture cross sections (in 10^{-16} cm 2) for α -particles colliding with alkali targets. Curves for different colliding systems are clearly marked.

region, where it exhibits Stuckelberg–Landau–Zener oscillations (see [5]). Except for this oscillation, the above curve is found to have similar energy dependence as possessed by the α -K curve, especially beyond 15 keV. The capture cross sections in both the systems monotonically decrease with increase in impact energy as we pass to the intermediate-energy region. Also, in terms of the selectivity of the capture process, these two systems appear to be closer. For example, the α -Na system has a selectivity of 90% in terms of capture into He^+ ($n = 3$ manifold) up to an impact energy 21 keV, whereas the α -K pair possesses this kind of selectivity even at higher energies. In the case of $Rb-\alpha$, the preferential population of He^+ ($n = 3$) falls below 90% much earlier (at 12 keV of projectile energy). Perhaps this is the most important aspect that separates this system from the other

two interacting pairs. With increase in the impact energy, the contribution of new channels of charge transfer becomes increasingly significant, perhaps imparting an altogether different energy dependence to the electron capture cross section in α -Rb.

The above-stated fact also supports the idea of looking into the target dependency of the capture cross sections for alkali atoms. These atoms apparently present a pseudo-one-electron character for the incoming bare nuclei. But when it comes to the transfer of that outermost weakly bound electron, the internal structure of the target atom seems to enter into the scheme. The striking similarity between the α -Na and α -K pairs is perhaps a manifestation of the fact that these target atoms have, more or less, a similar core. In both cases, the outermost electron (ns^1) is backed by a core which has the configuration $(n - 1)s^2(n - 1)p^6$. But as

the d -shell enters into the picture, the core for the $5s^1$ electron of Rb changes. This is perhaps reflected by an altogether different energy dependence of the electron capture cross section for the colliding system α -Rb. One may argue at this stage that the pseudopotential approach, which has been employed by us in the present study, does not include any core orbital, and, hence, such a conclusion seems to be a bit far-fetched. But it should be noted that the parameters used for the pseudopotential were extracted from the spectroscopic data (see Bardsley [10]) which has all the information about the core structure embedded in it. At this stage, we not only agree with the observations of Schweinzer and Winter [6] that the α -K pair needs to be further investigated, but also feel that a systematic study on all alkali targets, both theoretically and experimentally, should be carried out to decipher the role played by their cores toward target dependency of these charge-transfer cross sections, especially in the low- and intermediate-energy regions.

We have thus carried out a close-coupling calculation, using the MO *expansion* method in a semiclassical approximation, to estimate single-electron capture cross sections by α -particles from K and Rb in the low- and intermediate-energy regions. Along with the total capture cross sections, we also calculated the partial cross sections for various individual channels. These calculated results are found to be in satisfactory agreement with the available experimental measurements except at very low impact energies. This may, in part, be due to the use of a semiclassical approach, although we have reasons to believe that cross sections calculated by this method should provide a satisfactory account of experiments even at these energy values. We certainly need a more detailed and systematic study on these target atoms, where the selective population of excited states of He^+ dominates in low energy. Also, the issue of the target dependency of these cross sections and the

possible role played by their cores therein needs to be looked into.

ACKNOWLEDGMENTS

This work was supported, in part, by NASA (Grant No. NAGS-6831), by the NSF-CREST Cooperative Agreement HDR-9707076, and by Army High Performance Computing Research Center under the auspices of the Department of the Army, Army Research Laboratory Cooperative Agreement No. DAAH04-95-2-0003/Contract No. DAAH04-95-C-0008, the content of which does not necessarily reflect the position or the policy of the government, and no official endorsement should be inferred. One of us (B. C. S.) would like to acknowledge the support of the Research Corp. A grant of computer time by the Florida State University is gratefully acknowledged as well.

References

1. R. K. Janev and H. Winter, Phys. Rep. **117**, 265 (1985).
2. W. Fritsch and C. D. Lin, Phys. Rep. **202**, 1 (1991).
3. T. G. Heil, S. E. Butler, and A. Dalgarno, Phys. Rev. A **23**, 1100 (1981).
4. H. Sato and M. Kimura, Phys. Lett. A **96**, 286 (1983).
5. A. Kumar, N. F. Lane, and M. Kimura, Phys. Rev. A **42**, 3861 (1990).
6. J. Schweinzer and H. Winter, J. Phys. B **23**, 3881 (1990).
7. M. B. Shah and H. B. Gilbody, J. Phys. B **7**, 637 (1974).
8. T. Nagata, J. Phys. Soc. Jpn. **48**, 2068 (1980).
9. A. Kumar, N. F. Lane, and M. Kimura, Phys. Rev. A **39**, 1020 (1989).
10. J. N. Bardsley, Case St. At. Phys. **4**, 299 (1974).
11. M. Kimura, R. E. Olson, and J. Pascale, Phys. Rev. A **26**, 3113 (1982).
12. M. Kimura and N. F. Lane, Adv. At. Mol. Phys. **26**, 79 (1990).
13. M. Gargaud, R. McCarroll, and P. Valiron, J. Phys. B **20**, 1555 (1987).
14. O. G. Larsen and K. Taulbjerg, J. Phys. B **17**, 4523 (1984).

Bethe–Bloch Stopping-Power Parameters for GaAs and ZnSe

L. E. PORTER

Washington State University, Pullman, Washington 99164-1302

Received 21 February 1998; accepted 27 February 1998

ABSTRACT: If one is to calculate the stopping power for a specified projectile-target combination within the energy interval of applicability of modified Bethe–Bloch theory, values of several parameters appearing in the formulation must be ascertained. In the past, the author has established such values for numerous target materials through fits of stopping-power measurements with modified Bethe–Bloch theory. However, the semiconductor materials ZnSe and GaAs have not yet been thus characterized. A set of very recent measurements of the stopping powers of each compound for low-energy protons and alpha particles, reported by members of the Helsinki group, has been analyzed in order to remedy this dearth of parameter values. Moreover, some corresponding measurements for ^7Li ions traversing ZnSe have been analyzed for the purpose of obtaining the value of a single effective charge parameter. Results of these studies are reasonably consistent with expectations, and values are recommended for the mean excitation energy and the Barkas-effect parameter for each compound. © 1998 John Wiley & Sons, Inc. *Int J Quant Chem* 70: 919–924, 1998

Introduction

The energy lost by an ion while traversing matter often must be known with considerable accuracy, both for tests of theories in physics and for application to numerous, diverse areas of experimental physics. Energy-loss measurements for every projectile-target combination would be a formidable undertaking indeed. Hence, the availability of a reliable method of calculation is essential. The modified Bethe–Bloch theory of stopping power has great utility for a broad range of projec-

tile velocities, provided that values of several parameters appearing in the theory are known [1–5]. If the target material features aggregation effects, for example, compounds or alloys, Bragg's rule of the (linear) additivity of stopping effects must be invoked [6]. A method of energy-loss calculation in this type of target has been set forth previously [2, 5, 7].

The stopping powers of two compound semiconductor materials for protons and alpha particles have been reported in the past 2 years [8, 9]. In the first experiment [8], the stopping powers of GaAs for 0.3–2.5 MeV protons and alpha particles were measured using both Rutherford backscatter-

ing spectrometry (RBS) and foil transmission methods. In the second experiment [9], the stopping cross sections of ZnSe for 0.4–2.2 MeV protons and alpha particles and for 1.6–8.9 MeV ^7Li ions were measured using the RBS technique. Neither of these targets has yet been adequately characterized in terms of Bethe–Bloch stopping-power parameters. Hence, the author elected to analyze both sets of measurements [8, 9] in order to provide recommended parameter values. In the case of GaAs targets [8], the measurements made with each of the two methods, RBS and foil transmission, were analyzed separately for the sake of subsequent comparisons. Finally, measurements for ^7Li ions in the energy interval 4.0–8.9 MeV were selected for analysis in order to determine the value of an effective charge parameter for this projectile–target combination.

Theory

The modified Bethe–Bloch stopping power formalism and the procedure utilized in the analysis of stopping-power data for the extraction of values of the various parameters contained in the formalism have been extensively described in previous studies [2, 5, 7, 10, 11]. In the case of an elemental target of atomic number Z and atomic weight A , the stopping power S for a projectile of atomic number z and velocity $v = \beta c$ is given by

$$S = \frac{0.30706}{\beta^2} z^2 \frac{Z}{A} L \quad (1)$$

in units of MeV cm²/g. In this expression, L , signifying the (dimensionless) stopping number per target electron, consists of three terms:

$$L = L_0 + \xi z L_1 + L_2, \quad (2)$$

where the basic stopping number, L_0 , is

$$L_0 = \ln \left(\frac{2mc^2\beta^2}{1 - \beta^2} \right) - \beta^2 - \ln I - C/Z - \delta/2. \quad (3)$$

The symbol I in this equation represents the target mean excitation energy, mc^2 denotes the rest mass energy of the electron, C signifies the sum of target shell corrections, and δ is the density effect correction required for highly relativistic projectiles [12]. The mean excitation energy can be determined in a fit of accurate stopping-power measurements. Shell

corrections can be evaluated by the method of Bichsel [1], whereby Walske K - and L -shell corrections [13] are employed with scaling factors assigned to the L -shell correction in order to obtain the M - and N -shell corrections:

$$C = C_K(\beta^2) + V_L C_L(H_L \beta^2) + V_M C_L(H_M \beta^2) + V_N C_L(H_N \beta^2). \quad (4)$$

Here, C_K and C_L denote the K - and L -shell corrections, respectively, and the V_i and H_i (with $i = L, M, N$) represent the scaling factors.

The (zL_1) and L_2 terms of Eq. (2) signify two necessary correction terms of higher order in the projectile atomic number (z). The (zL_1) term has been named the Barkas-effect term, whereas the L_2 term is known as the Bloch term [14]. These corrections have recently been reviewed in the course of a random-phase approximation evaluation of the L_1 term [15]. This term was calculated by the author on the basis of the formalism that demonstrably best agreed with a large body of experimental data [3], namely, the formalism prepared by Ashley et al. [16–19], that is, the Barkas-effect term was obtained for analyses in the current study from the expression [16–19]

$$L_1 = \frac{F(b/x^{1/2})}{Z^{1/2} x^{3/2}}, \quad (5)$$

where F denotes a function graphed in [16], $x = (18787)\beta^2/Z$, and b represents the sole free parameter of the formalism. ξ precedes the Barkas-effect term as an adjustable parameter that was introduced for the study of a controversy over the inclusion of close-collision contributions to the term [2, 7, 10]. In recognition of the conclusion drawn by the author [2, 7, 10] and others [20] that the controversy could not be resolved through fits to stopping-power measurements, the value of ξ is now generally set at unity. The Bloch term [14], originally introduced as a correction term to make the transition from the first Born approximation to classical scattering at low projectile velocities [15], is obtained as

$$L_2(y) = \psi(1) - \text{Re}[\psi(1 + iy)], \quad (6)$$

where ψ denotes the digamma function [21] and $y = z\alpha/\beta$, with α representing the fine structure constant.

A complete discussion of data-fitting strategies, especially in the case of a target evincing aggrega-

tion effects, can be found in [5]; that is, stopping-power measurements generally are provided with a fit by modified Bethe-Bloch theory, in the course of which best-fit values of I and b are established. The figure of merit employed in the fitting procedure is the root-mean-square relative deviation of calculated from measured stopping powers, σ . This quantity is defined as

$$\sigma = \sqrt{\frac{1}{N} \sum_{i=1}^N \left(\frac{S_m - S_c}{\Delta S_m} \right)_i^2}, \quad (7)$$

for measurements at N energies, with S_m denoting the measured stopping power; S_c , the calculated stopping power; and ΔS_m , the uncertainty in the measured value. Hence, a resulting value of σ near unity implies that agreement between theory and experiment is acceptable.

The additivity test usually applied to the value of mean excitation energy is based on a Bragg value (I_B) calculated from the expression [22, 23]

$$\ln I_B = \sum_j n_j Z_j \ln I_j / \sum_j n_j Z_j, \quad (8)$$

where I_j , Z_j , and n_j , respectively, denote the mean excitation energy, atomic number, and atomic concentration of the j th component of the composite target material. In the present investigation, this test has little value, since of the four components of GaAs and ZnSe only one (Zn) has had its mean excitation energy determined previously.

One further modification in the Bethe-Bloch formula must be made in order to account for the gain and loss of electrons by the projectile when its velocity has decreased to a value comparable to those of atomic electrons. This method of extending downward the projectile energy of applicability of the Bethe-Bloch formula is often effected by incorporating some form of projectile effective charge [10, 24]. The form utilized by the author has proved successful in one quite comprehensive study of heavy ion stopping powers [10], wherein the projectile charge ze is replaced by an effective charge γze , with

$$\gamma = 1 - \zeta e^{-\lambda v_r}. \quad (9)$$

Here, v_r represents the ratio of projectile velocity in the laboratory frame (v) to the Thomas-Fermi velocity (e^2/h) $z^{2/3}$, so that $v_r = \beta/\alpha z^{2/3}$, and ζ and λ stand for the effective-charge parameters whose values must be established for any given projectile-target combination [10]. This method

was used in the present study for analysis of the stopping-power measurements with ^7Li projectiles and ZnSe targets [9].

Analyses and Results

The basic procedure utilized was that described previously [2, 5, 7, 10, 11], that is, shell-correction values were calculated by the Bichsel method [1] and ξ was set at unity so as to ascertain best-fit values of I and b . The values of the known parameters, including the average atomic number (\bar{Z}) and atomic weight (\bar{A}), are displayed in Table I. The values of I_B shown there were obtained from Eq. (8), and the constituent I values, from the one value based on measurement (Zn) and three estimates, all from [1]: $I = 334$ eV for Ga, 347 eV for As, (330 ± 10) eV for Zn, and 348 eV for Se. This method was used for analyses of all light projectile measurements.

In selecting measurements for analysis, it is important to know the lowest-energy data point that can be included without employing a charge-state correction (i.e., an effective charge formalism). The answer to this question has been established in earlier studies with protons [11, 25, 26] and with alpha particles [27, 28]. The lower bound for proton energy inclusion without an appreciable distortion of extracted parameter values is 300 keV, whereas that for alpha particles is 1.0 MeV. Thus, the energy intervals selected were consistent with this constraint.

Results are displayed in Table II. To assess the relative credibility of results for each experiment, uncertainties in the extracted parameters (ΔI and Δb) were evaluated according to the procedure described in detail previously [10]. The values of uncertainties reflect the number, accuracy, and internal consistency of the measurements analyzed.

TABLE I
Average atomic number (\bar{Z}) and atomic weight (\bar{A}), shell correction scaling parameters (V_L, H_L, V_M, H_M), and Bragg value of mean excitation energy (I_B) for both compound targets.

Target	\bar{Z}	\bar{A}	V_L	H_L	V_M	H_M	I_B (eV)
GaAs	32	72.32	1.0	1.0	2.25	5.39	340.6
ZnSe	32	72.17	1.0	1.0	2.25	5.39	339.4

TABLE II
Projectile-target combination, projectile energy interval utilized, and type of experiment, with corresponding best-fit values of mean excitation energy (I), Barkas-effect parameter (b), and figure of merit (σ).

Target	Projectile	E (MeV)	Expt.	I	b	σ
ZnSe	Proton	0.4–2.2	RBS	320.1	2.77	0.73
	Alpha	1.0–2.2	RBS	328.1	1.99	0.65
GaAs	Proton	0.6–2.5	RBS	315.1	2.70	1.55
	Alpha	1.0–2.2	RBS	323.9	2.00	0.37
	Proton	0.3–2.4	Transmission	301.9	3.42	1.40
	Alpha	1.0–2.1	Transmission	309.6	2.20	0.43

Results, which are shown in Table III, will be discussed further below.

A final aspect of the analyses described in this investigation was the assignment of a value of a single effective charge parameter [λ in Eq. (9)] to measurements of ^7Li energy loss in ZnSe targets [9] in the energy interval 4.0–8.9 MeV. For this portion of the study, a value of 324 eV was assigned to the mean excitation energy (I) and a value of 2.0 to the Barkas-effect parameter (b). The resulting value of λ was 1.35, with a figure of merit (σ) of 0.56. This outcome compared favorably with those from similar studies with targets of kapton ($\lambda = 1.28 \pm 0.08$) [29] and mylar ($\lambda = 1.30$) [24], but less favorably with those from a study on nickel ($\lambda = 1.04$) and havar ($\lambda = 1.16$) [30].

Discussion

The experiments analyzed in this study [8, 9] were conducted with thin-film transmission and Rutherford backscattering techniques, as was the case in a similar previous study with polystyrene as a target material [5]. An inspection of the results in Table II does suggest possible systematic outcomes based on the type of experiment. (This possibility will be explored below.)

The figure of merit (σ) exceeded unity in two cases, one for each type of experiment but both for the proton–GaAs projectile–target combination. Indeed, the graphical data presentation indicates considerable scatter for each of those two sets of measurements [8]. Salient characteristics of the parameter values extracted from the experimental data, displayed in Table III, will be explained on a quantitative basis.

In the final stages of developing the Barkas-effect formalism employed herein [16–19], two of the authors recommended that, in general, $b = 1.4 \pm 0.1$ [19]. In fits to measurements, extracted b values often stray considerably from this guideline [5, 9, 11, 27]. However, one might assign higher plausibility to the reported measurements which provide extracted b values in the vicinity of the guideline value, assuming that the modified Bethe–Bloch theory is correct. In Table III, three rather high values of b are observed, notably those for protons in GaAs (transmission experiment). In fact, all three of these values arose from the proton measurements. Indeed, the calculated uncertainties in both I and b were high for all three sets of proton measurements; this outcome reflects some scatter in the two cases of GaAs targets, but scatter was only moderate in the case of a ZnSe target [9].

There is no firm guideline for extracted I values, since the Bragg values (I_B) are based on recommended constituent I values [1] that are tenuous indeed. An alternate set of recommended I values for the constituent elements, published much earlier [31], were generally lower than those of [1]: $I = 290.6$ eV for As, 301.8 eV for Ga, 300.9 eV for Se, and 323.1 eV for Zn. Hence, the Bragg values calculated from these constituent values would lie considerably lower than those given in Table I (approximately 310 eV for ZnSe and 295 eV for GaAs). Since the experiment-based value of I for Zn [1] was (330 ± 10) eV, and since the observed I values for compounds are generally expected to exceed additivity-based values, one might lend higher credence to the extracted I values for the two subject compounds that lie in the vicinity of the range cited for Zn.

To assess the outcome of the current analysis systematically and quantitatively, the extracted

TABLE III

Projectile-target combination, projectile energy interval utilized, and type of experiment, with corresponding experimental relative uncertainty ($\Delta S / S$), number of data points analyzed (N), and calculated uncertainties in mean excitation energy (ΔI) and Barkas-effect parameter (Δb).

Target	Projectile	E (MeV)	Expt.	$\Delta S / S$ (%)	N	$I \pm \Delta I$ (eV)	$b \pm \Delta b$
ZnSe	Proton	0.4–2.2	RBS	4.0	11	320.1 ± 9.2	2.77 ± 0.52
	Alpha	1.0–2.2	RBS	4.0	9	328.1 ± 3.4	1.99 ± 0.04
GaAs	Proton	0.6–2.5	RBS	3.5	17	315.1 ± 8.2	2.70 ± 0.63
	Alpha	1.0–2.2	RBS	4.0	5	323.9 ± 3.3	2.00 ± 0.06
	Proton	0.3–2.4	Transmission	3.0	27	301.9 ± 4.0	3.42 ± 0.25
	Alpha	1.0–2.1	Transmission	2.0	27	309.6 ± 1.3	2.20 ± 0.03

parameter values were combined for average values, weighted according to the uncertainties in the extracted values as shown in Table III. The results of this approach are given in Table IV.

Uncertainties in the extracted parameter values were definitely lower in the experiments with alpha particle projectiles. Hence, the weighted average values closely approach those from the alpha-particle experiments for both ZnSe and GaAs targets. In the case of GaAs targets, two other comparisons were possible: one by type of experiment (RBS or foil transmission) and one by type of projectile (proton or alpha particle). Since the smallest uncertainties by far were obtained for the alpha particle in the GaAs (transmission) experiment, the parameter values characterizing that experiment clearly dominated all comparisons, as readily observed by viewing Tables III and IV. In light of the remarkably high value of b and low value of I associated with the proton in the GaAs (transmission) experiment, it appears reasonable to suggest that some difficulties attended those measurements, but there is no rationale for excluding

any other experiment from the six available. Although the alpha-particle measurements manifested the greater internal consistency, for example, the proton measurements covered an energy interval that was twice as large. On the basis of the systematics observed in the results of the foregoing analysis, the author has risked a recommendation of parameter values for each target. The recommendations appear in Table V.

Summary

Very recent measurements of the stopping powers of two semiconductor compounds, GaAs and ZnSe, for protons and alpha particles [8, 9] were analyzed in terms of modified Bethe-Bloch theory to extract values of the mean excitation energy and Barkas-effect parameter. Results of this study are quite consistent with general expectations. Moreover, a single effective charge parameter for ^7Li ions in ZnSe targets [9] was evaluated, with results comparable to those of several similar previous studies [24, 29, 30]. Recommended values of the mean excitation energy and Barkas-effect parameter for each compound, shown in Table V, will

TABLE IV

Comparison of weighted average values of mean excitation energy (\bar{I}) and Barkas-effect parameter (\bar{b}) by target and group of measurements.

Target	Group	\bar{I} (eV)	\bar{b}
ZnSe	All	327.1	1.99
GaAs	All	310.8	2.18
GaAs	RBS	322.7	2.01
	Transmission	308.9	2.22
GaAs	Proton	304.4	3.32
	Alpha	311.5	2.16

TABLE V

Recommended values of the Bethe-Bloch parameters, mean excitation energy (I), and Barkas-effect parameter (b) for both compounds.

Target	I (eV)	b
ZnSe	325 ± 5	2.0 ± 0.1
GaAs	315 ± 5	2.2 ± 0.1

have to await the advent of experiments more accurate than those analyzed [8, 9] in order to be confirmed or revised.

References

1. See, e.g., *Stopping Power and Ranges for Protons and Alpha Particles*, ICRU Report No. 49 (International Commission on Radiation Units and Measurements, Bethesda, MD, 1993).
2. L. E. Porter, E. Rauhala, and J. Räisänen, Phys. Rev. B **49**, 11543 (1994).
3. L. E. Porter and H. Lin, J. Appl. Phys. **67**, 6613 (1990).
4. L. E. Porter, Appl. Phys. Lett. **61**, 360 (1992).
5. L. E. Porter, Int. J. Quantum Chem. **65**, 997 (1997).
6. W. H. Bragg and R. Kleeman, Philos. Mag. **10**, 318 (1905).
7. L. E. Porter, Phys. Rev. A **50**, 2397 (1994).
8. M. Rajatora, K. Väkeväinen, T. Ahlgren, E. Rauhala, J. Räisänen, and K. Rakennus, Nucl. Instrum. Methods B **119**, 457 (1996).
9. K. Väkeväinen, Nucl. Instrum. Methods B **122**, 187 (1997).
10. L. E. Porter, Radiat. Res. **110**, 1 (1987).
11. L. E. Porter, Nucl. Instrum. Methods B **88**, 211 (1994).
12. R. M. Sternheimer, M. J. Berger, and S. M. Seltzer, At. Data Nucl. Data Tab. **30**, 261 (1994).
13. M. C. Walske, Phys. Rev. **88**, 1283 (1952); *Ibid.* **101**, 940 (1956).
14. F. Bloch, Ann. Phys. (Leipzig) **16**, 285 (1933).
15. J. M. Pitärke, R. H. Ritchie, and P. M. Echenique, Phys. Rev. B **52**, 13883 (1995).
16. J. C. Ashley, R. H. Ritchie, and W. Brandt, Phys., Rev. B **5**, 2393 (1972).
17. J. C. Ashley, R. H. Ritchie, and W. Brandt, Phys. Rev. A **8**, 2402 (1973).
18. J. C. Ashley, Phys. Rev. B **9**, 334 (1974).
19. R. H. Ritchie and W. Brandt, Phys. Rev. A **17**, 2101 (1978).
20. G. Basbas, Nucl. Instrum. Methods B **4**, 227 (1984).
21. M. Abramowitz and I. A. Stegun, Eds., *Handbook of Mathematical Functions* (National Bureau of Standards, Washington, DC, 1964), p. 259.
22. U. Fano, Annu. Rev. Nucl. Sci. **13**, 1 (1963).
23. W. H. Barkas and M. J. Berger, in *Studies in Penetration of Charged Particles in Matter*, National Academy of Sciences—National Research Council Publication No. 1133 (NAS-NRC, Washington, DC, 1967).
24. L. E. Porter, J. Appl. Phys. **80**, 1901 (1996).
25. L. E. Porter, Nucl. Instrum. Methods B **12**, 50 (1985).
26. L. E. Porter, Nucl. Instrum. Methods B **93**, 203 (1994).
27. L. E. Porter, Nucl. Instrum. Methods B **69**, 39 (1992).
28. L. E. Porter, Nucl. Instrum. Methods B **95**, 285 (1995).
29. L. E. Porter, Nucl. Instrum. Methods B **115**, 181 (1996).
30. L. E. Porter, Nucl. Instrum. Methods B **96**, 643 (1995).
31. J. F. Janni, At. Data Nucl. Data Tab. **27**, 341 (1982).

Searches on the Potential Energy Hypersurfaces of GeCH_2 , GeSiH_2 , and Ge_2H_2

AMY J. BOONE,^{1,*} DAVID H. MAGERS,¹ JERZY LESZCZYŃSKI²

¹Department of Chemistry, Mississippi College, Clinton, Mississippi 39058

²Department of Chemistry, Jackson State University, Jackson, Mississippi 39217

Received 30 March 1998; accepted 19 May 1998

ABSTRACT: Optimum geometries are computed at both the SCF level of theory and the level of second-order perturbation theory for several isomers on the potential energy hypersurfaces of GeCH_2 , GeSiH_2 , and Ge_2H_2 , including linear structures, methylene-carbenelike structures, dibridged structures, and monobridged structures. In addition, harmonic vibrational frequencies are computed to characterize these structures as local minima or transition states. All computations employ basis sets of triple-zeta quality on valence electrons with *d* and *f* polarization functions on the heavy atoms and *p* functions on hydrogen. This investigation is the first systematic study to include all of these germanium systems and to employ *f*-type polarization functions in such a study. Previous investigations of ours indicate that large basis sets such as those employed in this study can, in part, compensate for the lack of a more advanced treatment of electron correlation. While a dibridged global minimum is confirmed for both Ge_2H_2 and GeSiH_2 systems, the C_{2v} isomer, methylenegermene, is found to be the most stable structure for GeCH_2 . © 1998 John Wiley & Sons, Inc. Int J Quant Chem 70: 925–932, 1998

Introduction

The isomerization of acetylene to methylenecarbene (Fig. 1) has been one of the most thoroughly studied unimolecular reactions [1–4] and has led to interest in various isoelec-

tronic species. Research of silicon derivatives has been of particular importance due to the increasing interest in the development of silicon thin films [5]. In 1983, an ab initio study predicted that disilyne (Si_2H_2) prefers a butterfly, double-bridged geometry (Fig. 2) instead of a linear structure similar to that of acetylene [6, 7]. The first experimental evidence of this dibridged structure was reported in 1991 by Bogey and coworkers using microwave spectroscopy [8]. The very next year, a *cis* monobridged isomer (Fig. 3) of disilyne was predicted by Grev and Schaefer to be the second most stable

Correspondence to: D. H. Magers.

*Mississippi College CATALYSTS Undergraduate Research Fellow. Current address: Department of Chemistry, University of Florida, Gainesville, FL 32611.

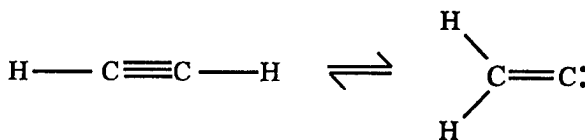


FIGURE 1. Isomerization of acetylene to methylenecarbene.



FIGURE 2. Disilyne.

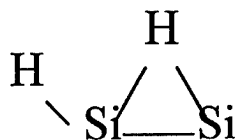


FIGURE 3. *cis*-HSiHSi.

isomer on the surface [9] and was discovered experimentally that same year by Cordonnier and coworkers [10]. Similar structures have also been predicted for Ge_2H_2 [11, 12].

Discovery of these three-centered bonding structures has sparked interest in the possibility of similar isomers of other isoelectronic systems, particularly those containing only one silicon atom [13–15]. Investigations have mapped out a complete potential energy surface for SiCH_2 , with the C_{2v} isomer methylenesilene being observed experimentally in the gas phase as confirmed by neutralization–reionization mass spectroscopy [16]. Other minima on this surface include another C_{2v} isomer, silylenecarbene (CSiH_2), as well as a planar *trans*-bent structure [14, 17, 18].

The goal of this present study was to extensively examine the potential energy surfaces of three germanium systems isoelectronic to the systems mentioned above, namely, Ge_2H_2 , GeSiH_2 , and GeCH_2 . A former computational study from our research group of linear and methylenecarbene-like C_{2v} structures on each of these surfaces has offered insight into bonding trends of these systems [19]. This study builds on this previous work by investigating not only linear and C_{2v} structures, but butterfly dibridged, *cis*-monobridged, *trans*-monobridged, *trans*-bent, and planar dibridged conformations as well.

Computational Details

In the present study, optimum equilibrium geometries, harmonic vibrational frequencies, and corresponding electronic energies were determined for the singlet ground states of various minima and transition structures on the surfaces of Ge_2H_2 , GeSiH_2 , and GeCH_2 . These computations were performed at both the SCF level and the level of second-order perturbation theory (MP2) using the Gaussian94 program package [20]. The SCF computations were performed only for reference, and, therefore, they are not reported in tabular form here.

In all of the second-order calculations reported in this study, core molecular orbitals (MOs) are frozen. For example, in GeCH_2 , 14 MOs corresponding to the germanium $1s$, $2s$, three $2p$, $3s$, three $3p$, and five $3d$ functions and one MO corresponding to the carbon $1s$ function are frozen. No virtual orbitals are deleted for any of the correlated calculations.

A basis set of triple-zeta quality for valence electrons is employed for each molecular system. For hydrogen, carbon, and silicon, the basis set is the standard Gaussian94 6-311G(2df, 2p). The 6-311G basis is a split-valence basis set comprising a single-zeta core description and a triple-zeta description for valence orbitals [21]. A similar basis set developed by Huzinaga and coworkers is employed for germanium [22]. This basis set also consists of a triple-zeta description for valence orbitals and is referred to as TZV(2df, 2p). Throughout this study, the overall basis set for a molecular system is denoted only as TZV(2df, 2p) for simplicity. The (2df, 2p) represents the number and types of polarization functions included on the heavy atoms and on the hydrogens, respectively. Each *d* function represents five degenerate complex *d* functions, while the *f* function comprises seven degenerate complex *f* functions. The exponents for the two *d* functions and the *f* function used for germanium are 0.108, 0.382, and 0.450, respectively. The number of functions included in the basis sets employed for the various molecular systems ranges from 91 functions for GeCH_2 to 104 functions for Ge_2H_2 . Previous investigations of ours have shown that large basis sets can, in part, compensate for the lack of a more advanced treatment of electron correlation [23].

Results and Discussion

Optimum equilibrium geometries and corresponding energetics for six stationary points located on the potential energy hypersurface of Ge_2H_2 are reported in Table I. Computation of the harmonic vibrational frequencies of these structures reveal that four are minima and two are transition states. At least five of these structures were investigated in previous studies. In 1990, Grev and coworkers predicted that the global minimum of Ge_2H_2 exhibits a C_{2v} double-bridged butterfly form (Fig. 4) analogous to that found for Si_2H_2 [11]. The present study reveals that this dibridged structure is only about 8.7 kcal/mol lower in energy than the next minimum on the surface at the MP2/TZV(2df, 2p) level of computation. This next local minimum is a planar (C_s) *cis*-monobridged isomer (Fig. 5) which was first predicted in 1993 by Palágyi and Schaefer to exist as a minimum at correlated levels and as a transition state at the SCF level [12]. This result is interesting in light of the fact that similar isomers of Si_2H_2 , Al_2H_2 , and Ga_2H_2 are shown to exist as minima at both the SCF level and correlated levels of theory [24].

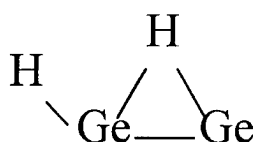
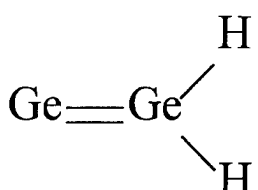
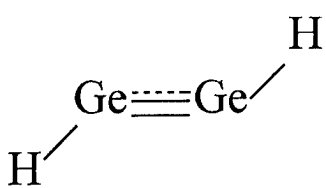
Examination of the results reported in Table I reveals another structure which lies energetically between the dibridged global minimum and the *cis*-monobridged isomer. A planar D_{2h} dibridged transition state is found to lie about 8.4 kcal/mol above the dibridged isomer at the MP2/TZV(2df, 2p) level. This structure appears to be the transition between the "flip-flop" or inversion of the C_{2v} dibridged isomer and exists as a transition state on both the SCF and the MP2 potential energy surfaces.

Two other minima are found on the Ge_2H_2 MP2 surface, namely, germylenegermene, a C_{2v} isomer (Fig. 6) analogous to methylenecarbene, and a planar (C_{2h}) *trans*-bent structure (Fig. 7) [11]. At the MP2/TZV(2df, 2p) computational level, GeGeH_2 possesses an energy about 13.7 kcal/mol higher than the dibridged isomer, while the *trans*-bent isomer, resting about 17.7 kcal/mol above the global minimum, is only slightly higher in energy. It is interesting to note that the *trans*-bent isomer, like the planar *cis*-monobridged structure, only exists at correlated levels, but, in contrast, possesses two imaginary vibrational frequencies at the SCF level. When observing bond lengths, it is

TABLE I
Energies and equilibrium geometries of the structural isomers of Ge_2H_2 determined at the MP2 / TZV(2df, 2p) level of theory.^a

	GehHGe dibridged (C_{2v})	GehHGe planar (D_{2h})	HGeHGe <i>cis</i> -monobridged planar (C_s)	GeGeH ₂ germylenegermene planar (C_{2v})	HGeH <i>trans</i> -bent planar (C_{2h})	HGeGeH ^b linear (D_{2h})
Energy (au)	-4148.25237	-4148.23904	-4148.23852	-4148.23059	-4148.22421	-4148.18486
Relative energy (kcal / mol)	0.00	8.36	8.69	13.67	17.67	42.36
$r(\text{Ge} - \text{Ge})$ (Å)	2.365	2.543	2.234	2.298	2.188	2.067
$r(\text{Ge} - \text{H})$ (Å)	1.745	1.678	1.789 (H_B) ^c	1.528	1.535	1.492
$r(\text{Ge} - \text{H})$ (Å)	1.745	1.678	1.534 (H_T) ^d	1.528	1.535	1.492
$\angle(\text{H} - \text{Ge} - \text{Ge})$	47.34°	40.72°	48.77° (H_B) ^c	124.19°	125.54°	180°
$\angle(\text{H} - \text{Ge} - \text{H})$			110.70° (H_T) ^d	180°	180°	180°
$\angle(\text{H} - \text{Ge} - \text{Ge} - \text{H})$	105.83°	180°	180°	180°	180°	180°

^a Core molecular orbitals are frozen; no virtual orbitals are deleted. Germanium atoms employ the TZV(2df) basis set (see [22]); all other atoms employ a 6-311G(2df, 2p) basis set (see [21]).
^b A transition state.
^c A bridge hydrogen is involved in the bond or bond angle.
^d A terminal hydrogen is involved in the bond or bond angle.

**FIGURE 4.** GeHHGe (C_{2v}).**FIGURE 5.** HGeHGe (C_s).**FIGURE 6.** GeGeH_2 (C_{2v}).**FIGURE 7.** HGeGeH (C_{2h}).

found that the Ge—Ge bond distance in this structure is somewhat shorter than that of the double bond found in GeGeH_2 ; however, it is slightly longer than that of the triple bond observed in a linear structure. This fact suggests that the *trans*-bent isomer can best be described as a biradical with two unpaired π electrons localized on the terminal atoms and weakly coupled into the observed singlet electronic state. The prototypical example of this type of biradical nature is ozone [25].

One other structure is reported in Table I. A linear structure analogous to acetylene is found to be over 40 kcal/mol higher in energy than the global minimum at the MP2/TZV(2*d*, 2*p*) level and collapses directly to the *trans*-bent isomer. The HGeGeH structure is a transition state with two degenerate imaginary frequencies corresponding to the out-of-line hydrogen motion of π_g symmetry. The existence of the linear structure as a high-

energy transition state seems to be in direct contrast with the corresponding stable acetylene isomer. This contrast may be explained by taking a closer look at the electronic structures of C_2H_2 and Ge_2H_2 .

The relative energy levels of the molecular orbitals in linear Ge_2H_2 are quite different from those in acetylene. In both molecules, the occupied molecular orbital with the highest energy (HOMO) has π_u symmetry and the unoccupied molecular orbital with the lowest energy (LUMO) has π_g symmetry. However, the HOMO-LUMO energy gap in Ge_2H_2 is much smaller than is the corresponding gap in acetylene. The LUMO in Ge_2H_2 is lower in energy than is the LUMO in acetylene and the HOMO in Ge_2H_2 is higher in energy. When the linear symmetry of Ge_2H_2 breaks into the C_{2h} symmetry of the *trans*-bent isomer, the degenerate π_u HOMO splits into two nondegenerate orbitals. One has a_u symmetry, and one has b_u symmetry. The highest occupied σ_u (σ^*) orbital of the linear structure also becomes an orbital of b_u symmetry in the nonlinear isomer. The reduced symmetry of this *trans* configuration allows mixing of these b_u orbitals, which leads to an overall lower energy in Ge_2H_2 . This type of stabilization is referred to as second-order Jahn-Teller stabilization. Of course, the same type of orbital mixing can occur in a *trans* configuration of C_2H_2 , but the original molecular orbital energy levels in the linear isomer of this molecular system are qualitatively different. In C_2H_2 , this b_u mixing in the *trans* configuration does not lead to an overall energy more stable than that of acetylene. A discussion similar to the above was given by Colegrove and Schaefer in their article on Si_2H_2 in which a *trans*-bent isomer is one of the local minima reported [26].

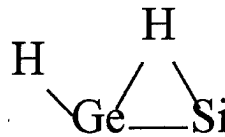
With the exception of the existence of the planar *cis*-monobridged transition state at the SCF level, no monobridged transition states have been discovered as yet on the Ge_2H_2 energy surface. However, there is sufficient evidence to support the existence of such stationary points on this surface. Known isomers of Ge_2H_2 are analogous to those found for Si_2H_2 . The latter exhibits two different monobridged transition states, namely, a nonplanar structure, as well as a planar *trans* structure [12].

The GeSiH_2 potential energy surface shares many features with that of Ge_2H_2 . The current study examined eight different stationary points on the potential surface of GeSiH_2 . Optimum equi-

librium geometries and corresponding energies and relative energies of these eight structures are given in Table II. The global minimum on the GeSiH_2 surface at the correlated level is a di-bridged butterfly structure with C_s symmetry similar to the global minima of Si_2H_2 and Ge_2H_2 . Another relatively low-lying local minimum on this surface is silyenegermene, a C_{2v} isomer with the lone electron pair residing on the germanium (GeSiH_2). At the MP2/TZV(2df, 2p) computational level employed in this study, this structure is about 8.4 kcal/mol higher in energy than the di-bridged isomer. However, at the SCF level, this C_{2v} isomer is the global minimum, with the di-bridged structure being slightly over 1 kcal/mol higher in energy [TZV(2df, 2p)].

A similar C_{2v} isomer with the lone pair residing on the silicon (SiGeH_2) is also a local minimum. However, this structure, germylenesilene, possesses the highest energy of all the minima on the GeSiH_2 surface at both computational levels employed. The energy difference between SiGeH_2 and the di-bridged isomer is almost 20 kcal/mol [MP2/TZV(2df, 2p)]. The stability of silyenegermene (GeSiH_2) relative to germylenesilene (SiGeH_2) is due to the ability of germanium's diffuse electron cloud to accommodate a lone electron pair more easily than can silicon. Another local minimum discovered on this potential surface is a planar (C_s) *trans*-bent structure [15] that exists with an energy about 17.5 kcal/mol higher than the di-bridged isomer. Like the similar structure found for Ge_2H_2 , this *trans*-bent isomer, due to its biradical nature, only exists at the correlated level.

Two additional minima were previously reported to exist on the GeSiH_2 surface: Two planar (C_s) *cis*-monobridged isomers were first discovered in 1995 by O'Leary and coworkers [15] and the present study concurs. The first of these monobridged isomers has the terminal hydrogen on the silicon (Fig. 8). This structure is about 6 kcal/mol higher in energy than the di-bridged isomer, putting it lower in energy than the GeSiH_2 C_{2v} isomer at the highest computational level employed in this

FIGURE 9. HGeHSi (C_s).

study. However, this monobridged structure only exists at the correlated level and collapses to the C_{2v} GeSiH_2 isomer at the SCF level. The other monobridged structure (Fig. 9) with the terminal hydrogen on the germanium is the last local minimum that we located on the GeSiH_2 surface. At the MP2/TZV(2df, 2p) level, it has an energy about 11.5 kcal/mol above that of the di-bridged isomer. This second monobridged structure is also a minimum only at the correlated level, but it exists as a transition state at the SCF level [15].

Three transition states on the GeSiH_2 surface have been revealed in this study. Similar to Ge_2H_2 , a linear structure exists as a transition state and possesses an energy of about 40 kcal/mol [MP2/TZV(2df, 2p)] above that of the di-bridged isomer. As previously mentioned with Ge_2H_2 , the instability of the linear structure is due to Jahn-Teller stabilization of the *trans*-bent isomer. A second transition state that is similar to one found on the Ge_2H_2 surface is a planar di-bridged structure with C_{2v} symmetry. At the highest computational level employed in this study, this structure is about 10.3 kcal/mol higher in energy than the C_s di-bridged isomer and, as before, probably represents the inversion of the latter. A third transition state not reported in Table II appears to exist. It is a nonplanar *trans*-monobridged structure (Fig. 10) with the terminal hydrogen on the silicon. Preliminary MP2 calculations using a smaller basis set [TZV(d, p)] place this structure about 11.2 kcal/mol higher in energy than the di-bridged isomer. Such a structure could easily represent the barrier between the C_{2v} GeSiH_2 isomer and the di-bridged isomer. If this is true, a similar nonplanar *trans*-monobridged structure with the terminal hydrogen on the germanium might also exist as the barrier from the C_{2v} SiGeH_2

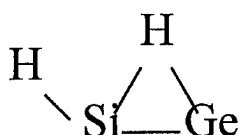
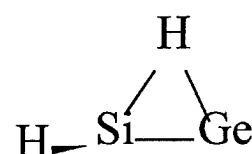
FIGURE 8. HSiHGe (C_s).FIGURE 10. HSiHGe (C_1).

TABLE II
Energies and equilibrium geometries of the structural isomers of GeSiH_2 determined at the MP2 / TZV(2df, 2p) level of theory.^a

	HSiHGe	GeSiH ₂	GeHHSi ^b	HGeSiH	SiGeH ₂	HGeSiH ^b
	cis-monobridged planar (C_s)	silylenegermene planar (C_{2v})	cis-monobridged planar (C_s)	trans-bent planar (C_s)	germylenesilene planar (C_{2v})	linear ($C_{\infty v}$)
Energy (au)	-2363.70691	-2363.69738	-2363.69349	-2363.69053	-2363.68858	-2363.67893
Relative energy (kcal/mol)	0.00	5.98	8.42	10.28	11.50	17.56
$r(\text{Ge} - \text{Si})$ (Å)	2.291	2.187	2.263	2.461	2.172	2.144
$r(\text{Ge} - \text{H})$ (Å)	1.766	1.821 (H_B) ^c	1.677	1.532 (H_T) ^d	1.533	1.526
$r(\text{Si} - \text{H})$ (Å)	1.657	1.484 (H_T) ^d	1.479	1.599	1.695 (H_B) ^c	1.485
$\angle(\text{Si} - \text{Ge} - \text{H})$	45.99°	46.64 (H_B) ^c	40.12°	158.85 (H_T) ^d	127.60°	124.01°
$\angle(\text{Ge} - \text{Si} - \text{H})$	50.03°	107.82° (H_T) ^d	42.52°	51.11° (H_B) ^c	123.32°	180°
$\angle(\text{H} - \text{Ge} - \text{Si} - \text{H})$	104.44°	180°	180°	180°	180°	180°

^{a-d} See footnotes a-d to Table I.

isomer to the global minimum. Future study is required.

Lastly, this study has revealed six different stationary points on the GeCH_2 potential surface. Optimum equilibrium geometries and the corresponding energies of these structures are reported in Table III. Two different structures analogous to methylenecarbene with C_{2v} symmetry exist as minima on this energy surface. Methylenegermene (GeCH_2) has the lone electron pair residing on the germanium, and, the other, germylenecarbene (CGeH_2), has the lone pair residing on the carbon. Methylenegermene, with an energy over 42 kcal/mol lower than any other stationary point on the potential surface, is the global minimum.

The next local minimum on the surface is a planar (C_s) *trans*-bent form which only exists at the correlated level. As noted with the previous two systems, this fact is due to the biradical properties of this isomer. The third and last local minimum revealed in this study is the previously mentioned CGeH_2 C_{2v} structure. It possesses an energy over 104 kcal/mol higher than that of the global minimum at the highest computational level employed in this study.

Three transition states have also been found on this GeCH_2 energy hypersurface. As with the previous two systems, a linear structure exists as a transition state due to Jahn-Teller stabilization of the *trans*-bent isomer. More interestingly, two planar (C_s) *trans*-monobridged structures were located and characterized as transition states. One has the terminal hydrogen on the carbon (Fig. 11), and the other has the terminal hydrogen on the germanium (Fig. 12).

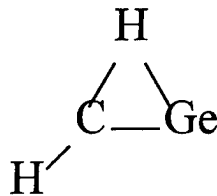


FIGURE 11. HCHGe (C_s).

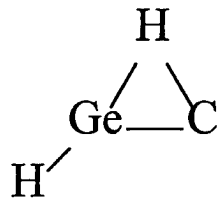


FIGURE 12. HGeHC (C_s).

TABLE III
Energies and equilibrium geometries of the structural isomers of GeCH_2 determined at the MP2 / TZV(2df, 2p) level of theory.^a

	GeCH_2 methylgermene planar (C_{2v})	HCGeH trans-bent planar (C_s)	HCGeH ^b linear ($C_{\infty v}$)	HCHGe ^b trans-monobridged planar (C_s)	CGeH ₂ germylene carbene planar (C_{2v})	HGeHC ^b <i>trans</i> -monobridged planar (C_s)
Energy (au)	-2112.69542	-2112.62785	-2112.62180	-2112.59953	-2112.52921	-2112.52505
Relative energy (kcal / mol)	0.00	42.40	46.20	60.17	104.30	106.91
$r(\text{Ge} - \text{C})$ (Å)	1.796	1.698	1.668	1.735	1.851	1.819
$r(\text{Ge} - \text{H})$ (Å)		1.499	1.482	1.564 (H_B) ^c	1.518	1.513 (H_T) ^d
$r(\text{C} - \text{H})$ (Å)	1.087	1.079	1.069	1.081 (H_T) ^d		2.261 (H_B) ^c
$\angle(\text{C} - \text{Ge} - \text{H})$			148.66°	86.75° (H_B) ^c		155.43° (H_T) ^d
$\angle(\text{Ge} - \text{C} - \text{H})$	122.72°	139.94°	180°	165.44° (H_T) ^d	121.58°	42.89° (H_B) ^c

^{a-d} See footnotes a-d to Table I.

The minima and transition-state structures found in this study appear to adequately describe the entire GeCH_2 potential energy hypersurface at the MP2 level. The *trans*-monobridged structure with the terminal hydrogen on the carbon appears to be the transition state between the GeCH_2 C_{2v} global minimum and the *trans*-bent isomer. The energy barrier for this transition is about 60 kcal/mol [MP2/TZV(2df, 2p)] from the GeCH_2 C_{2v} isomer. Continuing along the surface, the linear structure serves as the transition between mirror images of the *trans*-bent isomer. Note, however, that these mirror images are superimposable and, therefore, represent the same structure. This transition has an energy barrier of only around 4 kcal/mol at the computational level employed. Next, the other *trans*-monobridged structure with the terminal hydrogen on the germanium is probably the transition between the *trans*-bent isomer and the CGeH₂ C_{2v} isomer, with the barrier being over 60 kcal/mol [MP2/TZV(2df, 2p)] from the *trans*-bent structure.

The GeCH_2 surface is quite similar to that of SiCH_2 [15]. It is interesting to note that both of these surfaces are planar, unlike the other two systems studied in this work. This deviation is due to the extreme differences between the atomic radius of carbon and those of germanium and silicon. This difference is, of course, typical of second-row atoms when compared to third- and fourth-row atoms. Carbon's electron cloud is much smaller than that of the heavier atoms and is consequently less diffuse. Another major distinction is the fact that carbon is more electronegative than is hydrogen, whereas the reverse is true for hydrogen and the heavier atoms. Both of these variations tend to make it difficult for carbon to accommodate a lone pair of electrons, as would be the case in a di-bridged structure. This fact becomes evident when observing that the local minimum CGeH₂, which has the lone electron pair residing on the carbon, possesses the highest energy of all the minima on that surface.

Conclusions

This study revealed, collectively, 20 different stationary points on the potential energy surfaces of the isoelectronic systems Ge_2H_2 , GeSiH_2 , and GeCH_2 . These various stationary points demonstrate certain bonding trends of these particular

systems and also present the tendency of the heavier atoms to form nonclassical dibridged and monobridged structures. However, planar *trans*-bent and C_{2v} minima as well as linear transition states were found native to all three surfaces. It is interesting to note the differences in these correlated results and SCF computations. All three of the correlated surfaces contain *trans*-bent local minima; SCF results predict these structures to be transition states or not to be stationary points at all. SCF theory predicts the global minimum of GeSiH₂ to be the C_{2v} isomer silyenegermene, while correlated calculations reveal the dibridged structure to be the global minimum. On this same surface, the MP2 results predict a *cis*-monobridged isomer to be the second most stable local minimum. At the SCF level, this structure rearranges to the corresponding C_{2v} structure. Obviously, and not surprisingly, correlated treatments are required to adequately handle such systems with nonclassical structures.

Of the 20 stationary points reported here, seven are transition states. Tentative positions for these transition states were hypothesized in this current study, but future work will include intrinsic reaction coordinate computations for definitive placement of these states on their respective surfaces. In addition, nonplanar *trans*-monobridged transition states still need to be found and characterized for the two larger systems so that their entire potential energy surfaces can be completely described.

References

1. C. E. Dykstra and H. F. Schaefer, III, *J. Am. Chem. Soc.* **100**, 1378 (1978).
2. M. P. Conrad and H. F. Schaefer, III, *J. Am. Chem. Soc.* **100**, 7820 (1978).
3. Y. Osamura, H. F. Schaefer, III, S. K. Gray, and W. H. Miller, *J. Am. Chem. Soc.* **103**, 1904 (1981).
4. R. Krishnan, M. J. Frisch, J. A. Pople, and P. Von Schleyer, *Chem. Phys. Lett.* **79**, 408 (1981).
5. B. S. Meyerson, *Sci Am.* **270**, 62 (1994).
6. H. Lischka and H. Köhler, *J. Am. Chem. Soc.* **105**, 6646 (1983).
7. J. S. Binkley, *J. Am. Chem. Soc.* **106**, 603 (1984).
8. M. Bogey, C. D. Bolvin, and J. L. Destombes, *Phys. Rev. Lett.* **66**, 413 (1991).
9. R. S. Grev and H. F. Schaefer, III, *J. Chem. Phys.* **97**, 7990 (1992).
10. M. Cordonnier, M. Bogey, C. Demuynck, and J. Destombes, *J. Chem. Phys.* **97**, 7984 (1992).
11. R. S. Grev, B. J. DeLeeuw, and H. F. Schaefer, III, *Chem. Phys. Lett.* **165**, 257 (1990).
12. Z. Palágyi and H. F. Schaefer, III, *J. Am. Chem. Soc.* **115**, 6901 (1993).
13. M. R. Hoffman, Y. Yoshioka, and H. F. Schaefer, III, *J. Am. Chem. Soc.* **105**, 1084 (1983).
14. A. C. Hopkinson, M. H. Lien, and I. G. Csizmadia, *Chem. Phys. Lett.* **95**, 232 (1983).
15. P. O'Leary, J. R. Thomas, H. F. Schaefer, III, B. J. Duke, and B. O'Leary, *Int. J. Quantum Chem.* **29**, 593 (1995).
16. R. Srinivas, D. Sülzle, and H. J. Schwarz, *J. Am. Chem. Soc.* **113**, 52 (1991).
17. A. C. Hopkinson and M. H. Lien, *J. Chem. Soc. Chem. Commun.* 107 (1980).
18. M. S. Gordon and J. A. Pople, *J. Am. Chem. Soc.* **103**, 2945 (1981).
19. H. K. Brody, D. H. Magers, and J. Leszczyński, *J. Struct. Chem.* **6**, 293 (1995).
20. M. J. Frisch, G. W. Trucks, H. B. Schlegel, P.M. W. Gill, B. G. Johnson, M. A. Robb, J. R. Cheeseman, T. Keith, G. A. Petersson, J. A. Montgomery, K. Raghavachari, M. A. Al-Laham, V. G. Zakrzewski, J. V. Ortiz, J. B. Foresman, C. Y. Peng, P. Y. Ayala, W. Chen, M. W. Wong, J. L. Andres, E. S. Replogle, R. Gomperts, R. L. Martin, D. J. Fox, J. S. Binkley, D. J. Defrees, J. Baker, J. P. Stewart, M. Head-Gordon, C. Gonzalez, and J. A. Pople, *Gaussian 94, Revision B.2* (Gaussian, Inc., Pittsburgh PA, 1995).
21. A. D. McLean and G. S. Chandler, *J. Chem. Phys.* **72**, 5639 (1980).
22. S. Huzinaga, J. Andzelm, M. Klobukowski, E. Radzio-Andzelm, Y. Sakai, and H. Tatewski, *Gaussian Basis Sets for Molecular Calculations* (Elsevier, New York, 1984).
23. D. H. Magers, R. B. Hood, and J. Leszczyński, *Int. J. Quantum Chem., Quantum Chem. Symp.* **28**, 579 (1994).
24. Y. Yamaguchi, B. J. DeLeeuw, C. A. Richards, Jr., H. F. Schaefer, III, and G. Frenking, *J. Am. Chem. Soc.* **116**, 11922 (1994).
25. J. F. Stanton, R. J. Bartlett, D. H. Magers, and W. N. Lipscomb, *Chem. Phys. Lett.* **163**, 333 (1989).
26. B. T. Colegrove and H. F. Schaefer, III, *J. Phys. Chem.* **94**, 5593 (1990).

Excited-State Potential Energy Curves from Time-Dependent Density-Functional Theory: A Cross Section of Formaldehyde's 1A_1 Manifold

MARK E. CASIDA, KIM C. CASIDA, DENNIS R. SALAHUB

Département de Chimie, Université de Montréal, C.P. 6128, Succursale centre-ville, Montréal,
Québec H3C 3J7, Canada

Received 24 March 1998; revised 30 June 1998; accepted 10 July 1998

ABSTRACT: This work reports the first density-functional theory (DFT) treatment of excited-state potential energy surfaces exhibiting avoided crossings. Time-dependent DFT (TD-DFT) results, using a recently proposed asymptotically corrected local density approximation functional, are compared with multireference doubles configuration interaction (MRD-CI) results for the 1A_1 manifold of the CO stretching curves of planar formaldehyde. TD-DFT is found to reproduce the qualitative features essential for understanding the spectroscopy of this manifold, specifically the strong mixing of the ${}^1(\pi, \pi^*)$ with Rydberg transitions and the resultant avoided crossings. © 1998 John Wiley & Sons, Inc. *Int J Quant Chem* 70: 933–941, 1998

Key words: time-dependent density-functional theory; excited state surfaces; avoided crossings

1. Introduction

The well-established place of photochemistry within the greater domain of chemistry stems from the fact that different reaction pathways are available, and different products may be obtained,

Correspondence to: M. E. Casida.

Contract grant sponsors: Natural Sciences and Engineering Research Council (NSERC) of Canada; Fonds pour la formation des chercheurs et l'aide à la recherche (FCAR) of Quebec.

from photochemical as opposed to thermal processes. Photochemical pathways are important in synthesis, in state-selective chemistry, in decomposition of chemicals released into the environment, and in the pursuit of materials with novel optical properties. A detailed understanding of photochemical reactions begins with an understanding of the manifold of excited-state potential energy surfaces of the molecular species involved. The very features which can make the description of these surfaces difficult are also the ones which are important for photochemistry: the number and

density of states and their various types of encounters (i.e., crossings, avoided crossings, conical intersections.) These encounter regions are of particular interest because, for example, avoided crossings significantly alter the shapes of the adiabatic surfaces.

Clearly the theoretical methods used to calculate excited-state surfaces need to be capable of describing the interactions between surfaces in the encounter regions, and correctly reproducing the resultant shapes of the surfaces. While some avoided crossings are simply due to avoided crossings at the orbital level, many are due to configuration mixing at the n -electron level and thus require a theoretical method capable of describing this mixing. Various correlated ab initio methods can handle this. However, production of multiple excited-state surfaces is a computationally demanding task, and this is especially true for the medium and large sized molecules of interest for practical applications. Thus, an inexpensive yet accurate method which could obtain such avoided crossings would be very useful.

Hohenberg–Kohn–Sham density-functional theory (DFT) [1, 2] has proven remarkably successful at providing a variety of ground-state properties to an accuracy comparable to that of correlated ab initio methods, at a fraction of the computational cost. Thus, the ability to study the structure of excited-state surfaces via DFT would be valuable. However, the DFT treatment of excited states is not yet as fully developed as is the ground-state theory. To our knowledge, no previously published study using any DFT method has ever reported an avoided crossing due to configuration mixing.

In molecular applications of DFT, excited states have traditionally been treated by simply applying ground-state DFT to excited states. This is based, in the first instance, on the theorem that the energy of the lowest excited state of each symmetry may be obtained by minimizing a functional of its charge density ([3] pp. 204–205) and is, for example, the usual way to treat the lowest triplet excited state of a closed-shell molecule in DFT. Excitation energies are then simply obtained by the ΔSCF (self-consistent field) or related transition orbital method. This same approach is often applied with impunity to treat higher excited states. Another formal problem (usually ignored) is that the functional needed for each excited state need not be the same as that used for the ground state. However, the primary difficulty with this method

is practical as well as formal. The so-called excited-state multiplet problem originates in the intrinsic limitation to n -occupied Kohn–Sham orbitals when constructing excited-state wave functions. This is frequently insufficient to construct open-shell reference wave functions such as in the very simple and notable case of singlet excited states of a closed-shell molecule where $n + 2$ orbitals are actually needed to construct the singlet wave function, $\Phi \rightarrow (1/\sqrt{2})(\hat{a}_{a\uparrow}^\dagger \hat{a}_{i\downarrow} + \hat{a}_{a\downarrow}^\dagger \hat{a}_{i\uparrow})\Phi$. A group-theoretic method has been devised which partially addresses this problem, but it is, of course, not able to describe important configuration mixing arising from other effects besides symmetry [4–7]. In cases where nonsymmetry-related mixing of configurations is expected, e.g., based on experimental results, a *post hoc* configuration-interaction-like correction can sometimes be applied (e.g., [8] p. 5025) at the risk of double counting correlation effects. However, this is of limited utility for predictive purposes, and it is clearly not a very natural, nor well justified, way to treat the structure of excited-state surfaces where avoided crossings involving configuration mixing are important.

For atoms and simplified cluster models, photoabsorption spectra have long been calculated using a time-dependent generalization of the Kohn–Sham equation,

$$\left(-\frac{1}{2}\nabla^2 + v(\mathbf{r}, t) + \int \frac{\rho(\mathbf{r}, t)}{|\mathbf{r} - \mathbf{r}'|} d\mathbf{r}' + v_{xc}[\rho_t](\mathbf{r}) \right) \times \psi_j(\mathbf{r}, t) = i \frac{\partial}{\partial t} \psi_j(\mathbf{r}, t), \quad (1.1)$$

within the adiabatic approximation. Here $v_{xc}[\rho_t](\mathbf{r}) = \delta E_{xc}/\delta\rho_t(\mathbf{r})$, where $\rho_t(\mathbf{r}) = \rho(\mathbf{r}, t)$. In this approach, a scattering theory formalism is used, and spectra are obtained in the form of a spectral strength function [9–16]. This scattering theory approach precludes the treatment of spectroscopically dark states, and, although it is a natural way to treat the continuum part of the spectrum, artificial line broadening is required for treatment of the discrete spectrum.

Although time-dependent DFT (TD-DFT) was initially *ad hoc*, a substantial body of work has now given it a rigorous formal footing [17–26] (see especially reviews by Gross and co-workers [27–29]). The dynamic response of the charge density for a system, initially in its ground stationary state, that is exposed to a time-dependent perturbation, is described via the time-dependent

Kohn–Sham equation (1.1). Excitation energies, ω_I , and oscillator strengths, f_I , may then be obtained from the poles and residues of the dynamic polarizability,

$$\bar{\alpha}(\omega) = \sum_I \frac{f_I}{\omega_I^2 - \omega^2}, \quad (1.2)$$

using the well-known sum-over-states theorem [30]. We have formulated [30] and implemented [31] this approach in a manner suitable for molecular applications. The excitation energies and oscillator strengths, respectively, are the eigenvalues and eigenvectors obtained by solving a matrix eigenvalue problem,

$$\Omega \mathbf{F}_I = \omega_I^2 \mathbf{F}_I, \quad (1.3)$$

where (in the spin density formalism)

$$\begin{aligned} \Omega_{ia\sigma, jb\tau} &= \delta_{\sigma\tau} \delta_{ij} \delta_{ab} (\epsilon_{a\sigma} - \epsilon_{i\sigma})^2 \\ &+ \sqrt{\epsilon_{a\sigma} - \epsilon_{i\sigma}} [ia | \delta V_{\text{SCF}}^\sigma / \delta \rho_\tau | jb] \\ &\times \sqrt{\epsilon_{b\tau} - \epsilon_{j\tau}} \end{aligned} \quad (1.4)$$

[30–32] is constructed from the Kohn–Sham orbitals and orbital energies for the unperturbed self-consistent field problem (i.e., calculated in the SCF step). This provides a natural way to treat discrete spectra and yields dark as well as bright states. It should be emphasized that Eq. (1.3) is completely rigorous, involving no further approximations beyond the finite basis set model and the functionals used in TD-DFT. In the adiabatic approximation, which will be used in this work, Ω is independent of ω , so this is an ordinary eigenvalue problem. (See Ref. [30] for a discussion of the nonadiabatic case.) The presence of configuration mixing in this method follows from the configuration interaction (CI)-like nature of Eq. (1.3) as does the ability to generate entire manifolds of excitation energies in a one-shot process. This method is thus a natural candidate for a computationally simple treatment of excited-state surfaces.

In order for TD-DFT to be able to describe, even qualitatively, surfaces exhibiting avoided crossings due to configuration mixing, two factors are important: (1) the structure of the TD-DFT coupling matrix ($\delta V_{\text{SCF}} / \delta \rho$) and (2) the functional. Although our formulation of TD-DFT resembles time-dependent Hartree–Fock (TDHF), the TD-DFT coupling matrix differs significantly from that

of TDHF (see Ref. [30]). TD-DFT appears to do quite well at describing the configuration mixing responsible for multiplet splittings, in which case the mixing is due primarily to symmetry [31, 33]. We have also noted the occurrence of significant configuration mixing that does not arise from symmetry [31], however, its correctness has not been examined explicitly. A severe test is to see whether TD-DFT can describe the strong configuration mixing responsible for avoided crossings. The present study demonstrates that TD-DFT can give at least a qualitatively correct description in the difficult case of avoided crossings due to mixing of valence and Rydberg excitations in the 1A_1 manifold of formaldehyde.

The simultaneous description of valence and Rydberg excitations is a demanding task for the functional. The TD-DFT method has been found to give remarkably good results for low-lying vertical excitations, when the local density approximation (LDA) is used [31, 33, 34]. We have also shown that correction of the asymptotic behavior of the exchange–correlation potential, v_{xc} , used in the SCF step, is crucial for treating higher excitations [33]. Quite reasonable results are obtained by using the asymptotically correct potential of van Leeuwen and Baerends [35] in the SCF step, combined with the time-dependent local density approximation (TDLDA) for the post-SCF step [33, 36]. We have improved on this by combining the LB94 potential in the asymptotic region with the LDA in the “bulk” region of the molecule where $v_{\text{xc}}^{\text{LDA}}$ is more nearly parallel to the exact potential than is $v_{\text{xc}}^{\text{LB94}}$, while at the same time shifting $v_{\text{xc}}^{\text{LDA}}$ down to compensate for the fact that we are approximating the exact v_{xc} which has a particle number discontinuity by an approximate functional which has no derivative discontinuity [37]. Specifically,

$$v_{\text{xc}}^{\text{AC-LDA}}(\mathbf{r}) = \text{Max}[v_{\text{xc}}^{\text{LDA}}(\mathbf{r}) - \Delta, v_{\text{xc}}^{\text{LB94}}(\mathbf{r})], \quad (1.5)$$

where

$$\Delta = I + \epsilon_{\text{HOMO}} \quad (1.6)$$

is the difference between the Δ SCF ionization potential and the negative of the highest occupied molecular orbital (HOMO) energy, in the LDA. This asymptotically corrected LDA (AC-LDA) will be used in the present work (i.e., we use the TDLDA/AC-LDA functional, meaning that the AC-LDA is used for the SCF step and then combined with the TDLDA coupling in the post-SCF

step). The AC-LDA energy expression is

$$\begin{aligned} E^{\text{AC-LDA}} = & \sum_i \epsilon_i - \int v_{\text{xc}}^{\text{AC-LDA}}(\mathbf{r}) \rho(\mathbf{r}) d\mathbf{r} \\ & - \frac{1}{2} \iint \frac{\rho(\mathbf{r}_1) \rho(\mathbf{r}_2)}{r_{12}} d\mathbf{r}_1 d\mathbf{r}_2 + E_{\text{xc}}^{\text{LDA}}[\rho], \end{aligned} \quad (1.7)$$

and gives total energies very close to those of the LDA since $v_{\text{xc}}^{\text{AC-LDA}}$ and $v_{\text{xc}}^{\text{LDA}}$ differ by no more than a rigid shift in the energetically important regions of space [37]. Using the TDLDA/AC-LDA functional, we obtained most of the first 20–30 vertical excitations of formaldehyde and 3 other small molecules to within 0.5 eV [37]. Although there are a few states with larger errors (~ 1 eV), indicating a need for continued improvement of the functional, the results from the AC-LDA functional are good enough that we are now in a position to hope that TD-DFT will be able to describe photochemically interesting phenomena involving both valence and Rydberg excitations, and configuration mixing between the two.

As a first trial, we have chosen to focus on the CO-stretch cross section of the 1A_1 manifold of formaldehyde. These surfaces exhibit avoided crossings due to configuration mixing, and this mixing has been found to be essential for a resolution of the longstanding enigma of why the ${}^1(\pi, \pi^*)$ transition has never been observed experimentally [38–40]. As will be seen, TD-DFT is able to describe this phenomenon.

2. Computational Details

The TD-DFT calculations were performed using version 2 of our program deMon- (for “densité de Montréal”) DynaRho (for “dynamic response of ρ ”) [41]. Version 4.0 of deMon-KS (for “Kohn-Sham”) [42] was used for the SCF step due to its automated orbital symmetry assignments [43]. Both of these programs use the same auxiliary basis sets, which improve computational scaling both through the elimination of four-center integrals and by reducing the number of grid points needed to evaluate exchange-correlation terms.

Since TD-DFT produces transition densities, rather than the n -electron wave functions for the excited states, a complete assignment of term symbols for the transitions obtained typically requires

that some additional approximation be introduced. Following Ref. [30], we assume that the wave function, Ψ_I , for the I th excited state has the form,

$$\Psi_I = \sum_{ij\sigma}^{f_{i\sigma} > f_{j\sigma}} \sqrt{\frac{\epsilon_{j\sigma} - \epsilon_{i\sigma}}{\omega_I}} F_{ij\sigma}^I \hat{a}_{j\sigma}^\dagger \hat{a}_{i\sigma} \Phi + \dots, \quad (2.1)$$

where Φ is the single determinant of Kohn-Sham orbitals occupied in the ground-state noninteracting system and the creation and annihilation operators, $\hat{a}_{j\sigma}^\dagger$ and $\hat{a}_{i\sigma}$, refer to the Kohn-Sham molecular orbital representation. This approximation appears to be quite adequate, and is used in the present work, for the qualitative purpose of assigning term symbols to the quantitative transition energies and oscillator strengths obtained by solving the eigenvalue problem Eq. (1.3) and for analyzing the orbital promotions associated with each excitation.

We studied the CO-stretch cross section of the surfaces, holding the CH_2 moiety frozen at its experimental ground-state equilibrium geometry ($R_{\text{CH}} = 2.0796$ bohrs, $\angle \text{HCH} = 116.3^\circ$), the same as used in Ref. [38]. The zero energy is taken to be the minimum of the ground-state CO stretching curve. The excited-state surfaces were obtained by adding the TDLDA/AC-LDA transition energy to the AC-LDA ground-state energy, for each geometry.

Gaussian-type orbital (GTO) basis sets are used for both orbital and auxiliary basis sets. We used the Sadlej+ basis set of Ref. [33], which consists of the Sadlej basis [44, 45] supplemented with two diffuse s and one set each of diffuse p and d functions, for a total of 102 contracted GTOs. The deMon library (4, 4; 4, 4) auxiliary set was used for C and O. For H, a (4, 1; 4, 1) auxiliary basis set was obtained by supplementing the deMon library (3, 1; 3, 1) basis with a diffuse s function with exponent 0.06.

The deMon “extrafine” “random” grid (with 32 radial and 194 angular points per atom) constructed using C_{2v} symmetry was used. The SCF convergence criteria were a change of less than 10^{-8} a.u. in the charge density fitting coefficients and, simultaneously, less than 10^{-8} hartree in the total energy.

3. Results and Discussion

One of the strengths of our response theory formulation of TD-DFT is that the ability to de-

scribe configuration mixing, which is important for avoided crossings, is present in the formalism. In this section, we verify that this works in practice, by comparing our TDLDA/AC-LDA excited-state surfaces with the multireference doubles configuration interaction (MRD-CI) results of Hachey, Bruna, and Grein [38] for the 1A_1 manifold of formaldehyde.

We will use orbital promotion labels for the primary components of the transitions in order to interpret our surfaces. Placing CH₂O in its canonical orientation [46] with CO along the z axis and the hydrogens in the (y, z) plane, DFT with the AC-LDA functional gives the following ordering of valence-type orbitals:

$$[1b_2(\sigma')]^2[5a_1(\sigma)]^2[1b_1(\pi)]^2[2b_2(n)]^2[2b_1(\pi^*)]^0, \quad (3.1)$$

followed by the Rydberg orbitals,

$$\begin{aligned} &[6a_1(3s)]^0[7a_1(3p_z)]^0[3b_2(3p_y)]^0[3b_1(3p_x)]^0 \\ &\times [8a_1(3d_{x^2-y^2})]^0[4b_2(3d_{yz})]^0 \\ &\times [9a_1(3d_{z^2})]^0[1a_2(3d_{xy})]^0, \end{aligned} \quad (3.2)$$

in order of increasing energy. The “chemical names” are traditional [47], up to minor variations. For ease of comparison, we use the same chemical names as Hachey, Bruna, and Grein [38]. Note also that our distinction between “valence” and “Rydberg” is simply the one already well-established in the formaldehyde literature [47].

It is worthy of note that, in contrast to Hartree-Fock, all of the above unoccupied molecular orbitals are bound, and their ordering reflects the ordering of the Rydberg excited states [37]. In fact, when a sufficiently good exchange-correlation potential is used, DFT orbital energy differences provide a remarkably good approximation to Rydberg excitation energies [37, 48, 49]. This is illustrated in Table I, which also gives an idea of the level of agreement between our TDLDA/AC-LDA vertical excitation energies and the MRD-CI results of Hachey, Bruna, and Grein [38].

Since our excited-state surfaces are obtained by adding the TD-DFT transition energies to the ground-state energy, we begin with a look at our ground-state surface (Fig. 1). Note that the LDA and AC-LDA curves are virtually indistinguishable. This is as it should be, since the AC-LDA was designed to be an asymptotic correction which would leave the LDA orbitals (and hence total energy) essentially unaltered in the energetically important ‘bulk’ region of the molecule [37]. Although the AC-LDA and LDA curves are quite similar to the MRD-CI curve near the potential minimum, the difference increases significantly for large CO distances, where the AC-LDA and LDA curves go from being 0.1 eV too high at $R_{\text{CO}} = 2.6$ bohrs to 0.4 eV too high at 3.2 bohr. This error will be inherited by our excited-state curves. Since the error in the shape of the ground-state curve can be diminished by using a gradient-corrected functional [50], it is worth noting that the asymptotic correction paradigm applied to create the AC-LDA

TABLE I
Comparison of AC-LDA orbital energy differences, TDLDA / AC-LDA, and MRD-CI excitation energies at the experimental ground-state equilibrium geometry ($R_{\text{CO}} = 2.2739$ bohrs, [38, 54]).^a

Transition	A_1 Vertical Excitation Energies (eV)	TDLDA / AC-LDA	$\Delta\epsilon^c$
	MRD-CI ^b		
${}^1(n, 3d_{yz})$	9.06 (1A_1)	10.13 (1A_1)	9.76
$(n, 3d_{yz})$			
${}^3(n, 3d_{yz})$	9.18 (3A_1)	9.62 (3A_1)	
${}^1(n, 3p_y)$	7.99 (1A_1)	8.02 (1A_1)	7.99
$(n, 3p_y)$			
${}^3(n, 3p_y)$	7.92 (3A_1)	7.85 (3A_1)	
${}^1(\pi, \pi^*)$	9.65 (1A_1)	9.48 (1A_1)	7.42
(π, π^*)			
${}^3(\pi, \pi^*)$	6.15 (3A_1)	6.23 (3A_1)	

^aNote that the ${}^1(n, 3d_{yz})$ and ${}^1(\pi, \pi^*)$ configurations are heavily mixed at this geometry (see text).

^bRefs. [38, 54], basis set B.

^cAC-LDA orbital energy difference.

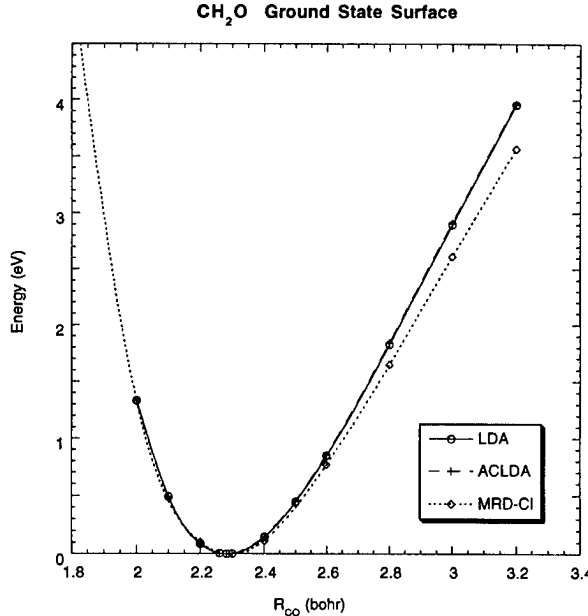


FIGURE 1. Comparison of ground-state CO-stretch potential energy curves of planar formaldehyde calculated using DFT (LDA and AC-LDA functionals) with the MRD-CI curve of Hachey, Bruna, and Grein [38] (CI data courtesy of Michel Hachey). All curves have been shifted so that their minima are at zero energy. Note that the LDA and AC-LDA curves are essentially coincident.

could equally well be used with a gradient-corrected functional, and would be expected to lead to improved excited-state surfaces.

The calculation of the 1A_1 excited-state surfaces played an important role in understanding the spectroscopy of formaldehyde. A classic puzzle has been the placement of the $^1(\pi, \pi^*)$ state. Despite an expected large oscillator strength, this transition has never been observed experimentally [38]. Hachey, Bruna, and Grein's calculation of the CO-stretch cross section of the 1A_1 manifold of excited-state surfaces has done much to give a definitive resolution to this enigma [38–40, 51, 52]. They found that the $^1(\pi, \pi^*)$ diabatic curve is indeed present, but that it is so strongly perturbed by Rydberg states that what is actually observed are strong mixtures of $^1(\pi, \pi^*)$ and Rydberg states. The resulting avoided crossings can be clearly understood in terms of the $^1(\pi, \pi^*)$, $^1(n, 3p_y)$, and $^1(n, 3d_{yz})$ diabatic curves (Fig. 2). (Although the diabatic curves are not shown, as such, in this figure, they are evident from the labeling of the primary components present in various portions of the adiabatic curves.) Since the $^1(\pi, \pi^*)$ diabatic curve is dissociative, Hachey, Bruna, and Grein

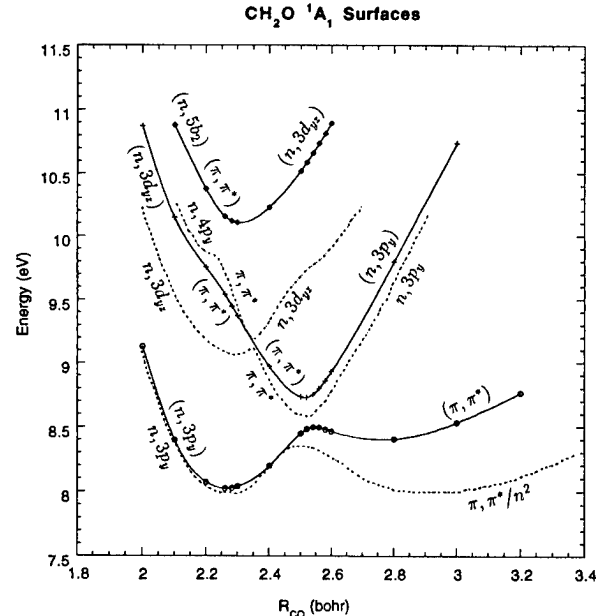


FIGURE 2. Comparison of TDLDA / AC-LDA (solid) with MRD-CI [38] (dashed) 2, 3, and 4 1A_1 CO-stretch potential energy curves of planar formaldehyde. The energy zeros are the minima of the corresponding (AC-LDA or MRD-CI) ground-state CO-stretch potential energy curves. The major orbital promotions found from the analysis of the TDLDA / AC-LDA “wave function” [Eq. (2.1)] have been indicated (in parentheses), as have the major orbital promotions for the MRD-CI curves given in Ref. [38] (no parentheses).

attribute the observed absorption continuum above about 7.5 eV to predissociating interactions. (The vertical ionization potential of CH_2O is 10.88 eV [53].)

This kind of global description of what is going on in the spectroscopy of the first several states in the 1A_1 manifold of formaldehyde is exactly the sort of information we would like to be able to obtain from TD-DFT. Our goal in the present work is not so much quantitative agreement with the MRD-CI results (since functionals for TD-DFT are still undergoing rapid development, and different basis sets are used), but rather to ascertain whether TD-DFT yields the same global picture as MRD-CI.

Figure 2 shows our TDLDA/AC-LDA excited-state CO-stretch curves. Analysis of the components of our TD-DFT excitations shows that the same three diabatic curves, $^1(\pi, \pi^*)$, $^1(n, 3p_y)$, and $^1(n, 3d_{yz})$, are present as in the MRD-CI calculation. The TDLDA/AC-LDA $^1(n, 3p_y)$ curve is within about 0.2 eV of the MRD-CI $^1(n, 3p_y)$ curve. The TDLDA/AC-LDA $^1(\pi, \pi^*)$ diabatic curve is

also close to the MRD-CI ${}^1(\pi, \pi^*)$ diabatic curve, for R_{CO} less than 2.5 bohrs. However, the difference increases going toward large R_{CO} , becoming about 0.7 eV at $R_{\text{CO}} = 3.2$ bohrs. This increasing error at large R_{CO} is partly due to the error in the AC-LDA ground-state surface in this region. When this is taken into account, the difference in the ${}^1(\pi, \pi^*)$ curves at 3.2 bohr reduces to 0.3 eV. Overall, the largest differences between the TDLDA/AC-LDA and MRD-CI diabatic curves are seen for the ${}^1(n, 3d_{yz})$ curves where the TDLDA/AC-LDA diabatic curve is consistently about 1 eV higher than the corresponding MRD-CI diabatic curve, though this difference reduces to 0.5 eV for small R_{CO} (2.0–2.1 bohr). Our tests at the equilibrium geometry indicate that differences in orbital basis set, and the choice of auxiliary basis, change these excitation energies only by about 0.1 eV or so. The substantial observed difference between the TDLDA/AC-LDA and MRD-CI ${}^1(n, 3d_{yz})$ diabatic curves thus appears to be due primarily to limitations of the functional.

The most striking feature of the TDLDA/AC-LDA curves is the appearance of avoided crossings. Although avoided crossings can arise simply from avoided crossings of the orbital energy curves, that is not the case for the present curves. Rather, the avoided crossings seen here are due to configuration mixing between n -electron states. The $[1b_1(\pi), 3b_1(\pi^*)]/[2b_2(n), 3b_2(3p_y)]$ avoided crossing is of this type, with

$$\begin{aligned} |3^1A_1\rangle &\cong -0.79[1b_1(\pi), 3b_1(\pi^*)]\rangle \\ &+ 0.53[2b_2(n), 3b_2(3p_y)]\rangle \\ &+ 0.29[2b_2(n), 4b_2(3d_{yz})]\rangle, \\ |2^1A_1\rangle &\cong 0.40[1b_1(\pi), 3b_1(\pi^*)]\rangle \\ &+ 0.91[2b_2(n), 3b_2(3p_y)]\rangle, \end{aligned} \quad (3.3)$$

at 2.5 bohr. Because our formulation of TD-DFT is a response theory method based upon ground-state orbitals, multiconfiguration descriptions of excitations may arise both from relaxation effects and from true configuration mixing. While the combination of the last two terms in the 3A_1 expansion may be simply interpreted as arising from a single excitation with relaxation,

$$\begin{aligned} 2b_2(n) \rightarrow 3b'_2 &= 0.88 \times 3b_2(3p_y) \\ &+ 0.48 \times 4b_2(3d_{yz}), \end{aligned} \quad (3.4)$$

and so could be described with a single excited-state configuration, $[2b_2(n), 3b'_2]$, the presence of combinations of $b_1 \rightarrow b_1$ with $b_2 \rightarrow b_2$ terms cannot. Thus, this avoided crossing does indeed involve true configuration mixing. Note that the resulting energy separation (between the 2A_1 and 3A_1 curves) is about the same in the TD-DFT and MRD-CI results.

Examination of the components of the 3A_1 and 4A_1 states reveals strong configuration mixing of ${}^1(\pi, \pi^*)$ and ${}^1(n, 3d_{yz})$, in the region around 2.3–2.4 bohr and indicates an avoided crossing of these two curves. However, since the TDLDA/AC-LDA diabatic ${}^1(n, 3d_{yz})$ curve is about 1 eV higher than the corresponding MRD-CI curve, it is not surprising that the appearance of the respective avoided crossings is different. In the TDLDA/AC-LDA results, the 4A_1 transition at $R_{\text{CO}} = 2.1$ bohr is predominantly ${}^1(n, 5b_2)$, where the $5b_2$ is an unbound unoccupied orbital to which we have not attempted to assign a “chemical” name. In view of the proximity to the molecular ionization potential, the orbital and auxiliary basis sets, as well as the functional, should be further investigated before attaching too much significance to the points approaching 11 eV.

The TDLDA/AC-LDA 1A_1 CO-stretch curves are qualitatively similar to the MRD-CI curves, and the TDLDA/AC-LDA does yield the important mixing of the ${}^1(\pi, \pi^*)$ with the ${}^1(n, 3p_y)$ and the ${}^1(n, 3d_{yz})$ Rydberg excitations, thus giving the same global picture found by Hachey, Bruna, and Grein [38] to explain why the long sought ${}^1(\pi, \pi^*)$ transition has never been observed. A Δ SCF-based DFT study of these excited-state curves would have been far more difficult (if it were possible), involving multiple Δ SCF (or Slater transition orbital) calculations for each geometry. Even so, it is difficult to see how the extensive configuration mixing at these energies could be described by the Δ SCF-based approach without the introduction of *post hoc* second-order corrections [7] of a non-DFT nature.

4. Conclusion

In this work, we have presented the first DFT calculation of excited-state surfaces exhibiting avoided crossings. The present results with the TDLDA/AC-LDA functional show that TD-DFT is capable of describing the important configuration

mixing effects intrinsic to the behavior of these surfaces, and that TD-DFT yields the same global picture of the spectroscopy of the long-enigmatic A_1 manifold of formaldehyde as was found in the MRD-CI study of Hachey, Bruna, and Grein [38]. While the TDLDA/AC-LDA already gives a good qualitative description, and is quantitative (agreement within a few tenths of an eV) for some portions of these surfaces, further improvement in the functional will be needed in order to make the results fully quantitative.

ACKNOWLEDGMENTS

One of us (M.E.C.) would like to thank Dr. Michel Hachey for useful discussions and for sending some data. Financial support through grants from the Natural Sciences and Engineering Research Council (NSERC) of Canada and the Fonds pour la formation des chercheurs et l'aide à la recherche (FCAR) of Quebec is gratefully acknowledged.

References

1. P. Hohenberg and W. Kohn, Phys. Rev. **136**, B864 (1964).
2. W. Kohn and L. J. Sham, Phys. Rev. **140**, A1133 (1965).
3. R. G. Parr and W. Yang, *Density-Functional Theory of Atoms and Molecules* (Oxford University Press, New York, 1989).
4. R. P. Messmer and D. R. Salahub, J. Chem. Phys. **65**, 779 (1976).
5. T. Ziegler, A. Rauk, and E. J. Baerends, Theor. Chim. Acta **43**, 261 (1977).
6. C. Daul, Int. J. Quant. Chem. **52**, 867 (1994).
7. C. A. Daul, K. G. Doclo, and A. C. Stückel, in *Recent Advances in Density Functional Methods, Part II*, D. P. Chong, Ed. (World Scientific, Singapore, 1997), p. 61.
8. A. Bencini, F. Totti, C. A. Daul, P. Fantucci, and V. Barone, Inorg. Chem. **36**, 5022 (1997).
9. A. Zangwill and P. Soven, Phys. Rev. A **21**, 156 (1980).
10. K. Nuroh, M. J. Stott, and E. Zaremba, Phys. Rev. Lett. **49**, 862 (1982).
11. G. Bertsch, Comp. Phys. Comm. **60**, 247 (1990).
12. M. Brack, Rev. Mod. Phys. **65**, 677 (1993).
13. A. Rubio, J. A. Alonso, X. Blase, L. C. Balbás, and S. G. Louie, Phys. Rev. Lett. **77**, 247 (1996).
14. A. Liebsch, *Electronic Excitations at Metal Surfaces* (Plenum, New York, 1997).
15. Z. H. Levine and P. Soven, Phys. Rev. Lett. **50**, 2074 (1983).
16. Z. H. Levine and P. Soven, Phys. Rev. A **29**, 625 (1984).
17. V. Peuckert, J. Phys. C **11**, 4945 (1978).
18. S. Chakravarty, M. B. Fogel, and W. Kohn, Phys. Rev. Lett. **43**, 775 (1979).
19. L. J. Bartolotti, Phys. Rev. A **24**, 1661 (1981).
20. L. J. Bartolotti, Phys. Rev. A **26**, 2243 (1982).
21. B. H. Deb and S. K. Ghosh, J. Chem. Phys. **77**, 342 (1982).
22. E. Runge and E. K. U. Gross, Phys. Rev. Lett. **52**, 997 (1984).
23. H. Kohl and R. M. Dreizler, Phys. Rev. Lett. **56**, 1993 (1986).
24. A. K. Dhara and S. K. Ghosh, Phys. Rev. A **35**, 442 (1987).
25. D. Mearns and W. Kohn, Phys. Rev. A **35**, 4796 (1987).
26. R. van Leeuwen, Phys. Rev. Lett. **80**, 1280 (1998).
27. E. K. U. Gross and W. Kohn, Adv. Quant. Chem. **21**, 255 (1990).
28. E. K. U. Gross, C. A. Ullrich, and U. J. Gossmann, in *Density Functional Theory*, E. K. U. Gross and R. M. Dreizler, Eds., NATO ASI Series (Plenum, New York, 1994), p. 149.
29. E. K. U. Gross, J. F. Dobson, and M. Petersilka, in *Density Functional Theory II*, Vol. 181 of *Topics in Current Chemistry*, R. F. Nalewajski, Ed. (Springer, Berlin, 1996), p. 81.
30. M. E. Casida, in *Recent Advances in Density Functional Methods, Part I*, D. P. Chong, Ed. (Singapore, World Scientific, 1995), p. 155.
31. C. Jamorski, M. E. Casida, and D. R. Salahub, J. Chem. Phys. **104**, 5134 (1996).
32. M. E. Casida, in *Recent Developments and Applications of Modern Density Functional Theory, Theoretical and Computational Chemistry*, Vol. 4, J. M. Seminario, Ed. (Elsevier Science, Amsterdam, 1996) p. 391.
33. M. E. Casida, C. Jamorski, K. C. Casida, and D. R. Salahub, J. Chem. Phys. **108**, 4439 (1998).
34. R. Bauernschmitt and R. Ahlrichs, Chem. Phys. Lett. **256**, 454 (1996).
35. R. van Leeuwen and E. J. Baerends, Phys. Rev. A **49**, 2421 (1994).
36. S. J. A. van Gisbergen, F. Kootstra, P. R. T. Schipper, O. V. Gritsenko, J. G. Snijders, and E. J. Baerends, Phys. Rev. A **57**, 2556 (1998).
37. M. E. Casida and D. R. Salahub, to appear.
38. M. R. J. Hachey, P. J. Bruna, and F. Grein, J. Phys. Chem. **99**, 8050 (1995).
39. M. R. J. Hachey and F. Grein, Chem. Phys. Lett. **256**, 179 (1996).
40. F. Grein and M. R. J. Hachey, Int. J. Quant. Chem. Symp. **30**, 1661 (1996).
41. M. E. Casida, C. Jamorski, and D. R. Salahub, deMon-DynaRho version 2, University of Montreal.
42. (a) A. St-Amant and D. R. Salahub, Chem. Phys. Lett. **169**, 387 (1990); (b) Alain St-Amant, Ph.D. Thesis, University of Montreal (1992); (c) M. E. Casida, C. Daul, A. Goursot, A. Koester, L. G. M. Pettersson, E. Proynov, A. St-Amant, and D. R. Salahub principal authors, H. Duarte, N. Godbout, J. Guan, C. Jamorski, M. Leboeuf, V. Malkin, O. Malkina, M. Nyberg, L. Pedocchi, F. Sim, L. Triguero, and A. Vela contributing authors, deMon-KS version 4.0, deMon Software, 1997.
43. Added to deMon-KS by Mats Nyberg and Lars G. M. Pettersson.
44. A. J. Sadlej, Coll. Czech. Chem. Comm. **53**, 1995 (1988).
45. A. Sadlej, Theor. Chim. Acta **79**, 123 (1991).
46. J. Chem. Phys. **23**, 1997 (1955).

EXCITED-STATE POTENTIAL ENERGY CURVES

47. D. C. Moule and A. D. Walsh, Chem. Rev. **75**, 67 (1975).
48. C. Filippi, C. J. Umrigar, and X. Gonze, J. Chem. Phys. **107**, 9994 (1997).
49. A. Savin, C. J. Umrigar, and X. Gonze, in *Electronic Density Functional Theory: Recent Progress and New Directions*, J. F. Dobson, G. Vignale, and M. P. Das, Eds. (Plenum, New York, 1997).
50. Unpublished calculations by the authors.
51. M. Hachey, P. J. Bruna, and F. Grein, J. Chem. Soc. Faraday Trans. **90**, 683 (1994).
52. M. R. J. Hachey, P. J. Bruna, and F. Grein, J. Molec. Spectr. **176**, 375 (1996).
53. C. R. Brundle, M. R. Robin, N. A. Kuebler, and H. Basch, J. Am. Chem. Soc. **94**, 1452 (1972).
54. P. J. Bruna, M. R. J. Hachey, and F. Grein, J. Phys. Chem. **99**, 16576 (1995).

Effective Potential for e-Neon and e-Argon Scattering by DCS Minimization at Intermediate Energies

JOSEPH M. PAIKEDAY, AMBER LONGSTREET

Southeast Missouri State University, Cape Girardeau, Missouri 63701

Received 26 February 1998; revised 24 July 1998; accepted 27 July 1998

ABSTRACT: The differential scattering cross-section (DCS) for electrons scattered elastically by neon and argon atoms is studied using a model potential. In the present study the long-range polarization potential is represented by an energy-dependent function, and the short-range part is constructed from the nonrelativistic Hartree-Fock wave function of the target atom. The computed differential cross section obtained using the approximate effective interaction potential for electrons scattered by neon and argon atoms in their ground state is compared with available published results. In the present study the parameters contained in the energy-dependent effective potential are determined by the minimization of the DCS with respect to angle θ and the incident energy. The resulting DCS in the angular range $2^\circ < \theta < 178^\circ$ is found to be in good agreement with the available experimental and theoretical results in the intermediate energy range. © 1998 John Wiley & Sons, Inc. *Int J Quant Chem* 70: 943–950, 1998

Key words: electron scattering; effective potential

Introduction

The present work is a continuation of the differential cross-section (DCS) computations of electrons scattered by the neon atom reported earlier [1]. The method has been refined and applied to argon as well as neon over the intermediate

Correspondence to: J. M. Paikeday.

Contract grant sponsor: Grants and Research Funding Committee and the College of Science and Technology of Southeast Missouri State University.

energy range. Electron scattering by atoms and selected molecules has been a topic of considerable interest as evidenced by a large number of experimental and theoretical works published over the last decade. The theoretical work has progressed mostly along the application of *R*-matrix theory [2] while the semiempirical calculations based on the optical potential models [3] with or without adjustable parameters have increased over the last few years owing to their simplicity and the ease of computations leading to the DCS over a wide range of incident energy. In the present study, the model potential is based on the dipole polarizabil-

ity α_d of the target atom and two parameters contained in the energy-dependent polarization potential determined by minimizing the DCS at the critical angle [4] with the condition that the computed integral cross section agrees with the experimental value of the integral cross section for two selected incident energies. The significance of the DCS minimum at the critical angle can be understood on the basis of the phenomenon of low-energy electron diffraction associated with the interaction between the incident electron and the atomic target. While the reported differential cross-section data for a given target atom varied from 5 to 13% depending on the incident energy, the integral cross section is known to have less uncertainty for most closed-shell atoms over the intermediate energy range. In the present study, the critical minima and the integral cross section of the computed DCS are shown to depend on the values of the parameters so that one can vary them to find the set that minimizes the DCS at the critical angle and corresponds to the correct integral cross section within the uncertainty of the experimental data at a selected incident energy. Using this set of parameters, the differential cross section for the target atom is computed over the energy range $20 < E < 500$ eV and the angular range $2^\circ < \theta < 180^\circ$. The computed DCS are found to be in good agreement with recently reported experimental and theoretical cross-section data for neon and argon atoms over the intermediate energy range.

Approximation to the Effective Potential

The effective potential is constructed from the Hartree-Fock orbitals [5] of the target atom and is of the form given by

$$V_e = V_{\text{ex}}(r) + V_p(E, r) + \left(\frac{2Z}{r}\right) \sum_k \sum_n A_n R_n(r) \exp(-B_k r), \quad (1)$$

where $V_{\text{ex}}(r)$ and $V_p(E, r)$ are the exchange and polarization potentials, respectively, and the values of A_n and B_k ($k = 1, 2, \dots, M$, $M < 10$) are determined from the Hartree-Fock wave function [5] of the target atom, and the function R_n is an n th order polynomial in r . The approximate function representing the short-range part of the potential and the exchange potential is then represented

by the following truncated potential given by

$$V_s(r) = (2Z/r) \sum_n C_n \exp(-nC_0 r). \quad (2a)$$

The coefficients C_n ($n = 1$ to 7 for argon and 1 to 6 for neon) for this representation of the effective potential is computed from the following equations:

$$C_n = \sum_j \sum_k [B]_{nk}^{-1} [\exp(-kC_0 r_j)] \times \{\langle \Phi_0 | V(r_j) | \Phi_0 \rangle + V_{\text{ex}}(r_j)\}, \quad (2b)$$

where Φ_0 is the wave function of the target atom and the $(N \times N)$ matrix B is defined by

$$\begin{aligned} B_{nk} &= \sum_i \Psi(n, i) \Psi(i, k); \\ \Psi(n, i) &= A_n \exp(-nr_i); \\ \Psi(i, k) &= A_n \exp(-kr_i). \end{aligned} \quad (3)$$

In Eq. (3), the value of $r_i = (i - 0.5) \Delta r$ is based on the stepsize $\Delta r = r_{\text{max}}/M$, where M is the number of subdivisions (30–60) of the range over which the potential is approximated ($0 < r < 30a_0$) and the sum over i is from 1 to M ($M > N$). The values of M and N entering in this algorithm is optimized with the condition that the computed DCS obtained from this approximating potential agree with that obtained from the initial potential within 1% or less. This leads to six constants for the neon target and seven values of C_n for the argon atom. For neon, and argon the values of the constants are listed in Table I. The truncated form of the potential increases the efficiency of the minimization algorithm over the intermediate energy range to produce the DCS surface over an energy

TABLE I
Constants C_n for the e-neon and e-argon potentials defined in Eq. (2a).

n	C_n	
	Neon	Argon
0	1.37079301	1.03130210
1	1.114661(-7)	0.391702(-6)
2	1.259580(1)	0.136716(1)
3	-0.129429(0)	0.111888(0)
4	0.858429(0)	-0.253920(1)
5	-0.274376(1)	-0.158640(1)
6	1.736750(0)	0.726041(1)
7	—	-0.360875(1)

grid of 15 and angular grid of 90. The operator $V(r_k)$ contained in the equation for C_n represents the Coulomb interaction between the incident electron and the target atom.

The energy-dependent polarization potential used in the present study is of the form:

$$V_p(E, r) = \alpha_d / [r + \xi(a, b, E)]^4, \quad (4)$$

where α_d is the experimentally known dipole polarizability [6] of the target atom (for neon atom, $\alpha_d = 2.66$ atomic units and 11.09 for argon) and $\xi(a, b, E)$ is an energy-dependent function given by $\xi = a + bE$, where a and b are parameters determined by the DCS minimization code. In the present study, the values of a and b are $a = 1.13$, $b = 0.0036$ for neon and $a = 2.932$, $b = 0.00245$ for argon target. This form of the polarization potential is based on a localization of the nonlocal potentials resulting from the well-known polarized orbital method of Temkin and Lamkin [7]. With this choice of the polarization potential, the function ξ has the effect of a cut-off parameter making the minimum value of the radial distance to be energy-dependent and at large distances from the atom, the polarization potential has the correct asymptotic form [3]. The inclusion of the dipole polarizability takes into account the excited states [8] of the target atom which contribute to the polarizability and thus to the polarization potential. Because of the long-range effect of the polarization potential, at intermediate energies ($50 < E < 500$ eV) of the incident electron, a large number of phase shifts (200 or more) have to be determined from direct numerical solution of the Schrödinger equation and the Born approximation.

Computation of Differential Cross Section

The effective interaction potential used in the present study is represented by the sum of the short-range term and the energy-dependent long-range polarization terms given by

$$V_e(r) = \langle \Phi_0 | V(r) | \Phi_0 \rangle + \alpha_d / [r + \xi(a, b, E)]^4 + V_{\text{ex}}, \quad (5)$$

where Φ_0 is the ground-state Hartree-Fock [5] wave function of the target atom, the operator $V(r)$ contains the electron-electron and electron

nuclear potentials, α_d is the dipole polarizability of the target atom, and the parameters a and b contained in $\xi(a, b, E)$ are to be determined for selected incident energies E of the electron. The form of the exchange potential V_{ex} is similar to the one used in an earlier study [9]. The differential scattering cross section $I(k, \theta)$ is then computed from the scattering amplitude $f(k, \theta)$ as a function of the wave number k and scattering angle θ given by

$$f(k, \theta) = \left(\frac{1}{2} ik \right) \sum_l (2l + 1) \times [\exp(2i\delta_l) - 1] P_l(\cos \theta), \quad (6)$$

where the phase shifts δ_l are computed by solving the radial part of the Schrödinger equation for angular momentum in the range $0 \leq l < 12$ using the Numerov algorithm [10] from which the zeros of the wave functions are used in the argument of Bessel and Neumann functions to compute the phase shifts accurate to four decimal places. In Eq. (6), the functions $P_l(\cos \theta)$ are the Legendre polynomials of order l [11]. For higher partial waves, the Born approximation is used in the range $11 < l < 30$ with a 32-point Gauss quadrature method for the numerical integration. The phase shifts for higher partial waves are computed using an analytical expression [12] for the phase shift in terms of integrals involving Bessel functions of fractional order for values of l up to 200. It has been found that for scattering angles $> 2^\circ$, not more than 200 partial waves are needed for the DCS to converge to an accuracy of $\pm 0.1\%$. However, for angles less than 0.1° , it was found that more than 1000 partial waves were needed for convergence to the listed accuracy. All the computations were performed in double precision using an IBM4381 and the DCS data reduction in graphics form was done with a Pentium PC. For scattering angles in the small-angle range, it was found that a faster algorithm was required to efficiently execute the minimization routine. For this, the electron-atom interaction was represented by a truncated least-square fitted function containing fewer terms which substantially reduced the computing time of the forward scattering amplitude and the resulting integral cross section. For the higher partial waves, the approximation to the short-range interaction did not significantly affect the final results since phase shifts depend mostly on the polarization potential. This enabled the determination of the approximate values of param-

ters a and b appearing in $V_p(E, r)$ for neon and argon atoms that satisfy the specified conditions with a few minutes of computer time for each incident energy for a given target atom.

Discussion of Results

The variation of computed integral cross-section σ with the parameters contained in the polarization potential $\xi(a, b, E)$ is shown in Figure 1. As the value of ξ was varied from 1 to 4, the value of the integral cross-section σ varied from 25.2 to 16.7 at the selected incident energy of 100 eV. Using the approximate experimental value of 17.82 (a.u.) for σ , the value of ξ is determined to be 3.177. Then, from the minimization of the DCS surface [1], the values of a and b contained in $\xi(a, b, E)$ were determined to be 2.932 and 0.00245, respectively, for argon. A similar procedure was used for the neon target for which the values of the parameters are 1.13 and 0.0036. Thus, using the potential given by Eq. (5), the DCS and the integral cross-section σ at all energies in the range $50 < E < 500$ eV were then computed. Comparison of the computed $\sigma(E)$ and other available theoretical [13] and experimental data [14] as a function of energy E is shown in Figure 2. The variation of σ with ξ is shown in Table II for argon for the incident energy of 100 eV. The comparison of the computed integral cross-section σ with other theoretical and experimental data for various energies in the range $50 < E < 500$ eV is shown in Table III.

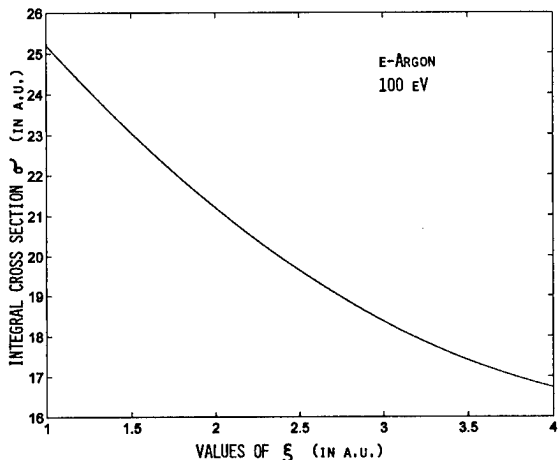


FIGURE 1. Change of the integral cross-section σ (in units of a_0^2) with the parameter ξ in the range 1–4 for e-argon system at an incident energy of 100 eV.

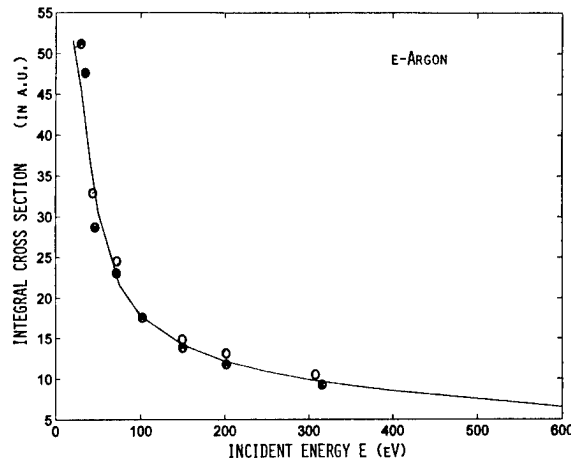


FIGURE 2. Comparison of the computed integral cross section for e-argon scattering for incident energy in the range 50–600 eV. Solid line, the computed σ . Open circles are theoretical results [13] and closed circles are the experimental results [14].

At the energy of 50 eV, the computed σ was found to be greater than the experimental values from different sources. At larger energies, the computed σ is in good agreement with theory and experiment in the intermediate energy range. For all energies, the computed σ appears to be larger than the experimental values. Comparison of the computed DCS with other theoretical and experimental data is shown in Tables IV and V. At these energies, the theoretical values of DCS are greater than the experimental results at all angles. However, the critical angle at 100 eV appears to be in good agreement with the published results. For the determination of the critical angle and energy

TABLE II
Variation of integral cross-section σ with ξ for e-argon system at incident energy $E = 100$ eV.^a

ξ	σ
2.246	20.650
2.446	19.751
2.646	19.053
2.846	18.490
3.046	18.052
3.246	17.699
3.446	17.409
3.646	17.183
3.846	17.001
4.046	16.840

^a Experimental value of $\sigma = 17.82 \pm 0.5$ (a_0^2) from Ref. [14].

TABLE III
Comparison of the computed integral cross-section σ with theory and experiment at various incident energies for e-argon scattering.^a

E	σ^b	σ^c	σ^d
50	30.49	33.28	26.0, 25.6, 21.8, 22.0
75	21.63	23.37	24.3
100	17.81	19.21	18.7, 16.5, 17.3, 17.0, 18.0, 19.3
150	14.18	15.02	12.0, 13.0, 10.9, 12.7
200	12.21	12.80	11.5, 10, 10.9, 12.7
250	10.89		
300	9.91	10.32	8.7, 8.0, 8.9, 10.2
350	9.14		
400	8.51		
450	7.97		
500	7.52		

^a σ is in units of a_0^2 .^b Present results.^c Theoretical results from Ref. [13].^d Experimental data from Ref. [14].

TABLE V
Comparison of the differential cross section with experimental and other theoretical results for argon at 100 eV.^a

Angle θ	Theory		Experiment Ref. [14]
	Present	Ref. [13]	
0	42.6	50.5	
10	22.5	23.2	
20	9.61	10.7	6.48
30	3.74	4.19	2.16
40	1.17	1.40	0.79
50	0.37	0.46	0.26
60	0.32	0.32	0.16
70	0.54	0.50	0.25
80	0.71	0.71	0.43
90	0.70	0.75	0.43
100	0.47	0.55	0.33
110	0.18	0.24	0.18
120	0.01	0.02	0.04
130	0.15	0.13	0.06
140	0.66	0.66	
150	1.48	1.54	
160	2.32	2.52	
170	3.05	3.29	
180	3.19	3.58	

^a Units in a_0^2 / ster .

TABLE IV
Comparison of the differential cross section with experimental and other theoretical results for argon at the incident energy of 50 eV.^a

Angle θ	Theory		Experiment	
	Present	Ref. [13]	Ref. [15]	Ref. [14]
0	46.6	48.9	57.4	
10	29.9	29.3	33.9	
20	17.3	17.7	19.6	13.7
30	9.31	9.86	10.8	6.80
40	4.08	4.71	5.29	3.10
50	1.13	1.62	1.91	1.15
60	0.06	0.22	0.30	0.11
70	0.26	0.16	0.13	0.09
80	1.00	0.90	0.82	0.54
90	1.63	1.74	1.63	1.08
100	1.75	2.08	2.01	1.19
110	1.35	1.72	1.73	0.97
120	0.69	0.92	0.99	0.58
130	0.18	0.24	0.26	0.20
140	0.12	0.14	0.04	
150	0.58	0.80	0.57	
160	1.33	1.92	1.59	
170	2.03	2.96	2.56	
180	2.27	3.38	2.94	

^a Units in a_0^2 / ster .

(θ_c, E_c), the DCS surface was generated over a grid of 15×90 with the width in energy and angle was reduced to obtain the surface near the critical region. The DCS surface for e-Neon system is shown in Figure 3 in which the approximate (θ_c, E_c) is shown to be approximately (65°, 100 eV) as can be seen in the corresponding contour plot of Figure 4. Once the approximate critical region is known, the

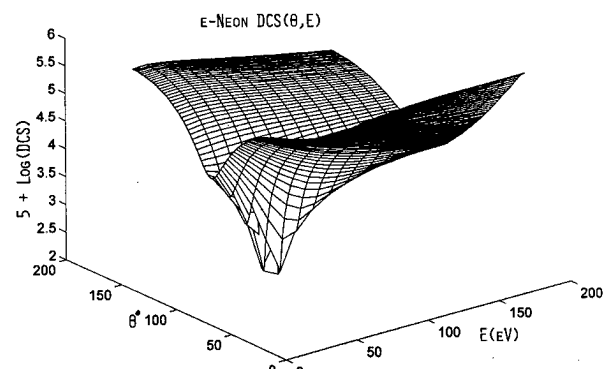


FIGURE 3. Differential cross section (DCS in atomic units) surface for e-neon system showing a minimum near (95°, 65 eV).

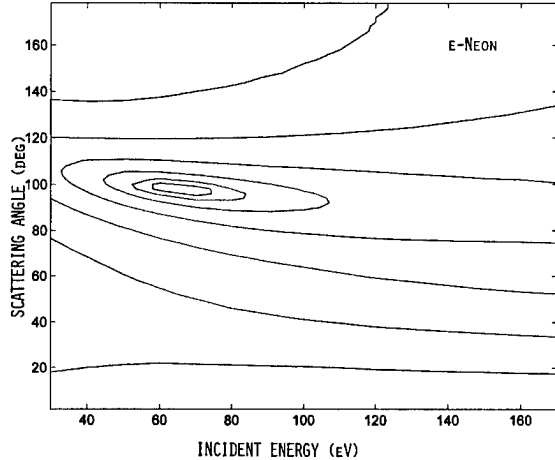


FIGURE 4. Contour plot corresponding to Figure 3 showing the approximate minimum of the surface at $(95^\circ, 65 \text{ eV})$.

grid size was reduced to about $\Delta\theta = 0.1^\circ$ and $\Delta E = 2 \text{ eV}$. The DCS surface near the critical region for e-Ne system is shown in Figure 5 and the corresponding contour plot is shown in Figure 6. Thus the value of (θ_c, E_c) is seen to be about $(65^\circ, 98 \text{ eV})$ for e-neon system. This is in excellent agreement with the published results [16]. The DCS surface for the e-argon system is shown in Figure 7 for a grid of $(\Delta\theta = 2^\circ, \Delta E = 10 \text{ eV})$ and the approximate value of (θ_c, E_c) is seen to be about $(120^\circ, 120 \text{ eV})$ in the contour plot of Figure 8. Using a smaller grid size of $(\Delta\theta = 0.1^\circ, \Delta E = 2$

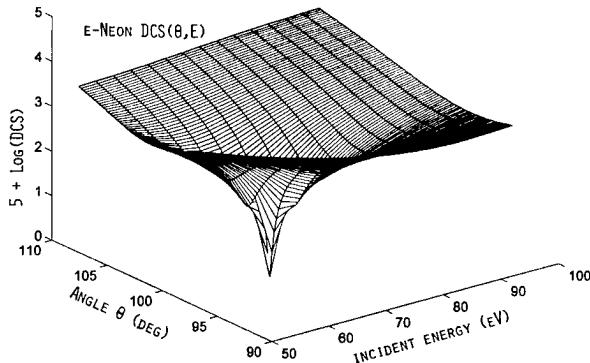


FIGURE 5. Differential cross section (DCS in atomic units) surface for e-neon system over a smaller grid of $(\Delta\theta = 0.2^\circ, \Delta E = 3 \text{ eV})$ showing a minimum near $(98^\circ, 65 \text{ eV})$.

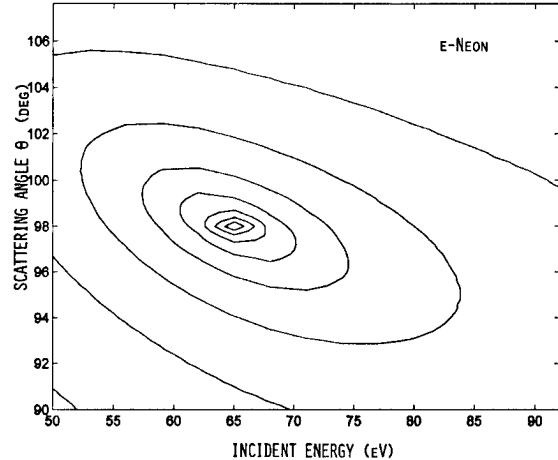


FIGURE 6. Contour plot corresponding to Figure 5.

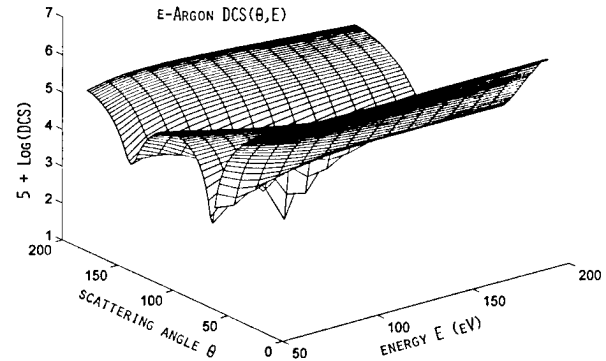


FIGURE 7. Differential cross section (DCS in atomic units) surface for e-argon system showing a minimum near $(120^\circ, 120 \text{ eV})$.

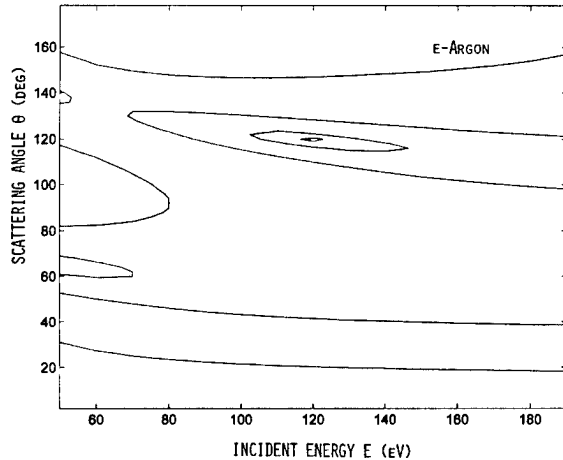


FIGURE 8. Contour plot corresponding to Figure 7 showing the approximate minimum of the surface at $(120^\circ, 120 \text{ eV})$.

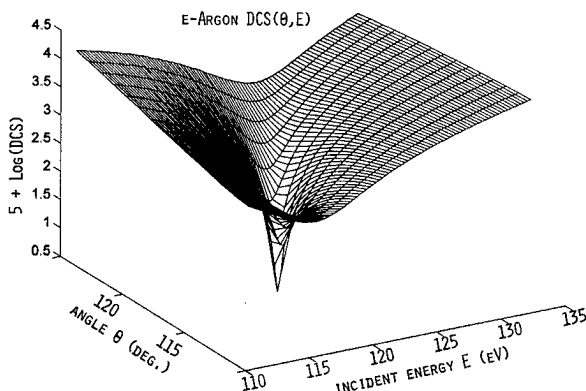


FIGURE 9. Differential cross section (DCS in atomic units) surface for e-argon system over a smaller grid of ($\Delta\theta = 0.1^\circ$, $\Delta E = 2 \text{ eV}$) showing a minimum near $(117.4^\circ, 120 \text{ eV})$.

eV), the DCS surface for e-argon system shown in Figure 9 appears to have a sharp minimum near the critical value of $(117.4^\circ, 120 \text{ eV})$ as is seen in the corresponding contour plot of Figure 10. Thus the present model calculations for DCS are in good agreement with available published data except at lower energies for which more accurate experimental data is needed for further analysis. At present a second-order function $\xi(a, b, c, E)$ is being tested to determine the DCS the critical angle and energy for other atoms to determine the limitations of the effective interaction potential for the

computation of DCS in the intermediate energy range. In conclusion, the usefulness of the model potential used in the present study is clearly for intermediate energies where a large number of partial waves are needed to obtain converged values of the differential scattering cross section for low scattering angles. For low energies, where fewer number of partial waves will be sufficient for the convergence of DCS, the close-coupling calculations have the advantage of being more accurate at all angles.

ACKNOWLEDGMENTS

This research has been supported by grants received from the Grants and Research Funding Committee and the College of Science and Technology of Southeast Missouri State University. Authors wish to thank Ms. Tessy Paikeday, Yale University, for the final proofreading of this manuscript.

References

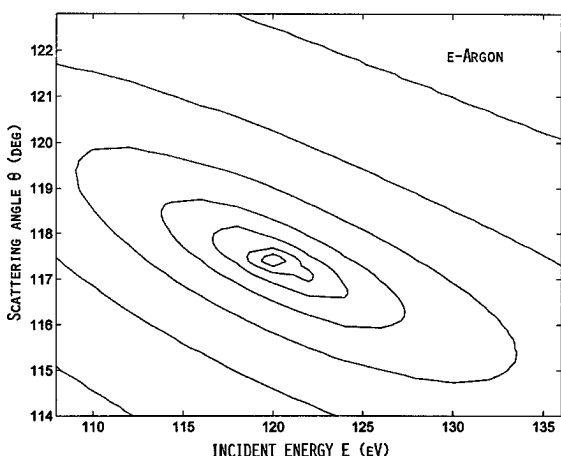


FIGURE 10. Contour plot corresponding to Figure 9.

1. J. M. Paikeday, Int. J. Quant. Chem. **65**, 585 (1997).
2. W. C. Fon, K. A. Berrington, and A. Hibbert, J. Phys. B **14**, 323 (1981). R. P. McEachran and A. U. Stauffer, J. Phys. B **16**, 4023 (1983). Arati Dasgupta and A. K. Bhatia, Phys. Rev. A **30**, 1241 (1984). H. P. Saha, Phys. Rev. A **39**, 5048 (1988).
3. W. Ihra and H. Friedrich, Phys. Rev. A **45**, 5278 (1992). D. Basu, Shankar K. Data, Pritikana Kahn, and A. S. Ghosh, Phys. Rev. A **35**, 5255 (1987). A. W. Pangantiwar and R. Srivastava, Phys. Rev. A **40**, 2346 (1989). Arvin Kumar Jain and A. N. Tripathi, Phys. Rev. A **42**, 6912 (1990).
4. J. M. Wadehra, T. S. Stein, and W. E. Kauppila, Phys. Rev. A **29**, 2912 (1984).
5. Carlos F. Bunge and Jose A. Barrientos, Atomic Data and Nuclear Data Tables **53**, 113 (1993). E. Clementi and C. Roetti, Atomic Data Nuclear Data Tables **14**, 177 (1974).
6. M. Horbatsch, J. W. Darewych, and R. F. McEachran, J. Phys. B **16**, 4451 (1983).
7. A. Temkin, Phys. Rev. **107**, 1004 (1957); **116**, 358 (1959). A. Temkin and J. C. Lamkin, Phys. Rev. **121**, 788 (1961). A. Temkin and A. K. Bhatia, J. Chem. Phys. **42**, 644 (1965). A. Temkin and K. V. Vasavada, Phys. Rev. **160**, 109 (1967). W. M. Duxler and R. T. Poe, Phys. Rev. A **4**, 1935 (1971).
8. Spyros I. Themelis and Cleanthes A. Nicolaides, Phys. Rev. A **46**, R21 (1992); J. Stiehler and J. Hinze, J. Phys. B **28**, 4055 (1995).
9. R. Vanderporten, J. Phys. B **8**, 926 (1975); A. W. Pangantiwar and R. Srivastava, Phys. Rev. A **40**, 2346 (1989).

10. J. M. Paikeday, *J. Chem. Phys.* **65**, 397 (1976).
11. M. Abramowitz and I. A. Stegun in *Handbook of Mathematical Functions* (Dover Publ., New York, 1970), Chapter 8.
12. Equation (3.14) and Eq. (3.15) of Ref. [7].
13. S. N. Nahar and J. M. Wadehra, *Phys. Rev. A* **35**, 2051 (1987).
14. J. P. Bromberg, *J. Chem. Phys.* **61**, 963 (1974). J. F. Williams and B. A. Willis, *J. Phys. B* **8**, 1670 (1975). R. H. J. Jansern and F. J. de Heer, *J. Phys. B* **9**, 185 (1976). L. Vuskovic and M. V. Kurepa, *J. Phys. B* **9**, 837 (1976). R. D. Dubois and M. E. Rudd, *J. Phys. B* **9**, 2657 (1976). F. J. de Heer, R. H. Jansen, and W. van der Kaay, *J. Phys. B* **12**, 979 (1979). S. K. Srivastava, H. Tanaka, A. Chutjian, and S. Trajmar, *Phys. Rev. A* **23**, 2156 (1981).
15. H. P. Saha, *Phys. Rev. A* **43**, 4712 (1991).
16. D. F. Register and S. Trajmar, *Phys. Rev. A* **29**, 1785 (1984). D. F. Register, S. Trajmar, and S. K. Srivastava, *Phys. Rev. A* **21**, 1134 (1980).

Ab Initio SCF-MO Study of the Topology of the Charge Distribution of Acid Sites of Zeolites

HUMBERTO SOSCÚN,¹ JAVIER HERNÁNDEZ,¹
OLGA CASTELLANO,¹ GILBERTO DÍAZ,² ALAN HINCHLIFFE³

¹ Sección de Teoría Cuántica y Diseño Molecular, Laboratorio de Química Inorgánica Teórica, Departamento de Química, Facultad de Ciencias, La Universidad del Zulia, Ap. 526, Grano de Oro, Maracaibo, Venezuela

² CeCalcula, Universidad de Los Andes, La Hechicera, Mérida, Venezuela

³ Department of Chemistry, UMIST, P.O. Box 88, M60 1QD, United Kingdom

Received 22 February 1998; accepted 25 June 1998

ABSTRACT: The structural, electronic, vibrational, and topologic properties of a series of acid sites of zeolites were studied at different levels of ab initio molecular orbital theory. The zeolite acid sites were modeled by using the following molecular clusters: silanol H_3SiOH (B_0) and the clusters $\text{H}_3\text{SiO}(\text{H})\text{AlH}_3$ (B_1), $(\text{OH})_3\text{SiO}(\text{H})\text{Al}(\text{OH})_3$ ($B_1-\text{OH}$), and $\text{H}_3\text{SiO}(\text{H})\text{Al}(\text{OH})_2\text{SiH}_3$ (B_2). The calculation of geometries and properties of these clusters were performed at the Hartree-Fock level, and, additionally, second-order Møller-Plesset (MP2) and density functional BLYP calculations were carried out for silanol and B_1 clusters. Geometries were fully optimized by following C_s symmetry restrictions. The standard STO/6-31 + G(D, P) basis set, which includes polarization and diffuse functions, was used for all the calculations. The topologic properties of the zeolite acid clusters, based on the theory of atoms in molecules, were analyzed in terms of the total density and the Laplacian density properties, both evaluated at the position of the bond critical points. The calculations showed that the frequency of the OH vibrational modes of the zeolite acid sites, often used as an infrared index for characterizing the acidity of zeolites, is linearly related to the total density of the charge at the critical points of the OH bonds, with a correlation coefficient of $r^2 = 0.97$. These results indicate that the total density of the electronic charge at the critical point of the OH bond can be used as a tool for interpreting the structural and electronic features of the zeolite hydroxyl groups. A relationship between the Mulliken population of the H atom of the OH bond and the OH frequency gives a correlation coefficient of 0.67. On the other hand, the

Correspondence to: H. Soscún.

Contract grant sponsor: CONICIT.

Contract grant number: 95-001617.

values of the Laplacian density calculated at the critical points of the bonds of the acid sites indicate that the zeolite structure is dominated by a network of Si—O and Al—O ionic interactions, while the O—H bonds are characterized as covalent bonds, with different extents of charge concentration. © 1998 John Wiley & Sons, Inc. Int J Quant Chem 70: 951–960, 1998

Introduction

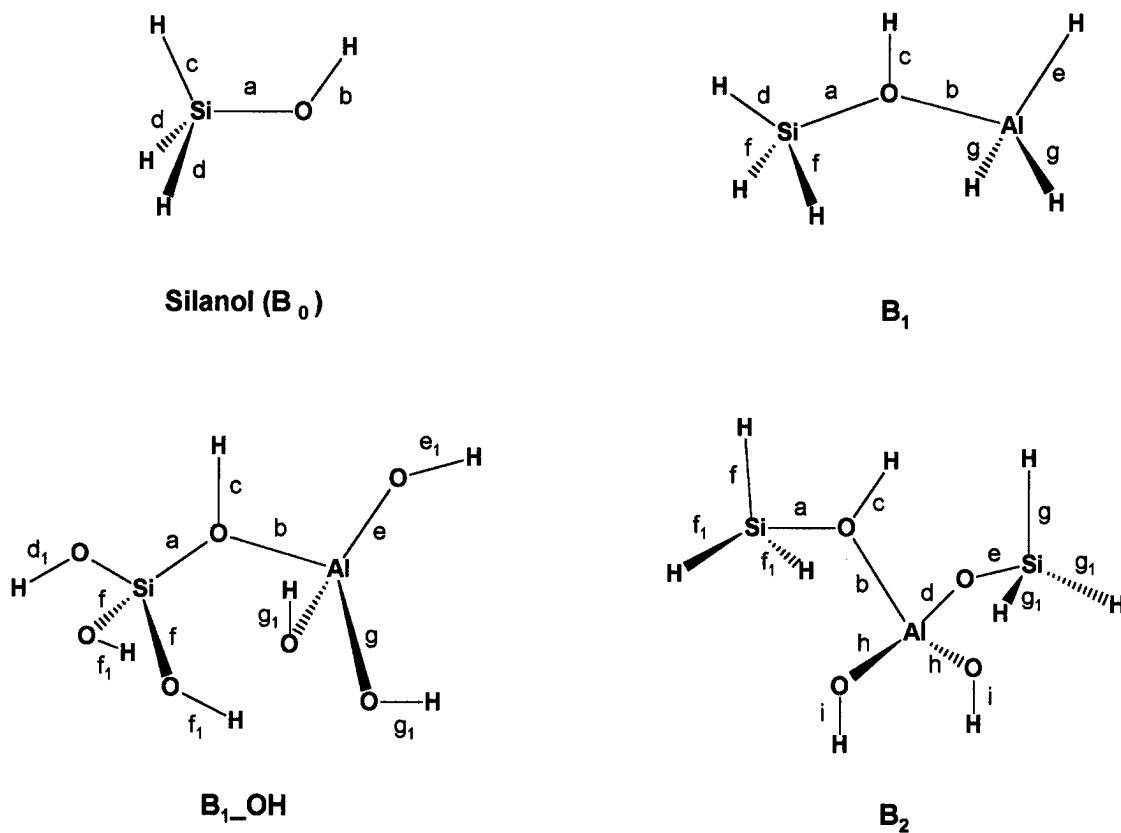
Zeolites are crystalline aluminosilicate compounds widely used as molecular sieves and acid catalysts in many important industrial processes [1–3]. The acidic properties of these materials arise from the presence of hydroxyl groups named acid sites of zeolites, where two different acid sites are distinguished [4]. One of them is the isolated hydroxyl group denoted as SiOH, which is found in amorphous silica and named terminal hydroxyl groups of zeolites, whose acidic features are moderate, allowing for the interaction with basic molecules leading to the formation of H bonds. The other acid group is referred as a Brönsted acid site of zeolites and are formed by surface hydroxyl groups that are inserted between the Al and Si atoms of the zeolite network. In fact, these Al and Si atoms are bonded as tetrahedral oxide units $[SiO_4]^{4-}$ and $[AlO_4]^{5-}$ through the OH bridge to give a Brönsted Si(OH)Al acid function. These acid sites are located at the internal surface of the zeolite channels. The Si(OH)Al group is a very strong acid site, being the main species responsible for the catalytic properties of zeolites. Both of these groups, Brönsted and terminal OH sites, the main acid sites of zeolites, are able to interact with different substrates, particularly with those species with electronic lone pairs [5].

The zeolite acidity can be characterized by using either experimental or theoretical determinations. Experimentally, IR techniques have been very useful for understanding the nature of the isolated and bridging surface hydroxyls. IR allows one to determine the vibrational properties of zeolite-adsorbed molecules [4, 5]. The dominant vibrational properties of these hydroxyl groups correspond to the OH valence-stretching mode, ν_{OH} . These OH modes were observed at 3744 cm^{-1} and in the region of 3520 and 3630 cm^{-1} for the SiOH and Al(OH)Si groups, respectively. This property is directly related to the force constant of the OH bond; in consequence, the value of ν_{OH} is considered an important index for the zeolite acidity. The

known values of this index for OH bonds in zeolites indicate that the Brönsted sites are more acidic than are the SiOH terminal groups [6]. Much attention has been dedicated to the problem of zeolite acidity; both experimental [7, 8] and theoretical [9, 10] investigations have been performed to establish relationships between the catalytic activity of zeolites and the determined structural and electronic properties, such as Al/Si ratio, gas phase acidity, and protonation energy.

The main aim of this article was to investigate the fundamental factors that govern the acid sites in zeolites from the structural and electronic points of view. To gain insight in this direction, we started a theoretical research program to characterize zeolites by using the topologic theory of atoms in molecules developed by Bader et al. [11, 12] as implemented by Ciowslowsky et al. [13] in the Gaussian packages [14]. This theory, based on the topological properties of the molecular charge distribution $\rho(r)$ and their associated fields, the gradient of $\rho(r)$ and the Laplacian of $\rho(r)$, is able to characterize locally the bonds, the global structure, the stability of a molecular system and its reactivity. In particular, ionic and covalent bonds and chemical reactivity can be clearly differentiated from the topological properties of the Laplacian of $\rho(r)$ [12].

This article reports the first investigation about the topologic properties of the electronic charge distribution, at the ab initio level, of a series of hydroxyl acid sites of zeolites. These zeolite hydroxyl groups are represented by silanol H_3SiOH (BO) and by two kinds of differently sized clusters of the bridged and terminal hydroxyl groups, namely, $H_3Si(OH)AlH_3$ (B1) and $(HO)_3Si(OH)Al(OH)_3$ (B1_OH), and $H_3Si(OH)Al(OH)_2SiH_3$ (B2) and $(HO)_3Si(OH)Al(OH)_2Si(OH)_3$ (B2_OH) (see Scheme 1). In addition, structural and vibrational features of the selected acidic groups of zeolites were studied to explore relationships between these properties and the topologic properties of zeolites. The results, analyzed in terms of the available theoretical and experimental data, have shown that the density of $\rho(r)$, calculated at the



SCHEME 1

position of the critical point of the OH bonds, is linearly related to the frequency of the OH vibration mode.

Theory and Computational Details

Quantum mechanic methods have become useful for studying the bonding interactions that occur between zeolites, represented by clusters of different chemical composition, and small molecules [5, 15]. These theoretical studies are limited by the complexity of the interacting molecules and, more significantly, for the size of the cluster taken as model for representing the zeolite active site. These limitations and the availability of computational resources define the levels of the theory that should be employed. This article concerns applications of the standard SCF-MO calculations at Hartree-Fock and post-Hartree-Fock methods and the application of the topologic theory of a molecular charge distribution. The first

deals with the levels of theory for the calculations and the second one is based on the theory of atoms in molecules [11, 12]. This theory deals with the topologic characterization of the electronic charge distribution of a molecular system, based in the properties of $\rho(r)$ and the Laplacian of $\rho(r)$.

THEORY OF ATOMS IN MOLECULES

The theory of atoms in molecules, developed by Bader et al. [11], is based on the topologic properties of a molecular charge distribution $\rho(r)$, which are characterized by the nature of the extreme of $\rho(r)$, known as the critical points of $\rho(r)$. These critical points are defined as the points where the gradient vector field of $\rho(r)$ vanishes [$\nabla\rho(r) = 0$] and are classified according to the three curvatures of $\rho(r)$, which are determined by the three eigenvalues (λ_1 , λ_2 , and λ_3) of the diagonalized Hessian matrix of $\rho(r)$ [$H_{ij} = \partial^2\rho(r)/\partial x_i \partial x_j$]. Each critical point can be labeled by two numbers: D and S , where D corresponds to the number of nonzero

eigenvalue, and S is the difference between the nonzero and the negative eigenvalues. The set (D, S) is often called the signature of the extreme. The label for a maxima critical point is $(3, -3)$ because all the three eigenvalues of H are nonzero and negative, being $S = 3$ and $D = -3$, while a label for a minima is $(3, +3)$. In a molecular system, the maxima, minima, and saddle points in $\rho(r)$ are defined as attractors, cage, and either bond $(3, -1)$ or ring points $(3, +1)$, respectively. The regions where the $\nabla\rho(r)$ is zero lead to the existence of a zero-flux surface that splits the molecule in fragments linked by bond paths characterized as $(3, -1)$. These regions, demarcated by the zero-flux surfaces, are named the basins. Attractors of basins are often located at the position of the nuclei, while bond critical points are located between two bonded atoms and correspond to a local maxima in two directions and a local minima in the third direction. The set of $(3, -1)$ critical points defines the network of bond paths and describes the molecular structure by the characterization of all their atomic interactions. Along each bond path, the charge density is a maximum with respect to any neighboring line. The value of the electron density at the bond critical point [$\rho_c(r)$] has been referred as an useful index for representing the corresponding bond order [11]. This is a property that accounts for the degree of charge concentration on the bond path. In the present work, we use this parameter for rationalizing the electronic properties of the OH bonds in the acid sites of zeolites, particularly for interpreting the frequency of the OH vibrational stretching mode that is used as an index for the zeolite acidity.

The characterization of how the electronic density is rearranged according to the concentrations and depletions of the charge is described by the properties of the Laplacian of $\rho(r), \nabla^2\rho(r)$. In particular, the sign of $\nabla^2\rho(r)$ determines the regions where the charge density is locally concentrated [$\nabla^2\rho(r) < 0$] or locally depleted [$\nabla^2\rho(r) > 0$] [12]. These regions identify the chemical reactivity of a molecule. For instance, if the Laplacian is calculated at the position of a bond critical point, $\nabla^2\rho_c(r)$, positive values are indicative of ionic interactions, while negative values are associated with covalent bonds. In the present work we used these properties of the Laplacian of $\rho(r)$ for characterizing the bond features of zeolites through the atomic inter-

actions within the clusters and for describing the differential reactivity of the OH bonds in terminal and Brönsted acid sites of zeolites.

CLUSTER MODELS FOR THE ZEOLITE ACID SITES

An accurate selection of the cluster size and their chemical composition is crucial for understanding at the theoretical level the geometric and electronic features of the acid sites of zeolites. Furthermore this information is important to rationalize the observed tendencies in the reactivity of different zeolites. In the present work we studied silanol (B_0) $H_3Si(OH)AlH_3$, (B_1) $(HO)_3Si(OH)Al(OH)_3$, (B_1-OH), and $H_3Si(OH)Al(OH)_2SiH_3$ (B_2) clusters. Geometric optimizations of B_0 , B_1 , and B_2 were referenced elsewhere [15], whereas for B_1-OH , no report has been published yet. We performed new electronic structural, and vibrational calculations for B_0 , B_1 , and B_2 models in order to be consistent with the comparisons.

CALCULATIONS

For silanol and B_1 clusters, the calculations of geometry optimizations and IR frequencies were performed at three levels of theory: Hartree–Fock Møller–Plesset [16] at second order of perturbation MP2, and density functional theory with the BLYP hybrid methods [17]. MP2 methods account for the second-order electronic correlation effects and BLYP density functional methods evaluate correlation and exchange electronic effects. For the B_1-OH and B_2 clusters calculations for geometry optimizations and IR spectra were carried out at the Hartree–Fock level. Different basis sets were employed for the calculations but in this work, we only report the results obtained by using the standard STO/6-31 + G(D,P) basis set [18]. Polarization and diffuse functions in the heavy atoms are included in this basis set. The geometry of clusters were fully optimized following C_s symmetry restrictions via the optimization method of Berny [19] and vibrational frequencies were evaluated by analytic methods within the harmonic approximation. The GAUSSIAN-94W, GAUSSIAN94 [14], and GAMESS [20] quantum chemistry packages were employed for the calculations, which were done on PC, IBM RS/6000, and Silicon Graphics workstations, respectively.

Results and Discussion

Zeolite clusters of different sizes and different chemical compositions were investigated in order to obtain reliable information about the changes in their properties according to the variations in the chemical environment around the acid sites, both the terminal and Brönsted ones. Particularly, for the clusters, calculations of geometry optimizations, IR frequency in the harmonic approximation, and topological properties of the electronic charge were performed to explore the existent relationships among themselves. It was expected that the introduced structural modifications in the cluster models were able to reflect the rearrangements in the electronic density of the OH hydroxyl groups by perturbation of the systematic increasing of the size of the clusters.

Here, we report the results of ab initio SCF-MO calculations of four different clusters to represent the acid sites in zeolites—silanol H_3SiOH , $\text{H}_3\text{SiO}(\text{H})\text{AlH}_3$, $(\text{HO})_3\text{Si}(\text{OH})\text{Al}(\text{OH})_3$, and $\text{H}_3\text{Si}(\text{OH})\text{Al}(\text{OH})_2\text{SiH}_3$, which will be denoted in the following as B_0 , B_1 , $\text{B}_1\text{--OH}$, and B_2 clusters, respectively. These models consider the effects of the addition of the AlH_3 group to B_0 to give the B_1 cluster; the substitution of the H atoms that are linked to Si and Al atoms by OH groups, giving the $\text{B}_1\text{--OH}$ cluster; and the formation of B_2 from

B_1 with the substitution of H atoms bonded to Al by OH groups. The B_0 and B_1 clusters represent a single terminal acid site and a single Brönsted acid site without environment perturbations, respectively, while $\text{B}_1\text{--OH}$ and B_2 are single Brönsted acid sites with environment perturbations. In all of these clusters there are three Brönsted acid sites and nine terminal acid sites. We expected that the behavior of the electronic density of the hydroxyl groups of these acid centers of zeolites will be representative for understanding at electronic level their acidity as interpreted in terms of the OH vibrational mode. Additionally, we expected that the Laplacian of the electronic charge of the selected acid sites can give to us reliable information about the nature of the bonding interactions that occur in the Si—O, Al—O, and O—H network bonds of zeolites.

GEOMETRIC STRUCTURE OF THE ACID SITES OF ZEOLITES

Tables I and II report the results of bond distances in angstroms and bond angles in degrees for the fully Cs optimization geometry performed for the B_0 , B_1 , $\text{B}_1\text{--OH}$, and B_2 clusters. For B_0 and B_1 , these optimizations were carried out at the Hartree-Fock, MP2, and BLYP levels of theory and the standard STO/6-31 + G(D,P) basis set. Total energies in atomic units are also reported for

TABLE I
Optimized bond lengths of B_0 , B_1 , $\text{B}_1\text{--OH}$, and B_2 , symmetry Cs.

Bond length (angstroms)	B_0			B_1			$\text{B}_1\text{--OH}$	B_2
	HF/6-31 + G(d,p)	MP2/6-31 + G(d,p)	BLYP/6-31 + G(d,p)	HF/6-31 + G(d,p)	MP2/6-31 + G(d,p)	BLYP/6-31 + G(d,p)	HF/6-31 + G(d,p)	HF/6-31 + G(d,p)
a	1.6495	1.6768	1.6920	1.7027	1.7225	1.7369	1.7012	1.7043
b	0.9413	0.9618	0.9733	2.0409	2.0352	2.0808	1.9331	1.9482
c	1.4687	1.4657	1.4880	0.9467	0.9660	0.9755	0.9474	0.9485
d	1.4768	1.4745	1.4981	1.4693	1.4675	1.4896	1.6127	1.7153
d1							0.9417	
e				1.6002	1.5937	1.6111	1.7086	
e1							0.9373	
f				1.4635	1.4625	1.4846	1.6087	1.4692
f1							0.9523	1.4626
g				1.5956	1.5891	1.6049	1.7314	1.4813
g1							0.9401	1.4786
h								1.7145
i								0.9378
$-\text{E}/\text{E}_h$	366.14701	366.45314	367.11059	609.79466	610.18922	611.30803	1059.40606	1124.73743

TABLE II
Optimized bond angles of B_0 , B_1 –OH, and B_2 , symmetry Cs.

Bond length (angstroms)	B_0			B_1			B_1 –OH	B_2
	HF/6-31 + G(d,p)	MP2/6-31 + G(d,p)	BLYP/6-31 + G(d,p)	HF/6-31 + G(d,p)	MP2/6-31 + G(d,p)	BLYP/6-31 + G(d,p)	HF/6-31 + G(d,p)	HF/6-31 + G(d,p)
ab	121.61	118.84	117.51	131.08	130.54	132.24	120.52	133.00
ac	106.70	105.46	105.22	118.80	118.41	118.08	120.44	119.31
be				95.03	94.43	93.31	99.17	
bd								93.37
ad	111.02	111.31	111.63	105.71	105.66	106.00	103.85	
cd	110.04	110.36	110.22					
ad1								
dd	108.04	108.07	107.92					
dd1							123.32	
ee1							132.15	
ed								162.85
af				107.84	107.44	107.58	106.21	105.07
af1								108.09
bg							98.68	
bh								101.56
dh								117.55
eg				118.30	118.58	118.46	121.65	109.75
ff				111.73	111.80	111.66	114.75	
ff1							117.26	111.67
f1f1								111.89
gg				116.68	116.72	117.22	109.67	
eg1								111.58
gg1							124.05	107.88
g1g1								108.00
hh								117.92
hi								128.64

these clusters. For the B_1 –OH and B_2 clusters, geometry optimizations are reported at the HF/6-31 + G(D,P) level of theory. Scheme 1 shows the cluster figures, indicating the corresponding geometric parameters. Table I shows that the electronic correlation effects at the MP2 level of theory and the electronic exchange and correlation combined effects at the BLYP level of theory increase the Si–O and O–H bond lengths if the Hartree–Fock quantities are taken as references, following the order HF < MP2 < BLYP with the STO/6-31 + G(D,P) basis set. For silanol and a similar cluster to B_1 , reported with the STO/6-31G** basis set [15], the correlation effects follow the same order as in the present work with a most extended basis set. For the B_1 cluster, MP2 calculations decrease the Al–O bond length, while the BLYP effects increase it with respect to the Hartree–Fock ones. Regarding to the rest of the clusters, B_1 –OH and B_2 , the Hartree–Fock OH

bond lengths, b for silanol and c for B_1 , B_1 –OH, and B_2 , increase regularly with the size of the cluster, from B_0 to B_2 . This tendency indicates that there is a structural effect in the chemical environment of these acid zeolite clusters that is directly reflected in the studied OH bonds. These results indicate that there is increasing Brønsted acidity of these clusters with increasing of the size. At the Hartree–Fock level, the Si–O bond lengths are approximately constants in the Brønsted acid sites B_1 , B_1 –OH, and B_2 and are slightly larger in the silanol molecule. On the other hand, the Al–O bond decreases from B_1 to B_1 –OH and B_2 . No systematic behavior, however, was found for the rest of geometric parameters with respect to the variation of the clusters. For the terminal OH bonds in B_1 –OH and in the B_2 clusters, the OH distances lie in the known range of OH zeolite bond lengths.

Table II shows the bond angles corresponding to the geometry optimizations of the clusters. These

TABLE III
Vibrational properties of the zeolite clusters.

Bond	OH Vibrational Mode (cm ⁻¹)		
	HF	MP2	BLYP
Silanol cluster			
b (O—H)	4236	3955	3750
B₁ cluster			
b (O—H)	4160	3871	3728
B₁_OH cluster			
c (O—H)	4154		
d1 (O—H)	4239		
e1 (O—H)	4301		
f1 (O—H)	4045		
g1 (O—H)	4258		
B₂ cluster			
c (O—H)	4131		
i (O—H)	4290		

bond angles are consistent with previous calculations [15].

VIBRATIONAL PROPERTIES

Table III shows the IR frequencies of the OH vibrational modes, of the Brönsted acid sites, and of the OH terminal, calculated in the harmonic approximation for the studied clusters. The tendencies observed in the values of the OH frequencies at the Hartree–Fock level gives an account of the environment and the size effects of the clusters of B₀ to B₂. It is important to note that the OH frequency values decrease systematically with increasing of the number of tetrahedral sites in the clusters. These results also show that the OH frequencies are larger in the OH terminal than in the bridged ones, being in the O—H fl mode in B₁_OH. The larger OH frequencies indicate that these groups are less acidic than are the OH bridged groups.

TOPLOGICAL PROPERTIES

Density of Charge

The topological properties of the charge distribution of the zeolite clusters, according to Scheme 1, are reported in Table IV. This table reports for the clusters the values of the total density, $\rho_c(r)$, and the Laplacian density, $\nabla^2\rho_c(r)$, calculated at the position of the critical points of the bond paths.

The labels for these bond paths correspond to the labels for the geometric parameters of clusters (Scheme 1). In addition to these results, Mulliken populations were also calculated. For silanol and B₁, the topological properties were calculated at the HF and MP2 levels, while for B₁_OH and B₂, they were calculated at the HF level only. All these calculations were performed with the STO/6-31 + G(D, P) basis set. The set of $\rho_c(r)$ values gives a consistent pattern of values for the Si—O, O—H, and Al—O bonds, where the degree of charge concentration follows the order O—H > Si—O > Al—O. Regarding the OH bonds, the charge density is bigger in terminal OH than in bridge OH, following similar tendencies as observed for the OH IR frequencies, indicating that the bridged OH are stronger acids than are the terminal ones. Figure 1 shows the relationship between the frequency of the OH mode and the charge density calculated at the critical point of the OH bonds, with a lineal correlation coefficient of $r^2 = 0.98$. In fact, this value of charge density gives a measure of the degree to which electronic charge is locally accumulated between the O and H nuclei of the OH bond in zeolites. These results indicate that the charge density, calculated at the position of the OH critical point is a reliable theoretical index to characterize zeolite acidity. On the other hand, Mulliken population at the position of the H atom of the OH bond gives a relationship with the OH frequency vibration of $r^2 = 0.68$ (see Fig. 2).

Laplacian of the Charge Density

The distribution of the Laplacian of the charge density is a property that is the contribution of the three diagonal elements of the second derivative matrix of the density in each point of the space. The Laplacian features are determined by the signs of the $\nabla^2\rho(r)$ that at each point of the space determines the regions where the charge density is locally concentrated [$\nabla^2\rho(r) < 0$] or locally depleted [$\nabla^2\rho(r) > 0$]. These regions are clearly identified by the signs of the Laplacian and determine the chemical reactivity in a particular cluster. For instance, these charge concentrations determine the nature of the bonding interactions, either ionic or covalent ones. Also, this property gives information about the sites of electrophilic attack (local concentration) and the sites for nucleophilic attack (local depletion).

For a Brönsted acid, such as the B₁ cluster, the distribution of Laplacian of $\rho(r)$ performed with

TABLE IV
Topological properties on critical points of zeolite clusters.

Bond path	Total density		Density of Laplacian	
	HF	MP2	HF	MP2
Silanol cluster				
A (Si—O)	0.125	0.119	0.102	0.863
B (O—H)	0.382	0.357	-2.460	-2.033
C (Si—H)	0.120	0.122	0.280	0.267
D (Si—H)	0.122	0.120	0.283	0.261
B_1 cluster				
A (Si—O)	0.108	0.104	0.826	0.716
B (Al—O)	0.036	0.038	0.259	0.252
C (O—H)	0.373	0.349	-2.521	-2.076
D (Si—H)	0.123	0.123	0.283	0.263
E (Al—H)	0.075	0.076	0.279	0.275
F (Si—H)	0.126	0.125	0.283	0.262
G (Al—H)	0.076	0.077	0.281	0.278
B_1 OH cluster				
A (Si—O)	0.109		0.827	
B (Al—O)	0.049		0.387	
C (O—H)	0.369		-2.533	
D (Si—O)	0.141		1.175	
D1 (O—H)	0.378		-2.495	
E (Al—O)	0.095		0.908	
E1 (O—H)	0.385		-2.436	
F (Si—O)	0.141		1.202	
F1 (O—H)	0.363		-2.505	
G (Al—O)	0.092		0.841	
G1 (O—H)	0.384		-2.398	
B_2 cluster				
A (Si—O)	0.107		0.819	
B (Al—O)	0.046		0.365	
C (O—H)	0.370		-2.539	
D (Al—O)	0.091		0.867	
E (Si—O)	0.133		1.162	
F (Si—H)	0.123		0.284	
F1 (Si—H)	0.126		0.282	
G (Si—H)	0.118		0.279	
G1 (Si—H)	0.119		0.278	
H (Al—O)	0.095		0.892	
I (O—H)	0.386		-2.411	

the MOLDEN program [21] is depicted in Figure 3, where the positive and negative regions are shown. The positive regions are located around the Si, O, and Al atoms, while the negative regions are concentrated around the H atoms. In Table IV are reported the values of the Laplacian density, calculated at the position of the critical points in the acid cluster of zeolites according to Scheme 1. These results indicate that for zeolite acid clusters

the Si—O and O—Al network of bonds are dominated by ionic interactions, while the Laplacian of the O—H groups indicate that these bonds are covalent ones. The ionicity of the OH bonds, according to the negative value of the Laplacian that parallel the charge density, increases within the following order: $B_0 < B_1 < B_1\text{-OH} < B_2$. This order is the same for the increasing of the acidity in these clusters according to the OH frequency.

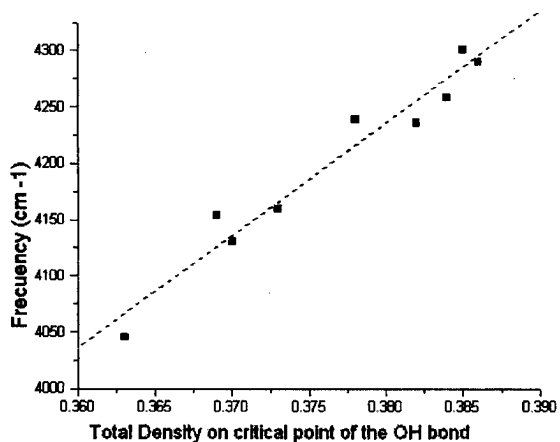


FIGURE 1. Relationship between the HF / 6-31 + G(d, p) calculated frequency of the OH vibrational mode and the HF / 6-31 + G(d, p) total density, calculated at the position of the critical point of OH bonds in the zeolite cluster acid sites. Linear correlation coefficient is $r^2 = 0.98$.

Conclusions

The present work has shown that ab initio calculations of the topology of the charge density of a selected number of zeolite clusters, used for modeling zeolite acid sites, can be used for rationalizing the IR observation of zeolites. In particular, we showed that the total density, evaluated at the position of the critical point of the OH bond, gives

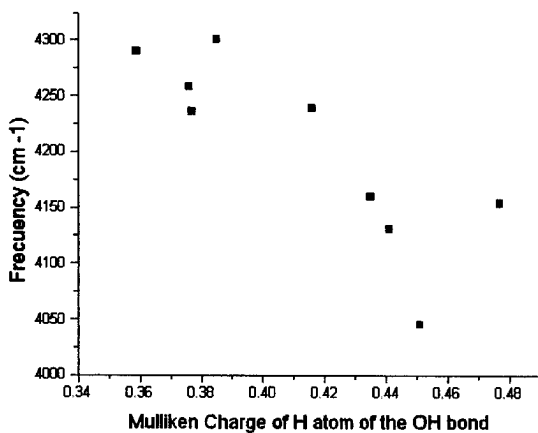


FIGURE 2. Relationship between the HF / 6-31 + G(d, p) calculated frequency of the OH vibrational mode and the HF / 6-31 + G(d, p) Mulliken population of the H atom of the OH bonds in the zeolite cluster acid sites.

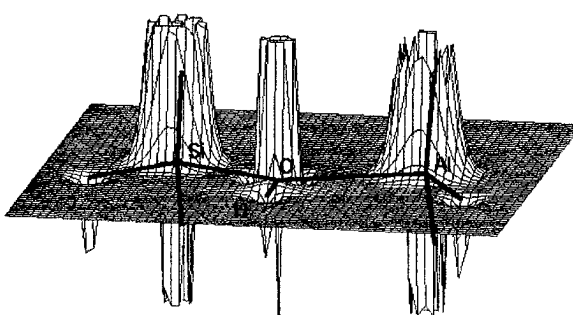


FIGURE 3. A relief map of the distribution of the Laplacian of electron density for a Brønsted acid site of zeolite as represented in the B₁ cluster. The map has been oriented taking as reference the plane of the cluster, containing the H-Si-O(H)-Al-H nuclei.

a real measure of the extent of acidity of the zeolite cluster. Mulliken populations, calculated at the position of the H atom of the OH bond, give an incomplete interpretation about the acidity of zeolite acid clusters. The results of the Laplacian distribution clearly indicate the presence of Al—O and Si—O ionic bonding in the zeolite clusters, whereas the OH bonds are of covalent nature. These properties allow us to characterize topologically the nature of the charge distributions and the network bonds in a zeolite molecular system.

ACKNOWLEDGMENTS

This work was partially supported by CONICIT, under Project Contract Number 95-001617. We also acknowledge a grant of computer time at the Manchester Computing Centre under Project mcdi009 and at the CeCalULA, Centro de Cálculo Científico de La Universidad de Los Andes.

References

1. A. Corma, Chem. Rev. **97**, 2373 (1997).
2. E. F. Vansant, J. Mol. Catal. A: Chem. **115**, 379 (1997).
3. P. A. Jacobs, in *Catalysis by Zeolites*, B. Imelik, et al., Eds. (Elsevier: Amsterdam, 1980), p. 293.
4. P. A. Jacobs, and R. von Ballmoos, J. Phys. Chem. **86**, 3050 (1982).
5. J. Sauer, P. Ugliengo, E. Garrone, and V. R. Saunders, Chem. Rev. **94**, 2095 (1994).
6. J. Szanyi and M. T. Paffett, Micropor. Matt. **7**, 201 (1996), and references therein.

7. J. Klinowski, *Anal. Chim. Acta* **283**, 929 (1993); G. Mirth, J. A. Lercher, M. W. Anderson, and J. Klinowski, *J. Chem. Soc., Faraday Trans.* **86**, 3039 (1990).
8. L. Smith, A. K. Cheetham, R. E. Norris, L. Marchese, J. M. Thomas, P. A. Wright, and J. Chen, *Science* **271**, 799 (1996).
9. A. K. Chandra, A. Goursi and F. Fajula, *J. Mol. Catal. A: Chem.* **119**, 45 (1997); F. Haase and J. Sauer, *J. Am. Chem. Soc.* **117**, 3780 (1995).
10. S. Damoun, W. Langenaecker, and P. Geerlings, *J. Phys. Chem. A* **101**, 6951 (1997).
11. R. F. W. Bader, *Atoms in Molecules—a Quantum Theory* (Clarendon Press, Oxford, UK, 1990); R. F. W. Bader and P. J. MacDougall, *J. Am. Chem. Soc.* **107**, 6788 (1985).
12. R. F. W. Bader, T. S. Slee, D. Cremer, and E. Kraka, *J. Am. Soc.* **105**, 5061 (1983).
13. J. Cioslowsky and S. T. Mixon, *J. Am. Chem. Soc.* **113**, 4142 (1991); J. Cioslowsky and P. R. Surján, *J. Mol. Struct. (Theochem)* **255**, 9 (1992).
14. M. J. Frisch, G. W. Trucks, H. B. Schlegel, P. M. W. Gill, B. G. Johnson, M. A. Robb, J. R. Cheeseman, T. Keith, G. A. Petersson, J. A. Montgomery, K. Raghavachari, M. A. Al-Laham, V. G. Zakrzewski, J. V. Ortiz, J. B. Foresman, J. Cioslowski, B. B. Stefanov, A. Nanayakkara, M. Challacombe, C. Y. Peng, P. Y. Ayala, W. Chen, M. W. Wong, J. L. Andres, E. S. Replogle, R. Gomperts, R. L. Martin, D. J. Fox,
15. J. S. Binkley, D. J. Defrees, J. Baker, J. P. Stewart, M. Head-Gordon, C. Gonzalez, and J. A. Pople, *Gaussian 94, Revision E.1* (Gaussian, Inc., Pittsburgh PA, 1995).
16. H. J. Soscún, P. J. O'Malley, and A. Hinchliffe, *J. Mol. Struct. (Theochem)* **341**, 237 (1995); H. V. Brand, A. Redondo, and P. J. Hay, *J. Mol. Catal. A: Chem.* **121**, 45 (1997); S. Bates and J. Dwyer, *J. Mol. Struct. (Theochem)* **306**, 57 (1994); S. Bates and J. Dwyer, *J. Phys. Chem.* **97**, 5897 (1993); K. J. Farnworth and P. J. O'Malley, *J. Phys. Chem.* **100**, 1814 (1996).
17. C. Lee, W. Yang, and R. G. Parr, *Phys. Rev. B* **37**, 785 (1988).
18. M. J. Frisch, J. A. Pople, and J. S. Binkley, *J. Chem. Phys.* **80**, 3265 (1984), and references therein.
19. H. B. Schlegel, *J. Comp. Chem.* **3**, 214 (1982).
20. Gamess, Ver. April 1997, M. W. Schmidt, K. K. Baldridge, J. A. Boatz, S. T. Elbert, M. S. Gordon, J. H. Jensen, S. Koseki, N. Matsunaga, K. A. Nguyen, S. J. Su, T. L. Windus, M. Dupuis, J. A. Montgomery, *J. Comp. Chem.* **14**, 1347 (1993).
21. G. Schaftenaar, CAOS/CAMM Center, University of Nijmegen, The Netherlands, <http://www.caos.kun.nl/staff/schaft.html>.

Singlet-Triplet Splitting and the Activation of C—H Bond for (η^5 -C₅H₅)M(CO) Isoelectronic Fragments: A Theoretical Study

MING-DER SU, SAN-YAN CHU

Department of Chemistry, National Tsing Hua University, Hsinchu 30043, Taiwan, Republic of China

Received 18 March 1998; accepted 17 August 1998

ABSTRACT: A density functional study was used to investigate potential energy surfaces of the oxidative addition reaction CpM(CO) + CH₄ → CpM(CO)(H)(CH₃) (M = Ru⁺, Os⁺, Rh, Ir, Pd⁺, and Pt⁺). A qualitative model which is based on the theory of Pross and Shaik was applied to develop an explanation for the barrier heights. As a result, our theoretical findings suggest that the singlet-triplet splitting ($\Delta E_{st} = E_{triplet} - E_{singlet}$) of the CpM(CO) species can be a guide to predict its reaction activity and enthalpy for oxidative additions. A better linear correlation was found between the latter two quantities. Considering the nature of the metal center, the following conclusions therefore emerged: For the 16-electron CpM(CO) system, a heavier transition-metal center (i.e., the third-row) will lead to a smaller ΔE_{st} and, in turn, will facilitate the oxidative addition reactions to alkane C—H bonds. In contrast, a lighter transition-metal center (i.e., the second row) will result in a larger ΔE_{st} and then tend to undergo the reductive elimination reactions of the C—H bond-forming. The results obtained are in good agreement with the available experimental results and allow a number of predictions to be made. © 1998 John Wiley & Sons, Inc. Int J Quant Chem 70: 961–971, 1998

Introduction

In 1982, Janowicz and Bergman reported the first well-characterized example of a simple oxidative addition of an unactivated alkane to a

Correspondence to: S.-Y. Chu.

Contract grant sponsor: National Science Council of Taiwan.

homogeneous metal complex using a permethylcyclopentadienyl iridium complex. This observation generated tremendous excitement in academic and industrial communities, as it led to the employment of alkanes in homogeneous organometallic reactions [1–3]. Although several theoretical studies have confirmed the low activation barrier in the case of CpM(CO) (Cp = η^5 -C₅H₅; M = Rh, Ir) [4], we believe that a somewhat different ap-

proach and some new aspects emphasized here may supplement their results. In addition, no previous calculational work has to our knowledge been published on the dependence in the reaction on the barrier height as a function of the nature of the transition-metal center. In the present study, we therefore chose the 16-electron CpM(CO) ($M = \text{Ru}^-, \text{Os}^-, \text{Rh}, \text{Ir}, \text{Pd}^+$, and Pt^+) complexes as models to reveal their mechanisms and the reactivities of the oxidative addition to the C—H bond of CH_4 .

Our aim was to explain the trend of the reactivities in numerous variations in the central metal atoms and to bring out the determined factor that controls the activation barrier for the 16-electron CpM(CO) reactions. It will be shown that the singlet–triplet gap of the 16-electron CpM(CO) complex correlates nicely with its reaction activity and thus can be a guide to predict its reactivity for oxidative addition reactions.

Origin of the Barrier and Reaction Enthalpy for Oxidative Addition of CpM(CO)

To highlight the questions which formed the basis for this study, it is perhaps worthwhile to review briefly the electronic structure of the CpML fragment. A general outline of the valence molecular orbitals (MOs) in CpML , which are explicitly shown in Figure 1, was given previously [5]. They are identified as $1a'$, $1a''$, $2a'$, $2a''$, and $3a'$ orbitals under C_s symmetry. Basically, the former three orbitals ($1a'$, $1a''$, and $2a'$) have more or less bonding interactions between the central metal M and the ancillary ligand L , so that they all lie in lower energy. At highest energy are the two metal-based orbitals, $2a''$ and $3a'$, composed primarily of d_{xz} and d_{yz} orbitals, respectively. Note that it is the two frontier levels, $2a''$ and $3a'$, that allow one to view 16-electron CpML as organometallic analogs of CH_2 [6]. Accordingly, when the CpML complex and methane interact with each other, the main interaction is between the HOMO ($2a''$) of the former and the low vacant σ_{CH}^* of the latter, yielding an important back-bonding electron transfer. Likewise, the interaction between the occupied σ_{CH} orbital of methane and the high LUMO ($3a'$) of the CpML group is strong as well.

Before proceeding further, we shall use a simple valence-bond model as illustrated in Figure 2 to

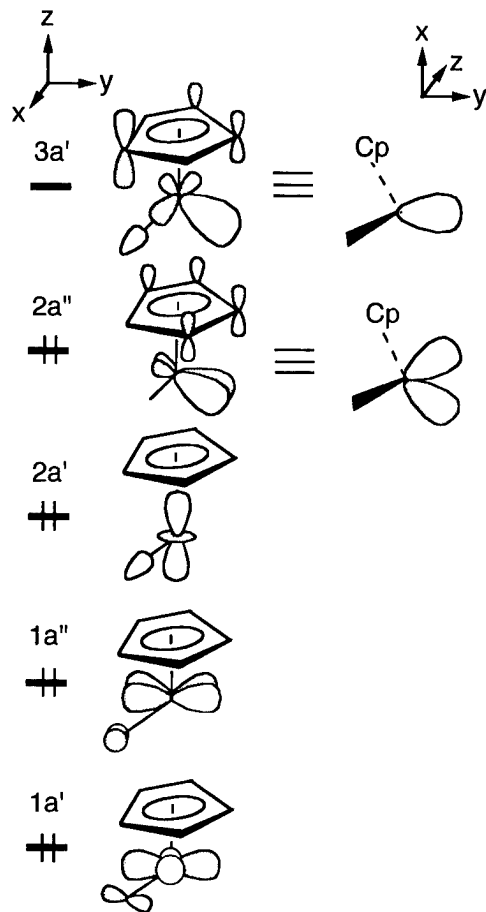


FIGURE 1. The valence molecular orbital correlation of the 16-electron CpML complex.

develop an explanation for the activation of alkane by CpML . According to Su's study [7] based upon the configuration mixing (CM) model described by Pross and Shaik [8], it was suggested that the singlet–triplet gap of carbene plays a crucial role in insertion reactions, that is, the relative stabilities of the lowest singlet and triplet states are, in turn, a sensitive function of the barrier height for carbonic reactivity. Since, as mentioned above, 16-electron CpML is isolobal to CH_2 : [6], one may envision that those predictions for carbonic reactivity should also apply to the 16-electron CpML systems. We therefore take the oxidative addition reaction $\text{CpML} + \text{CH}_4$ as an example by using the CM model as shown in Figure 2 to understand the origin of the barrier height and bonding nature of the CpML species.

Basically, the oxidative addition reaction may exist in a number of predetermined states, each of which may be approximated by the appropriate

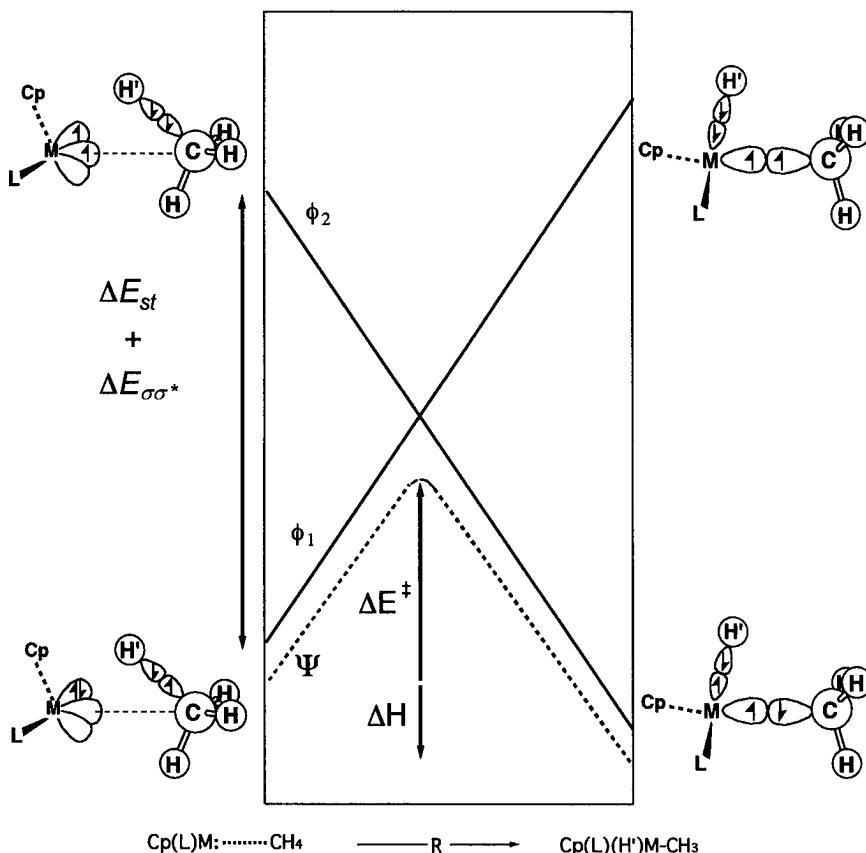


FIGURE 2. Energy diagram for an oxidative addition reaction showing the formation of a state curve (Ψ) by mixing two configurations: the reactant configuration (ϕ_1) and the product configuration (ϕ_2). It can be seen that both the activation energy (ΔE^\ddagger) and reaction enthalpy (ΔH) is linear with respect to ΔE_{st} ($= E_{triplet} - E_{singlet}$ for the 16-electron CpML) and $\Delta E_{\sigma\sigma^*}$ ($= E_{triplet} - E_{singlet}$ for CH_4). See the text.

molecular orbital configuration. However, as shown in Figure 2, there are only two predominant configurations that contribute considerably to the total wave function Ψ and, in turn, that affect the shape of the singlet surface. One is the reactant ground-state configuration ϕ_1 that ends up as an excited configuration in the product region. The other is the excited configuration of the reactants, ϕ_2 , that correlates with the ground state of the products. In consequence, the reaction complex at any point on the reaction profile can be described by Ψ , a linear combination of ϕ_1 and ϕ_2 , and the character of the transition state will reflect the extent of mixing between ϕ_1 and ϕ_2 in the region of the avoided crossing. It is notable that the product configuration (ϕ_2) is doubly excited with respect to the reactant configuration (ϕ_1), forms an overall singlet state, and allows both M—H and M—C bond formation and simultaneous C—H' bond breaking. Indeed, from the valence-bond

point of view (right side in Fig. 2), the bonding in the product can be recognized as bonds formed between a triplet CpML and two doublet radicals (overall singlet), a methyl radical, and a hydrogen atom. This is much in the same way as the bonding in the water molecule can be viewed: as bonds formed between a triplet oxygen atom and two doublet hydrogen atoms. Consequently, avoiding crossing of these two configurations (ϕ_1 and ϕ_2) leads to the simplest description of the ground-state energy profiles for the oxidative addition reactions of 16-electron CpML complexes.

As demonstrated in Figure 2, it is apparent that the barrier height (ΔE^\ddagger), as well as the reaction enthalpy (ΔH), may be expressed in terms of the initial energy gap between the reactant and product configurations. In other words, the reactivity of such oxidative additions will be governed by the singlet-triplet excitation energies for each of the reactants, that is, ΔE_{st} ($= E_{triplet} - E_{singlet}$ for

CpML) and $\Delta E_{\sigma\sigma^*}$ ($= E_{triplet} - E_{singlet}$ for CH_4). Accordingly, if $\Delta E_{\sigma\sigma^*}$ is a constant, then a smaller value of ΔE_{st} leads to (1) reduction of the reaction barrier since the intended crossing of ϕ_1 and ϕ_2 is lower in energy, and (2) production of a larger exothermicity since the energy of the product is now lower than that of the reactant. In short, the smaller the ΔE_{st} of CpML is, the lower the barrier height and the larger the exothermicity and, in turn, the faster the oxidative addition reaction. Note that the predictions from the CM model are basically in accordance with Hammond's postulate [9]. We shall see the calculational results supporting these predictions below.

Methodology

All geometries were fully optimized by employing the density functional theory (DFT) without imposing any symmetry constraints. For DFT calculations, the hybrid gradient-corrected exchange functional proposed by Becke [10a,b] was combined with the gradient-corrected correlation functional of Lee, Yang, and Parr [10c]. Henceforth, we will denote this functional as B3LYP, which has been shown to be quite reliable both in geometry and in energies for semiquantitative discussions [11].

Effective core potentials (ECPs) were used to represent the 28 innermost electrons of the ruthenium, rhodium, and palladium (up to the 3d shell) [12]. Likewise, ECPs were used to represent the 60 innermost electrons of the osmium, iridium, and platinum (up to the 4f shell) atoms [12]. For these atoms, the basis set was that associated with the pseudopotential [12], with a standard LANL2DZ contraction [13]. For hydrogen, carbon, and oxygen atoms, the double-zeta basis of Dunning-Huzinaga was used [14]. Hence, the B3LYP calculation is denoted by B3LYP/LANL2DZ.

Vibrational frequencies at stationary points were calculated at the B3LYP/LANL2DZ level of theory to identify them as minima (zero imaginary frequencies) or transition states (one imaginary frequency). All calculations were performed using the GAUSSIAN94 package [13].

Results and Discussion

The optimized geometries for the reactants, precursor complexes, transition states, and products

for the various metals are given in Figures 3–5, respectively. Also, the total and relative B3LYP energies are reported in Table I. The potential energy profiles based on the data in Table I are therefore summarized in Figure 6. Four interesting results can be drawn from this figure:

First, it is readily seen that the oxidative addition reactions of the Ru, Os, and Ir systems are much more favorable than are those of Rh, Pd, and Pt kinetically and thermodynamically. For instance, the activation barriers from the precursor complex to the transition state at the B3LYP level of theory increase in the order Os(0.621 kcal/mol) < Ir(1.91 kcal/mol) < Ru(3.24 kcal/mol) < Rh(12.9 kcal/mol) < Pt(14.5 kcal/mol) < Pd(29.4 kcal/mol). Likewise, the reaction enthalpies decrease in the order Pd(19.3 kcal/mol) > Rh(-4.24 kcal/mol) > Pt(-6.30 kcal/mol) > Ru(-27.2 kcal/mol) > Ir(-31.8 kcal/mol) > Os(-49.1 kcal/mol). This theoretical finding is in accordance with the conventional concept mentioned by Bergman et al. [1b,c] and Jones and Feher [2j].

Second, as seen in Figure 6, it is obvious that the energy of the transition state for the Rh, Pd, and Pt cases is apparently higher than that of the reactants, while in the other cases, the energy of the transition state is below the energy of the reactants. This result strongly implies that the CpM(CO) (M = Ru, Os, and Ir) intermediates should readily overcome the intrinsic barrier and then undergo insertion into the saturated C—H bonds in a concerted fashion, whereas for Pd, Pt, and Rh homologs, the process might be significantly more difficult.

Third, considering the reverse process, that is, the reductive elimination from the alkyl hydride for the CpM(CO) species (right to left in Fig. 1), it is apparent that the barriers to reductive elimination for Ru, Os, and Ir systems are much higher in energy than those for Rh, Pd, and Pt analogs. For example, the barrier energies increase in the order Pd(0.141 kcal/mol) < Pt(9.85 kcal/mol) < Rh(10.8 kcal/mol) < Ru(23.5 kcal/mol) < Ir(24.1 kcal/mol) < Os(39.6 kcal/mol).

Fourth, our model calculations also suggest that the oxidative additions of the third-row transition metals would be preferable to those of the second-row transition metals, since it is demonstrated not only that the former is thermodynamically favorable but also that the kinetic barriers associated with them are typically small. For instance, as seen in Figure 6 and Table I, the facile oxidative addi-

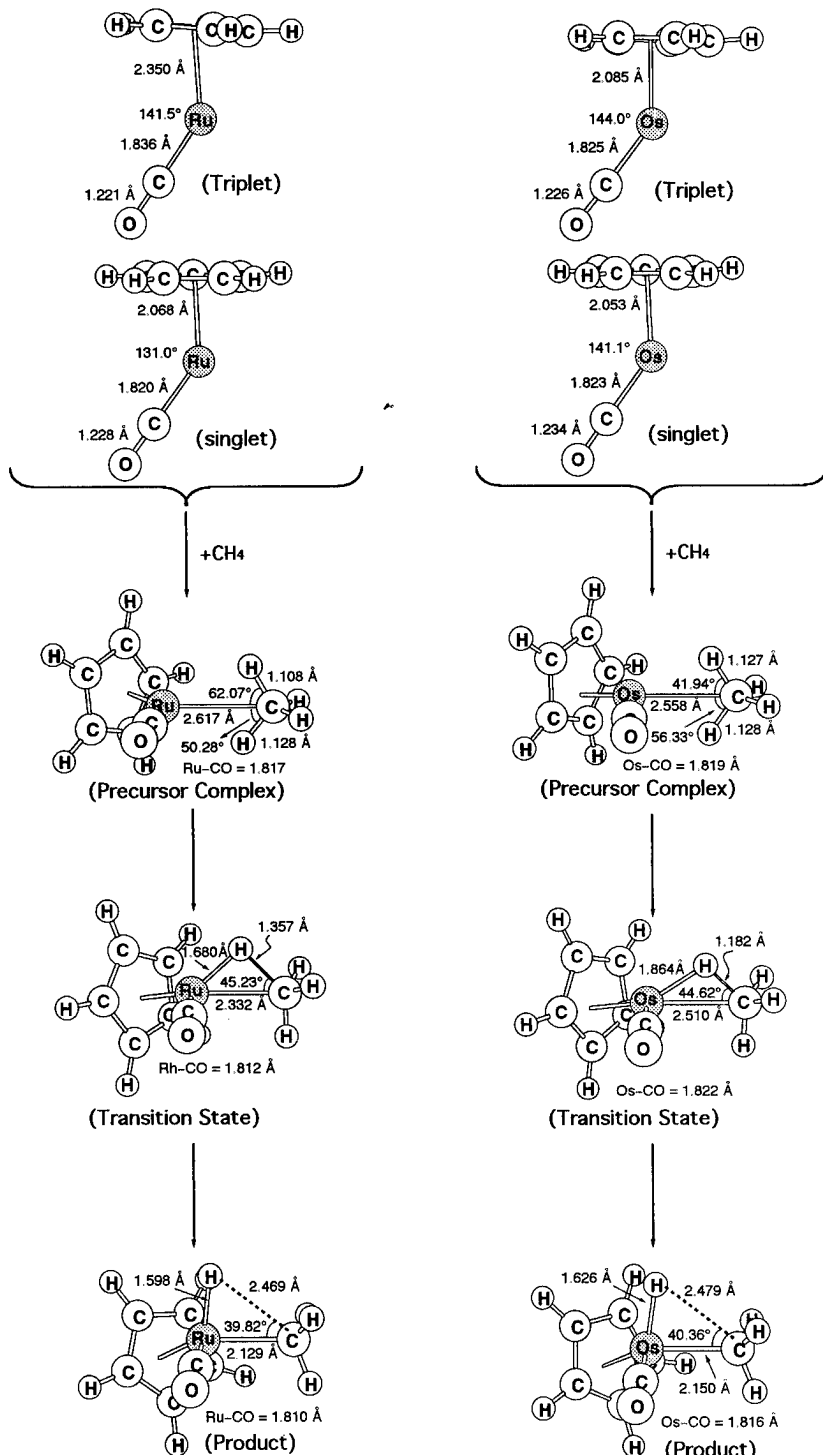


FIGURE 3. Optimized structures at the B3LYP / LANL2DZ level for the $[\text{CpRu}(\text{CO})]^-$ and $\{\text{CpOs}(\text{CO})\}^-$ systems.

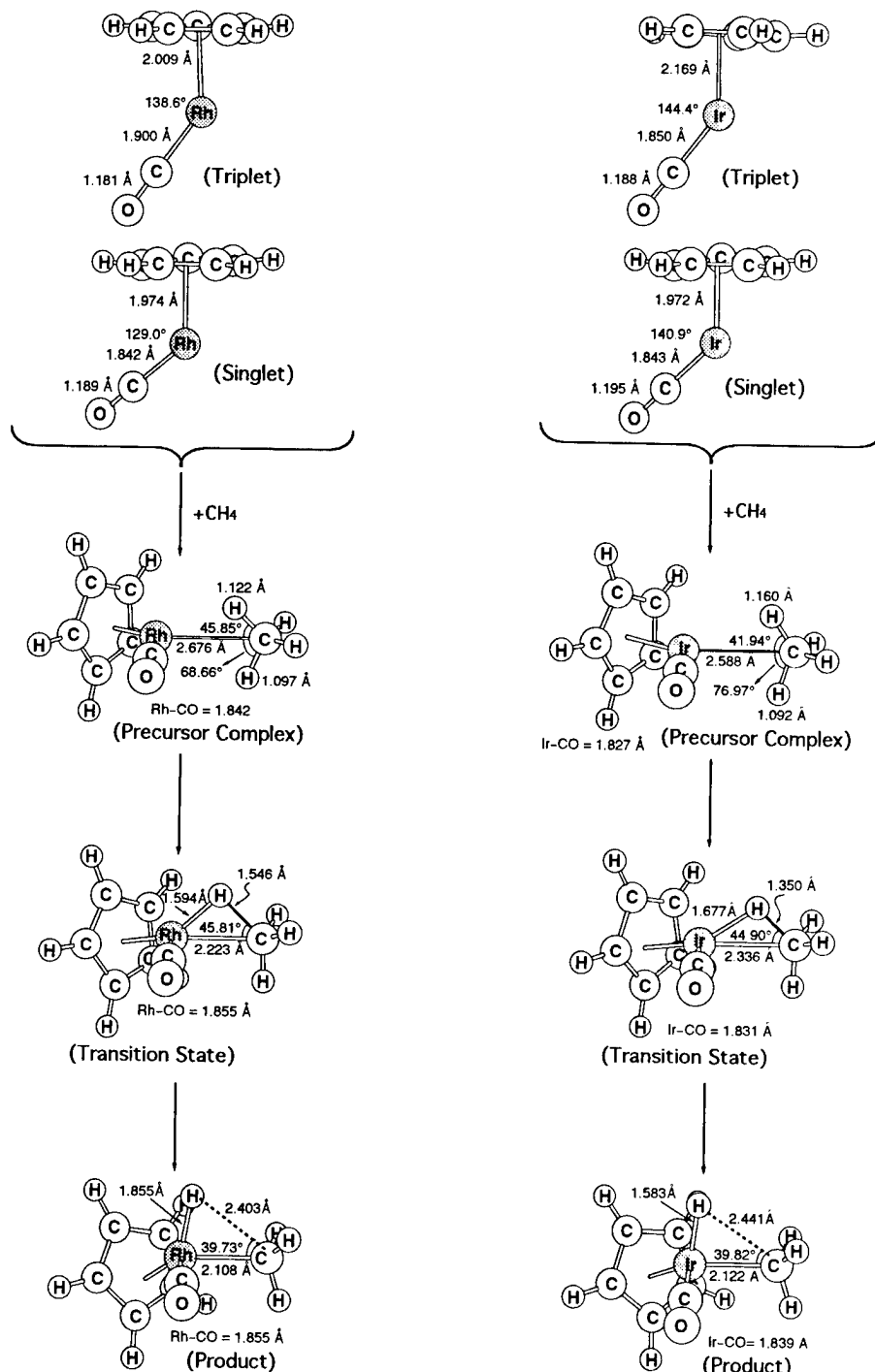


FIGURE 4. Optimized structures at the B3LYP / LANL2DZ level for the $[CpRh(CO)]$ and $\{CpIr(CO)\}$ systems.

SINGLET-TRIPLET SPLITTING FOR ACTIVATION OF C—H BOND

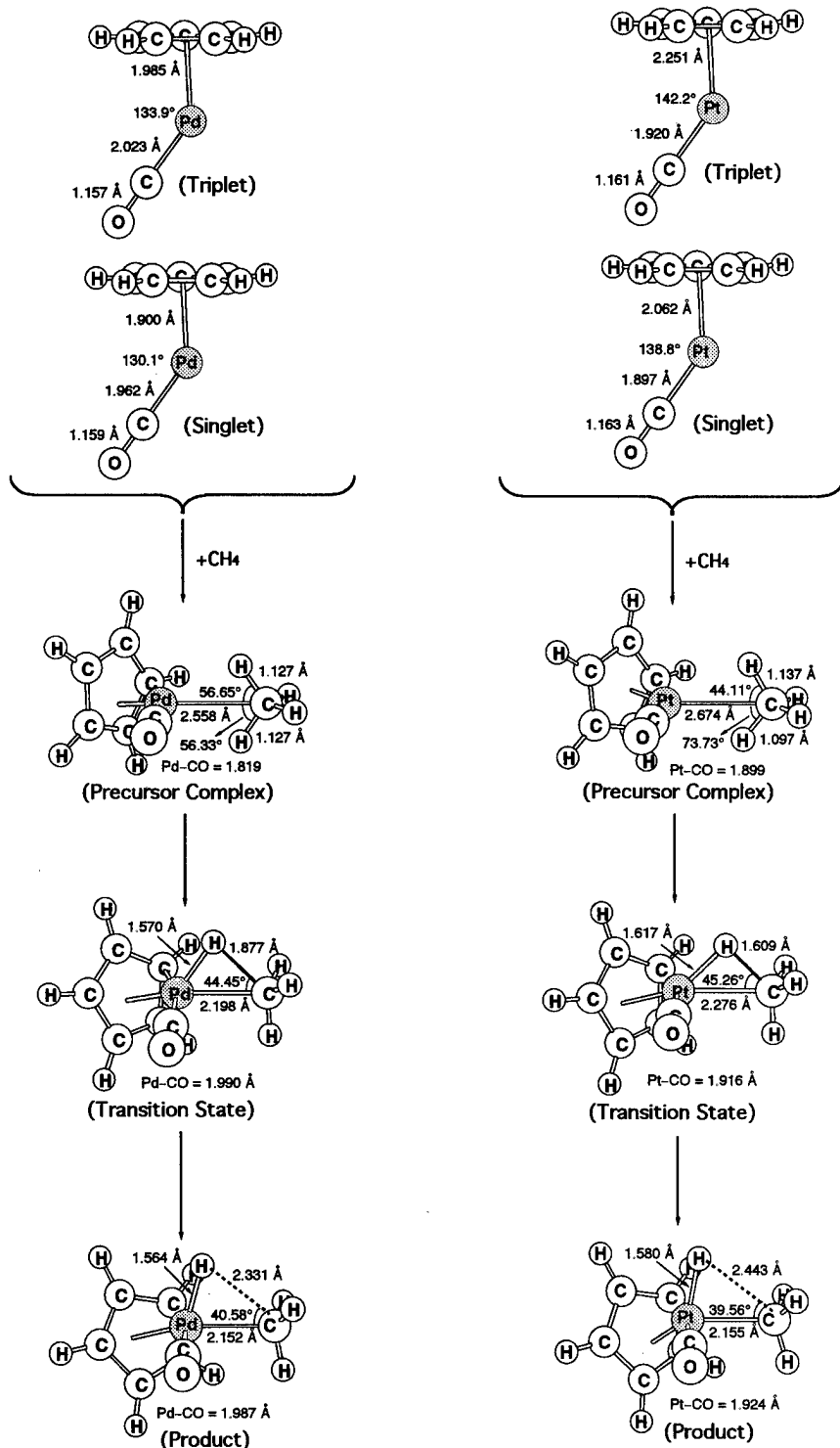


FIGURE 5. Optimized structures at the B3LYP / LANL2DZ level for the $[\text{CpPd}(\text{CO})]^+$ and $\{\text{CpPt}(\text{CO})\}^+$ systems.

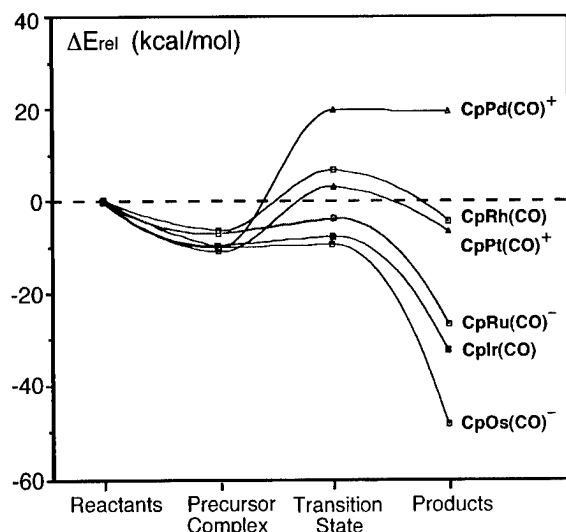


FIGURE 6. The potential energy profile of the reaction of $\text{CpM}(\text{CO})$ ($\text{M} = \text{Ru}^-$, Os^- , Rh , Ir , Pd^+ , and Pt^+) with CH_4 . All the energies were calculated at the B3LYP/LANL2DZ level.

tion is in the order $\text{Os} > \text{Ru}, \text{Ir} > \text{Rh}$, and $\text{Pt} > \text{Pd}$. Additionally, these trends are consistent with the electronegativity of the central metal, that is, the electronegativity of the third-row metal is larger than that of the second-row element (such as Ru (1.42) < Os (1.52), Rh (1.45) < Ir (1.55) and Pd (1.35) < Pt (1.44) [15]). Furthermore, the reductive elimination of the second-row metals is more favorable than that of the third-row homologs. To the best of our knowledge, the experimentally supporting evidence comes from the fact that, in comparison of oxidative additions of the iridium and rhodium intermediates to alkane C—H bonds, the products formed in the latter case are much less stable and undergo reductive elimination at -20°C [1b,c].

Furthermore, as mentioned earlier, a strong correlation between ΔE_{st} and the activation energy as well as the reaction enthalpy is expected [16]. For instance, the B3LYP calculations suggest that ΔE_{st} increases in the order $\text{Os}(-14.4 \text{ kcal/mol}) < \text{Ru}(-11.7 \text{ kcal/mol}) < \text{Ir}(-3.58 \text{ kcal/mol}) < \text{Rh}(0.112 \text{ kcal/mol}) < \text{Pd}(1.03 \text{ kcal/mol}) < \text{Pt}(3.26 \text{ kcal/mol})$, while the barrier height also increases

TABLE I
Energies for singlet and triplet CpML fragments and for the process $\text{CH}_4 + \text{CpML} \rightarrow$ precursor complex \rightarrow transition state \rightarrow product.^a

System	Singlet (Hartrees)	Triplet ^b (Hartrees)	Reactant ^c (Hartrees)	Precursor complex ^d (Hartrees)	Transition state ^e (Hartrees)	Product ^f (Hartrees)
$\text{CpRu}(\text{CO})^-$	-400.71041	-400.72904 (-11.7)	-441.22489	-441.23584 (-6.87)	-441.23067 (+3.24)	-441.26818 (-27.2)
$\text{CpOs}(\text{CO})^-$	-397.85012	-397.87309 (-14.4)	-438.36459	-438.38068 (-10.1)	-438.37969 (+0.62)	-438.44286 (-49.1)
$\text{CpRh}(\text{CO})$	-416.31084	-416.31066 (+0.11)	-456.83208	-456.83547 (-6.37)	-456.81495 (+12.9)	-456.83208 (-4.24)
$\text{CpIr}(\text{CO})$	-411.48311	-411.48882 (-3.58)	-451.99759	-452.01296 (-9.64)	-452.00991 (+1.91)	-452.04833 (-31.8)
$\text{CpPd}(\text{CO})^+$	-433.26482	-433.26318 (+1.03)	-473.77930	-473.79516 (-9.96)	-473.74836 (+29.4)	-473.74859 (+19.3)
$\text{CpPt}(\text{CO})^+$	-425.67850	-425.67330 (+3.26)	-466.19298	-466.21041 (-10.9)	-466.18733 (+14.5)	-466.20302 (-6.30)

^a At the B3LYP / LANL2DZ level.

^b The value in the parentheses is ΔE_{st} ($= E_{triplet} - E_{singlet}$, units in kcal / mol).

^c The B3LYP / LANL2DZ energy of CH_4 is -40.51448 Hartrees.

^d The values in the parentheses represent the stabilization energy of the precursor complex (ΔE_{int} , units in kcal / mol), which is relative to the corresponding reactant.

^e The values in the parentheses represent the activation energy (ΔE_{act} , units in kcal / mol), which is relative to the corresponding precursor complex.

^f The values in the parentheses represent the reaction enthalpy (ΔH , units in kcal / mol), which is relative to the corresponding reactants.

in the order Os(−9.47 kcal/mol) < Ir(−7.73 kcal/mol) < Ru(−3.63 kcal/mol) < Pt (3.55 kcal/mol) < Rh(6.51 kcal/mol) < Pd(19.4 kcal/mol). Again, the enthalpy follows the same trend as in the ΔE_{st} : Os(−49.1 kcal/mol) < Ir(−31.8 kcal/mol) < Ru(−27.2 kcal/mol) < Pt(−6.30 kcal/mol) < Rh(−4.24 kcal/mol) < Pd(19.3 kcal/mol). Additionally, as seen in Figure 7, the DFT calculations indicate that there exists a linear correlation between the activation energy and the reaction enthalpy, namely, our theoretical results confirm the Hammond postulate considerations as discussed earlier. This investigation makes it quite obvious that in order to find a good model for the facile oxidative addition of 16-electron CpML to C—H bonds an understanding of the singlet–triplet gap ΔE_{st} of the coordinatively unsaturated CpML is crucial, namely, oxidative additions in which 16-electron CpML complexes have large singlet–triplet gaps will have larger barriers as well as smaller exothermicity than will reactions whose corresponding complexes have small singlet–triplet gaps. *The smaller the ΔE_{st} of 16-electron CpML is, the lower the barrier height and, in turn, the faster the oxidative addition reaction is, the larger the exothermicity.*

Finally, one may wonder why the oxidative addition of a third-row metal is preferable to that of a second-row one. The reason for this can be traced to the singlet–triplet energy gap (ΔE_{st}) of

CpML. As analyzed above, the smaller the ΔE_{st} of CpML (if $\Delta E_{\sigma\sigma^*}$ is a constant), the lower the barrier height and the larger the exothermicity, and, in turn, the faster the oxidative addition reaction. Furthermore, as studied previously [16], the Os atoms have a quintet d^6s^2 ground state with a relatively high excitation energy of 32 kcal/mol to the triplet d^7s^1 state. On the other hand, the Ru atom has a quintet d^7s^1 ground state with a low excitation energy of 19 kcal/mol to the triplet d^7s^1 state. Likewise, the Ir atom has a quartet d^7s^2 ground state with a high excitation energy to the doublet d^9 state of 61 kcal/mol. For the Rh atom, the ground state is quartet d^8s^1 but with a relatively low excitation energy to the doublet d^9 state of 7.8 kcal/mol. Again, the ground state of the Pt atom is triplet s^1d^9 (with the d^{10} state lying 21.9 kcal/mol), while that of the Pd atom is singlet d^{10} (with the s^1d^9 state lying 11.0 kcal/mol). These results strongly imply that the third-row metals would prefer to remain in high-spin states, whereas the second-row metals favor low-spin states. It is reasonable to expect that the promotion energy from the singlet state to the triplet state should be smaller for the former than for the latter. Our B3LYP/LANL2DZ results as shown earlier are consistent with the above prediction. For this reason, insertion into a C—H bond is more easier and more exothermic for the third-row system than for its second-row counterpart.

In summary, our study has shown that the singlet–triplet gap ΔE_{st} ($= E_{triplet} - E_{singlet}$) based on the CM model can provide a useful basis for understanding and rationalizing the relative magnitude of the activation barriers as well as reaction enthalpies for the activation of alkane by CpML. With the above analyses in hand, we are confident in predicting that *for the 16-electron CpM(CO) system a more electronegative as well as a heavier transition-metal center (i.e., the third row) will lead to a smaller ΔE_{st} and, in turn, will facilitate the oxidative addition reactions to alkane C—H bonds. In contrast, a less electronegative and a lighter transition-metal center (i.e., the second row) will result in a larger ΔE_{st} and then tend to undergo the reductive elimination reactions of the C—H bond-forming.* Despite the fact that the estimated magnitude of the barrier and the predicted geometry of the transition state for such reactions appear to be dependent on the calculational level applied, our qualitative predictions are in accord with the calculational results presented here as well as the available experimen-

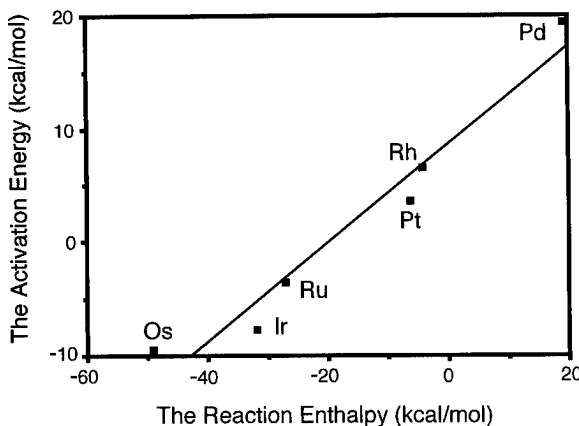


FIGURE 7. The reaction enthalpy (x) versus the activation energy (y) for the oxidative addition of methane to $\text{CpM}(\text{CO})$ ($\text{M} = \text{Ru}^-, \text{Os}^-, \text{Rh}, \text{Ir}, \text{Pd}^+, \text{and Pt}^+$). All were calculated at the B3LYP / LANL2DZ level (see Table I). The linear regression equation is $y = 8.62x + 0.433$, and the correlation coefficient $R = 0.951$.

tal observations.*[†] It is hoped that our study will stimulate further research into the subject.

ACKNOWLEDGMENTS

We are very thankful to the National Center for High-Performance Computing of Taiwan and the Computing Center at Tsing Hua University for generous amounts of computing time. We also thank the National Science Council of Taiwan for financial support. We are also grateful to a referee for critical comments of the manuscript.

References

- For reviews, see (a) G. W. Parshall, *Acc. Chem. Res.* **8**, 113 (1975). (b) R. G. Bergman, *Science* **223**, 902 (1984). (c) A. H. Janowicz, R. A. Periana, J. M. Buchanan, C. A. Kovac, J. M. Struker, M. J. Wax, R. G. Bergman, *Pure Appl. Chem.* **56**, 13 (1984). (d) C. L. Hill, *Activation and Functionalization of Alkanes*, (Wiley, New York, 1989). (e) J. Halpern, *Inorg. Chim. Acta* **100**, 41 (1985). (f) M. Ephritikhine, *New J. Chem.* **10**, 9 (1986). (g) W. D. Jones, F. Feher, *J. Acc. Chem. Res.* **22**, 91 (1989). (h) A. D. Ryabov, *Chem. Rev.* **90**, 403 (1990). (i) J. A. Davies, P. L. Watson, J. F. Liebman, A. Greenberg, *Selective Hydrocarbon Activation, Principles and Progress*, (VCH, New York, 1990). (j) R. G. Bergman, *J. Organomet. Chem.* **400**, 273 (1990). (k) R. G. Bergman, *Adv. Chem. Ser.* **230**, 211 (1992). (l) E. P. Wasserman, C. B. Moore, R. G. Bergman, *Science* **255**, 315 (1992). (m) R. H. Crabtree, *Angew. Chem. Int. Ed. Engl.* **32**, 789 (1993). (n) D. Schroder, H. Schwarz, *Ibid.* **34**, 1937 (1995). (o) A. J. Lees, A. A. Purwoko, *Coord. Chem. Rev.* **132**, 155 (1994). (p) B. A. Amdtson, R. G. Bergman, T. A. Mobley, T. H. Peterson, *Acc. Chem. Res.* **28**, 154 (1995).
- (a) A. J. Oliver, W. A. G. Graham, *Inorg. Chem.* **10**, 1 (1971). (b) A. H. Janowicz, R. G. Bergman, *J. Am. Chem. Soc.* **104**, 352 (1982). (c) J. K. Hoyano, W. A. G. Graham, *Ibid.* **104**, 3723 (1982). (d) W. D. Jones, F. Feher, *Ibid.* **104**, 4240 (1982). (e) A. H. Janowicz, R. G. Bergman, *Ibid.* **105**, 3929 (1983). (f) J. K. Hoyano, A. D. McMaster, W. A. Graham, *Ibid.* **105**, 7190 (1983). (g) W. D. Jones, F. J. Feher, *Organometallics* **2**, 562 (1983). (h) *Ibid.* **2**, 686 (1983). (i) R. A. Periana, R. G. Bergman, *J. Am. Chem. Soc.* **106**, 7272 (1984). (j) W. D. Jones, R. J. Feher, *Ibid.* **106**, 1650 (1984). (k) A. J. Rest, I. Whitwell, W. A. G. Graham, J. K. Hoyano, A. D. McMaster, *J. Chem. Soc. Chem. Commun.* **624** (1984). (l) M. J. Wax, J. M. Stryker, J. M. Buchanan, A. K. Caroline, R. G. Bergman, *J. Am. Chem. Soc.* **106**, 1121 (1984). (m) R. A. Perlana, R. G. Bergman, *Organometallics* **3**, 508 (1984). (n) W. D. Jones, F. J. Feher, *Inorg. Chem.* **23**, 2376 (1984). (o) P. O. Stoutland, R. G. Bergman, *Ibid.* **107**, 4581 (1985). (p) W. D. McGhee, R. G. Bergman, *Ibid.* **107**, 3388 (1985). (q) T. M. Gilbert, R. G. Bergman, *Ibid.* **107**, 3502 (1985). (r) L. J. Newman, R. G. Bergman, *Ibid.* **107**, 5314 (1985). (s) W. D. Jones, F. J. Feher, *Ibid.* **107**, 620 (1985). (t) J. M. Buchanan, J. M. Stryker, R. G. Bergman, *J. Am. Chem. Soc.* **108**, 1537 (1986). (u) W. D. Jones, F. J. Feher, *Ibid.* **108**, 4814 (1986). (v) R. A. Periana, R. G. Bergman, *Ibid.* **108**, 7332 (1986). (w) *Ibid.* **108**, 7346 (1986). (x) W. D. McGhee, R. G. Bergman, *Ibid.* **108**, 5621 (1986). (y) D. M. Haddleton, *J. Organomet. Chem.* **311**, C21 (1986).
- (a) S. P. Nolan, C. D. Hoff, P. O. Stoutland, L. J. Newman, J. M. Buchanan, R. G. Bergman, G. K. Yang, K. S. Peters, *J. Am. Chem. Soc.* **109**, 3143 (1987). (b) D. E. Marx, A. J. Lees, *Inorg. Chem.* **27**, 1121 (1988). (c) P. O. Stoutland, R. G. Bergman, S. P. Nolan, C. D. Hoff, *Polyhedron* **7**, 1429 (1988). (d) P. E. Bloyce, A. J. Rest, I. Whitwell, W. A. G. Graham, R. Holmes-Smith, *Chem. Commun.* **846** (1988). (e) D. M. Haddleton, A. McCamley, R. N. Perutz, *J. Am. Chem. Soc.* **110**, 1810 (1988). (f) M. B. Sponsler, B. H. Weiller, P. O. Stoutland, R. G. Bergman, *Ibid.* **111**, 6841 (1989). (g) S. T. Belt, F.-W. Grevels, W. E. Klotzbucher, A. McCamley, R. N. Perutz, *Ibid.* **111**, 8373 (1989). (h) B. H. Weiller, E. P. Wasserman, R. G. Bergman, C. B. Moore, G. C. Pimentel, *Ibid.* **111**, 8288 (1989). (i) T. W. Bell, D. M. Haddleton, A. McCamley, M. G. Partridge, R. N. Perutz, H. Willner, *Ibid.* **112**, 9212 (1990). (j) C. Barrientos, C. K. Ghosh, W. A. G. Graham, M. J. Thomas, *J. Organomet. Chem.* **394**, C31 (1990). (k) B. H. Weiller, E. P. Wasserman, C. B. Moore, R. G. Bergman, *Ibid.* **115**, 4326 (1993). (l) P. Burger, R. G. Bergman, *Ibid.* **115**, 10462 (1993). (m) R. H. Schultz, A. A. Bengali, M. J. Tauber, B. H. Weiller, E. P. Wasserman, K. R. Kyle, C. B. Moore, R. G. Bergman, *Ibid.* **116**, 7369 (1994). (n) A. A. Bengali, R. H. Schultz, C. B. Moore, R. G. Bergman, *Ibid.* **116**, 9585 (1994). (o) J. E. Veltheer, P. Burger, R. G. Bergman, *Ibid.* **117**, 12478 (1995). (p) A. D. Selmezy, W. D. Jones, R. Osman, R. N. Perutz, *Organometallics* **14**, 5685 (1995). (q) B. A. Arndtsem, R. G. Bergman, *J. Organomet. Chem.* **504**, 143 (1995). (r) S. E. Bromberg, T. Lian, R. G. Bergman, C. B. Harris, *J. Am. Chem. Soc.* **118**, 2069 (1996).
- For theoretical works, see (a) T. Ziegler, V. Tschinke, L. Fan, A. D. Becke, *J. Am. Chem. Soc.* **111**, 9177 (1989). (b) J. Song, M. B. Hall, *Organometallics* **12**, 3118 (1993). (c) D. G. Musaev, K. Morokuma, *Ibid.* **117**, 799 (1995). (d) P. E. M. Siegbahn, *Ibid.* **118**, 1487 (1996). (e) R. Jimenez-Catano, M. B. Hall, *Organometallics* **15**, 1889 (1996). (f) M. Couty, C. A. Bayse, R. Jimenez-Catano, M. B. Hall, *J. Phys. Chem.* **100**, 13976 (1996).
- P. Hoffmann, M. Padmanabhan, *Organometallics* **2**, 1273 (1983).
- R. Hoffmann, *Angew. Chem. Int. Ed. Engl.* **21**, 711 (1982).
- M.-D. Su, *Inorg. Chem.* **34**, 3829 (1995).

[†] Besides the nature of the transition metals, the ligand effect which can modulate the electron density at the reacting metal center will also play a dominant role in the activation of the C—H bonds of alkanes. See [18].

* Our DFT calculations suggest that the ground states of the $[CpRh(CO)]$, $[CpPd(CO)]^+$, and $[CpPt(CO)]^+$ fragments are singlets, whereas other complexes are triplets. This implies that a complex with the triplet ground state might insert into the saturated C—H bond via a diradical type of mechanism. Nevertheless, it is well established that whenever a reactant contains a heavy atom center which is not necessarily directly involved in the reaction, a strong spin-orbit coupling may be obtained. In other words, a triplet reactant, via the agency of the heavy atom, can provide a spin-inversion process for transferring to the singlet reactant and then undergoing the singlet reaction. See [17].

SINGLET-TRIPLET SPLITTING FOR ACTIVATION OF C—H BOND

8. (a) S. Shaik, H. B. Schlegel, S. Wolfe, *Theoretical Aspects of Physical Organic Chemistry*, (Wiley, New York, 1992). (b) A. Pross, *Theoretical and Physical Principles of Organic Reactivity*, (Wiley, New York, 1995).
9. G. S. Hammond, J. Am. Chem. Soc. **77**, 334 (1954).
10. (a) A. D. Becke, Phys. Rev. A **38**, 3098 (1988). (b) A. D. Becke, J. Chem. Phys. **98**, 5648 (1993). (c) C. Lee, W. Yang, R. G. Parr, Phys. Rev. B **37**, 785 (1988).
11. (a) P. J. Stevens, F. J. Devlin, C. F. Chabowski, M. J. Frisch, J. Phys. Chem. **98**, 11623 (1994). (b) A. Ricca, C. W. Bauschlicher, Theor. Chim. Acta. **92**, 123 (1995).
12. J. P. Hay, W. R. Wadt, J. Chem. Phys. **82**, 299 (1985).
13. M. J. Frisch, G. W. Trucks, H. B. Schlegel, P. M. W. Gill, B. G. Johnson, M. A. Robb, J. R. Cheeseman, T. Keith, G. A. Petersson, J. A. Montgomery, K. Raghavachari, M. A. Al-Laham, V. G. Zakrzewski, J. V. Ortiz, J. B. Foresman, J. Cioslowski, B. B. Stefanov, A. Nanayakkara, M. Challacombe, C. Y. Peng, P. Y. Ayala, W. Chen, M. W. Wong, J. L. Andres, E. S. Replogle, R. Gomperts, R. L. Martin, D. J. Fox, J. S. Binkley, D. J. Defrees, J. Baker, J. P. Stewart, M. Head-Gordon, C. Gonzalez, J. A. Pople, *Gaussian 94, Revision B.2*, (Gaussian, Pittsburgh, PA, 1995).
14. T. H. Dunning, P. J. Hay, In *Modern Theoretical Chemistry* H. F. Schaefer, Ed. (Plenum, New York, 1976); pp 1–28.
15. (a) A. L. Allred, E. G. Rochow, J. Inorg. Nucl. Chem. **5**, 264 (1958). (b) E. J. Little, Jr., M. M. Jones, J. Chem. Ed. **37**, 231 (1960).
16. (a) M.-D. Su, S.-Y. Chu, J. Am. Chem. Soc. **119**, 5373 (1997). (b) M.-D. Su, S.-Y. Chu, J. Am. Chem. Soc. **119**, 10178 (1997). (c) M.-D. Su, S.-Y. Chu, J. Phys. Chem. **101**, 6798 (1997). (d) M.-D. Su, S.-Y. Chu, Organometallics **16**, 1621 (1997). (e) M.-D. Su, S.-Y. Chu, Chem. Phys. Lett. **282**, 25 (1998). (f) M.-D. Su, S.-Y. Chu, Inorg. Chem. **37**, 3400, (1998).
17. M.-D. Su, Chem. Phys. **205**, 277 (1996), and references therein.
18. M.-D. Su, S.-Y. Chu, Organometallics, in press.

Structural and Electronic Properties of Silicon Nitride Materials

F. DE BRITO MOTA,^{1,2} J. F. JUSTO,¹ A. FAZZIO¹

¹*Instituto de Física da Universidade de São Paulo, CP 66318, CEP 05315-970 São Paulo—SP, Brazil*

²*Instituto de Física da UFBA, Campus Universitario de Ondina CEP 40210-340 Salvador—BA, Brazil*

Received 23 February 1998; revised 21 April 1998; accepted 30 April 1998

ABSTRACT: We developed an empirical potential for interactions between Si and N to describe silicon nitride systems using the Tersoff functional form. With this model, we explored the structural properties of amorphous silicon nitride through the Monte Carlo simulations and compared them to available experimental data. The empirical model provided a very good description of such properties for $a - \text{SiN}_x$ ($0 < x < 1.5$). Electronic structure of amorphous and point defects in crystalline silicon nitride were then studied using first-principles calculations. For such calculations, the configurations were created by the empirical model, with the relaxed structures used as input for the first-principles calculations. Atomic relaxation was later allowed in the first-principles calculations.

© 1998 John Wiley & Sons, Inc. *Int J Quant Chem* 70: 973–980, 1998

Introduction

Silicon nitride is a material of great technological interest due to its mechanical and electronic properties allowing a number of applications [1]. Due to its high melting temperature, low mechanical stress, chemical inertness, and strong resistance against thermal shock, it is suitable for high-temperature applications [2]. It has high dielectric constant, large electronic gap, and high

resistance against radiation. Due to these properties, silicon nitride has been widely used in micro-electronic devices as a gate dielectric in thin-film transistors and as a charge storage medium in nonvolatile memories. This wide range of applications led to intensive studies aiming to understand its microscopic properties. The electronic properties of amorphous silicon nitride have received special attention [3–5]. This is because applications as a gate dielectric in thin-film transistors or as a charge storage medium require the understanding of the properties of charge trapping centers in the material [6]. These centers, associated with Si and N dangling bonds, are related to gap levels which appear in the amorphous matrix.

Correspondence to: A. Fazzio.

Contract grant sponsors: Brazilian Agencies Capes and CNPq; FAPESP.

Methods involving electronic calculations have been successful in describing a number of microscopic properties of silicon nitride [7, 8], but computational cost hinders their use to systems larger than a few hundreds atoms. However, many important problems require thousands of atoms for a proper description. Since these problems are too expensive to be explored using such methods, empirical models have been alternatives in studying structural properties. These methods are computationally efficient and can handle systems involving thousands to millions of atoms. Two empirical models were developed [9, 10] for silicon nitride. However, their *transferability* to a wide range of silicon nitride compositions, such as low nitrogen content, was never tested. The problem is that those models lack reliability when describing the Si—Si interactions. The Tersoff potential [11–13], originally developed for pure silicon, has been successfully used and tested over the last few years [14]. In that sense, this functional form appears to be the best choice for an empirical potential to describe silicon nitride.

Here we introduce an empirical potential for Si—N interactions using the Tersoff functional. Using this empirical model to generate a relevant silicon nitride system, we study the electronic properties of point defects in crystalline β — Si_3N_4 and of amorphous SiN_x . The electronic properties are computed within the framework of density functional theory (DFT) using local density approximation (LDA). This study is organized as follow: In the following section we discuss the interatomic potential. In the third section we discuss the fitting strategy to find the set of parameters which best describes relevant properties of silicon nitride, and in the fourth section we use the empirical model to study structural properties of amorphous SiN_x system using Monte Carlo simulations. In the fifth section, we discuss electronic properties from ab initio calculations of amorphous silicon nitride and defects in silicon nitride. Finally, in the last section, we present final remarks.

Interatomic Potential

The Tersoff potential [11–13] is a bond-order potential composed of a two-body expansion which depends on the local environment. These bond-order models have been shown to describe reason-

ably well the chemical properties of bonding in covalent materials [15, 16].

The total potential energy E is given by the sum over all n atoms of the energy of site i , (E_i):

$$E = \sum_{i=1}^n E_i = \frac{1}{2} \sum_{i \neq j} V_{ij}, \quad (1)$$

where V_{ij} is the interaction energy between atoms i and j and is a combination of repulsive and attractive terms.

$$V_{ij} = f_c(r_{ij}) \{f_R(r_{ij}) + b_{ij}f_A(r_{ij})\}, \quad (2)$$

where r_{ij} is the distance between atoms i and j .

$$f_R(r_{ij}) = A_{ij} \exp(-\lambda_{ij}r_{ij}), \quad (3)$$

$$f_A(r_{ij}) = -B_{ij} \exp(-\mu_{ij}r_{ij}), \quad (4)$$

$$f_c(r_{ij}) = \begin{cases} 1, & \text{if } r_{ij} < R_{ij} \\ \frac{1}{2} + \frac{1}{2} \cos x_{ij}, & \text{if } R_{ij} < r_{ij} < S_{ij} \\ 0, & \text{if } r_{ij} > S_{ij} \end{cases} \quad (5)$$

where $x_{ij} = \pi(r_{ij} - R_{ij})/(S_{ij} - R_{ij})$.

The parameter b_{ij} defines the strength of the attractive interaction as function of local environment.

$$b_{ij} = \chi_{ij}(1 + \beta_i^n \zeta_{ij}^{n_i})^{-1/2 n_i}, \quad (6)$$

$$\zeta_{ij} = \sum_{k \neq i, j} f_c(r_{ik}) g(\theta_{ijk}), \quad (7)$$

$$g(\theta_{ijk}) = 1 + \frac{c_i^2}{d_i^2} - \frac{c_i^2}{d_i^2 + (h_i - \cos \theta_{ijk})^2}, \quad (8)$$

where θ_{ijk} is the angle between ij and ik bonds.

All the parameters take into account the atom type to describe the interaction. For atoms i and j of different types, the parameters are given by:

$$A_{ij} = (A_i \times A_j)^{1/2}, \quad (9)$$

$$B_{ij} = (B_i \times B_j)^{1/2}, \quad (10)$$

$$\lambda_{ij} = \frac{\lambda_i + \lambda_j}{2}, \quad (11)$$

$$\mu_{ij} = \frac{\mu_i + \mu_j}{2}, \quad (12)$$

$$R_{ij} = (R_i \times R_j)^{1/2}, \quad (13)$$

$$S_{ij} = (S_i \times S_j)^{1/2}, \quad (14)$$

where the parameters with single index describe the interaction between atoms of the same type.

The parameter χ takes into account the strengthening or weakening of heteropolar bonds. For interactions between atoms of the same type, this term is normally taken equal to 1. For a bond involving atoms of different types, this number weakens the attractive interaction as a result of the bond polarity. In our model, while this parameter is set to 1 for Si—Si interaction, it is set to zero for the N—N interaction, i.e., the N—N interaction has only repulsive terms. This choice was motivated by the fact that the N—N interaction to form N_2 molecule is so strong, with binding energy of 9.8 eV that when N_2 is formed inside a silicon nitride sample, it essentially does not interact with other atoms and diffuses through the system to evaporate on the surface. To keep nitrogen atoms stable inside the crystalline structure, we take $\chi_{N-N} = 0$. The best value for the parameter χ for Si—N interaction, was 0.65, which is considerably smaller than the value 0.9776 found for Si—C previously [13]. This can be explained by the difference in electronic affinity between Si and N which is considerably larger than the one between Si and C.

Fitting Procedure and Tests

In this section we describe the procedure used to search for the best set of parameters for all interactions. The fitting procedure combined two ingredients: the choice of a database of ab initio or experimental results and the strategy of finding the parameters which best describe the properties chosen in the database. We considered a database of ab initio and experimental properties, including experimental lattice parameter of the crystalline β - Si_3N_4 [17], ab initio value for average binding energy [8], experimental interatomic distance and binding energy of the N_2 molecule [18], and the ab initio result for the structure of the N—Si bonds in the Si_3NH_9 molecule. [The structure of the Si_3NH_9 was found with ab initio calculations using the density functional theory with an extended basis function 6-31G(p,d).]

For the Si—Si interactions, we used the parameters from the original Tersoff model [13], which provides a reliable description of silicon [14]. For other interactions, the best set of parameters are determined using a least-squares approach [19, 20]. A multidimensional cost function of all the

fitting parameters is defined as a sum:

$$\Phi = \sum_k \left(\frac{E^k - E_t^k}{\sigma^k} \right)^2, \quad (15)$$

where the index k runs over all the configurations in the database, E^k is the property calculated using the empirical model for configuration k , E_t^k is the corresponding target result (ab initio or experimental data), and σ^k is the tolerance which controls the weight of each configuration in the cost function. Simulated annealing was used to find a minima of Φ . The procedure for minimization was as follow: for a given set of parameters, the cost function is computed. The temperature in the beginning of the annealing process is very high, and after a large number of Monte Carlo steps, the temperature is reduced every few thousand steps with all parameters allowed to vary at once. In the simulations, the initial parameters are used as reasonable guesses, for example, the cut-offs were guessed around 2.5 Å, corresponding only to first-neighbor interactions. As a convergence criteria for the cost function, the best set of parameters were found to always converge within a reasonable range no matter the initial set of parameters used. Table I gives the best set of parameters for all interactions.

The reliability of this empirical potential in describing silicon nitride systems was tested over several properties. The tests were performed using Monte Carlo simulations [20] at room temperature

TABLE I _____
Best set of the parameters that define the
Si—Si [13], and the Si—N interactions obtained
from a simulated annealing fit to the database
described in the text.

	N	Si
A (eV)	6.36814×10^3	1.8308×10^3
B (eV)	5.11760×10^2	4.7118×10^2
$\lambda (\text{\AA}^{-1})$	5.43673	2.4799
$\mu (\text{\AA}^{-1})$	2.70000	1.7322
β	5.29380×10^{-3}	1.1000×10^{-6}
n	1.33041	7.8734×10^{-1}
c	2.03120×10^4	1.0039×10^5
d	2.55103×10^1	1.6217×10^1
h	-5.62390×10^{-1}	-5.9825×10^{-1}
$R (\text{\AA})$	1.80	2.70
$S (\text{\AA})$	2.10	3.00
χ_{Si-N}		0.65

(300 K) with periodic boundary conditions and 756 atoms. The statistical sampling is taken after initial equilibration of a few thousand steps. The internal stress is released by allowing relaxation of the simulation cell volume (NPT ensemble) in the Monte Carlo scheme [20].

There are two stable crystalline phases for Si_3N_4 : α and β [17]. For both phases the local bonding is similar, differing mostly by the number of atoms in the primitive cell. In the simpler structure (β), and believed to be the most stable, the N atoms form bonds with the three Si first neighbors in a planar structure (sp^2 hybridization). The Si atoms form bonds with the four N first neighbors in a tetrahedral structure (sp^3 hybridization). Table II compares the results of binding energy and lattice parameter of the β - Si_3N_4 to experimental and ab initio data. Due to the strong bond between Si and N atoms, silicon nitride has a large bulk modulus. The bulk modulus in the β phase is found to be 2.40 Mbar, in very good agreement with ab initio [8] and experimental results [21]. The good description of local bonding and mechanical strength shows the reliability of this model for silicon nitride. This model now can be used for predicting properties of other silicon nitride systems. In the following section we study the a - SiN_x and compare structural properties to recent experimental data [4, 5].

Structural Properties of Amorphous SiN_x

We now discuss the structure of a - SiN_x ($0 < x < 1.5$) and compare the results with experimental data [4, 5, 22, 23]. The a - SiN_x was created by a simulated annealing process, using 756 atoms and periodic boundary conditions. The relaxation of both the atoms and the simulation cell volume was allowed during the simulations. For each x , the simulation started at a very high temperature ($T > 6000$ K), when the material is essentially liquid. After allowing equilibration at such temperature, so that any memory of crystalline phase is lost, the temperature is slowly reduced in a schedule until it reaches $T = 300$ K. Then the statistical properties are computed over a large number of configurations.

Figure 1 shows the density as a function of x . The density of the material increases as x increases, consistent with experimental findings [5]. For all nitrogen contents, this model provides a

TABLE II
Properties of β crystalline phase computed using this model as compared with ab initio and experimental data.^a

	Experiment	Ab initio	This work
a (Å)	7.606 ^b 7.595 ^a	7.61 ^d 7.586 ^e	7.513
E_B (eV)	—	-5.307 ^d -5.342 ^e	-5.305
ρ (g / cm ³)	3.19 ^c	3.17 ^d	3.32
B (Mbar)	2.56 ^f	2.65 ^d	2.40 2.82 ^e

^a Binding energies (E_B) are given in eV/atom, lattice parameter (a) in Å, and bulk modulus (B) in Mbar.

^b Ref. [30].

^c Ref. [17].

^d Ref. [8].

^e Ref. [31].

^f Ref. [21].

reasonably good description of the density as compared to experimental data [5]. Figure 2 shows the total radial distribution function $g(r)$ for $x = 0, 0.5, 1.0, 1.33$, and 1.5 . As x increases, $g(r)$ changes its behavior considerably. At $x = 0$, the system is a -Si and $g(r)$ shows a peak around 2.4 Å which is the first-neighbor average distance of Si-Si. As x increases, the peak corresponding to Si-Si bonds decreases and a peak appears at a shorter distance (1.73 Å) corresponding to the Si-N. In

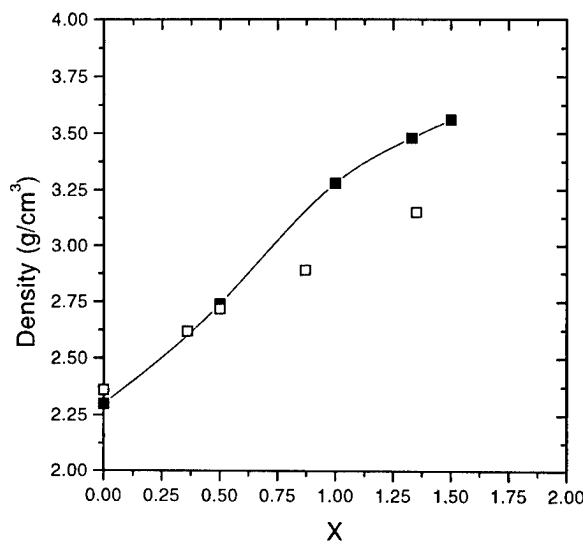


FIGURE 1. Density (in g / cm³) of amorphous silicon nitride (SiN_x) computed by Monte Carlo simulations compared to experimental results (□) [5].

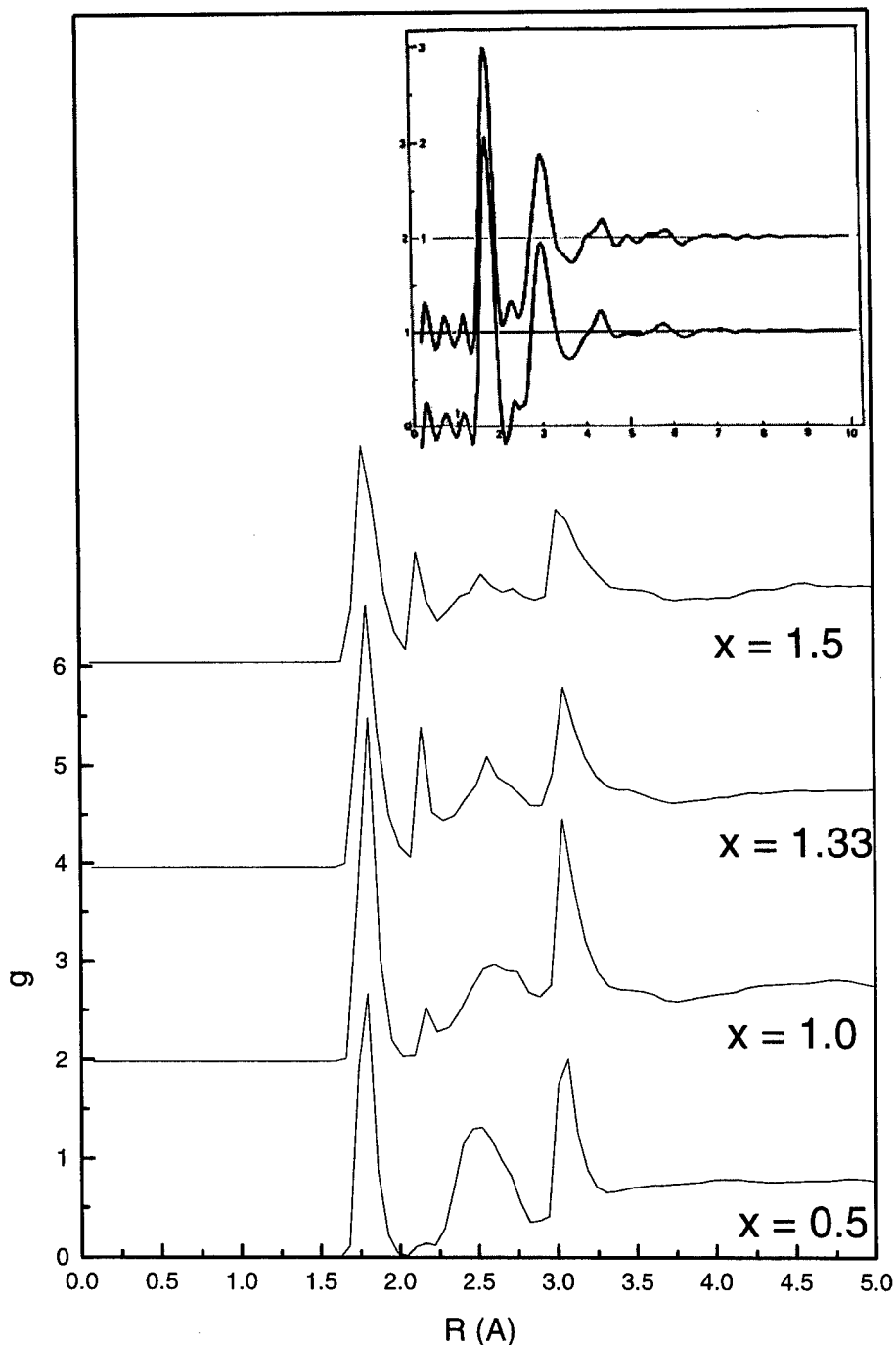


FIGURE 2. Total radial distribution function $g(r)$ for $x = 0.5, 1.0, 1.33$, and 1.5 . The experimental result [22] for the $x = 1.33$ is presented in the insert.

the case of $x = 1.33$, where there is available experimental data, $g(r)$ is in very good agreement with experimental results reached by x-ray scattering [22] shown in the insert of the figure.

Figure 3 compares the average coordination number at Si and N centers as a function of x with

experimental data [5]. The coordination number is computed as the area under the radial distribution function inside the covalent radius. The figure shows the coordination $n_A(B)$, the average number of neighbors A for atom type B . For $x = 0$ (a —Si) each Si atom has an average coordination

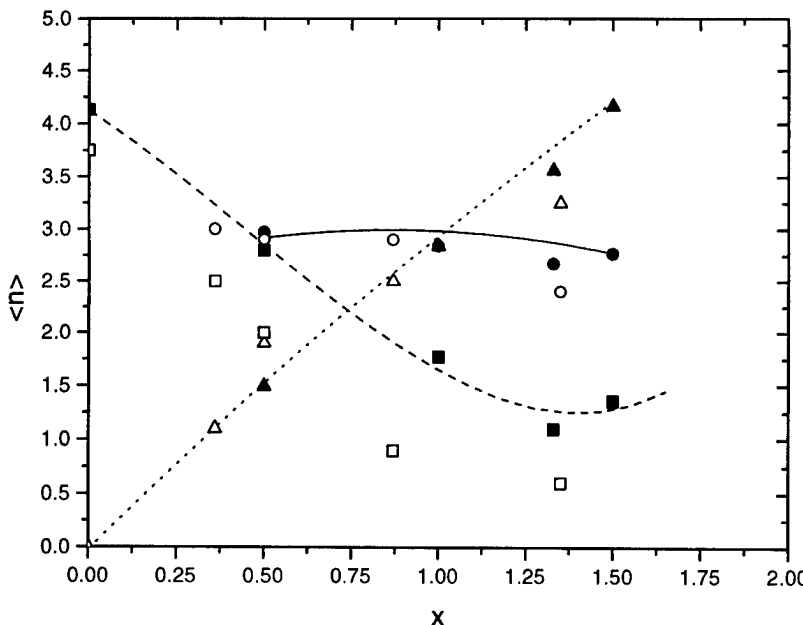


FIGURE 3. Average coordination number at Si and N sites as function of x . The simulation results (solid symbols) are compared to experimental data (open symbols) [5]. The figure shows (\square) $\langle n_{\text{Si}}(\text{Si}) \rangle$, (\triangle) $\langle n_{\text{N}}(\text{Si}) \rangle$, and (\circ) $\langle n_{\text{Si}}(\text{N}) \rangle$.

of 4.13. As x increases, the N atoms compete with Si atoms to form bonds, so that the coordination $n_{\text{Si}}(\text{Si})$ falls from 4.13 at $x = 0$ to about 0.9 at $x = 1.5$. On the other hand, the coordination $n_{\text{Si}}(\text{N})$ grows linearly for $x < 1$ from zero to four. The coordination $n_{\text{Si}}(\text{N})$ is about 3 for all the range of x . This is consistent with the fact that N atom has a preference to bind to three Si atoms [24, 25]. These results agree very well with experimental data [5]. However, this comparison should be taken with caution. The samples in which the experiments were performed had considerably high hydrogen concentration. Hydrogen competes with Si and N, to form Si—H and N—H bonds instead of Si—N or Si—Si. Theoretical coordinations are larger than the experimental ones because in our case there is no H competing to form bonds.

Electronic Properties of Defects in Silicon Nitride

Empirical models have been used as alternative methods to study structural properties of materials. More recently, these models have been combined to first-principles calculations to explore electronic structure [25]. Since thermodynamical properties are not feasible using the first-principles calculations, empirical models can be used to cre-

ate configurations which are used as input for the electronic calculations. We studied the electronic properties of SiN systems using an empirical model to generate relevant equilibrium structures. Then, we computed the electronic properties within the framework of DFT/LDA framework [26]. The Khon–Sham equations were solved using Car–Parrinello scheme [27] with Troullier–Martins type pseudopotentials [28] in Kleinmann–Bylander form [29]. The basis sets were expanded in plane waves, with kinetic energy of 60 Ry. The number of atoms in the large unit cell (LUC) varied depending on the structure analyzed, but no LUC comprised more than 56 atoms.

We studied the electronic properties of the crystalline Si_3N_4 , a — $\text{SiN}_{1.33}$, N-type vacancy, and Si antisite ($\text{Si}_{[\text{N}]}$). Figure 4 shows the density of states (DOS) for all those systems. In all cases, the zero in energy corresponds to the top of the valence band. Figure 4(a) shows the DOS for the crystalline β — Si_3N_4 which agrees very well with experimental results [3] and other theoretical calculations [7]. The electronic structure shows clearly the valence band split in two subbands, with a pseudogap located around 11 eV below the top of the valence band. The states located at the bottom of the valence band arise from the N 2s-orbitals. The peak in the top of the valence band arises from the N 2p-lone pairs.

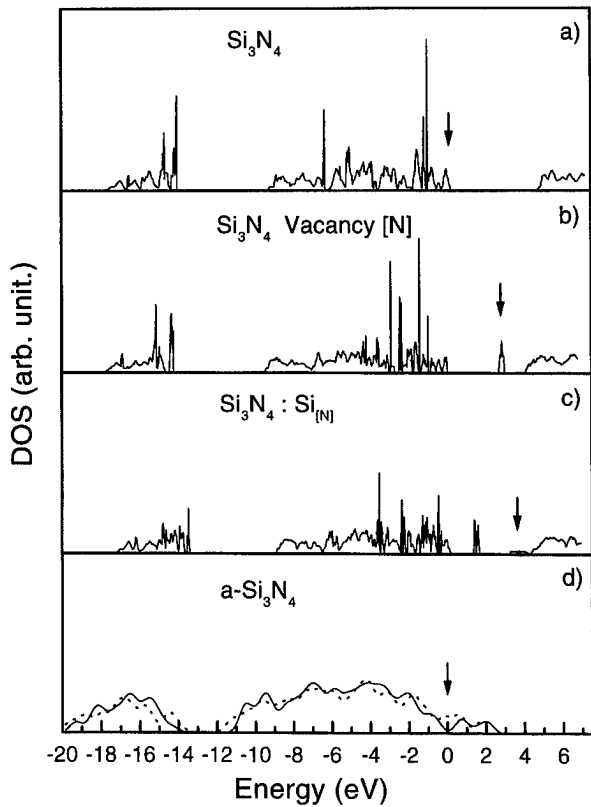


FIGURE 4. Density of states (DOS) for: (a) the crystalline β - Si_3N_4 , (b) a N vacancy in crystalline Si_3N_4 , (c) a Si antisite in crystalline Si_3N_4 , and (d) the a - $\text{SiN}_{1.33}$. The arrows in the figure represent the Fermi levels.

A number of defect centers related to Si and N dangling bonds have been studied [6]. The K center involves a Si dangling bond (Si bounded to three N atoms), the N_2 center involves an N dangling bond (N bounded to two Si atoms). Here we search for a different kind of dangling bond which may appear in amorphous silicon nitride, those coming from antisite configurations. Figure 4(b) shows the DOS for the N vacancy. This defect introduces a singly occupied dangling-bond orbital located in the middle of the gap. Removing a nitrogen atom gives rise to three Si atoms with one dangling bond each, as shown schematically in Figure 5. Two of them form a bond state located at the top of the valence band leaving one dangling bond state in the gap.

Figure 4(c) shows the DOS results for the $\text{Si}_{[\text{N}]}$ antisite. Due to the small size of the LUC, with 28 atoms, the removal of one N atom causes a nonnegligible decrease in the DOS from the levels coming from the N-lone pair. The localized mini-

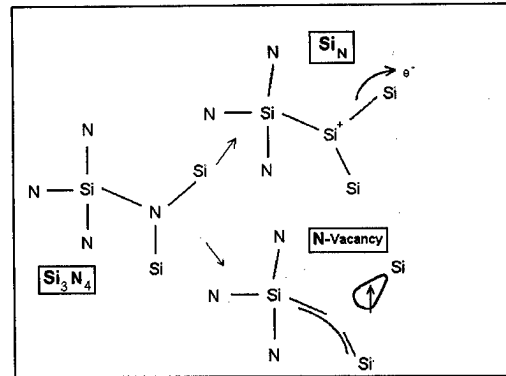


FIGURE 5. Schematic representation of a Si antisite and a N vacancy in crystalline Si_3N_4 .

band which appears in the middle of the energy gap comes from the Si—Si wrong bonds fully occupied. The extra electron appears close to the top of the conduction band, with a localized character. These results show that Si antisite behaves as Si^+ . This kind of structural defect should present a diamagnetic behavior around the Si antisite. In Figure 5, this process is shown schematically.

Figure 4(d) shows the DOS for the a - $\text{SiN}_{1.33}$. The empirical model, described in the previous sections, was used to generate the amorphous structure. We started with a cell containing 56 atoms in the ideal β phase. The crystal was melted using the Monte Carlo scheme (NPT ensemble). After thermalization, the temperature was slowly decreased to $T = 300$ K. The final structure was used as input for the ab initio calculation. Figure 4(d) shows the DOS with the dashed line referring to the results without lattice relaxations (only fully electronic self-consistent calculations), while the solid line describes the results after full relaxation until all the Hellman–Feynman forces are lower than 0.01 eV/A. Both results are in reasonably good agreement showing that the empirical model describes reasonably well the structural properties of the amorphous material. However, we should point out that the atomic relaxations in the ab initio calculations are important to describe the gap region, consequently, the microscopic properties related to transport in disordered systems. After relaxation, a small gap forms. We did not expect a large gap in this prototypical amorphous for two reasons: (i) the number of atoms in the unit cell is too small that the system has high concentration of structural defects (Si and N dangling bonds and Si—Si wrong bonds) which introduce states in the gap; (ii) to reduce the DOS in

the gap, hydrogen atoms should be incorporated in the cell to passivate the dangling bonds.

Final Remarks

In summary, we presented a new empirical model for the silicon nitride system using the Tersoff functional form. The potential provides a considerably reliable description of crystalline and amorphous silicon nitride over a wide range of configurations and systems. Using the empirical model, we created relevant defect structures to study electronic properties through ab initio calculations. The vacancy and antisite defects create energy gap levels, which are electrically active.

ACKNOWLEDGMENTS

Partial support was provided to FBM and AF by Brazilian Agencies Capes and CNPq. JFJ acknowledges support from FAPESP.

References

1. F. H. P. M. Habraken and A. E. T. Kuiper, *Mat. Sci. Eng. R* **12**, 123 (1994).
2. R. N. Katz, *Science* **208**, 841 (1980).
3. R. Kärcher, L. Ley, and R. L. Johnson, *Phys. Rev. B* **30**, 1896 (1984).
4. M. M. Guraya, H. Ascolani, G. Zampieri, J. I. Cisneros, J. H. Dias da Silvia, and M. P. Cantão, *Phys. Rev. B* **42**, 5677 (1990).
5. M. M. Guraya, H. Ascolani, G. Zampieri, J. H. Dias da Silvia, M. P. Cantão, and J. I. Cisneros, *Phys. Rev. B* **49**, 13446 (1994).
6. J. Robertson, W. L. Warren, and J. Kanicki, *J. Non-Cryst. Mater.* **187**, 297 (1995).
7. S.-Y. Ren and W. Y. Ching, *Phys. Rev. B* **23**, 5454 (1981).
8. A. M. Liu and M. L. Cohen, *Phys. Rev. B* **41**, 10727 (1990).
9. N. Umesaki, N. Hirosaki, and K. Hirao, *J. Non-Cryst. Solids* **150**, 120 (1992).
10. P. Vashishta, R. K. Kalia, J. P. Rino, and I. Ebbsjö, *Phys. Rev. B* **41**, 12197 (1990).
11. J. Tersoff, *Phys. Rev. Lett.* **56**, 632 (1986).
12. J. Tersoff, *Phys. Rev. B* **37**, 6991 (1988).
13. J. Tersoff, *Phys. Rev. B* **39**, 5566 (1989).
14. H. Balamane, T. Halicioglu, and W. A. Tiller, *Phys. Rev. B* **46**, 2250 (1992).
15. A. P. Horsfield, A. M. Bratkovsky, M. Fearn, D. G. Pettifor, and M. Aoki, *Phys. Rev. B* **53**, 12694 (1996).
16. M. Z. Bazant, E. Kaxiras, and J. F. Justo, *Phys. Rev. B* **56**, 8542 (1997).
17. R. Grün, *Acta Cryst. B* **35**, 800 (1979).
18. G. Herzberg, *Diatom Molecules* (VNR, New York, 1945).
19. R. Fletcher and J. D. Powell, *Comput. J.* **6**, 163 (1963).
20. M. P. Allen and D. J. Tildesley, *Computer Simulation of Liquids* (Oxford Univ. Press, Oxford, 1987).
21. O. Borgen and H. M. Seip, *Acta Chem. Scand.* **15**, 1789 (1961).
22. T. Aiyama, T. Fukunaga, K. Niihara, and K. Susuki, *J. Non-Cryst. Solids* **33**, 131 (1979).
23. M. Misawa, T. Fukunaga, K. Niihara, T. Hirai, and K. Suzuki, *J. Non-Cryst. Solids* **34**, 313 (1979).
24. C. Cunha, S. Canuto, and A. Fazzio, *Phys. Rev. B* **48**, 17806 (1993).
25. P. P. M. Venezuela and A. Fazzio, *Phys. Rev. Lett.* **77**, 546 (1996).
26. P. Hohenberg and W. Kohn, *Phys. Rev.* **136**, 864B (1964); W. Kohn and L. J. Sham, *Phys. Rev.* **140**, 1133A (1965).
27. R. Car and M. Parrinello, *Phys. Rev. Lett.* **55**, 2471 (1985).
28. N. Troullier and J. L. Martins, *Phys. Rev. B* **43**, 1993 (1991).
29. L. Kleinmann and D. M. Bylander, *Phys. Rev. Lett.* **48**, 1425 (1982).
30. R. W. G. Wyckoff, *Crystal Structures*, 2nd ed. (Krieger, Malabar, 1986).
31. Y. Xu and W. Y. Chiang, *Physica B* **150**, 32 (1988).

Analysis of Three-Dimensional Molecular Shape Using Surface Area and Molecular Volume Scaling Descriptors

GUSTAVO A. ARTECA

Département de Chimie et Biochimie, Laurentian University—Université Laurentienne,
Ramsey Lake Road, Sudbury, Ontario, Canada P3E 2C6

Received 23 February 1998; accepted 23 June 1998

ABSTRACT: Continua of molecular surfaces have been proposed in the past as realistic approaches to modeling molecular shape. A continuum of fused-sphere surfaces combines the simplicity of computations involving hard spheres with a more accurate description of the “fuzzy” boundary of a molecule. In this work, we study some simple properties of a continuum of molecular surfaces derived by *linearly scaling the van der Waals radii*. We introduce some molecular shape descriptors derived from surface area and volume and study their dependence on a scaling parameter that “swells” the molecular surface. As one moves away from the nuclei, any transitions in molecular shape are reflected by changes in the descriptors. These descriptors convey *essential* shape features, in the sense that they are rather insensitive to molecular size. Even though the geometrical descriptors characterize the continuum globally, their behavior appears to be strongly determined by local molecular shape features. The procedure can also be extended to more realistic electron density surfaces. As a tool, the method can be helpful in assessing molecular similarity, as well as in studying properties of local neighborhoods within large clusters. © 1998 John Wiley & Sons, Inc. Int J Quant Chem 70: 981–992, 1998

Key words: molecular similarity; electron density contours; fused-sphere surfaces; van der Waals radii; hydrocarbons

Contract grant sponsors: Fonds de Recherche de l'Université Laurentienne (FRUL); Natural Sciences and Engineering Research Council (NSERC) of Canada.

Introduction

The three-dimensional “body” of a molecule is commonly described by an envelope surface. The simplest model is the van der Waals (or “fused-sphere”) surface, defined by interpenetrating atomic spheres. This model has a long established history in the study of gases, solids, and liquids [1]. In modern molecular modeling, alternative surfaces can be used, depending on whether one wants to convey an accurate electron density surface or simply map properties around the molecule [2, 3]. (For an up-to-date review on molecular surface models, see Ref. [4].) Despite their idiosyncrasies, all fused-sphere models share one weakness: *they assign a “clear-cut” boundary to the molecule*. Not only is this unphysical from a rigorous viewpoint, but also the set of *fixed* atomic radii used to build the surface is not uniquely defined. This situation creates inconsistencies between calculated properties [5] and difficulties in obtaining an unbiased comparison of molecular shapes [6]. In this work, we deal with an improved version of the fused-sphere molecular surface that takes into account the “fuzzy” nature of this boundary, yet conserves the simplicity of the computations.

The possibility of using “adjustable” atomic radii (i.e., varying from molecule to molecule) has been proposed [5a]. Here, we take a more physical stand. We study molecular shape features averaged over a range of atomic radii. To this end, we replace the notion of a single molecular surface by a continuum of surfaces [7, 8]. This ensemble is defined by a scaling parameter acting on a set of atomic radii. By studying the continuum as a function of the scaling parameter, one can extract essential shape properties over all size scales. In this work, we analyze the behavior of a family of shape descriptors derived from simple properties of the continuum, namely, the molecular surface area and the volume of the scaled surfaces.

Molecular surface area (S) and volume (V) are the most important geometric properties of hard-sphere models. Actually, all thermodynamic properties of a system composed of packed hard spheres are determined by the volume and surface area of the free space accessible to the spheres [9, 10]. (In this latter case, one must deal with the geometry of the

actual molecules as well as the voids between them [11, 12].) Despite their simplicity, hard-sphere models describe well a number of properties of real systems in the limit of *infinite dilution*. This is the situation found in molecular modeling and drug design applications, which are frequently based on single-molecule simulations. Molecular surface areas computed at equilibrium geometries correlate well with experimental properties. In hydrophobic molecules, relative solvent affinity can be completely characterized in terms of surface areas, as these are found to be proportional to the logarithm of the partition coefficient between immiscible liquids (e.g., $\log p_{o/w}$ for *n*-octanol-water) [13]. Similarly, solvation free energies [14–16], critical parameters [17–19], and diffusion coefficients [20] can be computed from molecular surface areas and related properties.

In contrast, these parameters are problematic for assessing similarity. Molecular surface area and volume do not discriminate well between molecules. There have been some attempts to build better shape descriptors from S and V . Two descriptors proposed by Meyer [21] are relevant to the present work: the *molecular rugosity* (G_1) and the *molecular globularity* (G_2).

The rugosity, defined as the ratio $G_1 = S/V$, takes large values if the molecule has indentations and protuberances. As a descriptor, it has some drawbacks. Note that, for a sphere, G_1 is proportional to the reciprocal radius. Therefore, two molecules with similar *shape* but different *size* will be assigned different rugosities. In other words, G_1 will not be invariant if we scale isotropically the molecular surface. The globularity is defined as the ratio $G_2 = S_e/S$, where S_e is the surface area of a sphere with the same volume V as the molecule in question. In contrast with the rugosity, G_2 is scaling invariant in a sphere. Thus, we can expect that molecules (or interstitial voids in clusters) with similar G_2 values could share similar essential shape features, even if they differ in size. This is a valuable feature when assessing molecular similarity [3]. Note, however, that the globularity of nonspherical molecules may depend on how the molecular “boundary” is defined. In this work, we improve on this approach by *extending the concept of molecular globularity to a continuum of scaled surfaces* [8]. We propose to use the scaling behavior of a globularity-like property as a shape descriptor for molecules or clusters.

The work is organized as follows. In the next section, we introduce the molecular shape descriptors and analyze some of their properties. In the following section, the descriptors are tested on a series of hydrocarbons. Another section discusses the extension to other molecules, including the comparison of large- and small-scale shape features in proteins. We close with remarks on how the method can be extended to more realistic surfaces.

Molecular Shape Descriptors for a Continuum of Scaled Surfaces

The key idea of our method is as follows. Let $\{\rho_1, \rho_2, \dots, \rho_n\}$ be the series of "standard" van der Waals (VDW) radii characterizing a molecule of n nuclei, in a spatial configuration indicated by nuclear positions $(\mathbf{R}_1, \dots, \mathbf{R}_n)$. The VDW envelope surface is defined by the set of points, $F(\mathbf{r})$, that lie on the surface of an atomic sphere and are not enclosed by any other one:

$$F(\mathbf{r}) = \left\{ \mathbf{r} \in \Re^3 : \|\mathbf{r} - \mathbf{R}_i\| = \rho_i, \text{ and } \|\mathbf{r} - \mathbf{R}_j\| \geq \rho_j, \forall j \neq i \right\}. \quad (1)$$

If we now consider that the molecular boundary is fuzzy, we can replace (1) by a continuum. The simplest approach is to derive a series of molecular surfaces that differ from (1) by a scaling parameter f modifying the VDW radii: $\rho_i \rightarrow f\rho_i$. This scaled surface will be indicated by $F_f(\mathbf{r})$:

$$F_f(\mathbf{r}) = \left\{ \mathbf{r} \in \Re^3 : \|\mathbf{r} - \mathbf{R}_i\| = f\rho_i, \text{ and } \|\mathbf{r} - \mathbf{R}_j\| \geq f\rho_j, \forall j \neq i \right\}, \quad f > 0. \quad (2)$$

The continuum comprises all scaled surfaces, i.e., $\{F_f(\mathbf{r}), f > 0\}$. Note that $F_f(\mathbf{r})$ differs from other "augmented" surfaces, such as the solvent accessible surface [2]. In the latter case, a constant (the "solvent radius") is added to the atomic radii.

Whereas the surface area and volume change continuously upon scaling, a ratio such as $(\text{area}) \times (\text{volume})^{-2/3}$ would be constant in a sphere, but not in a nonspherical surface. Therefore, by studying this descriptor as a function of the scaling parameter f , we could distinguish among molecular surfaces. We generalize this simple notion by introducing *geometrical* shape descriptors that pre-

sent a rich behavior upon scaling. The changes in these descriptors (as functions of f) can be correlated with "transitions" in molecular shape as one moves away from the nuclei.

Let $S(f)$ and $V(f)$ be the surface area and volume, respectively, associated with the scaled surface $F_f(\mathbf{r})$. (There are several techniques for computing $S(f)$ and $V(f)$ [22–28]. Here, we use the method proposed in Ref. [25].) First, we introduce a function of $S(f)$ and $V(f)$ as follows:

$$Q(f) = \frac{S(f)}{(36\pi)^{1/3} V(f)^{2/3}}. \quad (3)$$

The function $Q(f)$ is the reciprocal of the molecular globularity as defined in Ref. [21]. The denominator in Eq. (3) ensures that $Q(f) = 1$ in a sphere, for all values of the scaling parameter f . Note that all molecules reach this limit if $f \rightarrow \infty$. This is consistent with the asymptotic behavior of the electron density, whereby all molecules look spherical at vanishingly small density values.

As a descriptor, $Q(f)$ has some disadvantages:

1. For $f \ll 1$, the surface becomes a series of disconnected spheres. In this case, we find a limit behavior $Q(f) \sim n^{1/3}$. As a result, $Q(f)$ will have a strong dependence on molecular size.
2. The value of $Q(f)$, while describing a continuum of surfaces, depends on the initial VDW radii used for scaling.

Both these problems can be solved by using a "relative" $Q(f)$ function. Let $Q_0(f)$ be the value of the Q function when computed with a "standard" set of radii. (In our case, we will use the set of atomic radii proposed by Gavezzotti [29]. The corresponding surface area and volume will be indicated by $S_0(f)$ and $V_0(f)$, respectively.) The molecular envelope described by this function can be bounded by two "virtual" surfaces. Let $Q_m(f)$ be the value of Eq. (3) when *all the nuclei* are given the *smallest* value for a radius (i.e., when the VDW radii are taken as $\rho_j = \min\{\rho\}$, for all j). This surface will be characterized by surface area and volume denoted by $S_m(f)$ and $V_m(f)$, respectively. Let $Q_M(f)$ be the value of Eq. (3) when *all the nuclei* are given the *largest* value for a radius (i.e., when the VDW radii are taken as $\rho_j = \max\{\rho\}$, for

all j). In this case, the surface area and volume will be denoted by $S_M(f)$ and $V_M(f)$, respectively. Finally, we associate the following shape descriptors with a given molecule:

$$q_m(f) = Q_0(f)/Q_m(f) = (S_0/S_m)(V_m/V_0)^{2/3}, \quad (4a)$$

$$q_M(f) = Q_0(f)/Q_M(f) = (S_0/S_M)(V_M/V_0)^{2/3}. \quad (4b)$$

These parameters are ratios of surface areas and molecular volumes computed by using two scales of atomic radii. We shall refer to $q_m(f)$ and $q_M(f)$ as the *relative globularities* (lower and upper bounds, respectively). An intuitive analysis suggests the type of information conveyed in the descriptors $q_m(f)$ and $q_M(f)$:

1. In the descriptor $q_m(f)$, atoms are replaced by the smallest atomic spheres. Therefore, the major changes in globularity will be caused by the number and location of the *largest* atomic spheres. Therefore, the variations in $q_m(f)$ as a function of f will reflect global shape features associated with the positions of bulky (usually, nonhydrogen) atoms.
2. In the descriptor $q_M(f)$, atoms are replaced by the largest atomic spheres. Therefore, the major changes in globularity will be caused by the number and location of the *smallest* atomic spheres. We would thus expect that the variations in $q_M(f)$ as a function of f will normally be related to the number of hydrogen atoms and their spatial positions.

In other words, we expect $q_m(f)$ and $q_M(f)$ to reflect the interplay between *local geometry* (i.e., the distribution and relative position of different atoms) and *global shape features* (i.e., the ratios of surface area and volume). The simultaneous use of $q_m(f)$ and $q_M(f)$ should provide a "signature" of molecular shape.

Note that $q_s(f) \rightarrow 1$ ($s = m, M$) when $f \rightarrow \infty$ (i.e., all molecules become asymptotically spherical). When $f \rightarrow 0^+$, $q_m(f)$ and $q_M(f)$ become a constant whose value depends only on the initial set of atomic radii. For a general n -atom molecule,

a simple calculation gives:

$$\lim_{f \rightarrow 0^+} q_m(f) = \lim_{f \rightarrow 0^+} q_M(f) = n^{-1/3} \frac{\sum_{i=1}^n \rho_i^2}{\left[\sum_{i=1}^n \rho_i^3 \right]^{2/3}} = C. \quad (5)$$

For most molecules, the constant C is found to be between 0.96 and 1.00. For intermediate values of f , the changing contacts of atomic spheres will cause variations of surface area and volume, and this will be reflected in the descriptors $q_m(f)$ and $q_M(f)$. As discussed before, we do not expect these descriptors to be too sensitive to differences in molecular size.

A simple example serves to illustrate the qualitative behavior of the $q_s(f)$ descriptors. Consider the fused-sphere model of a homonuclear diatomic molecule. In this case, we have two identical spheres with VDW radii $\rho_1 = \rho_2 = \rho$, separated by a bond distance $d < 2\rho$. Let ρ be the corresponding "standard" atomic radius. Let $\rho_m < \rho$ be a reasonable lower bound to ρ (e.g., the smallest VDW radius, $\rho_m = 1.17 \text{ \AA}$, corresponding to hydrogen [29]). A simple calculation gives the exact volume and area for the surface built with the radius ρ : $V = (4\pi\rho^3/3)(1 + d/2\rho)$ and $S = 4\pi\rho^2(1 + d/2\rho)$. We can now calculate the $Q_0(f)$ descriptor for the molecular surfaces with scaled radius $f\rho$. Considering that the spheres are disjointed whenever $f\rho < d/2$, the result is:

$$Q_0(f) = \begin{cases} 2^{1/3}, & \rho f \leq d/2 \\ (1 + d/2\rho f)^{1/3}, & \rho f \geq d/2 \end{cases}. \quad (6)$$

A similar result holds for the descriptor $Q_m(f)$ computed with the smaller radius $\rho_m < \rho$. Finally, we evaluate the relative descriptor $q_m(f)$ as a continuous function of the scaling parameter:

$$q_m(f) = \begin{cases} 1, & f \leq d/2\rho \\ [(2\rho f + d)/4\rho f]^{1/3}, & d/2\rho \leq f \leq d/2\rho_m \\ [(2\rho f + d)/(2\rho_m f + d)]^{1/3} (\rho_m/\rho)^{1/3}, & f \geq d/2\rho_m \end{cases}. \quad (7)$$

Note that $q_m(f) = 1$ when $f \rightarrow 0$, as required by Eq. (5) in the case of identical VDW radii. For completeness, we note how $q_m(f)$ tends to unity as the surface becomes asymptotically large:

$$q_m(f) \approx 1 - \frac{d(\rho - \rho_m)}{6f\rho\rho_m} + O(f^{-2}). \quad (8)$$

Figure 1 translates schematically the behavior in Eq. (7). The regions denoted by *A*, *B*, and *C* represent three topologically different situations for a diatomic molecule: (a) the atomic spheres are disjoint, *A*; (b) the spheres fuse in the regime of large atomic radii, *B*; and (c) the spheres fuse also in the regime of small atomic radii, *C*. These three regimes represent the different molecular shapes expected in a continuum of diatomic surfaces “grown” from a range of initial VDW surfaces. By using information related to the nuclear geometry and connectivity, the descriptor $q_m(f)$ manages to capture these essential shape features. As such, it provides a one-dimensional descriptor of molecular shape.

The “transitions” in $q_m(f)$ values are indicative of the changes in shape that accompany the scaling of the molecular surface. A similar analysis can be made for the complementary descriptor, $q_M(f)$, defined by the upper bound to the atomic radii. In this case, $q_M(f)$ exhibits a *maximum* in terms of f . This maximum corresponds also to a transition in spherical contacts. These results are representative of the qualitative scaling dependence of the *relative globularity* for most molecules.

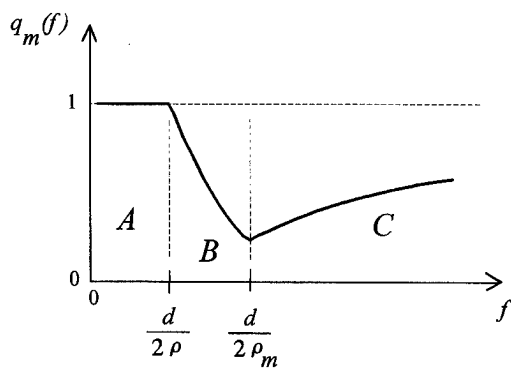


FIGURE 1. Schematic dependence of the $q_m(f)$ descriptor upon scaling for a homonuclear diatomic molecule [cf. Eq. (7)]. (The minimum indicates the region of atomic radii where the spheres fuse.)

If the molecule contains two *different* types of atoms, we will compute $q_m(f)$ and $q_M(f)$ with a simple choice for the “reference” surfaces. In this case, $q_m(f)$ will be defined over a surface where all atoms have the radius of the smallest atom of the two. Similarly, $q_M(f)$ will be defined over a surface where all atoms have the radius of the largest atom. As the geometry becomes more complicated, further information can be retrieved from the behavior of $q_m(f)$ and $q_M(f)$ in terms of f . For example, we can expect new transitions in $q_m(f)$ if the contacts between atomic spheres lead to cycles, cages, or voids. Similarly, the transitions in $q_m(f)$ values will depend on the range of atomic radii used to “grow” the continuum of surfaces. In the next section, we compute these descriptors for hydrocarbons and discuss in more detail their behavior and interpretation.

Shape Descriptors for Scaled Surfaces of Hydrocarbons

The VDW surfaces of hydrocarbons are defined by their equilibrium geometries and two atomic radii. By choosing the “minimum radius” as $\rho_m = \rho_{\text{Hydrogen}} = 1.17 \text{ \AA}$ [29] and the “maximum radius” as $\rho_M = \rho_{\text{Carbon}} = 1.75 \text{ \AA}$ [29], we can compute the relative globularity descriptors. Molecular shape features can then be assessed from the behavior of $q_m(f)$ and $q_M(f)$ during scaling.

The details of the computations are as follows. Since the surface area and volume are rather insensitive to small changes in nuclear geometries, we have used minimum energy conformations optimized with molecular mechanics. (We employ the force field MM2 [30], as implemented and modified in the molecular modeling program HyperChem [31]. This force field (MM+) is well-tested and reliable for stable hydrocarbon conformations.) In the case of several accessible conformers, we have always used the global minimum. The surface area and volume are computed with the program GEPOL [25, 26]. This program calculates the surface area by a recurrence of triangulations on an atomic sphere. We have used the highest precision allowed by the program (i.e., 5 levels of triangulation over an initial C_{60} -like polyhedron per atomic sphere). Using this method, we have computed areas and volumes for values of the scaling

factor f between 0.10 and 3.00, in steps of 0.05. For all molecules discussed in this work, $f = 3$ corresponds to the regime of spheroidal surfaces (i.e., $q_m(f) \rightarrow 1$, $q_M(f) \rightarrow 1$).

As a first example, Figure 2 shows the results for $q_m(f)$ (full line) and $q_M(f)$ (dotted line) in a number of linear saturated hydrocarbons. Both $q_m(f)$ and $q_M(f)$ show changes in terms of f as the chain lengthens. Some important observations are:

1. All hydrocarbons present a sharp peak in $q_M(f)$ (dotted line) for $f < 1$. This peak defines the region of atomic radii where one changes from disjoint spheres to hydrogen–carbon spherical contacts. A second peak ($f \approx 1$) occurs for hydrocarbons other than methane. This second peak is associated with the fusion of adjacent carbon spheres, as well as the fusion of hydrogen atomic spheres located in these adjacent carbons. [Note that hydrogen atoms are assigned a larger radius when computing $q_M(f)$.] The larger the number of such contacts, the larger the change on the relative globularity. As a result, the height of this peak increases with the length of the chain. This observation is consistent with our discussion in the previous section, whereby $q_M(f)$ was expected to be strongly dependent

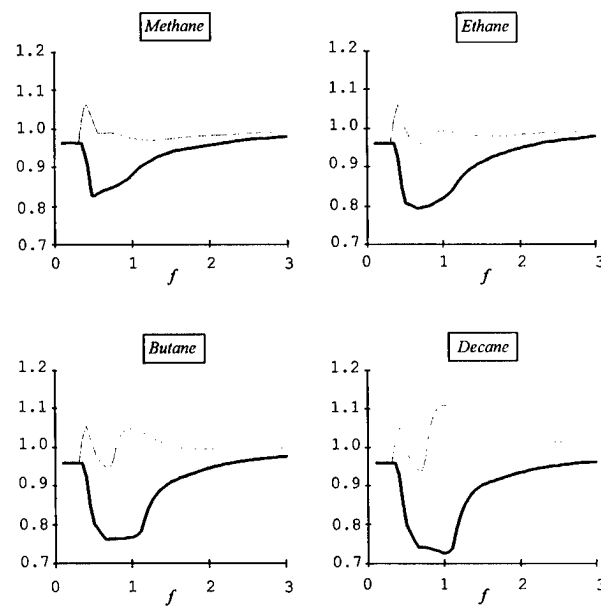


FIGURE 2. Relative globularity descriptors $q_m(f)$ (full line) and $q_M(f)$ (dotted line) for methane and some saturated linear hydrocarbons.

on the number and position of the *smallest* atoms.

2. The function $q_m(f)$ (full line) shows a minimum in all hydrocarbons. The minimum becomes broader, deeper, and shifts as the chain lengthens. In methane, the minimum indicates the transition from disjoint to fused hydrogen–carbon spheres. [Note that the minimum in $q_m(f)$ is found at larger f values than the maximum in $q_M(f)$.] This is expected because $q_m(f)$ uses the lower bound to the atomic radii, and thus the first spherical contacts will be found in more “swollen” surfaces.] As in the example above, the longer chains shift the minimum in $q_m(f)$ due to the presence of carbon–carbon and hydrogen–hydrogen contacts between neighbor groups.

The relative importance of carbon–carbon vs. hydrogen–hydrogen contacts can be assessed by comparing molecules with the same number of carbons in similar geometries, but different number of hydrogens. This is done in Figure 3, where *n*-hexane and hexa-1,3,5-triene are compared (both in *all-trans* conformations). The results indicate that the height of the second peak in $q_M(f)$ is most influenced by the number of hydrogen–hydrogen spherical contacts. These contacts have a smaller influence on the depth of the second minimum in $q_m(f)$.

Figure 4 complements the analysis of Figure 3. Here, we compare the series of cyclic hydrocarbons from cyclohexane (in chair conformation) to benzene. The effect on the $q_M(f)$ descriptor is clear. With each double bond, two hydrogen spheres on adjacent carbons are removed. This is reflected in a decrease in the second maximum. In benzene, this maximum is barely noticeable.

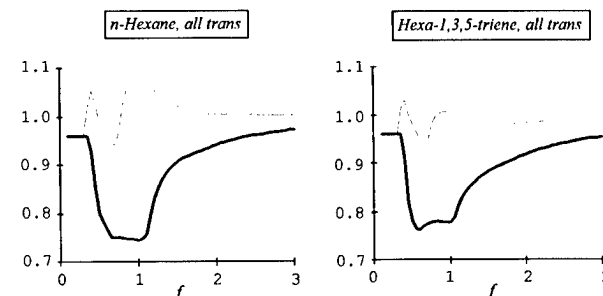


FIGURE 3. Compared behavior of the $q_m(f)$ (full line) and $q_M(f)$ (dotted line) descriptors in two molecules with similar carbon skeletons but different number of hydrogen atoms.

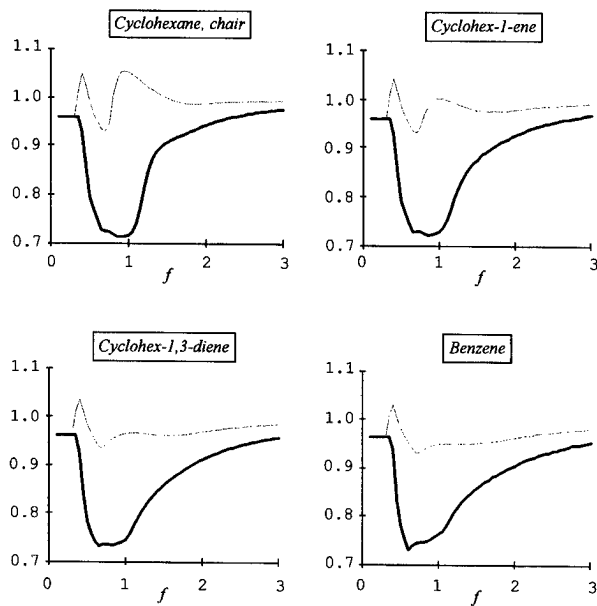


FIGURE 4. Relative globularity descriptors $q_m(f)$ (full line) and $q_M(f)$ (dotted line) for cyclic molecules with varying number of hydrogen atoms. [Note the disappearance of a maximum in $q_M(f)$ as the number of hydrogen atoms decreases.]

The role of the carbon–carbon contacts is well illustrated in the behavior of $q_m(f)$ in Figure 4. Note that the minimum in benzene appears as a secondary minimum or “shoulder” for the other hydrocarbons. This feature in common must be associated with two characteristics: a local environment consisting of —CH— groups and a global cyclic connectivity. If we compare *n*-hexane (Fig. 3) and cyclohexane (Fig. 4), we can estimate the relative weight of these two factors. In the cyclic molecule, the main difference is found in the additional carbon–carbon contacts. This difference appears to translate in a lowering of the minimum in $q_m(f)$.

The results in Figures 2–4 show the interplay between *local* and *global* shape features in the relative globularity. Even though we use global properties (volume and surface area), the $q_m(f)$ and $q_M(f)$ descriptors appear to be quite sensitive to the local environments around the atoms. As the scaling parameter f increases, the changes in $q_m(f)$ and $q_M(f)$ will reflect the modulation of surface area and volume by the fusion of neighboring atomic spheres. Consequently, we can expect that two molecules whose atoms have similar neighborhoods over a range of atomic radii will have similar $q_m(f)$ and $q_M(f)$ descriptors. In this

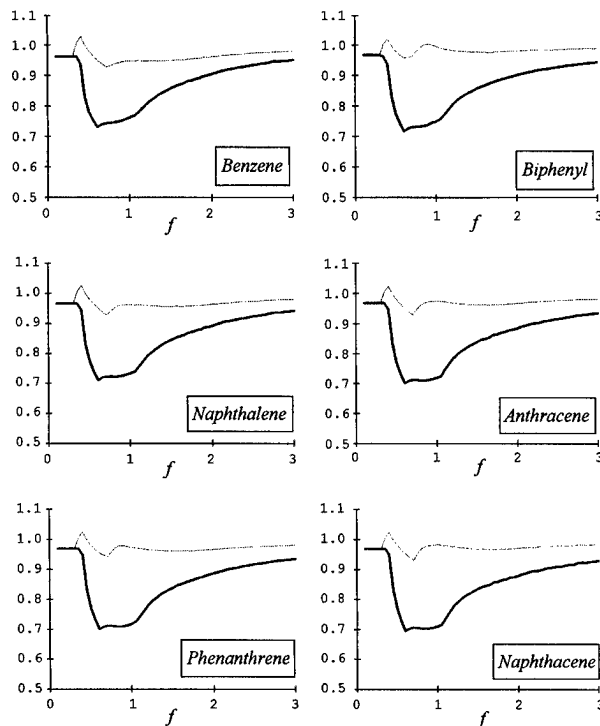


FIGURE 5. Relative globularity descriptors $q_m(f)$ (full line) and $q_M(f)$ (dotted line) for polycyclic aromatic hydrocarbons. (Planar benzenoid polycycles are virtually indistinguishable from benzene. Biphenyl shows the difference caused by a different pattern of spherical contacts around the C–C bond connecting the two rings.)

case, these two molecules will be said to be (q_m, q_M) -equivalent within a given range of scaling factors.

This notion can be further tested by studying other hydrocarbons with common local neighborhoods. Figure 5 compares the results for $q_m(f)$ and $q_M(f)$ in benzene, biphenyl, and a series of polycyclic aromatic hydrocarbons: naphthalene (2 fused benzenoid rings), anthracene and phenanthrene (3 fused benzenoid rings), and naphthacene (4 benzenoid rings fused in a row). Two observations can be made from Figure 5:

1. The $q_s(f)$ ($s = m, M$) values for benzene and the polycycles are virtually identical. In other words, as the molecular surfaces are scaled up, their properties are completely determined by the cyclic connectivity and by the occurrence of three nearest neighbors around each carbon atom.

2. The only noticeable difference in shape descriptors is found in $q_m(f)$ for biphenyl. This difference reflects the fact that four hydrogen atoms in biphenyl have a distinct neighborhood (the hydrogens are staggered about the C—C bond linking the two rings).

As indicated by observation 2, the notion of "local neighborhoods" should be understood as a region in space where an atomic sphere can "fuse" with others. This region is determined by nuclei close in space, and *not* just by simple bond connectivity. Depending on molecular structure and conformation, the effect of nonbonded atoms on the globularity can be important. This can be illustrated by studying nonplanar polycyclic hydrocarbons.

We have computed $q_m(f)$ and $q_M(f)$ for a number of planar polycycles and helicenes. For clarity, Figure 6 shows some of the key structural features of the molecules being compared. On the one hand, we have benzo[*a*]phenanthrene as a planar polycycle with 4 benzenoid rings in C_{2v} symmetry. If one more ring is added terminally, the molecule releases stress by becoming the nonplanar [5]helicene, with only C_2 symmetry (Fig. 6). If further rings are added in sequence, the molecule curls in

space and adopts a left-handed helical conformation. As an example, Figure 6 shows two views of [8]helicene. We should expect that these molecules belong to a different equivalence class of molecular shape than the planar polycycles.

By stacking benzenoid rings with every helical turn, helicenes introduce new atoms into the neighborhood of the "lower" rings. Accordingly, we find marked changes in relative globularity as the molecular surface is enlarged. From the selected results displayed in Figure 7, we make the following observations:

1. Benzo[*a*]phenanthrene and [5]helicene show similar behavior for $q_M(f)$, whereas the second minimum in $q_m(f)$ is slightly deeper in [5]helicene. These small differences are due to the fact that [5]helicene shows no ring stacking but only some close contacts between the terminal rings.
2. Once a turn of the helix is completed (e.g., in [8]helicene), $q_M(f)$ develops a *third maximum*. The height of this new maximum increases with the number of turns (cf. [14]helicene, which has two complete turns). This third maximum is due to the hydrogen–carbon and carbon–carbon contacts between spheres belonging to stacked rings, i.e., for neighbors along the helical axis.

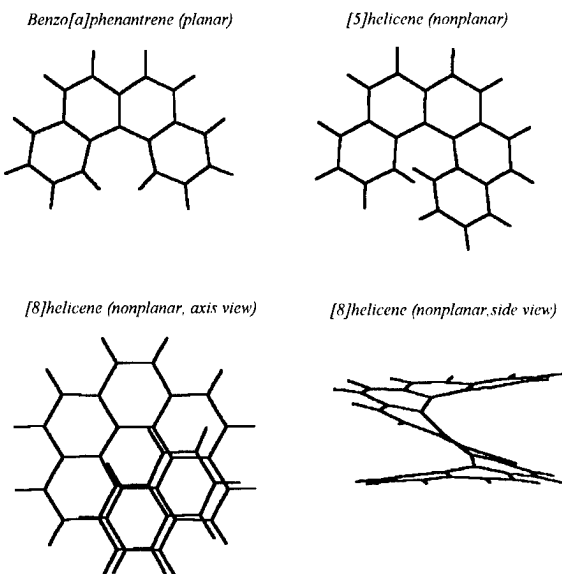


FIGURE 6. Equilibrium geometries for some planar and nonplanar aromatic polycycles. (Note that [5]helicene is nonplanar but exhibits few ring–ring contacts. In contrast, the full helical turn causes strong contacts between two stacked rings in [8]helicene.)

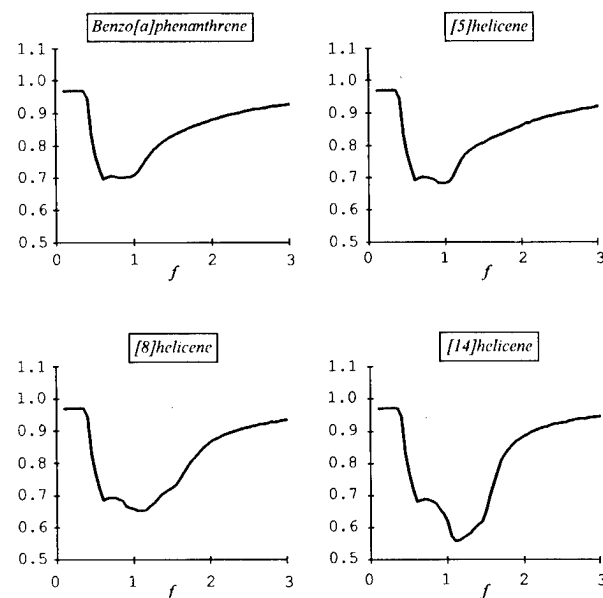


FIGURE 7. Relative globularity descriptors $q_m(f)$ (full line) and $q_M(f)$ (dotted line) for a planar benzenoid polycycle and a number of helicenes.

3. In helicenes with more than one helical turn, the descriptor $q_m(f)$ develops a deep second minimum. This second minimum is also due to changes in molecular surface area and volume caused by helical contacts between the atomic spheres of nonbonded atoms. The effect of molecular size on the $q_m(f)$ minimum is more marked than the effect on the $q_M(f)$ maximum.

In summary, the spherical contacts between nonbonded atoms can translate into important changes in the shape descriptors as a function of the scaling parameter. In linear hydrocarbons, these contacts exist but they are limited to second neighbors along the chain. In the case of stacking, these "distant" neighbor contacts are widespread. As a result, relative globularity descriptors correctly classify helicenes in a different molecular shape class than the planar polycycles. Similar differences could be expected in other molecules, particularly in flexible polymers. In this case, the shape of the molecular surfaces will vary differently upon scaling depending on whether we deal with "swollen" or "compact" polymer conformations.

Shape Descriptors for General Molecular Surfaces

The VDW surfaces of hydrocarbons can be naturally bound between the surfaces defined by assigning either ρ_{Hydrogen} or ρ_{Carbon} to all atoms. In molecules with at least three different atoms, the choice of the reference radii ρ_m and ρ_M is less clear. For the sake of simplicity, one could still use the same values employed for hydrocarbons, considering that carbon and hydrogen represent the extreme values of VDW radii among the common "organic" elements (i.e., H, C, O, N). We provide below some exploratory examples of the behavior of $q_m(f)$ and $q_M(f)$ for general molecules, using the scale of radii tested for hydrocarbons.

As an illustration, we have computed the relative globularity descriptors for some α -amino acids, in their neutral form (i.e., $\text{H}_3\text{N}-\text{CHR}-\text{COOH}$, where R is the side chain). The nuclear geometries are taken as the global minima derived with the molecular mechanics force field AMBER 3.0 [32], as implemented in the molecular modeling program HyperChem [31].

Figure 8 shows the results for glycine, alanine, valine, and leucine [with R : —H, —CH₃, —CH(CH₃)₂, and —CH₂CH(CH₃)₂, respectively]. The qualitative behavior of $q_m(f)$ and $q_M(f)$ is similar in all cases, although the values of the $q_M(f)$ maxima and $q_m(f)$ minima depend on the molecule. Not surprisingly, the differences in shape between valine and leucine are marginal.

A comparison between Figures 8 and 2 reveals also a close similarity between the shape description of these amino acids and some hydrocarbons. Whereas the $q_m(f)$ and $q_M(f)$ functions of glycine and alanine resemble those of propane and butane, the descriptors for valine and leucine resemble those of nonane and decane. These similarities indicate that the dominant shape features of their molecular surfaces are determined by the underlying presence of short saturated chains. Note that leucine and valine contain branched chains with 8 and 9 nonhydrogen atoms, respectively. Since short branches in hydrocarbons do not introduce large changes in spherical contacts, the coincidence between the three-dimensional shapes of the molecular surfaces of amino acids and some linear or branched hydrocarbons is not surprising.

However, the packing of amino acids in proteins presents the possibility of different shape features. In globular proteins, hydrophobic side chains will tend to group near the core, thus largely

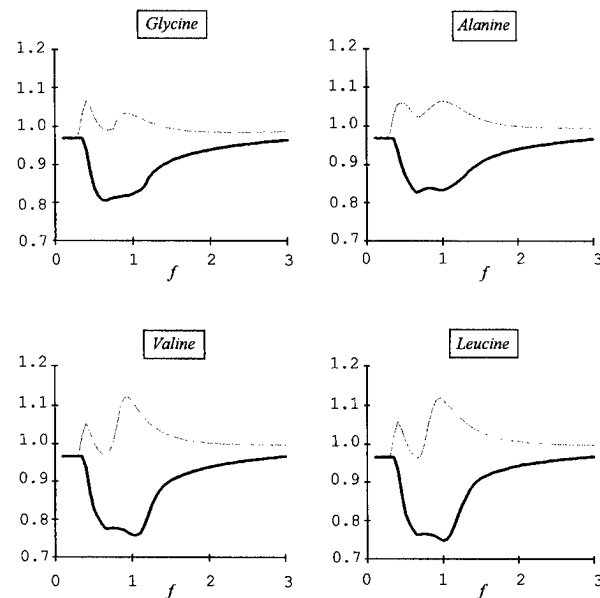


FIGURE 8. Relative globularity descriptors $q_m(f)$ (full line) and $q_M(f)$ (dotted line) for some α -amino acids, in neutral form.

increasing the contacts between neighboring atomic spheres. A comparable situation would not likely be found in long hydrocarbons, as the latter lack native structure and do not form stable hydrophobic cores.

To illustrate this idea, we have computed $q_m(f)$ and $q_M(f)$ in proteins. In this case, we have used the experimental geometries deposited in the Brookhaven Protein Data Bank (PDB) [33]. (Entries normally contain coordinates for all nonhydrogen atoms derived from X-ray diffraction or nuclear magnetic resonance (NMR) spectroscopy. On these structures, we have restored any "missing" hydrogens, assuming standard bond distances and bond angles. In the case of multimeric proteins, only the first monomer listed in the PDB entry was considered. On the resulting *complete* structures, we have computed surface areas, volumes, and shape descriptors.)

Figure 9 shows the results for three small proteins: 8PTI (bovine pancreatic trypsin inhibitor, with 56 residues), 2LZT (hen lysozyme, with 129 residues), and 1MBS (seal metmyoglobin, with 151 residues). Qualitatively, the results are quite similar for all proteins. This is an indication that *protein molecular surfaces consist of similar local neighborhoods*, despite differences in tertiary structure.

The $q_m(f)$ and $q_M(f)$ descriptors reveal some shape features not seen in other molecules. Most remarkable is the occurrence of a broad, intense maximum in $q_M(f)$. As seen in the previous section, the $q_M(f)$ maxima are dominated by the spherical contacts involving hydrogen atoms. In a compact protein, the contacts between nonbonded atomic spheres are more frequent due to the packing of amino acids. This effect is much larger than the one observed in helicenes.

In conclusion, some essential shape features about general molecular surfaces can be retrieved by using measures of relative globularity. These descriptors indicate how large-scale properties of the surface relate to the nature of the local neighborhoods about the atoms. As far as we know, these features are not captured by commonly used shape parameters.

Further Comments and Conclusions

The descriptors introduced in this work allow one to study subtle aspects of the molecular shape

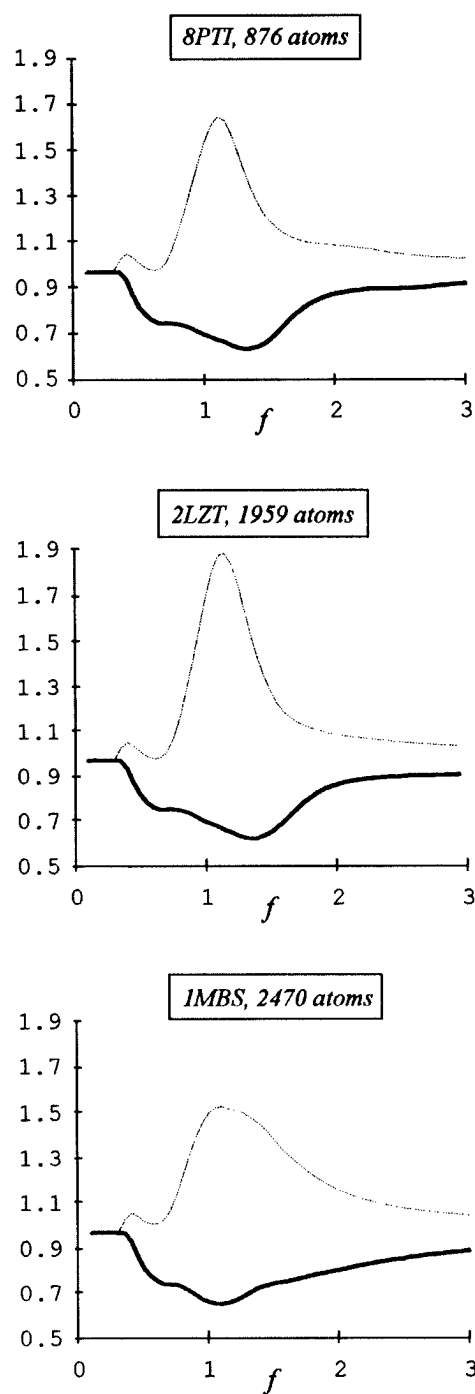


FIGURE 9. Illustrative results for globularity descriptors $q_m(f)$ (full line) and $q_M(f)$ (dotted line) in some selected proteins. (Proteins are labeled according to their entry code in the Brookhaven Protein Data Bank. The number of atoms listed includes all hydrogens "missing" from the X-ray structures. The latter have been added with a molecular modeling program [31].)

of a continuum of surfaces. Interestingly, although our geometrical descriptors characterize the entire continuum, their central properties are determined by the interrelation between local and global shape features.

For this reason, these descriptors may be suitable for applications other than similarity analysis between single molecules. We believe these descriptors are also well adapted for the study of molecular clusters, including liquids, glasses, and polymer networks. Note that, when modeling these systems, one normally studies clusters of increasing size and looks for intrinsic properties that remain invariant. Consequently, a detailed characterization of a given cluster is not particularly interesting because it is bound to be size dependent. Rather, one would be interested in describing the shape features associated with "local neighborhoods" around the atoms. In particular, the volume and surface area of the *intermolecular voids* are specially important for liquids [11]. As the clusters increase in size, their time-averaged local shape features should reach stability. The descriptors introduced in this work can be used to extract the state of these local neighborhoods from the data of the entire cluster.

In closing, we should mention that the present procedure can also be generalized to more realistic molecular surfaces. The extension of our analysis to electron densities is immediate, once we "label" the surfaces in an electron density continuum in terms of a single "scaling" parameter. In order to transform isodensity surfaces into a family of surfaces $F_f(\mathbf{r})$ similar to those in Eq. (2), we proceed as follows. Let $\rho(\mathbf{r})$ be the one-electron (or "marginal") electron density at a point \mathbf{r} in space. Let ρ^* be the maximum value of $\rho(\mathbf{r})$ anywhere in space. (This maximum will be located, normally, on the nucleus corresponding to the atom with the largest number of electrons.) As $\rho(\mathbf{r})$ approaches ρ^* , a constant electron density contour will comprise disjoint, spheroidal surfaces centered about the atoms. This situation is comparable to the limit $f \rightarrow 0^+$ in the scaled VDW surface. As the electron density decreases, some of these separate surfaces will "fuse." In the limit $\rho(\mathbf{r}) \rightarrow 0$, the isodensity surfaces become asymptotically spherical, a situation that is equivalent to the limit $f \rightarrow \infty$ in the scaled VDW surfaces. Accordingly, we can label a continuum of isodensity surfaces in terms of a

"scaling" parameter f as follows:

$$F_f(\mathbf{r}) = \{\mathbf{r} \in \Re^3 : \rho(\mathbf{r}) = \rho^*/(1 + f)\}, \quad f > 0. \quad (9)$$

By computing the molecular surface area and volume for an isodensity surface $F_f(\mathbf{r})$, we can define the reciprocal globularity $Q_0(f)$ as in Eq. (3). To compute *relative globularity* descriptors [Eq (4)], a number of choices are possible. For example, we can measure the globularity relative to a "virtual" electron density with minimal electron contributions to bonds. A relevant choice would be a total electron density obtained from a superposition of the electron densities of the *isolated* atoms at the *same* nuclear geometry. In this case, the $Q_m(f)$ computed with this virtual density would reflect the changes in surface area and volume brought about by the actual interaction between the atoms. The relative globularity descriptor defined as $q_m(f) = Q_0(f)/Q_m(f)$ could then be used to monitor the effects of local geometry on surface area or for high-quality molecular similarity assessments.

ACKNOWLEDGMENT

I thank N. D. Grant (Sudbury) for her comments on the manuscript. This work was supported by the Fonds de Recherche de l'Université Laurentienne (FRUL) and a grant from the Natural Sciences and Engineering Research Council (NSERC) of Canada.

References

1. A. Bondi, *Physical Properties of Molecular Crystals, Liquids, and Glasses* (Wiley, New York, 1968).
2. (a) B. Lee and F. M. Richards, *J. Mol. Biol.* **55**, 379 (1971). (b) F. M. Richards, *Annu. Rev. Biophys. Bioeng.* **6**, 151 (1977).
3. P. G. Mezey, in *Reviews in Computational Chemistry*, K. B. Lipkowitz and D. B. Boyd, Eds. (VCH, New York, 1990), Vol. 1, pp. 265–294.
4. M. L. Connolly, *Molecular Surfaces: A Review*, Network-Science, 1996 [<http://www.netsci.org/Science/Comp-chem/feature14.html>].
5. (a) W. J. Becktel and L. M. Rellick, in *Techniques in Protein Chemistry*, R. H. Angeletti, Ed. (Academic, San Diego, 1983). (b) L. M. Rellick and W. J. Becktel, *Biopolymers* **42**, 191 (1997).
6. P. G. Mezey, *Shape in Chemistry* (VCH, New York, 1993).
7. G. A. Arteca and P. G. Mezey, *J. Phys. Chem.* **93**, 4746 (1989).
8. G. A. Arteca, in *Reviews in Computational Chemistry*, K. B. Lipkowitz and D. B. Boyd, Eds. (VCH, New York, 1996), Vol. 9, pp. 191–253.

9. R. J. Speedy, J. Chem. Soc. Faraday Trans. II **76**, 693 (1980).
10. R. J. Speedy and H. Reiss, Mol. Phys. **72**, 999 (1991).
11. S. Sastry, D. S. Corti, P. G. Debenedetti, and F. H. Stillinger, Phys. Rev. E **56**, 5524 (1997).
12. S. Torquato, B. Lu, and J. Rubinstein, Phys. Rev. A **41**, 2059 (1990).
13. C. Hansch and A. Leo, *Exploring QSAR: Fundamentals and Applications in Chemistry and Biology* (ACS, Washington, DC, 1995).
14. C. Chothia, Nature **248**, 338 (1974).
15. P. L. Privalov and S. J. Gill, Adv. Protein Chem. **39**, 191 (1988).
16. E. Silla, I. Tuñón, and J. L. Pascual-Ahuir, J. Comp. Chem. **12**, 1077 (1991).
17. S. Grigoras, J. Comp. Chem. **11**, 493 (1990).
18. J. S. Murray, P. Lane, T. Brinck, K. Paulsen, M. E. Grice, and P. Politzer, J. Phys. Chem. **97**, 9369 (1993).
19. R. C. Mebane, C. D. Williams, and T. R. Rybolt, Fluid Phase Equilibria **124**, 111 (1996).
20. P. Politzer, J. S. Murray, and P. Flodmark, J. Phys. Chem. **100**, 5538 (1996).
21. A. Y. Meyer, J. Comp. Chem. **9**, 18 (1988).
22. M. L. Connolly, J. Appl. Crystallogr. **16**, 548 (1983).
23. M. L. Connolly, Science **221**, 709 (1983).
24. F. M. Richards, Meth. Enzymol. **115**, 440 (1985).
25. J. L. Pascual-Ahuir and E. Silla, J. Comp. Chem. **11**, 1047 (1990).
26. J. L. Pascual-Ahuir, E. Silla, and I. Tuñón, J. Comp. Chem. **15** 1127 (1994).
27. A. A. Bliznyuk and J. E. Gready, J. Comp. Chem. **17**, 962 (1996).
28. Y. N. Vorobjev and J. Hermans, Biophys. J. **73**, 722 (1997).
29. A. Gavezzotti, J. Am. Chem. Soc. **105**, 5220 (1983).
30. U. Burkert and N. L. Allinger, *Molecular Mechanics*, ACS Monograph 177 (ACS, Washington, DC, 1982).
31. HyperChem 4.0 for Windows, Hypercube Inc., Waterloo (Canada), 1994.
32. (a) S. J. Weiner, P. A. Kollman, D. A. Case, U. C. Singh, C. Ghio, G. Alagona, S. Profeta, Jr., and P. Weiner, J. Am. Chem. Soc. **106**, 765 (1984). (b) U. C. Singh, P. K. Caldwell, and P. A. Kollman, AMBER 3.0, University of California, San Francisco.
33. F. C. Bernstein, T. F. Koetzle, G. J. B. Williams, E. F. Meyer, Jr., M. D. Brice, J. R. Rogers, O. Kennard, T. Shimanouchi, and M. Tasumi, J. Mol. Biol. **112**, 535 (1977) [For updated information, see the PDB website at <http://www.pdb.bnl.gov>].

Approximations of the Mulliken Charges for the Oxygen and Silicon Atoms of Zeolite Frameworks Calculated with a Periodic Hartree–Fock Scheme

A. V. LARIN,* D. P. VERCAUTEREN

Institute for Studies in Interface Sciences, Laboratoire de Physico-Chimie Informatique, Facultés Universitaires Notre Dame de la Paix, Rue de Bruxelles 61, B-5000 Namur, Belgium

Received 21 February 1998; accepted 8 June 1998

ABSTRACT: Distributed multipole analysis (DMA) on the basis of periodic Hartree–Fock (PHF) calculations, using the CRYSTAL code, is applied to five different all-siliceous zeolite models: chabazite, gmelinite, merlinoite, montesommaite, and RHO. Mulliken charges of the framework atoms were calculated with a pseudopotential ps-21G* basis set for silicon and a 6-21G* basis for oxygen. The charge values of the silicon atoms were approximated by a simple one-dimensional function with respect to the average Si—O distance within the respective SiO_4 tetrahedra, whereas a two-dimensional function with respect to the average Si—O distance and the Si—O—Si angle was used for the oxygen atoms. Both dependences were then utilized to evaluate the Mulliken atomic charges of 10 other frameworks with a larger number of atoms per unit cell. The validity of such application is confirmed by comparison with results obtained through direct PHF calculation for all-siliceous mordenite. © 1998 John Wiley & Sons, Inc.
Int J Quant Chem 70: 993–1001, 1998

Key words: Mulliken charges; zeolite; periodic Hartree–Fock

*Permanent address: Laboratory of Molecular Beams, Department of Chemistry, Moscow State University, Vorob'evy Gory, Moscow, B-234, 119899, Russia.

Correspondence to: D. P. Vercauteren.

Contract grant sponsor: FNRS-FRFC.

Contract grant number: 9.4595.96.

Contract grant sponsor: Russian Foundation of Basic Researches.

Contract grant number: 96-03-33771.

Introduction

Aluminosilicate zeolite frameworks with a high Si/Al ratio, such as MCM-22 (Si/Al = 10–14), ZSM-5 (Si/Al = 20–50), Beta (Si/Al = 5–15), etc. constitute an important class of adsorbent and catalyst materials. The necessity to consider accurate electrostatic interactions to locate the preferential positions of an adsorbed species is now confirmed by direct ab initio Hartree–Fock calculations on systems such as the all-siliceous form of ZSM-5, i.e., silicalite [1]. All-siliceous forms are the simplest models which can be considered by three-dimensional (3D) periodic ab initio Hartree–Fock (PHF) computations and whose study could provide a deeper knowledge to simulate electrostatic interaction effects. The modeling of the behavior of an adsorbed molecule then requires the most accurate estimation of the field which is created only by the silicon and oxygen atoms of the all-siliceous frameworks (or mainly by these atoms within zeolites with high Si/Al ratio). Therefore, the largely used cluster embedded models require to consider the long-range interactions between the adsorbed molecule and the inert rest of the zeolite structure. In the case of embedded cluster models, which include a molecule near a cation or near a bridged hydroxyl group linked to the closest aluminum atom [2], the electrostatic long-range interactions have often been estimated as created by these last two types of framework atoms only.

A conventional way to evaluate the electrostatic field is through the derivation of the atomic multipole moments for the total host–guest system for which we can calculate the wave function. The distributed multipole analysis (DMA) scheme related to the atomic positions developed by Saunders et al. [3] allows to express these moments in terms of internal geometric coordinates. For the case of zeolite frameworks, the application of the DMA scheme was proposed first through ab initio computations of some zeolite models with a relatively small number of atomic orbitals (AO) per elementary unit cell (UC) considering basis sets of a relatively advanced level [4, 5]. More particularly, it allowed to derive simple analytical approximations of the calculated multipole moments with respect to some internal geometric characteristics of each atom, which interestingly can be

applied to other zeolites with a higher number of AOs per UC, those latter constituting most of the materials effectively used in various types of chemical catalytic processes.

In our previous works, the Mulliken charges (moments of zeroth order) were calculated with the ab initio Hartree–Fock linear combination of atomic orbital (LCAO) code CRYSTAL92 [6] for two types of periodic systems [4, 5]. One-dimensional expressions with respect to the average T–O distance (T = Al, P, Si) were then fitted to represent the Mulliken charges of the silicon atoms within all-siliceous structures [4] and of both the aluminum and phosphorus atoms within aluminophosphates (Al/P = 1) [5]. It has also been shown that various distortions of the TO_4 tetrahedra do not influence strongly the charge value of the T atoms. A two-dimensional type dependence was obtained for the Mulliken oxygen charges within all-siliceous analogs and a three-dimensional one for the Mulliken charges and dipolar atomic moments of oxygens within the aluminophosphate (ALPO) frameworks [5].

In order to verify our method of estimating the multipole moment dependences for any arbitrary siliceous zeolite or ALPO based on the approximate results obtained for structures with a relatively small number of AOs per UC, the behavior of both types of dependence of each multipole moment and their convergence need to be confirmed with different basis sets. To our knowledge, this has so far been discussed only for the Mulliken charges [7–9], but not for their dependences with the internal geometric characteristics of the respective atom.

In our previous study treating a series of all-siliceous zeolites [4], we confirmed the use of a same type of two-dimensional analytical dependence for the Mulliken oxygen charges and of a one-dimensional expression for the silicon charges with two basis sets, i.e., the STO-3G and a 6-21G type quality basis. In this study, we analyze the evaluation of their dependences with higher quality basis sets, including a split valence pseudopotential ps-21G* (Durant–Barthelat) on Si and 6-21G* on O, for 5 all-siliceous zeolites, i.e., chabazite (CHA), gmelinite (GME), merlinoite (MER), montesommaite (MON), and RHO. In total, this amounts of 6 different types of silicon atoms and 19 types of oxygens.

In the next section, we briefly discuss the basis sets together with the characteristics of the frameworks. In the third section, we present the fitting

of the atomic Si and O charges with respect to the internal geometric parameters using the dependences obtained previously [4, 5]. In the last section, the approximations using the herein computed parameters are applied to predict the Mulliken charges of 10 siliceous zeolites with a larger number of AOs per UC, for which the direct solution can hardly be achieved with the most modern available computing platforms and electronic structure codes. The validity of such an application is confirmed by comparison with available results obtained by direct PHF calculation for all-siliceous mordenite with a basis set of 6-21G* quality [10].

Theoretical Aspects

The theoretical bases for the solution of the Schrödinger electronic problem in three dimensions considering periodic boundary conditions have already largely been described in the literature [3, 6, 11, 12]. The choice of the siliceous structures was done on the basis of a relatively small number of atoms per UC, hence a reasonable number of two-electronic Coulomb and exchange integrals to evaluate. The characteristics of the 5 all-siliceous frameworks, which were treated with the CRYSTAL92 code, have been taken from the MSI database [13] (Table I). The characteristics of the other 10 all-siliceous forms whose charge values were predicted on the basis of the herein derived approximations are presented in Table II.

The pseudopotential Durant-Barthelat ps-21G* basis set on silicon atoms [26] and 6-21G* on

oxygens [27] with conventional exponents for the *d*-polarization functions, i.e., 0.5 and 0.92 a.u.⁻² for Si and O, respectively, was applied to all zeolites considered in Table I. An exponent value of 0.35 a.u.⁻² for the oxygen *d*-polarization function was optimized in the case of the MON zeolite, but we held the value of 0.92 a.u.⁻² providing acceptable computation limits for all 5 frameworks. No convergence could be reached for DAC and MON, whereas the other zeolites could not be treated with the ps-21G*(Si)/6-21G*(O) basis set because the number of atomic orbitals in their UC was too large.

Computations with the CRYSTAL92 code were carried out partly on an IBM RISC 6000 model 560 workstation (with 256 Mb of memory) and partly on an IBM 15-node (120 MHz) Scalable POWER-parallel platform (with 1 Gb of memory/CPU). For all cases, the thresholds for the calculations were fixed to 10⁻⁵ for the overlap Coulomb, the penetration Coulomb, and overlap exchange, to 10⁻⁶ and 10⁻¹¹ for the pseudo-overlap exchange, and to 10⁻⁵ for the pseudopotential series.

Approximation of the Mulliken Charges of the Si and O Atoms in Small Size Type Zeolites

Omitting *d*-polarization functions on the oxygen atom, we first wished to compare the quality of the basis sets chosen with available results of Apra et al. for the "Opt3" model of silico-chabazite [8]. The Mulliken total silicon charge 12.230 |*e*| calculated with the CRYSTAL92 code and ps-21G*

TABLE I
Symbol, number of different silicon and oxygen types, of total atoms, and of atomic orbitals (AO) per unit cell (UC) using the ps-21G*(Si) / 6-21G*(O) basis set, and symmetry group of the considered zeolite frameworks.^a

Name	Symbol ^b	<i>n</i> _{Si} / <i>n</i> _O	Atoms / UC	AO / UC	Symmetry group
Montesommaite	MON	1/3	24	328 ^d	I4 ₁ / amd
Chabazite ^c	CHA	1/4	36	492	R3c
Merlinoite	MER	2/6	48	656	Immm
Gmelinite	GME	1/4	72	984	P6 ₃ / mmc
RHO	RHO	1/2	72	984	Im3m

^aAll coordinates are from Ref. [13] if no other reference is given.

^bRef. [14].

^cRef. [6, 8].

^d368 for basis set 6-21G* on both atoms.

TABLE II
Symbol, number of different silicon and oxygen types, of total atoms, and of atomic orbitals (AO) per unit cell (UC) using the STO-3G basis set, and symmetry group of the zeolite frameworks whose charge distributions were predicted on the basis of the estimations with functions (1) and (2).

Name	Symbol ^a	$n_{\text{Si}}/n_{\text{O}}$	Ref.	Atoms / UC	AO / UC (STO-3G)	Symmetry group
Ferrierite	FER	4/8	15	54	342	I _{mmm}
ZSM-57	MFS	8/14	16	54	342	I _{mm2}
Mordenite	MOR	4/9	17	72	456	C _{m2} c ₁
ZSM-12	MTW	7/14	18	84	532	C ₂ /c
Mazzite	MAZ	2/6	19	108	684	P _{6₃} /mcm
VPI-5	VFI	2/6	20	108	684	P _{6₃} /mcm
ZSM-11	MEL	7/15	21	144	912	I _{4m2}
Beta	BEA	9/17	22	192	1216	P _{4,22}
NU-87	NES	17/34	23	204	1292	P _{2₁} /c
MCM-22	MCT ^b	8/12	24	216	1368	P _{6₃} /mmm
Silicalite	MFI	12/26	25	288	1824	Pnma

^aRef. [14].^bSymbol from Ref. [13].

basis coincides exactly with the value given in [8] (below for simplicity, we consider the difference between the number of electrons of the neutral atom, i.e., 14 |e| for Si and 8 |e| for O, and the Mulliken charge).

The PHF computation of the 5 all-siliceous frameworks allowed us to obtain the Mulliken charges with the ps-21G* basis set for 6 different types of silicon atoms and 19 types of oxygens (Table I). Then, a fitting of the Si charges (|e|) was made using a simple 1D expression with respect to the average Si—O distance $R = (\sum_{k=1}^4 R_{\text{Si}O_k})/4$ (Å) of each Si atom within its respective SiO₄ tetrahedron [4]:

$$Q_0^0(R) = a_1 e^{a_2(R - a_3)} \quad (1)$$

with $a_1 = 2.019$, $a_2 = -0.771$, and $a_3 = 1.517$ being obtained by fitting. For the oxygen charges (|e|), we fitted the calculated values with a 2D function depending on the average Si—O distance of each O atom $R' = (R_{\text{OSi}2} + R_{\text{OSi}1})/2$ (Å) and Si—O—Si angle (ϑ , radian) [5]:

$$Q_0^0(R', \vartheta) = b_1 e^{nR'} + b_2 e^{m(R' - R_0)} \cos(\vartheta - \vartheta_0) \quad (2)$$

with $b_1 = -1.373$, $n = -0.277$, $b_2 = 0.198$, $m = -0.595$, $R_0 = -0.139$, and $\vartheta_0 = 0.091$ being obtained by fitting. The root mean square deviation (RMSD) values for the approximate Mulliken charges obtained with the ps-21G* basis for the Si and O atoms are 0.40 and 1.23%, respectively. Function (2) leads to a better RMSD for the two

STO-3G and 8-31G(Si)/6-21G(O) basis sets, i.e., 1.57 and 0.77%, respectively, as compared to 2.0 and 1.2% presented earlier [4]. The positions of the calculated Si charge values (open circles) relative to the approximate function (1) is presented in Figure 1 together with the other results obtained with STO-3G (diamonds) and with a basis of 6-21G quality (triangles) [4]. One can remark a very slight variation of the slope of the new dependence (1) obtained for the different basis sets. But the principal conclusion is that the conservation of the same type of approximate functions with all three basis sets for both the Si and O atomic charges is clearly verified.

The quality of function (1) obtained here with only 6 silicon charge values needed to be tested. For this, we compared our results with those calculated with the 6-21G* basis [10] for siliceous mordenite. The closeness between the 6-21G* and ps-21G* basis sets suggests that dependence (1) corresponding to 6-21G* could be estimated using a simple shift by a constant value (vertical arrow in Fig. 1) from the charge values obtained with ps-21G* (Table III). Namely, a value of 0.223 |e| obtained as the difference between the Si charge values 2.102 (triangles in Fig. 1) and 1.879 |e| obtained for MON with the 6-21G* and ps-21G* basis, respectively. The average Si charge value 1.872 |e| evaluated with dependence (1) for the MOR framework was corrected accordingly to 2.095 |e| (corresponding to the average value over the 4 charges depicted by *) which nearly coin-

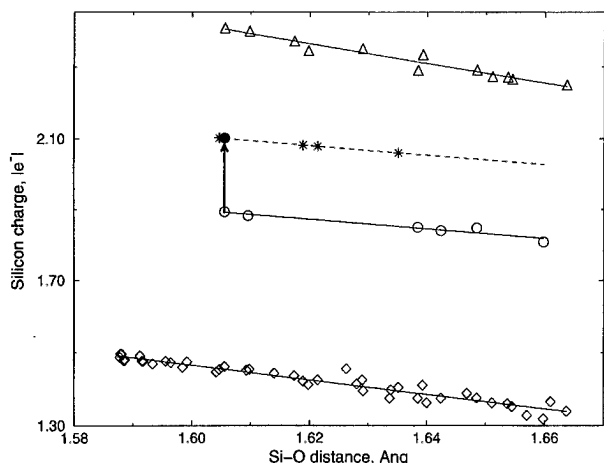


FIGURE 1. Mulliken Si charge values (in $|e|$) of various zeolite models calculated with: STO-3G (diamonds, Ref. [4]), 8-31G (Si) / 6-21G (O) (triangles, Ref. [4]), ps-21G* (empty circles), and 6-21G* (filled circles, MON zeolite) compared to the approximate dependence [eq. (1)] (solid lines) versus the average Si—O distance $R = (\sum_{k=1}^4 R_{\text{Si}O_k}) / 4$ (in Å). The dashed line corresponds to function (1) corrected for the 6-21G* level charges (stars) in the case of MOR. The vertical arrow depicts the difference between the charges of MON estimated with ps-21G* and 6-21G* basis sets.

cides with $2.09 |e|$ [10]. An analogous correction of the average O charge $-0.935 |e|$ for the same framework in the opposite direction by half of the upper estimated correction ($-0.112 |e|$) led to $-1.047 |e|$ also in agreement with the direct PHF calculated value $-1.04 |e|$ [10] (Table IV).

TABLE III
Mulliken silicon charges ($|e|$) for the MOR zeolite approximated via function (1) including the average Si—O distance $R = (\sum_{k=1}^4 R_{\text{Si}O_k}) / 4$ using the parameters fitted over the Mulliken charges calculated with ps-21G* for five smaller size type zeolites.

Type	R , Å	Q_0^0
2	1.6047	1.893
1	1.6189	1.874
4	1.6214	1.870
3	1.6352	1.851
Average		1.872
Correction ^a		0.223
Corrected		2.095
Calculated with 6-21G* basis set [10]		2.09

^aFrom the calculation with the MON zeolite (see text).

TABLE IV
Mulliken oxygen charges ($|e|$) for the MOR zeolite approximated via function (2) including the average Si—O distance $R' = (R_{\text{OSi}1} + R_{\text{OSi}2}) / 2$ and Si—O—Si angle (ϑ) using the parameters fitted over the Mulliken charges calculated with ps-21G* basis sets for five smaller size type zeolites.

Type ^a	R' , Å	ϑ , degree	$-Q_0^0$
7	1.5872	180.00	0.955
2	1.6060	158.00	0.942
3	1.6115	168.45	0.945
4	1.6116	144.37	0.931
5	1.6243	150.52	0.932
6	1.6295	137.26	0.920
1	1.6313	145.81	0.927
9	1.6373	146.80	0.926
8	1.6408	147.17	0.925
Average		0.935	
Correction ^b		0.112	
Corrected		1.047	
Calculated with 6-21G* basis set [10]		1.04	

^aNumbering from Ref. [10].

^bFrom the calculation with the MON zeolite (see text).

These results suggest that function (1) is precise enough despite the small number of charge values. It also proves the validity of a similar behavior of dependence (1) obtained with the ps-21G* and 6-21G* basis sets here applied. We hence conclude that functions [(1) and (2)] for the Si and O charges conserve their types with all three basis sets. However, on the other hand, this coincidence could be due to the relative short differences between the Si—O distances within the mordenite framework (stars in Fig. 1). Further studies would thus be useful to clearly ascertain the extrapolation of one dependence versus another corresponding to a different basis set.

Evaluation of the Mulliken Charges of the Si and O Atoms in Larger Size Zeolites

The good agreement obtained above between the calculated and approximate [functions (1) and (2)] charge values for the mordenite framework permits us to evaluate the charge distributions of some other all-siliceous zeolites. Moreover, this work is very useful considering the absence, to our

knowledge, of any data about the electrostatic field for most of the herein studied zeolite forms. Thus, we chose some zeolite forms whose UC sizes make the direct calculation with a periodic Hartree-Fock approach and an advanced basis set (like ps-21G*) either rather "expensive" or even nonrealistic. The simple charge evaluations with formulas (1) and (2) for the chosen zeolites can indeed be easily performed knowing the geometric parameters of all types of silicon (i.e., R) and oxygen (i.e., R' and ϑ) within the frameworks (Table V and VI).

TABLE V
Mulliken oxygen charges $Q_0^0(|e|)$ approximated with function (2) including the average Si—O distance
 $R' = (R_{\text{OSi}1} + R_{\text{OSi}2}) / 2$ (in Å) and Si—O—Si angle ϑ (in degree).

Type	Atom numb. ^a	R'	ϑ	$-Q_0^0$
BEA	16	1.6155	154.80	0.938
	4	1.6158	153.27	0.937
	2	1.6158	148.29	0.933
	9	1.6159	137.46	0.924
	8	1.6159	162.35	0.942
	15	1.6160	149.23	0.934
	12	1.6160	144.86	0.930
	5	1.6160	148.28	0.933
	17	1.6160	150.62	0.935
	6	1.6161	157.91	0.939
	13	1.6161	154.81	0.937
	1	1.6161	163.02	0.942
	10	1.6161	143.84	0.930
	3	1.6161	156.45	0.938
	14	1.6162	165.58	0.943
FER	7	1.6162	154.53	0.937
	11	1.6163	137.45	0.924
	6	1.5910	153.26	0.944
	5	1.5916	180.00	0.954
	4	1.5974	157.95	0.945
	8	1.6029	147.35	0.936
	7	1.6108	152.85	0.938
	2	1.6148	152.67	0.936
	1	1.6179	169.27	0.944
	3	1.6251	153.52	0.934
MAZ	6	1.6403	136.64	0.917
	2	1.6407	171.19	0.938
	3	1.6414	146.54	0.925
	4	1.6429	144.74	0.923
	5	1.6488	137.34	0.915
	1	1.6558	149.24	0.923
	1	1.4457	180.00	0.997
MCT	11	1.5194	157.04	0.966
	6	1.5632	164.50	0.958
	9	1.5874	159.45	0.948

TABLE V
(Continued)

Type	Atom numb. ^a	R'	ϑ	$-Q_0^0$
MEL	10	1.5952	143.22	0.935
	3	1.6093	136.21	0.925
	5	1.6225	180.00	0.945
	4	1.6323	145.83	0.927
	2	1.6409	142.13	0.921
	12	1.6458	145.82	0.923
	8	1.6482	151.18	0.926
	7	1.6502	159.31	0.931
	14	1.5578	165.13	0.959
	9	1.5619	158.57	0.955
	3	1.5800	150.96	0.945
	7	1.5855	151.92	0.944
	13	1.5871	165.27	0.951
	2	1.5895	146.59	0.939
	12	1.5983	145.64	0.936
	15	1.6006	160.43	0.945
MFS	6	1.6049	147.55	0.936
	1	1.6148	149.77	0.934
	8	1.6155	144.07	0.930
	4	1.6171	161.00	0.941
	11	1.6291	145.37	0.927
	10	1.6326	159.10	0.935
	5	1.7452	120.59	0.874
	8	1.5814	162.19	0.951
	3	1.5818	162.32	0.951
	2	1.5842	158.00	0.948
	6	1.5851	157.17	0.948
	4	1.5854	158.00	0.948
	13	1.5855	158.95	0.948
MTW	10	1.5898	154.93	0.945
	11	1.5916	149.55	0.941
	7	1.5938	148.56	0.939
	12	1.5944	147.58	0.939
	9	1.5955	147.69	0.938
	14	1.5961	146.67	0.937
	1	1.5981	145.40	0.936
	5	1.6043	145.13	0.934
	6	1.5641	144.77	0.945
	8	1.5673	155.57	0.952
MCT	2	1.5685	156.21	0.952
	13	1.5777	146.09	0.942
	3	1.5877	146.37	0.940
	14	1.5891	145.86	0.939
	10	1.5926	152.09	0.943
	12	1.5936	144.86	0.937
	5	1.6014	148.05	0.937
	7	1.6042	156.91	0.942
	4	1.6228	157.94	0.938
	1	1.6236	158.59	0.938
	11	1.6292	152.79	0.933
	9	1.6340	134.39	0.917

TABLE V
(Continued)

Type	Atom numb. ^a	R'	θ	-Q ₀ ⁰
VFI	4	1.4339	164.41	0.995
	1	1.5766	180.00	0.958
	3	1.6074	131.02	0.920
	6	1.6250	156.52	0.936
	2	1.6551	174.48	0.935
	5	1.7025	167.59	0.920
NES	3	1.5713	136.21	0.935
	17	1.5714	156.91	0.951
	18	1.5749	151.91	0.947
	19	1.5764	153.04	0.947
	16	1.5787	166.49	0.954
	2	1.5847	168.10	0.953
	20	1.5875	145.64	0.939
	7	1.5876	170.98	0.953
	22	1.5880	145.19	0.938
	27	1.5883	150.87	0.943
	10	1.5890	141.46	0.935
	8	1.5898	164.28	0.950
	5	1.5905	143.54	0.936
	23	1.5906	148.84	0.941
	14	1.5910	157.54	0.946
	9	1.5922	148.73	0.940
	29	1.5925	145.98	0.938
	33	1.5939	143.91	0.936
MFI	34	1.5942	156.27	0.944
	28	1.5948	143.37	0.935
	4	1.5949	154.64	0.943
	6	1.5953	160.26	0.946
	31	1.5956	137.72	0.930
	21	1.5963	140.07	0.932
	12	1.5982	149.76	0.939
	30	1.5995	140.75	0.932
	26	1.6016	146.65	0.936
	32	1.6020	164.84	0.947
	15	1.6101	145.91	0.933
	13	1.6107	158.69	0.941
	11	1.6191	146.81	0.931
	1	1.6287	167.36	0.940
	24	1.6301	157.03	0.935
	25	1.6358	150.57	0.929
	17	1.5378	149.61	0.956
	19	1.5538	171.81	0.963
	13	1.5608	175.00	0.962
	15	1.5620	157.40	0.954
	10	1.5704	159.94	0.953
	3	1.5724	174.01	0.958
	6	1.5736	162.62	0.954
	22	1.5788	149.49	0.944
	4	1.5808	162.14	0.951
	7	1.5811	156.40	0.948

TABLE V
(Continued)

Type	Atom numb. ^a	R'	θ	-Q ₀ ⁰
	12	1.5819	155.59	0.948
	2	1.5839	145.18	0.940
	11	1.5839	158.93	0.949
	14	1.5852	166.54	0.952
	21	1.5859	150.86	0.943
	24	1.5910	142.85	0.936
	25	1.5930	152.73	0.943
	9	1.5947	153.39	0.943
	5	1.5982	146.12	0.936
	26	1.6049	145.84	0.934
	18	1.6148	139.89	0.927
	8	1.6156	155.37	0.938
	20	1.6165	148.21	0.933
	1	1.6223	142.61	0.927
	23	1.6375	156.04	0.932
	16	1.6554	151.94	0.925

^aNumbering of the atoms from references given in Table II.**TABLE VI**
Mulliken silicon charges Q₀⁰(|e|) approximated with
function (1) including the average Si—O distance
 $R = (\sum_{k=1}^4 R_{SiO_k}) / 4$ (in Å).

Type	Atom numb. ^a	R	Q ₀ ⁰
BEA	8	1.6159	1.878
	5	1.6159	1.878
	1	1.6159	1.878
	9	1.6159	1.878
	4	1.6160	1.878
	3	1.6160	1.878
	6	1.6161	1.877
FER	2	1.6161	1.877
	7	1.6163	1.877
	4	1.5964	1.905
	3	1.5984	1.902
	1	1.6140	1.880
MAZ	2	1.6263	1.864
	2	1.6405	1.844
	1	1.6513	1.830
	7	1.5485	1.972
	6	1.5801	1.927
MCT	5	1.5861	1.919
	2	1.5914	1.912
	4	1.5932	1.909
	3	1.6071	1.890
	8	1.6268	1.863
	1	1.6604	1.818

TABLE VI
(Continued)

Type	Atom numb. ^a	R	Q_0^0
MEL	2	1.5617	1.954
	6	1.5783	1.930
	3	1.6048	1.893
	7	1.6050	1.893
	5	1.6170	1.876
	1	1.6290	1.860
	4	1.6596	1.819
	2	1.5948	1.907
VFI	1	1.6064	1.891
	4	1.5878	1.917
	2	1.5879	1.917
	7	1.5881	1.916
	1	1.5886	1.916
MFS	3	1.5912	1.912
	6	1.5915	1.911
	5	1.5917	1.911
	8	1.5933	1.909
	1	1.5677	1.945
MTW	3	1.5901	1.913
	2	1.5971	1.904
	7	1.5984	1.902
	5	1.6007	1.859
	6	1.6094	1.887
	4	1.6146	1.880
	8	1.5814	1.926
	2	1.5841	1.922
	14	1.5849	1.921
	15	1.5852	1.920
NES	1	1.5867	1.918
	3	1.5868	1.918
	16	1.5877	1.917
	7	1.5904	1.913
	6	1.5910	1.912
	17	1.5940	1.908
	9	1.5958	1.905
	11	1.6023	1.896
	12	1.6057	1.892
	10	1.6079	1.889
	13	1.6082	1.888
	4	1.6095	1.887
	5	1.6211	1.871

Two evident features of the charge estimations can be emphasized. First, all the charge values are strictly related to the spatial models referenced in Table II. Any optimization of these initial coordinate sets would alter the internal geometry and hence the charge distribution. But evidently, a

TABLE VI
(Continued)

Type	Atom numb. ^a	R	Q_0^0
MFI	8	1.5610	1.955
	6	1.5734	1.937
	10	1.5756	1.934
	11	1.5768	1.932
	4	1.5769	1.932
	5	1.5831	1.923
	3	1.5874	1.917
	9	1.5935	1.909
	7	1.5941	1.908
	1	1.6007	1.899
MTW	2	1.6137	1.881
	12	1.6257	1.864

^aNumbering of atoms from references given in Table II.

spatial optimization using empirical type potentials could lead to reasonable results if the dependences [(1) and (2)] are also taken into account. Second, the charge distribution obtained herein with the ps-21G* basis set can be corrected to the level corresponding to 6-21G* considering the simple shift by a constant value of 0.223 |e| for the Si charges and by -0.112 |e| for the O charges. Caution should, however, be taken if the zeolite system under study has very large Si—O bond lengths. The boundaries for the hopeful estimates applying the charge distribution shift may be evaluated from the extremal values of the Si—O distances for the 4 types of Si charges of mordenite, i.e., 1.605 to 1.635 Å.

Conclusions

The Mulliken charges for 5 all-siliceous zeolites, i.e., chabazite, gmelinite, merlinoite, montesommaite, and RHO, were calculated using the CRYSTAL92 code with a pseudopotential ps-21G* (Durant-Barthelat) basis set on the silicon and 6-21G* on the oxygen atoms. The Si charge values were approximated by a simple one-dimensional function with respect to the average Si—O distance within the respective SiO_4 tetrahedra. A two-dimensional function with respect to the average Si—O distance and Si—O—Si angle was con-

sidered for the O atomic charges. Both types of approximate functions were found to be appropriate to fit the charge values computed with this presently proposed basis set in the same way as it was shown previously for charges obtained with STO-3G and 6-21G sets [4, 5]. The comparison between the atomic charges computed directly with the CRYSTAL92 code for mordenite showed a good agreement with our estimations based on the two simple proposed analytical functions. This also allowed to evaluate the charge distribution for some zeolites with a larger number of atoms per elementary unit cell without the necessity to pass thru the direct solution of the electronic problem.

The knowledge of the Mulliken charges only provides a rather qualitative level for the evaluation of the electrostatic field [3, 9]; however, it is useful to estimate an order of magnitude for the electrostatic field of the considered host system and hence to propose preferential positions of any adsorbed molecule. We hope that the approximate charge (multipole moments of zeroth order) dependences for both the silicon and oxygen atoms could be completed later by similar types of approximate dependences for the hydrogen and aluminum atoms obtained on the basis of analogous fitting of the charges and higher order multipole moments for a series of H-form zeolite models with a small number of atomic orbitals per UC. The direct calculations of these moments with the CRYSTAL code are presently in progress.

ACKNOWLEDGMENTS

All authors wish to thank the FUNDP for the use of the Namur Scientific Computing Facility (SCF) Centre. They acknowledge financial support of the FNRS-FRFC, the "Loterie Nationale" for the convention no. 9.4595.96, IBM Belgium for the Academic Joint Study on "Cooperative Processing for Theoretical Physics and Chemistry," and MSI for the use of their software in the framework of the "Catalysis and Sorption" consortium. One of us (A.V.L.) acknowledges the PAI 3-49, "Science of Interfacial and Mesoscopic Structures," the "Services du Premier Ministre des Affaires Scientifiques, Techniques et Culturelles" of Belgium for his Postdoctoral stage and the Russian Foundation of Basic Researchers for financial support (Grant No 96-03-33771).

References

1. J. C. White and A. C. Hess, *J. Phys. Chem.* **97**, 8703 (1993).
2. M. Brändle and J. Sauer, *J. Mol. Cat.* **119**, 19 (1997).
3. V. R. Saunders, C. Freyria-Fava, R. Dovesi, L. Salasco, and C. Roetti, *Mol. Phys.* **77**, 629 (1992).
4. A. V. Larin, L. Leherte, and D. P. Vercauteren, *Chem. Phys. Lett.* **287**, 169 (1998).
5. A. V. Larin and D. P. Vercauteren, *J. Mol. Cat.*, submitted.
6. R. Dovesi, V. R. Saunders, and C. Roetti, *CRYSTAL92, An Ab Initio Hartree-Fock LCAO Program for Periodic Systems*, User Manual, 1992.
7. B. Silvi, P. D'Arco, and M. Causa, *J. Chem. Phys.* **93**, 7225 (1990).
8. E. Apra, R. Dovesi, C. Freyria-Fava, C. Pisani, C. Roetti, and V. R. Saunders, *Modelling Simul. Mater. Sci. Eng.* **1**, 297 (1993).
9. J. B. Nicolas and A. C. Hess, *J. Am. Chem. Soc.* **116**, 5428 (1996).
10. J. C. White and A. C. Hess, *J. Phys. Chem.* **97**, 6398 (1993).
11. C. Pisani, R. Dovesi, and C. Roetti, *Hartree-Fock Ab Initio Treatment of Crystalline Systems* (Springer, New York, 1988).
12. R. Dovesi, V. R. Saunders, C. Roetti, M. Causa, N. M. Harrison, R. Orlando, and E. Apra, *CRYSTAL95 User's Manual*, 1996.
13. (a) J. M. Newsam and M. M. J. Treacy, *ZeoFile—A Stack of Zeolite Structure Types, Catalysis and Sorption software and databases from Molecular Simulations Inc.*, San Diego, 1995; (b) J. M. Newsam and M. M. J. Treacy, *Zeolites* **13**, 183 (1993).
14. R. M. Barrer, *Pure Appl. Chem.* **51**, 1091 (1979).
15. P. A. Vaughan, *Acta Crystallogr.* **21**, 983 (1966).
16. J. L. Schlenker, J. B. Higgins, and E. W. Valyocsik, *Zeolites* **10**, 293 (1990).
17. A. Alberti, P. Davoli, and G. Vezzalini, *Z. Kristallogr.* **175**, 249 (1986).
18. C. A. Fyfe, H. Gies, G. T. Kokotailo, B. Marler, and D. E. Cox, *J. Phys. Chem.* **94**, 3718 (1990).
19. E. Galli, *Cryst. Struct. Commun.* **3**, 339 (1974).
20. J. W. Richardson, J. V. Smith, and J. J. Pluth, *J. Phys. Chem.* **93**, 8212 (1989).
21. C. A. Fyfe, H. Gies, G. T. Kokotailo, C. Pasztor, E. H. Strobl, and D. E. Cox, *J. Am. Chem. Soc.* **111**, 2470 (1989).
22. J. M. Newsam, M. M. J. Treacy, W. T. Koetsier, and C. B. deGruyter, *Proc. Roy. Soc. A420*, 375 (1988).
23. M. D. Shannon, J. L. Casci, P. A. Cox, and S. J. Andrews, *Nature* **353**, 417 (1991).
24. M. E. Leonowicz, J. A. Lawton, S. L. Lawton, and M. K. Rubin, *Science* **264**, 417 (1994).
25. D. H. Olson, G. T. Kokotailo, S. L. Lawton, and W. M. Meier, *J. Phys. Chem.* **85**, 2238 (1981).
26. P. Durand, J.-C. Barthelat, *Theor. Chim. Acta* **38**, 283 (1975).
27. W. J. Hehre, L. Radom, P. v. R. Schleyer, and J. A. Pople, *Ab Initio Molecular Orbital Theory* (Wiley, New York, 1986).

Structure and Properties of NH_5^{2+} : A Dication with Two 2-Electron 3-Center Bonds

JANET E. DEL BENE,¹ JOHN D. WATTS,² RODNEY J. BARTLETT²

¹*Department of Chemistry, Youngstown State University, Youngstown, Ohio 44555*

²*Quantum Theory Project, P.O. Box 118435, University of Florida, Gainesville, FL 32611*

Received 30 March 1998; revised 1 July 1998; accepted 13 July 1998

ABSTRACT: The dication NH_5^{2+} has been studied by state-of-the-art quantum chemical techniques. NH_5^{2+} is a square-based pyramid with C_{4v} symmetry. The apical H is bonded to N with a 2-electron covalent bond, while the other H atoms are bonded to N through degenerate 2-electron 3-center bonds. No other local minimum exists on the potential energy surface. A C_{2v} transition state linking equivalent C_{4v} structures is only 1.35 kcal mol⁻¹ higher in energy. The barrier to deprotonation is 26.4 kcal mol⁻¹. © 1998 John Wiley & Sons, Inc. Int J Quant Chem 70: 1003–1007, 1998

Key words: dications; coupled-cluster calculations; penta coordinate nitrogen

Introduction

Although the dication NH_5^{2+} has not been observed experimentally, it is an interesting species for several reasons.

1. NH_5^{2+} is isoelectronic with the pentahydrides BH_5^- and CH_5^+ , which have been the subjects of several theoretical [1] and experimental [2] studies.

Correspondence to: J. D. Watts.

Contract grant sponsor: U.S. Air Force Office of Scientific Research.

Contract grant number: AFOSR-F 49620-95-1-0130.

2. NH_5^{2+} continues the known isoelectronic series NH_2^- , NH_3 , and NH_4^+ , which we examined recently [3].
3. Olah and Rasul [4] have noted that NH_5^{2+} is isolobal with the gold complex $[(\text{C}_6\text{H}_5)_3\text{PAu}]_5\text{N}^{2+}$ [5], which features a trigonal bipyramidal nitrogen.

In this study we report a series of coupled-cluster calculations with extended basis sets on NH_5^{2+} . The aims of this work were to determine the structure and energetics of local minima and other important stationary points, to compute vibrational frequencies, which might be useful for future experimental studies, to analyze the bonding, and to compare with isoelectronic analogs. Since

experimental study of small multiply charged species is very difficult, high-quality calculations may provide useful data, as well as valuable insight into the bonding in these species. During the final stages of this work, Olah et al. [6] reported an attempt to generate NH_5^{2+} and $(\text{CH}_3)_4\text{NH}^{2+}$ by protonating NH_4^+ and $(\text{CH}_3)_4\text{N}^+$ in superacid media, but these were not successful. They also reported some ab initio calculations on NH_5^{2+} with the MBPT(2) and QCISD methods and 6-31G** and 6-311G** basis sets. These calculations are much less extensive than the ones reported in this work, but both studies lead to similar structures and energetics.

Computational Methods

Calculations were performed with the ACES II program [7, 8]. The methods used were second-order many-body perturbation theory [MBPT(2)] and coupled-cluster singles and doubles with non-iterative triples [CCSD(T)] [9]. The basis sets used were the augmented correlation-consistent polarized valence triple-zeta basis set (aug-cc-pVTZ) [10], and this basis set without diffuse functions on hydrogen (denoted aug'-cc-pVTZ). Geometries were determined at the MBPT(2)/aug-cc-pVTZ, CCSD(T)/aug-cc-pVTZ, and CCSD(T)/aug'-cc-pVTZ levels. Since the CCSD(T) structures of NH_5^{2+} computed with the two basis sets are essentially identical, only CCSD(T)/aug'-cc-pVTZ harmonic vibrational frequencies were computed. Geometry optimizations of BH_5 and CH_5^+ were performed at the MBPT(2)/aug-cc-pVTZ level for comparison. In all calculations, the 1s electrons of the nonhydrogen atom (B, C, or N) were not correlated. Spherical harmonic *d* and *f* functions were used throughout.

Results and Discussion

The potential energy surface of NH_5^{2+} was first searched at the MBPT(2)/aug-cc-pVTZ level. Stationary points were then further investigated at the CCSD(T)/aug-cc-pVTZ level. Unless otherwise stated, energy differences quoted below are from CCSD(T)/aug-cc-pVTZ calculations. The stationary points on the NH_5^{2+} surface are shown in Figure 1, and their total energies, along with those of several other relevant species, are given in Table I.

The lowest energy structure of NH_5^{2+} (**1**) has C_{4v} symmetry, and is a local minimum. The geometries of **1** obtained at three levels of theory are reported in Table II. The next lowest energy stationary point is **2**. This is a transition structure of C_{2v} symmetry, which is only 1.35 kcal mol⁻¹ higher in energy than **1**. Structure **2** is the saddle point for interchange of apical and basal hydrogen atoms in **1**, and so connects equivalent C_{4v} structures. A second transition state of importance is that for deprotonation of NH_5^{2+} , which is structure **3**. As expected, decomposition to $\text{NH}_4^+ + \text{H}^+$ is highly exothermic (98 kcal mol⁻¹), but the barrier to deprotonation is significant (26.4 kcal mol⁻¹). Elongation of one of the basal N—H bonds leads to the transition state for deprotonation. This transition state was expected to have only C_s symmetry, since elongation of one of the four equivalent N—H bonds reduces the symmetry to C_s . However, closer examination showed it to have C_{3v} symmetry, as reported by Olah et al. [6], which is the highest symmetry possible for $\text{NH}_4^+ + \text{H}^+$. Elongation of the apical N—H bond appears to lead to unfavorable homolytic dissociation, rather than deprotonation. The trigonal bipyramidal structure of NH_5^{2+} (**4**) is only 2.7 kcal mol⁻¹ higher in energy than **1**, but it is neither a local minimum nor a transition state. It has a doubly degenerate imaginary frequency. This mode leads to the C_{4v} structure, the two axial H atoms of **4** become basal H atoms in **1**, and one of the equatorial H atoms in **4** becomes the apical H atom in **1**. Structure **4** provides another pathway for interchange of apical and basal H atoms of **1**.

In the equilibrium structure of NH_5^{2+} (**1**), four of the H atoms (H_b) are at the base of a pyramid, and the fifth H atom (H_a) is at the apex. All of the N—H distances are similar. The N— H_a distance is slightly smaller than the N— H_b distance. The shortest H—H distance is 1.46 Å, which is the distance between adjacent basal H atoms. By no means, then, is NH_5^{2+} a complex between NH_5^{2+} and H_2 . What, therefore, is the bonding in C_{4v} NH_5^{2+} ? A qualitative and plausible description can be obtained by examining the occupied molecular orbitals (MOs). The most stable valence MO in the MO in the C_{4v} structure has a_1 symmetry and is essentially the 2s N orbital, but is largely non-bonding. Higher in energy are the degenerate *e* orbitals, which form the bonds between the N and the four equivalent H_b atoms. If one pair of H_b atoms lies along the *x* axis and the other along the

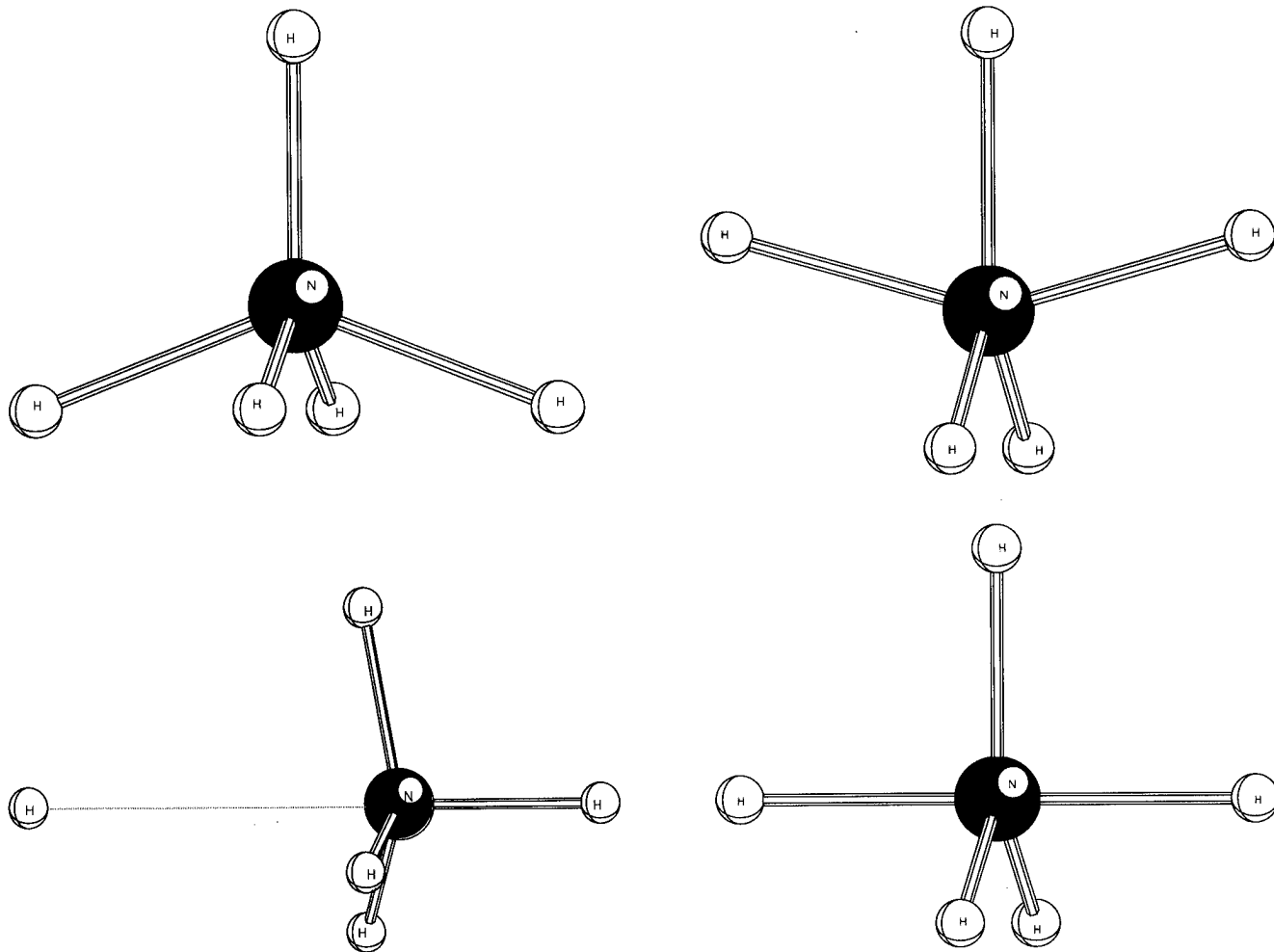


FIGURE 1. Four stationary points on the NH_5^{2+} potential energy surface. The point group symmetries of **1**, **2**, **3**, and **4** are C_{4v} , C_{2v} , C_{3v} , and D_{3h} , respectively.

y axis, one *e* orbital consists largely of an N p_x orbital overlapping with an antisymmetric combination of a pair of H_b *s* orbitals, and the other is of the same type, but with the N p_y orbital and the *s* orbitals of the other pair of H_b atoms. Since the N

atom lies 0.4 Å above the base of the pyramid (Table II), the bonds between the N and basal H atoms may be described as two bent 2-electron, 3-center bonds. The highest occupied MO, which is almost degenerate with the *e* MOs, has a_1 symme-

TABLE I
Total energies (Hartrees) and relative energies (kcal mol^{-1}) of stationary points **1**, **2**, **3**, and **4** of NH_5^{2+} and some other relevant species.^a

	Symmetry	MBPT(2)	CCSD(T)
NH_5^+ (1)	C_{4v}	-56.64071 (0.0)	-56.66145 (0.0)
NH_5^{2+} (2)	C_{2v}	-56.63842 (1.4)	-56.65930 (1.3)
NH_5^{2+} (3)	C_{3v}	-56.59862 (26.4)	-56.61935 (26.4)
NH_5^{2+} (4)	D_{3h}	-56.63959 (2.6)	-56.65720 (2.7)
NH_4^+	T_d	-56.79615 (-97.5)	-56.81802 (-98.2)
NH_3^+	D_{3h}	-55.22365	-55.24923
H_2	$D_{\infty h}$	-1.16502	-1.17264

^a Energies obtained with the aug-cc-pVTZ basis set.

TABLE IIDistances (\AA) and angles ($^\circ$) in $C_{4v} \text{NH}_5^{2+}$.

	MBPT(2) / aug-cc-pVTZ	CCSD(T) / aug-cc-pVTZ	CCSD(T) / aug'-cc-pVTZ
$r(\text{N}-\text{H}_a)^a$	1.0517	1.0524	1.0522
$r(\text{N}-\text{H}_b)^b$	1.1068	1.1074	1.1072
$r(\text{N}-\text{X})^c$	0.4063	0.4068	0.4066
$r(\text{H}-\text{H})^d$	1.4559	1.4566	1.4564
$\theta(\text{H}_a \text{NH}_b)^e$	111.5	111.6	111.5

^aThe distance from N to the apical H atom (H_a).^bThe distance from N to one of the basal H atoms (H_b).^cThe perpendicular distance from N to the basal plane.^dThe distance between adjacent basal H atoms.^eThe $\text{H}_a \text{NH}_b$ angle.

try and constitutes the bonding MO between the N and the apical H atom.

The bonding in $C_{4v} \text{NH}_5^{2+}$ contrasts strongly with that in BH_5 and CH_5^+ . BH_5 is best described as a species in which H_2 is attached to an almost unperturbed BH_3 molecule, with the complex stabilized by overlap of the H_2 bonding orbital and the empty p orbital on BH_3 . At the MBPT(2)/aug-cc-pVTZ level, the H_2 bond length in BH_5 is 0.79 \AA , compared with 0.74 \AA in free H_2 . Similarly, CH_5^+ can be described as a complex between CH_3^+ and H_2 , but in this case the interaction is stronger, and the H—H distance (0.98 \AA) is significantly larger than in free H_2 . That the nature of the bonding in NH_5^{2+} is unlike that in BH_5 and CH_5^+ is further illustrated by a comparison of the energies required to remove H_2 . In the series BH_5 , CH_5^+ , NH_5^{2+} , the energy for removal of H_2 increases considerably, as expected. At the MBPT(2)/aug-cc-pVTZ level of theory, ΔH° val-

ues for the reactions $\text{BH}_5 \rightarrow \text{BH}_3 + \text{H}_2$, $\text{CH}_5^+ \rightarrow \text{CH}_3^+ + \text{H}_2$, and $\text{NH}_5^{2+} \rightarrow \text{NH}_3^+ + \text{H}_2$ are 0.6, 43.7, and 115.5 kcal mol⁻¹, respectively. Are there stable C_{4v} structures for BH_5 and CH_5^+ and how do these compare with the equilibrium C_s structures? At MBPT(2)/aug-cc-pVTZ, C_{4v} structures of BH_5 and CH_5^+ are 18 and 3 kcal mol⁻¹ less stable than the C_s structures and are not local minima.

CCSD(T)/aug'-cc-pVTZ and MBPT(2)/aug-cc-pVTZ harmonic frequencies and infrared intensities for the C_{4v} structure of NH_5^{2+} are given in Table III, along with approximate descriptions of the normal modes. There are no low-frequency vibrational modes in NH_5^{2+} . This suggests that if this dication could be formed, it should be stable at low temperature. Moreover, the lowest frequency mode does not lead to decomposition. Rather, it reduces the symmetry to C_{2v} , and is the initial motion toward the C_{2v} transition state for exchange of apical and basal H atoms. The most

TABLE IIIMBPT(2) / aug-cc-pVTZ and CCSD(T) / aug'-cc-pVTZ harmonic frequencies (cm⁻¹) and infrared intensities (km mol⁻¹) for $C_{4v} \text{NH}_5^{2+}$.^a

Symmetry	MBPT(2)		CCSD(T)		Description
	ω	I	ω	I	
b_2	620	0	624	0	Antisymmetric $\text{H}_a \text{NH}_b$, bend
e	674	930	643	936	$\text{H}_b \text{NH}_b$ “rocking” motion
a_1	1352	266	1352	263	Symmetric $\text{H}_a \text{NH}_b$ bend (“umbrella” mode)
e	1536	75	1538	77	$\text{H}_a \text{NH}_b$ bend
b_1	1627	0	1618	0	In-plane $\text{H}_b \text{NH}_b$ bend (“scissor”)
b_2	2369	0	2368	0	Antisymmetric N—H _b stretch
e	2653	2041	2654	1963	N—H _b stretch
a_1	2755	148	2755	143	Symmetric N—H _b stretch
a_1	3146	471	3144	441	N—H _a stretch

^a H_a and H_b are the apical and basal H atoms.

intense band in the infrared spectrum of NH₅²⁺ is predicted to occur around 2650 cm⁻¹. This band is due to a degenerate antisymmetric stretching mode involving the basal H atoms and N. This mode reduces the symmetry to C_s, which is the initial motion along the pathway leading to deprotonation.

Finally, it should be noted that although C_{4v} NH₅²⁺ is a local minimum, exchange of hydrogen atoms is likely to be rapid, as the transition state is of low energy and tunneling may be important. Accordingly, except on very short time scales, the H atoms will be effectively equivalent. Some of these features of the behavior of CH₅⁺ have previously been noted [1(d), (e)], and there have been a few dynamical studies of that system [11]. Unlike CH₅⁺, however, NH₅²⁺ does not have any very low vibrational frequencies.

ACKNOWLEDGMENTS

This work has been supported by the U.S. Air Force Office of Scientific Research (Grant No. AFOSR-F49620-95-1-0130). The Ohio Supercomputer Center is thanked for provision of facilities for the development of the ACES II program system and for some of the calculations. Kenneth J. Wilson is thanked for preparing the figures.

References

- (a) J. F. Stanton, W. N. Lipscomb, and R. J. Bartlett, *J. Am. Chem. Soc.* **111**, 5173 (1989). (b) P. R. Schreiner, H. F. Schaefer III, and P. von R. Schleyer, *J. Chem. Phys.* **101**, 7625 (1994). (c) J. D. Watts and R. J. Bartlett, *J. Am. Chem. Soc.* **117**, 825 (1995). (d) P. R. Schreiner, S.-J. Kim, H. F. Schaefer III, and P. von R. Schleyer, *J. Chem. Phys.* **99**, 3716 (1993). (e) H. Müller, W. Kutzelnigg, J. Noga, and W. Klopper, *J. Chem. Phys.* **106**, 1863 (1997).
- (a) T. J. Tague and L. Andrews, *J. Am. Chem. Soc.* **116**, 4970 (1994). (b) D. W. Boo and Y. T. Lee, *Chem. Phys. Lett.* **211**, 358 (1993). (c) D. W. Boo and Y. T. Lee, *J. Chem. Phys.* **103**, 514 (1995).
- R. J. Bartlett, J. E. Del Bene, S. A. Perera, and R. P. Mattie, *J. Mol. Struct. (THEOCHEM)* **400**, 157 (1997).
- G. A. Olah and G. Rasul, *J. Am. Chem. Soc.* **118**, 12922 (1996).
- A. Grohmann, J. Riede, and H. Schmidbaur, *Nature* **345**, 140 (1990).
- G. A. Olah, A. Burrichter, G. Rasul, and G. K. S. Prakash, *J. Am. Chem. Soc.* **119**, 4594 (1997).
- J. F. Stanton, J. Gauss, J. D. Watts, W. J. Lauderdale, and R. J. Bartlett, *Int. J. Quant. Chem. Symp.* **26**, 879 (1992).
- ACES II is a program product of the Quantum Theory Project, University of Florida. Authors: J. F. Stanton, J. Gauss, J. D. Watts, M. Nooijen, N. Oiphant, S. A. Perera, P. G. Szalay, W. J. Lauderdale, S. R. Gwaltney, S. Beck, A. Balková, D. E. Bernholdt, K.-K. Baeck, P. Rozyczko, H. Sekino, C. Huber, and R. J. Bartlett. Integral packages included are VMOL (J. Almlöf and P. R. Taylor); VPROPS (P. R. Taylor); ABACUS (T. Helgaker, H. J. Aa. Jensen, P. Jørgensen, J. Olsen, and P. R. Taylor).
- (a) G. D. Purvis III and R. J. Bartlett, *J. Chem. Phys.* **76**, 1910 (1982). (b) M. Urban, J. Noga, S. J. Cole, and R. J. Bartlett, *J. Chem. Phys.* **83**, 4041 (1985). (c) K. Raghavachari, G. W. Trucks, J. A. Pople, and M. Head-Gordon, *Chem. Phys. Lett.* **157**, 479 (1989).
- (a) T. H. Dunning, Jr., *J. Chem. Phys.* **90**, 1007 (1989). (b) R. A. Kendall, T. H. Dunning, Jr., and R. J. Harrison, *Ibid.*, **96**, 6796 (1992).
- (a) P. R. Bunker, *J. Mol. Spectrosc.* **176**, 297 (1996). (b) D. Marx and M. Parrinello, *Nature* **375**, 216 (1995). (c) M. Kolbuszewski and P. R. Bunker, *J. Chem. Phys.* **105**, 3649 (1996).

C_{60} Carbyne Knots (from O_1 to 6_3): Theoretical NMR Spectra

JAN CZ. DOBROWOLSKI,^{1,2} ALEKSANDER P. MAZUREK²

¹*Industrial Chemistry Research Institute, 8, Rydygiera Street, 01-793 Warsaw, Poland*

²*Drug Institute, 30-34, Chełmska Street, 00-725 Warsaw, Poland*

Received 21 February 1998; revised 3 June 1998; accepted 6 June 1998

ABSTRACT: The structure, stability, and theoretical ^{13}C -NMR spectra of nonlinear C_{60} carbon clusters of the carbyne type have been estimated by ab initio calculations. Semiempirical AM1 calculations have shown the knot-cycle energy difference to increase with the number of knot crossings and to decrease with the number of atoms constituting the molecule. Some C_{60} carbyne prime knots belong to the following symmetry point groups: D_{30h} for cycle, D_3 for trefoil, C_1 for figure eight (but S_4 for the C_{64} figure eight), C_2 for cinquefoil and the other five-crossing knot, and C_1 for six crossing knots. Knot symmetry and the calculated ^{13}C -NMR qualitative spectra provide the basis for experimental identification of the knotted carbyne structures. © 1998 John Wiley & Sons, Inc. Int J Quant Chem 70: 1009–1015, 1998

Key words: ab initio; carbon allotrope; carbyne; ^{13}C -NMR; topological isomerism; knot

Introduction

Knot theory has been developed by mathematicians and physicists since the 18th century [1–3], and although knotted chemical structures are still bizarre for chemists, several DNA knots are already well known and well characterized [4–18]. Knotted structures have also been considered in polymer science [19–23]. Knots, links, and various other topological isomers have been discussed in monographs on chemical conformation and chirality [24].

Correspondence to: J. Cz. Dobrowolski.

Contract grant sponsor: Drug Institute, Warsaw.

Carbynes, that is, carbon allotropes with pure sp -hybridization, were expected to be synthesized in the last quarter of the 19th century [25, 26] and the first quarter of the 20th century [27]. Then, in the 1950s, small carbon molecules (up to C_8) were identified by mass spectrometry [28–30] and studied theoretically [31, 32]. Now, the spectroscopy of small carbon clusters (including carbynes) is becoming a field of increasing interest [33–40]. Carbynes are considered to be chainlike carbon allotropes [41, 42], likely to occur in interstellar dust [43]. Those with even numbers of C atoms prefer the cycle to the linear chain [44–46] and are better described as $(C \equiv C -)_n$ rather than as $(C = C =)_n$ [47, 48]. Interaction of a cyclic carbyne with lanthanum has recently been observed [49] and stud-

ied theoretically [50–53]. We have studied cyclic, knotted (trefoils), and linked carbyne compounds [54, 55] and introduced the name *cycarbynes* for unknotted cyclic carbynes, *knocarbynes* for knotted carbynes, and *catecarbynes* for carbyne links. We have also proposed [55] supplementing the knocarbynes and the cycarbynes names with the topological symbol [56] denoting the topological type of knot or link.

So far, several knots and various other topological (carbon) isomers have been described in general terms of mathematical chemistry [57–66]. We have shown [54, 55] that the energy difference between 3_1 knotted (trefoil) and 0_1 unknotted (cyclic) C_n carbyne structures ($C \equiv C -$)_{*n*} diminishes as *n* increases and should become negligible at $n \approx 150$. The theoretical IR and NMR spectra of C_{30} , C_{40} , C_{50} , and C_{60} cycarbynes and trefoil 3_1 knocarbynes [54] (cyclic and knotted carbynes) and also NMR theoretical spectra of two C_{60} catecarbynes, that is, carbyne links of the C_{30} and C_{20} carbon rings, 2_1 catecarbyne ($C_{30}C_{30}$), and 6_2^3 catecarbyne ($C_{20}C_{20}C_{20}$) (Borromean rings) [55], show how such topological isomers can be identified and distinguished experimentally.

This article sets out to describe the structure, energetics, and theoretical ^{13}C -NMR spectra of C_{60} knocarbynes endowed with not more than six crossings. Comparison of the calculated spectral properties with those of C_{60} fullerene provides the basis for experimental identification of C_{60} knotted structures, which may have implications in interstellar dust spectroscopy.

Computations

Preliminary molecular modeling, that is, structure building and AM1 optimization, was performed using the *Spartan 5* package of programs with a graphical interface [67]. The ab initio calculations were carried out with the *Gaussian 94* [68] system of programs. Both programs were executed on SGI computers. Full optimization was done at the HF/STO-3G//HF/STO-3G level. Theoretical ^{13}C -NMR chemical shifts were calculated using the CHF-GIAO approach [69] based on the HF/DZP-HB single-point calculations for both the HF/STO-3G and AM1-optimized structures of the molecules (where DZP-HB denotes the double-zeta DZP-CGTO basis of Hansen and Bouman [70] composed for carbon atoms of (721/221/1) AO con-

tracted to [3s3p1d]). The double-zeta basis set [70] used here has already been shown to be efficient for chemical-shift calculations [71–75].

Results and Discussion

A schematic representation of the knots studied and their optimized ab initio structures are shown in Figure 1.

ENERGETICS—ENERGY DIFFERENCE:

Cyclic versus Knotted Structures

We have shown the energy difference between 3_1 knotted (trefoil) and 0_1 unknotted (cyclic) C_n carbynes to diminish as *n* is increased and have estimated that it should become negligible at $n \approx 150$ [54]. The semiempirical AM1 heats of formation for the cycle and the knot-cycle heat-of-formation differences for the first seven carbyne prime knots (i.e., 3_1 , 4_1 , 5_1 , 5_2 , 6_1 , 6_2 , and 6_3) for the molecules composed of 40, 50, 60, 70, 80, 90, and 100 carbon atoms are listed in Table I and presented graphically in Figure 2. The energy differences between the knotted and cycle carbyne structures decrease as the number of carbon atoms is increased; for the C_{100} molecule, the differences range from only 50 to 200 kcal/mol for trefoil and the 6_3 carbyne knot, respectively. Moreover, the AM1 energy differences were consistent with the HF/STO-3G values and the basis-set extension together with inclusion of correlation effects remarkably reduced the difference for the trefoil [54]. This results from the decrease in the structural strain both in cyclic and knotted carbynes, especially for the latter. For six-crossing C_{60} knocarbynes, for which the structural strain is large, the AM1 energy predictions agree less with those calculated at the HF/DZP-HB//HF/STO-3G level (Table I). Obviously, as the number of C atoms in knocarbynes is increased, the degree of packing and the strength of repulsive interactions decrease in the vicinity of the crossings. The increase in strains with the increasing number of knot crossings can be read from Figure 2. Indeed, for C_{40} carbynes, only cycle, trefoil, figure eight, and cinquefoil knocarbynes are stable at the AM1 level. Then, for the C_{50} , C_{60} , and C_{70} structures, the energy increases in line within the knot-type series, except for the 6_1 knocarbynes, for which two stable forms were found.

C₆₀ CARBYNE KNOTS (FROM 0₁ TO 6₃)

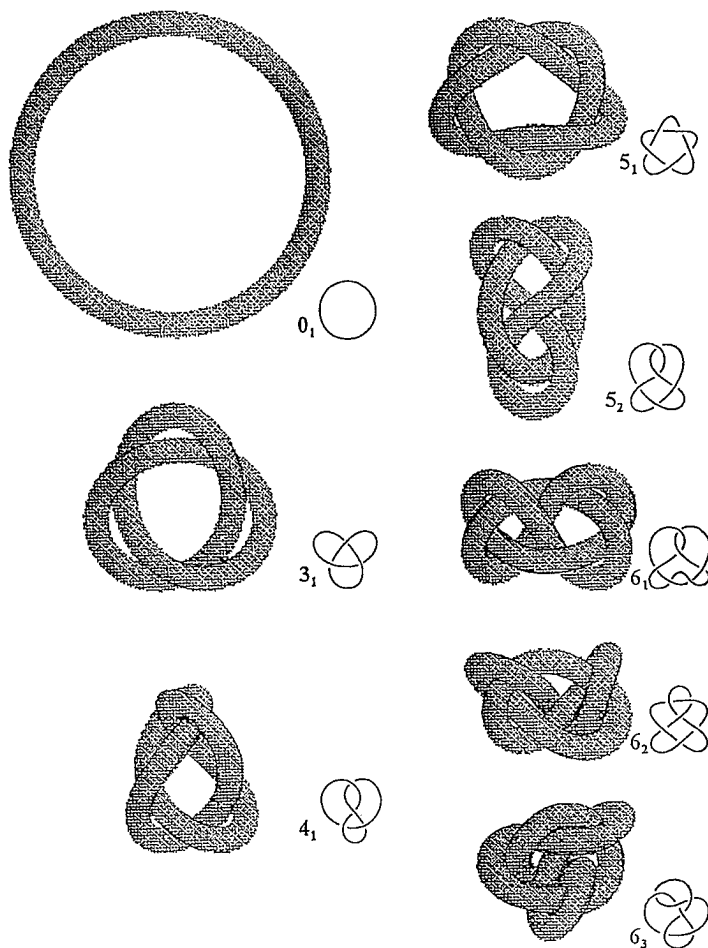


FIGURE 1. A schematic representation of the knots studied and their optimized ab initio structures.

TABLE I
AM1 heat-of-formation for cyclic carbynes and knot cycle heat-of-formation difference (kcal / mol) for carbynes with 40, 50, ..., 100 carbon atoms.

No. C atoms	Topological type of carbyne molecule							
	0 ₁	3 ₁	4 ₁	5 ₁	5 ₂	6 ₁	6 ₂	6 ₃
40	1059.44	231.38	544.85	1067.97	nc	nc	nc	nc
50	1307.31	145.59	308.02	502.00	554.48	1152.42 (nc) ^a	1079.75	1169.35
	1557.73	106.58	210.96	320.27	341.31	606.45 (566.78) ^a	577.87	622.69
60	2242.194032 ^b	104.51	202.88	307.70	334.28	669.91	637.74	695.01
	2270.637542 ^c	98.16	189.00	301.41	329.66	673.35	647.23	699.36
70	1809.57	84.62	162.43	228.45	241.80	414.53 (382.37) ^a	390.29	417.99
80	2062.32	70.28	134.32	178.45	186.76	283.07 (283.21) ^a	289.55	308.27
90	2315.66	60.12	115.26	147.42	154.14	223.82	230.10	241.90
100	2569.43	52.52	101.09	122.97	132.35	185.03	192.41	200.55

nc, not converged.

^aTwo different conformers are observed.

^bRHF/STO-3G // RHF/STO-3G calculations.

^cHF/DZP-HB // HF/STO-3G calculations.

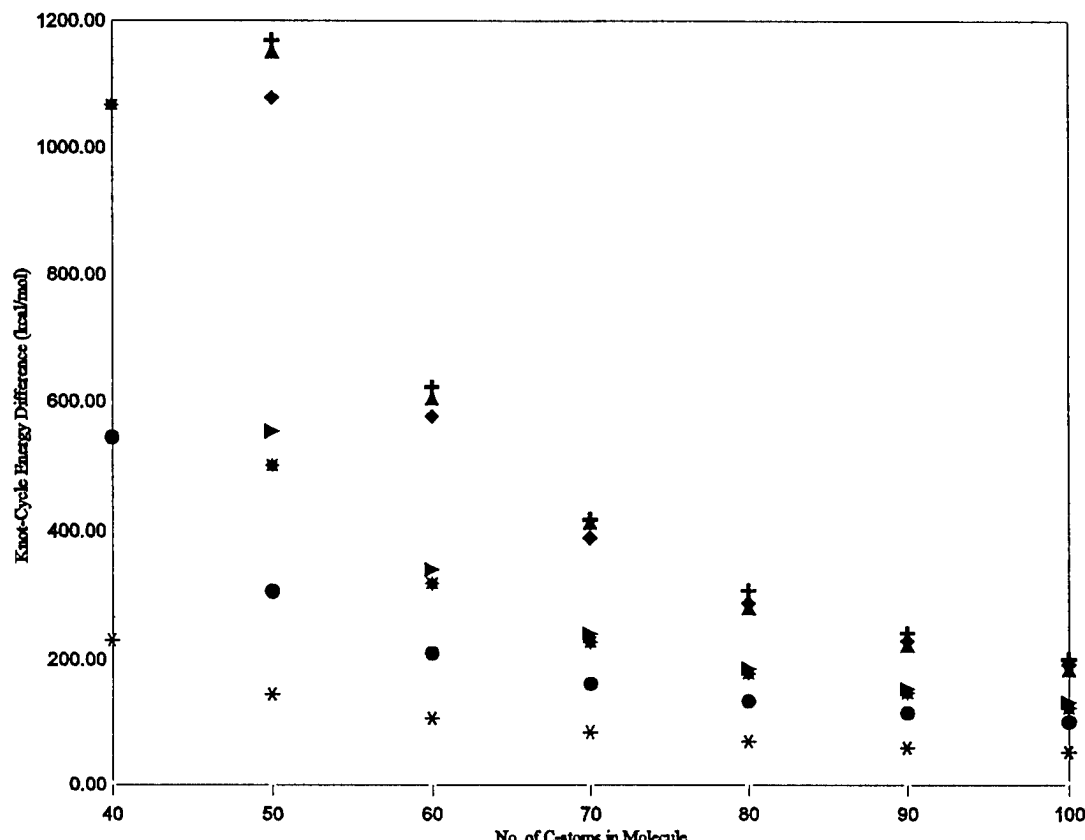


FIGURE 2. The AM1 knot-cycle heat-of-formation differences for the first seven carbyne prime knots for the molecules composed from 40 to 100 carbon atoms: (asterisks) 3₁ knots; (circles) 4₁ knots; (suns) 5₁ knots; (wedges) 5₂ knots; (triangles) 6₁ knots; (diamonds) 6₂ knots; and (crosses) 6₃ knots.

KNOCARBYNES SYMMETRY AND QUALITATIVE ¹³C-NMR SPECTRA

Symmetry

In mathematical knot theory [1, 56, 76, 77], the knot group is a concept based on the fundamental group method. This results in a very effective knot classification and construction of different knot invariants. However, when chemical molecules of knotted structures are studied, geometrical parameters again become important and classification with respect to point symmetry groups is again of use. So, the cyclohexyne C_{2n} molecule ($n = k$, $k = 20, 30, \dots, 50$) constitutes a $2n$ -gon with the sides alternately equal, belonging to the D_{nh} point group symmetry. Thus, the C_{60} cyclohexyne belongs to the D_{30h} point group symmetry (but the C_{100} cyclohexyne to the D_{50h} point group). The carbyne trefoil C_{2n} molecules ($n = 3k$, $k = 5, 6, \dots$, and so also the C_{60} trefoil) belong to the D_3 point group of symmetry, whereas the other trefoil molecules

belong to the C_2 or C_1 point group of symmetry. The carbyne figure-eight C_{2n} knots ($n = 4k$, $k = 5, 6, \dots$) belong to the S_4 symmetry group; the other figure-eight knocarbynes have no symmetry. Thus, the 4₁ C_{60} knocarbyne has no symmetry, whereas the 4₁ C_{56} and 4₁ C_{64} structures have the reoreflection S_4 axis. The C_{2n} knocarbyne molecules with five crossings ($n = 5k$, $k = 4, 5, \dots$), both the 5₁ and the 5₂ types, belong to the C_2 point group symmetry. All the six-crossing knocarbynes possess only a trivial symmetry element, that is, they belong to the C_1 point group.

Qualitative ¹³C-NMR Spectra

The medium-size Hansen-Bouman double-zeta basis [70] was used to calculate ¹³C-NMR shielding constants. The spectra were calculated for knot geometries using the STO-3G basis set and, for comparison, for those optimized at the AM1 level.

Qualitatively, the spectra calculated for the STO-3G and AM1 geometries are identical but, the

latter are dispersed over a wider spectral range. Probably, the AM1-based spectra are less accurate because the HF/DZP-HB//AM1 energies are much higher than the HF/STO-3G//HF/STO-3G energies: from ca. 0.007 (fullerene) to 0.08 Hartree (6₃ knocarbyne).

The C₆₀ buckminsterfullerene belongs to the icosahedral symmetry group I_h and all its atoms are equivalent. The same is true for the C₆₀ cycarbene which has the D_{30h} symmetry. However, its single signal is placed in a completely different region of the ¹³C-NMR spectrum [54] (Table II). In the case of the C_{2n} trefoil with D₃ symmetry, n/3 equal signals should be observed [54], which, for the C₆₀ trefoil, implies that 10 NMR signals of equal intensity should appear [54, 55] (Table II). The C₆₀ figure-eight knocarbyne has no symmetry, but, in fact, the calculated spectrum consists of 30 NMR doublets. However, the C_{2n} figure-eight knocarbynes of series (n = 4k, k = 5, 6, ...) belong to the S₄ symmetry group; therefore, for the C₆₄ figure-eight knocarbyne, 16 signals should be observed, and for C₅₆, only 14. All five-crossing knocarbynes belong to the C₂ point group; therefore, for the 5₁ and 5₂ C₆₀ knocarbynes, 30 signals of equal intensity are expected (Table II). Because the six-crossing knocarbynes possess no symmetry, 60 separate signals of equal intensity should be observed in all three cases (Table II).

The calculated chemical shifts (Table II) illustrate qualitatively the possible locations of signals that might be assigned to different topological isomers. Table II demonstrates also the complexity of the spectrum determined by the knot type and its symmetry and the tendencies of the signals to shift with the increasing number of knot crossings. We showed earlier [54] that, with the increasing n (decreasing bending stress and repulsive interaction), both the ¹³C-NMR signal for the cycle and signals for the C_n trefoil shift up-field and that the signals of the C₆₀ trefoil are expected to occur between the signal of the C₆₀ buckminsterfullerene and the signal of the C₆₀ cycle. Now, it seems that those knocarbynes that are relatively slightly strained (trefoil and figure eight) exhibit the ¹³C-NMR signals between the fullerene and cycle signals. With the increase in strain as the number of knot crossings increases, the signals cover a wider spectral region which does not extend beyond the limit set by the fullerene signal but includes the signal originating from the cycarbene.

Conclusions

1. By using ab initio and semiempirical quantum chemical methods, several knotted car-

TABLE II
¹³C-NMR chemical shifts (ppm) calculated for C₆₀ carbyne-knotted topological isomers.

C ₆₀ molecular	No. equal signals	Chemical shift ^a
Fullerene [54]	1	161.19 (156.61)
Cycle [54]	1	71.88 (72.86)
Trefoil [54]	10	99.23 98.96 96.90 94.03 92.02 85.98 83.93 77.70 74.11 72.24 (129.67 126.99 122.89 112.66 110.10 95.23 84.88 77.52 66.02 64.66)
Figure 8	30 (doublets)	133.12–77.88 (168.05–51.70)
C ₆₄ figure 8	16	118.49 117.58 115.95 114.96 107.15 101.42 98.71 93.86 89.82 85.10 81.87 79.00 76.07 72.46 70.17 68.01 (160.34 160.34 149.53 148.24 142.13 141.76 115.43 113.63 102.06 98.33 78.43 74.71 67.25 63.83 56.77 51.49
5 ₁ (cinquefoil)	30	138.10–65.19 (189.81–37.13)
5 ₂	30	133.54–58.60 (200.93–36.02)
6 ₁	60	130.30–31.67 (233.19–51.91)
6 ₂	60	142.16–43.26 (232.10–39.94)
6 ₃	60	142.37–36.81 (230.66–30.09)

The Hansen and Bouman double-zeta basis set was used to calculate chemical shifts: values calculated for the STO-3G geometries (in parentheses, results for AM1 geometries).

^aChemical shifts are calculated against the ¹³C atoms of TMS (shielding constant, 201.05 ppm for STO-3G and 195.40 for AM1 geometries).

- bynes have been predicted to exist and to be identifiable by the NMR method.
2. The energy differences between the C_n knotted and cycle carbyne structures decrease with n and for the C_{100} molecule, the differences range from only 50 to 200 kcal/mol for trefoil and the 6_3 carbyne knot, respectively.
 3. The energy differences increase in line with the knot-type series.
 4. Some of the C_{2n} knocarbynes exhibit the following symmetries:
 - 0_1 of series $n = 2k, k = 5, 6, 7, \dots$ belong to the D_{nh} point symmetry group,
 - 3_1 of series $n = 3k, k = 5, 6, 7, \dots$ belong to the D_3 point symmetry group,
 - 4_1 of series $n = 4k, k = 5, 6, 7, \dots$ belong to the S_4 point symmetry group,
 - 5_1 of series $n = 5k, k = 5, 6, 7, \dots$ belong to the C_2 point symmetry group,
 - six-crossing knocarbyns possess no symmetry.
 5. In the ^{13}C -NMR spectrum of C_{60} knocarbynes, the following numbers of signals should be observed:
 - one for 0_1 ,
 - 10 for 3_1 ,
 - 30 doublets for 4_1 ,
 - 30 for 5_1 and 5_2 , and
 - 60 for $6_1, 6_2$, and 6_3 .
 6. Our research in that area may serve as a model study on knotted structures for DNA, RNA [78–83], and other macromolecules.

ACKNOWLEDGMENTS

This work was financially supported by the Drug Institute, Warsaw.

References

1. J. H. Przytycki, *Węzły. Podejście kombinatoryczne do teorii węzłów* (SCRIPT, Warszawa, 1995).
2. J. H. Przytycki, *Aport. Mat. Com.*, **11**, 173 (1992).
3. P. Van de Griend, *The History of Knot Theory* (Aarhus University, Denmark, 1992).
4. M. Suffczynski, *Pol. J. Chem.*, **69**, 157 (1995).
5. B. Holmes, R. N. Brodgen, and D. M. Richards, *Drugs*, **30**, 482 (1985).
6. S. A. Wasserman and N. R. Cozzarelli, *Proc. Natl. Acad. Sci. U.S.A.*, **82**, 1079 (1985).
7. S. A. Wasserman and N. R. Cozzarelli, *Science*, **232**, 951 (1986).
8. D. M. Walba, T. C. Homan, R. M. Richards, and R. C. Halitwanger, *New J. Chem.*, **17**, 661 (1993).
9. C. O. Dietrich-Buchecker and J. P. Sauvage, *Angew. Chem., Int. Ed. Engl.*, **28**, 189 (1989).
10. D. W. Sumners, *Studies in Physical and Theoretical Chemistry* (Elsevier, Amsterdam, 1987), Vol. 51, p. 3.
11. D. W. Sumners, *Math. Intel.*, **12**, 71 (1990).
12. R. Kanaar and N. R. Cozzarelli, *Curr. Opin. Struct. Biol.*, **2**, 369 (1992).
13. V. V. Rybenkov, N. R. Cozzarelli, and A. V. Volgotskii, *Proc. Natl. Acad. Sci. U.S.A.*, **90**, 5307 (1993).
14. A. V. Volgotskii and N. R. Cozzarelli, *J. Mol. Biol.*, **232**, 1130 (1993).
15. M. C. Tesi, E. J. J. van Rensburg, E. Orlandini, D. W. Sumners, and S. G. Whittington, *Phys. Rev. E*, **49**, 868 (1994).
16. C. Ernst and D. W. Sumners, *Math. Proc. Camb. Philos. Soc.*, **108**, 489 (1990).
17. S. J. Spengler, A. Stasiak, and N. R. Cozzarelli, *Cell*, **42**, 325 (1985).
18. K. A. Rayan, T. A. Shapiro, C. A. Rauch, J. D. Griffith, and P. T. Englund, *Proc. Natl. Acad. Sci. U.S.A.*, **85**, 5844 (1988).
19. S. R. Quake, *Phys. Rev. Lett.*, **73**, 3317 (1994).
20. M. L. Mansfield, *Macromolecules*, **27**, 5924 (1994).
21. M. Muthukumar and K. G. Koniaris, *Polym. Mater. Sci. Eng.*, **71**, 634 (1994).
22. K. Iwata and M. Tanaka, *J. Phys. Chem.*, **96**, 4100 (1992).
23. K. Iwata, *J. Phys. Chem.*, **96**, 4111 (1992).
24. H. Dodziuk, *Modern Conformational Analysis. Elucidating Novel Exciting Molecular Structures. The Methods in Stereochemical Analysis*, A. P. Marchand, Series Ed. (VCH, New York, Weinheim, Cambridge, 1995).
25. A. Baeyer, *Ber. Deut. Chem. Ges.*, **18**, 674 (1885).
26. A. Baeyer, *Ber. Deut. Chem. Ges.*, **18**, 2269 (1885).
27. G. Tammann, *Z. Anorg. Allg. Chem.*, **115**, 145 (1921).
28. R. E. Honig, *J. Chem. Phys.*, **22**, 126 (1954).
29. W. A. Chupka and M. G. Inghram, *J. Chem. Phys.*, **22**, 1472 (1954).
30. W. A. Chupka and M. G. Inghram, *J. Phys. Chem.*, **59**, 100 (1955).
31. K. S. Pitzer and E. Clementi, *J. Am. Chem. Soc.*, **81**, 4477 (1959).
32. S. J. Strickler and K. S. Pitzer, in *Molecular Orbitals in Chemistry, Physics and Biology*, P.-O. Lowdin and B. Pulman, Eds. (Academic Press, New York, 1964), p. 281.
33. V. Parasuk and J. Almlöf, *J. Chem. Phys.*, **87**, 2191 (1989).
34. K. Raghavachari, *Chem. Phys. Lett.*, **171**, 249 (1990).
35. L. Adamowicz, *Chem. Phys. Lett.*, **182**, 45 (1991).
36. J. Szczepanski and M. J. Vala, *J. Phys. Chem.*, **95**, 2792 (1991).
37. D. W. Arnold, S. E. Bradforth, T. N. Kitsopoulos, and D. M. Neumark, *J. Chem. Phys.*, **95**, 8753 (1991).
38. J. Szczepanski, S. Ekern, and M. Vala, *J. Phys. Chem. B*, **101**, 1841 (1997).
39. J. Szczepanski, Ch. Wehlburg, and M. Vala, *J. Phys. Chem. A*, **101**, 7039 (1997).

40. S. L. Wang, C. M. L. Rittby, and W. R. M. Graham, *J. Chem. Phys.*, **107**, 6032 (1997).
41. Yu. Kudryavtsev, S. Evsyukov, M. Guseva, V. Babaev, and V. Khvostov, *Chem. Phys. Carbon*, **25**, 1 (1997).
42. Yu. P. Kudryavtsev, R. B. Heimann, and S. E. Evsyukov, *J. Mater. Sci.*, **31**, 5557 (1996).
43. C. T. Pillinger, *Philos. Trans. R. Soc. Lond., Ser. A*, **343**, 73 (1993).
44. K. Raghavachari and J. S. Binkley, *J. Chem. Phys.*, **87**, 2191 (1987).
45. J. M. L. Martin and J. P. Francois, *J. Mol. Struct.*, **294**, 21 (1993).
46. J. M. L. Martin and P. R. Taylor, *J. Chem. Phys.*, **102**, 8270 (1995).
47. W. Weltner, Jr. and R. J. van Zee, *Chem. Rev.*, **89**, 1713 (1989).
48. W. Weltner, Jr. and D. McLeod, Jr., *J. Chem. Phys.*, **45**, 3096 (1966).
49. K. B. Shelimov, D. E. Clemmer, and M. F. Jarrold, *J. Phys. Chem.*, **99**, 11376 (1995).
50. D. L. Strout and M. B. Hall, *J. Comput. Chem.*, **100**, 18007 (1996).
51. S. Roszak and K. Balasubramanian, *J. Chem. Phys.*, **106**, 158 (1997).
52. A. Ayuela, G. Seifert, and R. Schmidt, *Z. Phys. D*, **41**, 69 (1997).
53. D. L. Strout and M. B. Hall, *J. Phys. Chem. A*, **102**, 641 (1998).
54. J. Cz. Dobrowolski and A. P. Mazurek, *Pol. J. Chem.* (1998).
55. J. Cz. Dobrowolski and A. P. Mazurek, *J. Phys. Chem. A*, **102**, 5260 (1998).
56. D. Rolfsen, *Knots and Links* (Publish or Perish, Berkeley, 1976).
57. W. J. Ambs, *Mendel Bull.*, **17 / Spring**, 26 (1953).
58. H. L. Frisch and E. Wasserman, *J. Am. Chem. Soc.*, **83**, 3789 (1961).
59. E. Wasserman, *Sci. Am.*, **207**, 94 (1962).
60. D. M. Walba, in *Chemical Applications of Topology and Graph Theory*, R. B. King, Ed. (Elsevier, Amsterdam, 1983).
61. Z. Slanina, *Contemporary Theory of Chemical Isomerism* (Academia, Prague, 1986).
62. T. G. Schmalz, W. A. Seitz, D. J. Klein, and G. E. Hite, *J. Am. Chem. Soc.*, **110**, 1113 (1988).
63. D. J. Klein, *J. Chem. Inf. Comput. Sci.*, **34**, 453 (1994).
64. D. J. Klein and X. Liu, *Int. J. Quantum Chem.*, **28**, 501 (1994).
65. K. Mislow, *Croat. Chem. Acta*, **69**, 485 (1996).
66. D. J. Klein and H. Zhu, in *From Chemical Topology to Three-Dimensional Geometry*, A. T. Balaban, Ed. (Plenum Press, New York, 1997).
67. Spartan version 5.0. (Wavefunction, Inc., 18401 Von Karman Ave., #370, Irvine, CA 92715; © Wavefunction, Inc.).
68. M. J. Frisch, G. W. Trucks, H. B. Schlegel, P. M. W. Gill, B. G. Johnson, M. A. Robb, J. R. Cheeseman, T. A. Keith, G. A. Petersson, J. A. Montgomery, K. Raghavachari, M. A. Al-Laham, V. G. Zakrzewski, J. V. Ortiz, J. B. Foresman, J. Cioslowski, B. B. Stefanov, A. Nanayakkara, M. Challacombe, C. Y. Peng, P. Y. Ayala, W. Chen, M. W. Wong, J. L. Andres, E. S. Replogle, R. Gomperts, R. L. Martin, D. J. Fox, J. S. Binkley, D. J. Defrees, J. Baker, J. P. Stewart, M. Head-Gordon, C. Gonzales, and J. A. Pople, *Gaussian 94 (Revision D.4)* (Gaussian, Inc., Pittsburgh, PA, 1995).
69. K. Wolniński, J. F. Hinton, and P. Pulay, *J. Am. Chem. Soc.*, **112**, 8251 (1990).
70. A. E. Hansen and T. D. Bouman, *J. Chem. Phys.*, **82**, 5035 (1985).
71. A. Barszczewicz, M. Jaszuński, and K. Jackowski, *Chem. Phys. Lett.*, **203**, 404 (1993).
72. A. Barszczewicz, M. Jaszuński, and L. Stefaniak, *Chem. Phys. Lett.*, **186**, 313 (1991).
73. K. Jackowski, A. Barszczewicz, and K. Woźniak, *Solid State NMR*, **2**, 265 (1993).
74. M. Pecul, K. Jackowski, K. Woźniak, and J. Sadlej, *Solid State NMR*, **8**, (1997).
75. M. Pecul and J. Sadlej, *Chem. Phys.*, (1998).
76. G. Burde and H. Zieschang, *Knots* (Walter de Gruyter, Berlin, New York, 1985).
77. R. H. Crowell and R. H. Fox, *Introduction to Knot Theory* (Ginn, Boston, 1963).
78. H. Wang, S. M. Su, and N. C. Seeman, *J. Biomol. Struct. Dyn.*, **10**, 853 (1993).
79. W. M. Stark, C. N. Parker, S. E. Halford, and M. R. Boocock, *Nature*, **368**, 76 (1994).
80. S. M. Du, and N. C. Seeman, *Biopolymers*, **34**, 31 (1994).
81. S. M. Du, H. Wang, Y. C. Tse-Dinh, and N. C. Seeman, *Biochemistry*, **34**, 673 (1995).
82. H. Wang, R. J. Di Gate, and N. C. Seeman, *Proc. Natl. Acad. Sci. USA*, **93**, 9477 (1996).
83. V. V. Rybenkov, A. V. Volgotskii, and N. R. Cozzarelli, *Nucleic Acids Res.*, **25**, 1412 (1997).

Perturbed Ellipsoidal Wave Functions for Quantum Scattering

T. LEVITINA,* E. J. BRÄNDAS

Department of Quantum Chemistry, Uppsala University, Box 518, S-751 20 Uppsala, Sweden

Received 22 February 1998; accepted 18 March 1998

ABSTRACT: The scattering data of a potential, separable in ellipsoidal coordinates, are expanded in perturbed Lamé wave functions. These functions arise when variables in the Schrödinger equation are separated in the ellipsoidal coordinate system. Preliminary calculations are displayed for the total cross section and the scattering amplitude versus direction. The quicker the potential vanishes at infinity the more pronounced is the dependence on the incident direction. © 1998 John Wiley & Sons, Inc. Int J Quant Chem 70: 1017–1022, 1998

Key words: scattering; ellipsoidal coordinates; Fourier method; Lamé wave functions; optical theorem

Introduction

In a recent paper [1] we expressed the scattering matrix and the far-field or scattering amplitude of a potential $V(\mathbf{r})$, separable in dimensionless ellipsoidal coordinates, in the form of a series in perturbed ellipsoidal wave functions arising when

*Permanent address: Department of Numerical Methods, Computing Center of Russian Academy of Sciences, Vavilova str. 40, 117967 Moscow GSP-1, Russia.

Correspondence to: E. J. Brändas.

Contract grant sponsor: Russian Foundation for Basic Research.

Contract grant number: 96-01-00951.

Contract grant sponsor: Swedish Defence Research Establishment.

Contract grant number: FOA Project E 6022.

Contract grant sponsor: Swedish Institute.

the variables in the Schrödinger equation

$$\Delta\Psi + (k^2 - V(\mathbf{r}))\Psi = 0, \quad \mathbf{r} \in \mathbb{R}^3 \quad (1)$$

are separated. Here Δ is the Laplacian and $k = |\mathbf{k}|$ is a wave number. In what follows we will derive the expansion of the total scattering cross section, as well as give a proof of the optical theorem, for the potentials under study. Unexpected behavior will be discussed and explained. The general character of the ellipsoidal coordinate system is also emphasized.

Perturbed Ellipsoidal Wave Functions

To introduce the ellipsoidal coordinates, we fix the ellipsoid S : $x^2/a^2 + y^2/b^2 + z^2/c^2 = 1$ of semiaxes $a > b > c > 0$ and consider the equation

(with respect to ξ)

$$\frac{x^2}{(a^2 - b^2)\xi} + \frac{y^2}{(a^2 - b^2)(\xi - 1)} + \frac{z^2}{(a^2 - b^2)(\xi - \rho^2)} = 1 \quad (2)$$

with $\rho^2 = (a^2 - c^2)/(a^2 - b^2) > 1$. This equation defines a family of confocal surfaces specified by the variable ξ . For each point (x, y, z) , $xyz \neq 0$, there are exactly three different roots: $\xi_1 \in I_1 = (0, 1)$, $\xi_2 \in I_2 = (1, \rho^2)$, and $\xi_3 \in I_3 = (\rho^2, \infty)$. If $\xi = \xi_1$, the surface, defined by Eq. (2) above, is a hyperboloid of two sheets; for $\xi = \xi_2$ it is a hyperboloid of one sheet, and for $\xi = \xi_3$ it is an ellipsoid [e.g., the equation $\xi_3 = \xi_3^* = a^2/(a^2 - b^2)$ defines S].

The above three families of confocal surfaces form an orthogonal curvilinear coordinate system related to Cartesian coordinates within each octant (e.g., $x \geq 0, y \geq 0, z \geq 0$) by the one-to-one correspondence

$$\begin{aligned} x^2 &= (a^2 - b^2)\xi_1\xi_2\xi_3/\rho^2, \\ y^2 &= -(a^2 - b^2)(\xi_1 - 1)(\xi_2 - 1)(\xi_3 - 1)/(\rho^2 - 1), \\ z^2 &= (a^2 - b^2)(\xi_1 - \rho^2)(\xi_2 - \rho^2)(\xi_3 - \rho^2)/[(\rho^2 - 1)\rho^2]. \end{aligned}$$

(See also [2].)

The most general appearance of a separable potential is here given by (see, e.g., [3])

$$V(\xi_1, \xi_2, \xi_3) = \frac{(\xi_3 - \xi_2)\alpha_1(\xi_1) + (\xi_1 - \xi_3)\alpha_2(\xi_2) + (\xi_2 - \xi_1)\alpha_3(\xi_3)}{(\xi_1 - \xi_2)(\xi_2 - \xi_3)(\xi_3 - \xi_1)}. \quad (3)$$

Here $\alpha_i(\xi_i)$, $i = 1, 2, 3$, are arbitrary functions.

By separating variables, we arrive at a system of three identical equations

$$\begin{aligned} \sqrt{f(\xi_i)} \frac{d}{d\xi_i} \left\{ \sqrt{f(\xi_i)} \frac{d\Lambda_i}{d\xi_i} \right\} \\ + \frac{1}{4}(q(\xi_i, h, l, \omega) - \alpha_i(\xi_i))\Lambda_i = 0, \quad \xi_i \in I_i, \\ i = 1, 2, 3, \end{aligned} \quad (4)$$

which in the case $V(\xi_1, \xi_2, \xi_3) = 0$ coincide with the Lamé wave equations. Here h, l are separation constants, $f(\xi) = \xi(\xi - 1)(\xi - \rho^2)$, $q(\xi, h, l, \omega) = h\rho^2 - l\rho^2\xi + \omega^2\xi^2$, $\omega^2 = k^2(a^2 - b^2)$.

A particular solution to (1), i.e., the product $\Lambda_1(\xi_1) \times \Lambda_2(\xi_2) \times \Lambda_3(\xi_3)$, must be either odd or even with respect to each of coordinate planes $x = 0$, $y = 0$, and $z = 0$ (see below). Hereafter we will specify the parity properties of a partial solution by a triplet of binaries (i_x, i_y, i_z) , equal to 0 or 1 depending on the parity requirement with respect to the corresponding plane. Thus functions

$\Lambda_i(\xi_i)$ are subject to

$$\begin{aligned} \text{either } \lim_{\xi_1 \rightarrow +0} \left(\sqrt{f(\xi_1)} \Lambda_1(\xi_1) \right) = 0 \quad \text{or} \\ \lim_{\xi_1 \rightarrow +0} \Lambda_1(\xi_1) = 0; \\ \text{either } \lim_{\xi_1 \rightarrow 1-0} \Lambda_1(\xi_1) = \lim_{\xi_2 \rightarrow 1+0} \Lambda_2(\xi_2) = 0, \\ \text{or } \lim_{\xi_1 \rightarrow 1-0} \left(\sqrt{f(\xi_1)} \Lambda_1(\xi_1) \right) \\ = \lim_{\xi_2 \rightarrow 1+0} \left(\sqrt{-f(\xi_2)} \Lambda_2(\xi_2) \right) = 0; \\ \text{either } \lim_{\xi_2 \rightarrow \rho^2-0} \left(\sqrt{-f(\xi_2)} \Lambda_2(\xi_2) \right) \\ = \lim_{\xi_3 \rightarrow \rho^2+0} \left(\sqrt{f(\xi_3)} \Lambda_3(\xi_3) \right) = 0, \\ \text{or } \lim_{\xi_2 \rightarrow \rho^2-0} \Lambda_2(\xi_2) = \lim_{\xi_3 \rightarrow \rho^2+0} \Lambda_3(\xi_3) = 0. \end{aligned} \quad (5)$$

The functions $\Lambda_1(\xi_1)$ and $\Lambda_2(\xi_2)$ form the eigenfunction $\Xi(\xi_1, \xi_2) = \Lambda_1(\xi_1) \times \Lambda_2(\xi_2)$ of a two-parameter self-adjoint eigenvalue problem. That is, one must find such a couple of values

(l, h) for the separation constants, called the eigenvalue, that Eq. (4) has nontrivial solutions both on I_1 and on I_2 , which satisfy the boundary condi-

tions (5) determined by (i_x, i_y, i_z) . According to general multiparameter spectral theory [4] the eigenfunctions normalized by

$$\int_{\Pi} \int \frac{[\Xi_n^m(\xi_1, \xi_2)]^2 (\xi_2 - \xi_1)}{[-\xi_1 \xi_2 (\xi_1 - 1)(\xi_2 - 1)(\xi_1 - \rho^2)(\xi_2 - \rho^2)]^{1/2}} d\xi_1 d\xi_2 = \frac{1}{2}$$

constitute a complete system in $\mathcal{L}^2(\Pi)$, where $\Pi = I_1 \times I_2$, m and $n - m$ are the number of internal zeros for $\Lambda_1^{n,m}(\xi_1)$ and $\Lambda_2^{n,m}(\xi_2)$, respectively, $n = 0, 1, \dots, m = 0, 1, \dots, n$. Let $S^0: \xi_3 = \xi_3^0$ be an arbitrary ellipsoid. As (ξ_1, ξ_2) vary over Π , the points (ξ_1, ξ_2, ξ_3^0) cover one-eighth part of S^0 . Therefore, we continue each function $\Xi_n^m(\xi_1, \xi_2)$ according to its parity properties (i_x, i_y, i_z) over the whole ellipsoid. Note that in the absence of a potential these functions coincide with the surface ellipsoidal wave functions analogous to the spherical harmonics in the case of spherical symmetry. The perturbed surface ellipsoidal wave functions of all possible parities build up a complete system in $\mathcal{L}^2(S^0)$.

The perturbed radial ellipsoidal wave function $\Lambda_3^{n,m}(\xi_3)$ —i.e., the solution to (4) and (5) on $\xi_3 \in I_3$ —behaves at infinity as follows:

$$\Lambda_3^{n,m}(\xi_3) = \frac{D}{\sqrt{\xi_3}} \sin(\omega \sqrt{\xi_3} + \Delta_n^m) + O\left(\frac{1}{\xi_3}\right),$$

$$\xi_3 \rightarrow \infty.$$

Here the limit phase Δ_n^m is determined by the potential, and D is an arbitrary constant.

To calculate the perturbed functions, we applied the methods proposed in [5, 6], see also Refs. [7, 8], which provide an efficient and economic way to calculate ellipsoidal wave functions at a wide range of parameter variations.

Scattering Data Representations

For details on the expansion of the scattering matrix \hat{S} as well as the far-field amplitude $f(\mathbf{n}, \mathbf{n}_0)$ we refer to [1, 9, 10]. We will here present the fundamental expressions:

$$\hat{S}(\mathbf{n}, \mathbf{n}_0) = \sum_{(i_x, i_y, i_z)} \sum_{n=0}^{\infty} \sum_{m=0}^n [\exp(2i\tilde{\Delta}_n^m) \times \Xi_n^m(\xi_1, \xi_2) \Xi_n^m(\xi_1^0, \xi_2^0)]_{(i_x, i_y, i_z)}, \quad (6)$$

$$f(\mathbf{n}, \mathbf{n}_0) = \frac{2\pi}{ik} \sum_{(i_x, i_y, i_z)} \sum_{n=0}^{\infty} \sum_{m=0}^n \{ [\exp(2i\tilde{\Delta}_n^m) - 1] \times \Xi_n^m(\xi_1, \xi_2) \Xi_n^m(\xi_1^0, \xi_2^0) \}_{(i_x, i_y, i_z)}, \quad (7)$$

where the unit vectors $\mathbf{n} = \mathbf{r}/r = (1, \varphi, \theta)$ and $\mathbf{n}_0 = \mathbf{k}/k = (1, \varphi^0, \theta^0)$ indicate the observation and incident directions, respectively. Note that the angle ellipsoidal coordinates ξ_1, ξ_2 connect in (6) and (7) with the spherical angle coordinates as given by

$$\xi_1 \xi_2 = \rho^2 \cos^2 \theta,$$

$$(\xi_1 - 1)(\xi_2 - 1) = -(\rho^2 - 1)\sin^2 \theta \cos^2 \varphi,$$

$$(\xi_1 - \rho^2)(\xi_2 - \rho^2) = \rho^2(\rho^2 - 1)\sin^2 \theta \sin^2 \varphi,$$

where θ is measured in relation to the x -axis. The coordinate ξ_3 plays the role of the radius:

$$(a^2 - b^2)\xi_3 = r^2 + \mathcal{O}(1), \quad r \rightarrow \infty. \quad (8)$$

In Eqs. (6) and (7) we have extracted the phase shift $\tilde{\Delta}_n^m$ from the limit phase Δ_n^m , i.e.,

$$\Delta_n^m = \tilde{\Delta}_n^m - \pi[i_x + i_y + i_z]/2 \pmod{\pi}.$$

We can now use formula (7) to expand the total scattering cross section Ω for the class of potentials given by (3).

Substituting in the definition

$$\Omega(\theta^0, \varphi^0) = \int_0^{2\pi} \int_0^\pi |f(\theta, \varphi, \theta^0, \varphi^0)|^2 \sin \theta d\theta d\varphi \quad (9)$$

the series (7) as well as the orthogonality relations, see Ref. [1].

$$\int_0^{2\pi} \int_0^\pi [\Xi_n^m(\theta, \varphi)_{(i_x, i_y, i_z)} \Xi_{n'}^{m'}(\theta, \varphi)_{(i'_x, i'_y, i'_z)}] \sin \theta \, d\theta \, d\varphi \\ = 8 \int_{\Pi} \int \frac{[\Xi_n^m(\xi_1, \xi_2)_{(i_x, i_y, i_z)} \Xi_{n'}^{m'}(\xi_1, \xi_2)_{(i'_x, i'_y, i'_z)}] (\xi_2 - \xi_1)}{4[-\xi_1 \xi_2 (\xi_1 - 1)(\xi_2 - 1)(\xi_1 - \rho^2)(\xi_2 - \rho^2)]^{1/2}} \, d\xi_1 \, d\xi_2 = \delta_{n, n'} \delta_{m, m'} \delta_{(i_x, i_y, i_z), (i'_x, i'_y, i'_z)}, \quad (10)$$

we obtain

$$\Omega(\mathbf{n}_0) = \frac{16\pi^2}{k^2} \sum_{(i_x, i_y, i_z)} \sum_{n=0}^{\infty} \sum_{m=0}^n \left\{ \sin^2(\tilde{\Delta}_n^m) \times \left[\Xi_n^m(\xi_1^0, \xi_2^0) \right]^2 \right\}_{(i_x, i_y, i_z)}. \quad (11)$$

In comparing the last formula with (7), we recognize the well-known optical theorem [11]:

$$\Omega(\mathbf{n}_0) = \frac{4\pi}{k} \mathcal{I}[f(\mathbf{n}_0, \mathbf{n}_0)].$$

Note that total cross section depends on the incident direction, and that the optical theorem holds for all n_0 .

Results and Discussion

We have calculated here several examples of cross sections for potentials that vanish at infinity as r^{-n} , where $n = 2, 4, 6, 12$. We found, for $n = 2$, and $n = 4$, that the scattering cross section did not depend very much on \mathbf{n}_0 (for k not too large), while for $n \geq 6$ the nonspherical effects became clearly visible. In Figure 1 we display preliminary calculations for the potential

$$V(\mathbf{r}) = \gamma_0[(\xi_3 - \xi_2)(\xi_3 - \xi_1)]^{-1} \left\{ \frac{\sigma^{12}}{\xi_3^4} - \frac{\sigma^6}{\xi_3} \right\},$$

which, according to (8), vanishes at infinity as the well-known Lennard-Jones potential, used in molecular physics, i.e.,

$$V(\mathbf{r}) = \gamma_0 \left\{ \frac{\sigma^{12}}{r^{12}} - \frac{\sigma^6}{r^6} \right\}, \quad r \rightarrow \infty.$$

We have presented the scattering data in Figure 1 with the total cross section in the first column and the scattering amplitude for various incident directions in the next three columns. See figure caption for details. We have chosen $k^2 = 1.0$ and $\gamma_0 = 1.0$ to be constant in all plots, while the other param-

ters are varied as shown. The accuracy of the auxiliary ordinary differential equation (ODE) calculation is $\epsilon = 10^{-6}$.

We have found that when the potential is small enough, the phase $\tilde{\Delta}_n^m$ scales nearly linearly with the parameter γ_0 , similarly to previous observations [1]. Therefore, according to (7) and (11), small values of γ_0 preserve the shape of $\Omega(\theta^0, \varphi^0)$ as well as of $f(\mathbf{n}, \mathbf{n}_0)$.

It is important to note that the scattering data is entirely dependent on the values of ω and ρ . Compare, for instance, the spherical case, when we have a simple scale dependence on kR where R is the characteristic size of the scattering scenario. While the latter case implies a simple but useful reciprocal law, the ellipsoidal formula embodies a more flexible invariance. For example, in Figure 1 scattering data (up to the factors k^2 and k , respectively) on the second row may correspond to either

$$a^2 = \underbrace{1.00\dots02}_{1997}, \quad b^2 = \underbrace{1.00\dots01}_{1997}, \quad c^2 = 1.0, \quad (12)$$

on

$$a^2 = 200.\underbrace{00\dots 01}_{1997}, \quad b^2 = 100.\underbrace{00\dots 01}_{1997}, \\ c = 0.\underbrace{00\dots 01}_{1997} \quad (13)$$

provided $k^2 = 10^{1999}$ or $k^2 = 10^{-1}$, respectively, i.e., values of both ρ and ω remain as presented in the figure. In [12] we have observed that the surface ellipsoidal wave functions and the corresponding spherical functions behave similarly for ω small (and coincide for $\omega = 0!$) independently of ρ . The simple explanation is, of course, that by varying geometrical parameters one may come as close to a sphere as desired, see, e.g., (12) above, keeping ρ constant. On the contrary one can also vary ρ arbitrarily while remaining in the vicinity of the spherical case.

As is well-known there are exactly 11 coordinate systems in which the Helmholtz equation is

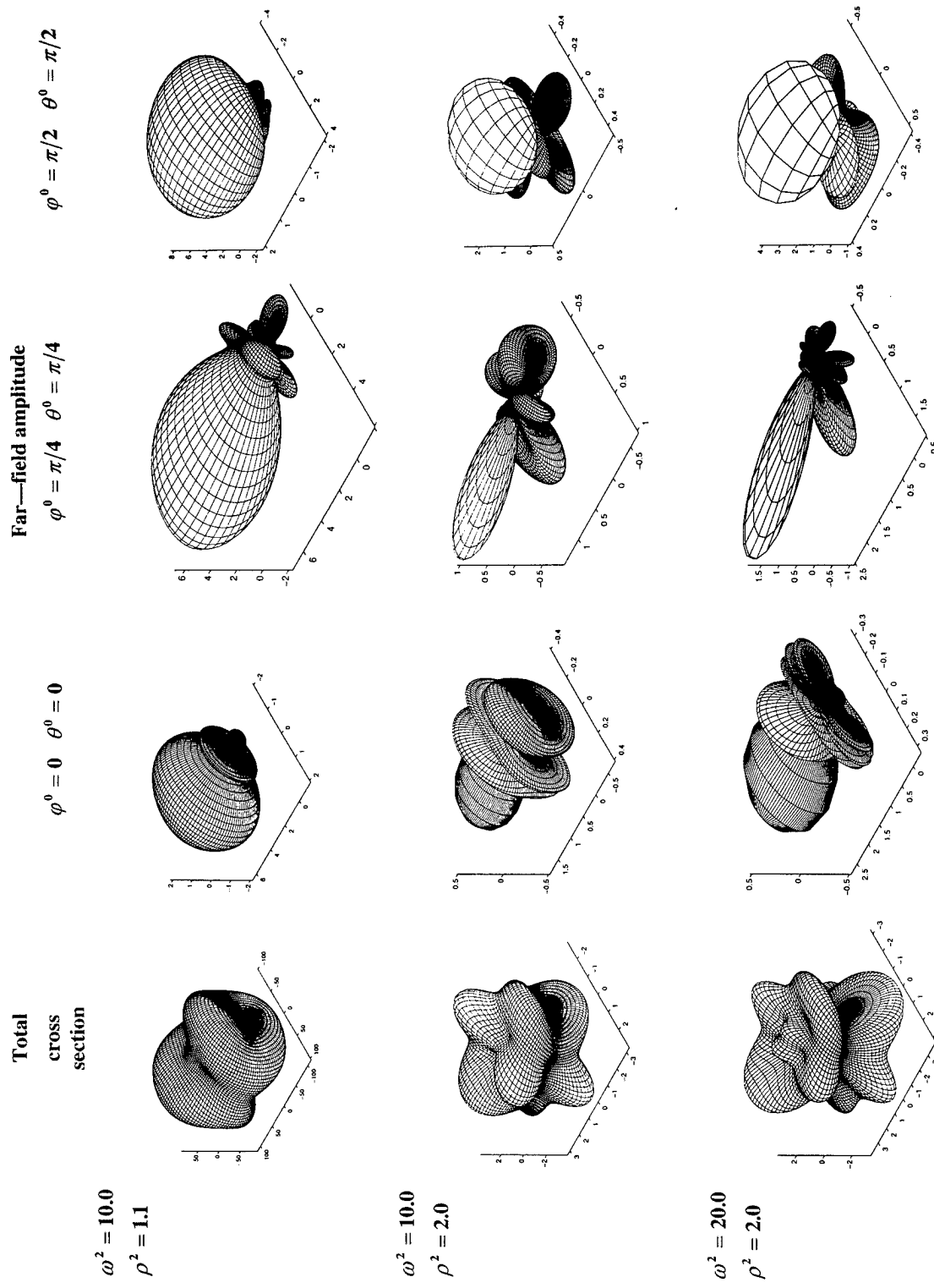


FIGURE 1. In the first column we present the total cross section as a function of the incident direction for different values of ω and ρ . In the next three columns the far-field amplitudes are displayed as functions of the observation direction, for three different values of the incident angles. The potential under consideration is described in the text. Note that the grid is produced by conventional (spherical) angle variables.

separable. The ellipsoidal system is the most general one as the remaining 10 of them can be obtained by special limits of its parameter values [2]. Letting the semiaxes a , b , and c go to these limits one may approach any of the above 10 symmetries. Note that in the limit cases, corresponding to nonspherical symmetry, small values of k will give the same scattering data as in a nearly spherical case for large k , as soon as the values of ω and ρ are the same. This is to some extent an explanation of the well-known fact that for small values of the wave number $|k|$, scattering data of a sphere is a good approximation for other cases.

On the other hand this means that even small deviations from spherical symmetry may produce essential influences upon the scattering scenario, provided $|k|$ is large enough.

ACKNOWLEDGMENTS

This work was partly supported by the Russian Foundation for Basic Research under Grant No. 96-01-00951, the Swedish Defence Research Establishment, FOA Project E 6022, and by the Swedish Institute through expert-exchange program.

References

1. T. Levitina and E. J. Brändas, *Int. J. Quant. Chem.* **65**, 601 (1997).
2. P. M. Morse and H. Feshbach, *Methods of Theoretical Physics, Part 1* (McGraw-Hill, New York, 1953).
3. L. P. Eisenhart, *Phys. Rev.* **74**(1), 87 (1948).
4. A. Källström and B. D. Sleeman, *Proceed. Royal Soc. Edinburgh* **74A**, 145 (1974/75).
5. A. A. Abramov, A. L. Dyshko, N. B. Konyukhova, and T. V. Levitina, *USSR Comput. Maths., Math. Phys.* **29**(3), 119 (1989).
6. A. A. Abramov, A. L. Dyshko, N. B. Konyukhova, and T. V. Levitina, *USSR Comput. Maths., Math. Phys.* **31**(2), 25 (1991).
7. T. V. Levitina, Thesis, *Vychisl. Tsentr Akad. Nauk SSSR, Moscow* (1991).
8. N. B. Konyukhova, S. Ye. Masalovich, and I. B. Staroverova, *USSR Comput. Maths., Math. Phys.* **35**(3), 287 (1995).
9. Yu. N. Demkov and V. S. Rudakov, *Zh. Eksp. Teor. Fiz.* **59**(6), 2035 (1970).
10. I. V. Komarov, L. I. Ponomarev, and S. Yu. Slavyanov, *Spheroidal and Coulomb Spheroidal Functions* (Nauka, Moscow, 1976).
11. A. G. Sitenko, *Lectures in Scattering Theory* (Pergamon, Oxford, 1971).
12. T. Levitina and E. J. Brändas, *Int. J. Quant. Chem.* **60**, 1217 (1996).

Photochemical Reaction Pathways of Ethylene

LARS FREUND, MARTIN KLESSINGER

Organisch-Chemisches Institut der Westfäl, Wilhelms-Universität, D-48149 Münster, Germany

Received 23 February 1998; revised 26 May 1998; accepted 1 June 1998

ABSTRACT: Conical intersections are a common feature in most nondiabatic singlet photoreactions. For ethylene, several S_1-S_0 conical intersections could be located by CASSCF calculations. The energetically lowest one is different from the one determined by Ohmine [J. Chem. Phys. 83, 2348 (1985)]; its geometry suggests that *cis-trans* isomerization and a [1,2]hydrogen shift occur via the same funnel. © 1998 John Wiley & Sons, Inc. Int J Quant Chem 70: 1023–1028, 1998

Introduction

The mechanism of photochemical *cis-trans* isomerization has been the subject of many studies [1]. Of particular interest is the nonadiabatic transition from the low-lying excited to the ground state. In recent years, conical intersections have been located using ab initio calculations for a large variety of photoreactions [2], and it can be assumed that the occurrence of this topological phenomenon, previously believed to be quite improbable, is more likely to be the rule than an exception. Several models have been proposed to predict the structure of a conical intersection. Robb and Bernardi [3] showed that in the framework of a 2×2 VB model the nature of the surface-crossing region may be predicted on the basis of the geometry dependence of the VB exchange inte-

grals. Particularly useful is the two-electron two-orbital model (2-in-2 model) of Michl and Bonačić-Koutecký [1, 4].

For 90°-twisted ethylene, the p orbitals are orthogonal and degenerate; the pericyclic geometry of C_{2v} symmetry [Fig. 1(b)] corresponds to a perfect biradical with a very large gap between S_1 and S_0 [1]. A heterosymmetric perturbation δ (electronegativity difference of the localized p orbitals) reduces the energy gap, but calculations show that pyramidalization of one of the methylene groups alone [Fig. 1(c)] does not represent a perturbation δ sufficient for reaching a conical intersection [5]. Ohmine showed, however, that an additional distortion of one of the CH bonds toward the other carbon causes a crossing of S_1 and S_0 potential energy surfaces, thus explaining the experimentally observed fast photoreaction [6].

Ohmine restricted his calculation to C_s symmetry with one hydrogen migrating within the mirror plane from a planar CH_2 group to a pyramidal

Correspondence to: M. Klessinger.

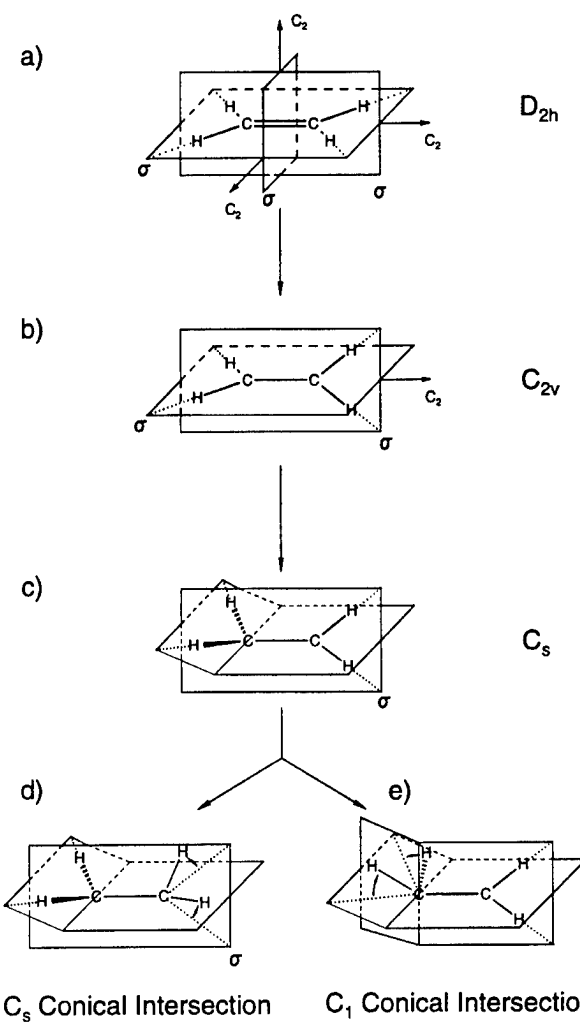


FIGURE 1. Ethylene symmetries: (a) ground state (D_{2h}); (b) 90°-twisted (C_{2v}); 90°-twisted and pyramidalized (C_s); (d, e) conical intersections (C_s and C_1 , respectively).

one as shown in Figure 1(d). In view of the fact that conical intersections in general occur at structures with no symmetry [2], the question arises as to how relaxing the C_s symmetry will affect the results. As hydrogen motion is apparently involved in efficient excited-state relaxation, another open question is whether the [1,2]hydrogen shift and *cis-trans* isomerization reactions will proceed via the same conical intersection or whether different excited-state reaction paths lead to different conical intersections for these two reactions.

A complete determination of the outcome of a photochemical reaction requires detailed dynamics calculations. As the first step toward this goal, we present here a discussion of the S_0 and S_1 surfaces

and of their topology which allows some of the questions to be answered.

Method of Calculation

Preliminary calculations were carried out using the semiempirical MNDOC-CI method [7]. Final results on the ab initio CASSCF level of theory were obtained using the GAUSSIAN 94 [8] and MOLPRO 96.4 [9] software. 6-31G and 6-31G** basis sets were employed; the neglect of diffuse basis functions is justified by the fortunate circumstance that in contrast to planar geometries at the photochemically important twisted geometries of ethylene the lowest excited states are all purely valence character while the Rydberg states are high in energy [1a]. For calculating energy surfaces, the active space consists of four orbitals; final results were obtained with six electrons in an active space of six orbitals. The optimization of conical intersections was achieved in the $(f - 2)$ -dimensional intersection space using the method of Bearpark et al. [10] implemented in the GAUSSIAN 94 program.

Results and Discussion

The lowest-energy intersection point of the S_1 and S_0 potential energy surfaces of ethylene was located using the GAUSSIAN 94 package and the CASSCF (4,4) procedure with a 6-31G basis. If the optimization procedure was started at a point of C_s symmetry, the result of Ohmine [6] was recovered and the conical intersection shown in Figure 2 was obtained. If, however, the C_s symmetry is relaxed, another conical intersection some 15 kcal/mol lower in energy (see Table I) is reached, which is shown in Figure 3. Geometry parameters and total electronic energies for these conical intersections are collected in Table I, with the numbering of atoms being shown in Scheme 1, where H_1 is the migrating hydrogen atom. The geometry at the conical intersection of C_1 symmetry is shown in Figure 4. The main difference between the two structures of C_s and C_1 symmetry is found, apart from the dihedral angles, for the CC distance, which is longer, and the angle $C_2C_1H_2$, which is considerably smaller in the nonsymmetrical case.

The same conical intersection was found if the optimization was started at any point with C_1

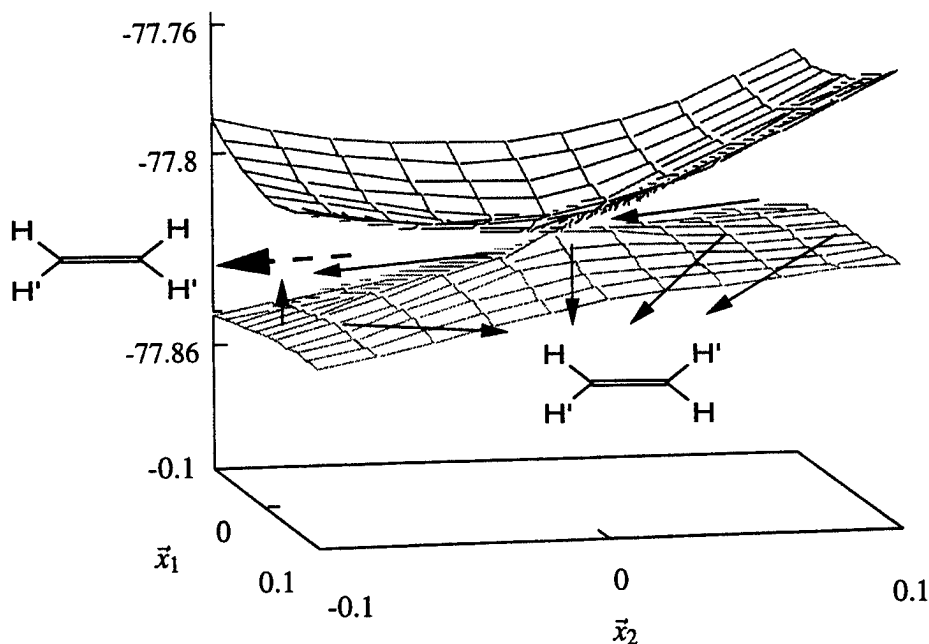


FIGURE 2. Conical intersection of the S_0 and S_1 surfaces of ethylenes; calculation started in C_s symmetry.

TABLE I
Energies (in au) and geometries (distances r in Å, angles a and dihedral angles d in degrees) of the conical intersections of ethylene.

	Method				
	MRDCI ^a	CAS(4,4)	CAS(4,4)	CAS(6,6)	MNDOC-CI
	Basis				
DZ ₊ ^b	6-31G	6-31G	6-31G**	/	/
	Symmetry				
C_s	Nearly C_s	C_1	C_1	C_1	C_1
Energy in Hartrees	-77.98	-77.8141	-77.8389	-77.9063	
$r(C_1C_2)$	1.373	1.364	1.419	1.405	1.393
$r(C_1H_1)$	1.295	1.217	1.297	1.221	1.240
$r(C_1H_2)$	1.067	1.053	1.086	1.086	1.091
$r(C_2H_3)$	1.101	1.089	1.076	1.118	1.109
$r(C_2H_4)$	1.101	1.089	1.076	1.081	1.095
$a(C_2C_1H_1)$	67.0	67.9	73.0	77.2	73.1
$a(C_2C_1H_2)$	173.9	165.7	121.4	119.7	122.9
$a(C_1C_2H_3)$	123.8	123.8	125.7	125.8	129.9
$a(C_1C_2H_4)$	123.8	123.8	119.6	120.7	119.4
$d(H_1C_1C_2H_2)$	180.0	180.0	-86.0	-89.0	-95.0
$d(H_1C_1C_2H_3)$	90.0	-87.7	-62.1	-58.3	-69.9
$d(H_3C_2C_1H_4)$	180.0	-175.0	-172.9	-168.3	-169.1

^a See [6].

^b Dunning and Huzinaga basis.

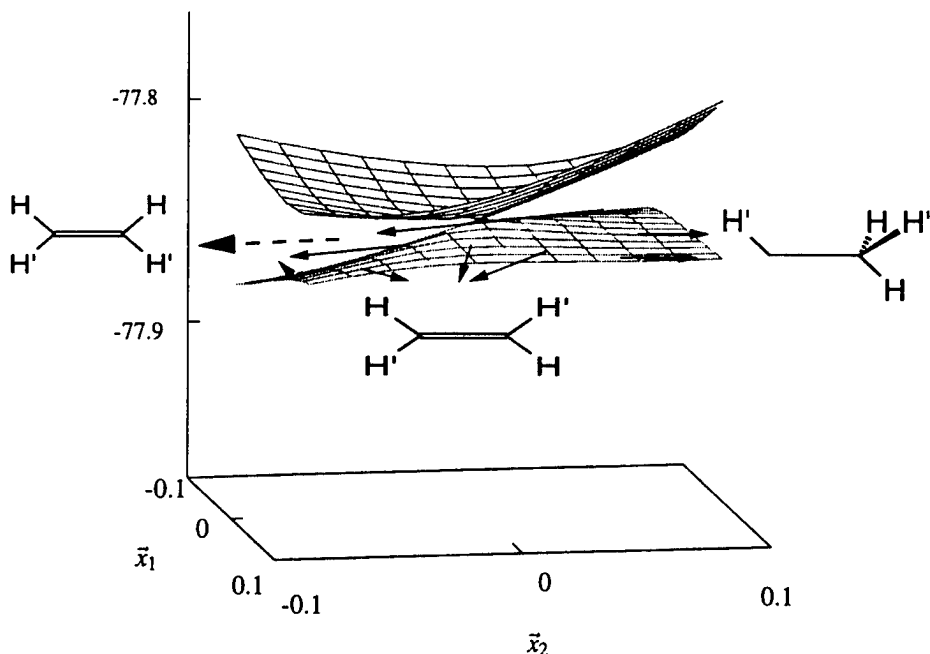
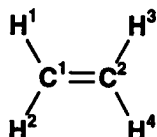


FIGURE 3. Nonsymmetrical conical intersection of the S_0 and S_1 surface of ethylene calculation started in C_2 symmetry.



SCHEME 1.

symmetry, for example, from an initial structure obtained by pyramidalizing one of the methylene groups and distorting one of the CH bonds of the same methylene group [cf. Fig. 1(e)]. Hence, it is concluded that this is the energetically lowest minimum of the S_1-S_0 intersection space, while symmetry restriction leads to another stationary point in the same intersection space. Since even very small deviations from C_s symmetry yield the nonsymmetrical conical intersection, the C_s -symmetrical stationary point first reported by Ohmine [6] is most likely a transition state between the two equivalent nonsymmetrical conical intersections, which result from the C_s symmetric one by altering the $\text{H}_1\text{C}_1\text{C}_2\text{H}_2$ dihedral angle in a positive or negative sense, respectively.

In the diagrams of Figures 2 and 3, the energies of the lowest two singlet states S_0 and S_1 are

plotted against x_1 and x_2 ; the coordinate x_1 is the gradient difference vector given by

$$x_1 = \partial(E_0 - E_1)/\partial \mathbf{q},$$

where \mathbf{q} is a vector of nuclear displacement coordinates. x_2 is the gradient of the interstate coupling vector given by

$$x_2 = \langle \mathbf{C}_0 (\partial \mathbf{H} / \partial \mathbf{q}) \mathbf{C}_1 \rangle,$$

where \mathbf{C}_0 and \mathbf{C}_1 are configuration interaction (CI) eigenvectors and \mathbf{H} is the corresponding CI Hamiltonian. The vector x_2 is parallel to the nonadiabatic coupling vector $\mathbf{g}(\mathbf{q}) = \langle \psi_0 | \partial \psi_1 / \partial \mathbf{q} \rangle$. The vectors x_1 and x_2 are depicted in Figures 5 and 6 for the C_s conical intersection [cf. Fig. 1(d)] and the C_1 conical intersection [cf. Fig. 1(e)], respectively. To show clearly all atomic displacement vectors, the perspective had to be slightly changed with respect to Figure 4. These vectors illustrate the nuclear motion at the conical intersection: Trajectories through the tip of the cone will follow the slope of the cone wall most likely in a direction close to the x_1 vector; trajectories that miss the cone tip have some probability of performing a jump onto the lower surface, and an amount of

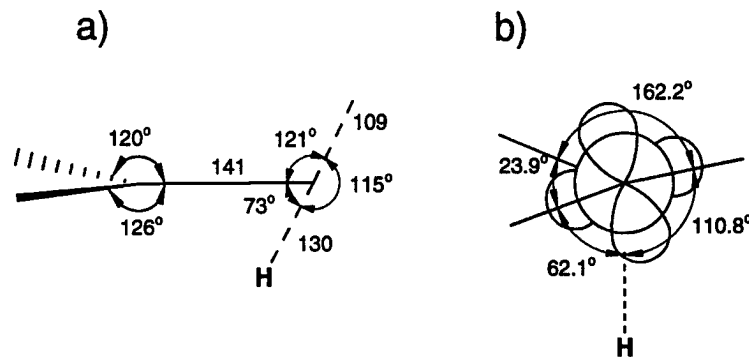


FIGURE 4. Geometry of the nonsymmetrical (C_1) conical intersection of the S_0 and S_1 surfaces of ethylene; (a) side view; (b) Newman projection with localized nonbonding orbitals.

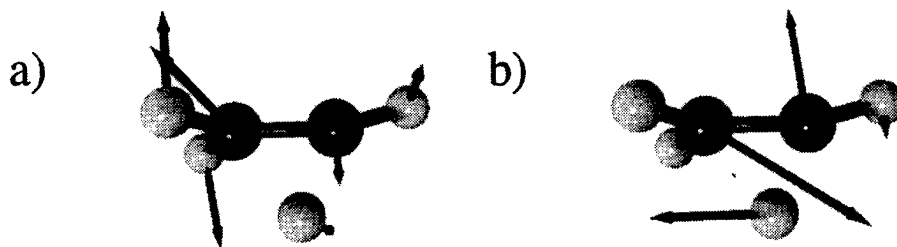


FIGURE 5. Three-dimensional representation of (a) the gradient difference vector x_1 and (b) the nonadiabatic coupling vector x_2 at the conical intersection shown in Figure 2.

energy equal to the height of the jump is converted into a component of motion in a direction given by the x_2 vector.

In the immediate vicinity of the apex of a conical intersection, the reaction path can follow any direction in the x_1 , x_2 plane and may reach different reaction valleys that develop on the S_0 surface. To establish which valleys can be reached in the

case of ethylene, the structures of various points on the seam of the S_0 surfaces shown in Figures 2 and 3 were optimized, yielding ethylene with the two possible arrangements of the hydrogens corresponding to *cis*- and *trans*-configurations as well as methylcarbene. This demonstrates that, starting from the conical intersection, the products of both *cis-trans* isomerization and the [1,2]hydrogen shift

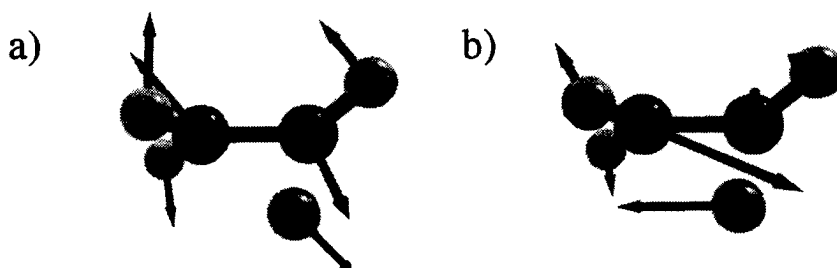


FIGURE 6. Three-dimensional representation of (a) the gradient difference vector x_1 and (b) the nonadiabatic coupling vector x_2 at the conical intersection shown in Figure 3.

as well as that of the initial reactant can be reached on a barrier-less ground-state relaxation pathway.

The results are similar for both conical intersections. The restriction to C_s symmetry, however, considerably reduces the probability of reaching the reaction valley of the [1,2]hydrogen shift, as may be verified particularly from the atomic components of the gradient difference vector x_1 shown in Figures 2 and 4. In contrast to the nonsymmetrical conical intersection, only two of 20 optimizations produced methylcarbene.

As shown in Table I, CASSCF(6,6) calculations with a 6-31G** basis confirm the results for the nonsymmetrical conical intersection. The same conical intersection could also be obtained on a semiempirical level including full valence configuration interaction [11] by minimizing the projection of the gradient into the ($f - 2$)-dimensional subspace orthogonal to x_1 and x_2 according to the method of Bearpark et al. [10].

Conclusion

Radiationless decay from S_1 to S_0 of ethylene occurs via a conical intersection, which, in agreement with the generally observed situation [2], occurs at a very unsymmetrical structure. Starting from this conical intersection, the products of both the *cis-trans* isomerization and the [1,2]hydrogen shift reactions as well as the initial reactant can be reached on a barrier-less ground-state relaxation path. The conical intersection of C_s symmetry which was first obtained by Ohmine [6] corresponds to a stationary point in the same intersection space and is presumably a transition state between the two equivalent nonsymmetrical conical intersections.

References

- (a) J. Michl and V. Bonačić-Koutecký, *Electronic Aspects of Organic Photochemistry* (Wiley, New York, 1990); (b) M. Klessinger and J. Michl, *Excited States and Photochemistry of Organic Molecules* (VCH, New York, 1995).
- (a) F. Bernardi, M. Olivucci, and M. A. Robb, *Chem. Soc. Rev.* **321** (1996); H. M. Klessinger, *Angew. Chem., Int. Ed. Engl.* **34**, 549 (1995), and references therein.
- F. Bernardi, M. Olivucci, and M. A. Robb, *Isr. J. Chem.* **33**, 265 (1993).
- V. Bonačić-Koutecký, J. Koutecký, and J. Michl, *Angew. Chem., Int. Ed. Engl.* **26**, 170 (1987).
- R. J. Buenker, V. Bonačić-Koutecký, and L. Pogliani, *J. Chem. Phys.* **73**, 1836 (1980).
- I. Ohmine, *J. Chem. Phys.* **83**, 2348 (1985).
- M. Klessinger, T. Pötter, and Ch. v. Wüllen, *Theoret. Chim. Acta* **80**, 1 (1991).
- M. J. Frisch, G. W. Trucks, H. B. Schlegel, P. M. W. Gill, B. G. Johnson, M. A. Robb, J. R. Cheeseman, T. Keith, G. A. Petersson, J. A. Montgomery, K. Raghavachari, M. A. Al-Laham, V. G. Zakrzewski, J. V. Ortiz, J. B. Foresman, J. Cioslowski, B. B. Stefanov, A. Nanayakkara, M. Challacombe, C. Y. Peng, P. Y. Ayala, W. Chen, M. W. Wong, J. L. Andres, E. S. Replogle, R. Gomperts, R. L. Martin, D. J. Fox, J. S. Binkley, D. J. Defrees, J. Baker, J. P. Stewart, M. Head-Gordon, C. Gonzalez, and J. A. Pople, *GAUSSIAN 94, Revision B.2* (Gaussian, Inc., Pittsburgh PA, 1995).
- H.-J. Werner, P. J. Knowles, J. Almlöf, R. D. Amos, A. Berning, M. J. O. Deegan, F. Eckert, S. T. Elbert, C. Hampel, R. Lindh, W. Meyer, A. Nicklass, K. Peterson, R. Pitzer, A. J. Stone, P. R. Taylor, M. E. Mura, P. Pulay, M. Schuetz, H. Stoll, T. Thorsteinsson, and D. L. Cooper, *MOLPRO 96.4 Program Package* (1996); *MCSCF/CASSCF*; H.-J. Werner and P. J. Knowles, *J. Chem. Phys.* **82**, 5053 (1985); P. J. Knowles and H.-J. Werner, *Chem. Phys. Lett.* **115**, 259 (1985).
- M. J. Bearpark, M. A. Robb, and H. B. Schlegel, *Chem. Phys. Lett.* **223**, 269 (1994).
- R. Izzo, Ph.D. Thesis, Westf. Wilhelms-Universität Münster (1998).

Theoretical Studies on Hydrogen Activation by Iridium Dimers

S. CASTILLO,¹ V. BERTIN,² E. SOLANO-REYES,¹
H. LUNA-GARCÍA,¹ A. CRUZ,³ E. POULAIN⁴

¹Área de Física, CBI, UAM-A, Av. San Pablo 180, 02200, México, D.F., México

²Dep. de Química, CBI, UAM-I, A.P. 55-534, 09340, México, D.F., México

³Subdirec. de Transformación Industrial, IMP, A.P. 14-805, 07730, México D.F., México

⁴Div. de Est. de Posgrado e Invest., ITTLA, A.P. 750, 54070 Tlalnepantla de Baz, Méx. México

Received 23 February 1998; accepted 20 April 1998

ABSTRACT: The basic and fundamental mechanisms governing the catalytic reaction of small iridium clusters with H₂ are presented here with the purpose to determine its behavior in hydrogenation reactions. The iridium dimer's lowest states in interaction with H₂ potential energy surface were obtained using ab initio multiconfigurational self-consistent-field calculations (MC-SCF), with relativistic pseudopotentials. The electronic correlation contribution was included by configurations interaction (CI) calculations, which considered a variational part plus a second-order perturbative part. The Ir₂ + H₂ reactions were developed in the C_{2v} symmetry. The Ir₂'s five lowest electronic states were determined, ⁵Π_g, ³Π_g, ¹Σ_g⁺, ³Σ_u⁺, and ⁵Σ_g, and studied when reacted with H₂. It was found that the iridium dimer, in these five states, might capture and break the H—H bond, spontaneously in certain cases and after surmounting activation barriers in other cases. © 1998 John Wiley & Sons, Inc. Int J Quant Chem 70: 1029–1035, 1998

Introduction

That metallic iridium adsorbs H₂ without activation is observed in many experiments. The adsorption occurs both as a molecular reaction and

in a dissociative way [1]: in the last mode, in a 1:1 H and Ir rate, with an adsorption heat of 18.40 kcal/mol in the (110) plane [1]. But in increasing the iridium dispersion over a support, each Ir atom can adsorb two or three H atoms [2]. The dispersion is increased easily in iridium-supported catalysts, reaching almost a 100% value [3], by far different from other transition metals, as platinum, where the atoms have the tendency to sinter.

Correspondence to: E. Poulain.

Contract grant sponsor: CONACYT (Mexico).

Contract grant number: 3494PE.

Iridium has been employed to improve the Pt/Al₂O₃ reforming catalyst, but the resulting bimetallic catalyst is not easily regenerated, so its industrial application is difficult. Better applications have iridium catalysts in a variety of hydrogenation or dehydrogenation reactions, as, for example, in cyclohexene, benzene [4], and linoleic acid hydrogenation [5], with the purpose to obtain products with a large added value. Iridium catalysts also have been employed in hydrogenolysis reactions. Also, iridium complexes (phosphynes, carbonyls) are currently employed [4].

The Ir ground state is an ⁴F(5d⁷6s²) configuration. Ir reacts very quickly and easily with alkenes, but does not react with methane and other alkanes. This behavior has to be explained in terms of the ground and excited states' electronic configuration [6] and topology.

It was suggested that the 6s orbital lanthanide contraction modifies the 5d series atoms reactivity. Also, the positive Ir ion is efficient, the most efficient among transition-metal ions. For instance, among other characteristics, in gas-phase methane dehydrogenation, the Ir ion easily changes its spin value [7]. Ir monomers have been studied theoretically, where some characteristics were presented; particularly, studies of the Ir + H₂ and Ir + CH₄ reactions are shown in [8, 9].

Theoretically and experimentally [10–24], the H₂ reaction with many metals has been the object of intense work in our laboratory. Due to, in particular, that the Ir + H₂ interaction is a preliminary not yet well-determined catalytic reaction, many steps of these reactions are in process. Moreover, they are especially important in petrochemical processes [25], where in these reaction types, the hydrogen is a reactant or a product and is employed to activate the catalysts. For instance, the H₂ interaction with metal is a powerful reaction test, which has produced the greatest number of experimental reports [26].

Pd and Pt are the most employed metals in catalysis because of their electronic properties. The most important catalyzed reactions using them are the CO, H₂, and alkane activations [27, 28]. But there are other metals also with important catalytic properties. Iridium is one of these metals. Some iridium organometallic complexes may activate and break the C—H alkane bonds by inserting an Ir atom in the bonds and forming a carbon–metal–hydrogen complex [29].

Method of Calculation

The potential energy states (PES) parameters' determination in each point is done and initiated using ab initio Hartree–Fock self-consistent-field (HF–SCF) calculations with the PSHONDO program [30], with relativistic pseudopotentials, also called relativistic effective core potentials (RECP). The Ir pseudopotential is a xenon core type [31]. These calculations are followed by small multiconfigurational (MC) SCF calculations, which gives the initial energy value and the initial wave function. The electronic correlation is considered and added to the energy value previously described throughout configuration interaction (CI) methods. This term is obtained by CI variational and perturbative calculations, where an energy value is determined by making a variational calculation, modified by a perturbative calculation upon second order, using the CIPSI algorithm [32]. The iridium atomic basis functions are Gaussians taken from [31], contracted to a triple zeta scheme (3s3p4d)/[111/21/211]. The hydrogen functions are of double-zeta quality [33] plus two polarization functions [34].

Results and Discussion

IRIDIUM ATOM CALCULATIONS

As the first step of the Ir₂ + H₂ reaction study, the Ir atomic basis and the Ir pseudopotential were tested. Here, we used the best set from the literature reproducing the experimental iridium atomic energy spectra; Table I presents the calculated and the reported energies [35] of the atomic iridium's three low-lying F states. These results show that

TABLE I
Experimental and calculated splitting of the three lowest F iridium atom states.

Atomic state	ΔE (this work) (kcal / mol)	ΔE (experimental ^a) (kcal / mol)
⁴ F(5d ⁷ 6s ²)	0.0	0.0
⁴ F(5d ⁸ 6s ¹)	13.6	9.2
² F(5d ⁸ 6s ¹)	19.3	26.0

^aFrom [34], the J-averaged values over all spin-orbit components.

by using the selected functions we obtained a satisfactory description of the Ir states.

H₂ in C_{2v} Approach to the Ir(⁴F:5d⁷6s²) and Ir(⁴F:5d⁸6s¹) Atoms

The hydrogen molecule activation by a single iridium atom was studied previously [36] and recently by Gropen et al. [8]. In both calculations, it was found that the iridium atom in its ⁴F ground state captures H₂ after surmounting a small barrier. In addition, the former authors found that the iridium atom in its lowest ²F excited state spontaneously inserts between the H atoms. These configurations were calculated by us and the results presented in the mentioned work were reproduced. It seems not relevant to include them here.

Table II shows that the iridium atom, in its ground state ⁴F:5d⁷6s², captures and breaks the hydrogen molecule. These PES reactions are ⁴A₁ and ⁴B₁ excited states. The ⁴A₁ and ⁴B₂ PES of the first iridium excited state present, first, an attractive character, arriving at an avoided crossing region with the ⁴A₂ and ⁴B₁ PES. After that, they change to a repulsive character. The ⁴A₂ and ⁴B₁ states of the ⁴F:5d⁷6s² + H₂ reaction are initially repulsive curves. After the avoided crossing, these PES became attractive, showing potential wells, where the H₂ is captured and the H—H rupture occurs. The potential barriers presented in these interactions are in all cases a consequence of avoided crossings.

H₂ C_{2v} Approach to the Ir(²F:5d⁸6s¹) Atom

For the iridium in the doublet state, we found that in the ²F:5d⁸6s¹ + H₂ reaction the ²A₁, ²A₂, and ²B₁ states spontaneously occur, capturing and breaking the hydrogen molecule. Our results are in very good agreement with those of [36].

IRIDIUM DIMER CALCULATIONS

The electronic configurations of the iridium dimer's lowest most important states were calculated. The energies and interatomic distance for these configurations are presented in Table III. As we can see from this table, the Ir₂ ground state is a quintuplet, where the excited-state energy gap difference is similar and the metal–metal distance presents a very interesting behavior. The electronic configuration of the Ir₂ ⁵P_g ground state as well as the first ³P_g excited state have the same four single-occupied molecular orbitals: σ_u (Ir(s) + Ir(-s)), π_g (Ir(d_{yz}) + Ir(d_{yz})), δ_g (Ir(d_{xy}) + Ir(d_{xy})), and δ_u (Ir(d_{xy}) + Ir(-d_{xy})).

POTENTIAL ENERGY SURFACES FOR THE Ir₂ + H₂ INTERACTION

The PES reactions of the five Ir₂ lowest states in the reaction with H₂ were determined. The hydrogen molecule approached the iridium dimer in the C_{2v} symmetry in two ways: one in which both systems are in the same plane, and in the other, where the two systems are in perpendicular planes.

TABLE III
The five lowest Ir₂ states.

Molecular electronic state	Relative energy (kcal / mol)	Ir–Ir distance (au)
⁵ P _g : $\pi_u^2 \pi_u^2 \delta_u^2 \sigma_g^2 \delta_u^2 \pi_g^2 \sigma_g^2 \pi_g^1 \delta_g^1 \sigma_u^1 \delta_u^1$	0.0	4.6
³ P _g : $\pi_u^2 \pi_u^2 \delta_u^2 \sigma_g^2 \delta_u^2 \pi_g^2 \sigma_g^2 \pi_g^1 \delta_g^1 \sigma_u^1 \delta_u^1$	15.9	4.4
¹ S _g ⁺ : $\pi_u^2 \pi_u^2 \sigma_g^2 \delta_g^2 \delta_u^2 \pi_g^2 \pi_g^2 \delta_g^2 \sigma_u^2$	21.6	4.4
³ S _u ⁺ : $\pi_u^2 \pi_u^2 \delta_g^2 \sigma_g^2 \delta_u^2 \pi_g^2 \pi_g^2 \delta_g^2 \sigma_g^1 \sigma_u^1$	29.6	4.6
⁵ S _g : $\pi_u^2 \pi_u^2 \sigma_g^2 \delta_g^2 \delta_u^2 \pi_g^2 \pi_g^2 \sigma_g^2 \sigma_g^1 \delta_g^1 \sigma_u^1 \delta_u^1$	35.3	4.8

TABLE II
H₂ C_{2v} approach to an Ir atom.

Ir electronic state	d(Ir—mcH ₂) (au)	d(H—H) ^a (au)	% H—H relax	Depth of well (kcal / mol)	Barrier (kcal / mol)
⁴ A ₁			No capture for this state		
⁴ A ₂	2.5	3.0	113	11.2	15.0
⁴ B ₁	2.1	4.0	184	11.8	4.5
⁴ B ₂			No capture for this state		

^ad(H—H) nonactivated = 1.41 au.

Both Systems in the Same Plane: Side on C_{2v} Approach of H_2 to Ir_2

In this reaction mode (Table IV), it was found that Ir_2 activates the H_2 in its four low-lying states, $^5\Pi_g$, $^3\Pi_g$, $^1\Sigma_g^+$, $^3\Sigma_u^+$, where capture and dissociation of H_2 is obtained, but with barriers present, whereas in the highest state, $^5\Sigma_g$, the H_2 capture and dissociation occurs spontaneously. But, this last state is a very high one, hardly important in catalyzed reactions.

From Table IV, we can see that all the well depths (adsorption heats) are larger than the experimental adsorption heat (18.40 kcal/mol). All the capture distances are similar, and, in general, the captures need to be activated.

The $Ir_2(^5\Pi_g) + H_2$ PEs ground-state reaction shows a well only surmounting a potential barrier of 13 kcal/mol. This barrier is produced by an avoided crossing of this PES with an attractive PES coming from a high quintuplet state, whose separate fragments correlate with an iridium dimer in a quintuplet state and the hydrogen molecule is in the ground state. Similar to this case, all the potential barriers in this reaction mode are produced by avoided crossings.

Let us now analyze the molecular orbitals of the system. The Ir_2H_2 in equilibrium resulting from the $Ir_2(^5\Pi_g) + H_2$ reaction present the following molecular orbital elements: a bonding a_1 orbital, due to the overlap of the $Ir(s + d_{z2} + d_{yz}) + Ir(s + d_{z2} - d_{yz})$ orbitals with the $H(1s) + \bar{H}(1s)$ orbital; and a bonding a_2 orbital coming from the overlap of the orbital $Ir(s + d_{z2} + d_{yz})$ orbital + $Ir(-s - d_{z2} + d_{yz})$ with the antibonding $H(1s) + H(-1s)$ orbital.

Considering the bond formation, the following reaction mechanism is proposed to explain the $Ir_2(^5\Pi_g) + H_2$ interaction in the lowest state: At the beginning, the $H_2 \sigma^*$ empty orbital started to populate from the singled occupied $Ir_2 \sigma_u [Ir(s) + Ir(-s)]$ orbital, later interacted with the double-occupied $\pi_g [Ir(dz_2) + Ir(-dz_2)]$, due to that at the beginning the σ_u orbital has a higher energy than has the π_g orbital, but when the reaction progresses, the π_g becomes more important and both interactions contribute to generate the a_2 orbital. In the barrier zone, the a_2 orbital formation is in competition with a repulsive interaction of the occupied $Ir(s) + Ir(s)$ with the $H_2 \sigma$ orbital and the bonding a_1 orbital of the Ir_2H_2 in equilibrium system.

H_2 in C_{2v} , Perpendicular Approach to One of the Ir of the Ir Dimer

In this approach, the metal and the hydrogen are in a plane and Ir_2 in its five $^5\Pi_g$, $^3\Pi_g$, $^1\Sigma_g^+$, $^3\Sigma_u^+$, and $^5\Sigma_g$ low-lying states captures and activates H_2 without need of activation (see Table V). In the two lowest states, $^5\Pi_g$ and $^3\Pi_g$, the hydrogen molecule is only relaxed, whereas in the next three highest states of the metal, the hydrogen molecule is clearly dissociated. In addition, the adsorption heat is lower in the lowest metal states, being quite close to the reported values. The $Ir_2(^5\Sigma_g) + H_2$ PES depth of the potential well differs < 2 kcal/mol with the Ir adsorption heat in the (110) plane. This is the minor adsorption heat found in the present study. The capture distances are smaller for the highest metal states.

TABLE IV
 $H_2 C_{2v}$ lateral approach to Ir_2 reaction parameters.

Ir_2 electronic state	$d(Ir_2-H_2)^a$ (au)	$d(H-H)^b$ (au)	% H—H relax	Depth of well (kcal / mol)	Barrier (kcal / mol)
$^5\Pi_g$	2.8	5.6	297	33.4	13.3
$^3\Pi_g$	2.8	4.6	226	49.2	16.7
$^1\Sigma_g^+$	3.0	4.0	184	54.3	8.5
$^3\Sigma_u^+$	3.0	4.6	226	66.0	13.0
$^5\Sigma_g$	3.0	4.6	226	50.2	No

^aMass center–mass center distance.

^bCompared with $d(H-H)$ nonactivated = 1.41 au.

TABLE V
 $H_2 C_{2v}$ perpendicular approach to one Ir of the Ir_2 , both species in the same plane.

Ir_2 electronic state	$d(Ir_2-H_2)^a$ (au)	$d(H-H)^b$ (au)	% H—H relax	Depth of well (kcal / mol)	Barrier (kcal / mol)
$^5\Pi_g$	3.0	1.8	28	17.0	No
$^3\Pi_g$	3.0	1.8	28	29.2	No
$^1\Sigma_g^+$	3.0	4.7	233	34.8	No
$^3\Sigma_u^+$	1.5	5.0	255	52.2	No
$^5\Sigma_g$	2.5	4.6	226	42.7	No

^aIr—Ir bond bisecting the H—H bond.

^bAs in Table IV.

This reaction mode is the most similar one to the direct reaction of a single Ir atom with the hydrogen molecule. Comparing the one and two Ir atoms' reactions with H_2 and comparing with the platinum case, we can see that there are at least two differences: A ground-state single Ir atom can activate H_2 , whereas a single Pt atom only can activate H_2 from an excited state. Also, the second Ir atom does not poison the reaction of one Ir atom and the Pt dimer is able to activate the H_2 , but in an excited state, with a lower angle (almost one-half of a single Pt atom) because of the poisoning of the second atom.

The 100% dispersed Ir catalysts are easily prepared and adsorb H_2 [3], whereas it is very difficult to have Pt catalysts with this dispersion. In some experiments, by introducing Pt in small porous zeolites, it is possible to get such a dispersion, but in any of these cases, Pt does not adsorb H_2 [37].

H_2 in C_{2v} Approach to Ir_2 , Both Systems in Perpendicular Planes

Again, for Ir_2 in the four lowest states, $^5\Pi_g$, $^3\Pi_g$, $^1\Sigma_g^+$, and $^3\Sigma_u^+$, for this reaction mode, activation is necessary to induce the dissociative capture of H_2 , especially in the ground state (Table VI). But we have to remark that this approach is not a comparable scheme with the experimental results, due to the following: This model does not consider the Ir atoms of the subjacent plane.

In the experimental situation, the hydrogen molecule falls over the Ir crystal plane but not on a single isolated dimer. However, it is useful to consider the characteristics of this approach over an isolated and naked cluster because the H_2 can rotate.

From Table VI, we can observe, that in this approach mode, the distances between the metal dimer and the hydrogen are the smallest. In all the

TABLE VI
 C_{2v} approach of H_2 to Ir_2 , both dimers in perpendicular planes.

Ir_2 electronic state	$d(Ir_2-H_2)^a$ (au)	$d(H-H)^b$ (au)	% H—H relaxation	Depth of well (kcal / mol)	Barrier (kcal / mol)
$^5\Pi_g$	0.8	3.8	170	22.1	39.8
$^3\Pi_g$	0.0	3.8	170	32.5	9.1
$^1\Sigma_g^+$	0.0	4.4	212	48.7	13.7
$^3\Sigma_u^+$	0.8	4.2	198	35.1	27.5
$^5\Sigma_g$	1.5	3.4	141	24.0	No

^{a,b}See footnotes a and b to Table IV.

cases presented, the H—H bond is completely ruptured with a very different well depth, depending on the electronic state, but all the five metal states show dissociative capture. In the $^5\Sigma_g$ highest state, the dissociative H_2 adsorption is spontaneous, that is, it does not present a barrier.

For the $Ir_2(^3\Pi_g)$ — H_2 and $Ir_2(^1\Sigma_g^+)$ — H_2 interactions, it was found that the metal–hydrogen distance is null, that is, the hydrogen atoms are between the Ir atoms, forming a bridged structure (Table VI). This structure is presented in organometallic compounds [38]. Comparing the results of Tables V and VI, there are some similar behaviors. This can be explained by considering that it is possible to change the reaction mode from the same plane to the perpendicular planes, with a simple rotation.

This reaction mode for the equilibrium Ir_2H_2 system, the $Ir_2(^5\Pi_g)$ — H_2 interaction, presents, among others, the following orbitals: a bonding a_1 orbital, resulting from the overlap of the $\sigma_g[Ir(s) + Ir(s)]$ orbital, with the $H_2(\sigma_g)$ orbital. Also, there is a bonding b_1 orbital from the overlap $\pi_u[Ir(d_{xy}) + Ir(-d_{xy})]$ orbital with the $\sigma^*(H_2)$ orbital. The bond arises from the following proposed mechanism: The empty $\sigma^*(H_2)$ orbital may be populated and form a bond with the Ir_2 doubly occupied $\pi_u[Ir(d_{xy}) + Ir(-d_{xy})]$ orbital; nevertheless, at the beginning of the reaction, this Ir_2 orbital is much deeper in energy than are the other Ir_2 partially occupied orbitals, so the $\sigma^*(H_2)\gamma\pi_u(Ir_2)$ cannot overlap completely. In advancing the reaction, the overlap is produced and the described equilibrium geometry is achieved.

The interaction of both orbitals led to the $Ir_2H_2b_1$ orbital formation. Also, at the beginning of the reaction, the b_1 orbital formation is in competition with the repulsive interaction of the occupied $Ir(s) + Ir(s)$ with the σ (H_2) orbital. This last interaction produces the bonding a_1 Ir_2H_2 orbital. As a consequence, in this approach mode, a high barrier appears in the $Ir_2(^5\Pi_g)$ — H_2 interaction. When the reactants are in the same plane, they show from the beginning an attractive interaction compared with the high barrier existence in this approach and is in agreement with a less favorable directional character of the molecular orbitals in the reaction with the metal dimer and the hydrogen in perpendicular planes.

The present study shows that the iridium dimer, in the ground state, as in its four low-lying excited states, can activate the hydrogen molecule. In catalytic processes, the excited states' contribution is

quite probable, mainly because the ligands may modify the electronic structure of the metal's leading to many active states, giving the best catalyst [8, 20].

Conclusions

From the Ir dimer study, we obtain the molecular configuration, the equilibrium interatomic distances, and the energies of the five lowest states, $^5\Pi_g$ being the ground state, and $^3\Pi_g$, $^1\Sigma_g^+$, $^3\Sigma_u^+$, and $^5\Sigma_g$, the four lowest excited states.

Ir_2 could capture and activate the hydrogen molecule in almost all the cases studied. In the perpendicular reaction mode, where H_2 and Ir_2 are in the same plane, both the molecular and the dissociative capture of H_2 is obtained. As experimentally observed, no barriers are presented.

The participation of some of the metal excited states must be considered because they also have a dissociative reaction with H_2 . Other modes of reaction may be considered as important because the excited states are also active, but the presence of avoided crossings generate high barriers which make it more difficult to reach these states.

ACKNOWLEDGMENTS

We wish to thank once again our colleagues at the University of Toulouse, France, and at the University of Barcelona, Spain, for the PSHF-GMCP-CIPSI chain of programs. This work was partially supported from CONACYT (México) Project No. 3494PE. The calculations were done with an Aspen Alpha Durango II 533 MHz computer provided by the mentioned project.

References

1. K. R. Christmann, in *Hydrogen Effects in Catalysis*, Z. Paál and P. G. Menon, Eds. (Marcel Dekker, New York, 1988).
2. V. F. Kiselev and O. V. Krylov, in *Adsorption and Catalysis on Transition Metals and Their Oxides*, R. Gomer, Ed. (Springer-Verlag, Berlin, Heidelberg, 1989).
3. L. Tournayan, H. Charcosset, R. Frety, C. Leclercq, and P. Turlier. *Thermochim. Acta* **27**, 95 (1978).
4. P. N. Da Silva, M. Guenin, C. Leclercq, and R. Frety. *Appl. Catal.* **54**, 203 (1989).
5. Y. Kitayama, M. Muraoka, M. Takahashi, T. Kodama, E. Takahashi, and M. Okamura, *J. Am. Oil Chem. Soc.* **74**, 525 (1997).
6. J. Carroll, J. John, J. C. Weisshaar, and C. James. *J. Phys. Chem.* **100**, 12355 (1996).

HYDROGEN ACTIVATION BY IRIDIUM DIMERS

7. J. K. Perry, G. Ohanessian, and W. A. Goddard, *Organometallics* **13**, 1870 (1994).
8. O. Gropen, M. Sjovoll, H. Stromsnes, E. Karlsen, O. Swang, and K. Faegri, Jr., *Theor. Chim. Acta* **87**, 373 (1994).
9. O. Swang, K. Faegri, Jr., and O. Gropen, *J. Phys. Chem.* **98**, 3006 (1994).
10. S. Castillo, E. Poulain, V. Bertin, and A. Cruz, *Int. J. Quantum Chem.* **S29**, 207 (1995).
11. S. Castillo, A. Cruz, A. Cuán, A. Ramírez-Solís, E. Poulain, and G. Del Angel, *Int. J. Quantum Chem.* **S29**, 550 (1995).
12. E. Poulain, A. Cruz, S. Castillo, and V. Bertin, *J. Mol. Catal. A: Chem.* **116**, 385 (1997).
13. S. Castillo, A. Cruz, V. Bertin, E. Poulain, J. S. Arellano, and G. Del Angel, *Int. J. Quantum Chem.* **62**, 29 (1997).
14. G. Del Angel, V. Bertin, A. Pérez, and R. Gómez, *React. Kinet. Catal. Lett.* **48**, 259 (1992).
15. R. Gómez, V. Bertin, M. A. Ramírez, T. Zamudio, P. Bosch, I. Schifter, and T. López, *J. Non-Cryst. Solids* **147 & 148**, 748 (1992).
16. R. Gómez, V. Bertin, P. Bosch, T. López, P. Del Angel, and I. Schifter, *Catal. Lett.* **21**, 309 (1993).
17. G. Del Angel, R. Meléndrez, V. Bertin, J. M. Domínguez, P. Marcot, and J. Barbier, *Stud. Surf. Sci. Catal.* **78**, 171 (1993).
18. V. Bertin, P. Bosch, G. Del Angel, R. Gómez, J. Barbier, and P. Marécot, *J. Chim. Phys.* **92**, 120 (1995).
19. G. Aguilar-Ríos, M. Valenzuela, P. Salas, H. Armendáriz, P. Bosch, G. Del Toro, R. Silva, V. Bertin, S. Castillo, A. Ramírez-Solis, and I. Schifter, *Appl. Catal. A: Gen.* **127**, 65 (1995).
20. E. Poulain, V. Bertin, S. Castillo, and A. Cruz, *J. Mol. Catal. A: Chem.* **116**, 385 (1997).
21. R. Gómez, V. Bertin, T. López, I. Schifter, and G. Ferrat, *J. Mol. Catal. A: Chem.* **109**, 55 (1996).
22. R. Gómez, T. López, V. Bertin, R. Silva, P. Salas, and I. Schifter, *J. Sol-Gel Sci. Tech.* **8**, 847 (1997).
23. T. López, R. Silva, V. Bertin, J. Sánchez, and R. Gómez, *React. Kinet. Catal. Lett.* **61**, 49 (1997).
24. A. Cruz, S. Castillo, V. Bertin, G. Del Angel, and E. Poulain, *Int. J. Quantum Chem.* (in press).
25. S. Bathia, F. Engelke, M. Pruski, B. C. Gerstein, and T. S. King, *J. Catal.* **147**, 455 (1994).
26. J. Barbier, E. Lamy-Pitara, and P. Marecot, *Actas XV Simp. Iberoam. Cat.* **1**, TI39 (1996).
27. S. R. de Miguel, A. A. Castro, O. A. Scelza, and J. Soria, *Catal. Lett.* **32**, 281 (1995).
28. A. Sárkány, Z. Zsoldos, Gy. Stefler, J. W. Hightower, and L. Guczi, *J. Catal.* **157**, 179 (1995).
29. A. H. Janowicz and R. G. Bergman, *J. Am. Chem. Soc.* **104**, 352 (1982).
30. J. P. Daudey, PSHF Pseudopotential Program, based on the original HONDO-76, QCPE Program No. 338 (1977) by M. Dupuis, J. Rys, and H. F. King.
31. R. B. Roos, J. M. Powers, T. Atashroo, and W. C. Ermler, L. A. LaJohn, and P. A. Christiansen, *J. Chem. Phys.* **93**, 6654 (1990).
32. B. H. Huron, J. P. Malrieu, and P. Rancurel, *J. Chem. Phys.* **58**, 5745 (1973). CIPSI code written by J. P. Daudey, M. Périsier, J. P. Malrieu, S. Evangelisti, F. Spiegelmann and D. Maynau.
33. F. B. Van Duijneveldt, *IBM Research Report RJ*, 1971, p. 445.
34. E. Poulain, J. García-Prieto M. E. Ruiz, and O. Novaro, *Int. J. Quantum. Chem.* **29**, 1181 (1986).
35. C. E. Moore, *Atomic Energy Levels* U.S. National Bureau of Standards (Washington, D.C., 1971).
36. K. Balasubramanian and D. Dai, *J. Chem. Phys.* **93**, 7243 (1990).
37. A. Alarcón and P. Gazelot, *J. Catal.* **39**, 334 (1975).
38. F. A. Cotton and R. A. Walton, *Multipole Bond Between Metal Atoms* (Wiley, New York, 1982).

Electron Propagator Theory of Conformational Effects on Anisole and Thioanisole Photoelectron Spectra

O. DOLGOUNITCHEVA,¹ V. G. ZAKRZEWSKI,¹ J. V. ORTIZ,¹
G. V. RATOVSKI²

¹ Department of Chemistry, Kansas State University, Manhattan, Kansas 66506-3701

² Institute of Petroleum and Coal Synthesis, Irkutsk State University, Irkutsk, 664000, Russia

Received 30 March 1998; revised 15 July 1998

ABSTRACT: Electron propagator calculations in two diagonal self-energy approximations, partial third order and the outer valence Green's function, are employed in interpretation of the photoelectron spectra of anisole and thioanisole. Major features of the spectra are accurately predicted and are associated to canonical molecular orbitals. Contributions from planar and orthogonal rotational structures are responsible for minor features of the spectra that are dependent on temperature. Correlation effects are large and change the order of final states in thioanisole. Partial third-order calculations are more accurate than outer valence Green's function results. © 1998 John Wiley & Sons, Inc.
Int J Quant Chem 70: 1037–1043, 1998

Key words: anisole; thioanisole; conformations; propagator theory; photoelectron spectra

Introduction

Substituted anisoles (phenyl alkyl ethers) and thioanisoles (phenyl alkyl sulfides) have low barriers to internal rotation of alkyl groups about C—O and C—S bonds [1]. The conformational

Correspondence to: V. G. Zakrzewski.

Contract grant sponsor: National Science Foundation.

Contract grant number: CHE-9321434.

Contract grant sponsor: Petroleum Research Fund.

Contract grant number: 29848-AC6.

Contract grant sponsor: Gaussian, Inc.

behavior of these compounds remains controversial despite numerous experimental and theoretical attempts to determine energetically preferred conformations. Estimates of rotation barriers vary from 0.8 to 3.0 kcal/mol for anisoles and from 0.3 to 1.4 kcal/mole for thioanisoles. Conformational isomerism in these compounds has attracted interest because of their regioselective chemical properties. Recent work has shown that anisole and thioanisole form distinctive complexes with NO⁺. While anisole forms a π -complex, thioanisole forms an n -complex at the sulfur atom [2]. This observation suggests that the highest occupied molecular

orbital of thioanisole has dominant sulfur, lone-pair character. Photoelectron spectra (PES) may provide additional insights into the electronic structure and reactivity of these compounds.

PES of anisole have appeared in a number of publications [3–7]. In all but one of these works, the peaks were interpreted in terms of a single, planar conformation. The presence of a second, less stable conformation was hypothesized in Ref. [6]. A shoulder at ~ 8.8 eV and a low amplitude feature at 10.0–10.4 eV were assigned to this conformation. A 91:9 planar-to-orthogonal abundance ratio and an energy difference of ~ 1.4 kcal/mol were inferred from the temperature dependence of PES band intensities. These features are seen in other published spectra as well [3, 5].

Spectra of thioanisole [3, 4, 8, 9] have been interpreted in terms of rotational isomerism. The first attempts of this kind were based on qualitative models and Koopmans's theorem [3]. To assign unusually wide bands, Dewar and co-workers [4] postulated a conformational equilibrium between planar (major) and orthogonal (minor) rotational isomers. This assumption was used widely to explain photoelectron, ultraviolet, and infrared spectra of several substituted thioanisoles [10]. In contrast, an assumption of free rotation [11] provided a consistent interpretation of PES.

In this work, PES of anisole and thioanisole are interpreted with electron propagator methods [12]. Relationships between vertical ionization energies and initial state conformations are examined. Computational predictions are compared with PES. Results then are explained in terms of a one-electron picture of electronic structure that is based on correlated generalizations of molecular orbital concepts.

Electron Propagator Theory

The recently developed, partial third-order approximation (P3) [13] has predictive and computational advantages that have facilitated a variety of applications to large aromatic and heteroaromatic systems [14]. The outer valence Green's function method [15] (OVGF) is used as well. These two methods employ the diagonal approximation in the self-energy matrix. While relaxation and correlation effects (i.e., corrections to Koopmans's theorem results) are included in the vertical ionization energies calculated here, the Feynman-Dyson

amplitudes (FDA),

$$\begin{aligned}\phi^{\text{FDA}}(x_1) = & \int \Psi_{N-1}^*(x_2, x_3, x_4, \dots, x_N) \\ & \times \Psi_N(x_1, x_2, x_3, \dots, x_N) \\ & \times dx_2 dx_3 dx_4 \dots x_N,\end{aligned}$$

remain equal to canonical orbitals. These one-electron functions are overlaps between initial, N -electron states and final states with $N - 1$ electrons. In this picture of electronic structure, electrons assigned to uncorrelated molecular orbitals are subject to an effective, correlated, energy-dependent potential represented by the diagonal elements of the self-energy matrix. The Dyson equation reduces to

$$E = \epsilon_i + \Sigma_{ii}(E),$$

where ϵ_i and $\Sigma_{ii}(E)$ are the i th canonical orbital energy and the i th diagonal element of the self-energy matrix, respectively. Propagator poles (ionization energies and electron affinities) are values of E that satisfy the previous equation. Pole searches iterate on E and generally converge in three iterations.

Correlated photoionization intensities are proportional to pole strengths, P , that are less than unity and greater than zero. The OVGF and P3 approximations remain valid only for outer valence ionization energies for which $P > 0.80$. In these cases, the sum of the squares of all orbital coefficients in the normalized ionization operator ($\hat{O}^{\text{ioniz.}}$) that contains h (occupied orbital), p (virtual orbital), $2h - p$ (shakeup) and $2p - h$ (shakeon) contributions, where

$$\begin{aligned}\hat{O}^{\text{ioniz.}} = & \sum_h^{\text{occ}} C_h a_h + \sum_p^{\text{vir}} C_p a_p \\ & + \sum_{h_1, h_2}^{\text{occ}} \sum_p^{\text{vir}} C_{h_1 h_2 p} a_p^\dagger a_{h_1} a_{h_2} \\ & + \sum_{p_1, p_2}^{\text{vir}} \sum_h^{\text{occ}} C_{p_1 p_2 h} a_h^\dagger a_{p_1} a_{p_2},\end{aligned}$$

is given by

$$\sum_h^{\text{occ}} |C_h|^2 + \sum_p^{\text{vir}} |C_p|^2 = P > 0.80.$$

For outer valence ionization energies of closed-shell molecules, contributions to a given FDA from the

Koopmans orbital in question generally dominate those of other canonical orbitals. The P3 and OVGF methods used here neglect the non-Koopmans orbital operators, so that for ionization energies,

$$\hat{O}^{\text{ioniz.}} = C_{\text{Koopmans}} a_{\text{Koopmans}} + \sum_{h_1, h_2}^{\text{occ}} \sum_p^{\text{vir}} C_{h_1 h_2 p} a_p^\dagger a_{h_1} a_{h_2} + \sum_{p_1, p_2}^{\text{vir}} \sum_h^{\text{occ}} C_{p_1 p_2 h} a_h^\dagger a_{p_1} a_{p_2}.$$

Pole strengths are evaluated according to

$$P_i = \left[1 - \frac{d\Sigma_{ii}(E_{\text{pole}})}{dE_{\text{pole}}} \right]^{-1}.$$

Lowered pole strengths usually indicate enhanced shakeup character in the final states. In the uncorrelated case, where the self-energy matrix is neglected, the Koopmans theorem (KT) value corresponds to a pole strength equal to unity. For all states studied here, the pole strengths are sufficiently large to justify use of the OVGF and P3 methods.

Computational Methods

GAUSSIAN 95 (development version) [16] was used for all calculations. A semidirect algorithm [17] for the P3 and OVGF methods was utilized. All molecular orbitals (MOs) except for core orbitals were included in electron propagator calculations.

Geometry optimization for all molecules was first performed at the Hartree-Fock (HF) level with the 6-31G* basis set [18]. Analytical second derivatives [19] were calculated at every optimization step due to poor self-consistent field convergence. Planar and orthogonal conformations of anisole and thioanisole were reoptimized with a density functional recipe, B3LYP [20], and the same basis set. HF optimizations with the 6-311G* basis [21] also were done for thioanisole. Optimized geometries were used in OVGF and P3 calculations.

Structural diagrams were generated with the MOLDEN program [22].

Results and Discussion

The atomic numbering scheme is given in Figure 1. In the planar forms [Fig. 1(a)], the C₇—

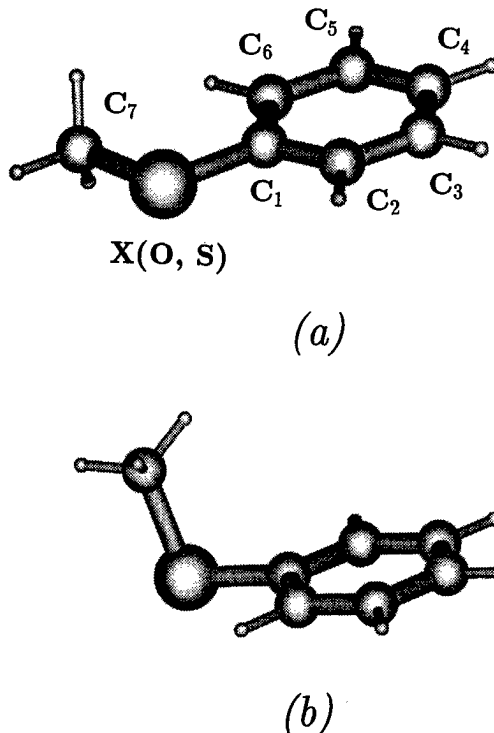


FIGURE 1. Anisole and thioanisole in planar (a) and orthogonal (b) forms.

X—C₁—C₆ dihedral angle is zero. For the orthogonal forms [Fig. 1(b)], the optimized value of this angle is closer to 90°.

ANISOLE

Structures of planar and orthogonal conformers have been fully optimized with HF/6-31G* and B3LYP/6-31G* total energies. All stationary points have a reflection plane of symmetry. Planar isomers are more stable in each case. The following energy differences between the conformers were obtained: 1.4 (HF) and 3.0 kcal/mol (B3LYP). These values are in excellent agreement with the estimate of 1.4 kcal/mol that was based on the temperature dependence of the PES [6]. Harmonic frequency analyses were performed in each case. At the HF level, both stationary points are minima. However, at the B3LYP level, the stationary point corresponding to an orthogonal form becomes a transition state. Because the ionization process is much faster than internal rotation, two poorly resolved ionization bands observed in the PES of anisole [3,6] may be produced by nonplanar conformers.

TABLE I
Planar anisole: vertical ionization energies (eV) and pole strengths.

State	HF geometry			B3LYP geometry			Expt. [3, 4, 5, 6, 7]
	KT	OVGF	P3	KT	OVGF	P3	
$^2A''$	8.42	8.06	8.31	8.42	8.07	8.32	8.39–8.46
		0.90	0.89		0.91	0.89	
$^2A''$	9.23	9.05	9.18	9.20	9.02	9.16	9.22–9.32
		0.90	0.89		0.90	0.89	
$^2A''$	12.69	11.31	11.20	12.65	11.25	11.14	11.02–11.14
		0.87	0.86		0.87	0.86	
$^2A'$	13.04	11.57	11.59	13.05	11.58	11.62	11.52–11.76
		0.90	0.90		0.90	0.89	
$^2A'$	13.94	12.44	12.50	13.90	12.40	12.48	12.33–12.76
		0.90	0.89		0.90	0.89	

Two basis sets were initially used for OVGF calculations: the correlation-consistent, polarized, valence double- ζ set (cc-pVDZ) [23] and 6-311G** [21]. While producing essentially the same ionization energies, the latter basis set required significantly less time for semidirect calculations [17]. All further propagator calculations therefore were performed with the 6-311G** basis set.

Propagator calculations were performed with HF and B3LYP geometries. Differences in the initial state's structure produce discrepancies in the ionization energies that are less than 0.06 eV. These energies and experimental peak positions are presented in Tables I and II for planar and orthogonal forms of anisole.

Results for five final states of the planar isomer are considered here. Correlation corrections to KT results may be as large as 1.4 eV, but there are no

reorderings of final states that follow. All pole strengths are above 0.85; this result implies that shakeup features lie at considerably higher energies. There is close agreement between P3 results and the principal spectral features listed in Table I. In each case, the predicted ionization energy is within 0.1 eV of the experimental range. Somewhat larger discrepancies occur for the OVGF calculations.

When similar calculations are performed for the orthogonal isomer, it is possible to account for the minor spectral features mentioned above. The lowest ionization energy increases by ~ 0.55 eV at the P3 level. Pole strengths are not significantly affected by the conformational change. (Note that the symmetry label for this state changes from $^2A''$ in the planar case to $^2A'$ in the orthogonal case.) This result provides a compelling explanation

TABLE II
Orthogonal anisole: vertical ionization energies (eV) and pole strengths.

State	HF geometry			B3LYP geometry			Expt. [3, 4, 5, 6, 7]
	KT	OVGF	P3	KT	OVGF	P3	
$^2A'$	8.88	8.71	8.88	8.87	8.72	8.86	8.8–8.9
		0.90	0.89		0.90	0.89	
$^2A''$	9.25	9.13	9.25	9.22	9.09	9.23	9.22–9.32
		0.90	0.89		0.90	0.89	
$^2A''$	11.95	10.28	10.10	11.98	10.29	10.12	10.0–10.4
		0.90	0.90		0.90	0.90	
$^2A'$	13.27	11.89	11.80	13.23	11.83	11.76	11.52–11.76
		0.86	0.85		0.86	0.84	
$^2A'$	13.83	12.37	12.40	13.74	12.36	12.36	12.33
		0.90	0.89		0.88	0.86	

for the temperature-dependent shoulder seen at ~ 8.8 eV. Because the FDA for the second state is insensitive to the structural change (it remains a nearly unperturbed π -orbital on the benzene ring), the corresponding ionization energy changes little. In the orthogonal structure, the third FDA is considerably more localized on oxygen. P3 predictions for this state account for the low-intensity feature seen between 10.0 and 10.4 eV.

THIOANISOLE

Geometries of thioanisole were optimized in the same manner as those of anisole. HF optimizations obtained minima for orthogonal conformations and transition states for the planar ones. B3LYP optimizations gave the opposite result. Total energies of the orthogonal form relative to the planar form are -1.20 , -1.49 , and 0.42 kcal/mol, respectively, at the HF/6-31G*, HF/6-311G*, and B3LYP/6-31G* levels. Values for the lowest harmonic frequency are no higher than 46 cm^{-1} for minima and are no lower than -15.1 cm^{-1} for transition states. These data imply a shallow potential energy surface near the stationary points. Low rotation barriers, small absolute values of harmonic frequencies, and contradictions between HF and B3LYP results suggest that nearly free rotation of the methyl group about the S—C bond occurs in thioanisole.

As was the case with anisole, two basis sets were used in the OVGF and P3 calculations, cc-pVDZ and 6-311G**. The P3 method combined

with the 6-311G** basis set gave much closer agreement with PES maxima while demanding significantly less computer resources than either the OVGF method or the cc-pVDZ basis set. All further discussion pertains to the P3 method and the 6-311G** basis set.

Calculated ionization energies obtained for geometries optimized at different theory levels are displayed in Table III and IV. Agreement with experiment is close and provides a consistent assignment of observed features. All pole strengths exceed 0.85. Propagator corrections to KT results are especially large for the last three states of the planar structure and for the first and last two states of the orthogonal structure. In the latter geometry, correlation reorders the final states and provides an explanation for the feature at 8.55–8.71 eV. The FDA for the lowest final state has a pronounced ring-sulfur antibonding relationship in the planar geometry. In the orthogonal structure, the FDA for the lowest ionization energy is dominated by sulfur $3p$ contributions. HF and B3LYP geometries lead to different orderings of the next two states. For the second FDA (according to the ordering provided by the HF geometries), almost no change in the ring-localized π -orbital pattern takes place as the C—S bond is rotated and the ionization energy varies relatively little (from 9.26 to 9.05 eV at the P3 level). In the third FDA of the planar form, sulfur $3p$ contributions are in a bonding relationship with a benzene π -pattern. This stabilizing interaction is lost and localization on the ring is accentuated in the orthog-

TABLE III
Planar thioanisole: vertical ionization energies (eV) and pole strengths.

State	HF geometry		B3LYP geometry		Expt. [3, 4, 8, 9]
	KT	P3	KT	P3	
$^2A''$	8.02	7.82	8.11	7.82	8.01–8.07
		0.89		0.89	
$^2A''$	9.20	9.26	9.29	9.22	9.25–9.30
		0.88		0.88	
$^2A''$	10.77	10.05	10.84	10.01	10.1–10.20
		0.88		0.88	
$^2A'$	12.01	11.00	12.10	11.02	11.10
		0.89		0.89	
$^2A'$	13.29	12.12	13.33	12.09	11.90
		0.89		0.89	

TABLE IV
Orthogonal thioanisole: vertical ionization energies (eV) and pole strengths.

State	HF geometry		B3LYP geometry		Expt. [3, 4, 8, 9]
	KT	P3	KT	P3	
$^2A''$	9.44	8.64	9.46	8.47	8.55–8.71
		0.90		0.90	
$^2A''$	9.23	9.16	9.18	9.12	9.25–9.30
		0.88		0.88	
$^2A'$	9.33	9.05	9.30	9.18	9.25–9.30
		0.89		0.88	
$^2A'$	12.07	11.01	12.06	11.01	11.10
		0.89		0.88	
$^2A'$	13.34	12.06	13.24	12.04	11.90
		0.86		0.86	

onal form. This leads to a lower ionization energy (from 10.05 to 9.16 eV) in the latter structure. Other states are relatively insensitive to conformational changes.

Conclusions

Application of correlated electron propagator methods to the analysis of rotational isomerism in anisole and thioanisole reveals the linkage between ground state energies and vertical ionization energies. Rotations about C—O and C—S bonds account for the appearance of extra spectral features. A correlated treatment of vertical ionization energies is required for a consistent assignment. The P3 method with the 6-311G** basis set obtained very close agreement with PES and permitted assignment of unassigned bands. Correlation affects the order of final states in thioanisole. P3 results are more accurate and are easier to obtain than their OVGF counterparts.

ACKNOWLEDGMENTS

This work was supported by the National Science Foundation under grant CHE-9321434, the Petroleum Research Fund under grant 29848-AC6, and by Gaussian, Incorporated.

References

- (a) H. M. Seip and R. Seip, *Acta. Chem. Scand.* **27**, 4024 (1973); (b) P. Palmieri, F. Tullini, B. Velino, and C. Zauli, *Gazz. Chim. Italiana* **105**, 61 (1975); (c) D. G. Lister,
- P. Palmier, and C. Zauli, *J. Mol. Struct.* **35**, 299 (1976); (d) T. Matsushita, Y. Osamura, N. Misawa, K. Nishimoto, and Y. Tsuno, *Bull. Chem. Soc. Jpn.* **52**, 2521 (1979); (e) T. Schaefer and G. H. Penner, *J. Mol. Struct. (Theochem)* **152**, 179 (1987); (f) J. I. Seeman, H. V. Secor, P. J. Breen, and E. R. Bernstein, *J. Chem. Soc. Chem. Commun.* 393 (1988); (g) P. J. Breen, E. R. Bernstein, H. V. Secor, and J. I. Seeman, *J. Am. Chem. Soc.* **1989**, 1958 (1989); (h) T. Schaefer and R. Sebastian, *Can. J. Chem.* **67**, 1148 (1989); (i) V. Baliah and V. Premasagar, *J. Indian Chem. Soc.* **68**, 614 (1991); (j) V. M. Bzhezovsky, V. V. Penkovsky, A. B. Rozhenko, S. V. Iksanova, N. V. Kondratenko, and L. M. Yagupolsky, *J. Fluor. Chem.* **69**, 41 (1994); (k) D. Chmielewski, N. H. Werstiuk, and T. A. Wildman, *Can. J. Chem.* **71**, 1741 (1993); (l) T. M. Krygowski, R. Anulewics, A. Jarmula, T. Bak, D. Rasala, and S. Howard, *Tetrahedron* **50**, 13155 (1994).
- G. I. Borodkin, V. A. Podryvanov, M. M. Sakirov, and V. G. Shubin, *J. Chem. Soc. Perkin Trans. 2* 1029 (1995).
- (a) H. Bock, G. Wagner, and J. Kröner, *Tetrahedron Lett.*, 3713 (1971). (b) H. Bock, G. Wagner, and J. Kröner, *Chem. Ber.* **105**, 3850 (1972).
- P. S. Dewar, E. Ernstbrunner, J. R. Gilmore, M. Godfrey, and J. M. Mellor, *Tetrahedron* **30**, 2455 (1974).
- (a) T. Kobayashi and S. Nagakura, *Bull. Chem. Soc. Japan* **47**, 2563 (1974); (b) T. Kobayashi and S. Nagakura, *J. Electron Spectrosc. Relat. Phenom.* **6**, 421 (1975).
- H. Frieg and M. Klessinger, *Chem. Ber.* **112**, 1614 (1979).
- L. Klasinc, B. Kovač, and H. Güsten, *Pure Appl. Chem.* **55**, 289 (1983).
- A. Schweig and N. Thon, *Chem. Phys. Lett.* **38**, 482 (1976).
- R. G. Glass, J. L. Broeker, and M. E. Jatcko, *Tetrahedron* **45**, 1263 (1989).
- G. V. Ratovskii, O. L. Shivernovskaya, A. M. Panov, and I. A. Aliev, *Russ. J. Gen. Chem.* **59**, 2273 (1989) and references therein.
- (a) E. Honegger and E. Heilbronner, *Chem. Phys. Lett.* **81**, 615 (1981); (b) M. Mohraz, W. Jian-qi, E. Heilbronner, A. Solladie-Cavallo, and F. Matloubi-Moghadam, *Helv. Chim. Acta* **64**, 97 (1981).
- (a) J. Lindberg and Y. Öhrn, *Propagators in Quantum Chemistry* (Academic, New York, 1973); (b) B. T. Pickup and

ANISOLE AND THIOANISOLE PHOTOELECTRON SPECTRA

- O. Goschinski, Mol. Phys. **26**, 1013 (1973); (c) J. Simons, Theor. Chem. Adv. Persp. **3**, 1 (1978); (d) M. F. Herman, K. F. Freed, and D. L. Yeager, Adv. Chem. Phys. **48**, 1 (1981); (e) Y. Öhrn and G. Born, Adv. Quant. Chem. **13**, 1 (1981).
13. J. V. Ortiz, J. Chem. Phys. **104**, 7599 (1996).
14. (a) J. V. Ortiz, V. G. Zakrzewski, and O. Dolgounitcheva, in *Conceptual Trends in Quantum Chemistry* Vol. 3, E. S. Kryachko ed. (Kluwer, Dordrecht, 1997); (b) V. G. Zakrzewski, O. Dolgounitcheva, and J. V. Ortiz, J. Chem. Phys. **105**, 8748 (1996); (c) V. G. Zakrzewski, O. Dolgounitcheva, and J. V. Ortiz, J. Chem. Phys. **107**, 7906 (1997); (d) O. Dolgounitcheva, V. G. Zakrzewski, and J. V. Ortiz, J. Phys. Chem. **101**, 8554 (1997).
15. W. von Niessen, J. Schirmer, and L. S. Cederbaum, Comput. Phys. Rep. **1**, 57 (1984).
16. M. J. Frish, G. W. Trucks, H. B. Schlegel, P. M. W. Gill, B. G. Johnson, M. A. Robb, J. R. Cheeseman, T. A. Keith, G. A. Petersson, J. A. Montgomery, K. Raghavachari, M. A. Al-Laham, V. G. Zakrzewski, J. V. Ortiz, J. B. Foresman, J. Cioslowski, B. B. Stefanov, A. Nanayakkara, M. Challacombe, C. Y. Peng, P. Y. Ayala, W. Chen, M. W. Wong, J. L. Andres, E. S. Replogle, R. Gomperts, R. L. Martin, D. J. Fox, J. C. Binkley, D. J. Defrees, J. Baker, J. J. P. Stewart, M. Head-Gordon, C. Gonzalez, and J. A. Pople, *Gaussian 95, Revision B.2*, Gaussian, Inc., Pittsburgh, PA, 1995.
17. V. G. Zakrzewski and J. V. Ortiz, Int. J. Quant. Chem. **53**, 583 (1995).
18. W. J. Hehre, R. Ditchfield, and J. A. Pople, J. Chem. Phys. **56**, 2257 (1972); P. C. Hariharan and J. A. Pople, Theor. Chim. Acta **28**, 213 (1973).
19. (a) H. B. Schlegel, J. Comp. Chem. **3**, 214 (1982); (b) J. A. Pople, R. Krishnan, H. B. Schlegel, and J. S. Binkley, Int. J. Quant. Chem. Symp. **13**, 325 (1979).
20. A. D. Becke, J. Chem. Phys. **98**, 5648 (1993).
21. R. Krishnan, J. S. Binkley, R. Seeger, and J. A. Pople, J. Chem. Phys. **72**, 650 (1980); A. D. McLean and G. S. Chandler, J. Chem. Phys. **72**, 5639 (1980).
22. G. Schaftenaar, MOLDENCAOS/CAMM Center, The Netherlands, 1991.
23. T. H. Dunning, J. Chem. Phys. **90**, 1007 (1989).

Advantages of the Fourier Space RHF Band Structure Approach: Application to Polyoxymethylene Using a Distributed Basis Set of *s*-Type Gaussian Functions

I. FLAMANT,¹ J. G. FRIPIAT,² J. DELHALLE¹

¹*Laboratoire Interdisciplinaire de Spectroscopie Electronique, Facultés Universitaires Notre-Dame de la Paix, Rue de Bruxelles 61, B-5000 Namur, Belgium*

²*Laboratoire de Chimie Théorique Appliquée, Facultés Universitaires Notre-Dame de la Paix, Rue de Bruxelles 61, B-5000 Namur, Belgium*

Received 22 February 1998; accepted 19 May 1998

ABSTRACT: In this contribution, we outline the Fourier space-restricted Hartree–Fock (FS-RHF) approach to the calculation of the band structure of polyoxymethylene (POM) using a distributed basis set of *s*-type Gaussian functions (DSGF) to simulate *p*-type functions. The band structure results are compared to those obtained using minimal STO-3G basis sets, within the conventional RHF direct space (DS) approach, and subminimal floating spherical Gaussian orbital (FSGO) basis sets. While the FSGO basis sets are unable to describe correctly the oxygen lone pairs and their interactions, the DSGF basis set reproduces qualitatively the features of the band structure observed with the minimal basis set. We show that minor differences between the FS and DS results originate in difficulties of lattice summations within the DS approach, illustrating the advantages of the FS method compared to the conventional DS approach. © 1998 John Wiley & Sons, Inc. *Int J Quant Chem* 70: 1045–1054, 1998

Key words: restricted Hartree–Fock; Fourier space; Gaussian-type functions; polymers; band structure

Correspondence to: I. Flamant.

Contract grant sponsor: FNRS–FRFC.

Contract grant sponsor: Loterie Nationale.

Contract grant number: 9.4553.92.

Contract grant sponsor: FNRS/Belgian Ministry of Science.

Contract grant number: D.4511.93.

Introduction

Restricted Hartree–Fock (RHF) linear combination of atomic orbitals (LCAO) calculations on extended chains with one-dimensional periodicity [1, 2] have become close to routine for systems containing small to moderate-sized unit cells [3]. Extended chains represent an increasingly important class of materials because of a number of their properties, for example, non-linear optical responses and electrical properties, which make them interesting potential candidates for integration in many devices. Computed electronic band structures, densities of states, total energies, etc., can be correlated with experimentally determined properties of existing systems. The success of such correlations serves as a basis for quantum chemistry-aided design of new molecular structures with improved properties [4, 5].

RHF calculations on infinite model chains face numerical and algorithmic difficulties posed by, for example, lattice summations, and basis-set extension and possible pseudo-linear dependencies [6], since they can affect the quality of the results. It should be noted that essentially all practical calculations in this area are carried out in the direct space (DS) approach.

In the DS approach, the Coulomb and exchange contributions are treated on a different footing. The Coulomb sums are computed generally via a multipole expansion of the two-electron integrals in the asymptotic regime of small overlap of the interacting charge distributions [7, 8]. The implementation of such an algorithm is more difficult for the exchange summations, the convergence of which is fixed by the decay of the LCAO density matrix elements [9, 10], and the usual practice still amounts to guessing the limits of these lattice summations. The situation is worst in the case of metallic systems since a very large number of interacting cells is required to stabilize the exchange summations and the reproduction of the genuine features of the Hartree–Fock description of the metallic situation is impossible in practice [11]. This raises questions on the meaning of applying schemes going beyond the HF level if the starting point is not a proper description of a symmetry-constrained metallic solution.

A Fourier representation of the RHF equations for band structure calculations on infinite chains

has been proposed to evaluate the Coulomb and exchange lattice sums on a consistent basis [12]. It has been shown that combining the Poisson formula [13] and the Ewald technique [14] in the context of Gaussian basis sets can be used to compute accurately and efficiently these summations and that the Fourier representation method yields the special exchange behavior of metallic chains [15]. Our Fourier transform code (FTCHAIN) is still in the prototype phase, and at the current stage of development, only *s*-type Gaussian atomic orbitals can be considered. Nevertheless, it has already illustrated successfully the applicability and the merits of the FS–RHF scheme (FS for Fourier space) in the context of calculations of the electronic structure of extended chains [16, 17].

In previous work [18], the success of the floating spherical Gaussian orbital (FSGO) basis set [19–22] in the identification of conformational signatures in the valence band of polyethylene has led us to consider polyoxymethylene (POM) in which lone pairs on oxygen atoms, which replace alternate CH₂ units, could lead to interesting geometry-dependent electronic characteristics. This study has shown that the approach based on the use of FSGOs provides a simple and computationally fast scheme of calculation that reproduces correctly the bonding trends in polymeric chains, but that important discrepancies are observed in the band structures of POM obtained using the subminimal FSGO and minimal STO-3G basis sets. Moreover, few optimized exponents and positions of FSGOs for extended systems are available in the literature, and the use of FSGOs for practical applications and quantitative results is not realistic. Indeed, the procedure of optimization of FSGO exponents and positions is not trivial and has to be done for each case studied.

In this contribution, we outline the FS–RHF approach to the calculation of the band structure of POM using a distributed basis set of *s*-type Gaussian functions (DSGF) to simulate *p*-type functions. The aim of the present work is twofold: First, we aim to show that, contrary to the FSGO basis sets, which are unable to describe correctly the oxygen lone pairs and their interactions, the DSGF basis set reproduces qualitatively the features of the band structure observed with minimal basis set. To do this, the band structure results are compared to those obtained in [18] in which STO-3G basis sets [23] (within the conventional DS–RHF approach) and FSGO basis sets are used. Second,

we aim to highlight the differences and advantages of the FS approach compared to the conventional DS approach. Overall, the FS and DS results are in good agreement, but we show that minor differences originate in difficulties of lattice summations within the DS approach, illustrating the advantages of the FS method.

The article is planned as follows: In the Theoretical Considerations section, the basic RHF equations which are used and some computational aspects are introduced. In the Results and Discussion section, we assess qualitatively the performance of the DSGF basis set in the description of long-range interactions in POM, and we analyze the numerical results on the POM chain obtained with the FS and DS approaches. Finally, we make a few concluding remarks.

Theoretical Considerations

RELEVANT RHF EXPRESSIONS

The RHF–Bloch states $\varphi_n(k, \mathbf{r})$ are doubly occupied up to the Fermi energy E_F and orthonormalized as shown in the following equation:

$$\int d\mathbf{r} \varphi_{n'}^*(k', \mathbf{r}) \varphi_n(k, \mathbf{r}) = \delta_{k'k} \delta_{n'n}, \quad (1)$$

where k and n are the wavenumber and the band index, respectively. In our notation, the wavenumber k is expressed in units of $2\pi/a_0$ and is defined in the Brillouin zone (BZ), that is, $k \in [-\frac{1}{2}, \frac{1}{2}]$. The Bloch states

$$\varphi_n(k, \mathbf{r}) = \sum_p C_{pn}(k) b_p(k, \mathbf{r}) \quad (2)$$

are expressed in terms of Bloch sums $b_p(k, \mathbf{r})$:

$$\begin{aligned} b_p(k, \mathbf{r}) &= N^{-1/2} \sum_{m=-\infty}^{\infty} \exp(i2\pi mk) \\ &\quad \times \chi_p(\mathbf{r} - (\mathbf{R}_p + m\mathbf{e}_z)a_0) \\ &= N^{-1/2} \sum_{m=-\infty}^{\infty} \exp(i2\pi mk) \chi_p^m(\mathbf{r}), \end{aligned} \quad (3)$$

where p and the vector \mathbf{R}_p (in units of cell length a_0) represent the label and the position of the atomic function, χ_p , in the reference unit cell, respectively. $N^{-1/2}$ is the normalization factor for a polymer containing N cells. Indices p, q, r , and s

denote the atomic functions and the lattice sites are identified by the integers m, m' , and m'' ($= 0, \pm 1, \pm 2, \dots$). Density matrix elements $P_{pq}(k)$ are given by

$$P_{pq}(k) = \sum_n C_{pn}^*(k) C_{qn}(k) \theta_n(k), \quad (4)$$

with the occupation function $\theta_n(k)$ defined as

$$\theta_n(k) = \begin{cases} 2 & \text{if } E_n(k) \leq E_F \\ 0 & \text{if } E_n(k) > E_F, \end{cases}$$

where $E_n(k)$ is the energy of band n .

Expansion coefficients $C_{pn}(k)$ and one-electron energy eigenvalues $E_n(k)$ are solutions of the following system of equations:

$$\sum_q F_{pq}(k) C_{qn}(k) = E_n(k) \sum_q S_{pq}(k) C_{qn}(k), \quad (5)$$

where $S_{pq}(k)$ and $F_{pq}(k)$ are the overlap and Fock matrix elements, respectively, given by

$$S_{pq}(k) = \langle b_p(k, \mathbf{r}) | b_q(k, \mathbf{r}) \rangle \quad (6)$$

and

$$F_{pq}(k) = T_{pq}(k) + V_{pq}(k) + J_{pq}(k) + X_{pq}(k), \quad (7)$$

where $T_{pq}(k)$ is the kinetic term,

$$T_{pq}(k) = \left\langle b_p(k, \mathbf{r}) \left| -\frac{1}{2} \nabla^2(\mathbf{r}) \right| b_q(k, \mathbf{r}) \right\rangle; \quad (8)$$

$V_{pq}(k)$, the electron–nuclear attraction term,

$$\begin{aligned} V_{pq}(k) &= \left\langle b_p(k, \mathbf{r}) \left| \sum_{A=1}^M Z_A \right. \right. \\ &\quad \times \sum_m |r - (\mathbf{R}_A + m\mathbf{e}_z)a_0|^{-1} \left. \left| b_q(k, \mathbf{r}) \right. \right\rangle; \end{aligned} \quad (9)$$

$J_{pq}(k)$, the electron–electron repulsion term,

$$J_{pq}(k) = N \int_{BZ} dk' \sum_{r,s} P_{rs}(k') J_{pqrs}(k, k'), \quad (10)$$

where

$$\begin{aligned} J_{pqrs}(k, k') &= \left\langle b_p(k, \mathbf{r}_1) b_q(k, \mathbf{r}_1) \right. \\ &\quad \times |\mathbf{r}_1 - \mathbf{r}_2|^{-1} \left. \left| b_r(k', \mathbf{r}_2) b_s(k', \mathbf{r}_2) \right. \right\rangle; \end{aligned} \quad (11)$$

and $X_{pq}(k)$, the exchange term,

$$X_{pq}(k) = -\frac{1}{2} N \int_{BZ} dk' \sum_{r,s} P_{rs}(k') X_{pqrs}(k, k'), \quad (12)$$

where

$$X_{pqrs}(k, k') = \langle b_p(k, \mathbf{r}_1) b_s(k', \mathbf{r}_1) | |\mathbf{r}_1 - \mathbf{r}_2|^{-1} | b_r(k', \mathbf{r}_2) b_q(k, \mathbf{r}_2) \rangle. \quad (13)$$

Z_A and the vector \mathbf{R}_A define the nuclear charge and the position of atom A , respectively, and M is the number of atoms. The analysis of the problems associated with these terms with respect to the convergence of the lattice sums which enter in their definition, the analytic properties of the LCAO density matrix elements $P_{pq}(k)$ in the BZ , and the consequences on the RHF results have been documented [10, 24, 25].

COMPUTATIONAL ASPECTS

POM, with the unit cell $-\text{CH}_2-\text{O}-$, is the simplest polymer related to polyethers. We consider, in this study, a hypothetical zigzag planar conformation of the POM chain. This conformer, denoted PZZ, corresponds to a $\text{C}-\text{O}-\text{C}-\text{O}$ dihedral angle of 180° . Tetrahedral angles have been assumed between the $\text{C}-\text{O}-\text{C}$, $\text{O}-\text{C}-\text{O}$, $\text{H}-\text{C}-\text{O}$, and $\text{H}-\text{C}-\text{H}$ bonds, and the $\text{C}-\text{H}$ and $\text{C}-\text{O}$ distances have been set equal to 1.1066 and 1.4306 Å, respectively. This unit cell geometry is illustrated in Figure 1. The xz plane is defined by the carbon and oxygen atoms and the direction of periodicity is the z -axis.

The DSGF basis set for the POM translational unit cell consists of the standard nuclear centered STO-1G exponents for the carbon and oxygen $1s$ and $2s$ orbitals and for the hydrogen $1s$ orbitals, and of s -type Gaussian orbitals (s -GTO's) to simu-

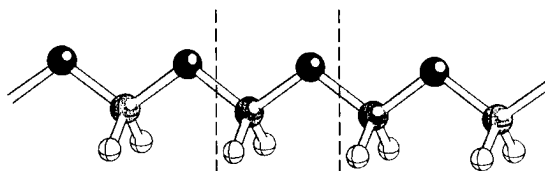


FIGURE 1. Geometry of the zigzag planar (PZZ) conformation of the POM chain. The unit cell boundaries are denoted by dotted lines.

TABLE I Exponents and positions (distance from the atom) of the distributed basis set of s -type Gaussian functions for the POM translational unit cell.

Basis function	Exponent	Distance from the atom (Å)
H_{1s}	0.27095	0.0
C_{1s}	8.71074	0.0
C_{2s}	0.25911	0.0
$s\text{-C}_{2p}$	0.656	0.55751
O_{1s}	15.89814	0.0
O_{2s}	0.50786	0.0
$s\text{-O}_{2p}$	0.62	0.39822

$s\text{-C}_{2p}$ and $s\text{-O}_{2p}$ are the s -GTOs that simulate the C and O $2p$ orbitals, respectively.

late the C and O $2p$ orbitals. Each $2p$ orbital is represented by two identical s -GTOs symmetrically centered about the nucleus, at distances corresponding to the position of the maxima of the standard STO-1G $2p$ function. The exponent of the s -GTOs simulating the C and O $2p$ orbitals has been optimized by minimizing the total energy of the CH_4 and H_2O molecules, respectively, using the GAMESS program [26]. The exponents and positions of the basis functions used are listed in Table I. The results obtained with the DSGF basis set are compared to those obtained using the FSGO basis set. For the POM chain, the FSGO basis set consists of two core orbitals (C_{1s} , O_{1s}), four optimized bond-centered orbitals (two $\text{C}-\text{O}$, two $\text{C}-\text{H}$), and two optimized orbitals to represent oxygen lone pairs (O-LP).

Contrary to an approach based on the use of FSGOs, where the number of basis functions is equal to the number of electron pairs, the density matrix is not uniquely defined as the inverse of the overlap matrix and the iterative self-consistent-field (SCF) procedure is thus no longer avoided. The criterion for convergence of the iterative SCF procedure on the density matrix elements is set equal to 10^{-6} . The band structures obtained by the FS approach using the DSGF basis set were checked against ab initio band structure calculations in a conventional DS approach using the PLH-93 program [3].

Results and Discussion

In this section, we first assess qualitatively the performance of the distributed basis set of s -type

Gaussian functions in the description of long-range interactions in POM. We then analyze the numerical results on the POM chain obtained with the FS and DS approaches.

ELECTRONIC STRUCTURE OF THE POM CHAIN

To assess the performance of the DSGF basis set in the calculation of the electronic structure of POM, we compare the occupied valence band structures and the occupied valence band density of states (DOS) of POM obtained using the DSGF basis set to the results obtained in [18] in which FSGO and STO-3G basis sets are used. The total energies E_T per $-\text{CH}_2-\text{O}-$ unit and occupied valence band energies at selected k -points using the FSGO, DSGF, and STO-3G basis sets are listed in Table II, and the valence band structures and valence band DOS are plotted in Figure 2.

Comparison of the inner-valence band structures (labeled bands 1 and 2) and DOS plotted in Figure 2 shows that the FSGO, DSGF, and STO-3G results are in good agreement qualitatively. The

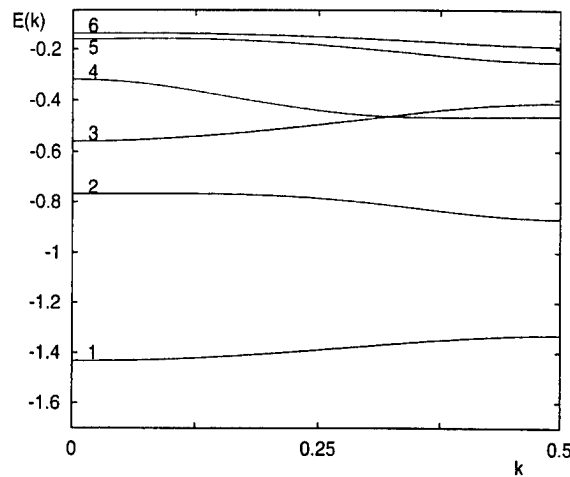
high intensity ratio of the inner-valence peak II, relative to peak I, which fingerprints the PZZ conformation, is obvious from the graphs of the FSGO, DSGF, and STO-3G valence band DOS (Fig. 2, right-hand side). As can be seen from the inner-valence band structures (Fig. 2, left-hand side), the top of band 2 is characterized by a small dispersion. The bandwidth between $k = 0$ and $k = 0.25$ is equal to 0.02000, 0.01281, and 0.00992 au for the FSGO, DSGF, and STO-3G basis sets, respectively. There is an improved agreement between the DSGF and STO-3G results compared to the FSGO results.

The characteristic sharpening of peak II is due to the stabilization of band 2 towards the point $k = 0$ (Fig. 2, left-hand side). To understand the origin of the stabilization of the uppermost part of the inner-valence band, it is useful to analyze the composition of the crystalline orbitals at $k = 0$ for bands 1 and 2, schematically represented in the case of the STO-3G basis set in Figure 3. The FSGOs contributing most to bands 1 and 2 at $k = 0$ are the C—O, and C—H and O-lone pair (O-LP) bond orbitals, respectively. Similarly, for the STO-3G basis set, there is a switching in the composition of the crystalline orbitals from a $\text{C}_{2s}-\text{O}_{2s}$ in character (band 1) to another nodal structure enriched in H_{1s} atomic functions and C_{2p_x} and O_{2p_x} atomic functions in the plane of the polymer backbone and perpendicular to the direction of periodicity (band 2). In the case of the DSGF basis set, there is also a change in the composition of the crystalline orbitals which goes from being $\text{C}_{2s}-\text{O}_{2s}$ in character (band 1) to $\text{C}_{2s}-\text{O}_{2s}$, H_{1s} , and antisymmetric combinations of s-GTOs simulating the C_{2p_x} and O_{2p_x} atomic functions (band 2). The symmetries of band 1 and 2 with the DSGF basis set are the same as those using the FSGO and STO-3G basis sets. This mixing of states enables the development of long-range stabilizing interactions between successive methylene groups (hyperconjugation) and between lone pairs oriented in parallel directions.

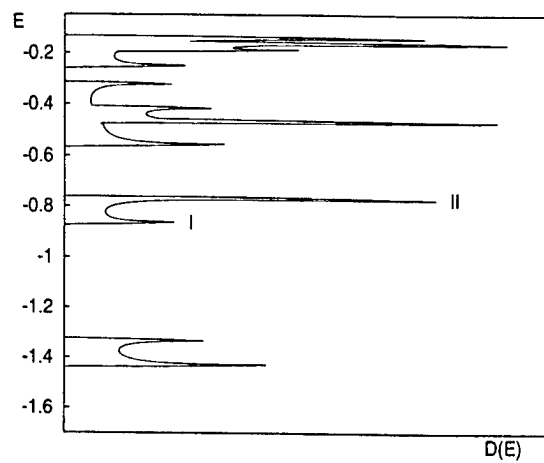
While the graphs of the outer-valence band structures obtained using the FSGO and STO-3G basis sets show significant differences such as the width of band 5 [Fig. 2(a,c), left-hand side], the DSGF and STO-3G results compare very well, except for the crossing of bands 3 and 5 towards $k = 0.5$ observed in the case of the DSGF basis set [Fig. 2(b,c), left-hand side]. As can be seen from the valence band energies listed in Table II, while the FSGO and STO-3G calculated widths of band 5

TABLE II
Total energy E_T per $-\text{CH}_2-\text{O}-$ unit,
occupied valence band energies at selected
 k -points, $E_n(k)$, and total bandwidths,
 W_n (n being the band index) for the zigzag planar
(PZZ) conformation of POM chain using the FSGO,
DSGF, and STO-3G basis sets (energies in
atomic units).

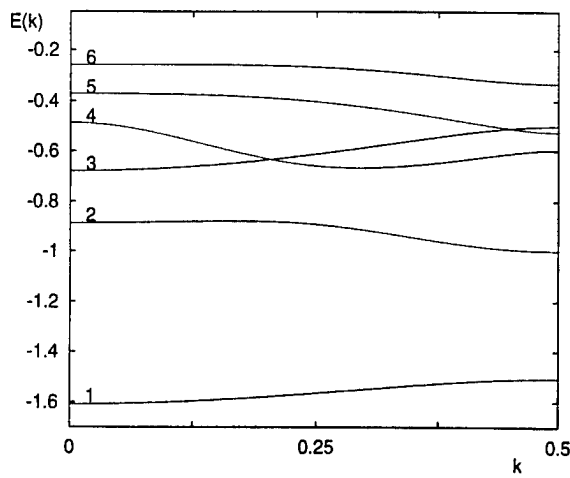
	FSGO	DSGF	STO-3G
E_T	-96.08581	-97.28808	-112.41214
$E_1(0.0)$	-1.43273	-1.60798	-1.37784
$E_1(0.25)$	-1.38940	-1.56461	-1.33023
$E_1(0.5)$	-1.33065	-1.50768	-1.25672
W_1	0.10208	0.10030	0.12112
$E_2(0.0)$	-0.76795	-0.88688	-0.84458
$E_2(0.25)$	-0.78795	-0.89210	-0.84046
$E_2(0.5)$	-0.86726	-0.99849	-0.94098
W_2	0.09931	0.11920	0.10632
$E_5(0.0)$	-0.16132	-0.37118	-0.38238
$E_5(0.25)$	-0.18576	-0.40269	-0.42273
$E_5(0.5)$	-0.25331	-0.52460	-0.51917
W_5	0.09249	0.15342	0.13679
$E_6(0.0)$	-0.13846	-0.25760	-0.34417
$E_6(0.25)$	-0.15367	-0.26691	-0.35703
$E_6(0.5)$	-0.19089	-0.33091	-0.41233
W_6	0.05243	0.07359	0.06816



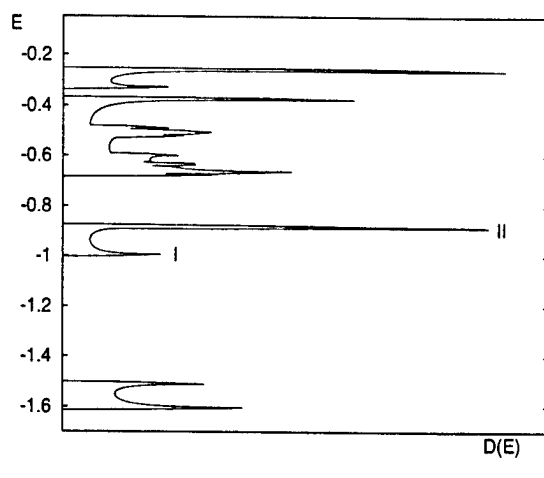
(a)



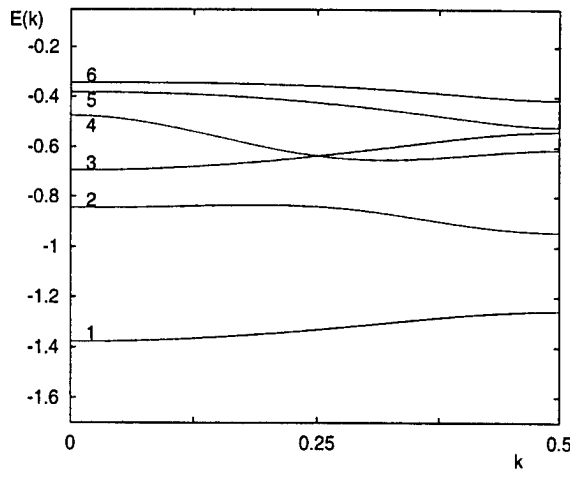
(a)



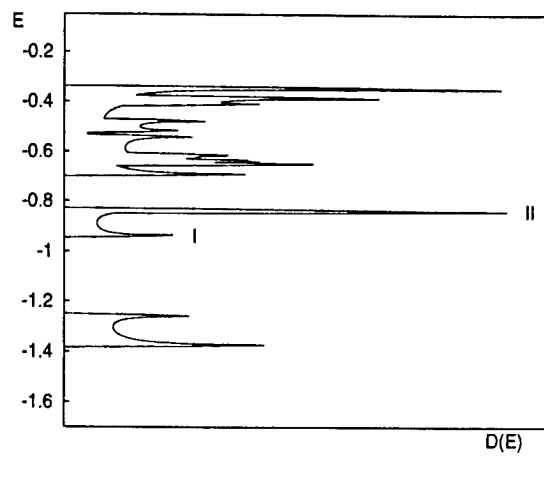
(b)



(b)



(c)



(c)

FIGURE 2. The valence band structures (left-hand side) and valence-band density of states (DOS) (right-hand side) of POM in zigzag planar form obtained using the (a) FSGO, (b) DSGF, and (c) STO-3G basis sets. Energy values are in atomic units and the DOS values are in arbitrary units.

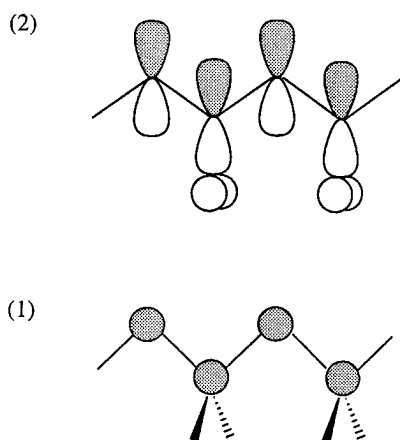


FIGURE 3. Sketch of the crystalline orbitals at $k = 0$ in terms of atomic orbitals (STO-3G basis set) for bands 1 and 2 in the case of the PZZ chain of POM.

[Fig. 2(a,c), left-hand side] are very different (0.09249 and 0.13679 au, respectively), the DSGF and STO-3G widths of band 5 [Fig. 2(b,c), left-hand side] are more comparable (0.15342 and 0.13679 au).

In the case of the STO-3G basis set, the atomic functions contributing most to band 5 are the O_{2p_x} and C_{2p_x} orbitals and the O_{2s} and C_{2s} orbitals. Similarly, for the DSGF basis set, the functions contributing most to band 5 are the O_{2s} and C_{2s} orbitals and antisymmetric combinations of s -GTOs simulating the O_{2p_x} and C_{2p_x} orbitals. The strong dispersion of the energy levels at the bot-

tom of band 5 is due to through-space interactions between the O_{2p_x} and C_{2p_x} favored by the relative position of atoms in the PZZ chain. Contrary to the FSGO basis set, the DSGF basis set does succeed in describing the interactions between the oxygen lone pairs in the POM chain.

COMPARISON OF THE FS AND DS APPROACHES

To highlight the differences and advantages of the FS approach compared to the conventional DS approach, we analyze the DSGF results on the POM chain obtained with the two methods. Overall, the FS and DS results compare fairly well and the graphs of the occupied valence band structures and of the occupied valence band DOS obtained within the two methods are indeed indistinguishable. Selected occupied and unoccupied valence band energies computed with the FS and DS approaches are listed in Table III. As can be seen from the data in Table III, the FS and DS occupied valence band energies are in good agreement (to 5 or 6 significant digits), while there are discrepancies between the results obtained for the unoccupied bands. See, for example, band 16, for which the results at $k = 0$ and $k = 0.25$ compare to 3 significant digits only.

To identify the origin of these discrepancies, we computed the eigenvalues of the three contributions to the Fock matrix elements: the kinetic energy term, $T_{pq}(k)$, the Coulomb term, $C_{pq}(k)$, which

TABLE III
Selected occupied and unoccupied valence band energies, $E_n(k)$ (n being the band index) for the POM chain using the DSGF basis set, and within the Fourier space (FS) and direct space (DS) approaches (energies in atomic units).

	$k = 0$		$k = 0.25$		$k = 0.5$	
	FS	DS	FS	DS	FS	DS
Occupied						
E_1	-1.60798	-1.60797	-1.56461	-1.56461	-1.50768	-1.50767
E_2	-0.88688	-0.88693	-0.89210	-0.89212	-0.99849	-0.99849
E_3	-0.67888	-0.67886	-0.65892	-0.65891	-0.59550	-0.59550
E_4	-0.48603	-0.48601	-0.61160	-0.61160	-0.52460	-0.52459
E_5	-0.37118	-0.37117	-0.40269	-0.40268	-0.52460	-0.52459
E_6	-0.25760	-0.25758	-0.26691	-0.26689	-0.33091	-0.33088
Unoccupied						
E_{13}	1.19752	1.19758	1.43530	1.43555	1.47829	1.47822
E_{14}	1.90760	1.90758	1.73804	1.73804	1.59900	1.59905
E_{15}	2.45067	2.45032	2.20492	2.20465	1.95252	1.95263
E_{16}	3.08117	3.06786	2.89753	2.87218	2.72459	2.72427

TABLE IV

Eigenvalues at selected k -points of the kinetic energy term, $T(k)$, Coulomb term, $C(k)$, and exchange term, $X(k)$, obtained for band 16 using the DSGF basis set, and within the Fourier space (FS) and direct space (DS) approaches (energies in atomic units).

	$k = 0$		$k = 0.25$		$k = 0.5$	
	FS	DS	FS	DS	FS	DS
$T(k)$	26.86613	26.86616	26.88931	26.88930	26.90580	26.90580
$C(k)$	-0.16053	-0.16123	-0.16188	-0.16182	-0.16005	-0.16010
$X(k)$	-0.06666	-0.06524	-0.07121	-0.07110	-0.07208	-0.07155

includes the electron–nuclear attraction and the electron–electron repulsion contributions, and the exchange term, $X_{pq}(k)$. The results corresponding to band 16 obtained within the FS and DS approaches are listed in Table IV. As one can expect, in the case of the kinetic terms, for which the convergence of lattice sums entering their definition does not pose any problem, the eigenvalues obtained within the two approaches compare very well (7 significant digits). On the contrary, the maximum relative differences between the FS and DS results are of the order of 10^{-3} and 10^{-1} for the Coulomb and exchange terms, respectively.

To understand further the origin of this disagreement between the FS and DS results, we computed the band structures of POM using a more localized basis set within the two ap-

proaches. To do this, we multiplied the exponents of the s -type Gaussian functions by four. Selected occupied and unoccupied valence band energies and the eigenvalues corresponding to band 16 are listed in Tables V and VI, respectively. As one can see from the data in Tables V and VI, the FS and DS results are in perfect agreement and improve upon the situation observed with the initial basis set. In the case of the Coulomb term, the better agreement between the FS and DS results is due to the fact that the more localized basis set improves the reliability and accuracy of the multipole expansion method used in the PLH program to evaluate the long-range corrections. Within the FS approach, a multipole expansion technique as an approximation for long-range interactions is not used, and the rapid and accurate calculation of the

TABLE V

Selected occupied and unoccupied valence band energies, $E_n(k)$ (n being the band index) for the POM chain using the DSGF basis set with all exponents multiplied by four, and within the Fourier space (FS) and direct space (DS) approaches (energies in atomic units).

	$k = 0$		$k = 0.25$		$k = 0.5$	
	FS	DS	FS	DS	FS	DS
Occupied						
E_1	-0.07163	-0.07163	-0.06914	-0.06914	-0.06651	-0.06651
E_2	-0.00588	-0.00588	-0.00496	-0.00496	-0.00404	-0.00404
E_3	0.26054	0.26054	0.26468	0.26468	0.26831	0.26831
E_4	1.02083	1.02083	0.88065	0.88065	0.79456	0.79456
E_5	1.11486	1.11486	1.08486	1.08486	1.02928	1.02928
E_6	1.27060	1.27060	1.27044	1.27044	1.27029	1.27029
Unoccupied						
E_{13}	4.66369	4.66369	4.55049	4.55049	4.39950	4.39950
E_{14}	4.70919	4.70919	4.65357	4.65357	4.61279	4.61279
E_{15}	12.15199	12.15200	12.13294	12.13295	12.11404	12.11404
E_{16}	21.23576	21.23577	21.21351	21.21350	21.19142	21.19142

TABLE VI

Eigenvalues at selected k -points of the kinetic energy term, $T(k)$, Coulomb term, $C(k)$, and exchange term, $X(k)$, obtained for band 16 using the DSGF basis set with all exponents multiplied by four, and within the Fourier space (FS) and direct space (DS) approaches (energies in atomic units).

	$k = 0$		$k = 0.25$		$k = 0.5$	
	FS	DS	FS	DS	FS	DS
$T(k)$	95.12429	95.12429	95.11660	95.11660	95.10896	95.10896
$C(k)$	-0.34294	-0.34294	-0.34297	-0.34297	-0.34300	-0.34300
$X(k)$	-0.13233	-0.13233	-0.13266	-0.13266	-0.13292	-0.13292

lattice summations is ensured by the use of a combination of the Ewald technique and the Poisson formula.

A multipole expansion technique is more difficult to implement for the exchange contributions and the practice in the PLH program is to guess the limits of the lattice summations appearing in the exchange term. The DS results have been obtained with $N_x = 21(\pm 10$ cells), the maximum number of interacting cells that can presently be taken into account in the PLH program to compute the exchange contributions. Within the DS approach, the convergence of the exchange lattice sums is fixed by the decay with respect to the lattice indices of the Fourier transform density matrix elements, P_{pq}^{0m} ,

$$P_{pq}^{0m} = \frac{a_0}{2\pi} \int_{BZ} P_{pq}(k) \exp(i2\pi mk) dk. \quad (14)$$

The FS method avoids the systematic use of the density matrix elements, P_{pq}^{0m} , and the exchange contributions are accurately evaluated on the same footing as the Coulomb term. We have checked that the density matrix elements corresponding to the more localized basis set decay faster than those corresponding to the initial basis set. Thus, the larger discrepancy between the FS and DS results noted for the less localized basis set indicate that the number of interacting cells, $N_x = 21$, used within the DS approach is not enough to evaluate the exchange contributions correctly, leaving an error of the order of 10^{-1} .

Concluding Remarks

In this contribution, it has been shown that, contrary to the FSGO basis set, the distributed basis set of s -type Gaussian functions (DSGF) describes correctly the interactions between the lone

pairs in the polyoxymethylene chain, restoring nicely the qualitative agreement with the band structure observed with the STO-3G basis set. Additionally, it has been seen that DSGF results obtained within the Fourier space (FS) and direct space (DS) approaches are in good overall agreement. This comparison constitutes a test of the reliability of the FTCHAIN prototype code.

Minor differences between the FS and DS results have been shown to originate in difficulties of lattice summations within the DS approach. It must be stressed that these differences are already observed for a localized basis set which behaves better from a numerical point of view in the lattice summations. Indeed, it has been demonstrated that the more localized the basis set is the better the agreement between the two approaches. Even if the situation is not dramatic in the case studied here, a similar analysis on results obtained with richer basis sets (STO-3G, 3-21G, 6-31G, 6-31G*, ...) is necessary when the FS code is able to treat s , p , and d Gaussian-type functions. Moreover, we have seen that the disagreement between the FS and DS results is more marked in the unoccupied valence bands. This has important consequences in the use of methods including electron correlation effects, since the energies of the unoccupied valence bands are involved in the expressions [27, 28].

Finally, we can conclude that the FS approach permits equally efficient handling of delocalized and localized basis sets and avoids the problem of selecting the number of interacting cells needed in a particular situation. The numerical consistency of the results for a given level of approximation is ensured by the use of the FS approach.

ACKNOWLEDGMENTS

I. F. thanks Dr. D. H. Mosley for useful discussions and practical help. The calculations reported

were carried out at the "Namur Scientific Computing Facility" with the financial support of the FNRS-FRFC, the "Loterie Nationale" (9.4553.92), and the FNRS/Belgian Ministry of Science "Action d'impulsion à la recherche fondamentale" (D.4511.93).

References

1. G. Del Re, J. Ladik, and G. Biczo, Phys. Rev. **155**, 977 (1967).
2. J. M. André, L. Gouverneur, and G. Leroy, Int. J. Quantum Chem. **1**, 427 (1967).
3. J. M. André, D. H. Mosley, B. Champagne, J. Delhalle, J. G. Fripiat, J. L. Brédas, D. J. Vanderveken, and D. P. Vercauteren, *Methods and Techniques in Computational Chemistry* (METECC-94), E. Clementi, Ed. (Stef. Cagliari, 1993), Vol. B.
4. J. M. André, D. H. Mosley, B. Champagne, and J. M. André, PLH-93 from METECC-94.
5. J. M. André and J. Delhalle, Chem. Rev. **91**, 843 (1991).
6. S. Suhai, P. S. Bagus, and J. Ladik, Chem. Phys. **68**, 467 (1982).
7. L. Piela and J. Delhalle, Int. J. Quantum Chem. **13**, 605 (1978).
8. J. Delhalle, L. Piela, J. L. Brédas, and J. M. André, Phys. Rev. B **22**, 6254 (1980).
9. H. J. Monkhorst and M. Kertesz, Phys. Rev. B **24**, 3015 (1981).
10. J. Delhalle and J. L. Calais, J. Chem. Phys. **85**, 5286 (1986).
11. J. Delhalle, M. H. Delvaux, J. G. Fripiat, J. M. André, and J. L. Calais, J. Chem. Phys. **88**, 3141 (1988).
12. J. Delhalle and F. E. Harris, Phys. Rev. B **31**, 6755 (1985).
13. P. Henrici, *Applied and Computational Complex Analysis* (Wiley, New York, 1977), Vol. 2.
14. P. P. Ewald, Ann. Phys. **64**, 253 (1921).
15. J. Delhalle, J. Cizek, I. Flamant, J. L. Calais, and J. G. Fripiat, J. Chem. Phys. **101**, 10717 (1994).
16. I. Flamant, J. G. Fripiat, and J. Delhalle, Int. J. Quantum Chem. **60**, 1487 (1996).
17. I. Flamant, J. Delhalle, and J. G. Fripiat, Int. J. Quantum Chem. **63**, 709 (1997).
18. I. Flamant, J. G. Fripiat, and J. Delhalle, Theor. Chem. Acc. **98**, 155 (1997).
19. A. A. Frost, J. Chem. Phys. **47**, 3707 (1967).
20. A. A. Frost, J. Chem. Phys. **47**, 3714 (1967).
21. B. V. Cheney and R. E. Christoffersen, J. Chem. Phys. **56**, 3503 (1972).
22. R. E. Christoffersen, D. Spangler, G. G. Hall, and G. M. Maggiora, J. Am. Chem. Soc. **95**, 8526 (1973).
23. R. F. Stewart, J. Chem. Phys. **52**, 431 (1970).
24. H. J. Monkhorst, Phys. Rev. B **20**, 1504 (1979).
25. J. Delhalle and J. L. Calais, Phys. Rev. B **35**, 9460 (1987).
26. M. W. Schmidt, K. K. Baldridge, J. A. Boatz, S. T. Elbert, M. S. Gordon, J. H. Jensen, S. Koseki, N. Matsunaga, K. A. Nguyen, S. J. Su, T. L. Windus, M. Dupuis, and J. A. Montgomery, J. Comput. Chem. **14**, 1347 (1993).
27. J. Q. Sun and R. J. Bartlett, J. Chem. Phys. **104**, 8553 (1996).
28. J. Q. Sun and R. J. Bartlett, J. Chem. Phys. **106**, 5554 (1997).

Periodic INDO Calculations of Organic Adsorbates on a TiO₂ Surface

PETTER PERSSON,* ARVIDS STASHANS,[†] ROBERT BERGSTRÖM,
STEN LUNELL

Department of Quantum Chemistry, Uppsala University, Box 518, S-751 20 Uppsala, Sweden

Received 22 February 1998; revised 29 May 1998; accepted 3 June 1998

ABSTRACT: A new parametrization for use in periodic semiempirical quantum-chemical INDO calculations is proposed. Parameter sets for C and N atoms are tested on a number of C- and N-containing molecules, giving reasonably good agreement with experimental data and/or ab initio results. The new parametrization is intended for studies of organic adsorbates on oxide surfaces using a periodic large unit cell (LUC) model. As an example, two possible adsorption geometries for bi-isonicotinic acid on a TiO₂ rutile(110) surface were investigated, and structural effects involved in the adsorption are discussed. © 1998 John Wiley & Sons, Inc. *Int J Quant Chem* 70: 1055–1066, 1998

Key words: periodic INDO; bi-isonicotinic acid; adsorption; TiO₂ surface; rutile

Introduction

The adsorption of large organic molecules on oxide surfaces is rapidly gaining in technological importance, for example, in dye-sensitization of solar cells [1]. Understanding and improving the molecule–surface linkages in these systems

is an important step in developing such molecular devices [2]. Much less is, unfortunately, known about oxide surfaces than metal ones, and theoretical studies are urgently needed in this general area, especially in view of the difficulty of interpreting experimental observations for these systems [3]. Some detailed studies of oxide-adsorbate structures do exist; the orientation of acetate on a TiO₂ (110) surface has, for example, recently been investigated experimentally [4], and several accurate theoretical studies on systems involving small adsorbates using DFT-pseudopotential [5, 6] or periodic HF [7, 8] methods have been published in the last few years.

For larger adsorbates, typically containing more than one aromatic ring, many experimental studies have been made on interesting spectroscopic and

Correspondence to: P. Persson.

* Also at the University College of Gävle/Sandviken, Box 6052, S-800 06 Gävle, Sweden.

[†] Present address: Departamento de Física, Facultad de Ciencias, Escuela Politécnica Nacional, Apt. 17 01 2759, Quito, Ecuador.

Contract grant sponsors: Swedish Research Council for Engineering Sciences (TFR); Swedish Natural Science Research Council (NFR); European Community Joule III Program.

chemical properties, but usually the detailed structure is hard to determine. Theoretically, these systems are difficult to treat due to their inherent complexity, but some advances have been made recently to study, for example, hydrocarbon adsorption using atomistic simulations [9]. Simulation techniques do, however, not give any electronic structure information which often is of interest for systems with optical applications. Thus, semiempirical quantum-chemical methods may still be a useful tool for these types of systems.

The INDO method employed here [10] uses periodically repeated large unit cells (LUCs) [11, 12] and is designed for the calculation of the total energy and electronic structure of crystals. The exchange interaction is carefully treated. However, the calculation scheme of the modified crystal INDO method has so far only been applied to calculations of the electronic structure of perfect and defective crystals.

The objective of this work was to extend the method to include organic complexes. In particular, we are concerned with the parametrization of carbon and nitrogen, two main components of organic matter. The parametrization includes studies of carbon- and nitrogen-containing molecules of different sizes, with the aim of reproducing their spatial structure and charge distribution. The results are compared to available experimental data or GAUSSIAN94 [13] ab initio computations.

The obtained parameters are primarily intended for studies of organic adsorbates on metal oxide surfaces. In this article, we study two possible adsorption structures of bi-isonicotinic acid (4,4'-dicarboxy-2,2'-bipyridine) on the TiO_2 rutile(110) surface. This is a model for the surface-dye contact in the above-mentioned solar cells.

Computational Details

The INDO method modified for crystal calculations, as implemented in the CLUSTERD computer code [10], was used in the calculations. The approach is based on semiempirical molecular orbital (MO) theory [14] with a specific parametrization scheme [15]. There are two main models incorporated into the computer code: (i) the periodic LUC model [11], which calculates both the electronic structure and the total energy of the crystal via MO as linear combinations of atomic orbitals (LCAOs), and (ii) the embedded molecular cluster

(EMC) model [16]. Additionally, one can use a so-called molecular model to study free molecules. During the parametrization procedure, the molecular model was applied, while the periodic LUC model was used later on to simulate an infinite rutile(110) surface. We preferred to use the LUC model because of its advantages compared to the EMC model, for example, a better treatment of the exchange interaction. A full discussion of the computational relations for calculating the total energy of the crystal within the framework of the LUC approach was given in [10–12]. Here, we shall only outline the basic idea of the method.

In the LUC $\mathbf{k} = \mathbf{0}$ approximation, the Fock matrix elements are made self-consistent through terms of the form

$$\frac{1}{N} \sum_{\mathbf{k}} P_{pq}(\mathbf{k}) \exp(i\mathbf{kR}_v), \quad (1)$$

where the summation is carried out over all the values \mathbf{k} in the reduced Brillouin zone (RBZ) of the large unit cell. The method is not fully self-consistent because of the nature of the approach: We only obtain information about the density matrices $P_{pq}(\mathbf{k})$ at the point $\mathbf{k} = \mathbf{0}$. However, it has been proven that the computation of the electronic structure of the unit cell at $\mathbf{k} = \mathbf{0}$ in the RBZ is equivalent to a band calculation at those BZ \mathbf{k} points which transform to the RBZ center on extending the unit cell [17, 18]. As indicated by numerous studies, a fourfold- or eightfold-symmetric extension of the unit cell proves to be completely sufficient to correctly reproduce the electronic-density distribution in the crystal [17]. The modified INDO, using both the LUC and EMC models, has been applied to a vast number of materials and has shown its reliability in describing different properties of perfect and defective crystals (see [10, 19] and references therein). Recent applications include, for example, studies of various properties and phenomena in such complex oxides as $\alpha\text{-Al}_2\text{O}_3$ [20], WO_3 [21], and a series of computations on TiO_2 [22–24].

Parametrization Results

The Fock matrix elements in the modified INDO approximation contain a number of semiempirical parameters. The orbital exponent ζ enters the radial part of the Slater-type atomic orbitals. A valence basis set including 4s, 4p, and 3d atomic

orbitals (AO) on Ti, 2s and 2p on O, C, and N, and 1s on H was used. The diagonal matrix elements of the interaction of an electron occupying the k 'th valence AO on atom A with its own core are calculated as

$$U_{kk}^A = -E_{neg}^A(k) - \sum_m (P_{mm}^{0A} \gamma_{km} - \frac{1}{2} P_{mm}^{0A} K_{km}) \quad (2)$$

where P_{mm}^{0A} are the diagonal elements of the density matrix (= m th AO populations), E_{neg}^A is the k th AO electronegativity, and γ_{km} and K_{km} are one-center Coulomb and exchange integrals, respectively. The matrix elements of the interaction of an electron in the k 'th AO belonging to an atom A with the core of another atom B take the form

$$V_{kb} = Z_B \left\{ \frac{1}{R_{AB}} + \left[\langle kk | mm \rangle - \frac{1}{R_{AB}} \right] \times \exp(-\alpha_{kB} R_{AB}) \right\}, \quad (3)$$

where R_{AB} is the distance between atoms A and B, Z_B is the core charge of atom B, α_{kB} is an adjustable parameter characterizing the nonpoint character of the atomic core B and additionally the diffuseness of the k 'th AO, $\langle kk | mm \rangle$ is the two-center Coulomb integral. Finally, the so-called resonant integral parameter β_{AB} , enters the nondiagonal Fock matrix:

$$F_{km}^u = \beta_{AB} S_{km} - P_{km}^u \langle kk | mm \rangle, \quad (4)$$

where the k 'th AO belongs to atom A and the m th AO to atom B, u is an electron subsystem with α or β spin, S_{km} is the overlap integral matrix between the k th and m th AO's, and P_{km}^u is the

spin-density matrix. The parametrization scheme thus contains the five parameters ζ , E_{neg} , P^0 , α , and β . It is useful to define the values of the AO populations (parameters P^0) to be equal to those of the free atoms (C and N atoms in our case). Additionally, special attention has to be paid to reproduce the ionization potentials (IPs) for the C and the N atoms.

PARAMETRIZATION OF CARBON

As the first step, the parameters for the C atom were fitted to get reliable values for the IPs and interatomic distances. The results are presented in Tables I–III. As one can see, the ionization potentials are generally well reproduced up to the fourth IP. The geometries of the C-containing molecules are, with some exceptions, very close to the experimental results. We did, however, not manage to get fully satisfactory results for the interatomic distances of the CO₂ and CO molecules (Table II), nor to fully reproduce the difference in bond length between the single and the double bonds in formic acid (Table III). The experimental values are 1.20

TABLE I
Calculated and experimental ionization potentials for the carbon atom (in eV).

	INDO	Experiment ^a
1st	9.44	11.26
2nd	25.21	24.48
3rd	47.47	47.47
4th	64.47	64.48

^a [25].

TABLE II
C-containing molecules: calculated and experimental geometries (in Å and degrees).

Molecule	Property	INDO	Exp. ^a	Standard INDO
CH ₄	R_e (C—H)	1.06	1.1068	1.116
C ₂ H ₂	R_e (C—C)	1.22	1.2031	1.20
	R_e (C—H)	1.05	1.0608	1.05
C ₂ H ₄	R_e (C—C)	1.31	1.339	1.31
	R_e (C—H)	1.03	0.085	1.11
	Θ (H—C—H)	118	117.83	124.3
CO ₂	R_e (C—O)	1.24	1.16	1.162
CO	R_e (C—O)	1.21	1.128323	1.196

^a [26].

TABLE III
Formaldehyde and formic acid: calculated and experimental geometries (in Å and degrees).

Molecule	Property	INDO	Exp. ^a
HCHO	$R_e(C-O)$	1.23	1.2078
	$R_e(C-H)$	1.05	1.1161
	$\Theta(H-C-H)$	114	116.5
HCOOH	$R_e(C-O_1)$	1.24	1.202
	$R_e(C-O_2)$	1.29	1.343
	$R_e(C-H_1)$	1.10	1.097
	$R_e(O_2-H_2)$	0.97	0.972
	$\Theta(H_1-O_2-C)$	105	106.3
	$\Theta(H_2-C-O_1)$	124	124.1
	$\Theta(O_1-C-O_2)$	124	124.9

The numbering of the atoms for HCOOH is the same as Figure 1(a).

^a [26].

and 1.34 Å for the C—O double and single bonds, respectively. Our corresponding INDO values are 1.24 and 1.29 Å, constituting the best compromise between a good description of a single and a double bond, respectively.

We also note that the geometries calculated by our method are very close to those obtained using the standard Pople–Beveridge INDO parametrization scheme [14] (except for CO₂) as shown in the Table II. This is an encouraging fact as our method was primarily developed for crystal computations and has never before been used for isolated molecules.

PARAMETRIZATION OF NITROGEN

The same procedure was used to optimize parameters for the N atom. The ionization potentials

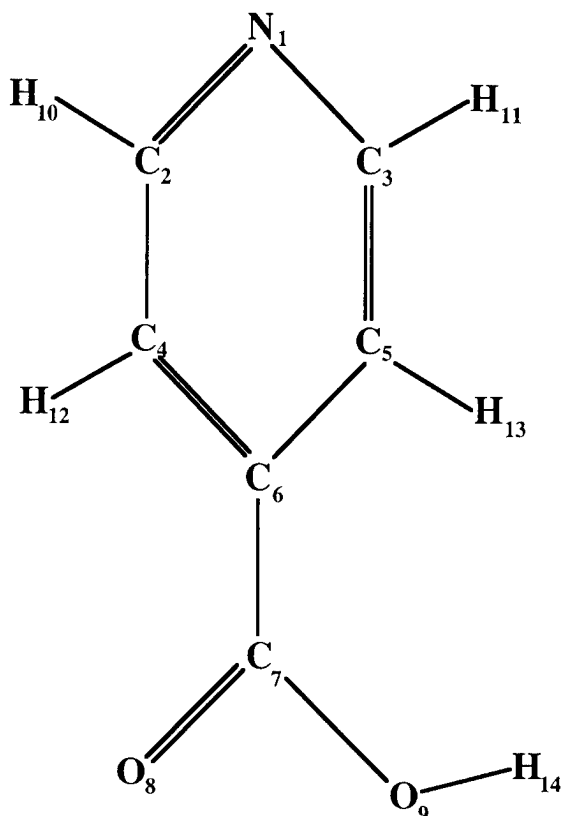


FIGURE 1. (continued)

for the free N atom (Table IV) and the geometries of N-containing molecules (Table V) were calculated in order to fit available experimental data and/or ab initio results. The comparison shows, in general, good agreement between experimental and calculated results, confirming the reliability of the N parameters.

Computations on free isonicotinic acid was another test for the modified INDO method and the new parametrization. Due to the lack of experimental data on the isonicotinic acid geometry, we

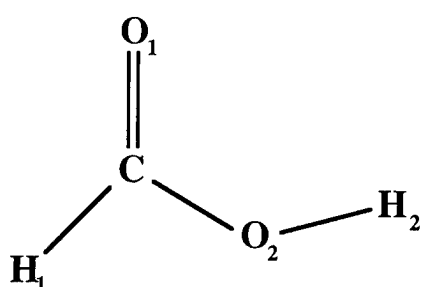


FIGURE 1. (a) Formic acid; the numbering of the atoms corresponds to that in Table III; (b) isonicotinic acid; the numbering of the atoms corresponds to that in Table VI.

TABLE IV
Calculated and experimental ionization potentials for the N atom (in eV).

	INDO	Experiment ^a
1st	14.95	14.53
2nd	30.30	29.593
3rd	45.66	47.426
4th	70.97	77.45
5th	92.22	97.863

^a [25].

TABLE V
N-containing molecules: calculated and experimental geometries (in Å and degrees).

Molecule	Property	INDO	Exp. ^a
CN ₂	$R_e(C-N)$	1.29	1.232
N ₂ O	$R_e(N-N)$	1.26	1.1284
	$R_e(N-O)$	1.21	1.1841
N ₂ O ₄	$R_e(N-N)$	1.49	1.782
	$R_e(N-O)$	1.21	1.190
	$\Theta(O-N-O)$	154	135.4
	$\Theta(O-N-N)$	103	112.5
NH ₃	$R_e(N-H)$	1.04	1.0116
	$\Theta(H-N-H)$	107	106.68

^a [26].

fitted INDO results for this molecule to HF/6-311G** ab initio calculations. The results for interatomic distances and net atomic charges are shown in Table VI. We managed to reproduce the geometry of the molecule very well and the electron distribution satisfactorily. The trends in atomic charges are consistent between the two methods within the expected deviations. We also note that the charges obtained by the ab initio calculations are basis-dependent, which makes a direct comparison of ab initio and semiempirical charges less relevant.

To find nondiagonal α parameters between Ti and C and between Ti and N, the TiC and TiN molecules were used. The correct ground-state configurations $^3\Sigma^+$ (for TiC) and $^2\Sigma$ (for TiN) were obtained. The interatomic distance for TiC was fitted to match the corresponding ab initio value of 1.733 Å obtained by using the multireference configuration interaction (MRCI) method [27], and that for TiN was fitted to the experimental value of 1.582 Å [28]. The results are shown in Table VII. The necessity of including nondiagonal α parameters follow from the fact that we have to describe the interaction between the rutile(110) surface and the adsorbate, in particular, the interaction between Ti and C as well as between Ti and N.

To reproduce the Ti—O interaction is more complicated since it exists both within the crystal framework and also between atoms in the adsorbate and the surface. In general, the computer program allows the definition of different parameter sets for the same type of atom and one might use two parameter sets for the O atoms in the crystalline framework and the adsorbate, respectively. In our previous studies [22–24], the standard oxygen parameters [10] were used, giving reliable results. This was the reason why we retained standard O parameters also for the O atoms in the adsorbate. We made use of the standard H parameters [10] as well, except for a few α values

TABLE VI
Isonicotinic acid: INDO and ab initio HF / 6-311G** geometries (in Å and degrees), and atomic charges (in e).

Property	INDO	Ab initio	Property	INDO	Ab initio
$R_e(N_1-C_2)$	1.32	1.35	$R_e(N_1-C_3)$	1.32	1.35
$R_e(C_2-C_4)$	1.37	1.40	$R_e(C_3-C_5)$	1.37	1.40
$R_e(C_4-C_6)$	1.35	1.41	$R_e(C_5-C_6)$	1.35	1.41
$R_e(C_6-C_7)$	1.48	1.48	$R_e(C_7-O_8)$	1.24	1.24
$R_e(C_7-O_9)$	1.31	1.38	$R_e(O_9-H_{14})$	0.96	0.99
$R_e(C_2-H_{10})$	1.06	1.09	$R_e(C_3-H_{11})$	1.06	1.09
$R_e(C_4-H_{12})$	1.07	1.09	$R_e(C_5-H_{13})$	1.09	1.09
$q(N_1)$	-0.13	-0.39	$q(O_8)$	-0.60	-0.46
$q(C_2)$	0.08	0.15	$q(O_9)$	-0.86	-0.47
$q(C_3)$	0.07	0.15	$q(H_{10})$	0.17	0.13
$q(C_4)$	-0.26	-0.16	$q(H_{10})$	0.16	0.13
$q(C_5)$	-0.26	-0.17	$q(H_{12})$	0.22	0.14
$q(C_6)$	0.13	-0.14	$q(H_{13})$	0.26	0.14
$q(C_7)$	0.57	0.66	$q(H_{14})$	0.46	0.30

The numbering of the atoms is the same as in Figure 1(b).

TABLE VII

Properties of TiC and TiN molecules: interatomic distances (in Å) and dipole moments (in D, and corresponding to Ti^+X^- polarity, where X is C or N).

Molecule	Property	INDO	Ab initio	Experimental
TiC	$R_e(\text{Ti—C})$	1.72	1.733 ^a	
	μ	4.04	2.73 ^a	
TiN	$R_e(\text{Ti—N})$	1.58	1.61 ^b	1.582 ^b
	μ	2.56	3.25 ^b	3.56 ^b

^a [27].^b [28].

($\alpha_{\text{O—H}}$, $\alpha_{\text{H—O}}$, $\alpha_{\text{H—H}}$) which were modified in order to fit some interatomic distances more precisely. Finally, parameters for Ti were derived in one of our previous studies [22]. The parameters are given in Tables VIII and IX.

Application: Adsorption Geometries for Bi-Isonicotinic Acid on a TiO_2 Rutile(110) Surface

We studied two possibilities of molecular adsorption of bi-isonicotinic acid (BINA) to a TiO_2 rutile(110) surface. BINA is a bipyridine-type molecule believed to be the ligand responsible for the adsorbate–surface binding in a variety of proposed solar cells [29]. In particular, a link to the surface can be expected through the carboxyl groups which are known to bind to oxide surfaces, at least for smaller carboxylic acids [4]. The geometric constraints imposed by the molecular structure may, however, prevent the best local carboxyl–surface links to form.

TABLE VIII
INDO parameter set.

Atom	AO	ζ (au)	E_{neg} (eV)	$-\beta$ (eV)	P^0 (e)
H	1s	1.2	4.0	2.0	0.8
C	2s	1.72	19.8	8.7	2.0
	2p	1.48	2.0	8.7	0.66
N	2s	2.15	20.6	9.8	2.0
	2p	1.72	4.8	9.8	1.0
O	2s	2.27	4.5	16.0	1.97
	2p	1.86	-12.6	16.0	1.96
Ti	4s	1.4	1.4	0.5	0.65
	4p	1.1	-10.0	0.5	0.04
	3d	1.93	-2.9	9.0	0.62

Our starting geometries were chosen because of the visually good fit between surface and adsorbate and because they were consistent with preliminary experimental information [30]. While there are several other chemisorption possibilities, we feel that our study illustrates the kind of geometric and electronic effects which are essential to adsorption of large organic molecules on oxide surfaces, and the potential of the present method to elucidate this type of problem.

The present results are based on periodic calculations using the LUC method with a unit cell containing 146 atoms: 120 surface atoms, and the 26 BINA atoms. The unit cell has surface dimensions of 12.988 and 14.790 Å in the (-110) and (001) directions, respectively. This is large enough for BINA to fit above the surface part of one unit cell comfortably. The cells used are shown in Figures 2 and 3, respectively.

Since it is known that the carboxylic acid dissociates upon adsorption, the H^+ ions were initially positioned and optimized on top of surface oxygens some distance away from the Ti—O surface–adsorbate bonding sites. They were then locked in these positions throughout the calculations.

TABLE IX
The derived electron–core interaction parameters $\alpha_{\mu B}$ (au⁻¹), where $\mu \in A$.

A	B				
	Ti	O	H	C	N
Ti				0.16	0.11
O			0.42	0.16	0.11
H		0.23	0.33	0.38	0.03
C	0.36	0.14	0.22	0.12	0.00
N	0.55	0.11	0.34	0.30	0.04

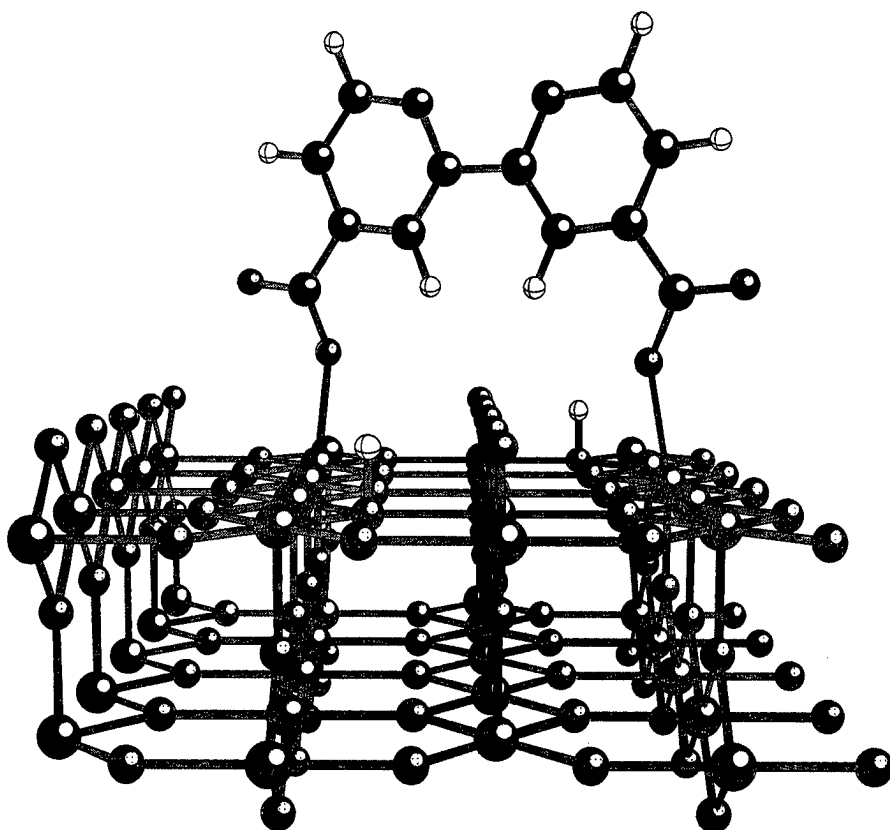


FIGURE 2. 1M-monodentate adsorption of BINA on TiO_2 rutile(110): (a) perspective view of one unit cell along the [001] direction; (b) bird's eye view along the [110] direction.

Partially optimized adsorption structures were obtained by performing series of single-point calculations with controlled variations of the most important bond lengths, angles, etc. No relaxation of the surface was allowed in this study. Experimentally, the TiO_2 surface has been characterized as quite stable [31], and adsorbate-induced relaxations are expected to be less important for low coverages [4], as is the case here.

The different adsorption cases are labeled according to the type of surface-adsorbate bonding for each of the two carboxyl groups. In the first case, there are two 1M-monodentate bonds, and in the second case, there are two 2M-bidentate bonds.

1M-MONODENTATE ADSORPTION

Vertical binding of BINA diagonally across a row of bridging oxygens with on-top binding of one oxygen per carboxyl group and without internal twisting of the BINA was considered as one option (Fig. 2). The adsorption geometry which

gives the best overall fit to the surface is such that the Ti atoms to which the BINA binds lie one step shifted along the (001) direction relative to each other, making an angle, Θ , of 60° between BINA and the (001) direction. The most important structural parameters for the best adsorption geometry are given in Table X, and a graphical representation of the system is shown in Figure 2. The preferred adsorption distance between the fivefold surface Ti atoms and the adsorbate oxygens was investigated, and the results are shown in Figure 4. The optimal adsorption distance according to these calculations is 2.2 \AA , but with a rather small variation in energy in the range $2.0\text{--}2.2 \text{ \AA}$. An effect of the additional Ti—O bonds coming from the carboxyl group is the creation of an effective six-coordination of the involved Ti atoms. This is expected to be favorable, as it is the natural environment of bulk Ti. The bond formed is, however, somewhat longer than the bulk Ti—O distance of ca. 1.9 \AA . One explanation for the discrepancy is that the

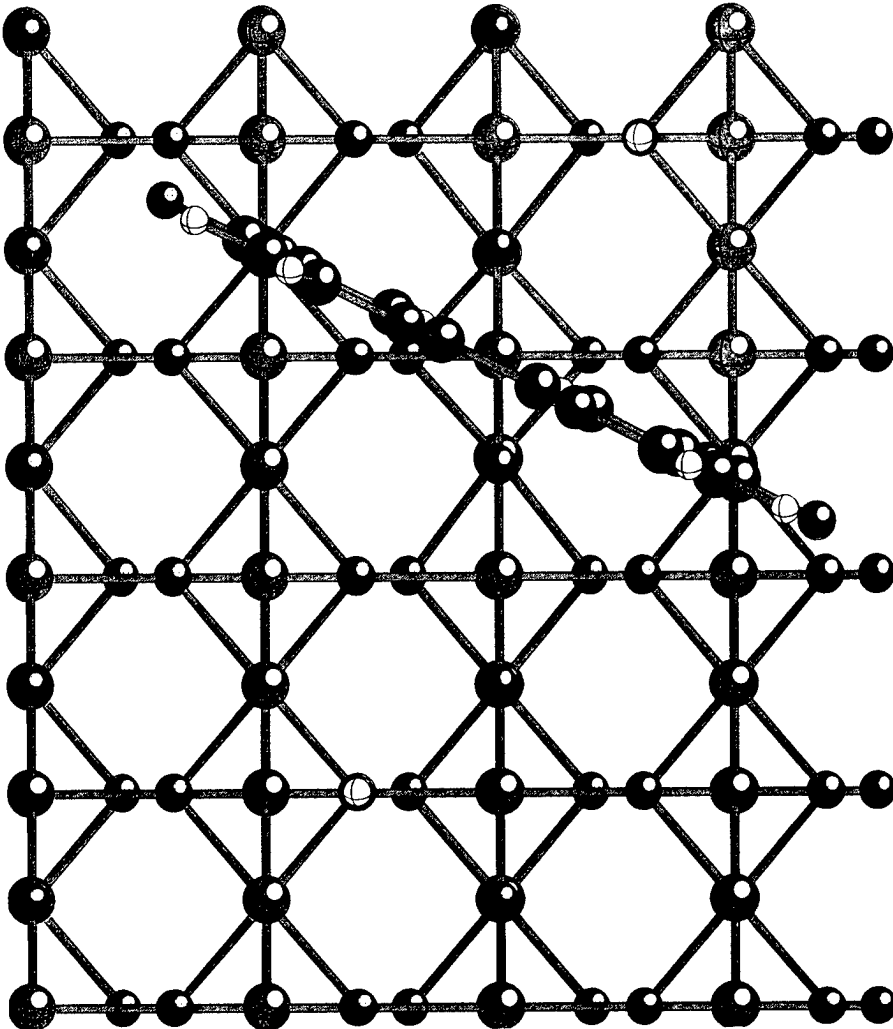


FIGURE 2. (continued)

distance between the two BINA oxygens directly involved (6.3 \AA) does not exactly match the distance between the two relevant surface Ti atoms (7.1 \AA). This introduces some strain into the system. The surface–adsorbate bonding can only be optimized at the expense of deforming the adsorbate and/or the surface. This balance between optimizing the local surface–adsorbate bond, and keeping a favorable overall adsorbate structure is an effect which does not play a significant role for small adsorbates with a single contact point to the surface, but which is anticipated to be a recurring consideration in the detailed study of large adsorbates on complicated, site-specific, surfaces such as oxides.

2M-BIDENTATE ADSORPTION

Like the 1M-monodentate example, this system involves adsorption diagonally across a row of bridging oxygens, but now we consider a nonplanar adsorbate where internal twists between the functional units of the molecule are introduced in order to accommodate four surface–adsorbate bonds (Fig. 3). Bonding of a carboxyl group to TiO_2 rutile(110) surfaces with both oxygens coordinated to a Ti atom, in a 2M-bidentate way, has been found to be favorable for small carboxylic acids such as acetic acid [4], but will only be advantageous for large and relatively rigid molecules such as BINA if such a configuration is

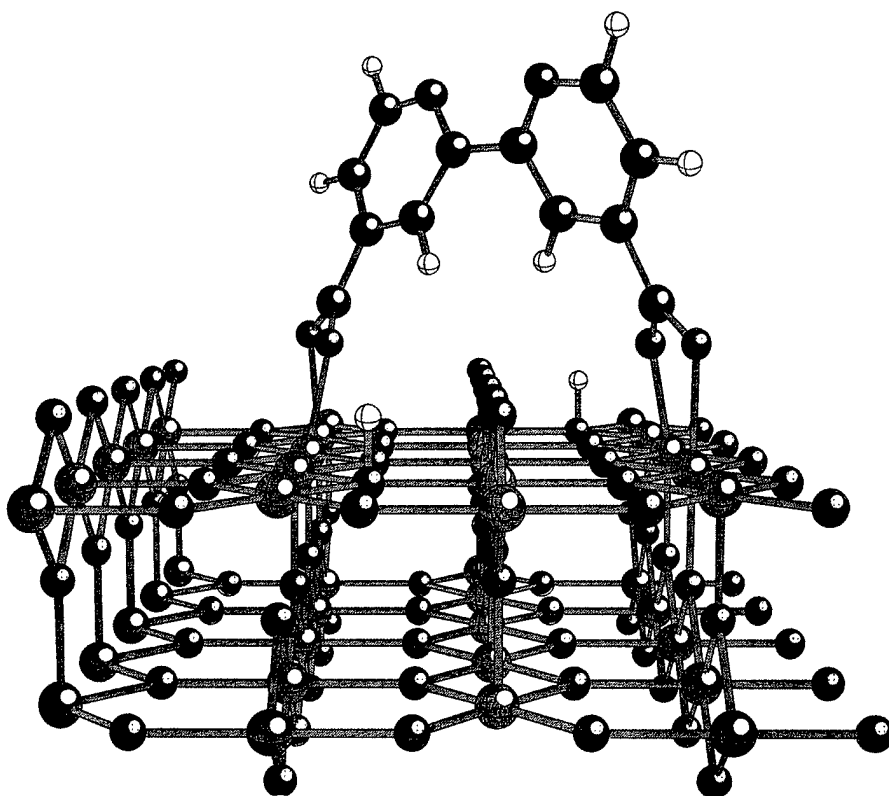


FIGURE 3. 2M-bidentate adsorption of BINA on TiO₂ rutile(110): (a) perspective view of one unit cell along the [001] direction; (b) bird's eye view along the [110] direction.

compatible with the additional geometric constraints and if the disadvantage of straining the adsorbate is compensated for by improved linkage to the surface. As Figure 3 shows, a structure with two 2M-bidentate bonds can be realized with relatively moderate adsorbate distortions. Again, the most important geometrical features are listed in Table X. The most significant modifications are a 34° twist between the two pyridine rings, as well as a 25° twist between each ring and the attached carboxyl group.

The optimum adsorption distance according to these calculations is 2.0 Å, which is 0.2 Å shorter than for the 1M-monodentate case and closer to the bulk value of 1.9 Å. The shorter Ti-adsorbate distances in the 2M-bidentate case can be understood from the fact that although there is an initial distortion of BINA to form the 2M-bidentate bonding arrangement the additional distortion in changing the adsorption distance from 2.2 to 2.0 Å is small, whereas for the 1M-monodentate configuration, the incompatibility between adsorbate and

surface grows in importance as the bond distance is shortened. However, once shorter bonds than the favored 2.0 Å are considered, the 2M-bidentate system is destabilized more rapidly as there are four rather than two bonds with close-range repulsion. This explains the steeper slope of the 2M-bidentate case compared to the 1M-monodentate case for short Ti—O distances in Figure 4.

Conclusions

The INDO model modified for crystal calculations was extended to include organic species. Parameters for C and N, including the electron–core interaction parameters $\alpha_{\mu B}$, needed for studies of systems containing H, C, N, O, and Ti, were determined and shown to work satisfactorily for a representative sample of molecules. The method was used to study two molecular adsorption possibilities of bi-isonicotinic acid on a TiO₂ rutile(110) surface, where new considerations due to the addi-

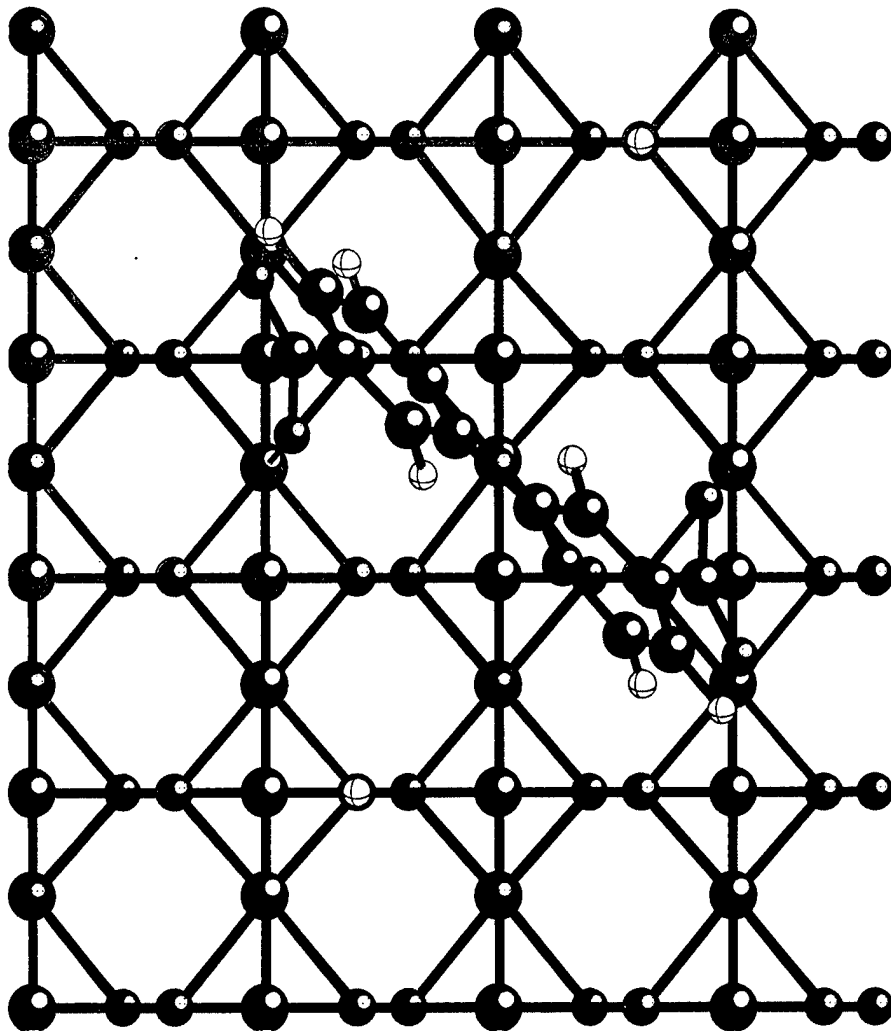


FIGURE 3. (continued)

TABLE X
Geometries (distances in Å and angles in degrees) as obtained by the modified INDO calculations for (i) the 1M-monodentate and (ii) the 2M bidentate models.

Property	1M-monodentate model	2M-bidentate model
R_e	2.2	2.0
Θ	60	45
α	0	34
β	0	25

R_e is the Ti—O_{ads} distance. Θ is the angle between the BINA orientation and the surface (001) direction. α and β are the dihedral angles between the two pyridine rings and a pyridine ring and its carboxyl group, respectively.

tional strain arising from several surface-adsorbate contact points emerge, compared to most previously studied adsorbates with only a single contact point to the surface.

For the two cases considered here, it appears that the configuration with two 2M-bidentate bonds interacts more favorably with the surface, having the best binding energy and the deeper adsorption well. The favoring of the 1M-monodentate system at large adsorption distances reflects the fact that the planar structure is more stable than is the nonplanar one for an isolated BINA molecule.

The present study is, however, not exhaustive: Further adsorption possibilities and other factors

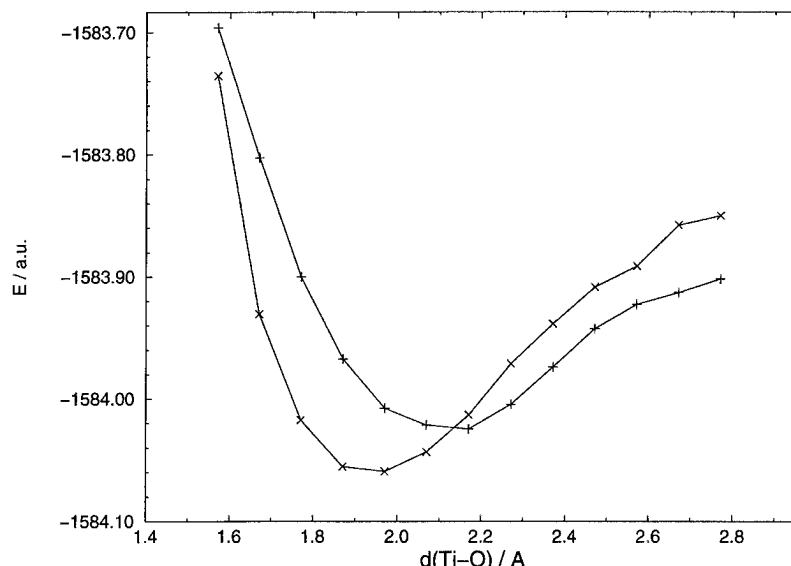


FIGURE 4. Total energy of one unit cell as a function of surface–adsorbate bond distance for (—+) the 1M-monodenate and the (-×-) 2M-bidentate models.

such as coverage dependence could be considered. Experiments like NEXAFS and XPS can give indirect information about, for example, molecular orientations or atomic environments in the naturally occurring situation, and such information could be compared to results expected from theoretically predicted structures. There is a wide field of related systems of great practical interest, involving the adsorption of large organic molecules on oxide surfaces, where the present methods could be useful. Some such studies are underway and will be published elsewhere.

ACKNOWLEDGMENTS

This work was supported by the Swedish Research Council for Engineering Sciences (TFR), the Swedish Natural Science Research Council (NFR), and the European Community Joule III program.

References

1. B. O'Regan and M. Grätzel, *Nature* **353**, 737 (1991).
2. T. A. Heimer, S. T. D'Arcangelis, F. Farzad, J. M. Stipkala, and G. J. Meyer, *Inorg. Chem.* **35**, 5319 (1996).
3. H.-J. Freund, H. Kuhlenbeck, and V. Staemmler, *Rep. Prog. Phys.* **59**, 283 (1996).
4. Q. Guo, I. Cocks, and E. M. Williams, *J. Chem. Phys.* **106**, 2924 (1997).
5. M. C. Payne, M. P. Teter, D. C. Allan, T. A. Arias, and J. D. Joannopoulos, *Rev. Mod. Phys.* **64**, 1045 (1992).
6. M. J. Gillan, L. N. Kantorovich, and P. J. D. Lindan, *Curr. Opin. Solid State Mater. Sci.* **1**, 820 (1996).
7. C. Pisani, R. Dovesi, and C. Roetti, *Ab Initio Treatment of Crystalline Solids*, Lecture Notes in Chemistry **48** (Springer, Berlin, 1988).
8. D. Ferry, P. N. M. Hoang, J. Suzanne, J.-P. Biberian, and M. A. Van Hove, *Phys. Rev. Lett.* **78**, 4237 (1997).
9. P. de Sainte Claire, K. C. Hass, W. F. Schneider, and W. L. Hase, *J. Chem. Phys.* **106**, 7331 (1997).
10. E. V. Stefanovich, E. K. Shidlovskaya, A. L. Shluger, and M. K. Zakharov, *Phys. Stat. Sol. B* **160**, 529 (1990).
11. R. A. Evarestov and V. A. Lovchikov, *Phys. Stat. Sol. B* **79**, 743 (1977).
12. P. V. Smith, J. E. Szymanski, and J. A. D. Matthews, *J. Phys. C* **18**, 3157 (1985).
13. M. J. Frisch, G.W. Trucks, H. B. Schlegel, P. M. W. Gill, B. G. Johnson, M. A. Robb, J. R. Cheeseman, T. Keith, G. A. Petersson, J. A. Montgomery, K. Raghavachari, M. A. Al-Laham, V. G. Zakrewski, J. V. Ortiz, J. B. Foresman, J. Cioslowski, B. B. Stefanov, A. Nanayakkara, M. Challacombe, C. Y. Peng, P. Y. Ayala, W. Chen, M. W. Wong, J. L. Andres, E. S. Replogle, R. Gomperts, R. L. Martin, D. J. Fox, J. S. Binkley, D. J. Defrees, J. Baker, J. J. P. Stewart, M. Head-Gordon, C. Gonzalez, and J. A. Pople, *Gaussian 94, Revision B.2* (Gaussian, Inc., Pittsburgh, PA, 1995).
14. J. Pople and D. Beveridge, *Approximate MO Theories* (McGraw-Hill, New York, 1970).
15. A. Shluger, *Theor. Chim. Acta* **66**, 355 (1985).

16. L. N. Kantorovich, J. Phys. C **21**, 5041 (1988).
17. R. A. Evarestov, *Quantum-Chemical Methods of Solid State Theory* (Leningrad State University, Leningrad, 1982).
18. A. Shluger and E. Stefanovich, Phys. Rev. B **42**, 9664 (1990).
19. P. W. M. Jacobs, E. A. Kotomin, A. Stashans, E. V. Stefanovich, and I. Tale, J. Phys.: Condens. Mat. **4**, 7531 (1992).
20. Yu. F. Zhukovskii, A. A. Sokol, E. A. Kotomin, C. R. A. Catlow, and R. M. Nieminen, J. Phys. Condens. Mat. **9**, 3559 (1997).
21. A. Stashans and S. Lunell, Int. J. Quantum Chem. **63**, 729 (1997).
22. A. Stashans, S. Lunell, and R. W. Grimes, J. Phys. Chem. Solids **9**, 1293 (1996).
23. A. Stashans, S. Lunell, R. Bergström, A. Hagfeldt, and S.-E. Lindquist, Phys. Rev. B **53**, 159 (1996).
24. S. Lunell, A. Stashans, L. Ojamäe, H. Lindström, and A. Hagfeldt, J. Am. Chem. Soc. **119**, 7374 (1997).
25. R. C. Weast, Ed., *CRC Handbook of Chemistry and Physics* (CRC Press, Boca Raton, FL, 1979).
26. K.-H. Hellwege and A. M. Hellwege, Eds., *Landolt-Börnstein Numerical Data and Functional Relationship in Science and Technology*, Vol. 7, *Structural Data of Free Polyatomic Molecules* (Springer-Verlag, Berlin, 1976).
27. M. D. Hack, R. G. A. R. MacLagan, G. E. Scuseria, and M. S. Gordon, J. Chem. Phys. **104**, 6628 (1996).
28. J. F. Harrison, J. Phys. Chem. **100**, 3513 (1996).
29. A. Hagfeldt and M. Grätzel, Chem. Rev. **95**, 49 (1995).
30. L. Patthey, private communication.
31. L. Patthey, PhD Thesis (Faculté des Sciences de l'Université de Lausanne, 1995).

Sign of the Interaction Parameter in Disordered Fe-Al Alloys

SIMON DORFMAN,¹ DAVID FUKS,² VLAD LIUBICH²

¹*Department of Physics, Technion-Israel Institute of Technology, 32000 Haifa, Israel*

²*Materials Engineering Department, Ben-Gurion University of the Negev, Beer-Sheva, Israel*

Received 21 February 1998; revised 22 June 1998; accepted 23 June 1998

ABSTRACT: In the framework of the coherent potential approximation we show that the interaction parameter for disordered Fe-Al alloy strongly depends on the concentration. The calculations were provided within linear muffin-tin orbital formalism in the atomic sphere approximation. Calculation data for B2 phase for different concentrations were used to extract the interaction parameter, $V(0)$, for disordered solid solutions and were compared with the parameter treated from the X-ray scattering data. The concentration dependence of $V(0)$ leads to the failure of the application of the regular solid solution model to the study of the phase relations in the Fe-Al system. Parameter $V(\mathbf{k}_s)$, which is responsible for ordering tendency, also depends on concentration, and it is in accordance with the experimental data. © 1998 John Wiley & Sons, Inc. *Int J Quant Chem* 70: 1067–1073, 1998

Key words: Fe-Al alloys; electronic structure calculations; ordering; phase transitions

Introduction

Intermetallic compounds (intermetallics for short) have attracted considerable interest during recent decades because of fundamental as well as technological reasons [1]. The fundamental interest is mainly concern with structural instabilities of the relatively simple lattices, sometimes

exhibiting cubic symmetry for different concentrations in a wide temperature range. In Fe-Al systems the structural instabilities manifest themselves in a series of phase transitions which may be of first or second order. Fe-Al alloys form one of the classical alloy systems of long-standing interest. It represents magnetic and structural phase transformations, which may be driven by the magnetic interactions and by other factors, such as volume per atom, relaxation, etc.

The increasing interest in aluminides due to their technological importance has recently triggered studies on Fe-Al intermetallics [2–6]. Monte Carlo study of Fe-Al systems was carried out by

Correspondence to: D. Fuks.

Contract grant sponsor: German–Israel Binational Science Foundation.

Contract grant number: GI-418-038.10/95.

Schmid and Binder in the framework of the Ising–Heisenberg model [7]. The energy parameters used in this work were extracted from the experimental data. In Ref. [8] the theoretical study of ordering in Fe–Al alloys based on a density-functional generalized perturbation method was performed. It was found that ordering tendencies in Fe–Al systems strongly depend on the underlying magnetic structure as well as the local magnetic moments. Ordering tendencies show a significant dependence on the Wigner–Seitz radius in the alloy. It is concluded that the concentration dependence of the pair interactions in the ferromagnetic model is significant.

Fe–Al alloy has a complicated phase diagram [9]. For equiatomic composition the paramagnetic disordered body-centered cubic (bcc) phase (A2) transfers into paramagnetic B2 phase at 1068°C. At the atomic fraction of iron equal to 0.75 the paramagnetic A2 phase undergoes at 612°C a phase transition to the two-phase mixture, where the B2 paramagnetic phase coexists with the ferromagnetic A2 phase. Further, at 552°C, this state changes into a DO_3 paramagnetic phase which is mixed with a small amount of ferromagnetic A2. After 510°C the DO_3 phase becomes ferromagnetic. A study of phase competition of these phases in a wide concentration range demands the concentration-dependent effective potentials of interatomic interactions. The procedure described in Ref. [10] to estimate the parameters of the effective mixing potential may be realized for different phases with the stoichiometric composition. Taking into consideration, for example, only phases that are stable from the Lifshitz criterion [11] and writing down the formula, analogous to those represented for the B2 phase in the ground state, it is possible to evaluate the effective mixing potential for the different concentrations, corresponding to the stoichiometric compositions. The equilibrium between coexisting phases is described by the competition of the mixing energy term and the entropy of mixing. Typically the modeling of the mixing energy is carried out in terms of regular or subregular solid solutions. Parameters of these models are phenomenological constants, but in the common case they may be concentration-dependent. Such a dependence reflects the changes of the interatomic interaction of alloy constituents.

Band structure calculations based on the density-functional theory allow to obtain a quantitative description of the ground-state properties of

absolutely ordered alloys. Application of these methods to the calculations of the thermodynamic properties of partially ordered or random alloys is discussed for example in Refs. [12–14]. The formalism presented in [12] allows to derive the cluster variables from a series of density-functional calculations on ordered compounds and to apply the theory of cluster expansions to estimate the energy of disordered system from first principles. In this case, the total energies of a number of atomic configurations are calculated by the ab initio method, after which the Connolly–Williams (CW) procedure is used for matching calculated total energies to their phenomenological expression in terms of multisite interactions. One may find the application of this approach for example in [15, 16]. Some difficulties appear in this scheme when the atomic volumes of components are different. In this case it is impossible to calculate the interatomic interactions on the set of equilibrium volumes, because even in simple metals the equilibrium is defined mostly by the contributions which cannot be expressed in terms of interatomic interactions (i.e., ion–electron, electron–electron interactions, exchange and correlation effects, etc.). A detailed review on first-principles approaches which are combined with the CW procedure or with the generalized perturbation method (GPM) [17] is presented in [18]. Recently a fast version of the linear muffin-tin orbitals–coherent potential approximation (CPA–LMTO) method was proposed [19] which reduces the computational time of electronic structure calculations for random solid solutions. The most attractive feature of the single-site coherent potential approximation (CPA) is the ability to apply this scheme to the direct calculations of the electronic structure of random or partially ordered alloys [14]. Applications of the CPA scheme show that this method allows to reproduce accurately lattice parameters, bulk moduli, and enthalpies of formation (see, e.g., Refs. [20–23] and references therein). This accuracy is adequate to the accuracy of the electronic structure density-functional methods for completely ordered phases.

Hence in this work we study the concentration dependence of the energy parameters which describe the stability of the disordered Fe–Al alloy and the phase transformation in B2 phase. Band structures of Fe–Al alloys at different concentrations are calculated within the CPA–LMTO procedure described in [23]. We decided to use this code

as the fastest scheme for the direct calculations of electronic structure of the alloy under consideration. With the self-consistently obtained bands we calculated the total energies of the completely ordered B2 phase, partially ordered and random phases in the paramagnetic state. In the approach that we are suggesting in our study the description of the temperature dependences of the long-range order parameter and of the free energy of ordering is done according to the static concentration wave (SCW) theory [24]. The SCW method allows to take into account interatomic interactions at arbitrary distances. It establishes the relation between the statistical theory and the Landau–Lifshitz thermodynamic theory of second-order transformations in the ordering of an alloy. This method provides the possibility to predict the structure of the ordered phase if the pairwise interatomic interactions are estimated. Thus SCW theory overcomes several principal difficulties of the traditional theories of ordering [25, 26]. We combine the SCW theory with the first-principles calculations of the interatomic interaction and evaluate the above-mentioned concentration and temperature dependences.

Study of the Energy Parameters for Fe-Al Alloy

CONCENTRATION WAVE APPROACH

The Gibbs free energy of Fe-Al alloy, G , may be written in the form

$$G = c_{\text{Fe}}G_{\text{Fe}} + c_{\text{Al}}G_{\text{Al}} + \Delta G(c_{\text{Fe}}, c_{\text{Al}}), \quad (1)$$

where ΔG is the Gibbs free energy of mixing. This value depends nonlinearly on the molar fractions of components and may be presented by means of different models for solid solutions: regular solid solutions, subregular solid solutions, etc. ΔG contains the enthalpy of mixing, ΔH , and the excess entropy of mixing. For ambient pressure ΔH is practically identical to the internal energy of mixing, ΔU .

Description of the temperature dependences of the long-range order (LRO) parameter and of the free energy of ordering may be performed according to the SCW theory [24]. In the framework of this theory the internal mixing energy of ordering phase ΔU may be written in terms of pairwise

interactions

$$\Delta U = \frac{1}{2}V(0)c_{\text{Fe}}(c_{\text{Fe}} - 1) + \frac{1}{2}\sum_s \gamma_s^2 \eta_s^2 V(\mathbf{k}_s). \quad (2)$$

where η_s is the long-range order parameters that describe the ordering in the superstructure, and γ_s is the structural constants which depend on the symmetry of the ordering phase. $V(\mathbf{k}_s)$ is the Fourier transform of the mixing potential $V(R) = V_{\text{Fe-Fe}}(R) + V_{\text{Al-Al}}(R) - 2V_{\text{Fe-Al}}(R)$ that is calculated for the superstructure reciprocal lattice vectors \mathbf{k}_s

$$V(\mathbf{k}_s) = \sum_{\mathbf{R}} V(\mathbf{R}) e^{i\mathbf{k}_s \cdot \mathbf{R}}, \quad (3)$$

$V(0)$ is just the same as (3) but for $\mathbf{k}_s = 0$. Vectors \mathbf{k}_s belong to the stars of vectors which describe the superstructure. The summation in Eq. (3) is produced over the stars of vectors satisfying the Lifshitz criterion [11]. In the case of CsCl-type (B2) superstructure, for example, the vector \mathbf{k}_s that is responsible for the formation of this phase from the disordered bcc solid solution is $\mathbf{k}_s = 2\pi/a(111)$. As shown in Ref. [24] $\gamma_s = \frac{1}{2}$ for this structure. The vector \mathbf{k}_s defines the site occupation probabilities for the ordered phase that is stable with respect to the formation of the antiphase domains in an alloy. The site occupation probability, $n(R)$, for B2 superstructure is

$$n(R) = c_{\text{Fe}} + \frac{1}{2}\eta e^{2\pi i(x+y+z)}, \quad (4)$$

where x , y , and z are the coordinates of the bcc lattice sites. At $c_{\text{Fe}} = \frac{1}{2}$ and $\eta = 1$ this equation describes the completely ordered phase. With Eq. (3) for this \mathbf{k}_s it is easy to obtain

$$V(\mathbf{k}_s) = -8V(R_1) + 6V(R_2) + 12V(R_3) - 24V(R_4) + 8V(R_5), \quad (5)$$

and

$$V(0) = 8V(R_1) + 6V(R_2) + 12V(R_3) + 24V(R_4) + 8V(R_5). \quad (6)$$

Here we restricted ourselves by only five coordination shells of the Ising lattice. Now we can get the expression for the mixing energy of B2 phase in the stoichiometric composition in the form

$$\Delta U = \frac{3}{2}V(R_2) + 3V(R_3) + 2V(R_5). \quad (7)$$

It is obvious that this mixing energy in the ground state depends only on the interaction potential between atoms in such a binary phase. If such potential is known it is possible to calculate the temperature dependence of the long-range order parameter using the equation of the Bragg-Williams (BW) type

$$\ln \left[\frac{(1 - c_{\text{Fe}} - 1/2\eta)(c_{\text{Fe}} - 1/2\eta)}{(1 - c_{\text{Fe}} + 1/2\eta)(c_{\text{Fe}} + 1/2\eta)} \right] = \frac{V(\mathbf{k}_s)}{kT} \eta, \quad (8)$$

and the temperature of the order-disorder phase transition

$$T_c = - \frac{c_{\text{Fe}}(1 - c_{\text{Fe}})V(\mathbf{k}_s)}{k}. \quad (9)$$

Here k is the Boltzmann constant. Substituting $\eta(T)$ dependence into Eq. (2) one can immediately obtain the temperature dependence of the internal energy.

In the framework of the SCW theory the expression for the Gibbs free energy of mixing ΔG (neglecting the $p\Omega$ term) is

$$\begin{aligned} \Delta G = & \frac{1}{2}V(0)c_{\text{Fe}}(c_{\text{Fe}} - 1) + \frac{1}{8}V(\mathbf{k}_s)\eta^2 \\ & + \frac{1}{2}kT[(c_{\text{Fe}} + \frac{1}{2}\eta) \\ & \times \ln(c_{\text{Fe}} + \frac{1}{2}\eta) \\ & + (1 - c_{\text{Fe}} - \frac{1}{2}\eta)\ln(1 - c_{\text{Fe}} - \frac{1}{2}\eta) \\ & + (c_{\text{Fe}} - \frac{1}{2}\eta)\ln(c_{\text{Fe}} - \frac{1}{2}\eta) \\ & + (1 - c_{\text{Fe}} + \frac{1}{2}\eta)\ln(1 - c_{\text{Fe}} + \frac{1}{2}\eta)]. \end{aligned} \quad (10)$$

The values of $V(0)$ and $V(\mathbf{k}_s)$ may be obtained from diffuse X-ray scattering data as discussed in Ref. [27], where $V(0)$ is constant [$V(0)/k = 5800$ K] while $V(\mathbf{k}_s)$ depends on concentration (see Fig. 1).

Concentration dependence of $V(\mathbf{k}_s)$ leads to the substantial change in the temperature dependences of LRO for different concentrations. Turning to Eq. (8) with obtained values $V(\mathbf{k}_s)$ we may study the influence of the concentration dependence of $V(\mathbf{k}_s)$ on the temperature dependence of the long-range order parameter η . Results of calculations of the temperature dependence of the long-range order parameter for different concentrations of iron in B2 Fe-Al phase are presented in Figure 2. Bold lines in this figure are plotted for the constant value $V(\mathbf{k}_s) = -5400$ K. Even slight change of $V(\mathbf{k}_s)$ values with concentration detected in experiment

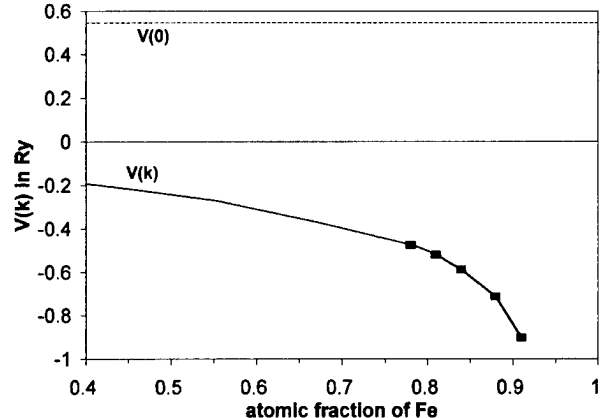


FIGURE 1. $V(0)$ and $V(\mathbf{k}_s)$ from Ref. [22] vs. concentration. $V(0)$ is a constant value and is given by a dashed line. $V(\mathbf{k}_s)$ values are presented by squares and the extrapolation of the experimental data is shown by the bold line.

moves these dependences to the lower temperature region.

NONEMPIRICAL CALCULATIONS

The selection of the interaction parameters of SCW $V(0)$ and $V(\mathbf{k}_s)$ may be carried out by the fitting of the $V(R)$ to the volume dependence of the mixing energy. The choice of the functional dependence of $V(R)$ for this fitting has some freedom and, for example, in our work [28] it was

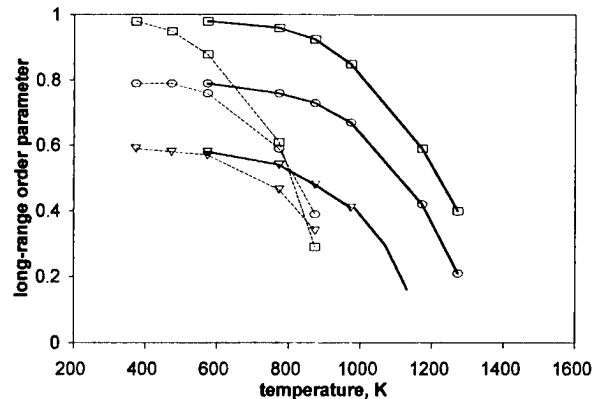


FIGURE 2. Temperature dependence of the long-range order parameter for different concentrations of iron with (dashed lines) and without (bold lines) concentration dependence of $V(\mathbf{k}_s)$. Atomic fractions of iron 0.5, 0.6, and 0.7 are shown as squares, circles, and triangles, respectively.

selected as the Morse-type function. The alternative way is to calculate the mixing energy for the B2 phase in the form

$$\Delta U = \frac{1}{2}V(0)c_{\text{Fe}}(c_{\text{Fe}} - 1) + \frac{1}{8}V(\mathbf{k}_s)\eta^2. \quad (11)$$

For the completely disordered phase (A2) the long-range order parameter η equal to zero and we calculate the concentration dependence of $V(0)$ from the nonempirical CPA-LMTO calculations of the mixing energy.

From a series of CPA-LMTO calculations for B2 and A2 phases with different volumes per atom we calculated the equilibrium states for different concentrations. The calculations have been performed in the scalar-relativistic approach with the Perdew-Zunger parametrization of the exchange-correlation potential [29]. Core electrons were frozen after initial atomic calculations. All calculations were done in the framework of the atomic sphere approximation (ASA) [30]. In all calculations the individual atomic sphere radii were set equal to the radius of the average atomic Wigner-Seitz sphere of the alloy. The convergence criteria for the total energy was 0.001 mRy. The equilibrium lattice parameter and corresponding ground-state energy of a given alloy were obtained on the basis of a set of self-consistent calculations of the total energy close to the equilibrium lattice parameter with a fit to a Morse-type equation of state [31]. The integration over the Brilloin zone has been performed with the special points technique.

The resulting values of $V(0)$ for different atomic fractions of iron are shown in the Figure 3. Calculated values are marked by squares on this plot. The straight line illustrates the linear tendency of the $V(0)$ concentration dependence if we consider only values of $V(0)$ for atomic fraction of iron less than 0.7. Assuming such a linear dependence of $V(0)$ vs. c_{Fe} we obtain a change of the sign of $V(0)$ for $c_{\text{Fe}} = 0.75$. The expression $\frac{1}{2}V(0)c_{\text{Fe}}(c_{\text{Fe}} - 1)$ represents the mixing energy in absolutely disordered solid solution ($\eta = 0$). The change of the sign of the mixing energy leads to decay of the solid solution. After calculation of $V(0)$ for few values of $c_{\text{Fe}} > 0.7$ we see the change of the character of the concentration dependence of $V(0)$, which remains negative. This result is in a contradiction with the treatment of diffuse X-ray measurements [27]. In this work the absence of the $V(0)$ concentration dependence was assumed on

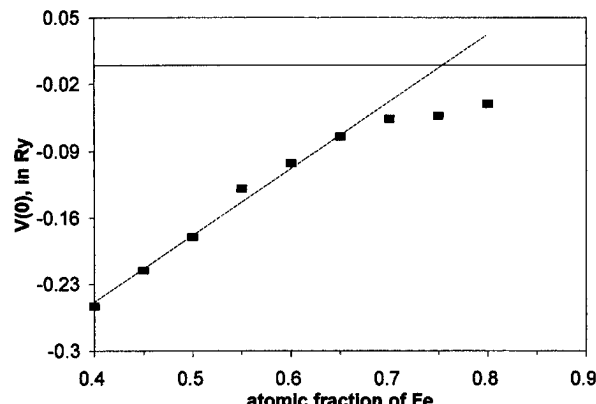


FIGURE 3. Nonempirically calculated values of the energy parameter $V(0)$. Calculated values are shown by squares. The straight line shows the tendency of the concentration dependence of $V(0)$.

the basis of the analysis of the data close to the pure Fe side of the phase diagram. Taking few right points of the plot we also can see very slow dependence of $V(0)$ on the concentration.

The data on $V(\mathbf{k}_s)$ may be received from the calculations of the mixing energy for the completely ordered B2 phase. Using Eq. (11) we simply subtract from these mixing energy values the term with the calculated data of $V(0)$ for the completely disordered phase. In these calculations we used the maximum value of the long-range order parameter η for each concentration. We put nonempirically calculated values $V(\mathbf{k}_s)$ into Eq. (9) and compare concentration dependences of the temperature of order-disorder transition with the values obtained on the basis of experimental data [27]. The experimental data is shown in Figure 4 by triangles. The slope of the calculated and experimental curves is approximately the same.

Summary

In this study we carried out CPA-LMTO calculations of the mixing energy for Fe-Al system in a wide concentration range. We discussed the possible schemes of calculations of the energy parameters $V(\mathbf{k}_s)$ and $V(0)$, which determine the thermodynamic properties of absolutely disordered A2 phase and ordering B2 phase. We calculated these parameters and used the obtained data to study concentration dependences of the temperature of order-disorder phase transition in B2 Fe-Al. The

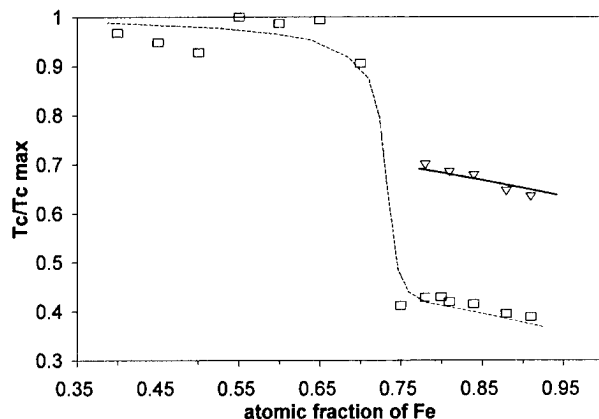


FIGURE 4. Comparison of calculated values (squares) and extracted from the diffuse X-ray measurements (triangles) of T_c / T_c^{\max} dependences on the atomic fraction of iron.

results show that $V(k_s)$ vs. concentration dependence change the temperature dependence of η for different concentrations. This means, by the way, that T_c is not a parabolic function of the concentration [see Eq. (9)]. This result is an extension of the Bragg–Williams description of second-order phase transition and explains the possibility of existence of a nonsymmetric behavior of $T_c(c)$ even for the ordering phases with equiatomic stoichiometric composition. $V(0)$ is also obtained concentration dependent and shows thus that the phase equilibrium in disordered Fe–Al systems cannot be described in the simple model of regular solid solutions.

An important result of our study is that the energy parameters $V(0)$ and $V(k_s)$ are intimately linked with the interatomic interaction potentials and their concentration dependence reflects the concentration dependence of interatomic interactions in alloys. These results support the study of short-range order properties for Al–transition metal alloys performed in Ref. [32]. Although the concentration dependence of $V(k_s)$ in the region of disordered Fe–Al solid solutions was already discussed in [30], its application to Bragg–Williams approach means some effective account of correlations when the ordering process for different concentrations is considered. The dependence $V(0)$ on concentration was not obtained in experimental studies. Perhaps it was a sequence of the very narrow concentration range of alloys investigated. Nevertheless this dependence may be of principle importance because it shows the deviation from

the model of regular solid solutions, still widely used in the study of the phase competition.

ACKNOWLEDGMENTS

This research was supported by the grant GI-418-038.10/95 from the German–Israel Binational Science Foundation (GIF) and by the special program of the Israel Ministry of Absorption.

References

- R. W. Cahn, *Metals, Materials, Processes* **1**, 1 (1989); F. Mondolfo, *Aluminum Alloys: Structure and Properties* (Buttersworths, Boston, 1976).
- R. Feldwisch, B. Sepiol, and G. Vogl, *Acta Metall. Mater.* **43**, 2033 (1995).
- H. Mehrer, M. Eggersmann, A. Gude, M. Salamon, and B. Sepiol, *Proceedings of the 4th International Conference on High-Temperature Intermetallics*, San Diego, 1997, to appear.
- H.-E. Schaefer, R. Würschum, M. Sob, T. Zak, W. Z. Yu, W. Eckert, and F. Banhart, *Phys. Rev. B* **41**, 11869 (1990).
- H.-E. Schaefer and K. Badura-Gergen, *Defect Diffusion Forum* **143–147**, 193 (1997).
- J. Wolff, M. Franz, A. Broska, and Th. Hehenkamp, *Defect Diffusion Forum* **143–147**, 239 (1997).
- K. Binder and D. W. Heermann, *Monte Carlo Simulation in Statistical Physics*, Springer Series in Solid-State Sciences, Vol. 80 (Springer, Berlin, 1992).
- S. K. Bose, V. Drchal, J. Kudrnovsky, O. Jepsen, and O. K. Andersen, *Phys. Rev. B* **55**, 8184 (1997).
- O. Kubaschewski, *Iron-Binary Phase Diagrams* (Springer, Berlin, 1982), p. 5.
- D. Fuks and S. Dorfman, *Solid State Commun.* **90**, 773 (1994).
- E. M. Lifshitz, *Fiz. Zh.*, **7**, 61 (1942); *Fiz. Zh.*, **7**, 251 (1942).
- J. W. D. Connolly and A. R. Williams, *Phys. Rev. B* **27**, 5169 (1983).
- A. Zunger, S.-H. Wei, L. G. Ferreira, and J. E. Bernard, *Phys. Rev. Lett.* **65**, 353 (1990).
- J. S. Faulkner, *Progr. Mater. Sci.* **27**, 1 (1982).
- A. E. Carlsson, *Phys. Rev. B* **35**, 4858 (1987).
- A. E. Carlsson and J. M. Sanchez, *Solid State Comm.* **65**, 527 (1988).
- F. Ducastelle and F. Gautier, *J. Phys. F* **6**, 2039 (1976).
- R. Monnier, *Phil. Mag. B* **75**, 67 (1997).
- I. A. Abrikosov, Yu. H. Vekilov, and A. V. Ruban, *Phys. Lett. A* **154**, 407 (1991).
- Z. W. Lu, S.-H. Wei, and A. Zunger, *Phys. Rev. Lett.* **66**, 1753 (1991).
- P. P. Singh, A. Gonis, and P. E. A. Turchi, *Phys. Rev. Lett.* **71**, 1605 (1991).

22. P. P. Singh, and A. Gonis, Phys. Rev. B **49**, 1642 (1994).
23. A. V. Ruban, I. A. Abrikosov, and H. L. Skriver, Phys. Rev. B **51**, 12958 (1995).
24. A. G. Khachaturyan, *Theory of Structural Transformations in Solids* (Wiley, New York, 1983).
25. W. L. Bragg and E. J. Williams, Proc. Roy. Soc. A**145**, 699 (1934); **A152**, 231 (1935); J. G. Kirkwood, J. Chem. Phys. **6**, 70 (1938).
26. R. Kikuchi, Phys. Rev. **81**, 988 (1951); J. Chem. Phys. **60**, 1071 (1974).
27. S. V. Semenovskaya, Physica Status Solidi B **64**, 291 (1974); S. V. Semenovskaya and D. M. Umidov, Physica Status Solidi B **64**, 627 (1974).
28. D. Fuks and S. Dorfman, J. de Physique, C2, **5**, 135 (1995).
29. J. Perdew and A. Zunger, Phys. Rev. B **23**, 5048 (1981).
30. O. K. Andersen, Phys. Rev. B **12**, 3060 (1975); H. L. Skriver, *The LMTO Method* (Springer, New York, 1984).
31. V. L. Moruzzi, J. F. Janak, and K. Schwarz, Phys. Rev. B **37**, 790 (1988).
32. A. E. Carlsson, Phys. Rev. B **40**, 912 (1989).

Possibility of Charge-Mediated Superconductors in the Intermediate Region of Metal–Insulator Transitions

HIDEMI NAGAO,¹ MASAKI MITANI,² MASAMICHI NISHINO,²
YASUTERU SHIGETA,² YASUNORI YOSHIOKA,²
KIZASHI YAMAGUCHI²

¹*Institute for Molecular Science, Myodaiji, Okazaki 444, Japan*

²*Department of Chemistry, Graduate School of Science, Osaka University, Toyonaka, Osaka 560, Japan*

Received 21 February 1998; revised 28 May 1998; accepted 2 June 1998

ABSTRACT: Some molecular systems for a charge-mediated superconductor are proposed from the viewpoint of the metallic side and the insulator side. An approach to the charge-transfer (CT) model is presented. Expressions of the effective electron–electron interaction in the charge-fluctuation models is also derived by a field-theoretical approach.

© 1998 John Wiley & Sons, Inc. *Int J Quant Chem* 70: 1075–1084, 1998

Introduction

The superconductivity in usual metal has been well explained by the BCS theory [1–6]. Characteristic electrons in the metal are described by the free fermion gas model, for the electron correlation effect is small. The electron–electron interaction becomes attractive through the electron–phonon interaction in this case. On the other hand, the high-temperature superconductivity has been realized in copper oxides [7] with an appropriate hole concentration. The copper oxides are antiferromagnetic insulators before doping. Electrons in the antiferromagnetic insulator are local-

ized at the copper atoms because of strong electron–electron interaction. The electron correlation is found to be still strong [8] even if the medium becomes a metallic conductor after doping holes. The high-temperature superconductivity in copper oxides is, therefore, intrinsically related to the electron correlation. The high- T_c copper oxide has been investigated by many approaches [9–24].

The discovery of high- T_c copper oxide suggested the idea that doping in an antiferro- or ferromagnetic system, more generally, molecular charge-transfer (CT) insulators, may provide several exotic electronic phases [25–27], which are as follows: (1) a ferromagnetic metal or insulator; (2) spin glasses; (3) a paramagnetic metal; (4) an antiferromagnetic metal; (5) a ferrimagnetic metal or insulator; and (6) a charge- or spin-mediated

Correspondence to: H. Nagao.

superconductor. From these works, we have therefore started our theoretical attempts to search for possible models for charge- or spin-mediated superconductivity and have presented the hypotheses about the possibilities of the superconductivity in the intermediate region of the metal-insulator transition in a previous article [28].

Concerning charge-mediated superconductivity, the introduction of charge fluctuation from the metallic side was already examined by Little [29] in the case of conductive polymers. On the other hand, the possible role of the CT excitation from the non-magnetic insulator side in the intermediate region of metal-insulator transitions has not been elucidated yet.

In this article, we propose some molecular systems, which may be the charge-mediated superconductor and the CT models from the viewpoint of the metallic side and the insulator side. We also present a Hamiltonian for the CT model. The polarization properties of the models were investigated by the field-theoretical approach. In the charge-fluctuation model, the effective electron-electron interaction through the CT or the exciton is derived.

General Discussion

Two possible approaches to charge-mediated superconductivity are illustrated in Figure 1. Several approaches from the metallic side in Figure 1 were performed by Little et al. [29–39]. In this section, from two viewpoints, from the metallic and nonmagnetic insulator sides, some models which may be charge-mediated superconductivity are proposed.

POLYMER NETWORK SYSTEM

Little [29] considered a molecule consisting of two parts: a long chain called the spine in which electrons fill various levels and might or might not be a conducting system, and, second, a series of atoms or side chains attached to the spine as shown in Figure 2. He assumed that the spine was a conjugated chain of double and singlet bonds resonating between the two at each link. This corresponds, in the band theory of a metal, to a band which is half-filled and ideally is a metallic conductor. The individual side-chain molecules were chosen so as to have a low-lying excited state such

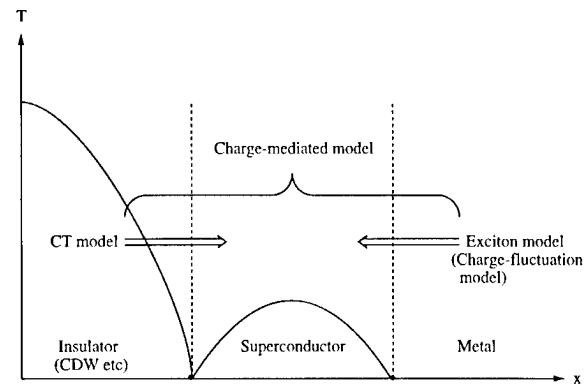


FIGURE 1. Two approaches to obtain charge-mediated superconductors in the intermediate region of the metal-insulator transition.

that transition from the ground state to its excited state corresponds classically to an oscillation of charge from end to end of the molecule. This can provide an interaction between the electrons moving in the spine. If the interaction is sufficiently attractive, we have a necessary condition that the superconducting state results.

On the other hand, in the spin-mediated system, Hirsch and Scalapino pointed out a strong-coupling mechanism of high- T_c superconductivity expected for weakly coupled double-valence fluctuating molecules [40, 41]. Strongly or intermediately electron-correlated systems have received continuous

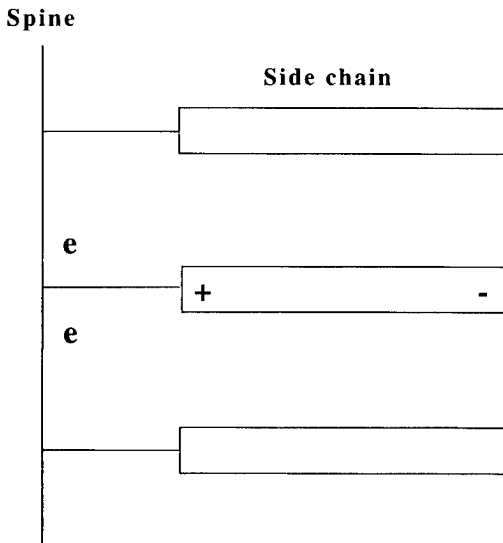


FIGURE 2. An infinitely long conjugated chain molecule (spine) substituted by dye molecules (side chain). The electron passing through the spine polarizes the side chain.

interest in relation to both magnetism and (super)conductivity.

First, from this analogy, we propose a charge-fluctuation model instead of the Little model. The model systems have the charge transferring from the spine (side chain) to the side chain (spine) as shown in Figure 3(a). The side chains consist of donors or acceptors. This model is different from the Little model in relation to the CT.

Next, we present a model from the metallic side to extend the Little model. The model system consists of the spine and the side chain with the interaction between side chains as shown in Figure 3(b). The side chain is a zwitterionic structure of the A-B-C species. In the next section, we present a model for the polymer network system (see Fig. 7).

CRYSTAL SYSTEM

Recently, several types of molecular magnetic compounds were synthesized and their magnetic properties were thoroughly investigated [42, 43]. Fujiwara et al. [44] designed new types of fer-

romagnetic or ferrimagnetic polymers composed of heteropoly transition-metal tetrathioliates [poly(M₁T_M₂)_n; T: tetrathioliates] on the basis of the orbital-symmetry rules for superexchange couplings of unpaired electrons via anionic ligands, which have been derived from previous ab initio calculations of the binuclear complex (HS)₂M₁T_M₂(SH)₂ [45]. Spin-fluctuations also play important roles in spin-mediated exotic materials. Theoretical results are utilized for the molecular design of ferromagnetic metals, dense Kondo and spin-mediated superconductors composed of the segregated columns of trinuclear complexes (L)₂M₂T_M₁(L)₂ (L = proper ligand) [46]. The isologous analogy among these inorganic systems and TTF derivatives with radical groups are clearly shown on the basis of the Anderson-type Hamiltonian.

We present charge-fluctuation models instead of spin-fluctuation models of TTF derivatives as shown in Figure 4. The models consist of donors and acceptors instead of isoelectrons. The systems have the CT between the conducting sites and the local charge sites of the donors or acceptors.

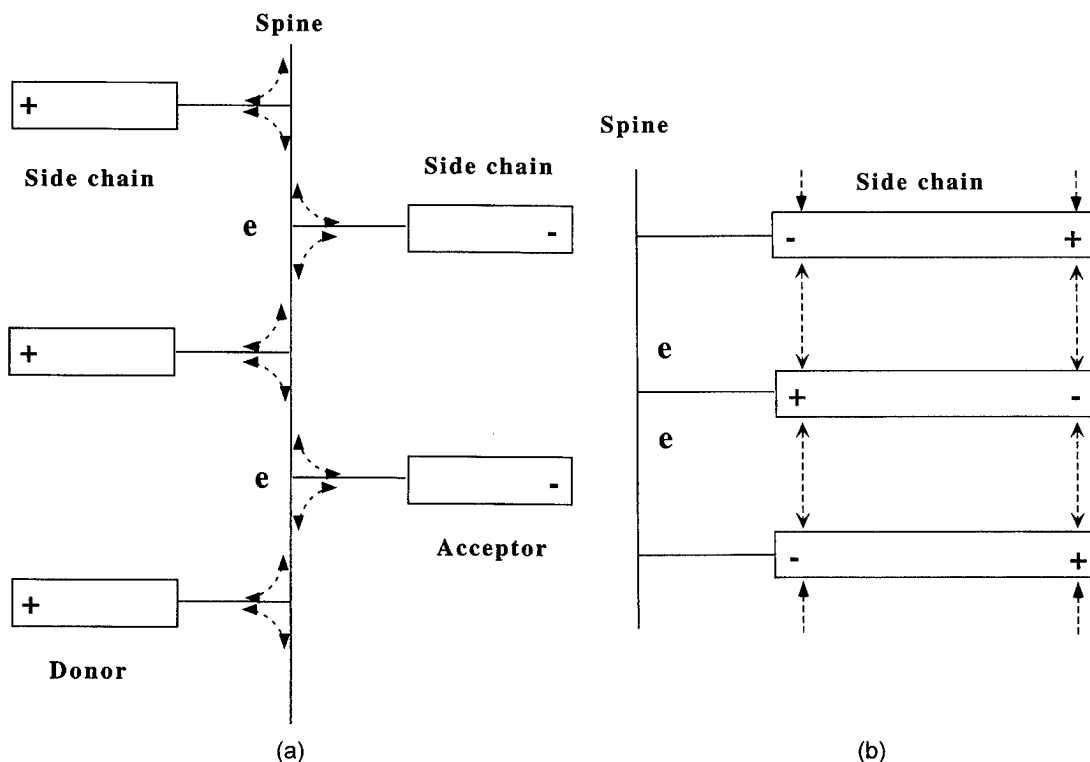


FIGURE 3. CT polymer network models. (a) depicts a model which consists of the spine and the side chain with the CT between the spine and the side chain. The electron transfer is illustrated as arrows. In (b), another model interacting between side chains is shown.

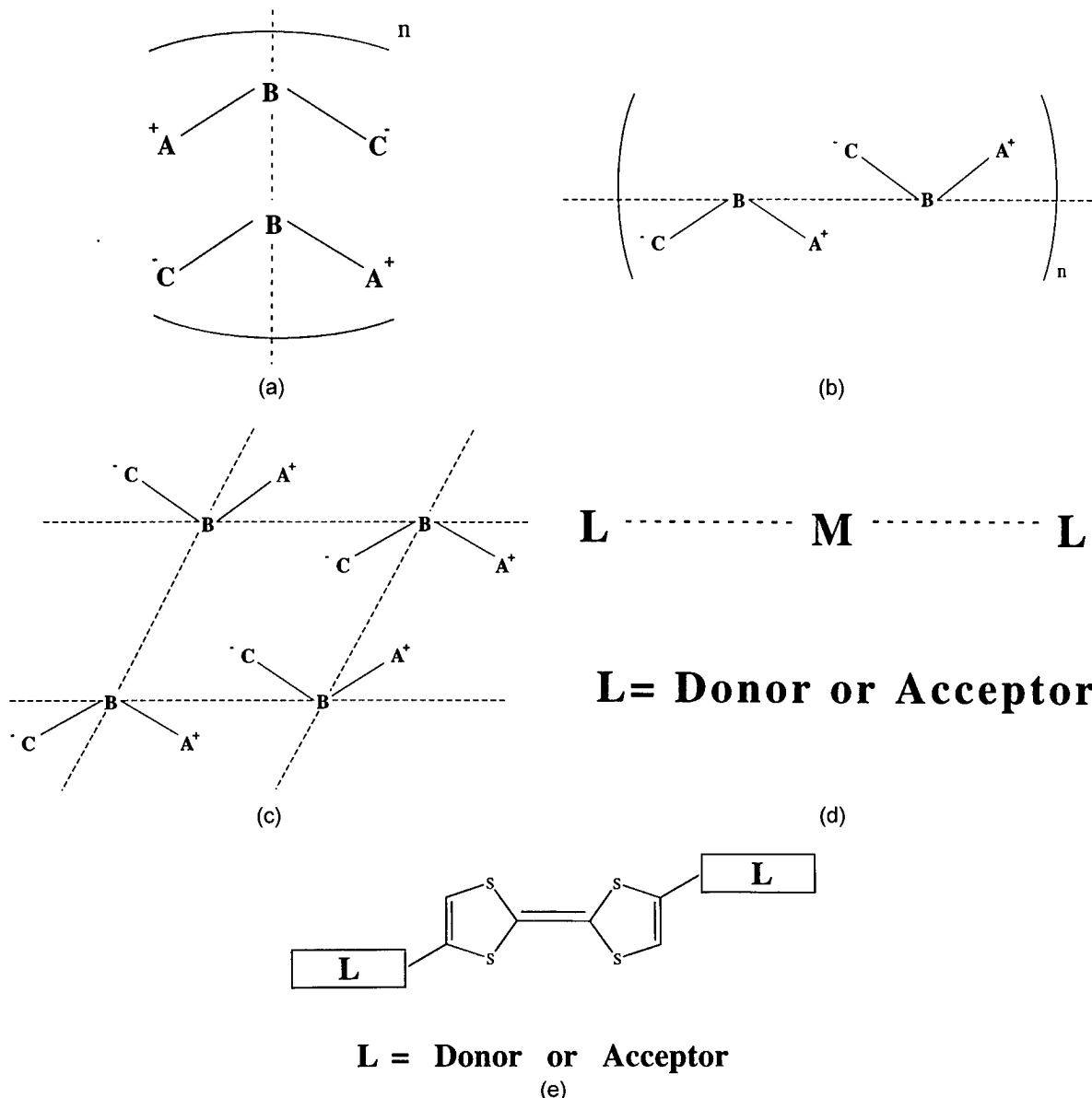


FIGURE 4. Crystal systems for charge transfer model. In (a–c), the systems consist of zwitterionic structures, and the dotted lines mean the through space electron transfer. In (d, e), L is a donor or an acceptor.

Finally, we propose composite systems consisting of the polymer network and crystal systems as shown in Figure 5. We also present some models for the crystal system in the next section (see Fig. 7).

General Theory for Charge-mediated Superconductivity

Little's calculation was criticized by Paulus [30] using two points: (1) Little used the screened

Coulomb interaction for the electron–electron interaction in the unsaturated spine, but this is not the case. Attractive coupling of two electrons in the spine, if it occurs, results when one of them polarizes the charge distribution in a side chain and then the second one is attracted to the resulting excess of positive charge near the spine. However, since this polarization is an electronic effect, the distorted charge distribution will relax very rapidly back to the undistorted one, so that the second electron must be very close, in both space and time, to the first one in order to feel any

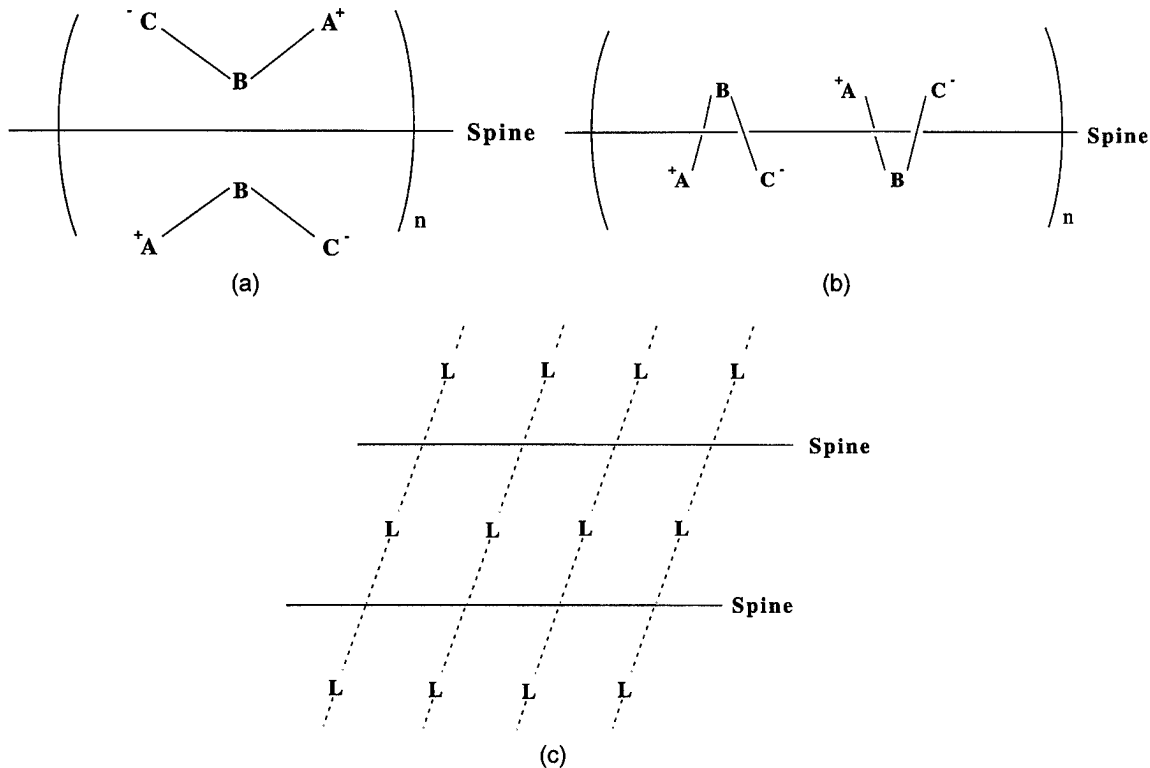


FIGURE 5. Composite models for the CT model. (a, b) show the system which consists of a spine and zwitterionic side chains. The electron transfers between the spine and the side chains through space. (c) illustrates the system of spines and donors / acceptors.

appreciable effect due to the distortion. The spine electron will move at velocities comparable to those of the substituent electrons, so that there will be no time to screen the Coulomb repulsion of the two spine electrons before the distortion in the side-chain charge distribution disappears again. (2) Little used two opposite point charges at the ends of each side chain to represent its polarized distribution. This is a large overestimation of the effective polarization and of the consequent coupling between the spine electrons. Paulus concluded that it is unlikely that any substituent can be found which provides sufficient coupling between the spine electrons to make overall interaction attractive.

As to the second point, Salem [32] pointed out that it was possible, at least in principle, to build a side-chain molecule in which the transition density was effectively localized at the ends of the molecule; in other words, Little's estimate would be reasonable. Further, he showed that, due to the resulting large coupling, the superconducting state will be possible, if other conditions are met.

In this section, we present a Hamiltonian in the model system as shown in figure 3(a) in the previous section. Differences between the Little model and our CT model will be clearly shown.

HAMILTONIAN

The total Hamiltonian for a many-electron system in the CT model as shown in Figure 3(a) is written as

$$H = H_0^a + H_{int}^a + H_0^b + H_{int}^b + H^{ab} + H_{int}^{ab}, \quad (1)$$

where

$$H_0^a = \sum_{r,s,\sigma} h_{rs}^a a_{r\sigma}^\dagger a_{s\sigma}, \quad (2)$$

$$H_{int}^a = \frac{1}{2} \sum_{r,s,t,u} \sum_{\sigma,\rho} V_{rstu}^{\sigma\rho\rho\sigma} a_{r\sigma}^\dagger a_{sp}^\dagger a_{t\rho} a_{u\sigma}, \quad (3)$$

$$H_0^b = \sum_{r,s,\sigma} h_{rs}^b b_{r\sigma}^\dagger b_{s\sigma}, \quad (4)$$

$$H_{int}^b = \frac{1}{2} \sum_{r,s,t,u} \sum_{\sigma,\rho} V_{rstu}^{\sigma\rho\rho\sigma} b_{r\sigma}^\dagger b_{s\rho}^\dagger b_{t\rho} b_{u\sigma}, \quad (5)$$

$$H^{ab} = \sum_{r,s,\sigma} t_{rs} [a_{r\sigma}^\dagger b_{s\sigma} + b_{r\sigma}^\dagger a_{s\sigma}], \quad (6)$$

$$H_{int}^{ab} = \sum_{r,s,t,u} \sum_{\sigma,\rho} V_{rstu}^{\sigma\rho\rho\sigma} a_{r\sigma}^\dagger b_{s\rho}^\dagger b_{t\rho} a_{u\sigma} + 12 \text{ terms.} \quad (7)$$

The first and second terms are the Hamiltonian for the spine and the third and fourth terms describe the side-chain part. Other terms imply the mixing terms between the spine and side-chain parts. $a_{r\sigma}^\dagger$ ($a_{r\sigma}$) is the creation (annihilation) operator for the r -th site with spin σ in the spine. $b_{r\sigma}^\dagger$ ($b_{r\sigma}$) is that for the side chain.

In the next subsection, we study the possibility of the charge-mediated superconductivity in relation to the effective electron-electron interaction in two cases of the charge-fluctuation model and the CT model.

CHARGE-FLUCTUATION MODEL

For the charge-fluctuation model as for the Little model, the Hamiltonian, H_{CF} , is derived from Eq. (1):

$$H_{CF} = H_0^a + H_0^b + H_{int}, \quad (8)$$

where other terms in Eq. (1) are ignored. The Hamiltonian for the many-electron system in the spine is rewritten as

$$H = H_0 + H_{int}, \quad (9)$$

where

$$H_0 = \sum_{i,\sigma} \epsilon_i a_{i\sigma}^\dagger a_{i\sigma}, \quad (10)$$

$$H_{int} = \frac{1}{4} \sum_{i,j,k,l} \sum_{\alpha,\beta,\gamma,\delta} \Gamma_{ijkl}^{\alpha\beta\gamma\delta} a_{i\alpha}^\dagger a_{j\beta}^\dagger a_{k\gamma} a_{l\delta}. \quad (11)$$

The first and the second terms imply the kinetic and the interaction parts, respectively. $a_{i\alpha}^\dagger$ ($a_{i\alpha}$) is the creation (annihilation) operator for the i -th orbital with spin σ . Γ is the bare vertex part:

$$\Gamma_{ijkl}^{\alpha\beta\gamma\delta} = \langle i\alpha j\beta | k\gamma l\delta \rangle \delta_{\alpha\delta} \delta_{\beta\delta} - \langle i\alpha j\beta | l\delta k\gamma \rangle \delta_{\alpha\gamma} \delta_{\beta\delta}, \quad (12)$$

with

$$\langle i\alpha j\beta | k\beta l\alpha \rangle = \int dr_1 dr_2 \phi_{i\alpha}^*(r_1) \phi_{j\beta}^*(r_2) V(r_1, r_2) \times \phi_{k\beta}(r_2) \phi_{l\alpha}(r_1). \quad (13)$$

The effective electron-electron interaction, $V(r_1, r_2, \omega)$, satisfies the following integral equation:

$$V(r_1, r_2, \omega) = V_0(|r_1 - r_2|) + \iint dr dr' V_0(|r_1 - r|) \times \pi(r, r', \omega) V(r', r_2, \omega), \quad (14)$$

where $V_0(|r_1 - r_2|)$ is the bare potential and $\pi(r, r', \omega)$ is the frequency-dependent polarization part or the irreducible particle-hole propagator. This equation is usually represented diagrammatically as shown in Figure 6. All the coordinates assume N discrete values, so that the equation may be written in the matrix form as

$$V(\omega) = V_0 + V_0 \pi(\omega) V(\omega). \quad (15)$$

Therefore, the effective interaction becomes

$$V = [1 - V_0 \pi]^{-1} V_0. \quad (16)$$

We divide this into two parts, P and Q . The former refers to the spine, and the latter, to the side chain. Then, Eq. (16) becomes

$$\begin{aligned} & \begin{pmatrix} V_{PP} & V_{PQ} \\ V_{QP} & V_{QQ} \end{pmatrix} \\ &= \left[1 - \begin{pmatrix} V_{0PP} & V_{0PQ} \\ V_{0QP} & V_{0QQ} \end{pmatrix} \begin{pmatrix} \pi_{PP} & \pi_{PQ} \\ \pi_{QP} & \pi_{QQ} \end{pmatrix} \right]^{-1} \\ & \quad \times \begin{pmatrix} V_{0PP} & V_{0PQ} \\ V_{0QP} & V_{0QQ} \end{pmatrix}. \end{aligned} \quad (17)$$

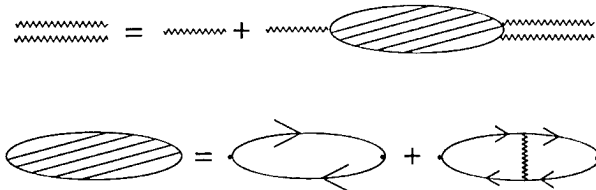


FIGURE 6. The Dyson equation for electron-electron interaction and the approximation for the polarization part.

The effective electron-electron interaction in the spine is written as

$$\begin{aligned} V_{PP} = & \left[1 - V_{0PP}\pi_{PP} - V_{0PQ}\pi_{QP} \right. \\ & - (V_{0PP}\pi_{PQ} + V_{0PQ}\pi_{QQ}) \\ & \times (1 - V_{0QP}\pi_{PQ} - V_{0QQ}\pi_{QQ})^{-1} \\ & \times (V_{0QP}\pi_{PP} + V_{0QQ}\pi_{QP}) \Big]^{-1} \\ & \times \left[V_{0PP} + (V_{0PP}\pi_{PQ} + V_{0PQ}\pi_{QQ}) \right. \\ & \times (1 - V_{0QP}\pi_{PQ} - V_{0QQ}\pi_{QQ})^{-1} V_{0QP} \Big]. \end{aligned} \quad (18)$$

Without Charge Transfer Between Spine and Side Chain

To proceed further, we assume that $\pi_{PQ} = \pi_{QP} = 0$, which implies that the CT between the spine and the side chain is neglected. There is a single bond between them. We get

$$\begin{aligned} V_{PP} = & \left[1 - V_{0PP}\pi_{PP} \right. \\ & - V_{0PQ}\pi_{QQ}(1 - V_{0QQ}\pi_{QQ})^{-1} V_{0QP}\pi_{PP} \Big]^{-1} \\ & \times \left[V_{0PP} + V_{0PQ}\pi_{QQ}(1 - V_{0QQ}\pi_{QQ})^{-1} V_{0QP} \right]. \end{aligned} \quad (19)$$

If we restrict ourselves to retain the first-order term with respect to π_{QQ} , we get

$$V_{Little} = (1 - V_{0PP}\pi_{PP})^{-1} V_{0PP} + V_{0PQ}\pi_{QQ} V_{0QP}, \quad (20)$$

which is the Little approximation. The first term in Eq. (20) may be positive. The first term implies the screened Coulomb interaction in the spine. The second term will be negative through the exciton in the side chain. In the Little approximation, the effective electron-electron interaction may be negative in an appropriate model. On the other hand, in the approximation of Eq. (19), it is unlikely that the effective interaction becomes attractive [33–35].

We consider that the polarization π_{QQ} is large in Eq. (19). The second factor in the right hand of

Eq. (19) is rewritten as

$$\begin{aligned} V_{0PP} + V_{0PQ}\pi_{QQ}(1 - V_{0QQ}\pi_{QQ})^{-1} V_{0QP} \\ = V_{0PP} + V_{0PQ}(\pi_{QQ}^{-1} - V_{0QQ})^{-1} V_{0QP} \quad (21) \\ \cong V_{0PP} - V_{0PQ}V_{0QQ}^{-1}V_{0QP}. \quad (22) \end{aligned}$$

If the second term is larger than the first term, this factor becomes negative. Therefore, in the infinite limit of the polarization π_{QQ} , the effective interaction in Eq. (19) becomes

$$\begin{aligned} V_{PP} = & \left[1 - V_{0PP}\pi_{PP} + V_{0PQ}V_{0QQ}^{-1}V_{0QP} \right]^{-1} \\ & \times \left[V_{0PP} - V_{0PQ}V_{0QQ}^{-1}V_{0QP} \right]. \end{aligned} \quad (23)$$

In the small polarization, the effective interaction will also become positive.

It is found that although in the Little approximation the effective electron-electron interaction is negative it becomes positive in Eq. (19) by the field-theoretical procedure because of the small polarization, π_{QQ} , in the side chain consisting of the organic system. Thus, we are inclined to conclude that the organic superconductor is unlikely to occur at this stage.

With Charge Transfer Between Spine and Side Chain

We consider the CT between the spine and the side chain. When the polarizations of π_{PQ} are large, the second factor on the right-hand side of Eq. (18)

$$\begin{aligned} & V_{0PP} + (V_{0PP}\pi_{PQ} + V_{0PQ}\pi_{QQ}) \\ & \times (1 - V_{0QP}\pi_{PQ} - V_{0QQ}\pi_{QQ})^{-1} V_{0QP} \end{aligned}$$

approximately becomes

$$-V_{0PQ}\pi_{QQ}\pi_{PQ}^{-1}. \quad (24)$$

Thus, the effective electron-electron interaction is written as

$$\begin{aligned} V_{PP} = & - \left[1 - (V_{0PQ} - V_{0PP}V_{0QP}^{-1}V_{0QQ})\pi_{QP} \right. \\ & + V_{0PQ}\pi_{QQ}\pi_{PQ}^{-1}(\pi_{PP} + V_{0QP}^{-1}V_{0QQ}\pi_{QP}) \Big]^{-1} \\ & \times V_{0PQ}\pi_{QQ}\pi_{PQ}^{-1}, \end{aligned} \quad (25)$$

where

$$\pi_{QQ} \ll \pi_{PQ}. \quad (26)$$

It may be attractive in the polymer system with the CT between the spine and the side chain.

From the viewpoint of the possibility of the organic superconductor, the sign of the interaction is essential. When the CT between the spine and the side chain is larger than that in the side chain, the effective interaction of Eq. (25) may be attractive.

Another Charge-fluctuation Model

Next, we consider the charge-fluctuation model as shown in Figure 3(b). In this system, electrons transfer between the side chains and between the spine and the side chain. The Hamiltonian, H_{CF2} , is derived from Eq. (1):

$$\begin{aligned} H_{CF2} = & t_a \sum_{r, s, \sigma} a_{r\sigma}^\dagger a_{s\sigma} + t_b \sum_{i, j\sigma} b_{i\sigma}^\dagger b_{j\sigma} \\ & + t_{ab} \sum_{i, r, \sigma} [a_{r\sigma}^\dagger b_{i\sigma} + b_{i\sigma}^\dagger a_{r\sigma}] \\ & + \frac{1}{4} \sum_{r, s, \sigma, \rho} \Gamma_{rs}^{\alpha\sigma\rho} a_{r\sigma}^\dagger a_{s\rho}^\dagger a_{s\rho} a_{r\sigma} \\ & + \frac{1}{4} \sum_{i, j, \sigma, \rho} \Gamma_{ij}^{b\sigma\rho} b_{i\sigma}^\dagger b_{j\rho}^\dagger b_{j\rho} b_{i\sigma} \\ & + \frac{1}{4} \sum_{r, i, \sigma, \rho} \Gamma_{ri}^{ab\sigma\rho} a_{r\sigma}^\dagger b_{i\rho}^\dagger b_{i\rho} a_{r\sigma}. \quad (27) \end{aligned}$$

Here, we consider that the transfer between the spine and the side chain is small:

$$t_a \gg t_{ab}, \quad t_b \gg t_{ab}. \quad (28)$$

The effective electron-electron interaction, V_{PQ} , between the spine and the side chain is then written as

$$\begin{aligned} V_{PQ} = & [1 - V_{0PP}\pi_{PP} - V_{0PQ}\pi_{QP} \\ & - (V_{0PP}\pi_{PQ} + V_{0PQ}\pi_{QQ}) \\ & \times (1 - V_{0QP}\pi_{PQ} - V_{0QQ}\pi_{QQ})^{-1} \\ & \times (V_{0QP}\pi_{PP} + V_{0QQ}\pi_{QP})]^{-1} \\ & \times [V_{0PQ} + (V_{0PP}\pi_{PQ} + V_{0PQ}\pi_{QQ}) \\ & \times (1 - V_{0QP}\pi_{PQ} - V_{0QQ}\pi_{QQ})^{-1} V_{0QQ}]. \quad (29) \end{aligned}$$

Although the polarizations of π_{PQ} and π_{QQ} are very small, the effective interaction in this case may be negative:

$$\begin{aligned} V_{PQ} \cong & [1 - V_{0PP}\pi_{PP} - V_{0PQ}\pi_{QP}]^{-1} \\ & \times [V_{0PQ} + V_{0PP}\pi_{PQ}V_{0QQ} + V_{0PQ}\pi_{QQ}V_{0QQ}]. \quad (30) \end{aligned}$$

Because the second term in the second factor on the right-hand of Eq. (30) becomes largely negative, the effective interaction of electrons between the spine and the side chain will be attractive. If the attractive part is over a longer time scale than the short time scale repulsion, they will form a dielectron pair with a very short lifetime. In this case, we will have the gapless superconducting state as $(TMTSF)_2X$.

From these estimations for the charge-fluctuation system, we present some models for the polymer network and the crystal systems as shown in Figure 7. Figure 7(a) shows a polymer network system which consists of two spines connected with side chains. L in Figure 7 means a side chain of a donor or an acceptor. Crystal systems are illustrated in Figures 7(b-d). The series of M correspond to conducting part connecting with side chains. We chose the conducting part as BEDT-TTF or TMTSF or $Ni(dmt)_2$. In these cases, the effective interaction between electrons in each spine may be attractive.

CHARGE-TRANSFER MODEL

In the CT model, the total Hamiltonian is written as Eq. (1). This Hamiltonian reduces to the Anderson Hamiltonian:

$$\begin{aligned} H_{CT} = & t_a \sum_{r, s, \sigma} a_{r\sigma}^\dagger a_{s\sigma} + t_b \sum_{i, j\sigma} b_{i\sigma}^\dagger b_{j\sigma} \\ & + t_{ab} \sum_{i, r, \sigma} [a_{r\sigma}^\dagger b_{i\sigma} + b_{i\sigma}^\dagger a_{r\sigma}] \\ & + \frac{1}{4} \sum_{r\sigma} \Gamma_r^{\alpha\sigma-\sigma} a_{r\sigma}^\dagger a_{r-\sigma}^\dagger a_{r-\sigma} a_{r\sigma} \\ & + \frac{1}{4} \sum_{i\sigma} \Gamma_i^{b\sigma-\sigma} b_{i\sigma}^\dagger b_{i-\sigma}^\dagger b_{i-\sigma} b_{i\sigma}. \quad (31) \end{aligned}$$

The solution of the Hamiltonian of Eq. (31) should be studied by the nonperturbation theory. Unfortunately, we cannot analytically solve the equation. If the superconducting state occurs in such system, we expect the high- T_c charge- or spin-

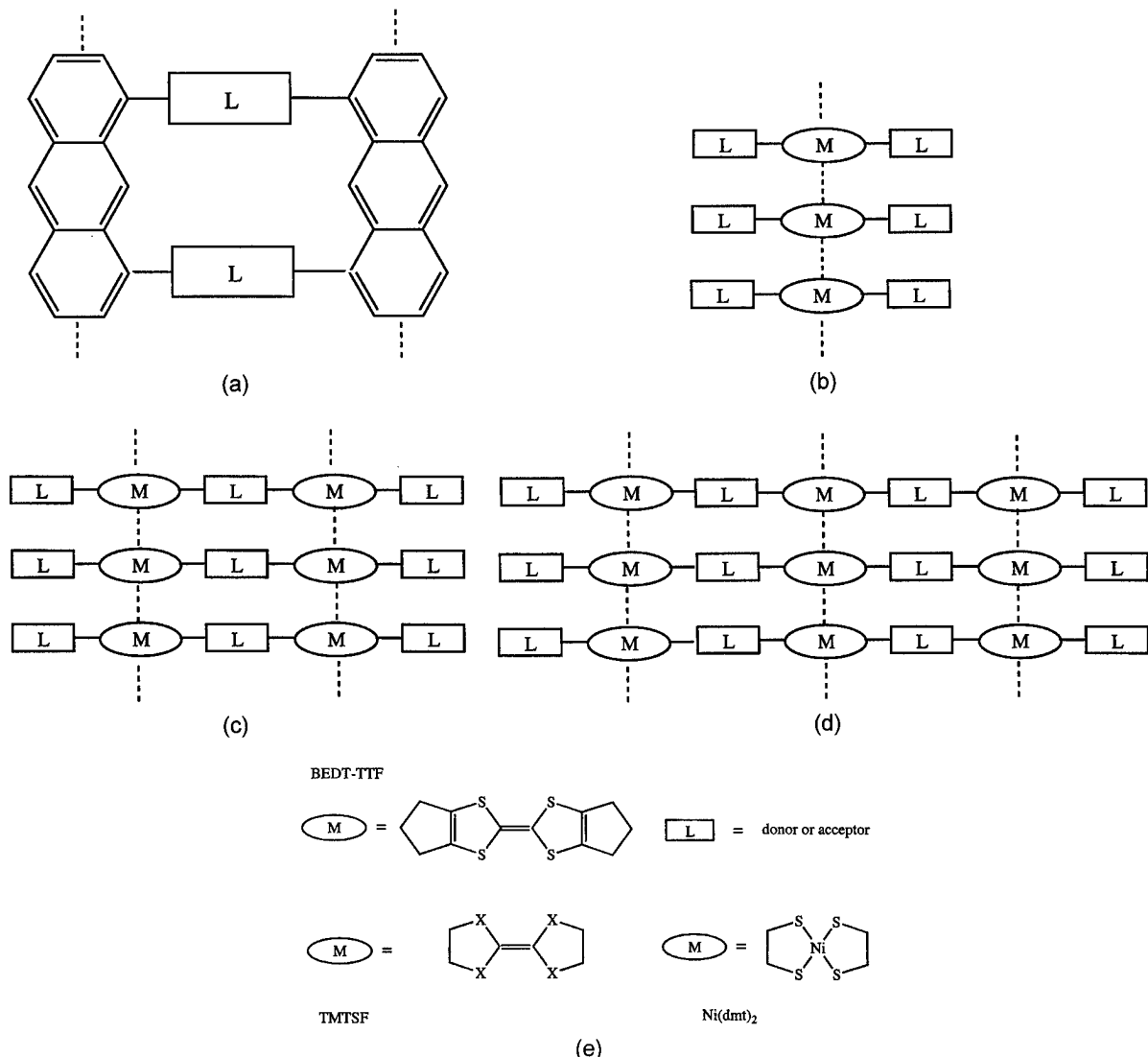


FIGURE 7. Some possible models of polymer network and crystal systems for the superconductor.

mediated or charge plus spin-mediated (namely, cooperative mechanism) superconductivity.

Concluding Remarks

We propose some molecular models which may be the charge-mediated superconductivity. The models are classified into the polymer network system, the crystal system, and the composite system. These models are different from the Little model. The models have the CT between the spine and the side chain. A Hamiltonian for the CT model is also presented.

We provide a Hamiltonian for the charge-fluctuation model, and the effective electron-electron interaction in the spine for the charge-fluctuation model is also derived. We point out that the CT between the spine and the side chain is important in the model systems and that the effective interaction will be attractive in such models with the CT between the spine and the side chain. If the attractive part is over a longer time scale than the short time scale repulsion, the state will exhibit the superconductivity. The bandwidth effect and the consideration of the dynamic polarization are future problems in the course of our treatment.

ACKNOWLEDGMENTS

The authors would like to thank Prof. S. Aono for his continued encouragement and helpful discussions throughout this work. We also wish to express our grateful acknowledgment to Prof. K. Nishikawa, Prof. T. Sakurai, Dr. M. Nakano, and Dr. H. Kawabe for our instructive discussions.

References

1. J. Bardeen, L. N. Cooper, and J. R. Schrieffer, Phys. Rev. **108**, 1175 (1957).
2. P. G. de Gennes, *Superconductivity of Metals and Alloys* (W. A. Benjamin, New York, 1966).
3. G. Rickayzen, *Theory of Superconductivity* (Wiley, New York, 1965).
4. J. R. Schrieffer, *Theory of Superconductivity* (W. A. Benjamin, New York, 1964).
5. A. A. Abrikosov, L. P. Gorkov, and I. E. Dzyaloshinskii, *Methods of Quantum Field Theory in Statistical Physics* (Prentice-Hall, Englewood Cliffs, NJ, 1963).
6. A. L. Fetter and J. D. Walecka, *Quantum Theory of Many-particle Systems* (McGraw-Hill, New York, 1971).
7. J. G. Bednorz and K. A. Müller, Z. Phys. B **64**, 189 (1986).
8. A. P. Kampf, Phys. Rep. **249**, 219 (1994).
9. G. Baskaran, Z. Zou, and P. W. Anderson, Solid State Commun. **63**, 973 (1987).
10. H. Fukuyama and K. Yoshida, Jpn. J. Appl. Phys. **26**, L371 (1987).
11. V. J. Emery, Phys. Rev. Lett. **58**, 2794 (1987).
12. J. E. Hirsch, Phys. Rev. B **31**, 4403 (1985); *Ibid.*, Phys. Rev. Lett. **55**, 1317 (1985).
13. F. C. Zhang and T. M. Rice, Phys. Rev. B **37**, 3759 (1988).
14. M. S. Hybertsen, E. B. Stechel, M. Schlüter, and D. R. Jennison, Phys. Rev. B **41**, 11068 (1990).
15. W. E. Pickett, Rev. Mod. Phys. **61**, 433 (1989).
16. K. Yamaguchi, M. Nakano, H. Namimoto, and T. Fueno, Jpn. J. Appl. Phys. **27**, L1835 (1988).
17. P. W. Anderson, Science **235**, 1196 (1987).
18. E. Fradkin, *Field Theories of Condensed Matter Systems* (Addison Wesley, Reading, MA, 1991).
19. P. W. Anderson, Mater. Res. Bull. **8**, 153 (1973).
20. A. E. Ruckenstein, P. J. Hirschfeld, and J. Apple, Phys. Rev. B **36**, 857 (1987).
21. P. W. Anderson and Z. Zou, Phys. Rev. Lett. **60**, 132 (1988).
22. N. Nagaosa and P. A. Lee, Phys. Rev. Lett. **64**, 2450 (1990); *Ibid.*, Phys. Rev. B **46**, 5621 (1992).
23. S. Yamamoto, K. Yamaguchi, and K. Nasu, Phys. Rev. B **42**, 266 (1990).
24. D. Wechsler and J. Ladik, Phys. Rev. B **55**, 8544 (1997).
25. K. Yamaguchi and T. Fueno, Kagaku **41**, 372 (1986).
26. K. Yamaguchi, T. Takahara, T. Fueno, and K. Nasu, Jpn. J. Appl. Phys. **26**, L1362 (1987); *Ibid.*, **26**, L2037 (1987); *Ibid.*, **27**, L509 (1987).
27. K. Yamaguchi, Int. J. Quantum Chem. **37**, 167 (1990).
28. H. Nagao, M. Mitani, M. Nishino, Y. Yoshioka, and K. Yamaguchi, Int. J. Quantum Chem. **65**, 947 (1997).
29. W. A. Little, Phys. Rev. A **134**, 1416 (1964).
30. K. F. G. Paulus, Mol. Phys. **10**, 381 (1966).
31. R. E. Peierls, *Quantum Theory of Solids* (Oxford University Press, Oxford, 1955), Chap. 5.
32. L. Salem, Mol. Phys. **11**, 499 (1966).
33. J. Yoshida, K. Nishikawa, and S. Aono, Prog. Theor. Phys. **50**, 830 (1973).
34. D. Davis, H. Gutfrund, and W. A. Little, Phys. Rev. B **13**, 4766 (1976).
35. M. Kimura, H. Kawabe, K. Nishikawa, and S. Aono, Bull. Chem. Soc. Jpn. **61**, 4245 (1988).
36. J. Ladik, G. Biczo, and A. Zawadowski, Phys. Lett. **18**, 257 (1965).
37. J. Ladik, G. Biczo, and J. Redly, Phys. Rev. **188**, 710 (1969).
38. J. Ladik and A. Bierman, Phys. Lett. A **29**, 636 (1969).
39. T. C. Collins, M. Seel, J. Ladik, M. Chandrasekhar, and H. R. Chandrasekhar, Phys. Rev. B **27**, 140 (1983).
40. J. E. Hirsch and D. J. Scalapino, Phys. Rev. B **32**, 5639 (1985).
41. M. R. Schafroth, J. M. Blatt, and S. T. Butler, Helv. Phys. Acta **30**, 93 (1957).
42. J. S. Miller, J. C. Calabrese, H. Rommelmann, S. R. Chittipeddi, J. H. Zhang, W. M. Reiff, and A. J. Epstein, J. Am. Chem. Soc. **109**, 769 (1987).
43. Yu Pei, O. Kahn, K. Nakatani, E. Codjovi, C. Mathoniere, and J. Sltern, J. Am. Chem. Soc. **113**, 6558 (1987).
44. M. Fujiwara, S. Takamizawa, W. Mori, and K. Yamaguchi, Mol. Cryst. Liq. Cryst. **279**, 1 (1996).
45. M. Fujiwara, T. Matsushita, and K. Yamaguchi, Synth. Met. **41–43**, 3267 (1991).
46. K. Yamaguchi, M. Okumura, T. Fueno, and K. Nakasuiji, Synth. Met. **41–43**, 3631 (1991).

Embedded Cluster and Supercell Study of the Structure of the Interstitial Cu–C Solid Solutions

DONALD E. ELLIS,¹ SIMON DORFMAN,² DAVID FUKS,³
RONIT EVENHAIM,³ KLEBER C. MUNDIM¹

¹*Department of Physics and Astronomy, Northwestern University, Evanston, Illinois 60208*

²*Department of Physics, Technion—Israel Institute of Technology, 32000 Haifa, Israel*

³*Materials Engineering Department, Ben-Gurion University of the Negev, Beer-Sheva, Israel*

Received 21 February 1998; revised 1 May 1998; accepted 22 May 1998

ABSTRACT: The preferable carbon occupation in copper-based solid solutions is modeled in different Cu–C lattice cells and clusters. A study is based on the comparative analysis of electronic density distributions for different interatomic distances, supercell configurations, and compositions of carbon. For these solid solutions we use the linear muffin-tin orbitals (LMTO) and discrete variation method (DVM) computer codes which allow us to calculate equilibrium positions of carbon atoms. We study the concentration dependence of the lattice parameter in Cu–C solid solution and discuss the charge transfer in this system. © 1998 John Wiley & Sons, Inc. *Int J Quant Chem* 70: 1085–1092, 1998

Key words: electronic structure calculations; microstructure; composites; solid solutions

Introduction

The study of solid solutions that are usually formed in interface regions of composite materials is not only an academic problem: Because of

the increasing interest in composites as structural materials and conducting materials for modern micromachinery devices, understanding the tendencies of formation and bonding in such solid solutions gives a powerful tool for the design of new technologically important materials [1]. The problem of stability of copper–carbon solid solutions is significant for the development of modern metal matrix composites with the aim of adding improved mechanical properties to the excellent electrical and thermal conductivity properties of copper (see, e.g. [2, 3]). Of particular interest is the

Correspondence to: S. Dorfman.

Contract grant sponsor: United States–Israel Binational Science Foundation.

Contract grant number: 94-00044.

Contract grant sponsor: Israel Ministry of Absorption.

possibility of developing improved high-temperature strength. Addition of particulate graphite to copper matrices permits considerable improvements in tribological properties. Thus copper–carbon composites see regular application in sliding electrical contacts applications.

Carbon is insoluble in copper up to very high temperatures; its solubility does not exceed 0.02 at %. Thus a problem of wettability of carbon fibers by copper arises. This wettability is extraordinarily small [4] and does not allow one to fabricate the composite material. So the interface bonding in copper–carbon composites is extremely weak [5]. Formation of very dilute Cu–C interstitial solid solution at the interface may be diffusion controlled.

Study of copper–carbon solid solutions formed at the interface between the copper host and carbon fibers [6] shows that the interface region in these composites is very narrow and does not exceed 100 nm. The experimental investigation of the properties of these interfaces is a complicated task. This is why theoretical studies of interface alloys have to be appreciated. The modeling of diffusion of interstitial carbon atoms may be a unique opportunity in the understanding of cohesion and wetting at copper–carbon interfaces [7]. To predict the diffusion behavior of carbon atoms, we have to study the structure and interatomic interactions in such alloys.

In this study we focus on nonempirical embedded cluster and supercell studies of the structure of the interstitial Cu–C solid solutions. However, the experimental data on these solutions are very limited, and it would be very attractive to produce comparative study of Cu–C alloys by nonempirical density functional embedded cluster and supercell schemes.

Methodology

Density functional (DF) theory is a first-principles self-consistent approach to electronic structure, which has wide applications to molecules and solids [8]. Even the crudest approximation, local density approximation (LDA), to the density functional theory has been successfully applied to predict structural and dynamical properties of a large variety of materials. Equilibrium volumes, elastic constants, phonon frequencies, surface reconstruction, and magnetism are just some exam-

ples of properties which could be successfully calculated for systems without particularly strong electron correlations within the LDA (an LSDA, the local spin-density approximation). The LDA usually leads to some overbinding in solids (equilibrium volumes are typically 1–3% underestimated). Considerably larger errors are found in cases where the LDA is not sufficiently accurate; the ionic compounds like MgO serve as examples when the simple LDA fails.

In order to study the effects of chemical bonding in copper-based solid solutions on the electronic density distributions we model different Cu–C lattice cells and calculate electronic density distributions based on the linear muffin-tin orbitals (LMTO) [9] and discrete variation method (DVM) computer codes. Such a study is based on the analysis of electronic density distributions for different interatomic distances, supercell configurations, and compositions of carbon. Changes in the concentration will lead to two results:

1. Changes of the positions of atoms in the supercell, i.e., the reconstruction of the cell
2. Changes in the character of the bonding forces

Our own development of the embedded cluster scheme permits a spatially localized expansion of electronic wave functions, densities, and derived properties by treating fragments of the extended system [10]. This approach gives a feasible methodology for self-consistently treating large systems with low symmetry, and is thus particularly well suited for problems of impurities, surfaces, and interfaces [11]. Extraction of the interior “seed” volume of each cluster, and alignment of equivalent partial densities of states (equivalent Fermi energies) completes the self-consistent fragment matching procedure. The DF wave functions for each embedded cluster are obtained by the well-developed discrete variational (DV) method [8], using the DF potential derived from the total electronic density.

LMTO even in the crudest atomic sphere approximation (ASA) approach is a well-established technique to study metals, alloys, and also perovskites and different phases with sometimes non-trivial very complicated structures (see, e.g., Refs. [12–14]). In recent years it was successfully applied to the study of surface alloys (see, e.g. [15]). In the case of dilute alloys the properties of Fe embedded in V and Cr matrices was successfully

studied [16]. It seems that today this scheme is one of the most promising techniques in band structure studies due to the ability to calculate very fast electronic structures for various crystal lattices.

Study of Bonding in Cu-C Solid Solutions

SUPERCELL CALCULATIONS

In Ref. [17] the interatomic Cu-C potential was used to calculate the carbon atom energies in different interstitial (octahedral and tetrahedral) positions, u_o and u_t , respectively. Interactions in the first- and the second-coordination shells were accounted for in these calculations. The energies u_o and u_t were used to study the temperature dependence of the relative concentrations c_o and c_t of carbon in octahedral and tetrahedral positions. These results show clearly that the probability of finding carbon atoms in octahedral positions is much higher than in tetrahedral ones. Only after heating over a temperature $T \sim 1000$ K the occupation probability of octahedral positions decreases to 80% and tetrahedral positions will be occupied by 20% of atoms. Thus we are convinced to use the model of the interstitial occupation of carbon atoms in Cu-C solid solution with the carbon atoms randomly situated in octahedral positions. This model is valid up to $T \sim 1000$ K.

The LDA calculations for Cu-C supercells (tetrahedral and octahedral occupation of carbon atom) with 20% carbon concentration performed in the framework of LMTO formalism [9] yield an equilibrium lattice parameter for tetrahedral occupation 5.21 a.u. and for octahedral occupation 7.12 a.u. The octahedral occupation was modeled in the cubic supercell with carbon situated in position $a\{0.5, 0, 0\}$ and copper atoms in positions $a\{0, 0, 0\}$, $a\{0.5, 0.5, 0\}$, $a\{0.5, 0, 0.5\}$, and $a\{0, 0.5, 0.5\}$. The tetrahedral supercell differs by the position of a carbon atom, which is put in the position $a\{0.25, 0.25, 0.25\}$.

The calculated density of states (DOSs) for both types of supercells are shown on the applied Figures 1 and 2. Fermi energy for supercell with a carbon atom in octahedral position (O) is much less than for the tetrahedral occupation (T). The differences in DOSs are mainly expressed in p -band occupation. We can see that in O-case p -band is unoccupied and is much narrower than in T-case. The p -band in T-case supercell simulations is

highly smashed. Positions of main p -band peaks of carbon and copper in O and T occupation coincide. The lower p -band peak positions in T- and O-cases are situated at distances 0.3 and 0.45 Ry under Fermi energy, respectively. These data were a basis of the chemical bonding study in DVM formalism, as we supposed that the lower position of p -band in O-sites shows the tendency to formation of weak chemical bonding.

We calculated the equation of states for O- and T-occupations. These equations are plotted in Figures 3(a) and 3(b), respectively. The equilibrium tetrahedral supercell is much more compressed than the octahedral one. In Figure 4 we show the dependence of the equilibrium lattice parameter in Cu-C solid solution with octahedral occupation of carbon on the displacement of the carbon atom along the path $\{0.5-x, x, 0\}$. This path represents the diffusion path of the interstitial atom between two nearest interstitial positions in face-centered cubic (fcc) copper host lattice (see Ref. [17]). Our results show the minimal value of the lattice parameter of the cell with the displaced carbon atom. This displacement is $x = 0.02$ and reflects the weak bonding of carbon in this off-center position. As will be shown later, this result correlates very well with the calculations of a charge redistribution in the vicinity of displaced and nondisplaced interstitial carbon atom in the copper host matrix. In Figure 5 we present the data for the calculated dependence of the lattice parameter in Cu-C solid solutions vs. atomic fraction of carbon. This dependence was modeled by inclusion of additional carbon atoms in the previously described supercell. In our simulations these carbon atoms occupied $a\{0.5, 0.5, 0.5\}$, $a\{0, 0.5, 0\}$, and $a\{0, 0, 0.5\}$ additional sites in the cubic cell. The increasing number of carbon atoms in the supercell allowed us to calculate the energies and the lattice parameter for the following atomic fraction of carbon: $\frac{1}{3}$, $\frac{3}{7}$, and $\frac{1}{2}$. The last concentration corresponds to the total occupation of octahedral positions in fcc lattice. The lattice parameter vs. atomic fraction dependence is nonmonotonic and reflects the changes of the quasielastic response of the lattice on the occupation of interstitial positions. Analogous behavior of the concentration dependence of the lattice parameter is a well-known fact for interstitial Ti-C, Zr-C, and other carbides with a wide homogeneity region on a phase diagram. Even in the Kanazaki force formalism it happens that for small atomic fraction of interstitial atoms the lattice ex-

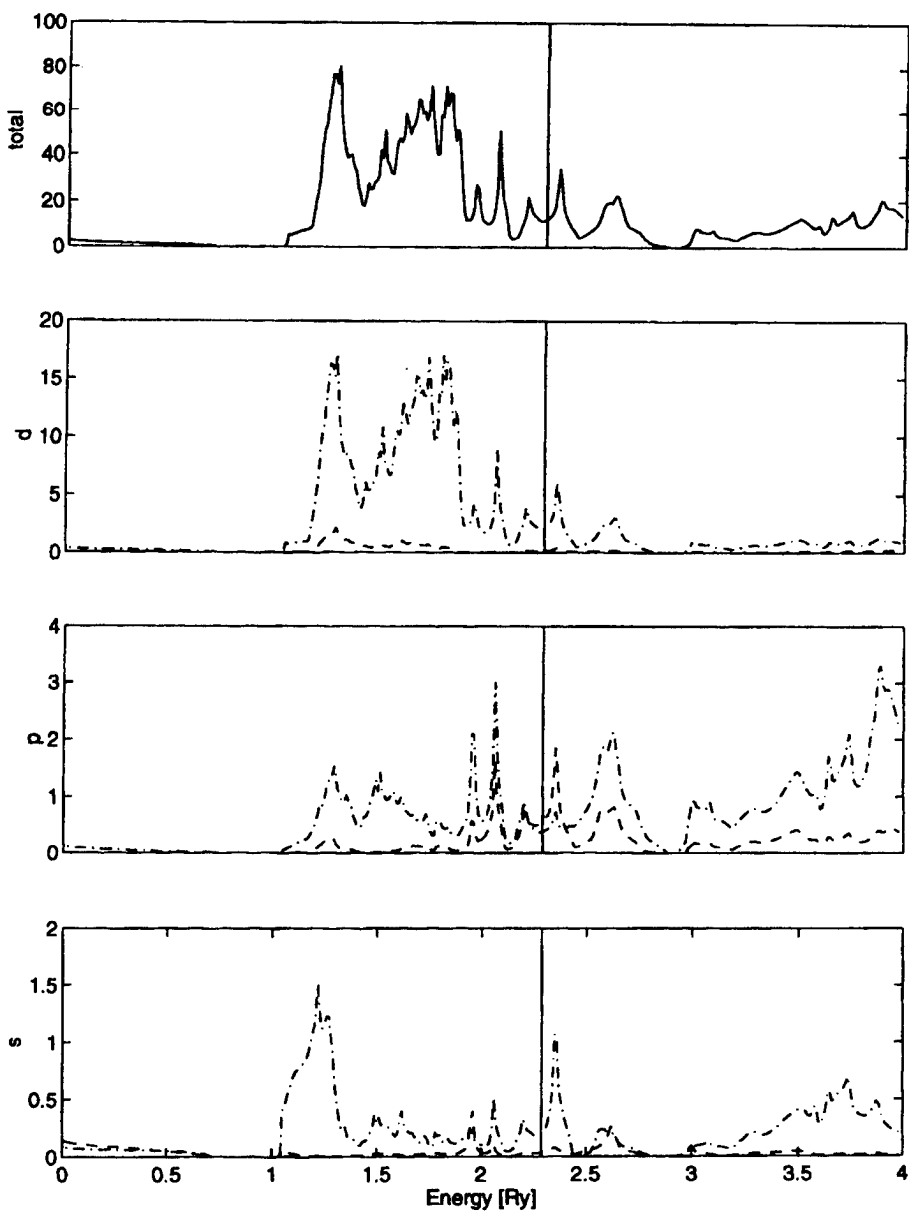


FIGURE 1. Density of states for the copper–carbon supercell with 20% of carbon. Carbon occupies the tetrahedral interstitial position.

pansion concentration coefficient

$$u = \frac{1}{a} \frac{da}{dc}$$

(a is a lattice parameter and c is an atomic fraction) is positive. Increase of atomic fraction of interstitial atoms leads to compensation of Kanzaki forces (starting from some atomic fraction). It results in a change of sign of u and in a decrease in

the equilibrium lattice parameter of solid solutions.

CLUSTER CALCULATIONS

The first-principles density functional theory has been used to calculate electronic structure of carbon present as substitutional and interstitial impurities in copper. Using the embedded cluster formalism and localized orbitals, we have obtained

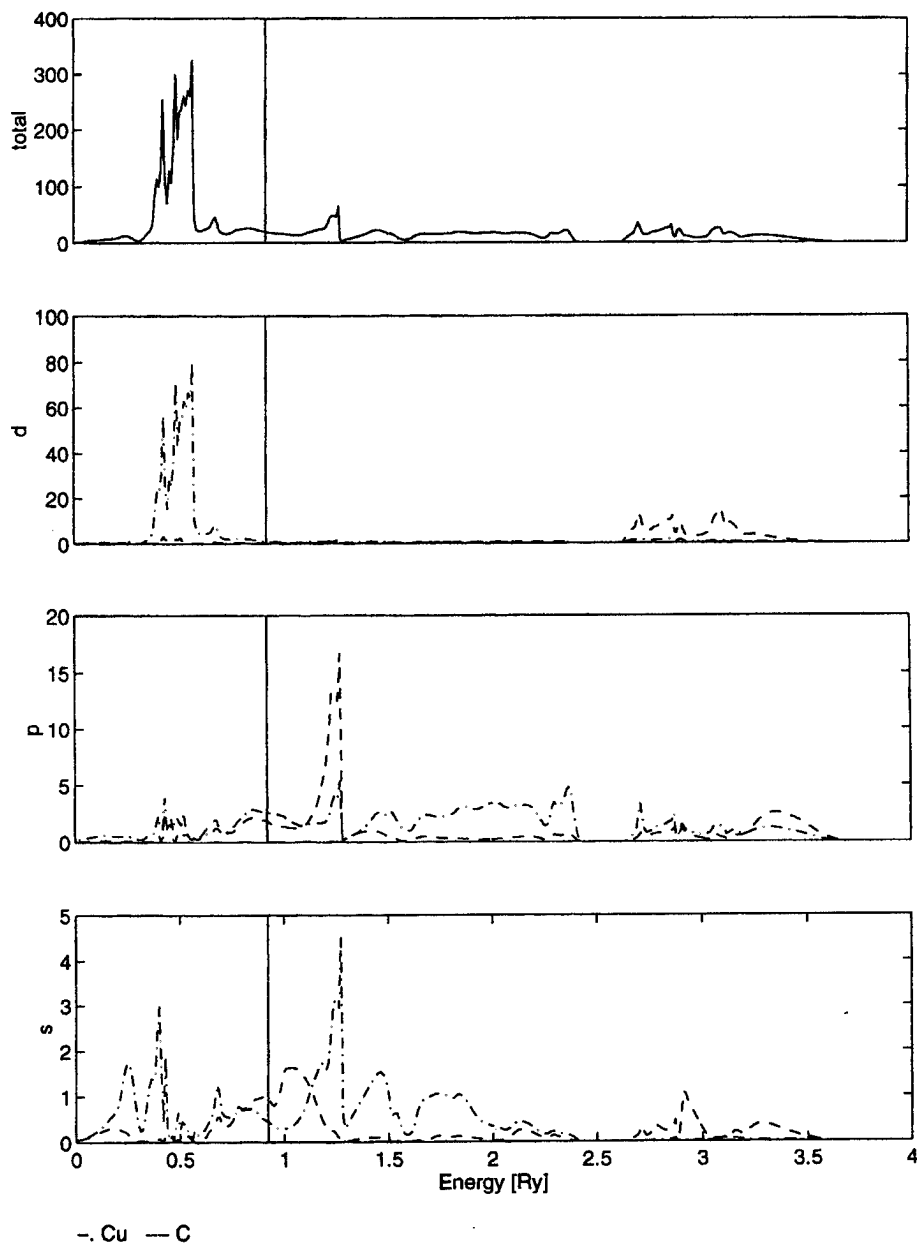


FIGURE 2. Density of states for the copper–carbon supercell with 20% of carbon. Carbon occupies the octahedral interstitial position.

energy levels and wave functions for finite molecular fragments within the infinite copper host. Three coordination shells were included in the cluster with the center in the octahedral interstitial position. The following sites were treated: substitutional, octahedral interstitial, and tetrahedral interstitial. In all cases displacements of the C atom from the site of high symmetry were studied, with the objective of determining response of the Cu lattice to the impurity and the relative energy

versus position. Symmetric relaxation of the first shells of Cu atoms around the impurity was also considered. Mulliken population analysis of the self-consistent wave functions shows that C is generally a weak electron acceptor, with net charge ranging from -0.1 to -0.3 depending upon location. In the highly improbable substitutional site, C is found to be a net electron donor. The copper populations show the expected s - d hybridization, with typical configuration of $3d^{9.74} s^{0.94} p^{0.5}$. Net Cu

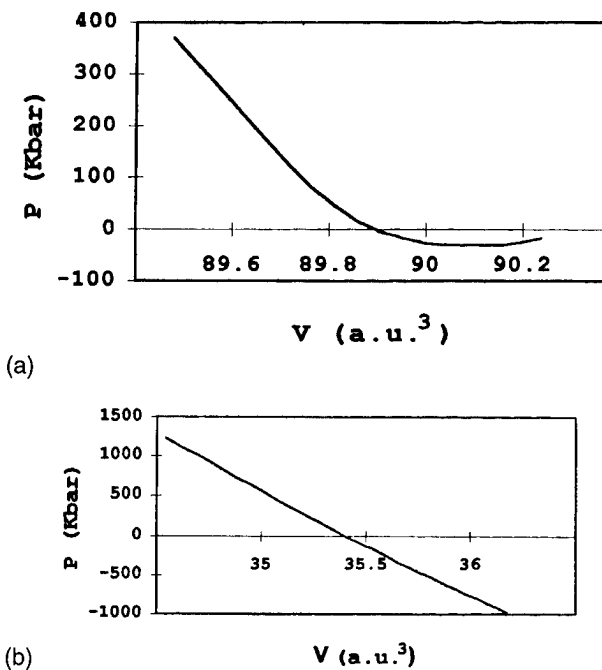


FIGURE 3. Equation of states for the copper–carbon solid solution with 20% of carbon. (a) Carbon atom occupies the octahedral interstitial position and (b) carbon atom occupies the tetrahedral interstitial position.

charges are found to be inversely proportional to distance from C. For example, in the highly stressed tetrahedral site, net Cu charges of +0.39, +0.02, and -0.02 are found for first, second, and third neighbors, respectively. These charges are a manifestation of the Ruderman–Kittel oscillations predicted in simpler (electron gas) models of impurity

response. A DOS diagram [18] shows that for the octahedral interstitial site the occupied portion of the valence band is 5 eV in width, and there is little overlap between major C 2s, 2p features with that of the Cu 3d. We reduced a number of atoms in the cluster (“microscope”) by a factor of 3 and received the energy and volume charge curves with just the same tendencies. Analysis of total energy results versus carbon displacement and Cu shell relaxation (see Figs. 6 and 7) suggests that the minimum energy configuration lies off the octahedral site, toward the fcc cube center. The microscope approach (Fig. 7) completely reproduces the energy decrease with the off-center shift of carbon. We complement the present data with calculations of the volume carbon charge along the same {0.5- x , x , 0} path. Our simulations show the tendency to the formation of the chemical bonding between the displaced carbon and copper atoms (see Figs. 8 and 9). Reduction of number of atoms in the cluster (Fig. 9) does not influence sufficiently the character of bonding and confirms the formation of weak chemical bonding in the system with the off-center shift of carbon atom. These results correlate with the supercell calculation (see above). Comparing Figures 6 and 8 we see that the position of the energy minimum with carbon displacement from the center of octahedral position is surprisingly well and corresponds to the minimal value of the carbon volume charge and is equal to $x = 0.04$. This result is only twice as large as obtained in LMTO calculations where the carbon concentration was much larger. The decrease of the binding energy after $x = 0.12$ is related to

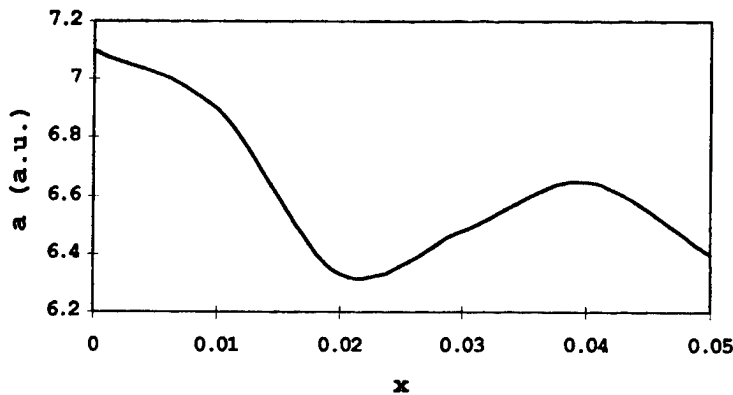


FIGURE 4. Equilibrium lattice parameter dependence on the displacement of carbon atom along the path {0.5- x , x , 0} for the copper–carbon solid solution with 20% of carbon. Carbon occupies the octahedral interstitial position.

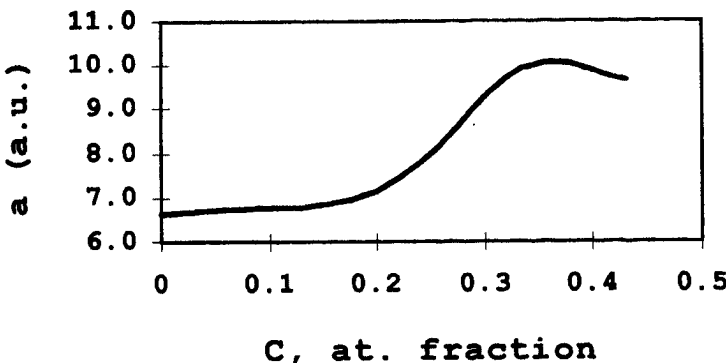


FIGURE 5. Calculated dependence of the lattice parameter in Cu-C solid solutions vs. atomic fraction of carbon.

influence of cluster boundaries in embedded cluster simulations.

Summary

The DF cluster and supercell results correspond in predicting the off-center displacements of the carbon atom and indicate a charge transfer of $\sim 1 e$ to carbon, mostly from the first-neighbor shell, in all relaxed environments studied. Bond-order data display the Cu-C interaction to be bonding in nature. Densities of states show the interaction to be primarily C 2p-Cu 3d in nature, dominated by the nearest-neighbor coordination shell in all environments.

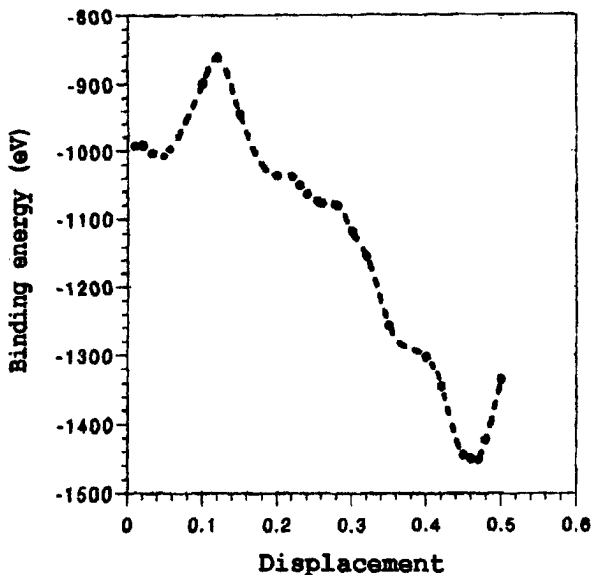


FIGURE 6. Binding energy as a function of carbon atom displacements. The path of the carbon motion is $\{0.5-x, x, 0\}$, the data of the embedded cluster density functional calculations.

Inclusion of the electrostatic charge-transfer component of the Cu-C interaction, accompanied with a refinement of initial force field parameters, should permit accurate future atomistic simulations not only of relaxation, but also of diffusion processes. Work in progress on copper-carbon interfaces is aimed at addressing the process of diffusion from carbon fibers into the metallic host at elevated temperatures, and to provide a detailed interpretation of the interface bonding region which we have observed with microscopy studies [6].

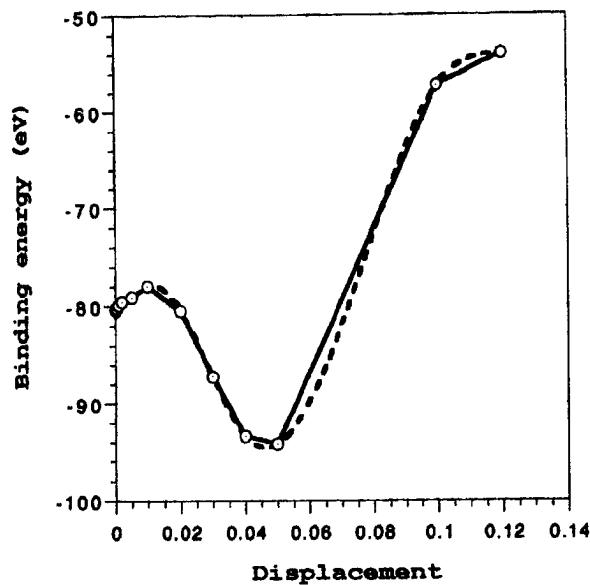


FIGURE 7. Binding energy as a function of carbon atom displacements. The path of the carbon motion is $\{0.5-x, x, 0\}$, the data of the embedded cluster density functional calculations. Number of atoms in the cluster reduced by a factor of 3 (microscope). A dashed line is a spline interpolation.

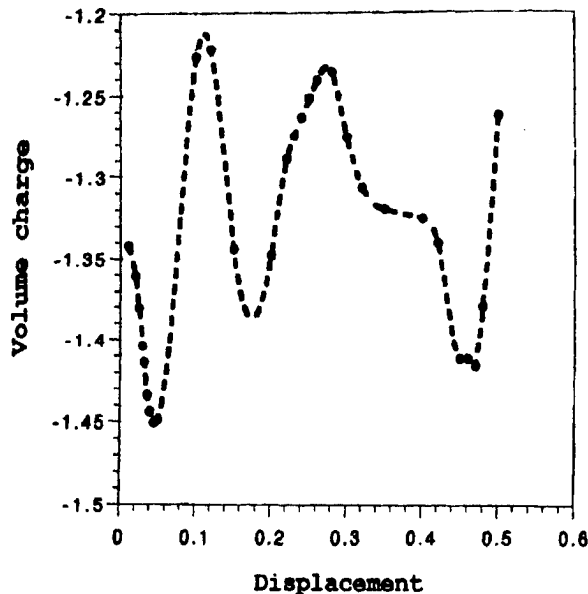


FIGURE 8. Volume carbon atom charge as a function of carbon atom displacements. The path of the carbon motion is $\{0.5-x, x, 0\}$, the data of the embedded cluster density functional calculations.

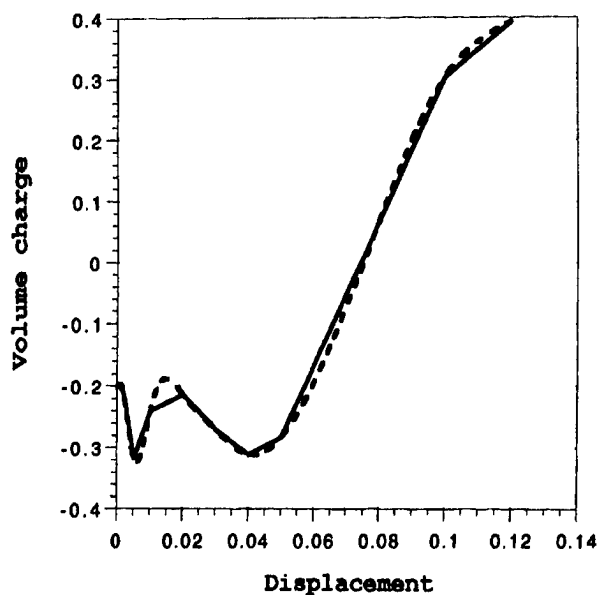


FIGURE 9. Volume carbon atom charge as a function of carbon atom displacements. The path of the carbon motion is $\{0.5-x, x, 0\}$, the data of the embedded cluster density functional calculations. Number of atoms in the cluster reduced by a factor of 3 (microscope). A dashed line is a spline interpolation.

ACKNOWLEDGMENTS

This research was supported by the grant no. 94-00044 from the United States-Israel Binational Science Foundation (BSF), Jerusalem, Israel, and by the special program of the Israel Ministry of Absorption.

References

- R. F. Gibson and G. M. Newaz, Eds., *Proceedings of the American Society for Composites*, 12th Technical Conference, October 6-8, 1997, Dearborn, Michigan (Technomic, Lancaster, 1997).
- X. Kuang, G. Caronuto, Z. Zhou, and L. Nicolais, *Sci. Eng. Composite Mater.* **50**, 9 (1996).
- S. Dorfman and D. Fuks, *Composites* **27A**, 697 (1996).
- D. A. Mortimer and M. J. Nicholas, *J. Mater. Sci.* **5**, 149 (1970).
- S. J. Sun and M. D. Zhang, *J. Mater. Sci.* **26**, 5762 (1991).
- R. Evenhaim, D. Fuks, S. Dorfman, A. Berner, and D. E. Ellis, submitted.
- S. Dorfman and D. Fuks, *Composite Interfaces* **3**, 431 (1996).
- D. E. Ellis, Ed., *Electronic Density Functional Theory of Molecules, Clusters, and Solids* (Kluwer, Dordrecht, 1994).
- O. K. Andersen, *Phys. Rev. B* **12**, 3060 (1975); H. L. Skriver, *The LMTO Method* (Springer, New York, 1984).
- D. E. Ellis, J. Guo, and D. J. Lam, *Rev. Solid State Sci.* **5**, 227 (1991).
- D. E. Ellis, E. Baggio-Saitovich, and D. J. Lam, *Physica C* **198**, 57 (1992); J. Guo, D. E. Ellis, and D. J. Lam, *Phys. Rev. B* **45**, 13647 (1992).
- O. Eriksson, B. Johansson, M. S. S. Brooks, H. L. Skriver, *Phys. Rev. B* **40**, 9519 (1989).
- V. N. Antonov, B. Yu. Yavorsky, A. P. Shpak, Vi. N. Antonov, O. Jepsen, G. Guizzetti, and F. Marabelli, *Phys. Rev. B* **53**, 15631 (1996).
- C. Felser, J. Kohler, A. Simon, and O. Jepsen, *Phys. Rev. B* **57**, 1510 (1998).
- A. Christensen, A. V. Ruban, P. Stoltze, K. W. Jacobsen, H. L. Skriver, J. K. Nørskov, and F. Besenbacher, *Phys. Rev. B* **56**, 5822 (1997); A. I. Landa, A. V. Ruban, I. A. Abrikosov, P. Wynblatt, and H. L. Skriver, *Structure and Evolution of Surfaces*, R. C. Cammarata, E. H. Chason, T. L. Einstein, and E. D. Williams, *MRS Symposium Proceedings* **440**, 467 (1997).
- S. Mirbt, I. A. Abrikosov, B. Johansson, and H. L. Skriver, *Phys. Rev. B* **55**, 67 (1997).
- S. Dorfman and D. Fuks, in *Proceedings of the American Society for Composites*, R. F. Gibson and G. M. Newaz, Eds., 12th Technical Conference, October 6-8, 1997, Dearborn, Michigan (Technomic, Lancaster, 1997), p. 1151.
- D. E. Ellis, DVM-X _{α} calculations (unpublished).

Atomic Motion at Germanium Surfaces: Scanning Tunneling Microscopy and Monte Carlo Simulations

JEAN-POL VIGNERON, ABOUD BENAISSE,* ISABELLE DERYCKE,
ALAIN WIAME, R. SPORKEN

Institute for Studies in Interface Sciences, Facultés Universitaires Notre-Dame de la Paix, rue de Bruxelles 61, 5000 Namur, Belgium

Received 21 March 1998; accepted 2 April 1998

ABSTRACT: The observation of the motion of an adatom on the reconstructed Ge (111) is a rare event, which will be examined by way of simple adatom-surface interaction models. Estimations of the residence time of adatoms on energetically favorable sites indicate that a thermal excitation can account for casual adatom motion and that a strong tip-surface interaction is not obviously needed to explain the changes found in sequences of scanning tunneling microscopy (STM) images of the same surface areas. © 1998 John Wiley & Sons, Inc. *Int J Quant Chem* 70: 1093–1097, 1998

Key words: surface; STM; germanium

Introduction

The (111) surface of elemental semiconductors like Ge usually assumes a rather complex structure, and several types of reconstructions ($1 \times 2, 2 \times 8 \dots$) can be identified [1]. The long-range regularity of the reconstructions encountered on this surface is easily disrupted by the presence of defects, and this fragility of the surface order is expected to have some impact on the

thermally activated self-diffusion [2]. The direct observation of the Ge (111) surface by scanning tunneling microscopy (STM), and the new computer tools that can be used to achieve a better interpretation of the images provide a new direct way of studying the diffusion processes that take place on these systems.

Crystalline Structure of the Germanium (111) Surface

The crystalline structure of bulk Ge can be viewed as a succession of parallel, equidistant, rumpled planes lying normal to the [111] direction. The thickness of these rumpled planes is about

*Facultés des Sciences et Techniques de Settat, Université Hassanier, Settat, Marokko.

Correspondence to: J.-P. Vigneron.

Contract grant sponsor: Belgian Programs on Interuniversity Attraction, Belgian National Fund for Scientific Research.

$a/7$ ($a = 5.658 \text{ \AA}$), while the gap between two of these planes is nearly twice as large ($a/4$). A clean surface in this direction can be created by cutting off the crystal between two of these rumpled planes, creating an ideal 1×1 surface, in which each terminating atom reinforces the surface energy by its associated dangling bond. The surface tension is immediately partially released by a substantial flattening of the last rumpled plane (surface relaxation) and by a change in the native crystal translational symmetry. At some temperature, the Ge (111) surface presents a 2×1 reconstruction [3], which is usually observed after a direct cleavage under high-vacuum conditions. After high-temperature annealing, the surface is usually found in a 2×8 reconstruction state, in which the number of dangling bonds is reduced by an exact factor of 2. Here, the near-ideal surface is covered with supplementary Ge adatoms, which find their place in a so-called T_4 site, right on top of one of the lower atoms in the surface rumpled plane. The surface rumpled plane indeed defines an outer surface layer made of an hexagonal arrangement of atoms, leaving us with two types of triangular sites: the site T_4 is at the center of a triangle occupied by one of the atoms in the second atomic plane. The site at the center of the other type of triangle, usually called H_3 , is empty. The T_4 appellation reminds of the fact that the adatom lies on top of the second-plane shallow surface atom, and will there experience the contact with four nearest neighbors. The hollow site where the adatom interacts only with three neighbors (H_3) is, as will be shown below, substantially higher in energy, but is also clearly a possible adatom meta-stable state.

Interpretation of the Adatom STM Image

The STM image of the (111) surface of Ge under positive sample bias is easily understood in terms of the tunneling from the occupied states of the tip into the unoccupied states are essentially localized at the same lateral coordinates as the adatoms, so that under these bias conditions, these adatoms are easily located: in a 2×8 configuration, four of these high-current density spots are observed, attributed to the protruding adatoms stabilized on the T_4 site. The STM image can easily be simulated by a method presented a few years ago at this conference [5], and which has been extended to

allow deriving semiconductor surface STM currents. Equation (29) of Ref. [5], which expresses the tunnel conductance for electrons flowing between a metallic tip and a metallic sample at zero bias ($V = 0$) should be modified, for positive bias V , to include all electrons flowing from occupied tip states to unoccupied Ge states (from $E_F - eV$ to E_F). All electrons from any incidence (summed over all wave numbers $g + q_{\parallel}$) compatible with the tunneling energy attempt to cross the bias-dependent tip barrier and tunnel, except if reflected back to the tip, an event which arises with the probability amplitude $a_{g'gI}^-$ when scattered from a plane-wave state g' into a plane-wave state g :

$$eJ(V) = -\frac{2e}{4\pi^2 h} \int_{BZ} dq_{\parallel} \int_{E_F - eV}^{E_F} dE \sum_g \Theta(k_{gI}^2) \times \left[1 - \sum_{g'} \frac{k_{g'I}}{k_{gI}} |a_{g'gI}^-(eV)|^2 \Theta(k_{g'I}^2) \right]. \quad (1)$$

In this expression, $\Theta(x)$ is the Heaviside function, which filters out evanescent waves (wave vectors k_{gI} , when they are imaginary) and the transfer amplitudes $a_{g'gI}^-$ are computed with the transfer-matrix technique. Figure 1 shows the result of a simulation of the constant-height tunnel current (5 Å above the adatom layer) for the scattering by

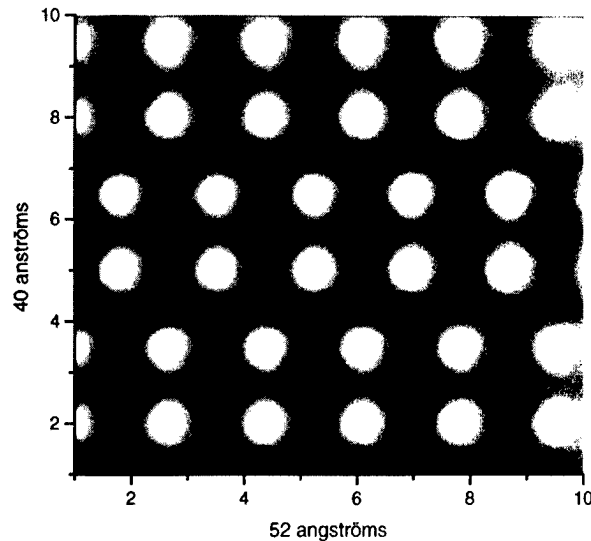


FIGURE 1. Results of a transfer-matrix simulation of the constant-height STM image of the 2×8 reconstructed (111) surface of Ge, under positive-sample bias. Light spots are located at the surface coordinates of the adatoms.

a 2×8 germanium surface, with Ge atoms represented by a (non-self-consistent) local Gaussian pseudopotential based on parameters given by Cohen and Bergstresser [6]. Contrasting the experimental images, this simulation does not show the presence of the so-called restatoms in the first surface layer, which are atoms not bound to adatoms, and then still presenting a dangling bond. This discrepancy is due to the fact that the simulation has been carried out at constant tip height, while experimental images are usually obtained under constant-current conditions. Figure 2 shows a pair of STM images of the same area of the (111) Ge surface, taken 5 min one after the other. Most of the adatoms seen on the first picture are found again at the same site a few minutes later, which demonstrates the stability of the adatoms on their (T_4) surface grid at room temperature. However, it is clearly apparent that one of the adatom (indicated by an arrow) has moved to a neighboring site between the STM snapshots. A question arises as to whether the move could be induced by the tip-adatom mechanical interaction during the measurements or is the result of the thermal excitation of the adatom during the few minutes elapsed during the experiment. The following discussion of the energetics of the adatom-sample

interaction can bring some information relevant to this question.

Adatom Diffusion Energy Map

The energy variations of the adatom when moved over the various sites of the surface define several properties related to the atomic self-diffusion. The changes in energy experienced by an adatom when relocated at different places over the Ge (111) surface can be defined in the following way. We consider an isolated adatom on an otherwise clean, but fully relaxed Ge (111) surface. We position this adatom at fixed lateral (x, y) coordinates and change the adatom-surface distance while relaxing the surface atoms in the vicinity of the adatom. We use a simple Metropolis algorithm [7] and a classical Tersoff representation [8] of the system to achieve a complete relaxation of the substrate for each elevation of the adatom. We then look in a systematic way for a total energy minimum (golden-section search algorithm [9]) with respect to the adatom altitude. This gives the map represented on Figure 3. It is seen that the less comfortable site for an adatom is, by far, to sit on top of one of the terminal surface layer atom,

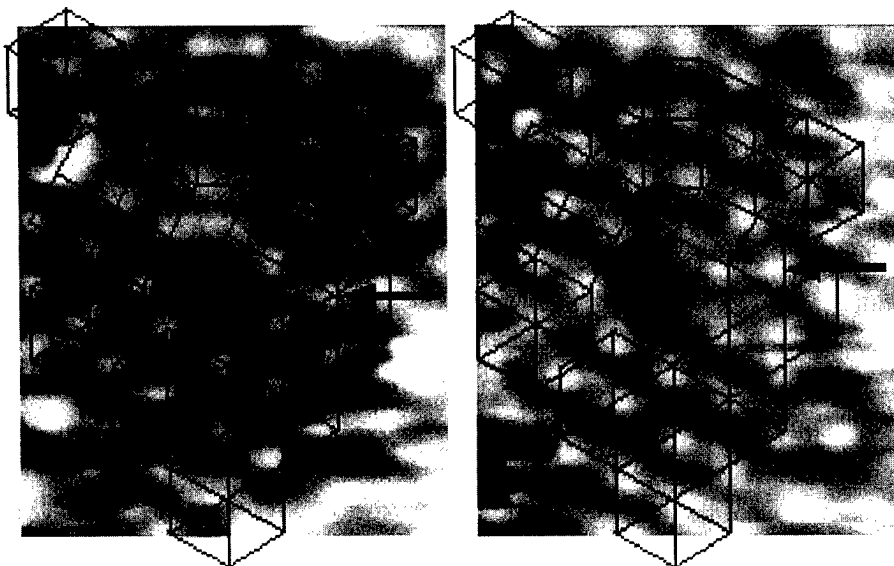


FIGURE 2. Two successive STM images of the same area of the (111) Ge. Most of the adatoms seen on the first picture are found again at the same site a few minutes later, but it is clearly apparent that one of the adatom (indicated by an arrow) has moved to a neighboring site between the STM snapshots.

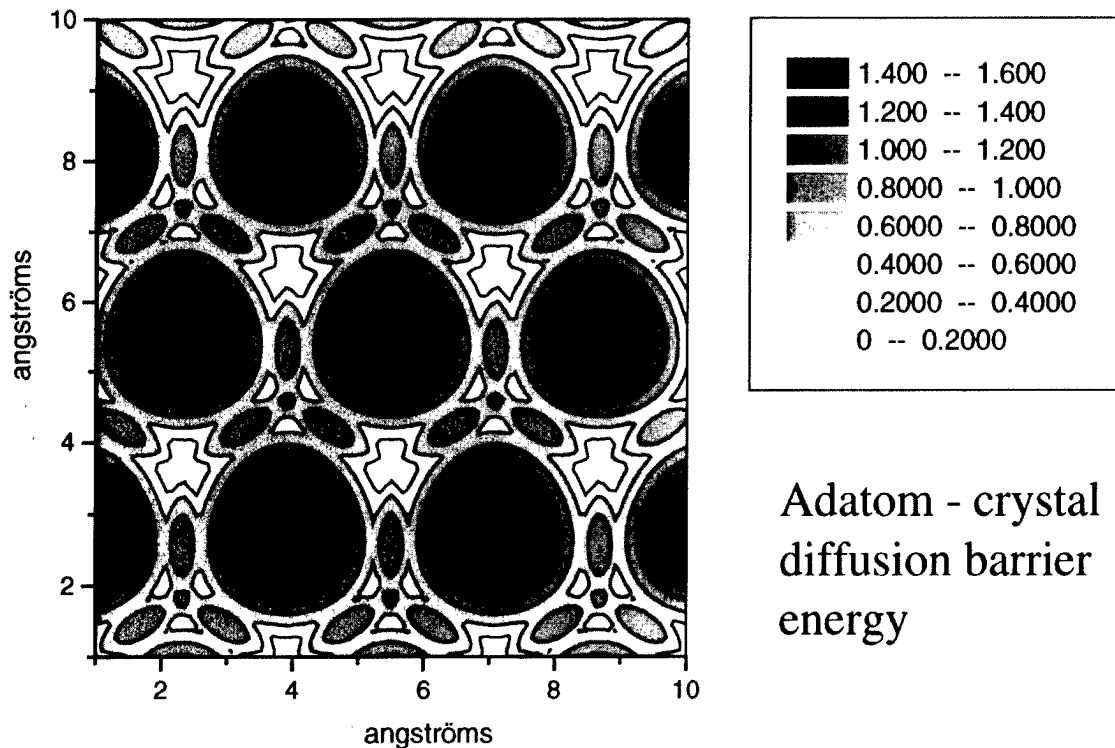


FIGURE 3. Energy of an adatom, mapped against the (111) Ge clean surface, showing the adatom stable sites.

where it can only passivate one dangling bond, while reintroducing itself several new expensive empty states. The better gain in energy concerns, as expected, the threefold symmetric T_4 site, on top of a subsurface layer atom. There, the adatom rebonds to four very close neighbors, and passivates a maximum number of dangling bonds. The H_3 site is found to lie about 0.6 eV above the energy of the T_4 site, but can also be described as a stable point, as more energy (0.2 eV) is needed to leave this site before returning to the T_4 site. The path for connecting two neighboring T_4 sites passes through an N_3 site, as most experimental studies indicate today [10–12]. The stability of the adatom at the T_4 site is large: The lifetime of a Ge adatom at this site at room temperature can be estimated from Arrhenius law:

$$\tau = \nu^{-1} \exp(E/kT) \quad (2)$$

to a few seconds, a time much longer than the time of residence on a H_3 site, which amounts to 10^{-10} s (we use an attempt frequency ν of the order of 10^{13} s⁻¹). This leaves the possibility of a very slow transfer from T_4 to T_4 sites via H_3 by thermal excitation at room temperature. At higher

temperatures (e.g., at 600 K, the residence time on a T_4 site would drop to about 10^6 s), the adatom mobility is much better understandable.

Conclusions

In light of the present discussion, we cannot rule out the possibility that the STM might have produced adatom motion at room temperature during the scan, but the energetics of the adatoms on the (111) surface indicates that this motion, though relatively slow, can be thermally excited at room temperature. Further work is in progress to examine the influence of adatom disorder and the influence of the presence of an impurity on the shape and height of the T_4 – H_3 – T_4 diffusion barrier.

ACKNOWLEDGMENTS

This work is partly supported by the Belgian Programs on Interuniversity Attraction and by an FRFC contract with the Belgian National Fund for Scientific Research.

References

1. M. Brousseau, *Physique du Solide, propriétés électroniques* (Masson, Paris, 1992).
2. I. S. Hwang, S. K. Theiss, and J. A. Golovchenko, *Science* **265**, 490 (1994).
3. copy W. Monch, *Semiconductor Surfaces and Interfaces*, 2nd ed. (Springer, Berlin, 1995).
4. H. J. Güntherodt and R. Wiesendanger, *Scanning Tunneling Microscopy* (Springer, Berlin, 1995).
5. I. Derycke, J. P. Vigneron, Ph. Lambin, Th. Laloyaux, and A. A. Lucas, *Int. J. Quant. Chem.: Quant. Chem. Symp.* **25**, 687 (1991).
6. M. Cohen and W. Bergstresser, *Phys. Rev.* **141**, 789 (1966).
7. N. Metropolis, A. W. Rosenbluth, M. N. Rosenbluth, A. H. Teller, and E. Teller, *J. Chem. Phys.* **21**, 1087 (1953).
8. J. Tersoff, *Phys. Rev. B* **37**, 6991 (1988).
9. W. H. Press, S. A. Teukolsky, W. T. Vetterling, and B. P. Flannery, *Numerical Recipes in Fortran: The Art of Scientific Computing*, 2nd ed. (Cambridge University Press, Cambridge, 1992), see p. 390.
10. N. Takeuchi, A. Selloni, and E. Tossatti, *Phys. Rev. B* **49**, 10757 (1994).
11. N. Takeuchi, A. Selloni, and E. Tossatti, *Surf. Sci.* **755**, 307 (1994).
12. N. Takeuchi, A. Selloni, and E. Tossatti, *Phys. Rev. B* **51**, 10844 (1995).

**Published Symposia of the
*International Journal of Quantum Chemistry***

- 1967 QUANTUM CHEMISTRY SYMPOSIUM NO. 1
(Proceedings of the International Symposium on Atomic, Molecular, and Solid-State Theory)
- 1968 QUANTUM CHEMISTRY SYMPOSIUM NO. 2
(Proceedings of the International Symposium on Atomic, Molecular, and Solid-State Theory and Quantum Biology)
- 1969 QUANTUM CHEMISTRY SYMPOSIUM NO. 3 PART 1
(Proceedings of the International Symposium on Atomic, Molecular, and Solid-State Theory and Quantum Biology)
- 1970 QUANTUM CHEMISTRY SYMPOSIUM NO. 3 PART 2
(Proceedings of the International Symposium on Atomic, Molecular, and Solid-State Theory and Quantum Biology)
- 1971 QUANTUM CHEMISTRY SYMPOSIUM NO. 4
(Proceedings of the International Symposium on Atomic, Molecular, and Solid-State Theory and Quantum Biology)
- 1971 QUANTUM CHEMISTRY SYMPOSIUM NO. 5
(Proceedings of the International Symposium on Atomic, Molecular, and Solid-State Theory and Quantum Biology)
- 1972 QUANTUM CHEMISTRY SYMPOSIUM NO. 6
(Proceedings of the International Symposium on Atomic, Molecular, and Solid-State Theory and Quantum Biology)
- 1973 QUANTUM CHEMISTRY SYMPOSIUM NO. 7
(Proceedings of the International Symposium on Atomic, Molecular, and Solid-State Theory and Quantum Biology)
- 1974 QUANTUM CHEMISTRY SYMPOSIUM NO. 8
(Proceedings of the International Symposium on Atomic, Molecular, and Solid-State Theory and Quantum Statistics)
QUANTUM BIOLOGY SYMPOSIUM NO. 1
(Proceedings of the International Symposium on Quantum Biology and Quantum Pharmacology)

- 1975** QUANTUM CHEMISTRY SYMPOSIUM NO. 9
(Proceedings of the International Symposium on Atomic, Molecular, and Solid-State Theory and Quantum Statistics)
QUANTUM BIOLOGY SYMPOSIUM NO. 2
(Proceedings of the International Symposium on Quantum Biology and Quantum Pharmacology)
- 1976** QUANTUM CHEMISTRY SYMPOSIUM NO. 10
(Proceedings of the International Symposium on Atomic, Molecular, and Solid-State Theory and Quantum Statistics)
QUANTUM BIOLOGY SYMPOSIUM NO. 3
(Proceedings of the International Symposium on Quantum Biology and Quantum Pharmacology)
- 1977** QUANTUM CHEMISTRY SYMPOSIUM NO. 11
(Proceedings of the International Symposium on Atomic, Molecular, and Solid-State Theory, Collision Phenomena, and Computational Methods)
QUANTUM BIOLOGY SYMPOSIUM NO. 4
(Proceedings of the International Symposium on Quantum Biology and Quantum Pharmacology)
- 1978** QUANTUM CHEMISTRY SYMPOSIUM NO. 12
(Proceedings of the International Symposium on Atomic, Molecular, and Solid-State Theory, Collision Phenomena and Computational Methods)
QUANTUM BIOLOGY SYMPOSIUM NO. 5
(Proceedings of the International Symposium on Quantum Biology and Quantum Pharmacology)
- 1979** QUANTUM CHEMISTRY SYMPOSIUM NO. 13
(Proceedings of the International Symposium on Atomic, Molecular, and Solid-State Theory, Collision Phenomena, Quantum Statistics, and Computational Methods)
QUANTUM BIOLOGY SYMPOSIUM NO. 6
(Proceedings of the International Symposium on Quantum Biology and Quantum Pharmacology)
- 1980** QUANTUM CHEMISTRY SYMPOSIUM NO. 14
(Proceedings of the International Symposium on Atomic, Molecular, and Solid-State Theory, Collision Phenomena, Quantum Statistics, and Computational Methods)
QUANTUM BIOLOGY SYMPOSIUM NO. 7
(Proceedings of the International Symposium on Quantum Biology and Quantum Pharmacology)

- 1981** QUANTUM CHEMISTRY SYMPOSIUM NO. 15
(Proceedings of the International Symposium on Atomic, Molecular, and Solid-State Theory, Collision Phenomena, and Computational Quantum Chemistry)
QUANTUM BIOLOGY SYMPOSIUM NO. 8
(Proceedings of the International Symposium on Quantum Biology and Quantum Pharmacology)
- 1982** QUANTUM CHEMISTRY SYMPOSIUM NO. 16
(Proceedings of the International Symposium on Quantum Chemistry, Theory of Condensed Matter, and Propagator Methods in the Quantum Theory of Matter)
QUANTUM BIOLOGY SYMPOSIUM NO. 9
(Proceedings of the International Symposium on Quantum Biology and Quantum Pharmacology)
- 1983** QUANTUM CHEMISTRY SYMPOSIUM NO. 17
(Proceedings of the International Symposium on Atomic, Molecular, and Solid-State Theory, Collision Phenomena and Computational Quantum Chemistry)
QUANTUM BIOLOGY SYMPOSIUM NO. 10
(Proceedings of the International Symposium on Quantum Biology and Quantum Pharmacology)
- 1984** QUANTUM CHEMISTRY SYMPOSIUM NO. 18
(Proceedings of the International Symposium on Atomic, Molecular, and Solid-State Theory, and Computational Quantum Chemistry)
QUANTUM BIOLOGY SYMPOSIUM NO. 11
(Proceedings of the International Symposium on Quantum Biology and Quantum Pharmacology)
- 1985** QUANTUM CHEMISTRY SYMPOSIUM NO. 19
(Proceedings of the International Symposium on Atomic, Molecular, and Solid-State Theory, Scattering Problems, Many Body Phenomena, and Computational Quantum Chemistry)
QUANTUM BIOLOGY SYMPOSIUM NO. 12
(Proceedings of the International Symposium on Quantum Biology and Quantum Pharmacology)
- 1986** QUANTUM CHEMISTRY SYMPOSIUM NO. 20
(Proceedings of the International Symposium on Atomic, Molecular, and Solid-State Theory, Scattering Problems, Many Body Phenomena, and Computational Quantum Chemistry)

- 1986** QUANTUM BIOLOGY SYMPOSIUM NO. 13
(Proceedings of the International Symposium on Quantum Biology and Quantum Pharmacology)
- 1987** QUANTUM CHEMISTRY SYMPOSIUM NO. 21
(Proceedings of the International Symposium on Quantum Chemistry, Solid-State Theory, and Computational Methods)
QUANTUM BIOLOGY SYMPOSIUM NO. 14
(Proceedings of the International Symposium on Quantum Biology and Quantum Pharmacology)
- 1988** QUANTUM CHEMISTRY SYMPOSIUM NO. 22
(Proceedings of the International Symposium on Quantum Chemistry, Solid-State Theory, and Computational Methods)
QUANTUM BIOLOGY SYMPOSIUM NO. 15
(Proceedings of the International Symposium on Quantum Biology and Quantum Pharmacology)
- 1989** QUANTUM CHEMISTRY SYMPOSIUM NO. 23
(Proceedings of the International Symposium on Quantum Chemistry, Solid-State Theory, and Molecular Dynamics)
QUANTUM BIOLOGY SYMPOSIUM NO. 16
(Proceedings of the International Symposium on Quantum Biology and Quantum Pharmacology)
- 1990** QUANTUM CHEMISTRY SYMPOSIUM NO. 24
(Proceedings of the International Symposium on Quantum Chemistry, Solid State Physics, and Computational Methods)
QUANTUM BIOLOGY SYMPOSIUM NO. 17
(Proceedings of the International Symposium on Quantum Biology and Quantum Pharmacology)
- 1991** QUANTUM CHEMISTRY SYMPOSIUM NO. 25
(Proceedings of the International Symposium on Quantum Chemistry, Solid State Physics, and Computational Methods)
QUANTUM BIOLOGY SYMPOSIUM NO. 18
(Proceedings of the International Symposium on Quantum Biology and Quantum Pharmacology)

- 1992** QUANTUM CHEMISTRY SYMPOSIUM NO. 26
(Proceedings of the International Symposium on Atomic, Molecular, and Condensed Matter Theory and Computational Methods)
QUANTUM BIOLOGY SYMPOSIUM NO. 19
(Proceedings of the International Symposium on the Application of Fundamental Theory to Problems of Biology and Pharmacology)
- 1993** QUANTUM CHEMISTRY SYMPOSIUM NO. 27
(Proceedings of the International Symposium on Atomic, Molecular, and Condensed Matter Theory and Computational Methods)
QUANTUM BIOLOGY SYMPOSIUM NO. 20
(Proceedings of the International Symposium on the Application of Fundamental Theory to Problems of Biology and Pharmacology)
- 1994** QUANTUM CHEMISTRY SYMPOSIUM NO. 28
(Proceedings of the International Symposium on Atomic, Molecular, and Condensed Matter Theory and Computational Methods)
QUANTUM BIOLOGY SYMPOSIUM NO. 21
(Proceedings of the International Symposium on the Application of Fundamental Theory to Problems of Biology and Pharmacology)
- 1995** QUANTUM CHEMISTRY SYMPOSIUM NO. 29
(Proceedings of the International Symposium on Atomic, Molecular, and Condensed Matter Theory and Computational Methods)
QUANTUM BIOLOGY SYMPOSIUM NO. 22
(Proceedings of the International Symposium on the Application of Fundamental Theory to Problems of Biology and Pharmacology)
- 1996** QUANTUM CHEMISTRY SYMPOSIUM NO. 30
(Proceedings of the International Symposium on Atomic, Molecular, and Condensed Matter Theory and Computational Methods)
QUANTUM BIOLOGY SYMPOSIUM NO. 23
(Proceedings of the International Symposium on the Application of Fundamental Theory to Problems of Biology and Pharmacology)
- 1997** QUANTUM CHEMISTRY SYMPOSIUM NO. 31
(Proceedings of the International Symposium on Atomic, Molecular, and Condensed Matter Theory and Computational Methods)
QUANTUM BIOLOGY SYMPOSIUM NO. 24
(Proceedings of the International Symposium on the Application of Fundamental Theory to Problems of Biology and Pharmacology)

- 1998** QUANTUM CHEMISTRY SYMPOSIUM NO. 32
(Proceedings of the International Symposium on Atomic, Molecular, and Condensed Matter Theory)
QUANTUM BIOLOGY SYMPOSIUM NO. 25
(Proceedings of the International Symposium on the Application of Fundamental Theory to Problems of Biology and Pharmacology)

All of the above symposia can be individually purchased from the Subscription Department,
John Wiley & Sons.

COPYRIGHT TRANSFER AGREEMENT

Date:

To:

Production/Contribution

ID# _____

Publisher/Editorial office use only

Re: Manuscript entitled _____ (the "Contribution")
for publication in _____ (the "Journal")
published by John Wiley & Sons, Inc. ("Wiley").

Dear Contributor(s):

Thank you for submitting your Contribution for publication. In order to expedite the publishing process and enable Wiley to disseminate your work to the fullest extent, we need to have this Copyright Transfer Agreement signed and returned to us as soon as possible. If the Contribution is not accepted for publication this Agreement shall be null and void.

A. COPYRIGHT

1. The Contributor assigns to Wiley, during the full term of copyright and any extensions or renewals of that term, all copyright in and to the Contribution, including but not limited to the right to publish, republish, transmit, sell, distribute and otherwise use the Contribution and the material contained therein in electronic and print editions of the Journal and in derivative works throughout the world, in all languages and in all media of expression now known or later developed, and to license or permit others to do so.
2. Reproduction, posting, transmission or other distribution or use of the Contribution or any material contained therein, in any medium as permitted hereunder, requires a citation to the Journal and an appropriate credit to Wiley as Publisher, suitable in form and content as follows: (Title of Article, Author, Journal Title and Volume/Issue Copyright © [year] John Wiley & Sons, Inc. or copyright owner as specified in the Journal.)

B. RETAINED RIGHTS

Notwithstanding the above, the Contributor or, if applicable, the Contributor's Employer, retains all proprietary rights other than copyright, such as patent rights, in any process, procedure or article of manufacture described in the Contribution, and the right to make oral presentations of material from the Contribution.

C. OTHER RIGHTS OF CONTRIBUTOR

Wiley grants back to the Contributor the following:

1. The right to share with colleagues print or electronic "preprints" of the unpublished Contribution, in form and content as accepted by Wiley for publication in the Journal. Such preprints may be posted as electronic files on the Contributor's own website for personal or professional use, or on the Contributor's internal university or corporate networks/intranet, or secure external website at the Contributor's institution, but not for commercial sale or for any systematic external distribution by a third party (e.g., a listserve or database connected to a public access server). Prior to publication, the Contributor must include the following notice on the preprint: "This is a preprint of an article accepted for publication in [Journal title] © copyright (year) (copyright owner as specified in the Journal)". After publication of the Contribution by Wiley, the preprint notice should be amended to read as follows: "This is a preprint of an article published in [include the complete citation information for the final version of the Contribution as published in the print edition of the Journal]", and should provide an electronic link to the Journal's WWW site, located at the following Wiley URL:
<http://www.interscience.Wiley.com/>. The Contributor agrees not to update the preprint or replace it with the published version of the Contribution.
2. The right, without charge, to photocopy or to transmit online or to download, print out and distribute to a colleague a copy of the published Contribution in whole or in part, for the Contributor's personal or professional use, for the advancement of scholarly or scientific research or study, or for corporate informational purposes in accordance with Paragraph D.2 below.

3. The right to republish, without charge, in print format, all or part of the material from the published Contribution in a book written or edited by the Contributor.
4. The right to use selected figures and tables, and selected text (up to 250 words, exclusive of the abstract) from the Contribution, for the Contributor's own teaching purposes, or for incorporation within another work by the Contributor that is made part of an edited work published (in print or electronic format) by a third party, or for presentation in electronic format on an internal computer network or external website of the Contributor or the Contributor's employer.
5. The right to include the Contribution in a compilation for classroom use (course packs) to be distributed to students at the Contributor's institution free of charge or to be stored in electronic format in datarooms for access by students at the Contributor's institution as part of their course work (sometimes called "electronic reserve rooms") and for in-house training programs at the Contributor's employer.

D. CONTRIBUTIONS OWNED BY EMPLOYER

1. If the Contribution was written by the Contributor in the course of the Contributor's employment (as a "work-made-for-hire" in the course of employment), the Contribution is owned by the company/employer which must sign this Agreement (in addition to the Contributor's signature), in the space provided below. In such case, the company/employer hereby assigns to Wiley, during the full term of copyright, all copyright in and to the Contribution for the full term of copyright throughout the world as specified in paragraph A above.
2. In addition to the rights specified as retained in paragraph B above and the rights granted back to the Contributor pursuant to paragraph C above, Wiley hereby grants back, without charge, to such company/employer, its subsidiaries and divisions, the right to make copies of and distribute the published Contribution internally in print format or electronically on the Company's internal network. Upon payment of the Publisher's reprint fee, the institution may distribute (but not resell) print copies of the published Contribution externally. Although copies so made shall not be available for individual re-sale, they may be included by the company/employer as part of an information package included with software or other products offered for sale or license. Posting of the published Contribution by the institution on a public access website may only be done with Wiley's written permission, and payment of any applicable fee(s).

E. GOVERNMENT CONTRACTS

In the case of a Contribution prepared under U.S. Government contract or grant, the U.S. Government may reproduce, without charge, all or portions of the Contribution and may authorize others to do so, for official U.S. Government purposes only, if the U.S. Government contract or grant so requires. (U.S. Government Employees: see note at end).

F. COPYRIGHT NOTICE

The Contributor and the company/employer agree that any and all copies of the Contribution or any part thereof distributed or posted by them in print or electronic format as permitted herein will include the notice of copyright as stipulated in the Journal and a full citation to the Journal as published by Wiley.

G. CONTRIBUTOR'S REPRESENTATIONS

The Contributor represents that the Contribution is the Contributor's original work. If the Contribution was prepared jointly, the Contributor agrees to inform the co-Contributors of the terms of this Agreement and to obtain their signature to this Agreement or their written permission to sign on their behalf. The Contribution is submitted only to this Journal and has not been published before, except for "preprints" as permitted above. (If excerpts from copyrighted works owned by third parties are included, the Contributor will obtain written permission from the copyright owners for all uses as set forth in Wiley's permissions form or in the Journal's Instructions for Contributors, and show credit to the sources in the Contribution.) The Contributor also warrants that the Contribution contains no libelous or unlawful statements, does not infringe on the rights or privacy of others, or contain material or instructions that might cause harm or injury.

CHECK ONE:

Contributor-owned work

Contributor's signature

Date

Type or print name and title

Co-contributor's signature

Date

Type or print name and title

ATTACHED ADDITIONAL SIGNATURE PAGE AS NECESSARY

Company/Institution-owned work
(made-for-hire in the
course of employment)

Company or Institution (Employer-for-Hire)

Date

Authorized signature of Employer

Date

U.S. Government work

Note to U.S. Government Employees

A Contribution prepared by a U.S. federal government employee as part of the employee's official duties, or which is an official U.S. Government publication is called a "U.S. Government work," and is in the public domain in the United States. In such case, the employee may cross out Paragraph A.1 but must sign and return this Agreement. If the Contribution was not prepared as part of the employee's duties or is not an official U.S. Government publication, it is not a U.S. Government work.

U.K. Government work (Crown Copyright)

Note to U.K. Government Employees

The rights in a Contribution prepared by an employee of a U.K. government department, agency or other Crown body as part of his/her official duties, or which is an official government publication, belong to the Crown. In such case, the Publisher will forward the relevant form to the Employee for signature.

DISK SUBMISSION INSTRUCTIONS

**Please return your final, revised manuscript on disk as well as hard copy.
The hard copy must match the disk.**

The Journal strongly encourages authors to deliver the final, revised version of their accepted manuscripts (text, tables, and, if possible, illustrations) on disk. Given the near-universal use of computer word-processing for manuscript preparation, we anticipate that providing a disk will be convenient for you, and it carries the added advantages of maintaining the integrity of your keystrokes and expediting typesetting. Please return the disk submission slip below with your manuscript and labeled disk(s).

Guidelines for Electronic Submission (also available at <http://www.interscience.wiley.com>)

Text

Storage medium. 3-1/2" high-density disk in IBM MS-DOS, Windows, or Macintosh format.

Software and format. Microsoft Word 6.0 is preferred, although manuscripts prepared with any other microcomputer word processor are acceptable. Refrain from complex formatting; the Publisher will style your manuscript according to the Journal design specifications. Do not use desktop publishing software such as Aldus PageMaker or Quark XPress. If you prepared your manuscript with one of these programs, export the text to a word processing format. Please make sure your word processing program's "fast save" feature is turned off. Please do not deliver files that contain hidden text: for example, do not use your word processor's automated features to create footnotes or reference lists.

File names. Submit the text and tables of each manuscript as a single file. Name each file with your last name (up to eight letters). Text files should be given the three-letter extension that identifies the file format. Macintosh users should maintain the MS-DOS "eight dot three" file-naming convention.

Labels. Label all disks with your name, the file name, and the word processing program and version used.

Illustrations

All print reproduction requires files for full color images to be in a CMYK color space. If possible, ICC or ColorSync profiles of your output device should accompany all digital image submissions.

Storage medium. Submit as separate files from text files, on separate disks or cartridges. If feasible, full color files should be submitted on separate disks from other image files. 3-1/2" high-density disks, CD, Iomega Zip, and 5 1/4" 44- or 88-MB SyQuest cartridges can be submitted. At authors' request, cartridges and disks will be returned after publication.

Software and format. All illustration files should be in TIFF or EPS (with preview) formats. Do not submit native application formats.

Resolution. Journal quality reproduction will require greyscale and color files at resolutions yielding approximately 300 ppi. Bitmapped line art should be submitted at resolutions yielding 600–1200 ppi. These resolutions refer to the output size of the file; if you anticipate that your images will be enlarged or reduced, resolutions should be adjusted accordingly.

File names. Illustration files should be given the 2- or 3-letter extension that identifies the file format used (i.e., .tif, .eps).

Labels. Label all disks and cartridges with your name, the file names, formats, and compression schemes (if any) used. Hard copy output must accompany all files.

Detach and return with labeled disk(s)

Corresponding author's name _____ E-mail address: _____ Telephone: _____

Manuscript number: _____ Type of computer: _____ Program(s) & version(s) used: _____

Miscellaneous: _____

I certify that the material on the enclosed disk(s) is identical in both word and content to the printed copy herewith enclosed.

Signature: _____ **Date:** _____

International Journal of Quantum Chemistry

Information for Contributors

1. Manuscripts should be submitted in triplicate and accompanied by an executed Copyright Transfer Form to the Editorial Office, International Journal of Quantum Chemistry, Quantum Chemistry Group, University of Uppsala, Box 518, S-75120 Uppsala, Sweden. Authors may also submit manuscripts to the Editorial Office, International Journal of Quantum Chemistry, Quantum Theory Project, 2301 NP Building #92, P.O. Box 118435, Museum Road and North South Drive, University of Florida, Gainesville, Florida 32611-8435.
All other correspondence should be addressed to the Publisher, Professional, Reference, & Trade Group, John Wiley & Sons, Inc., 605 Third Ave., New York, NY 10158.
2. It is the preference of the Editors that papers be published in the English language. However, if the author desires that his paper be published in French or German, it is necessary that a particularly complete and comprehensive synopsis be furnished in English.
3. Manuscripts should be submitted in triplicate (one *original*, two carbon copies) typed *doubled spaced* throughout and on one side of each sheet only, on a *heavy* grade paper with margins of at least 2.5 cm on all sides. Copyright: No article can be published unless accompanied by a signed publication agreement, which serves as a transfer of copyright from author to publisher. A publication agreement may be obtained from the editor or the publisher. A copy of the publication agreement appears in most issues of the journal. Only original papers will be accepted and copyright in published papers will be vested in the publisher. It is the author's responsibility to obtain written permission to reproduce material that has appeared in another publication. A copy of that agreement, executed and signed by the author, is now required with each manuscript submission. (If the article is a "work made for hire," the agreement must be signed by the employer.)
4. A short synopsis (maximum length 200 words) is required. The synopsis should be a summary of the entire paper, not the conclusions alone. If the paper is written in French or German, a synopsis in English should also be prepared. The paper should be reasonably subdivided into sections and, if necessary, subsections.
5. A list of five key words or phrases for indexing must accompany each submission.
6. Authors are cautioned to type—wherever possible—all mathematical and chemical symbols, equations, and formulas. If these must be handwritten, please print clearly and leave ample space above and below for printer's marks; please use only ink. All Greek or unusual symbols should be identified in the margin the first time they are used. Please distinguish in the margins of the manuscript between capital and small letters of the alphabet wherever confusion may arise (e.g., k, K, k). Please underline with a wavy line all vector quantities. Use fractional exponents to avoid root signs.
7. The nomenclature sponsored by the International Union of Pure and Applied Chemistry is requested for chemical compounds. Unit abbreviations should follow the practices of the American Institute of Physics. Chemical bonds should be correctly placed, and double bonds clearly indicated. Valence is to be indicated by superscript plus and minus signs.
8. The references should be numbered consecutively in the order of their appearance and should be complete, including authors' initials and—for unpublished lectures or symposia—the title of the paper, the date, and the name of the sponsoring society. Please compile references on a separate sheet at the end of the manuscript. Abbreviations of journal titles should conform to the *Bibliographic Guide for Editors & Authors* published by the American Chemical Society.
References should be limited to literature citations. Explanatory or supplementary material should be treated either as footnotes to text or appendices. Examples:
 - [1] D. N. Zubarev, *Nonequilibrium Statistical Thermodynamics* (Consultants Bureau, Plenum, New York, 1974).
 - [2] H. Adachi, M. Tsukada, and C. Satoko, *J. Phys. Soc. Jpn.* **45**, 875 (1978).
 - [3] K. Fukui, T. Yonezawa, C. Nagata, H. Katou, A. Imamura, and K. Morokuma, in *Introduction to Quantum Chemistry* (Kagakudojin, Kyoto, 1963), Vol. 1, p. 197.
8. A limited number of color figures that are of critical importance and that significantly enhance the presentation will be considered for publication at the publisher's expense. Color separations or

transparencies (negatives or positives) are optimal. Color slides are preferable to color prints. Any cropping of the color figure should be clearly indicated. Final decision on publication of color figures will be at the discretion of the Editor.

9. Each table should be supplied on a separate sheet (not interspersed with text). Please supply numbers and titles for all tables. All table columns should have an explanatory heading.
10. Please supply legends for all figures and compile these on a separate sheet.
11. Figures should be professionally prepared and submitted in a form suitable for reproduction (camera-ready copy). Computer-generated graphs are acceptable only if they have been printed with a good quality laser printer. Artwork is generally reduced so that the type in the figures is about 2.5 mm high. The maximum final size of figures for this journal is 16 x 21 cm after reduction.

Good glossy photographs are required for halftone reproductions. If in doubt about the preparation of illustrations suitable for reproduction, please consult the publisher at the address given in paragraph 1.

12. Senior authors will receive 50 reprints of their articles without charge. Additional reprints can be ordered and purchased by filling out the form enclosed with the proof.
13. The publisher will do everything possible to ensure prompt publication. It will therefore be appreciated if manuscripts and illustrations conform from the outset to the style of the journal. Contributors should use the *Style Manual* of the American Institute of Physics; papers will otherwise have to be returned to the author for revision.

Corrected proofs must be sent back to the publisher within two days to avoid the risk of the author's contribution having to be held over to a later issue.

New in ...

Quantum Physics

TEXTBOOK

Bachor, H.-A.
A Guide to Experiments in Quantum Optics

1997. Approx XVI, 400 pages,
170 figs.
Softcover. Approx \$70.00
ISBN 3-527-29298-5
Publication date: November 1997

This book differs from other excellent but theoretical texts in that it focuses on actual experiments and explains the underlying physics. It addresses limitations of equipment, what is measurable and what are the future goals.

TEXTBOOK

Zubarev, D. / Morozov, V. / Röpke, G.
Statistical Mechanics of Nonequilibrium Processes

Volume 1: Basic Concepts, Kinetic Theory
1996. 375 pages, 19 figs.
Hardcover. Approx \$70.00
ISBN 3-05-501708-0

Volume 2: Relaxation and Hydrodynamic Processes
1997. 375 pages, 12 figs.
Hardcover. Approx \$ 98.00
ISBN 3-05-501709-9

In the first part of this two-volume textbook a unified approach to the modern statistical theory of nonequilibrium processes is given. Applications to classical and quantum kinetic theory of nonideal gases, to plasmas and solid state physics are presented. In Volume 2 applications of the general approach given in the first volume are considered. Applications in transport theory, relaxation processes, and hydrodynamics are presented.

TEXTBOOK

Dittrich, T. et al.
Quantum Transport and Dissipation

1997. X, 372 pages, approx 96 figs.
Hardcover. Approx \$70.00
ISBN 3-527-29261-6
Publication date: November 1997

For those who need a compact and clear introduction at a graduate level to the theory that underlies research into mesoscopic systems, this book is highly recommended.

TEXTBOOK

Murayama, Y.
Mesoscopic Systems

1998. Approx XII, 325 pages, 90 figs.
Hardcover. Approx \$69.95
ISBN 3-527-29376-0
Publication date: April 1998

Future high-tech applications such as nanotechnology require a deep understanding of the physics of Mesoscopic systems. This introduction discusses a variety of typical surface, optical, transport, and magnetic properties of Mesoscopic systems with reference to many experimental observations. It is written for physics, materials science and engineering students who want to catch up with current research or high-tech development.

MONOGRAPH

Gramß, T. et al.
Non-Standard Computation
Molecular Computation — Cellular Automata — Evolutionary Algorithms — Quantum Computers

1997. Approx XVI, 230 pages, 80 figs.
Softcover. Approx \$70.00
ISBN 3-527-29427-9
Publication date: November 1997

This exciting book provides the first overview of and introduction to the chemical, biological and physical non-standard computation concepts which promise to solve highly computationally intensive problems by a massive parallelism and a clever use of other effects: Molecular and Quantum Computers, and Genetic Algorithms.

TEXTBOOK

Schleich, W.P. / Mayr, E. / Krähmer, D.
Quantum Optics in Phase Space

1997. Approx XII, 270 pages, 80 figs.
Softcover. Approx \$70.00
ISBN 3-527-29435-X
Publication date: December 1997

Based on a two-semester graduate course given at the University of Ulm, Germany, this book provides a compact introduction to the theory. It gives a good preparation for research and can either be used alone or with other books.

Prices are subject to change without notice.

The new
global
force in
scientific
publishing

 **WILEY-VCH**

Available on
STN International

Look no further than
your own computer terminal
to find the results of
worldwide polymer research
with . . .

CHEMICAL JOURNALS
ONLINE

WILEY POLYMER JOURNALS
(CJ Wiley)

now available as part of CHEMICAL JOURNALS
ONLINE, comprises three authoritative journals
published by John Wiley & Sons, Inc.:

JOURNAL OF APPLIED POLYMER SCIENCE

JOURNAL OF POLYMER SCIENCE

BIOPOLYMERS

With CHEMICAL JOURNALS ONLINE, you will have the capability to search and display original polymer research • vital experimental data • experimental procedures • new preparation techniques • literature citations • crossover to other chemical information including CAS Online.

Easily accessible and cost-effective, CHEMICAL JOURNALS ONLINE (which also includes journals from the Royal Society of Chemistry and the American Chemical Society) will enable you to obtain immediate results without even leaving your desk!

To find out more about how CJ Wiley — and the *entire* CHEMICAL JOURNALS ONLINE database — can work for you, call toll-free 800-227-5558. An American Chemical Society sales representative will be pleased to answer any questions you might have.

You can also write to the Marketing/Communications Department, American Chemical Society, 1155 Sixteenth Street, N.W., Washington, D.C. 20036.



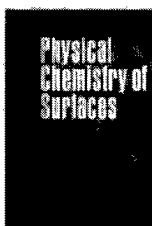
The Computer-Powered
Full-Text Search System
From The American
Chemical Society

CHEMICAL JOURNALS
ONLINE

Essential Resources from JOHN WILEY & SONS, Inc.

PHYSICAL CHEMISTRY of SURFACES, Sixth Edition

Arthur W. Adamson & Alice P. Gast



This thoroughly updated edition of the standard work on surface science contains thorough coverage of modern surface chemistry, spectroscopy and solid-gas interfaces.

0-471-14873-3 784pp.
1997 \$79.95

STATISTICAL MECHANICS for CHEMISTS

Jerry Goodisman

This book introduces the concepts and equations of statistical mechanics for the chemist. Presents a rigorous treatment of the fundamentals, beginning with ideas and functions followed by demonstration of applications and thermodynamic properties.

0-471-16812-2 344pp. 1997 \$69.95

ELECTROCHEMISTRY:

An Introduction for Chemists

C.H. Hamann, A. Hamnett & W. Vielstich

This text/reference provides a concise introduction to the fundamental principles of modern electrochemistry. Includes discussions of everyday applications such as electrochemical batteries, coatings and chemical analysis.

A WILEY-VCH PUBLICATION
3-527-29096-6 approx. 450pp. 1997 \$59.95 (pb)

INFRARED and RAMAN SPECTRA of INORGANIC and COORDINATION COMPOUNDS, Fifth Edition

Kazuo Nakamoto

PART A: THEORY and APPLICATIONS in INORGANIC CHEMISTRY

This self-contained volume provides the fundamentals of infrared and raman spectroscopy such as the origin of molecular spectra, symmetry and point groups.

0-471-16394-5 387pp. 1997 \$69.95

PART B: APPLICATIONS in COORDINATION, ORGANOMETALLIC and BIOINORGANIC CHEMISTRY

This stand-alone volume focuses on the applications of the basic theories of vibrational spectroscopy to large and complex models.

0-471-16392-9 384pp. 1997 \$69.95

SAVE! 2-Volume Set:
0-471-19406-9 1997 \$120.00

MODERN SPECTROSCOPY, 3E

J.M. Hollas

Presenting both fundamental principles and applications, this new edition provides an introduction to all aspects of modern spectroscopy.

0-471-96522-7 416pp. 1996 \$95.00 (cl)
0-471-96523-5 416pp. 1996 \$39.95 (pb)

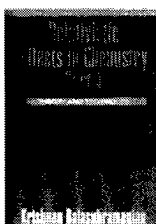
RELATIVISTIC EFFECTS in CHEMISTRY

Krishnan Balasubramanian

PART A: THEORY and TECHNIQUES

This work describes the basic techniques of relativistic quantum chemistry. Its systematic five-section format begins with a detailed exposition of Einstein's special theory of relativity, the significance of relativity in chemistry, and the nature of relativistic effects.

0-471-30400-X 301pp. 1997 \$84.95



PART B: APPLICATIONS

The second volume contains specific experimental and theoretical results on the electronic states of molecules containing very heavy atoms as well as their spectroscopic properties and electronic structures.

0-471-17991-4 527pp. 1997 \$89.95

SAVE! 2-Volume Set:
0-471-18184-6 1997 \$145.00

SURFACE ANALYSIS:

The Principal Techniques

John C. Vickerman

This introductory-level text describes the various techniques for analyzing surfaces and the theory required for understanding the results.

0-471-95939-1 457pp.
1997 \$98.00 (cl)

0-471-97292-4 457pp. 1997 \$44.95 (pb)



An INTRODUCTION to MOLECULAR DYNAMICS and CHEMICAL KINETICS

Gert D. Billing & Kurt V. Mikkelsen

This book covers both molecular reaction dynamics and chemical kinetics (useful in calculating the probability of chemical reactions occurring) with a complete discussion of theory and thorough mathematical presentations.

0-471-12739-6 200pp. 1996 \$49.95

ADVANCED MOLECULAR DYNAMICS and CHEMICAL KINETICS

Gert D. Billing & Kurt V. Mikkelsen

This self-contained reference combines all of the theories of molecular reaction dynamics and chemical kinetics into a single location, including a complete discussion of the theoretical as well as mathematical presentation of the technique.

0-471-12740-X 288pp. 1997 \$64.95

SAVE! 2-Volume Set
0-471-18203-6 1997 \$95.00



LIQUID INTERFACES in CHEMISTRY and BIOLOGY

Alexander Volkov, David Deamer,
Darrell Tanelian, & Vladislav Markin

This book offers comprehensive treatment of surface science theory and its application in biology and chemistry. Includes both theoretical and experimental studies on charge and energy transfer.

0-471-14872-5 approx. 568pp. 1997 \$95.00

NOW AVAILABLE in PAPERBACK!

ADVANCES in CHEMICAL PHYSICS SERIES

Series Editors: I. Prigogine & Stuart Rice

NEW METHODS in COMPUTATIONAL QUANTUM MECHANICS: Volume 93

This self-contained volume surveys a number of recent accomplishments in computational quantum chemistry. Examples include Quantum Monte Carlo methods in chemistry and the Redfield Equation in condensed-phase quantum dynamics.

0-471-19127-2 812pp. 1997 \$54.95 (pb)

POLYMERIC SYSTEMS: Volume 94

"... highly recommended to scientists in every branch of chemical physics." - Polymer News
0-471-19143-4 742pp. 1997 \$54.95 (pb)

SURFACE PROPERTIES: Volume 95

This special topic volume brings together contributions from leading researchers treating some of the most crucial aspects of the experimental and theoretical study of surface.

0-471-19956-7 432pp. 1997 \$49.95 (pb)

For orders inside North America, contact:

John Wiley & Sons, Inc.

605 Third Avenue

New York, NY 10158

Attn: A. Yee, 9th Floor

Tel: 1-800-225-5945

Fax: (212) 850-8888

E-mail: custserv@wiley.com

For orders outside North America, contact:

John Wiley & Sons, Ltd.

Distribution Centre

Southern Cross Trading Estate

1 Oldlands Way

Bognor Regis

Sussex PO 22 9SA

England

Tel: 011-44 (0243) 779777

Fax: 011-44 (0243) 820250

E-mail: cs-books@wiley.co.uk

JOIN WILEY ONLINE

Netscape: John Wiley & Sons, Inc., Publishers

Back Forward Home Reload Images Open Print Find Stop N

Netsite: <http://www.wiley.com/>

What's New? What's Cool? Destinations Net Search People Software

[about wiley](#) | [products](#) | [order](#)
[what's new](#) | [for authors](#) | [search](#)


WILEY



Document: Done.

Drop in and explore. Get the very latest information on new books, journals, and other publications along with special promotions and publicity.

Discover a variety of online services, including online journals.

Download a sample chapter or software.

And much more.

STOP BY TODAY!
www.wiley.com/



WILEY

Publishers Since 1807



0020-7608(1998)70:4/5;1-#

19990329 039